PENNSTATE

Susan Lavan
Director of Research Administration
College of Earth and Mineral Sciences

The Pennsylvania State University
248B Deike Building
University Park, PA 16802-5000, USA

+1 814 865-7650
+1 814 865-2084 (Fax)
sal5@ems.psu.edu

March 31, 2008

AAD Document Control
MS 921-143
U.S. Department of Energy
National Energy Technology Laboratory
P.O. Box 10940
Pittsburgh, PA 15236-0940

Re: Gas Storage Technology Consortium
        DE-FC26-03NT41779
        Mr. Joel Morrison, Consortium Director

In keeping with the terms of Cooperative Agreement DE-FC26-03NT41779, I am submitting the accompanying third-party final technical reports received by Penn State on behalf of the Gas Storage Technology Consortium for work funded through December 31, 2007.

Each final report includes details of the work performed during the award period in a comprehensive manner and where appropriate includes findings and/or conclusions produced as a consequence of the work.

We have provided copies of these reports to assure the technical report deliverables under this Cooperative Agreement are submitted in a publicly releasable form and should be considered as an addendum to the 17th Quarterly Technical Progress Report that was submitted in January 2008.

We hope this information will prove to be satisfactory.

Sincerely,

Sue Lavan
Associate Director Grants and Contracts
College of Earth and Mineral Sciences

U.S. DEPARTMENT OF ENERGY

REQUEST FOR PATENT CLEARANCE FOR
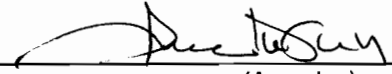# RELEASE OF CONTRACTED RESEARCH DOCUMENTS

TO: ☑ For Technical Reports
AAD Document Control
MS 921-143
U.S. Department of Energy - NETL
P.O. Box 10940
Pittsburgh, PA 15236-0940

◆ Award No.

DEFC26-03NT41779 Addendum # 1

Name & Phone No. of DOE COR

Martin Brynes   412/386-4486

☐ For Technical Papers/Journal Articles/Presentations
Mark P. Dvorscak
U.S. Department of Energy
9800 S. Cass Avenue
Argonne, IL 60439
FAX: (630) 252-2779

A.   AWARDEE ACTION (AWARDEE COMPLETES PART A. 1-5)

1.   Document Title: Gas Storage Technology Consortium (GSTC) Quarterly Report Addendum

2.   Type of Document: ☐ Technical Progress Report   ☐ Topical Report   ☐ Final Technical Report

☐ Abstract   ☐ Technical Paper   ☐ Journal Article   ☐ Conference Presentation

☑ Other (please specify) Final Technical Reports from Subawards funded under GSTC

3.   Date Clearance Needed: _____

◆4.   Results of Review for Possible Inventive Subject Matter:

a.   ☑   No Subject Invention is believed to be disclosed therein.

b.   ☐   Describes a possible Subject Invention relating to _____

   i.   Awardee Docket No.: _____

   ii.   A disclosure of the invention was submitted on _____

   iii.   A disclosure of the invention will be submitted by the following date: _____

   iv.   A waiver of DOE's patent rights to the awardee: ☐ has been granted, ☐ has been applied for, or

   ☐ will be applied for by the following date: _____

◆5.   Signed _____   Date 3/31/2008
                        (Awardee)

Name & Phone No. Sue Lavan, Assoc. Director Grants & Contracts/Earth & Mineral Sciences

Address 248B Deike Building, University Park, PA 16802

B.   DOE PATENT COUNSEL ACTION

☐ Patent clearance for release of the above-identified document is granted.

☐ Other: _____

Signed _____   Date _____
         (Patent Attorney)

◆ **Must be** completed by the awardee.

Appendix A 2004 Reports

- [Gas Storage Field Deliverability Enhancement and Maintenance: An Intelligent Portfolio Management Approach](#)- *West Virginia University*

- [Real Time Well Bore Integrity Monitoring](#) - *Colorado School of Mines*

- [Compact Separators for Gas Storage Field Applications](#)- *Colorado Engineering Experiment Station, Inc. (no report, no funds expended)*

- [Renovation of Produced Waters from Underground Natural Gas Storage Facilities: A Feasibility Study Using Hybrid Constructed Wetland Technology](#)- *Clemson University*

Appendix B 2005 Reports

- [Demonstration-Scale Constructed Wetland System for Treatment of Produced Waters from Underground Gas Storage](#)- *Clemson University*

- [Scale Remediation Using Sonication: Pre-Commercial Test Project](#) – *TechSavants (no report)*

- [Gas Storage Field Deliverability Enhancement and Maintenance: and Intelligent Portfolio Management Approach, Phase II](#)- *West Virginia University*

- [Cement Evaluation in Gas Filled Borehole](#) - *Baker Atlas*

- [New Comprehensive Inventory Analysis Tool](#)- *Schlumberger Consulting Services*

- [Smart Gas: Using Chemicals to Improve Gas Deliverability](#)- *Correlations Company*

- [Temperature Effects on Threaded Couplings in Caverns](#)- *RESPEC*

- [Wellbore Cement Bond Integrity](#)- *University of Texas*

Appendix C 2006 Reports

- [Storage Field Wellbore Flow Data Containing Water and Hydrates](#) - *Colorado Engineering Experiment Station, Inc. (no report)*

- [Protocol Evaluation fro Scale Prevention and Remediation in Gas Storage Reservoirs and Formations](#)- *Colorado School of Mines (no report, no funds expended)*

- [Predicting and Mitigating Salt Precipitation](#)- *Correlations Company*

- [State-of-the-Art Assessment of Alternative Casing Repair Methods](#) - *Edison Welding Institute*

- [Effects of Tensile Loading on the Remaining Strength of Corroded Casing](#)- *Kiefner and Associates, Inc. (project extended)*

- [Brine String Integrity-Case History Survey and Model Evaluation](#) - *PB Energy Storage Services, Inc. (project extended)*

- [Wellbore Cement Bond Integrity](#) - *University of Texas*

- [Technical Feasibility Evaluation of Non-Intrusive Optical Detection, Monitoring and Preliminary Characterization of Casing Cement Leaks for Gas Wells](#)- *URS Group, Inc. (project extended)*

Appendix A 2004 Reports

Gas Storage Field Deliverability Enhancement and Maintenance: An Intelligent Portfolio Management Approach.

First Year
Final Report

Report prepared by:
Shahab D. Mohaghegh, Ph.D.
Principal Investigator
Petroleum & Natural Gas Engineering

West Virginia University
Morgantown, WV 26506
Telephone: 304.293.7682 Ext. 3405
Fax: 304.293.5708
Email: Shahab@wvu.ed

Report prepared for:
GSCT Consortium Director
PSU/Energy Institute
The Pennsylvania State University
C211 Coal Utilization Laboratory
University Park, PA 16802-2309
Telephone: 814.865.0531
Fax: 814.685.3248
Email: jlm9@psu.edu

DISCLAIMER

This report was prepared as an account of work sponsored by an agency of the United States Government. Neither the United States Government nor any agency thereof, nor any of their employees, makes any warranty, expressed or implied, or assumes nay legal liability or responsibility for the accuracy, completeness, or usefulness of any information, apparatus, product, or process disclosed, or represents that its use would not infringe privately owned rights. Reference herein to any specific commercial product, process, or service by trade name, trademark, manufacturer, or otherwise does not necessarily constitute or imply its endorsement, recommendation, or favoring by the United States Government or any agency thereof. The views and opinions of authors expressed herein do not necessarily state or reflect those of the United States Government or any agency thereof.

ABSTRACT

Portfolio management, a common practice in the financial market, is essentially an optimization problem that attempts to increase return on investment. The objective this project is to apply the state-of-the-art in optimum portfolio management to the gas storage field in order to optimize the return on investment associated with well remedial operations.

Each year gas storage operators spend hundreds of thousands of dollars on workovers, re-completions, and re-stimulations of storage wells in order to battle the decline in deliverability due to well damage with time. A typical storage field has tens if not hundreds of production wells. Each well will respond to a remedial operation in its own unique way that is a function of a set of uncontrollable parameters such as porosity and permeability and a set of controllable parameters such as completion and stimulation practices.

The objective of this project is to identify the combination of best candidate wells for the remedial operations that will result in the most successful program each year, and consequently provides the highest return on investment. The project deliverable is a Windows-based software application that would perform the analysis and provide the list of wells and their corresponding remedial operation for each year base on the budget constraints identified by the user.

The state-of-the-art in intelligent systems application that is currently being used extensively in the Wall Street is the methodology to achieve the objectives of this proposed project. This methodology includes a hybrid form of artificial neural networks, genetic algorithms and fuzzy logic. The principal investigator of this project is a pioneer in application of intelligent systems in the oil and gas industry and has a successful track record in developing intelligent applications for our industry.

Columbia Gas Transmission Corporation will be the industry partner of this project and will cooperate with the research and development team in order to ensure successful completion of the project.

At the end of the first year of the project the database was completed. The database includes modules for interpretation of gas storage wells pressure test data as it is demonstrated in this report.

TABLE OF CONTENTS

LIST OF FIGURES

INTRODUCTION

Each year Gas Storage operators spend hundreds of thousands of dollars to combat the inevitable decline in the deliverability of their production wells. The decline in deliverability with time has two major contributors. The first contributor is geology and reservoir characteristics that are uncontrollable parameters. The second sets of parameters that contribute to the decline are associated with well damage that is addressed by well remedial operations such as workovers, re-completions, and re-stimulation of the producing wells. The parameters associated with these remedial operations can be controlled by the operator.

It is a fact that every well will respond to a specific remedial operation in a unique way. For example the deliverability of well "A" will increase two folds if a proper restimulation is performed on it while the same operation performed on well "B" will result in little or no deliverability enhancement. Same is true for workovers. Finding the best candidate for restimulation or workover, each year, from among the tens or hundreds of wells is a challenging task. Consider another situation where well "C" will have a 70% increase if a restimulation is performed but it would have a 65% increase if a far less expensive workover is performed. Obviously performing a workover instead of a restimulation on well "C" would be more economical this year.

EXECUTIVE SUMMARY

Portfolio management, a common practice in the financial market, is essentially an optimization problem that attempts to increase return on investment. The objective this project is to apply the state-of-the-art in optimum portfolio management to the gas storage field in order to optimize the return on investment associated with well remedial operations.

Each year gas storage operators spend hundreds of thousands of dollars on workovers, re-completions, and re-stimulations of storage wells in order to battle the decline in deliverability due to well damage with time. A typical storage field has tens if not hundreds of production wells. Each well will respond to a remedial operation in its own unique way that is a function of a set of uncontrollable parameters such as porosity and permeability and a set of controllable parameters such as completion and stimulation practices.

The objective of this project is to identify the combination of best candidate wells for the remedial operations that will result in the most successful program each year, and consequently provides the highest return on investment. The project deliverable is a Windows-based software application that would perform the analysis and provide the list of wells and their corresponding remedial operation for each year base on the budget constraints identified by the user.

The state-of-the-art in intelligent systems application that is currently being used extensively in the Wall Street is the methodology to achieve the objectives of this proposed project. This methodology includes a hybrid form of artificial neural networks, genetic algorithms and fuzzy logic. The principal investigator of this project is a pioneer in application of intelligent systems in the oil and gas industry and has a successful track record in developing intelligent applications for our industry.

Columbia Gas Transmission Corporation will be the industry partner of this project and will cooperate with the research and development team in order to ensure successful completion of the project.

At the end of the first year of the project the database was completed. The database includes modules for interpretation of gas storage wells pressure test data as it is demonstrated in this report.

EXPERIMENTAL

No experimental work was performed during this project.

RESULTS & DISCUSSIONS

This is the detail report of the progress made so far in the above mentioned project, which consists of following components:

1-   Project Overview
2-   Data made available and it's format
3-   Database & Software

PROJECT OVERVIEW

The objective of this project is to apply state-of-the-art intelligent, optimum portfolio management to the gas storage field in order to optimize the return on investment associated with well remedial operations. Columbia Gas Transmission Corporation is the industry partner in this project and provided us with very valuable data and in-depth knowledge about their gas storage field operations.

The data in very crude form was provided to the research and development team in the last week of March, 2005. The team extracted valuable data and organized it in a form of database, with generic make up in order to be reusable. Windows-based software was developed which can help the user in viewing and later populating the data with easy to use interface. One of its modules provides the user with all the valid stimulations required as an input for Neural Network.

DATA MADE AVAILABLE AND IT'S FORMAT

The research and development (R & D) team was initially provided data in MS excel worksheets. On further request some pdf files with well schematics, well test files and well summary files were provided but still the required data especially relating to stimulations and well-tests was so scarce that the team in July, 2005 went to the Columbia Transmission Corporation Office in Charleston, WV to get more information. Retrieval of data from different files and thousands of microfiche was taking so long at the office that it was decided that West Virginia University lab facilities will be used to read thousands of microfiche. So for the next few weeks the team concentrated its efforts on data collection. That data could be segregated into five main tables, each relating to specific characteristic features of the gas storage wells. The five characteristic features are below:

1-   Well-bore data
2-   Completion Data
3-   Perforation Data
4-   Stimulation Data
5-   Well-Test Data

WELL BORE DATA
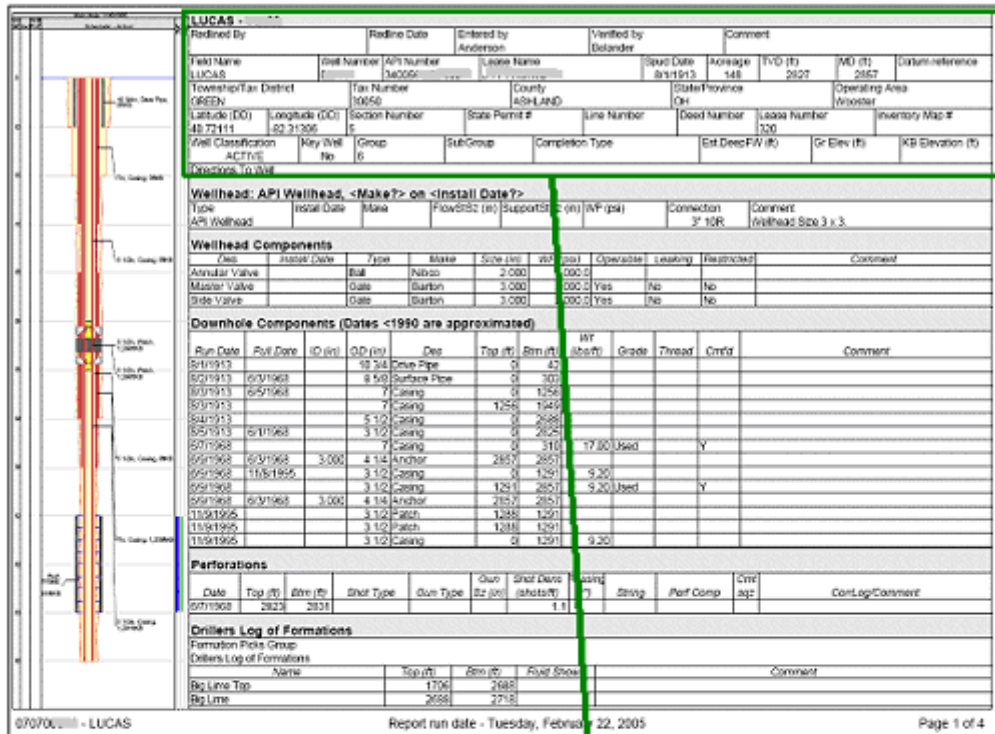
It includes basic features of the well like location, depth, well name … etc. Data about well-bore was retrieved mostly from well schematics and well summary reports. The data already provided by Columbia Transmission Corporation was also verified. The complete list of the data type retrieved is below

1.   API Number
2.   Field Name
3.   Well
4.   Lease Name
5.   Classification
6.   Latitude (Lat)
7.   Longitude (Long)
8.   Section
9.   Township
10. County
11. State
12. Operator
13. Total Vertical Depth
14. Formation

Picture of one of the form from which this data was retrieved is on next page

Fig1. Well-bore data retrieved from a file

The tables contained many minor mistakes like wrong Well API number length and many spelling mistakes. A picture of this correction is below:

Fig2. Correction of Wrong API number in data

GRAPHICAL ANALYSIS OF RAW DATA vs. REFINED DATA

WELLBORE DATA															
DATA FIELDS	API Number	Field Name	Well	Lease Name	Classification	Lat	Long	Section	Township	County	State	Operator	Total Vertical Depth	Formation
INITIIAL DATA AVAILABLE	430	427	430	430	427	429	430	430	430	430	430	430	425	430
FINAL DATA AVAILABLE	430	430	430	430	430	430	430	430	430	430	430	430	430	430

Fig3. Data addition and refinement for Well-bore Data

COMPLETION DATA

Completion data mostly relates to the type and depth of casing/liner/tubing run in the gas storage wells. The data type retained for the database includes following

1. API Number
2. Field Name
3. Well Name (Well)
4. Completion Description (Des)
5. Date Tubing Run (Dt Tm Rn)
6. Outer Diameter (OD)
7. Top of Casing
8. Bottom of Casing(Bot)
9. Casing Weight (Weight)
10. Casing Grade (Grade)

Unfortunately the data was mostly in an excel file and had to be verified with well schematic drawings. This led to the most unusual step in this project as it lead to reduction of valuable data available to us. This was due to the erroneous and multiple data entry originally in the completion table. Identification of the multiple entries and their removal from table was the most focused act of cleaning the data, as omission of desirable records was unacceptable. Following pictures show one of such flawed multiple data entries which were removed.

	A	B	C	D	E	F	G	H	I	J	K	L
1	Field Name	Well	API	Des	DtTmRun	OD	Top	Bot	Weight	Grade		
71	LUCAS	00873	34-005-90873	Casing	03-Oct-17	7.00	0	2043	20.00			
72	LUCAS	00873	34-005-90873	Casing	02-Mar-64	5.50	0	2908	17.00	Seamless		
73	LUCAS	01981	34-005-91981	Drive Pipe	01-Nov-24	10.75	0	33	40.00			
74	LUCAS	01981	34-005-91981	Surface Pipe	02-Nov-24	8.63	0	299	24.00			
75	LUCAS	01981	34-005-91981	Casing	03-Nov-24	7.00	1893	1931	20.00			
76	LUCAS	01981	34-005-91981	Casing	04-Nov-24	5.50	0	2681	17.00			
77	LUCAS	01981	34-005-91981	Casing	02-Nov-63	3.50	0	2694	9.20	Used		
78	LUCAS	01981	34-005-91981	Packer	03-Nov-63	5.50	2694	2694		Straight Anchor		
79	LUCAS	01981	34-005-91981	Packer	03-Nov							
80	LUCAS	01981	34-005-91981		03-Nov					Straight Anchor		
81	LUCAS	02008	34-005-92008	Drive Pipe	01-Jul				00			
82	LUCAS	02008	34-005-92008	Surface Pipe	02-Ju				.00			
83	LUCAS	02008	34-005-92008	Packer	02-Jul-25	8.63	1829	1839		Larkin Lead B.H.		
84	LUCAS	02008	34-005-92008	Packer	03-Jul-25	8.63	1829	1839				
85	LUCAS	02008	34-005-92008	Casing	03-Jul-25	7.00	1793	1839	20.00			
86	LUCAS	02008	34-005-92008	Packer	04-Jul-25	7.00	2500	2510				
87	LUCAS	02008	34-005-92008	Packer	04-Jul-25	7.00	2500	2510		OWS Midget		
88	LUCAS	02008	34-005-92008	Casing	04-Jul-25	5.50	0	2510	17.00			
89	LUCAS	02008	34-005-92008	Casing	02-Oct-63	5.50	0	2654				
90	LUCAS	02008	34-005-92008	Packer	02-Oct-63	5.50	2551	2561				
91	LUCAS	02008	34-005-92008	Anchor	02-Oct-63	5.50	2561	2571				
92	LUCAS	02008	34-005-92008	Packer	02-Oct-63	5.50	2551	2561				
93	LUCAS	02008	34-005-92008	Anchor	02-Oct-63	5.50	2561	2571				
94	LUCAS	02060	34-005-92060	Casing	01-Oct-25	10.75	0	64	40.00			

Fig4. Multiple Data Entries in Completion Table

In the completion table the following notations used as casing description were replaced in place of different notations being used to have a standard definition

NOTATION KEPT IN DATABASE	Surface casing
NOTATIONS DISCARDED	Drive pipe
	Driver Pipe
	Swedge
	Two stage

Completion data was mostly re- checked for accuracy from the documents, picture of which is shown below for a Well

Fig5. Well-bore data retrieved from a file

Run Date	Pull Date	ID (in)	OD (in)	Des	Top (ft)	Btm (ft)	Wt (lbs/ft)	Grade	T
8/1/1913			10 3/4	Drive Pipe	0	42			
8/2/1913	6/3/1968		8 5/8	Surface Pipe	0	303			
8/3/1913	6/5/1968		7	Casing	0	1256			
8/3/1913			7	Casing	1256	1949			
8/4/1913			5 1/2	Casing	0	2688			
8/5/1913	6/1/1968		3 1/2	Casing	0	2825			
6/7/1968			7	Casing	0	310	17.00	Used	
6/9/1968	6/3/1968	3.000	4 1/4	Anchor	2857	2857			
6/9/1968	11/8/1995		3 1/2	Casing	0	1291	9.20		
6/9/1968			3 1/2	Casing	1291	2857	9.20	Used	
6/9/1968	6/3/1968	3.000	4 1/4	Anchor	2857	2857			
11/9/1995			3 1/2	Patch	1288	1291			
11/9/1995			3 1/2	Patch	1288	1291			
11/9/1995			3 1/2	Casing	0	1291	9.20		

ANALYSIS OF RAW DATA vs. REFINED DATA

Please note that multiple data entry was the major reason for the reduction in the refined data from the initial

DATA FIELDS	COMPLETION DATA										
	Total Completions Run	API Number	Field Name	Well	Description	Date Tubing Run	OD	Top Casing	Bot	Weight	Grade
INITIIAL DATA AVAILABLE	2910	431	431	431	2909	2909	2909	2909	2909	1781	1607
FINAL DATA AVAILABLE	2413	430	431	431	2413	2413	2413	2413	2413	1723	1607

Fig6. Data addition and refinement for Completion Data

PERFORATION DATA

This data set contains mostly all the information relating to the perforations done on the gas storage well like perforation top & bottom depth and shots per feet. Following are the data types included in this type of data set are below

1.   Well API Number
2.   Field Name
3.   Well Name
4.   Completion Type
5.   Perforation Date (Perf Date)
6.   Perforation Top (Perf Top)
7.   Perforation Bottom (Perf Btm)
8.   Shot Type
9.   Shot Per feet (Shot Per ft)

The picture of a document showing this information is shown below

Fig7. Perforation data retrieved from a file

ANALYSIS OF RAW DATA vs. REFINED DATA

PERFORATION DATA										
DATA FIELDS	Total Perforations	API Number	Field Name	Well Name	Completion Type	Perf Date	Perf Top	Perf Bottom	Shot Type	Shot Per ft
INITIIAL DATA AVAILABLE	392	57	57	57	48	392	392	392	209	383
FINAL DATA AVAILABLE	392	57	57	57	48	392	392	392	209	383

PERFORATION DATA

Fig8. Data addition and refinement for Perforation Data

STIMULATION DATA

Stimulation data is the one of the most significant dataset about the storage wells. Because of this it was very important that we have maximum records of valid stimulations. Following data type is used to represent stimulation

1.   API Well Number
2.   Well Name
3.   Size of String
4.   Stimulation From
5.   Stimulation To
6.   No Of Shots
7.   Fractured by
8.   Stimulation Type
9.   Stimulation Date
10.   Water
11.   Acid
12.   Gel
13.   Foam
14.   Nitrogen
15.   Alcohol
16.   Cushion
17.   Flush
18.   Sand Quantity
19.   Sand Type
20.   Injection Rate
21.   Total Fluid
22.   Breakdown Pressure
23.   ISIP

Unfortunately initially we didn't have much data about the stimulations being done in this Lucas field. With this in mind every record with Columbia Transmission Corporation was carefully examined. The largest source of stimulation data came from the thousands of microfiche with some data being found in well summary reports. Following is a picture of data in well summary reports.

LUCAS - ...

Name	Top (ft)	Btm (ft)	Fluid Shows	Comment
Clinton Sand	2817	2827		
TD	2827	2827		
DOTD	2857	2857		

ELog Formations(Record Log & Date in Comments)

Formation Picks Group
ELog Formations(Record Log & Date in Comments)

Name	Top (ft)	Btm (ft)	Fluid Shows	Comment
Big Lime				
Clinton Sand				
DOTD				
Logger's TD				
Big Lime Top				

Stimulations: Water Fracture on 7/1/1968

Date	Stim Type	Stim/Treat Company	Stim Trade Name
7/1/1968	Water Fracture		

Zone		Top (ft)	Bottom (ft)	Est. Pore Press (psig) (psi)
		2823	2831	

Breakdown Pressure (psi)	Avg Treat Press (psi)	Avg BH rate (bpm)	Instant. Shut-in Pressure (psi)	Flush Fluid Density (ppg)

Fluid Volume Pumped (bbl)	Nitrogen Amount (mcf)	Proppant Type & Mesh	Proppant Amount (lb)	Max BH sand conc.(lb/gal)

Comment
Clinton

breakdown 2500 #, ave press 2434 #, ISIP 1000 #, 10,500 lb. sand.

Build-Up Tests

Start Date	Type	c	a	kh	Skin	True Skin	DDRate (mcf/day)	AOF (mcf/day)	Comment
8/1/1913	Open-Flow								
4/13/1964	Open-Flow								
9/21/1966	Open-Flow								
4/5/1967	Open-Flow								
9/7/1967	Open-Flow								
7/29/1968	Open-Flow								
10/9/1968	Open-Flow								
4/8/1969	Open-Flow								
10/2/1969	Open-Flow								
4/1/1970	Open-Flow								
10/7/1970	Open-Flow	0.454	0.750				4765.96	18054.40	
4/2/1973	Open-Flow								
5/13/1981	Open-Flow								
6/14/1993	Multi-Point	0.047	0.750				497.89	1886.94	Repair casing / wellhead as necessary, re-perforate and frac.Historical comparison of BP curve indicates significant loss of delivery. Analysis of flow test not possible, very ambiguous.Fill in well Coiled tubing cleanout to original TD. Reperf and frac well.

070700323 - LUCAS   Report run date - Tuesday, February 22, 2005   Page 2 of 4

Stimulations: Water Fracture on 7/1/1968

Date	Stim Type	Stim/Treat Company	Stim Trade Name
7/1/1968	Water Fracture		

Zone		Top (ft)	Bottom (ft)	Est. Pore Press (psig) (psi)
		2823	2831	

Breakdown Pressure (psi)	Avg Treat Press (psi)	Avg BH rate (bpm)	Instant. Shut-in Pressure (psi)	Flush Fluid Density (ppg)

Fluid Volume Pumped (bbl)	Nitrogen Amount (mcf)	Proppant Type & Mesh	Proppant Amount (lb)	Max BH sand conc.(lb/gal)

Comment
Clinton

breakdown 2500 #, ave press 2434 #, ISIP 1000 #, 10,500 lb. sand.

Fig9. Perforation data retrieved from a file

MICROFICHE TO DATABASE

Each Microfiche contained dozens of documents from invoices to valuable stimulation and well-test data

Microfiche were read by digital Microfilm scanners

Each scanned image of the microfiche was searched and read for valuable data

Prints were taken of the documents containing data

Data was entered in the database

Following are pictures of some types of data formats for fracture jobs found in the records

Fig10. Different formats of Nitrogen Amount

During the data entry different sign conventions and unit conversions were carried out as follows

MEASURED QUANTITY	UNITS IN RECORDS	UNITS USED IN DATABASE
SAND	1 sack 1 sks	100 lbs
NITROGEN	52M	52,000 SCF
LIQUID	1 bbl	42 gal
PERFORATIONS	2000-2005 ft, 10 shots 10/5	2 shots /ft

The following notations were used in place of different notations being used in the tables

NOTATIONS USED IN DATABASE	WATER GEL FRAC	PETRO GEL FRAC	FOAM FRAC	NITRO SHOT	WATER/N2 FRAC	WATER FRAC	10/20 SAND
NOTATIONS THAT WERE REPLACED	Gelled water frac	Petrl gel	Foam	Shot	Water / N2	water	10/20
	Water Gel	Petro Gel Petro gel fracture	foam Frac foam fracture		Water N2 Fracture Water nitrogen		Sand 10/20
					Water/N2 assist Water Fracture w/N2 assist		

All records of Nitro-shots were discarded for this database as they have no stimulation parameters on record and are part of history now plus they also damage the well. Above all they will tend to degrade the Neural Network.

GRAPHICAL ANALYSIS OF RAW DATA vs. REFINED DATA

DATA FIELDS	Total Stimulations	API Number	Well	Size Of String	Stim From	Stim To	No Of Shots	Fractured by	Type	Stim Date	Water	Acid	Gel	Foam	N2	Alcohol	Cushion	Flush	Sand Quantity	Sand Type	Injection Rate	Total Fluid	Breakdown Pressure	ISIP
STIMULATION DATA																								
INITIIAL DATA AVAILABLE	32	32	32	32	32	32	32	32	32	32	0	0	0	0	0	0	0	0	32	32	25	0	27	24
FINAL DATA AVAILABLE	390	430	430	308	388	388	156	354	370	391	85	293	294	157	249	21	277	302	368	266	263	317	181	345

Fig11. Data addition and refinement for Stimulation Data

WELL TEST DATA

Well-test data is the most extensive dataset that our R & D team worked on. It has the max amount of records nearly 3365 and 29 data types that control every aspect of a well-test. The data type selected for a well-test representation consists of following

1. Well API Number
2. Field Name
3. Test Date
4. Test Type
5. Time 1
6. Field Pressure 1
7. Flowing Pressure 1
8. Rate 1
9. Time 2
10. Field Pressure 2
11. Flowing Pressure 2
12. Rate 2
13. Time 3
14. Field Pressure 3
15. Flowing Pressure 3
16. Rate 3
17. Time Extended
18. Field Pressure Extended
19. Flowing Pressure Extended
20. Rate Extended
21. kh
22. Skin
23. True Skin
24. Non Darcy Co-efficient
25. n Value
26. C Value
27. Delta Pressure Squared
28. Peak Day Rate
29. Absolute Open Flow

Lot of data was missing in this dataset so it was decided that values of n, C, PDrate & AOF will be interpreted manually and on the other side work on software will continue to automatically do this interpretation procedure with little input from user. This program will be discussed in great detail latter.

ESTIMATION OF n, C, PEAK DAY RATE & ABSOLUTE OPEN FLOW

EMPIRICAL APPROACH

SINGLE/OPEN FLOW TESTS

The values used for point 1 and 2 are from different well-tests

    1-   Find ΔP^2

    3- $\dfrac{1}{n} = \dfrac{\log(\overline{p}^2 - p_{wf}^2)_2 - \log(\overline{p}^2 - p_{wf}^2)_1}{\log q_2 - \log q_1}$ (Where q is in MMcfD)

    4- $C = \dfrac{q_g}{(\overline{p}^2 - p_{wf}^2)^n}$ (Where q is in McfD)

    5- $AOF = C(1150^2 - 0^2)^n$ McfD

    6- $PDRate = (C \times 250,000)^n$ McfD

MULTI-POINT TESTS

Estimation of n, C, PD rate & AOF:

    1-   Same as above except that the points used are from the same test

NOTE: The n, C, PD rate & AOF values for more than 400 well-tests were manually calculated

ESTIMATION OF KH, SKIN, TRUE SKIN, NON-DARCY COEFFICIENT

1- From extended draw-down test plot (P_i-P_{wf}) vs. time on log-log paper. Draw unit-line for un-stimulated wells and half-slope line for Stimulated wells. Find end of well-bore storage effects after 1-1/2 log time cycle

2- Find values of viscosity, z-factor, compressibility of storage gas at different pressure assuming Gas gravity = 0.585 & temperature = 75 F = 535 R

DRAW-DOWN TEST

1- Plot P_{wf}^2 vs. time
2- Draw straight line after pseudo-steady state starts
3- Find slope m and $P^2 1hr$

4- $$kh = \frac{1637qTzu}{m}$$

5- $$S = 1.151\left[\frac{p^2 - p^2_{1hr}}{m} - \log\left(\frac{k}{\phi\mu c r_w^2}\right) + 3.23\right]$$

6- Plot skin vs. flow-rate. It should be a straight line
7- Slope of this line is D
8- Find True Skin (S') at q=0.

BUILD-UP TEST

1- Plot P_{wf}^2 vs. (tp+dt)/dt on semi-log paper
2- Draw straight line after well-bore storage effects diminishes
3- Find slope m and $P^2 1hr$

4- $$kh = \frac{1637qTzu}{m}$$

5- $$S = 1.151\left[\frac{p^2_{1hr} - p^2}{m} - \log\left(\frac{k}{\phi\mu c r_w^2}\right) + 3.23\right]$$

6- Plot skin vs. flow-rate. It should be a straight line
7- Slope of this line is D
8- Find True Skin (S') at q=0.

We require time, flow-rate & Bottom hole pressure from the data which is present in two txt files as bottom hole & surface recording files. The flow rates are at Wellhead so we match the bhp & THP with time.
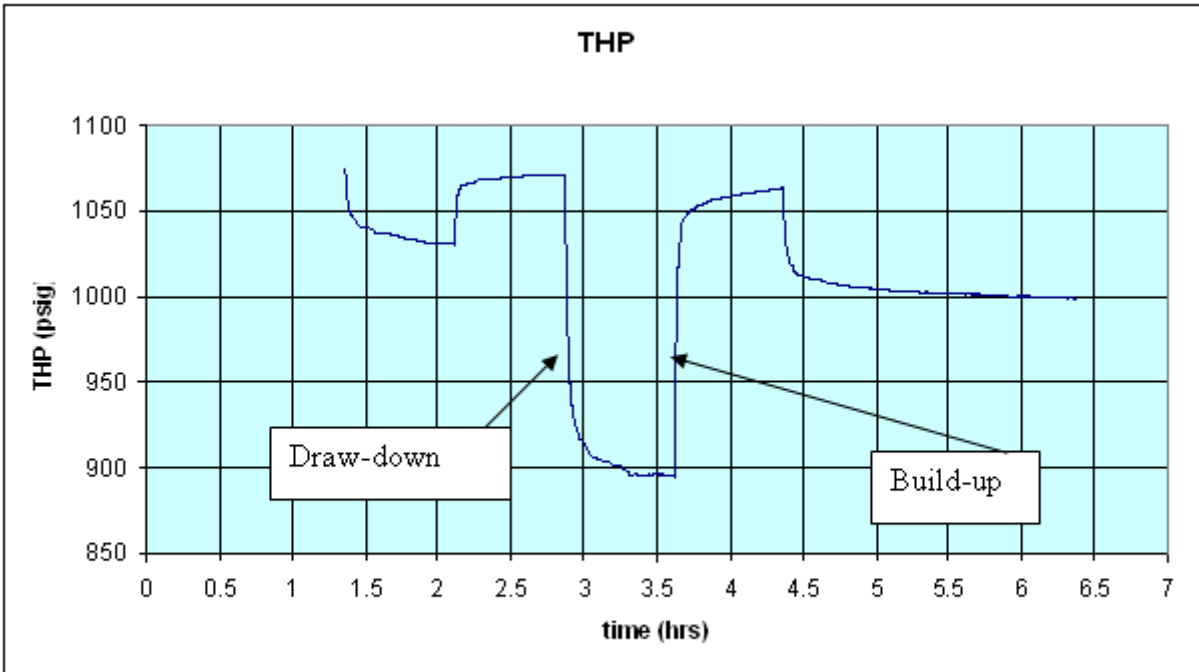
Fig12. Tubing Head Pressure profile for Multi-point test
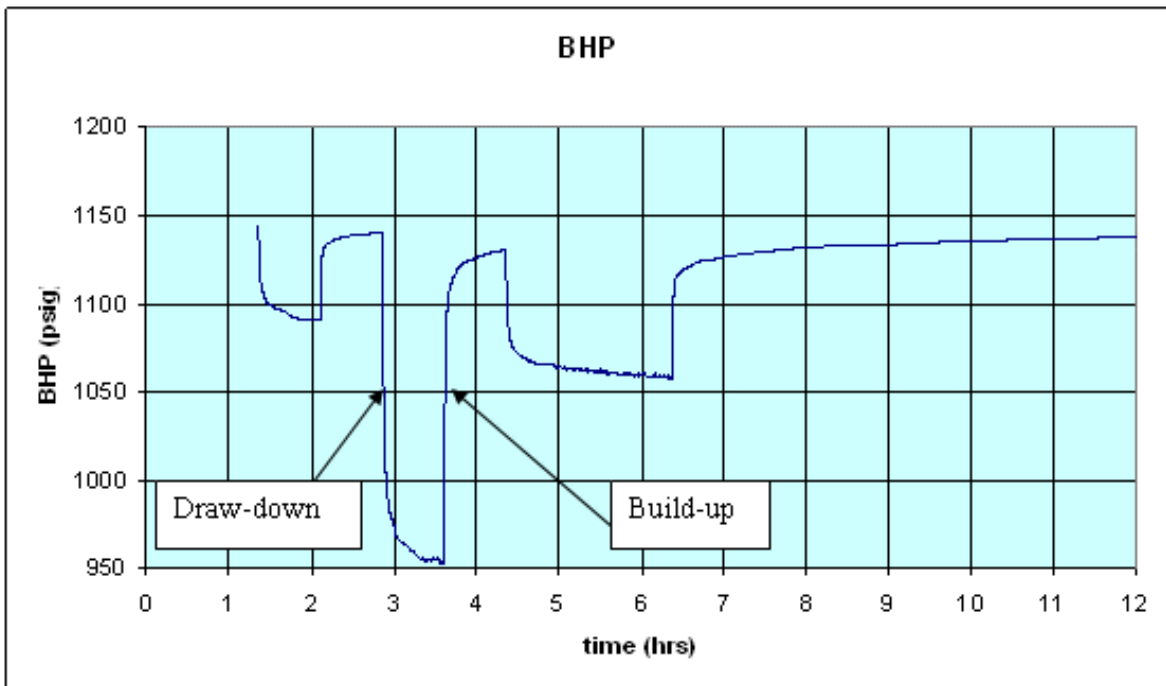
Fig13. Bottom Hole Pressure profile for Multi-point test

The multipoint-test data is divided into Draw-down & build-up test and each one is analyzed separately.

DRAW-DOWN TEST

Analysis of drawdown tests was done as described above and following graphs were obtained
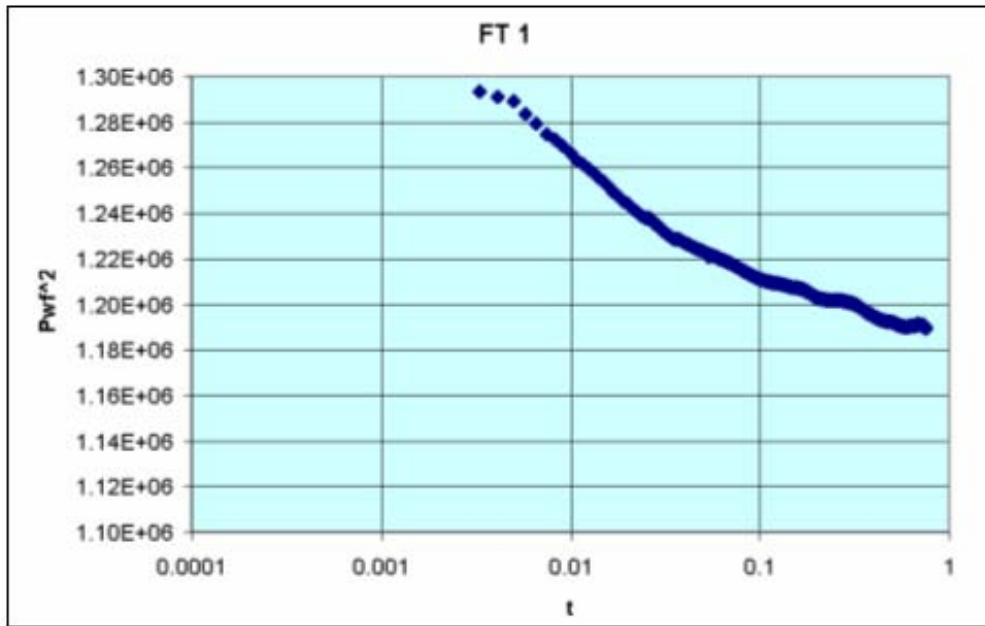
Fig14. Flow Test 1 – Delta pressure squared vs. time
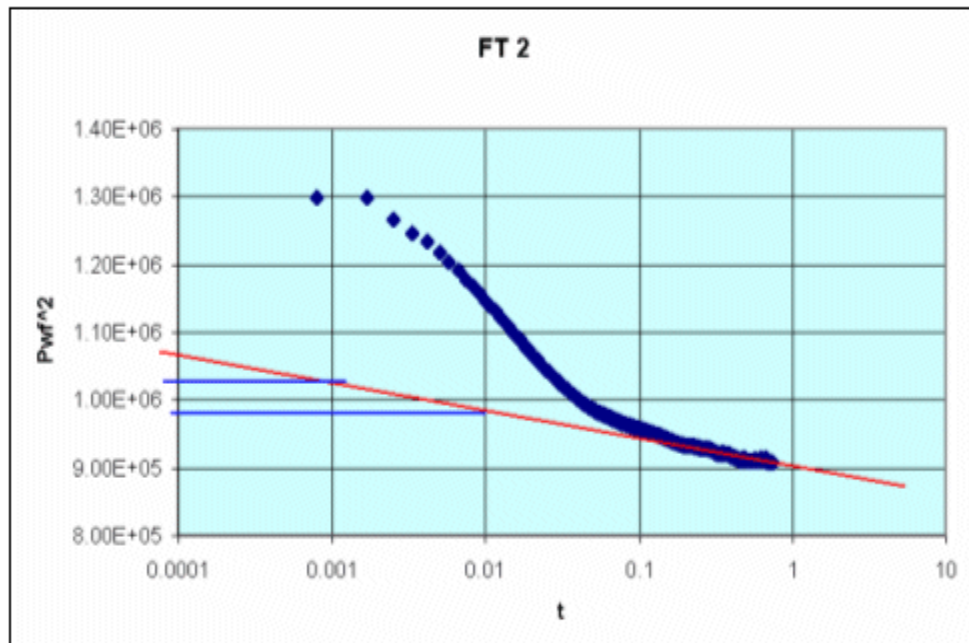
Fig15. Flow Test 2 – Delta pressured squared vs. time
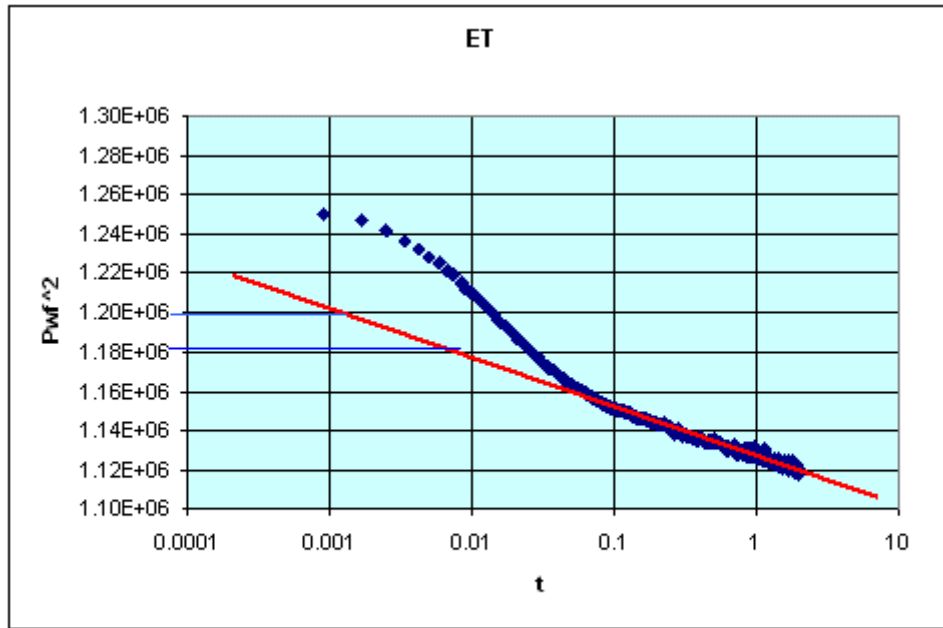
Fig16. Extended Flow Test – Delta pressured squared vs. time
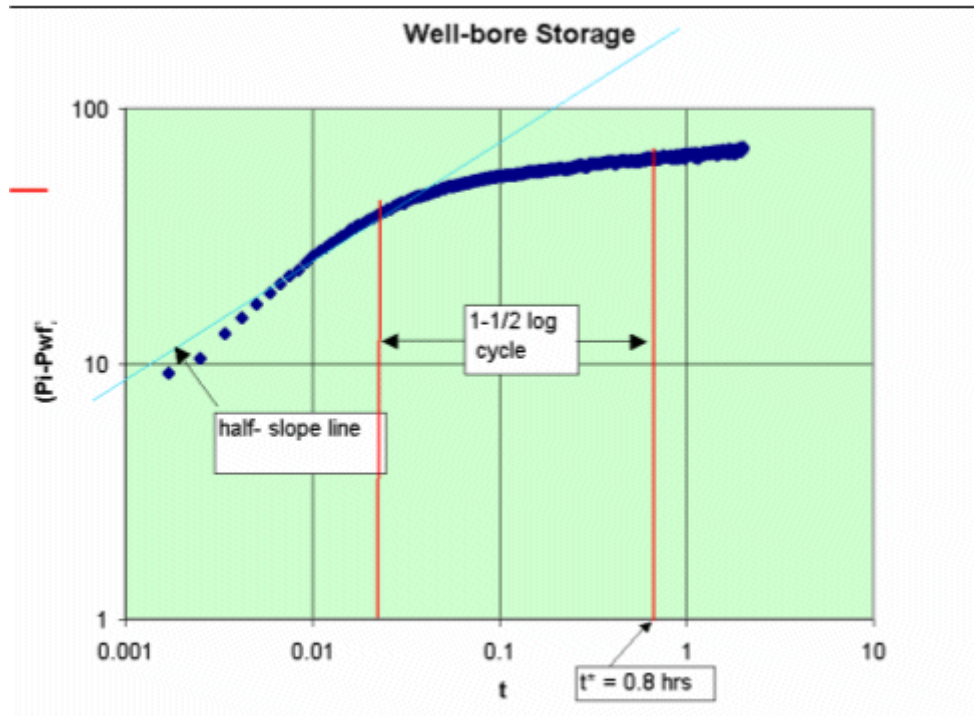
Fig17. log-log graph

For well-tests after fracture half-slope line is drawn and for un-simulated wells unit slope line is drawn to find end of well-bore effects and start of pseudo-steady state.

Gas production Simulator was used to find the values of viscosity, z-factor and compressibility of storage gas at different pressure assuming Gas gravity = 0.585 & Temperature = 75 F = 535 R that are also used by Columbia Trans.
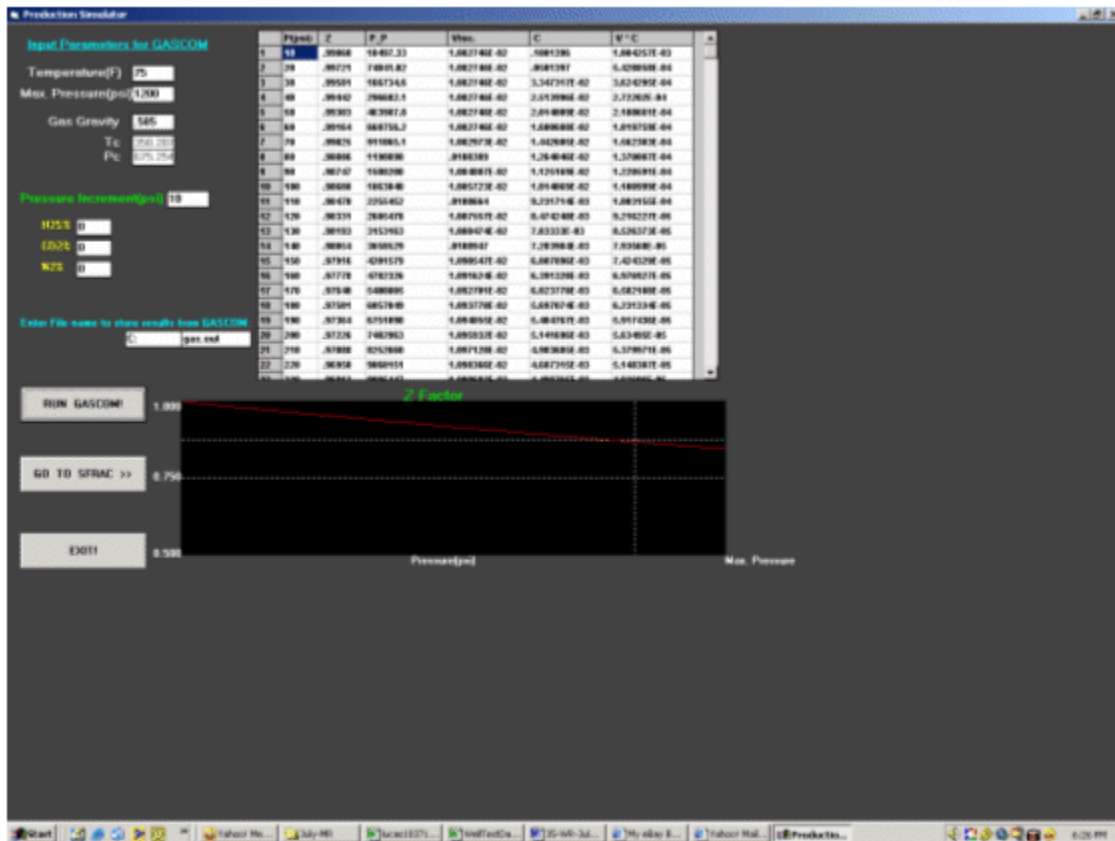
Fig18. Gas properties Simulator

The slope from Pwf^2 vs. time on semi-log graph was used to find kh & then skin. The three values of skin were plotted on Q vs. S graph and extrapolated to Q = 0 to get True skin (S').
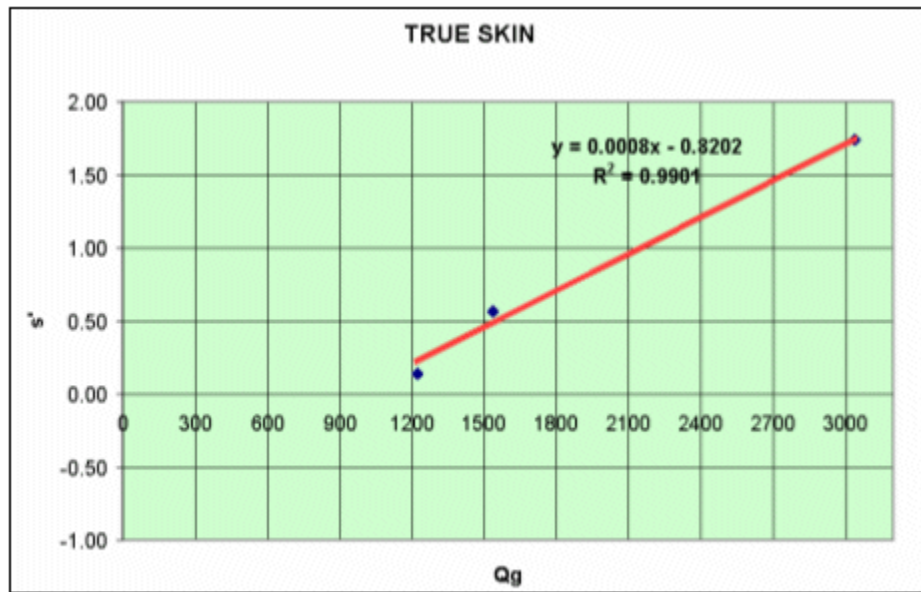
Fig19. Calculation of True skin

DRAW-DOWN TEST RESULTS

	FLOW TEST 1	FLOW TEST T2	EXTENDED TEST
porosity	0.14	0.14	0.14
rw	0.1458333	0.1458333	0.1458333
Ct	1.02E-03	1.08E-03	1.04E-03
Uav	1.28E-02	1.26E-02	1.27E-02
Zav	0.8558691	0.8635354	0.859119
P	1143	1140	1127.3
Qav	1223.8668	3038.7039	1536.1134
Tav	533	533	533
h	10	10	10
m	2.00E+04	5.40E+04	2.20E+04
kh	5.86E+02	5.36E+02	6.67E+02
k	5.86E+01	5.36E+01	6.67E+01
p1hr^2	1.185E+06	9.000E+05	1.128E+06
S	0.14	1.74	0.57
S'	-0.8202		
D	0.0008		

BUILD-UP TEST

In build-up tests, the slope drawn for Horner plot is after the time when well-bore storage effects were found to be minimum from previous draw-down test. This slope is then used to find the values of kh & skin. The True skin is found the similar way as in draw-down test.
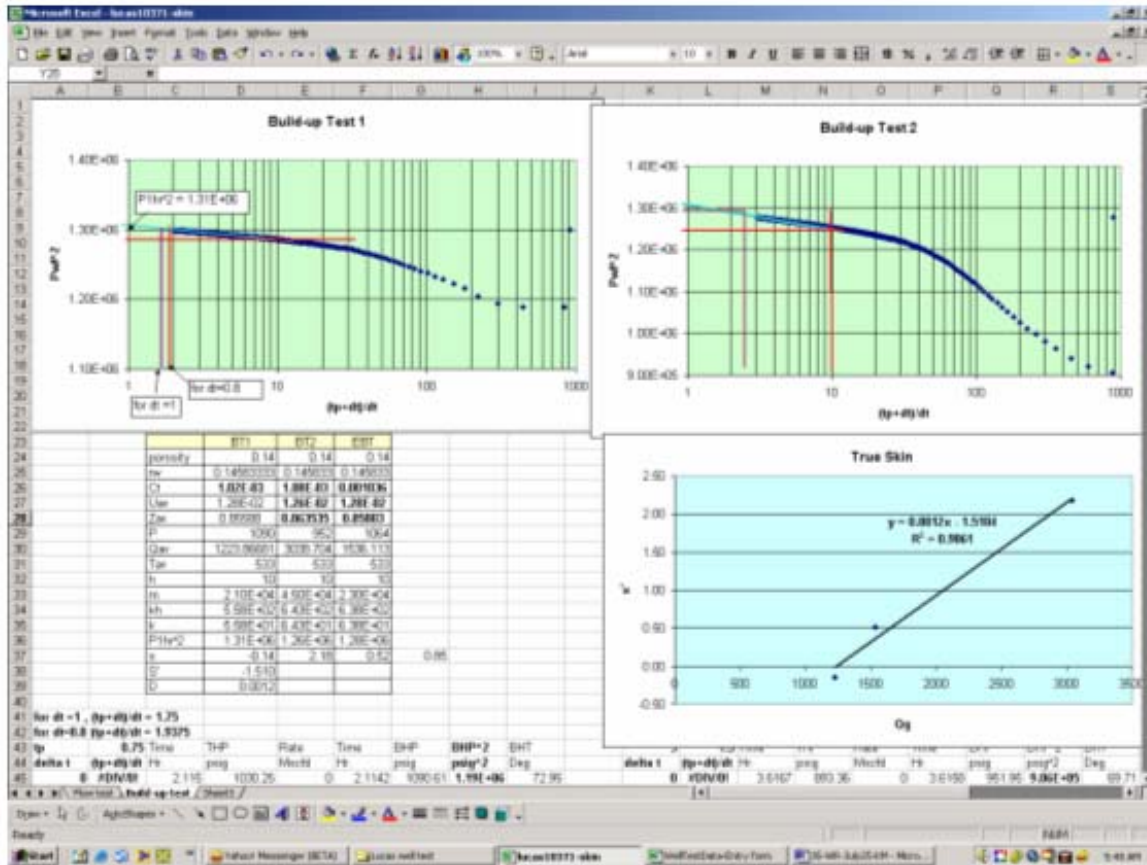
Fig20. Calculation of True skin from Build-up test

BUILD-UP TEST RESULTS

	BUILD-UP TEST 1	BUILD-UP TEST 2	EXTENDED BUILD-UP TEST
porosity	0.14	0.14	0.14
rw	0.14583333	0.145833	0.145833
Ct	1.02E-03	1.08E-03	0.001036
Uav	1.28E-02	1.26E-02	1.28E-02
Zav	0.85588	0.863535	0.85803
P	1090	952	1064
Qav	1223.86681	3038.704	1536.113
Tav	533	533	533
h	10	10	10
m	2.10E+04	4.50E+04	2.30E+04
kh	5.58E+02	6.43E+02	6.38E+02
k	5.58E+01	6.43E+01	6.38E+01
P1hr^2	1.31E+06	1.26E+06	1.28E+06
s	-0.14	2.18	0.52
S'	-1.510		
D	0.0012		

AVERAGED RESULTS

	DRAW-DOWN	BUILD-UP	AVERAGE	ACTUAL
S'	-0.8202	-1.510	-1.165	-1.17
D	0.0008	0.0012	0.0010	.00126

Due to large errors corresponding to estimating skin and kh values manually, it was decided that for time being these values will not entered in the database.

Following are some pictures of the documents to show the different format in which the data was present in files and microfiche.
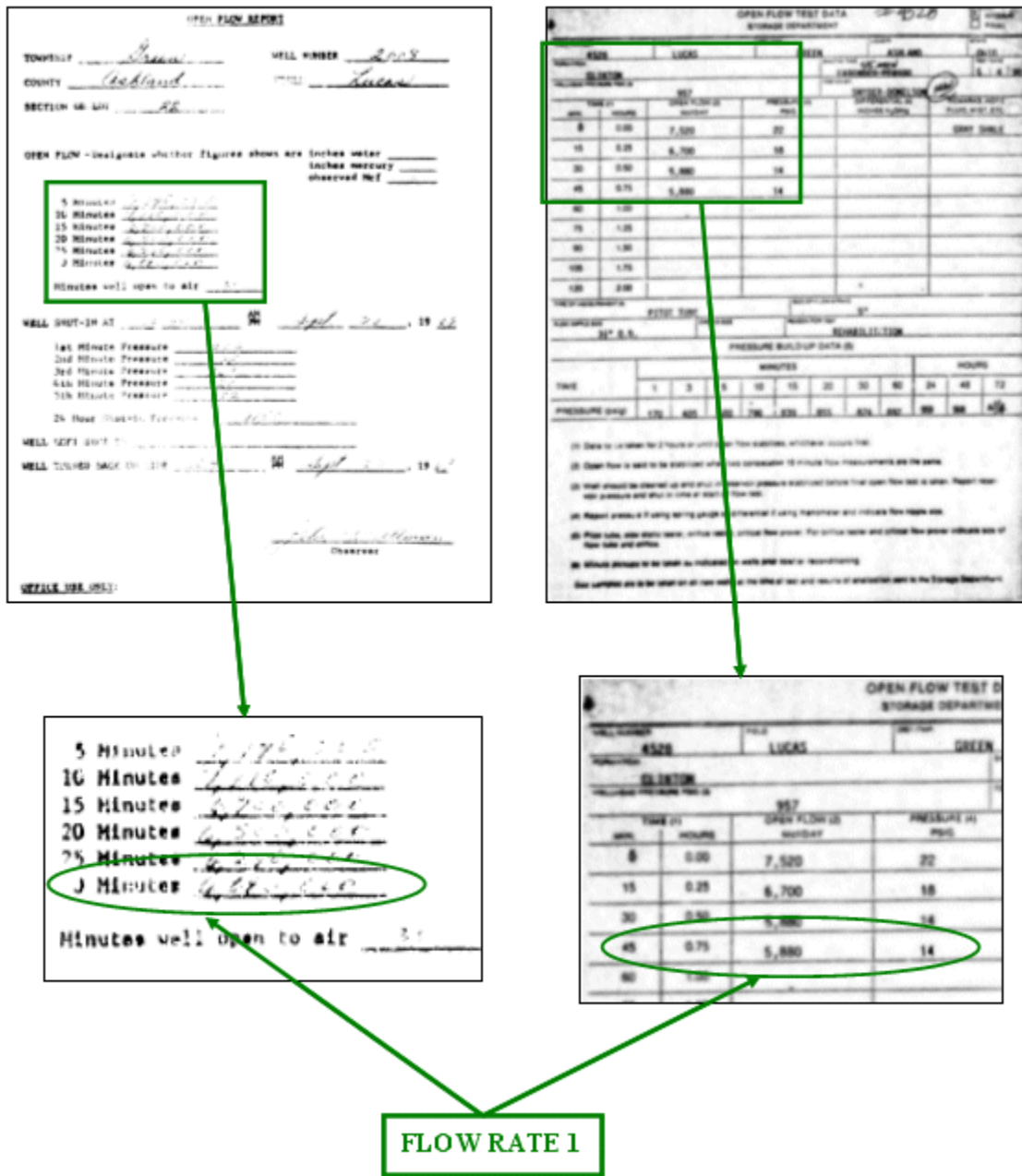
Fig21. Retrieving flow-rate of an open-flow test

GRAPHICAL ANALYSIS OF RAW DATA vs. REFINED DATA

WELL TEST DATA																														
DATA FIELDS	Total Well-Tests	API Number	Field Name	Well	Test Date	Test Type	Time1	FieldPress1	FlowingPress1	Rate1	Time2	FieldPress2	FlowingPress2	Rate2	Time3	FieldPress3	FlowingPress3	Rate3	Time Extended	Field Pressure Ext	Flowing Pressure Ext	Rate Ext	kh	Skin	True Skin	Non Darcy Coefficient	n-Value	C-Value	Delta P Squared	Peak Day Rate	Absolute Open Flow
INITIAL DATA AVAILABLE	3223	431	431	431	3223	3223	3223	3223	3223	3223	347	347	347	347	292	292	292	292	345	345	345	345	191	182	163	163	916	916	916	916	916
FINAL DATA AVAILABLE	3365	431	431	431	3365	3365	3365	3365	3365	3365	347	347	347	347	292	292	292	292	345	345	345	345	194	185	166	166	1362	1362	1362	1362	1362

WELL TEST DATA

Number of Data Entries

□ INITIAL DATA AVAILABLE   ■ FINAL DATA
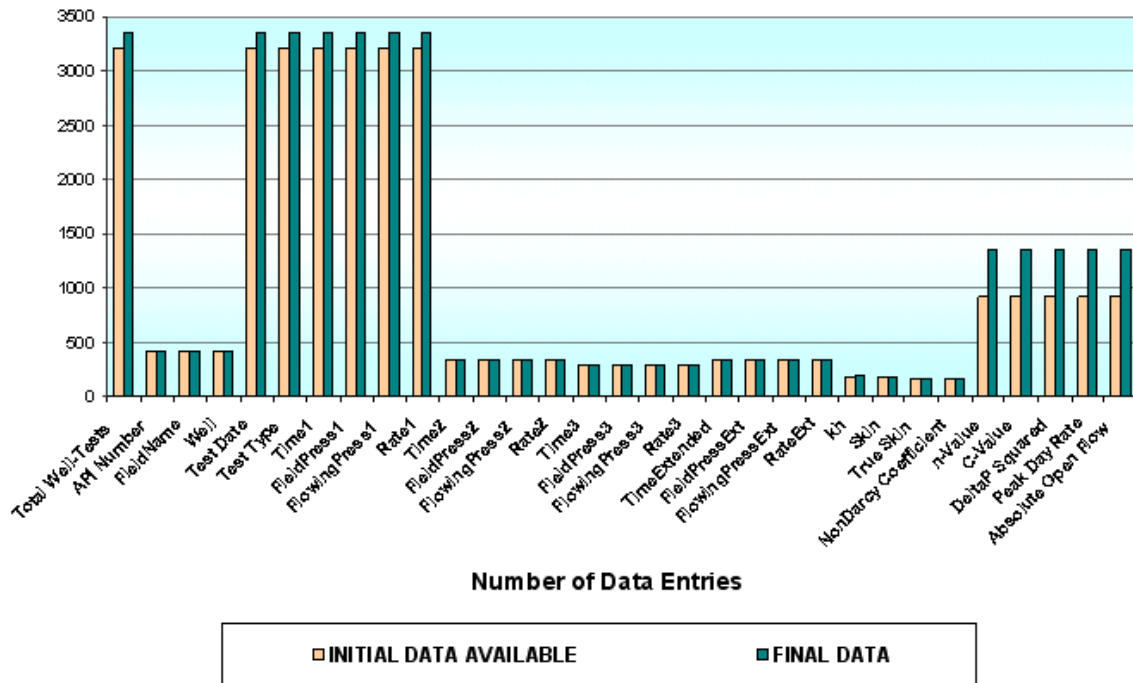
Fig22. Data addition and refinement for well test data

DATABASE & SOFTWARE

SOFTWARE BASICS

This software allows you to add/edit well data in the database and choose the data that you want to look at, for a selected well. It also has a Well Test Analysis tool which calculates the well deliverability parameters like n, C, Peak Day rate & Absolute Open Flow

The database for this software consists of five tables

1. Well bore Data
2. Completion Data
3. Perforation Data
4. Stimulation Data
5. Well Test Data

The **API number** of a well is the primary key in this database so it must be known before adding a record and cannot be duplicated
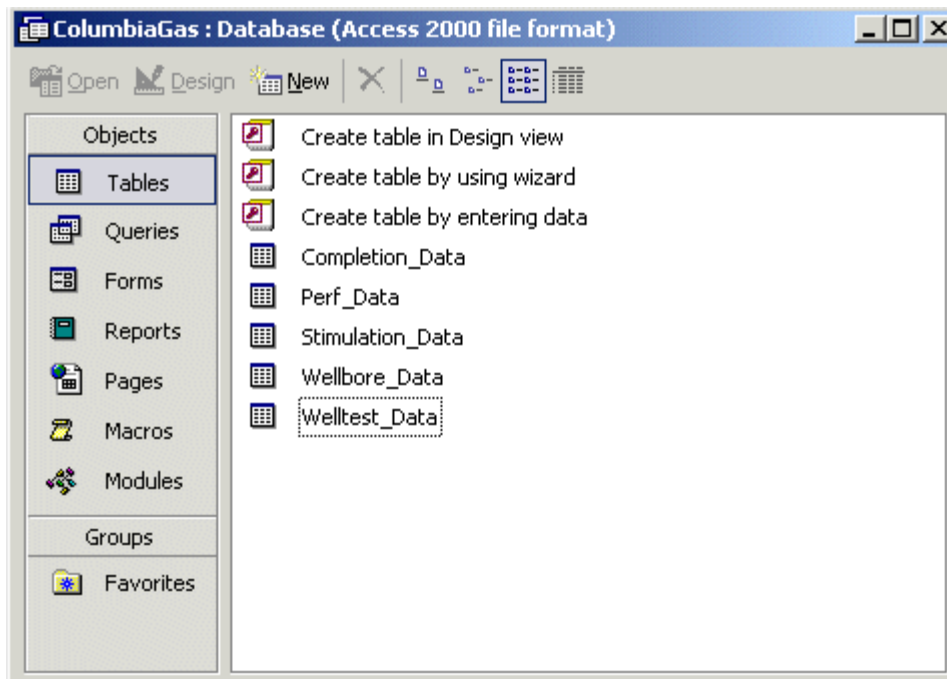
Fig23. Screen shot of database showing different tables

The software starts with the main menu screen with six options

Fig24. Main Screen of software

Editing / Viewing Data

To edit/view well data or do a Well Test Analysis

Select Well Data

To choose the well data that you want to look at for selected wells

Exit

To Exit from the Program

Tutorial [Tutorial]

To open the Help file / Tutorial for this program

About [About]

To get general information about the developing of thus project

EDIT / VIEW WELL DATA

This screen has all the well data in the form of five tabs (for five database tables) that can be edited / viewed or a Well Test Analysis can be performed in the Well Test tab

Fig25. Browsing through the well-bore data

To browse between different wells

To move to the first well, previous well, next well & the last well in the record click on the button assigned to it. The records are assorted in ascending order according to well number

API Number & Well Count

The progress bar shows the relative position of the record and well count shows the current well position in the well bore database out of the total records. The API number of the current well is also displayed

Back to main menu

Takes you back to the very first screen of the program

Editing Tools

These buttons will help you to add a new record, edit or delete it or find a well for which you want the data to be retrieved if you know its API number

DIFFERENT TABS

WELL BORE

Fig26. Well-bore tab

This tab contains all the data pertaining to the name, location & some main features of the current well

COMPLETION

Fig27. Completion tab

This tab contains all the data relating to different completion run in the well

To browse between different Completions

To move to the first completion, previous completion, next completion & the last completion in the record, click on the button assigned to it. The completions are assorted in ascending order according to date tubing run for current well

PERFORATION

Fig28. Perforation tab

To browse between different Perforations

To move to the first perforation, previous perforation, next perforation & the last perforation in the record, click on the button assigned to it. The perforations are assorted in ascending order according to perforation date for current well

STIMULATION

Fig29. Stimulation tab

To browse between different Stimulations

To move to the first stimulation, previous stimulation, next stimulation & the last stimulation in the record, click on the button assigned to it. The stimulations are assorted in ascending order according to stimulation date for current well

WELL TEST

Fig30. Well-test tab

To browse between different Well Tests

To move to the first well test, previous well test, next well test & the last well test in the record, click on the button assigned to it. The well tests are assorted in ascending order according to well test date for current well

Adding a new data

One can add a complete new well or just only a new well-bore/completion/perforation/ stimulation/well-test data by following method

Adding a complete new well data

1- Click on the Add New button [Add New] while keeping your well bore tab as active
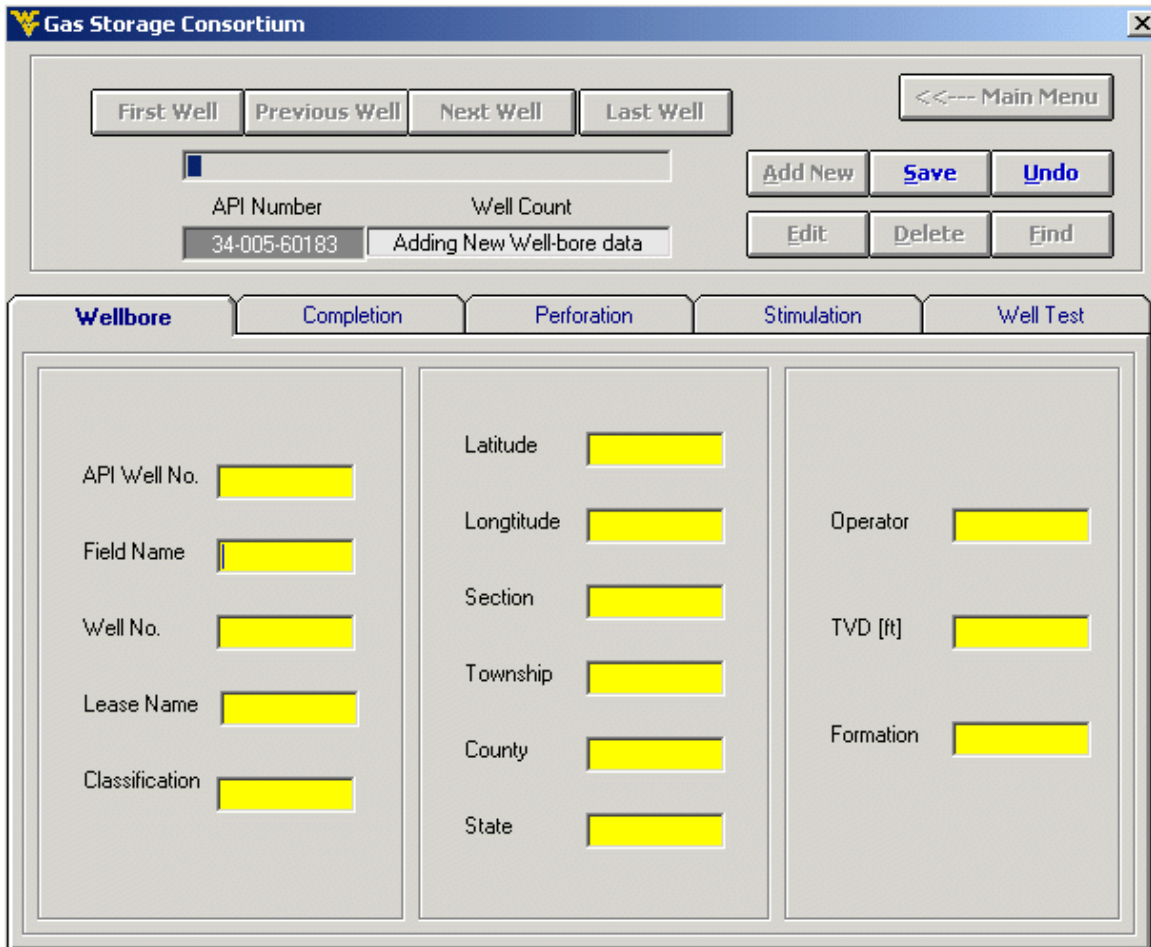
Fig31. Adding a complete new Well – well-bore tab

The following messages will pop-up. If you want to add the complete new well-bore data then click No button [No].

If you don't have the dates of Stimulation, Completion, Perforation & Well-Test data then click Yes [Yes] and then add them one-by one
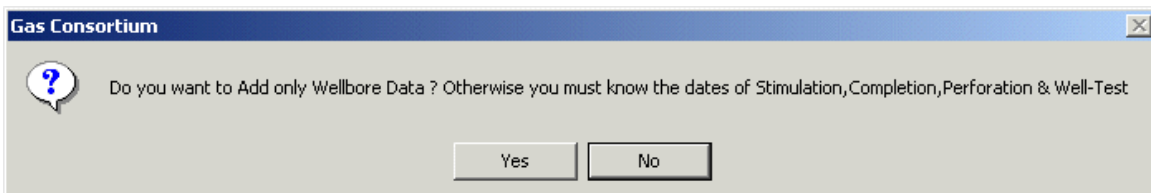
Following screen appears if No is clicked

Fig32. Adding a complete new Well - completion tab

The background color of text boxes of all tabs including well-bore tab will be yellow indicating that they are ready for entering data

2- Enter the data in all the tabs. The dates for completion, perforation, stimulation & well test job should be known

Fig33. Adding a complete new Well – entering data for wellbore

Fig34. Adding a complete new Well – entering data for perforation

Fig35. Adding a complete new Well – entering data for stimulation

Fig36. Adding a complete new Well – entering data for well test

3- Click the Save button

RESULT OF ADDING A COMPLETE NEW WELL DATA
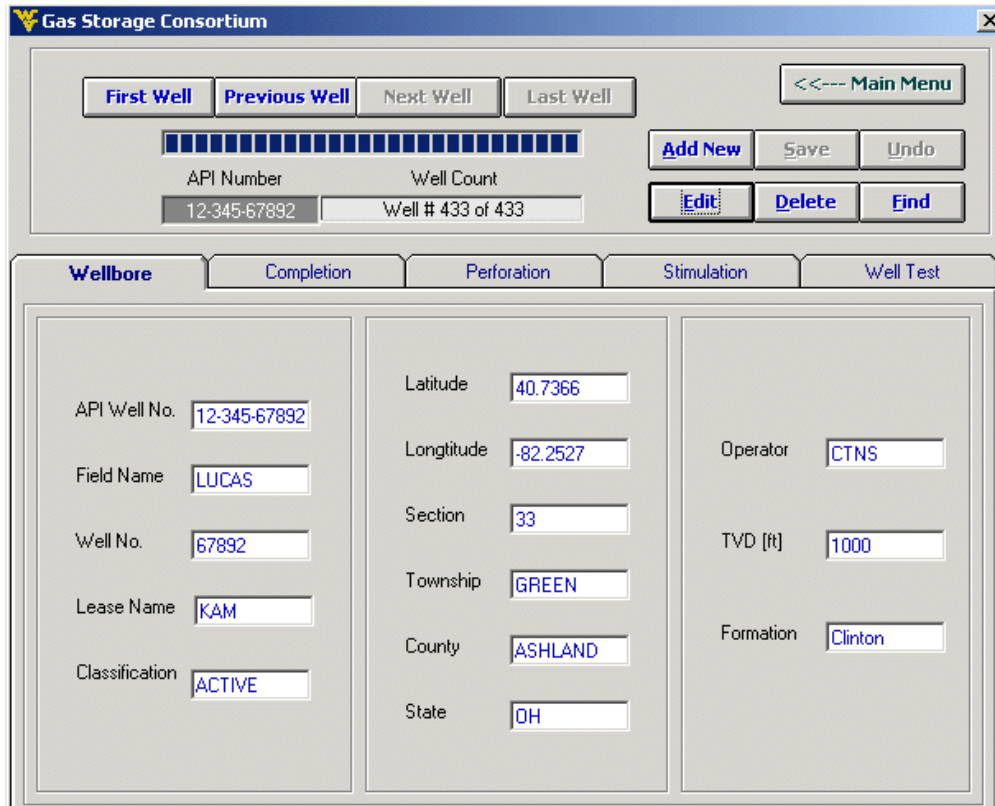
Fig37. Result of adding a complete new well

Warnings – If API Number is not entered
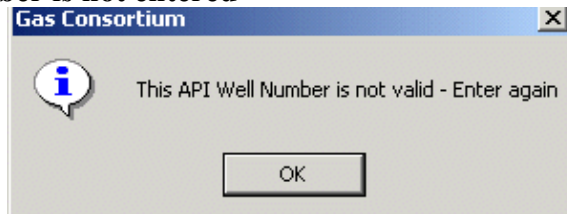
Warnings – If API Number entered is already in the database
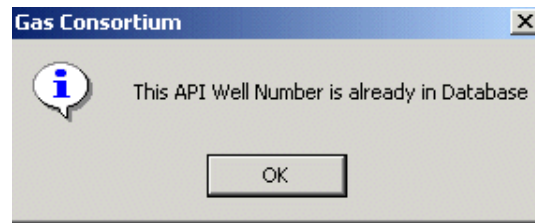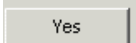
ADDING ONLY WELL-BORE/COMPLETION/PERFORATION/ STIMULATION/ WELL-TEST DATA

1- Click on the Add New button while keeping that tab active for which you want to add the data.

      Only for well-bore tab following message pops-up
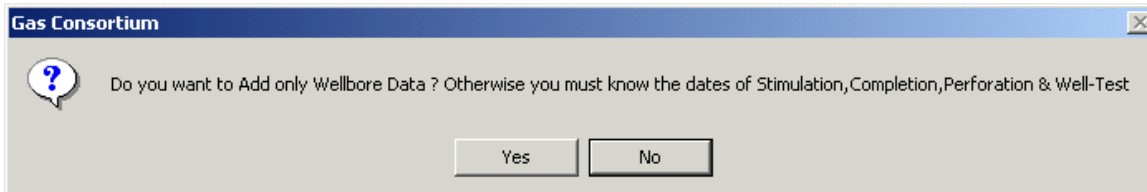
      Click Yes button to add only Well-bore data

The background color of all text boxes of that tab will be yellow indicating that they are ready for entering data

2- Enter the data. The dates for completion, perforation, stimulation & well test job should be known

3- Click the Save button

Editing data
One can edit complete well or just only a new well-bore/completion/perforation/ stimulation/well-test data by following methods

Editing a complete well data

1- Click on the Edit button while keeping your well bore tab as active

Following screen pops-up
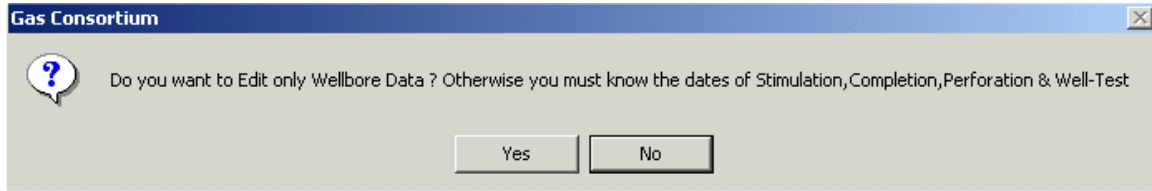
Select accordingly
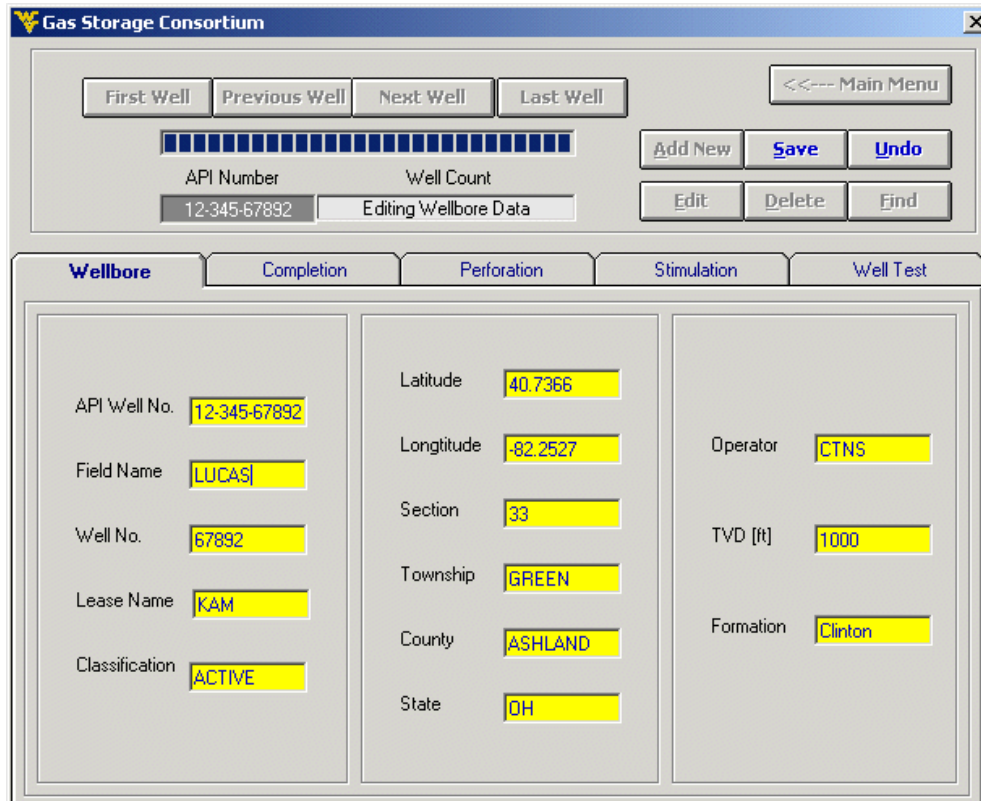
Fig38. Editing well data

Fig39. Editing completion data

The background color of text boxes of all tabs including well-bore tab will be yellow indicating that they are ready for entering data

2- Enter the data in all the active tabs. The dates for completion, perforation, stimulation & well test job should be known

3- Click the Save button [Save]

EDITING ONLY COMPLETION/PERFORATION/ STIMULATION/WELL-TEST DATA

1- Click on the Edit button **Edit**   while keeping that tab active for which you want to edit the data except well bore tab

Fig40. Saving completion data

The background color of all text boxes of that tab will be yellow indicating that they are ready for entering data

2- Enter the data. The dates for completion, perforation, stimulation & well test job should be known

3- Click the Save button **Save**

RESULT OF EDITING ONLY COMPLETION DATA

Fig41. Saved completion data

DELETING DATA

One can delete complete well or just only delete completion/perforation/ stimulation/well-test data by following methods

Deleting a complete well data

1- Click on Delete button [Delete] while keeping your well bore tab as active

Editing only completion/perforation/ stimulation/well-test data

1- Click on Delete button [Delete] while keeping that tab active of which you want to delete the data except well bore tab

Fig42. Deleting perforation record

You will be greeted with the above message to make sure that delete button is not accidentally pressed

2- Click on yes [Yes] if you want the selected record to be deleted

UNDO THE EDIT / ADD OPERATION

To undo the edit or add operation before they can be saved click undo button **Undo**

FINDING A WELL

Follow the following procedure to find a well for which you have some idea of its API well number

Click on Find button **Find**

The following screen is displayed
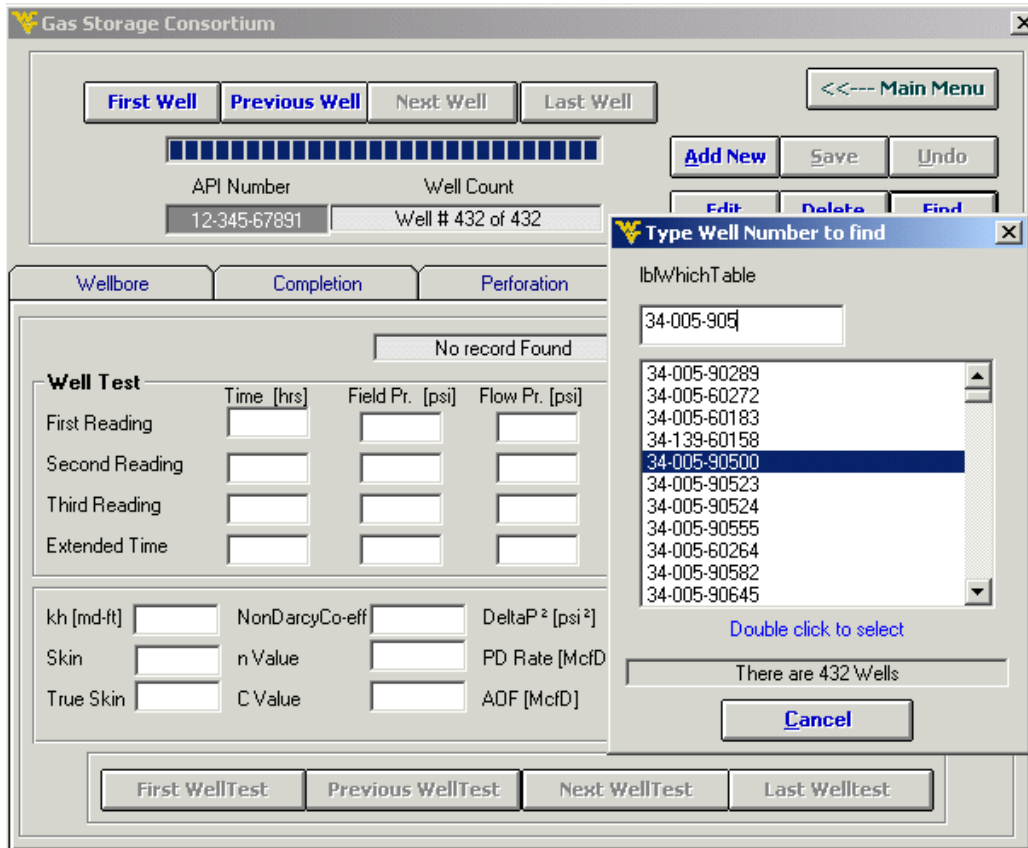
Fig43. Finding a well

1- Type the API number to find the well and then double click it in the list

If the API number is found then the message below is displayed and the data for that well is retrieved
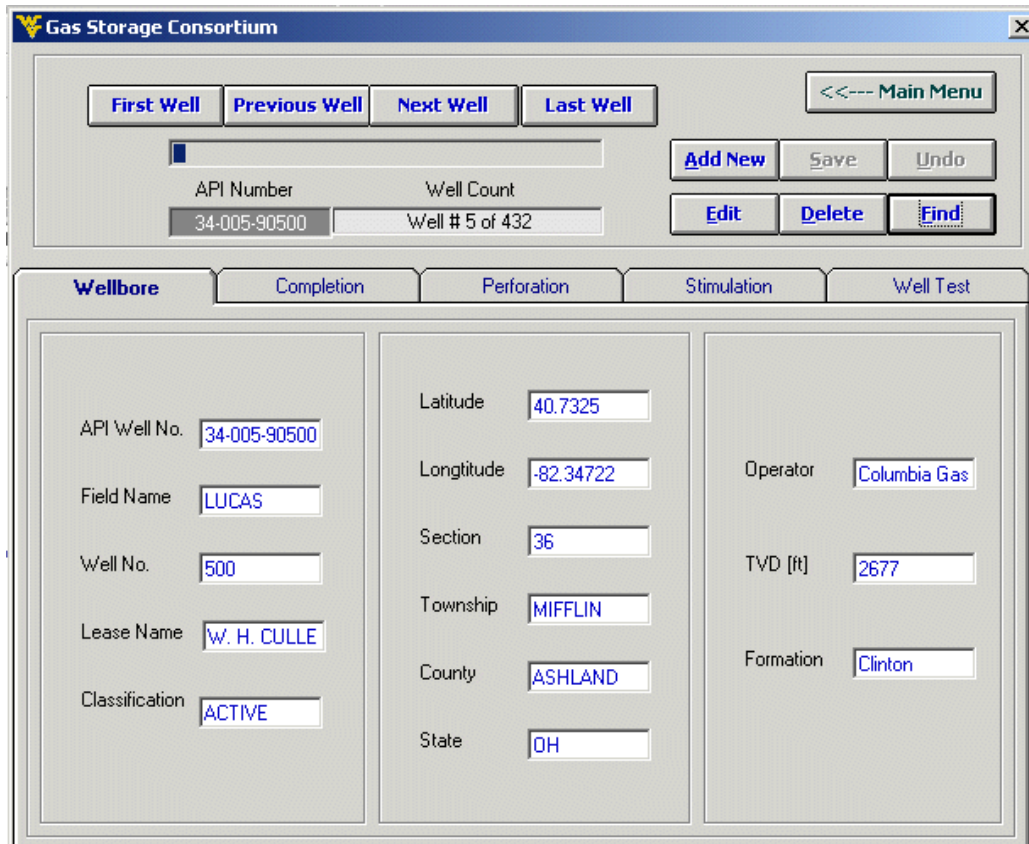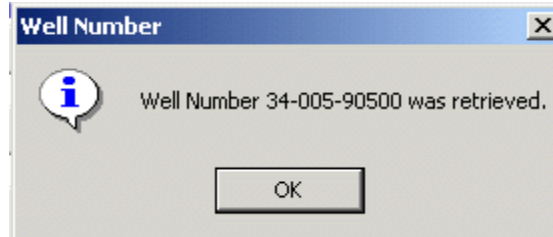
Fig44. Retrieving the data

WELL TEST ANALYSIS

To do the well test analysis on the well and to draw graph of Peak day rate and Absolute open flow use the option / command buttons below
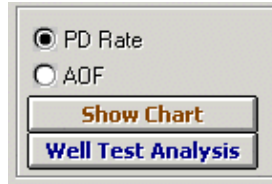
Fig45. Well-test Analysis Option in well-test tab

PEAK DAY / AOF GRAPH

Select **PD rate** / **AOF** option button and click **Show Chart** button ![Show Chart]. The following screens will appear according to the option selected
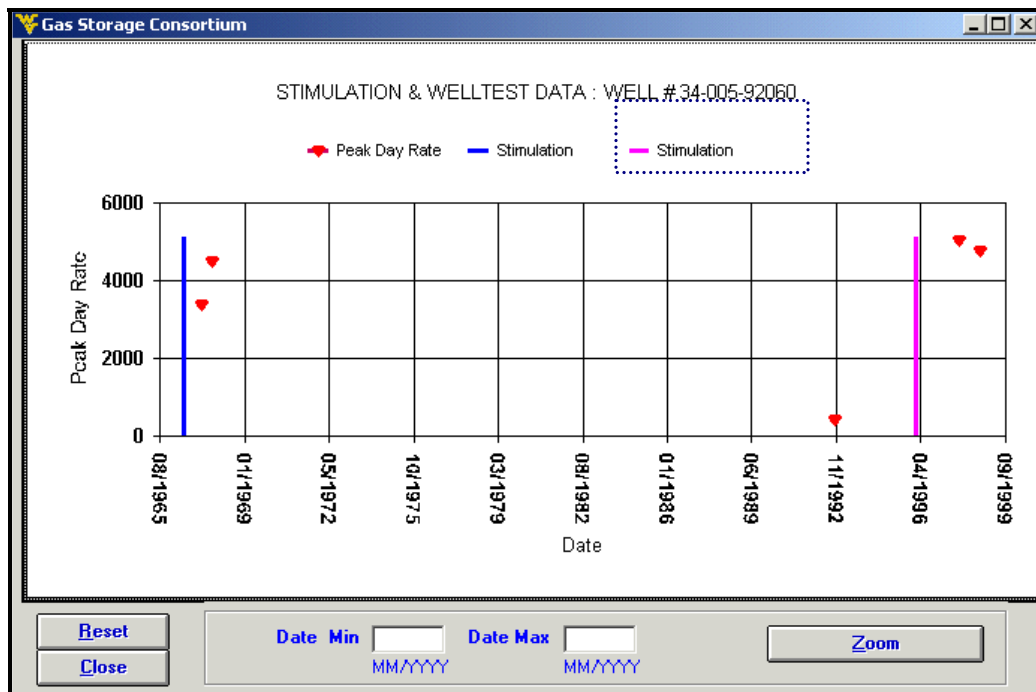
Fig46. Show Chart – Peak Day Rate
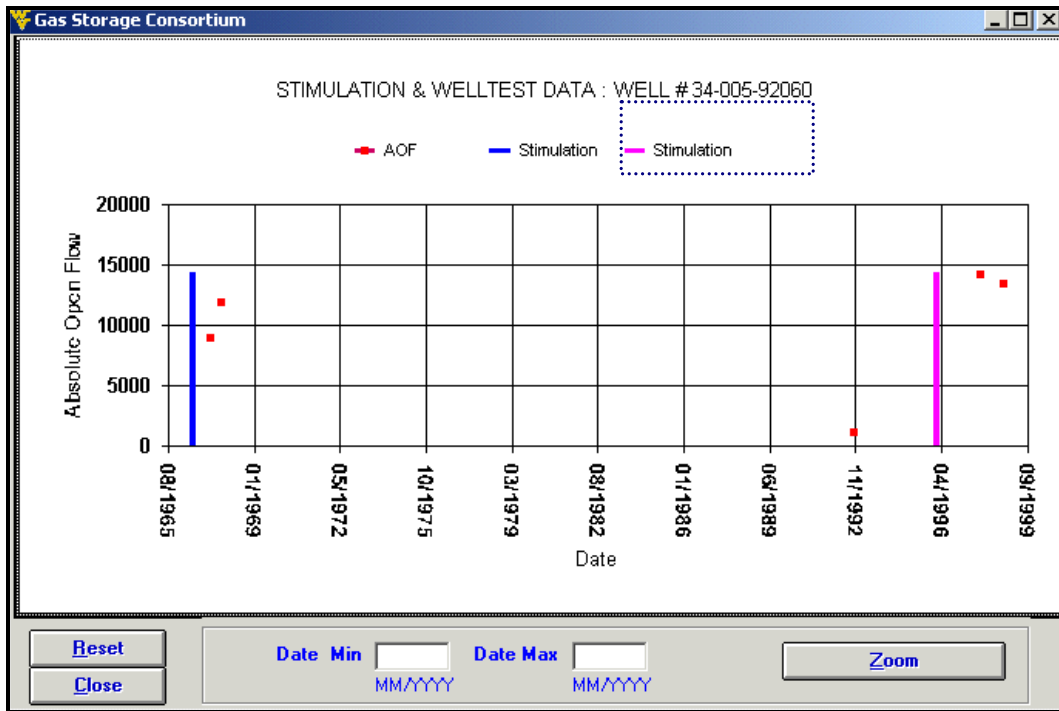
Fig47. Show Chart – Absolute Open Flow

WELL TEST ANALYSIS TOOL

Click the **Well Test Analysis** button [Well Test Analysis] and the following screen will pop up indicating different types of well tests that have done on the selected well
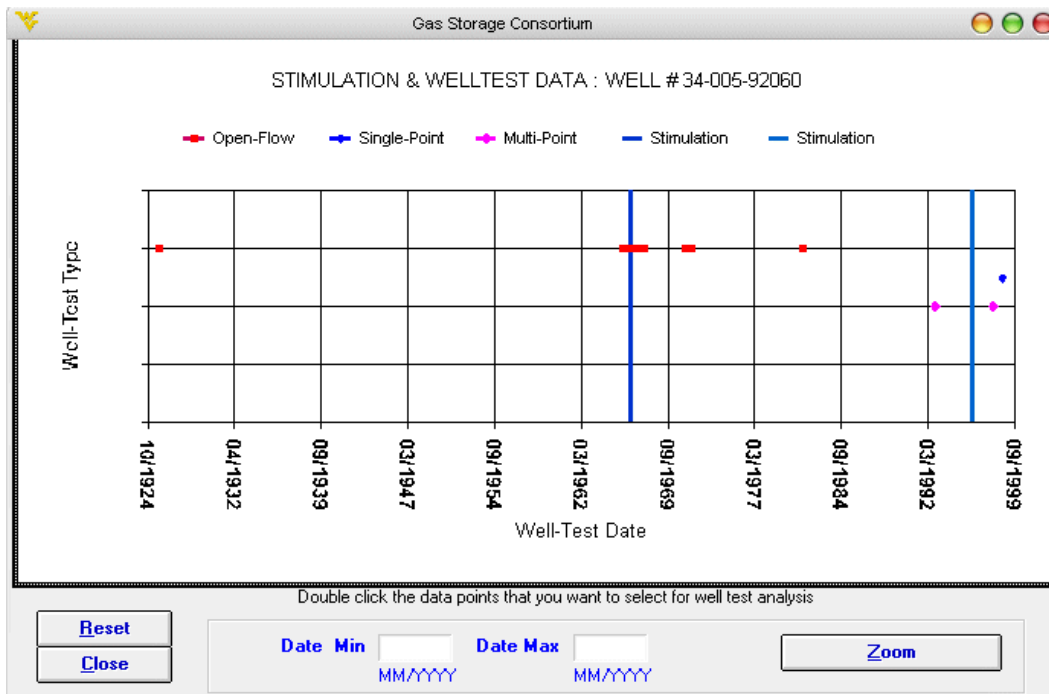
Fig48. Well Test analysis – Showing types of tests

To zoom the screen, type minimum and maximum date and press **Zoom** button. The screen will be zoomed between the dates typed
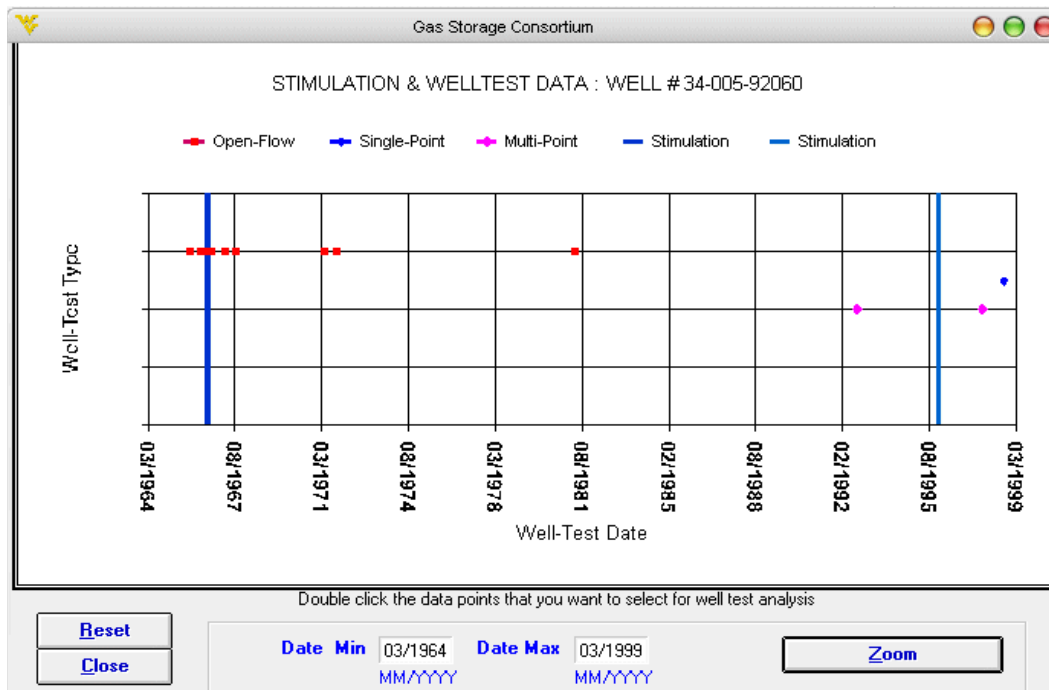
Fig49. Well Test analysis – zoomed

SELECTING WELL TESTS TO PLOT

Double click on the data points that you want to select for well test analysis. These points will be added in the Selected Well Tests list box.

You can remove the points from Selected Well Tests list box by selecting the well tests and then press Remove points button
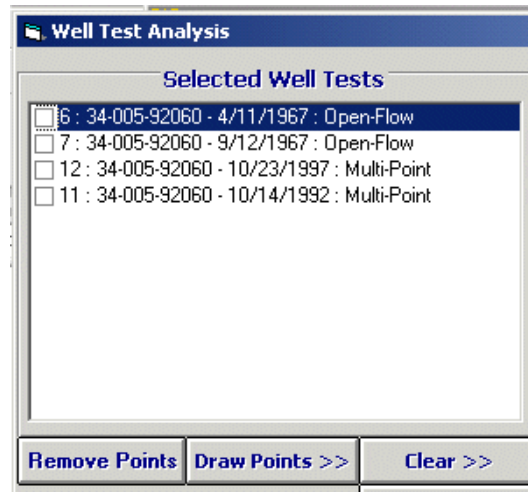
Fig50. Well-tests selected for analysis

Select the well tests that you want to draw and draw them by clicking 'Draw Points' button
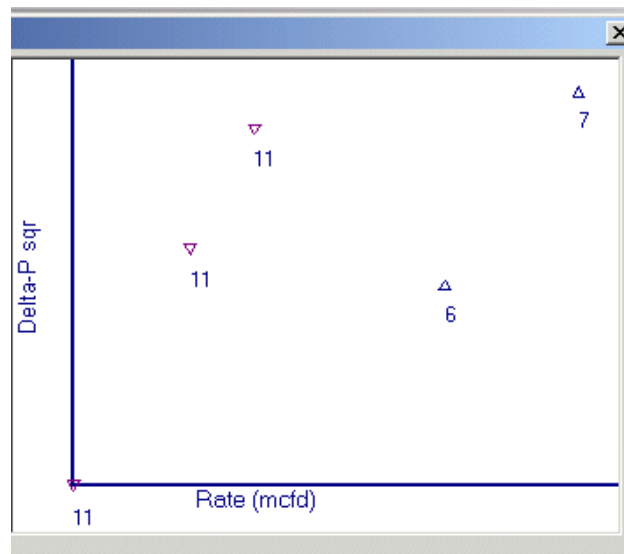
Fig51. Well-tests selected to find value of 'n'

CALCULATING SLOPE 'N'

Draw a line in the picture box keeping left mouse button held down
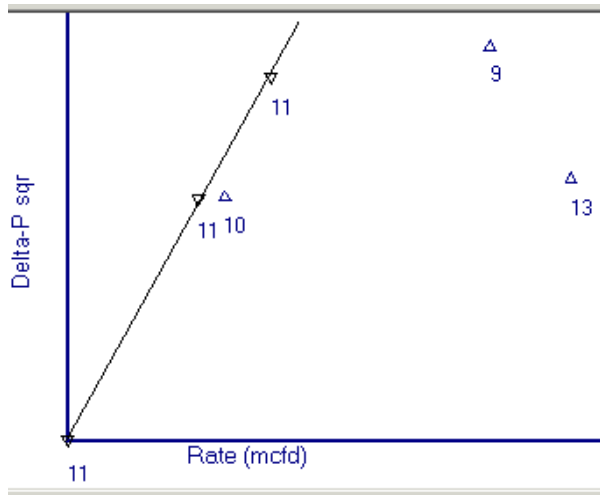
Fig52. Draw a line to find value of 'n'

Press Calculate n button to find the slope the drawn line
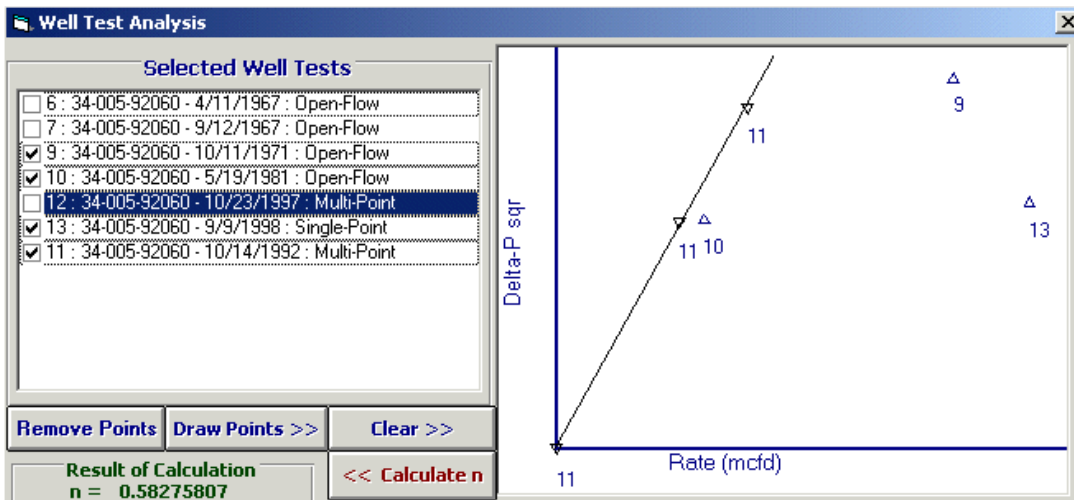
Fig53. Calculating value of 'n'

CALCULATING C, PEAK DAY, AOF

Press the **Calculate C, PDrate, AOF** button to find these values
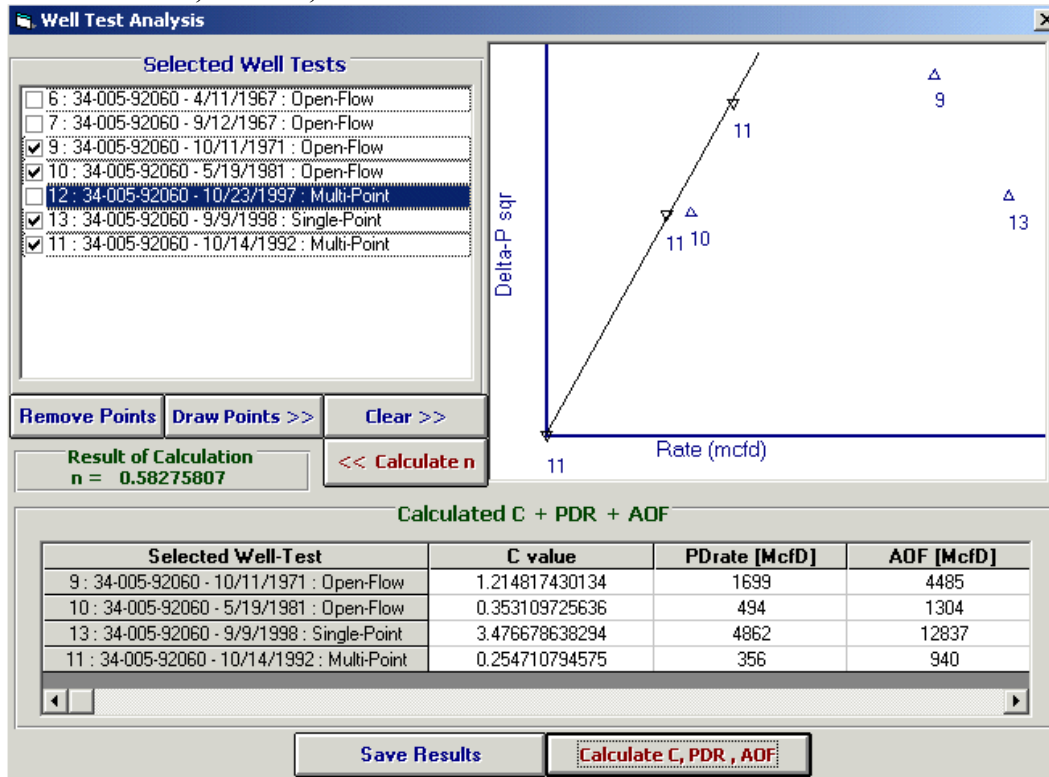
Fig54. Calculating C, PDR & AOF

SAVING THE WELL DELIVERABILITY PARAMETERS CALCULATED

To save the results click the **Save Results** ![Save Results] button. The new calculated well deliverability parameters would be added in the database
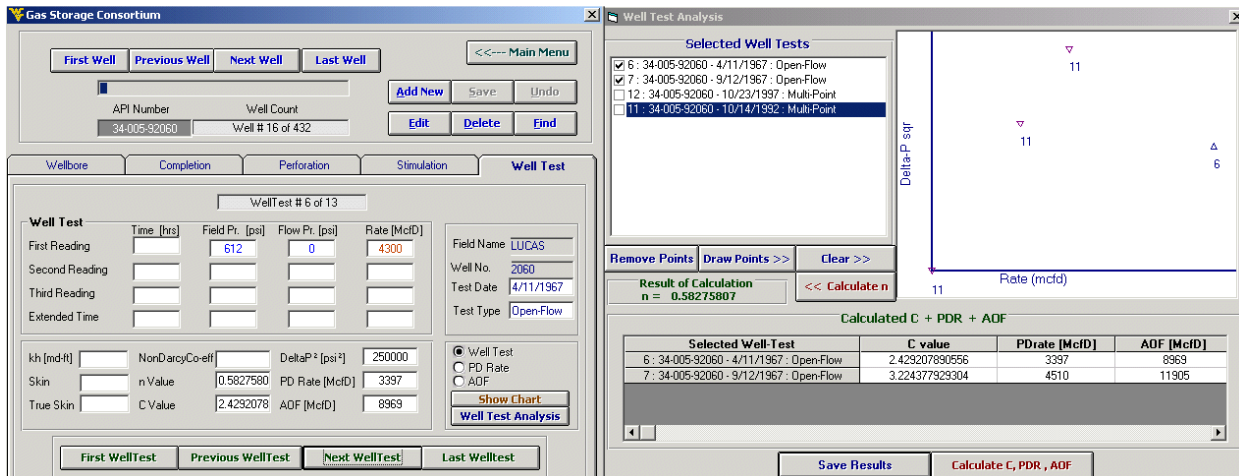
Fig55. C, PDR & AOF values saved in the database

SELECT WELL DATA

In this form the user can choose to select the data of the wells that he wants to look at. Following are a few ways he can choose the data

SELECTING A WELL BY STATE /COUNTY

The user selects the state first and then the county. All the wells will be selected for that county in the selected wells list box

Fig56. Selecting Ohio County

SELECTING A WELL BY STIMULATION YEAR

The user can select the option button for stimulated year and input the year values. If Select Wells button [Select Wells] is clicked then all the wells that have been stimulated between these years will be shown in the selected wells list box
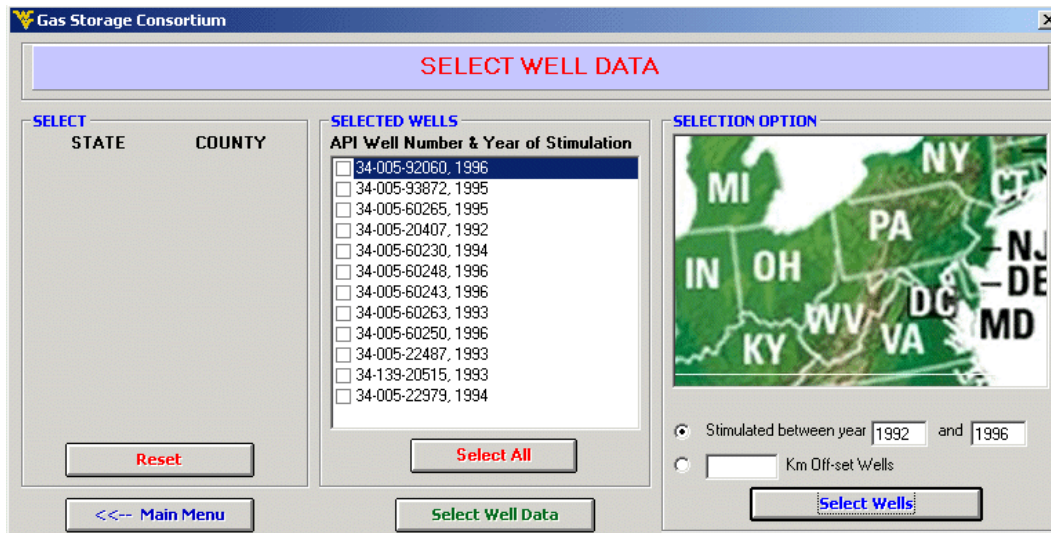
Fig57. Selecting wells according to stimulation year

SELECTING OFFSET WELLS TO A WELL

The user selects the offset option and the well near which he wants to find the off-set wells, and then enters the distance of off-set in kilometers. If Select Wells button is clicked then all the wells that are off-set of the selected well will be shown in the selected wells list box
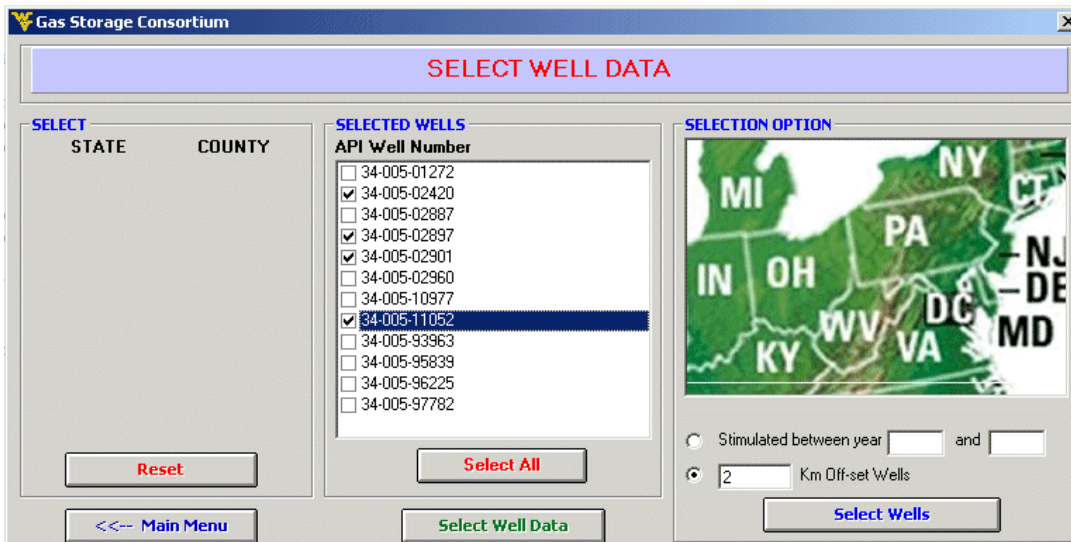
Fig58. Offset wells

SELECTING WELL DATA TO DISPLAY

When the wells for which the user want the data to be retrieved have been selected, click the Select Well Data button [Select Well Data] and select the parameters
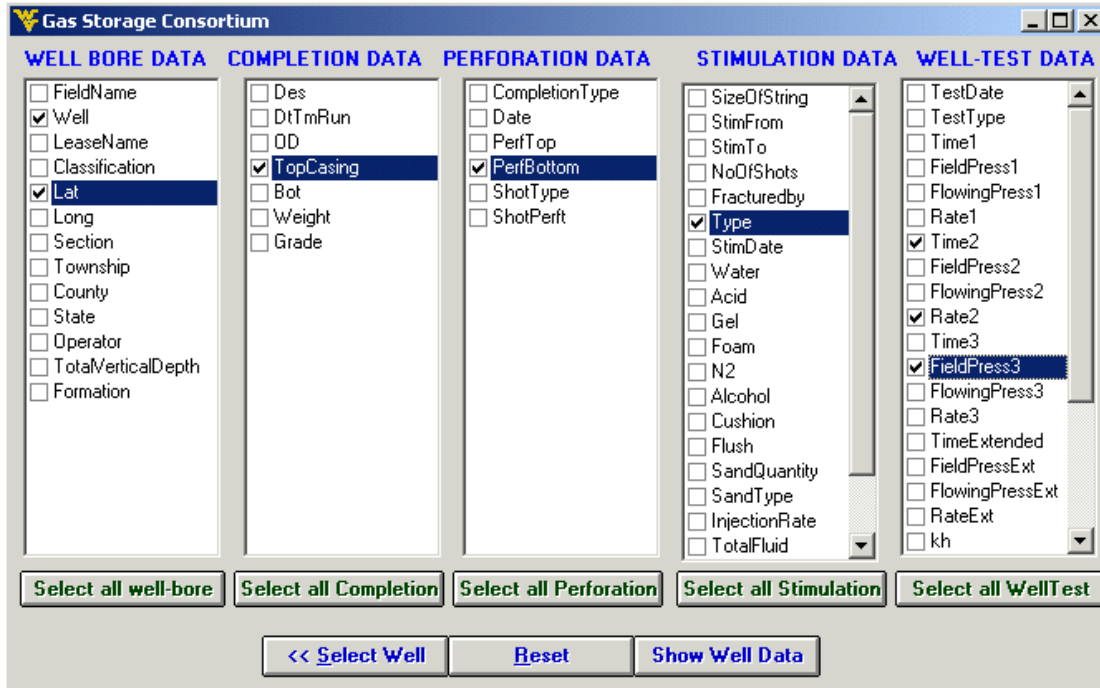
Fig59. Selecting Well Parameters

Click Show Well Data [Show Well Data] to retrieve the data
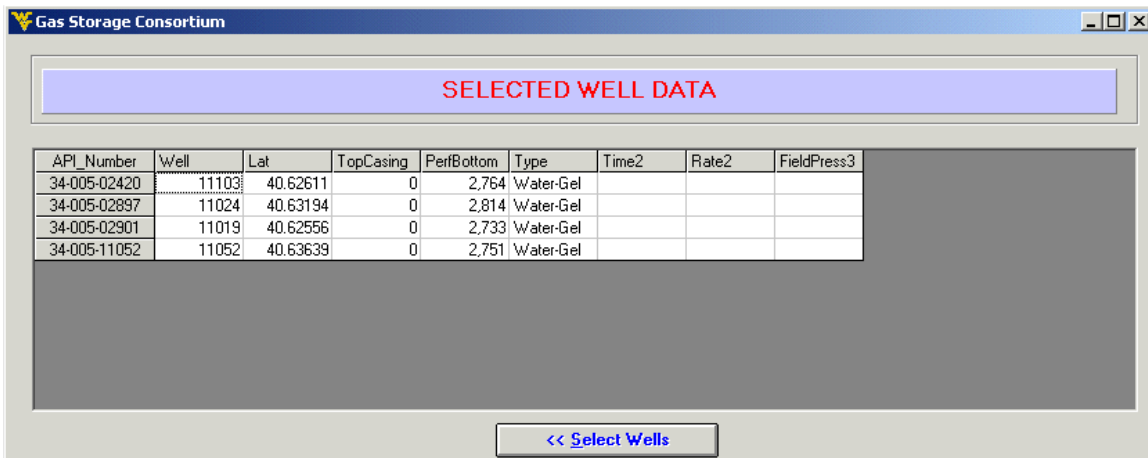
Fig60. Result of the wells & parameters selected

CONCLUSIONS

The first year of the project was completed successfully. A database software application was developed that included a module for gas storage well test interpretation. This software package was compiled and together with a user manual was included as part of this report. The software package is included in the accompanying CD.

Real-time Wellbore Integrity Monitoring

FINAL Report

Reporting Period Start Date: September 1, 2004
Reporting Period End Date: December 31, 2005

Principal Author:
Professor L. G. Chorn

Issue Date: May, 2006

DOE Award Number:
2809-CSM-DOE-1779

Colorado School of Mines
Department of Petroleum Engineering
1500 Illinois Street
Golden, CO 80401

Subcontractor:
WellDynamics Inc.
445 Woodline Drive
Spring, Texas 77386

DISCLAIMER:

"This report was prepared as an account of work sponsored by an agency of the United States Government. Neither the United States Government nor any agency thereof, nor any of their employees, makes any warranty, express or implied, or assumes any legal liability or responsibility for the accuracy, completeness, or usefulness of any information, apparatus, product, or process disclosed, or represents that its use would not infringe privately owned rights. Reference not necessarily constitute or imply its endorsement, recommendation, or favoring by the United States Government or any agency thereof. The views and opinions of authors expressed herein do not necessarily state or reflect those of the United States Government or any agency thereof."

Abstract

This report describes the work done under DOE Award Number 2809-CSM-DOE-1779, for the Gas Storage Technology Consortium during the period from October 1, 2004 through December 31, 2005, addressing the application of continuous pressure and temperature monitoring hardware to assess the integrity of tubing and casing in wells linking reservoirs used for natural gas storage with surface facilities.

The principal investigator, a graduate student, and representatives of WellDynamics, Inc performed the work described in this report. Successful results were achieved in the following subtasks:

- Compute and validate the theoretical pressure drop in a flowing wellbore during production operations, if the wellbore has pressure integrity, using OLGA™, a multiphase flow simulator.
- Acquire data sets (different wellbore architectures, reservoir conditions, and flow rates) from gas storage field operators to calibrate a multiphase flow model using Dun and Ros correlations for dry gas vertical flow.
- Develop a database of simulation results for use in model development leading to a nomograph for tubing integrity.
- Modify OLGA™ to predict flowing tubing pressure losses in vertical and deviated wellbores for a range of perforation sizes, tubing diameters, flow rates, gas compositions, and wellhead temperatures and pressures.
- Develop a nomograph for field operators to use pressure/temperature/flow rate data to evaluate tubing integrity.
- Identify suitable hardware for real time data acquisition.

Based on the results of these subtasks, it is clear that gas storage field operators may use this approach to monitor wellbore integrity in some architectures above a threshold flow rate.

Unsatisfactory results were obtained for the following subtasks:

- Identification of a suitable sensor hardware assembly with a low drift rate for permanent installation.

Based on the outcome of this subtask, gas storage field operators will not be able to permanently install pressure/temperature sensors at bottomhole to apply these results. Sensors may be run-in on a wireline to acquire an instantaneous measurement for integrity analysis.

Details of the research are provided in the body of the report.

Table of Contents

List of Graphical Materials

List of Tables

Introduction

Mechanical failures, water-loading, scale deposition and sand production in wellbore tubulars in long-lived natural gas storage reservoirs and salt domes represents a loss of efficiency in injection and withdrawal. Wellbore reliability is a priority for operators and state regulators.

The underground natural gas storage industry has an outstanding safety record and is striving to maintain its record by seeking out new, comprehensive methods to monitor tubular status. Testing presently requires extended shut-ins of wells and reservoirs to stabilize the system and then monitor the wellhead pressure; or running a wellbore caliber tool in the wellbore. Both of these techniques are expensive and subject to inaccurate results.

Conveniently, the petroleum industry has recently experienced dramatic advances in wellbore monitoring and flow control through the linkage of sensors at the reservoir – wellbore interface with remotely actuated valves. The sensors provide real-time data (pressure, temperature, fluid property, and flow rate) to the operator who can adjust subsurface valve settings to control oil, gas, and water influx to the well. "Downhole" sensors have longevity and reliability in high temperature, high pressure, and corrosive environments. Drift in absolute measurement value remains problematic. The ability to observe conditions in the wellbore with relatively inexpensive sensors offers the underground gas storage operator the tool to monitor the reservoir-to-surface link and demonstrate system reliability. Efficient wellbore performance is demonstrated by matching predicted "no-leak" pressure differentials between the wellhead and the formation to measured data.

Application of this technology to the natural gas storage industry's wellbore management issue requires the following technology advances:

- a non-isothermal transient flow gas well model with compositional phase behavior to predict pressure and temperature profiles between the well perforations and the wellhead under different flow rates;
- testing of downhole flow sensors (P and T) for their differential measurement sensitivity.

This research program delivers a predictive analysis tool to the Gas Storage industry that allows low cost, reliable testing capabilities.

Computational Work

Background

As part of the cost share structure of the research program Scandpower provided a limited license for the use of OLGA™, a multiphase tubing flow simulator with heat transfer and fluid property calculation capability. OLGA™ is the industry standard flow simulation tool developed collaboratively by Scandpower and several members of the international petroleum industry, using extensive databases of flowing well conditions.

OLGA™ was installed on a single user Windows operating system computer with a 1.2 Megahertz processor and 512K memory. Mr. Ryan London, M.S. candidate in Petroleum Engineering, began testing the software with example problems provided by Scandpower. A member of Scandpower's technical staff visited Colorado School of Mines and provided a brief user introduction session for Mr. London and the PI.

The simulator is designed to handle two and three-phase flow conditions in vertical and horizontal tubing configurations. One-dimensional, multiphase flow regimes accurately represented in OLGA™ include mist, annular, wavy, and slug flows for hydrocarbon and aqueous liquid phases flowing simultaneously with natural gas. The computational scheme subdivides the tubular along the axis of flow into segments and solves for pressure, temperature, phase velocities, and phase saturations. Heat transfer and phase properties are modeled at each time step along the tubular axis. The user can subdivide the tubular as finely or grossly as desired, but finer gridding results in dramatic increases in computation time.

Conservation of mass and momentum equations are solved using an analytic structure described by Ansara, A.M., et al[1],

$$-\left[\frac{dp}{dz}\right]_c = \left[\frac{g\rho_c}{g_c} + \frac{f_c V_c^2 \rho_c}{2g_c d(1-2\delta)}\right]$$

$$-\left[\frac{dp}{dz}\right]_l = \left[\frac{g\rho_l}{g_c} + \frac{2f_{lF} V_{sl}^2 (1-E)^2 \rho_l}{64 g_c d\delta^3 (1-2\delta)^3} - \frac{f_c V_c^2 (1-2\delta)\rho_c}{2g_c d\delta(1-\delta)}\right]$$

where variable nomenclature is standard for fluid dynamics. Subscripts refer to phases in the tubular. OLGA™ solves these simultaneous equations sequentially up the wellbore to forecast wellhead pressure and temperature.

Prediction of gas density and viscosities are required to predict pressure loss per unit distance. Both gas properties vary with temperature and pressure. As a consequence, any wellbore

---

[1] Ansara, A.M., et al[1], "A Comprehensive Mechanistic Model For Upward Two-Phase Flow in Wellbores," SPEPF, (1994).

modeling attempt requires property correlations or an equation of state. Accuracy in the density prediction is particularly critical to the successful pressure loss calculation.

No-Leak Nomograph Development

OLGA™ is a valuable modeling tool but represents a very large investment for gas storage operators. As a consequence, one goal for this project was the development of a simple, yet accurate vertical gas flow simulation tool. Mr. London developed a Visual Basic program that utilized the Duns and Ros Method to predict pressure gradient in a flowing well. The Basic program was fine-tuned against OLGA™ predictions over a wide variety of wellbore architecture and flow rate combinations.

The London program uses standard relationships for estimating fluid properties and multiphase flow relationships, as described below.

For fluid properties estimation, the user has the option of entering gas composition, specific gravity, or specific gravity and pseudo-critical properties. The molecular weight, if given specific gravity, is:

$$MW = 28.964 * specific\ gravity \tag{1}$$

Pseudo-critical temperature and pressure are:

$$T_{PC} = 169.2 + (349.5 * specific\ gravity) - (74 * specific\ gravity^2) \tag{2}$$

$$P_{PC} = 756.8 - 131 * specific\ gravity - 3.6 * specific\ gravity^2 \tag{3}$$

Reduced pseudo-critical properties are computed by dividing wellhead temperature and pressure by T_{PR} and P_{PR}, respectively.

The gas Z-factor must be computed by iteration. The initial Z_{guess} is set to one and the iteration proceeds as follows:

$$\rho_{PR} = (0.27 * P_{PR})/(T_{PR} * Z_{guess}) \tag{5}$$

$$Z = 1 + C_1 * \rho_{PR} + C_2 * \rho_{PR}^2 - C_3 * \rho_{PR}^5 + C_4$$

$$where:$$

$$C_1 = 0.3265 - 1.07/T_{PR} - 0.5339/T_{PR}^3 + 0.01569/T_{PR}^4 - 0.05165/T_{PR}^5 \tag{6}$$

$$C_2 = 0.5475 - 0.7361/T_{PR} + 0.1844/T_{PR}^2$$

$$C_3 = 0.1056 * (-0.7361/T_{PR} + 0.1844/T_{PR}^2)$$

$$C_4 = 0.6134 * (1 + 0.721 * \rho_{PR}^2) * \rho_{PR}^2 / T_{PR}^3 * e^{(-0.721 * \rho_{PR}^2)}$$

This calculation proceeds until a tolerance of 10^{-5} is reached.

Viscosities and densities are computed from the following relationships:

$$\mu = 1.*10^{-4} * K * e^{(X*rho^{Y})}$$

$$\begin{aligned}
&where: \\
&K = (9.379 + 0.01607 * MW)/(209.2 + 19.26 * MW + T_{WH}) * T_{WH}^{1.5} \\
&X = 3.448 + (986.4 / T_{WH}) + 0.01009 * MW \\
&Y = 2.447 - 0.224 * X \\
&rho = 1.4935 * 10^{-3} * P_{WH} * MW /(Z * T_{WH})
\end{aligned}$$

(7)

$$\rho = 144/1545 * P_{WH} * MW /(Z * T_{WH}) \tag{8}$$

Confirmation of the consistency of the London program with the results of the more robust OLGA™ program provides the gas storage operator with a predictive tool appropriate for withdrawal operation monitoring in a wellbore with no thru-tubing leaks.

By applying the principles of conservation of mass and linear momentum, the steady-state pressure gradient equation is:

$$\left(\frac{dp}{dL}\right)_{total} = \left(\frac{dp}{dL}\right)_{friction} + \left(\frac{dp}{dL}\right)_{hydrostatic} + \left(\frac{dp}{dL}\right)_{acceleration} \tag{9}$$

The acceleration term can be neglected at higher pressures so the last term on the right hand side of equation (1) can be discarded. Given that measurements take place only at the sand face and the wellhead, we will assume an average pressure difference between the two points can be described as:

$$(\Delta p)_{total} = (\Delta p)_{friction} + (\Delta p)_{hydrostatic} \tag{10}$$

where:

$$(\Delta p)_{total} = (p_{bh} - p_{wh})$$

$$(\Delta p)_{friction} = \frac{f\rho L V^2}{D}$$

$$(\Delta p)_{hydrostatic} = \rho g h$$

The density and velocity terms can be accurately calculated from the pressure, temperature, flowrate and pipe characteristics leaving the friction factor the only unknown. There is one equation, and one unknown:

$$(\Delta p)_{friction} = (\Delta p)_{total} - (\Delta p)_{hydrostatic}$$

$$(\Delta p)_{friction} = (p_{bh} - p_{wh}) - \rho g h$$

$$\frac{f\rho L V^2}{D} = (p_{bh} - p_{wh}) - \rho g h \qquad (11)$$

$$f_{Method1} = \frac{[(p_{bh} - p_{wh}) - \rho g h]D}{\rho L V^2}$$

This calculation for friction factor assumes that the friction pressure loss term is responsible for all pressure loss remaining after the elevation pressure loss term is accounted for. This term is the average friction factor throughout the length of the pipe at steady state conditions.

Next, the friction factor will be calculated through correlations that approximate the Moody friction factor diagram.

$$f = f(N_{Re}, \frac{\varepsilon}{D})$$

$$N_{Re} = \frac{\rho D V}{\mu}$$

$$\rho = f(p, M_w, z, T)$$

$$z = f(p, M_w, T) \qquad (12)$$

$$V = f(p, Q, D, T)$$

$$\mu = f(\rho, M_w, T)$$

Therefore, the friction factor is a function of the following variables:

$$f_{Method2} = f(p, T, \varepsilon, D, M_w) \qquad (13)$$

If the friction factor calculated using equation (11) is plotted versus the equation (13) approach, the result should be a straight line, the only deviation should be due to averaging, heat losses, and small contributions from the neglected acceleration term.

When a leak does occur, the value for friction factor in Method 1 will rise and be disproportionate to the value for friction factor in Method 2 because of how Method 1 calculates the friction factor. If a leak occurs, the individual pressure components will be:

$$(\Delta p)_{total} = (\Delta p)_{friction} + (\Delta p)_{hydrostatic} + (\Delta p)_{leak} \qquad (14)$$

However, equation (11) will still calculate the friction factor based upon:

$$(\Delta p)_{friction} = (\Delta p)_{total} - (\Delta p)_{hydrostatic} \qquad (15)$$

Thus, the total pressure drop will increase because of the leak, and Method 1 will errantly allocate the additional pressure drop to the friction term, thereby making the friction factor larger. However, Method 2 relies solely on the value of the pressure and temperature (instead of the difference) and will still be able to successfully calculate the correct friction factor. If Method 1 is

plotted against Method 2 and the points begin to bend upward, the numerical model will have successfully indicated to the operator that a leak has occurred.

The ultimate purpose of modeling the tubing flow regime and fluid properties is to determine the appropriate magnitude of pressure loss associated with frictional losses in the tubing. Frictional losses present themselves as a pressure loss. The pressure difference between the wellhead and the reservoir is a combination of the change in gravity head and the frictional losses. Gravity head calculation is sensitive to the aggregate density of the column of fluid loading the wellbore and exerting a pressure, ρgh, on the bottom of the well, at the reservoir interface. Because we are concerned with a gas-dominated flow, the frictional pressure loss will be quite low. The gravity head as shown in Figure 1 dominates the pressure difference between the wellhead and the reservoir for a dry gas flow. Figure 1 illustrates the magnitude of the gravity head contribution to the pressure difference as a function of wellhead flow rate and wellhead pressure. Wellhead pressure is a proxy for the relative density of the fluid column, assuming temperature gradient and fluid composition (gas and water weight fractions) are held constant.

As expected, the contribution of the frictional losses to the pressure difference is small, ranging from 10 to 35 percent for the field data examined. Any modeling of the wellbore must exhibit accurate density calculations for the fluid column. The addition of water to the gas phase, as a mist, will increase the column density. Data contributed by GSTC members showed only low water fractions, less than a few pounds of water per million standard cubic feet of gas. While gas density can change significantly with pressure and temperature, water density is relatively constant. Consequently, the wellbore flow model calculations assume only the aggregate density based on the weight fraction of water at wellhead conditions plus weight fraction of the gas phase times the empirical relationship for gas density as a function of pressure and temperature.
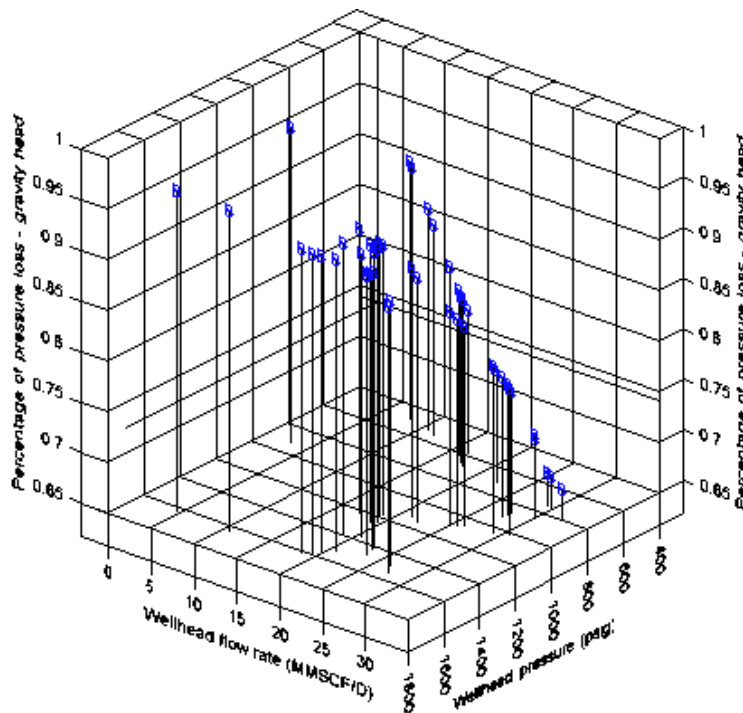
Figure 1. Fraction of flowing tubing pressure loss associated with gravity head, as a function of flow rate and wellhead pressure.

OLGA™ calculations

OLGA™ calculates the flow field profile from the bottom-hole conditions to the surface over small length steps. At each incremental length, coming up the tubing string, new temperature, pressure and fluid properties are computed which reflect volume changes of the gas/water mixture. The user must estimate heat transfer properties of the wellbore in addition to the geothermal gradient. Further, the relative surface roughness of the tubing must be estimated. The combination of these estimates provides for some fine-tuning latitude to match field measurements with computed values.

Figure 2 illustrates the effect of heat transfer and geothermal gradient estimates on the prediction. OLGA™ was run on a field data set with a measured bottomhole temperature of 568 °R and a measured wellhead temperature of 530 °R. The x-axis is the measured wellhead flow rate in MMSCF per day and the y-axis is the OLGA™-computed wellhead temperature. Three wellhead pressures are shown. A perfect agreement between measured and computed would result in a straight-line with a 0° slope at 530°R. The impact of this inaccuracy will be seen in the fluid properties and ultimately in the calculation of the gravity head, ρgh. This causes a limitation in the detection limit of a perforation at low tubing pressures.
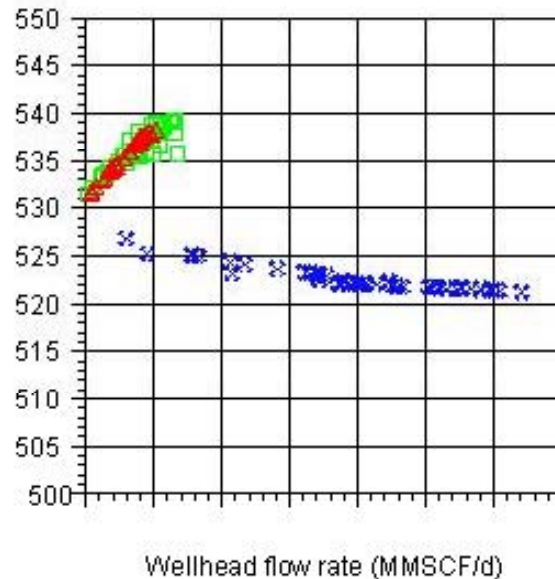
Figure 2. Effect of wellhead flow rate on Olga™-predicted wellhead temperature (°R).

Effect of Perforation(s) on Wellbore Pressure Profile

Small perforations or holes in the tubing will allow the release of gas into shallower zones above the reservoir. The loss of gas volume through the perforation will cause a non-linear pressure decrease in the tubing, deceleration and Joule-Thompson cooling of the gas flow field above the perforation, resulting in a lowered gas pressure at the wellhead.

The amount of gas released to the overburden is a function of tubing pressure, temperature, depth of the perforation (backpressure against outflow), and perforation diameter. There are no known theoretical approaches to estimate the gas flow rate through a perforation. Consequently an attempt was made to estimate the maximum volumetric loss rate using a simple orifice equation. This approach will over-estimate the loss rate since it assumes the orifice is in-line with the principle direction of flow, rather than at a 90° angle to the flow as with a perforation.

The equation[2] for orifice flow is:

$$Q = C_c A_o \sqrt{\frac{2\Delta p / \rho}{\left(1 - C_c^2 \left(\frac{A_o}{A}\right)^2\right)}}$$

$$C_c = 0.595 + 0.29 \left(\frac{A_o}{A}\right)^{2.5} \tag{16}$$

Examples of the volumetric loss rate, in SCFD, are shown in Figures 3 and 4 for representative tubing diameters, perforation sizes, and wellbore pressures at 100 and 250 feet deep locations. The results of the calculation indicate relatively low gas volumes per day will be lost under conditions typically observed under conditions commonly observed during withdrawal. However, over time, a shallow zone can be significantly pressured up with the "lost" gas resulting in migration updip and potentially release to the surface either through fractures or outcrops.

Using OLGA™ to Calculate Effect of Tubing Perforations on Wellbore Pressure Losses

The present release of OLGA™ incorporates an option to compute the effect of cross-flow between two zones. The option provides the ability to locate the zones vertically, set the size and number of perforations in each zone, and the pressures in the zones.

This option was used to simulate the effect of a tubing perforation near the surface, i.e., at a low backpressure. The depth of the tubing perforation fixes the backpressure by assuming a pressure gradient of 0.6 psi/ft.

One perforation in the tubing was assumed and the flow field computed. Six perforation diameters were considered (0.0625, 0.125, 0.25, 0.5, 0.75 and 1.0 inches) in the study. A matrix of results were compiled, including: bottomhole pressure and temperature, wellhead temperature and pressure, and bottomhole and wellhead flowrates for various wellbore architectures. A single gas composition was used for all simulations. The composition is shown in Table 1.

---

[2] E. Shashi Menon, Gas Pipeline Hydraulics, Taylor and Francis Publishers (2005).
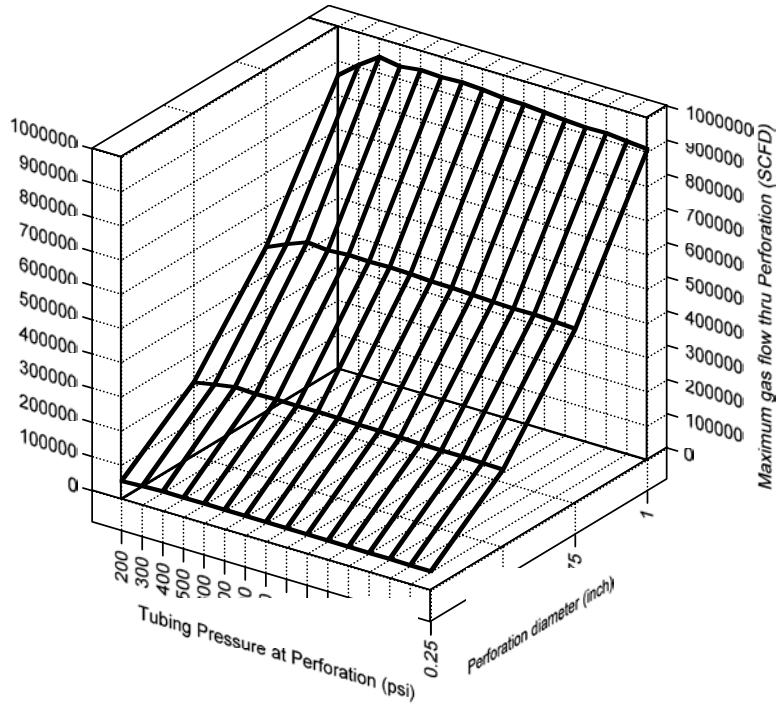
Figure 2. Maximum gas loss through a perforation at 100 feet (overburden pressure = 60 psi) given a perforation diameter (y-axis) and local tubing pressure (x-axis).
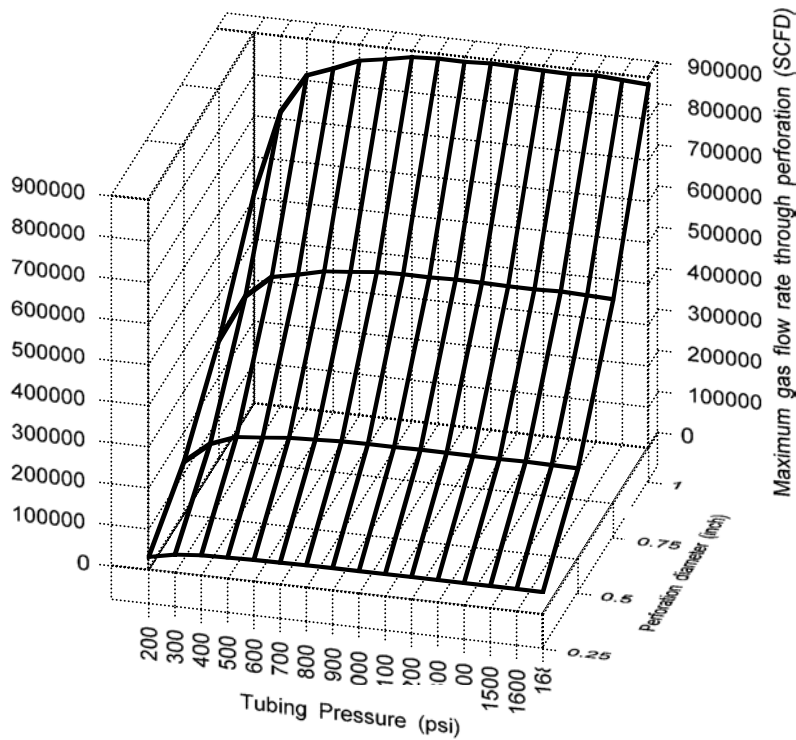
Figure 3. Maximum gas loss through a perforation at 250 feet (overburden pressure = 150 psi), given a perforation diameter (y-axis) and local tubing pressure (x-axis).

Gas Component	Mole Percent Composition
Carbon Dioxide	0.7095
Nitrogen	0.9105
Methane	95.6709
Ethane	2.3638
Propane	0.2499
n-Butane	0.0482
i-Butane	0.031
n-Pentane	0.0069
i-Pentane	0.007
n-Hexane	0.0023

Table 1. Gas Composition for simulations (based on a gas composition provided by a GSTC member)

Field Data Set Acquisition

Members of the Gas Storage Technology Consortium (GSTC) anonymously provided six data sets that were used for simulator calibration and to establish autoclave test conditions for the pressure and temperature sensor package.

The data sets contain hourly surface temperature, pressure and flow rate data over periods from as short as six months to as long as nine years. Reservoir temperatures and pressures are included in the data sets as measured in a shut-in observation well some distance from the well under study.

Description of Field Data

The following table gives the range of parameters within the six data sets.

	Minimum	Maximum
Wellhead tubing diameter	2.041 in	6.366 in
Bottom-hole tubing diameter	2.041 in	7.00 in
Wellhead temperature	530 °R	530 °R
Bottom-hole temperature	530 °R	590 °R
Liquid-Gas ratio (STB/SCF)	0.00	5×10^{-7} (20 lbs/MMSCF)
Wellhead pressure	315 psig	1855 psig
Bottom-hole pressure	349 psig	2084 psig
Measured delta p	33 psig	568 psig
Flow rate (MMSCF/day)	0.279	60.7

Table 2. Field data parameter ranges

All data and calculated results are reported in American engineering units (inches, °R, psig, MMSCF/day, feet/sec, ft/sec, stock tank barrels/standard cubic feet, lb_m/ft^3, etc.).

Data included 76 measurements with non-zero Gas-Liquid ratios. Analysis indicates that mist flow is the likely flow regime for these two-phase flow situations, but at these low liquid to gas

ratios the presence of water is inconsequential to the pressure loss calculations. Consequently, all OLGA™ simulations were performed with a zero water fraction.

Hardware testing

Research staff at WellDynamics, Inc. developed a qualification program in context with the objectives set out in the research proposal. The basic specifications for the new monitoring system are presented below.

ITEM	DESCRIPTION
Size:	3 ½" and 2 7/8" tubing compatible
Multi-Drop Capability:	6 x Dual
Data Rate:	2 gauges per second
Operating Voltage:	24.0 + 4.0/-12.0 VDC
Operating Temperature:	0º to 125º C, limit 150C
Temperature Accuracy:	± 1º C
Temperature Drift:	< 2º C/year
Pressure Range:	10,000 psi
Pressure Accuracy:	± 0.1% full scale
Pressure Resolution:	< 0.5 psi
Pressure Drift:	< 5.0 psi/year @100º C

Table 3. Outline specifications for low cost monitoring unit

The testing program was designed to address the following critical milestones for the low cost monitoring project;

- To complete the packaging concept for a dual pressure and temperature monitoring unit, with the ability to multi-drop these units in wells with multiple zones,

- Successfully complete a long term test at full rated temperature on the downhole electronics board, and

- Successfully verify the performance of a select piezo-resistive pressure transducer as a replacement to the high cost quartz sensors used in the offshore markets.

Following completion of the final packaging concept, a bench assembly of a fully populated mandrel assembly was executed with several minor design changes. These design changes were largely associated with the chassis and housing for the electronics that required some dimensional adjustment based on minor size discrepancies for the electronic components.

The production drawings were updated following the prototype assembly and new production builds were executed for the start of the full prototype qualification phase as per WellDynamics internal standards for pressure, temperature and vibration.

The production unit is shown in Figure 4, detailing a clamp-on style mandrel with 2 pressure sensors, electrical bus connections (in and out) and a 3rd electrical connection for a position sensor gauge (in wells where flow control systems may be run).
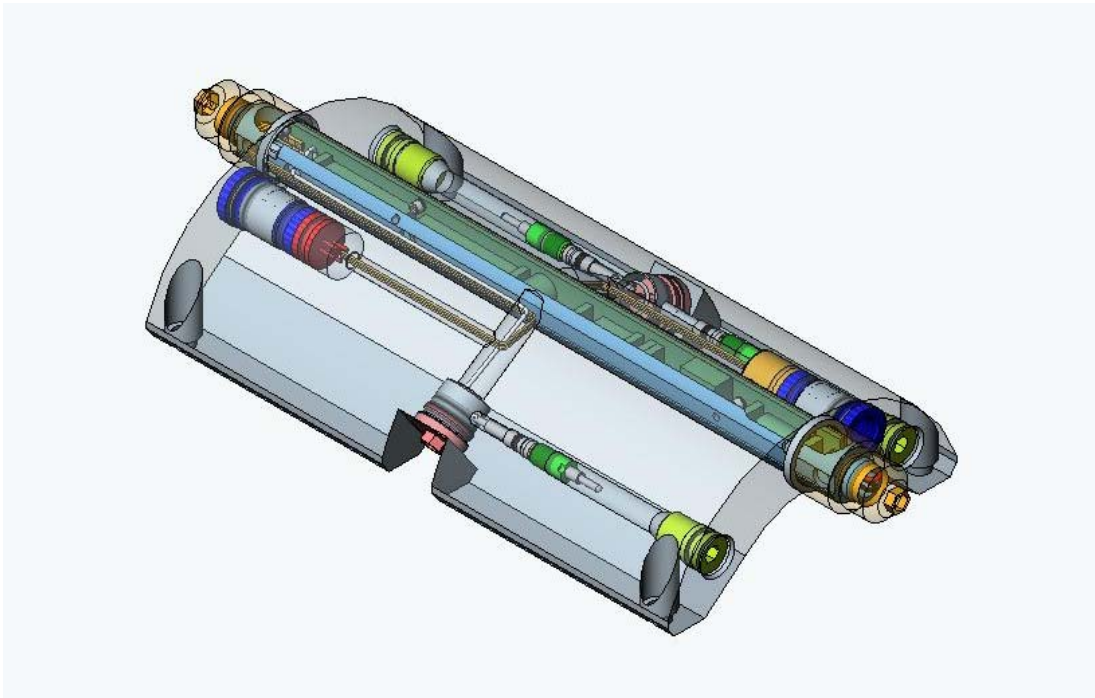
Figure 5: Solidworks™ layout drawing illustrating the clamp-on style,
low cost monitoring mandrel.

Results

Computational

The London model was used to predict "no-leak" pressure drops in wellbores. Screenshots from the London model are provided in Appendix A. The model allows the user to select several alternative data input approaches and two computational methods for determining bottomhole pressure, given a wellhead pressure, flowrate, gas composition and temperatures.

The London gas flow model was benchmarked against "no-leak" OLGA™ simulations.   The comparative accuracy of the London model was within pressure measurement tolerance. Computed bottom hole pressures were usually within five psig of the pressure measured in the field. The computed pressure difference (bottom hole minus wellhead) was always less than a 2.5 percent error compared to the measurements. Figure 6 shows the percentage error as a function of the wellhead gas flow rate (MMSCF/d) in a 6.34 inch ID wellbore with reservoir depth of approximately 2750 feet.

The error distribution indicates the pressure loss predictions may be inaccurate over the range of flow rates with increasing error magnitude at lower differential pressures. The pressure gauges used may not be sufficiently accurate to measure the small (order 7 percent of the reservoir pressure) differentials observed. Also, the bottom hole pressure was acquired at an offset well and may suffer from non-equilibrium conditions. Also of concern is the accuracy of gas density estimates at low tubing pressure. Errors in density propagate through the gravity head estimate and appear as differences in computed versus measured pressure drop.
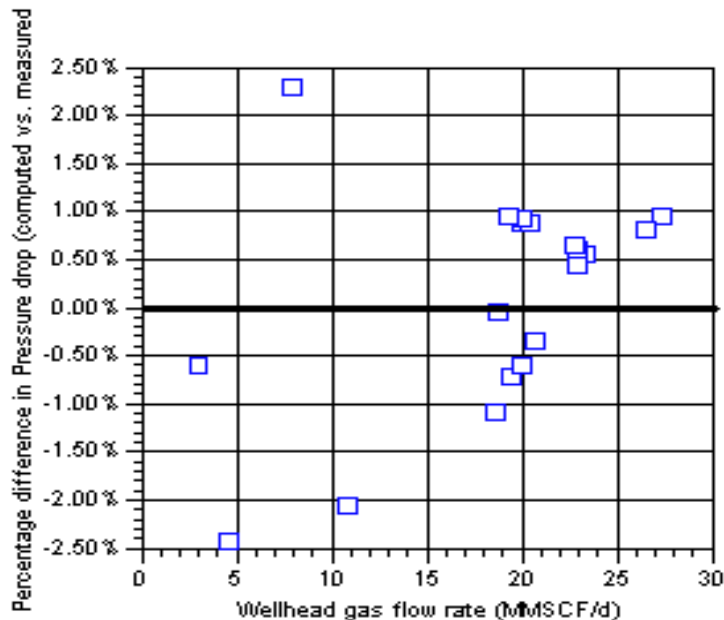
Figure 6. Example of error in computed versus measured pressure drop as a function of gas flow rate.

OLGA was used to simulate the effect of a single tubing perforation under different flowing conditions in the six wellbore architectures described by the field data sets. Approximately

24,000 simulations were performed to understand the combination of variables' effect on the computed pressure loss due to friction and loss of gas through the perforation.

A suite of results for a particular wellbore architecture are shown in Figures 6 through 10 as an illustration of the OLGA simulations. The total pressure loss (dP) between the wellhead and the reservoir is computed in combination with the gravity head of gas. The total pressure loss minus the gravity head is the flowing or frictional pressure loss of interest. The "no leak" data points are from the London model. The pressure loss estimates correlate well, as expected, with the wellhead gas Reynolds number ($\rho\mu DV/\mu$).
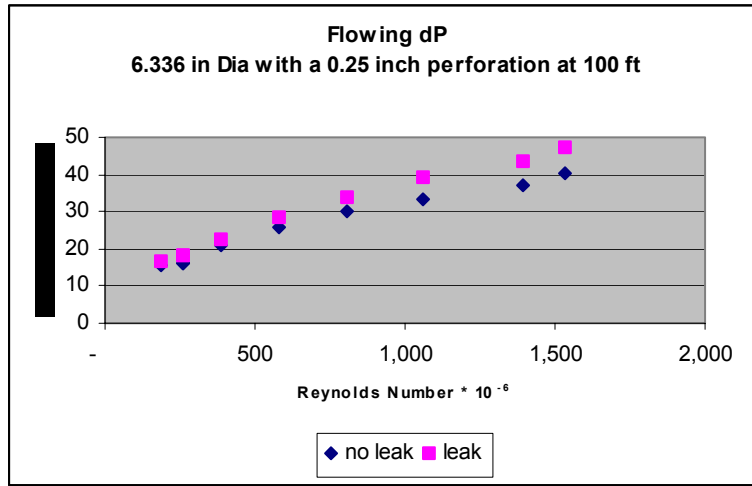
Figure 7. Frictional and leak pressure losses as a function of wellhead Reynolds number for a 0.25-inch diameter perforation at 100 feet below the wellhead.
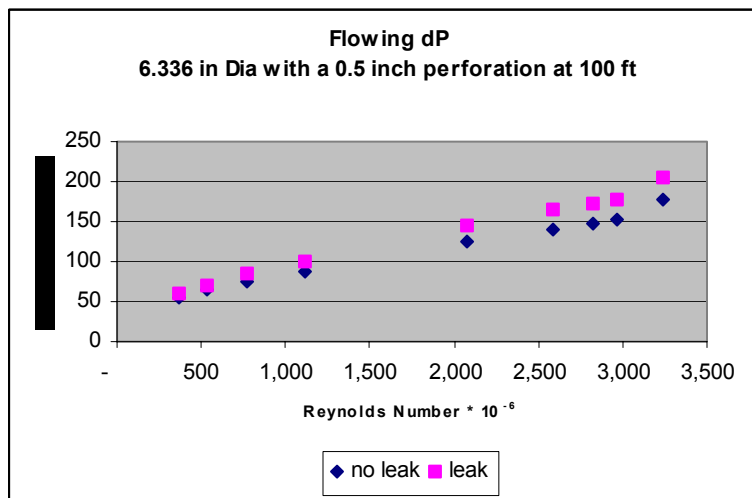
Figure 8. Frictional and leak pressure losses as a function of wellhead Reynolds number for a 0.5-inch diameter perforation at 100 feet below the wellhead.

Flowing dP
6.336 in Dia with a 0.75 inch perforation at 100 ft
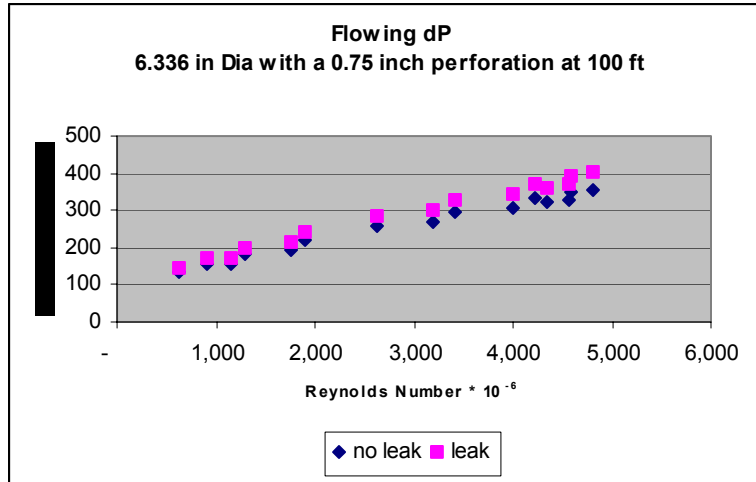
Figure 9. Frictional and leak pressure losses as a function of wellhead Reynolds number for a 0.75-inch diameter perforation at 100 feet below the wellhead.

Flowing dP
6.336 inch Dia with a 1.0 inch perforation at 100 ft
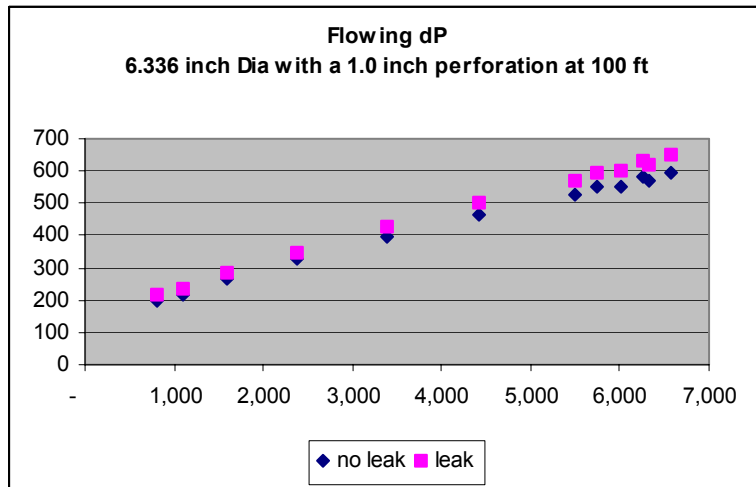
Figure 10. Frictional and leak pressure losses as a function of wellhead Reynolds number for a 1.00-inch diameter perforation at 100 feet below the wellhead.

The "no-leak" frictional pressure losses are a linear function of the wellhead Reynolds number, as expected, for such highly turbulent flows. Incremental pressure losses associated with the existence of a tubing leak are not linear functions of the Reynolds number. This is explained by the orifice calculations and illustrated in Figures 2 and 3. The pressure loss due to a tubing leak is also a function of tubing pressure that is indirectly associated with the gas flow rate in the tubing. Figure 11 shows the effect of perforation diameter on the incremental pressure loss due to a tubing leak.   It is clear that above a particular perforation diameter and differential pressure across the perforation, pressure loss due to a tubing perforation is independent of perforation diameter.

We compare the incremental pressure losses due to a tubing leak for a 6.336-inch diameter tubing with a 2.334-inch diameter tubing as a function of Reynolds number in Figure 12. Clearly, the effect is approximately the square of the tubing diameter of the total pressure loss. Consequently, small tubing perforations should be easier to detect in small diameter tubing.
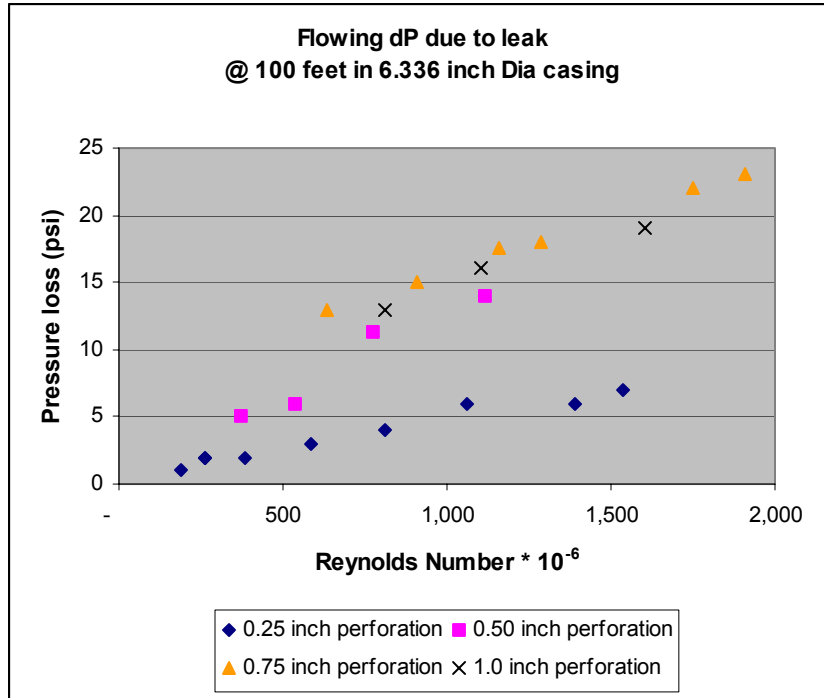
Figure 11. Effect of perforation size on pressure loss in a 6.336-inch diameter wellbore.
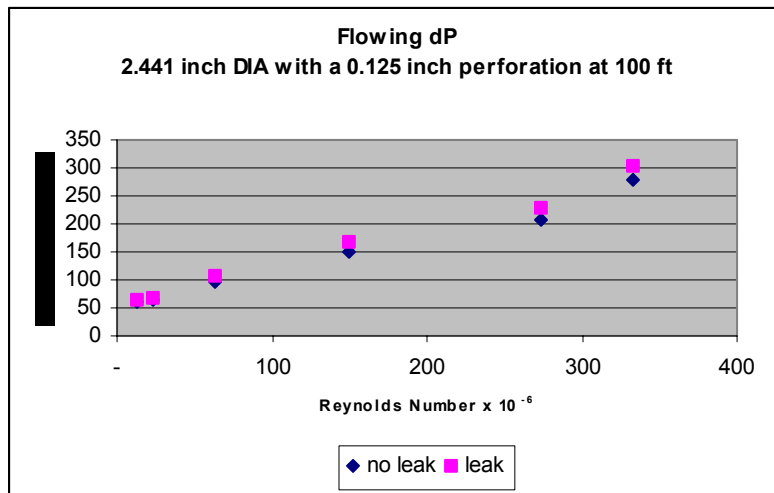
Figure 12. Effect of perforation on frictional pressure drop in a 2.441-inch diameter tubing.

For comparison with Figure 11, we consider the effect of perforation diameter at 100 feet in a 2.441-inch tubing on frictional pressure loss in Figure 13. It is clear that in small diameter tubing, the effect of perforation diameter on frictional pressure loss is independent of perforation size.

All comparisons, to this point, have been made for perforations at 100 feet below the wellhead. The impact on pressure should be at a maximum near the wellhead since backpressure from the formation is low, relative to wellhead pressure. OLGA™ simulations were performed for a suite

of perforation dimensions in a 2.441-inch tubing 250 feet below the wellhead. These results are shown in Figure 14. From this simulation suite, we see that the absolute frictional pressure loss is a strong function of tubing pressure, but is insensitive to perforation dimension.
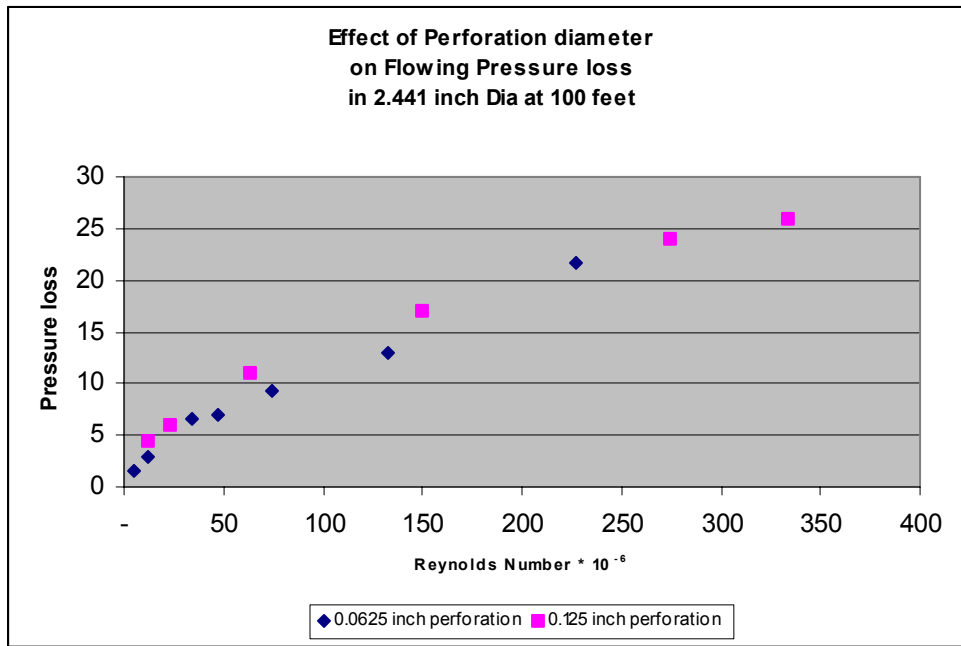
Figure 13. Effect of perforation diameter in a 2.441-inch tubing on pressure loss.
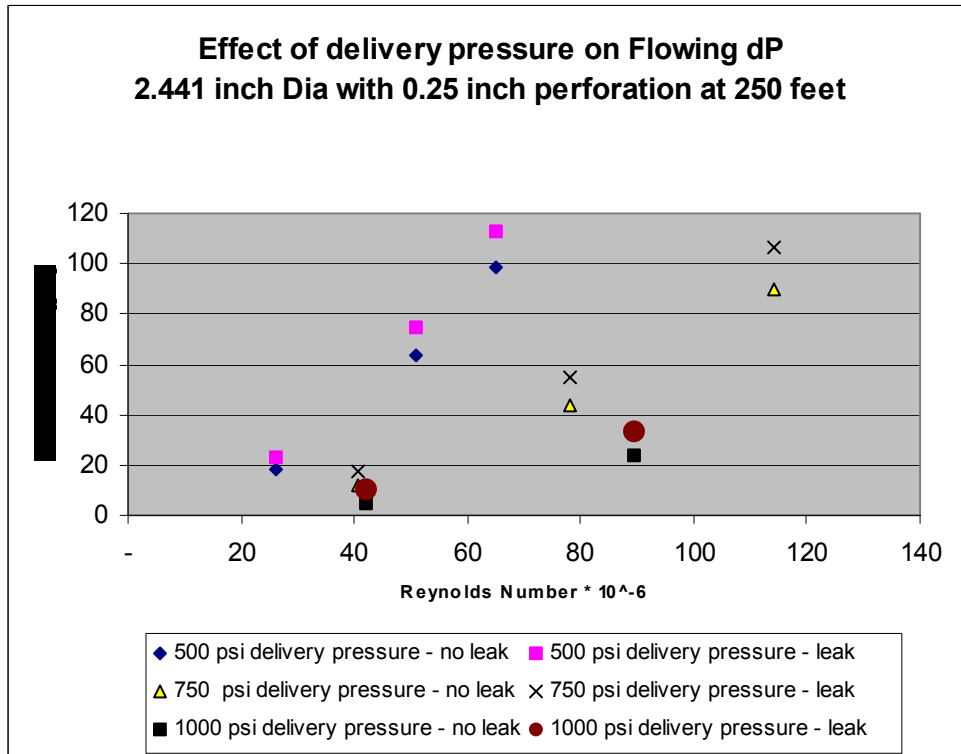
Figure 14. Effect of perforation diameter in a 2.441-inch tubing as a function of tubing pressure.

Hardware

Electronics

The basis of the electronics design was around reducing parts count, reducing assembly time and increasing reliability. The design is based on predominantly through-hole parts based on the fact that solder connections are more reliable and assembly requires less technician experience. Small robust micro-connectors were employed to speed overall assembly time.

The PCB assembly is shown in Figure 15, illustrating its compact size and relatively small number of electronic components.

The electronics were tested at the full rated temperature (125ºC) for more than 1 calendar year. The pressure was held at a constant 3,000 psi with cycling at calibration intervals. The reference pressure and temperature system is a quartz-based reference known for both its accuracy and repeatability.

No system failures were recorded during the long-term test.
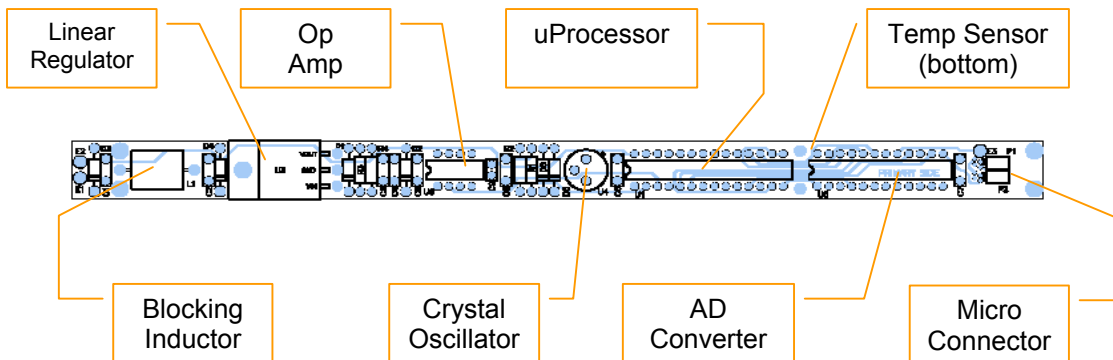
Figure 15. Downhole pressure/temperature electronics package.

Sensor Drift Testing

A collection of piezo-resistive sensors were tested with the electronics assemblies for a long period. These sensors are based on a strain bridge design where the arms of the bridge are of piezo-resistive material as illustrated in Figure 16.
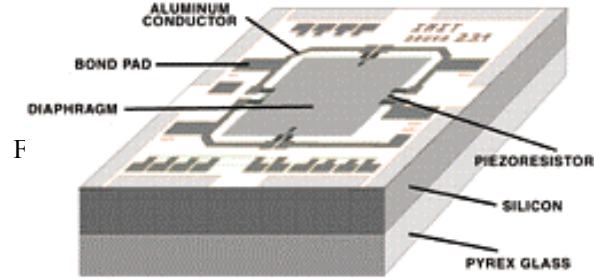
Figure 16. Schematic diagram of piezo-resistive sensor.

The piezo-resistive sensors were meant to be more stable than the first generation bonded counterparts as the strain bridge arms are physically part of the silicon rather than attached (glued).

In excess of 7,000 observations were taken at four temperatures to calculate the sensor coefficients for the test sample. The resulting pressure measurement is expressed as an error in PSI from the control calibration (a quartzdyne) unit.

The sensor was held at 3900 psi and 125ºC and calibration data was thn collected over four months with the error calculated using the initial coefficients vs. Quartzdyne reference. Note that the histogram "amplitude" indicates number of samples taken for the calibration.

The results for the long-term stability tests were not favourable indicating a drift characteristic well outside the stated specification range. Figure 17 shows the results obtained at the sample points.
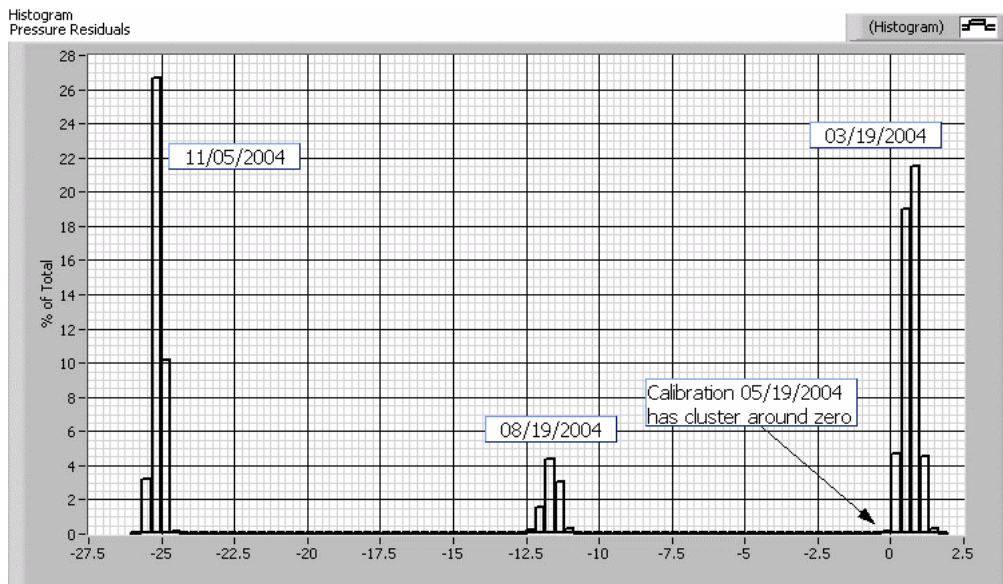
Figure 17. Histogram of pressure residuals collected for the sensor calibration test indicating significant drift of the piezo-resistive unit.

The drift issue has remained unresolved through the duration of this project.

Interpretation of Results

This program has successfully evaluated the effect of a tubing perforation on the frictional pressure loss over a range of wellbore architectures, flow rates, and delivery pressures. The results can be summarized as follows:

- Gas storage field operators can monitor wellbore integrity for wellbores above a particular suite of dimensions, gas flow rates and perforation sizes with existing pressure/temperature sensor technologies via wireline sensor package deployment.
- Gas losses from the wellbore to shallow zones do not exceed 1MMSCFD for perforations less than one-inch in diameter which is relatively easy to observe using this pressure monitoring protocol.
- For wellbore configurations of 2.5-inch diameter and less, the impact of perforations on flows with Reynolds numbers below $50x10^6$ and above delivery pressures of 500 psi is below the measurement threshold (10 psia incremental over "no leak" conditions), regardless of the depth of the perforation.
- For perforations with the most serious consequences, shallow and large diameter, existing sensor hardware will provide unequivocal indications at Reynolds number greater than $1x10^7$.
- For perforations located deeper in the wellbore, the incremental frictional pressure losses are small relative to the total losses and can be overlooked, since the incremental loss is a strong function of perforation diameter.
- A nomograph of the combination thresholds of tubing pressure, flow rate and perforation diameter for detection of a tubing perforation is provided in Table 4.
- Deviations in computed (via the London model) versus measured pressures greater than 10 psi should be viewed as suspect and further investigations of wellbore integrity are appropriate, particularly when the deviation cannot be related to the gradual buildup of scale in the wellbore.

For existing hardware sensitivity, we recommend a minimum of a ten psi incremental pressure above the predicted "no leak" pressure differential as the threshold for initiating additional tubing integrity tests. OLGA simulations indicate that the ten psi threshold will be exceed for perforation dimensions and depths shown below. Note that both a Reynolds number and wellhead pressure threshold are required in the tubing diameters indicated. The operator may assume a linear relationship for Reynolds number and wellhead pressure thresholds for tubing diameters between 2.441 and 6.336 inches.

Tubing diameter (inches)	Perforation Diameter (inches)	Perforation depth (feet)	Reynolds Number x10^{-6}	Wellhead Pressure (psi)
2.441	0.0625	100	70	500
2.441	0.125	100	50	500
2.441	0.25	250	50	500
2.441	0.25	250	80	750
2.441	0.25	250	120	1000
6.336	0.25	100	2,500	500
6.336	0.5	100	750	500
6.336	0.75	100	400	500
6.336	1.00	100	250	500
6.336	0.5	250	750	1000

Table 4. Threshold parameter values for detection of tubing perforations in gas wells
via pressure drop measurements

Summary

The research program has developed a nomograph of threshold flow conditions in standard gas storage wellbore architectures that will allow the operator to use a low cost pressure differential analysis technique to authenticate the integrity of the wellbore. The operator must consider both the Reynolds number and the wellhead pressure in determining the existence, dimension and probable location of a perforation.

The use of a ten psi minimum incremental pressure loss above that predicted by the London model for a "no leak" condition should minimize the occurrence of false positives yet provide enough sensitivity to allow the operator to detect perforations before a great deal of gas is lost to shallower zones.

In a fortuitous sense, the monitoring technique is most sensitive to shallow perforations where the greatest amount of gas is lost for a given perforation dimension and where it will have the largest deleterious effects.

Appendix

London model for gas flow in wellbores with NO perforations
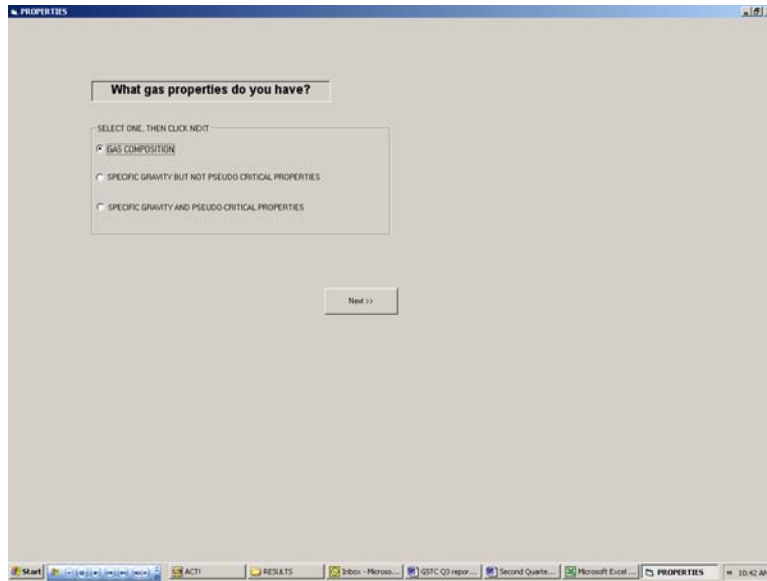
Figure A-1. Initial data input screen for the London gas flow model.

Figure A-2. Gas properties input screen for the London model.
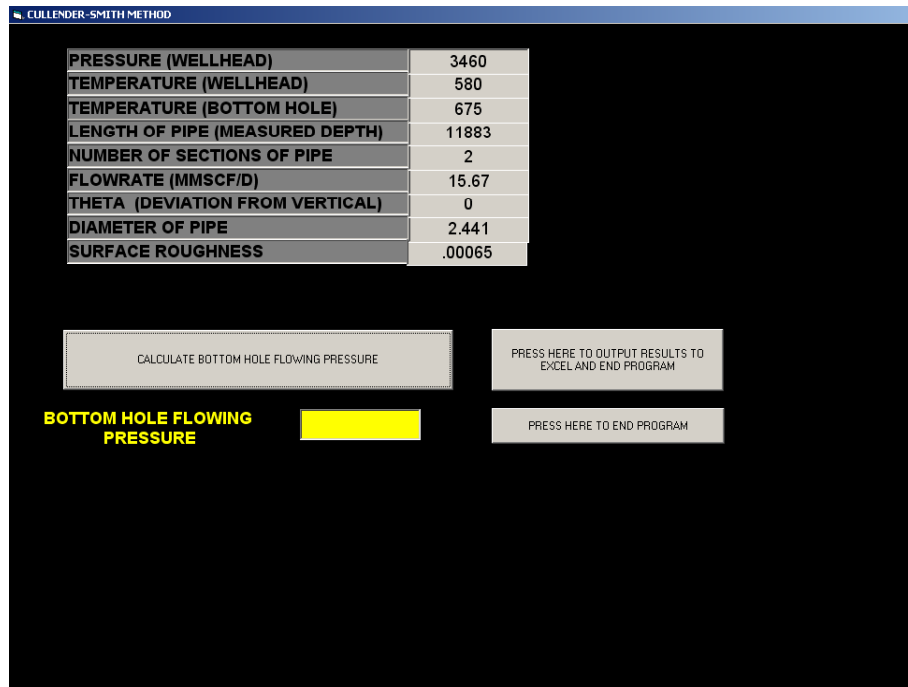
Figure A-3. Wellbore architecture input screen and bottomhole pressure calculation output for the London model.

Compact Separators for Gas Storage Field Applications

Jeffrey Savidge
Colorado Engineering Experiment Station
54043 WCR 37
Nunn, CO 80648

Project not completed, no funds expended

Renovation of Produced Waters from Underground Natural Gas Storage Facilities: A Feasibility Study Using Hybrid Constructed Wetland Technology

Final Report
September 1, 2004 – December 31, 2005

Submitted by:

James W. Castle (PI), Ph.D., Associate Professor, Clemson University
John H. Rodgers Jr. (Co-PI), Ph.D., Professor, Clemson University
Brenda M. Johnson, Graduate Research Assistant, Clemson University
Laura E. Ober, Graduate Research Assistant, Clemson University
Scott Brame, Research Associate, Clemson University

January 30, 2006

Clemson University
340 Brackett Hall
Clemson, SC 29634

Disclaimer

"This report was prepared as an account of work sponsored by an agency of the United States Government. Neither the United States Government nor any agency thereof, nor any of their employees, makes any warranty, express or implied, or assumes any legal liability or responsibility for the accuracy, completeness, or usefulness of any information, apparatus, product, or process disclosed, or represents that its use would not infringe privately owned rights. Reference herein to any specific commercial product, process, or service by trade name, trademark, manufacturer, or otherwise does not necessarily constitute or imply its endorsement, recommendation, or favoring by the United States Government or any agency thereof. The view and opinions of authors expressed herein do not necessarily state or reflect those of the United States Government or any agency thereof."

Abstract

The use of hybrid constructed wetland treatment systems offers an innovative approach for handling water produced from natural gas storage. Materials such as chlorides, metals, hydrocarbons, and corrosion inhibitors are often of concern in these waters. Specifically designed constructed wetland treatment systems have been used to treat each of these constituents independently, but this technology has not been demonstrated for produced waters from gas storage fields. Specific objectives of this study were: (1) to characterize produced waters; (2) to compare National Pollutant Discharge Elimination System (NPDES) standards in several situations where produced waters may be discharged or reused; (3) to design, construct, and monitor the performance of a pilot-scale constructed wetland system for treatment of water produced from gas storage fields; (4) to evaluate treatment effectiveness and performance of the pilot-scale system; and (5) to confirm design characteristics (hydrosoil, hydroperiod, vegetation, sizing, etc.) for field-scale constructed wetland treatment systems. Statistical data regarding the composition of gas storage produced waters were gathered and tabulated from industry and literature. Several gas storage companies provided actual samples of produced water for analysis. NPDES permits were obtained for Ohio, Pennsylvania, New York, and West Virginia, and these permits were compiled into a single model (comprehensive) permit that was utilized for treatment performance criteria for targeted constituents. A pilot-scale constructed wetland treatment system was designed, constructed, and allowed time to stabilize. Simulated produced waters treated by the pilot-scale system were formulated and mixed. Four experiments were completed in which Experiment 1 (fresh produced water), Experiment 2 (brackish produced water), Experiment 3 (saline produced water), and Experiment 4 (hyper-saline produced water), were run through the appropriate modules of the hybrid constructed wetland treatment system. As samples were collected during each of these experiments, analyses were performed and results were compared to the model NPDES permit. Design parameters were developed and refined to accomplish remediation of the specific produced waters. Data obtained during this study indicate that the pilot-scale hybrid CWTS provided effective treatment of simulated natural gas storage produced waters.

Table of Contents

List of Tables

List of Figures

Appendix: Tables

Introduction

One of the highest priorities identified by the Gas Storage Technology Consortium (GSTC) is the investigation of new approaches for handling produced water. Produced waters pose a challenge for treatment because they vary greatly in their composition. Expansion of existing gas storage fields and development of new fields are limited by the high costs associated with wastewater treatment and disposal. Currently there are two common methods for handling produced water. The first method is to transport the produced water to specialized treatment facilities followed by surface discharge of the treated water, and the second is to reinject the water to the subsurface. While volumes of produced water are increasing, conventional treatment methods are becoming exponentially more costly as surface discharge and re-injection regulations under the National Pollutant Discharge Elimination System (NPDES) and Clean Water Act (CWA) grow more stringent. Finding new approaches for handling produced waters is essential for continued operation of many existing storage fields and for the development of new storage capacities.

Water produced from gas storage facilities may be generated in relatively high volumes and contain a variety of constituents that limit disposal or reuse of the water. Materials such as chlorides, hydrocarbons, and corrosion inhibitors are of concern in these waters. Although salinity of some produced waters may be low enough to meet NPDES discharge limits, concentrations of other constituents in these waters may preclude discharge, resulting in a need for treatment or disposal. Generic parameters such as biochemical oxygen demand (BOD) and chemical oxygen demand (COD) may be targeted for treatment. Specifically designed constructed wetland treatment systems (CWTS) have been used to treat various constituents independently, but this technology has not been demonstrated for produced waters from gas storage fields. Wetlands possess unique reactions not occurring in other aquatic or terrestrial systems. Constructed wetlands can be poised or buffered to ensure that desired reactions (transfers and transformations) affecting the constituents targeted for treatment proceed at predictable rates over long periods of time (decades).

The use of CWTS is a readily implemented approach with the potential to reduce the costs of handling water produced from gas storage fields. The proposed approach offers the following specific advantages:
1. low construction cost;
2. low operational and maintenance costs;
3. reliability; and
4. flexibility in design, so the approach is applicable to many gas storage fields.

The purpose of the current research is to develop a low cost and readily implemented hybrid CWTS for treating produced water as part of a system integrated with surface facilities of gas storage fields. The approach is applicable to a wide range of waters produced from gas storage, as the composition and volumes of waters generated vary greatly among storage fields. A pilot-scale study serves to decrease uncertainties and confirm design features for future, field-scale constructed wetland treatment systems.

The pilot-scale study provides data regarding the feasibility of this approach for treating gas storage produced waters of various compositions. Specific objectives of this pilot-scale study are:

1. To characterize several produced waters;
2. To compare NPDES standards in several situations where produced waters may be discharged or reused;
3. To design, construct, and monitor the performance of a pilot-scale constructed wetland treatment system for treatment of water produced from gas storage fields;
4. To evaluate treatment effectiveness and performance of the pilot-scale system; and
5. To confirm design characteristics (hydrosoil, hydroperiod, vegetation, sizing, etc.) for future field-scale constructed wetland treatment systems.

A hybrid CWTS capable of effectively and consistently treating simulated produced waters in compliance with NPDES standards was designed and tested at a pilot-scale.

The major expected benefit of investigating CWTS technology for the handling of water produced from gas storage is significantly decreased costs for produced water management, which could potentially lead to expansion of existing storage fields. In addition, new geographic areas may be opened up for development of gas storage fields in light of the anticipated economic advantages.

Executive Summary

The first objective of this investigation was to characterize water produced from natural gas storage (Task 1). Two steps were involved with produced water characterization: 1) analysis of actual produced waters, and 2) statistical analysis of produced water composition data. To help accomplish the first step, sampling kits were sent to various natural gas storage facilities in order to obtain samples of actual produced waters for analysis. The second step in the characterization of produced water was the statistical analysis of data provided by various gas storage facilities. These data, which were obtained from industry members of the Gas Storage Technology Consortium, were statistically analyzed and compared using the Statistical Analysis System (SAS Institute, 2002). Based on results from analyses of these data, characteristics of the produced waters tend to cluster into four groups (based primarily on chloride concentrations):

    1.) fresh - characterized by low chloride concentrations ($\leq$ 400-2,500 mg/L);
    2.) brackish - characterized by medium chloride concentrations (2,500-15,000 mg/L);
    3.) saline - characterized by high chloride concentrations (15,000-40,000 mg/L); and
    4.) hyper-saline - characterized by extremely high chloride concentrations ($\geq$ 40,000 mg/L).

The data gathered from the statistical analysis of produced waters were utilized to formulate simulated produced waters. By using simulated produced waters, the specific characteristics of the water entering the system are known. When these characteristics are compared with those of the treated water leaving the system, the constituents removed by the system can be determined more accurately.

In order to develop reasonable treatment performance goals for the constructed wetland treatment systems (CWTS), the second objective of this research project was to obtain NPDES permits and to develop treatment performance goals based on these permits (Task 2). This objective required contacting various State regulatory and USEPA offices in Ohio, Pennsylvania, New York, and West Virginia, as well as gathering information from industry contacts in West Virginia and Pennsylvania. Concurrent with the work on this task, the USEPA released a website (USEPA, 2004) for easy access of NPDES permits which provided additional information. After analysis of approximately 50 NPDES permits from the aforementioned states, a model (comprehensive) permit was generated.

The third objective of the investigation was to design, construct, and monitor the performance of a pilot-scale constructed wetland system for treatment of water produced from gas storage fields (Task 3). The design of the hybrid CWTS includes five major components (or modules): (1) the produced water is retained in a detention basin; (2) the produced water is passed through an API oil/water separator; (3) the water from the oil/water separator progresses through two saltwater wetland cells in series containing quartz-sand hydrosoil and *Spartina alterniflora*; (4) the water from the saltwater cells is held in a second detention basin until passing through a reverse osmosis (RO) system; (5) if the water no longer shows toxicity to receiving system biota, it is directly discharged; if the water is still toxic, it is passed through a freshwater wetland system. Each module

has a different function in the treatment of produced water. Depending on the salinity of the produced water as well as the oil and grease concentration present in the water, various modules in this process may be bypassed. For example, the RO system will be used only for water with greater than 4,000 mg/L chlorides. The design for the pilot-scale system is shown in Figure 1.
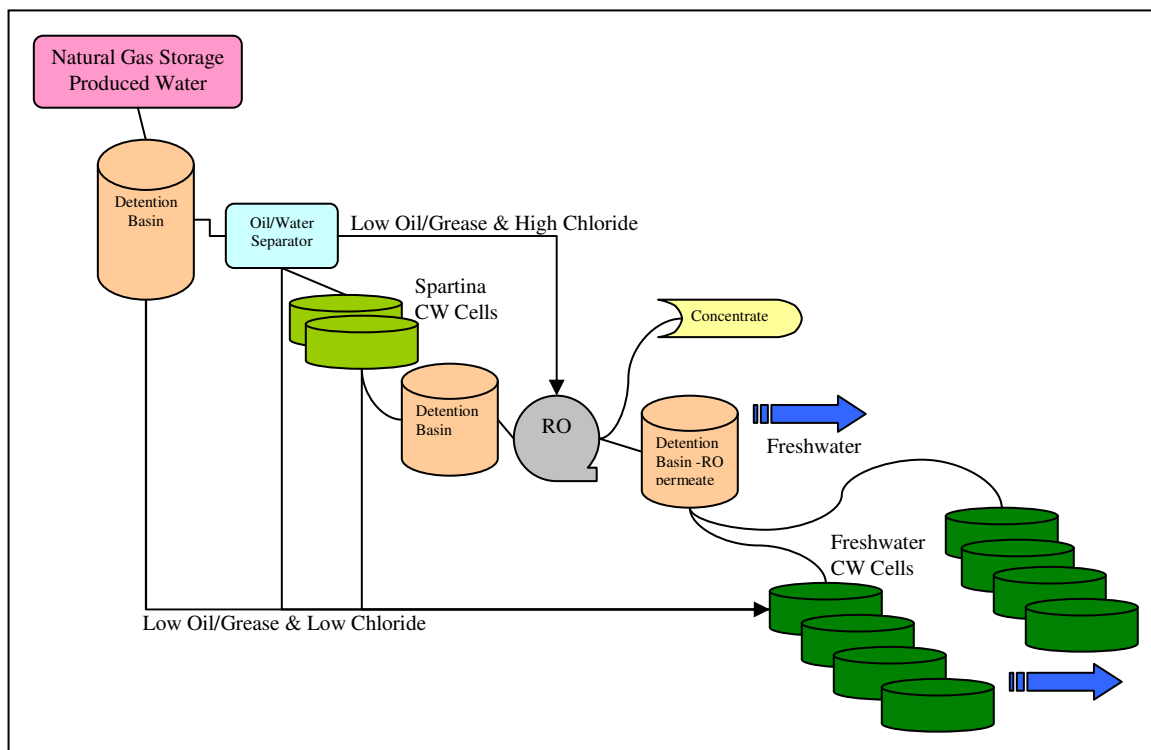
Figure 1. Schematic of the hybrid pilot-scale constructed wetland treatment system for water produced from natural gas storage. CW = constructed wetland; RO = reverse osmosis system.

Task 4 was to evaluate treatment effectiveness and performance of the pilot-scale CWTS. Standard operating procedures (SOPs) for analysis of water samples as well as sampling procedures were developed and confirmed. The first two experiments, Experiment 1 (simulated fresh produced water) and Experiment 2 (simulated brackish produced water), were run through only the freshwater wetland portion of the hybrid CWTS due to their low oil/grease and low chloride concentrations. For Experiment 3 (simulated saline produced water) and Experiment 4 (simulated hyper-saline produced water) it was necessary to run the water through the entire hybrid CWTS due to high oil/grease and high chloride concentrations (>4,000 mg/L chlorides). As water samples were collected, standard operating procedures for their analysis were followed and modified accordingly to optimize results. Task 5 was to confirm design characteristics (hydrosoil, hydroperiod, vegetation, sizing, etc.) for a demonstration-scale CWTS. Task 6 involved report preparation and documentation of results for transfer of the technology.

Experimental

Task 1: Characterize Produced Waters

Produced waters were characterized in Task 1 in order to determine realistic composition of water for use in the pilot-scale CWTS. Approximately 4,000 records of produced waters provided by several natural gas storage companies were analyzed using the Statistical Analysis System (SAS Institute, 2002). The results were grouped into four categories of water composition (fresh, brackish, saline, and hyper-saline) using primarily the median and quartiles of chloride concentrations (Table 1). Six targeted constituents are listed in Table 1, which are representative of produced water composition for the purpose of evaluating treatment effectiveness. These constituents were used in Task 4 to formulate simulated waters for treatment in the pilot-scale CWTS. The chemical source of each constituent is also listed in Table 1.

Table 1: Targeted constituents, inflow concentrations, and chemical sources for simulated produced water.

Constituent	Chemical Source	Fresh Target Inflow (mg/L)	Brackish Target Inflow (mg/L)	Saline Target Inflow (mg/L)	Hyper-Saline Target Inflow (mg/L)
Cadmium	$CdCl_2$	0.02	0.41	0.8	1.21
Copper	$CuCl_2 \cdot 2H_2O$	0.02	1.68	3.34	5
Lead	$PbCl_2$	0.1	5.47	6.84	10.2
Zinc	$ZnCl_2$	0.1	23	45.9	69
Oil/Grease	Motor Oil	3	19	49	78
Chlorides	$CaCl_2$, NaCl, $MgCl_2 \cdot 6H_2O$	<400- 2,500	2,500- 15,000	15,000- 40,000	>40,000

The utilization of simulated waters has many benefits. Simulated waters allow for a complete knowledge of system input, which in turn allows for a better comparison with system output. Simulated waters are also more cost effective for preliminary, pilot-scale experiments. The simulated natural gas storage produced waters are designed to closely replicate the composition of actual waters as shown by statistical analysis of the data and are in agreement with published data (Pope and Pope, 1999; USEPA, 2004; Veil et al., 2004).

Task 2: Obtain Discharge Permits and Develop Treatment Performance Goals

NPDES permits were obtained from a variety of sources including industry and government websites, the United States Environmental Protection Agency (USEPA), and natural gas storage companies. Several USEPA offices were contacted, including those

in Ohio, Pennsylvania, New York, and West Virginia, to obtain sample permits. While these data were gathered, the USEPA released a website (USEPA, 2004), providing easier access to NPDES permits. These NPDES permits were carefully examined and used to create a list of possible constituents of concern and a range of surface discharge limits for the constituents found in produced waters. This information was used to create a model NPDES permit for the project (Table 2). Values included in this table, when shown in the format X-Y, illustrate the range of values found for constituents of concern in various NPDES permits. This model permit delineates viable output or performance goals to apply to the hybrid constructed wetland treatment system for each of the constituents of concern.

Task 3: Design, Construct and Monitor Hybrid Treatment System

The first step of treatment involved storage of the simulated produced water in a 3780 L (1000 gallon) detention basin, allowing time for some solids to settle. From the detention basin the water was pumped by a Fluid Metering, Inc. [®] (FMI) piston pump to an American Petroleum Institute (API) oil/water separator at a rate of 149 mL/min. For this pilot study, the API oil/water separator was 116.8 cm (46 in) long by 55.9 cm (22 in) wide by 30.4 cm (12 in) deep. The body of the separator was fiberglass with a skimmer and baffle of Plexiglas. The water leaving the oil/water separator entered a pilot-scale saltwater wetland.

The second step utilized two saltwater wetland cells (Figure 1) with quartz sand hydrosoil and planted with both tall and short forms of *Spartina alterniflora.* The purpose of these cells was to remove any residual oil and grease from the produced water in order to prevent fouling of the reverse osmosis (RO) membrane. These cells provided an opportunity for retained organics to be oxidized and for precipitation of various metal compounds. The water leaving the pilot-scale saltwater wetland cells drained into a detention basin prior to treatment by the RO system. If the produced water is not saline (i.e. <4,000 mg/L as chlorides), then steps two and three could be omitted.

The third step targeted salt removal through the use of an RO system. The RO system was utilized when Experiment 3 (saline water) and Experiment 4 (hyper-saline water) passed though the CWTS. The primary purpose of the RO system was to decrease chloride concentration and total dissolved solids (TDS) concentrations in saline waters to a tolerable level for the freshwater wetland and aquatic life. This system was run in batches and the post-treatment water was collected in a detention basin before being pumped into the freshwater wetland portion of the treatment system at a rate of 97.2 mL/min.

The pilot-scale freshwater CWTS was designed to remove metals and organic compounds that remain after passing through the API oil/water separator, the saltwater wetland cells, and the RO system. The freshwater system may also be used independently (i.e., bypassing the *Spartina* cells and RO) for treatment of waters with less than 4,000 mg/L chloride concentrations. The freshwater wetland system served as a final clean-up or polishing step. Its primary purpose is to ensure that the post-treatment

Table 2: Model (comprehensive) NPDES Permit for discharge of natural gas storage produced waters.

CONSTITUENT	LIMITS	UNITS	CONSTITUENT	LIMITS	UNITS
PH	6-9	SU	OIL & GREASE	15	mg/L
BOD5(20*C)	29-57	mg/L	CARBON, TOTAL ORGANIC (TOC)	5	mg/L
CBOD5	25	mg/L			
COD	170-292	mg/L	BENZENE	0.06-2.88	µg/L
SOLIDS, TOTAL DISSOLVED	500	mg/L	TOLUENE	0.028-5.0	µg/L
SOLIDS, TOTAL SUSPENDED	30-70	mg/L	ETHYLBENZENE	0.142-5.0	µg/L
ALKALINITY/ACIDITY	alkalinity<acidity		ORTHO-XYLENE	5	µg/L
			XYLENE, META & PARA	0.01-100	µg/L
BARIUM	154	mg/L	BTEX	< 5.0	µg/L
CHLORIDES	5,000	mg/L			
CHLORINE, TOTAL RESIDUAL	0.038	mg/L	NAPTHALENE	0.2	mg/L
CHROMIUM, TOTAL	0.1-100	µg/L	1,1,1-TRICHLORO-ETHANE	0.05	mg/L
COPPER, TOTAL	0.37-1.0	mg/L	1,2-DICHLOROPROPANE	0.196	µg/L
CYANIDE, TOTAL	0.4	mg/L	ETHYLENE GLYCOL	50	µg/L
FLUORIDE, TOTAL	30	mg/L	PAH	2.8-12.2	mg/L
IRON, TOTAL	0.6-9.4	mg/L			
LEAD, TOTAL	2.6-400	µg/L	TOXICITY	Zero discharge of water containing toxic substances in concentrations that are toxic to human, animal or aquatic life.	
MANGANESE, TOTAL	1-4.4	mg/L			
MERCURY, TOTAL	0.004	mg/L			
NICKEL, TOTAL	2	mg/L			
NITROGEN, AMMONIA TOTAL (AS N)	1.5-6.6	mg/L			
PHOSPHOROUS, TOTAL	1	mg/L			
SULFIDE, TOTAL	0.21-1.0	mg/L			
TIN, TOTAL	50	µg/L			
ZINC, TOTAL	0.4-5.0	mg/L			

Note: Limits are based on New York, Ohio, Pennsylvania, and West Virginia NPDES permits.
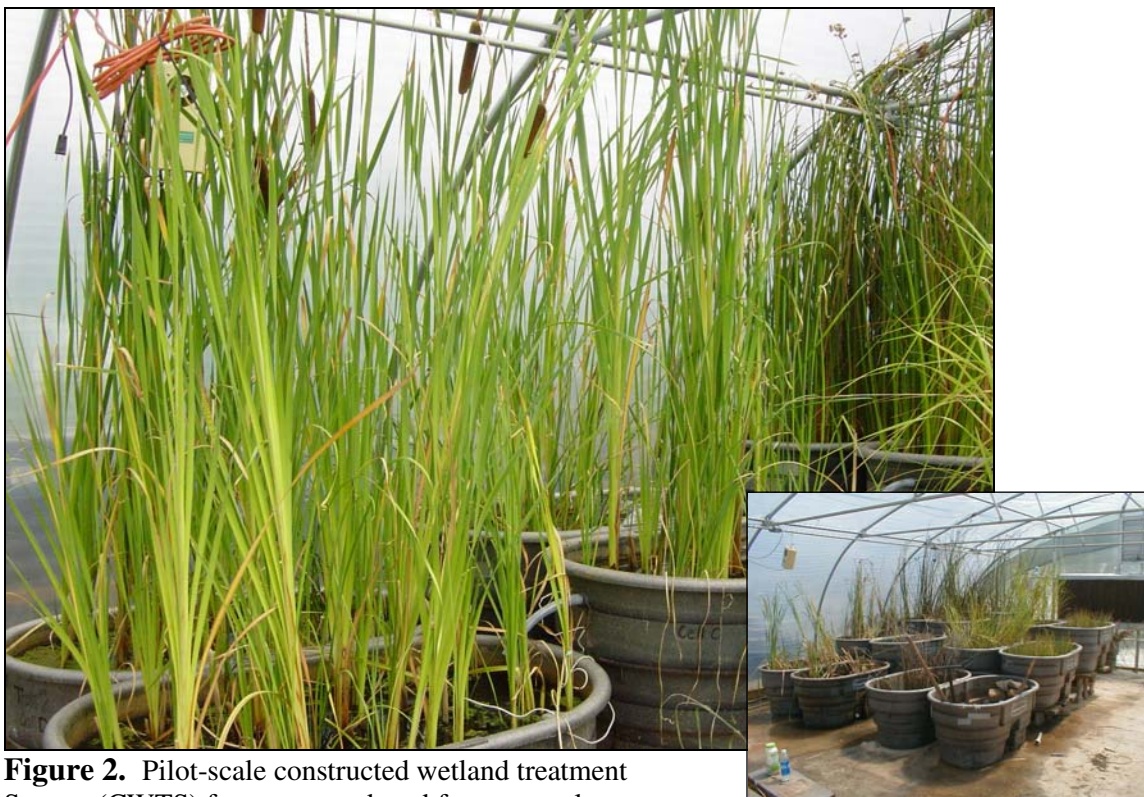
Figure 2. Pilot-scale constructed wetland treatment System (CWTS) for water produced from natural gas storage. The smaller photograph shows the system in its early stage of construction. The two trains on the left are the freshwater wetland cells that form the final stage of treatment. The two trains of wetland cells on the right contain *Spartina alterniflora,* which is used for the treatment of saline water. The larger photograph shows the CWTS in June 2005 following the successful establishment and growth of the wetland plants.

water is non-toxic. In the pilot-scale freshwater wetland system, there were two parallel trains consisting of four cells. Each cell was contained within a 121.9 cm (48 in) long by 77.5 cm (30.5 in) wide by 63.5 cm (25 in) deep, 378 L (100 gal) Rubbermaid® tub. The four cells in series provided adequate sampling locations and prevent "short circuiting" (water passing through without adequate treatment). The cells were connected by PVC pipe fittings and approximately 30 cm long segments of ¾" poly-tubing. The PVC pipe fittings were designed to maintain surface flow and were placed 6 cm below the top of each Rubbermaid® tub.

Each of the freshwater wetland cells (Figure 2) consisted of three macrofeatures: hydrosoil, macrophytes, and a hydroperiod. The first two cells in each train contained reducing hydrosoil (sediment collected from 18 Mile Creek, SC, amended with clay and organic materials) and were planted with *Schoenoplectus californicus* C.A. Meyer (California bulrush). The final two cells in each train contained oxidizing hydrosoil (quartz sand) and were planted with *Typha latifolia* L. (broadleaf cattail). Each cell contained approximately 140 L (37 gal) of water (not including pore water). By maintaining a flow rate of 97.2 mL/min, the hydroperiod or hydraulic retention time

(HRT) of the CWTS was maintained at 24 hours per cell or 96 hours for the entire freshwater system.

Upon the completion of the design and construction of the hybrid CWTS, monitoring of the CWTS began. Experiment 1, fresh produced water, was run through the freshwater wetland portion of the CWTS for four weeks. Two batches of simulated produced water were needed to run the experiment for this length of time. Water samples were collected progressively throughout the system according to the hydraulic retention time at the onset of the experiment and once in the middle of the experiment (following the mixing of the second batch of water).

Upon the completion of Experiment 1, well-water with a chloride concentration of approximately 2,500 mg/L and containing no oil or metals was run through the freshwater system to allow the plants to acclimate to the level of chlorides characteristic of Experiment 2, simulated brackish produced water. In Experiment 2, two batches of brackish produced water were pumped through the system over the course of four weeks. Based upon the concentrations of constituents found in the simulated produced water, Experiment 2, brackish produced water, was run through only the freshwater wetland portion of the CWTS. Again, samples were collected progressively throughout the system according to the hydraulic retention time at the onset of the experiment, and once in the middle of the experiment (following the mixing of the second batch of water).

To allow the plants in the freshwater system to acclimate to the level of chlorides expected in the permeate from RO in Experiment 3, well-water with a chloride concentration of approximately 1,500 mg/L and containing no oil or metals was run through the freshwater system for one week. Then well-water with no amendments was run through the freshwater system until this module was required for Experiment 3. Experiment 3 utilized the entire hybrid CWTS, including the API oil/water separator and the RO system, due to the concentrations of constituents found in this category of water. Samples were collected progressively throughout the system according to the hydraulic retention time at the onset of the experiment, and once in the middle of the experiment (following the mixing of the second batch of water).

The level of chlorides expected to reach the freshwater system during Experiment 4, simulated hyper-saline produced water, was expected to be similar to that found for Experiment 3. For this reason, well-water with no amendments was run through the freshwater system between Experiment 3 and Experiment 4. Experiment 4 utilized the entire hybrid CWTS; however, for this final experiment, a new oil/water separator was built and used in place of the API oil/water separator from the previous experiment. Samples were collected progressively throughout the system according to the hydraulic retention time at the onset of the experiment, and once in the middle of the experiment (following the mixing of the second batch of water).

Task 4: Evaluate Treatment Effectiveness and Performance of the Pilot-Scale System

As samples were collected throughout the experiments, the treatment effectiveness and performance were evaluated. Samples were analyzed for the parameters listed in Table 3 according to the associated standard operating procedures.

Table 3: Analytical methods for parameters monitored from the pilot hybrid constructed wetland treatment system.

Parameter	Method	Method Detection Limit
Temperature	Direct Instrumentation: YSI Model 52	0.5ºC
pH	Direct Instrumentation: Orion Model 420A	0.01
Conductivity	Direct Instrumentation: YSI 30	0.1 µS/cm
Alkalinity	Standard Methods: 2320 B	2 mg/L as $CaCO_3$
Hardness	Standard Methods: 2340 C	2 mg/L as $CaCO_3$
DO[1]	Direct Instrumentation: YSI Model 52	0.1 mg/L
COD[2]	Closed reflux colorimetry (HACH- modified from Standard Methods: 5220 D)	3 mg/L
BOD[3]	Standard Methods: 5210 B	0.1 mg/L
Chloride	High: HACH Drop Count Titration Method Low: HACH colorimetric method 8207	500 mg/L 25 mg/L
Sulfate	Standard Methods: 4500 E	1 mg/L
Metals	Atomic Absorption Spectrometry (AA)	Cd–0.002 mg/L Cu–0.010 mg/L Pb–0.050 mg/L Zn–0.005 mg/L
	Inductively Coupled Plasma-Atomic Emissions Spectrometry (ICP-AES): USEPA 200.8	Cd-0.010 mg/L Cu-0.010 mg/L Pb-0.015 mg/L Zn-0.010 mg/L
TDS[4]	Standard Methods: 2540 C	0.1 mg/L
TSS[5]	Standard Methods: 2540 D	0.1 mg/L
Oil and Grease	Flourometer	1.0 mg/L
Bulk Redox	Standard Voltmeter, Accumet® calomel reference electrode, and *in situ* platinum-tipped electrodes (Faulkner et al., 1989).	±10mV

[1] Dissolved Oxygen   [3] Biological Oxygen Demand   [5] Total Suspended Solid
[2] Chemical Oxygen Demand   [4] Total Dissolved Solids

Task 5: Confirm Design Characteristics

Upon completion of Experiment 1 and Experiment 2 excessive separation of oil was observed in the detention basin. For the remaining experiments, the waters were continuously mixed with a submersible pump in the initial detention basin. This reduced the settling of solids and the separation of the oil fraction, allowing a more representative sample to be pumped into the CWTS.

After Experiment 3, it was noted that a more effective oil/water separator was needed. The new model is approximately 122 cm (48 in) long by 61 cm (24 in) wide by 40.6 cm (16 in) deep. It incorporates some of the same baffle concepts as the initial oil/water separator but also utilizes dissolved air flotation, turbulence reduction, and filtering to separate the oil from the water.

Upon completion of Experiments 1 through 4, a second simulated brackish water was processed through the system. Experiment 1 showed no toxicity in inflow or outflow, and Experiment 2 showed toxicity in both the inflow and outflow. Thus a water with concentrations set at the minimum NPDES permit limits for the constituents of concern (Tables 1 and 2) was needed to assess the capabilities of the freshwater wetland module. This water was called Simulated Brackish Water II.

Results and Discussion

Task 1: Characterize Produced Waters

The composition of produced waters associated with natural gas production and storage varies greatly depending upon the geologic formation from which it originates, the extraction method utilized in the natural gas production process, and the treatment chemicals selected for the process. Data provided by several gas storage facilities show wide ranges of values for many produced water constituents. Chloride concentrations and total solids show the largest range in values from non-detect to 384,000 mg/L and non-detect to 494,000 mg/L, respectively. In order to characterize the produced waters, they were divided into four general categories based upon statistical analysis:

        1.) fresh - low chloride concentrations ($\leq$400-2,500 mg/L),

        2.) brackish - medium chloride concentrations (2,500-15,000 mg/L),

        3.) saline - high chloride concentrations (15,000-40,000 mg/L), and

        4.) hyper-saline - extremely high chloride concentrations ($\geq$40,000 mg/L).

Separate experiments conducted in Task 4, using simulated produced water, are defined by each of these four categories.

Chlorides play a major role in the character of produced water. Based on data provided by several major gas storage companies, it was determined that chlorides in produced waters are composed primarily of 47% sodium chloride (NaCl), 47% calcium chloride ($CaCl_2$), and 6% magnesium chloride ($MgCl_2$).

Based on statistical analysis and literature review, a large variety of metals may be present in produced waters (USEPA, 2000; Veil et al., 2004). Many of these metals are present in concentrations that are toxic to receiving system biota. This toxicity consequently leads to failure to meet NPDES permit limits. It is not feasible to study in great depth every metal present in produced waters. Due to time and cost, four metals, cadmium (Cd), copper (Cu), lead (Pb), and zinc (Zn), were chosen based on their presence in produced waters, toxicity to receiving system biota, and cost of experimentation.

In order to create the simulated produced waters, it was necessary to define the inflow concentrations of Cd, Cu, Pb and Zn. For the first (fresh) simulated produced water, the range of each metal concentration typically found in produced waters was examined and then compared to the risk-based concentration. The targeted inflow metal concentrations were chosen primarily based upon the risk to *Ceriodaphnia dubia* in 7-day toxicity experiments, which is referred to as the lowest observable effect concentration (LOEC), in the USEPA's ECOTOX database (USEPA, 2002). Metal concentrations for the other three experiments were determined by the published values for each metal. Simulated hyper-saline produced water was determined by the maximum published values, simulated saline water metal concentrations were determined by the 75th percentile, and simulated brackish water metal concentrations by the median. The goal was to test for the lowest effluent concentration that can be achieved by the system below the NPDES permitted level for the widest range of Cd, Cu, Pb, and Zn conentrations.

Task 2: Obtain Discharge Permits and Develop Treatment Performance Goals

A model NPDES permit (Table 2) was created from approximately fifty NPDES permits that were issued by Ohio, Pennsylvania, New York, and West Virginia. The tabulated permits were issued for various oil and gas industrial purposes including oil field services, natural gas transmission, petroleum refining, oil and gas general permitting, and industrial wastewater pollution control. These permits were utilized to create an initial list of constituents of concern and to provide an objective treatment output concentration for each constituent. The comprehensive model permit served as a means of measuring the success of the hybrid constructed wetland treatment system to effectively remove the constituents of concern. If the discharge from the system failed to meet the standards outlined in the model permit, necessary adjustments were made to fine tune the system until it was capable of meeting these requirements.
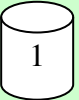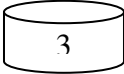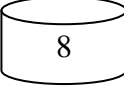
Task 3: Design, Construct and Monitor Hybrid Treatment System

The major components of the design plan included a detention basin, an API oil/water separator, two saltwater wetland cells, an RO system or nanofiltration unit, and two trains of four freshwater wetland cells each. The first two of the four freshwater wetland cells contained hydrosoil that created a bulk reducing environment which promoted the removal of metals and sulfates by the following processes: precipitation of metals, sorption, plant uptake, and biodegradation (Table 4). In order to create a reducing

environment, the hydrosoil must possess a sediment oxygen demand greater than the rate at which oxygen is supplied to the system. This can be accomplished by using a hydrosoil with high clay content and a relatively high amount of labile organic matter. When hydrosoil of this type is combined with plants that do not greatly oxygenate the rhizosphere, a reducing environment capable of the aforementioned removal processes can be established. The final two freshwater wetland cells contained hydrosoil that created a bulk oxidizing environment which promoted the removal of water soluble organics and metals through oxidative processes including biodegradation, sorption, plant uptake, and precipitation (Table 4). A bulk oxidizing environment is accomplished through hydrosoil with high sand content and little to no organic matter combined with plants that have high radial oxygen loss in the rhizosphere.

Due to the detrimental effects of high chloride concentrations on the growth and survival of the freshwater plants chosen for the CWTS, an RO system was included in the design for any produced water containing chloride concentrations greater than 4,000 mg/L. RO systems are capable of removing chlorides, TDS, and many other constituents; however, RO membranes are sensitive to oil and grease. In order to extend the life of the RO membrane (prevent membrane fouling and subsequent failure of the RO system), two saltwater wetland cells were added to the system as a method of pretreatment to the RO system. These cells were planted with *Spartina alterniflora*, a saltwater macrophyte, as a means of ensuring the removal of residual oil and grease that may not have been adequately removed by the API oil/water separator. These saltwater cells also provided additional benefits, such as an environment conducive to the precipitation of various metal compounds.

Table 4: Stages and processes of the hybrid constructed wetland treatment system

	Stage of Treatment		Processes		Constituents Removed
1	Detention Basin	→	Settling, Precipitation	→	Solids
2	Oil/Water Separator	→	Gravity/Density Settling	→	Solids & Oil
3	Spartina Cells (Oxidizing)	→	Sorption, Biodegradation, Sedimentation, Precipitation	→	Oil & Grease, Water Soluble Organics
4	Detention Basin	→	Settling, Precipitation	→	Solids
5	RO System	→	Membrane – Reverse Osmosis	→	TDS: Chlorides, Hardness, Salts, Metals, & Sulfates
6	Detention Basin	→	Settling, Precipitation	→	Solids
7	Schoenoplectus Cells (Reducing)	→	Precipitation, Sorption, Plant Uptake, Biodegradation	→	Metals
8	Typha Cells (Oxidizing)	→	Precipitation, Sorption, Plant Uptake, Biodegradation	→	Water Soluble Organics, Metals

Task 4: Evaluate Treatment Effectiveness and Performance of the Pilot-Scale System

Analytical methods to complete Task 4 were chosen (Table 3), standard operating procedures were written for each method, and a sampling plan was written prior to initiation of the experiments to ensure adequate and representative sampling and analysis.

The system was loaded according to the concentrations outlined in Table 1 for each experiment. The salts and metals were weighed in the laboratory. The specific gravity of the Shell ^{TM} Rotella T ^{TM} Multigrade SAE 15W-40 oil was found to be approximately 0.87 g/mL as determined by weighing a 50 mL volume on a laboratory balance. From this specific gravity, the appropriate concentration of oil and grease for each batch of water was measured by volume. The constituents were added to 1000 gallons of well-water for each batch. The water was mixed for 24 hours using a submersible pump to allow the salts to dissolve and organics to partition into the water. Following mixing, the simulated produced waters for Experiments 1 and 2 were given 24 hours to settle, before being pumped into the treatment system. It was assumed that by allowing time to settle, the simulated produced water would be more representative of actual produced water. For Experiment 3 and Experiment 4, the simulated produced waters were mixed continuously to prevent separation of oil from water in the initial detention basin.

In Experiments 1 (simulated fresh water) and 2 (simulated brackish water), the freshwater wetland system was the primary component utilized for treatment of produced water (PW). The water was pumped directly from the 1000 gal detention basin into each of the two freshwater wetland trains at a rate of 97.2 mL/min, in order to maintain a 24 hr hydraulic retention time for each wetland cell.

These freshwater wetlands are capable of processing a maximum of 4,000 mg/L chlorides due to the sensitivity of the macrophytes to chlorides. NPDES permits require chloride concentrations to be below 5,000 mg/L. Since the chloride concentrations in Experiment 1, fresh produced water (400 mg/L chlorides), and Experiment 2, brackish produced water (2,500 mg/L chlorides), are both below this limit, it was not necessary to send these waters through all the stages of the hybrid constructed wetland system. By bypassing the oil/water separator, the two saltwater wetland cells, and the RO system in cases where the chloride concentrations are relatively low, both time and money can be saved.

Figure 3: Reverse Osmosis System.

Experiment 3, saline produced water (15,000 mg/L chlorides), and Experiment 4, hyper-saline produced water (40,000 mg/L chlorides), used the entire hybrid CWTS. The water was pumped from the initial 1000 gal detention basin into the oil/water separator at a rate of 149 mL/min to maintain a 24 hour hydraulic retention time for each of the saltwater cells and a 22 hour hydraulic retention time for the oil/water separator. From the second saltwater cell (Spartina 2), the water was collected in a 550 gallon detention basin. From this first 550 gallon detention basin,

the water progressed through an RO system (Figure 3). Permeate from the RO system was collected in a second 550 gallon detention basin, while the concentrate was collected and treated separately. Permeate collected in the second 550 gallon detention basin became the inflow to the freshwater wetlands, being pumped into each of the two freshwater wetland trains at a rate of 97.2 mL/min, in order to maintain a 24 hr hydraulic retention time for each cell.

All of the metal analyses were conducted at Clemson University. Cadmium, copper and lead for Experiments 1 and 2 were analyzed by Atomic Absorption Spectrometry (AA-5100, Perkin-Elmer Corporation). For Experiments 1 and 2, zinc was analyzed by Inductively Coupled Plasma-Atomic Emission Spectrometry (ICP-AES, Spectro Flame Modula EOP, Spectro Analytical Inc.). All four metals for Experiment 3 and Experiment 4 were analyzed by Inductively Coupled Plasma-Atomic Emission Spectrometry (ICP-AES, Spectro Flame Modula EOP, Spectro Analytical Inc.).

Experiment 1: Simulated Freshwater

Metals
For Experiment 1, metal concentrations were loaded at approximately 0.02 mg/L Cd, 0.02 mg/L Cu, 0.1 mg/L Pb, and 0.1 mg/L Zn. Both Cu and Pb concentrations were below current detection limits of the AA utilized for analysis. The results for Cd are shown in Figure 4, and the results for Zn are shown in Figure 5.
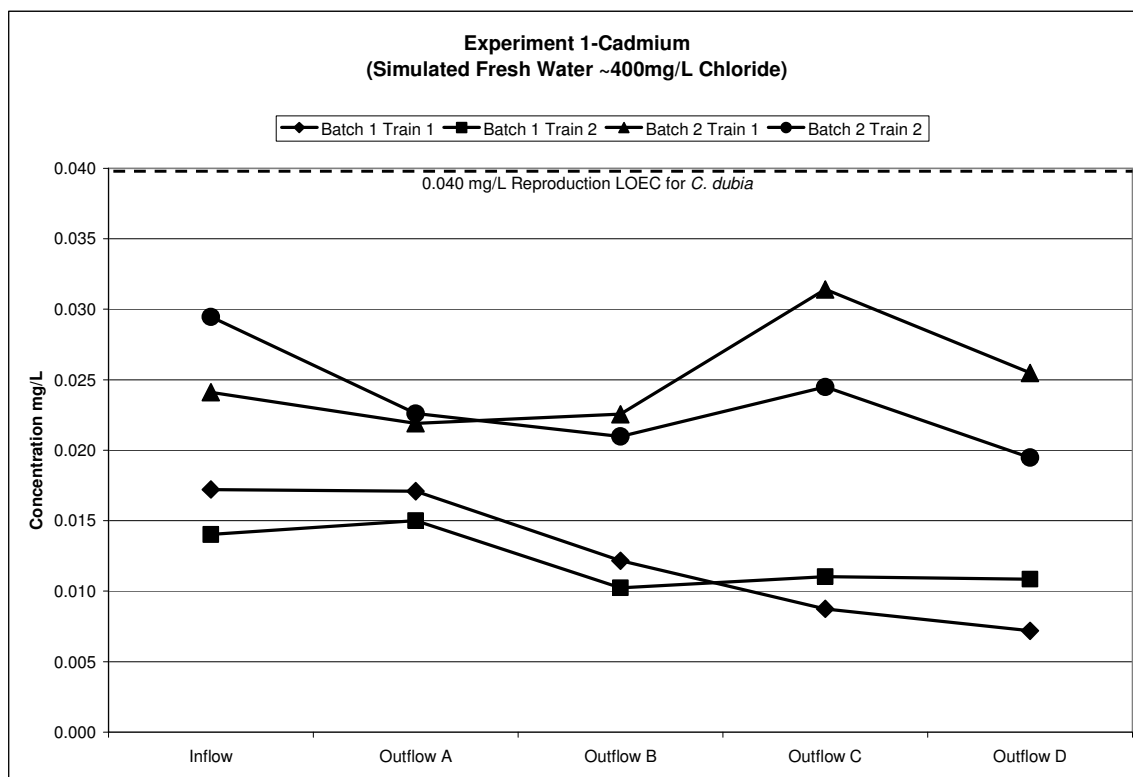
Figure 4. Experiment 1: Simulated freshwater metal analysis for cadmium performed by AA.

Cadmium was not found in any of the NPDES permits for the pertinent EPA regions; however, cadmium is found in produced waters at high concentrations and therefore is regulated by the NPDES permit limit that calls for zero toxicity. For this reason, the lowest observable effect concentration (LOEC) for reproduction of *C. dubia* was utilized as a target outflow concentration (USEPA, 2002). The inflow vs. final outflow concentrations for Batch 1: Train 1 and Train 2 were 0.017/0.007 mg/L and 0.014/0.011 mg/L respectively. For Batch 2: Train 1 and Train 2, the inflow vs. final outflow concentrations were 0.024/0.026 mg/L and 0.030/0.020 mg/L respectively. As shown in Figure 4, all Cd inflow and outflow concentrations for Experiment 1 fell below the target outflow limit.
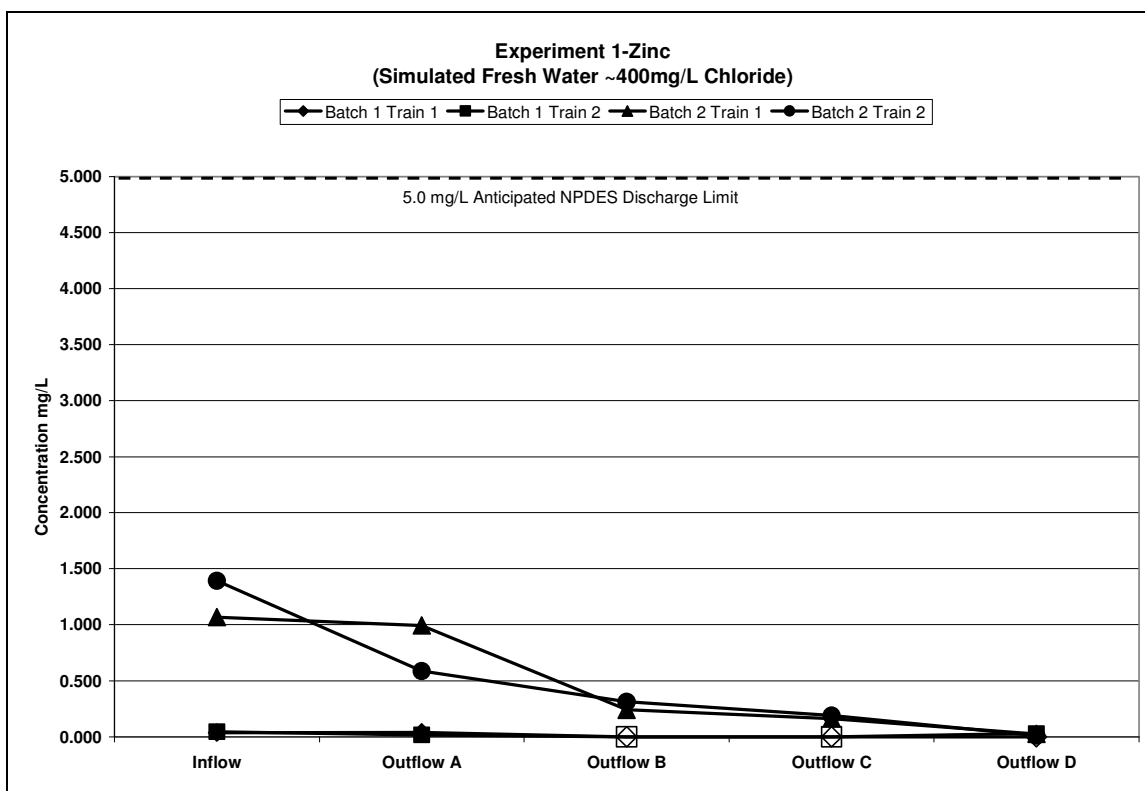
Figure 5. Experiment 1: Simulated freshwater metal analysis for zinc performed by ICP.

Zinc was loaded at a concentration of approximately 0.1 mg/L. The open symbols in Figure 5 indicate outflow values that were below the current detection limit of 10 μg/L. The inflow concentration of Batch 2 increased by an order of magnitude due to a calculation error. However, this error did not prove to have a significant effect on the final outflow concentration. The inflow vs. final outflow concentrations for Batch 1: Train 1 and Train 2 were 0.035 mg/L/non-detect and 0.044/0.029 mg/L respectively. For Batch 2: Train 1 and Train 2, they were 1.070/0.025 mg/L and 1.390/0.011 mg/L respectively. As shown in Figure 5, all inflow and outflow Zn concentrations for Experiment 1 fell below the anticipated NPDES limit. The "Anticipated NPDES Discharge Limit" is the outflow goal defined by the model NPDES permit (Task 2: Table 2).

Toxicity

For Experiment 1, 7-day toxicity tests were performed with *C. dubia* on inflow and final outflow waters from each batch and train. There was no significant difference between the controls and the inflow for mortality or reproduction. There was a significant increase in reproduction of *C. dubia* in the outflow of both trains when compared to the inflow and control results. Waters from Experiment 1 were not toxic to *C. dubia*.

Experiment 2: Simulated Brackish Water

Metals

For Experiment 2, metal concentrations were loaded at approximately 0.41 mg/L Cd, 1.68 mg/L Cu, 5.47 mg/L Pb, and 23 mg/L Zn.
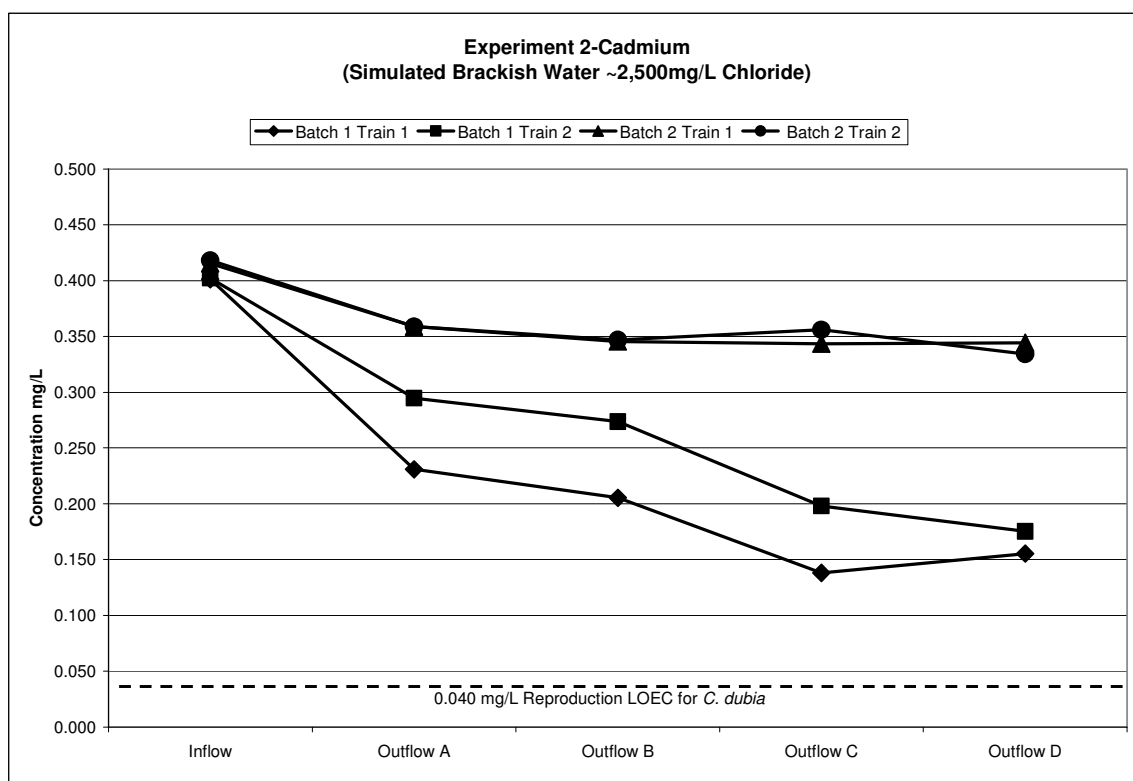
Figure 6. Experiment 2: Simulated brackish water metal analysis for cadmium performed by AA.

The inflow vs. final outflow cadmium concentrations for Batch 1: Train 1 and Train 2 were 0.401/0.155 mg/L and 0.402/0.175 mg/L. For Batch 2: Train 1 and Train 2, they were 0.415/0.344 mg/L and 0.418/0.334 mg/L respectively. As shown in Figure 6, all outflow Cd concentrations for Experiment 2 were greater than the target outflow limit. This indicates that further adjustments need to be made to the system in order to optimize it for the removal of Cd.
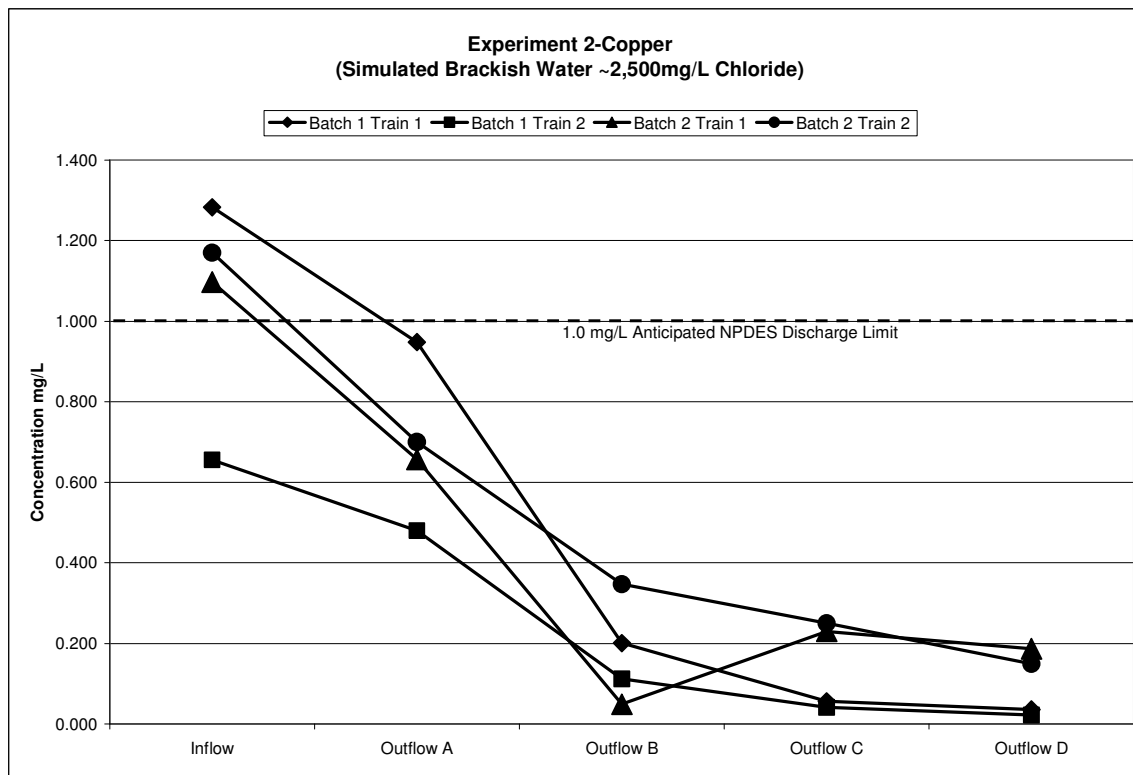
Figure 7. Experiment 2: Simulated brackish water metal analysis for copper performed by AA.

The NPDES permits for the regions examined provided a NPDES discharge limit of 1.0 mg/L for Cu. Two of the data points for Batch 1: Train 2 were lost due to a computer error during original analysis and were performed later on the ICP-AES. The inflow vs. final outflow concentrations for Batch 1: Train 1 and Train 2 were 1.283/0.036 mg/L and 0.656/0.022 mg/L. For Batch 2: Train 1 and Train 2, inflow vs. outflow concentrations were 1.097/0.187 mg/L and 1.170/0.149 mg/L respectively. As shown in Figure 7, all outflow Cu concentrations for Experiment 2 fell below the anticipated NPDES limit.
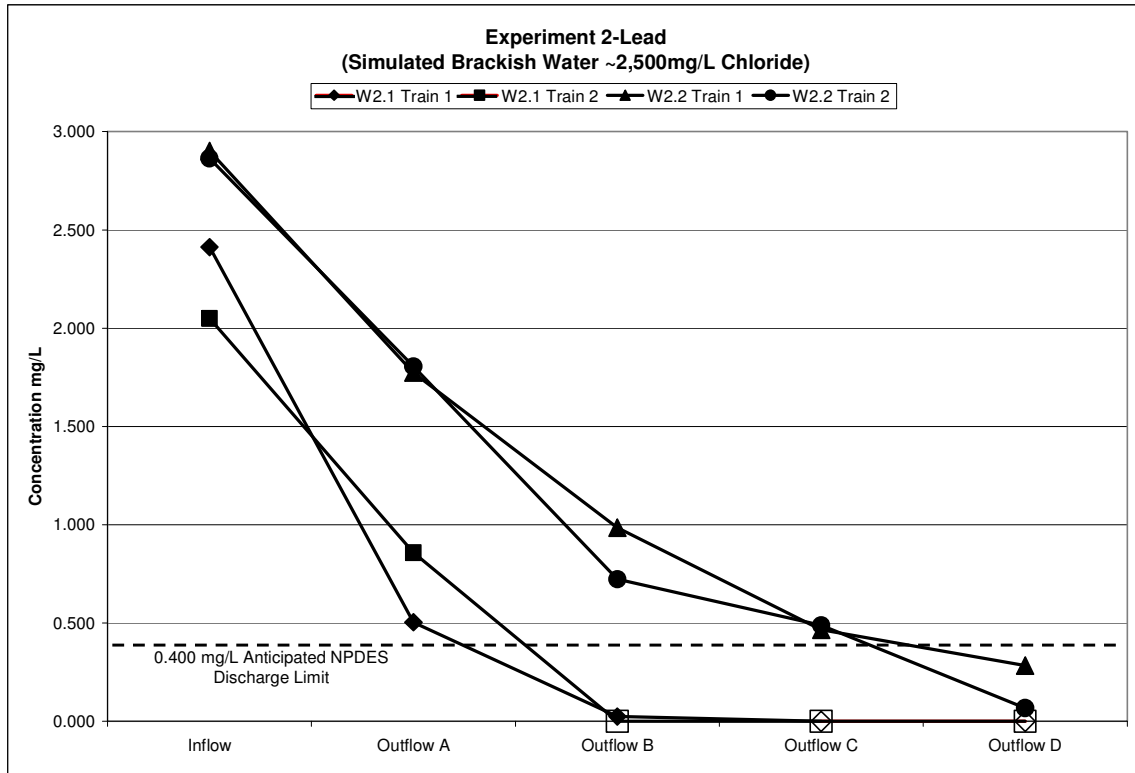
Figure 8. Experiment 2: Simulated brackish water metal analysis for lead performed by AA.

The NPDES permits for the regions examined provided a NPDES discharge limit of 0.400 mg/L for Pb. The open symbols in Figure 8 indicate values that were below the detection limit of the instrument used. The inflow vs. final outflow concentrations for Batch 1: Train 1 and Train 2 were 2.413/non-detect mg/L and 2.049/non-detect mg/L. For Batch 2: Train 1 and Train 2, they were 2.901/0.284 mg/L and 2.864/0.068 mg/L respectively. As shown in Figure 8, all outflow Pb concentrations for Experiment 2 fell below the anticipated NPDES limit.
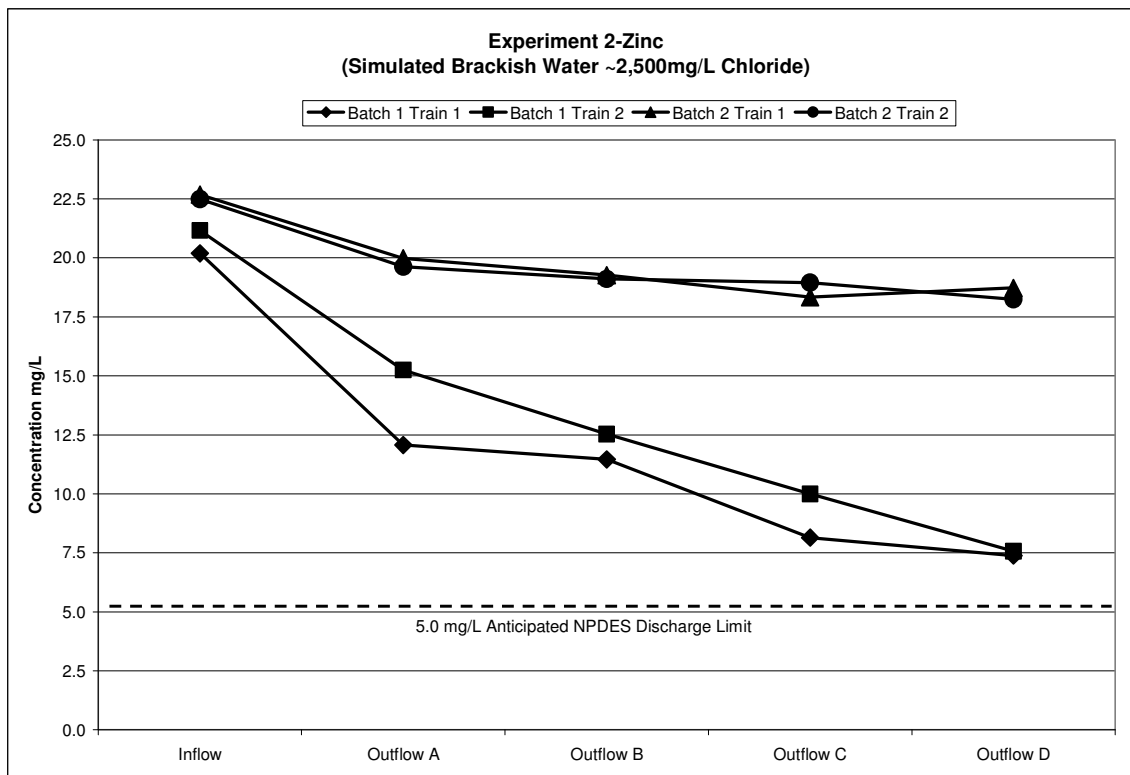
Figure 9. Experiment 2: Simulated brackish water metal analysis for zinc performed by ICP.

The NPDES permits for the regions examined provided a NPDES discharge limit of 5.0 mg/L for Zn. The inflow vs. final outflow concentrations for Batch 1: Train 1 and Train 2 were 20.19/7.39 mg/L and 21.16/7.57 mg/L. For Batch 2: Train 1 and Train 2, they were 22.68/18.73 mg/L and 22.49/18.25 mg/L respectively. As shown in Figure 9, all outflow Zn concentrations for Experiment 2 were greater than the anticipated NPDES limit. This indicates that further adjustments need to be made to the system in order to optimize it for the removal of Zn.

Toxicity
In Experiment 2, 7-day toxicity tests utilizing *C. dubia* were performed only on the waters from Batch 1 because of time constraints. Experiment 2: Batch 1 showed total mortality after 24 hours in 100%, 50%, and 5% final outflow water. From these preliminary screening tests, two full tests were run at 2.5% and 1.2% water for mortality and reproduction effects data, respectively. At the 2.5% dilution there was full mortality for the inflows to both trains, while there was no significant effect on mortality in the outflows from either of the two trains. At the 1.2% Dilution Train 1 shows significantly lower reproduction of *C. dubia* than the control in both inflow and outflow, while Train 2 shows significantly lower reproduction of *C. dubia* in the inflow but no significant difference between the control and the outflow.

Experiment 3: Simulated Saline Water

Metals

For Experiment 3, metals were loaded at concentrations of approximately 0.8 mg/L Cd, 3.34 mg/L Cu, 6.84 mg/L Pb, and 45.9 mg/L Zn.
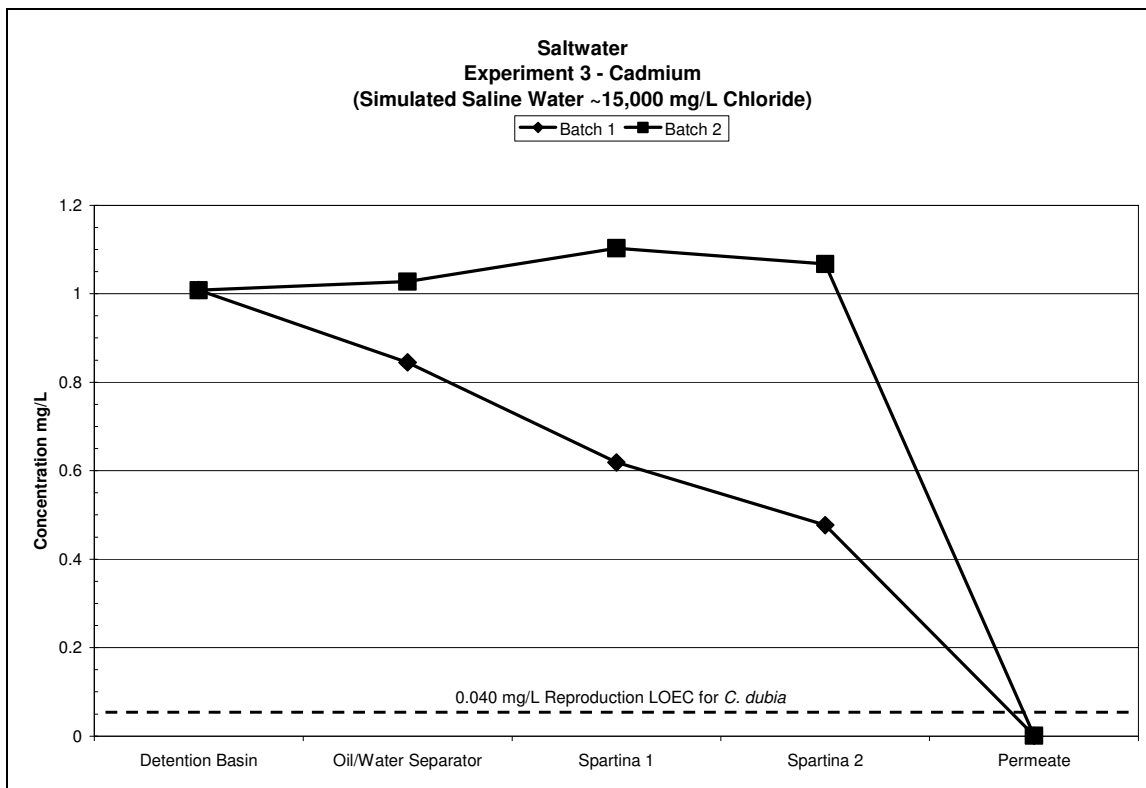
Figure 10. Saltwater module and RO permeate results for Experiment 3: Simulated saline water metal analysis of cadmium performed by ICP. The saltwater module is that portion of the hybrid constructed wetland treatment system occurring before the RO system (i.e., all points except "permeate"). The RO permeate is the outflow water from the RO system that is then pumped into the two freshwater wetland trains. For each batch of water in the above graph, the RO permeate concentration is the average of the inflow concentrations for each of the two freshwater wetland trains.
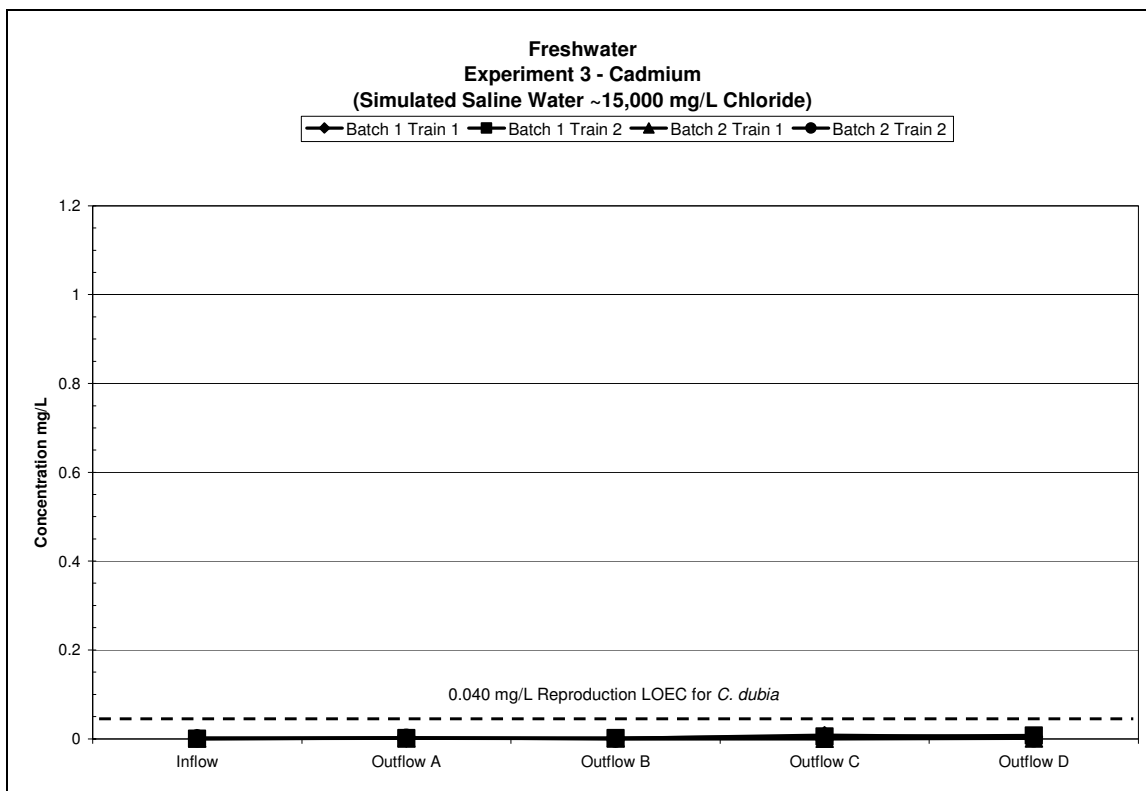
Figure 11. Freshwater module (post-RO system) results for Experiment 3: Simulated saline water metal analysis of cadmium performed by ICP.

The inflow cadmium concentrations to the entire hybrid CWTS were 1.008 mg/L and 1.0076 mg/L for Batch 1 and Batch 2, respectively, of the simulated saline produced water. As shown in Figure 10, the Cd concentrations decreased as the water flowed through the saltwater portion of the hybrid CWTS and the RO system took the concentrations below the target outflow limit. The inflow vs. final outflow concentrations for Batch 1: Train 1 and Train 2 of the freshwater system were 0.0017/0.0041 mg/L and 0.0001/0.0072 mg/L. For Batch 2: Train 1 and Train 2, they were 0.0004/ 0.0010 mg/L and 0.0011/0.0020 mg/L, respectively. As shown in Figure 11, the inflow water to each freshwater wetland train had low concentrations of Cd due to removal by the RO system. The inflow water to the freshwater system was below the target outflow limit based on the LOEC for reproduction of *C. dubia*. As the water flowed through the freshwater system, it remained below the target outflow limit.
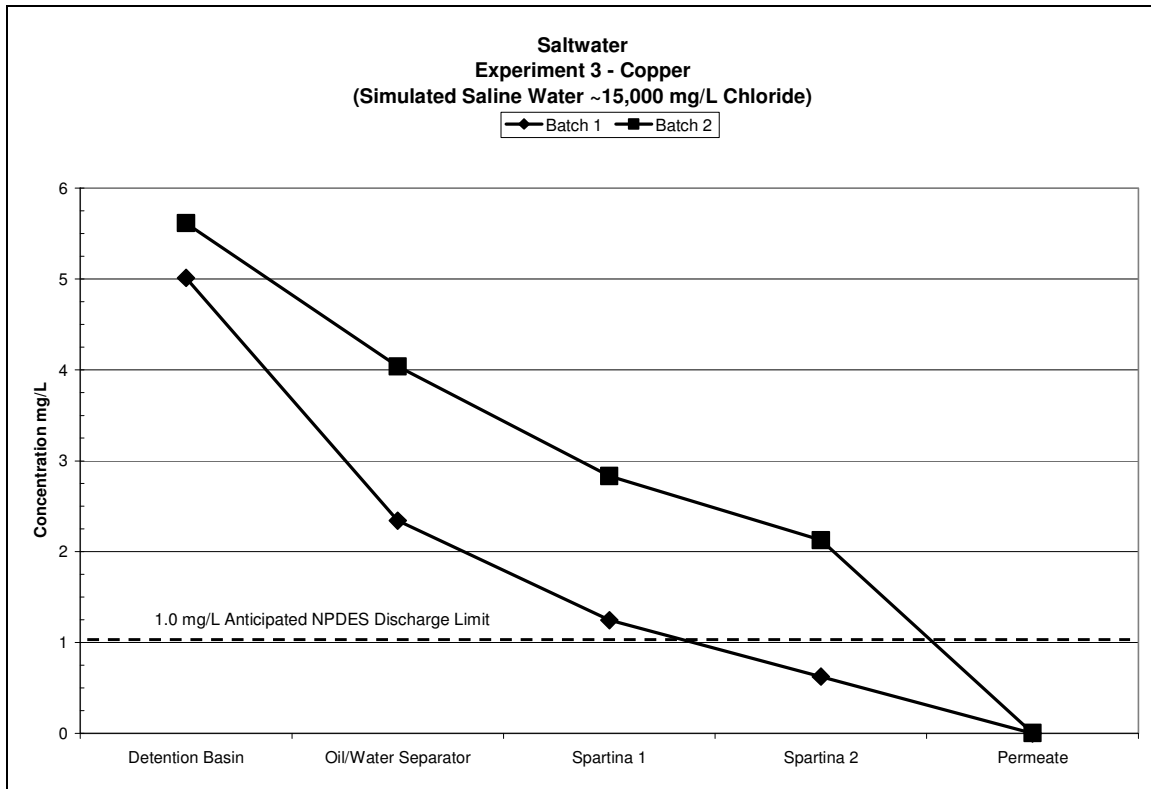
Figure 12. Saltwater module and RO permeate results for Experiment 3: Simulated saline water metal analysis of copper performed by ICP. The saltwater module is that portion of the hybrid constructed wetland treatment system occurring before the RO system (i.e., all points except "permeate"). The RO permeate is the outflow water from the RO system that is then pumped into the two freshwater wetland trains. For each batch of water in the above graph, the RO permeate concentration is the average of the inflow concentrations for each of the two freshwater wetland trains.
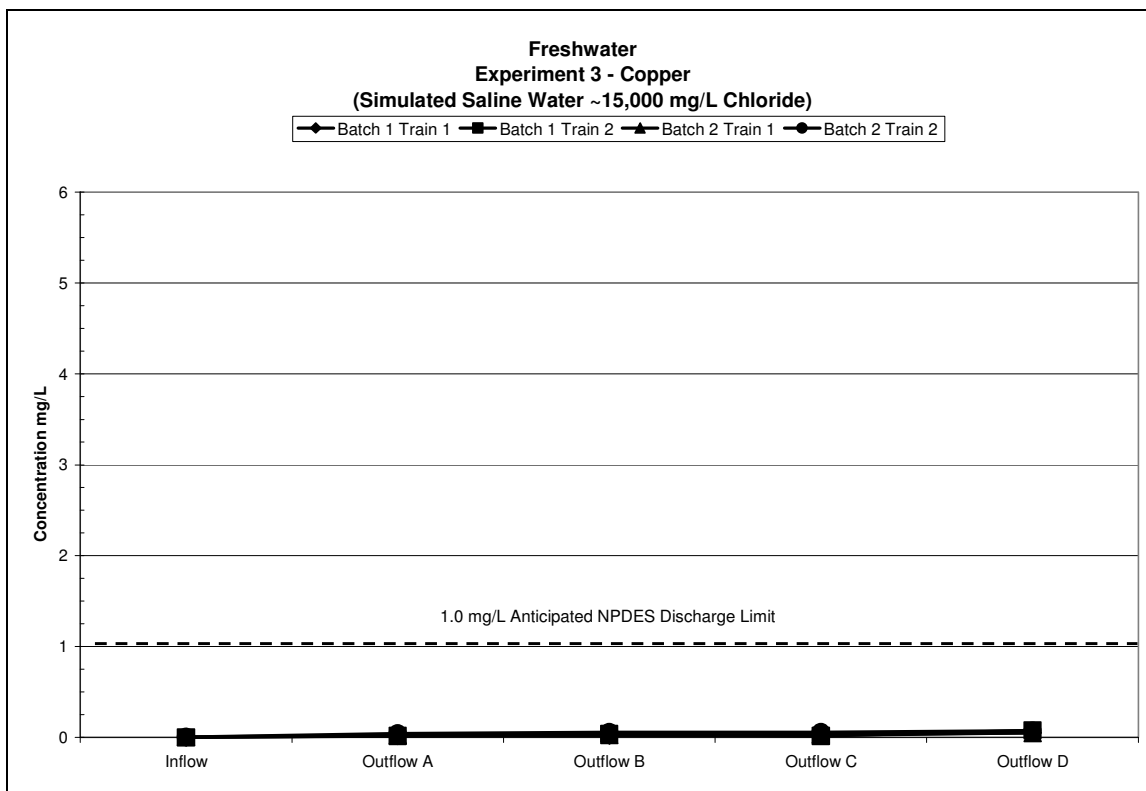
Figure 13. Freshwater module (post-RO system) results for Experiment 3: Simulated saline water metal analysis of copper performed by ICP.

The NPDES permits for the regions examined provided a NPDES discharge limit of 1.0 mg/L for Cu. The inflow concentrations to the entire hybrid constructed wetland system were 5.012 mg/L and 5.616 mg/L for Batch 1 and Batch 2 respectively. As shown in Figure 12, the Cu concentrations decreased as the water flowed through the saltwater portion of the hybrid CWTS, and the RO system took the concentrations below the target outflow limit set by the model NPDES permit. The inflow vs. final outflow concentrations for Batch 1: Train 1 and Train 2 of the freshwater system were 0.0005/0.0512 mg/L and 0.0009/0.0779 mg/L. For Batch 2: Train 1 and Train 2, they were 0.0050/0.0478 mg/L and 0.0050/0.0732 mg/L, respectively. As shown in Figure 13, all water samples for both batches of water collected after the RO system, the permeate (outflow from the RO system) through the outflow from Trains 1 and 2, met the NPDES discharge limit of 1.0 mg/L for copper.
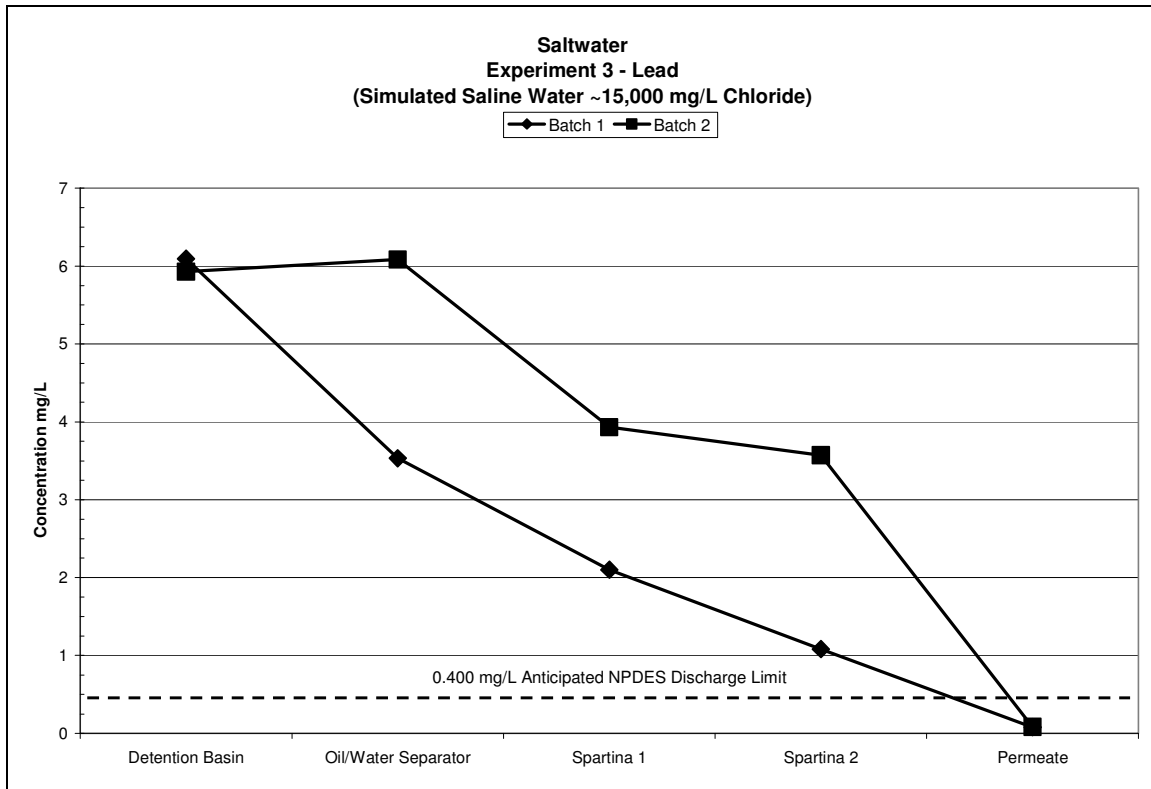
Figure 14. Saltwater module and RO permeate results for Experiment 3: Simulated saline water metal analysis of lead performed by ICP. The saltwater module is that portion of the hybrid constructed wetland treatment system occurring before the RO system (i.e., all points except "permeate"). The RO permeate is the outflow water from the RO system that is then pumped into the two freshwater wetland trains. For each batch of water in the above graph, the RO permeate concentration is the average of the inflow concentrations for each of the two freshwater wetland trains.
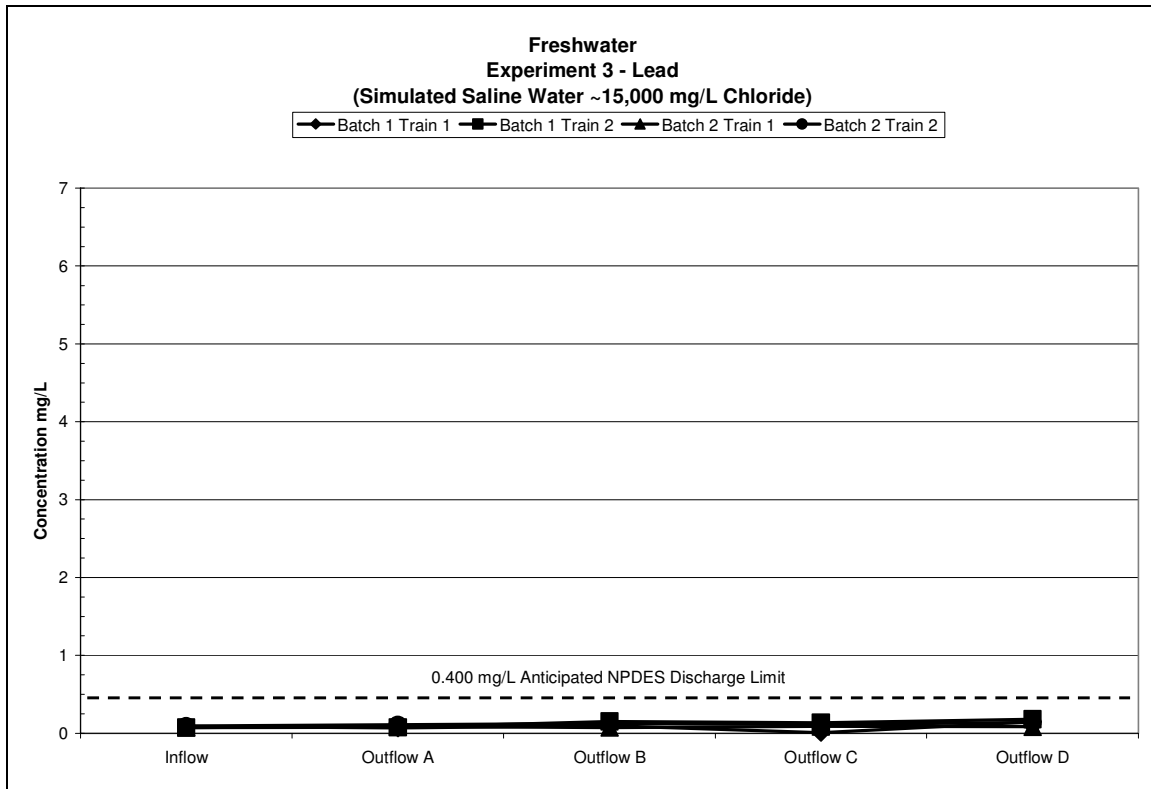
Figure 15. Freshwater module (post-RO system) results for Experiment 3: Simulated saline water metal analysis of lead performed by ICP.

The NPDES permits for the regions examined provided a NPDES discharge limit of 0.400 mg/L for Pb. The inflow concentrations to the entire hybrid constructed wetland system were 6.096 mg/L and 5.928 mg/L for Batch 1 and Batch 2, respectively. As shown in Figure 14, the Pb concentrations decreased as the water flowed through the saltwater portion of the hybrid CWTS and the RO system took the concentrations below the target outflow limit set by the model NPDES permit. The inflow vs. final outflows for Batch 1: Train 1 and Train 2 of the freshwater system were 0.0870/0.1455 mg/L and 0.0737/0.1795 mg/L. For Batch 2: Train 1 and Train 2, they were 0.0724/0.0821 mg/L and 0.0919/0.1365 mg/L, respectively. As shown in Figure 15, all water samples for both batches of water collected after the RO system, the permeate (outflow from the RO system) through the outflow from trains 1 and 2 met the NPDES discharge limit of 0.400 mg/L for lead.
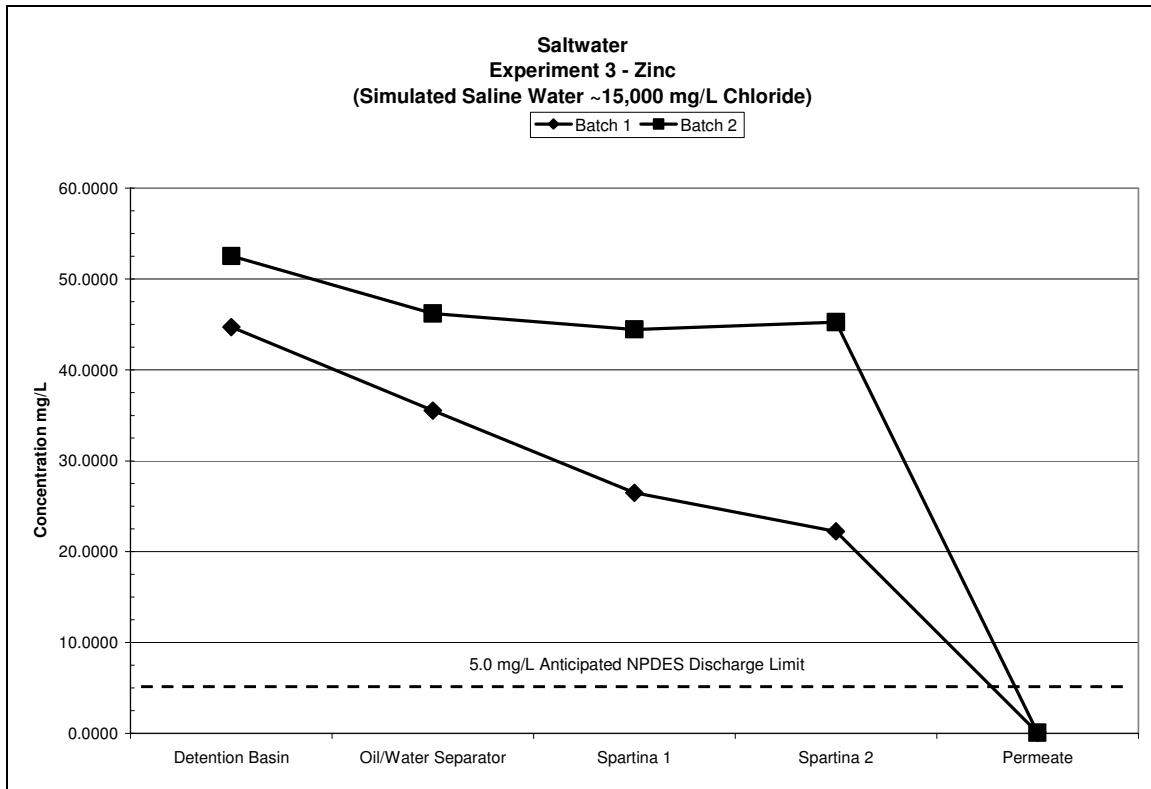
Figure 16. Saltwater module and RO permeate results for Experiment 3: Simulated saline water metal analysis of zinc performed by ICP. The saltwater module is that portion of the hybrid constructed wetland treatment system occurring before the RO system (i.e., all points except "permeate"). The RO permeate is the outflow water from the RO system that is then pumped into the two freshwater wetland trains. For each batch of water in the above graph, the RO permeate concentration is the average of the inflow concentrations for each of the two freshwater wetland trains.
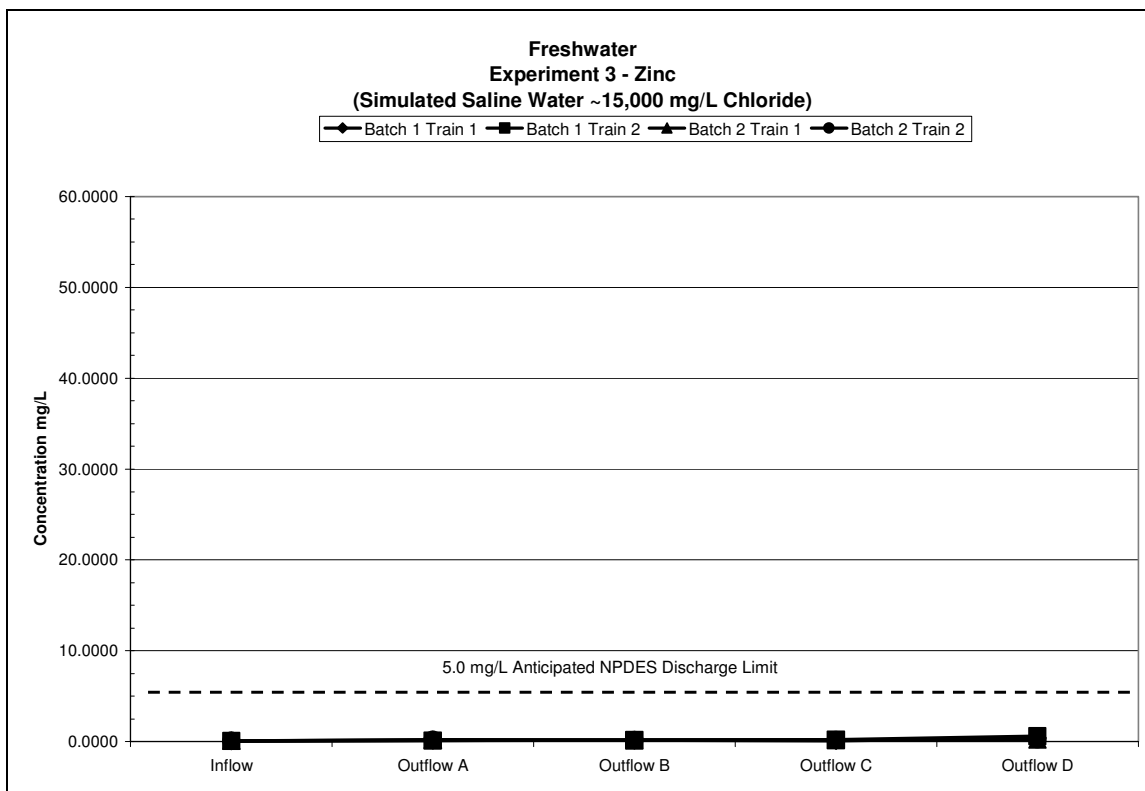
Figure 17. Freshwater module (post-RO system) results for Experiment 3: Simulated saline water metal analysis of zinc performed by ICP.

The NPDES permits for the regions examined provided a NPDES discharge limit of 5.0 mg/L for Zn. The inflow concentrations to the entire hybrid constructed wetland system were 44.7340 mg/L and 52.5340 mg/L for Batch 1 and Batch 2, respectively. As shown in Figure 16, the Zn concentrations decreased as the water flowed through the saltwater portion of the hybrid CWTS, and the RO system took the concentrations below the target outflow limit set by the model NPDES permit. The inflow vs. final outflow concentrations for Batch 1: Train 1 and Train 2 of the freshwater system were 0.0656/0.4025 mg/L and 0.0696/0.5895 mg/L. For Batch 2: Train 1 and Train 2, they were 0.0881/0.2482 mg/L and 0.0928/0.2568 mg/L, respectively. As shown in Figure 17, all water samples for both batches of water collected after the RO system, the permeate (outflow from the RO system) through the outflow from trains 1 and 2, met the NPDES discharge limit of 5.0 mg/L for zinc. Like the results for cadmium, copper, and lead, the low concentrations of zinc in the RO permeate support the proposed fine-tuning of the RO system for increased volumes of permeate and decreased amounts of concentrate.

Toxicity
In Experiment 3, 7-day toxicity tests utilizing *C. dubia* were performed only on the waters from Batch 2 due to time constraints. Experiment 3: Batch 2 samples from the saltwater module (detention basin, oil/water separator outflow, Spartina cell 1 outflow, and Spartina cell 2 outflow) were diluted to 3% sample water: 97% moderately hard water to prevent interference in toxicity results from chlorides. These waters showed total mortality after 24 hours. In the freshwater system, the inflow to Train 2 showed total

mortality after 24 hours. The inflow to Train 2 was also found to have a low pH which is likely the cause of these results. The outflow from Train 2 showed significantly decreased reproduction of *C. dubia* but no significant difference in mortality from the control. Train 1 showed no significant difference in reproduction or mortality of *C. dubia* from the control.

Experiment 4: Simulated Hyper-Saline Water

Metals
For Experiment 4, metals were loaded at concentrations of approximately 1.21 mg/L Cd, 5.0 mg/L Cu, 10.2 mg/L Pb, and 69.0 mg/L Zn.
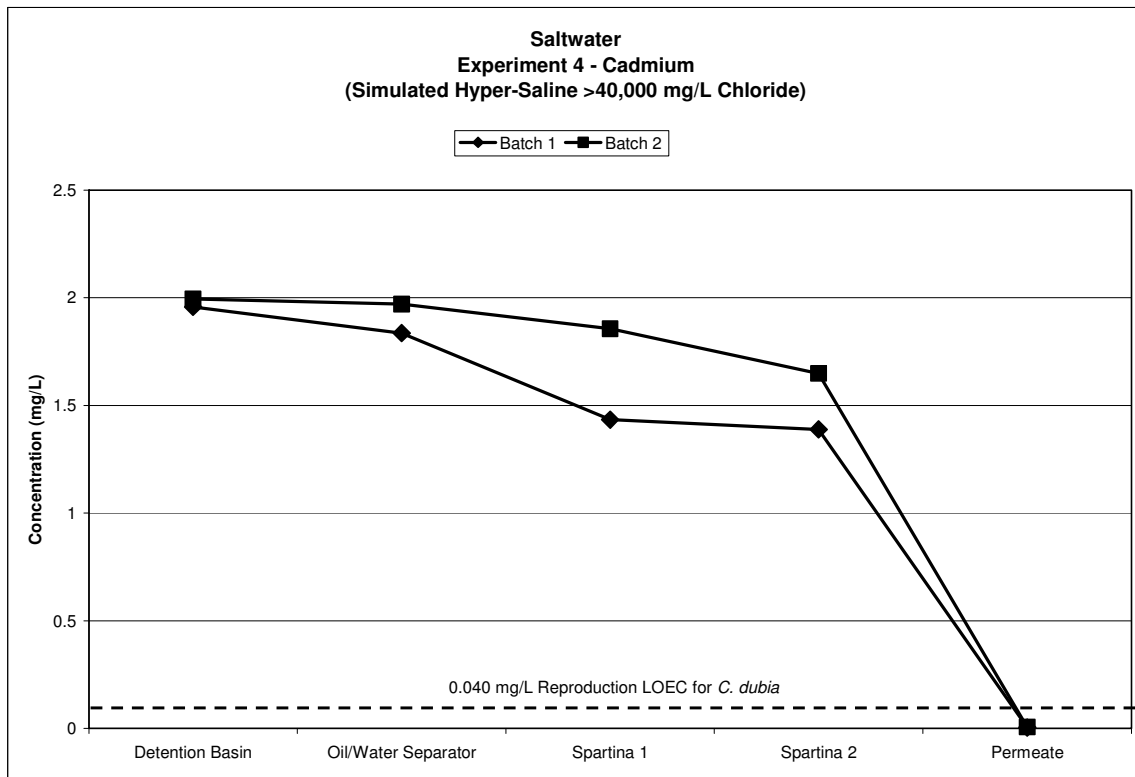
Figure 18. Saltwater module and RO permeate results for Experiment 4: Simulated hyper-saline water metal analysis of cadmium performed by ICP. The saltwater module is that portion of the hybrid constructed wetland treatment system occurring before the RO system (i.e., all points except "permeate"). The RO permeate is the outflow water from the RO system that is then pumped into the two freshwater wetland trains. For each batch of water in the above graph, the RO permeate concentration is the average of the inflow concentrations for each of the two freshwater wetland trains.
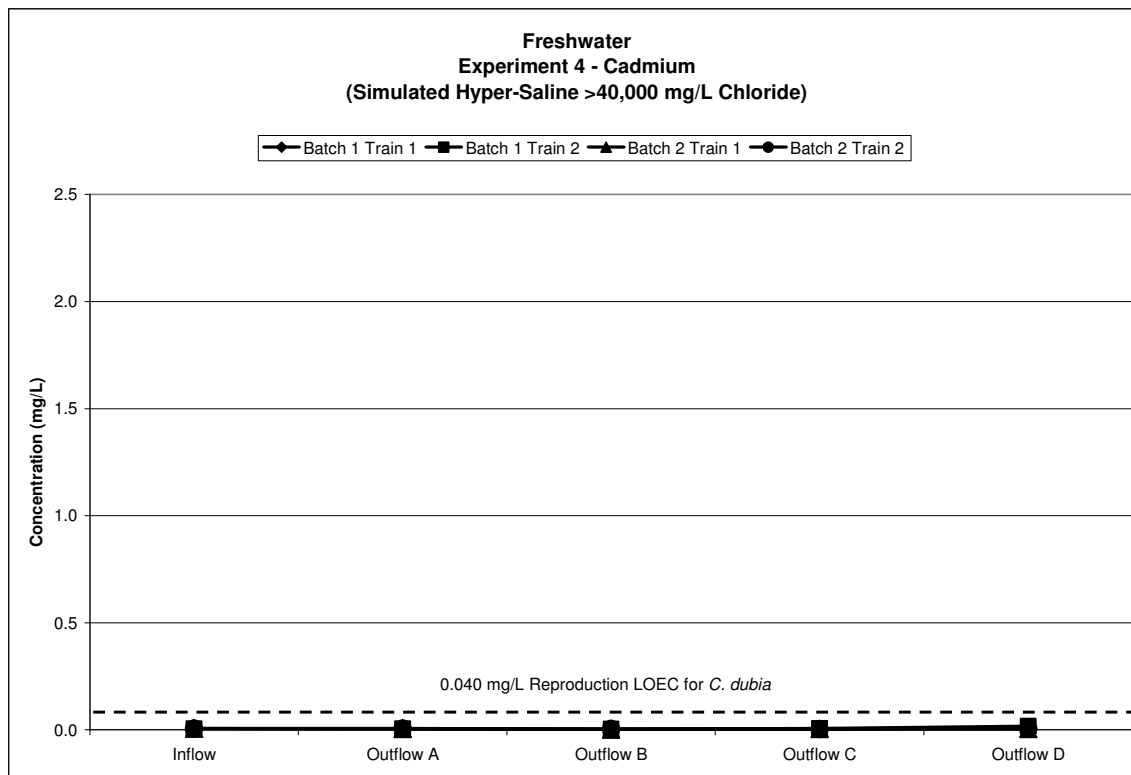
Figure 19. Freshwater module (post-RO system) results for Experiment 4: Simulated hyper-saline water metal analysis of cadmium performed by ICP.

The inflow cadmium concentrations to the entire hybrid CWTS were 1.958 mg/L and 1.994 mg/L for Batch 1 and Batch 2, respectively, of the simulated hyper-saline produced water. As shown in Figure 18, the Cd concentrations decreased as the water flowed through the saltwater portion of the hybrid CWTS. The inflow vs. final outflow concentrations for Batch 1: Train 1 and Train 2 of the freshwater system were 0.0069/.0076 mg/L and 0.0059/0.0168 mg/L. For Batch 2: Train 1 and Train 2, they were 0.0062/0.0039 mg/L and 0.0055/0.0043 mg/L, respectively. As shown in Figure 19, the inflow water to each freshwater wetland train had low concentrations of Cd due to removal by the RO system. The inflow water to the freshwater system was below the target outflow limit based on the LOEC for reproduction of *C. dubia*. As the water flowed through the freshwater system, it remained below the target outflow limit.
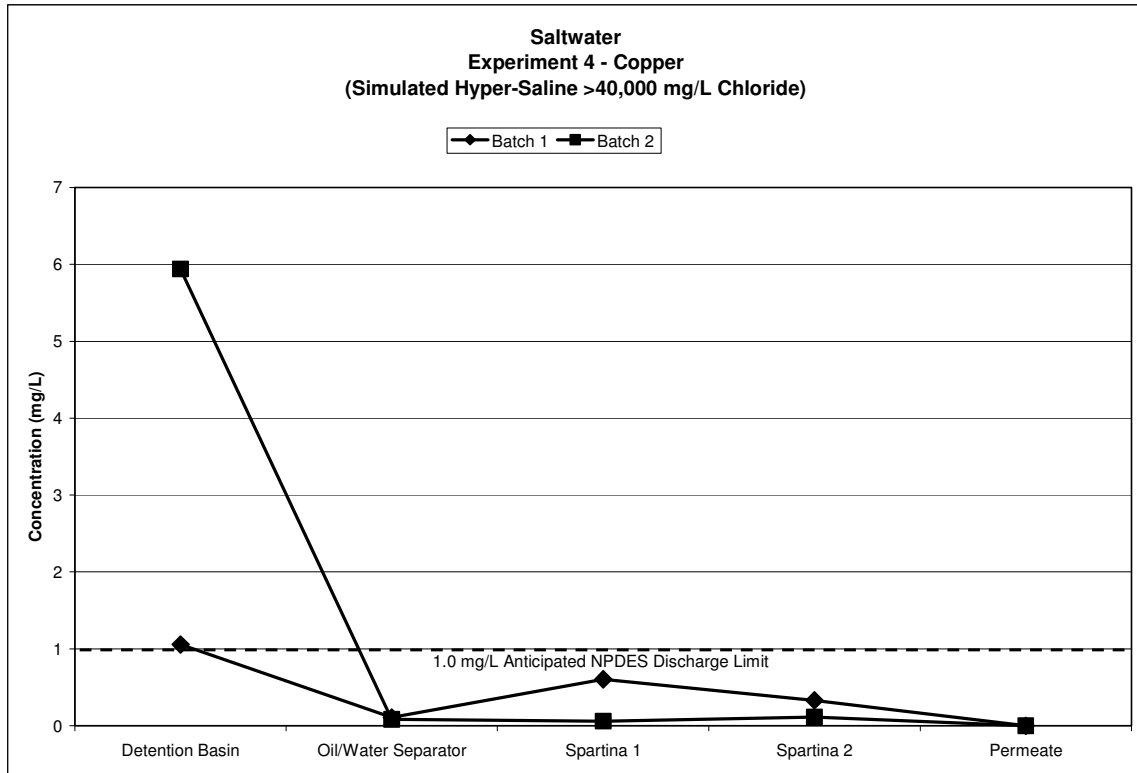
Figure 20. Saltwater module and RO permeate results for Experiment 4: Simulated hyper-saline water metal analysis of copper performed by ICP. The saltwater module is that portion of the hybrid constructed wetland treatment system occurring before the RO system (i.e., all points except "permeate"). The RO permeate is the outflow water from the RO system that is then pumped into the two freshwater wetland trains. For each batch of water in the above graph, the RO permeate concentration is the average of the inflow concentrations for each of the two freshwater wetland trains.
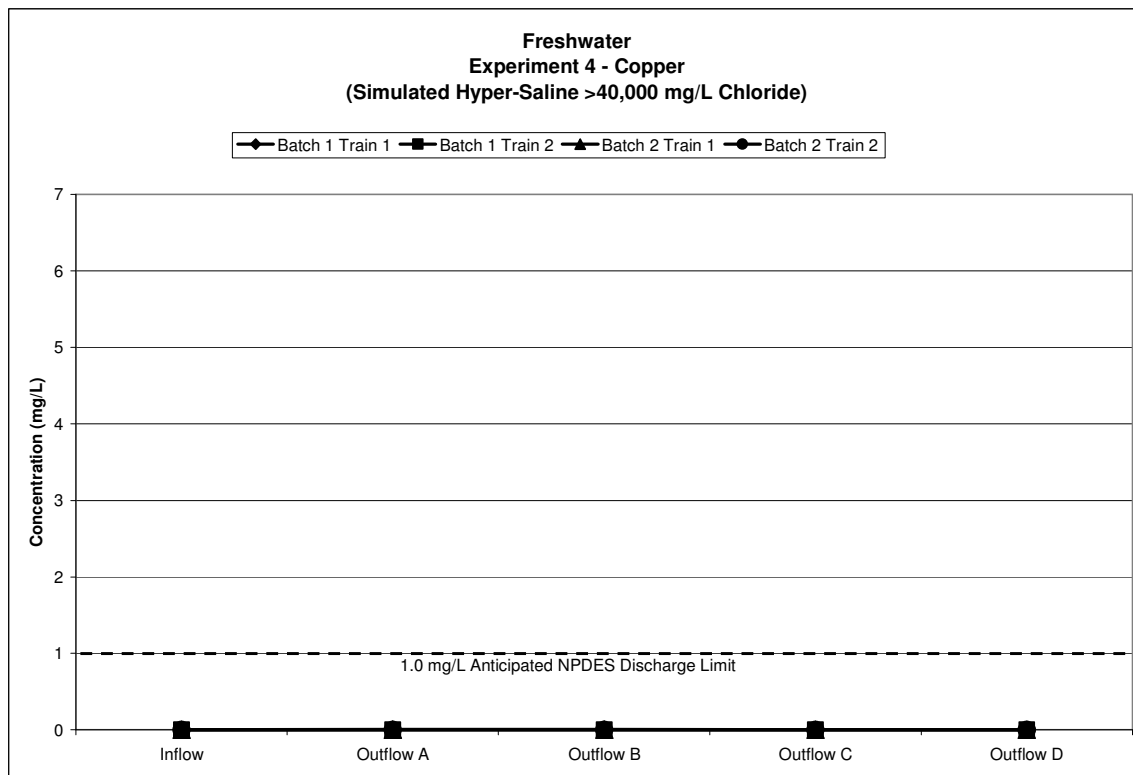
Figure 21. Freshwater module (post-RO system) results for Experiment 4: Simulated hyper-saline water metal analysis of copper performed by ICP.

The NPDES permits for the regions examined provided a NPDES discharge limit of 1.0 mg/L for Cu. The inflow concentrations to the entire hybrid constructed wetland system were 1.056 mg/L and 5.940 mg/L for Batch 1 and Batch 2, respectively. As shown in Figure 20, the Cu concentrations decreased to levels below the target outflow limit set by the model NPDES permit as the water flowed through the oil/water separator and into the saltwater portion of the hybrid CWTS. As the water continued through the system into the saltwater portion and through the RO system, the copper concentrations remained below the target outflow limit set by the model NPDES permit. The inflow vs. final outflow concentrations for the entire freshwater system were below method detection limits. As shown in Figure 21, all water samples for both batches of water collected after the oil/water separator, including water samples from the saltwater wetland cells, the RO system, and the freshwater wetland cells, met the NPDES discharge limit of 1.0 mg/L for copper.
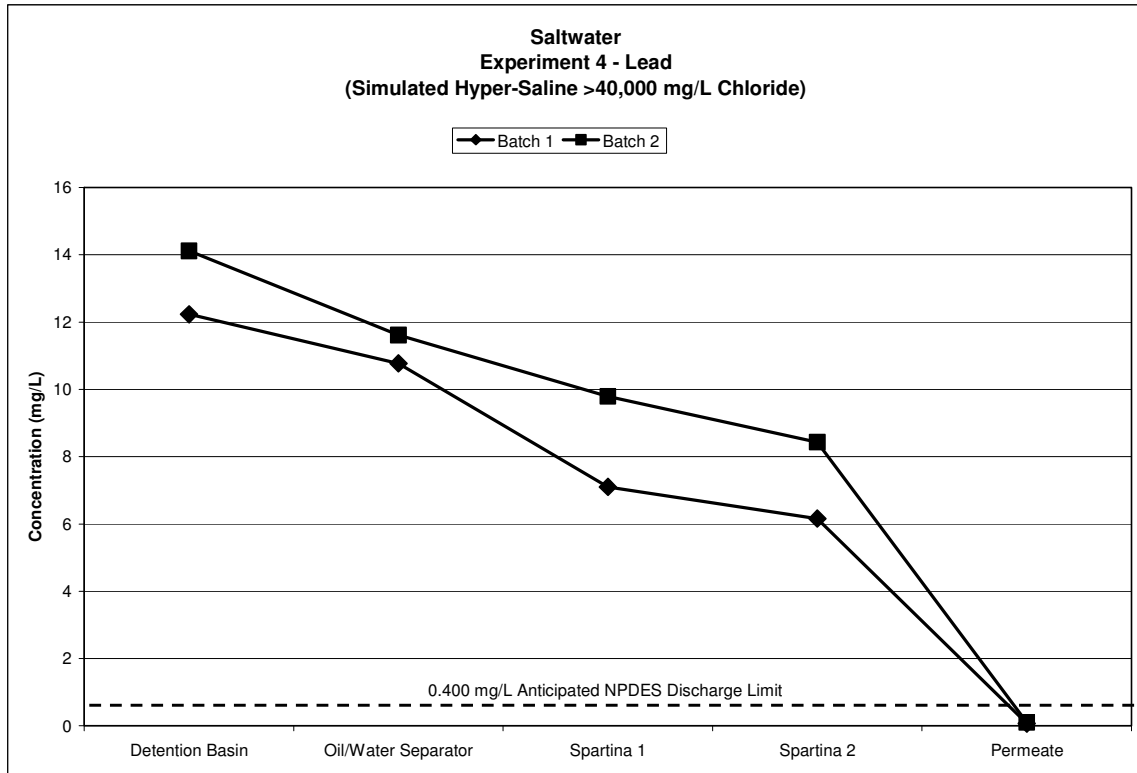
Figure 22. Saltwater module and RO permeate results for Experiment 4: Simulated hyper-saline water metal analysis of lead performed by ICP. The saltwater module is that portion of the hybrid constructed wetland treatment system occurring before the RO system (i.e., all points except "permeate"). The RO permeate is the outflow water from the RO system that is then pumped into the two freshwater wetland trains. For each batch of water in the above graph, the RO permeate concentration is the average of the inflow concentrations for each of the two freshwater wetland trains.
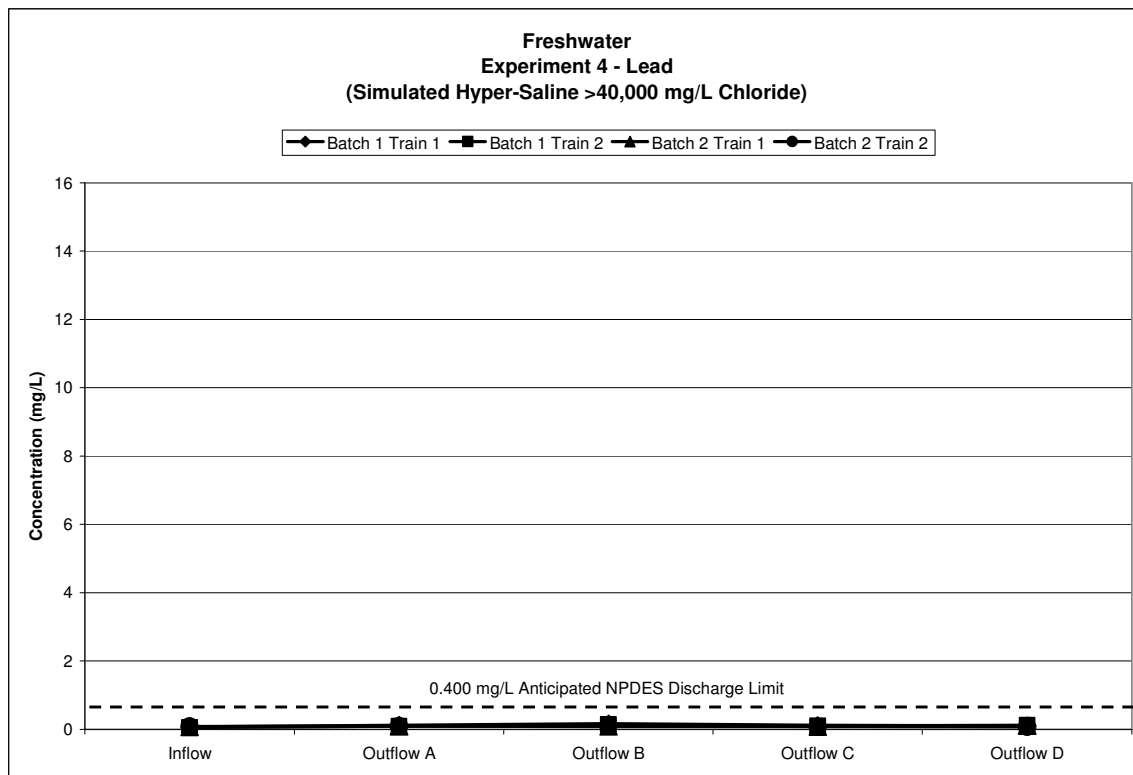
Figure 23. Freshwater module (post-RO system) results for Experiment 4: Simulated hyper-saline water metal analysis of lead performed by ICP.

The NPDES permits for the regions examined provided a NPDES discharge limit of 0.400 mg/L for Pb. The inflow concentrations to the entire hybrid constructed wetland system were 12.23 mg/L and 14.11 mg/L for Batch 1 and Batch 2 respectively. As shown in Figure 22, the Pb concentrations decreased as the water flowed through the saltwater portion of the hybrid CWTS, and the RO system took the concentrations below the target outflow limit set by the model NPDES permit. The inflow vs. final outflows for Batch 1: Train 1 and Train 2 of the freshwater system were 0.0683/0.0974 mg/L and 0.0510/0.1130 mg/L. For Batch 2: Train 1 and Train 2, they were 0.0679/0.1005 mg/L and 0.0847/0.0703 mg/L, respectively. As shown in Figure 23, all water samples for both batches of water collected after the RO system, the permeate (outflow from the RO system) through the outflow from trains 1 and 2 met the NPDES discharge limit of 0.400 mg/L for lead.
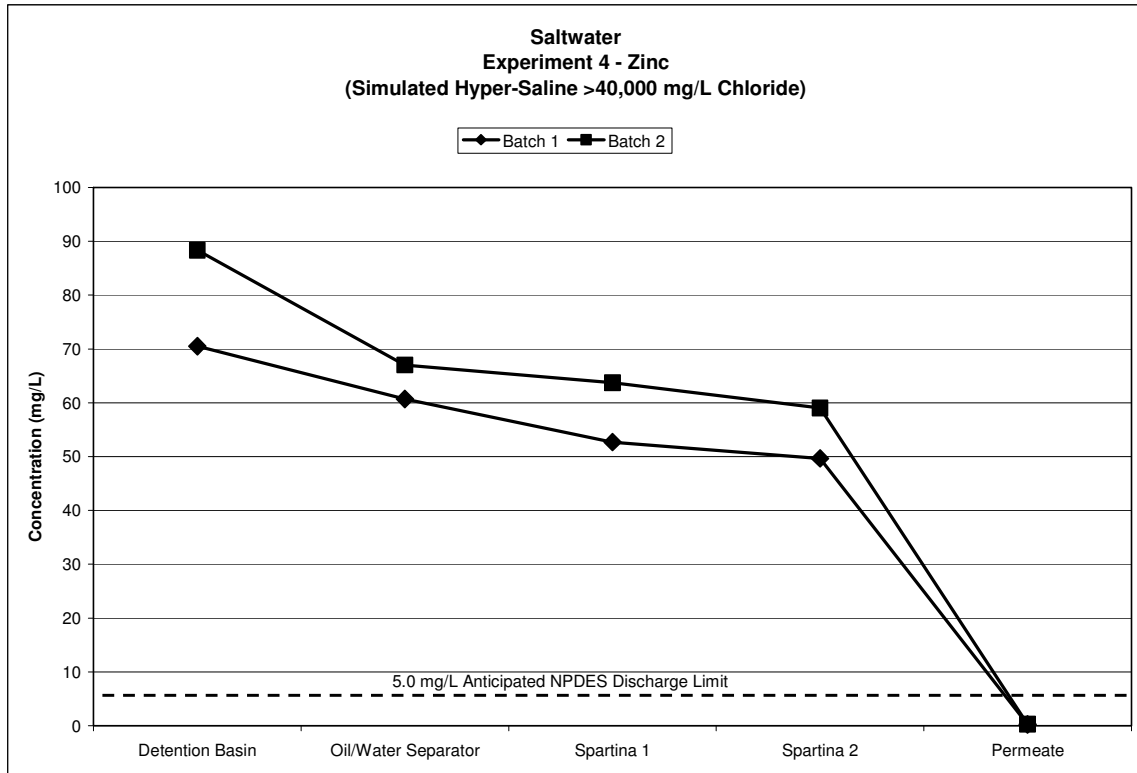
Figure 24. Saltwater module and RO permeate results for Experiment 4: Simulated hyper-saline water metal analysis of zinc performed by ICP. The saltwater module is that portion of the hybrid constructed wetland treatment system occurring before the RO system (i.e., all points except "permeate"). The RO permeate is the outflow water from the RO system that is then pumped into the two freshwater wetland trains. For each batch of water in the above graph, the RO permeate concentration is the average of the inflow concentrations for each of the two freshwater wetland trains.
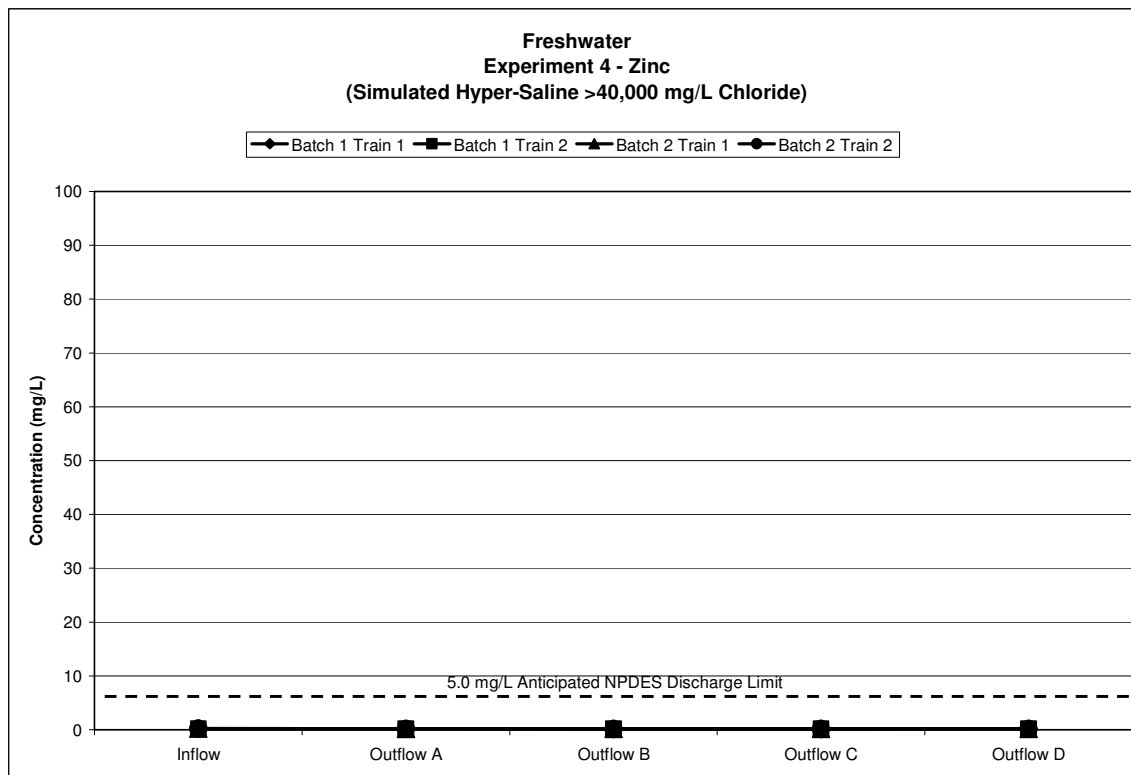
Figure 25. Freshwater module (post-RO system) results for Experiment 4: Simulated hyper-saline water metal analysis of zinc performed by ICP.

The NPDES permits for the regions examined provided a NPDES discharge limit of 5.0 mg/L for Zn. The inflow concentrations to the entire hybrid constructed wetland system were 70.5 mg/L and 88.3 mg/L for Batch 1 and Batch 2 respectively. As shown in Figure 24, the Zn concentrations decreased as the water flowed through the saltwater portion of the hybrid CWTS and the RO system took the concentrations below the target outflow limit set by the model NPDES permit. The inflow vs. final outflow concentrations for Batch 1: Train 1 and Train 2 of the freshwater system were 0.2498/0.1915 mg/L and 0.2346/0.1958 mg/L. For Batch 2: Train 1 and Train 2, they were 0.2368/0.1789 mg/L and 0.2361/0.1750 mg/L respectively. As shown in Figure 25, all water samples for both batches of water collected after the RO system, the permeate (outflow from the RO system) through the outflow from trains 1 and 2 met the NPDES discharge limit of 5.0 mg/L for zinc. Like the results for cadmium and lead, the low concentrations of zinc in the RO permeate support the proposed fine-tuning of the RO system for increased volumes of permeate and decreased amounts of concentrate.

Toxicity
In Experiment 4, 7-day toxicity tests utilizing *C. dubia* were performed on both the waters from Batch 1 and Batch 2. Experiment 4 samples from the saltwater module were diluted to 1.2% sample water, 98.8% moderately hard water to prevent chloride interference in toxicity results. In Experiment 4, both Batch 1 and Batch 2, showed survival of *C. dubia* as significantly less than the controls in each component of the

saltwater module. There was total mortality of *C. dubia* in both the detention basin water and oil/water separator outflow, and none of the organisms in either batch produced offspring.

The water tested in the freshwater module was run at 100% sample water for both experiments. The outflow from these wetland cells showed no significant differences in mortality or reproduction of *C. dubia* when compared to the control for both batches of water.

Oil-in-Water Data
Oil-in-water was measured by Turner Designs Hydrocarbon Instruments TD500 Handheld Oil in Water Meter. The methods used were adapted from Standard Methods fluorometric determination of oil-in-water. Measurements taken using this instrument indicate that the method has some interference, possibly from algae present in the water column.

General Water Chemistry
General water chemistry data provide an overview of the characteristics of each category of water as it flows through the system. To adequately assess the effectiveness of the system, each category of water was run through the CWTS for four weeks. For each category, two batches of water were mixed and analyzed. The general water chemistry results for each experiment and batch are shown in the Appendix.

Task 5: Confirm Design Characteristics

Task 5 focuses on confirming design characteristics and modifying the system to optimize performance.

Oil/Water Separator
The oil/water separator was one of the modules that was modified to improve performance. High values of oil-in-water were measured in the outflow from the Spartina 1 and Spartina 2 wetland cells during Experiment 3. While interference by algae may be the cause of the high concentrations of oil in water found in the outflows from these cells, visual inspection of the system suggested that the original oil/water separator (Figure 26) was not adequately removing the oil and grease from the water. Due to the detrimental effect excess hydrocarbon concentrations may have on the macrophytes, *Spartina alterniflora,* in the saltwater wetland cells and on the RO membrane, it was deemed necessary to make some adaptations to the oil/water separator in preparation for Experiment 4. In response to the above results and observations, a new oil/water separator was designed, built, and tested at a bench-scale. The new model incorporated some of the same baffle concepts used by the original oil/water separator and also utilized dissolved air flotation, turbulence reduction, and filtering techniques to separate the oil from the water. Following the successful removal of oil at the bench-scale by the new model, a pilot-scale oil/water separator was built with this design (Figure 27) and was incorporated into the hybrid CWTS for Experiment 4 in place of the previously used API oil/water separator.
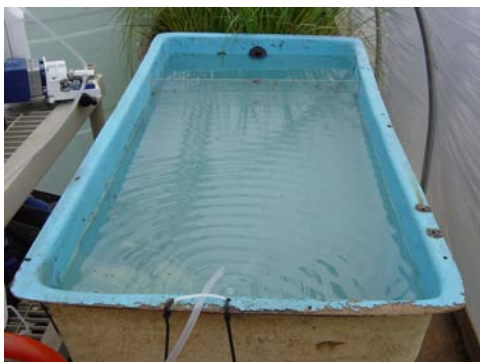
Figure 26: Oil/Water Separator used in Experiment 3.

Figure 27: Newly constructed Oil/Water Separator used in Experiment 4.

Reverse Osmosis System

The RO system also presents an opportunity for fine tuning the system and improving the system efficiency. Since the metal concentrations in the RO permeate are below the target outflow limits set forth in the NPDES permits, it may be beneficial to adjust the RO system (e.g. use less restrictive membranes) and allow more dissolved solids through, thus utilizing the freshwater wetland to its full potential. Also, by adjusting the RO system to create a larger volume of permeate, a smaller volume of concentrate is generated. Concentrate is the wastewater produced by the RO system requiring costly disposal. Since the freshwater system is capable of handling up to 4,000 mg/L chlorides, the RO system could be fine-tuned to produce a larger volume of permeate with higher concentrations of chlorides and metals. The freshwater system would then be used for decreasing the metal concentrations below the target outflow limits. By reducing the volume of concentrate and increasing the use of the freshwater system for metal removal, there is improved efficiency of the hybrid CWTS.

Simulated Brackish Water II

Metals

For Experiment 5, metals were loaded at concentrations emulating those of the model NPDES permit limit of approximately 0.37 mg/L Cu, 0.4 mg/L Pb, and 1.3 mg/L Zn. A concentration of 0.04 mg/L was used for Cd based on the lowest observable effect concentration (LOEC) for reproduction of *C. dubia* (USEPA, 2002). This experiment utilized the detention basin, the oil/water separator, and the freshwater module.
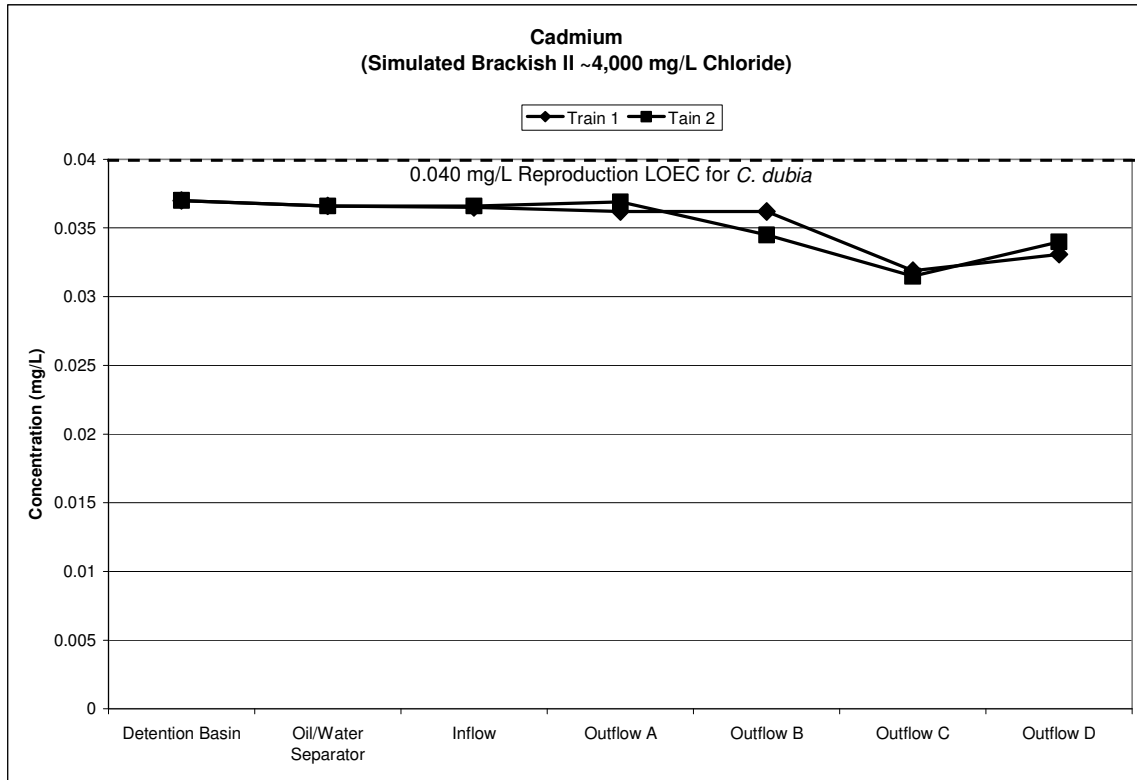
Figure 28. Results for simulated brackish water II metal analysis of cadmium performed by ICP.

The inflow cadmium concentration to the entire hybrid CWTS was 0.037 mg/L for the simulated brackish II produced water. As shown in Figure 28, the Cd concentrations decreased gradually as the water flowed through the CWTS. The final outflow concentrations for Train 1 and Train 2 were 0.0331 and 0.0340 mg/L, respectively. The inflow water to the freshwater system was below the target outflow limit based on the LOEC for reproduction of *C. dubia*. As the water flowed through the freshwater system, it remained below the target outflow limit.
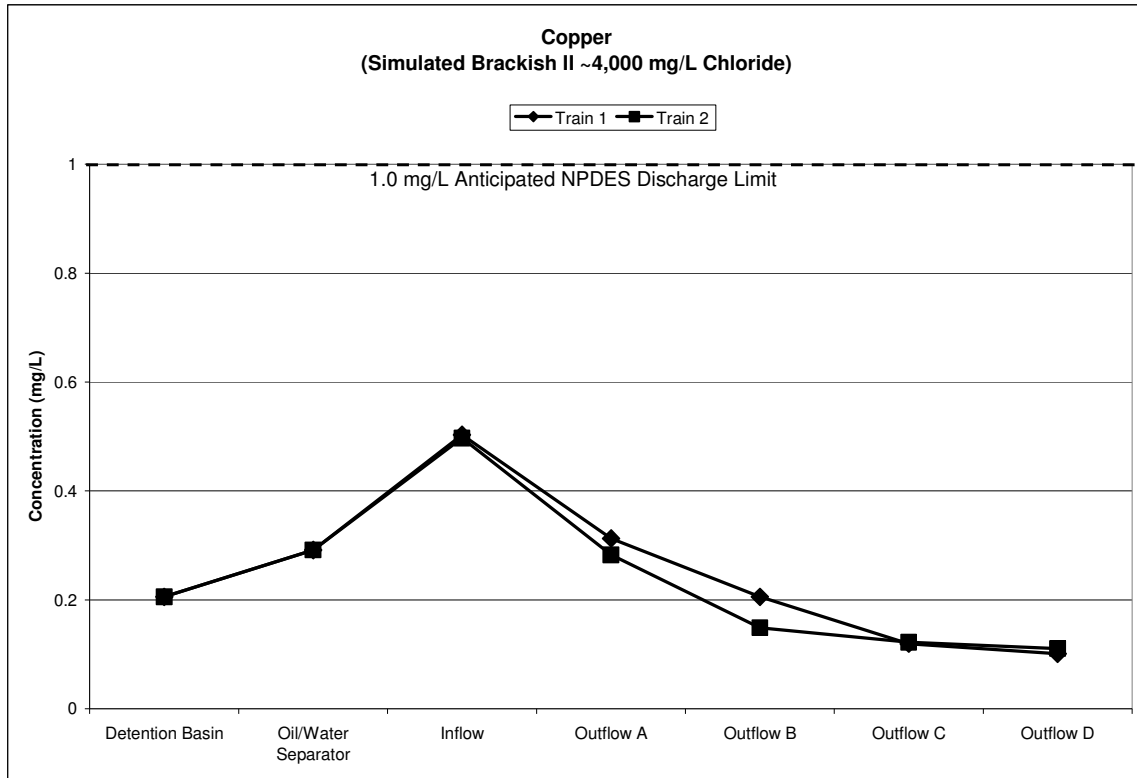
Figure 29. Results for simulated brackish water II metal analysis of copper performed by ICP.

The NPDES permits for the regions examined provided a NPDES discharge limit of 1.0 mg/L for Cu. The inflow concentration to the entire hybrid constructed wetland system was 0.2055 mg/L. The final outflow concentrations for Train1 and Train 2 were 0.1008 and 0.1105, respectively. As shown in Figure 29, the Cu concentrations remained below the target outflow limit set by the model NPDES permit as the water flowed through the oil/water separator and into the freshwater portion of the hybrid CWTS.
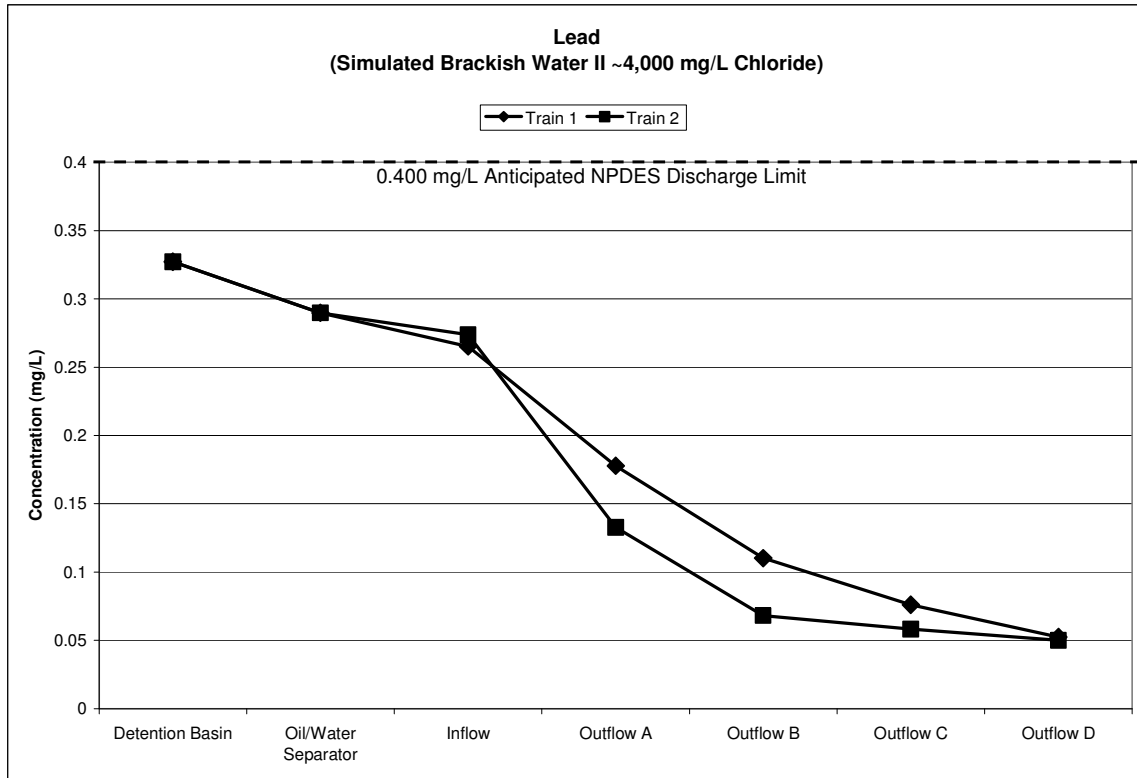
Figure 30. Results for simulated brackish water II metal analysis of lead performed by ICP.

The NPDES permits for the regions examined provided a NPDES discharge limit of 0.400 mg/L for Pb. The inflow concentration to the entire hybrid constructed wetland system was 0.3271 mg/L. The Pb concentrations decreased as the water flowed through the freshwater module. The final outflows for Train 1 and Train 2 were 0.052 and 0.0501 mg/L, respectively. As shown in Figure 30, the Pb concentrations were maintained below the NPDES limit.
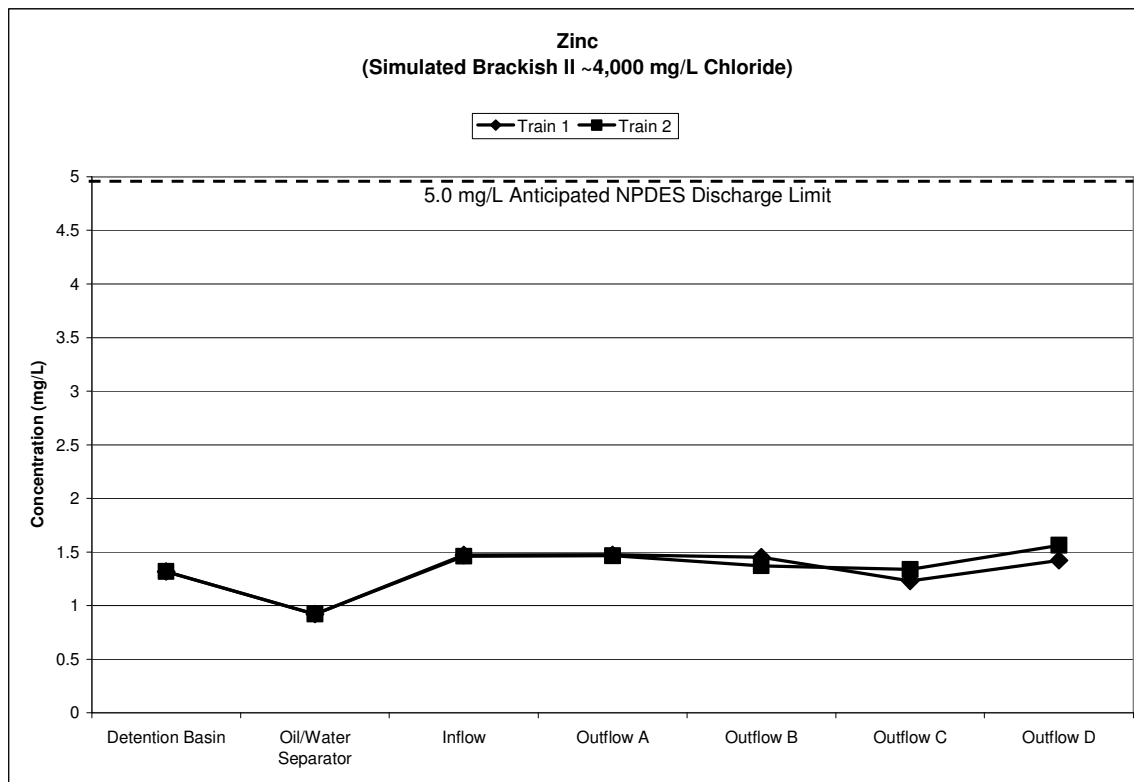
Figure 31. Results for simulated brackish water II metal analysis of zinc performed by ICP.

The NPDES permits for the regions examined provided a NPDES discharge limit of 5.0 mg/L for Zn. The inflow concentrations to the entire hybrid constructed wetland system were 1.318 mg/L. The final outflow concentrations for Train 1 and Train 2 were 1.562 and 1.423mg/L, respectively. As shown in Figure 31, the Zn concentrations were maintained below the NPDES limit.

Toxicity
In Experiment 5, 7-day toxicity tests utilizing *C. dubia* were performed. Experiment 5 samples were diluted to 20% sample water, 80% moderately hard water to reduce possible chloride interference in toxicity results. In Experiment 5 showed survival of *C. dubia* as significantly less than the controls for both inflows into the freshwater module. The outflow from each of the freshwater wetland cells showed no significant differences in mortality. The entire system showed significantly different reproduction of *C. dubia* as compared to the control. This may be due to increased chloride concentrations due to evaporation. As noted in Appendix Table 9, as the water flows through the system the chloride concentration increases, thus using the same dilution the concentration of chlorides in the outflow waters would be greater than the inflow waters.

Oil-in-Water Data
As in the other experiments, oil-in-water was measured by Turner Designs Hydrocarbon Instruments TD500 Handheld Oil in Water Meter. The methods used were adapted from

Standard Methods fluorometric determination of oil-in-water. Measurements taken using this instrument indicate that the method has some interference, possibly from algae present in the water column.

General Water Chemistry
The general water chemistry results for this experiment are shown in the Appendix-Table 9.

Conclusions

During the first quarter of the investigation, produced waters were characterized (Task 1), NPDES standards for treated produced waters were determined (Task 2), and the pilot-scale treatment system was designed and constructed (Task 3). Produced water composition varies widely based upon the geologic formation from which it originates, the extraction method utilized in the natural gas production process, and the treatment chemicals utilized in the process. A model NPDES permit was derived from a number of oil and gas permits issued by the states of Ohio, Pennsylvania, New York, and West Virginia. This model (comprehensive) permit serves as the performance goals for the pilot-scale constructed wetland treatment system. The treatment system is designed to target specific characteristics of natural gas storage produced waters. The design includes an API oil/water separator, saltwater wetland system, RO system, and freshwater wetland system.

During the second quarter of the investigation, Experiments 1 and 2 were completed. These experiments involved running the first two categories of produced water, simulated fresh and brackish, through the freshwater wetland portion of the CWTS. The API oil/water separator, the saltwater wetland cells, and the RO system were bypassed due to the relatively low oil and chloride concentrations found in these two categories of water. In Experiment 1 (simulated fresh produced water), the water showed no toxicity and the concentrations of metals as well as the concentrations of oil were below the limits defined by the model NPDES permit. In Experiment 2 (simulated brackish produced water), both the inflow and the final outflow showed toxicity. This can most likely be attributed to the high concentrations of cadmium and zinc in the final outflow remaining at levels above the model NPDES discharge limits. Copper and lead decreased as the water flowed through the system to concentrations below the model NPDES discharge limits. Oil concentrations remained relatively constant, increasing slightly in the final wetland cell of each train. This may be due to background levels of algae picked up by the fluorometer used to measure oil levels.

Experiment 3 (simulated saline produced water) was completed during the third quarter of the investigation. As water flowed through the oil/water separator and the saltwater portion of the hybrid CWTS, metal concentrations gradually decreased. The RO system reduced metal concentrations to levels below the model NPDES discharge limits (Task 2). The freshwater system maintained metal concentrations below the target outflow limits. By reducing the volume of concentrate and increasing the use of the freshwater system for metal removal, the efficiency of the hybrid CWTS could be improved. In

Experiment 3, the oil/water separator was introduced to decrease the amount of oil entering the saltwater wetland module. Due to high amounts of oil in water found in the water exiting from the original oil/water separator in Experiment 3, a new oil/water separator was designed, built, and tested.

Experiment 4 (simulated hyper-saline produced water) was completed during the fourth quarter of the investigation. As noted earlier, a new oil/water separator was incorporated into the hybrid CWTS for this experiment and proved to be successful at decreasing oil concentrations in the water. As water flowed through the oil/water separator and the saltwater portion of the hybrid CWTS, metal concentrations decreased. The RO system reduced metal concentrations to levels below the model NPDES discharge limits (Task 2), and the freshwater system maintained metal concentrations below the target outflow goals.

During the final four months of the investigation, a fifth experiment was run with simulated brackish water II. This experiment was added to enhance knowledge of the capabilities of the freshwater module. Constituents of concern were added at NPDES permit levels. The system was able to maintain or decrease concentrations of all four metals.

The low concentrations of cadmium, copper, lead, and zinc in the RO permeate from both Experiment 3 and Experiment 4 support the proposed fine-tuning of the RO system for increased volumes of permeate and decreased volumes of concentrate. By reducing the volume of concentrate and increasing the use of the freshwater system for metal removal, the efficiency of the hybrid CWTS could be improved. The new oil/water separator showed greatly improved results compared to the previously used oil/water separator, however, the residual oil contained in the saltwater wetland cells from Experiment 3 continued to flow through the system showing outflow concentrations above the model NPDES discharge limits (Task 2). Another probable cause for unexpectedly high oil-in-water measurements is the presence of algae in the samples; both chlorophyll-a and its phaeophytin derivative fluoresce in the same range as the hydrocarbons measured by the Turner Designs Handheld Oil-in-Water Meter.

Data obtained during the investigation indicate that the pilot-scale CWTS provided effective treatment of simulated natural gas storage produced water. Results are very encouraging as the work moves toward field demonstration of the technology.

References Cited

Faulkner, S.P., W.H. Patrick, Jr., R.P. Gambrell. 1989. Field Techniques for Measuring Wetland Soil Parameters. Soil Sci. Soc. Am. J. 53: 883-890.

Pope, D. H., and R.M. Pope. 1999. Diagnosis, Treatment, and Monitoring of Microbiologically Influenced Productivity in Natural Gas Storage Facilities. Gas Research Institute, Report GRI-00-0056.

SAS Institute. 2002. Statistical Analysis System. Version 9. SAS Institute Inc., Cary, North Carolina.

United States Environmental Protection Agency (USEPA). 2000. EPA Office of Compliance Sector Notebook Project: Profile of the Oil and Gas Extraction Industry. EPA/310-R-99-006.

United States Environmental Protection Agency (USEPA). 2002. ECOTOX User Guide: ECOTOXicology Database System. Version 3.0. Available: <http:/www.epa.gov/ecotox/>.

United States Environmental Protection Agency (USEPA). 2004. National Pollutant Discharge Elimination System: View NPDES Individual and General Permits. Available: <http://cfpub.epa.gov/npdes/permitissuance/genpermits.cfm>.

Veil, A., M.G. Puder, D. Elcock, and R.J. Redweik, Jr. 2004. A White Paper Describing Produced Water from Production of Crude Oil, Natural Gas, and Coal Bed Methane. United States Department of Energy, National Energy Technology Laboratory. Contract W-31-109-Eng-38.

Other Pertinent Publications

American Public Health Association (APHA), American Water Works Association, and Water Pollution Control Federation. 1998. Standard Methods for Examination of Water and Wastewater, 20th Ed. American Public Health Association, Washington, D.C.

Gillespie, Jr., W.B., W.B. Hawkins, J.H. Rodgers, Jr., M.L. Cano, and P.B. Dorn. 2000. Transfer and transformations of zinc in constructed wetlands: Mitigation of a refinery effluent. Ecological Engineering 14: 279-292.

Hawkins, W.B., J.H. Rodgers, Jr., A.W. Dunn, P.B. Dorn, and M.L. Cano. 1997. Design and construction of wetlands for aqueous transfers and transformations of selected metals. Ecotoxicology and Environmental Safety 36: 238-248.

Huddleston, G.M. III and J.H. Rodgers, Jr. *in press.* Integrated design of a constructed wetland system for treatment of copper-contaminated wastewater. Water Environment Research.

Huddleston, G.M. III, W.B. Gillespie, Jr., and J.H. Rodgers, Jr. 2000. Using constructed wetlands to treat biochemical oxygen demand and ammonia associated with a refinery effluent. Ecotoxicology and Environmental Safety 45:188-193.

Knight, R.L., R.H. Kadlec, and H.M. Ohlendorf. 1999. The use of treatment wetlands for petroleum industry effluents. Environmental Science & Tech. 33: 973-980.

Mastin, B.J., J.H. Rodgers, Jr. and Y.T. Shah. 2001. Hybrid cavitation/constructed wetland reactors for treatment of chlorinated and non-chlorinated organics. Chemical Engineering Tech. 24: 97A-105A.

Moore, M.T., J.H. Rodgers, Jr., S. Smith, Jr. and C.M. Cooper. 2001. Mitigation of metolachlor-associated agriculture runoff using constructed wetlands in Mississippi, USA. Agric. Ecosystems and Environ. 84: 169-176.

Moshiri, G.A. (ed.). 1993. Construction Wetlands for Water Quality Improvement: Lewis Publishers, Ann Arbor, Michigan.

Murray-Gulde, C., J.E. Heatley, T. Karanfil, J.H. Rodgers, Jr., and J.E. Myers. 2003. Performance of a hybrid reverse osmosis-constructed wetland treatment system for brackish water. Water Research 37: 705-713.

Myers, J.E. 2000. Constructed wetland overview for the petroleum industry. Society of Petroleum Engineers E&P Environmental Conference, Stavanger, Norway (SPE 61181).

Myers, J.E., L.M. Jackson, R.F. Bernier, and D.A. Miles. 2001. An evaluation of the Department of Energy Naval Petroleum Reserve No. 3 produced water bio-treatment facility. Society of Petroleum Engineers E&P Environmental Conference, San Antonio, TX (SPE 66522).

Appendix: General Water Chemistry Data

Table 1: General Water Chemistry Results for Experiment 1: Batch 1 (Simulated Fresh Produced Water).

Sample	pH	DO (mg/L)	Conductivity (mS/cm)	Temp (℃)	Alkalinity (mg/L)	Hardness (mg/L)	BOD$_5$ (mg/L)	Sulfate Conc. (mg/L)	COD (mg/L)	TSS (mg/L)	TDS (mg/L)	Chloride Conc. (mg/L)
1-A Inflow	7.42	9.16	1.4	19.0	12	288	0.82	ND	9.56	8.3	4532	462.5
2-A Inflow	7.36	8.24	1.4	18.6	12	268	ND	ND	4.25	7.9	1562	450
1-A Outflow	6.79	9.41	1.7	19.2	32	340	0.27	ND	10.81	17.1	1162	522.5
2-A Outflow	6.47	8.60	1.9	19.4	16	400	1.60	ND	5.19	14.7	1367	582.5
1-B Outflow	6.73	8.57	2.3	20.2	24	592	0.98	ND	16.75	16	1672	705
2-B Outflow	6.65	8.17	2.2	18.8	30	508	1.40	ND	7.69	7.6	1625	645
1-C Outflow	6.82	9.53	2.5	20.7	20	532	1.17	ND	16.13	8.5	1791	687.5
2-C Outflow	7.19	9.45	2.1	21.5	28	496	1.02	ND	12.69	14.6	1464	602.5
1-D Outflow	7.12	10.30	2.4	20.1	24	456	1.73	ND	12.69	16.2	1709	695
2-D Outflow	7.11	10.30	2.5	20.0	28	540	1.07	ND	5.19	8.2	48	697.5

*ND: Non-Detect

Table 2: General Water Chemistry Results for Experiment 1: Batch 2 (Simulated Fresh Produced Water).

Sample	pH	DO (mg/L)	Conductivity (mS/cm)	Temp. (°C)	Alkalinity (mg/L)	Hardness (mg/L)	BOD$_5$ (mg/L)	Sulfate Conc. (mg/L)	COD (mg/L)	TSS (mg/L)	TDS (mg/L)	Chloride Conc. (mg/L)
Equil. Basin	7.05	9.97	1.49	19.9	18	290	1.36	0.00	1.10	0.25	1149	610
1-A Inflow	7.14	9.89	1.50	21.1	12	330	0.86	13.75	0.57	0.55	1132	612.5
2-A Inflow	6.78	9.94	1.50	21.1	16	240	1.69	11.25	1.10	0.75	1116	635
1-A Outflow	6.98	9.54	1.40	21.2	14	340	0.77	11.25	0.04	0.45	1032	575
2-A Outflow	7.00	9.10	1.40	21.8	22	280	0.62	13.75	0.39	4.85	1113	575
1-B Outflow	6.86	9.34	1.40	21.9	22	250	0.76	8.75	0.21	0.95	1145	542.5
2-B Outflow	6.61	9.42	1.40	21.6	46	350	0.64	8.75	0.21	0.35	1181	555
1-C Outflow	6.90	9.78	1.50	23.3	16	290	1.56	8.75	0.57	1.15	1188	590
2-C Outflow	7.13	9.66	1.60	23.0	30	250	1.57	8.75	1.28	9.55	1208	557.5
1-D Outflow	7.24	10.58	1.55	20.1	14	300	2.07	6.25	1.10	0.75	1204	655
2-D Outflow	7.22	11.04	1.56	20.0	18	330	2.20	8.75	1.28	0.85	1244	605

Table 3: General Water Chemistry Results for Experiment 2: Batch 1 (Simulated Brackish Produced Water).

Sample	pH	DO (mg/L)	Conductivity (mS/cm)	Temp (°C)	Alkalinity (mg/L)	Hardness (mg/L)	BOD$_5$ (mg/L)	Sulfate Conc. (mg/L)	COD (mg/L)	TSS (mg/L)	TDS (mg/L)	Chloride Conc. (mg/L)
Equil. Basin	7.02	9.50	7.52	~20	14	1360	0.55	4.56	18.34	3.75	5674.5	3260
1-A Inflow	7.06	9.81	7.48	~20	10	1270	0.82	3.80	15.01	1.75	5447.5	2640
2-A Inflow	6.87	9.71	7.47	~20	10	1520	0.68	5.06	13.01	1.75	5782.5	2810
1-A Outflow	6.91	9.20	7.09	~20	22	620	0.91	7.85	8.67	2.85	5043.5	2450
2-A Outflow	6.94	9.30	7.32	~20	20	700	0.64	8.86	12.00	2.65	5369.5	2530
1-B Outflow	7.33	7.74	7.03	~20	26	610	0.44	25.57	10.67	2.15	5086.5	2620
2-B Outflow	7.05	8.26	7.47	~20	22	690	0.67	21.52	21.34	2.25	5459.5	2730
1-C Outflow	7.27	10.10	7.00	~20	24	630	0.91	31.90	11.34	3.25	5166.5	2580
2-C Outflow	7.22	9.90	7.17	~20	22	720	0.87	27.59	10.00	4.45	4297.5	2600
1-D Outflow	7.21	10.61	6.87	~20	18	520	1.43	32.91	9.34	8.65	5147.5	2560
2-D Outflow	7.04	10.13	7.15	~20	16	580	2.75	32.15	17.67	31.75	5454.5	2610

Table 4: General Water Chemistry Results for Experiment 2: Batch 2 (Simulated Brackish Produced Water).

Sample	pH	DO (mg/L)	Conductivity (mS/cm)	Temp (°C)	Alkalinity (mg/L)	Hardness (mg/L)	BOD5 (mg/L)	Sulfate Conc. (mg/L)	COD (mg/L)	TSS (mg/L)	TDS (mg/L)	Chloride Conc. (mg/L)
Equil. Basin	7.1	9.18	8.64	20.2	15	1600	0.59	10.38	NA	ND	6855	3050
1-A Inflow	7.1	9.15	8.85	22.2	14	1540	0.6	2.28	31.18	1.4	6657	2920
2-A Inflow	7.06	9.2	8.85	20.6	16	1670	0.46	3.29	30.47	4.5	6830	2950
1-A Outflow	6.92	7.87	8.49	22.2	18	1600	0.35	5.32	29.76	2.1	6491	2950
2-A Outflow	7.02	7.89	8.53	22	18	1630	0.24	8.35	30.47	-0.8	6244	3020
1-B Outflow	7.06	7.82	8.51	20.8	24	1730	0.98	11.90	29.76	1.1	6550	2950
2-B Outflow	6.84	8.91	8.92	21.1	20	1540	0.96	20.51	28.34	1.4	6640	2940
1-C Outflow	7.07	10.66	8.5	21.3	16	1580	0.85	11.65	28.34	1.8	6455	3020
2-C Outflow	7.07	10.45	8.72	17.6	44	1590	1.56	14.18	29.05	1.6	6650	3050
1-D Outflow	7.28	10.53	8.45	17.3	16	1680	1.3	11.14	29.05	3.6	6370	3000
2-D Outflow	7.25	11.04	8.6	19.4	46	1600	1.24	14.68	33.30	6.2	6566	3000

*ND: Non-Detect

Table 5: General Water Chemistry Results for Experiment 3: Batch 1 (Simulated Saline Produced Water).

Sample	pH	DO (mg/L)	Conductivity (mS/cm)	Temp. (℃)	Alkalinity (mg/L)	Hardness (mg/L)	BOD$_5$ (mg/L)	Sulfate Conc. (mg/L)	COD (mg/L)	TSS (mg/L)	TDS (mg/L)	Chloride Conc. (mg/L)
Equil. Basin	7.41	8.30	37.82	26	360	10800	8.3	ND	NA	31.2	28708	20000
O/W Sep.	7.15	7.81	33.5	23	260	10000	7.81	ND	NA	5.7	25928	20000
S-1 Outflow	7.00	7.89	28.74	20	260	8400	7.89	ND	NA	12.1	21517	15000
S-2 Outflow	6.81	4.02	26.46	20	220	7600	2.91	ND	NA	8.6	20740	15000
RO Outflow	5.57	8.05	0.281	20	4	6	0.87	ND	NA	1	174	115
1-A Inflow	6.59	9.15	0.176	21	2	16	0.85	ND	3.83	0.1	218	71
2-A Inflow	6.42	9.06	0.176	21	4	16	0.8	ND	7.37	0.2	211	52
1-A Outflow	7.11	10.23	0.248	22	12	38	1.43	ND	8.79	ND	154	83
2-A Outflow	7.12	10.52	0.254	22	12	42	0.96	ND	10.91	ND	162	86
1-B Outflow	7.13	9.42	0.298	21	20	64	1.34	ND	10.20	2.9	181	82
2-B Outflow	7.22	9.27	0.401	21	24	102	1.85	ND	10.91	4.6	252	92
1-C Outflow	7.38	11.64	0.324	21	18	68	3.7	ND	12.33	6.2	202	93
2-C Outflow	7.57	12.15	0.439	21	22	106	4.16	19.11	11.62	8.1	314	103
1-D Outflow	7.41	13.36	0.399	20	18	72	9.39	ND	15.87	11.1	212	92
2-D Outflow	7.41	13.21	0.473	20	22	100	10.05	23.56	18.71	27.5	284	115

*ND: Non-Detect.

*NA: Not Available

Table 6: General Water Chemistry Results for Experiment 3: Batch 2 (Simulated Saline Produced Water).

Sample	pH	DO (mg/L)	Conductivity (mS/cm)	Temp. (°C)	Alkalinity (mg/L)	Hardness (mg/L)	BOD5 (mg/L)	Sulfate Conc. (mg/L)	COD (mg/L)	TSS (mg/L)	TDS (mg/L)	Chloride Conc. (mg/L)
Equil. Basin	7.25	8.65	45.20	27.5	22	9000	0.24	18.00	NA	120.75	32811.5	20000
O/W Sep.	7.29	8.92	44.60	21.2	32	11000	0.69	17.69	NA	103.65	32568.5	20000
S-1 Outflow	6.64	7.61	43.30	25.0	30	11000	2.32	18.13	NA	356.65	33047.5	20000
S-2 Outflow	6.72	7.72	43.96	22.2	32	11000	1.10	15.34	NA	64.65	33329.5	20000
1-A Inflow	4.32	8.46	0.2646	26.1	0	14	0.46	ND	ND	51.05	188.5	101
2-A Inflow	5.24	8.34	0.2571	24.0	2	16	0.35	ND	ND	54.75	172.5	98
1-A Outflow	6.99	7.09	0.588	23.3	14	82	0.46	14.56	ND	56.75	406.5	156
2-A Outflow	7.31	6.95	0.602	23.8	12	94	1.20	21.13	ND	55.85	363.5	167
1-B Outflow	7.25	8.03	0.554	23.7	16	104	1.06	27.53	ND	55.05	335.5	153
2-B Outflow	7.21	7.80	0.724	25.3	30	148	1.86	49.25	ND	56.45	441.5	181
1-C Outflow	7.37	8.76	0.554	25.3	20	92	1.90	27.84	ND	56.15	325.5	154
2-C Outflow	6.87	8.19	0.698	26.1	26	132	7.95	49.56	ND	68.75	430.5	180
1-D Outflow	7.22	6.96	0.597	27.2	22	104	2.17	30.03	ND	59.35	368.5	255
2-D Outflow	7.15	6.89	0.744	27.2	20	140	5.32	53.94	ND	63.65	460.5	182

*ND: Non-Detect.

*NA: Not Available

Table 7: General Water Chemistry Results for Experiment 4: Batch 1 (Simulated Hyper-Saline Produced Water).

Sample	pH	DO (mg/L)	Conductivity (mS/cm)	Temperature (°C)	Alkalinity (mg/L)	Hardness (mg/L)	BOD$_5$ (mg/L)	Sulfate Conc. (mg/L)	COD (mg/L)	TSS (mg/L)	TDS (mg/L)	Chloride Conc. (mg/L)
Equil. Basin	7.41	7.40	87.7	23.2	42	12000	1.22	44.78	NA	53.55	86726	50000
O/W Sep.	7.38	7.47	81.8	23.2	34	20800	0.15	40.07	NA	6.85	71808	45000
S-1 Outflow	6.55	4.55	69.8	26.2	26	19600	1.15	32.57	NA	7.55	59766	40000
S-2 Outflow	6.40	5.16	70.7	27.7	30	19200	1.75	33.31	NA	14.25	60917	40000
RO Outflow	5.75	7.45	0.975	22.3	ND	ND	ND	ND	NA	2.75	1106	356
1-A Inflow	6.50	8.15	0.725	26.8	6	30	0.37	ND	ND	0.65	444	266
2-A Inflow	6.68	8.16	0.720	27.4	2	30	0.30	ND	ND	1.65	434	262
1-A Outflow	7.22	7.01	0.739	26.3	28	100	6.88	31.54	ND	1.75	507	234
2-A Outflow	7.32	9.93	0.758	27.4	20	94	8.44	17.72	ND	ND	500	236
1-B Outflow	7.26	6.51	0.719	25.4	32	96	5.26	29.63	ND	4.75	511	214
2-B Outflow	7.44	6.05	0.825	27.0	38	132	3.66	38.01	ND	1.75	596	224
1-C Outflow	7.29	6.47	0.665	24.8	32	104	1.44	27.87	ND	5.95	483	195
2-C Outflow	7.54	6.15	0.785	24.9	36	124	1.23	35.81	ND	2.05	599	222
1-D Outflow	7.14	6.44	0.644	26.5	32	96	1.92	25.51	ND	5.05	677	189
2-D Outflow	7.51	7.65	0.736	29.2	34	120	0.95	32.28	ND	1.45	567	205

 *ND: Non-Detect.

*NA: Not Available

Table 8: General Water Chemistry Results for Experiment 4: Batch 2 (Simulated Hyper-Saline Produced Water).

Sample	pH	DO (mg/L)	Conductivity (mS/cm)	Temp. (°C)	Alkalinity (mg/L)	Hardness (mg/L)	BOD5 (mg/L)	Sulfate Conc. (mg/L)	COD (mg/L)	TSS (mg/L)	TDS (mg/L)	Chloride Conc. (mg/L)
Equil. Basin	7.61	5.21	99.60	22.3	74	21200	ND	54.01	NA	76.55	82678	50000
O/W Sep.	7.50	6.61	97.40	26.7	34	24000	0.24	49.79	NA	11.75	76606	45000
S-1 Outflow	6.92	7.76	97.00	21.5	32	23600	0.35	45.14	NA	28.05	78150	50000
S-2 Outflow	6.69	6.48	97.20	28.7	30	25600	ND	39.37	NA	41.25	79991	45000
RO Out	6.36	9.26	1.73	21.0	6	28	NA	ND	NA	ND	1390	NA
1-A Inflow	5.41	7.51	0.954	29.0	4	18	1.10	ND	6.80	0.55	545	373
2-A Inflow	5.43	7.50	0.954	29.8	4	20	1.09	ND	6.30	4.05	500	341
1-A Outflow	6.98	5.24	0.831	28.5	14	58	0.87	ND	6.30	0.25	523	417
2-A Outflow	7.28	5.39	0.858	29.1	16	60	1.03	4.58	6.80	1.75	537	287
1-B Outflow	7.25	6.84	0.843	27.2	22	66	1.52	1.90	6.80	2.05	543	253
2-B Outflow	7.17	6.03	0.906	27.8	28	86	0.91	10.49	7.30	2.85	585	266
1-C Outflow	7.09	5.87	0.96	27.3	20	70	0.49	1.48	7.30	3.45	616	318
2-C Outflow	7.23	5.79	1.013	28.3	12	86	1.74	9.51	7.30	3.15	646	301
1-D Outflow	7.30	7.80	0.932	27.3	28	72	1.57	2.75	7.80	4.15	608	295
2-D Outflow	7.59	8.17	1.00	27.7	4	86	1.58	9.37	7.80	4.25	670	320

*ND: Non-Detect.

*NA: Not Available

Table 9: General Water Chemistry Results for Simulated Brackish Produced Water II.

Sample	pH	DO (mg/L)	Conductivity (mS/cm)	Temp. (°C)	Alkalinity (mg/L)	Hardness (mg/L)	BOD5 (mg/L)	Sulfate Conc. (mg/L)	COD (mg/L)	TSS (mg/L)	TDS (mg/L)	Chloride Conc. (mg/L)
Equil. Basin	8.03	5.21	9.97	22.3	20	1600	1.82	7.46	30.00	5.7667	5921	3500
O/W Sep.	7.33	6.61	10.80	22.2	20	1500	1.68	6.16	35.00	0.6667	5998	3675
1-A Inflow	7.08	7.51	9.48	22.4	18	1600	1.17	11.74	30.00	3.2667	6068	3950
2-A Inflow	7.05	7.50	9.35	22.6	20	1500	0.98	7.75	30.00	2.1667	6182	3600
1-A Outflow	7.08	5.24	9.71	55.6	20	1500	1.17	7.90	45.00	2.7667	6195	3725
2-A Outflow	6.95	5.39	8.51	22.6	18	1100	1.01	7.32	75.00	5.7667	6136	3500
				.								
1-B Outflow	6.78	6.84	8.94	21.8	22	1600	2.60	9.78	55.00	7.0667	6465	3600
2-B Outflow	6.98	6.03	9.38	22.2	26	1700	1.47	17.32	55.00	6.0667	7026	3825
1-C Outflow	7.40	5.87	10.45	22.6	28	1800	1.50	20.94	15.00	3.4667	7032	3950
2-C Outflow	7.30	5.79	10.11	22.5	22	2000	1.10	17.03	15.00	3.4667	7008	3975
1-D Outflow	7.16	7.80	9.91	22.3	28	1900	2.42	19.49	20.00	2.7667	7355	3950
2-D Outflow	7.09	8.17	9.97	22.2	26	1900	1.02	20.36	15.00	2.7667	7309	3950

Appendix B 2005 Reports

Demonstration-Scale Constructed Wetland System for Treatment of Produced Waters from Underground Gas Storage

Final Technical Report
October 1, 2005 – March 31, 2007

Submitted by:

James W. Castle (PI), Ph.D., Associate Professor, Clemson University
John H. Rodgers Jr. (Co-PI), Ph.D., Professor, Clemson University
Evan H. Cross, Graduate Research Assistant, Clemson University
Brenda M. Johnson, Graduate Research Assistant, Clemson University
Scott E. Brame, Research Associate, Clemson University
George M. Huddleston, Ph.D., Senior Staff Scientist, ENTRIX
Cynthia Murray-Gulde, Ph.D., Senior Staff Scientist, ENTRIX
Doug Mooney, P.E., Senior Project Engineer, ENTRIX

May 30, 2007

Clemson University
340 Brackett Hall
Box 340919
Clemson, SC 29634

Disclaimer

Abstract

The purpose of this investigation was to demonstrate the utility of a constructed wetland treatment system to effectively and consistently treat waters produced from an underground gas storage field. To ensure efficient disposal or reuse of waters produced from gas storage facilities, effective and reliable water treatment systems are needed. Presently, treatment or disposal of produced waters adds substantial operational costs to many gas storage facilities.

During the first quarter of this investigation, a demonstration-scale constructed wetland system was designed and constructed for onsite treatment of targeted constituents in water produced from a gas storage field. Design criteria for the demonstration-scale constructed wetland treatment system were developed based on a site visit and on data collected from the pilot-scale system constructed and evaluated during our previous GSTC-sponsored project. In the second quarter of this investigation, design schematics were finalized, and data regarding costs of treatment were analyzed. In the third quarter of the project, the demonstration-scale system was constructed. After construction of the system and planting, the wetland plants acclimated to storm water and produced water from the gas storage site.

Three experiments involving flow through the demonstration-scale constructed wetland treatment system were performed. In the first experiment, onsite storm water was used for flow through the system. For the second experiment, produced water was co-managed with storm water to create low-ionic strength water. The third experiment, which involved storm water co-managed with a larger fraction of produced water to create high-ionic strength water, showed successful treatment in terms of metal removal. Measurements from the constructed wetland indicated that the plants are healthy and that redox potential of the hydrosoil is within targeted levels.

Results demonstrate the utility of constructed wetland systems for onsite treatment of gas storage produced waters. The demonstration-scale treatment system was designed and constructed successfully, and treatment was confirmed.

TABLE OF CONTENTS

List of Figures

List of Tables

Introduction

Produced waters pose a challenge for treatment because they vary greatly in their composition. High costs associated with existing produced water treatment and disposal methods limit the expansion of existing gas storage fields as well as development of new fields. Currently, there are two common methods for handling produced water. The first method involves the transport of produced water to specialized treatment facilities followed by surface discharge of the treated water, and the second method is to reinject the water into the subsurface. While volumes of produced water increase, the cost of conventional treatment methods are escalating exponentially due to increasingly stringent surface discharge and re-injection regulations under the Clean Water Act (CWA) through the National Pollutant Discharge Elimination System (NPDES), and Safe Drinking Water Act through the Underground Injection Control (UIC). Development of new approaches for treatment of produced water is essential for continued operation of existing storage fields and construction of new facilities.

Water produced from gas storage facilities is often generated in relatively high volumes and can contain a variety of constituents that limit disposal or reuse of the water. Constituents such as chlorides, hydrocarbons, and metals are of concern in these waters. Although salinity of some produced waters may be low enough to meet NPDES discharge limits, concentrations of other constituents in these waters may preclude discharge, resulting in a need for treatment or disposal. Specifically designed constructed wetland treatment systems (CWTS) have been used to treat various constituents independently. However, these systems have yet to be applied at full scale to waters produced from gas storage fields. Wetlands facilitate unique reactions not occurring in other aquatic or terrestrial systems. Constructed wetlands can be poised or buffered to ensure that desired reactions (transfers and transformations) affecting the constituents targeted for treatment proceed at predictable rates over long periods of time (decades). The use of constructed wetland treatment systems offers the following specific advantages:

1. low construction cost;
2. low operational and maintenance costs;
3. reliability; and
4. flexibility in design, so the approach is applicable to a wide range of water quality and quantity.

In the previous Gas Storage Technology Consortium (GSTC) sponsored investigation that we recently completed, a pilot-scale CWTS was designed, constructed, and found to effectively treat simulated produced water. The approach is applicable to waters with a range of chloride concentrations, as well as varying concentrations of cadmium, copper, lead, zinc, and oil. The pilot-scale study provided data regarding the feasibility of this approach for treating gas storage produced waters of varied composition. Results from the pilot-scale study served to decrease uncertainties and confirm design features for the

demonstration-scale constructed wetland treatment system.

The purpose of our investigation is to develop a readily implemented method for treating produced water that can be integrated with surface facilities of gas storage fields while maintaining low costs. The goal of this phase of the project was to design and construct a demonstration-scale CWTS that effectively treats produced water from a field site. Specific tasks of this demonstration study were:

1. Design the demonstration-scale constructed wetland treatment system;
2. Obtain permits to construct;
3. Construct the demonstration-scale system;
4. Monitor treatment;
5. Evaluate performance; and
6. Document results and prepare reports.

The major expected benefit of investigating CWTS technology for handling water produced from gas storage is significantly decreased costs for produced water management, which could potentially lead to expansion of existing storage fields. In addition, new geographic areas may be opened for development of gas storage fields in light of the anticipated economic advantages.

Executive Summary

The goal of this investigation is to demonstrate the utility of a constructed wetland treatment system to treat waters produced from an underground gas storage field. To ensure efficient disposal or reuse of waters produced from gas storage, effective and reliable water treatment systems are needed. Produced waters are often generated in relatively high volumes and contain a variety of constituents that limit disposal or reuse. Presently, treatment or disposal of produced waters adds substantial operational costs to many gas storage fields. The purpose of this investigation by Clemson University in partnership with Dominion Transmission, Inc., and the Gas Storage Technology Consortium was to demonstrate a low cost and readily implemented method for treating produced water as part of a system integrated with surface facilities of a gas storage field. This approach is applicable to a range of produced waters, since the composition (including salinity) and volume of water produced from one gas storage field to another can vary greatly. The approach involves identifying and confirming targeted constituents, designing constructed wetlands for treatment based on biogeochemistry and macrofeatures (hydroperiod, hydrosoil, and vegetation), and conducting carefully designed pilot and demonstration-scale studies to confirm performance and function of the constructed systems. The current investigation utilized a demonstration-scale constructed wetland treatment system to confirm operation and performance under field conditions. The demonstration-scale system was designed and built specifically to treat targeted constituents in water produced from a gas storage facility. Produced water and storm water from the facility were co-managed and treated using the system, and performance was determined through comparison of inflow to outflow concentrations of targeted constituents in the water.

The approach of this investigation incorporated the use of sound theory and fundamental principles, such as the Laws of Thermodynamics and basic biogeochemistry. A major expected benefit of this investigation is that the results will contribute to reduced cost of water management, which will potentially lead to expansion of existing storage fields. In addition, new geographic areas may be opened for development of gas storage fields due to the anticipated economic advantages.

Experimental

Task 1: Design the Demonstration-Scale Constructed Wetland Treatment System

The purpose of Task 1 was to design a demonstration-scale CWTS at a field site so that the results will be applicable for designing future full-scale systems at additional sites. The comprehensive engineering report and schematic diagrams for the demonstration-scale CWTS were completed by ENTRIX (Figures 1-6).

Storm water collected within the gas storage facility often contains dilute concentrations of constituents found in natural gas storage produced water (NGSPW) as well as constituents from wastewater delivery trucks (e.g. oil and grease) that require treatment prior to discharge to receiving aquatic systems. NGSPW and storm water were co-managed in a 10,000 gallon storage tank to reduce chloride concentrations. For waters with chloride concentrations exceeding 4,000 mg/L, a reverse osmosis system can be used to reduce chloride concentrations to levels that can be tolerated by the wetland plants.

Produced water treatment costs were compiled in order to compare the treatment costs of several common conventional treatment methods to costs associated with produced water treatment utilizing a CWTS. This was done in order to demonstrate the potential economic benefits derived from use of a CWTS in comparison with conventional treatment methods.

Additional experiments were conducted utilizing the pilot-scale CWTS in order to obtain additional data which can be incorporated into the design of the demonstration-scale system to achieve optimal treatment performance.

Task 2: Obtain Permits to Construct

The objective of this task was to obtain any permits needed for construction of the demonstration-scale CWTS, including the greenhouse. This objective was omitted because outflow water from the CWTS is collected and treated by conventional methods.

Task 3: Construct the Demonstration-Scale System

This task involved construction of the demonstration-scale CWTS at a site in West Virginia. The first phase of construction included surveying the site. Site preparation, excavation, and plumbing were completed by Ryan Environmental. A HDPE liner was included to prevent leaching of water into or out of the CWTS. A 28 by 45 foot greenhouse was constructed to enable year-round monitoring of the demonstration-scale CWTS. The greenhouse and its support systems were installed by Jaderloon (Irmo, SC) at the excavated and lined site. Local topsoil was amended with gypsum, iron, and slow release fertilizer to prepare it for use as hydrosoil in the constructed wetland. The planted

area of the greenhouse was 20 by 33 feet (660 square feet). The first 330 square foot section of the wetland was planted with *Schoenoplectus californicus* (California bulrush) in order to support a reducing aquatic environment. The second 330 square foot section was planted with *Typha latifolia* (cattail) in order to support an oxidizing aquatic environment.

Task 4: Monitor Treatment

Samples were collected from inflow and outflow water of the CWTS. These samples were analyzed for concentrations of targeted constituents. The analyses were performed in laboratories at Clemson University using standard methods (*Standard Methods for the Examination of Water and Wastewater,* APHA et al., 1998). Sampling frequency was based on the hydraulic retention time of water in the system.

Task 5: Evaluate Performance

Performance of the CWTS was evaluated by comparing the concentrations of constituents of concern (e.g., metals) in the inflow to concentrations in the outflow. Analytical methods for the parameters monitored are listed in Table 1.

Task 6: Document Results and Prepare Reports

The reports included data collected during the various tasks, including composition of the produced water and monitoring data.

Results and Discussion

Task 1: Design the Demonstration-Scale Constructed Wetland Treatment System

The demonstration-scale CWTS was built at Dominion Transmission's Lightburn facility near Bridgeport, WV. In October, 2005, investigators from Clemson University along with collaborators from Dominion and ENTRIX visited the site. The specific location was selected, and field measurements were obtained for use in designing the system. Engineering drawings were produced by engineers at ENTRIX, and computer-assisted drafting of the design was completed.

Cost Comparison

The overall goal of this research is to find a cost effective means for handling NGSPW. Common treatment methods for NGSPW include deep-well injection and transport to specialized treatment facilities (Nakels et al., 2003). Depending on water composition, other treatment methods may be utilized to dispose of NGSPW. Examples of alternative disposal methods include evaporation ponds, treatment by publicly owned treatment works, road-spread, and surface discharge. Each of these methods has associated costs and restrictions depending on the composition, volume, and location of the water. A cost summary of these disposal/treatment methods and costs for operation and management of constructed wetland treatment systems are listed in Table 2.

Operating costs for CWTS are significantly less than conventional treatment methods. If a CWTS can be installed on site, the transport of produced water may be reduced or eliminated.

Additional Experimental Data for Design

Results from the previous pilot-scale study served to decrease uncertainties and confirm design features for the current demonstration-scale CWTS. To obtain additional data for scaling to a demonstration project, a second, simulated fresh produced water (freshwater 2) was investigated during the second quarter of the current project. Simulated produced waters were formulated according to the constituents and concentrations listed in Table 3. The metal concentration data aided in determining accurate rate coefficients (Table 4) for design of the demonstration-scale project.

Percent metal removal was calculated by:

$$\% \text{ removal} = \left(\frac{[A_0] - [A]}{[A_0]} \right) 100$$

Equation 1

where $[A]$ is the final outflow metal concentration (mg/L), and $[A_0]$ is the initial inflow metal concentration (mg/L).

6

Rate coefficients for removal of metals from the water column were estimated by assuming a first-order reaction rate:

$$k = \frac{- \ln \left([A]/[A_0] \right)}{t}$$

Equation 2

where k is the rate coefficient (day^{-1}), [A] is the final outflow metal concentration (mg/L), [A$_0$] is the initial inflow metal concentration (mg/L), and t is hydraulic retention time (days) of the entire system.

The pilot-scale experiments provide data concerning the biogeochemical conditions within the system during simulated NGSPW treatment. These data may be used for making adjustments and/or adding amendments to a demonstration-scale or field-scale CWTS in order to establish similar biogeochemical conditions for treating NGSPW. Also, improvements can be made to obtain optimal treatment performance at the pilot scale, which can be applied to the design of the demonstration- and field-scale systems to maximize performance.

Engineering Design
ENTRIX completed a very thorough engineering design and report for the demonstration-scale CWTS. The design covered all facets of construction, and the report described all components required for effective treatment of produced water at the demonstration scale including individual component description, specifications, manufacturer, and cost. Engineering design drawings are shown in Figures 1 through 6.

Task 2: Obtain Permits to Construct

Permitting needs have been investigated. Because the demonstration-scale CWTS was contained in a temporary greenhouse located on industrial property, building permits were not required for this project. Also, because outflow water from the demonstration-scale CWTS was monitored and then commingled with the existing produced water waste stream rather than released as surface discharge, NPDES permits were not needed.

Task 3: Construct the Demonstration-Scale System

The demonstration-scale CWTS is contained in an 8.5 by 13.7 m (28 by 45 foot) freestanding poly cover greenhouse. Jaderloon Greenhouse Company of Irmo, SC delivered and assembled the greenhouse on site. The site was cleared, leveled, and excavated to a depth of about 1 m (3 feet) by Ryan Environmental prior to covering by the greenhouse. The excavated area was lined with an HDPE liner, and approximately 45 cm (18 inches) of topsoil from the excavation was placed on top of the liner as hydrosoil for the CWTS. The remaining excavated soil was used to berm and slope storm water away from the greenhouse and the CWTS. The greenhouse includes a propane heater and an evaporative cooler. Following construction of the greenhouse and associated support systems (i.e. plumbing and electrical), pumps, an oil/water separator, and a reverse

osmosis system were installed. Soil amendments and plants were added. Construction photos are shown in Figures 7 and 8, and photographs of the planting process are shown in Figure 9.

Local soils were used as hydrosoil. The hydrosoil was analyzed and amended with gypsum, iron, and slow release fertilizer to achieve the appropriate redox conditions and promote plant growth. The demonstration-scale CWTS was densely planted (24 cm centers) with *S. californicus* and *T. latifolia.* Storm water was added to the wetland and maintained at a suitable depth during the wetland acclimation period.

The plants chosen for this project, *S. californicus* (Bulrush) and *T. latifolia* (Cattail)*,* behave differently after transplanting. Cattails typically maintain a deep green color after transplanting and begin to show signs of growth within approximately two to three weeks after planting. Commonly, bulrush brown as the roots develop within new hydrosoil and begin to show signs of growth four to five weeks after planting. The bulrush eventually establish roots, and after a period of time, they too show extensive growth.

Enclosure of the demonstration-scale CWTS in a greenhouse facilitated year-round monitoring of the wetland during this investigation. Conditions within the greenhouse can be regulated for assessment of the demonstration-scale system. Although enclosure within a greenhouse contributed to investigation of the demonstration-scale CWTS, the greenhouse may not be necessary for successful operation of the system at this site and at other sites in a similar climatic zone.

Construction included installing a metering pump, oil/water separator, reverse osmosis system, and inflow spreader pipe (Figure 10).

After initial construction of the demonstration-scale CWTS, the configuration of inflow to the wetland was modified to manage flow between the metering pump and the reverse osmosis (RO) system. The RO system includes an external charge pump that supplies water to the main RO pump and membranes. We recognized that reconfiguration was needed to control and maintain flow rate between the pumps. Overflow could cause loss of system performance, and underflow could cause pumps to burn up and possibly damage the RO membranes. The new control system includes multiple, water-level float devices in a tank between the metering pump and RO system. These float devices actuate relays that can turn the metering pump on and off as needed to maintain steady flow for the RO charge pump. The RO system is equipped with pressure sensors that shut down the RO system if pressure becomes too high or too low. The outputs from the RO pressure sensors are wired to relays so that a shutoff condition at the RO will turn off both the metering pump and charge pump. Additionally, if the float devices fail and the float tank overflows, a backup float sensor in an overflow tank will shut down the entire system. As a final safeguard, the overflow tank was plumbed to transfer excess overflow water directly to the waste tank.

Task 4: Monitor Treatment

Treatment was investigated by sampling the inflow and outflow water from the CWTS. The samples were analyzed to determine concentrations of targeted constituents including Zn, Cu, Cd, Pb, Fe, Se, oil & grease. The analysis was performed in laboratories at Clemson University using standard methods (*Standard Methods for the Examination of Water and Wastewater,* APHA et al., 1998). Sampling frequency was based on the hydraulic retention time of the water in the system, which was 7 days. Samples were collected from the wetland inflow on days 1 and 7 to monitor any compositional changes in inflow water throughout the retention time. Wetland outflow samples were collected on day 7.

Redox and plant density were measured at specific locations 3, 6, 8, and 10 months after planting. These data were used to assess both the biogeochemical conditions and plant health and vigor within the system. Redox (reduction/oxidation potential), which is a measure of the ability to donate or accept electrons, strongly influences the biogeochemical reactions occurring within the wetland. These measurements were taken using a platinum-tipped, insulated copper wire inserted several centimeters into the hydrosoil. Using a milli-volt reader, a reference electrode was connected to the negative pole of the meter and placed in the water column. The exposed copper wire was attached to an electrode connected to the positive pole of the meter. This measured the electrical potential in milli-volts between the platinum-tipped insulated copper wire and the reference probe. Redox values in the wetland changed favorably during the acclimation period (Figure 11).

Plant and shoot density values indicated strong growth and reproduction of both bulrush and cattails (Figures 12, 13, 14, 15, and 16). Plant and shoot density was measured by counting all individuals within the boundaries of a 1 m^2 PVC frame placed within the wetland at each data collection site (Figures 17 and 18). Shoots are defined as new plants that developed post-planting and were separated from the "plant" count by size and appearance. There were approximately 16 bulrush and 11 cattails per m^2 on the day of planting.

To promote reducing conditions, organic matter was added to the area of the wetland planted with bulrush. Redox in the bulrush half of the wetland continued to move toward targeted values less than -150 mV. The cattail half of the wetland progressed toward targeted redox values greater than -50 mV.

For the first six months after construction, plants acclimated to storm water in the wetland. This storm water contained many constituents found in NGSPW in very low concentrations and was therefore well suited for acclimation. A sample of this storm water was collected and analyzed (Table 5). The results of the storm water compositional analysis were used to simulate storm water introduced to a pilot-scale CWTS system at Clemson University for treatment assessment.

Three experiments involving flow through the system were performed to assess the wetland system. For the first experiment, storm water was delivered for flow through the system. Samples were collected from inflow and outflow, and the samples were analyzed (Table 6). Inflow concentrations of Cu, Se, and Oil & Grease were reduced from 0.04, 0.04, and 84 mg/L to 0.02, 0.01, and 53 mg/L respectively. For the second experiment, produced water was co-managed with the storm water to create low-ionic strength water containing slightly higher concentrations of chlorides, metals, metalloids, and organics. Results of sample analysis are shown in Table 7. Inflow concentrations of Zn and Oil & Grease were reduced from 3.53 and 23 mg/L to 1.8 and 13 mg/L respectively. The third experiment involved co-management of produced water with storm water to create a matrix of high ionic strength containing higher concentrations of chlorides, metals, metalloids, and organics. Results of sample analysis are shown in Table 8. Inflow concentrations of Cu, Zn, Cd, and Pb were reduced from 0.2, 8.78, 0.08, and 0.05 mg/L to non-detect, 1.37, 0.05, and 0.03 mg/L respectively.

Task 5: Evaluate Performance

Performance of the CWTS was evaluated by comparing the concentrations of constituents of concern in the inflow to concentrations in the outflow. For the first experiment, storm water containing ~500 mg/L chlorides was delivered to the wetland for treatment. Removal of Zn, Cu, Pb, Fe, Se, and oil & grease was achieved in varying degrees (Table 6). For the second experiment, 7,900 gallons of storm water collected from the wetland outflow during experiment 1 was mixed with 300 gallons of NGSPW to achieve a chloride concentration of ~1,500 mg/L. In this experiment, only zinc and oil & grease concentrations were reduced, and the remaining constituents were either non-detect in both inflow and outflow waters or were discharged at higher concentrations than in the inflow waters (Table 7). The higher discharge concentrations in experiment 2 may be the result of evapotranspiration (ET), as average ambient air temperatures for this experiment were higher than those measured during experiment 1. Low removal percentage of some constituents of concern during experiments 1 and 2 may be attributed to the system not yet being fully acclimated to conditions (e.g., redox potential) necessary to achieve targeted treatment performance. The third and final experiment utilized ~8,650 gallons of storm water and 350 gallons of produced water to achieve a chloride concentration of ~2,500 mg/L. Concentrations of Cu, Cd, Pb, and Zn were reduced during flow through the constructed wetland system (Table 8). Treatment effectiveness achieved during experiment 3 is attributed to the system being acclimated, as indicated by stable values of redox potential within the targeted range.

Task 6: Document Results and Prepare Reports

All quarterly technical reports were prepared and transmitted to GSTC on time in accordance with project reporting requirements.

Conclusion

Design criteria for the demonstration-scale CWTS were developed based on a site visit and on data from the pilot-scale CWTS evaluated during our previous GSTC-sponsored project. A design report completed by ENTRIX provided specifications for construction of the demonstration-scale CWTS. The CWTS was constructed and is enclosed in a greenhouse. Because outflow water from the CWTS is commingled into the existing produced water waste stream rather than released as surface discharge, a NPDES permit was not required. This allowed the project to proceed without waiting for regulatory action.

Information compiled concerning operating costs of produced water treatment using conventional methods and CWTS illustrates the economic benefit gained by utilizing a CWTS in the treatment of gas storage produced waters. Experimental data obtained from additional pilot-scale research support previous findings and provide data concerning specific biogeochemical conditions observed in an operating CWTS for treating NGSPW.

Storm water was introduced to the CWTS for acclimation of hydrosoil conditions and plants. This wastewater contained many constituents found in NGSPW in very low concentrations and was therefore well suited for acclimation. Both bulrush and cattails grew well during acclimation of the constructed wetland. Measurements confirmed the increase in plant and shoot densities. To promote reducing conditions, organic matter was added to the area of the wetland planted with bulrush. Redox potential in the wetland reached targeted values for treatment.

Three experiments involving flow through the demonstration-scale CWTS were performed. For the first experiment, storm water was used for flow through the system. In the second experiment, produced water was co-managed with storm water to create low-ionic strength water. For the third and final experiment, storm water was co-managed with a larger fraction of produced water to create high-ionic strength water. Samples were collected from inflow and outflow for each experiment. Treatment effectiveness was indicated by decreasing concentrations of constituents of concern during the third experiment.

Results demonstrate the utility of constructed wetland systems for onsite treatment of gas storage produced waters. The demonstration-scale treatment system was designed and constructed successfully, and treatment was confirmed.
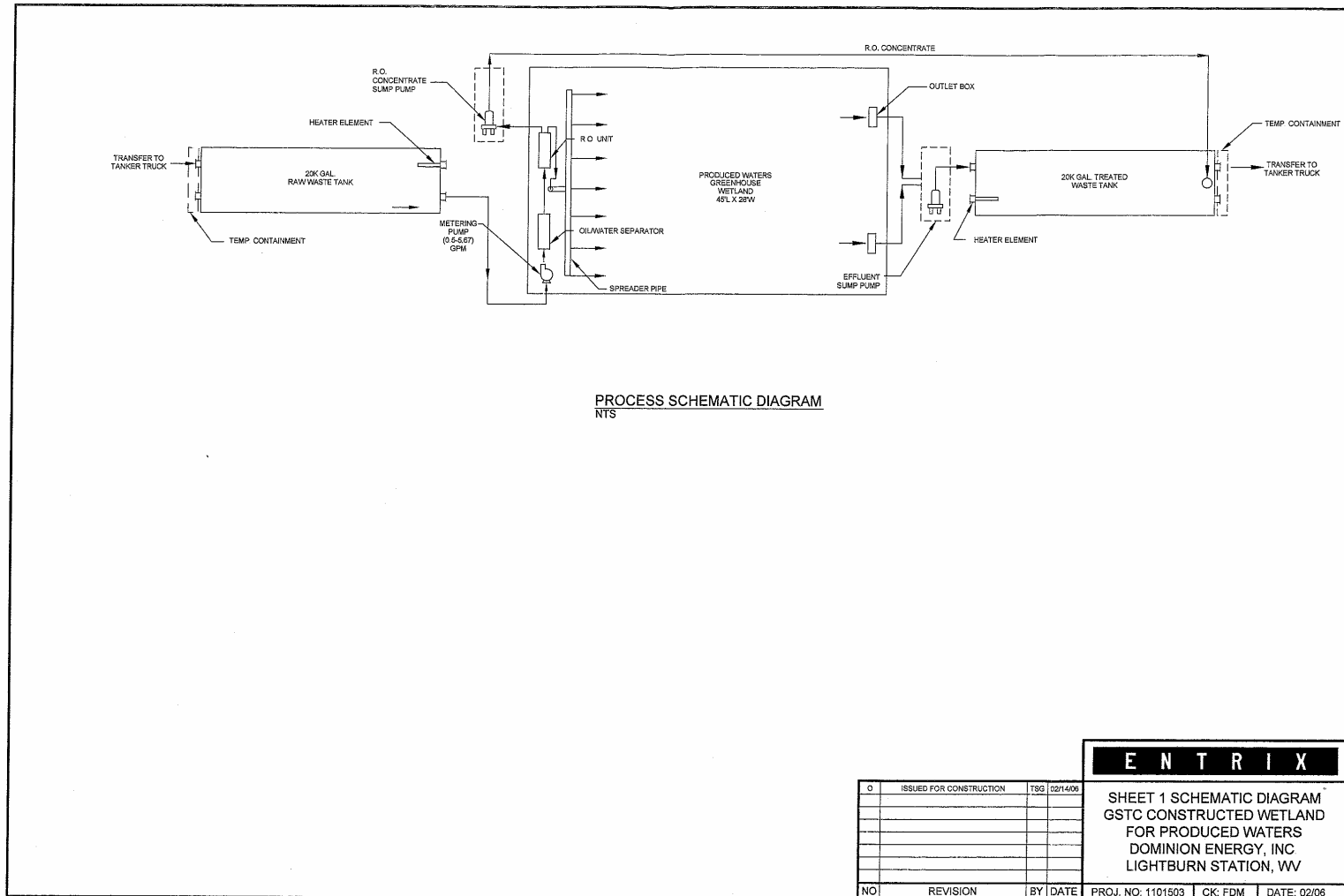
Figure 1. Process schematic diagram

Figure 2. Produced water treatment system layout.
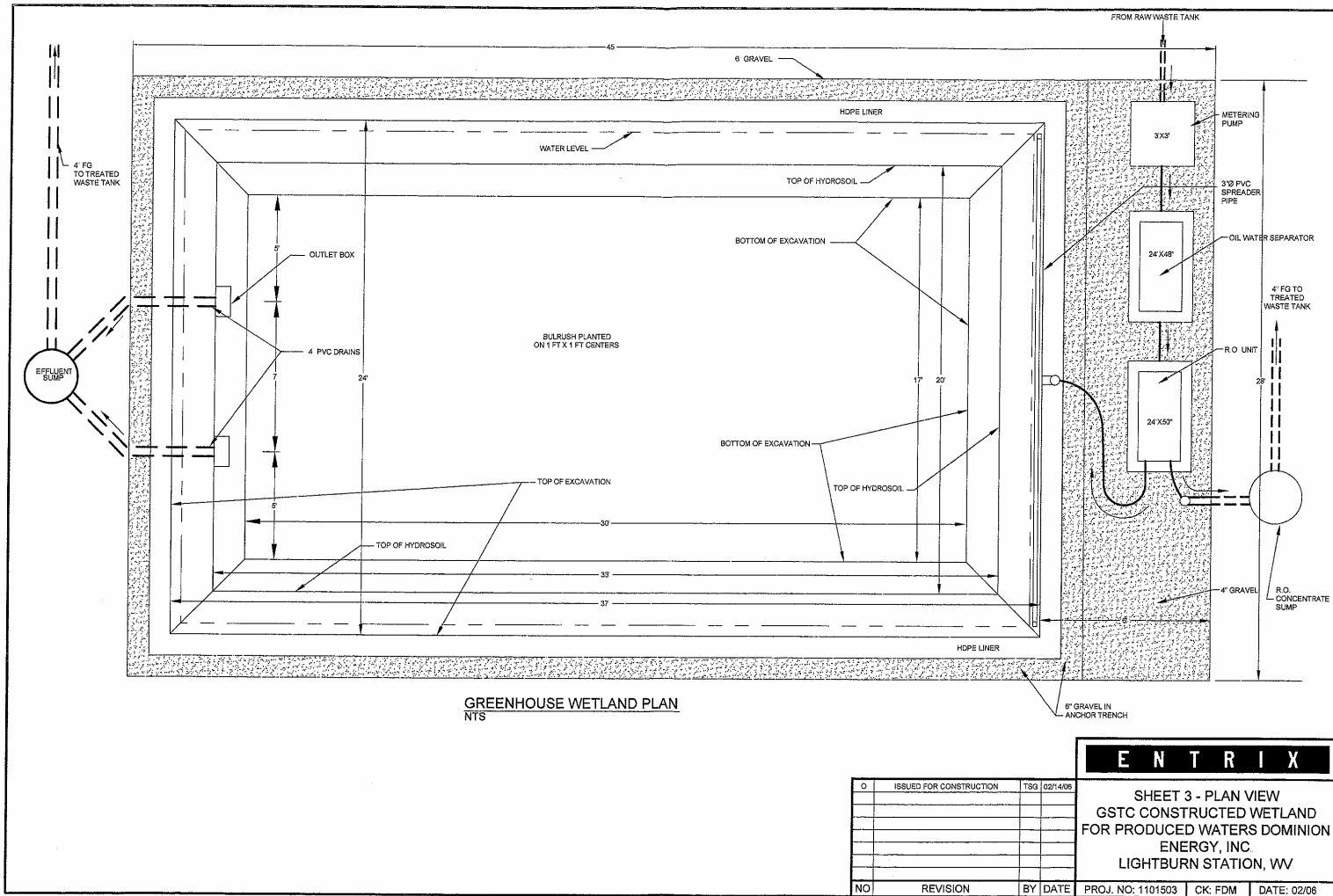
Figure 3. Greenhouse wetland plan.
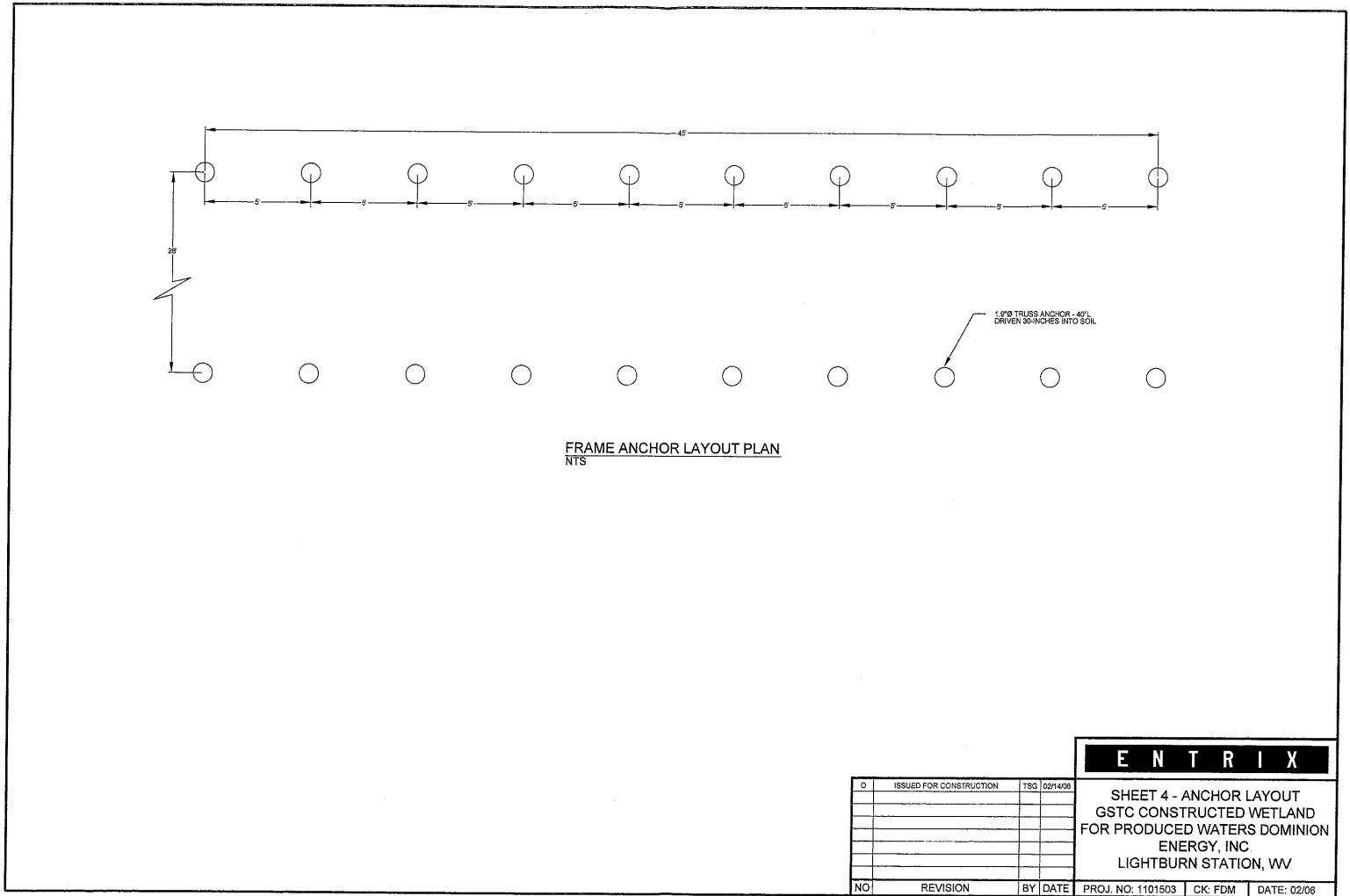
Figure 4. Frame anchor layout plan.
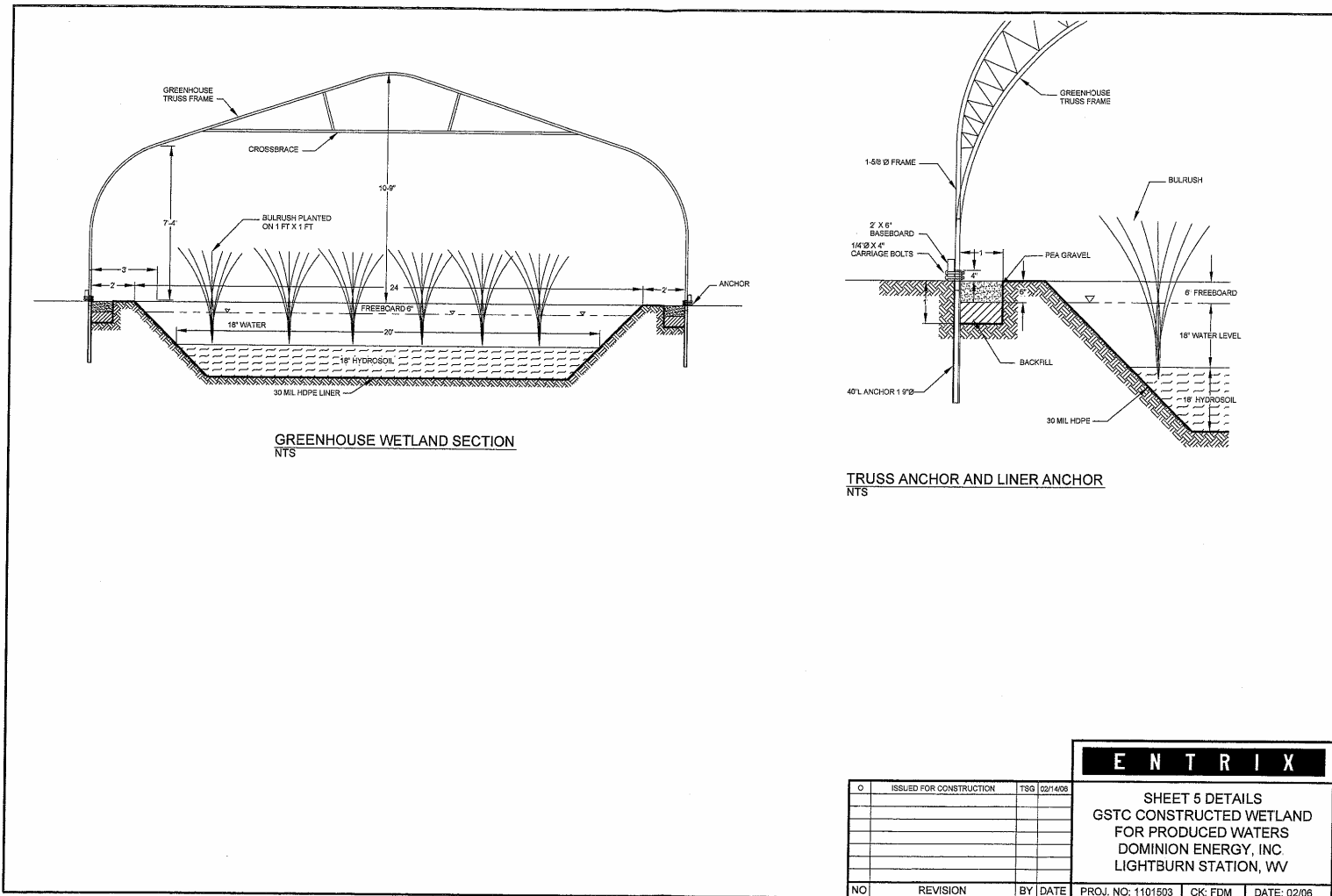
Figure 5. Greenhouse wetland, truss anchor, and liner anchor sections.

16
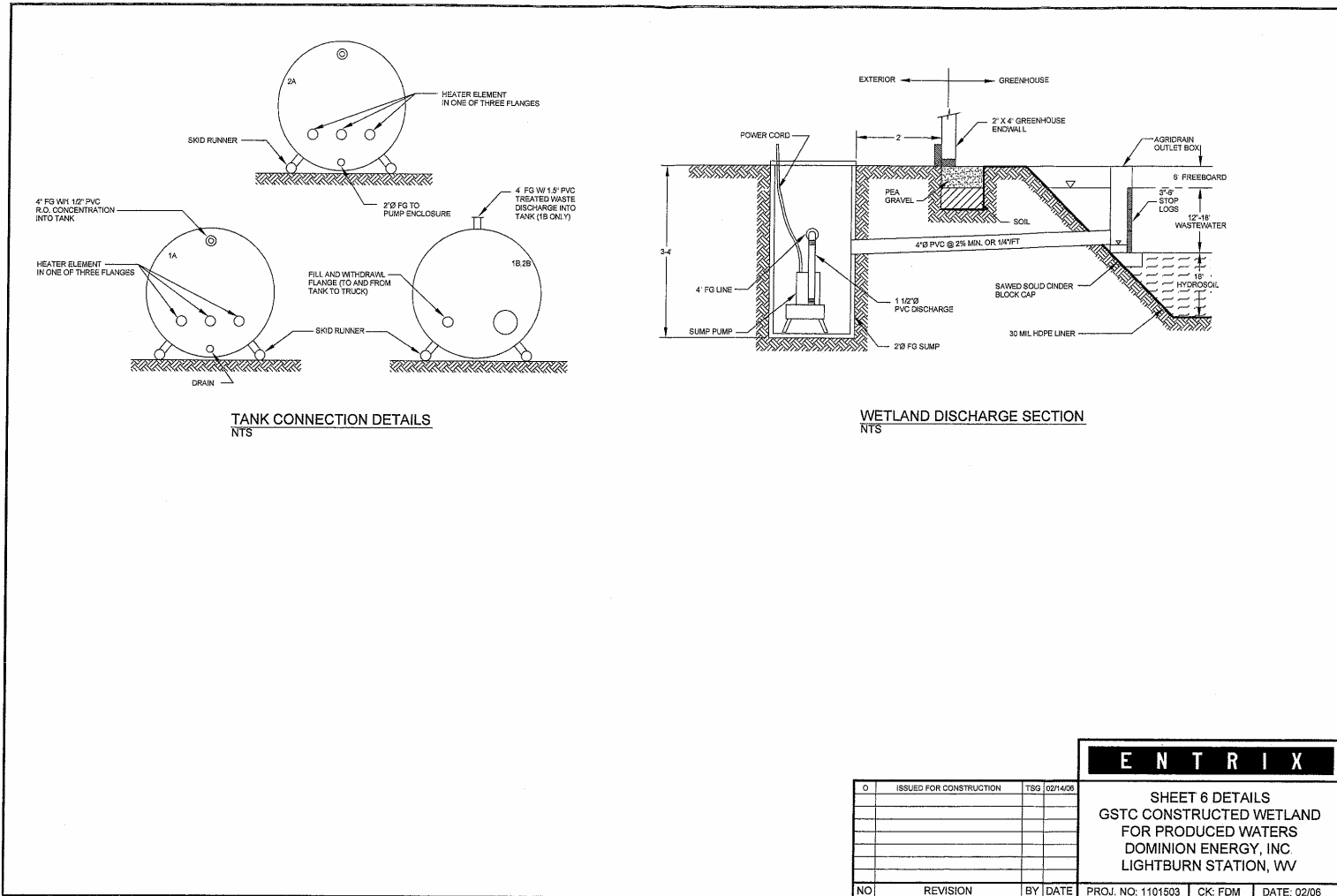
Figure 6. Tank connection details and wetland discharge section.

Figure 7. Exterior of greenhouse and tanks. Inflow tank is to the right, effluent tank is to the left.
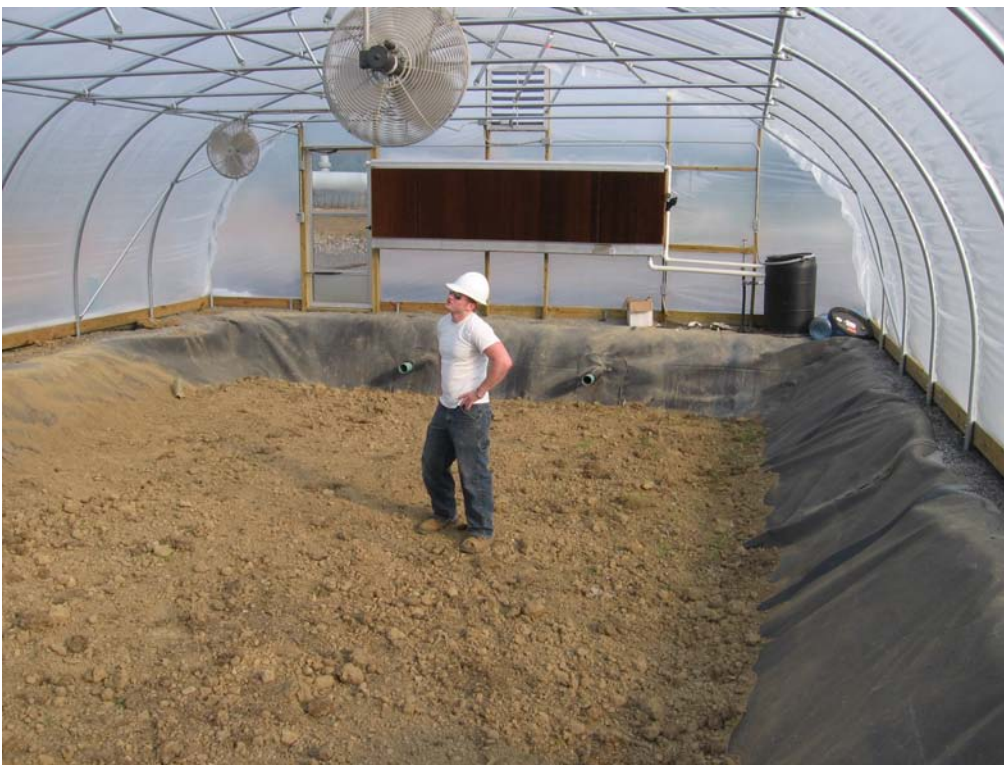
Figure 8. Interior of greenhouse including HDPE liner, hydrosoil and a graduate student.
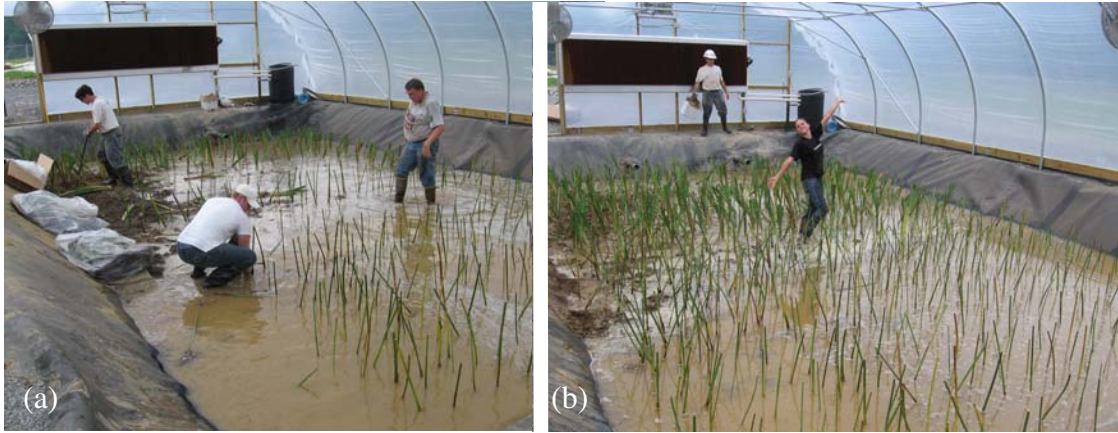
Figure 9. Planting of *S. californicus* and *T. latifolia*: (a) planting process (b) completed planting.
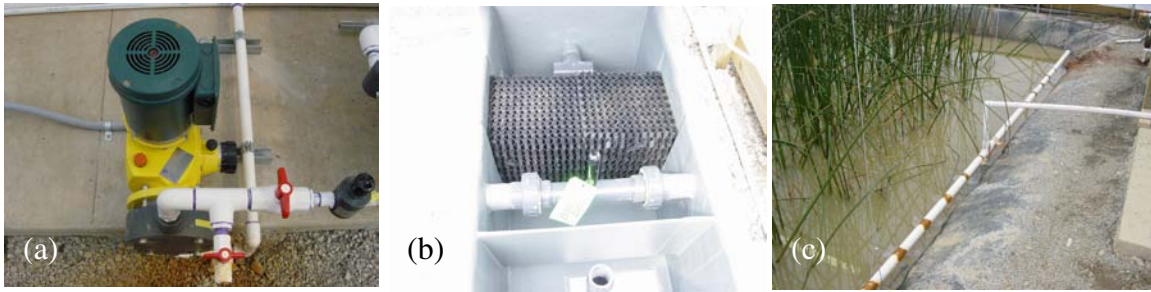
Figure 10. Components of the treatment system. (a) metering pump (b) oil-water separator (c) inflow spreader pipe.
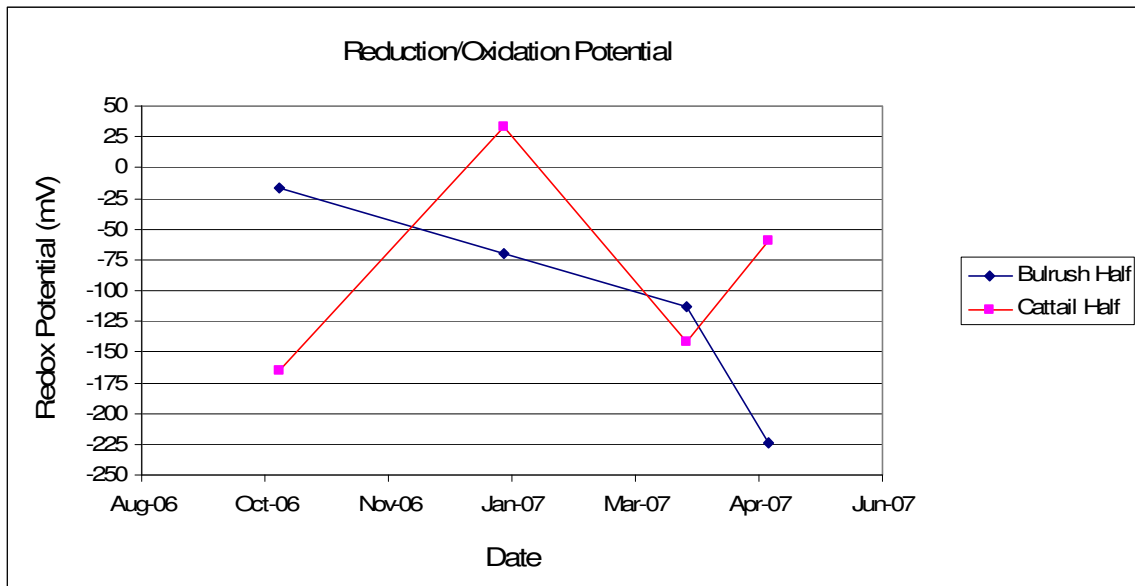
Figure 11. Redox potential in the wetland with time.

19
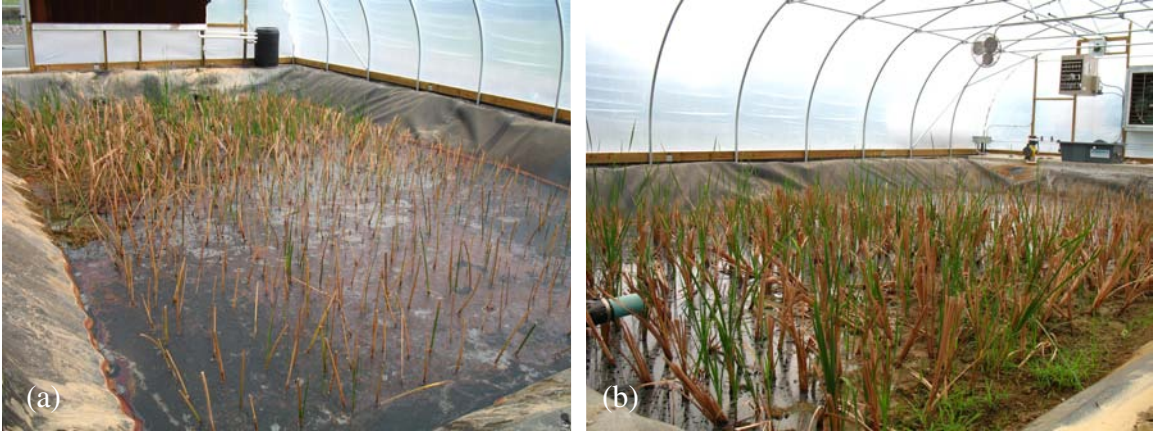
Figure 12. Wetland one month after planting: (a) bulrush side of wetland (b) cattail side of wetland
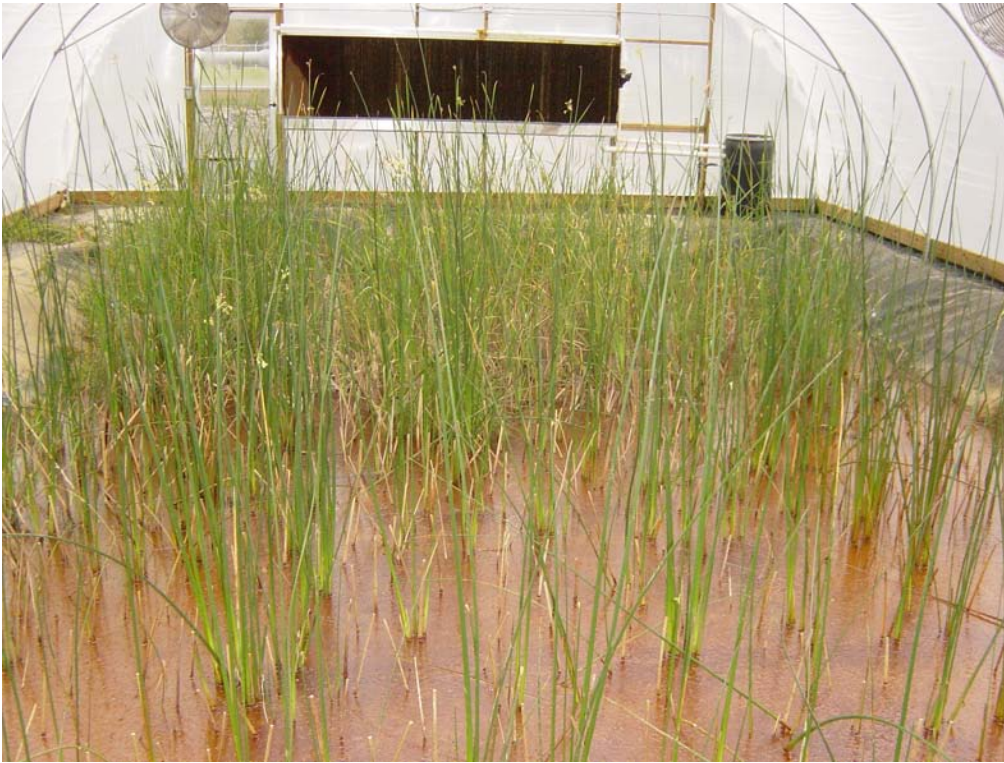
Figure 13. Wetland three months after planting. Bulrush are in the front, and cattails are in the back.

Figure 14. Wetland six months after planting. Bulrush are in the front and cattails are in the back. The mature bulrush have developed seed heads.

Figure 15. Wetland ten months after planting: (a) bulrush side of wetland (b) cattail side of wetland
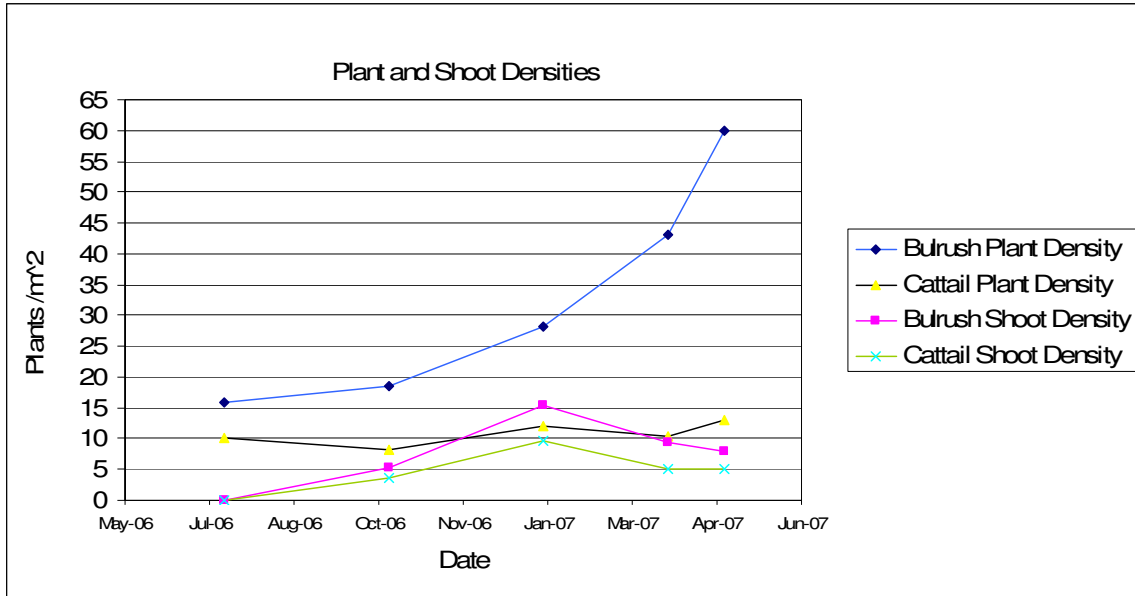
Figure 16. Plant and shoot densities in the wetland with time.
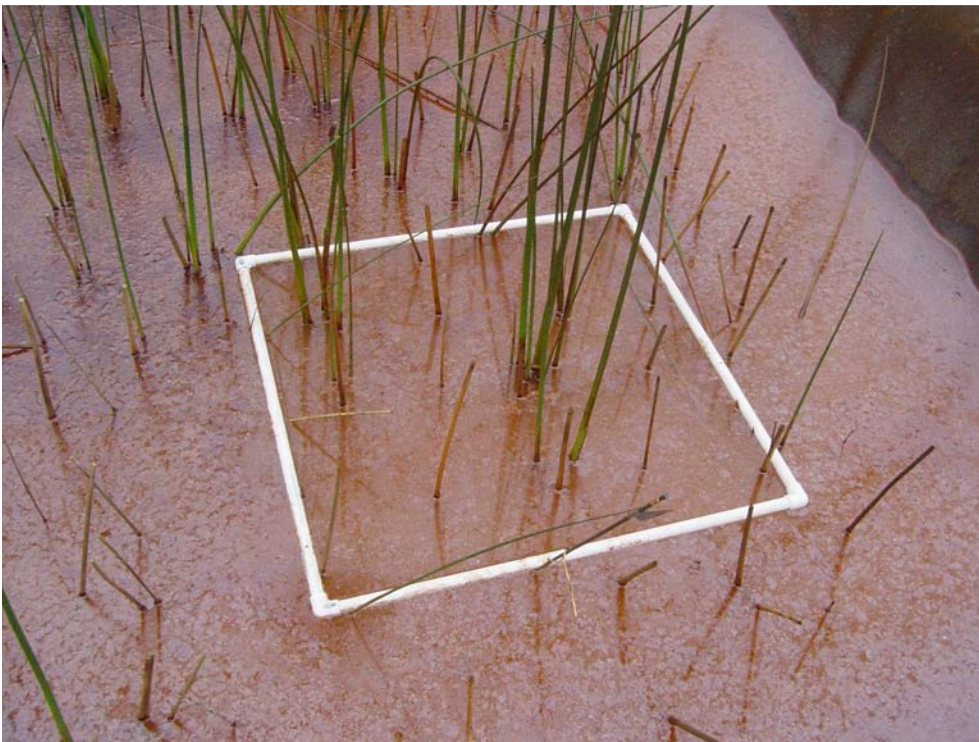
Figure 17. PVC frame (1 m^2) used for plant and shoot density measurements.
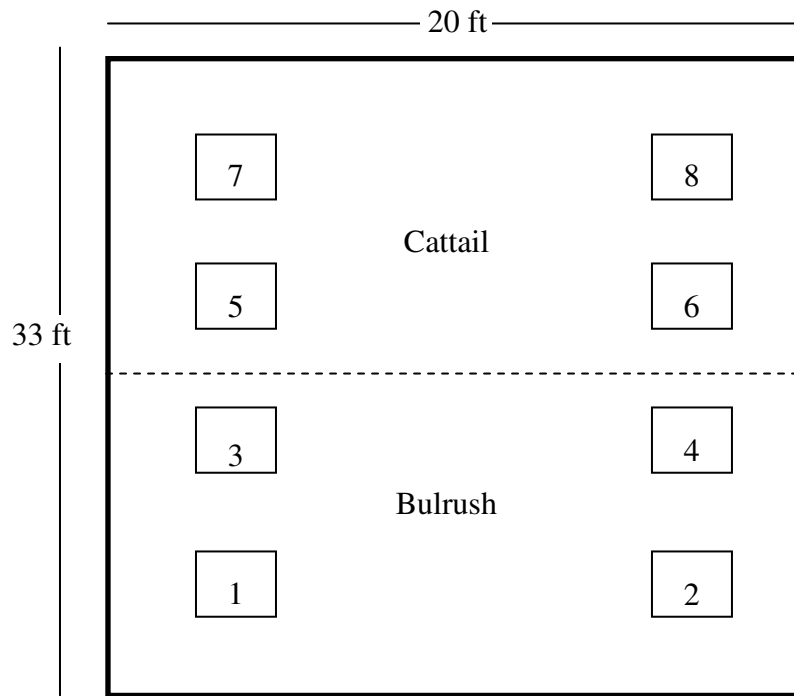
Figure 18. Schematic diagram showing measurement locations in wetland.

Table 1: Analytical methods for parameters monitored from the demonstration-scale constructed wetland treatment system.

Parameter	Method	Method Detection Limit
Temperature	Direct Instrumentation: YSI Model 52	0.5ºC
pH	Direct Instrumentation: Orion Model 420A	0.01
Conductivity	Direct Instrumentation: YSI 30	0.1 µS/cm
Alkalinity	Standard Methods: 2320 B (APHA, 1998)	2 mg/L as $CaCO_3$
Hardness	Standard Methods: 2340 C (APHA, 1998)	2 mg/L as $CaCO_3$
DO[1]	Direct Instrumentation: YSI Model 52	0.1 mg/L
COD[2]	Closed reflux colorimetry (HACH- modified from Standard Methods: 5220 D) (APHA, 1998)	3 mg/L
BOD[3]	Standard Methods: 5210 B (APHA, 1998)	0.1 mg/L
Chloride	High: HACH Drop Count Titration Method Low: HACH colorimetric method 8207	500 mg/L 25 mg/L
Sulfate	Standard Methods: 4500 E (APHA, 1998)	1 mg/L
Metals	Atomic Absorption Spectrometry (AA) (U.S. EPA, 1991)	Cd–0.002 mg/L Cu–0.010 mg/L Pb–0.050 mg/L Zn–0.005 mg/L
	Inductively Coupled Plasma-Atomic Emissions Spectrometry (ICP-AES): 200.8 (U.S. EPA, 1991)	Cd-0.010 mg/L Cu-0.005 mg/L Pb-0.015 mg/L Zn-0.010 mg/L
TDS[4]	Standard Methods: 2540 C (APHA, 1998)	0.1 mg/L
TSS[5]	Standard Methods: 2540 D (APHA, 1998)	0.1 mg/L
Oil and Grease	TOC[6] & TPH[7]	Undetermined
Bulk Redox	Standard Voltmeter, Accumet® calomel reference electrode, and *in situ* platinum-tipped electrodes (Faulkner et al., 1989).	±10mV
Toxicity	*Ceriodaphnia dubia*, (U.S. EPA, 2002)	

[1] Dissolved Oxygen   [3] Biological Oxygen Demand   [5] Total Suspended Solid
[2] Chemical Oxygen Demand   [4] Total Dissolved Solids   [6] Total Organic Carbons
[7] Total Petroleum Hydrocarbons

Table 2: Cost/barrel (Minimum-Maximum) for treatment of produced waters

Treatment Method	Cost ($/barrel)	State	Reference
Evaporation/injection	$0.01-$0.09	CA	(Veil, 1997)
Injection	$1.00	KY	(Veil, 1997)
Injection	$0.20-$4.50	LA	(Veil, 1997)
Evaporation	$0.25-$0.81	NM	(Veil, 1997)
Evaporation/injection	$0.69	NM	(Veil, 1997)
Injection	$0.69	NM	(Veil, 1997)
Injection	$0.30	OK	(Veil, 1997)
POTW	$0.65-$1.50	PA	(Veil, 1997)
POTW/Road Spread	$1.30-$4.20	PA	(Veil, 1997)
Treat/Discharge	$1.00-$2.10	PA	(Veil, 1997)
Treat/NPDES	$1.00-$2.10	PA	(Veil, 1997)
Treat/POTW	$1.25-$1.80	PA	(Veil, 1997)
Injection	$0.23-$4.50	TX	(Veil, 1997)
Evaporation	$0.50-$0.75	UT	(Veil, 1997)
Evaporation	$0.50-$2.50	WY	(Veil, 1997)
Injection	$0.60-$8.00	WY	(Veil, 1997)
Treat/injection or discharge	$0.96	WY	(Veil, 1997)
Treat/injection or NPDES	$0.96	WY	(Veil, 1997)
1.4 Acre CWTS	$0.007		(Mooney, 2006)
6.25 Acre CWTS	$0.034		(Mooney, 2006)
8 Acre CWTS	$0.015		(Mooney, 2006)
12.5 Acre CWTS	$0.019		(Mooney, 2006)
15 Acre CWTS	$0.022		(Mooney, 2006)
15 Acre CWTS	$0.017		(Mooney, 2006)

Table 3: Formulations of simulated natural gas storage produced waters by category based on chloride concentration. All waters except fresh water 2 were investigated in the previous pilot-scale project; freshwater 2 was investigated in the current demonstration-scale project.

Constituent (mg/L)	Simulated Source	Fresh Water Target Inflow		Brackish Water Target Inflow		Saline Water Target Inflow	Hyper-Saline Water Target Inflow
		1	2	1	2		
Cadmium	$CdCl_2$	0.02	0.4	0.04	0.40	0.8	1.21
Copper	$CuCl_2 \cdot 2H_2O$	0.02	0.8	0.67	1.0	3.34	5
Lead	$PbCl_2$	0.1	1	0.67	2.6	6.84	10.2
Zinc	$ZnCl_2$	0.1	5	1.31	21	45.9	69
Oil/Grease	Motor Oil	3	20	15	23	49	78
Chlorides	$CaCl_2$, NaCl, $MgCl_2 \cdot 6H_2O$	400		2,500		15,000	40,000
* Cadmium is not regulated by any reviewed NPDES permits							

Table 4: Average inflow/outflow, % removal, and estimated rate coefficients (k, units = d^{-1} = 1/days) for cadmium, copper, lead, and zinc using a pilot-scale CWTS. (Averages do not include non-detect values.)

Water Type	Sampling Point	Cadmium mg/L	Copper mg/L	Lead mg/L	Zinc mg/L
Simulated Fresh Produced Water 1	In	0.0212	ND	ND	0.635
	Out	0.0157	ND	ND	0.022
	% Removal	27%	NA	NA	97%
	k (d^{-1})	0.093	NA	NA	0.749
Simulated Fresh Produced Water 2	In	0.312	0.703	0.744	5.18
	Out	0.008	ND	ND	0.367
	% Removal	98%	>99.1%	>99%	93%
	k (d^{-1})	0.733	0.953	0.964	0.529
Simulated Brackish Produced Water 1	In	0.039	0.67	0.671	1.318
	Out	0.034	0.106	0.051	1.493
	% Removal	14%	84%	92%	-13%
	k (d^{-1})	0.03	0.37	0.514	-0.025
Simulated Brackish Produced Water 2	In	0.409	1.052	2.557	21.63
	Out	0.252	0.099	0.176	12.985
	% Removal	39%	91%	94%	41%
	k (d^{-1})	0.137	0.675	0.94	0.152
Simulated Saline Produced Water	In	1.008	5.012	6.096	44.734
	Out	0.004	0.063	0.136	0.374
	% Removal	>99%	99%	98%	99%
	k (d^{-1})	0.842	0.638	0.547	0.704
Simulated Hyper-Saline Produced Water	In	1.958	1.056	12.23	70.5
	Out	0.008	ND	0.095	0.185
	% Removal	>99%	>99%	99%	>99%
	k (d^{-1})	0.81	0.886	0.706	0.865
NA-Not Available ND-Non Detect					

Table 5: Chemical composition of storm water in wetland during initial acclimation.

Constituent	Concentration (mg/L)	EPA Method
Aluminum	0.098*	200.7
Antimony	ND	200.7
Arsenic	ND	200.7
Barium	0.047	200.7
Beryllium	ND	200.7
Cadmium	ND	200.7
Calcium	44.1	200.7
Chromium	ND	200.7
Cobalt	ND	200.7
Copper	ND	200.7
Iron	51.6*	200.7
Lead	0.0028	200.7
Magnesium	5.5	200.7
Manganese	0.52*	200.7
Nickel	ND	200.7
Potassium	15.8	200.7
Selenium	0.013	200.7
Silver	ND	200.7
Sodium	19.6	200.7
Thallium	ND	200.7
Tin	0.013	200.7
Vanadium	ND	200.7
Zinc	1.6*	200.7
Mercury	ND	245.1
Oil & Grease	8.4*	413.1
Total Petroleum Hydrocarbons	7.4*	413.1M
* Concentration exceeds EPA drinking water standards		ND-Non Detect

Table 6: Acclimation monitoring data from experiment 1, consisting of storm water with a chloride concentration of 500 mg/L.

Sample Location	Sample Concentrations (mg/L)						
	Cu	**Zn**	**Cd**	**Pb**	**Fe**	**Se**	**Oil and Grease**
Wetland Inflow	0.04	0.47	0.01	0.11	101.08	0.04	84.90
Wetland Outflow	0.02	0.41	0.01	0.01	94.24	0.01	51.85
% Removal	**52**	**12**	**NR**	**8**	**7**	**75**	**39**
NR - No Removal							

Table 7: Acclimation monitoring data from experiment 2, consisting of 7,900 gallons of storm water mixed with 300 gallons of NGSPW and a chloride concentration of 1,500 mg/L.

Sample Location	Sample Concentrations (mg/L)						
	Cu	**Zn**	**Cd**	**Pb**	**Fe**	**Se**	**Oil and Grease**
Wetland Inflow	ND	3.53	0.01	0.09	156.20	ND	23.00
Wetland Outflow	ND	1.80	0.01	0.12	194.23	ND	12.65
% Removal	**ND**	**49**	**NR**	**NR**	**NR**	**ND**	**45**
ND - Non-Detect							
NR - No Removal							

Table 8: Acclimation monitoring data from experiment 3, consisting of 8,600 gallons of storm water mixed with 350 gallons of NGSPW and a chloride concentration of 2,500 mg/L.

Sample Location	Sample Concentrations (mg/L)						
	Cu	**Zn**	**Cd**	**Pb**	**Fe**	**Se**	**Oil and Grease**
Wetland Inflow	0.20	8.78	0.08	0.05	443.39	ND	NA
Wetland Outflow	ND	1.37	0.05	0.03	438.64	ND	NA
% Removal	**100**	**84**	**39**	**44**	**1**	**ND**	**NA**
ND - Non-Detect							
NR - No Removal							

References Cited

American Public Health Association (APHA), American Water Works Association, and Water Pollution Control Federation. 1998. Standard methods for examination of water and wastewater, 20th Ed. American Public Health Association, Washington, D.C.

Faulkner, S.P., W.H. Patrick, Jr., R.P. Gambrell. 1989. Field techniques for measuring wetland soil parameters. Soil Sci. Soc. Am. J. 53: 883-890.

Mooney, Doug. 2006. Typical constructed wetlands operating costs. E-mail to Evan Cross, March 13, 2006.

Nakels, D.V., I. Oritx, and J. R. Frank. 2003. An analysis of management strategies for produced waters from natural gas production. *Produced Water: Technological /Environmental Issues and Solutions.* J. P. Ray, F.R. Engelhardt eds. Plenum Press. New York. Pp 151-162.

United States Environmental Protection Agency (U.S. EPA). 1991. *Methods for the Determination of Metals in Environmental Samples*, EPA/600/4-91/010. Cincinnati, OH.

United States Environmental Protection Agency (U.S. EPA). 2002. *Short-term Methods for Estimating Chronic Toxicity of Effluents and Receiving Water to Freshwater Organisms*, EPA/600/4-91/002. Cincinnati, OH.

Veil, John A.. 1997. Costs for off-site disposal of nonhazardous oil field wastes: salt caverns versus other disposal methods. U.S. Department of Energy, Assistant Secretary for Fossil Energy. W-31-109-Eng-38

Other Pertinent Publications

Gillespie, Jr., W.B., W.B. Hawkins, J.H. Rodgers, Jr., M.L. Cano, and P.B. Dorn. 2000. Transfer and transformations of zinc in constructed wetlands: Mitigation of a refinery effluent. Ecological Engineering 14: 279-292.

Hawkins, W.B., J.H. Rodgers, Jr., A.W. Dunn, P.B. Dorn, and M.L. Cano. 1997. Design and construction of wetlands for aqueous transfers and transformations of selected metals. Ecotoxicology and Environmental Safety 36: 238-248.

Huddleston, G.M. III and J.H. Rodgers, Jr. *in press.* Integrated design of a constructed wetland system for treatment of copper-contaminated wastewater. Water Environment Research.

Huddleston, G.M. III, W.B. Gillespie, Jr., and J.H. Rodgers, Jr. 2000. Using constructed wetlands to treat biochemical oxygen demand and ammonia associated with a refinery effluent. Ecotoxicology and Environmental Safety 45:188-193.

Knight, R.L., R.H. Kadlec, and H.M. Ohlendorf. 1999. The use of treatment wetlands for petroleum industry effluents. Environmental Science & Tech. 33: 973-980.

Mastin, B.J., J.H. Rodgers, Jr. and Y.T. Shah. 2001. Hybrid cavitation/constructed wetland reactors for treatment of chlorinated and non-chlorinated organics. Chemical Engineering Tech. 24: 97A-105A.

Moore, M.T., J.H. Rodgers, Jr., S. Smith, Jr. and C.M. Cooper. 2001. Mitigation of metolachlor-associated agriculture runoff using constructed wetlands in Mississippi, USA. Agric. Ecosystems and Environ. 84: 169-176.

Moshiri, G.A. (ed.). 1993. Construction wetlands for water quality improvement: Lewis Publishers, Ann Arbor, Michigan.

Murray-Gulde, C., J.E. Heatley, T. Karanfil, J.H. Rodgers, Jr., and J.E. Myers. 2003. Performance of a hybrid reverse osmosis-constructed wetland treatment system for brackish water. Water Research 37: 705-713.

Murray-Gulde, C.L., J. Bearr, and J.H. Rodgers, Jr. 2005. Evaluation of a constructed wetland treatment system specifically designed to decrease bioavailable copper in a wastestream. Ecotoxicology and Environmental Safety 61: 60-73.

Myers, J.E. 2000. Constructed wetland overview for the petroleum industry. Society of Petroleum Engineers E&P Environmental Conference, Stavanger, Norway (SPE 61181).

Myers, J.E., L.M. Jackson, R.F. Bernier, and D.A. Miles. 2001. An evaluation of the Department of Energy naval petroleum reserve No. 3 produced water biotreatment facility. Society of Petroleum Engineers E&P Environmental Conference, San Antonio, TX (SPE 66522).

Pope, D. H., and R.M. Pope. 1999. Diagnosis, treatment, and monitoring of microbiologically influenced productivity in natural gas storage facilities. Gas Research Institute, Report GRI-00-0056.

SAS Institute. 2002. Statistical Analysis System. Version 9. SAS Institute Inc., Cary, North Carolina.

United States Environmental Protection Agency (USEPA). 2000. EPA Office of Compliance Sector Notebook Project: Profile of the Oil and Gas Extraction Industry. EPA/310-R-99-006.

United States Environmental Protection Agency (USEPA). 2002. ECOTOX User Guide: ECOTOXicology Database System. Version 3.0. Available: <http:/www.epa.gov/ecotox/>.

United States Environmental Protection Agency (USEPA). 2004. National Pollutant Discharge Elimination System: View NPDES Individual and General Permits. Available: <http://cfpub.epa.gov/npdes/permitissuance/genpermits.cfm>.

Veil, A., M.G. Puder, D. Elcock, and R.J. Redweik, Jr. 2004. A white paper describing produced water from production of crude oil, natural gas, and coal bed methane. United States Department of Energy, National Energy Technology Laboratory. Contract W-31-109-Eng-38.

Scale Remediation Using Sonication: Pre-Commercial Test Project

Donald Johnson
TechSavants
36 Altura Road
Santa Fe, NM 87508

Final report not received, project report to be completed after
field tests are completed and evaluated

Gas Storage Field Deliverability Enhancement and Maintenance: An Intelligent Portfolio Management Approach.

Final Report

Report prepared by:
Shahab D. Mohaghegh, Ph.D.
Principal Investigator

Razi Gaskari, Ph.D.
Co-Principal Investigator

And Mr. Kazim Malik

Petroleum & Natural Gas Engineering

West Virginia University
Morgantown, WV 26506
Telephone: 304.293.7682
Fax: 304.293.5708

Subcontract No. 3040-WVRC-DOE-1779

Report prepared for:
GSCT Consortium Director
PSU/Energy Institute
The Pennsylvania State University
C211 Coal Utilization Laboratory
University Park, PA 16802-2309
Telephone: 814.865.0531
Fax: 814.685.3248
Email: jlm9@psu.edu

DISCLAIMER

This report was prepared as an account of work sponsored by an agency of the United States Government. Neither the United States Government nor any agency thereof, nor any of their employees, makes any warranty, expressed or implied, or assumes no legal liability or responsibility for the accuracy, completeness, or usefulness of any information, apparatus, product, or process disclosed, or represents that its use would not infringe privately owned rights. Reference herein to any specific commercial product, process, or service by trade name, trademark, manufacturer, or otherwise does not necessarily constitute or imply its endorsement, recommendation, or favoring by the United States Government or any agency thereof. The views and opinions of authors expressed herein do not necessarily state or reflect those of the United States Government or any agency thereof.

ABSTRACT

Portfolio management, a common practice in the financial market, is essentially an optimization problem that attempts to increase return on investment. The objective of this project is to apply the state-of-the-art in optimum portfolio management to the gas storage field in order to optimize the return on investment associated with well remedial operations.

Each year gas storage operators spend hundreds of thousands of dollars on workovers, re-completions, and re-stimulations of storage wells in order to battle the decline in deliverability due to well damage with time. A typical storage field has tens if not hundreds of production wells. Each well will respond to remedial operations in its own unique way. The well's response to the remedial operation is a function of a set of uncontrollable reservoir characteristics such as porosity and permeability and a set of controllable parameters such as completion and stimulation practices.

The objective of this project is to identify the combination of best candidate wells for the remedial operations that will result in the most successful program each year, and consequently provides the highest return on investment. The project deliverable is a Windows-based software application that would perform the analysis and provide the list of wells and their corresponding remedial operation for each year based on the budget constraints identified by the user.

The state-of-the-art in intelligent systems application that is currently being used extensively in the Wall Street is the methodology to achieve the objectives of this proposed project. This methodology includes a hybrid form of artificial neural networks, genetic algorithms and fuzzy logic. Columbia Gas Transmission Corporation is the industry partner of this project and cooperated with the research and development team in order to ensure successful completion of the project.

The software application that is the deliverable of this project and is explained in much detail in this report is available to public free of charge. One important note about the software is that the current, publicly available version of the software includes a neural network model that has been developed for our industry partner based on the data that they made available. Once a storage operator decides to implement this software, they should contact the principal investigator of this project *(Shahab D. Mohaghegh, Professor, Petroleum & Natural Gas Engineering, West Virginia University, Email: shahab@wvu.edu - Tel; 304-293-7682 ext. 3405 – Web Site: http://shahab.pe.wvu.edu)* and arrange for development of a neural network model for their specific storage field. In order to make the best use of capabilities of the software package, it is recommended that the storage filed have a minimum of 75 wells (wells with data that can be used for analysis).

TABLE OF CONTENTS

LIST OF FIGURES

LIST OF TABLES

INTRODUCTION

Each year Gas Storage operators spend hundreds of thousands of dollars to combat the inevitable decline in the deliverability of their production wells. The decline in deliverability with time has two major contributors. The first contributor is geology and reservoir characteristics that are uncontrollable parameters. The second sets of parameters that contribute to the decline are associated with well damage that is addressed by well remedial operations such as workovers, re-completions, and re-stimulation of the producing wells. The parameters associated with these remedial operations can be controlled by the operator.

It is a fact that every well will respond to a specific remedial operation in a unique way. For example, the deliverability of well "A" will increase two folds if a proper restimulation is performed on it while the same operation performed on well "B" will result in little or no deliverability enhancement. Same is true for workovers. Finding the best candidate for restimulation or workover, each year, among the tens or hundreds of wells is a challenging task. Consider another situation where well "C" will have a 70% increase if a restimulation is performed but it would have a 65% increase if a far less expensive workover is performed. Obviously performing a workover instead of a restimulation on well "C" would be more economical this year.

EXECUTIVE SUMMARY

Portfolio management, a common practice in the financial market, is essentially an optimization problem that attempts to increase return on investment. The objective of this project is to apply the state-of-the-art in optimum portfolio management to the gas storage field in order to optimize the return on investment associated with well remedial operations.

Each year gas storage operators spend hundreds of thousands of dollars on workovers, re-completions, and re-stimulations of storage wells in order to battle the decline in deliverability due to well damage with time. A typical storage field has tens if not hundreds of production wells. Each well will respond to remedial operations in its own unique way. The well's response to the remedial operation is a function of a set of uncontrollable reservoir characteristics such as porosity and permeability and a set of controllable parameters such as completion and stimulation practices.

The objective of this project is to identify the combination of best candidate wells for the remedial operations that will result in the most successful program each year, and consequently provides the highest return on investment. The project deliverable is a Windows-based software application that would perform the analysis and provide the list of wells and their corresponding remedial operation for each year based on the budget constraints identified by the user.

The state-of-the-art in intelligent systems application that is currently being used extensively in the Wall Street is the methodology to achieve the objectives of this proposed project. This methodology includes a hybrid form of artificial neural networks, genetic algorithms and fuzzy logic. Columbia Gas Transmission Corporation is the industry partner of this project and cooperated with the research and development team in order to ensure successful completion of the project.

The software application that is the deliverable of this project and is explained in much detail in this report is available to public free of charge. One important note about the software is that the current, publicly available version of the software includes a neural network model that has been developed for our industry partner based on the data that they made available. Once a storage operator decides to implement this software, they should contact the principal investigator of this project *(Shahab D. Mohaghegh, Professor, Petroleum & Natural Gas Engineering, West Virginia University, Email: shahab@wvu.edu - Tel; 304-293-7682 ext. 3405 – Web Site: http://shahab.pe.wvu.edu)* and arrange for development of a neural network model for their specific storage field. In order to make the best use of capabilities of the software package, it is recommended that the storage filed have a minimum of 75 wells (wells with data that can be used for analysis).

EXPERIMENTAL

No experimental work was performed during this project.

RESULTS & DISCUSSIONS

This is the detail report of the progress made so far in the above mentioned project, which consists of following components:

1-   Project Overview
2-   Data made available and its format
3-   Neural Network Model
4-   Genetic Optimization Model
5-   Database & Software

PROJECT OVERVIEW

The objective of this project is to apply state-of-the-art intelligent, optimum portfolio management to the gas storage field in order to optimize the return on investment associated with well remedial operations. Columbia Gas Transmission Corporation is the industry partner in this project and provided us with very valuable data and in-depth knowledge about their gas storage field operations.

The data in very crude form was provided to the research and development team in the last week of March, 2005. The team extracted valuable data and organized it in a form of database, with generic make up in order to be reusable. Windows-based software was developed which can help the user in viewing and later populating the data with easy to use interface. One of its modules provides the user with all the valid stimulations required as an input for Neural Network. A Neural Network was trained in order to predict skin for different stimulation parameters. A Genetic Optimization tool was developed and associated with the trained Neural Network in order to find the optimum stimulation parameters. The software ranks the well according to maximum change in skin value or/and stimulation cost for a well. Then a decision is made to re-stimulate a well or not accordingly.

DATA MADE AVAILABLE AND ITS FORMAT

The research and development (R & D) team was initially provided data in MS excel worksheets. On further request, some pdf files with well schematics, well test files and well summary files were provided but still the required data especially relating to stimulations and well-tests was so scarce that the team in July, 2005 went to the Columbia Transmission Corporation Office in Charleston, WV to get more information. Retrieval of data from different files and thousands of microfiche was taking so long at the office that it was decided that West Virginia University lab facilities will be used to read thousands of microfiche. So, for the next few weeks the team concentrated its efforts on data collection. That data could be segregated into five main tables, each relating to specific characteristic features of the gas storage wells. The five characteristic features are as below:

1-   Well-bore data
2-   Completion Data
3-   Perforation Data
4-   Stimulation Data
5-   Well-Test Data
6-   Reservoir Characteristic Data

WELL BORE DATA

It includes basic features of the well like location, depth, well name … etc. Data about well-bore was retrieved mostly from well schematics and well summary reports. The data already provided by Columbia Transmission Corporation was also verified. The complete list of the data type retrieved is as below:

1. API Number
2. Field Name
3. Well
4. Lease Name
5. Classification
6. Latitude (Lat)
7. Longitude (Long)
8. Section
9. Township
10. County
11. State
12. Operator
13. Total Vertical Depth
14. Formation

Picture of one of the forms from which this data was retrieved is on next page

Fig1. Well-bore data retrieved from a file

The tables contained many minor mistakes like wrong Well API number, length, and many spelling mistakes. A picture of this correction is shown below:

Fig2. Correction of Wrong API number in data

Analysis of raw data vs. refined data:

WELLBORE DATA														
DATA FIELDS	API Number	Field Name	Well	Lease Name	Classification	Lat	Long	Section	Township	County	State	Operator	Total Vertical Depth	Formation
INITIIAL DATA AVAILABLE	430	427	430	430	427	429	430	430	430	430	430	430	425	430
FINAL DATA AVAILABLE	430	430	430	430	430	430	430	430	430	430	430	430	430	430

Fig3. Data addition and refinement for Well-bore Data

COMPLETION DATA

Completion data mostly relates to the type and depth of casing/liner/tubing run in the gas storage wells. The data type retained for the database includes the following:

1. API Number
2. Field Name
3. Well Name (Well)
4. Completion Description (Des)
5. Date Tubing Run (Dt Tm Rn)
6. Outer Diameter (OD)
7. Top of Casing
8. Bottom of Casing(Bot)
9. Casing Weight (Weight)
10. Casing Grade (Grade)

Unfortunately the data was mostly in an excel file and had to be verified with well schematic drawings. This led to the most unusual step in this project as it lead to reduction of valuable data available to us.   This was due to the erroneous and multiple data entry originally in the completion table. Identification of the multiple entries and their removal from table was the most focused act of cleaning the data, as omission of desirable records was unacceptable. Following pictures show one of such flawed multiple data entries which were removed.

Fig4. Multiple Data Entries in Completion Table

In the completion table, the following notations used as casing description were replaced in place of different notations being used to have a standard definition

NOTATION KEPT IN DATABASE	Surface casing
NOTATIONS DISCARDED	Drive pipe
	Driver Pipe
	Swedge
	Two stage

Completion data was mostly re- checked for accuracy from the documents, picture of which is shown below for a Well.

Fig5. Well-bore data retrieved from a file

Analysis of raw data vs. refined data:

Please note that multiple data entry was the major reason for the reduction in the refined data from the initial data.

COMPLETION DATA											
DATA FIELDS	Total Completions Run	API Number	Field Name	Well	Description	Date Tubing Run	OD	Top Casing	Bot	Weight	Grade
INITIIAL DATA AVAILABLE	2910	431	431	431	2909	2909	2909	2909	2909	1781	1607
FINAL DATA AVAILABLE	2413	430	431	431	2413	2413	2413	2413	2413	1723	1607
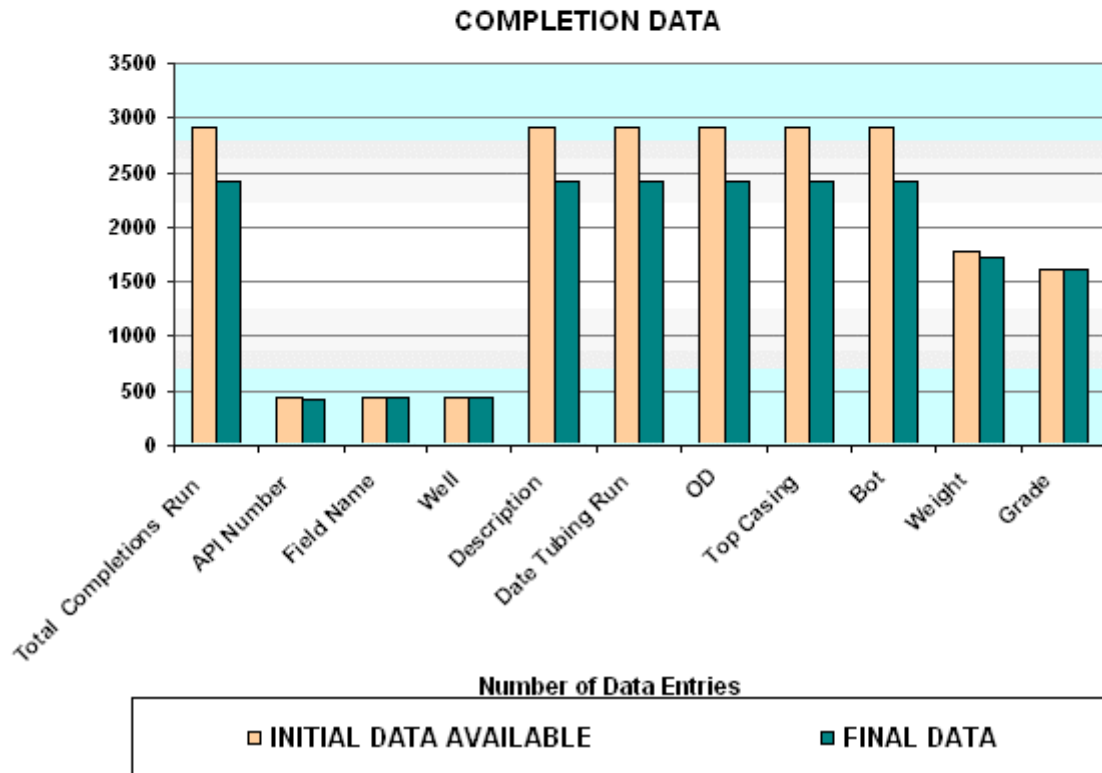
Fig6. Data addition and refinement for Completion Data

PERFORATION DATA

This data set contains all the information relating to the perforations done on the gas storage well like perforation top & bottom depth and shots per foot. Following are the data types included in this type of data set:

1. Well API Number
2. Field Name
3. Well Name
4. Completion Type
5. Perforation Date (Perf Date)
6. Perforation Top (Perf Top)
7. Perforation Bottom (Perf Btm)
8. Shot Type
9. Shot Per foot (Shot Per ft)

The picture of a document showing this information is shown below.

Fig7. Perforation data retrieved from a file

Analysis of raw data vs. refined data:

PERFORATION DATA										
DATA FIELDS	Total Perforations	API Number	Field Name	Well Name	Completion Type	Perf Date	Perf Top	Perf Bottom	Shot Type	Shot Per ft
INITIIAL DATA AVAILABLE	392	57	57	57	48	392	392	392	209	383
FINAL DATA AVAILABLE	392	57	57	57	48	392	392	392	209	383

PERFORATION DATA

Fig8. Data addition and refinement for Perforation Data

STIMULATION DATA

Stimulation data is one of the most significant datasets about the storage wells. Because of this, it was very important that we have maximum records of valid stimulations. Following data type is used to represent stimulation:

1. API Well Number
2. Well Name
3. Size of String
4. Stimulation From
5. Stimulation To
6. No Of Shots
7. Fractured by
8. Stimulation Type
9. Stimulation Date
10. Water
11. Acid
12. Gel
13. Foam
14. Nitrogen
15. Alcohol
16. Cushion
17. Flush
18. Sand Quantity
19. Sand Type
20. Injection Rate
21. Total Fluid
22. Breakdown Pressure
23. ISIP

Unfortunately, initially we didn't have much data about the stimulations being done in this Lucas field. With this in mind, every record with Columbia Transmission Corporation was carefully examined. The largest source of stimulation data came from the thousands of microfiche with some data being found in well summary reports. Following is a picture of data in well summary reports.

Fig9. Stimulation data retrieved from a file

Each Microfiche contained dozens of documents from invoices to valuable stimulation and well-test data

Microfiche were read by digital Microfilm scanners

Each scanned image of the microfiche was searched and read for valuable data

Prints were taken of the documents containing data

Data was entered in the database

Fig10. Microfiche to Database process

Following are pictures of some types of data formats for fracture jobs found in the records

Fig11. Different formats of Nitrogen Amount

During the data entry different sign conventions and unit conversions were carried out as follows:

MEASURED QUANTITY	UNITS IN RECORDS	UNITS USED IN DATABASE
SAND	1 sack 1 sks	100 lbs
NITROGEN	52M	52,000 SCF
LIQUID	1 bbl	42 gal
PERFORATIONS	2000-2005 ft, 10 shots 10/5	2 shots /ft

The following notations were used in place of different notations being used in the tables:

NOTATIONS USED IN DATABASE	WATER GEL FRAC	PETRO GEL FRAC	FOAM FRAC	NITRO SHOT	WATER/N2 FRAC	WATER FRAC	10/20 SAND
NOTATIONS THAT WERE REPLACED	Gelled water frac	Petrl gel	Foam	Shot	Water / N2	water	10/20
	Water Gel	Petro Gel Petro gel fracture	foam Frac foam fracture		Water N2 Fracture Water nitrogen		Sand 10/20
					Water/N2 assist Water Fracture w/N2 assist		

All records of Nitro-shots were discarded for this database as they have no stimulation parameters on record and are part of history now plus they also damage the well. Above all, they will tend to degrade the Neural Network.

Analysis of raw data vs. refined data:

STIMULATION DATA																								
DATA FIELDS	Total Stimulations	API Number	Well	Size Of String	Stim From	Stim To	No Of Shots	Fractured by	Type	Stim Date	Water	Acid	Gel	Foam	N2	Alcohol	Cushion	Flush	Sand Quantity	Sand Type	Injection Rate	Total Fluid	Breakdown Pressure	ISIP
INITIIAL DATA AVAILABLE	32	32	32	32	32	32	32	32	32	32	0	0	0	0	0	0	0	0	32	32	25	0	27	24
FINAL DATA AVAILABLE	390	430	430	308	388	388	156	354	370	391	85	293	294	157	249	21	277	302	368	266	263	317	181	345

Fig12. Data addition and refinement for Stimulation Data.

WELL TEST DATA

Well-test data is the most extensive dataset that our R & D team worked on. It has the maximum amount of records nearly 3365 and 29 data types that control every aspect of a well-test. The data type selected for a well-test representation consists of following:

1. Well API Number
2. Field Name
3. Test Date
4. Test Type
5. Time 1
6. Field Pressure 1
7. Flowing Pressure 1
8. Rate 1
9. Time 2
10. Field Pressure 2
11. Flowing Pressure 2
12. Rate 2
13. Time 3
14. Field Pressure 3
15. Flowing Pressure 3
16. Rate 3
17. Time Extended
18. Field Pressure Extended
19. Flowing Pressure Extended
20. Rate Extended
21. kh
22. Skin
23. True Skin
24. Non Darcy Co-efficient
25. n Value
26. C Value
27. Delta Pressure Squared
28. Peak Day Rate
29. Absolute Open Flow

Estimation of n, C, peak day rate & absolute open flow

Single/Open flow Tests:

The values used for point 1 and 2 are from different well-tests

1-   Find ΔP^2

3- $\dfrac{1}{n} = \dfrac{\log(\overline{p}^2 - p_{wf}{}^2)_2 - \log(\overline{p}^2 - p_{wf}{}^2)_1}{\log q_2 - \log q_1}$ (Where q is in MMcfD)

4- $C = \dfrac{q_g}{(\overline{p}^2 - p_{wf}{}^2)^n}$ (Where q is in McfD)

5- $AOF = C(1150^2 - 0^2)^n$ McfD

6- $PDRate = (C \times 250,000)^n$ McfD

Multi-Point Tests:

Estimation of n, C, PD rate & AOF:

Same as above except that the points used are from the same test

NOTE: The n, C, PD rate & AOF values for more than 400 well-tests were manually calculated

Estimation of kh, skin, true skin, non--darcy coefficient

1- From extended draw-down test plot (P_i-P_{wf}) vs. time on log-log paper. Draw unit-line for un-stimulated wells and half-slope line for Stimulated wells. Find end of well-bore storage effects after 1-1/2 log time cycle

2- Find values of viscosity, z-factor, compressibility of storage gas at different pressure assuming Gas gravity = 0.585 & temperature = 75 F = 535 R

Draw-Down Test:

1- Plot P_{wf}^2 vs. time
2- Draw straight line after pseudo-steady state starts
3- Find slope m and $P^2 1hr$
4- $kh = \dfrac{1637qTzu}{m}$
5- $S = 1.151\left[\dfrac{p^2 - p^2_{1hr}}{m} - \log\left(\dfrac{k}{\phi\mu cr_w^2}\right) + 3.23\right]$
6- Plot skin vs. flow-rate. It should be a straight line
7- Slope of this line is D
8- Find True Skin (S') at q=0.

Build-Up Test:

1- Plot P_{wf}^2 vs. (tp+dt)/dt on semi-log paper
2- Draw straight line after well-bore storage effects diminishes
3- Find slope m and $P^2 1hr$
4- $kh = \dfrac{1637qTzu}{m}$
5- $S = 1.151\left[\dfrac{p^2_{1hr} - p^2}{m} - \log\left(\dfrac{k}{\phi\mu cr_w^2}\right) + 3.23\right]$
6- Plot skin vs. flow-rate. It should be a straight line
7- Slope of this line is D
8- Find True Skin (S') at q=0.

We require time, flow-rate & Bottom hole pressure from the data which are present in two txt files as bottom hole & surface recording files. The flow rates are at Wellhead so we match the BHP & THP with time.
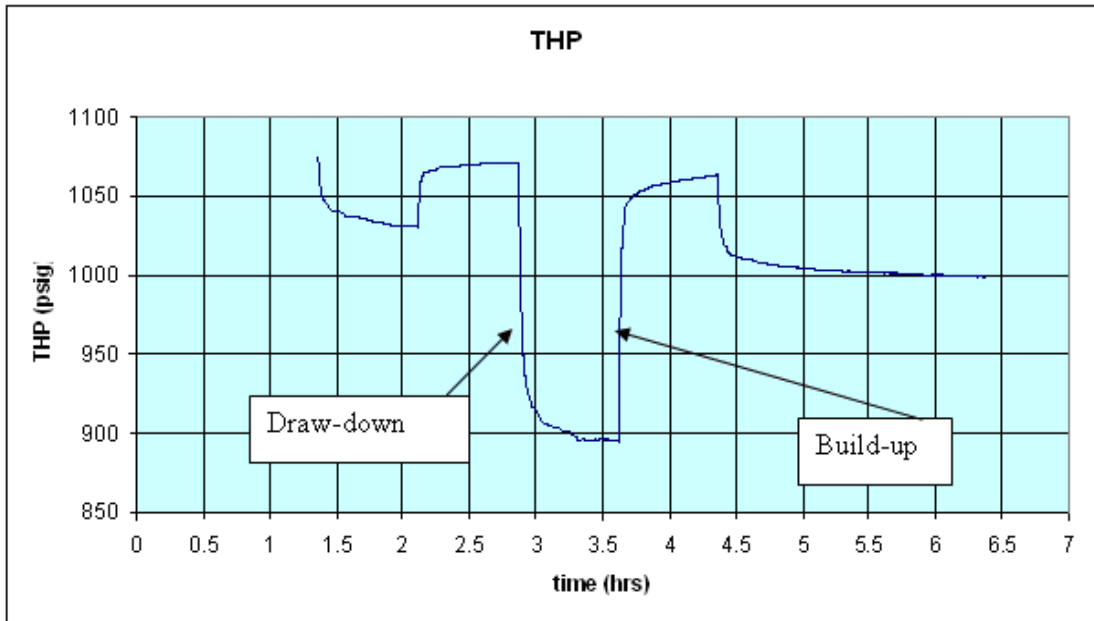
Fig13. Tubing Head Pressure profile for Multi-Point test
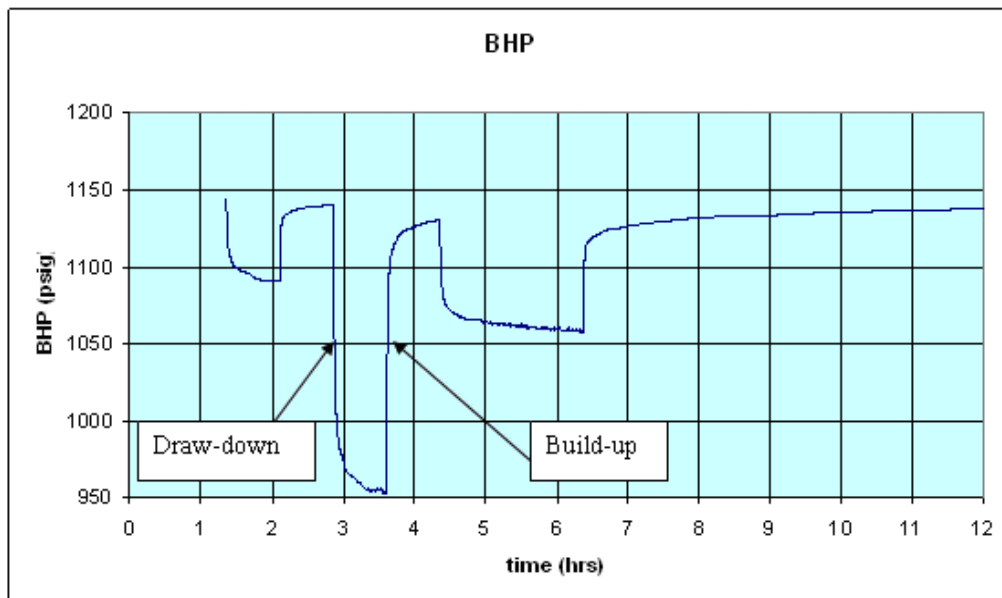
Fig14. Bottom Hole Pressure profile for Multi-Point test

The multipoint-test data is divided into Draw-down & build-up test and each one is analyzed separately.

Draw-down test

Analysis of drawdown tests was done as described above and following graphs were obtained
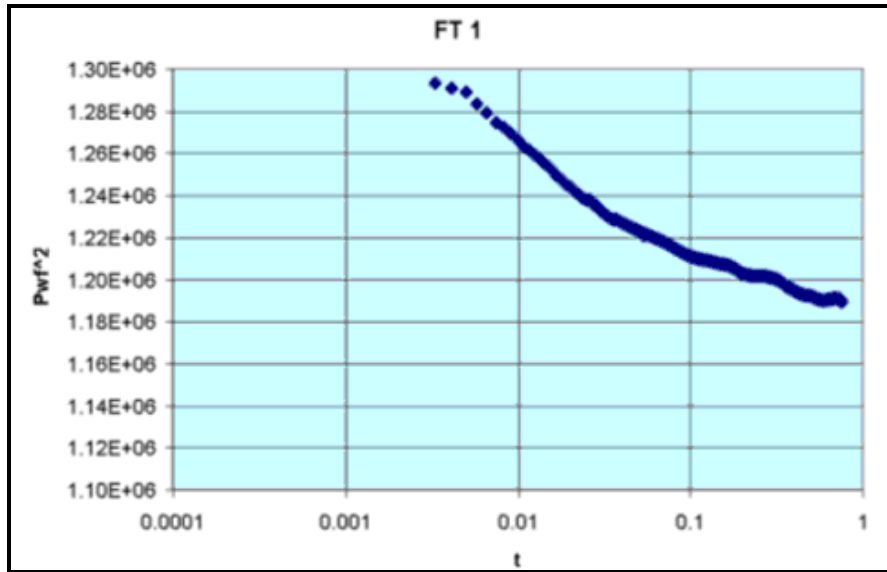
Fig15. Flow Test 1 – Delta pressure squared vs. time
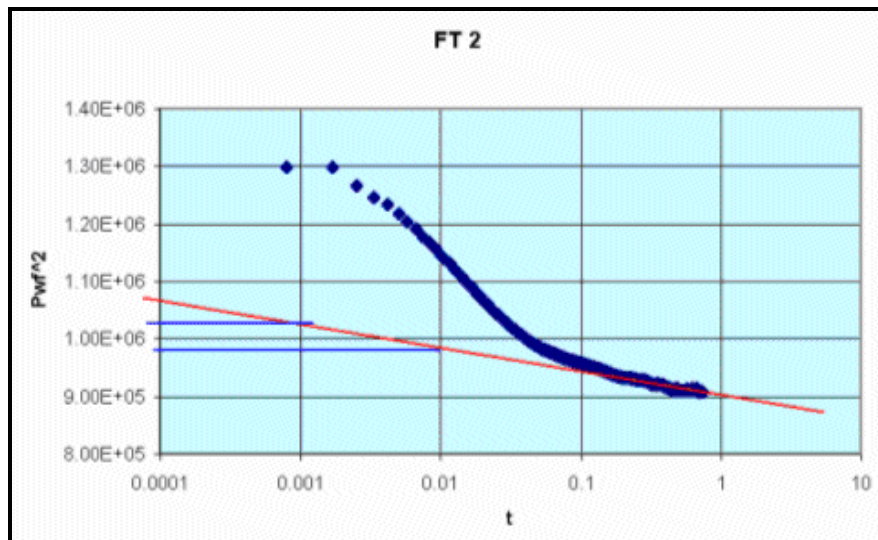
Fig16. Flow Test 2 – Delta pressure squared vs. time
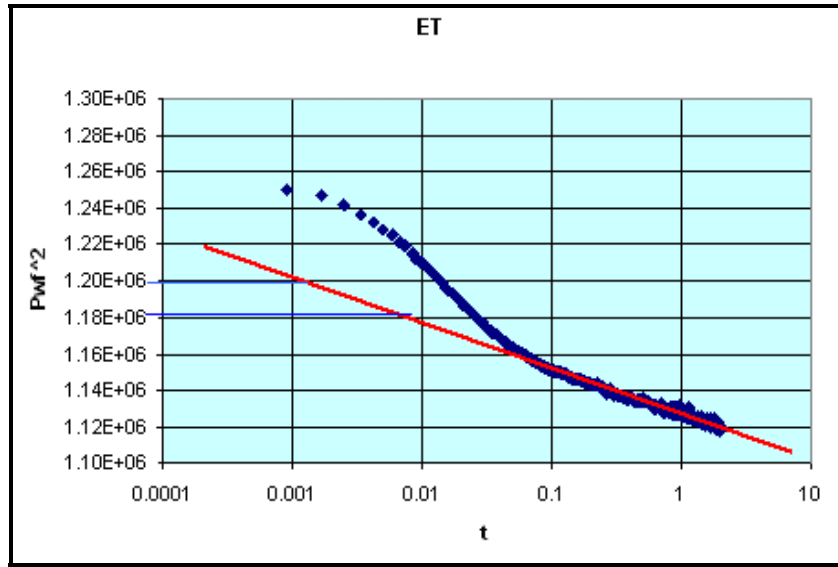
Fig17. Extended Flow Test – Delta pressure squared vs. time
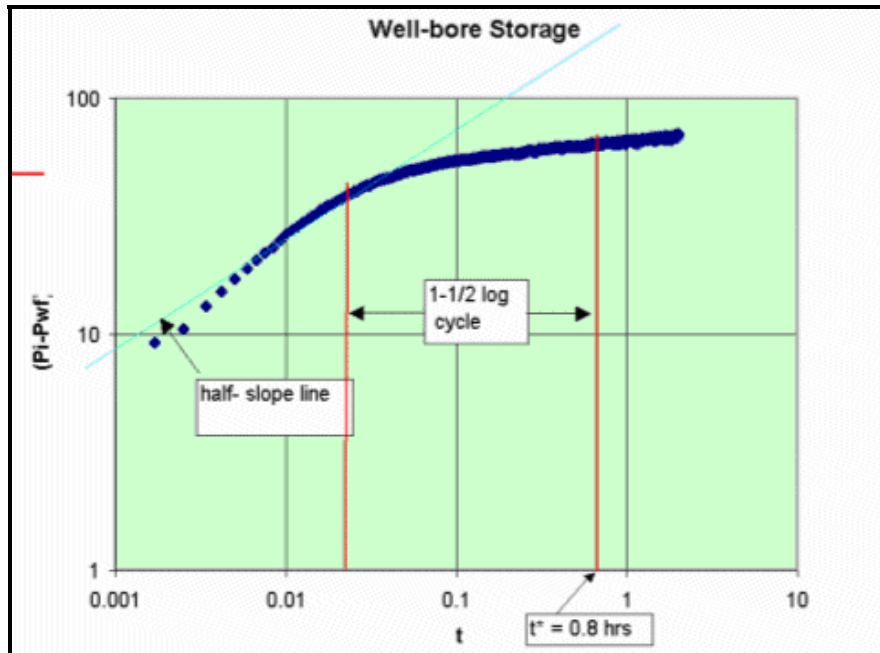
Fig18. Log-log graph

For well-tests after fracture half-slope line is drawn and for un-simulated wells unit slope line is drawn to find end of well-bore effects and start of pseudo-steady state.

Gas production Simulator was used to find the values of viscosity, z-factor and compressibility of storage gas at different pressure assuming Gas gravity = 0.585 & Temperature = 75 F = 535 R that are also used by Columbia Trans.
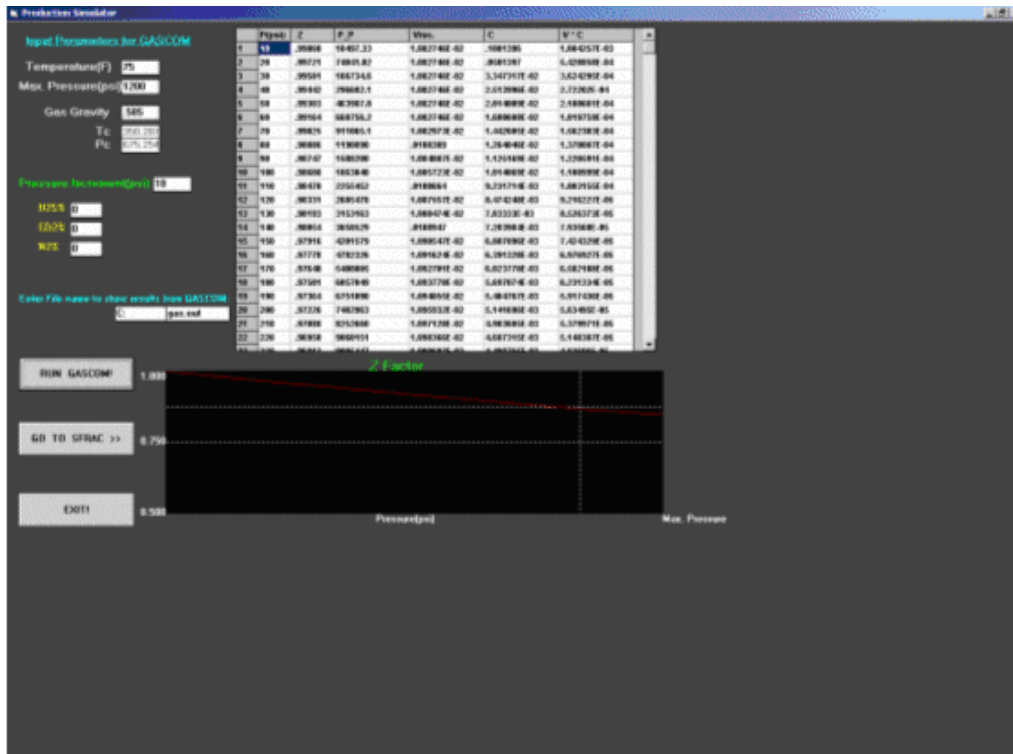
Fig19. Gas Properties Simulator

The slope from Pwf^2 vs. time on semi-log graph was used to find kh & then skin. The three values of skin were plotted on Q vs. S graph and extrapolated to Q = 0 to get True skin (S').
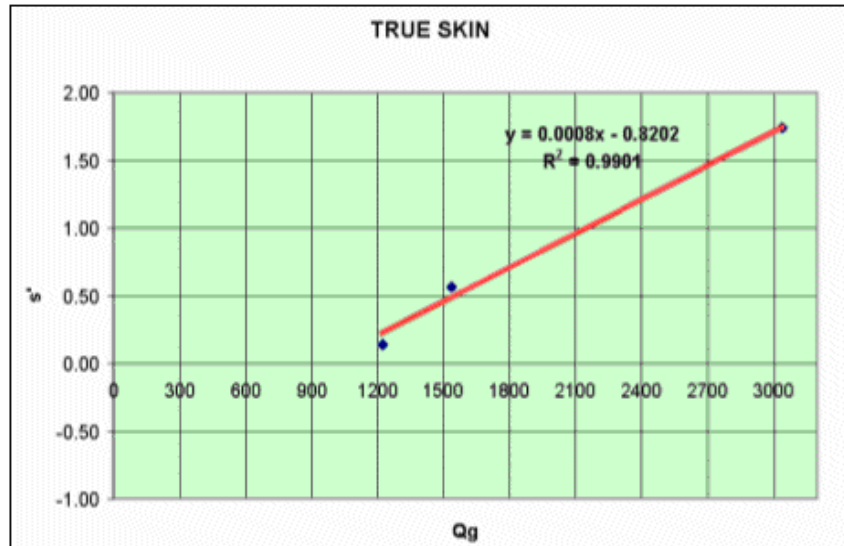
Fig20. Calculation of True skin

	FLOW TEST 1	FLOW TEST T2	EXTENDED TEST
porosity	0.14	0.14	0.14
rw	0.1458333	0.1458333	0.1458333
Ct	1.02E-03	1.08E-03	1.04E-03
Uav	1.28E-02	1.26E-02	1.27E-02
Zav	0.8558691	0.8635354	0.859119
P	1143	1140	1127.3
Qav	1223.8668	3038.7039	1536.1134
Tav	533	533	533
h	10	10	10
m	2.00E+04	5.40E+04	2.20E+04
kh	5.86E+02	5.36E+02	6.67E+02
k	5.86E+01	5.36E+01	6.67E+01
p1hr^2	1.185E+06	9.000E+05	1.128E+06
S	0.14	1.74	0.57
S'	-0.8202		
D	0.0008		

Table 1. Draw down Test Results

Build-up test

In build-up tests, the slope drawn for Horner plot is after the time when well-bore storage effects were found to be minimizing from previous draw-down test. This slope is then used to find the values of kh & skin. The True skin is found the similar way as in draw-down test.
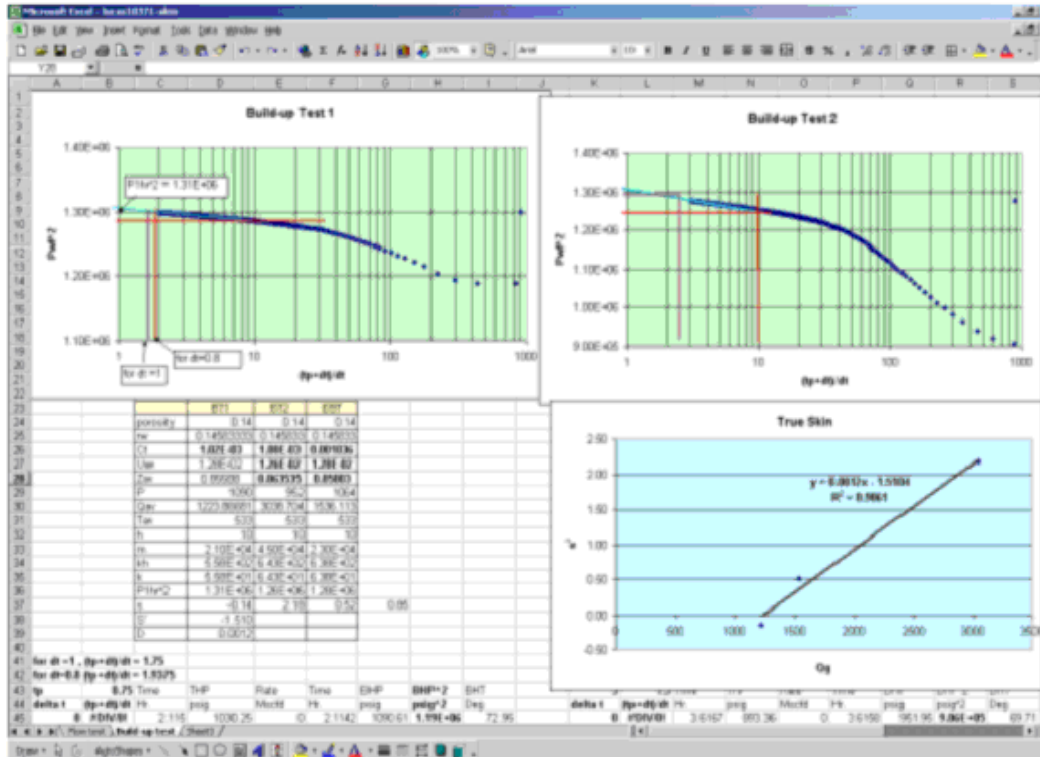
Fig21. Calculation of True skin Build-up test

	BUILD-UP TEST 1	BUILD-UP TEST 2	EXTENDED BUILD-UP TEST
porosity	0.14	0.14	0.14
rw	0.14583333	0.145833	0.145833
Ct	1.02E-03	1.08E-03	0.001036
Uav	1.28E-02	1.26E-02	1.28E-02
Zav	0.85588	0.863535	0.85803
P	1090	952	1064
Qav	1223.86681	3038.704	1536.113
Tav	533	533	533
h	10	10	10
m	2.10E+04	4.50E+04	2.30E+04
kh	5.58E+02	6.43E+02	6.38E+02
k	5.58E+01	6.43E+01	6.38E+01
P1hr^2	1.31E+06	1.26E+06	1.28E+06
s	-0.14	2.18	0.52
S'	-1.510		
D	0.0012		

Table 2. Build-up test results

	DRAW-DOWN	BUILD-UP	AVERAGE	ACTUAL
S'	-0.8202	-1.510	-1.165	-1.17
D	0.0008	0.0012	0.0010	.00126

Table 3. Average Results

Due to large errors corresponding to estimating skin and kh values manually, it was decided that for time being these values will not be entered in the database.

Following are some pictures of the documents to show the different format in which the data was presented in files and microfiche.
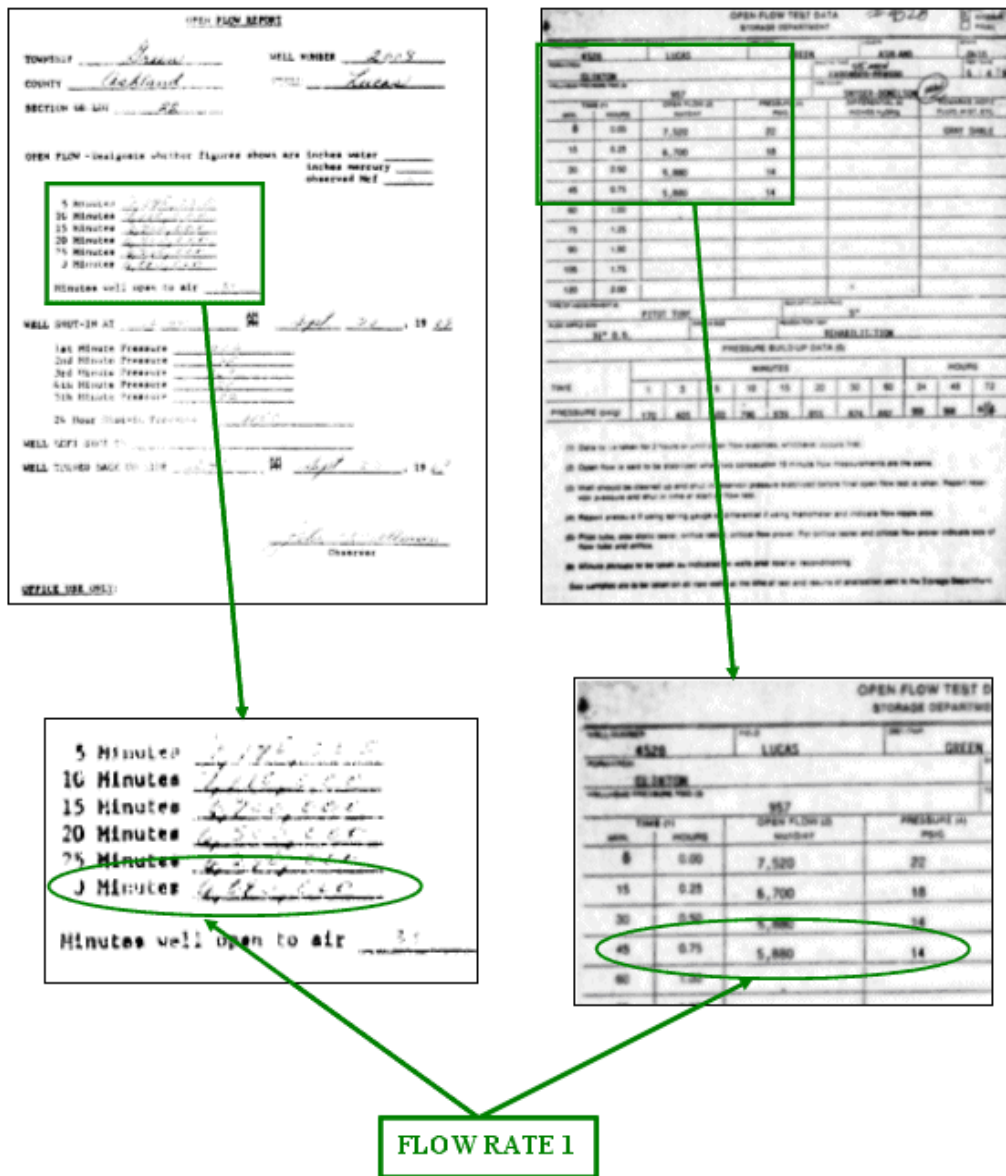
Fig22. Retrieving flow-rate of an open-flow test

Laminar Inertial Turbulent (LIT) Test

Analysis of data from isochronal type test using Laminar Inertial Turbulent (LIT) flow equation will yield considerable data. This method can also be used to find skin of a well from single-point test when the value of permeability of reservoir is known from prior multi-point test. The LIT equation is written as:

$$\Delta \psi = \overline{\psi}_R - \psi_{wf} = a_t q_{sc} + b q_{sc}^2$$

Pressure drop due to laminar flow and well conditions

Pressure drop due to inertial-turbulent flow
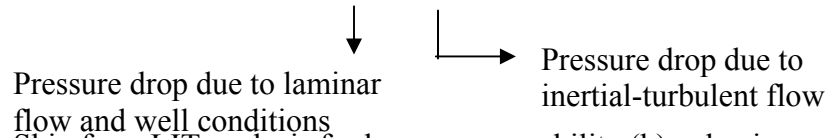
Procedure for calculating Skin from LIT analysis for known permeability (k) value is as shown below:

1. Calculate a_t and b from equations below:

$$a_t = \frac{\sum \frac{\Delta \Psi}{q_{sc}} \sum q_{sc}^2 - \sum q_{sc} \sum \Delta \Psi}{N \sum q_{sc}^2 - \sum q_{sc} \sum q_{sc}}$$

N= Number of data points

$$b = \frac{N \sum \Delta \Psi - \sum q_{sc} \sum \frac{\Delta \Psi}{q_{sc}}}{N \sum q_{sc}^2 - \sum q_{sc} \sum q_{sc}}$$

2. Plot $\left(\Delta \Psi - b q_{sc}^2 \right) vs. q_{sc}$ on a logarithmic scale. The transient data points should form a straight line. If they don't form a straight line, calculate a_t and b again with the data which forms the straight line.

3. Calculate Skin (S) with the formula.

$$S = \frac{1}{0.869} \left[a_t \times 10^6 \frac{kh}{1.632 \times 10^6 T} - \log \left(\frac{kt}{\phi \mu_i c_i r_w^2} \right) + 3.23 \right]$$

Where:
ΔΨ : Delta Pseudo Pressure
k : Effective permeability to gas, md
h : Net pay thickness, ft
t : Flow time, hrs
φ : Porosity, %
u_i : Initial Viscosity, cp
c_i : Initial compressibility, psi-1
T : Temperature of the reservoir, °R
r_w : Well-bore radius, ft
S : Skin, dimensionless

Flow Diagram of Well Test Analysis procedure

Following is the flow diagram of the well test analysis procedure and the type of values that we get from the data.
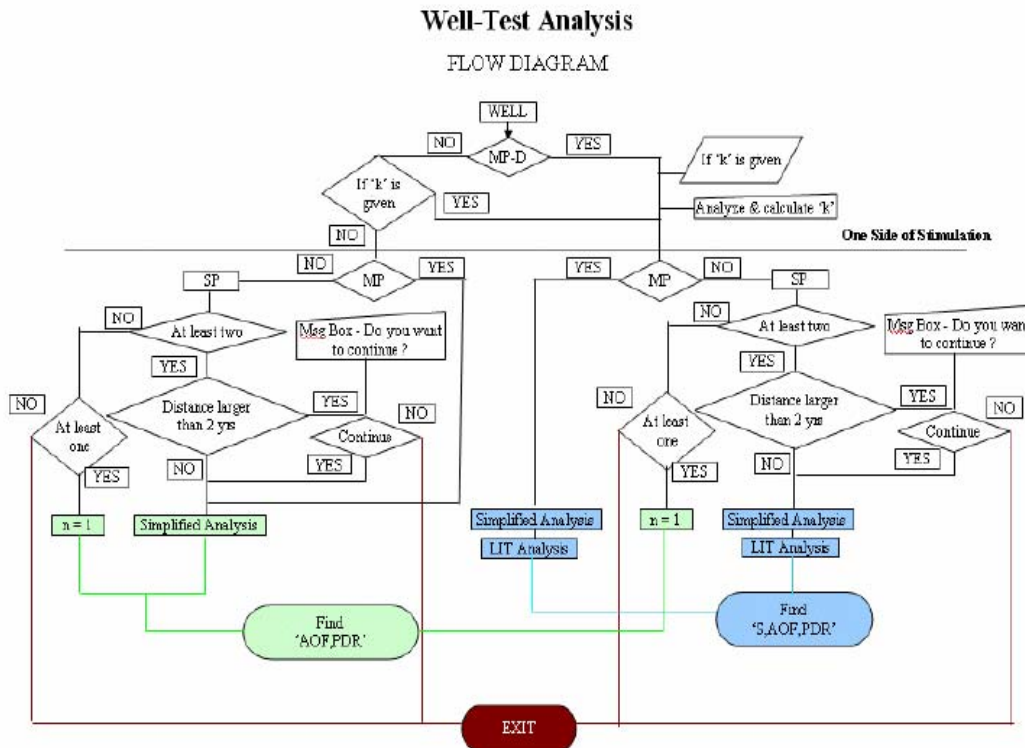
Fig23. Flow Diagram of Well Test Analysis procedure

RESERVIOR CHARACTERISTIC

It includes some reservoir properties. The complete list of the data type retrieved is shown below:

1. API Number
2. Well Radius
3. Reservoir Porosity
4. Reservoir Temperature
5. Gas Specific Gravity
6. Reservoir Thickness

NEURAL NETWORK MODULE

The Neural nets are very powerful in predicting non-linear relationships. As the relationship between skin and stimulation parameters is non-linear and very complicated, thus neural nets are used which are very good at it. With skin values before and after the stimulation calculated and stimulation parameters known, we can now use these valid stimulations to train the Neural Network to use it as a prediction tool. Intelligent Data Evaluation and Artificial Network IDEA® software by Intelligent Solutions Inc. was used to design the neural network. This software is very versatile in making different nets with different training algorithms. Generalized Regression Neural Net (GRNN) was used to train the neural net. The net had 11 inputs and 1 output as skin. The source of data for the neural net is given in Figure 24.

	Inputs	Source
1	Lat	Database
2	Long	Database
3	Sum Fluids	Sum of item 5,6,7,8
4	Prior-kh	Database
5	Water (bbls)	GA
6	Acid (bbls)	GA
7	Gel (bbls)	GA
8	Foam (bbls)	GA
9	N2 (Mcf)	GA
10	Sand Quantity (lbs)	GA
11	After-Test Type 3- Multi-Point 2- Single-Point 1- Open-Flow	GA

Fig24. Neural Network Inputs and their source

Out of the 78 valid stimulations available, the Neural net was trained on 60 data items while 14 were used as calibration data and 4 as verification data. The Neural network showed very good results for all three types of data. The screen shot taken from the IDEA software for training of the neural net is shown in Figure 25.
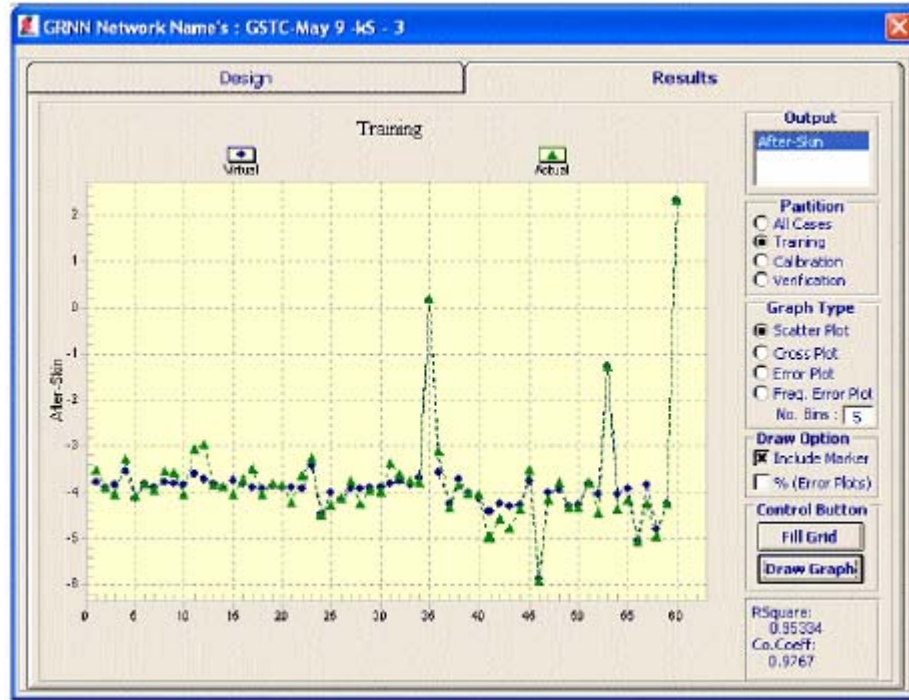
Fig25. Accuracy of training data for the Neural Net

The calibration and verification of the Neural net is shown in Figure 26 and Figure 27 respectively. After the accurate results of this GRNN, the software was updated to use the GRNN generated files to be used in the Genetic algorithm.
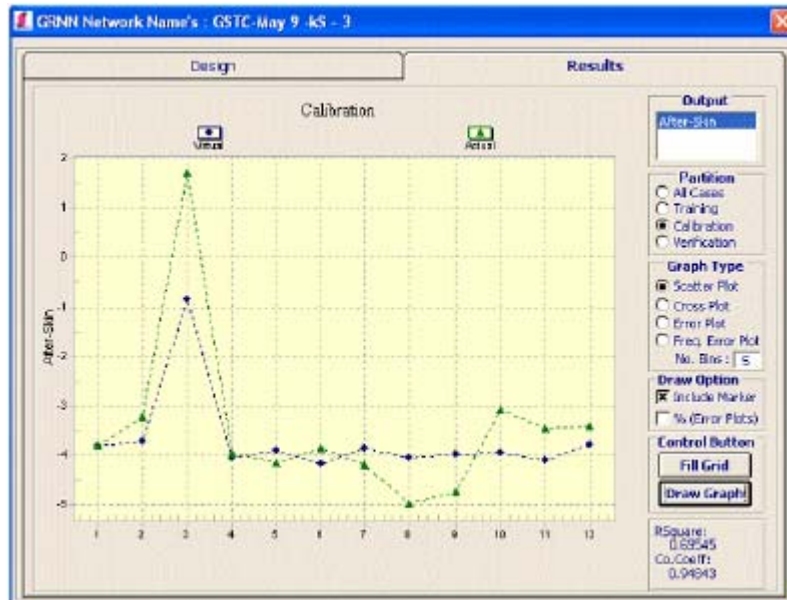
Fig26. Accuracy of calibration data for the Neural net
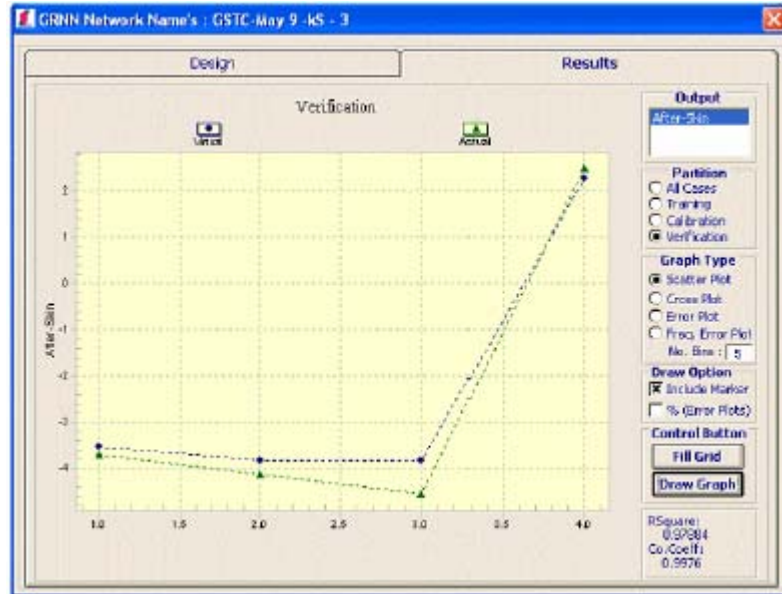
Fig27. Accuracy of verification data for the Neural net

GENETIC OPTIMIZATION MODEL

Genetic Algorithm was written to optimize the stimulation parameters used in the neural net. Out of the 11 input parameters, 7 can be varied to obtain optimum skin. The range of these variables was calculated and accuracy desired was determined to design the length of the chromosome of Genetic Algorithm (GA) that will be required. The calculation is shown in the table 4. for the chromosome length if all the parameters are selected.

	GA Input Parameter	Min	Max	Range	Accuracy Required	Accuracy Size	Range Size	Chromosome Size	Min Byte size	Max Byte size
1	Water (bbls)	0	345	345	1	1	345	9	2^8 =256	2^9=512
2	Acid (bbls)	0	11.9	11.9	0.01	100	1190	11	2^10 =1024	2^11=2048
3	Gel (bbls)	0	535	535	1	1	535	10	2^9=512	2^10=1024
4	Foam (bbls)	0	1.7	1.7	0.01	100	170	8	2^7 =128	2^8=256
5	N2(Mcf)	0	368	368	1	1	368	9	2^8 =256	2^9=512
6	Sand Quantity (lbs)	0	30000	30000	100	0.01	300	9	2^8 =256	2^9=512
7	After Test Type 3- Multi-Point 2- Single-Point 1- Open Flow	1	3	3	1	1	3	2	2^1=2	2^2 =4

Table 4. Calculation to determine the length of chromosome

The length of chromosome came out to be 9 + 11 +10 + 8 + 9 + 9 + 2 = 58.
The GA characteristics that were used are shown in Table 5. These were the best but can be changed as desired to suit other neural nets in the future.

GA CHARACTERISTICS	VALUE
Crossover rate	60 %
Mutation rate	10 %
Population size	500
No of Generations	10
Next Generation criteria	Top 30 % ranked from previous generation
Crossover criteria	Top 25 % has 75 % chance of Crossover

Table 5. CA characteristic

There are two optimization methods made available in this software. One is optimization just based on skin and other, based on both skin and cost. The optimization objective function is calculated using the following formula and GA minimizes this optimization objective function.

$$Optimization\ Objective\ Function = \frac{Skin - Skin_{min}}{Skin_{max} - Skin_{min}} \times Skin\ weight + \frac{Cost - Cost_{min}}{Cost_{max} - Cost_{min}} \times Cost\ weight$$

Software compatibility and variability:

In the software user has been given many options to accommodate the particular situation that he has and data availability if different from the data that we have used to verify the results from this software.
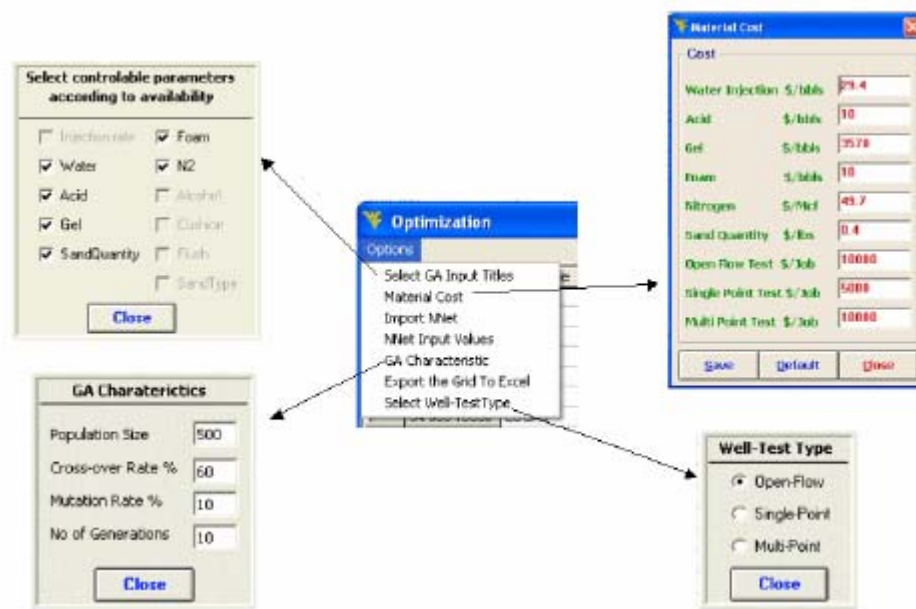
Fig28. Different options in the software that makes it versatile.

One of such variability introduced is that the software can use any other neural net if it is required. The option menu of the optimization screen has the option to import any other neural network. Plus, there is an option to select the available controllable parameters for the GA. For example, if the user does not want to use or does not have foam and nitrogen, then he can unselect them as shown in Figure 3.18. The length of GA will change according to the selection.

As the Neural Net has 'Well-Test Type' as its input, so the 'Select Well-Test Type' menu option gives the user an option to choose the test the user wants the neural net to interpret the well-test. With changing price of hydro-carbons, the petroleum industry is going through fluctuating material cost. The stimulation material prices change frequently and are a factor of demand and supply in that region. The software has the option to change the price of the stimulation material before applying the GA to the available data.

Analysis of raw data vs. refined data:

WELL TEST DATA																													
DATA FIELDS	Total Well-Tests	API Number	Field Name	Well	Test Date	Test Type	Time1	FieldPress1	FlowingPress1	Rate1	Time2	FieldPress2	FlowingPress2	Rate2	Time3	FieldPress3	FlowingPress3	Rate3	Time Extended	Field Pressure Ext	Flowing Pressure Ext	Rate Ext	Kh	Skin	True Skin	Non Darcy Coefficient	n-Value	C-Value	Delta P squared	Peak Day Rate	Absolute Open Flow
INITIIAL DATA AVAILABLE	3223	431	431	431	3223	3223	3223	3223	3223	3223	347	347	347	347	292	292	292	292	345	345	345	345	191	182	163	163	916	916	916	916	916
FINAL DATA AVAILABLE	3365	431	431	431	3365	3365	3365	3365	3365	3365	347	347	347	347	292	292	292	292	345	345	345	345	194	185	166	166	1362	1362	1362	1362	1362

Fig29. Data addition and refinement for well test data

DATABASE & SOFTWARE

SOFTWARE BASICS

This software allows you to add/edit well data in the database and choose the data that you want to look at, for a selected well. It also has a Well Test Analysis tool which calculates the well deliverability parameters like n, C, Peak Day rate & Absolute Open Flow

The database for this software consists of five main tables

1. Well bore Data
2. Completion Data
3. Perforation Data
4. Stimulation Data
5. Well Test Data
6. Reservoir Characteristic Data

The **API number** of a well is the primary key in this database so it must be known before adding a record and cannot be duplicated
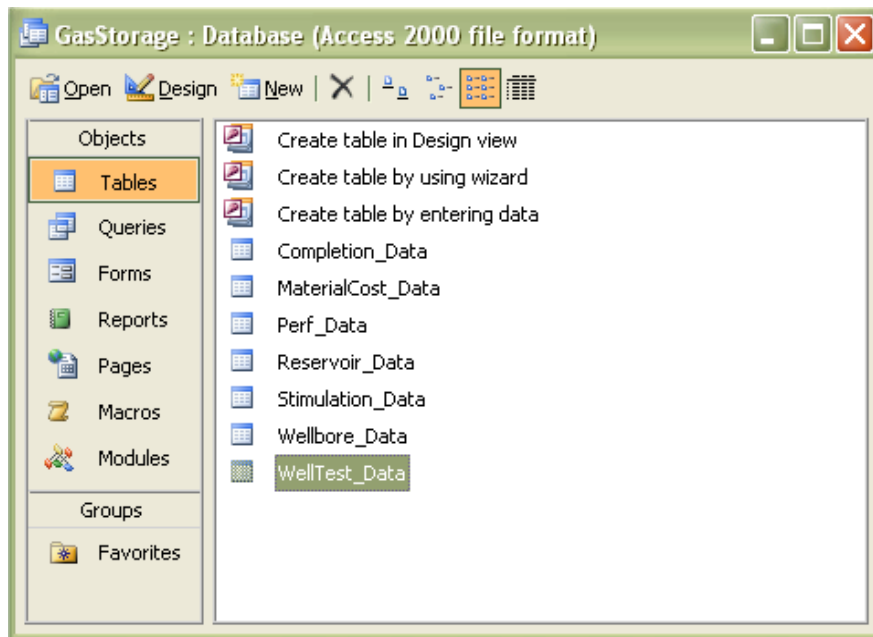
Fig30. Screen shot of database showing different tables

The software starts with the main menu screen with six options
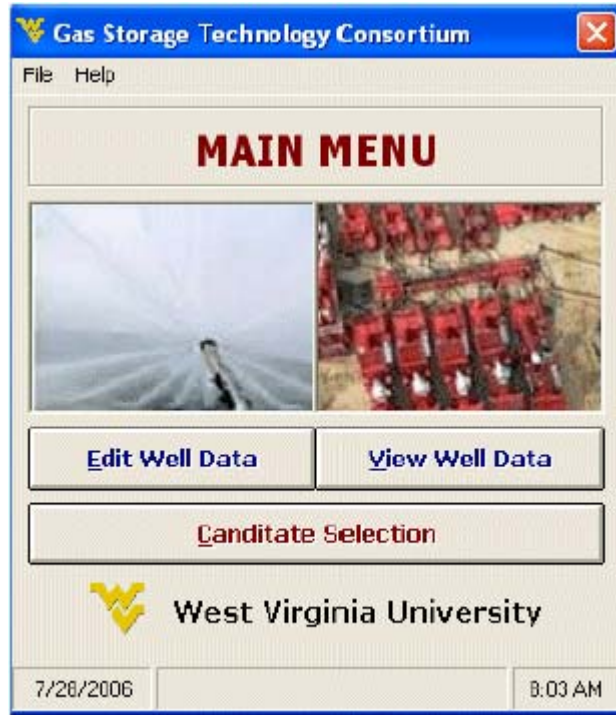
Fig31. Main Screen of software

Complete list of items and sub-items in the above command buttons is shown below:
File
 o Create Template
 o Import Data from filled-out Template
 o Remove all data from database
 o Exit
Help
 o User Manual
 o Formulas
 o About
Edit Well Data
 o Well bore
 o Completion
 o Stimulation
 o Perforation
 o Stimulation
 o Well Test
  • Well Test Analysis Tool
 o Reservoir
 o Find a Well
View Well Data

       o Select State & county
       o Select Wells
       o Selection Options
       o Select Well Data
Candidate Selection

File

The file menu can be accessed from the top left corner of menu bar. It contains four options.
       o   Create Template
       o   Import Data from filled-out Template
       o   Remove all data from database
       o   Exit
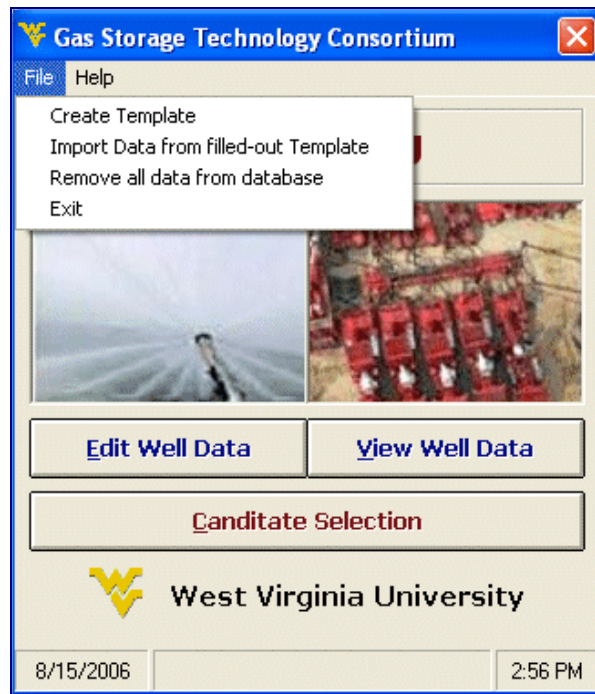
Fig32. File Menu options

Create Template

By executing this option first the user need to select a location in hard drive in order to save Template file.

Once the Template is successfully created in the hard drive, a message will appear indicating the user that the template file has been created.

Following is the screen shot of the Template file showing the Well bore data.
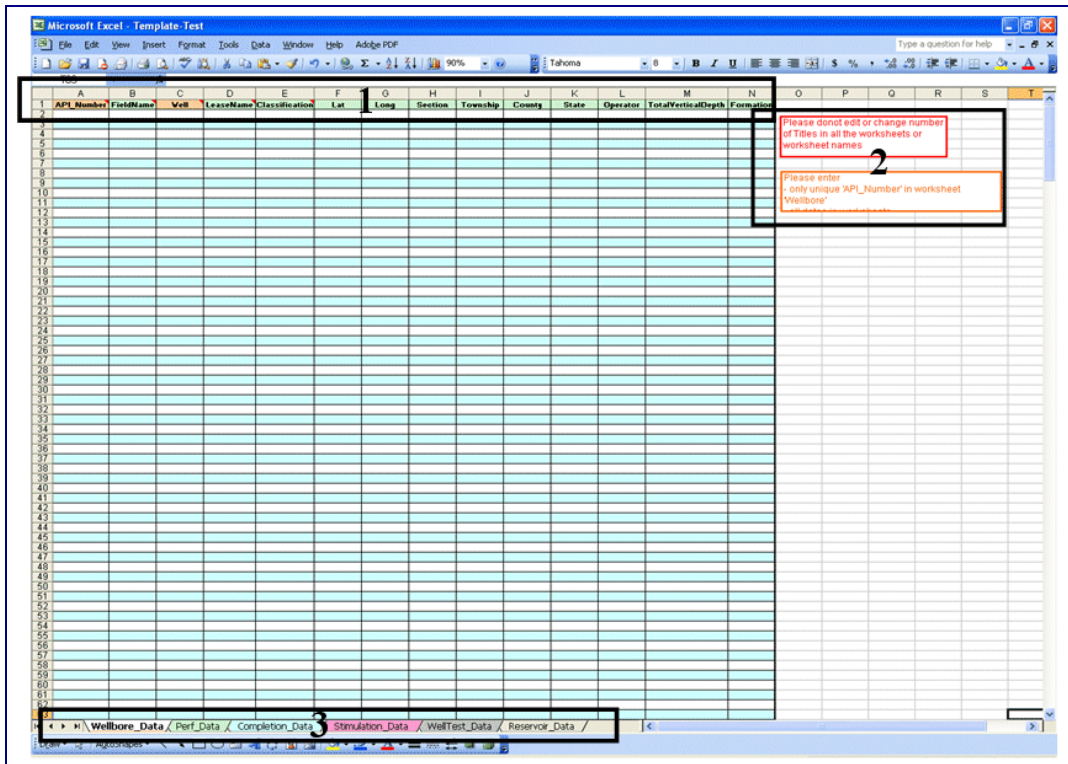
Fig33. Screen shot of Template file

It has six worksheets, each representing the table in the database of the software.
- o Well bore Data
- o Completion Data
- o Stimulation Data
- o Perforation Data
- o Stimulation Data
- o Well Test Data
- o Reservoir Characteristic

1. These are the fields of the table. Each field represents one characteristic of the table and each row is one record. If the user is not clear about any field, then he/she can drag the screen cursor to that field name and the comment will appear like in the picture below where it will give a little explanation, its format and an example so that the user understands what sort of data to enter in each field

Fig34. Comments that shows format of some cells in Template Excel file

2.   This section has two sets of warnings for the user entering data. One is to not edit or change number of Titles in all the worksheets or worksheet names and the other is to add only unique 'API Number' in worksheet 'Well bore Data' and all dates in worksheets where required.

This has been done as the data is retrieved from the template according to some specific format and non presence of any data in elementary field might stop program from using that record. All the elementary fields' background is orange/red while others are in green.

3.   This section shows all the worksheets in the Template file.

Import Data from filled-out Template
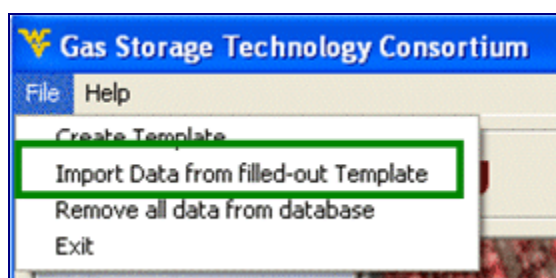
Fig35. Import data from filled-out Template

If this option is selected from the file menu, then the program will ask the user to select the filled Template file from the location. The new data will be appended to the existing data.

Remove all data from database

If the user doesn't want to append the data to the previous database but instead wants to up-load a whole new data, then there is an option in file menu as highlighted in the snapshot below. This option will remove all data in the previous database. After removing the data from previous database, the user can up-load the updated data from the template or enter it in the software.
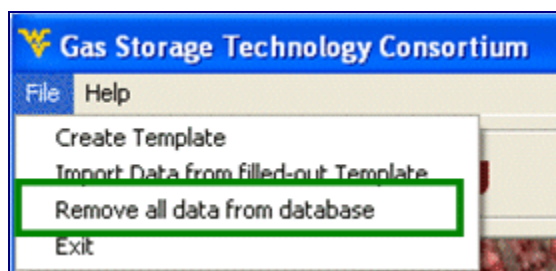
Fig36. Remove all data from database

Exit

The program can be exited by two options. One is to exit by using the file menu and selecting 'Exit' while the other is to select the cross on the top right corner as in normal windows based applications.
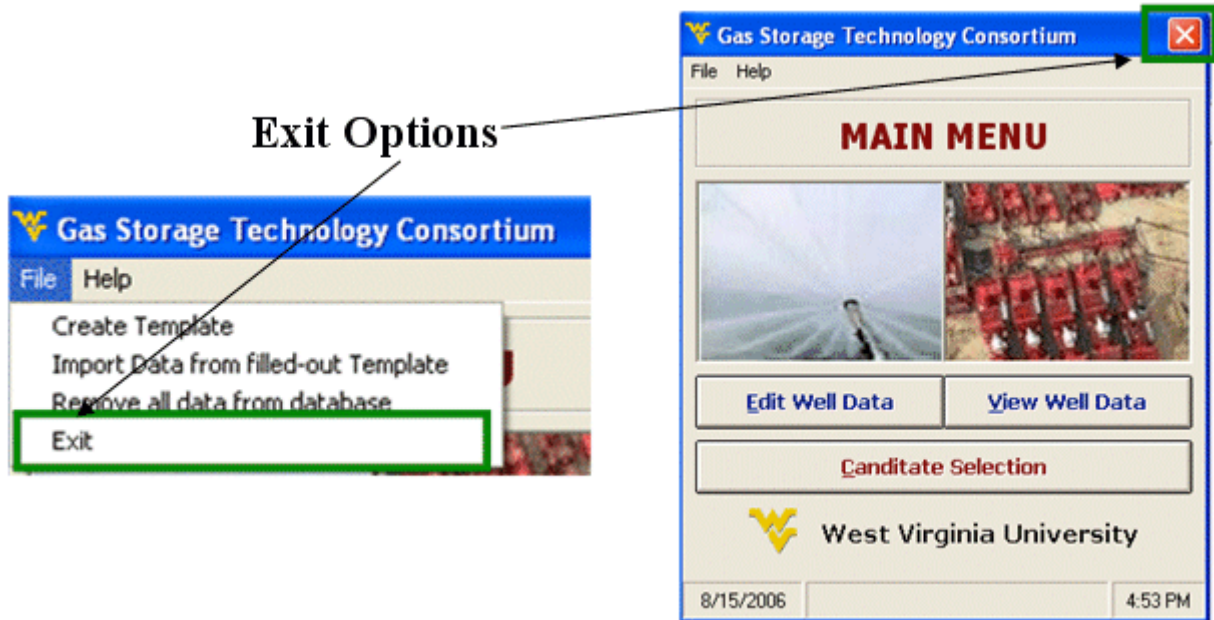
Fig37. Exit form file menu

Help
Another option that can be accessed from the menu bar on top of the main menu screen is the Help menu option.
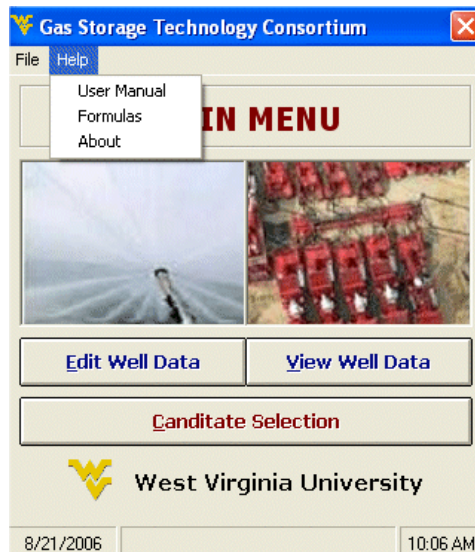
Fig38. Help menu options

It contains three types of information one is the User Manual for this software and second is the Formulas used in this software and third 'About' form which shows the system information and software contributors.
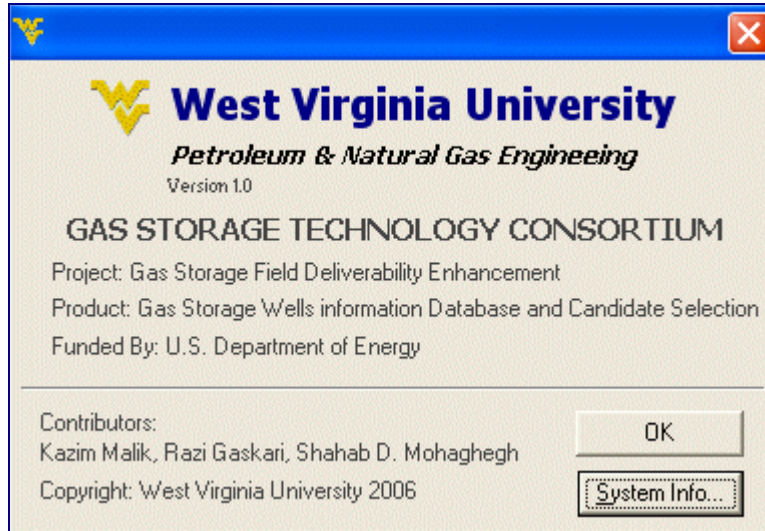
Fig39. "about" screen form help menu

Edit/View Well Data

This screen has all the well data in the form of five tabs (for five database tables) that can be edited / viewed or a Well Test Analysis can be performed in the Well Test tab.
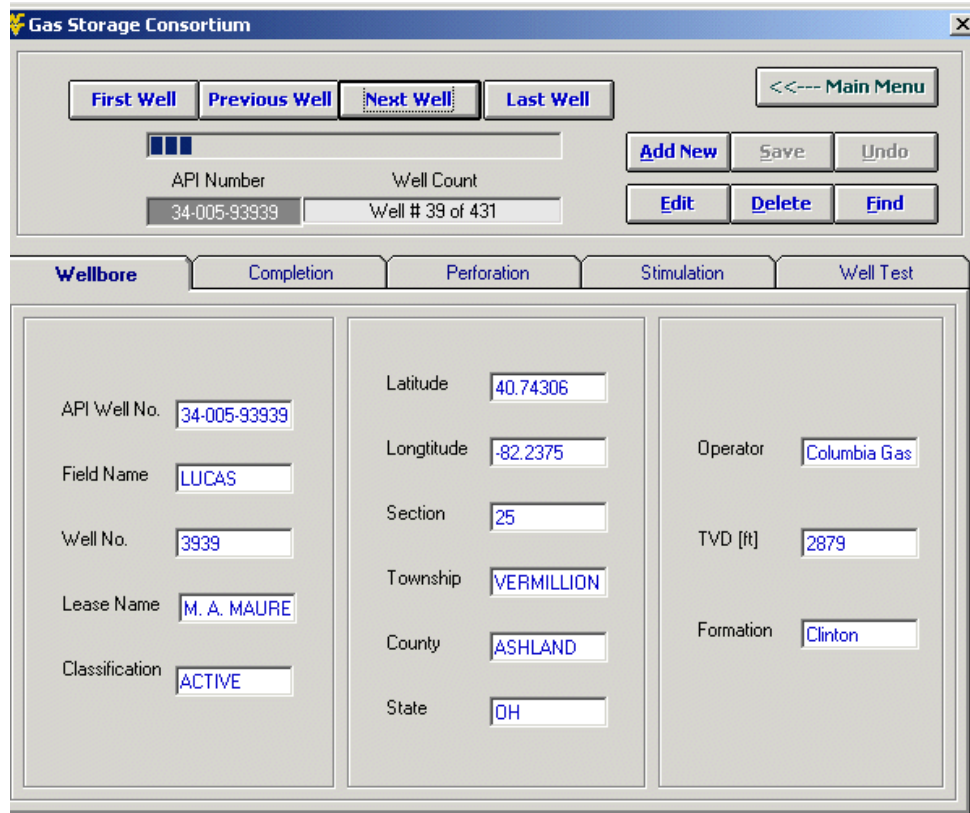
Fig40. Browsing through the well-bore data

To browse between different wells

To move to the first well, previous well, next well & the last well in the record, click on the button assigned to it. The records are sorted in ascending order according to well number

API Number & Well Count

The progress bar shows the relative position of the record and well count shows the current well position in the well bore database out of the total records. The API number of the current well is also displayed

Back to main menu

Takes you back to the very first screen of the program

Editing Tools

These buttons will help you to add a new record, edit or delete it or find a well for which you want the data to be retrieved if you know its API number.

Different Tabs

WELL BORE:

Fig41. Well-bore tab

This tab contains all the data pertaining to the name, location & some main features of the current well.

COMPLETION:

Fig42. Completion tab

This tab contains all the data relating to different completion run in the well.

To browse between different Completions

To move to the first completion, previous completion, next completion & the last completion in the record, click on the button assigned to it. The completions are assorted in ascending order according to date tubing run for current well.

PERFORATION:

Fig43. Perforation tab

To browse between different Perforations

To move to the first perforation, previous perforation, next perforation & the last perforation in the record, click on the button assigned to it. The perforations are sorted in ascending order according to perforation date for current well.

STIMULATION:

Fig44. Stimulation tab

To browse between different Stimulations

To move to the first stimulation, previous stimulation, next stimulation & the last stimulation in the record, click on the button assigned to it. The stimulations are sorted in ascending order according to stimulation date for current well.

WELL TEST:

Fig45. Well-test tab

To browse between different Well Tests

To move to the first well test, previous well test, next well test & the last well test in the record, click on the button assigned to it. The well tests are sorted in ascending order according to well test date for current well.

Adding a new data

One can add a complete new well or just only a new well-bore/completion/perforation/ stimulation/well-test data by following method

Adding a complete new well data

1- Click on the Add New button **Add New** while keeping your well bore tab as active.

Fig46. Adding a complete new Well – well-bore tab

The following messages will pop-up. If you want to add the complete new well-bore data then click No button [No] .

If you don't have the dates of Stimulation, Completion, Perforation & Well-Test data, then click Yes [Yes] and then add them one-by one.

Following screen appears if No is clicked:

Fig47. Adding a complete new Well - completion tab

The background color of text boxes of all tabs including well-bore tab will be yellow indicating that they are ready for entering data.

2- Enter the data in all the tabs. The dates for completion, perforation, stimulation & well test job should be known.

Fig48. Adding a complete new Well – entering data for wellbore

Fig49. Adding a complete new Well – entering data for perforation

Fig50. Adding a complete new Well – entering data for stimulation

Fig51. Adding a complete new Well – entering data for well test

3- Click the Save button **Save**

Result of adding of complete well data

Fig52. Result of adding a complete new well

Warnings – If API Number is not entered

Warnings – If API Number entered is already in the database

Note: The dates for completion, perforation, stimulation & well test should always be
             entered as the output of the software is directly dependent on the chronology of
             events. The format of date is also specified for the user where required. A close
             picture of that format is below:
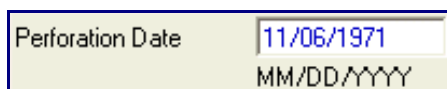
You need to enter API well number only once in the well-bore tab and it will be automatically
copied in the rest of tabs and procedure is the same for editing. The format for entering well API
Number is:
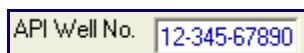
If wrong format or well API number is entered for a new well, then you will be greeted with the
following message

Adding only well-bore/completion/perforation/stimulation/well-test data

1- Click on the Add New button   while keeping that tab active for which
   you want to add the data.

   Only for well-bore tab following message pops up:

Click Yes [Yes] button to add only Well-bore data.

The background color of all text boxes of that tab will be yellow indicating that they are ready for entering data.

2- Enter the data. The dates for completion, perforation, stimulation & well test job should be known.

3- Click the Save button [Save].

Editing data
One can edit complete well or just only a new well-bore/completion/perforation/ stimulation/well-test data by following methods:

Editing a complete well data

1- Click on the Edit button [Edit] while keeping your well bore tab as active.

Following screen pops up:

Select accordingly.

Fig53. Editing well data

Fig54. Editing completion data

The background color of text boxes of all tabs including well-bore tab will be yellow indicating that they are ready for entering data.

2- Enter the data in all the active tabs. The dates for completion, perforation, stimulation & well test job should be known.

3- Click the Save button ![Save].

Editing only completion/perforation/stimulation/well-test data

1- Click on the Edit button [Edit] while keeping that tab active for which you want to
edit the data except well bore tab.

Fig55. Saving completion data

The background color of all text boxes of that tab will be yellow indicating that they are ready
for entering data.

Enter the data. The dates for completion, perforation, stimulation & well test job should be
known.

Click the Save button [Save].

Result of editing only completion data
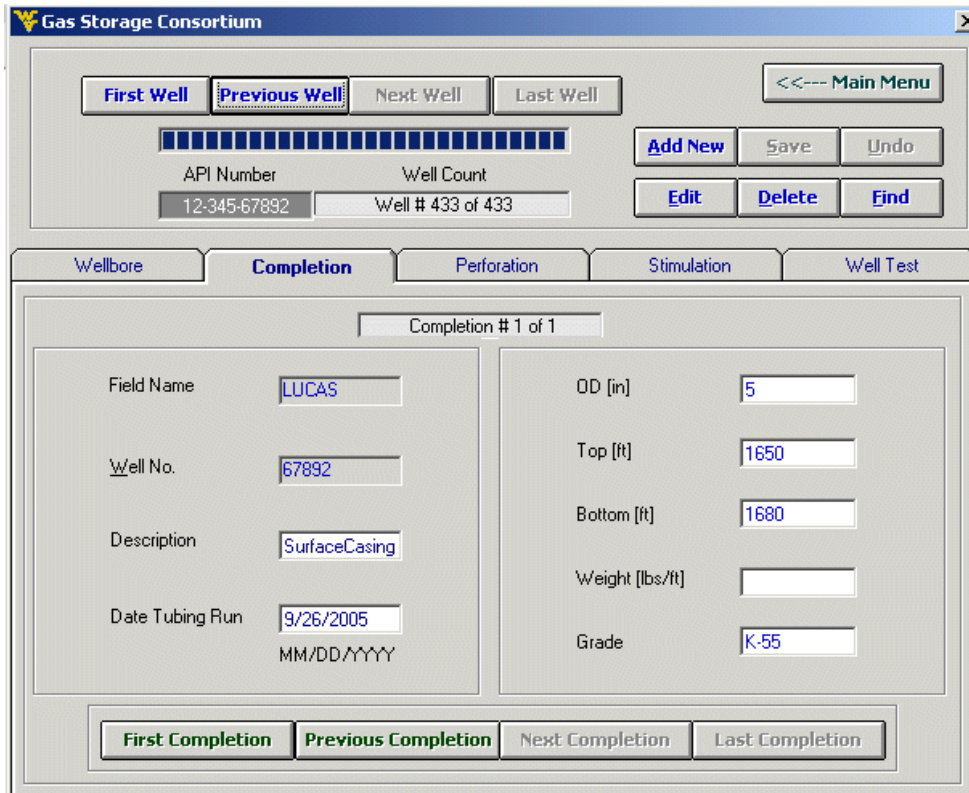
Fig56. Saved completion data

Deleting data

One can delete complete well or just only delete completion/perforation/ stimulation/well-test data by following methods:

Deleting a complete well data

1- Click on Delete button [Delete] while keeping your well bore tab as active

Editing only completion/perforation/ stimulation/well-test data

1- Click on Delete button [Delete] while keeping that tab active of which you want to delete the data except well bore tab.
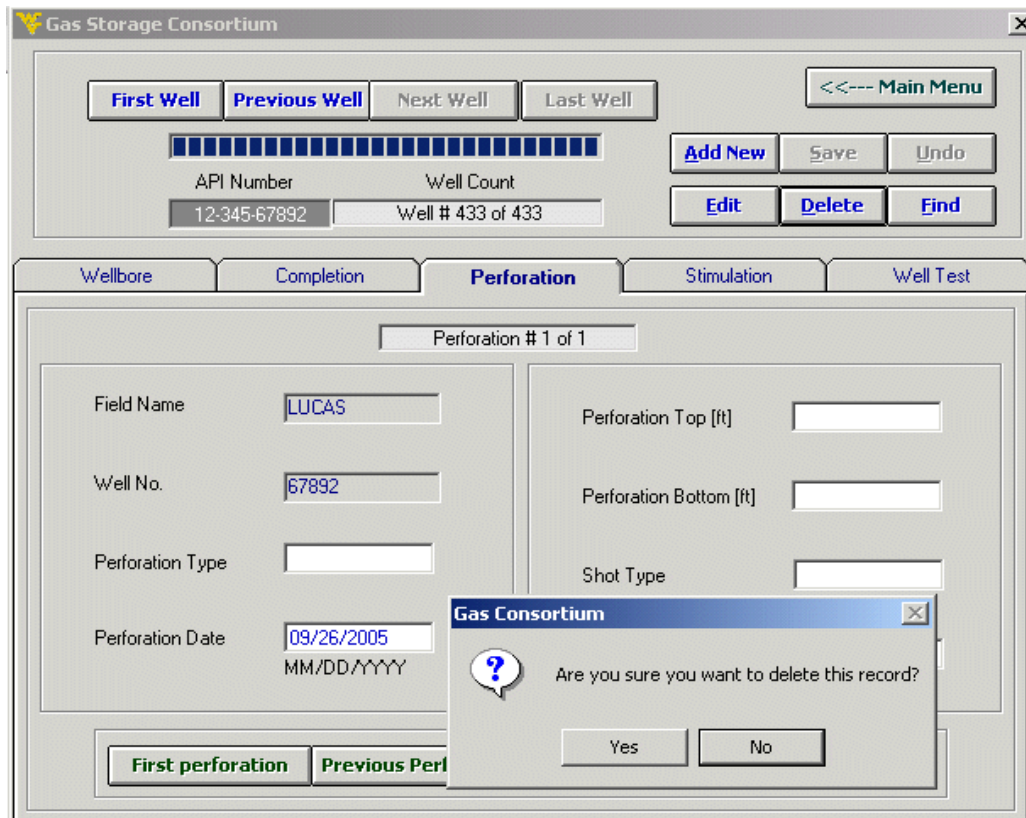
Fig57. Deleting perforation record

You will be greeted with the above message to make sure that delete button is not accidentally pressed.

2- Click on yes [Yes] if you want the selected record to be deleted.

Undo the edit/add operation:

To undo the edit or add operation before they can be saved click undo button ![Undo]

Finding a well

Follow the following procedure to find a well for which you have some idea of its API well number:

Click on Find button ![Find]

The following screen is displayed:
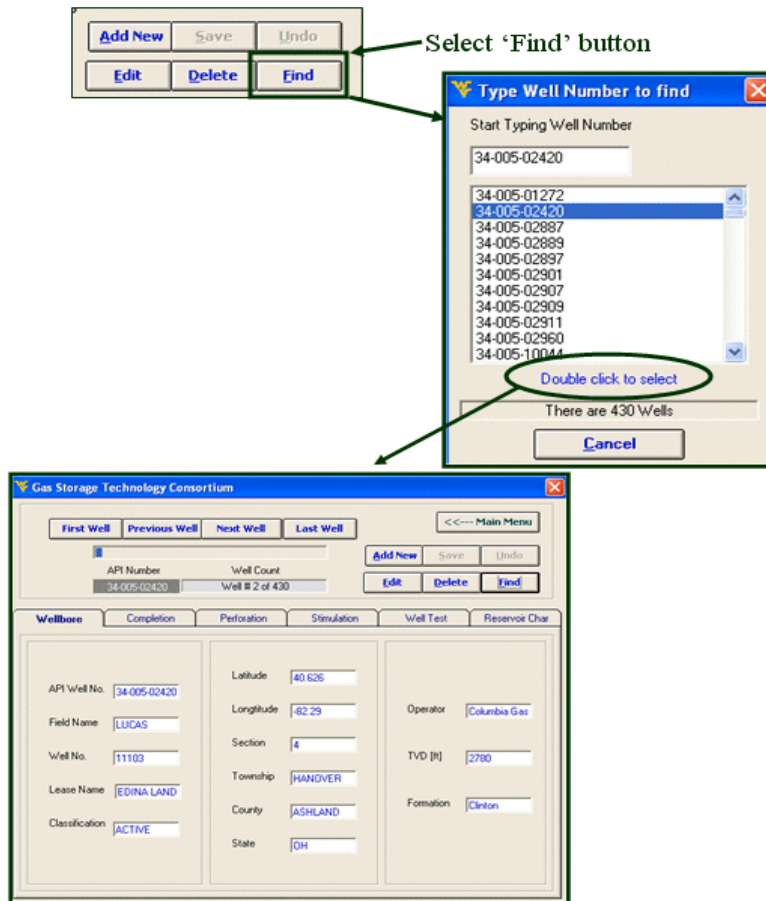
Fig58. Finding a well

WELL TEST ANALYSIS

To perform well test analysis on a well and draw graph of Peak day rate and Absolute open flow, use the option / command buttons below:
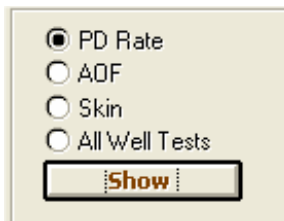
Fig59. Well-test Analysis Option in well-test tab

Peak day, AOF, Skin, and all well test graph

Select *PD rate , AOF, Skin or All well Tests* option button and then click on the **Show** button [Show]. The following screens will appear according to the option selected:
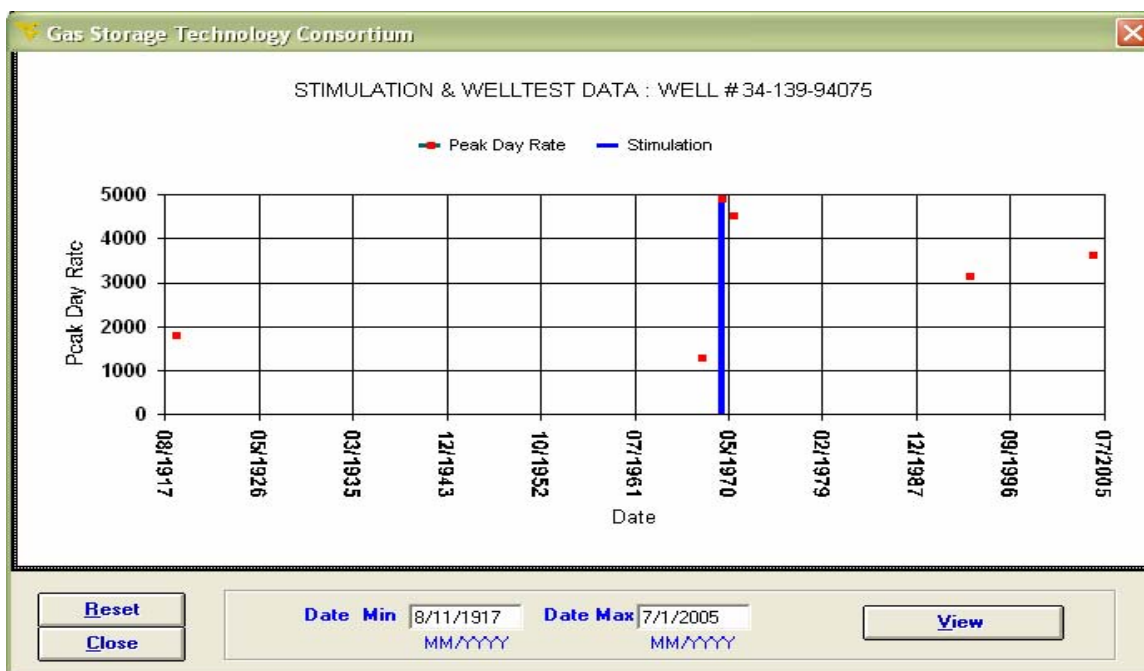
Fig60. Show Chart – Peak Day Rate
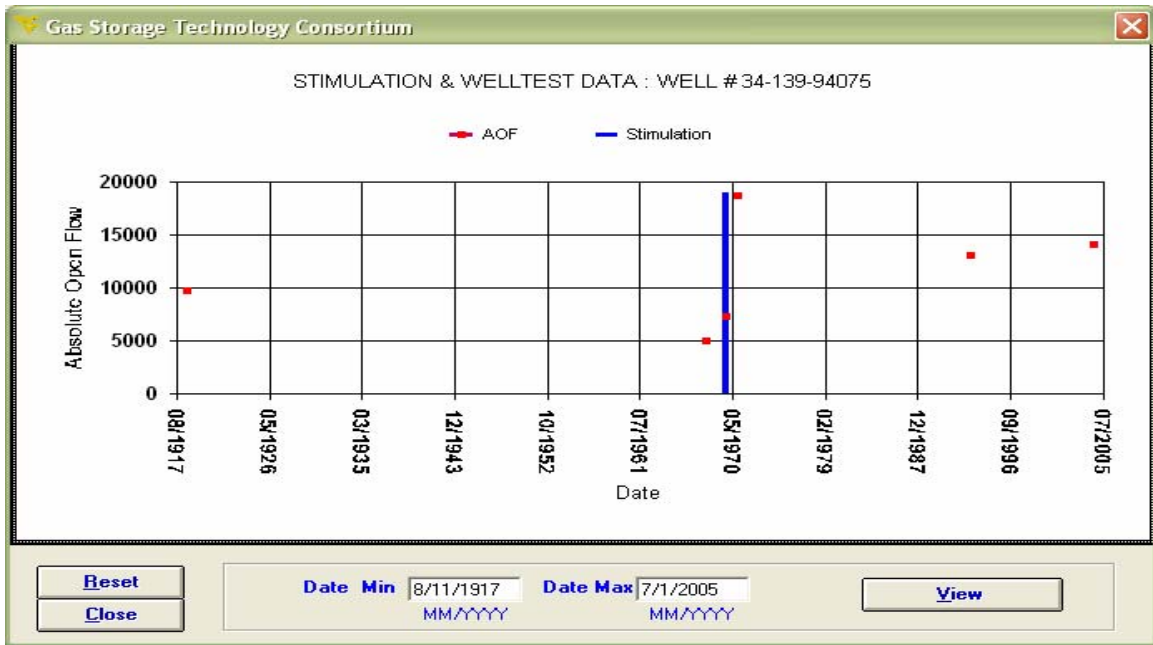
Fig61. Show Chart – Absolute Open Flow
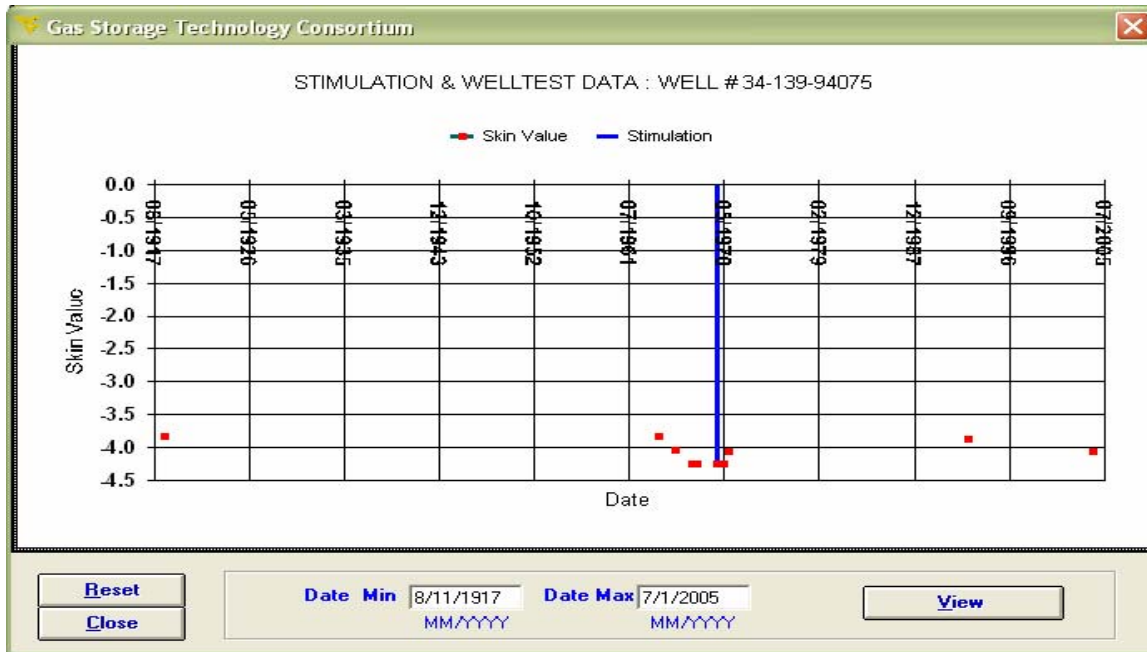
Fig62. Show Chart – Skin
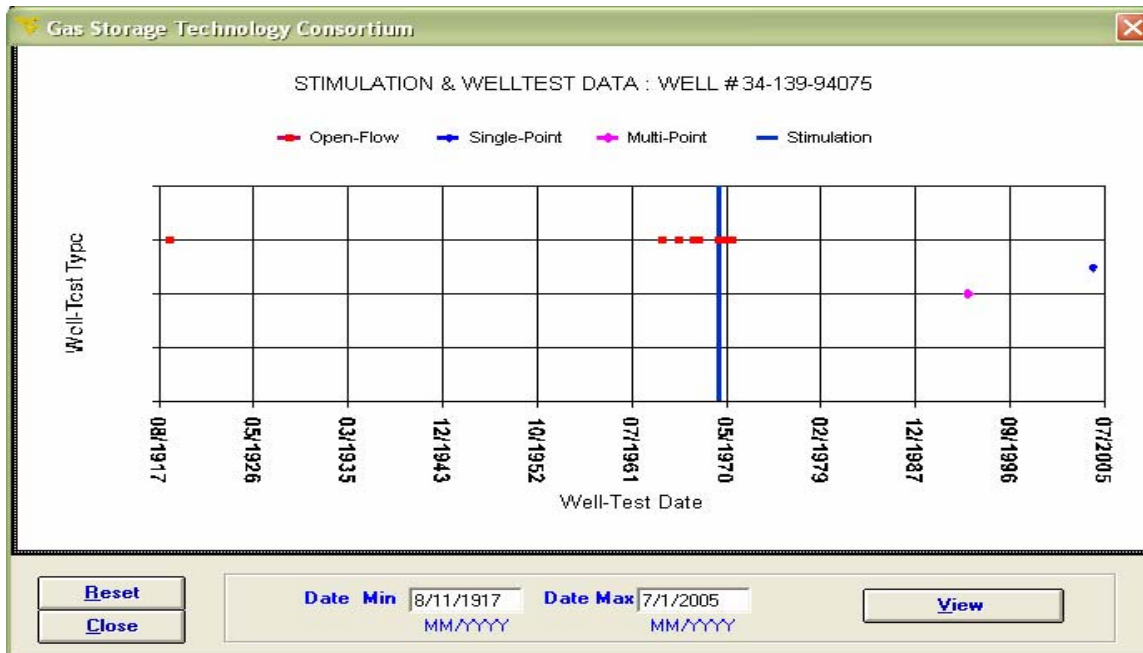
Fig63. Show Chart – All Well Tests

WELL TEST ANALYSIS TOOL

The user can do three types of Well Test Analysis in this software:
1- Simplified Analysis (for calculating n, C, PD rate & AOF)
2- LIT Analysis (for calculating Skin if 'k' is known)
3- Build-up Test Analysis (If Detailed Multi-Point Test data is available)
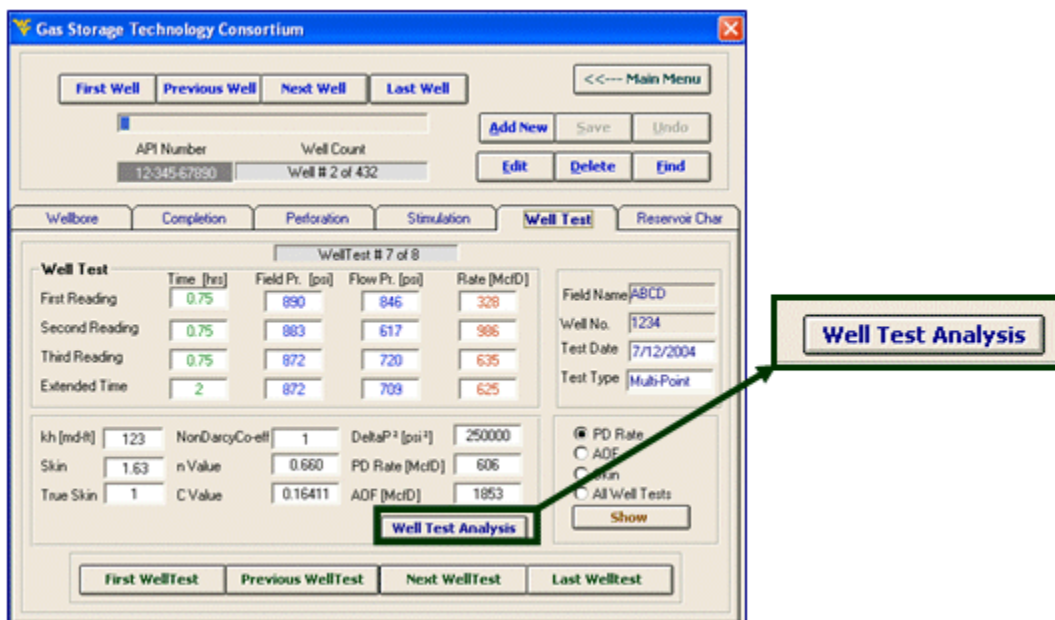
Fig64. Well Test Analysis button

The analysis tools are very similar for Simplified and LIT Analysis except where mentioned. The interface below will appear when you select 'Well Test Analysis' button. It will give you a glimpse of what has happened on the well since it was drilled.
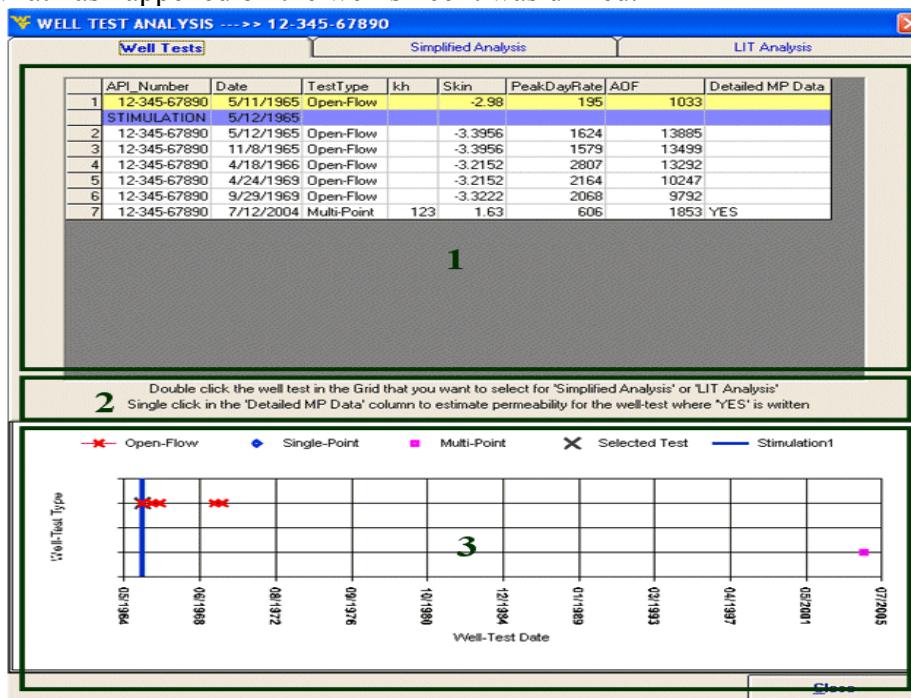
Fig65. Well Test Analysis Module

1. This section contains all the data in a grid form API Number, Date of well test, Test Type, kh value, Skin value, Peak Day rate, Absolute Open Flow and information in 'YES' or 'NO' form if the Detailed Multi-point data (Pressure profile & flow-rate vs.

time) is available for a given test or not. The back color of selected well-test is yellow while of stimulation is purple. The first well-test is selected by default.

2. This section contains instructions as how to select well-tests for analysis. Single click on any well-test will make it the current well-test with background changed to yellow and by double click; it will be selected for Simplified and LIT Analysis. If the Detailed MP Data for a well-test is given, then it can be selected for permeability analysis (build-up test) by single click on the cell where 'YES' is written. This way the build-up test analysis module will show up.

3. This section shows the time of different well tests which are indicated by three types of markers and stimulations on a well which are represented by straight blue vertical lines. The selected well have the similar marker according to its test-type but its color is dark green.

Once any well-test is double clicked, it is selected and added in the list box of simplified and LIT Analysis.

Simplified Analysis:

The screen shot of Simplified Analysis tab is below with Well-test # 2 to # 7 selected for analysis.
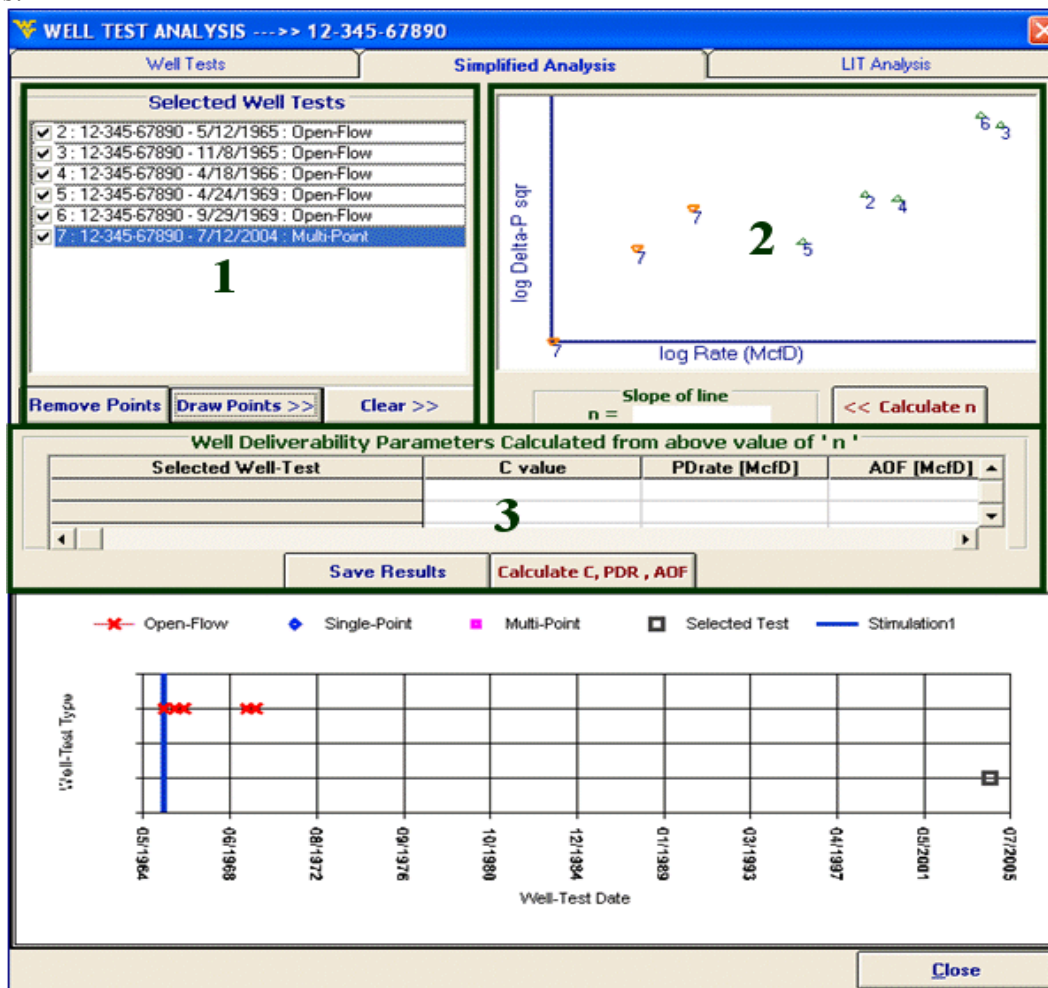
Fig66. Well Test analysis tool

1. This section contains the list box which has the entire well-tests selected for an analysis. Any test now again can be selected or de-selected by using the check-box in front of it. Once the well-tests are selected, then they can be drawn on log-log graph of Flow-rate (McfD) vs. Delta Pressure Square (Delta P sqr) by selecting the 'Draw Points' button. This graph can be cleared by selecting the 'Clear>>' button also if the well-tests drawn need to be changed.

2. Once the data points have been drawn, the user can draw a line in the picture box keeping left mouse button held down like shown below:
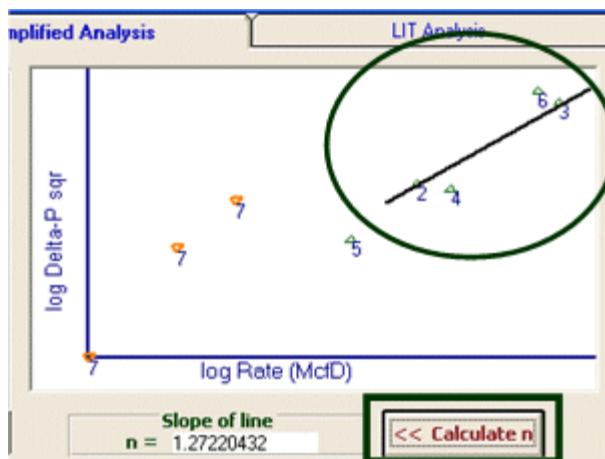
Fig67. Draw a line and calculate the slope

Select 'Calculate n' button to find the slope of the drawn line. The slope will be calculated in front of 'n' text box.

1. Now the user can select the well-tests that he/she intended to the simplified analysis on them. Then a line should draw based on the selected well tests in the picture box (Figure 68). The slop (n) will be calculated by mouse clicking on the "Calculate n" Button. The values of C, Peak Day Rate and Absolute Open Flow will be calculated and shown in the grid as shown in the picture shot on next page. These results can be saved in the database by selecting the 'Save' button.
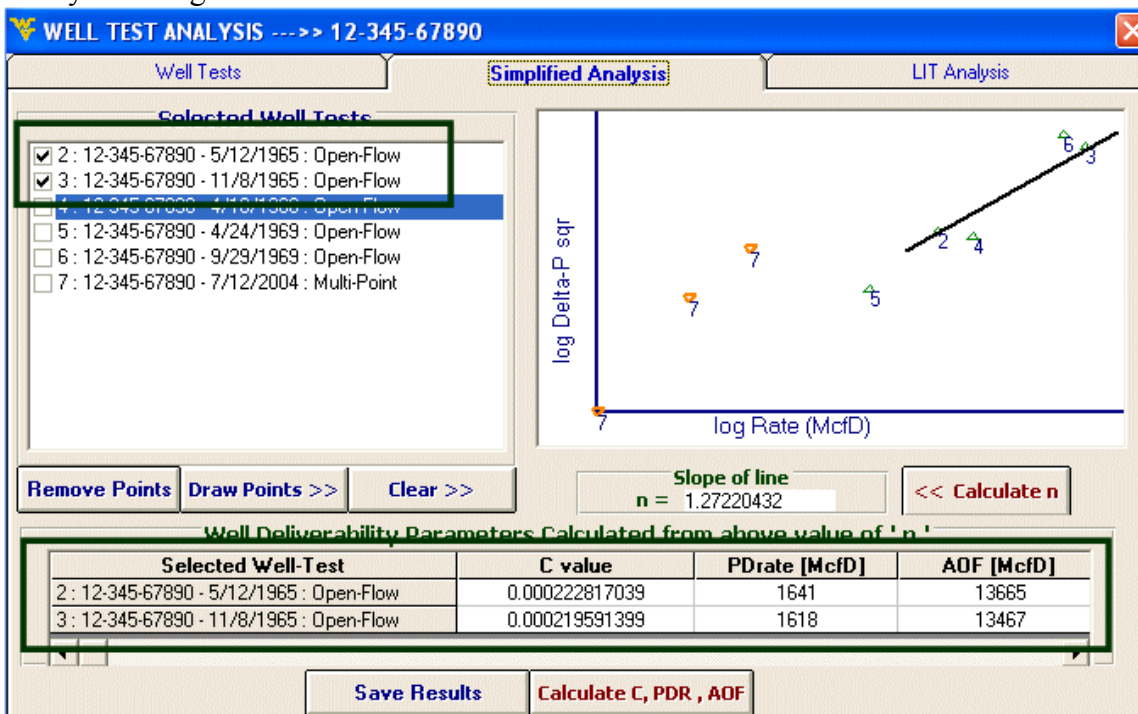
Fig68. Simplified well test analysis tool

Note: If there is only one well-test before or after the stimulation, then the value of *n* can be assumed and written in the textbox in front of label 'n' as shown in the picture below. The value of 'n' cannot be assumed for more than one well at a time so if there is more than one well-test for which the value of 'n' has to be assumed, then they should be selected one by one.
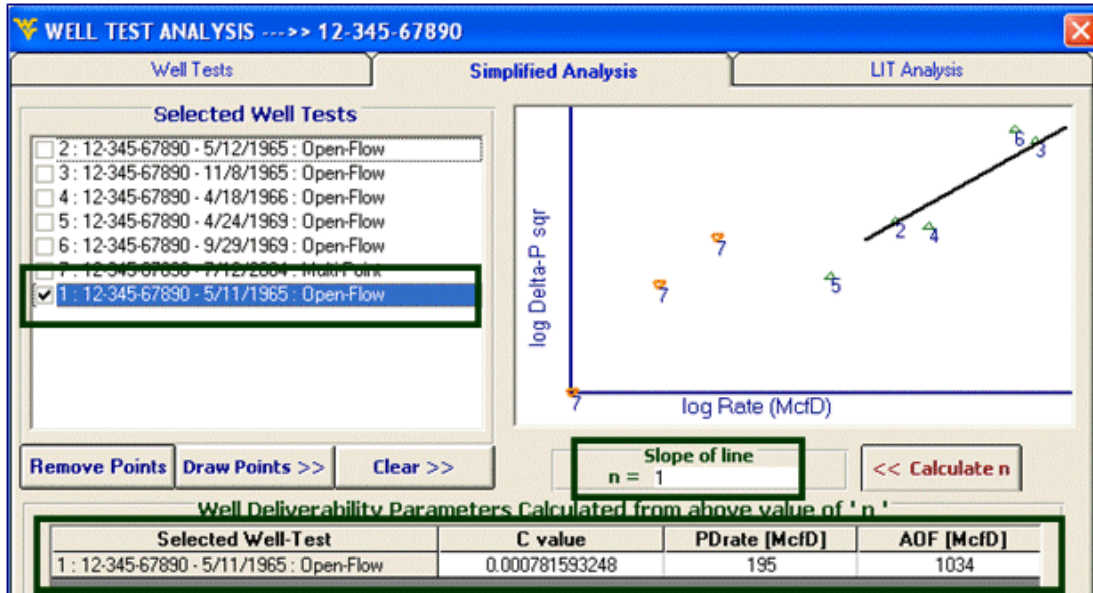
Fig69. Simplified well test with one well test before or after stimulation

Laminar Inertial Turbulent (LIT) test Analysis:

The screen shot of the LIT analysis is below:
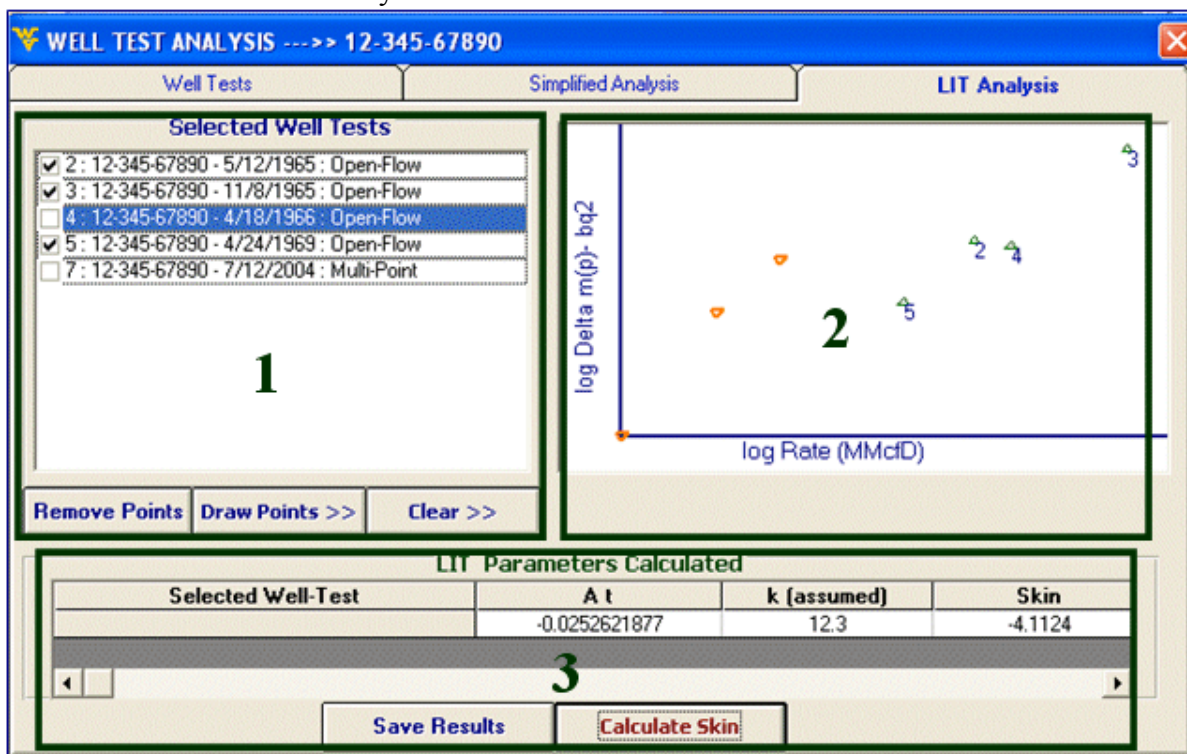
Fig70. LIT well test analysis

1.   This section is the same as for Simplified Analysis.

2.   In this section, the well-test points are drawn on log – log plot of 'Flow rate (MMcfD) vs. Delta pseudo pressure – bq^{2}' . There is no need to draw a slope line in this plot. Instead, the points can be selected by visual inspection that they form a straight line and that they were conducted preferably within 2 years. In the snapshot above, well test points 2,3 and 5 have been selected to calculate Skin.

3.   When the 'Calculate' button is pressed, the program uses the permeability value 'k' from the nearest well-test and calculates skin. The new value of skin can be saved in the database by selecting 'Save Results' button.

Note: Multi-point test points give erroneous calculations if selected with other well-tests as they are recorded one flow after another simultaneously, not like Open Flow and single point tests, which are recorded once a year.

If the selected well-tests are not within 2 years, then the following message will appear giving the user choice either to select other well-tests or continue with the well-tests selected.
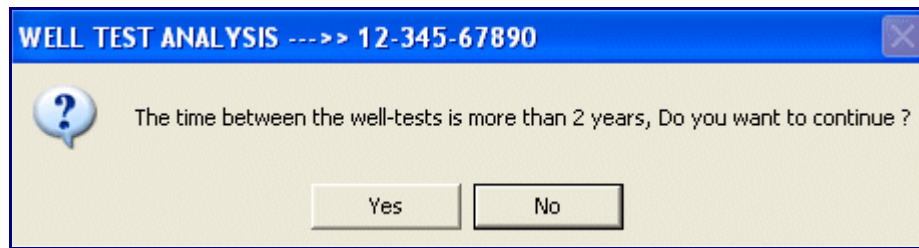
Build-up test Analysis:

If any Multi-point well test has a detailed data (pressure and flow-rate profile vs. time), then the 'Detailed MP Data' column in front of that test will show 'YES'. It means that the data for this well-test can be analyzed to estimate a value of permeability.
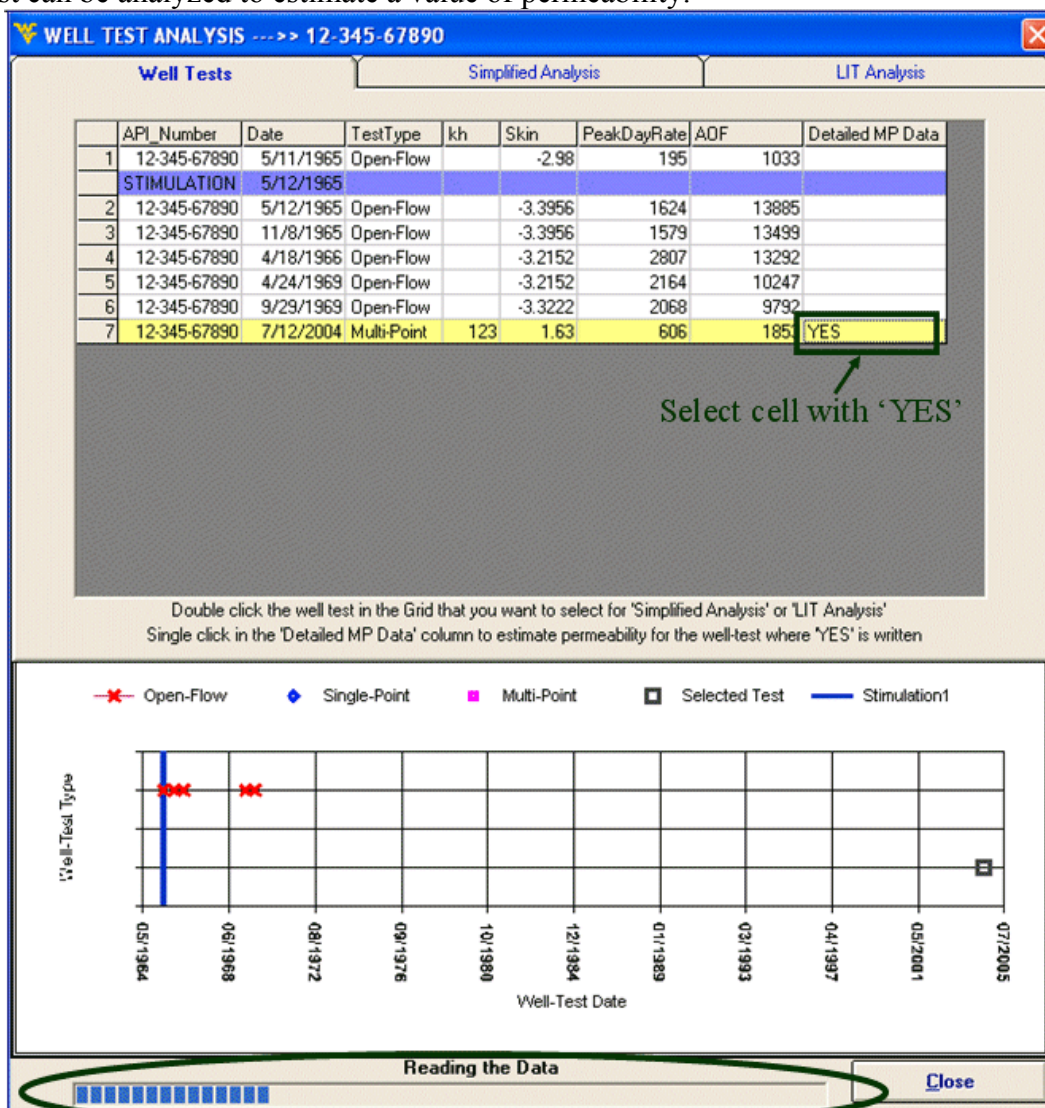
Fig71. Multi point well test analysis

If the cell with value 'YES' is selected the software will read the data from the excel file and progress bar will become visible like in the picture shot above showing that the data is being read.

After the complete data has been read by the software, the following screen will appear showing the pressure profile of the well-test.
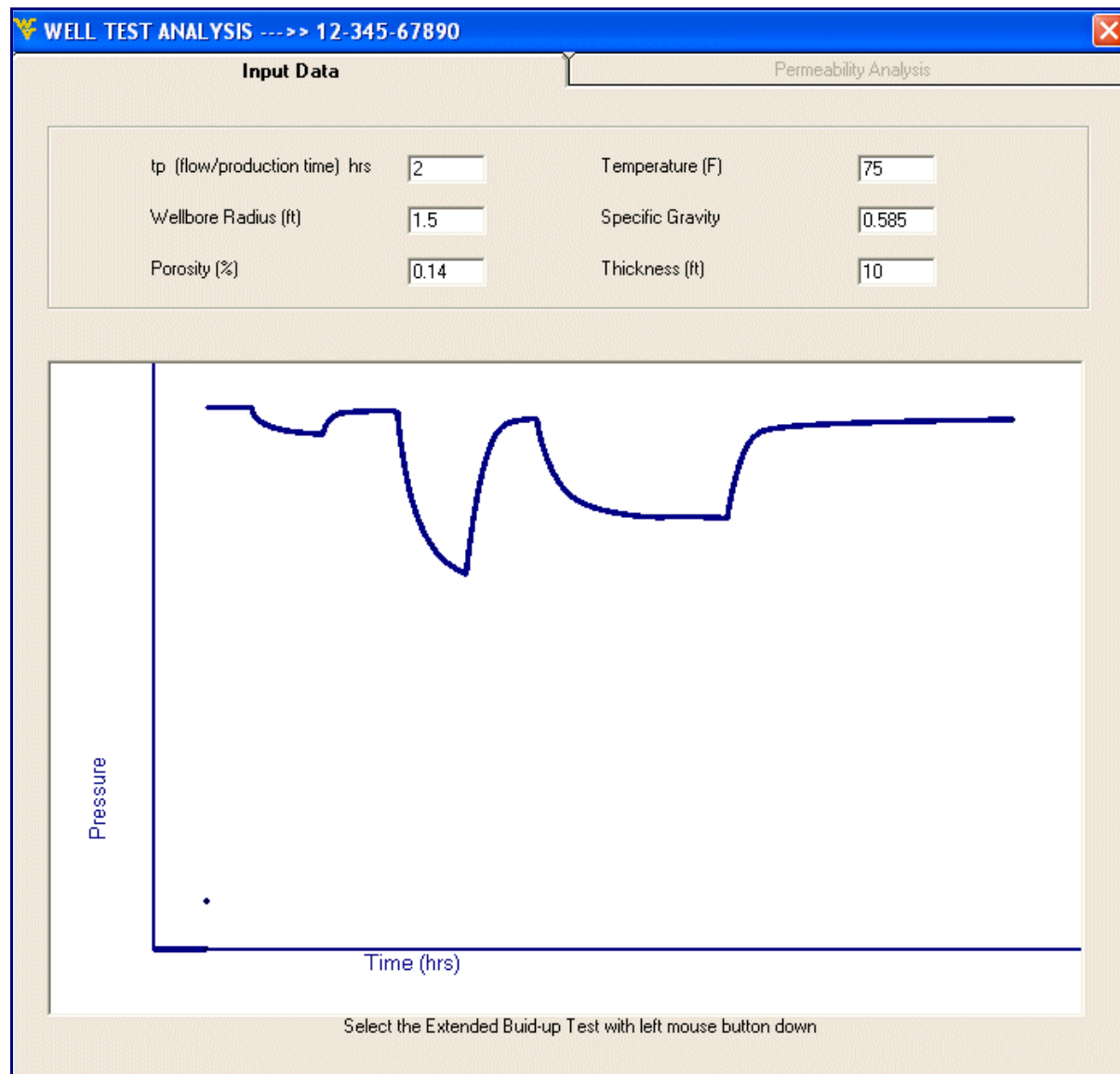
Fig72. Well extended pressure profile

All the Input data is retrieved from the database and if it is not found, then default values are inserted. The value 'tp (flow/production time' is 2 hrs by default but can be changed by the user. The Extended build-up test for 2 or more hours should be selected by keeping the left mouse button down. The green lines will indicate portion of build-up test selected.
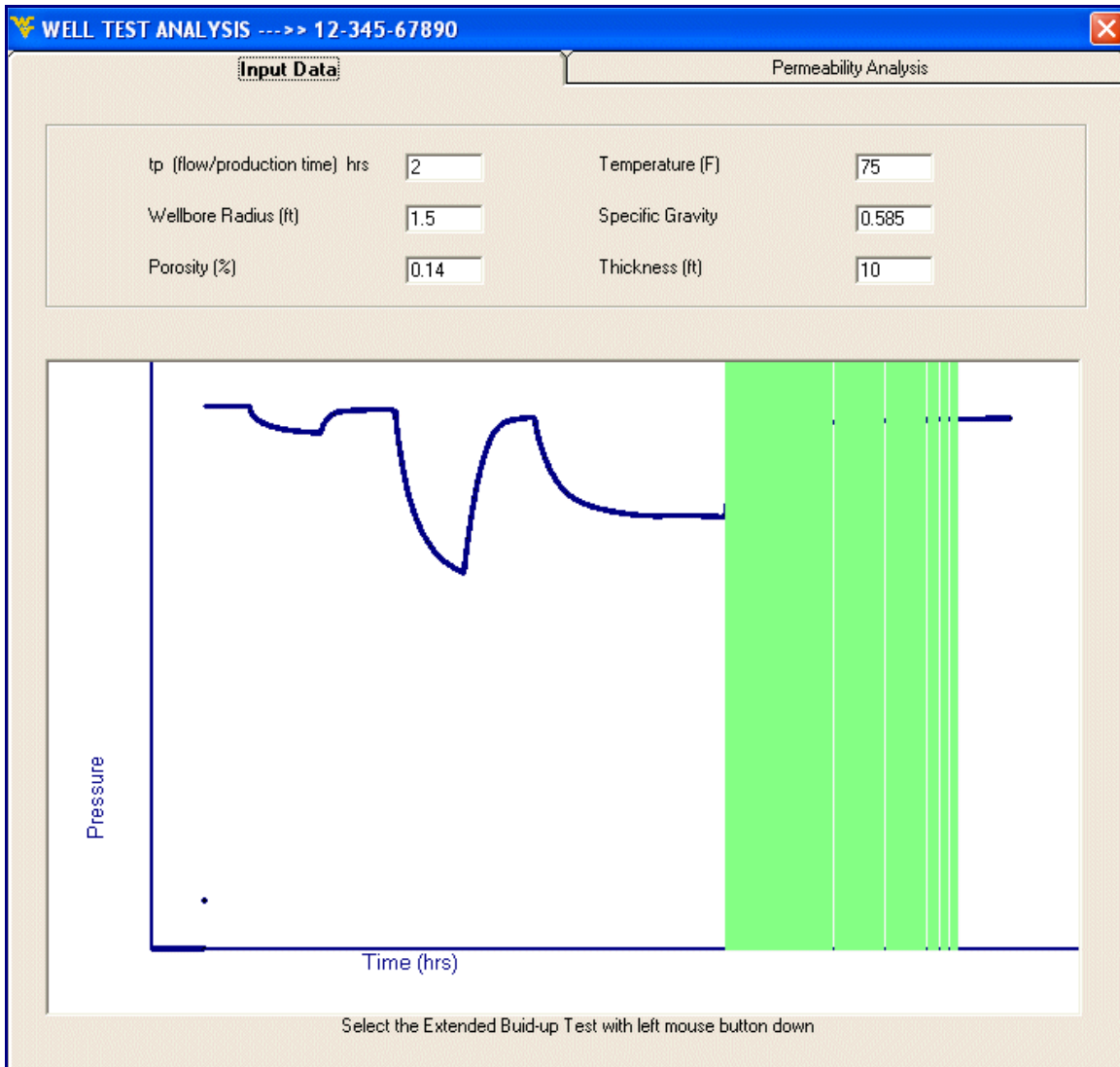
Fig73. Selecting the build-up section from pressure profile

If by mistake draw-down data is selected, then the following message will appear informing the user to select build-up data again.
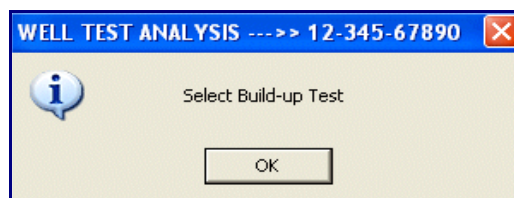
After the portion of build-up data has been correctly selected, the permeability analysis tab will show following graphs. The first one is the log-log diagnostic plot between 'Del Pressure' and 'Del Time'. The user should select the first point which does not fall on the unit slope line drawn by holding the left mouse button down. The initial pressure 'Pi' and flow rate text box values will be selected from the build-up portion of the extended well-test selected. The graphs will be drawn again with a green line drawn on the Horner plot indicating The End of Well-Bore Storage (tewbs).
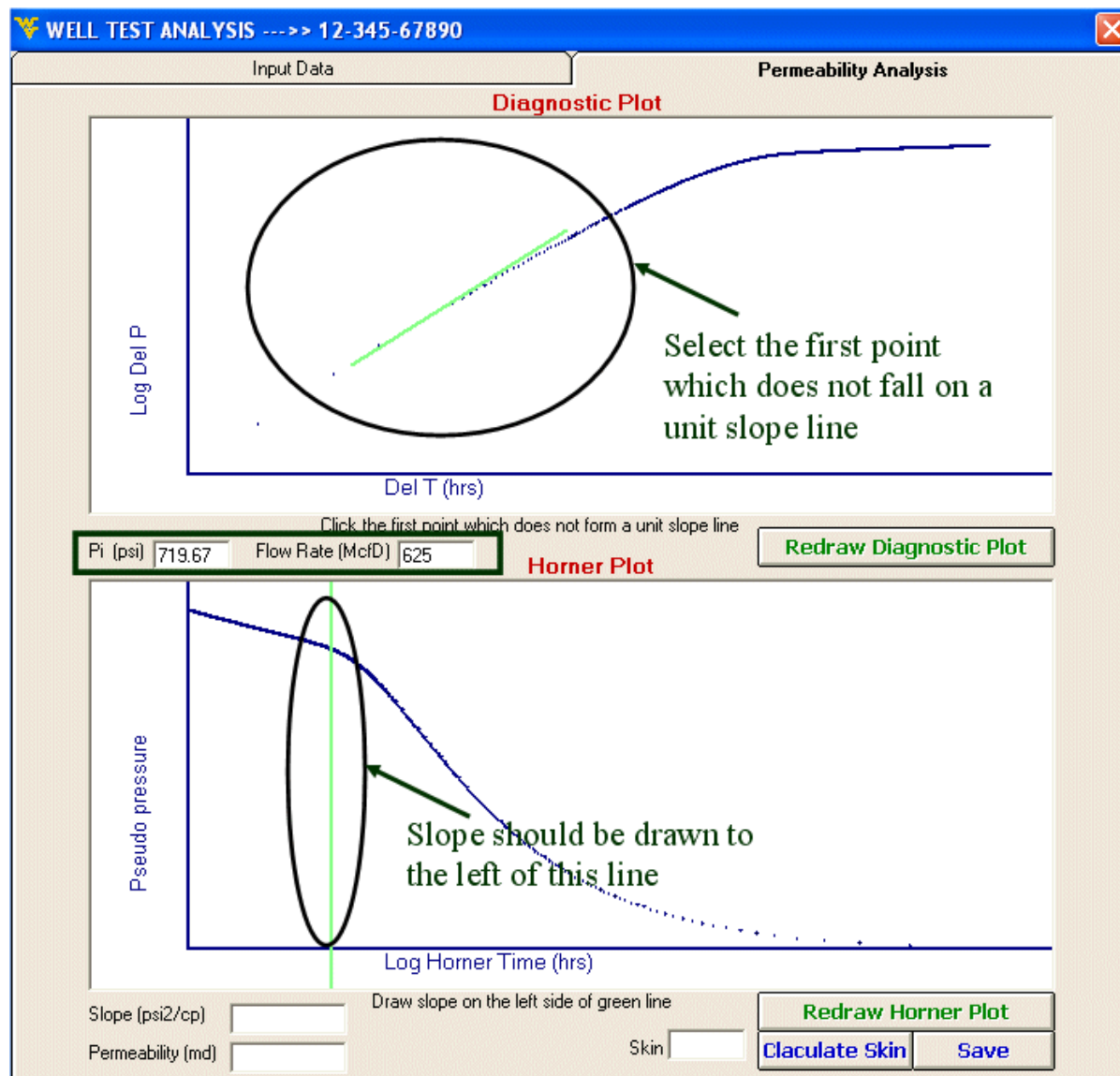
Fig74. Diagnostic plot analysis

The slope should be drawn on the Horner plot on the left side of the end of well bore storage line shown in green on Horner plot.
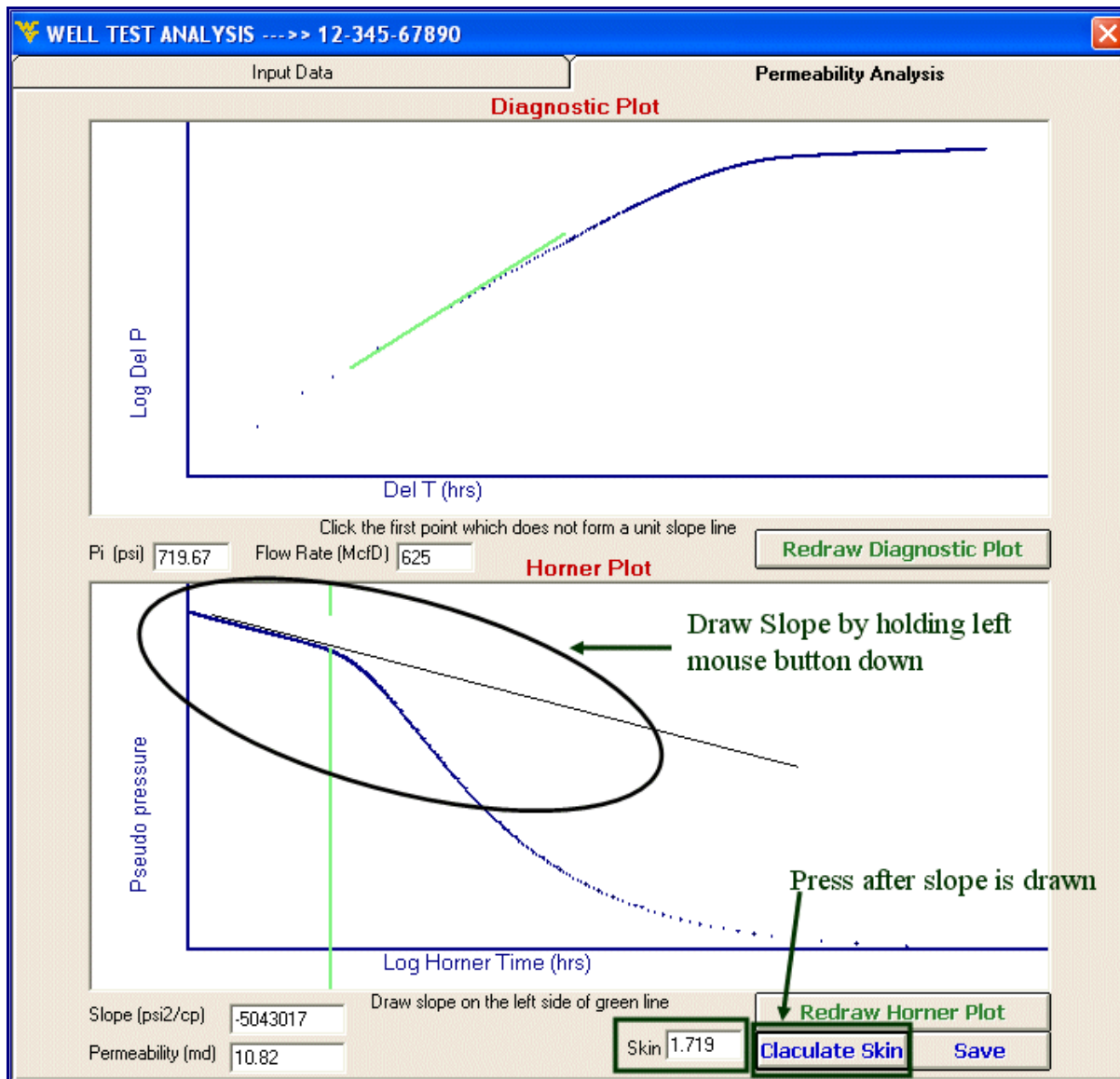
Fig75. Calculating skin from Hornet plot

After the slope is drawn, the user can select 'Calculate Skin' button to find the skin of the well. The respective graphs can be redrawn any time by selecting the 'Redraw Diagnostic Plot' or 'Redraw Horner Plot'.
The value of permeability and Skin can be saved in the database by selecting 'Save' button.

SELECT WELL DATA

In this form the user can choose to select the data of the wells that he wants to look at. Following are a few ways he can choose the data:

Selecting a well by State/County:

The user selects the state first and then the county. All the wells will be selected for that county in the selected wells list box:

Fig76. Selecting Ohio County

Selecting wells by stimulation year:

The user can select the option button for stimulated year and input the year values. If Select Wells button [Select Wells] is clicked, then all the wells that have been stimulated between these years will be shown in the selected wells list box
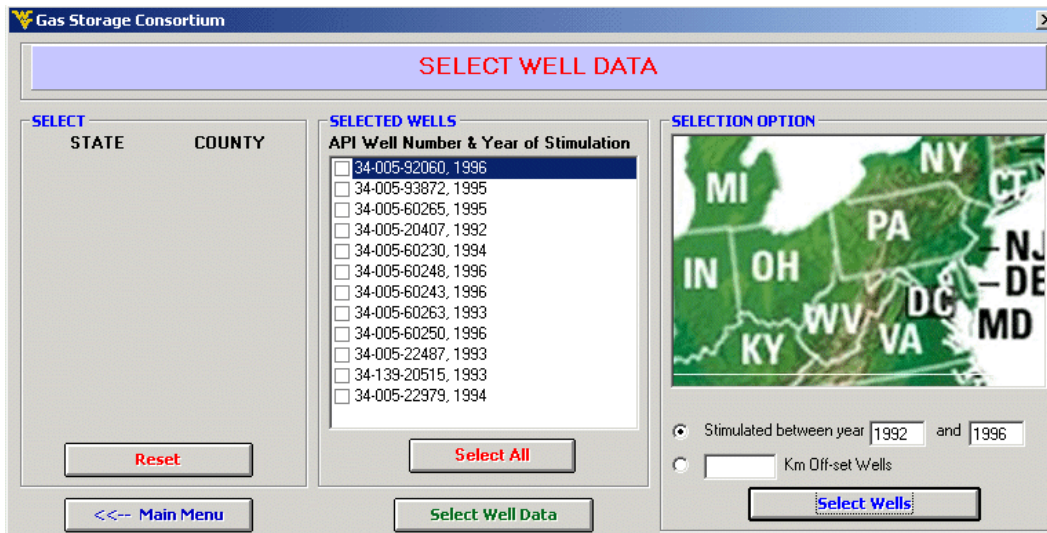
Fig77. Selecting wells according to stimulation year

Selecting offsets wells form a well:

The user selects the offset option and the well near which he wants to find the off-set wells, and then enters the distance of off-set in kilometers. If Select Wells button is clicked, then all the wells that are off-set of the selected well will be shown in the selected wells list box
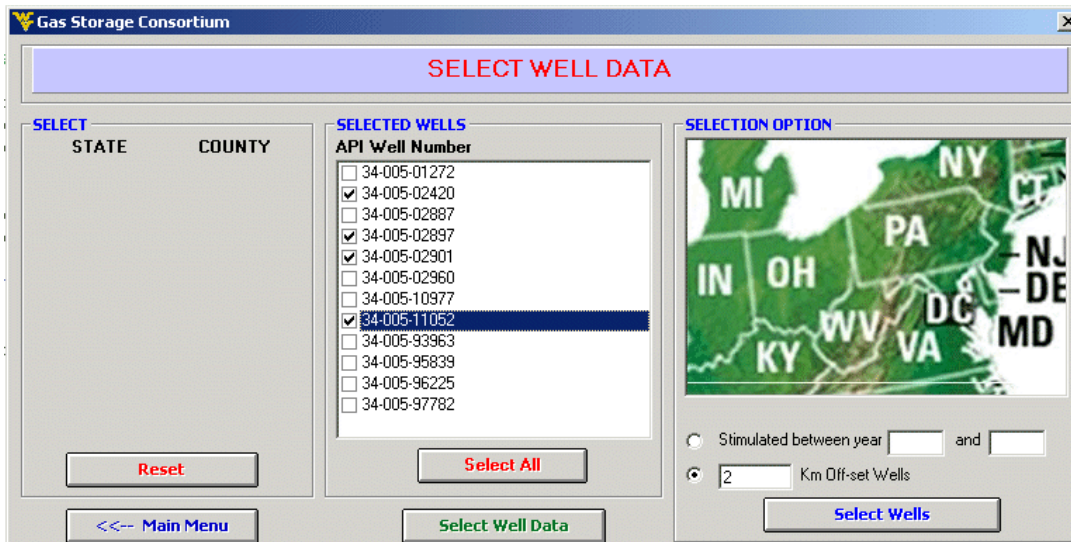
Fig78. Offset wells

Display the selected wells data:

When the wells for which the user want the data to be retrieved have been selected, click the Select Well Data button [Select Well Data] and select the parameters.

Fig79. Selecting Well Parameters

Click Show Well Data [Show Well Data] to retrieve the data.

Fig80. Result of the wells & parameters selected

CANDIDATE SELECTION

This module will appear on selecting the 'Candidate Selection' button from Main Menu.
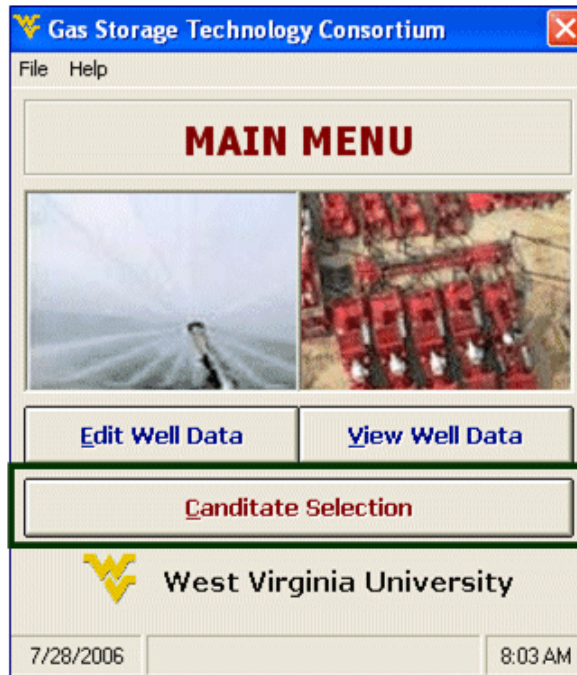
Fig81. Start Candidate Selection form main screen

For intelligent candidate selection of wells, it is very important that only valid data is given to the Neural Network (NN) for training. Valid data is one which will not degrade the performance of the NN and is useful in NN training.
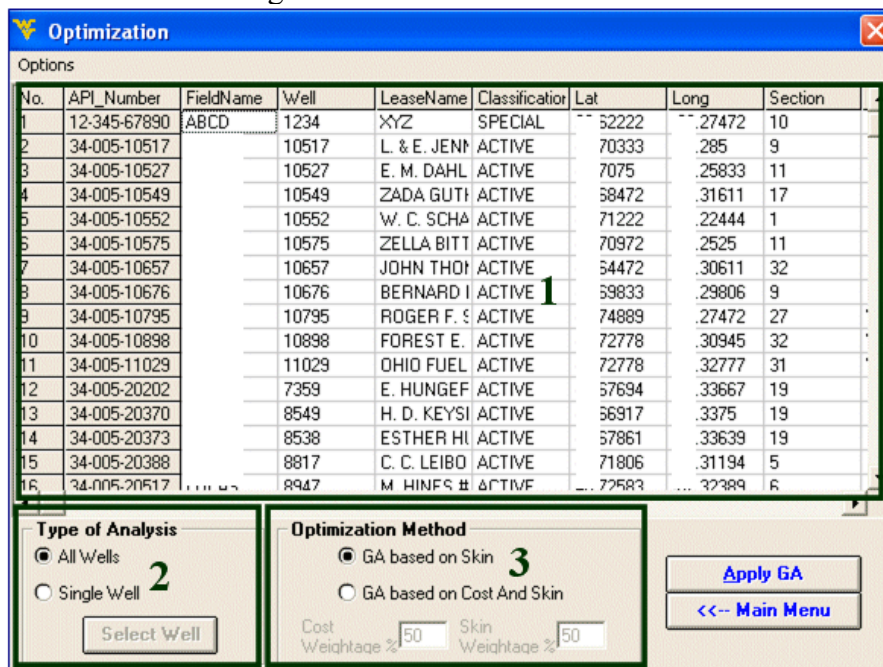
Fig82. Candidate Selection main screen

1.   When this module is loaded, each row in this section of the grid represents a valid
        stimulation as shown in figure above. Following, is the criteria for valid stimulation
        selection:

        Valid Stimulation – It should have skin value before & after stimulation.
        Valid Perforation – Perforation just before the stimulation.
        Valid Completion – The smallest size completion run before stimulation.
        Valid Well-test   – Well-test having skin value just before or after the well-test.
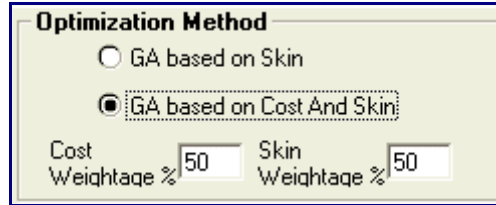
2.   Two types of analysis can be done on the wells: One option is to apply Genetic
        optimization on wells one at a time and the other is to apply it on all wells. If the 'All
        Wells' option is selected, then the 'Select Well' button will be enabled and the user can
        select the well the same way as shown in the previous section of the user Manual for –
        Find a well.
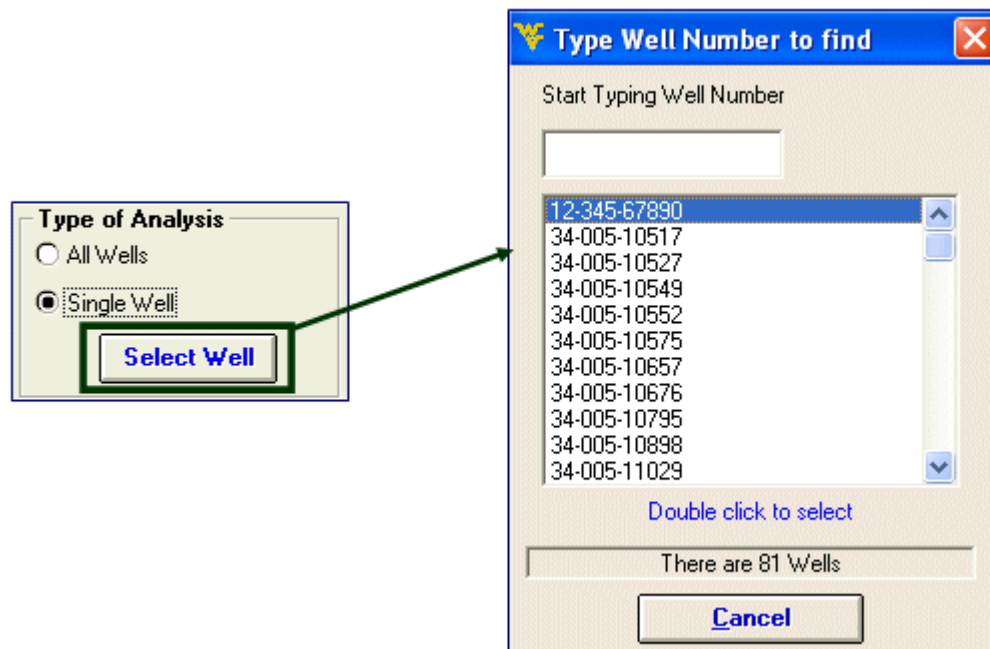
Fig83. Selecting a well for candidate selection process

3.   This section of module relates to the Optimization methods available. User can optimize
        the stimulations according to only change in skin criteria or may choose to select the 'GA
        based on cost and skin' option where he/she can give different weight ages to cost and
        skin.
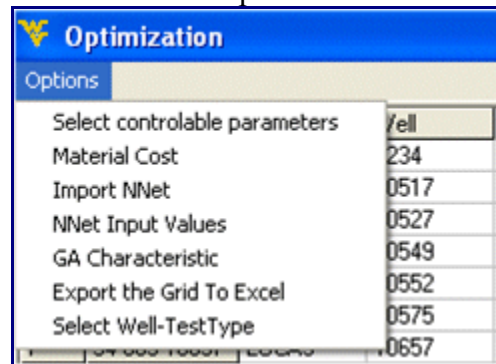
Options Menu:

This software can cater for many varied situations. These options can be selected from the 'options' menu bar on the top of the form. It contains following items:

- Select controllable parameters
- Material cost
- Import NNet
- NNet Input values
- GA characteristic
- Export the Grid to Excel
- Select Well-Test Type

Following is a screen shot of the items in the Options menu tool bar.

Fig84. Options to control Candidate Selection process

Material cost can be changed by the user as the prices fluctuate. These prices can be saved in the database by selecting 'Save' button and Default values can be retrieved by selecting ' Default' button. The screen shot of material cost is shown below and price is just an estimate and can be changed by user.

Fig85. Cost analysis module

Fig86.Inpurs that used to train the Neural Network

If the user wants to look at the Neural Network inputs being used, then 'NNet Input' option will take the user to a new form as shown above where all the inputs are shown. Keep in mind that this grid can only be seen once and that only after the Genetic optimization has been applied.

If some material is not available for stimulation, then still the user can optimize the stimulation by de-selecting that material from the 'Select controllable parameters' option. The materials not enabled are the ones that are not being used by the Neural Network in use.
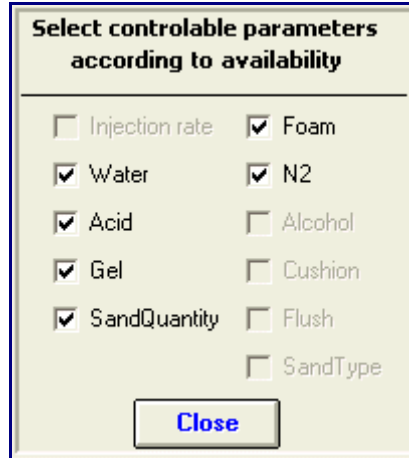
Fig87. Select the controllable parameters in optimization process

A new Neural Network can be used if the data is changed or appended by importing its 'ida' file. When a new Neural Network is imported, it might change the optimum GA parameters. The user can change them from 'GA characteristic' option. The default values are always loaded at startup as shown in figure below but can be changed by user.
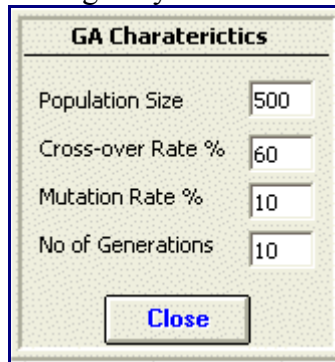
Fig88. Setup GA pentameters

If one of the Neural Net inputs is well test before stimulation, the type of the wells test in optimization process should specify here.
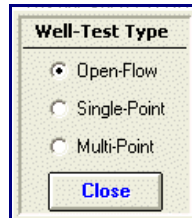
Fig89. Type of the wells test in optimization process.

When all the parameters for GA have been selected and user selects the 'Apply GA'

Apply GA button, then the screen below will appear showing the values of optimized stimulation slurry and change in skin due to this stimulation. The picture below shows the GA optimization done on well # 12-345-67890.
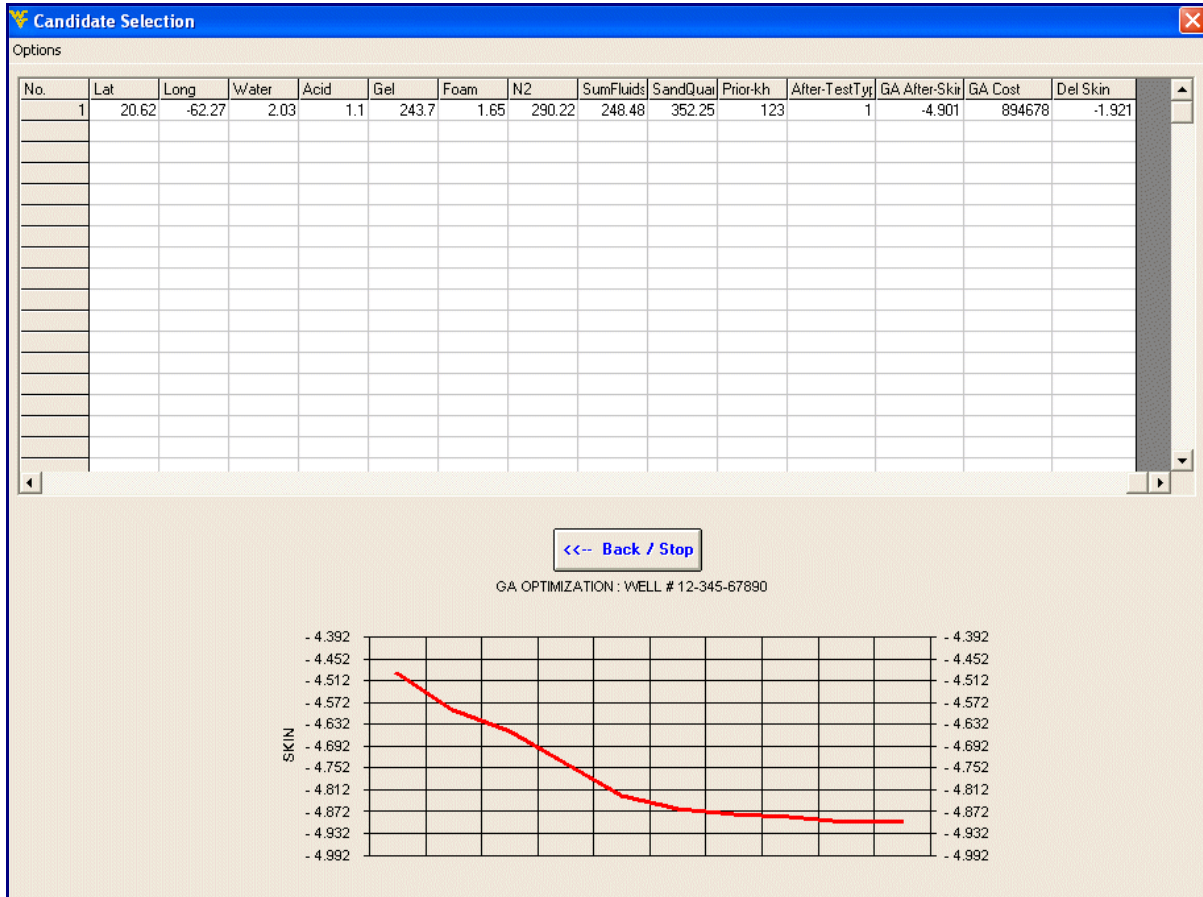
Fig90. Optimization process for one well

If the optimization is applied to all the wells, then we can rank the wells according to the change in skin by selecting 'Rank the wells' from Options menu bar on the top left corner of the form as shown in snapshot below.

Fig91. Optimization result for selected wells

The wells are ranked according to change in skin as shown in the figure below. These ranked wells and the optimized stimulation data now can be exported to excel by selecting 'Export to Excel' in the Option menu of Candidate Selection module.

Fig92.Rank the optimization result based on delta skin in order to find the best candidates

CONCLUSION

The main aim of this study was to find the re-stimulation candidate wells with the given data without trying to spend thousands of dollars on well-test and gas reservoir simulators. Detailed analysis of well-tests performed on the storage field was done and intelligent tools like Neural networks to predict the Skin and Genetic Algorithms were used to optimize the stimulation and to select the best stimulations for a well. The following conclusions can be drawn from this research:

1.   The Artificial Intelligence Tool can predict Skin with high degree of confidence.

2.   The Portfolio Management for re-stimulation candidate selection provides a cost effective method for taking full advantage of annual budget for remedial operations.

3.   This software is the first successful attempt to combine Data editing, Well-Test analysis and Artificial Intelligence in one software package.

REFERENCES

NONE

CEMENT EVALUATION IN GAS FILLED BOREHOLES

FINAL REPORT

Reporting Period Start Date: 05/01/2005

Reporting Period End Date: 12/31/2006

Edward Domangue

February 2007

DE-FC26-03NT41779

Baker Hughes Oilfield Operations, Inc.

Baker Atlas

2001 Rankin Road

Houston, TX 77073

ABSTRACT

Contained in this report is a description of efforts at determining the suitability of a new technology (EMATs) to perform cement evaluation in gas filled boreholes (e.g. gas storage wells). Also addressed is the issue of casing to cement microannulus using EMAT technology.

Included in the report are the following:

- Background/relevancy.
- Fundamentals of the new technology.
- Results of analytical modeling to establish feasibility.
- Experimental setup and data results.
- Conclusions

Findings of the investigation are that the technology will be suitable for the intended applications.

TABLE OF CONTENTS

1.0 EXECUTIVE SUMMARY

Beginning in 2002, Baker Atlas began looking at methods of improving cement evaluation in the new, lighter weight cements being introduced to the oil and gas industry. One avenue of investigation included the use of new acoustic sensors that broadened the type and frequency of acoustic signals that could be induced into the casing. A benefit of this sensor technology was that it did not rely on acoustic coupling of the signal through the borehole fluid, thus having the potential to work in gas-filled boreholes. Although such an application was not needed in conventional oil and gas development, Baker Atlas recognized the potential interest of the gas storage industry in such an application.

With the support of the Gas Storage Technology Consortium, Baker Atlas conducted a series of tests to determine whether this technology could indeed run cement evaluation logs in gas-filled boreholes. These additional tests were performed at Baker Atlas' Houston facility in conjunction with ongoing development of the new sensors. Furthermore, an additional evaluation of the ability of this technology to differentiate between uncemented pipe and a 'micro-annulus' was undertaken as such conditions are thought to be prevalent in older gas storage wells. The following report details these tests and their results.

The testing conducted under this program has shown that these new sensors are indeed capable of providing cement evaluation services in gas-filled boreholes. Although exact sensor response varied somewhat from the responses in liquid-filled boreholes, these differences are not material in terms of identifying a cement sheath around the casing. Finally, additional tests clearly show a method of differentiating between uncemented pipe and a micro-annulus.

Much work remains to be done to field an instrument and service usable in field work. Baker Atlas continues to work on this technology, however, and expects to conduct field trials of the new measurements in the future.

2.0 BACKGROUND

According to the Department of Energy, Office of Fossil Energy, there are approximately 110 operators maintaining more than 17,000 gas storage wells in over 415 underground storage facilities across the United States. [1]

In virtually every application, steel casing, cemented into place, serves to isolate the well from the underground formations forming part of the downhole completion hardware through which storage gas is injected and withdrawn under pressure.

The process of cementing wellbore casing in place provides two major benefits in gas storage wells. First, cement provides zonal isolation, preventing gas migration up the well bore between the formation and the casing. Second, cement transfers stress from the casing to the formation, increasing the effective strength and working pressure of the casing. [2] Unfortunately, reliable cement evaluation data does not exist on many wells in use for gas storage today.

Current cement evaluation techniques are designed to operate in fluid-filled holes typically on newly drilled but uncompleted wells. These techniques typically use an acoustic wave generated and then received by a logging tool within the wellbore to detect cement placed outside the casing and quantify several simple properties of this cement. A major restriction of all these services with respect to the gas storage industry, however, is their reliance on fluid in the casing to provide acoustic coupling between the logging tool and the casing. These tools are therefore unable to operate in gas-filled boreholes.

This report details the progress of efforts to confirm the validity of a new technique as well as the applicability of the technique for evaluating cement in gas-filled boreholes. The effort is part of a much larger project primarily intended to address the current shortfall within the industry for evaluation of highly modified, light-weight cements which normally have fluid-filled casings.

The ultimate benefit to the gas storage industry of a cement evaluation service capable of operating in a gas filled borehole is significant. First, it could provide direct proof of cement placement and zonal isolation in older gas wells (today, such a determination requires filling the well with fluid before logging). Second, the presence of cement between casing and the formation provides a method of transferring pressure-induced stress from the casing to the formation, greatly increasing the effective burst strength of the casing. Verification of cement placement should allow more realistic assessment of remaining casing burst strength, eliminating significant cost associated with unneeded

workovers. Finally, it is generally accepted that a sheath of competent cement on the exterior of the casing is beneficial in reducing the effects of corrosion on the casing wall.

3.0 EXPERIMENTAL

3.1 Overview

Prior generation cement evaluation techniques are fully capable of evaluating the placement of conventional cements in newly drilled wells. The most widely accepted technique uses a compressional acoustic wave generated and then received by a logging tool within the wellbore to detect cement placed outside the casing and quantify several simple properties of this cement. Due to the acoustic impedance mismatch between gas and steel, however, these instruments can not couple sufficient acoustic energy into the casing and cement to effectively make these measurements in gas filled boreholes. Prior to the effort contracted for and reported upon herein, Baker Atlas had identified that Electro Magnetic Acoustic Transducers (EMAT) were capable of generating controlled guided acoustic waves in electrically conductive material. Among these guided waves are Shear Horizontal (SH) and Lamb waves of both the symmetric and asymmetric types. SH waves are sometimes referred to as transversely polarized waves. In a steel place, SH particle displacement is tangential to the plate while direction of propagation is normal to the particle displacement. Lamb waves in a steel plate have particle displacement normal to the plate and again propagation is normal to the particle displacement. Because of these wave properties, Baker Atlas felt that EMATs would be able to provide capabilities beyond those of conventional cement evaluation devices. Subsequent analytical modeling further indicated those capabilities were probable.

Making use of EMATs, Baker Atlas is currently in the design phase of a new acoustic instrument intended for evaluation of light-weight cements. Because 100% of the current market for cement bond measurements is in fluid-filled boreholes, this effort is primarily directed towards those applications. Our work thus far indicates the instruments could be developed into a viable cement evaluation service for gas-filled boreholes.

This report provides certain details of our investigation techniques, observations, and conclusions as to the applicability of these concepts in gas-filled boreholes.

3.2 Cement models for testing lab instruments

Baker Atlas has applied for and has been granted a patent on several of these candidate techniques that could be used in gas-filled boreholes. [3] We are confident that these techniques will yield a suitable technique for eventual incorporation into a field measurement.

After initial evaluation for suitability, the selected measurement technologies have been built into test articles suitable for lab use only. Measurements with these devices have been made in several specially constructed cement test models (see Figures 1 and 2). These cement models were constructed with various cement formulations, casing thickness, and in a very special case, a controlled micro-annular condition.

Measurements were performed with both water and air in the borehole for direct comparison. Models were constructed so that they may be pressured internally to 1,000 psi to further simulate downhole conditions if needed (need was not demonstrated in the process of making measurements).

3.3 Micro-annulus study

When the first step was completed, the next required step in determining the feasibility of making cement evaluation measurements was to evaluate the effect of any potential 'microannulus' on the measurement. A microannulus is a very small gap between the cement and the casing. In typical completions, this gap is often caused by thermal casing expansion during cement curing and by wellbore pressure fluctuations (reduction of casing fluid weight, for example) subsequent to cement setting. Under conditions normally experienced during well completion, the size of the microannulus is typically no more than a few thousandths of an inch and is temporarily reversed for bond logging by increasing the fluid pressure within the well. In the case of gas storage wells, however, normal field operations imply that the thermal and pressure cycles may be large and last for months. It is thought that large microannuli are therefore possible in the gas storage well environment.

Prior to the effort contracted for and reported on herein, Baker Atlas was seeking new methods for evaluating cement in the presence of a microannulus without need for the conventional approach of pressuring up on the casing to swell the casing and close the microannulus. In the course of our search, we discovered that EMATs were capable of generating guided acoustic waves of several types in electrically conductive material. Further, our analytical modeling also indicated that one or a combination of two or more of these guided waves would be useful in the said cement evaluation.

In the case of a typical gas storage well simply increasing the borehole pressure, as is done in conventional wells, it is normally not possible since these wells usually have open perforations.

In order to fully understand this effect, a physical model was built so that actual transducer response in a microannulus can be studied. This model required a special "tapered" casing, which can be raised or lowered by means of a hydraulic jack, varying the size of the microannulus. A schematic of the model is shown in Figure 2.
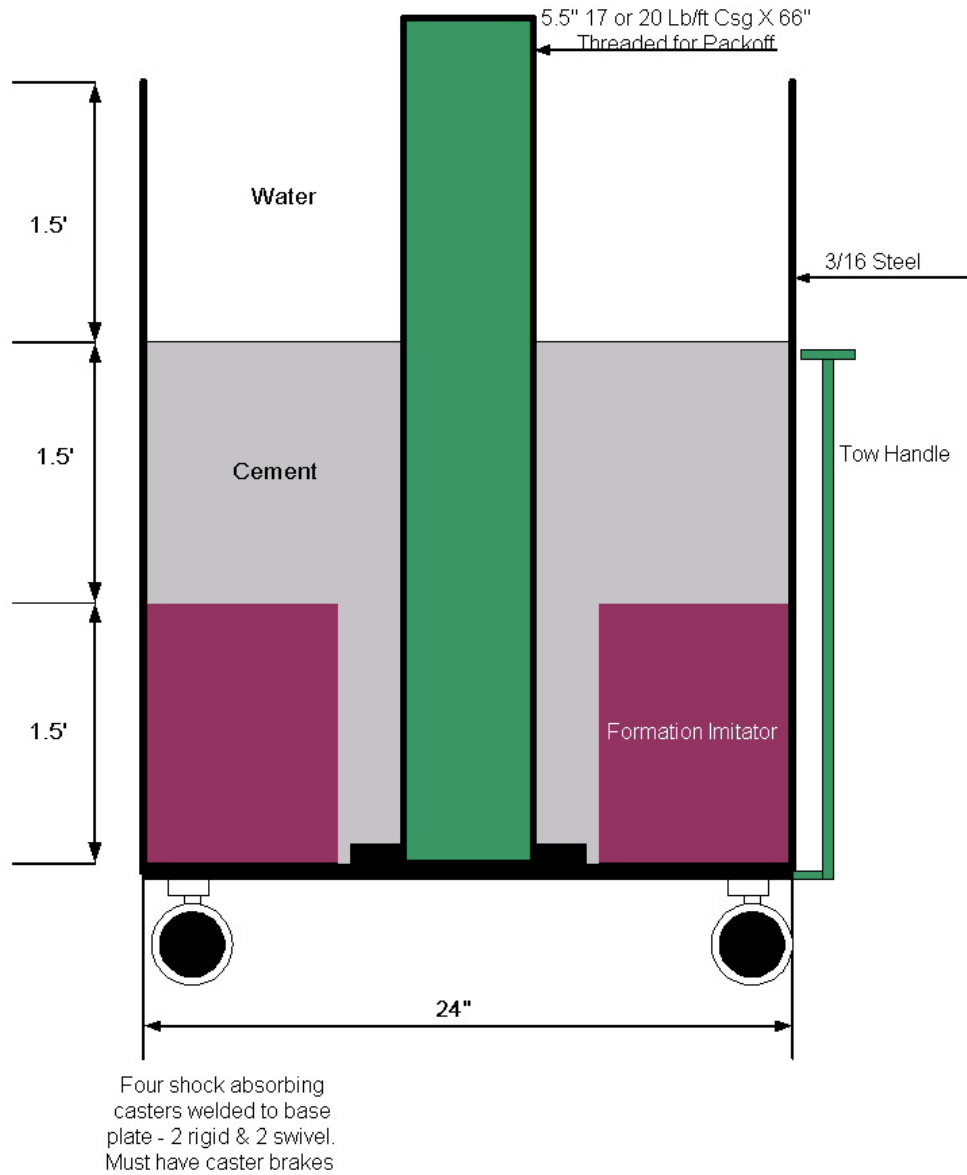
Figure 1

Drawing of a typical cement model for evaluation of new cement evaluation technology. Note central casing is welded to the bottom plate of the fixture during fabrication. The next step is to install the formation imitator which is actually a highly dense synthetic, cementitious material. The formation imitator was placed in all models save the microannulus fixture and the single free pipe model.
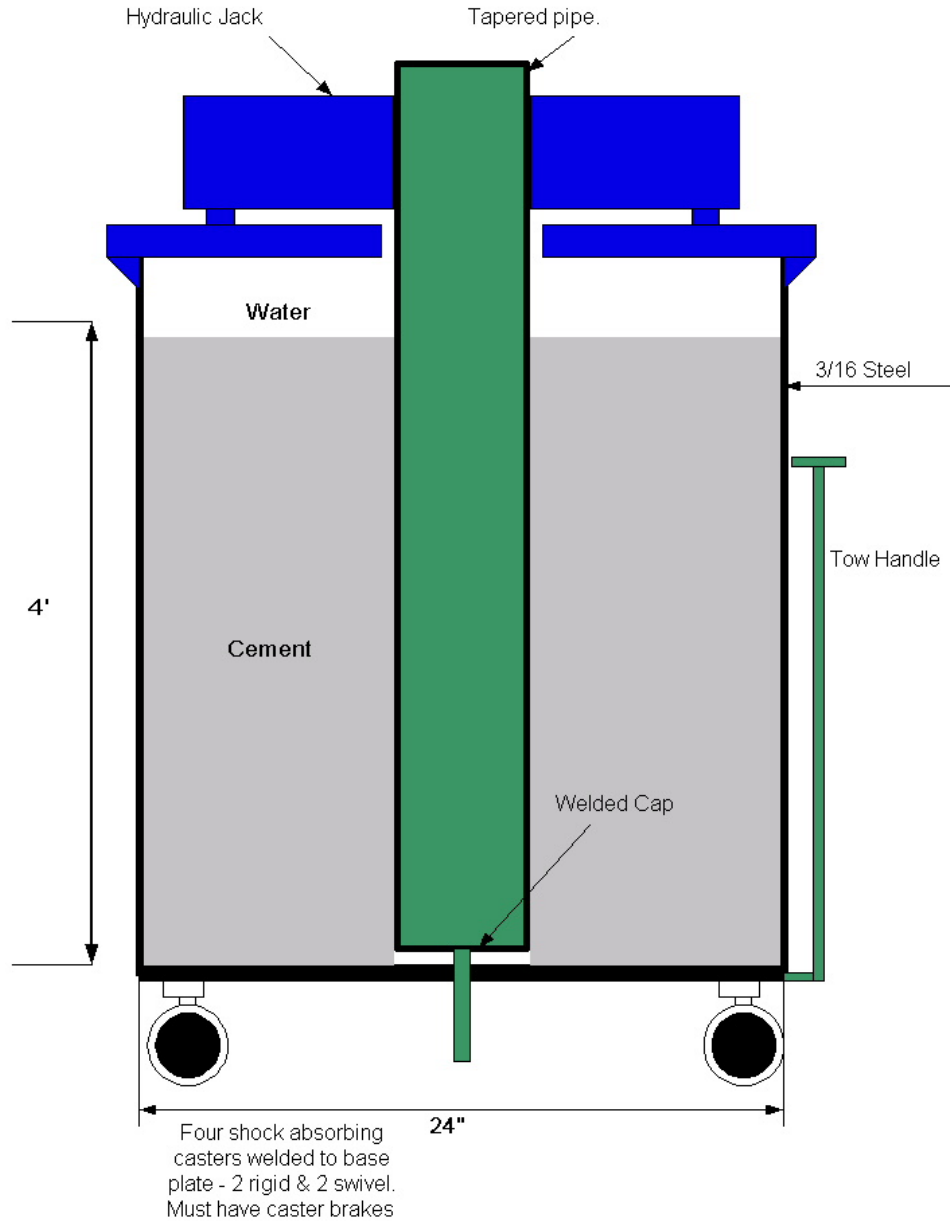
Figure 2

Drawing of a highly specialized version of cement model which permits investigation of microannular effects on the new cement evaluation techniques. The center casing is not attached to the bottom plate, but rather can be moved up and down in the cement column. The center casing is additionally tapered (smaller at the bottom), so that moving the casing up creates a controlled and progressively larger microannulus.

It should be pointed out that great care was exercised in the formulation, mixing, and placement of cement in the models. Nevertheless, the resulting specimens were not always of uniform quality and certain discontinuities in the cement column were present

10

as observed from the resulting data. More on this subject is offered later in the results and discussion section.

Eight cement models in total are constructed, but for purposes of this report, we will show data taken in three of the models.

3.4 Transducers

A review of the previously mentioned patent will reveal that our choice of transducer type is the Electro Magnetic Acoustic Transducer, or EMAT as they are known in the world of NDT. This transducer type was chosen for three principle reasons:

- By selection of the magnet and coil configuration and dimensions, the transducers are able to send and receive acoustic energy at different wavelengths as well as different modes of propagation.

- By excitation of multiple frequencies, the transducers are able to send and receive acoustic energy at different velocities and demonstrate varying degrees of sensitivity to casing and cement properties.

- The transducers do not require a liquid couplant to send and receive acoustic signals.

A simplified schematic of an EMAT can be observed in Fig. 3.

Figure 3

11
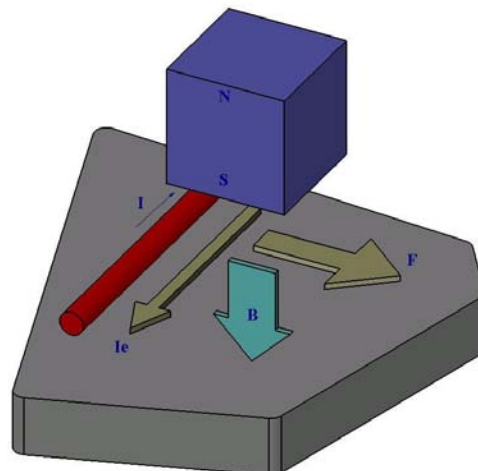
An EMAT uses non-contact electromagnetic transduction to impart physical stress to a conductive medium. A current I, in a wire near a conductive surface induces an equal and opposite eddy current Ie in the surface of the material. When a magnetic field is present, a force is created in the conductive surface known as a Lorentz force. This basic effect is the same as used in an electric motor to convert electrical energy into mechanical energy.

$$F = Ie \times B$$

This force generates particle displacement resulting in elastic waves. Selection of magnet and wire (coil) configuration and dimension controls a resulting Ultrasonic Guided wave. Common types of guided waves are Shear Horizontal (SH), also known as tangentially opposed, and Lamb waves of both symmetric and asymmetric type. Further information is available in published literature. [4]

3.5 Transducer configuration

For purposes of this study, a simple arrangement of transmitter and receivers was used consisting of only one transmitter and two receivers placed at equal distance radially. The arc between each transducer covers 120 Deg of the casing inner surface. Schematic of this arrangement can be observed in Figure 4.
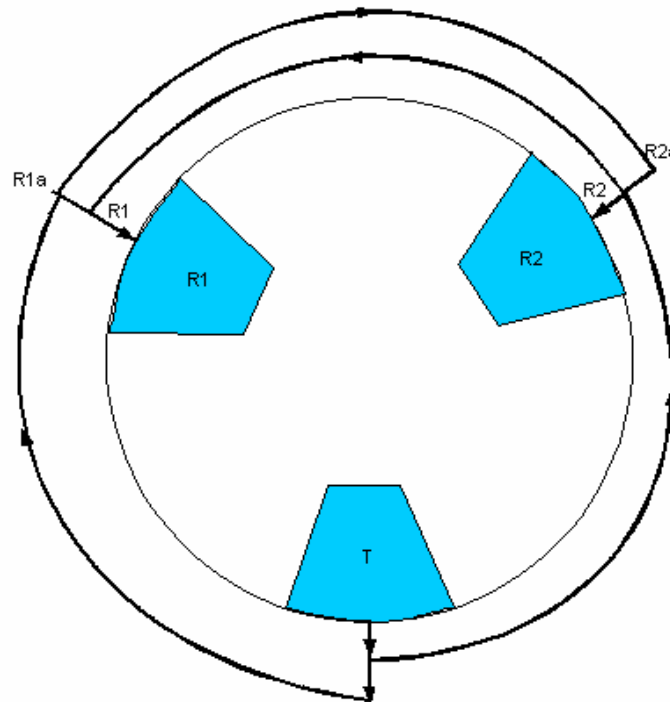
Figure 4

Using the above simple configuration, a single compensated measurement of attenuation can be made between Receivers One and Two using all three transducers. The calculation is made as follows using amplitudes from four arrivals. R1 and R2 measurements are made when the signals from the transmitter travel in one direction, and R1a and R2a are made as a result of signals traveling in the opposite direction.

$$Attn = \frac{-10}{\Delta} * Log \frac{R1}{R2} * \frac{R2a}{R1a}$$

This calculation approach provides an attenuation measurement compensated for transducer differences and is already widely accepted in the industry.

3.6 Modeling

Prior to entering the empirical phase of this project, a considerable amount of modeling was conducted in hopes of establishing the feasibility of going ahead with the larger effort. The results of one such model are presented in Figure 5. The intent of this model is to depict expected attenuation results for SH transducers from two specific cement density formulations across multiple casing wall thicknesses. Please keep in mind that the model assumes ideal contact with the cement as well as absolutely uniform placement and density. The results served as justification to commence with the experiments.

As will be evident from the results and discussion section, there is good numerical agreement with the case of low density cement. However, the model predicts much higher attenuation in the conventional 14 lb/gal cement slurry than was actually measured. Again, the model represents an ideal environment as well as an ideal instrument. In practice, measurements made with our transducers encountered signals in the far receivers that were below the threshold of noise. The resulting data therefore understates the actual acoustic attenuation rates present. It is our intention that further development will make use of improved technology which will permit us to more accurately measure actual attenuation rates.
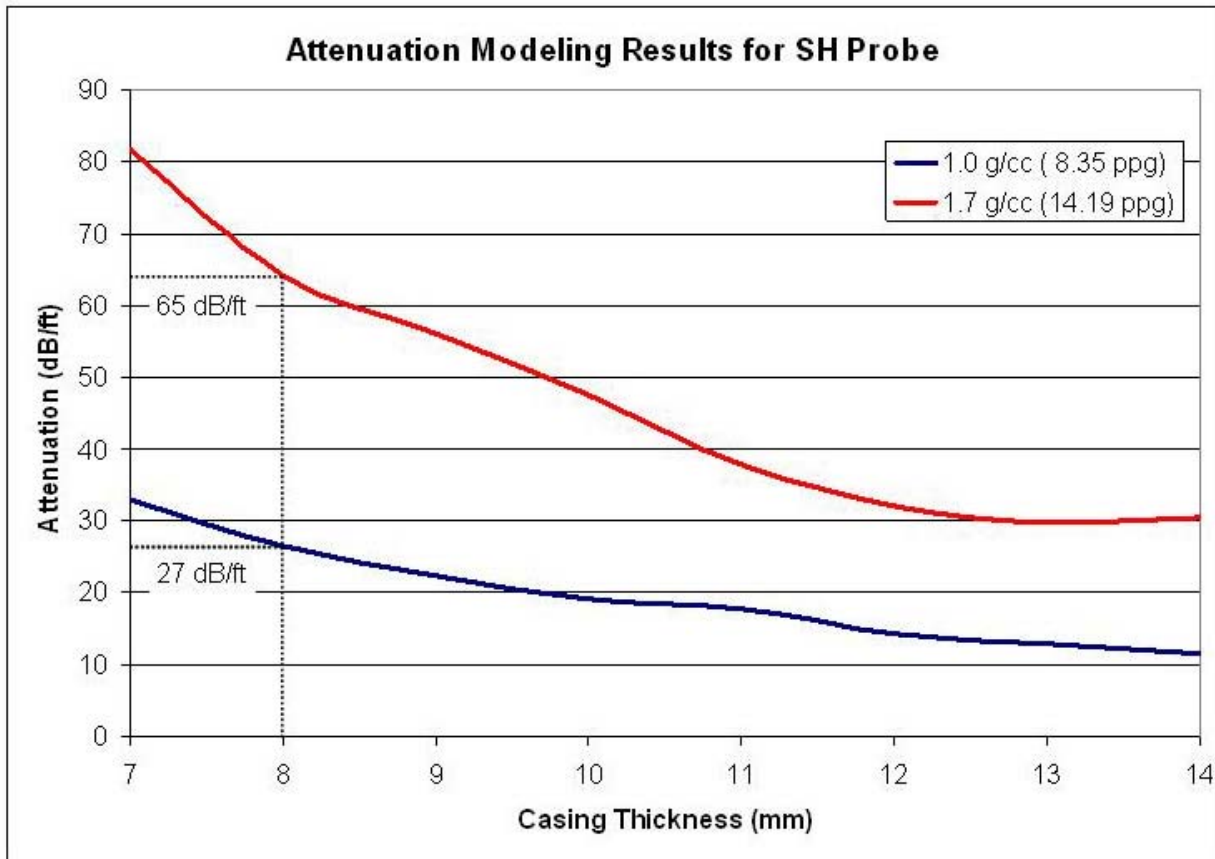
Figure 5

**Modeled attenuation obtained for SH waves for 2 different slurry densities for the
case of ideal contact between the pipe and cement. Highlighted results correspond to physical
configuration of model data presented in Figures 6 and 7.**

4.0 RESULTS AND DISCUSSION

In all cases, the following data was obtained beginning with the test instrument starting at the bottom of all three cement models and then pulled at an approximately constant rate to the top of the model. We would therefore expect that the instrument would detect cement in the lower sections and free pipe near the top (left to right on the data figures).

Figure 6 depicts a Shear Horizontal (SH) EMAT instrument response in terms of acoustic attenuation in the cement model with a fairly conventional 14 lb/gal extended slurry. Data is taken with and without fluid in the center casing. As previously mentioned, you will note that the quality of the cement is not as uniform and continuous as might be expected. Even so, a maximum attenuation rate of more than 40 dB/ft is observed in the cement with a contrasting attenuation of near 5 dB/ft in the free pipe section or a net 35 dB/ft contrast. By comparison, conventional cement evaluation systems demonstrate a net contrast of only approximately 10-12 dB/ft in a similar environment.
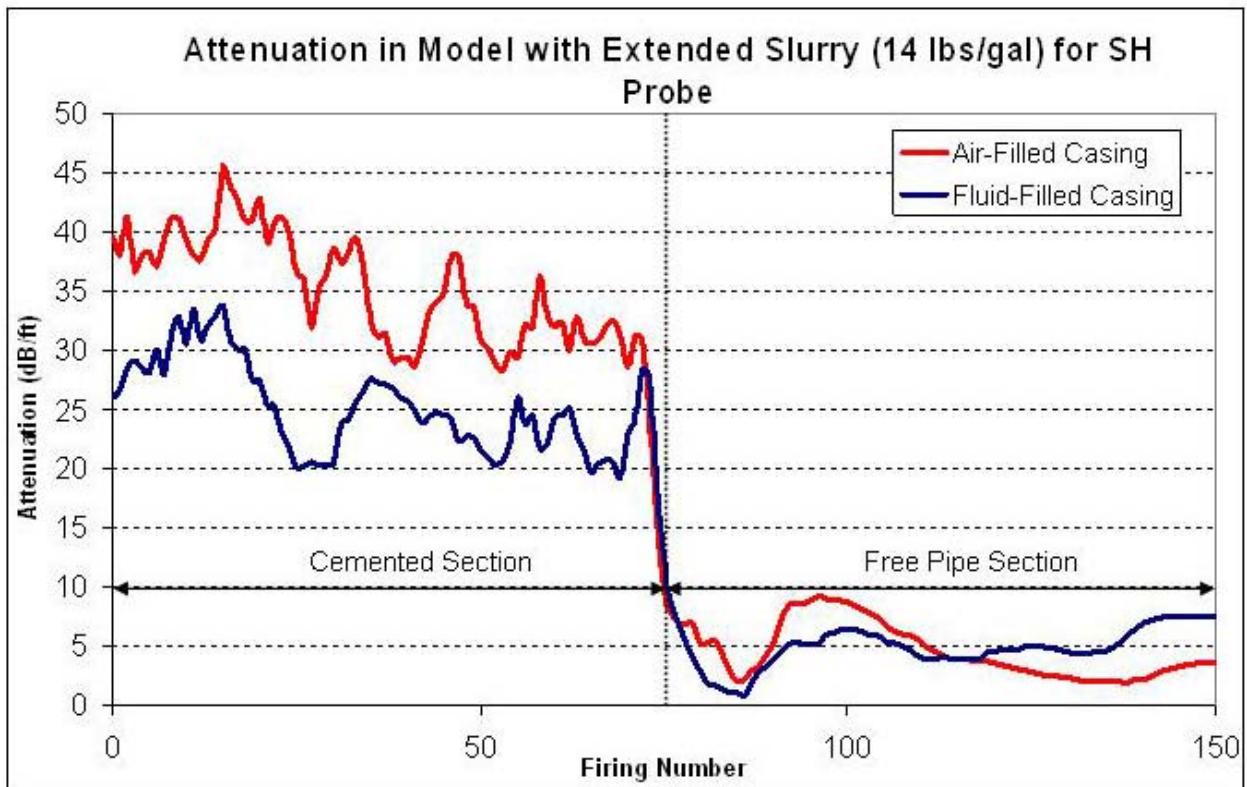
Figure 6

Attenuations obtained in experiments with SH probe for model with extended cement slurry contrasting air filled vs. fluid filled center casing.

Figure 7 depicts the data from the SH instrument in the cement model which contains extreme low density 7 lb/gal cement, again with and without fluid in the center casing. While the contrast between cemented and free pipe is not as high as in the prior example, the contrast still remains significant in terms of being able to identify the presence of cement. In this case, approximately 25 dB/ft maximum net contrast.
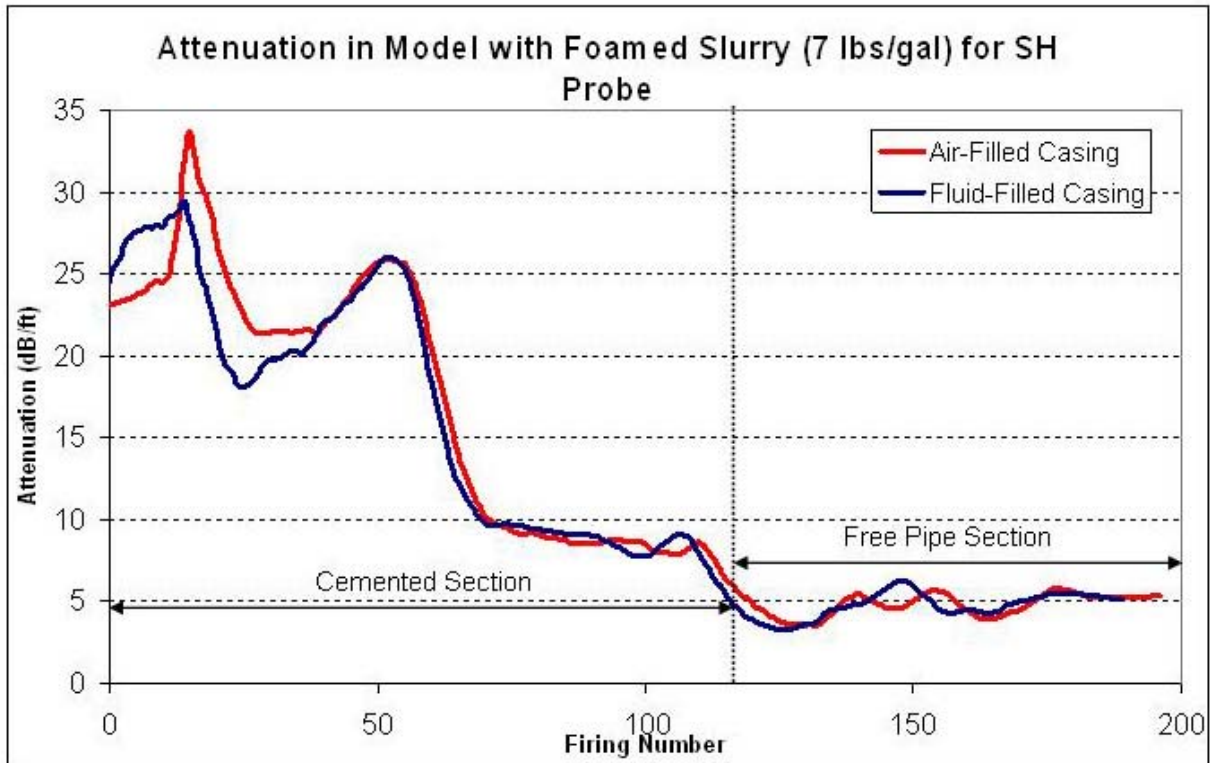
Figure 7

Attenuation obtained in experiments with SH probe for model with foamed cement slurry contrasting air filled vs. fluid filled center casing.

Figure 8 shows the data taken with the SH instrument from the microannulus cement model with fluid inside the center casing. Recall that the microannulus model has the additional capability over all the other models to move a tapered center casing up and down in the cement column creating a controlled microannulus of greater size as the pipe is moved up. In this model, the best cement encountered is just about halfway up the cement column. The black curve depicts cement conditions after cementing and before the casing was ever moved. All other curves represent varying degrees of microannulus size.

You will note that all the other curves are essentially equal-valued without regard to size of the microannulus present.
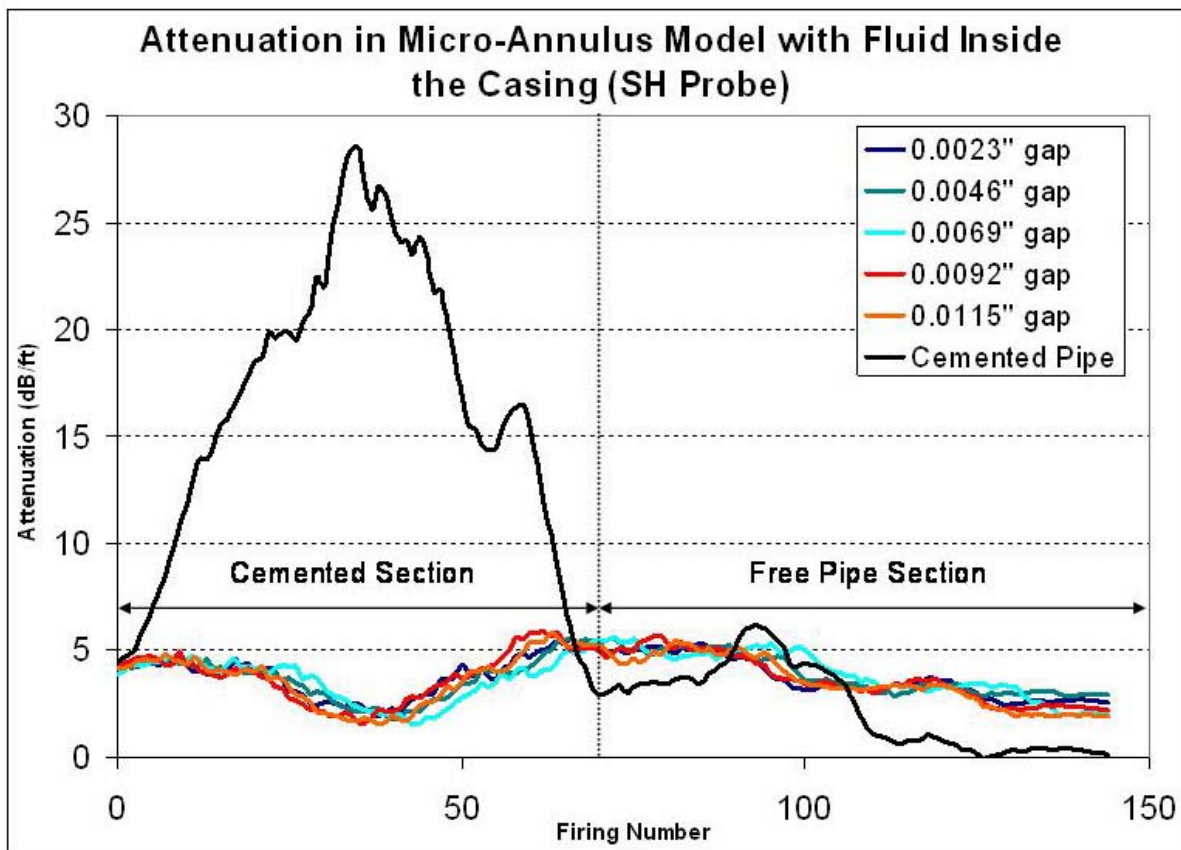
Figure 8

SH Probe results in the microannulus fixture with fluid inside the center casing first with fully cemented casing and then with varying microannulus size. Note that once a microannulus is present, all SH data is essentially equal valued.

17

Figure 9 displays the data results in the microannulus fixture over the same microannulus conditions as in the previous example, however in this case there is no fluid in the casing. In Figures 9 and 10, the first introduction of a microannulus results in free pipe readings. Please also note that there is essentially no difference in results from the air-filled and fluid-filled experiments.
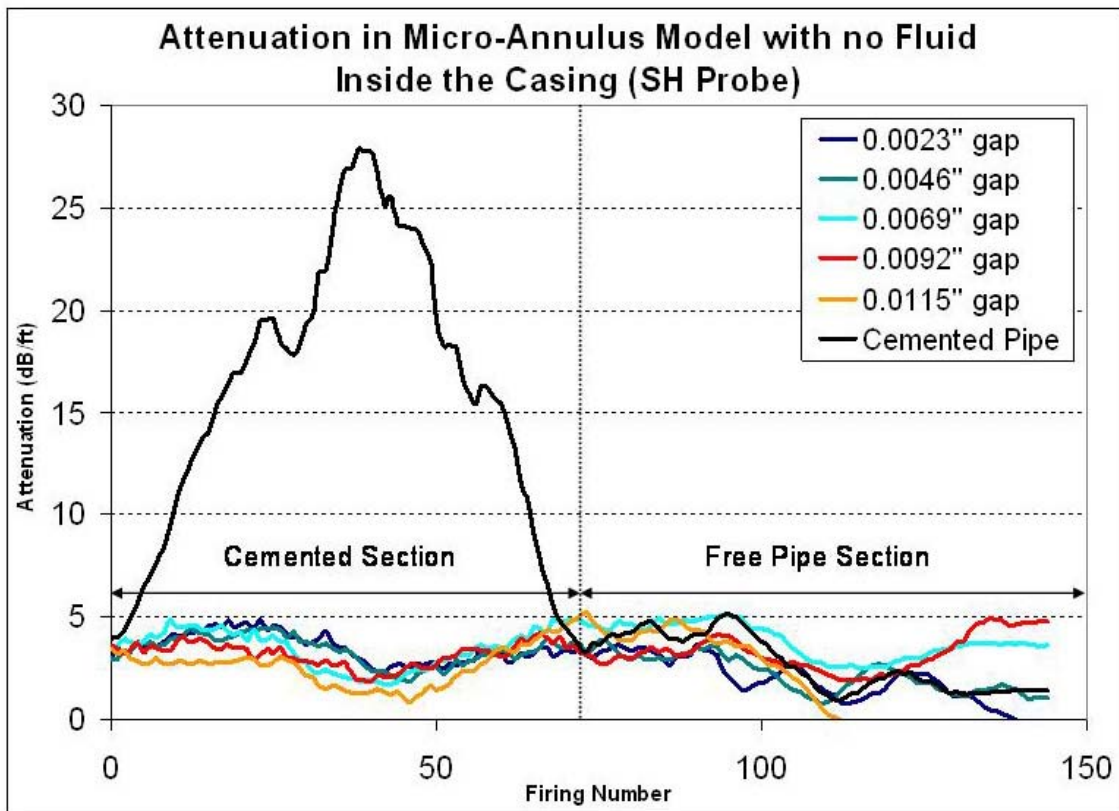
Figure 9

SH Probe results in the microannulus fixture with no fluid inside the center casing first with fully cemented casing and then with varying microannulus size. Note that once a microannulus is present, all SH data is essentially equal valued.

Figure 10 displays data taken with a flexural mode (LAMB) EMAT instrument in the microannulus model with the same microannulus conditions as in the prior two examples. Only data with no fluid inside the casing is presented. Again, the black curve represents data in the model after cementing and before the casing was ever moved. You will note that attenuation is present in all positions, even with a microannulus of 0.0115". You may also notice that the data appears to be offset from curve to curve. This is due to the apparatus used to transport the instrument up the casing. It was not possible to control the exact start time and velocity during the experiments. There is a nevertheless a high degree of similarity between all curves.

The attenuations observed tend to get larger as the microannulus also gets larger. The last two stations, however (0.0092" and 0.0115") seem to converge. The last station (0.0115") is the largest microannulus we can create with this model.

Figure 10

19
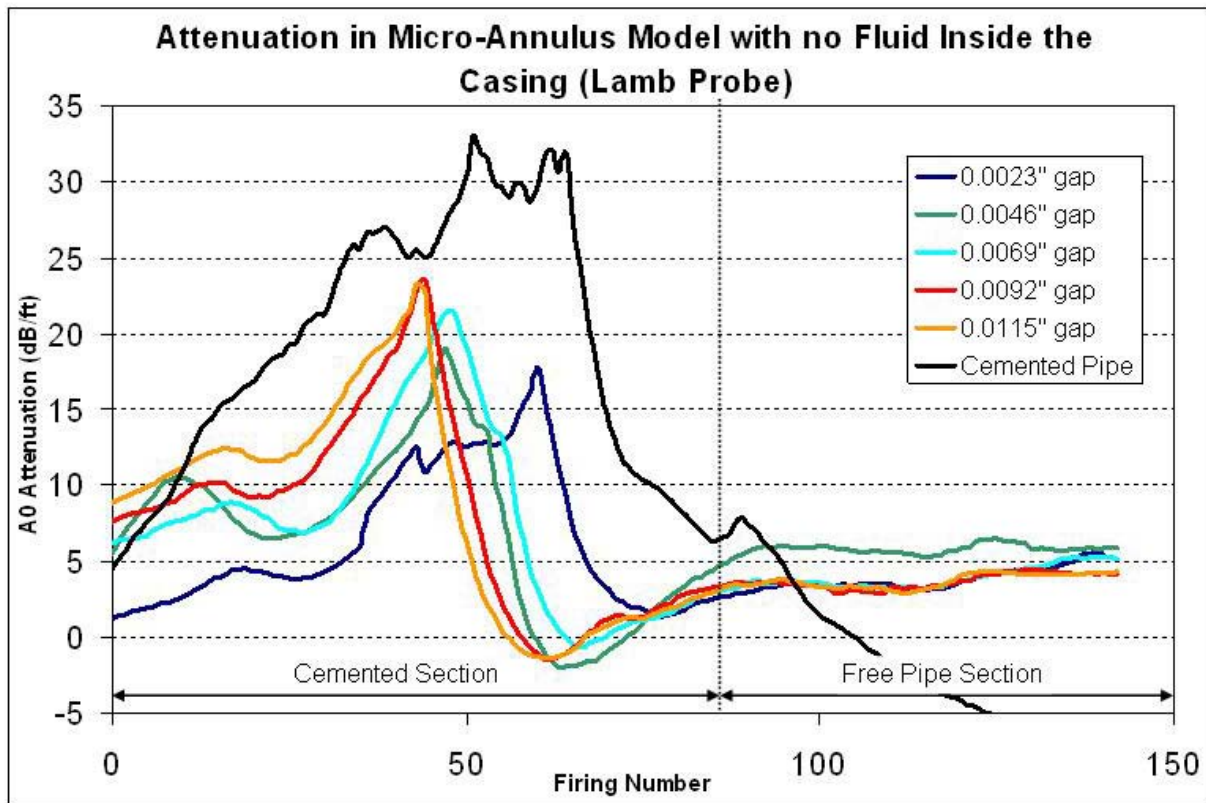
5.0 CONCLUSIONS

The data indicates that the SH EMAT instrument is clearly able to distinguish cemented pipe from free pipe without regard to whether there is fluid inside the measured casing. This is true even in the presence of extremely light weight (7 lb/gal) foamed cement.

As was predicted early on in the project, the SH EMAT instrument displays free pipe value whenever a microannulus is also present.

As was hoped at the outset of the project, the LAMB EMAT instrument is able to distinguish cemented pipe from free pipe even in the presence of a sizable microannulus (0.0115").

A combination of SH and LAMB EMAT sensors permits detection of cement presence even when a microannulus is also present. The condition is detectable without regard to whether there is fluid or air inside the casing.

6.0 REFERENCES

[1] Department of Energy, Office of Fossil Fuels; Website: *Gas Storage and Liquefied Natural Gas,* February 16,2004

[2] Fleckenstein, Eustes, & Miller, SPE 62596

[3] United States Patent 7,150,317 Barolak, et al. December 19, 2006

[4] NDT Resource Center website

United States Patent Application 20050190648 Method and apparatus for cement bond evaluation using transversely polarized shear waves

United States Patent Application 20060198243 Use of lamb waves in cement bond logging

New Comprehensive Inventory Analysis Tool

FINAL TECHNICAL REPORT

1 May 2005 – 31 May 2007

C. M. Boyer II, Project Director, Schlumberger
K. G. Brown, Principle Investigator, Schlumberger
W. K. Sawyer, Principle Consultant, Schlumberger

August 2007

Schlumberger
Consulting Services
1310 Commerce Drive
Park Ridge 1
Pittsburgh, PA 15275-1011

DISCLAIMER

This report was prepared as an account of work sponsored by an agency of the United States Government. Neither the United States Government nor any agency thereof, nor any of their employees, makes any warranty, express or implied, or assumes any legal liability or responsibility for the accuracy, completeness, or usefulness of any information, apparatus, product, or process disclosed, or represents that its use would not infringe privately owned rights. Reference herein to any specific commercial product, process, or service by trade name, trademark, manufacturer, or otherwise does not necessarily constitute or imply its endorsement, recommendation, or favoring by the United States Government or any agency thereof. The views and opinions of authors expressed herein do not necessarily state or reflect those of the Unites States Government or any agency thereof.

ABSTRACT

Inventory analysis is critical to proper management of underground gas storage (UGS) facilities. Often, basic inventory analysis plots (e.g., P/Z vs Inventory) are updated and reviewed once or twice a year, with additional scrutiny being applied if several cycles of data suggests possible inventory problems.

There are over a dozen useful diagnostic plots and techniques available for monitoring inventory and identifying potential causes of lost gas in storage reservoirs. However, many operators have given more and more responsibilities to fewer and fewer personnel in recent years, making truly comprehensive inventory analyses more difficult to accomplish in a reasonable timeframe. In addition, as new storage engineers enter the market to replace the graying retirees, unfamiliarity with the underlying assumptions and limitations inherent in the less known analysis techniques may cause undue hesitation to implement these techniques.

This report summarizes the work performed under contract DE-FC26-03NT41779. The primary objective of this project was to develop a comprehensive inventory analysis software tool that would:

- Allow easy importation of typical storage inventory data,

- Automatically generate pertinent raw data plots and diagnostic plots for the analyst's review and processing of inventory data,

- Provide on-line help that gives an overview of the inventory analysis process and explains the assumptions, applications, limitations, and processes used to analyze specific diagnostic plots, and

- Provide a "toolbox" application that would perform calculations useful in the process of inventory analysis.

This new tool significantly improves operators' ability to effectively monitor inventory and resolve gas loss issues by making inventory analysis processes much more automated and much more comprehensive. It also enhances the analysis process by guiding the engineer to the appropriate analysis techniques and away from the inappropriate analysis techniques via the on-line help tools.

In this report, the software development and design is briefly reviewed, including a summary of the major components of the software and online help features. An example dataset and analysis is presented. Recommendations for future improvements in the software are also discussed.

TABLE OF CONTENTS

APPENDIX I - SOFTWARE USER'S MANUALWITH EXAMPLE PROBLEM TUTORIAL

APPENDIX II - INVENTORY ANALYSIS PRIMER

APPENDIX III - LIST OF UNDERGROUND GAS STORAGE REFERENCES

APPENDIX IV - INVENTORY & DELIVERABILITY TERMINOLOGY

APPENDIX V - UNDERGROUND GAS STORAGE GLOSSARY

LIST OF FIGURES

1 INTRODUCTION

Some level of inventory analysis is routinely performed in virtually all gas storage fields, and is a critical to proper management of gas storage facilities. Often, basic inventory analysis plots (e.g., P/Z vs Inventory) are updated and reviewed once or twice a year. If several cycles of data suggests a possible inventory problem, the inventory data and analysis plots are given additional scrutiny. If additional scrutiny suggests significant gas losses, a major study may be initiated, in which inventory is analyzed more comprehensively, usually using two or three analysis techniques (e.g., P/Z vs Inventory analysis and inventory per pound (IPP) analysis).

There are over a dozen useful diagnostic plots and techniques available for monitoring inventory and identifying potential causes of lost gas in storage reservoirs. However, many operators have given more and more responsibilities to fewer and fewer personnel in recent years, making truly comprehensive inventory analyses more difficult to accomplish in a reasonable timeframe. In addition, as new storage engineers enter the market to replace the graying retirees, unfamiliarity with the underlying assumptions and limitations inherent in the less known analysis techniques may cause undue hesitation to implement these techniques. This is indeed unfortunate, since nearly every analysis technique will shed some useful light on inventory and gas loss issues.

Therefore, we proposed development of a user-friendly software package that would: 1) accept typical inventory data available for a field, 2) automatically generate and interactively interpret diagnostic plots, 3) provide on-line help screens summarizing the technical assumptions of each analysis technique, the applicability of the techniques to various types of storage reservoir, the inherent dangers of each technique, and example plots of each technique.

The result of this project is a software package that accomplishes the above objectives. This software significantly improves operators' ability to effectively monitor inventory and resolve gas loss issues by making inventory analysis processes much more automated and much more comprehensive. It also enhances the analysis process by guiding the engineer to the appropriate analysis techniques and away from the inappropriate analysis techniques via the on-line help tools.

2 EXECUTIVE SUMMARY

2.1 Objectives

The primary objectives of this project included:

- Develop and field test a software tool that:

  o Readily accepts inventory data available for a given field and

  o Automatically generates and interactively interprets diagnostic plots

- Develop on-line help tools within the software that provides:

  o The technical reference(s) on which the various inventory analysis technique are based

  o The technical assumptions inherent in each analysis technique

  o The applicability of each technique to various types of storage reservoirs

  o The inherent dangers of each technique

  o Example plots for each technique

  o A "toolbox" that would perform calculations useful for inventory analysis

  o A categorized list of references and technical papers that covers a broad range of underground gas storage topics

  o A glossary of underground gas storage terminology

2.2 Software Overview

This software was developed in the VisualBasic^{TM} programming environment, uses Microsoft ACCESS^{TM} for data storage, employs Microsoft EXCEL^{TM} as a "bridge" between users' data and the ACCESS^{TM} database, and exports reports to WORD^{TM}. EXCEL^{TM} was chosen for use as a template to hold data due to the ubiquitous use of EXCEL^{TM} in the UGS industry. ACCESS^{TM} was chosen due to its excellent data handling and data manipulation capabilities. Use of this software requires the installation of EXCEL^{TM} and WORD^{TM} on the user's computer, but not ACCESS^{TM}.

An EXCEL^{TM} spreadsheet was developed to facilitate transfer of data necessary for inventory analysis from the user to the software. This spreadsheet acts as a "template" to ensure the data types, order, and content are consistent with what the software expects upon import of the data.

There are five major areas or windows in the software work area (**Figure 1**), including:

- A Toolbar window, which contains several toolbars associated with different aspects of inventory analysis calculations and workflow (e.g., BHP and BHP/Z calculations, Inventory Per Pound (IPP) calculations, etc).

- A Data Table window, which displays data from the various tables containing the input and calculated data

- A Workflow window, which shows an outline (in tree structure) of the inventory analysis workflow employed in this software

- A Data/Plotting window, showing data contained in the highlighted table (in the Data Table window) or the diagnostic plot (highlighted in the Workflow window)

- A Plot Feature window, which contains various buttons that allow modification of various plot features.
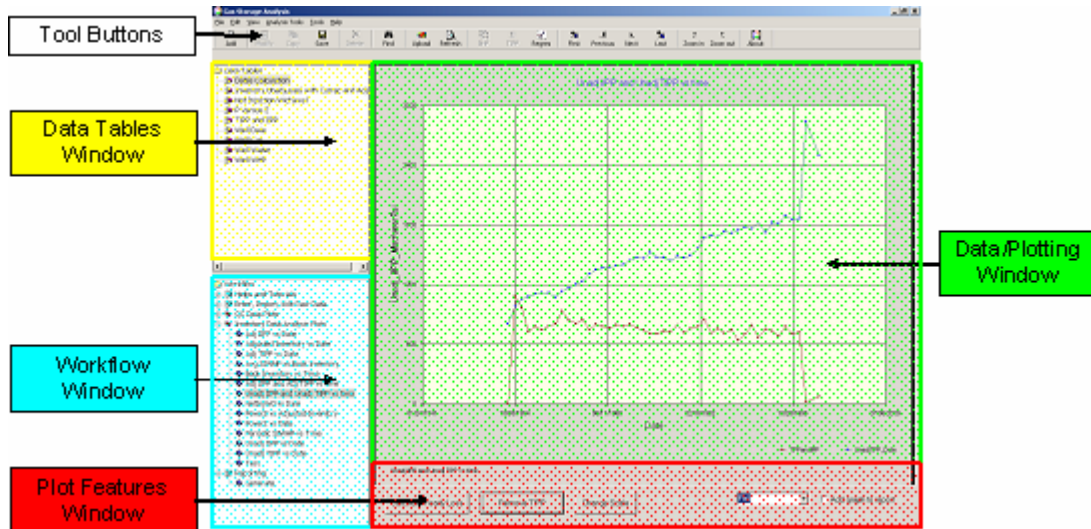
Figure 1: Major windows in the software work area

The development of comprehensive HELP features was considered a critical part of this project. Several HELP tools are available in two locations to guide the users as they use this software. All help features are available using the "help" menu at the top of the software window, and the HELP features typically used during the inventory analysis process are also included in the Workflow Window, under "Helps and Tutorials." The various HELP features include the following:

- Inventory Analysis Primer: This document provides a very concise summary of the objectives, theory, data required, diagnostic plots, and analyses techniques involved in inventory analysis. It also includes a sample dataset and the analysis of the sample dataset.

- Summary of References: This document summarizes various references and technical papers related to Underground Gas Storage. These references are not limited to inventory analysis, but cover a wide range of UGS topics including:

  - Introduction to Gas Storage

  - Gas Storage Field Design

  - Optimization

  - Migration and Monitoring

  - Inventory Verification

  - Deliverability Maintenance and Enhancement

- o Simulation of UGS Reservoirs

- o Top Twenty Technical Papers

- Inventory Analysis Toolbox: This is an EXCEL™ spreadsheet that summarizes and/or calculates various data useful in the process of inventory analysis, including:

  - o Estimated line losses as per a U.S. Bureau of Mines publication

  - o Estimated volume of gas vented during a wellbore blowdown

  - o Estimated volume of gas vented during a multi-rate well test

  - o Estimated volume of gas contained in a pipeline at specified inlet and outlet conditions.

  - o Estimated shut-in pseudopressure vs time for assumed reservoir properties (to estimate time to stabilized shut-in pressure).

  - o Estimate (first order) of minimum gas flow rate to continuously unload fluids from a wellbore of specified configuration.

  - o Units Conversion Table

  - o Chart of estimated residual gas saturation as a function of porosity

  - o Chart estimating (HP)/(MMscf/D) required to compress typical storage gas at 100 degrees F to 1000 psi using single stage compression.

- Input Template Help Information: There is help information for each input sheet in the EXCEL™ input template, including a description of the data needed and an example data input set.

- Technical Help for Diagnostic Plot Analysis: This document summarizes how various diagnostic plots are used and analyzed. In most cases, the following information is presented for each diagnostic plot:

  - o Example plot

  - o Purpose of the plot

  - o Assumptions inherent in construction/use of the plot

  - o Applicability of the plot

  - o Dangers associated with misuse of plot

  - o References

- Gas Storage Terminology and Gas Storage Glossary: This document lists and describes/defines various terms used in UGS, and includes a comprehensive glossary of terms.

The software tool has been tested using numerous actual field datasets to ensure the correct coding of all calculation processes. Nearly 20 datasets were loaded into the software and analyzed. These analysis results were compared to results previously obtained using manual analysis techniques to ensure the software gave consistent results.

2.3 Recommendations

We recommend that Gas Storage Technology Consortia (GSTC) members use this software for a period of time and provide the GSTC executive council with a list of additional features and upgrades the membership would like to incorporate into the software. Potential enhancements could include the following:

- Additional WHP-BHP correlations

- Additional Z-factor correlations

- Additional calculations/features in the "Toolbox"

- Additional diagnostic plots with associated calculations

- Enhanced interactive analysis features, such as

    o Enhanced data import features

    o Plot data points color-coded by date (e.g., P/Z vs Inventory plot)

    o Interactive selection of data point(s) to be included/excluded from analysis

    o Selection of *any* endpoints (not just actual data points) to draw plot lines

    o Expand the range of calculations made internally (e.g., have the software internally generate plot data required to construct the Cumulative Withdrawal vs Deliverability plot from raw input data instead of requiring the user to entering these calculated values in the input template).

3 EXPERIMENTAL

3.1 Introduction

Given the large number of useful diagnostic plots and techniques available for inventory analysis, we considered the ability of the software to automatically generate and interactively interpret inventory data to be of paramount importance in the development of the software.

Of nearly equal importance was the inclusion of HELP features that would allow storage engineers (especially inexperienced storage engineers) to more confidently employ the numerous graphical analysis techniques available, to fully appreciate the assumptions, limitations, and dangers associated with the application of these techniques to their specific reservoirs, and to provide the necessary technical references to more fully research the various inventory analysis methodologies.

All of this needed to be done in a software environment that allowed deployment of a product to users having a variety of types and versions of software available on their PC's. Therefore, careful consideration was given to the development platform used to develop the software, as well as any additional software requirements required for data importation into the software.

3.2 Software Development Platform and Layout

Given the above considerations, we decided to use Visual Basic^{TM} as the software development platform, EXCEL^{TM} to store raw inventory data for import into the software, and WORD^{TM} to export reports.

Visual Basic^{TM} was selected as the development platform to allow deployment of the software across a variety of platforms and minimizes the amount and type of specific software required to be installed on users' computer. EXCEL^{TM} and WORD^{TM} were selected because they are ubiquitous in the UGS industry.

There are five major areas or windows in the software work area (**Figure 2**):
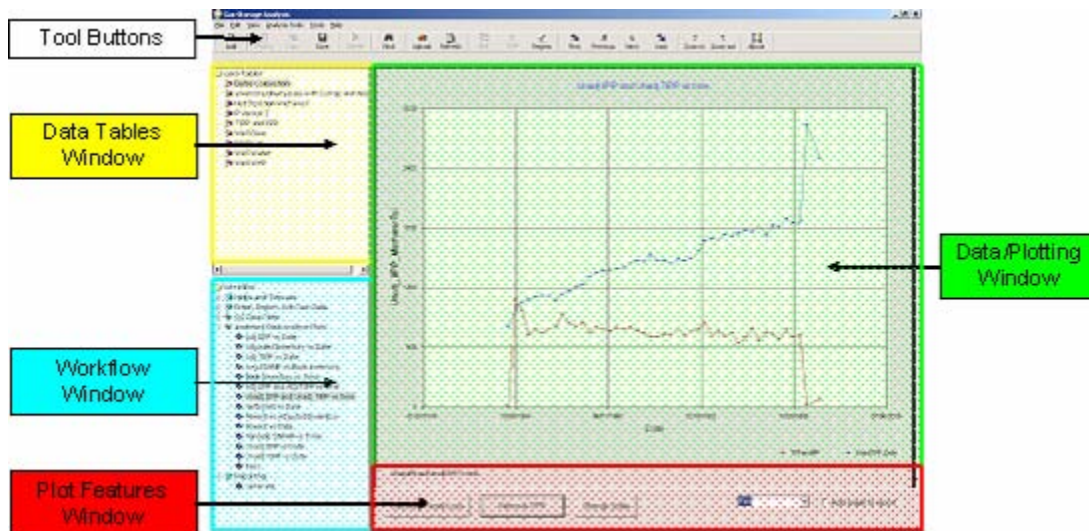
Figure 2: Major windows in the software work area

- At the extreme top of the work area (just below the various menus) are several toolbars associated with different aspects of inventory analysis calculations and workflow (e.g., BHP, BHP/Z, and Inventory Per Pound calculations, etc).

- On the top left portion of the screen is a window (highlighted in yellow) showing the tables containing input and calculated data.

- On the bottom left portion of the screen is a window (highlighted in blue) that shows an outline (in tree structure) of the workflow, including help options and reporting features.

- On the top right portion of the screen is a window (highlighted in green) that show table or plot information highlighted in the Data Table window or the Workflow window.

- On the bottom right portion of the screen is a window (highlighted in red) that contains various buttons that allow modification of various plot features.

The following sections provide a general description of software capabilities. For more comprehensive details and discussion of using this software can be found in the User's Manual (**Appendix I**).

3.3 Inventory Analysis Workflow

The general workflow followed for inventory analysis using this new software is summarized in **Figure 3**. This workflow is reflected in the structured order shown in the workflow window of the software, which was intentionally designed as such to promote use of proper inventory analysis workflow. For a more complete discussion of the inventory analysis process, see the Inventory Analysis Primer in **Appendix II**.
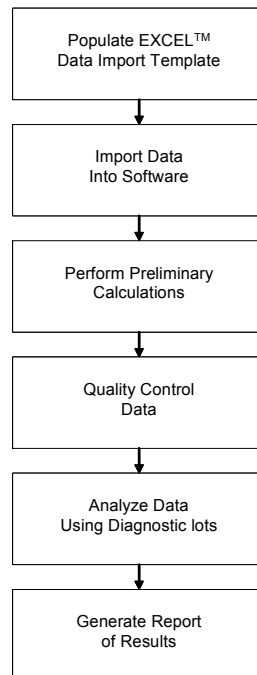
Figure 3: General workflow followed for inventory analysis using new software

The first step involves inputting raw inventory data into an EXCEL™ template. This data is then imported into the new software and stored in an ACCESS™ database for later manipulation. Next, basic calculations necessary to generate plots of historical operating parameters and specialized diagnostic plots are made. Several graphical control checks are then made of the data to identify any obvious errors in the raw and calculated data. Once the data QC process is completed, the user reviews and analyzes plots of historical operating data and interprets the specialized diagnostic plots that are pertinent to his specific field. Finally, the user constructs a draft report by selecting the specific plots to be included in the final report. Additional details of these processes are discussed below.

3.3.1 Populating Excel Input Template

Several potential options were available for data importation into the software. On the simplest end of the spectrum would be direct input of data into the software. Although this option would have been the easiest programming option, it was considered neither efficient nor user-friendly. On the complex end of the spectrum would be the interactive importation of data from *any* source (Access™, EXCEL™, ASCII, etc.) into the software. Although this would be the most user-friendly option, the level of programming effort to properly accomplish this was considered beyond the scope of this project.

Therefore, development of an EXCEL™ template which would act as an intermediate storage area for input data was considered a reasonable compromise, and was constructed. Selection of EXCEL™ for the template was strongly influenced by the fact that it is perhaps the most ubiquitous software used by storage engineers.

There are eight input sheets in the EXCEL™ template. Each input sheet includes a text box containing help information that 1) explains the type of data stored in the sheet, 2) describes the type, format, and units of the input items in the sheet (and whether they are required to be input by the user of if they are calculated by the program), and 3) and provides an example input data set. An example of an input sheet and the associated help information is shown in **Figure 4.**
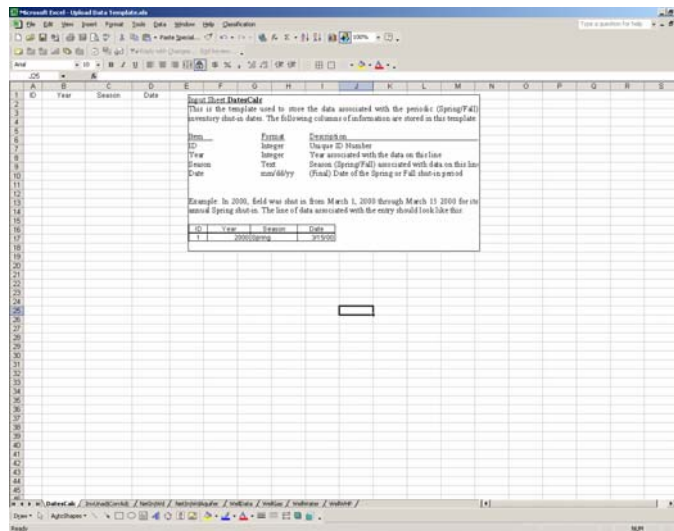
Figure 4: Example input sheet in EXCEL™ template and associated help information.

The first input sheet in the EXCEL^{TM} input template contains information related to the periodic (Spring/Fall) inventory shut-in dates. Four columns of information are stored in this sheet of the input template:

Item	Format	Description
StorageField	Text	Name of the Storage Field
Year	Integer	Year associated with the data on this line
Season	Text	Season (Spring/Fall) associated with data on this line
Date	mm/dd/yy	(Final) Date of the Spring or Fall shut-in period

Example data provided was as follows: In 2000, The Heap Big storage field was shut in from March 1, 2000 through March 15, 2000 for its annual Spring shut-in. In this case, the line of data associated with the entry should look like this:

StorageField	Year	Season	Date
Heap Big	2000	Spring	3/15/00

The second input sheet in the EXCEL^{TM} input template contains information related to book inventory and ADJUSTMENTS to the book inventory data. An ADJUSTMENT to book inventory is any modification to book inventory, including adjustments made for unknown losses, as well as known and quantified losses (e.g., well test in which gas was flared to atmosphere).

For example, if inventory analyses identify a total gas loss of 1 BCF between 2000 and 2003, but no specific cause of the loss can be identified, then an adjustment to the inventory necessary to correct the books is input here. Similarly, if a well is tested and flow rates and flow times are accurately measured during the test, then the volumes flared during the test would be considered an adjustment, since we know the date on which the test occurred and we measured the produced volumes.

The following columns of information are stored in this sheet of the input template:

Item	Format	Description
ID	Integer	Unique ID Number
Date	mm/dd/yy	Date
Unadjusted_Inventory_Bscf	Number	Unadjusted Book Inventory Volume, BCF
Corr_Vol	Number	Correction Vol – IGNORE THIS COLUMN
Cum_Corr	Number	Cumulative Correction Volume, BCF
Adj_Vol	Number	Adjustment Volume, BCF
Cum_Adj	Number	Cumulative Adjustment Volume, BCF
Inventoy_Corrected_Adjusted (Calc'd)	Number	Unadjusted Book Inventory Vol BCF

Note that "Corr_Vol" and "Cum_Corr" values are NOT used in the software at this time, and should be entered as zeros. These were included because we anticipate using these columns in future software upgrades.

Example data provided was as follows: Inventory analysis identified a total gas loss of 1 BCF between 1/1/2000 and 12/31/2003, which was booked on 12/31/2003. The Unadjusted Book Inventory on this date was 0.5 BCF. In this case, the entry should look like this (NOTE: the value in column Inventory_Corrected_Adjusted is calculated by the spreadsheet – it is not necessary to input this calculated number):

ID	Date	Unadjusted_Inventory_Bscf	Corr_Vol	Cum_Corr	Adj_Vol	Cum_Adj	Inventory_Corrected_Adjusted
1	12/31/03	0.500	-	-	1.000	1.000	1.500

The third input sheet in the EXCEL^{TM} input template contains information related to daily net injection/withdrawal volumes for the field. The following columns of information are stored in this sheet of the input template:

Item	Format	Description
ID	Integer	Unique ID Number
Date	mm/dd/yy	Date of recorded net INJ/WD for field
Net_InjWd_Mscf	number	Mscf of INJ(+) or WD(-) occurring on date

Example data might look as follows:

1	11/8/76	-4580
2	11/9/76	-5000
3	11/10/76	-5000
4	11/11/76	-5000
5	11/12/76	-728
6	11/13/76	0
7	11/14/76	0
8	11/15/76	0
9	11/16/76	0

The fourth input sheet in the EXCEL^{TM} input template contains information necessary to generate the plot most frequently used to assess inventory in aquifer storage fields (i.e., the deliverability versus cumulative withdrawal plot, sometimes displayed as the deliverability versus inventory plot). The following columns of information are stored in this sheet of the input template:

Item	Format	Description
ID	Integer	Unique ID Number
Date	mm/dd/yy	Date of recorded net INJ/WD for field
Net_InjWd_Mscf	Number	Mscf of INJ(+) or WD(-) occurring on date
Inventory	Number	Unadjusted Book Inventory Volume, BCF
CumWD	Number	Cum withdrawal since last Spring/Fall shut-in date
Abs_Q	Number	Absolute value of injection or withdrawal rate

Typical input data might look like the following:

ID	Date	Net_InjWd_Mscf	Inventory	CumWD	Abs_Q
8	08-Nov-76	-4580	1525420	4580	4580
9	09-Nov-76	-5000	1520420	9580	5000
10	10-Nov-76	-5000	1515420	14580	5000
11	11-Nov-76	-5000	1510420	19580	5000
12	12-Nov-76	-728	1509692	20308	728
13	13-Nov-76	0	1509692	20308	0
14	14-Nov-76	0	1509692	20308	0
15	15-Nov-76	0	1509692	20308	0
16	16-Nov-76	0	1509692	20308	0

The fifth input sheet in the EXCEL^{TM} input template contains individual well data. The following columns of information are stored in this sheet of the input template:

Item	Format	Description
Well ID	Text	Name of the Storage Well
Well Type	Text	Well Type (IW, OB, …)
Well Wt Fact	Number	Well Weighting Factor for BHP calculation
Resv Depth	Number	True Vertical Depth to Reservoir in Well
X	Number	X-Coordinate of Well Location
Y	Number	Y-Coordinate of Well Location

Data for a field having two IW wells and one OBS well might look like this:

Well_ID	Well_Type	Well_Wt_Fact	Resv_Depth	X	Y
3625	IW	1	2982	1	7
3667	IW	1	3092	1	8
3684	OB	1	3088.5	1	9

The sixth input sheet in the EXCEL^{TM} input template contains information related to individual well net gas Injection/Withdrawal volumes (e.g., flow rates measured at individual wellheads, if available). Four columns of information are stored in this sheet of the input template:

Item	Format	Description
ID	Integer	Unique Identifier
Date	Date	Date of recorded net injection for well
Well ID	Text	Name of the Storage Well
Net_Vol_Gas	Number	Net INJ(+) or WD(-) gas vol for well (Mscf)

Data for Field XYZ having has two IW wells might look like this:

ID	Date	Well_ID	Net_Vol_Gas
1	3/15/01	1	-2000
2	3/15/01	2	-1800
3	3/16/01	1	-1990
4	3/16/01	2	1780
5	3/17/01	1	1500
6	3/17/01	2	1200

The seventh input sheet in the EXCEL^{TM} input template contains information related to individual well produced water volumes (if available). Four columns of information are stored in this sheet of the input template:

Item	Format	Description
ID	Integer	Unique Identifier
Date	Date	Date of recorded net injection for well
Well ID	Text	Name of the Storage Well
Net_Vol_Wtr	Number	Net INJ(+) or WD(-) water vol (Bbls)

Data for a field XYZ having has two IW wells might look like this:

ID	Date	Well_ID	Net_Vol_Wtr
1	3/15/01	1	1
2	3/15/01	2	2
3	3/16/01	1	1
4	3/16/01	2	2
5	3/17/01	1	0.5
6	3/17/01	2	0.3

The last input sheet in the EXCEL^{TM} input template contains information related to individual wellhead pressure data. The following columns of information are stored in this sheet of the input template:

The following columns of information are stored in this template:

Item	Format	Description
ID	Integer	Unique Identifier
Well ID	Text	Name of the Storage Well
Date	mm/dd/yy	Date of recorded wellhead pressure
WHP_psig	Number	Measured wellhead pressure in psig
Comment	Text	Comment
Given_BHP*	Number	Given BHP (if given)
Calc_BHP	Number	Calc'd BHP (if BHP not given, enter zeros)

Example: Field has four IW wells. In this case, the entry might look like this (for one shut-in date):

ID	Well_ID	Date	WHP_psig	Comments	Given_BHP	Calc_BHP
1	1	9/15/50	55		0	0
2	2	9/15/50	67		0	0
3	3	9/15/50	49		0	0
4	4	9/15/50	50		0	0

* Note: Given_BHP values are NOT used in the software at this time, and should be entered as zeros. These were included because we anticipate using this column in future software upgrades.

3.3.2 Importing Data to Software

Use of the EXCEL^{TM} input template ensures uniformity of data type and format, which allows direct uploading of this data into the software. This process is completely automated, and required no user-intervention. Although this process may takes several seconds, depending on the dataset size, it only needs to be performed once.

3.3.3 Performing Preliminary Calculations

Several preliminary calculations are necessary before starting the inventory analysis process, including calculation of BHP's, Z-factors, and Inventory-Per-Pound (IPP) values. Numerous methodologies are available for these calculations. For the initial release of the software, we decided to include only the most popular calculations/correlations.

For conversion of WHP to BHP, the user can choose between the exponential equation and Cullender and Smith. For the Z-factor calculation, the user can choose between Abou-Kassem and Hall-Yarborough correlations. There are certainly more rigorous (and arguably more technically correct) methods for making BHP and Z-factor calculations. However, in the authors' experience, these seem to be the most popular methods employed by storage operators today. Understandably, they likely continue to use older calculation methodologies to maintain continuity with historical inventory calculations.

The IPP calculations (both Total IPP and Incremental IPP) were calculated based on the definition of these variables.

The total inventory per pound is defined as follows:

$$TIPP = \frac{G_b}{p/z}$$

where:

$TIPP$ = Total inventory per pound (total inventory per pressure unit)

G_b = Book inventory

$$p/z \quad = \quad \text{Average pressure divided by real gas deviation factor}$$

The incremental inventory per pound is defined as:

$$IIPP = \frac{\left(G_{bf} - G_{bs}\right)}{\left((p/z)_f - (p/z)_s\right)}$$

where

IIPP = Incremental inventory per pound (pressure unit)
G_b = Book inventory
P/z = Average pressure divided by real gas deviation factor
s = Spring, following withdrawal season
f = Fall, following injection season

3.3.4 Quality Controlling Input/Calculated Data
Several plots can be generated and reviewed to ensure calculations made within the software were performed properly. These QC plots include:

- SIWHP vs SIBHP for All Wells
- Average Field SIWHP vs Avg Field SIBHP
- Average Field BHP vs Field Z-Factor
- Average Field BHP vs Field BHP/Z-Factor

None of the correlations currently employed in the software should exhibit discontinuities. Therefore, all of these plots should exhibit smooth trends with no outlying data points. The presence of any outlying data points on the QC plots may indicate that calculations have not been performed properly, and should be brought to the attention of the software developers.

3.3.5 Analyzing Data Using Diagnostic Plots
There are a very large number of plots available in the software to allow for comprehensive analysis of available inventory data. These are discussed below:

3.3.5.1 Plots to review trends in basic operating data
Several plots are used to review and assess trends in basic operating data, including:

- Net Injection/Withdrawal Rates vs Time
- Unadjusted Book Inventory vs Time
- Adjustments to Book Inventory vs Time
- Adjusted Book Inventory vs Time
- SIWHP vs Time

Since most approaches to inventory analysis implicitly assume that the storage facility has been operated in a fairly consistent manner over time, it is important to verify

operational consistency using the above plots. Look for consistency in the pressures and inventory levels from year to year.

During this process, several very basic trends may be identified in the raw operational data that tip off the analyst concerning possible inventory problems. For example, if the historical plots of Spring/Fall inventory and pressure indicate that the same maximum pressure is reached at the end of each injection cycle, but the corresponding inventory levels are increasing over time, you can be sure the IPP plots will indicate ongoing losses (or perhaps increases in the non-effective gas volumes).

3.3.5.2   Diagnostic plots to identify/quantify gas losses
There are several diagnostic plots used to identify and quantify gas losses, including:

- o Unadjusted Book Inventory vs Time
- o Average SIWHP vs Time
- o P/Z vs Time
- o Avg SIWHP vs Unadjusted Book Inventory
- o Avg P/Z vs Unadjusted Book Inventory
- o Unadjusted TIPP vs Time
- o Unadjusted IIPP vs Time
- o Deliverability vs Cumulative Withdrawal
- o Deliverability vs Unadjusted Inventory

By using all of the plots above to assess potential inventory problems, the analyst will have a much higher confidence level in his conclusions, since those conclusions will be supported by the character of *all* the plots used in his analysis – not just one or two commonly used analysis plots.

3.3.5.3   Plots to verify that adjustments resolve discrepancies
After completing an inventory analysis and estimating loss rates and volumes, it is beneficial to generate the various diagnostic plots used in the analysis using post-analysis adjusted inventory volumes. If the diagnostic plots generated using the adjusted volumes (i.e., adjusted as per the results of your inventory analysis) indicate no ongoing losses, the analyst can be confident the appropriate adjustments have been determined.

These plots would include the following:
- o Avg SIWHP vs Adjusted Book Inventory
- o Avg P/Z vs Adjusted Book Inventory
- o Adjusted TIPP vs Time
- o Adjusted IIPP vs Time
- o Deliverability vs Adjusted Inventory

3.3.6 Generating Reports
In order to enhance the software's user-friendliness and practicality, we incorporated an option to automatically generate reports from within the software. This feature allows the user to check a box on each plot they wish to include in the report. After these boxes are

checked on all the plots the user wishes included in a report, the software will export to WORD^{TM} the reservoir input data and all of the plots having the "add graph to report" box checked.

Once exported to WORD^{TM}, the user can enhance the report by the addition of text to further document the input, processing, or analysis results. The final result will be a report in WORD^{TM} which summarizes the reservoir input data, all pertinent plots used in the analysis, and the analyst's comments and/or conclusions.

3.4 On-Line Help and References

Incorporation of extensive on-line help was considered a critical component of the project. Consequently, a considerable amount of time and effort was dedicated to making help options complete, informative, and useful to new or inexperienced engineers.

Help modules were constructed to help the user in the data input process, interpret the various diagnostic plots, perform on-the-fly calculations useful in inventory analysis, explain software features in detail, provide example inventory analysis problems and tutorials, explain commonly used gas storage terms and phases, and provide a comprehensive list of gas storage references and technical papers.

3.4.1.1   Help: Input Screens

Help is available for each sheet in the EXCEL^{TM} input template. This help provides a general description of the type of data requested on the sheet, the specific data items required, a brief description (including the data format) of each input data item, and an example input data set.

3.4.1.2   Help: Analysis Plots

Help is also available for the interpretation and analysis of each plot used in the inventory analysis process. Included is an example plot of typical data, a description of the purpose of the plot, a discussion of the assumptions that are inherent in the use of the particular plot, the applicability of the plot, the dangers of using the specific plot, and any pertinent technical references related to the diagnostic plot.

Also included for the diagnostic plots are typical "type curves" showing what the diagnostic plot might look like for the cases of gas losses, gas gains, gas bubble growth, and/or gas bubble shrinkage.

3.4.1.3   Help: Toolbox

A "toolbox" was developed to perform various calculations that may be useful in the process of inventory verification. EXCEL^{TM} was selected as the development platform for this toolbox due to the ease of performing calculations and generating graphics and because it is ubiquitous in the UGS industry. The tools in this toolbox include the following:

- Estimated line losses as per a U.S. Bureau of Mines publication

- Estimated volume of gas vented during a wellbore blowdown

- Estimated volume of gas vented during a multi-rate well test

- Estimated volume of gas contained in a pipeline at specified inlet and outlet conditions.

- Estimated shut-in pseudopressure vs time for assumed reservoir properties (to estimate time to stabilized shut-in pressure).

- Estimate (first order) of minimum gas flow rate to continuously unload fluids from a wellbore of specified configuration.

- Units Conversion Table

- Chert of estimated residual gas saturation as a function of porosity

- Chart estimating (HP)/(MMscf/D) required to compress typical storage gas at 100 degrees F to 1000 psi using single stage compression.

3.4.1.4   Help: Users Manual With Example Problem Tutorial
A comprehensive Users Manual has been written that describes the various features available in the software and how to use them. This Users Manual is included in **Appendix I**.

3.4.1.5   Help: Inventory Verification Primer
This document provides a very concise summary of the objectives, theory, data requirements, diagnostic plots, and analyses techniques involved in inventory analysis. It also includes a sample dataset and the analysis of the sample dataset. This Primer is included in **Appendix II**.

3.4.1.6   Help: References
A comprehensive list of references and technical papers (organized by topic) pertaining to the various aspects of underground natural gas storage have been prepared. These references are included in **Appendix III**.

3.4.1.7   Help: Storage Inventory and Deliverability Terminology
A list of the most common underground gas storage inventory and deliverability terms have been compiled and defined. These definitions are included in **Appendix IV**.

3.4.1.8   Help: Underground Gas Storage Glossary
A comprehensive glossary of the various terms used in the underground gas storage industry has been compiled, and is included in **Appendix V**.

4 RESULTS AND DISCUSSION

4.1 Software Developed

Work performed under contract DE-FC26-03NT41779 has resulted in the development of a comprehensive inventory analysis software tool that allows easy importation of typical storage inventory data, automatically generates pertinent raw data plots and analysis plots for the analysts review and processing, provides on-line help that provides an overview of the inventory analysis process and explains the assumptions, applications, limitations, and processes used to analyze specific diagnostic plots, and provide a "toolbox" application that would perform calculations useful in the process of inventory analysis.

This new tool significantly improves operators' ability to effectively monitor inventory and resolve gas loss issues by making inventory analysis processes much more automated and much more comprehensive. It also enhances the analysis process by guiding the engineer to the appropriate analysis techniques and away from the inappropriate analysis techniques via the on-line help tools.

4.2 Cost Benefit Assessment

In an effort to estimate the efficiency gains achievable using this newly developed software, we re-analyzed several sets of inventory data that we had already analyzed for previous clients. By recording the time required to re-analyze the inventory data and generate a draft report using the new software and comparing this to the estimated time it took us to manually analyze the data without the new software, we could quantify efficiency gains.

Based on the results of this testing, it is estimated that the time required to perform a "typical" comprehensive inventory analysis was reduced by at least 50%. In several cases, the time required to go from raw data to a finished report was reduced very significantly, and resulted in completion of a finished report in a matter of 1-2 man-days, whereas previous analysis of the same data without the newly developed software required 1-2 man-weeks.

Although these represent significant gains in efficiency for the practicing storage engineer, the real value of the product is derived from enabling storage engineers to more confidently quantify ongoing storage losses earlier than if traditional methods alone were employed. This would allow earlier deployment of loss mitigation efforts and reduce the amount of losses incurred by storage operators.

Assuming that the average UGS operator has only 1/2 of one percent annual loss rate, the ability to detect and mitigate these losses just 2 years earlier would save operators over $300 million at 2007 gas prices. Thus, even assuming the comprehensive inventory analysis software developed during this study has only a modest impact on inventory management, the financial impact to the industry is significant.

5 CONCLUSIONS

The development of a comprehensive inventory analysis software tool was completed and tested under contract DE-FC26-03NT41779. Benchmark testing suggests that operators' ability to efficiently analyze inventory data and resolve gas loss issues have been significantly improved.

Typical reductions in manpower requirements on the order of 50% were observed when the new software was used to perform typical comprehensive inventory analyses. The software also enhances the analysis process by helping the storage engineer use only the appropriate analysis techniques and avoid inappropriate techniques via the on-line help tools.

Deployment of this software in the UGS industry is expected to significantly reduce the time required to conduct inventory analysis and promote more accurate interpretation of inventory data, especially amongst young and/or inexperienced Gas Storage engineers.

Although the gains in efficiency for the practicing storage engineer are significant, the real value of the product is derived from enabling storage engineers to more confidently identify ongoing storage loss rates and volumes earlier than if traditional methods alone were employed. Conservative estimates suggest the economic impact could easily exceed $300 million.

6 REFERENCES

1. Piper, L.D., McCain, W.D. Jr., Corredor, J.H.: "Compressibility Factors for Naturally Occurring Petroleum Gases," paper SPE 26668 presented at the 1993 SPE Annual Technical Conference and Exhibition, Houston, Texas, 3-6 October.

2. McCain, W.D. Jr.: The Properties of Petroleum Fluids, 2nd ed., Pennwell, 1990.

3. Al-Hussainy, R., Ramey, H.J., Jr., and Crawford, P.B.: "The Flow of Real Gases Through Porous Media," JPT (May 1966) 624; Trans. AIME 237.

4. Cullendar, N.H. and Smith, R.V.: "Practical Solution of Gas Flow Equations for Wells and Pipelines With Large Temperature Gradients," Trans. AIME 207 (1956) 281-287.

5. Young, K.L.: "Effect of Assumptions Used to Calculate Bottom-Hole Pressures in Gas Wells," JPT (April 1967) 547-550.

6. Dranchuk, P.M., and McFarland, J.D.: "The Effect of the Time Rate of Change of Momentum on Bottom-Hole Pressure in Flowing Gas Wells," J. Cdn. Pet. Tech. (April-June 1974) 34-38.

7. Lee, W.J., Rollins, J.B., and Spivey, J.P.: Pressure Transient Testing, p. ???

8. Goode, P.A., and Thambanayagam, R.K.M.: "Pressure Drawdown and Buildup Analysis of Horizontal Wells in Anisotropic Media," SPEFE (December 1987) 683-697.

9. Odeh, A.S, and Babu, D.K.: "Transient Flow Behavior of Horizontal Wells: Pressure Drawdown and Buildup Analysis," SPEFE (March 1990) 7-15.

7 LIST OF ACRONYMS AND ABBREVIATIONS

AVG	=	Average
BHP	=	Bottom Hole Pressure
Deg F	=	Degrees Fahrenheit
Gb	=	Book Inventory
IIPP	=	Incremental Inventory Per Pound
MMSCF/D	=	Thousand Mscf/D
P/Z	=	Pressure divided by Z-factor
Psi	=	Pressure per square inch
SIBHP	=	Shut-In Bottom Hole Pressure
SIWHP	=	Shut-In Wellhead Pressure
SW	=	Software
TIPP	=	Total Inventory Per Pound
UGS	=	Underground Gas Storage
VBA	=	Visual Basic Application
WHP	=	Wellhead Pressure
Z	=	Z-Factor

8 NOMENCLATURE

Symbols

IPP	=	Inventory per "pound" (i.e., per p/z)
TIPP	=	Total Inventory per "pound" (i.e., per p/z)
IIPP	=	Incremental Inventory per "pound" (i.e., per p/z)
G	=	Inventory (Gas In Place)
p/z	=	pressure/z-factor
q	=	flow rate, Mscf/D

Subscripts

b	=	book
f	=	Fall
s	=	Spring

Appendix I

Comprehensive Inventory Analysis Software - Users Manual

Table of Contents

1 Overview

1.1 Background

This manual explains how to use the software developed under contract DE-FC26-03NT41779. The primary objective of the project was to develop a comprehensive inventory analysis software tool that would:

- Allow easy importation of typical storage inventory data,

- Automatically generate pertinent raw data plots and analysis plots for the analysts review and processing,

- Provide on-line help that provides an overview of the inventory analysis process and explains the assumptions, applications, limitations, and processes used to analyze specific diagnostic plots, and

- Provide a "toolbox" application that would perform calculations useful in the process of inventory analysis.

The software development and design is briefly reviewed, including a summary of the major components of the software and online help features. An example dataset and analysis is presented.

This software was developed in the VisualBasic^{TM} programming environment, uses Microsoft ACCESS^{TM} for data storage, employs Microsoft EXCEL^{TM} as a "bridge" between users' data and the ACCESS^{TM} database, and exports reports to WORD^{TM}. EXCEL^{TM} was chosen for use as a template to hold data due to the ubiquitous use of EXCEL^{TM} in the UGS industry. ACCESS^{TM} was chosen due to its excellent data handling and data manipulation capabilities. Use of this software requires the installation of EXCEL^{TM} and WORD^{TM} on the user's computer, but not ACCESS^{TM}.

1.2 Software Windows Layout

There are five major areas or windows in the software work area (**Figure 1**): 1) At the extreme top of the work area (just below the various menus) are several toolbars associated with different aspects of inventory analysis calculations and workflow (e.g., BHP and BHP/Z calculations, Inventory Per Pound calculations, etc). 2) On the top left portion of the screen is a window that show the tables containing the input and calculated data, 3) On the bottom left portion of the screen is a window that shows an outline (in tree structure) of the workflow, including help options and reporting features, 4) On the top right portion of the screen is a window that show table or plot information highlighted in the Data Table window or the Workflow window, and 5) On the bottom right portion of the screen is a window that contains various buttons that allow modification of various plot features.

Figure 1: Major windows in the software work area

1.3 Help Available

HELP tools are available to guide the users as they use this software. All of the HELP features are accessible from the HELP menu located at the top of the software screen. Select HELP items (those HELP items the user is likely to use during the inventory analysis process) are also located in the Workflow Window of the work area, under "Helps and Tutorials."
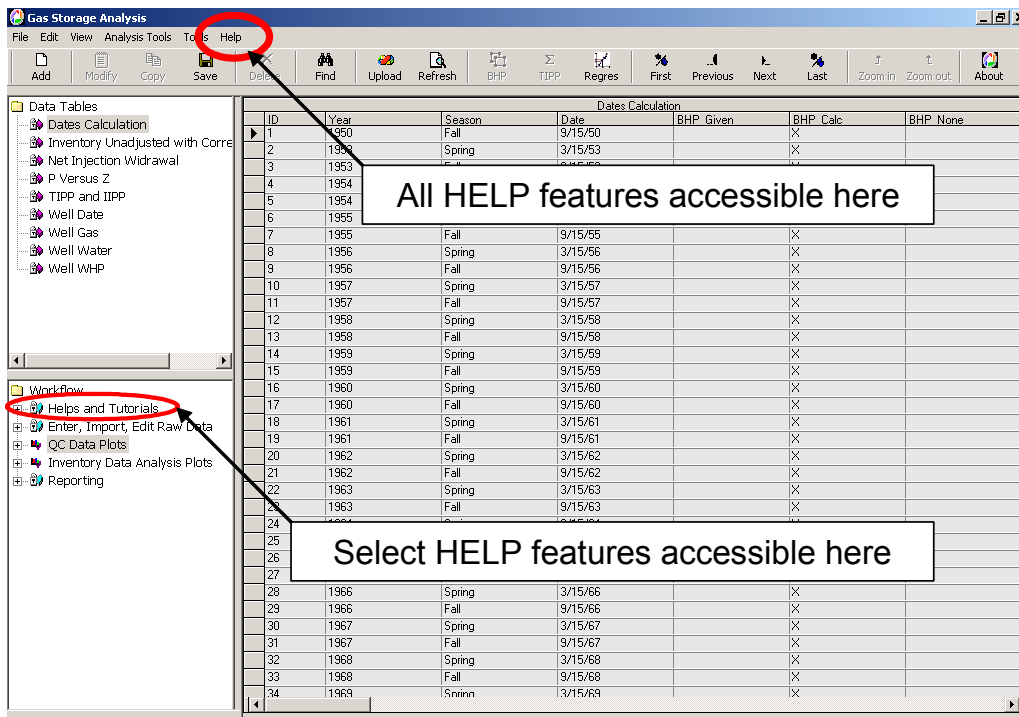
Figure 2: Location of Help Items

1.3.1 *Inventory Analysis Primer*

This is a document that summarizes the objectives, theory, data required, diagnostic plots, and analyses techniques involved in inventory analysis. It also includes a sample dataset and the analysis of the sample dataset.

1.3.2 *Summery of References and Papers*

This document summarizes references and technical papers related to Underground Gas Storage (these are not limited to inventory analysis, but cover a wide range of UGS topics) including:

- Introduction to Gas Storage
- Gas Storage Field Design
- Optimization
- Migration and Monitoring
- Inventory Verification
- Deliverability Maintenance and Enhancement
- Simulation of UGS Reservoirs
- Top Twenty Technical Papers

1.3.3 *Inventory Analysis Toolbox*

This is an EXCEL^{TM} spreadsheet that summarized and/or calculates various data useful in the process of inventory analysis, including:

- Estimated line loss rates/volumes as per a Bureau of Mines Publication
- Estimated volume of gas vented during a wellbore blowdown
- Estimated volume of gas vented during a multi-rate well test
- Estimated volume of gas contained in a pipeline at specified inlet and outlet conditions.
- Estimated shut-in pseudopressure vs time for assumed reservoir properties (to estimate time to stabilized shut-in pressure).
- Estimate (first order) of minimum gas flow rate to continuously unload fluids from a wellbore of specified configuration.
- Units Conversion Table
- Chert of estimated residual gas saturation as a function of porosity
- Chart estimating (HP)/(MMscf/D) required to compress typical storage gas at 100 degrees F to 1000 psi using single stage compression.

1.3.4 *Input Template Help Information*

There is help information, including a description of the data needed and an example data input set, for each input sheet in the EXCELTM input template.

1.3.5 *Technical Help for Diagnostic Plot Analysis*

This document summarizes how various diagnostic plots are used and analyzed. In most cases, the following information is presented for each diagnostic plot:

- Example plot

- Purpose of the plot

- Assumptions inherent in construction/use of the plot

- Applicability of the plot

- Dangers associated with misuse of plot

- References

1.3.6 *Gas Storage Inventory and Deliverability Terminology*

This document lists and describes/defines various inventory and deliverability terms.

1.3.7 *Underground Gas Storage Glossary*

This document lists and describes/defines various terms used in UGS industry, and is much broader in scope than the "Gas Storage Inventory and Deliverability Terminology: document above

2 Workflow

Figure 3 summarizes the basic workflow followed for inventory analysis using the new software.

Figure 3: General workflow followed for inventory analysis using new software

The first step involves inputting the raw inventory data into an EXCEL^{TM} template. This data is then imported into the new software and stored in an ACCESS^{TM} database for later manipulation. Next, basic calculations necessary to generate plots of historical operating parameters and specialized diagnostic plots are made. Several graphical control checks are then made of the data to identify any obvious errors in the raw and calculated data. Once the data QC process is completed, the user reviews and analyzes plots of historical operating data and interprets the specialized diagnostic plots that are pertinent to his specific field. Finally, the user constructs a report by selecting the specific plots to be included in a final report. Additional details of this process will be discussed in more detail later in this report.

2.1 Data Importing

An EXCEL^{TM} spreadsheet was created to facilitate transfer of data necessary for inventory analysis from the user to the software. This spreadsheet acts as a "template" to ensure the data types, order, and content are consistent with what the software expects upon import of the data. This template consists of an EXCEL^{TM} spreadsheet containing several worksheets, each containing similar data types.

Each sheet in the EXCEL^{TM} data template, and the input data contained in each of these sheets, is summarized below. Sample datasets for each sheet in the data template are also provided in the sheets and/or in the help screens shown on the right side of each sheet.

2.1.1 *DatesCalc InputTemplate*

This is the template used to store the data associated with the periodic (Spring/Fall) inventory shut-in dates and is shown with example data in **Figure 4**.
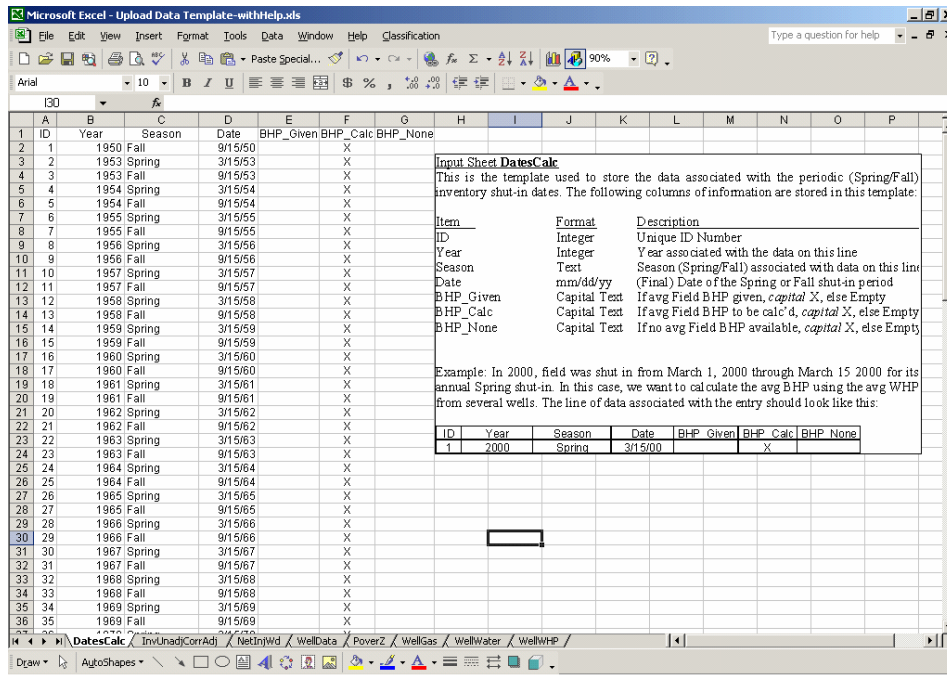
Figure 4: Template used to store the data associated with the periodic (Spring/Fall) inventory shut-in dates

The following columns of information are stored in this template:

Item	Format	Description
ID	Integer	Unique ID Number
Year	Integer	Year associated with the data on this line
Season	Text	Season (Spring/Fall) associated with data on this line
Date	mm/dd/yy	(Final) Date of the Spring or Fall shut-in period
BHP_Given	Capital Text	If avg Field BHP given, *capital* X, else Empty
BHP_Calc	Capital Text	If avg Field BHP to be calc'd, *capital* X, else Empty
BHP_None	Capital Text	If no avg Field BHP available, *capital* X, else Empty

Example: In 2000, field was shut in from March 1, 2000 through March 15 2000 for its annual Spring shut-in. In this case, we want to calculate the avg BHP using the avg WHP from several wells. The line of data associated with the entry should look like this:

ID	Year	Season	Date	BHP_Given	BHP_Calc	BHP_None
1	2000	Spring	3/15/00		X	

2.1.2 *InvUnadjCorrAdj* Input Template

This is the template used to store book inventory and ADJUSTMENTS to the book inventory data and is shown with example data in **Figure 5**.
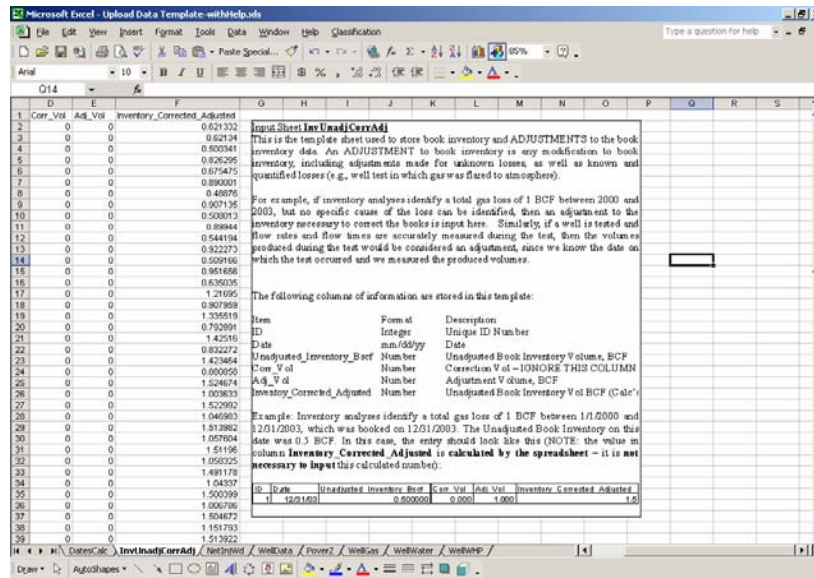
Figure 5: Template used to store book inventory and adjustments to the book inventory data

An ADJUSTMENT to book inventory is any modification to book inventory, including adjustments made for unknown losses, as well as known and quantified losses (e.g., well test in which gas was flared to atmosphere). For example, if inventory analyses identify a total gas loss of 1 BCF between 2000 and 2003, but no specific cause of the loss can be identified, then an adjustment to the inventory necessary to correct the books is input here. Similarly, if a well is tested and flow rates and flow times are accurately measured during the test, then the volumes produced during the test would be considered an adjustment, since we know the date on which the test occurred and we measured the produced volumes. The following columns of information are stored in this template:

Item	Format	Description
ID	Integer	Unique ID Number
Date	mm/dd/yy	Date
Unadjusted_Inventory_Bscf	Number	Unadjusted Book Inventory Volume, BCF
Corr_Vol	Number	Correction Vol – IGNORE THIS COLUMN
Adj_Vol	Number	Adjustment Volume, BCF
Inventoy_Corrected_Adjusted	Number	Unadjusted Book Inventory Vol BCF (Calc'd)

Example: Inventory analyses identify a total gas loss of 1 BCF between 1/1/2000 and 12/31/2003, which was booked on 12/31/2003. The Unadjusted Book Inventory on this date was 0.5 BCF. In this case, the entry should look like this (NOTE: the value in column **Inventory_Corrected_Adjusted** is **calculated by the spreadsheet** – it is **not necessary to input** this calculated number):

ID	Date	Unadjusted_Inventory_Bscf	Corr_Vol	Adj_Vol	Inventory_Corrected_Adjusted
1	12/31/03	0.500000	0.000	1.000	1.5

2.1.3 *NetInjWd Input Template*

This is the input template used to store daily net injection/withdrawal volumes for the field, and is shown with example data in **Figure 6**.
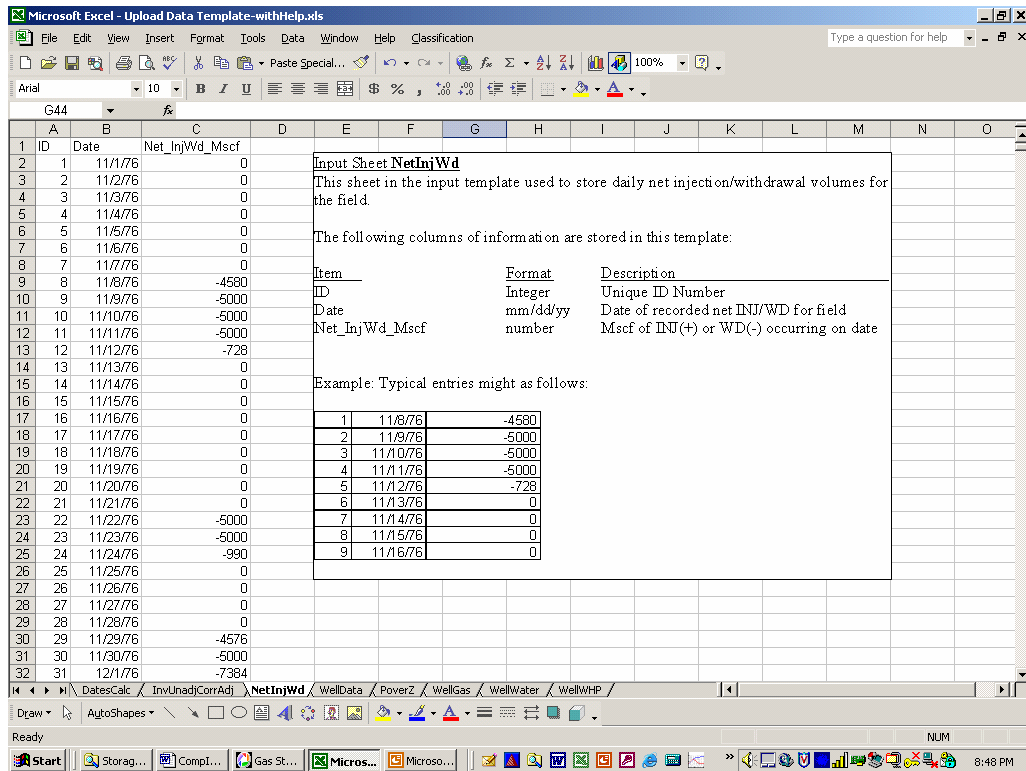
Figure 6: Template used to store daily net injection/withdrawal volumes for the field

The following columns of information are stored in this template:

Item	Format	Description
ID	Integer	Unique ID Number
Date	mm/dd/yy	Date of recorded net INJ/WD for field
Net_InjWd_Mscf	number	Mscf of INJ(+) or WD(-) occurring on date

Example: Typical entries might as follows:

1	11/8/76	-4580
2	11/9/76	-5000
3	11/10/76	-5000
4	11/11/76	-5000
5	11/12/76	-728
6	11/13/76	0
7	11/14/76	0
8	11/15/76	0
9	11/16/76	0

2.1.4 *WellData Input Template*

This template is used to store individual well data, and is shown with example data in **Figure 7**.
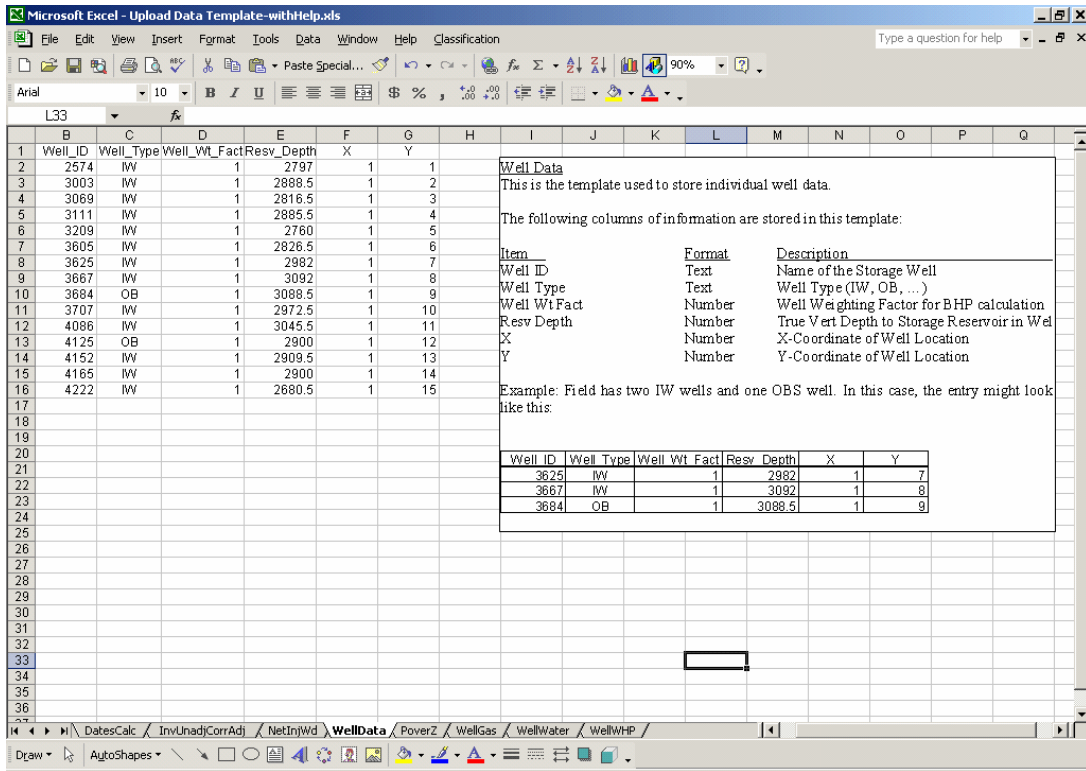
Figure 7: Template used to store individual well data

The following columns of information are stored in this template:

Item	Format	Description
Well ID	Text	Name of the Storage Well
Well Type	Text	Well Type (IW, OB, …)
Well Wt Fact	Number	Well Weighting Factor for BHP calculation
Resv Depth	Number	True Vert Depth to Storage Reservoir in Well
X	Number	X-Coordinate of Well Location
Y	Number	Y-Coordinate of Well Location

Example: Field has two IW wells and one OBS well. In this case, the entry might look like this:

Well_ID	Well_Type	Well_Wt_Fact	Resv_Depth	X	Y
3625	IW	1	2982	1	7
3667	IW	1	3092	1	8
3684	OB	1	3088.5	1	9

2.1.5 *WellGas* Input Template

This is the template used to store individual well net gas Injection/Withdrawal volumes (if available), and is shown in Figure 8.
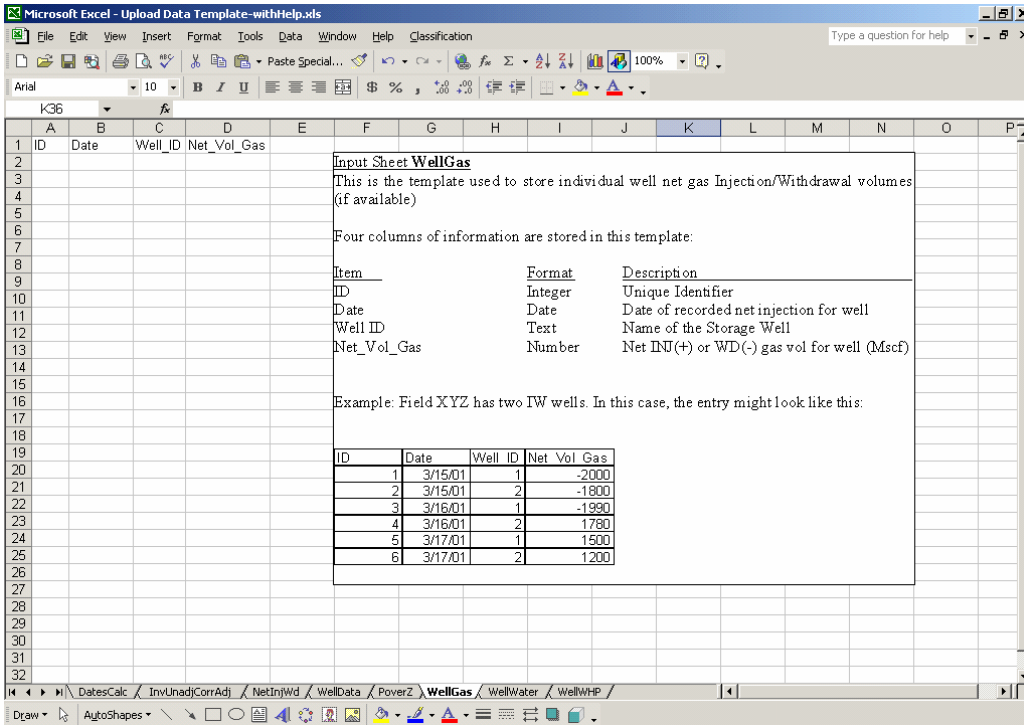
Figure 8: Template used to store individual well net gas Injection/Withdrawal volumes (if available)

Four columns of information are stored in this template:

Item	Format	Description
ID	Integer	Unique Identifier
Date	Date	Date of recorded net injection for well
Well ID	Text	Name of the Storage Well
Net_Vol_Gas	Number	Net INJ(+) or WD(-) gas vol for well (Mscf)

Example: Field XYZ has two IW wells. In this case, the entry might look like this:

ID	Date	Well_ID	Net_Vol_Gas
1	3/15/01	1	-2000
2	3/15/01	2	-1800
3	3/16/01	1	-1990
4	3/16/01	2	1780
5	3/17/01	1	1500
6	3/17/01	2	1200

2.1.6 *WellWater* Input

This is the template used to store individual well produced water volumes (if available), and is shown in
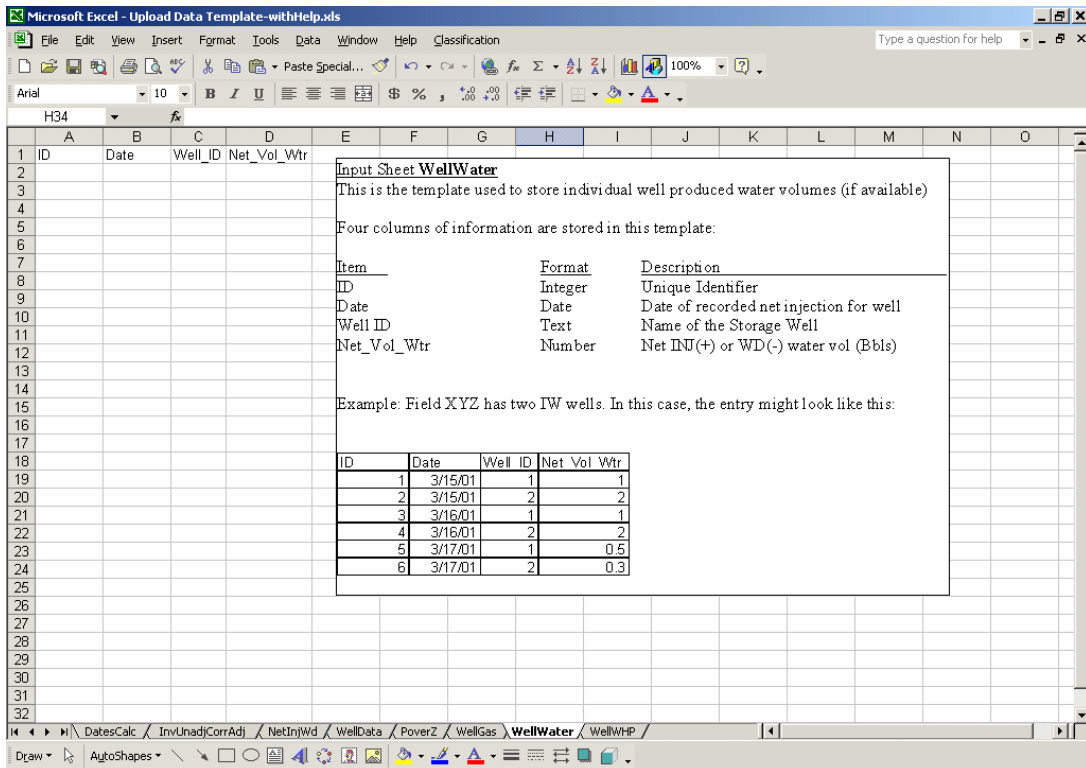
Figure 9: Template used to store individual well produced water volumes (if available)

Four columns of information are stored in this template:

Item	Format	Description
ID	Integer	Unique Identifier
Date	Date	Date of recorded net injection for well
Well ID	Text	Name of the Storage Well
Net_Vol_Wtr	Number	Net INJ(+) or WD(-) water vol (Bbls)

Example: Field XYZ has two IW wells. In this case, the entry might look like this:

ID	Date	Well_ID	Net_Vol_Wtr
1	3/15/01	1	1
2	3/15/01	2	2
3	3/16/01	1	1
4	3/16/01	2	2
5	3/17/01	1	0.5
6	3/17/01	2	0.3

2.1.7 *WellWHP Input Template*

This is the template used to store individual wellhead pressure data, and is shown with example data in **Figure 10**.
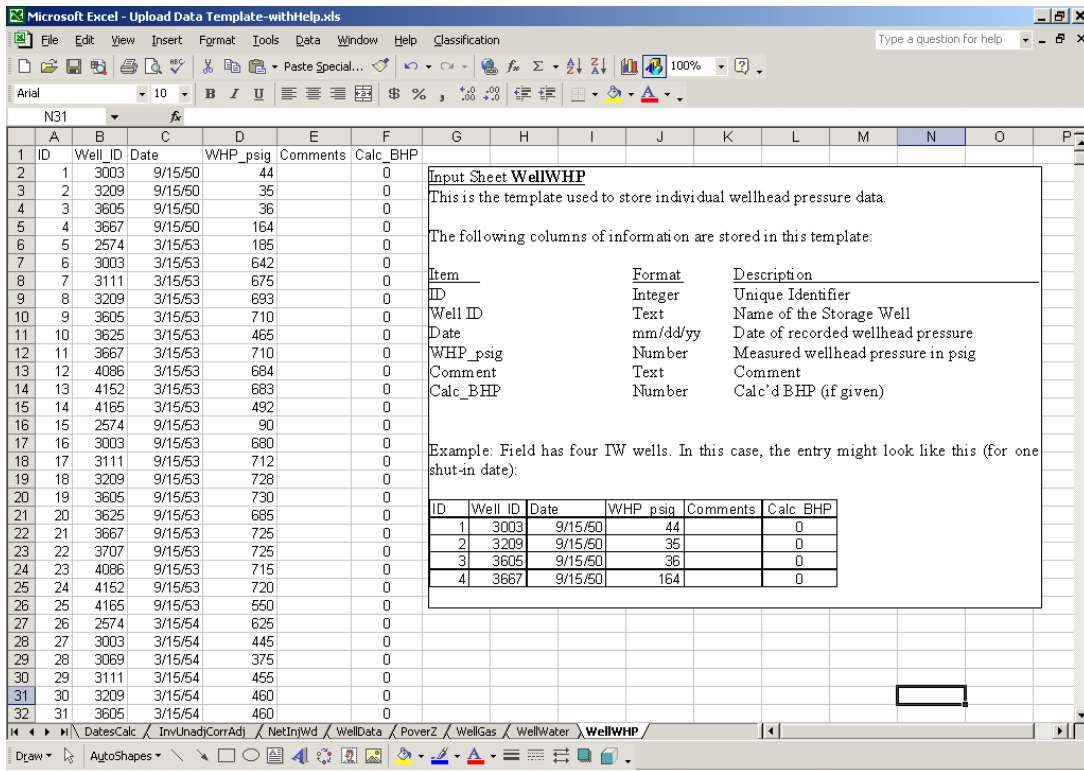
Figure 10: Template used to store individual wellhead pressure data

The following columns of information are stored in this template:

Item	Format	Description
ID	Integer	Unique Identifier
Well ID	Text	Name of the Storage Well
Date	mm/dd/yy	Date of recorded wellhead pressure
WHP_psig	Number	Measured wellhead pressure in psig
Comment	Text	Comment
Calc_BHP	Number	Calc'd BHP (if given)

Example: Field has four IW wells. In this case, the entry might look like this for one shut-in date:

ID	Well_ID	Date	WHP_psig	Comments	Calc_BHP
1	3003	9/15/50	44		0
2	3209	9/15/50	35		0
3	3605	9/15/50	36		0
4	3667	9/15/50	164		0

2.1.8 *Importing Data Into Software*

Once all necessary data is input into the data input template, we can import this data into the software. This is done using the **upload tool button**, or executing the "Upload to Database" command on the Tools Menu. This process may take a minute or so, so please be patient. This importing process is only necessary the first time data is uploaded to the software.
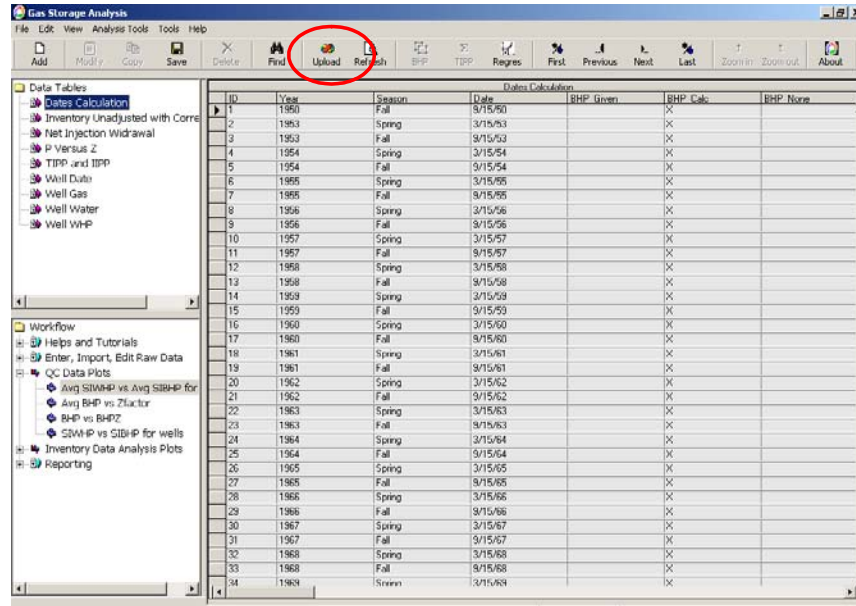
Figure 11: Location of Data Upload Tool Button

2.2 Data QC Process

There are several basic plots useful in identifying problems in input data and/or calculation results. These plots are shown in the Workflow Window, under the heading of **QC Data Plots**.
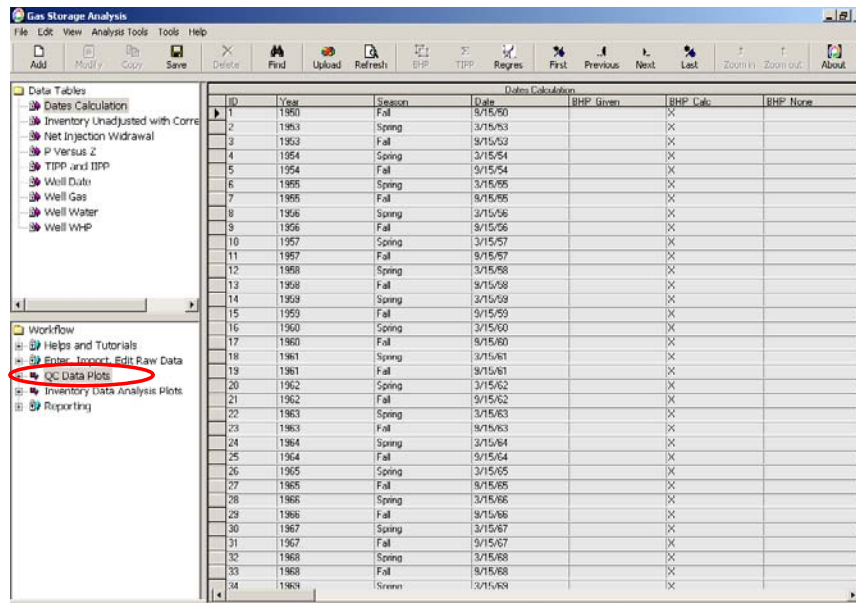
Figure 12: Location of QC Plots in Workflow Window

2.2.1 *Avg SIWHP vs Avg SIBHP QC Plot*

A plot of Avg SIWHP vs Avg SIBHP is shown in **Figure 13.** This plot should be a rather smooth line with no significant outlying points. Points that significantly deviate from the trend should be checked to ensure there are no errors in the calculation procedure.
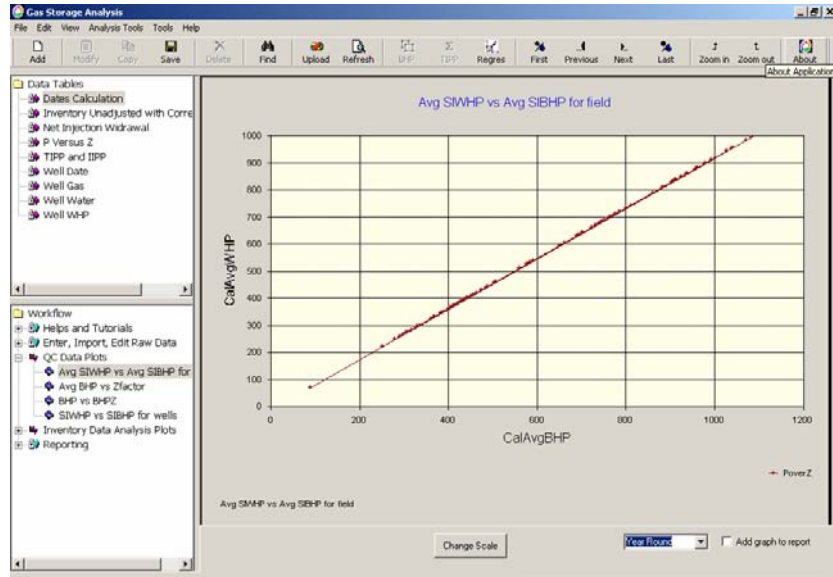
Figure 13: Example plot of Avg SIWHP vs Avg SIBHP

2.2.2 *Avg BHP vs Avg Z-Factor Plot*

A plot of Avg BHP vs Avg Z-Factor is shown in **Figure 15.** This plot should be a rather smooth line with no significant outlying points. Points that significantly deviate from the trend should be checked to ensure there are no errors in the calculation procedure.
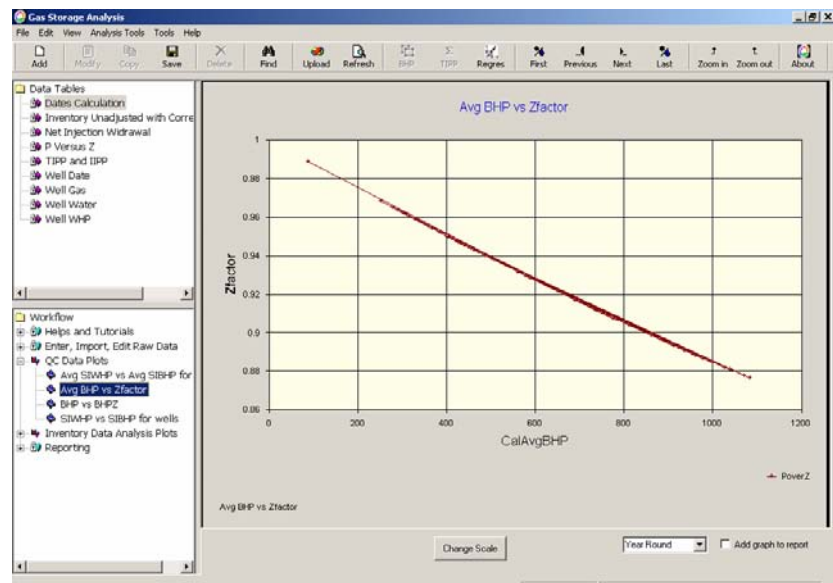
Figure 14: Example plot of Avg BHP vs Avg Z-Factor

2.2.3 *Plot of SIWHP vs SIBHP For All Wells*

A plot of SIWHP vs SIBHP For All Wells is shown in **Figure 15.** This plot should be a rather smooth line with no significant outlying points. Points that significantly deviate from the trend should be checked to ensure there are no errors in the calculation procedure.
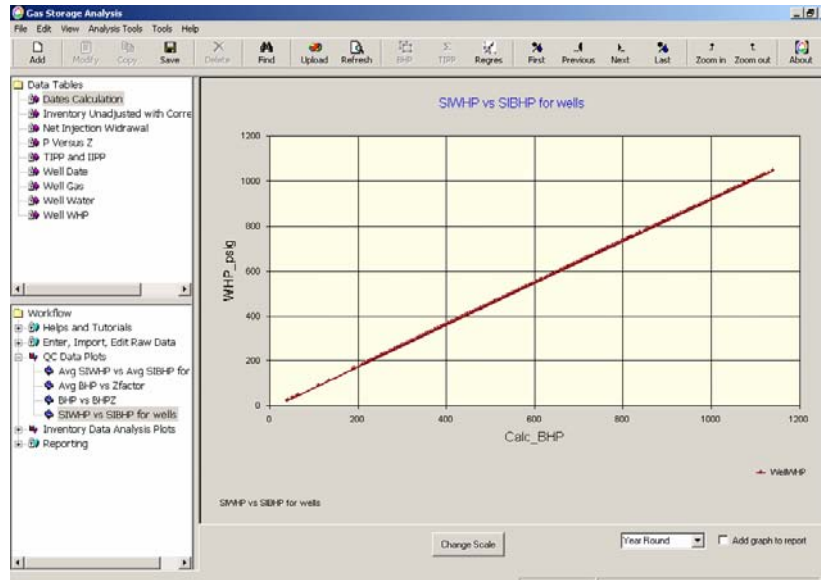
Figure 15: Example plot of SIWHP vs SIBHP For All Wells

2.3 Data Analysis Process

The inventory analysis (IA) process involves examining plots of historical operating data and other specialized diagnostic plots to identify trends indicative of gas losses, gas gains, gas bubble growth, and/or gas bubble shrinkage, and using graphical techniques to quantify the rates and volumes associated with these phenomena over time.

2.3.1 *Analysis of Unadjusted Inventory and Avg SIBHP/z vs Time Plots*

Typically, the first step in IA is to plot and review basic operating data. This usually involves looking for trends in the unadjusted inventory vs time plot, and the pressure (or P/z) vs time plot. If a volumetric reservoir is filled to the same inventory level each Fall, then we would expect the stabilized Fall shut-in pressure to be the same from year to year. We examine these two plots to look for deviations from this expected trend.

Examples of these two plots are shown in **Figure 16** and **Figure 17** below. The unadjusted inventory vs time plot shows that, since the 1960's, the reservoir has been filled to roughly the same inventory level at the end of each injection season. However, the BHP/z vs time plot shows that, since the 1960's, the BHP/z at the end of each injection season has been dropping.
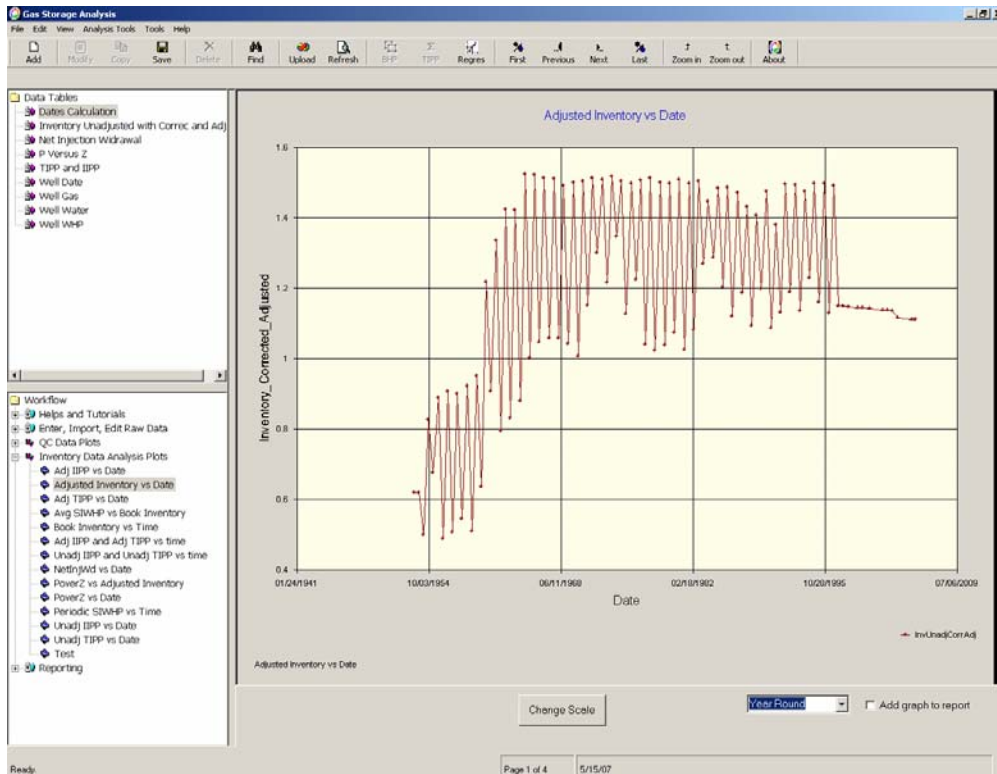
Figure 16: Unadjusted inventory vs time plot
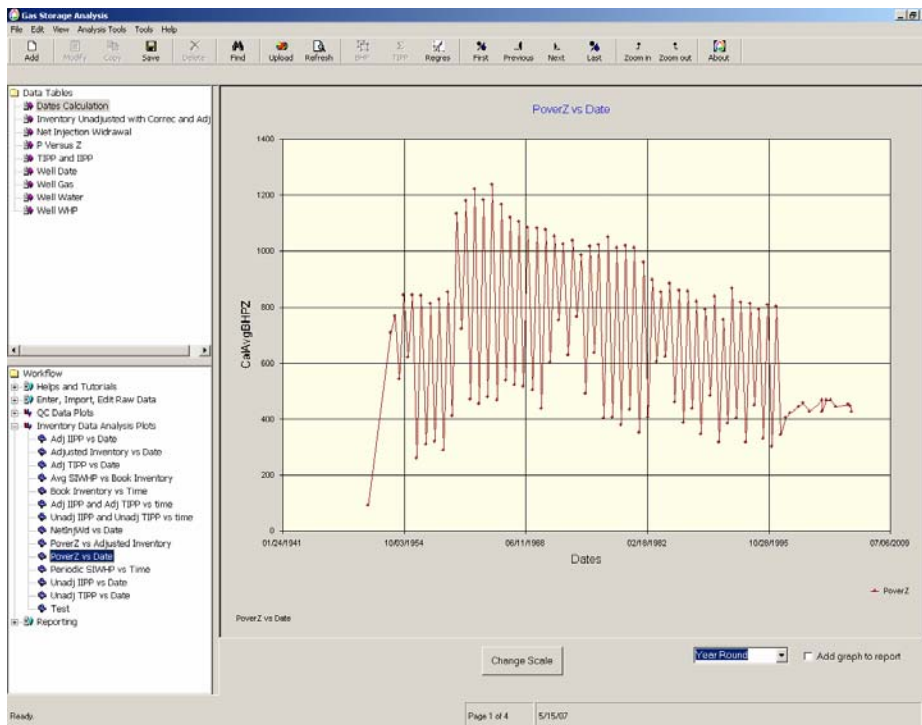
Figure 17: BHP/z vs time plot

Fall data points are considered by many storage engineers to be more reliable than Spring data points (due to the nature of injection vs withdrawal operations), and often times these plots are constructed using Fall points only. Examples of these two plots constructed using only Fall data points are shown in **Figure 18** and **Figure 19** below.
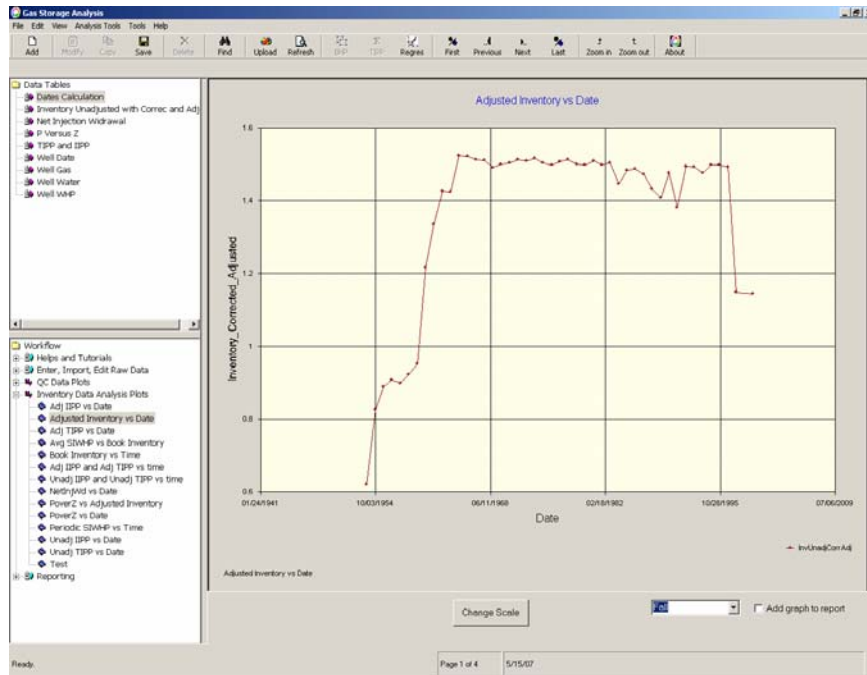
Figure 18: Unadjusted inventory vs time plot - Fall points only
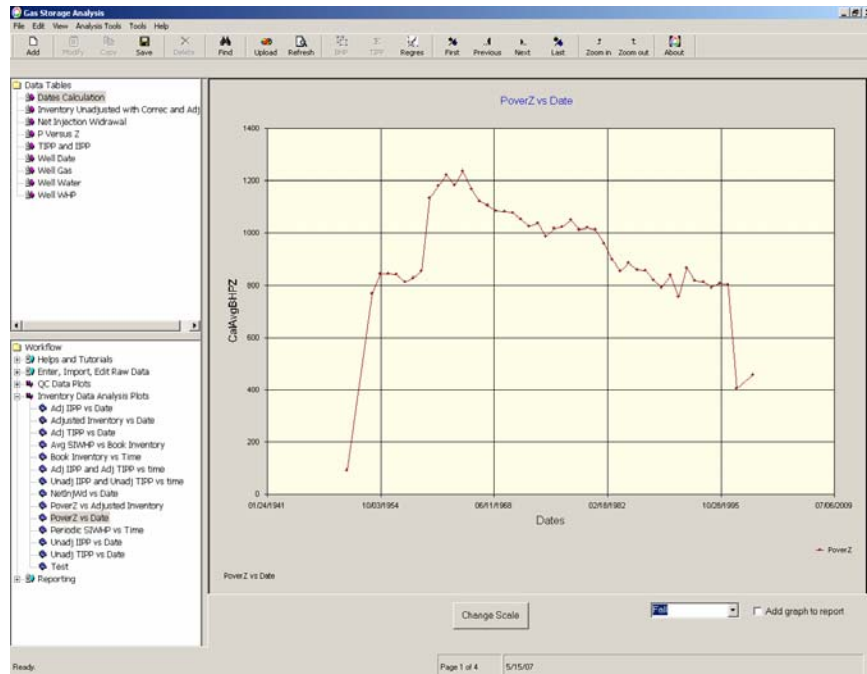
Figure 19: BHP/z vs time plot - Fall points only

2.3.2 *Analysis of P/z vs Unadjusted Book Inventory Plots*

A plot of P/z vs Unadjusted Inventory is very similar to what is typically referred to as a material balance plot (BHP/z vs Cumulative Production), often used to determine total GIP from primary production data in a volumetric gas reservoir. The difference is that the x-axis on this plot is the total unadjusted book inventory.

Theoretically, if a gas reservoir is volumetric, this plot should have the same slope (but different sign) as the material balance plot and pass through the origin. However, due to non-ideal conditions existing in most "volumetric" gas reservoirs reservoir, this is not the case, and deviations for ideal behavior can be used to estimate gas losses and changes in bubble size over time.

An example P/z vs Inventory plot is shown in **Figure 20**. The slope of the line on this plot remains roughly constant, but the position is changes (moves right) over time. This is indicative of ongoing gas losses.
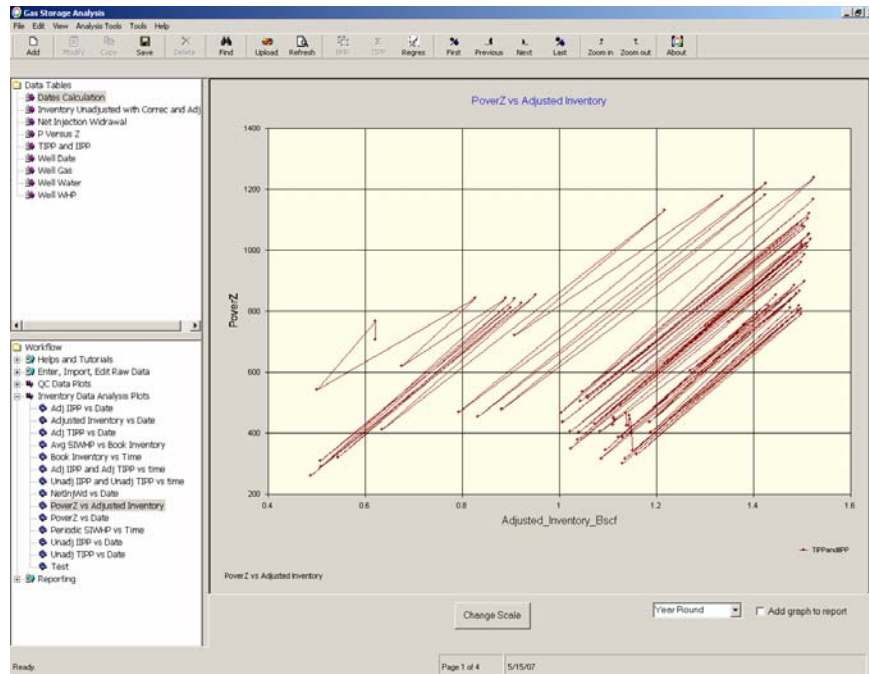
Figure 20: Example P/z vs Inventory plot

2.3.3 *Analysis of Inventory Per Pound (IPP) Plots*

Inventory Per Pound (IPP) plots are also used to estimate gas losses and/or gains as well as gas bubble growth and/or shrinkage (see the Inventory Primer for additional details on interpreting these diagnostic plots).

Two types of IPP plots are used. The Total IPP (TIPP) is defined as the total unadjusted book inventory divided by the BHP/z value corresponding to that inventory value. The Incremental IPP (IIPP) is defined as the *change* in the total unadjusted book inventory divided by the *change* in BHP/z value for a given injection or withdrawal cycle.

Examples of historical TIPP and IIPP values (using Fall data points only) are shown in **Figure 21**, and suggest that the subject field is experiencing ongoing gas losses. Note that we have the option of displaying or not displaying the TIPPP curve (controlled using the Add/Remove TIPP button in the Plot Features window.
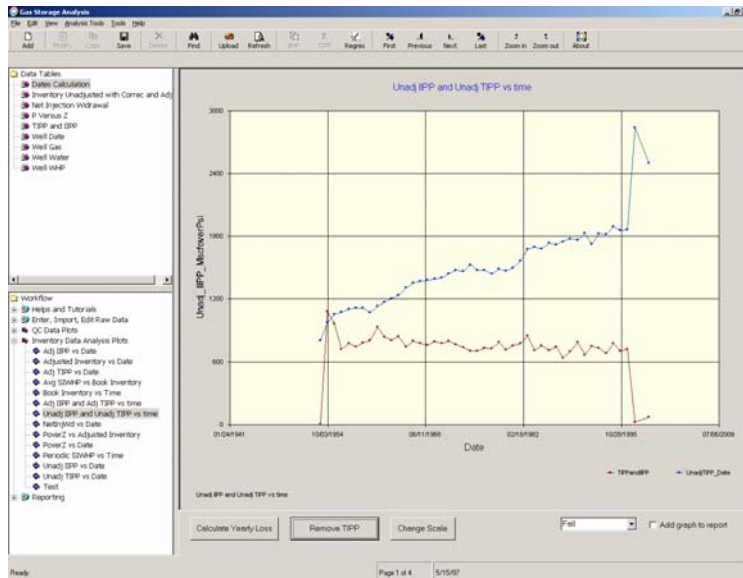
Figure 21: Examples of historical TIPP and IIPP values (using Fall data points only)

We can calculate the gas loss rate and total lost volume from this plot using the interactive analysis feature. In order to do this we first filter on Fall data only using the appropriate button in the plot feature window, then activate the TIPP graph (superimposed on the IIPP plot) using the appropriate button in the plot feature window (**Figure 22**). The resulting plot is what was shown in **Figure 21** above.
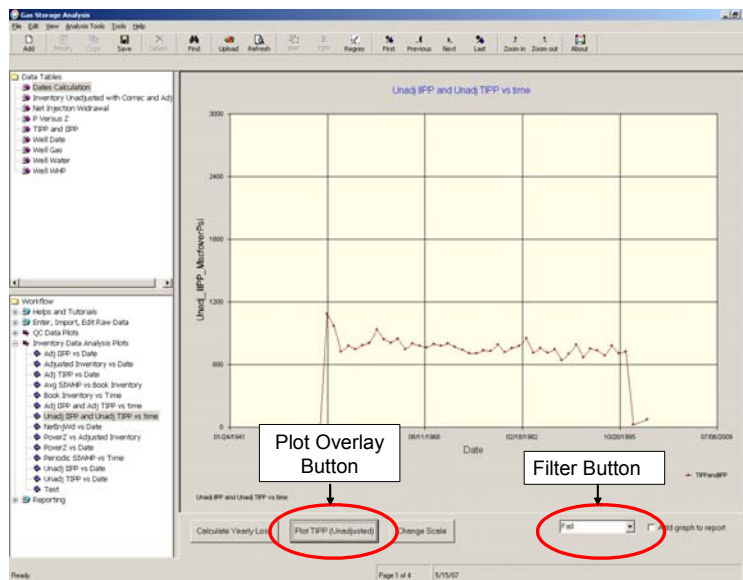
Figure 22: Location of Filter and Plot Overlay Buttons

Interpretation of this plot is initiated by clicking on the **Calculate Yearly Loss** in the plot feature window, which initially brings up a short description of the slope placement process. This

process consists of selecting a starting data point and an ending data point from the data points plotted on the TIPP plot.

After selecting the starting data point on the plot a calculation window will appear at the bottom of the plot. After selecting the ending data point, all of the calculation input data and the calculated loss rate and volume will be displayed in the calculation window at located at the bottom of the plot. Note that up to five separate lines can be used to determine five loss rates/volumes over the history of the storage field.

An example analysis of this data using 4 separate timeframes is shown in **Figure 23**.
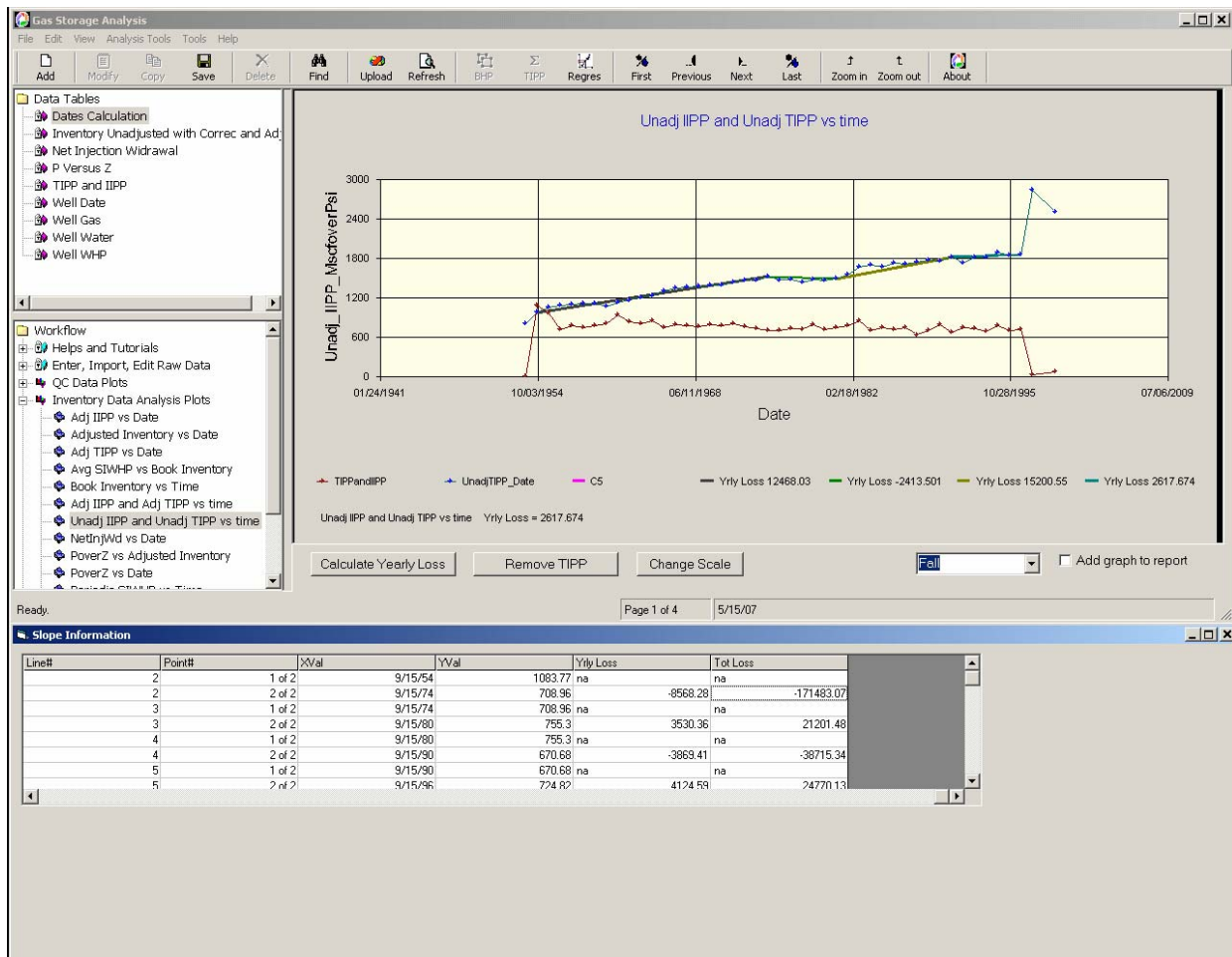
Figure 23: Example of graphical gas loss analysis and loss rate/volume calculations

2.4 Reporting

The reporting feature allows the user to easily capture the pertinent input data, IA plots, and analysis results, and export these data to a word processor for additional editing and formatting.

2.4.1 *Including Interpreted Plots in a Report*

An "Add graph to report" checkbox is located in right hand side of the plot features window. Checking this box while any particular plot is displayed will add the plot graphics (and any

analyses made using that plot) to a list of information to be included in an Inventory Analysis report. Every chart for which this box is checked will be included in a final report.

2.4.2 *Compiling Contents of a Report*

By simply checking the "Add graph to report" checkbox located in right hand side of the plot features window, the user can included all if the plots (and analyses) he wants to be included in the final report compiled by the software.

2.4.3 *Exporting and Editing a Report*

After checking the "Add graph to report" checkbox for all of the plots and analyses results the user wants to include in the final report, the user must click on "Generate" in the workflow window (under Reporting") to compile the report and export it to WORD^{TM} for further editing and inclusion of additional comments, text, and/or graphics not generated by the software.

3 Summary of Features in the Software Windows

3.1 Overall Window Layout

As noted earlier, there are five major areas or windows in the software work area (**Figure 1**): 1) At the extreme top of the work area (just below the various menus) are several toolbars associated with different aspects of inventory analysis calculations and workflow (e.g., BHP and BHP/Z calculations, Inventory Per Pound calculations, etc). 2) On the top left portion of the screen is a window that show the tables containing the input and calculated data, 3) On the bottom left portion of the screen is a window that shows an outline (in tree structure) of the workflow, including help options and reporting features, 4) On the top right portion of the screen is a window that show table or plot information highlighted in the Data Table window or the Workflow window, and 5) On the bottom right portion of the screen is a window that contains various buttons that allow modification of various plot features.

Figure 24: Major windows in the software work area

3.2 Tool Button Window

The tool button window is in the top of the software workspace, and contains all of the tool buttons, including tool buttons used to:

- Upload Data from the data input template
- Refresh the display in the active window
- Add, Delete, Modify, Save, and Copy data in tables
- Calculate the avg WHP, Avg BHP, avg BHP/Z and IPP values (TIPP and IIPP)
- Place a regression line on a plot
- Record navigation tool buttons for navigating data in tables:

- Go to first record in the table

- Go to next record in the table

- Go to previous record in the table

- Go to last record in the table

- Find data in the data tables

- Zoom into an area on a plot

- Zoom out of an area on a plot

3.3 Data Tables Window

The data table window contains all of the tables of data included in the database, including:

- Dates Calculation Table

- Unadjusted Book Inventory and Adjustments to Book Inventory

- Net Injection/Withdrawal Table

- P/z Table

- IIPP Table, which includes calculated values of TIPP andIIPP

- Well Data Table

- Well Water Table

- Well WHP Table

3.4 Workflow Window

The workflow window is arranged to reflect the order in which the various historical and diagnostic inventory analysis plots are analyzed, and includes the following selections:

- Various Helps, including

  - Inventory Primer

  - Inventory Analysis Toolbox

  - Technical References and Papers (grouped by Storage topic)

  - Glossary of Storage Terminology

  - Software Tutorial

- Data Manipulation features, including:

  - Data Importing (from EXCEL^{TM} template)

  - Manual Data Entry

  - Data Editing

- QC Data Plots, including:

- o Avg SIWHP vs Avg SIBHP

- o Avg SIBHP vs Avg Z-factor

- o Avg SIBHP vs Avg SIBHP/z

- o SIWHP vs SIBHP for all wells

- Inventory Analysis Plots of Historical Data, including:
  - o Date vs Unadjusted Total Field Book Inventory
  - o Date vs Adjustments to Total Field Book Inventory
  - o Date vs Adjusted Total Book Inventory
  - o Date vs Average Field Wellhead Pressure
  - o Date vs Average Field Bottom Hole Pressure
  - o Date vs Average Field (BHP/Z)

- Inventory Analysis Plots of Diagnostic Data, including:
  - o Field Avg BHP/Z vs Unadjusted Total Field Book Inventory
  - o Date vs UTIPP ([Unadjusted Total Inv]/[BHP/Z])
  - o Date vs UIIPP ([Unadjusted Incremental Inv]/[Incremental BHP/Z])
  - o Field Avg BHP/Z vs Adjusted Total Field Book Inventory
  - o Date vs ATIPP ([Adjusted Total Inv]/[BHP/Z])
  - o Date vs AIIPP ([Adjusted Total Inventory]/[BHP/Z])
  - o Non-Effective Gas vs Time
  - o Gas Loss Rate vs Time
  - o Total Lost Gas Volume vs Time

- Reporting
  - o Selection of this option will result in copies of reservoir input data and all plots selected for inclusion in the report to be compiled and sent to WORD^{TM} for additional editing.

3.5 Data/Plotting Window

If the user clicks on a data table in the Data/Plotting window, the data in the selected table is displayed. Once displayed in the Data/Plotting window, data can be added, deleted, and edited, as appropriate.

If the user clicks on a plot in the Workflow window, the selected plot will be displayed. Once displayed in the Data/Plotting window, the plot can be analyzed using the appropriate tools in the Plot Features window.

3.6 Plot Feature Window

Once displayed in the Data/Plotting window, the plot display can be modified and the plot data can be analyzed using the appropriate tools in the Plot Features window, which include:

- Change Scale Button: This button allows the user to modify the x-axis or y-axis scale limits and number of scale divisions.

- Filter Button: This button allows the user to display Spring, Fall, or All data points on the selected plot.

- Calculate Loss Button: This button allows the user to select the starting and ending points for up to 5 trend lines on the TIPP chart, which are then used to and calculate the loss rate(s) and volume(s) associated with each of the specified lines.

- Add Graph to Report Button: This button allows the user to add the graph – as displayed at the time button is activated – to an automatically generated report.

4 Example Problem

In this section of the manual, we will walk the user through a typical Inventory Analysis (IA) process using the example data below.

The Big Boy Field is a single-well dry gas field that produced from 1925 to 1940. The field remained shut-in from 1940-1949, at which time it was converted to storage (no additional wells were drilled). It has been an active storage facility since 1950. The storage reservoir is known have a small layer of lower permeability formation within the storage interval.

Historically, the storage field has operated between a minimum shut-in wellhead pressure of 650 psig and a maximum shut-in wellhead pressure of 1000 psig. Each Spring and Fall during storage operations, the operator measured the shut-in wellhead pressure in one IW well (Well ID 1) that is completed in the storage reservoir. The depth to the reservoir in this well is 5000 ft. The average wellhead temperature is 60 degrees F and the average reservoir temperature is 110 degrees F. Gas gravity is 0.58.

There is 1 mile of new (at conversion) 3" ID gathering line in the field. This line has custody transfer measurement facilities where it connects to a sales line that operates at 500 psi. From 1990 to 2000, separate measurement devices were "temporarily" installed at the sales lines to measure injected volumes. In 2000, this temporary injection measurement facility was removed.

Each year, when the wellhead pressures reach 700 psi, the one IW well is tested. During this test, the gas is vented into the atmosphere. These annual tests consist of three 15-minute flow periods (100 mscf/d, 200 mscd/d and 300 mscf/d) followed by a 45 minute extended flow (400 mscf/D).

At the end of withdrawal each year, a downhole camera is run in the IW well. Prior to running the camera, a bridge plug is set just above the bottom of the tubing (3" ID). There is a sealing packer at the bottom of the tubing, which is run inside casing (6" ID). Also at the end of withdrawal each year, the gathering line is blown down and pigged.

The Spring and Fall shut-in wellhead pressures recorded at the IW well and the corresponding unadjusted book inventory values are shown in the table on the following page.

Example Problem

Inventory Assessment Data

Date	Unadjusted Inventory (Bscf)	SIWHP psig
3/15/50	10.000000	650
9/15/50	15.000000	1000
3/15/51	10.100000	650
9/15/51	15.100000	1000
3/15/52	10.190000	650
9/15/52	15.190000	1000
3/15/53	10.270000	650
9/15/53	15.270000	1000
3/15/54	10.340000	650
9/15/54	15.340000	1000
3/15/55	10.400000	650
9/15/55	15.400000	1000
3/15/56	10.450000	650
9/15/56	15.450000	1000
3/15/57	10.490000	650
9/15/57	15.490000	1000
3/15/58	10.520000	650
9/15/58	15.520000	1000
3/15/59	10.540000	650
9/15/59	15.540000	1000
3/15/60	10.550000	650
9/15/60	15.550000	1000
3/15/61	10.550000	650
9/15/61	15.550000	1000
3/15/62	10.550000	650
9/15/62	15.550000	1000
3/15/63	10.550000	650
9/15/63	15.550000	1000
3/15/64	10.550000	650
9/15/64	15.550000	1000
3/15/65	10.550000	650
9/15/65	15.550000	1000
3/15/66	10.550000	650
9/15/66	15.550000	1000
3/15/67	10.550000	650
9/15/67	15.550000	1000
3/15/68	10.550000	650
9/15/68	15.550000	1000
3/15/69	10.550000	650
9/15/69	15.550000	1000
3/15/70	10.600000	650
9/15/70	15.600000	1000
3/15/71	10.650000	650
9/15/71	15.650000	1000
3/15/72	10.700000	650
9/15/72	15.700000	1000
3/15/73	10.750000	650
9/15/73	15.750000	1000
3/15/74	10.800000	650
9/15/74	15.800000	1000
3/15/75	10.850000	650
9/15/75	15.850000	1000
3/15/76	10.900000	650
9/15/76	15.900000	1000
3/15/77	10.950000	650
9/15/77	15.950000	1000
3/15/78	11.000000	650
9/15/78	16.000000	1000
3/15/79	11.050000	650
9/15/79	16.050000	1000
3/15/80	11.050000	650
9/15/80	16.050000	1000
3/15/81	11.050000	650
9/15/81	16.050000	1000
3/15/82	11.050000	650
9/15/82	16.050000	1000
3/15/83	11.050000	650
9/15/83	16.050000	1000
3/15/84	11.050000	650
9/15/84	16.050000	1000
3/15/85	11.050000	650
9/15/85	16.050000	1000
3/15/86	11.050000	650

Using the example data provided above:

- Load pertinent data into the EXCEL template

- Upload this data into the software

- Browse the data tables using the software

- Calculate BHP and BHP/Z values using the software

- Calculate TIPP and IIPP values using the software

- Peruse the various help features:

  - Open the Inventory Analysis Primer and peruse the document.

  - Open the Toolbox peruse the spreadsheet

  - Open the Help for input document and peruse the document.

  - Open the Help for analysis plots document and peruse the document.

  - Open the Storage Terms and peruse the document.

  - Open the Glossary and peruse the document.

  - Open the Summary of References and peruse the document.

- Browse the available analysis plots

- Review/Analyze appropriate diagnostic plots to calculate the inventory loss rates and volumes where appropriate

- Comment on the nature of the losses.

- Use the toolbox to determine if the losses can be reasonably explained by:

  - Line losses

  - Annual pigging of gathering lines

  - Annual well testing operations

  - Downhole camera 0perations

- Select several plots for inclusion in a report and generate a draft report

4.1 Loading Data Into EXCEL^{TM} Template

The first thing that needs to be done in any inventory analysis that utilizes the newly developed software is to reformat/reorganize the inventory data supplied by the operator. Generally, this is a fairly straightforward process, and simply involves cut/copy and paste commands within EXCEL, and perhaps some simple calculations within EXCEL to fill in necessary columns of input data.

We have installed the inventory analysis software on the D Drive, under the subdirectory called "Program Files." During the installation process, a subdirectory is created under the "Program Files" subdirectory called "EXCEL Template." In this subdirectory are several EXCEL files, including one named "Ex_Prob_Raw_Data.xls" in which is stored the raw data as collected by the operator. This file consists of a single sheet of data as shown above (see page with heading Example Problem Inventory Assessment Data). Open this file.

The EXCEL template used to import data into the software is in the same location, and is named "Upload Data Template.xls." Open this file also. The first sheet in the file ("DatesCalc") looks like this:

To populate this sheet, we will perform the following steps:

1. Copy data from cells A2–A113 in the raw data file (Ex_Prob_Raw_Data.xls) and past these values into Cells B2 – B113 in Sheet DatesCalc, in Excel template file (Upload Data Template.xls). Sheet DatesCalc in the "Upload Data Template.xls" should now look like this:

2. The **ID** column in this spreadsheet is simply a unique integer, or "auto-number," which we can populate by inputting a 1 in cell A2 and copying a formula in cells A3-A113 that adds one to the integer directly above it.

3. The **Year** column in this spreadsheet can be calculated using the YEAR function in EXCEL, using the date in column D as the input. For example cell B2 would contain the formula "Year(D2)." This formula can then be copied to D3-D113 to populate the remaining cells.

4. The **Season** column in this spreadsheet can be calculated using a conditional statement in EXCEL, using the date in column D as the input. For example cell C2 would contain the formula "IF(MONTH(D2)<6,"SPRING","FALL")." This formula can then be copied to D3-D113 to populate the remaining cells. Sheet DatesCalc in the "Upload Data Template.xls" is now populated and should now look like this:

The second sheet in "Upload Data Template.xls file ("InvUnadjCorrAdj") looks like this:

To populate this sheet, we will perform the following steps:

1. Copy the date and book inventory values from cells A2–B113 in the raw data file (Ex_Prob_Raw_Data.xls) and past these values into Cells B2–C113 in Sheet "InvUnadjCorrAdj", in Excel template file (Upload Data Template.xls).

2. The **ID** column in this spreadsheet is simply a unique integer, or "auto-number," which we can populate by inputting a 1 in cell A2 and copying a formula in cells A3-A113 that adds one to the integer directly above it.

3. **Corr_Vol, Cum_Corr, Adj_Vol, Cum_Adj, and Inventory_Corrected_Adjusted** columns in this spreadsheet are used to store corrections and/or adjustments and store the calculated values of cum corrections, cum adjustments, and corrected adjustmented book inventory. In this example, there are no corrections or adjustments to the book inventory, so all of these columns can be populated with zero's. Note the following about this input sheet:

    a. Although there are columns to input both "corrections" and "adjustments," the "corrections" columns are included in anticipation of a software upgrade wherein a distinction between a correction and an adjustment can be made. When using the current version of the software, input all changes made to the book inventory as adjustment.

    b. The values in columns labeled **Cum_Corr**, **Cum_Adj**, and **Inventory_Corrected_Adjusted,** are calculated within the software, and therefore zeros can be entered at this point

4. Sheet **InvUnadjCorrAdj** in the "Upload Data Template.xls" is now populated with data and should look like this:

No data was supplied in the example problem for the next two Sheets in the input template (**NetInjWd** and **NetInjWdAquifer),** so these will remain blank.

The **WellData** sheet contains information related to the one IW well. To populate this sheet, we will perform the following steps:

1. The **ID** column in this spreadsheet is simply a unique integer, or "auto-number," which we can populate by inputting a 1 in cell A2 and copying a formula in cells A3-A113 that adds one to the integer directly above it.

2. The **Well_ID** column contains a unique identifier for each well, and has the format of an integer. We identified the well in which the shut-in wellhead pressure is measured each spring and Fall as Well 1, so we will use a **Well_ID** of 1 to identify the well.

3. The **Resv_Depth** column contains the depth (TVD) to the reservoir in the well, which was given as 5000 ft.

4. The **X** and **Y** columns contains well location information for use in future upgrades and is not used in this version of the software. You can enter any number in these columns you want, as they are not used.

The **WellData** sheet is now populated with data and should look like this:

No data was supplied in the example problem for the next two Sheets in the input template (**WellGas** and **WellWater),** so these will remain blank.

The last sheet in "Upload Data Template.xls file ("WellWHP") looks like this:

To populate this sheet, we will perform the following steps:

1. Copy the Date and SIWHP in cells A2–A113 and cells C2-C113 in the raw data file (Ex_Prob_Raw_Data.xls) and past these values into cells C2–C113 and cells D2–D113 respectively in Sheet "SIWHP", in Excel template file (Upload Data Template.xls).

2. The **ID** column in this spreadsheet is simply a unique integer, or "auto-number," which we can populate by inputting a 1 in cell A2 and copying a formula in cells A3-A113 that adds one to the integer directly above it.

3. The **Well_ID** column should contain the Well_ID from the single well shown in sheet "WellID"

4. The **Comments** column can contain any text you wish to input. We will not input any comments in our file, so all rows under the header row in this sheet should be left blank.

5. The **Given_BHP** column is not used in this version of the software, and should be populated with zeros.

6. The **CalcBHP** column contains output calculated by the software after data is imported and should therefore contain all zeros at this point.

7. Sheet **SIWHP** in the "Upload Data Template.xls" is now populated with data and should look like this:

4.2 Uploading Data into Software

You have now completed populating the EXCEL file originally named, "Upload Data Templae.xls." It is now time to save this file using a different name, in a location you will remember. In this example, we will save the file in the same subdirectory as the Input Data Template was located (i.e., the subdirectory created on the D drive upon installation of the software, D:\Program Files\Gas Storage Software\Excel Template\) and name it KGB_EXAMPLE_Data Template-2.xls.

To upload this data into the IAS, open/start the software. The first screen you will see looks as follows:

Select the button **Click to create New Database,** and use the dialogue box that appears to name the ACCESS file that will be created to contain your uploaded data, in a location of your choice. In this example, we will create an ACCESS file named "KGB_Example-2.mdb" in the same subdirectory that the Input Data Template was located (i.e., the subdirectory created on the D drive upon installation of the software (D:\Program Files\Gas Storage Software\Excel Template\) and name it KGB_EXAMPLE_Data Template-2.xls.

After inputting the name you wish for the ACCESS database to be created, you will see the following dialogue box:

After you click OK, you will proceed to the reservoir data input screen, which looks as follows:

Populate the fields as shown in the following slide:

Note the following:

1. The average reservoir depth entered here is NOT the depth used to calculate SIBHP's from SIWHP's. We anticipate using this field in a later version of the software (allowing the user calculate all BHP's at the average reservoir depth or at the reservoir depth in each individual well). The depth associated with each individual well (entered on **WellData** sheet) is used to calculate BHP's from WHP's in each well.

2. Values entered for Reservoir Top and Base pressures are not used in this software version. We anticipate using them in later versions of the software. Values should be entered, but will not be used in the current software version.

3. Water specific gravity should be entered, but it is not used in dry gas wells.

4. When you click on the continue button, you will be asked if you want to save the changes – respond "yes."

At this point, you will be in the software, but nothing other than the reservoir data has been entered. You will see the following screen at this point:

It is now time to import the data from the EXCEL template file we created, "KGB_EXAMPLE_Data Template-2.xls." To do this, click on the "UPLOAD" tool button shown below:

You will then see the dialogue box below. Using this dialogue box, select the EXCEL input template file we created, ("KGB_EXAMPLE_Data Template-2.xls) from the location in which we stored it (D:\Program Files\Gas Storage Software\Excel Template\), and select "OPEN."

It will take a few moments to import the information from the EXCEL file, so be patient (this process is only required once). Upon completion of the import process, your screen should look as follows:

4.3 Browsing Data Tables and Performing BHP, p/z, and IPP Calculations

You can now browse the information located in the various tables by clicking on the table names in the Data Tables Window (upper left tree structure). Notice the following at this point:

1. The first two data tables ("Dates Calculation" and "Inventory Unadjusted…") contain data.

2. The third and fourth tables ("Net Injection Withdrawal" and "NetInjWdAquifer") contain no data because we did not input any data in these tables.

3. The fifth table ("PoverZ") contains no data because we have not yet calculated the BHP and Z values. To calculate the BHP and BHP/Z values, and populate this table with the calculated values, click on the "BHP" tool button shown below:

After clicking on the BHP tool button, the PoverZ table should look as follows:

4. The Sixth table ("TIPP and IIPP") contains no data because we have not yet calculated these values. To calculate TIPP and IIPP values and populate this table with the calculated values, click on the "TIPP" tool button shown below:

After clicking on the TIPP tool button, the "TIPP and IIPP table should look as follows:

5. The seventh table contains the well data we entered, and should look as follows:

6. The eighth and ninth tables ("Well Gas" and "Well Water") contain no data because we did not input any data in these tables.

7. The tenth table ("WellWHP") contains the SIWHP's input and the SIBHP's calculated from these SIWHP's, and should look as follows:

4.4 Perusing HELP features and Using the ToolBox

At this point, we will take a moment to briefly peruse the various HELP features in the softwareTo access the various HELP features of the software, go to the help menu at the top of the screen, as shown below:

This help button will bring up a menu of help items as shown below:

The various HELP menu items shown include the following:

Steps to work with Program

This is a very abbreviated Users' Manual compiled by the programmer that provides only the most essential information required to use the software.

Inventory Analysis Primer

This is a fairly complete introduction to inventory analysis, and includes discussions on the theory behind inventory analysis, the uses of various inventory analysis diagnostic plots, and references. The table of contents for this document is shown below.

Toolbox

Selecting this option opens a HELP document related to the EXCEL "Toolbox" that was developed as part of this software. The EXCEL Toolbox is accessed from within the workflow window, and will be discussed in more detail later.

Help for Input

Selecting this option activates a drop-down box to the right, which allows the user to select the input screen for which he needs help. Upon selection of an item in the drop-down box, a WORD file is opened that provides HELP information related to the selected input screen. A description of the data entered on this screen, including data names and formats are summarized.

Help for Analysis Plots

Selecting this option opens a WORD document that provides detailed help for each of the various data QC plots and the diagnostic plots used to estimate loss rates and volumes. The each plot, the purpose, assumptions, applicability, dangers of mis-use, examples, and references are discussed.

Storage Terms

Selecting this option opens a WORD document that provides a description of the various terms used in inventory analysis.

Glossary

Selecting this option opens a WORD document that provides a description of the various terms used in the underground gas storage industry. It is similar in purpose to the "Storage Terms" help above, but much broader in scope.

Summary of References

Selecting this option opens a WORD document that provides a list of various references and technical papers related to the gas storage industry. These references are listed by topic, and should look something like this:

<div style="border:1px solid black; padding:1em;">

Table of Contents

1. Introduction to Gas Storage

2. Gas Storage Field Design

3. Optimization

4. Migration and Monitoring

5. Inventory Verification

6. Deliverability Maintenance and Enhancement

7. Simulation of UGS Reservoirs

8. Special Topics

9. Top Twenty Papers

</div>

Example Data

Selecting this option opens an EXCEL document containing the Spring/Fall pressure and inventory example data.

Select HELP features are also accessible for the Workflow window, since we anticipate they will commonly be referenced during the inventory analysis process. In the Workflow Window, there are two Help items listed, the Inventory Primer and the Toolbox, as shown below:

Inventory Analysis Primer

As noted above, this is a fairly complete introduction to inventory analysis, and includes discussions on the theory behind inventory analysis, the uses of various inventory analysis diagnostic plots, and references.

Toolbox

Select this option and open the EXCEL "Toolbox."

After opening the EXCEL Toolbox, go to sheet **Bureau-of-Mines Est Line Losses**, and enter the data given in the example problem data set above to estimate the annual line losses each year we might expect from the 1 mile long gathering line carrying gas from the wellhead to the sales point.

After inputting the example data, your sheet should look like the following:

Obviously, the annual loss rate/volume calculated using the Bureau of Mines data is minimal, and we would not expect that potential loses in the gathering lines to contribute significant to any overall losses from the field.

Next, go to sheet **Est Wellbore Blowdown Volume**, and enter the data given in the example problem data set above to estimate the annual line losses each year we might expect from blowing down the well each year prior to running the camera. After inputting the example data, your sheet should look like the following:

Obviously, the annual lost volume due to blowing down the well prior to running a camera is minimal, and we would not expect that these losses contribute significant to any overall losses from the field.

Next, go to sheet **Est Well Test Volumes**, and enter the data given in the example problem data set above to estimate the annual losses associated with running the well test each year. After inputting the example data, your sheet should look like the following:

Obviously, the annual lost volume due to testing the well each year is minimal, and we would not expect that these losses contribute significant to any overall losses from the field.

Next, go to sheet **Est Pipeline Volumes**, and enter the data given in the example problem data set above to estimate the annual losses associated with blowing down the gathering line to run the pig each year. After inputting the example data, your sheet should look like the following:

Obviously, the annual lost volume due to pigging the gathering line each year is minimal, and we would not expect that these losses contribute significant to any overall losses from the field.

Note that not all of the calculations that can be made in this EXCEL Toolbox have been demonstrated here.

4.5 Performing Inventory Analysis and Generating Reports

At this point, all of the data from the example problem has been input/uploaded. We have perused the data tables and the help options, and we used the Toolbox feature to estimate any inventory losses due to field operations. The next step is to use the various plots to analyze loss rates and volumes over the entire life of storage operations.

At this point, it is recommended that you open a word processing document to keep notes about the trends observed during the inventory analysis process. These notes will prove to be extremely valuable after your analysis is complete and you generate a draft report.

We start by reviewing the data QC plots shown in the Workflow Window, under QC Data Plots (see below). Since none of these plots show any irregularities, it is safe to assume that no problems were encountered during the calculation processes we performed earlier.

After reviewing the data QC plots, we review plots of operational data to identify any operational trends that may provide preliminary, qualitative indications of ongoing losses and show timeframes wherein we need to be careful analyzing data due to widely varying operational practices.

The first two plots (**All SIWHP vs Date** and **Avg SIWHP vs Date**) are identical, since there is only one well in the field. For the purpose of this example, look at the **Avg SIWHP vs Date**, which should look like this (you may have to change the scale on the plot):

We observe from this plot that the field has consistently been operated between 650 psi and 1000 psi throughout its life. Therefore, we do not have to worry about wide fluctuations in minimum and maximum operating pressures skewing trends in other diagnostic plots.

We did not load any daily or monthly Net Injection information, so the next plot shows nothing:

The next plot in the workflow is the **UnadjBookInv vs Time**, which shows the book inventory prior to any adjustments as a function of time. This plot is revealing, especially in light of how

regularly the field was operated from a pressure perspective. This plot shows that various levels of inventory were required over the field life to achieve the same Spring and Fall shut-in pressures. This trend is a strong indicator, albeit qualitative indicator, that there have been losses and gains occurring during storage operations.

The next three plots, **Inv Adjs vs Date**, **Cum Inv Adjs vs Date**, and **Adjusted Inventory vs Date** are trivial, as no inventory adjustments have been booked during the life of the field. In addition, the two plots after these, **Avg WHP vs Date** and **Avg BHP vs Date**, are not noteworthy.

The next plot, **PoverZ vs Date**, reflects the same trends as the SIWHP vs time, and further demonstrates the uniformity of operations over the life of the storage field from a pressure perspective.

The next plot, **PoverZ vs UnadjInv**, is a plot of the unadjusted book inventory vs the BHP/Z. This plot shows movement to the right and left at various points during the life of storage

operations, which leads us to the conclusion the losses and gains have occurred during storage operations. This is consistent with the qualitative conclusions drawn from a review of the the operational plots (SIWHP vs Time and Unadjusted Book Inventoy vs Time).

The next plot, Unadj NEG vs Date, shows the non-effective gas (NEG) calculated for each cycle by back-extrapolating the BHP/Z vs Unadjusted Book Inventory plot for that cycle to a BHP/Z value of zero (i.e., the x-intercept of the plot). This plot clearly indicates the time periods experiencing losses, gains, and stability:

Note that the relative uniformity of injection operations compared to withdrawal operations lead some storage engineers to use only fall data to analyze NEG vs time plots and IPP vs time plots. By applying the FALL filter on this plot, we can generate the plot using only Fall data points:

The next plot is the Unadjusted TIPP vs time and Unadjusted IIPP vs time. These are perhaps the most widely used inventory analysis plots in the storage industry. Usually, these plots are generated using Fall only data points, since injection operations are relatively more uniform than withdrawal operations. Therefore, the Fall data points are generally thought to be less operationally influenced. A plot of IPP values vs time generated using Fall only data points is shown below:

This plot clearly shows the following:

1. Non-linear increase in the TIPP w/Flat IIPP in 1950's (GAIN)

2. Flat TIPP and IIPP during 1960's   (NO LOSS or GAIN)

3. Linear increase in the TIPP w/Flat IIPP in 1970's   (LOSS)

4. Flat TIPP and IIPP during 1980's   (NO LOSS or GAIN)

5. Non-linear decrease in the TIPP w/Flat IIPP in 1990's   (GAIN)

6. Flat TIPP and IIPP from 2000-2005   (NO LOSS or GAIN)

7.

In order to calculate the loss rates and volumes, we will use the TIPP plot generated with Fall only data points. This is accomplished by clicking on the UnadjTIPP vs Date plot in the Workflow window, filtering on Fall data points, and clicking on the "Calculate Yearly Loss" button (see below).

You can calculate losses for up to 5 time periods using the "Calculate Yearly Loss" button. Simply click the button, read the pop-up directions, and click OK to close the directions. Click on the data point closest to the start of the loss period, then click on the data point closest to the end of the loss period.

The software will automatically calculate annual loss rates for each period and display results on the plot. Using this information, we can calculate the total gains/losses by multiplying the gain/loss rate for each loss period by the number of years the gain/loss occurred, and summing the volumes for each period.

For this example, the TIPP vs Date used to calculate the loss rate looks like the following after loss analysis was performed:

The losses calculated using this plot can be summarized as follows:

- 80 MMscf/yr loss 1950-1955   (Lost Volume = 400 MMscf)
- 35 MMscf/yr loss 1955-1960   (Lost Volume = 175 MMscf)
- No Losses 1960-1970   Lost Volume =   0 MMscf)
- 50 MMscf/yr loss 1970-1980   (Lost Volume = 500 MMscf)
- No Losses 1980-1990   (Lost Volume =   0 MMscf)
- 50 MMscf/yr *gain* 1990-2000   (Lost Volume = -500 MMscf)
- No Losses 2000-2005   (Lost Volume =   0 MMscf)

Therefore, based on this analysis, the total net inventory lost over the time period 1950-2005 is 575 MMscf

4.6 Generating Reports

At the bottom right of each plot, there is a check box for the user to indicate if he wants that particular plot to be included in the report. By simply checking this box for the plots of interest, we can "collect" the plots we would like to include in this report.

For the purpose of this example, we will include all non-trivial plots in the report, so we will need to make sure each of these plots has the "Add Graph to Report" box checked. This would also be a good time to make sure all of the axes ranges are set appropriately. The figure below shows the location of the check box used to include plots in the report.

In addition, if the user has taken a few notes in a word processing document during the inventory analysis process (as recommended above), it is quite easy to merge the two documents into a final report that includes all of the pertinent plots used in the inventory analysis process. For the example problems, notes collected during the inventory analysis process might look something like the following:

QC Plots
None of the QC plots show any irregularities, so it is safe to assume that no problems were encountered during the calculation processes performed.

SIWHP vs Date Plots
The field has consistently been operated between 650 psi and 1000 psi throughout its life. Therefore, we do not have to worry about wide fluctuations in minimum and maximum operating pressures skewing trends in other diagnostic plots.

Unadjusted Inventory History
A plot of unadjusted inventory vs time is revealing, especially in light of how regularly the field was operated from a pressure perspective. This plot shows that various levels of inventory were required over the life of the field to achieve the same Spring and Fall shut-in pressures. This type of trend is a strong indicator, albeit a qualitative indicator, that there have been losses and gains occurring during over the life of storage operations

BHP/Z vs Unadj Book Inv
A plot of the unadjusted book inventory vs the BHP/Z shows movement to the right and left at various points during the life of storage operations, which leads us to the conclusion the losses and gains have occurred during storage operations. This is consistent with the qualitative conclusions drawn from a review of the operational plots (SIWHP vs Time and Unadjusted Book Inventoy vs Time).

NEG History
The plot of Unadjusted NEG vs Date clearly indicates the time periods experiencing losses, gains, and stability.

IPP History Plots
A plot of IPP values vs time generated with Fall data points clearly shows the following:

1. Non-linear increase in the TIPP w/Flat IIPP in 1950's   (GAIN)
2. Flat TIPP and IIPP during 1960's   (NO LOSS or GAIN)
3. Linear increase in the TIPP w/Flat IIPP in 1970's   (LOSS)
4. Flat TIPP and IIPP during 1980's   (NO LOSS or GAIN)
5. Non-linear decrease in the TIPP w/Flat IIPP in 1990's   (GAIN)
6. Flat TIPP and IIPP from 2000-2005   (NO LOSS or GAIN)

Loss Calculations using the TIPP Plot
Loss rates and volumes were calculated using the TIPP plot generated with Fall only data points. The losses calculated using this plot can be summarized as follows:

- 80 MMscf/yr loss 1950-1955   (Lost Volume = 400 MMscf)
- 35 MMscf/yr loss 1955-1960   (Lost Volume = 175 MMscf)
- No Losses 1960-1970   Lost Volume =   0 MMscf)
- 50 MMscf/yr loss 1970-1980   (Lost Volume = 500 MMscf)
- No Losses 1980-1990   (Lost Volume =   0 MMscf)
- 50 MMscf/yr *gain* 1990-2000   (Lost Volume = -500 MMscf)
- No Losses 2000-2005   (Lost Volume =   0 MMscf)

Therefore, based on this analysis, the total net inventory lost over the time period 1950-2005 is 575 MMscf

After checking the boxes on all of the charts you would like to be included in the report, go to the Workflow Window, expand the "Reporting" portion of tree directory to see the "Generate" option and click on the Generate option:

This will bring up a document preview window that will show all of the plots you have selected in thumbnail view. By clicking on the "Generate Report" button (see below), the information shown in thumbnail view will be exported to a WORD document for further editing.

After the report information was dumped to WORD and this file was opened, we opened the comments file we compiled during the analysis procedure (shown earlier). We then cut/pasted the information from the comments document into the WORD document, rearranged some information, added a report cover page.

The result is a first draft (or final draft, depending on requirements of the client) of an Inventory Analysis Report (see below):

Gas Storage Inventory Analysis

Big Boy Field

Summary of Reservoir Information

Field Name	Example
Field Type	Dry Gas
Average Reservoir Depth (ft)	5000
Average Reservoir Temperature (F)	110
Wellhead Temperature (F)	60
Reservoir Top Pressure (psia)	1000
Reservoir Base Pressure (psia)	650
Gas specific gravity	0.58
Water specific gravity	1.05
Total Number of wells	1
BHP correlation	Cullender and Smith
z-factor correlation	Hall-Yarborough

Review of Data QCPlots
None of the QC plots show any irregularities, so it is safe to assume that no problems were encountered during the calculation processes performed.

Review of Operational Plots
Based on a review of the SIWHP vs Date Plots, it is apparent that the field has consistently been operated between 650 psi and 1000 psi throughout its life. Therefore, we do not have to worry about wide fluctuations in minimum and maximum operating pressures skewing trends in other diagnostic plots.

Based on a review of the unadjusted inventory vs time, it is apparent that various levels of inventory were required over the life of the field to achieve the same Spring and Fall shut-in pressures. This type of trend is a strong indicator, albeit a qualitative indicator, that there have been losses and gains occurring during over the life of storage operations

---

Review of Diagnstic Plots
Based on a review of the unadjusted book inventory vs the BHP/Z plot, it is apparent that movement has occurred to the right and left at various points during the life of storage operations. This suggests that losses and gains have occurred during storage operations. This is consistent with the qualitative conclusions drawn from a review of the operational plots (SIWHP vs Time and Unadjusted Book Inventoy vs Time).

The plot of Unadjusted NEG vs Date clearly indicates the time periods experiencing losses, gains, and stability.

IPP History Plots
A plot of IPP values vs time generated with Fall data points clearly shows the following:

1. Non-linear increase in the TIPP w/Flat IIPP in 1950's (GAIN)
2. Flat TIPP and IIPP during 1960's (NO LOSS or GAIN)
3. Linear increase in the TIPP w/Flat IIPP in 1970's (LOSS)
4. Flat TIPP and IIPP during 1980's (NO LOSS or GAIN)
5. Non-linear decrease in the TIPP w/Flat IIPP in 1990's (GAIN)
6. Flat TIPP and IIPP from 2000-2005 (NO LOSS or GAIN)

Loss Calculations using the TIPP Plot
Loss rates and volumes were calculated using this plot generated with Fall only data points. The losses calculated using this plot can be summarized as follows:

- 80 MMscf/yr loss 1950-1955 (Lost Volume = 400 MMscf)
- 35 MMscf/yr loss 1955-1960 (Lost Volume = 175 MMscf)
- No Losses 1960-1970 Lost Volume = 0 MMscf
- 50 MMscf/yr loss 1970-1980 (Lost Volume = 500 MMscf)
- No Losses 1980-1990 Lost Volume = 0 MMscf
- 50 MMscf/yr gain 1990-2000 (Lost Volume = -500 MMscf)
- No Losses 2000-2005 (Lost Volume = 0 MMscf)

Based on this analysis, the total net inventory lost between 1950-2005 is 575 MMscf

Appendix II

UGS Inventory Verification Primer

Table of Contents

1. Introduction to Inventory Verification

Inventory verification is a way to keep track of amount of gas in storage through analysis of shut-in well pressures and injection and withdrawal volumes

1.1. Objectives

The objectives of inventory verification include the following:

- To verify book inventory is actually present in the reservoir and available for withdrawal

- If gas has been lost, to determine its magnitude

- To monitor growth or shrinkage of gas bubble in aquifer storage

1.2. Theory

Traditional inventory verification techniques are based on the real gas law (note: aquifer storage fields may require different analysis techniques – see section 4 below)

$$p\,V = znRT$$

If pressure varies from point to point within the reservoir, may need to calculate average pressure from individual well pressures

$$p_{avg} = \frac{\sum p_i h_i A_i}{\sum h_i A_i}$$

Where

A_i	=	Drainage area of well i
h_i	=	Thickness of reservoir in drainage area of well i
p_i	=	Pressure of well I
p_{avg}	=	Average reservoir pressure

It is important to note that virtually all of the industry-standard inventory analysis techniques (except reservoir simulation) assume that the storage field is operated in a similar manner from year to year, and that shut-in pressures used in the calculations are stabilized. The results of these industry-standard inventory analysis techniques should be interpreted with caution if significant changes in operations occur from year to year and/or shut-in periods are not of sufficient length to ensure stable shut-in if pressures.

1.3. *Data Required*

The amount and types of data required for the inventory analysis process will vary, depending on the type of reservoir being analyzed (dry gas or aquifer). Generally, the primary types of data used in the inventory analysis process include:

- Static field/reservoir data, including:

  - Field Name

  - Field Type (Dry Gas or Strong Aquifer)

  - Reservoir Depth

  - Reservoir Temperature

  - Reservoir Pressures (Base Pressure and Top Pressure)

  - Specific Gravity (Gas and Water)

- Static well data, including:

  - Well ID

  - Well Name

  - Well Type

  - Weighting Factor used in average pressure calculations

  - Depth to reservoir at well location

- Dynamic well data, including

  - Shut-in Pressure for each well, for each shut-in event

- Dynamic field inventory data, including

  - Book Inventory (Uncorrected and Unadjusted) vs date

  - Historical Inventory Corrections vs date

  - Historical Inventory Adjustments vs date

1.4. Key or Indicator Wells

Often, one or more wells are designated as key wells

- Typically they remain shut-in

- No injection or withdrawal from these wells

- Best if not even tied into surface header, to avoid erroneous pressures:

    o Cannot leak from header into well

    o Cannot leak from well into header

The next best thing to a key well as described above is pseudo-key well:

- Typically shut-in for a period of time only *periodically* (e.g., weekly)

    o Injection or withdrawal from these wells occur between shut-in's

    o Must be tied into surface header

Selection of key well locations should be such that pressures are representative of average reservoir pressure. If no key wells are available in a field, the operator usually shuts-in all I/W wells each spring and fall for a period of time sufficient for pressure stabilization

The number and types of calculations made during the inventory analysis process will vary, depending on the type of reservoir being analyzed (dry gas or aquifer). In nearly all analyses, however, it is necessary to calculate the average reservoir pressure from raw wellhead pressure data. The two most common calculation methods used are discussed below.

1.4.1. Calculated Average Reservoir Pressure from Keywell SIWHP's

Usually, a keywell is located such that the bottom hole pressure calculated from the pressure observed in this well is considered representative of the average reservoir pressure. In the rare instances where an operator has more than one keywell, it may be necessary to calculate an average bottom hole pressure.

1.4.2. Calculated Average Reservoir Pressures from IW Well SIWHP's

In most storage fields, operators use wellhead pressures collected from IW wells at the end of spring and fall shut-in periods to estimate average reservoir pressure. In this case, an average shut-in wellhead pressure is calculated using individual well SIWHP values at the end of the shut-in period. This average shut-in wellhead pressure is then converted to a bottom hole pressure assumed to be representative of the average reservoir pressure . Either an arithmetic or a weighted average technique can be used, depending on the characteristics of the reservoir.

2. Inventory Analysis Plots

2.1. Plot of Basic Operational Data

- Review plots of operational data to

  - Identify any operational trends that may provide preliminary, qualitative indications of ongoing losses and

  - Show timeframes wherein we need to be careful analyzing data due to widely varying operational practices.

- Example of such a plot is the BHP/z vs Time and Unadjusted Book inventory vs time plots shown below. In this example plot, we see that:

  - Unadjusted book inventory is remaining relatively steady over time while

  - BHP/Z values are declining over time

- The trends in this example suggest that losses may be occurring.
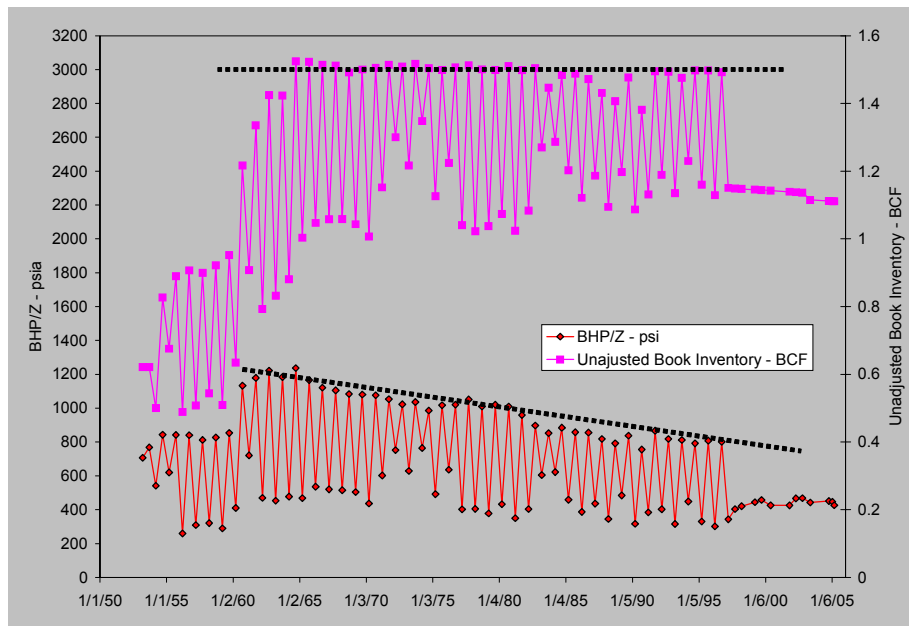
2.2. Gas Material Balance Plots: BHP/z vs Cum Production
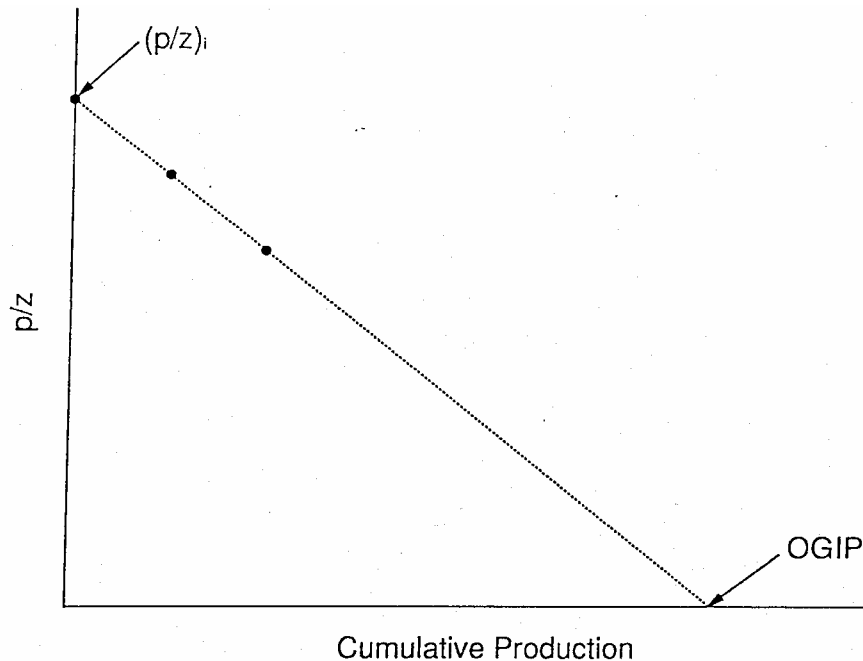
Gas material balance performance during primary depletion of volumetric gas reservoir.

- Graph

    o p/Z from

        ▪ Pressure survey

        ▪ One or more key wells

    o Vs. Cumulative production

- Often used during primary production to

    o Determine drive mechanism

    o Estimate original gas-in-place (prior to conversion to storage, this estimated GIP volume is often presumed to be a reasonable estimate of the total top gas in storage at initial reservoir pressure)

2.3. Pressure Content Plots – p/Z vs Inventory
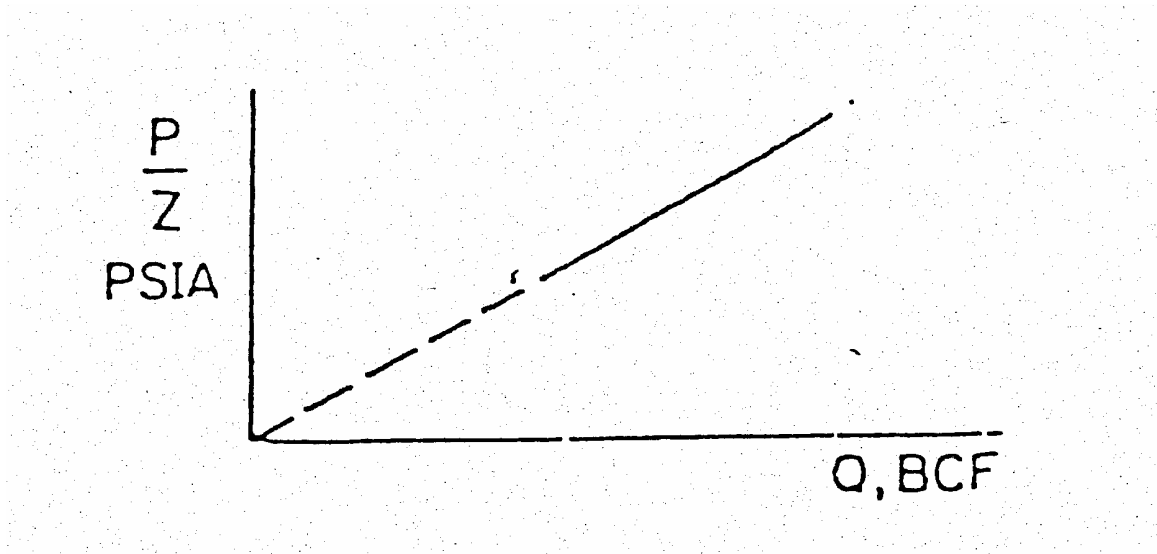
Pressure-content curve for a constant volume reservoir.

From Tek (1987).

- Graph

    - p/Z from

        - Pressure survey

        - One or more key wells

    - Vs. Inventory calculated from injection and withdrawal records (book inventory)

- Detection of Gas Loss

   o Line moves to the right with time

   o Changes in x-intercept indicate the amount of loss
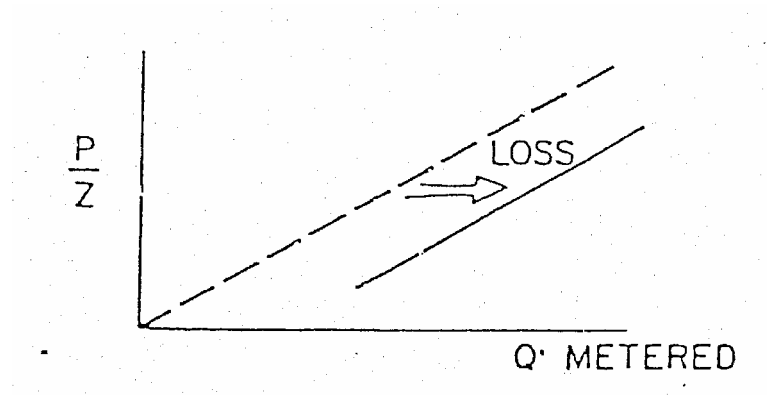
Effect of finite gas loss. From Tek (1987).

- Detection of Gas Gain

   o This might occur for a collector zone

   o Line moves to the left with time

   o Changes in x-intercept indicate the amount of gain
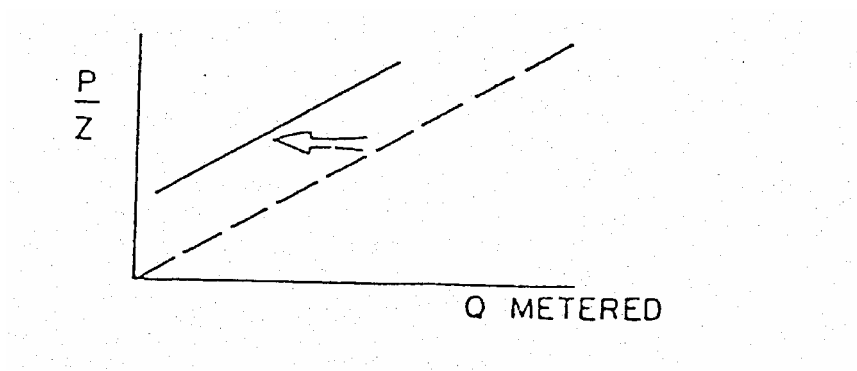
Effect of finite gas gain. From Tek (1987).

- <u>Detection of Gas Bubble Growth</u>

  o Slope of line decreases

  o x-intercept does not change
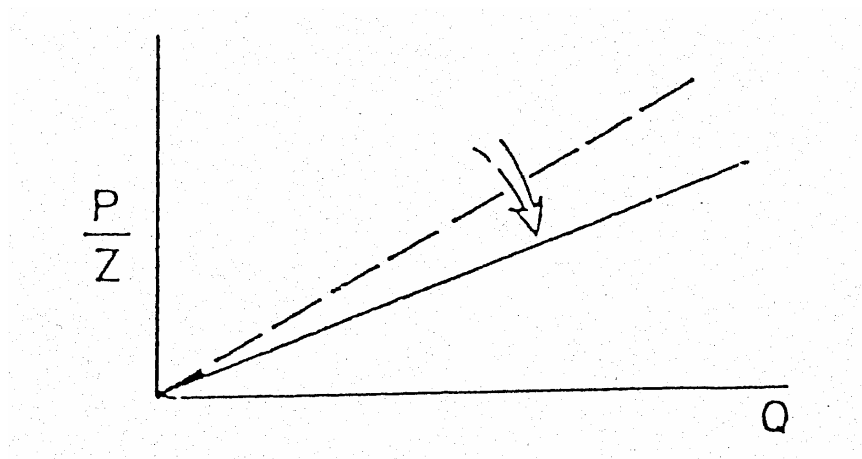
**Pressure-content curve for a reservoir subject to a volume increase.
From Tek (1987).**

- <u>Detection of Gas Bubble Shrinkage</u>

  o Slope of line increases

  o x-intercept does not change
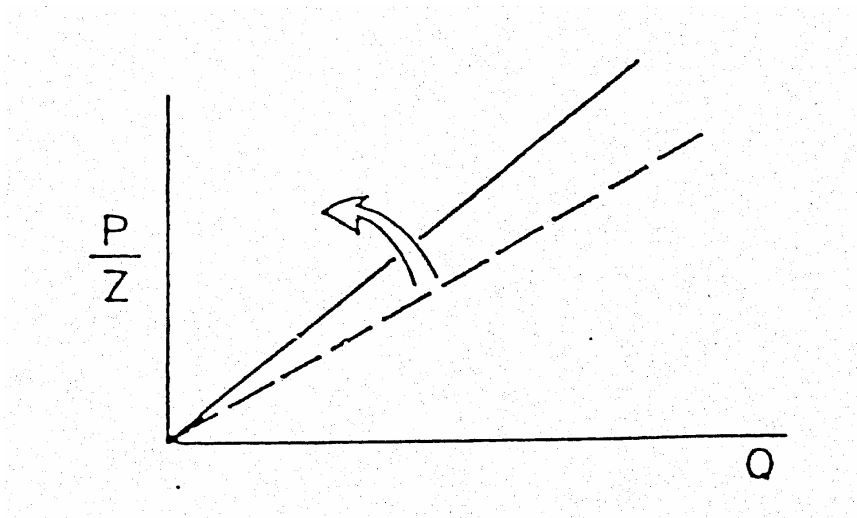
**Pressure-content curve for a reservoir subject to a volume decrease.
From Tek (1987).**

- <u>Detection of Combinations: Gas loss or gain and gas bubble growth or shrinkage</u>
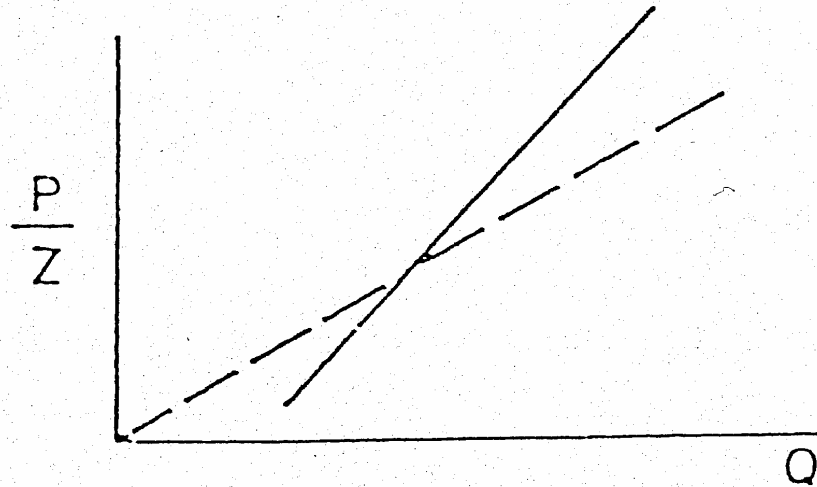
Pressure-content curve for a reservoir subject to a volume decrease and finite loss. From Tek (1987).
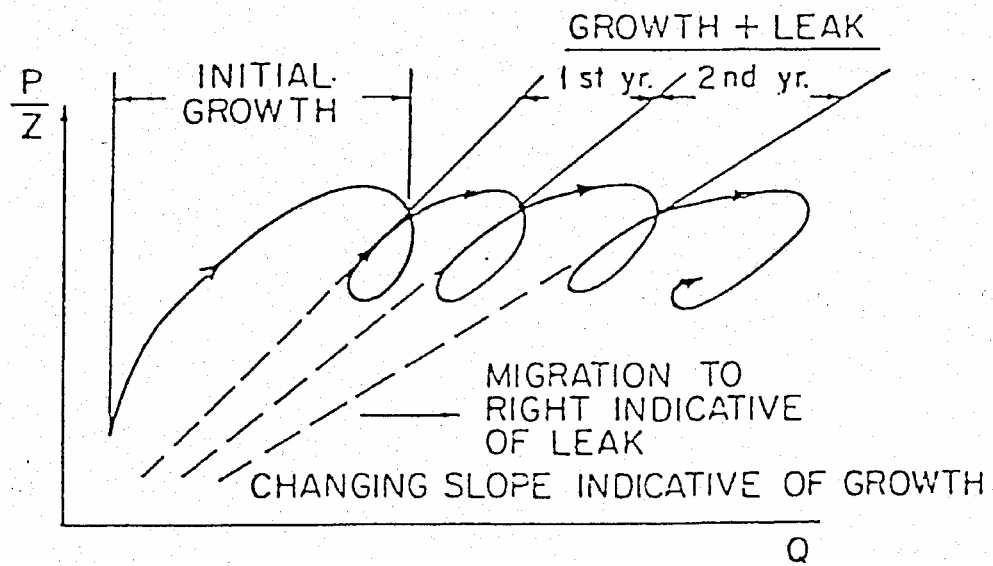
Pressure-content performance in an aquifer storage subject to growth and leak. From Tek (1987).

- <u>Hysteresis Curves</u>
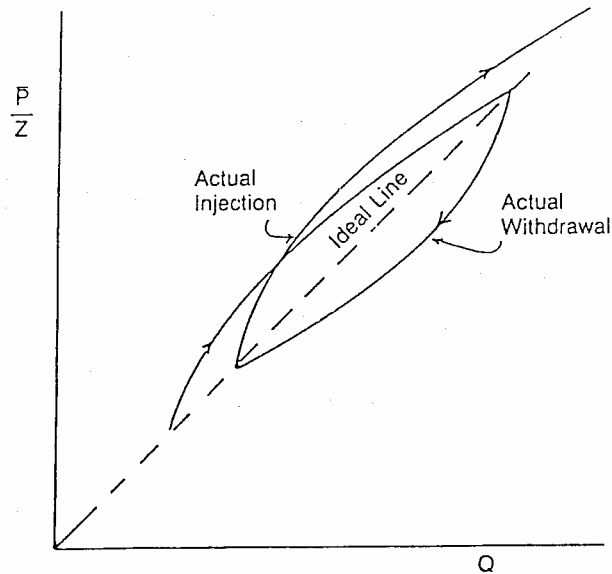
Pressure-content pattern on a volumetric storage reservoir showing hysteresis.
From Tek (1987).

- Often, p/Z vs inventory plots exhibit higher pressures at a given inventory level during injection than at the same inventory level during withdrawal

    - This is caused by not having full pressure equilibrium in the reservoir

    - Following injection, measured wellbore pressure may still be higher than average reservoir pressure, even after 7 day shut-in

    - Following withdrawal, measured wellbore pressure likely to be lower than average reservoir pressure

- Contributing factors

    o Low permeability

    o Layering - presence of layers may require one or two orders of magnitude longer to reach equilibrium than homogeneous system with same average permeability

    o Water movement in the aquifer.

- Ways to minimize the effect

  - Allow adequate time for pressure to. stabilize (may not be feasible)

  - Use pressures measured at observation wells which are not used for production

  - Use methods from pressure transient analysis to extrapolate pressure measurements to current average drainage area pressure

2.4. Inventory Per Pounds Plots

- Graph

  o Total inventory per pound: [(Book inventory) / (P/Z)] vs. Time

$$TIPP = \frac{G_b}{p/z}$$

  o where
    - TIPP   = Total inventory per pound (total inventory per pressure unit)
    - G_b = Book inventory
    - p/z   = Average pressure divided by real gas deviation factor

- Graph

  o Incremental inventory per pound vs. Time
    - (Change in book inventory) / (Change in p/Z for INJ or WD season)] vs. Time

$$IIPP = \frac{\left(G_{bf} - G_{bs}\right)}{\left((p/z)_f - (p/z)_s\right)}$$

  o where
    - IIPP   = Incremental inventory per pound (pressure unit)
    - G_b = Book inventory
    - P/z   = Average pressure divided by real gas deviation factor
    - s   = Spring, following withdrawal season
    - f   = Fall, following injection season

- Detection of constant volume reservoir

  o Total inventory per pound is constant with time

  o Incremental inventory per pound is also constant with time, and is approximately equal to the total inventory per pound

Inventory Per Pound Analysis Plot
No Gas Loss or Gain Example
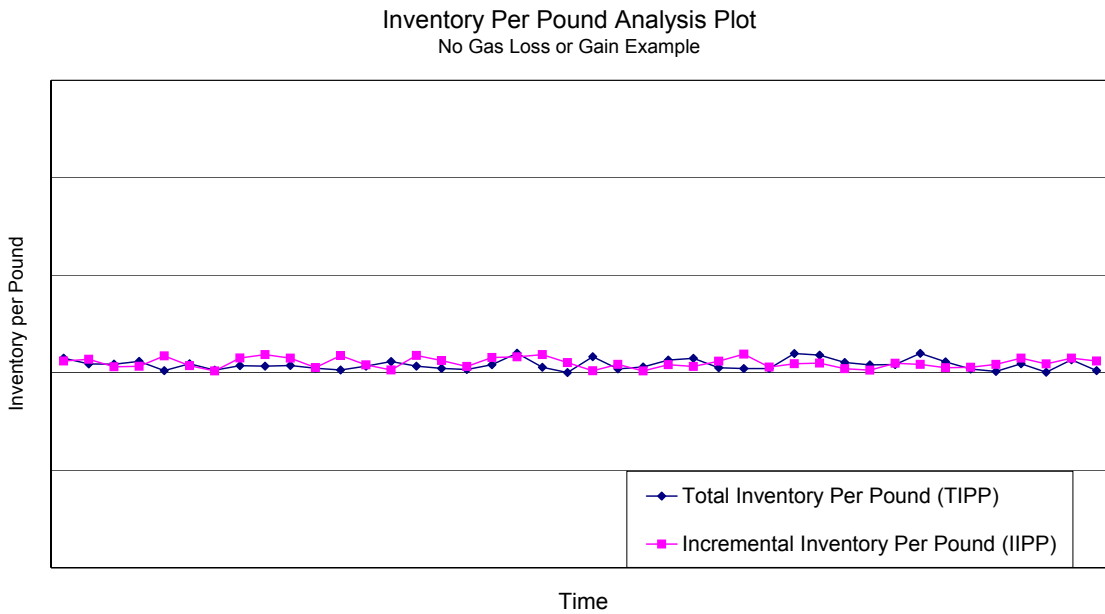
Example plot indicating no gas gains/losses

- Detection of gas bubble growth/gas loss

  o Total inventory per pound increases with time

  o Incremental inventory per pound

    ▪ Constant with time indicates an on-going gas loss

    ▪ Increasing with time indicates a growing gas bubble

Inventory Per Pound Analysis Plot
Ongoing Gas Loss Example
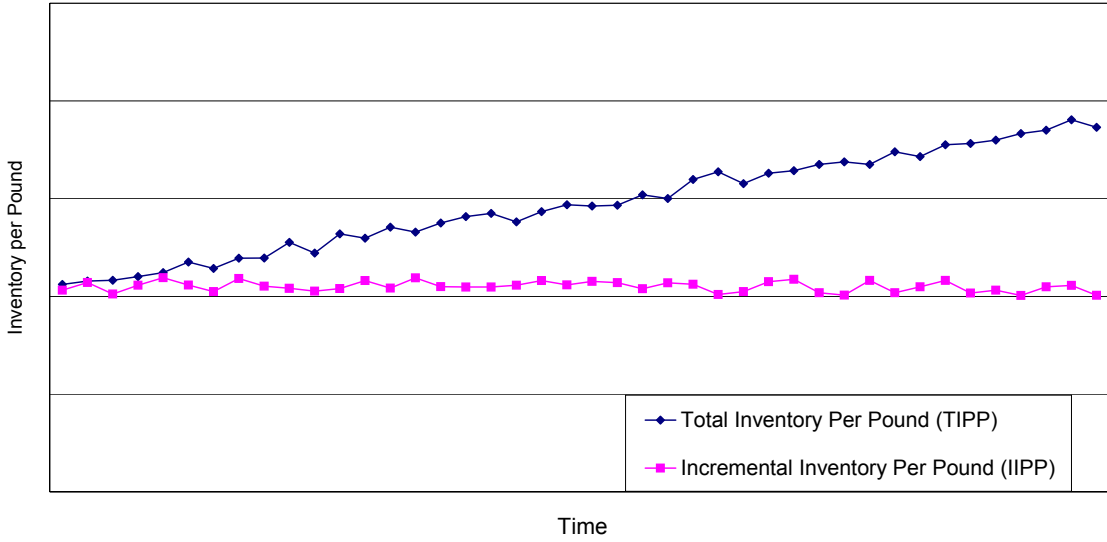
Example plot indicating ongoing gas losses

Inventory Per Pound Analysis Plot
Bubble Growth Example
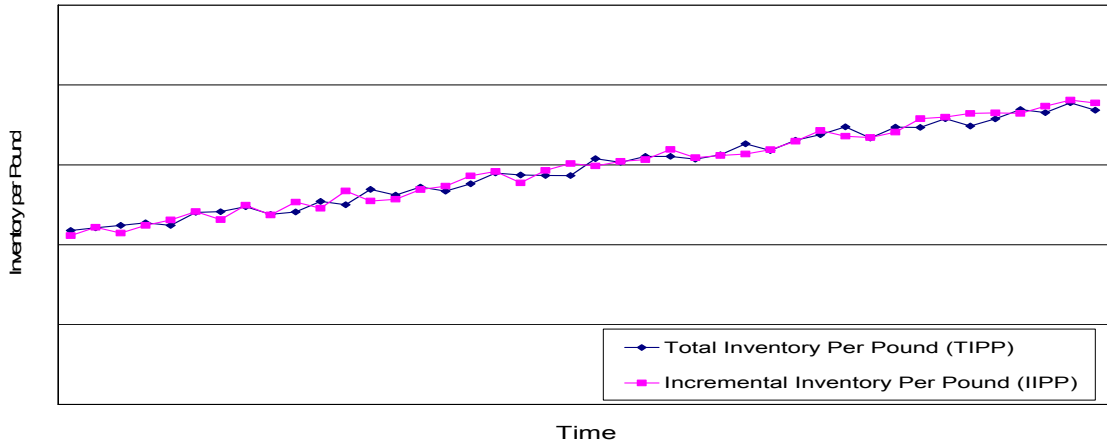
Example plot indicating bubble growth

- Detection of Gas bubble shrinkage/gas gain

  o Total inventory per pound decreases with time

  o Incremental inventory per pound

    ▪ Constant with time indicates an on-going gas gain

    ▪ Increasing with time indicates a shrinking gas bubble

Inventory Per Pound Analysis Plot
Ongoing Gas Gain Example

Legend:
◆ Total Inventory Per Pound (TIPP)
■ Incremental Inventory Per Pound (IIPP)

Y-axis: Inventory per Pound
X-axis: Time

Example plot indicating ongoing gas gains

Inventory Per Pound Analysis Plot
Bubble Shrinkage Example

Legend:
◆ Total Inventory Per Pound (TIPP)
■ Incremental Inventory Per Pound (IIPP)

Y-axis: Inventory per Pound
X-axis: Time
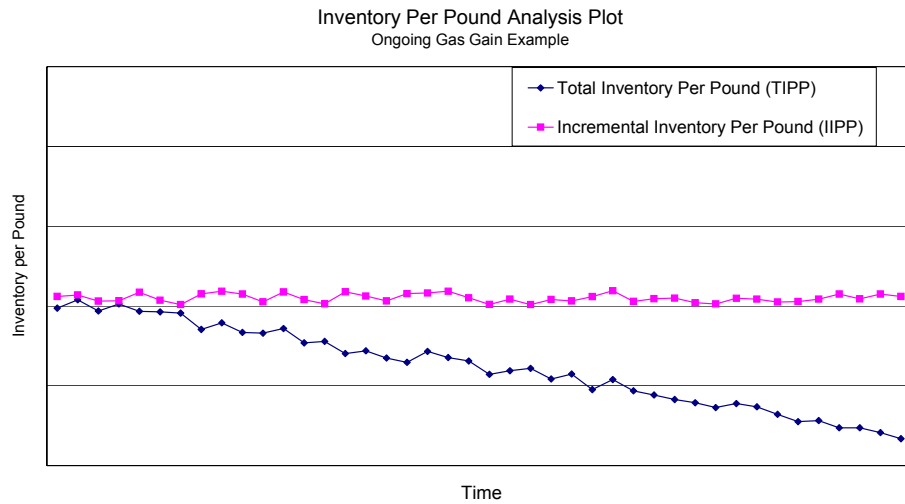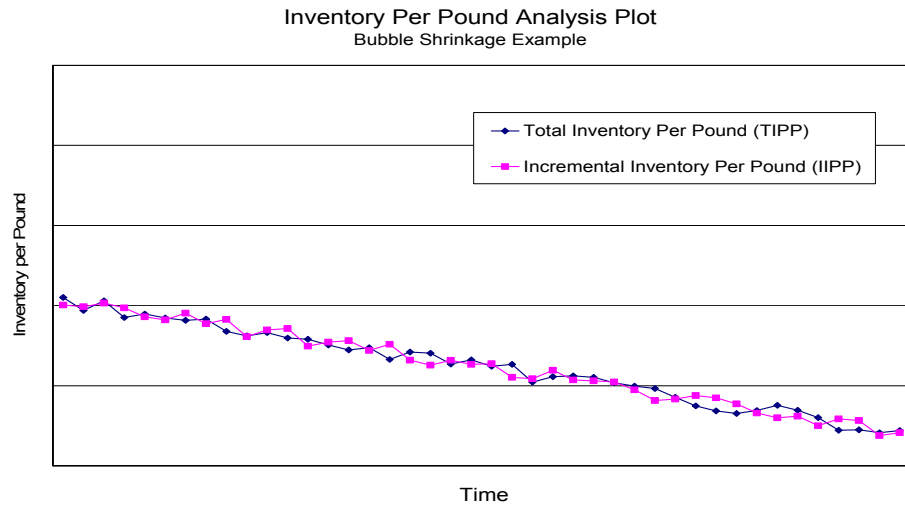
Example plot indicating bubble shrinkage

2.5. Non-Effective Gas
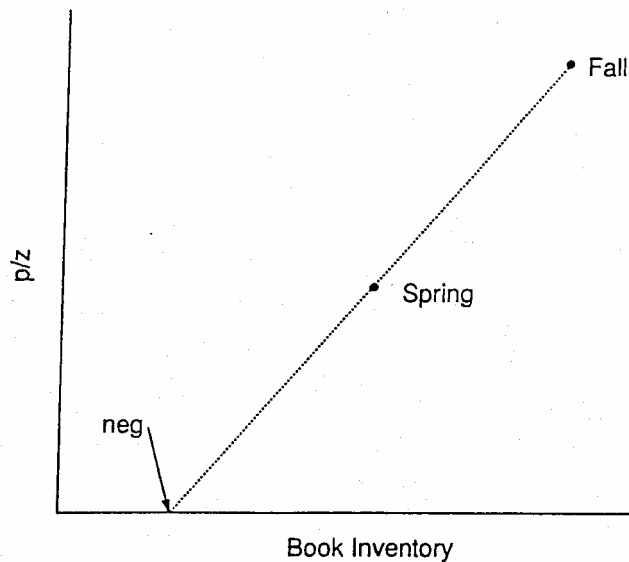
Extrapolation of fall-spring pressure content graph to zero p/z.

- Extrapolate fall-spring p/z vs. book inventory to p/z = 0

$$NEG = GIP_f - \left(\frac{p}{z}\right)_f \frac{\left(GIP_f - GIP_s\right)}{\left(\left(\frac{p}{z}\right)_f - \left(\frac{p}{z}\right)_s\right)}$$

where

NEG	=	"Non-effective gas"
GIP	=	Gas in place
p/z	=	Average reservoir pressure divided by real gas deviation factor
f	=	Fall conditions, at end of injection season
s	=	Spring conditions, at end of withdrawal season

- Graph

  - Non-effective gas

  - vs. Time

- Gives direct estimate of total gas lost as a function of time
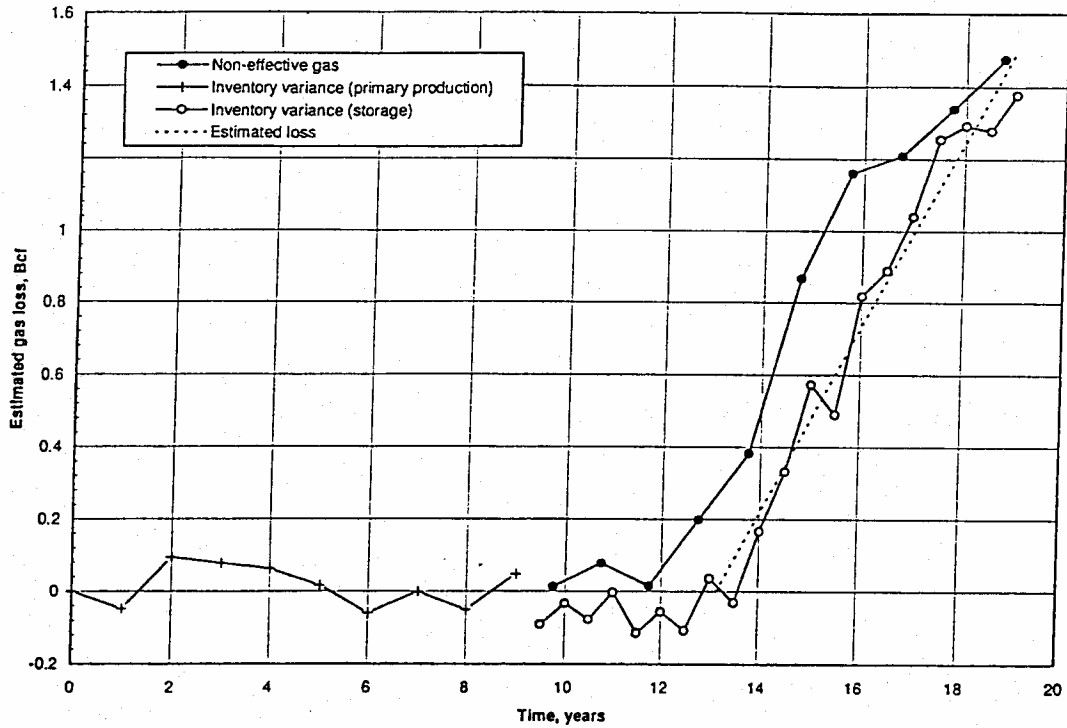
2.6. Pore Volume Ratio

- Ratio of reservoir volume occupied by book inventory to original gas pore volume

$$PVR = \frac{\left(G_b \middle/ \left(\frac{p}{z} \right) \right)}{\left(G \middle/ \left(\frac{p}{z} \right)_i \right)}$$

Where

PVR = Pore volume ratio

G = Original gas in place

G_b = Book inventory

(p/z) = Conditions at time of Book inventory

$(p/z)_i$ = Initial conditions

- Graph Pore volume ratio vs. Time

- Trends in the calculated PVR from unity indicate

  o Constant pore volume (PVR = 1)

  o Pore volume growth (PVR>1.0)

  o Pore Volume shrinkage (PVR<1.0)
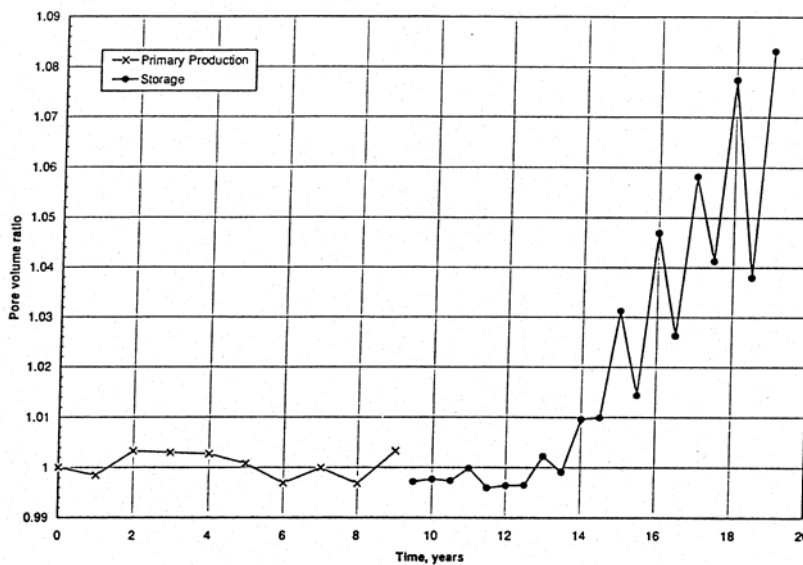
Pore volume ratio.

Plot of pore volume ratio showing pore volume growth

2.7. Inventory Variance From Material Balance

- Difference between book gas-in-place and gas-in-place from material balance calculation

$$\text{Variance} = G_b - G\frac{(p/z)}{(p/z)_i}$$

where

G	=	Original gas in place
G_b	=	Book inventory
(p/z)	=	Conditions at time of Book inventory
$(p/z)_i$	=	Initial conditions

- Graph Variance vs. Time

  - Gives direct estimate of total gas lost as a function of time

  - Very similar shape to non-effective gas graph

2.8. Inventory Analysis in Aquifer Storage

- A strong aquifer may provide enough pressure support that pressure content and inventory per pound plots cannot be used

- Graph Field deliverability vs. Cumulative seasonal withdrawal

  - If no loss is occurring, curves for consecutive seasons with overly each other

  - If there is loss, field deliverability will decrease at a given cumulative withdrawal with subsequent season
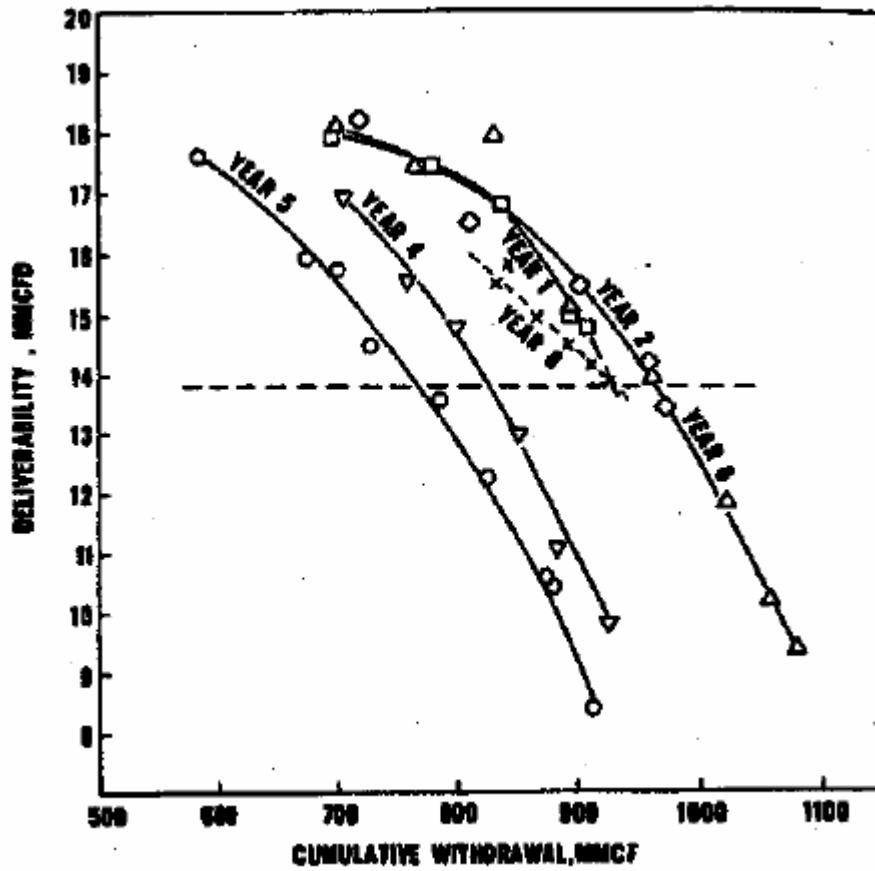
Plot of field deliverability vs. cumulative seasonal withdrawal indicating gas losses from Mayfield 1981

2.9. Inventory Analysis Nomenclature

For purposes of analysis techniques used in this software, we define the following terms:

Book Inventory

The book inventory at any point in time equals the estimated volume of gas in the reservoir at the time of conversion to storage, plus the cumulative net injected volume (cumulative net injected volume = total injections - total withdrawals). Caution should be exercised when evaluating data from storage operators, as the reporting of inventory is not standard between (and sometimes within) companies. For example, some report "Total *Injected* Book Inventory" (exclusive of native gas inventory), some report "Total *Working Gas* Inventory," and others report "*Total Gas in Place* Inventory" (using estimated native gas volumes).

Book Inventory Adjustment

Book inventory adjustments represent corrections to inventory volumes, and are usually taken/booked at a discrete point in time on storage company ledgers. These adjustments could be taken to correct for lost volumes due to known causes (e.g., gas produced from a well initially thought to be isolated from the storage reservoir which is later determined to be in communication with the storage reservoir), or unknown causes (e.g., the inventory analysis process may indicate ongoing losses are occurring from an undetermine cause). In both cases a book inventory adjustment is typically made by the storage operator.

It should be noted that adjustments to book inventory are not typically spread over the timeframe of the loss, but usually show up at a specific point in time on the storage company's ledger. A storage engineer performing inventory analysis may want to spread these adjustments over the time period during which the inferred losses are estimated to have occurred, in order to make the trends of the diagnostic plots used in inventory analysis consistent with the timing of the lost rates/volumes.

Non-Effective Gas

Non-Effective Gas (NEG) is gas inventory which has no observable impact on storage operations. The NEG volume usually manifests itself as an x-intercept on a plot of (Total GIP) vs (P/Z), where the Total GIP is plotted on the x-axis and the P/z is plotted on the y-axis. Non-effective gas may or may not be recoverable at the conclusion of storage operations, and therefore may or may not represent lost gas.

An example of *recoverable* non-effective gas may clarify the concept. There will often be a volume of gas that, over a $\pm$ 50-yr primary production life of a gas field, can be removed from portions of the reservoir having lower permeability than the portion of the reservoir volume with higher permeability (containing most of the storage working gas volume during storage operations).

After conversion of the producing gas field to storage, it will take several cycles of higher average operating pressures to replace gas volumes depleted from tighter portions of the field during primary production. During this time period, gas that is initially injected into the high perm

portion of the reservoir during early storage operations can "leak" into the lower perm portion of the reservoir and be "stored" in the lower perm reservoir volumes. Because these volumes have lower permeabilities, the gas cannot be effectively removed within the very short withdrawal periods associated with storage operations. Hence, from a P/z-analysis standpoint, it appears that these gas volumes are not present in the reservoir. Hence the term, "Non-Effective."

Note that not all NEG is recoverable, as lost gas is also non-effective during storage operations.

3. **Example Problem**

In this section of the manual, we will walk the user through a typical Inventory Analysis (IA) process using the example data below.

The Big Boy Field is a single-well dry gas field that produced from 1925 to 1940. The field remained shut-in from 1940-1949, at which time it was converted to storage (no additional wells were drilled). It has been an active storage facility since 1950. The storage reservoir is known have a small layer of lower permeability formation within the storage interval.

Historically, the storage field has operated between a minimum shut-in wellhead pressure of 650 psig and a maximum shut-in wellhead pressure of 1000 psig. Each Spring and Fall during storage operations, the operator measured the shut-in wellhead pressure in one IW well (Well ID 1) that is completed in the storage reservoir. The depth to the reservoir in this well is 5000 ft. The average wellhead temperature is 60 degrees F and the average reservoir temperature is 110 degrees F. Gas gravity is 0.58.

There is 1 mile of new (at conversion) 3" ID gathering line in the field. This line has custody transfer measurement facilities where it connects to a sales line that operates at 500 psi. From 1990 to 2000, separate measurement devices were "temporarily" installed at the sales lines to measure injected volumes. In 2000, this temporary injection measurement facility was removed.

Each year, when the wellhead pressures reach 700 psi, the one IW well is tested. During this test, the gas is vented into the atmosphere. These annual tests consist of three 15-minute flow periods (100 mscf/d, 200 mscd/d and 300 mscf/d) followed by a 45 minute extended flow (400 mscf/D).

At the end of withdrawal each year, a downhole camera is run in the IW well. Prior to running the camera, a bridge plug is set just above the bottom of the tubing (3" ID). There is a sealing packer at the bottom of the tubing, which is run inside casing (6" ID). Also at the end of withdrawal each year, the gathering line is blown down and pigged.

The Spring and Fall shut-in wellhead pressures recorded at the IW well and the corresponding unadjusted book inventory values are shown in the table on the following page.

Example Problem
Inventory Assessment Data

Date	Unadjusted Inventory (Bscf)	SIWHP psig
3/15/50	10.000000	650
9/15/50	15.000000	1000
3/15/51	10.100000	650
9/15/51	15.100000	1000
3/15/52	10.190000	650
9/15/52	15.190000	1000
3/15/53	10.270000	650
9/15/53	15.270000	1000
3/15/54	10.340000	650
9/15/54	15.340000	1000
3/15/55	10.400000	650
9/15/55	15.400000	1000
3/15/56	10.450000	650
9/15/56	15.450000	1000
3/15/57	10.490000	650
9/15/57	15.490000	1000
3/15/58	10.520000	650
9/15/58	15.520000	1000
3/15/59	10.540000	650
9/15/59	15.540000	1000
3/15/60	10.550000	650
9/15/60	15.550000	1000
3/15/61	10.550000	650
9/15/61	15.550000	1000
3/15/62	10.550000	650
9/15/62	15.550000	1000
3/15/63	10.550000	650
9/15/63	15.550000	1000
3/15/64	10.550000	650
9/15/64	15.550000	1000
3/15/65	10.550000	650
9/15/65	15.550000	1000
3/15/66	10.550000	650
9/15/66	15.550000	1000
3/15/67	10.550000	650
9/15/67	15.550000	1000
3/15/68	10.550000	650
9/15/68	15.550000	1000
3/15/69	10.550000	650
9/15/69	15.550000	1000
3/15/70	10.600000	650
9/15/70	15.600000	1000
3/15/71	10.650000	650
9/15/71	15.650000	1000
3/15/72	10.700000	650
9/15/72	15.700000	1000
3/15/73	10.750000	650
9/15/73	15.750000	1000
3/15/74	10.800000	650
9/15/74	15.800000	1000
3/15/75	10.850000	650
9/15/75	15.850000	1000
3/15/76	10.900000	650
9/15/76	15.900000	1000
3/15/77	10.950000	650
9/15/77	15.950000	1000
3/15/78	11.000000	650
9/15/78	16.000000	1000
3/15/79	11.050000	650
9/15/79	16.050000	1000
3/15/80	11.050000	650
9/15/80	16.050000	1000
3/15/81	11.050000	650
9/15/81	16.050000	1000
3/15/82	11.050000	650
9/15/82	16.050000	1000
3/15/83	11.050000	650
9/15/83	16.050000	1000
3/15/84	11.050000	650
9/15/84	16.050000	1000
3/15/85	11.050000	650
9/15/85	16.050000	1000
3/15/86	11.050000	650

Using the example data provided above:

- Load pertinent data into the EXCEL template

- Upload this data into the software

- Browse the data tables using the software

- Calculate BHP and BHP/Z values using the software

- Calculate TIPP and IIPP values using the software

- Peruse the various help features:

    o Open the Inventory Analysis Primer and peruse the document.

    o Open the Toolbox peruse the spreadsheet

    o Open the Help for input document and peruse the document.

    o Open the Help for analysis plots document and peruse the document.

    o Open the Storage Terms and peruse the document.

    o Open the Glossary and peruse the document.

    o Open the Summary of References and peruse the document.

- Browse the available analysis plots

- Review/Analyze appropriate diagnostic plots to calculate the inventory loss rates and volumes where appropriate

- Comment on the nature of the losses.

- Use the toolbox to determine if the losses can be reasonably explained by:

    o Line losses

    o Annual pigging of gathering lines

    o Annual well testing operations

    o Downhole camera 0perations

- Select several plots for inclusion in a report and generate a draft report

3.1. Loading Data Into EXCELTM Template

The first thing that needs to be done in any inventory analysis that utilizes the newly developed software is to reformat/reorganize the inventory data supplied by the operator. Generally, this is a fairly straightforward process, and simply involves cut/copy and paste commands within EXCEL, and perhaps some simple calculations within EXCEL to fill in necessary columns of input data.

We have installed the inventory analysis software on the D Drive, under the subdirectory called "Program Files." During the installation process, a subdirectory is created under the "Program Files" subdirectory called "EXCEL Template." In this subdirectory are several EXCEL files, including one named "Ex_Prob_Raw_Data.xls" in which is stored the raw data as collected by the operator. This file consists of a single sheet of data as shown above (see page with heading Example Problem Inventory Assessment Data). Open this file.

The EXCEL template used to import data into the software is in the same location, and is named "Upload Data Template.xls." Open this file also. The first sheet in the file ("DatesCalc") looks like this:

To populate this sheet, we will perform the following steps:

1. Copy data from cells A2–A113 in the raw data file (Ex_Prob_Raw_Data.xls) and past these values into Cells B2 – B113 in Sheet DatesCalc, in Excel template file (Upload Data Template.xls). Sheet DatesCalc in the "Upload Data Template.xls" should now look like this:

2. The **ID** column in this spreadsheet is simply a unique integer, or "auto-number," which we can populate by inputting a 1 in cell A2 and copying a formula in cells A3-A113 that adds one to the integer directly above it.

3. The **Year** column in this spreadsheet can be calculated using the YEAR function in EXCEL, using the date in column D as the input. For example cell B2 would contain the formula "Year(D2)." This formula can then be copied to D3-D113 to populate the remaining cells.

4. The **Season** column in this spreadsheet can be calculated using a conditional statement in EXCEL, using the date in column D as the input. For example cell C2 would contain the formula "IF(MONTH(D2)<6,"SPRING","FALL")." This formula can then be copied to D3-D113 to populate the remaining cells. Sheet DatesCalc in the "Upload Data Template.xls" is now populated and should now look like this:

The second sheet in "Upload Data Template.xls file ("InvUnadjCorrAdj") looks like this:

To populate this sheet, we will perform the following steps:

1. Copy the date and book inventory values from cells A2–B113 in the raw data file (Ex_Prob_Raw_Data.xls) and past these values into Cells B2–C113 in Sheet "InvUnadjCorrAdj", in Excel template file (Upload Data Template.xls).

2. The **ID** column in this spreadsheet is simply a unique integer, or "auto-number," which we can populate by inputting a 1 in cell A2 and copying a formula in cells A3-A113 that adds one to the integer directly above it.

3. **Corr_Vol, Cum_Corr, Adj_Vol, Cum_Adj, and Inventory_Corrected_Adjusted** columns in this spreadsheet are used to store corrections and/or adjustments and store the calculated values of cum corrections, cum adjustments, and corrected adjustmented book inventory. In this example, there are no corrections or adjustments to the book inventory, so all of these columns can be populated with zero's. Note the following about this input sheet:

    a. Although there are columns to input both "corrections" and "adjustments," the "corrections" columns are included in anticipation of a software upgrade wherein a distinction between a correction and an adjustment can be made. When using the current version of the software, input all changes made to the book inventory as adjustment.

    b. The values in columns labeled **Cum_Corr**, **Cum_Adj**, and **Inventory_Corrected_Adjusted,** are calculated within the software, and therefore zeros can be entered at this point

4. Sheet **InvUnadjCorrAdj** in the "Upload Data Template.xls" is now populated with data and should look like this:

No data was supplied in the example problem for the next two Sheets in the input template (**NetInjWd** and **NetInjWdAquifer**), so these will remain blank.

The **WellData** sheet contains information related to the one IW well. To populate this sheet, we will perform the following steps:

1. The **ID** column in this spreadsheet is simply a unique integer, or "auto-number," which we can populate by inputting a 1 in cell A2 and copying a formula in cells A3-A113 that adds one to the integer directly above it.

2. The **Well_ID** column contains a unique identifier for each well, and has the format of an integer. We identified the well in which the shut-in wellhead pressure is measured each spring and Fall as Well 1, so we will use a **Well_ID** of 1 to identify the well.

3. The **Resv_Depth** column contains the depth (TVD) to the reservoir in the well, which was given as 5000 ft.

4. The **X** and **Y** columns contains well location information for use in future upgrades and is not used in this version of the software. You can enter any number in these columns you want, as they are not used.

The **WellData** sheet is now populated with data and should look like this:

No data was supplied in the example problem for the next two Sheets in the input template (**WellGas** and **WellWater),** so these will remain blank.

The last sheet in "Upload Data Template.xls file ("WellWHP") looks like this:

To populate this sheet, we will perform the following steps:

1. Copy the Date and SIWHP in cells A2–A113 and cells C2-C113 in the raw data file (Ex_Prob_Raw_Data.xls) and past these values into cells C2–C113 and cells D2–D113 respectively in Sheet "SIWHP", in Excel template file (Upload Data Template.xls).

2. The **ID** column in this spreadsheet is simply a unique integer, or "auto-number," which we can populate by inputting a 1 in cell A2 and copying a formula in cells A3-A113 that adds one to the integer directly above it.

3. The **Well_ID** column should contain the Well_ID from the single well shown in sheet "WellID"

4. The **Comments** column can contain any text you wish to input. We will not input any comments in our file, so all rows under the header row in this sheet should be left blank.

5. The **Given_BHP** column is not used in this version of the software, and should be populated with zeros.

6. The **CalcBHP** column contains output calculated by the software after data is imported and should therefore contain all zeros at this point.

7. Sheet **SIWHP** in the "Upload Data Template.xls" is now populated with data and should look like this:

3.2. Uploading Data into Software

You have now completed populating the EXCEL file originally named, "Upload Data Templae.xls." It is now time to save this file using a different name, in a location you will remember. In this example, we will save the file in the same subdirectory as the Input Data Template was located (i.e., the subdirectory created on the D drive upon installation of the software, D:\Program Files\Gas Storage Software\Excel Template\) and name it KGB_EXAMPLE_Data Template-2.xls.

To upload this data into the IAS, open/start the software. The first screen you will see looks as follows:

Select the button **Click to create New Database,** and use the dialogue box that appears to name the ACCESS file that will be created to contain your uploaded data, in a location of your choice. In this example, we will create an ACCESS file named "KGB_Example-2.mdb" in the same subdirectory that the Input Data Template was located (i.e., the subdirectory created on the D drive upon installation of the software (D:\Program Files\Gas Storage Software\Excel Template\) and name it KGB_EXAMPLE_Data Template-2.xls.

After inputting the name you wish for the ACCESS database to be created, you will see the following dialogue box:

After you click OK, you will proceed to the reservoir data input screen, which looks as follows:

Populate the fields as shown in the following slide:

Note the following:

1. The average reservoir depth entered here is NOT the depth used to calculate SIBHP's from SIWHP's. We anticipate using this field in a later version of the software (allowing the user calculate all BHP's at the average reservoir depth or at the reservoir depth in each individual well). The depth associated with each individual well (entered on **WellData** sheet) is used to calculate BHP's from WHP's in each well.

2. Values entered for Reservoir Top and Base pressures are not used in this software version. We anticipate using them in later versions of the software. Values should be entered, but will not be used in the current software version.

3. Water specific gravity should be entered, but it is not used in dry gas wells.

4. When you click on the continue button, you will be asked if you want to save the changes – respond "yes."

At this point, you will be in the software, but nothing other than the reservoir data has been entered. You will see the following screen at this point:

It is now time to import the data from the EXCEL template file we created, "KGB_EXAMPLE_Data Template-2.xls." To do this, click on the "UPLOAD" tool button shown below:

You will then see the dialogue box below. Using this dialogue box, select the EXCEL input template file we created, ("KGB_EXAMPLE_Data Template-2.xls) from the location in which we stored it (D:\Program Files\Gas Storage Software\Excel Template\), and select "OPEN."

It will take a few moments to import the information from the EXCEL file, so be patient (this process is only required once). Upon completion of the import process, your screen should look as follows:

3.3. Browsing Data & Calculating BHP, p/z, and IPP Values

You can now browse the information located in the various tables by clicking on the table names in the Data Tables Window (upper left tree structure). Notice the following at this point:

1. The first two data tables ("Dates Calculation" & "Inventory Unadjusted…") contain data.

2. The third and fourth tables ("Net Injection Withdrawal" and "NetInjWdAquifer") contain no data because we did not input any data in these tables.

3. The fifth table ("PoverZ") contains no data because we have not yet calculated the BHP and Z values. To calculate the BHP and BHP/Z values, and populate this table with the calculated values, click on the "BHP" tool button shown below:

After clicking on the BHP tool button, the PoverZ table should look as follows:

4. The Sixth table ("TIPP and IIPP") contains no data because we have not yet calculated these values. To calculate TIPP and IIPP values and populate this table with the calculated values, click on the "TIPP" tool button shown below:

5.

After clicking on the TIPP tool button, the "TIPP and IIPP table should look as follows:

6. The seventh table contains the well data we entered, and should look as follows:

7. The eighth and ninth tables ("Well Gas" and "Well Water") contain no data because we did not input any data in these tables.

8.   The tenth table ("WellWHP") contains the SIWHP's input and the SIBHP's calculated from these SIWHP's, and should look as follows:

3.4. Perusing HELP features and Using the ToolBox

At this point, we will take a moment to briefly peruse the various HELP features in the softwareTo access the various HELP features of the software, go to the help menu at the top of the screen, as shown below:

This help button will bring up a menu of help items as shown below:

The various HELP menu items shown include the following:

Steps to work with Program

This is a very abbreviated Users' Manual compiled by the programmer that provides only the most essential information required to use the software.

Inventory Analysis Primer

This is a fairly complete introduction to inventory analysis, and includes discussions on the theory behind inventory analysis, the uses of various inventory analysis diagnostic plots, and references. The table of contents for this document is shown below.

Table of Contents

Toolbox

Selecting this option opens a HELP document related to the EXCEL "Toolbox" that was developed as part of this software. The EXCEL Toolbox is accessed from within the workflow window, and will be discussed in more detail later.

Help for Input

Selecting this option activates a drop-down box to the right, which allows the user to select the input screen for which he needs help. Upon selection of an item in the drop-down box, a WORD file is opened that provides HELP information related to the selected input screen. A description of the data entered on this screen, including data names and formats are summarized.

Help for Analysis Plots

Selecting this option opens a WORD document that provides detailed help for each of the various data QC plots and the diagnostic plots used to estimate loss rates and volumes. The each plot, the purpose, assumptions, applicability, dangers of mis-use, examples, and references are discussed.

Storage Terms

Selecting this option opens a WORD document that provides a description of the various terms used in inventory analysis.

Glossary

Selecting this option opens a WORD document that provides a description of the various terms used in the underground gas storage industry. It is similar in purpose to the "Storage Terms" help above, but much broader in scope.

Summary of References

Selecting this option opens a WORD document that provides a list of various references and technical papers related to the gas storage industry. These references are listed by topic, and should look something like this:

Table of Contents

Example Data

Selecting this option opens an EXCEL document containing the Spring/Fall pressure and inventory example data.

Select HELP features are also accessible for the Workflow window, since we anticipate they will commonly be referenced during the inventory analysis process. In the Workflow Window, there are two Help items listed, the Inventory Primer and the Toolbox, as shown below:

Inventory Analysis Primer

As noted above, this is a fairly complete introduction to inventory analysis, and includes discussions on the theory behind inventory analysis, the uses of various inventory analysis diagnostic plots, and references.

Toolbox

Select this option and open the EXCEL "Toolbox."

After opening the EXCEL Toolbox, go to sheet **Bureau-of-Mines Est Line Losses**, and enter the data given in the example problem data set above to estimate the annual line losses each year we might expect from the 1 mile long gathering line carrying gas from the wellhead to the sales point.

After inputting the example data, your sheet should look like the following:

Obviously, the annual loss rate/volume calculated using the Bureau of Mines data is minimal, and we would not expect that potential loses in the gathering lines to contribute significant to any overall losses from the field.

Next, go to sheet **Est Wellbore Blowdown Volume**, and enter the data given in the example problem data set above to estimate the annual line losses each year we might expect from blowing down the well each year prior to running the camera.

After inputting the example data, your sheet should look like the following:

Obviously, the annual lost volume due to blowing down the well prior to running a camera is minimal, and we would not expect that these losses contribute significant to any overall losses from the field.

Next, go to sheet **Est Well Test Volumes**, and enter the data given in the example problem data set above to estimate the annual losses associated with running the well test each year.After inputting the example data, your sheet should look like the following:

Obviously, the annual lost volume due to testing the well each year is minimal, and we would not expect that these losses contribute significant to any overall losses from the field.

Next, go to sheet **Est Pipeline Volumes**, and enter the data given in the example problem data set above to estimate the annual losses associated with blowing down the gathering line to run the pig each year. After inputting the example data, your sheet should look like the following:

Obviously, the annual lost volume due to pigging the gathering line each year is minimal, and we would not expect that these losses contribute significant to any overall losses from the field.

Note that not all of the calculations that can be made in this EXCEL Toolbox have been demonstrated here.

3.5. *Performing Inventory Analysis*

At this point, all of the data from the example problem has been input/uploaded. We have perused the data tables and the help options, and we used the Toolbox feature to estimate any inventory losses due to field operations. The next step is to use the various plots to analyze loss rates and volumes over the entire life of storage operations.

At this point, it is recommended that you open a word processing document to keep notes about the trends observed during the inventory analysis process. These notes will prove to be extremely valuable after your analysis is complete and you generate a draft report.

We start by reviewing the data QC plots shown in the Workflow Window, under QC Data Plots (see below). Since none of these plots show any irregularities, it is safe to assume that no problems were encountered during the calculation processes we performed earlier.

After reviewing the data QC plots, we review plots of operational data to identify any operational trends that may provide preliminary, qualitative indications of ongoing losses and show timeframes wherein we need to be careful analyzing data due to widely varying operational practices.

The first two plots (**All SIWHP vs Date** and **Avg SIWHP vs Date**) are identical, since there is only one well in the field. For the purpose of this example, look at the **Avg SIWHP vs Date**, which should look like this (you may have to change the scale on the plot):

We observe from this plot that the field has consistently been operated between 650 psi and 1000 psi throughout its life. Therefore, we do not have to worry about wide fluctuations in minimum and maximum operating pressures skewing trends in other diagnostic plots.

We did not load any daily or monthly Net Injection information, so the next plot shows nothing:

The next plot in the workflow is the **UnadjBookInv vs Time**, which shows the book inventory prior to any adjustments as a function of time. This plot is revealing, especially in light of how regularly the field was operated from a pressure perspective. This plot shows that various levels of inventory were required over the field life to achieve the same Spring and Fall shut-in pressures. This trend is a strong indicator, albeit qualitative indicator, that there have been losses and gains occurring during storage operations.

The next three plots, **Inv Adjs vs Date**, **Cum Inv Adjs vs Date**, and **Adjusted Inventory vs Date** are trivial, as no inventory adjustments have been booked during the life of the field. In addition, the two plots after these, **Avg WHP vs Date** and **Avg BHP vs Date**, are not noteworthy.

The next plot, **PoverZ vs Date**, reflects the same trends as the SIWHP vs time, and further demonstrates the uniformity of operations over the life of the storage field from a pressure perspective.

The next plot, **PoverZ vs UnadjInv**, is a plot of the unadjusted book inventory vs the BHP/Z. This plot shows movement to the right and left at various points during the life of storage operations, which leads us to the conclusion the losses and gains have occurred during storage operations. This is consistent with the qualitative conclusions drawn from a review of the the operational plots (SIWHP vs Time and Unadjusted Book Inventoy vs Time).

The next plot, Unadj NEG vs Date, shows the non-effective gas (NEG) calculated for each cycle by back-extrapolating the BHP/Z vs Unadjusted Book Inventory plot for that cycle to a BHP/Z value of zero (i.e., the x-intercept of the plot). This plot clearly indicates the time periods experiencing losses, gains, and stability:

Note that the relative uniformity of injection operations compared to withdrawal operations lead some storage engineers to use only fall data to analyze NEG vs time plots and IPP vs time plots. By applying the FALL filter on this plot, we can generate the plot using only Fall data points:

The next plot is the Unadjusted TIPP vs time and Unadjusted IIPP vs time. These are perhaps the most widely used inventory analysis plots in the storage industry. Usually, these plots are generated using Fall only data points, since injection operations are relatively more uniform than withdrawal operations. Therefore, the Fall data points are generally thought to be less operationally influenced. A plot of IPP values vs time generated using Fall only data points is shown below:

This plot clearly shows the following:

1. Non-linear increase in the TIPP w/Flat IIPP in 1950's   (GAIN)

2. Flat TIPP and IIPP during 1960's   (NO LOSS or GAIN)

3. Linear increase in the TIPP w/Flat IIPP in 1970's   (LOSS)

4. Flat TIPP and IIPP during 1980's   (NO LOSS or GAIN)

5. Non-linear decrease in the TIPP w/Flat IIPP in 1990's   (GAIN)

6. Flat TIPP and IIPP from 2000-2005   (NO LOSS or GAIN)

In order to calculate the loss rates and volumes, we will use the TIPP plot generated with Fall only data points. This is accomplished by clicking on the UnadjTIPP vs Date plot in the Workflow window, filtering on Fall data points, and clicking on the "Calculate Yearly Loss" button (see below).

You can calculate losses for up to 5 time periods using the "Calculate Yearly Loss" button. Simply click the button, read the pop-up directions, and click OK to close the directions. Click on the data point closest to the start of the loss period, then click on the data point closest to the end of the loss period.

The software will automatically calculate annual loss rates for each period and display results on the plot. Using this information, we can calculate the total gains/losses by multiplying the gain/loss rate for each loss period by the number of years the gain/loss occurred, and summing the volumes for each period.

For this example, the TIPP vs Date used to calculate the loss rate looks like the following after loss analysis was performed:

The losses calculated using this plot can be summarized as follows:

- 80 MMscf/yr loss 1950-1955   (Lost Volume = 400 MMscf)

- 35 MMscf/yr loss 1955-1960   (Lost Volume = 175 MMscf)

- No Losses 1960-1970   Lost Volume =   0 MMscf)

- 50 MMscf/yr loss 1970-1980   (Lost Volume = 500 MMscf)

- No Losses 1980-1990   (Lost Volume =   0 MMscf)

- 50 MMscf/yr *gain* 1990-2000   (Lost Volume = -500 MMscf)

- No Losses 2000-2005   (Lost Volume =   0 MMscf)

Therefore, based on this analysis, the total net inventory lost from 1950 to 2005 is 575 MMscf

3.6. Generating Reports

At the bottom right of each plot, there is a check box for the user to indicate if he wants that particular plot to be included in the report. By simply checking this box for the plots of interest, we can "collect" the plots we would like to include in this report.

For the purpose of this example, we will include all non-trivial plots in the report, so we will need to make sure each of these plots has the "Add Graph to Report" box checked. This would also be a good time to make sure all of the axes ranges are set appropriately. The figure below shows the location of the check box used to include plots in the report.

In addition, if the user has taken a few notes in a word processing document during the inventory analysis process (as recommended above), it is quite easy to merge the two documents into a final report that includes all of the pertinent plots used in the inventory analysis process. For the example problems, notes collected during the inventory analysis process might look something like the following:

QC Plots
None of the QC plots show any irregularities, so it is safe to assume that no problems were encountered during the calculation processes performed.

SIWHP vs Date Plots
The field has consistently been operated between 650 psi and 1000 psi throughout its life. Therefore, we do not have to worry about wide fluctuations in minimum and maximum operating pressures skewing trends in other diagnostic plots.

Unadjusted Inventory History
A plot of unadjusted inventory vs time is revealing, especially in light of how regularly the field was operated from a pressure perspective. This plot shows that various levels of inventory were required over the life of the field to achieve the same Spring and Fall shut-in pressures. This type of trend is a strong indicator, albeit a qualitative indicator, that there have been losses and gains occurring during over the life of storage operations

BHP/Z vs Unadj Book Inv
A plot of the unadjusted book inventory vs the BHP/Z shows movement to the right and left at various points during the life of storage operations, which leads us to the conclusion the losses and gains have occurred during storage operations. This is consistent with the qualitative conclusions drawn from a review of the operational plots (SIWHP vs Time and Unadjusted Book Inventoy vs Time).

NEG History
The plot of Unadjusted NEG vs Date clearly indicates the time periods experiencing losses, gains, and stability.

IPP History Plots
A plot of IPP values vs time generated with Fall data points clearly shows the following:

1. Non-linear increase in the TIPP w/Flat IIPP in 1950's   (GAIN)
2. Flat TIPP and IIPP during 1960's   (NO LOSS or GAIN)
3. Linear increase in the TIPP w/Flat IIPP in 1970's   (LOSS)
4. Flat TIPP and IIPP during 1980's   (NO LOSS or GAIN)
5. Non-linear decrease in the TIPP w/Flat IIPP in 1990's   (GAIN)
6. Flat TIPP and IIPP from 2000-2005   (NO LOSS or GAIN)

Loss Calculations using the TIPP Plot
Loss rates and volumes were calculated using the TIPP plot generated with Fall only data points. The losses calculated using this plot can be summarized as follows:

- 80 MMscf/yr loss 1950-1955   (Lost Volume = 400 MMscf)
- 35 MMscf/yr loss 1955-1960   (Lost Volume = 175 MMscf)
- No Losses 1960-1970   Lost Volume =   0 MMscf)
- 50 MMscf/yr loss 1970-1980   (Lost Volume = 500 MMscf)
- No Losses 1980-1990   (Lost Volume =   0 MMscf)
- 50 MMscf/yr *gain* 1990-2000   (Lost Volume = -500 MMscf)
- No Losses 2000-2005   (Lost Volume =   0 MMscf)

Therefore, based on this analysis, the total net inventory lost over the time period 1950-2005 is 575 MMscf

---

After checking the boxes on all of the charts you would like to be included in the report, go to the Workflow Window, expand the "Reporting" portion of tree directory to see the "Generate" option and click on the Generate option:

This will bring up a document preview window that will show all of the plots you have selected in thumbnail view. By clicking on the "Generate Report" button (see below), the information shown in thumbnail view will be exported to a WORD document for further editing.

After the report information was dumped to WORD and this file was opened, we opened the comments file we compiled during the analysis procedure (shown earlier). We then cut/pasted the information from the comments document into the WORD document, rearranged some information, added a report cover page.

The result is a first draft (or final draft, depending on requirements of the client) of an Inventory Analysis Report (see below):

Gas Storage Inventory Analysis

Big Boy Field

<u>Summary of Reservoir Information</u>

Field Name	Example
Field Type	Dry Gas
Average Reservoir Depth (ft)	5000
Average Reservoir Temperature (F)	110
Wellhead Temperature (F)	60
Reservoir Top Pressure (psia)	1000
Reservoir Base Pressure (psia)	650
Gas specific gravity	0.58
Water specific gravity	1.05
Total Number of wells	1
BHP correlation	Cullendar and Smith
z factor correlation	Hall-Yarborough

<u>Review of Data QC Plots</u>
None of the QC plots show any irregularities, so it is safe to assume that no problems were encountered during the calculation processes performed.

<u>Review of Operational Plots</u>
Based on a review of the SIWHP vs Date Plots, it is apparent that the field has consistently been operated between 650 psi and 1000 psi throughout its life. Therefore, we do not have to worry about wide fluctuations in minimum and maximum operating pressures skewing trends in other diagnostic plots.

Based on a review of the unadjusted inventory vs time, it is apparent that various levels of inventory were required over the life of the field to achieve the same Spring and Fall shut-in pressures. This type of trend is a strong indicator, albeit a qualitative indicator, that there have been losses and gains occurring during over the life of storage operations

---

<u>Review of Diagnostic Plots</u>
Based on a review of the unadjusted book inventory vs the BHP/Z plot, it is apparent that movement has occurred to the right and left at various points during the life of storage operations. This suggests that losses and gains have occurred during storage operations. This is consistent with the qualitative conclusions drawn from a review of the operational plots (SIWHP vs Time and Unadjusted Book Inventory vs Time).

The plot of Unadjusted NEG vs Date clearly indicates the time periods experiencing losses, gains, and stability.

<u>IPP History Plots</u>
A plot of IPP values vs time generated with Fall data points clearly shows the following:

1. Non-linear increase in the TIPP w/Flat IIPP in 1950's   (GAIN)
2. Flat TIPP and IIPP during 1960's   (NO LOSS or GAIN)
3. Linear increase in the TIPP w/Flat IIPP in 1970's   (LOSS)
4. Flat TIPP and IIPP during 1980's   (NO LOSS or GAIN)
5. Non-linear decrease in the TIPP w/Flat IIPP in 1990's   (GAIN)
6. Flat TIPP and IIPP from 2000-2005   (NO LOSS or GAIN)

<u>Loss Calculations using the TIPP Plot</u>
Loss rates and volumes were calculated using the TIPP plot generated with Fall only data points. The losses calculated using this plot can be summarized as follows:

- 80 MMscf/yr loss 1950-1955   (Lost Volume = 400 MMscf)
- 35 MMscf/yr loss 1955-1960   (Lost Volume = 175 MMscf)
- No Losses 1960-1970   (Lost Volume = 0 MMscf)
- 50 MMscf/yr loss 1970-1980   (Lost Volume = 500 MMscf)
- No Losses 1980-1990   (Lost Volume = 0 MMscf)
- 50 MMscf/yr gain 1990-2000   (Lost Volume = -500 MMscf)
- No Losses 2000-2005   (Lost Volume = 0 MMscf)

Based on this analysis, the total net inventory lost between 1950-2005 is 575 MMscf

4. References

Chierici, G. L., Gottardi, G. A., and Guidorzi, R. P. "Identified Models for Gas Storage Dynamics," *SPEJ* (April 1981) 151-159.

Dowdle, W.: "Inventory Verification in Gas Storage Reservoirs," presentation at the Gas Daily and Gas Storage Report Gas Storage Technical Seminar, April 14, 1994, Houston, Texas.

Hubbard, R. M., and Eienbaas, J. R." "Determining Gas-Filled Pore Volume in a Water-Drive Gas-Storage Reservoir," *JPT* (April 1964) 383-,388 •

Mayfield, "Inventory Verification of Gas Storage Fields," SPE 9391, *JPT* (Sept. 1981) 1730-34.

Molinard, J. E., Le Bitoux, P., Peice, V. and Tek, M. R. "Practical Model for Predicting Pressure in Gas-Storage Reservoirs," *SPERE* (Nov. 1 990) 576-580.

Tek, M. R.: *Underground Storage of Natural Gas*, Gulf, 1987.

Tutt, C. J" "A Practical Regression Model of Pressure/Inventory Hysteresis in Natural Gas Storage Fields," JPT (June 1978) 885-889.

Tutt, Charles, Jr." "Natural Gas Storage Field Inventory Verification by Statistical Analysis of Observation Well Pressures," AGA paper 84-DT-89, 1984 Operating Section Proceedings.

Appendix III

Underground Gas Storage References

Table of Contents

1. __Introduction to Gas Storage__

Coats, K. H.: "Some Technical and Economic Aspects of Underground Gas Storage," JPT (Dec. 1966) 1561-66.

Katz, D. L., and Tek, M. R.: "Overview on Underground Storage of Natural Gas," JPT (June 1981) 943-951.

Katz, D. L., et. al., Handbook of Natural Gas Engineering, McGraw-Hill, 1959.

Katz, D. L.: "Making Good Use of Observation Wells," Proc. AGA Transmission Conference, St. Louis (1977) T-251.

Katz, D. L.: "Monitoring Gas Storage Reservoirs," paper SPE 3287 presented at the 1971 Midwest Oil and Gas Industry Symposium, Chicago, April 1-2.

Tek, M. R.: Underground Storage of Natural Gas, Gulf, 1987.

The Potential for Natural Gas in the United States, National Petroleum Council, 1992.

Underground Storage, American Gas Association, 1990.

2. <u>Gas Storage Field Design</u>

Beyea, R. O. and Pinckney, K. D.: "Optimization of Cathodic Protection of Well Casing in the Texas Panhandle," paper SPE 24299, presented at the 1992 Mid-Continent Gas Symposium, Amarillo, TX, April 13-14.

Briggs, J. E. Jr., and Katz, D. L.: "Drainage of Water from Sand in Developing Aquifer Storage," paper SPE 1501 presented at the 1966 Annual Fall Meeting, Dallas, Oct. 2-5.

Coleman, S. B., Clay, H. B., McCurdy, D. G., and Norris, H. L. III: "A New Look at Predicting Gas-Well Load-Up," JPT (March 1991) 329-333.

Evernos, A. I., and Comer, A. G.: "On the Feasibility of Pressure Relief by Water Removal During Development and Operation of Gas Storage in Aquifers," paper SPE 4038 presented at the 1972 Annual Fall Meeting, San Antonio, Oct. 8-11.

Griffith, Howard D. Jr. and Rinehart, Richard D.: "Early Planning for Gas Storage Pays Off - A Case History of Kentucky's Largest Gas Field," paper SPE 3434 presented at the 46th Annual Fall Meeting of the Society of Petroleum Engineers, New Orleans, October 3-6, 1971.

Gober, W. H.: "Factors Influencing the Performance of Gas Storage Reservoirs Developed in Aquifers," paper SPE 1346 presented at the 1965 Gas Technology Symposium, Liberal, Kansas, November 18-19.

Hamlin, A. W.: "Cathodic Protection of Gas Storage Well Casings," AGA paper 91-DT-72, AGA 1991 Operating System Proceedings.

Henry, William A. and Fix, Frank F.: "Development of Aquifer Gas Storage Field with Minimum Environmental Impact," paper SPE 5139 presented at the 49th Annual Fall Meeting of the Society of Petroleum Engineers, Houston, October 6-9, 1974.

Katz, D. L., et. al., Handbook of Natural Gas Engineering, McGraw-Hill, 1959.

Katz, D. L., Vary, J. A., and Elenbaas, J. R.: "Design of Gas Storage Fields," Trans. AIME (1959) 216, 44-48.

Katz, D. L.: "Monitoring Gas Storage Reservoirs," paper SPE 3287 presented at the 1971 Midwest Oil and Gas Symposium, Chicago, April 1-2.

McMinn, R. E.: "Production Techniques for Aquifer-Type Storage Fields," paper SPE 1635 presented at the Gas Technology Symposium, Omaha, Nebraska, September 15-16, 1966.

Oden, R. D., and Jennings, J. W.: "Modification of the Cullender and Smith Equation for More Accurate Bottomhole Pressure Calculations in Gas Wells," SPE 17306

presented at the 1988 Permian Basin Oil and Gas Recovery Conference, Midland, Texas, March 10-11.

Peffer, J. W., Miller, M. A., and Hill, A. D.: "An Improved Method for Calculating Bottomhole Pressures in Flowing Gas Wells With Liquid Present," SPE 15655 presented at the 1986 Annual Technical Conference and Exhibition, New Orleans, Oct 5-8.

Smith, R. V.: "Determining Friction Factors for Measuring Productivity of Gas Wells," Trans. AIME (1950) 189, 73-82.

Stiff, H. A.: "The Interpretation of Chemical Water Analysis by Means of Patterns," Technical Note 84, Trans. AIME (1951) 192, 376-379.

Sukkar, Y. K., and Cornell, D.: "Direct Calculation of Bottom-Hole Pressures in Natural Gas Wells," Trans AIME (1955)204,43-48.

Tek, M. R.: Underground Storage of Natural Gas, Gulf, 1987. The Potential for Natural Gas in the United States, National Petroleum Council, 1992.

Turner, R. G., Hubbard, M. G., and Dukler, A. E.: "Analysis and Prediction of Minimum Flow Rate for the Continuous Removal of Liquids from Gas Wells," JPT (Nov. 1969) 1475-82.

U.S. Natural Gas Availability - Gas Supply Through the Year 2000, Office of Technology Assessment, 1985.

Wingerter, J. R.: "The Use of Inert Gas to Test Potential Gas Storage Aquifers," paper SPE 2770, 1969.

Witherspoon, P. A., Mueller, T. D., and Donovan, R. W.: "Evaluation of Underground Gas-Storage Conditions In Aquifers Through Investigations of Groundwater Hydrology," JPT (May 1962) 555-561.

Young, K. L.: "Effect of Assumptions Used to Calculate Bottom-Hole Pressures in Gas Wells," JPT (April 1967) 547-550.

3. <u>Optimization</u>

Coats, K. H.: "An Approach to Locating New Wells in Heterogeneous, Gas Producing Fields," JPT (May 1969) 549-558.

Duane, J. W.: "Gas Storage Field Development Optimization," JPT (March 1967) 323-330.

Henderson, J. H., Dempsey, J. R., and Tyler, J. C.: "Use of Numerical Models to Develop and Operate Gas Storage Reservoirs," JPT (Nov. 1968) 1239-1246.

Katz, D. L., et. al., Handbook of Natural Gas Engineering, McGraw-Hill, 1959.

McVay, D. A., and Spivey, J. P.: "Optimizing Gas Storage Reservoir Performance," SPE 28639 presented at the 1994 Annual Technical Conference and Exhibition, New Orleans, Sept. 25-28.

Misra, B. R.: "Graphical Design of Underground Gas Storage Developed From a Depleted Gas Field," SPE 7105, unsolicited paper, 1978.

Tek, M. R., Elenbaas, J. R., Whims, M. and Roberts, J. L.: "Design of Storage Fields With Minimum Temperature and Pressure Control at the Surface," paper SPE 8413 presented at the 1979 Annual Fall Technical Conference and Exhibition, Las Vegas, Sept. 23-26.

Van Horn, H. G., and Wienecke, D. R.: "A Method for Optimizing the Design of Gas Storage Systems," SPE 2966 presented at the 1970 Annual Fall Meeting, Houston, Oct. 4-7.

4. <u>Migration and Monitoring</u>

Araktingi, R. E., Benefield, M. E., Bessenyei, Z., Coats, K. H., and Tek, M. R.: "Leroy Storage Facility, Uinta County, Wyoming: A Case History of Attempted Gas-Migration Control," JPT (Jan. 1984) 132-140.

Chierici, G. L., Gottardi, G. A., and Guidorzi, R. P.: "Identified Models for Gas Storage Dynamics," SPEJ (April 1981) 151-159.

Coleman, D. D.: "The Use of Geochemical Fingerprinting To Identify Migrated Gas at the Epps Underground Gas Storage Field," paper SPE 24926 presented at the 1992 Annual Technical Conference and Exhibition, Washington, D.C., Oct. 4-7.

Coleman, D. D., Meents, W. F., Liu, Chao-Li, and Keough, R. A.: "Isotopic Identification of Leakage Gas from Underground Storage Reservoirs – A Progress Report," paper SPE 6491 presented at the 1977 Midwest Gas Storage and Production Symposium, Indianapolis, April 13-15.

Dake, L. P.: Fundamentals of Reservoir Engineering, Elsevier, 1978.

Gentges, Richard J.: "Monitoring Casing Corrosion in Natural Gas Storage Fields," AGA paper 85-DT-65, 1985 Operating Section Proceedings.

Katz, D. L.: "Containment of Gas in Storage Fields," AGA paper 78-T-79, 1978 Operating Section Proceedings.

Katz, D. L.: "Monitoring Gas Storage Reservoirs," paper SPE 3287 presented at the 1971 Midwest Oil and Gas Industry Symposium, Chicago, April 1-2.

Knepper, G. A., and Cuthbert, J. F.: "Gas Storage Problems and Detection Methods," paper SPE 8412 presented at the 1979 Annual Fall Technical Conference and Exhibition, Las Vegas, Sept. 23-26.

Tutt, C. J.: "A Practical Regression Model of Pressure/Inventory Hysteresis in Natural Gas Storage Fields," JPT (June 1978) 885-889.

Tutt, Charles, Jr.: "Natural Gas Storage Field Inventory Verification by Statistical Analysis of Observation Well Pressures," AGA paper 84-DT-89, 1984 Operating Section Proceedings.

5. <u>Inventory Verification</u>

Dowdle, W.: "Inventory Verification in Gas Storage Reservoirs," presentation at the Gas Daily and Gas Storage Report Gas Storage Technical Seminar, April 14, 1994, Houston Texas.

Hubbard, R. M., and Elenbaas, J. R.: "Determining Gas-Filled Pore Volume in a Water-Drive Gas-Storage Reservoir," JPT (April 1964) 383-388.

Mayfield, "Inventory Verification of Gas Storage Fields," SPE 9391, JPT (Sept. 1981) 1730-34.

Tek, M. R.: Underground Storage of Natural Gas, Gulf, 1987.

Mayfield, J. F.: "Inventory Verification of Gas Storage Fields," JPT (Sept. 1981) 1730-1734.

Hubbard, R. M., and Elenbaas, J. R.: "Determining Gas-Filled Pore Volume in a Water-Drive Gas-Storage Reservoir," JPT (April 1964) 383-388.

6. Deliverability Maintenance and Enhancement

Babu, D. K., and Odeh, A. S.: "Productivity of a Horizontal Well," SPERE (Nov. 1989) 417-421.

Bergin, S. R., and Shikari, Y. A.: "A Horizontal Well in Gas Storage: A Case Study," paper SPE 26165 presented at the 1993 Gas Technology Symposium, Calgary, June 28-30.

Cinco-Ley, H., and Samaniego-V., F.: "Transient Pressure Analysis for Fractured Wells," JPT (Sept. 1981) 1749-66.

Dereniewski, Edward; Hekim, Yusuf; and Roberts, Joseph L.: "Deliverability Interference in Gas Storage Reservoirs," AGA paper 82-T-20, 1982 Operating Section Proceedings.

Hall, J. Kevin, and Shikari, Yusuf: "Critical Parameters for Optimizing Horizontal Well Performance in Gas Storage Reservoirs," AGA paper 93-DT-50, 1993 Operating Section Proceedings.

Gredell, Mark E., and Benson, Mark A.: "Slim-hole Horizontal Well Improves Gas Storage Deliverability," OGJ (December 11, 1995) 66-70.Lee, W. J., Rollins, J. B., and Spivey, J. P.: Pressure Transient Testing, SPE Textbook Series, in progress.

State-of-Technology Assessment and Evaluation of Gas Storage Well Productivity Enhancement Techniques, GRI Topical Report GRI-93/0001.

7. <u>Simulation of UGS Reservoirs</u>

Wells & Evans, "Engineering Evaluation and Performance Analysis of the Loop Gas Storage Field," paper SPE 24922 presented at the 1992 Annual Technical Conference and Exhibition, Washington, D.C., Oct. 4-7.

8. <u>Special Topics</u>

Barron, Thomas F.: "Regulatory, Technical Pressures Prompt More U.S. Salt-cavern Gas Storage," OGJ Special, (September 12, 1994) 55-67.

Misrah, B. R., Foh, S. E., Shikari, Y. A., Berry, R. M., and Labaune, F.: "The Use of Inert Base Gas in Underground Natural Gas Storage," paper SPE 17741 presented at the 1988 Gas Technology Symposium, Dallas, June 13-15.

Herzog, R. A.: "Retrograde Vaporization of Residual Condensation in Storage Field Development," AGA paper 80-T-54, 1980 Operating Section Proceedings.

Weibel, Rudolph W.: "Gas Storage Enhances Oil Production," OGJ (January 21, 1991) 33-36.

9. Top Twenty Papers

Katz, Donald L., and Tek, M. Rasin: "Overview on Underground Storage of Natural Gas," JPT (June 1981) 943-951.

Griffith, Howard D. Jr. and Rinehart, Richard D.: "Early Planning for Gas Storage Pays Off - A Case History of Kentucky's Largest Gas Field," paper SPE 3434 presented at the 46th Annual Fall Meeting of the Society of Petroleum Engineers, New Orleans, October 3-6, 1971.

Katz, Donald L.: "Containment of Gas in Storage Fields," AGA paper 78-T-79, 1978 Operating Section Proceedings

Mayfield, J. F.: "Inventory Verification of Gas Storage Fields," JPT (Sept. 1981) 1730-1734.

Wells & Evans, "Engineering Evaluation and Performance Analysis of the Loop Gas Storage Field," paper SPE 24922 presented at the 1992 Annual Technical Conference and Exhibition, Washington, D.C., Oct. 4-7.

Knepper, G. A., and Cuthbert, J. F.: "Gas Storage Problems and Detection Methods," paper SPE 8412 presented at the 1979 Annual Fall Technical Conference and Exhibition, Las Vegas, Sept. 23-26.

Coleman, D. D.: "The Use of Geochemical Fingerprinting To Identify Migrated Gas at the Epps Underground Gas Storage Field," paper SPE 24926 presented at the 1992 Annual Technical Conference and Exhibition, Washington, D.C., Oct. 4-7.

Araktingi, R. E., Benefield, M. E., Bessenyei, Z., Coats, K. H., and Tek, M. R.: "Leroy Storage Facility, Uinta County, Wyoming: A Case History of Attempted Gas-Migration Control," JPT (Jan. 1984) 132-140.

Gober, W. H.: "Factors Influencing the Performance of Gas Storage Reservoirs Developed in Aquifers," paper SPE 1346 presented at the 1965 Gas Technology Symposium, Liberal, Kansas, November 18-19.

Hubbard, R. M., and Elenbaas, J. R.: "Determining Gas-Filled Pore Volume in a Water-Drive Gas-Storage Reservoir," JPT (April 1964) 383-388.

Henry, William A. and Fix, Frank F.: "Development of Aquifer Gas Storage Field with Minimum Environmental Impact," paper SPE 5139 presented at the 49th Annual Fall Meeting of the Society of Petroleum Engineers, Houston, October 6-9, 1974.

McMinn, R. E.: "Production Techniques for Aquifer-Type Storage Fields," paper SPE 1635 presented at the Gas Technology Symposium, Omaha, Nebraska, September 15-16, 1966.

Weibel, Rudolph W.: "Gas Storage Enhances Oil Production," OGJ (January 21, 1991) 33-36.

Herzog, R. A.: "Retrograde Vaporization of Residual Condensation in Storage Field Development," AGA paper 80-T-54, 1980 Operating Section Proceedings.

Dereniewski, Edward; Hekim, Yusuf; and Roberts, Joseph L.: "Deliverability Interference in Gas Storage Reservoirs," AGA paper 82-T-20, 1982 Operating Section Proceedings.

Hall, J. Kevin, and Shikari, Yusuf: "Critical Parameters for Optimizing Horizontal Well Performance in Gas Storage Reservoirs," AGA paper 93-DT-50, 1993 Operating Section Proceedings.

Gredell, Mark E., and Benson, Mark A.: "Slim-hole Horizontal Well Improves Gas Storage Deliverability," OGJ (December 11, 1995) 66-70.

Gentges, Richard J.: "Monitoring Casing Corrosion in Natural Gas Storage Fields," AGA paper 85-DT-65, 1985 Operating Section Proceedings.

Misrah, B. R., Foh, S. E., Shikari, Y. A., Berry, R. M., and Labaune, F.: "The Use of Inert Base Gas in Underground Natural Gas Storage," paper SPE 17741 presented at the 1988 Gas Technology Symposium, Dallas, June 13-15.

Barron, Thomas F.: "Regulatory, Technical Pressures Prompt More U. S. Salt-cavern Gas Storage," OGJ Special, (September 12, 1994) 55-67.

Appendix IV

Underground Gas Storage Inventory & Deliverability Terminology

Gas Storage Terminology

Inventory
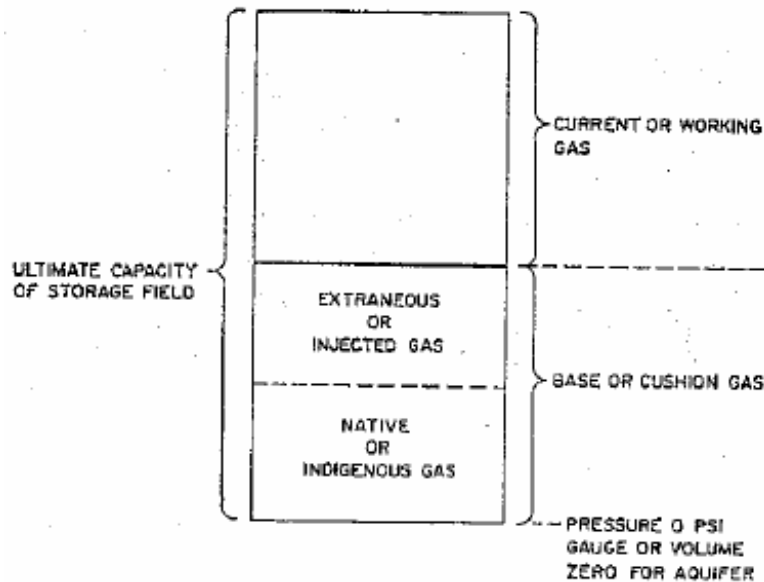
Gas volumes in storage fields. From Katz, *et. al.*, 1959.

- Cushion gas (base gas)

  – The volume of gas that must remain in the storage field to maintain an adequate deliverability rate throughout the withdrawal season

- Working gas (top gas)

  – The volume of gas in reservoir above the designed level of the cushion gas

  – May or may not be completely withdrawn during any particular output season

  – Conditions may permit the total working capacity to be used more than once during any season

- Native gas

  – Gas originally present in a depleted gas or oil field

  – After a reservoir is converted to storage, remaining gas becomes part of the cushion gas volume

- Injected gas

- Gas injected into a storage reservoir

- Likely to be different in composition from native gas
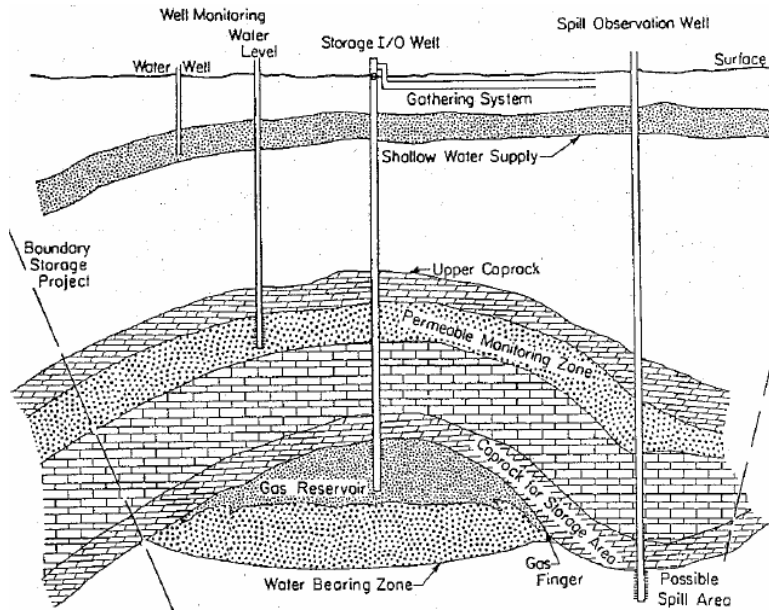
Cross section of gas storage field. From Katz, 1971.
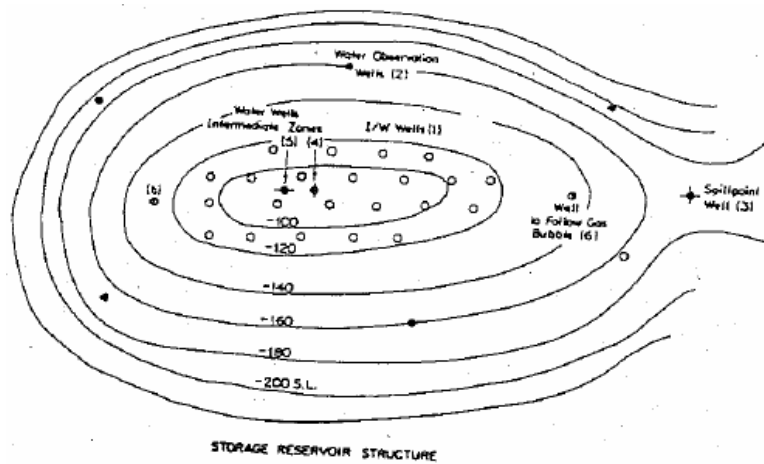
**Generalized structure map of gas storage field.
From Katz, 1977.**

- Spill point

  – Point on structure at which gas is most likely to escape

- Delta pressure

  – Operating pressure for a gas storage reservoir which is higher than original reservoir pressure

  – Aquifer storage reservoirs always have some delta pressure

  – Depleted gas and oil reservoirs may or may not be operated under delta pressure conditions

- Migration

  – Movement of storage gas beyond the storage area, so that it cannot be recovered through the wells completed in the storage zone

- Cycling

  – The process of injecting or withdrawing a percentage or all of a storage reservoir's working gas capacity during a particular season

Deliverability

- Deliverability

    – The maximum rate at which gas can be withdrawn from an underground reservoir under a given set of conditions

    – Deliverability depends on rock characteristics, reservoir pressure, and facilities such as wells, pipelines, and compressors

- Pipeline load factor

    – The ratio of the average annual pipeline flow rate to the design capacity

- Degree-day deficiency

    – Measure of space heating requirement for a given climate

    – Sum over a year or other time period of 65 °F - the mean daily temperature

    – On a graph of temperature vs. time in days, area between a horizonal line corresponding to a temperature of 65 °F and the mean daily temperature

- Sendout

    – Gas volume delivered to the transmission line or consumer

- Peak day

    – The day of maximum demand for natural gas service

    – Usually occurs on the coldest day of the year, when demand for natural gas for heating is at its highest

    – May occur on the hottest day of the year, when demand for space cooling drives electric generation demand to its highest levels

- Peak day deliverability

    – Deliverability required to meet peak day demand

- Design day deliverability

    – The rate of delivery at which a storage facility is designed to be used when storage withdrawals are at their maximum levels

    – Controls design of surface equipment capacity

- Peak-day sendout

  – Gas actually delivered to the transmission line or consumer on the peak day

- Base load

  – Average withdrawal rate during the withdrawal season

  – Obtained by dividing the working gas capacity by the number of days in the withdrawal season

- Peak shaving

  – Practice of providing for short-term (hours-days) demands using specially designed facilities

Appendix V

UGS Glossary

The following definitions were selected from a larger list published by the U.S. National Petroleum Council in 1992

American Gas Association (AGA) - The US gas utility industry trade association.

Base Gas - See "Cushion Gas".

BCF - Billion Cubic Feet. A volumetric unit of measurement for natural gas.

Certification Capacity - The maximum volume of gas that may be stored in an underground storage facility certificated by the Federal Energy Regulatory Commission. Absent a certificate, a reservoir's present developed operating capacity is considered to be its "certified" capacity.

Citygate - A point or measuring station at which a gas distribution company receives gas from a pipeline company or transmission system.

Citygate Sales Services - Interstate pipeline natural gas sales service where the title to gas sold changes at the pipeline's interconnection with the purchasing local distribution company.

Commercial Consumption - Gas consumed by non-manufacturing establishments or agencies primarily engaged in the sale of goods or services. Included are such establishments as hotels, restaurants, wholesale and retail stores, and other service enterprises; gas consumed by establishments engaged in agriculture, forestry, and fishers; and gas consumed by local, state, and federal agencies engaged in non-manufacturing activities.

Curtailments - The rationing of natural gas supplies to an end user when gas is in short supply, or when demand for service exceeds a pipeline's capacity, usually to an industrial user and/or power generator.

Cushion Gas - The volume of gas, including native gas, that must remain in the storage field to maintain an adequate reservoir pressure and deliverability rate throughout the withdrawal season.

Cycling - The process of injecting or withdrawing a percentage or all of a storage reservoir's working gas capacity during a particular season.

Deliverability - The rate at which gas can be withdrawn from an underground reservoir. Actual rates depend on rock characteristics, reservoir pressure, and facilities such as wells, pipelines, and compressors.

Delivered - The physical transfer of natural, synthetic, and/or supplemental gas from facilities operated by the responding company to facilities operated by others or to consumers.

Demand Charge - A charge levied in a contract between a pipeline and local distribution company, electric generator, or industrial user for firm gas pipeline transportation service. The demand charge must be paid whether or not gas is used up to the volume covered by the charge.

Demand Side Management - Programs designed to encourage customers to use less natural gas or other fuels or less electricity and to use it more efficiently (i.e., conservation) or to reduce peak demand (i.e., load management).

Demand Day Capacity - The volume of natural gas that a pipeline facility is designed to transport during one day, given the assumptions used in the design process, such as pressures, pipeline efficiency, and peak hourly rates.

Design Day Deliverability - The rate of delivery at which a storage facility is designed to be used when storage withdrawals are at their maximum levels.

Developed Operating Capacity - That portion of operating capacity which is currently available for storage use.

End User - Anyone who purchases and consumes natural gas.

Field - A single pool or multiple pools of hydrocarbons grouped on, or related to, a single structural or stratigraphic feature.

Firm Gas - Gas sold on a continuous and generally log-term contract.

Firm Service - Service offered to customers (regardless of class or service) under schedules or contracts that anticipate no interruptions. The period of service may be for only a specified part of the year as in off-peak service. Certain firm service contracts may contain clauses that permit unexpected interruption in case the supply to residential customers is threatened during an emergency.

Fracturing - Improvement of the flow continuity between gas-bearing reservoir rock and the wellbore by creating fractures which extend some distance into the reservoir.

Gas Condensate Well - A gas well producing from a gas reservoir containing considerable quantities of liquid hydrocarbons in the pentane and heavier range, generally describes as "condensate".

Gas Research Institute (GRI) - A US organization which funds research efforts in all phases of the natural gas industry, including exploration and production, transmission, storage, and end-use application.

Gas Well - A gas well completed for the production of natural gas from one or more gas zones or reservoir.

Gathering System - Facilities constructed and operated to receive natural gas from the wellhead and transport, process, compress, and deliver that gas to a pipeline, LDC, or end user. The construction and operation of gathering systems is not a federally regulated business, and in some states is not regulated by the state.

Hub - A hub is a location where gas sellers and gas purchasers can arrange transactions. The location of the hub can be anywhere multiple supplies, pipelines, or purchasers interconnect. "Market centers" are hubs located near central market areas. "Pooling points" are hubs located near center supply production areas. Physical hubs are found at processing plants, offshore platforms, pipeline interconnects, and storage fields. "Paper" hubs may be located anywhere parties arrange title transfers (changes in ownership) of natural gas.

Hydrates - Gas hydrates are physical combinations of gas and water in which the gas molecules fit into a crystalline structure similar to that of ice. Gas hydrates are considered a speculative source of gas.

Industrial Consumption - Natural gas consumed by manufacturing and mining establishments for heat, power, and chemical feedstock.

Interruptible Gas - Gas sold to customers with a provision that permits curtailment or cessation of service at the discretion of the distributing company or pipeline under certain circumstances, as specified in the service contract.

Local Distribution Company (LDC) - A company that distributes natural gas at retail to individual residential, commercial, and industrial consumers. LDCs are typically granted an exclusive franchise to serve a geographic area by state or local governments, subject to some requirement to provide universal service. Rates and terms and conditions or service are typically (but not always) subject to regulation.

Market Center - A place, located near natural gas market areas, where many gas sellers and gas buyers may arrange to buy/sell natural gas. See "Hub".

MCF/D - "Thousand cubic feet of natural gas per day". A volume unit of measurements for natural gas.

MMCF/D - "Million cubic feet of natural gas per day". A volume unit of measurement for natural gas.

Native Gas -The gas remaining in a reservoir at the end of a reservoir's producing life. After a reservoir is converted to storage, remaining gas becomes part of the cushion gas volume.

Off-Peak - Periods of time when natural gas pipeline facilities are typically not flowing natural gas at design capacity.

Operating Capacity - The maximum volume of gas an underground storage field can store. This quantity is limited by such factors as facilities, operational procedure, confinement, and geological and engineering properties.

Peak Day - The day of maximum demand for natural gas service. In any given area, the "peak day" usually occurs on the coldest day of the year, when demand for natural gas for heating is at its highest/ Because each part of the country experiences different weather conditions, the peak day for each region or area is usually different. In some parts of the country, such as the Southeast and the Southwest Central regions, the peak day may occur on the hottest day of the year, when demand for space cooling drives electric generation demand to is highest levels.

Peak-Day Deliverability - The rate of delivery at which a storage facility is designed to be used for peak days.

Pipeline - A continuous pipe conduit, complete with such equipment as valves, compressor stations, communications systems, and meters, for transporting natural and/or supplemental gas from one point to another, usually from a point in or beyond the producing field or processing plant to another pipeline or to points of use. Also refers to a company operating such facilities.

Reservoir Pressure - The force within a reservoir that causes the gas and/or oil to flow through the geological formation to the wells.

Residential Consumption - Gas consumed in private dwellings, including apartments, for heating, air conditioning, cooking, water heating, and other household uses.

Storage Additions - Volumes of gas injected or otherwise added to underground natural gas reservoirs or liquefied natural gas storage.

Storage Field - A facility where natural gas is stored for later use. A natural gas storage field is usually a depleted oil- or gas-producing field (but can also be an underground aquifer or salt cavern). The wells in these depleted fields are used to either inject or withdraw gas from the reservoir as circumstances require.

Storage Volume - The total volume of gas in a reservoir. It is comprised of the cushion and working gas volumes.

Storage Withdrawals - Volumes of gas withdrawn from underground storage or liquefied natural gas storage.

Top Gas - See "Working Gas".

Underground Storage - The storage of natural gas in underground reservoirs at a different location from which is was produced.

Underground Storage Injections - Gas from external sources put into underground storage reservoirs.

Underground Storage Withdrawals - Gas removed from underground storage reservoirs.

Vented - Gas released into the air on the base site or at processing plants.

Well Workover - Work done on a well that improves the mechanical condition of the well or work that treats the reservoir in order to improve gas flow.

Working Gas - The volume of gas in reservoir above the designed level of the cushion gas. It may or may not be completely withdrawn during any particular output season. Conditions may permit the total working capacity to be used more than once during any season.

Smart Gas: Using Chemicals to Improve Gas Deliverability

Final Report

Reporting Period Start Date:
May 1, 2005
Reporting Period End Date:
December 31, 2006

Principal Authors:
William W. Weiss
Xina Xie, Ph.D.

DOE Award No.
DE-FC26-03NT41779
Subaward No. 2909-CC-DOE-1779

Report Issue Date:
June 30, 2006

Prime Awardee
The Pennsylvania State University
110 Technology Center Building
University Park, PA 16802

Subawardee
Correlations Company
P.O. Box 730
115 Court Street
Socorro, NM 87801

Table of Contents

List of Tables

List of Figures

Abstract

Each year, more than 17,000 gas storage wells in the United States lose from 3–5% of their storage capacity and deliverability. In addition, the gas storage industry spends $80–100 million annually to revitalize existing wells; thus, there is an economic incentive to develop new stimulation methods. Limited laboratory information suggests that using surfactants to alter the wettability of the reservoir rock could increase deliverability of gas storage wells. The objective of this project was to develop new technology to improve deliverability from gas storage wells. Two cost-effective surfactants were selected from 11 candidates through preliminary screening tests for additional reservoir core tests. Reservoir cores from three gas storage facilities including sandstone and dolomite reservoirs were used to evaluate surfactant-gas-core systems. The imbibition and core flood tests showed that gas deliverability and storage capacity were improved in surfactant-treated sandstone cores. However, the surfactants had a very limited effect on dolomite cores. An engineering analysis was conducted to develop an analytical method to evaluate future field tests of the new technology. The aquifer storage facilities are candidates for field testing.

Executive Summary

The objective of this project was to develop new technology to improve deliverability from gas storage wells. The laboratory effort included preliminary surfactant-screening tests and work with reservoir cores to evaluate surfactant-gas-core systems. In addition to the use of capillary tubes to screen surfactants, a novel method based on the contact angle of water drops on reservoir cores was investigated. Concurrently, an engineering analysis was conducted to provide an inventory of storage facility reservoirs that are candidates for field testing and establish baseline metrics. Initially the potential fields included sandstone and dolomite reservoirs in dry gas fields and water aquifers. However, the laboratory tests failed to support the application of surfactants in dolomite gas storage reservoirs because the cores were not water-wet.

It is known that water-wet porous media imbibes water in a fashion similar to water rising in a glass capillary tube. In gas storage reservoirs, the imbibition force promotes the retention of water in the pore space, which curtails the deliverability of gas to the wellbore during periods of high demand. In a similar manner, the injection of gas during the fill cycle is restricted. The pore space occupied by irreducible water is also not available for gas storage. Adding surfactants to the well during the fill cycle could decrease the capillary pressure by changing the rock surface wettability.

Results from this project provide the foundation for a possible continuation project that would focus on field demonstrations of the new technology. Many variables could affect changes in well deliverability. New smart technology based on fuzzy logic and neural networks would be used to analyze the field test results and generate correlations that would optimize commercial applications.

Introduction

Each year, more than 17,000 gas storage wells in the United States lose from 3–5% of their storage capacity and deliverability. The gas storage industry spends $80–100 million annually to revitalize existing wells with methods such as mechanically removing debris, washing, injecting acids, and creating new perforations in the well pipe.[1] Improvements are limited and temporary. A principal cause of the loss of deliverability problem is the retention of water in the reservoir matrix, also known as relative permeability effects.[2] A solution to the reduced deliverability due to capillary forces is the subject of this final report. Here flow performance is characterized with a gas deliverability index defined as the quotient of flow rate divided by pressure drop, q/ΔP, across a core plug or into/out of the wellbore.

Many gas storage reservoirs are thought to be water-wet, which promotes the retention of water around the near-wellbore formation via capillary forces, or $P_c = \dfrac{2\sigma\cos\theta}{r}$, where P_c is the capillary pressure, σ is the gas-water surface tension, θ is the contact angle, and r is the equivalent capillary radius. The greater the capillary pressure, the more water retained. The problem becomes increasingly serious with decreased formation permeability due to the smaller pore sizes generating stronger capillary action. The retained water curtails the gas deliverability to the wellbores of gas storage wells during periods of high demand and in a similar manner restricts the injection of gas during the fill cycle. Notice that P_c is dependent on both the interfacial tension and the contact angle. Altering the interfacial tension depends on the presence of a fluid, whereas continuous presence of a fluid is not necessary when altering the contact angle. This is important if increased well deliverability is to remain following stimulation.

Others have investigated the effect of using surfactants and alcohol to reduce the interfacial tension in the laboratory and tested the effect in the field.[3–6] In fact, Fahes and Firoozabadi[6] used an expensive fluorochemical surfactant to permanently alter the wettability of water-wet sandstone core to intermediate wettability. A number of chemicals shown in Table 1 have been evaluated in gas deliverability laboratory studies.

Table 1. Potential gas wetting agents		
Chemical	**Description**	**Vendor**
WITCO 1276	Ammonium alkyl ether sulfate (hard acid)	Akzo Nobel
WITCO 1298	Alkylbenzenesulfonic acid (soft acid)	Akzo Nobel
Arquad 2HT-75	Quaternary ammonium cationic	Akzo Nobel
Stepanquat 300	Dicocodimethyl ammonium Chloride	Stepan Chemical
Accosoft 808	Methyl tallow amidoethyl tallow imidazolin sulphate	Stepan Chemical
Octyl Palmite	Palmitic acid-2-ethylhexyl alcohol ester	Stepan Chemical
FC 4430	Fluorosurfactant fluoroaliphatic polymeric esters	3M Corp
FC 4432	Fluorosurfactant fluoroaliphatic polymeric esters	3M Corp
FC 4434	Fluorosurfactant fluoroaliphatic polymeric esters	3M Corp
T91-8	Ethoxylated alcohol	Tomah Products
TomaDry N-4	Formulated cationic surfactant	Tomah Products
OSA	Oil-soluble amine	Oil-Chem
REDICOTE CS 392S	Fatty polyamine derivative–Sandstones	Akzo Nobel
REDICOTE CS 393L	Fatty polyamine derivative–Limestone & dolomites	Akzo Nobel
Quilon	Tetradecanoato chromic chloride hydroxide	DuPont

In the present study inexpensive methods were investigated to screen the chemicals prior to testing with field cores. The capillary rise method was developed to screen chemicals for sandstone reservoirs. The principle is demonstrated in Fig. 1 with water and food dye: the greater the rise, the more water-wet the system.

Figure 1. Capillary tube test.

A drop method illustrated with Fig. 2 from Fahes and Firoozabadi shows promise as an inexpensive surfactant-screening protocol. The spreading drop with a contact angle greater than 90° indicates a water-wet rock surface, while the beaded drop with a contact angle less than 90° indicates a non-water-wet surface.
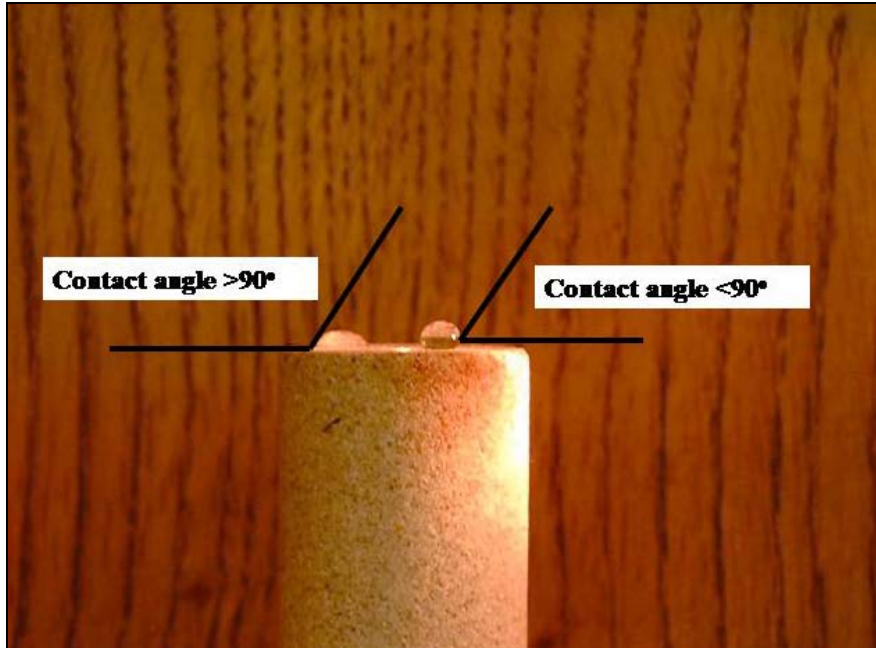
Figure 2. Surfactant drop screening method.[6]

After the surfactant screening with capillary tubes, surfactants were selected for imbibition tests with reservoir cores, followed by flow testing with reservoir cores and wet gas.

The imbibition of water into dry reservoir cores was determined by measuring the weight gain in cores with and without surfactant treatment as represented in Fig. 3.
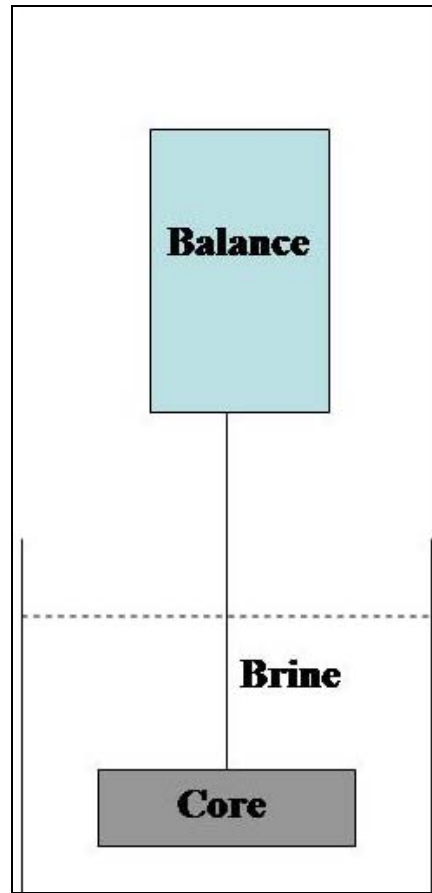
Figure 3. Representation of an imbibition test.

Constant pressure and temperature conditions were maintained during the laboratory imbibition experiments; therefore, the difference in weight gain of the treated vs. non-treated cores represents the change in the storage capacity of the core. Changes in the deliverabilty index of each core were measured with flow tests conducted with treated and non-treated cores. Since dry gas can volatilize the residual water trapped in the cores, wet-gas was used for all flow experiments. The dry/wet gas concept[7] is shown in Fig. 4 where the constant-flow rate pressure drop was measured independently in the first and second half of the core. Note that the pressure drop doubled in the area of the core where water had not yet vaporized.
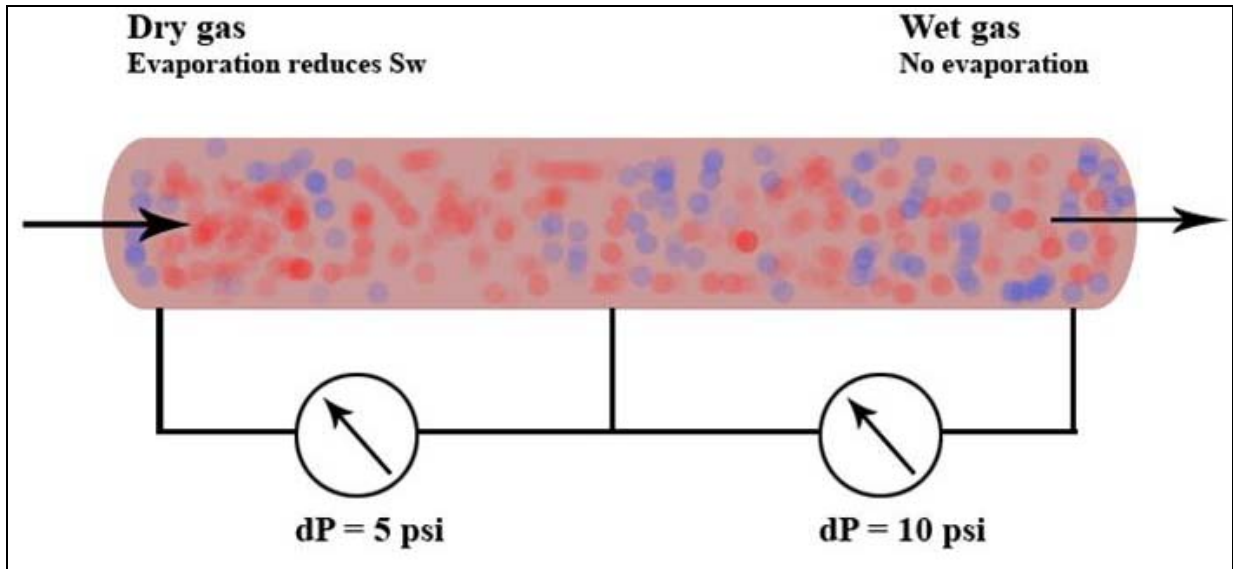
Figure 4. **Demonstration of the dry/wet gas concept where the constant-flow rate pressure drop was measured independently in the first and second half of the core. Note that dP in wet-gas half of the core is twice that of the dry gas area.**

Three operators offered data and cores for this project. Panhandle Energy provided sandstone cores and water analyses from their Waverly, St. Peter aquifer, storage facility along with production history of the withdrawal and fill cycles. Ameren Corp. provided sandstone sidewall cores and water analyses from their Mt. Simon sandstone aquifer, Sciota storage facility. Michigan Consolidated Gas provided dolomite cores (courtesy of William Harrison, Michigan Basin Core Research Laboratory, Western Michigan University) and production history from their Bell River Mills Niagaran reef storage facility. It was determined that field deliverability expressed as the wellhead flow rate divided by the difference in bottom hole pressure measured at an observation well and the flowing wellhead pressure generated trends that could be used to evaluate a field test of using surfactants to increase deliverability. Shown in Fig. 5 is a plot of the historical deliverability vs. cumulative withdrawals from Waverly well #91 during the 2004 season. Constructing the plot with cumulative withdrawals rather than time reduces the noise seen in time plots.
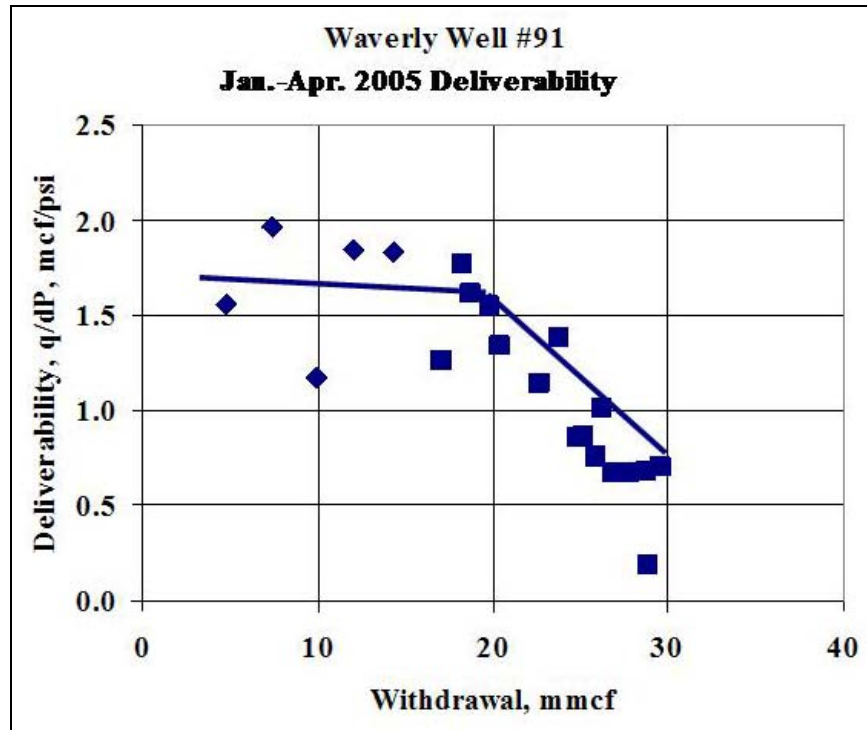
Figure 5. Deliverability history of the Waverly well #91 during the 2004 season.

Experimental Results

Laboratory Screening Tests

Capillary rise

      Capillary rise tests (Fig. 1) were the first step in the laboratory surfactant-screening procedure. Each surfactant was diluted with either methanol or water to prepare solutions of various concentrations. Clean capillary tubes with a diameter of about 1 mm were first soaked in surfactant solutions, drained, and then inserted in synthetic seawater. The greater the rise of water in the capillary tube, the greater the water-wetness of the testing system. The seawater composition is listed in Table 2.

Table 2. Synthetic seawater composition								
Composition	Na^+	K^+	Mg^{2+}	Ca^{2+}	Cl^-	HCO_3^-	SO_4^{2-}	TDS
Concentration, ppm	10890	490	1368	428	19700	124	2960	35960

      The capillary rise of seawater and dilute solutions of surfactants in seawater and methanol against air was measured with a cathetometer. The results obtained with 11 of the 14 surfactants are presented in Table 3. Vendors were not able to provide samples of three of the potential samples listed in Table 1.

Table 3. Capillary rise tests results			
Surfactants (bar chart code)	Capillary rises (cm) after soaking by different solutions (Methanol)	Capillary rises (cm) after soaking by different solutions (Water)	Observation
Stepanquat 300 (1)	1% ---0.76 0.1% ---0.79 0.01%--1.86	1% ---0.73 0.1% ---0.74 0.01% ---0.75 0.002%---0.83	
Witcolate 1276 (3)	1% ---1.63 0.1% ---2.18 0.01%---2.25	1% ---0.9 0.1% ---2.14 0.01% ---2.23	
Octyl Palmitate (5)	1% ---1.9 0.1% ---1.92 0.01%---1.99		Not soluble in water
Witconic 1298 (7)	1% ---0.77 0.1% ---1.04 0.01%---1.07	1% ---0.8 0.1% ---0.94 0.01%---2.08	
FC-4430 (9)	1% ---0.75 0.1% ---1.08 0.01%---2.25	1% ---0.89 0.1% ---1.67 0.01%---2.32	
FC-4432 (11)	1% ---0.83 0.1% ---1.2 0.01%---2.22	1% ---0.72 0.1% ---2.01 0.01%---2.28	
FC-4434 (13)	1% ---0.74 0.1% ---2.25 0.01%---2.33	1% ---1.38 0.1% ---1.79 0.01%---1.86	
Tomadol 91-8 (15)	1% ---0.78 0.1% ---0.98 0.01%---2.23	1% ---1.03 0.1% ---1.58 0.01%---2.42	
Tomadry N-4 (17)	1% ---0.7 0.1% ---0.72 0.01%---2.17	1% ---0.7 0.1% ---0.71 0.01%---0.71	
Accosoft 808 (90%) (19)	1% ---0.83 0.1% ---0.93 0.01%---2.2	1% ---0.72 0.1% ---0.76 0.01%---2.12	Dispersed in water
Arquad 2HT-75 (21)	1% ---0.82 0.1% ---1.09 0.01%---2.01		Not soluble in water
Capillary rise of clean tube: in (23) sea water = 2.51 cm, in (25) methanol = 0.87 cm			

The capillary rise experimental results with water as the diluent are presented graphically as bar charts in Figs. 6–10 (see Table 3 for reference code). The results are normalized with water as 1.0 and shown in Figs. 6–8 with water as the solvent and surfactant concentrations of 10,000, 1,000, and 100 ppm. Notice that the capillary rise of all surfactants is less than water indicating that the water-wetness of glass tubes was reduced.
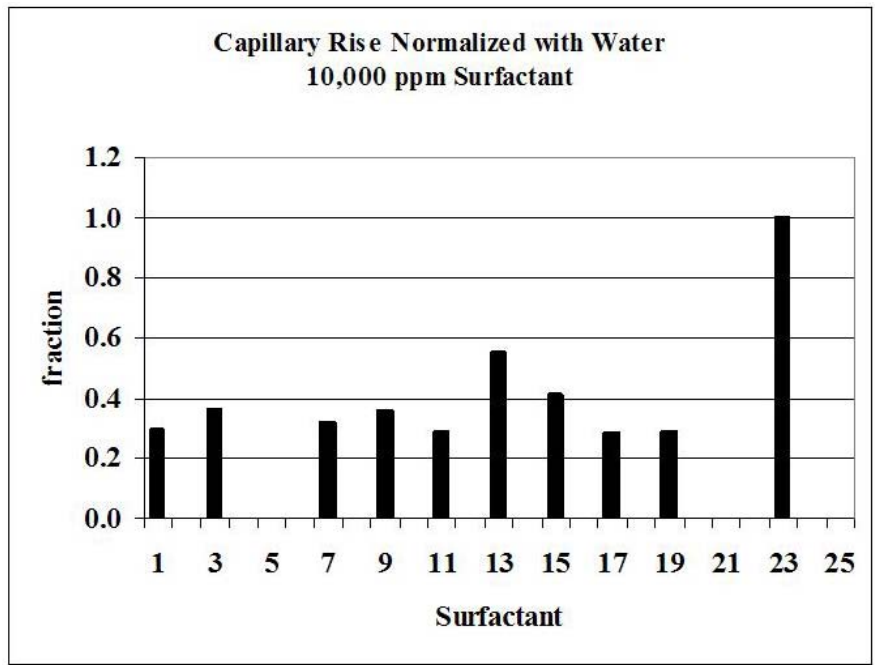
Figure 6. Capillary rise of surfactants at 10,000 ppm in water.
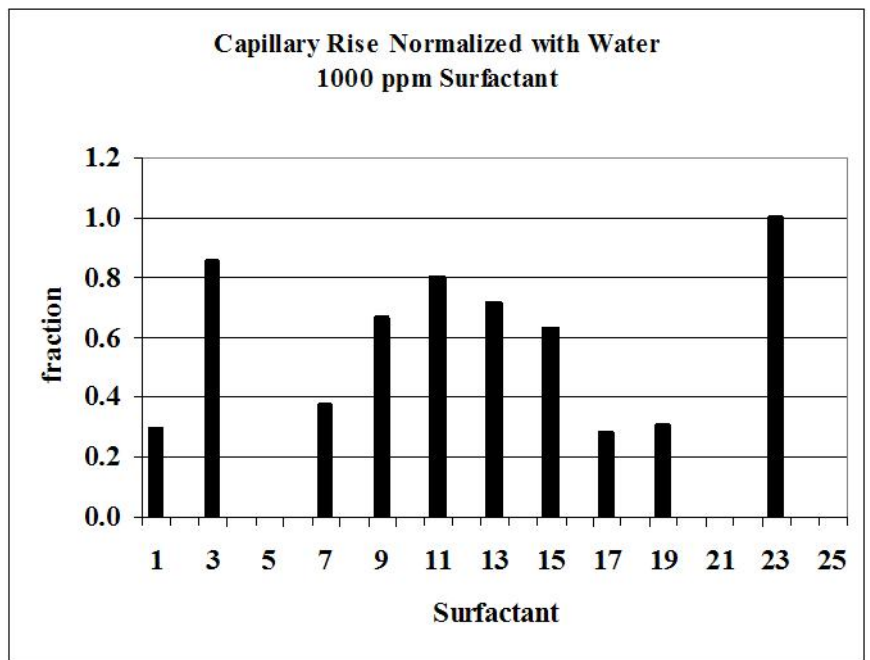
Figure 7. Capillary rise of surfactants at 1,000 ppm in water.

13
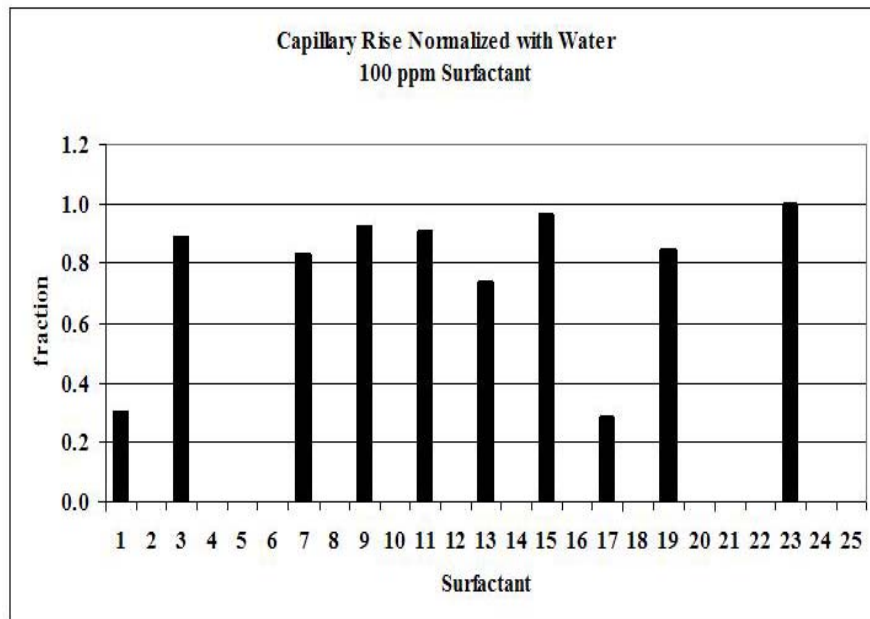
Figure 8. Capillary rise of surfactants at 100 ppm in water.

Shown in Figs. 9–11 are results of the capillary rise experiments using methanol as the diluent to ensure solubility of the surfactants. Surfactants dissolved in methanol do not significantly reduce the tube wettability as shown in Figs. 9–11. The capillary rise tests are summarized in the appendix (Fig. A1).
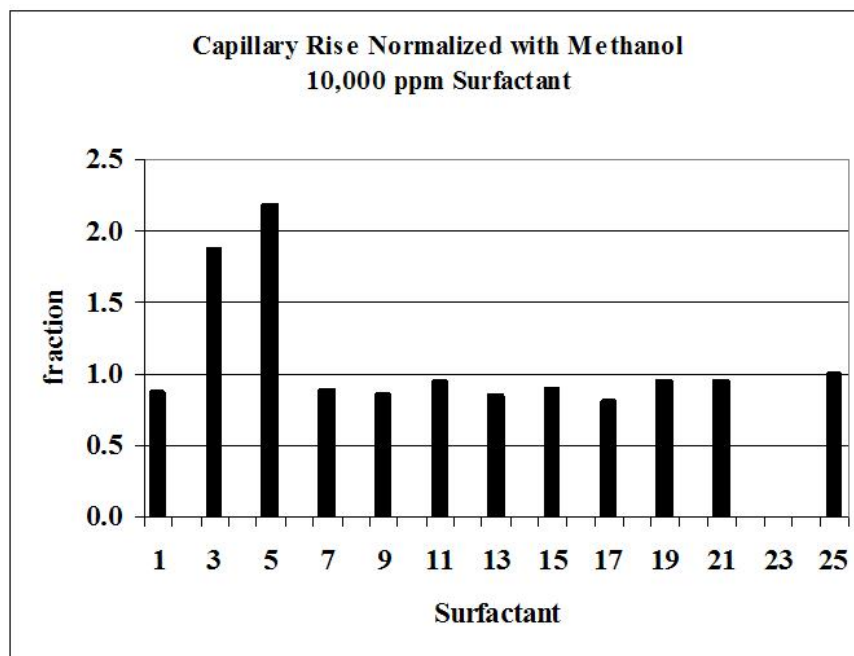
Figure 9. Capillary rise of surfactants at 10,000 ppm in methanol.
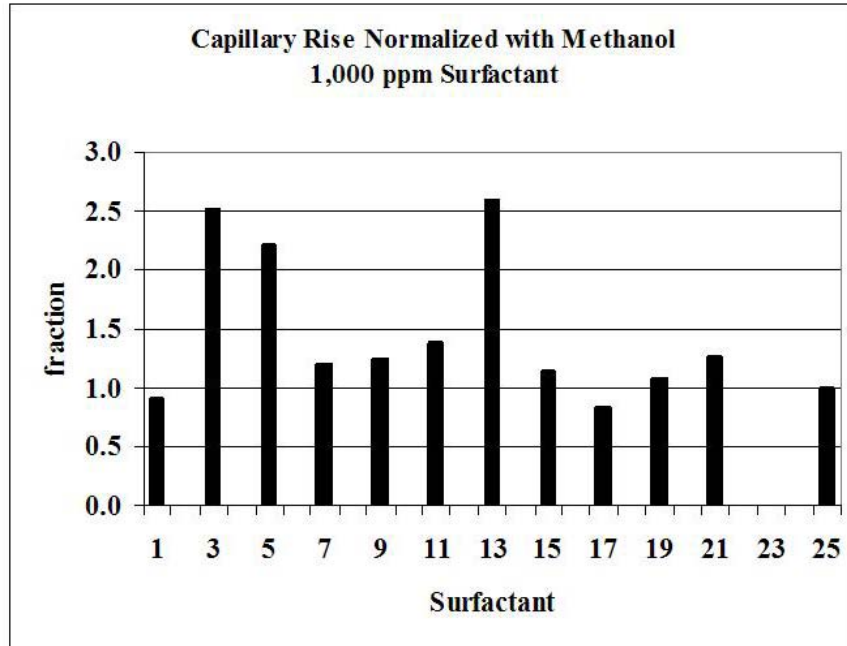
Figure 10. Capillary rise of surfactants at 1,000 ppm in methanol.
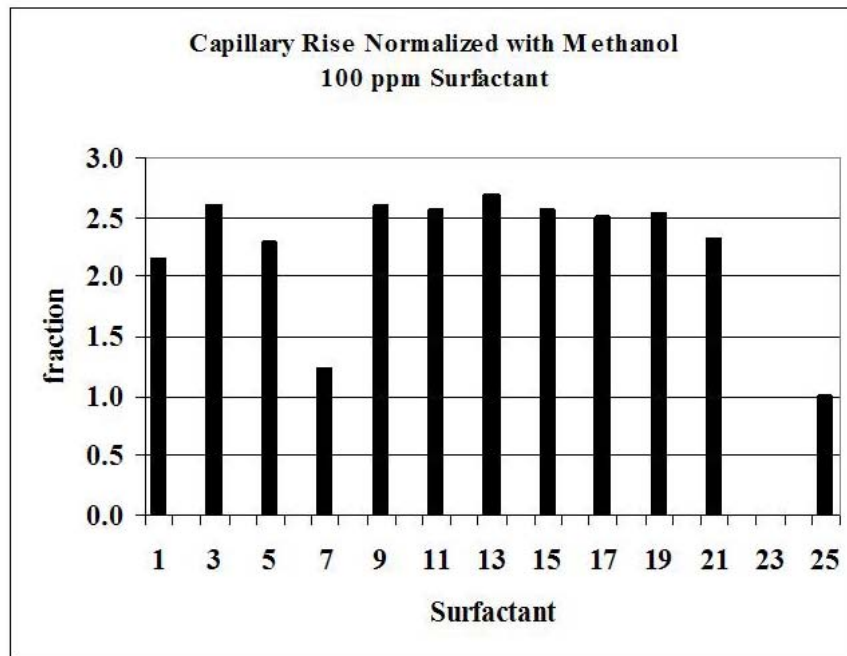
Figure 11. Capillary rise of surfactants at 100 ppm in methanol.

Critical micelle concentration

The critical micelle concentration (CMC) of both Stepanquat 300 and Tomadry N-4 was measured. CMC is the stabilized surface tension value measured at increasing surfactant concentrations in seawater using a DuNouy ring tensiometer. Fig. 12 shows that the CMC of both surfactants is about 10,000 ppm (1.0%). The surface tension of Stepanquat 300 (1) is 30.5

dyne/cm and Tomadry N-4 (17) is 41.7 at the CMC as shown in Table 4. The CMC is used to determine the application concentration.
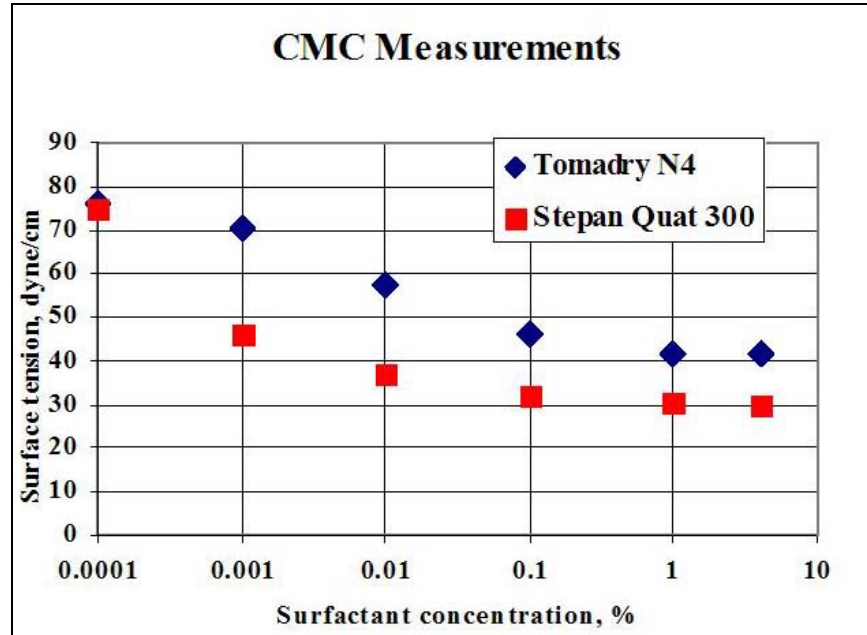
Figure 12. Critical micelle concentration test results.

Table 4. CMC test results			
Tomadry N-4		Stepanquat 300	
Concentration,%	IFT, mN/m	Concentration, %	IFT, mN/m
4	41.6	4	29.8
1	41.7	1	30.5
0.1	46.3	0.1	32.3
0.01	57.5	0.01	37.1
0.001	70.2	0.001	46.4
0.0001	76	0.0001	74.9
0	76.7	0	76.7

Contact angle (water drop)/core

A potential screening test consisting of observing the imbibition properties of a drop of water or dilute surfactant on the surface of reservoir core material was investigated. As shown in Fig. 2, a drop of water that beads on the surface of a treated Berea core suggests that the core is not water-wet. In a similar manner core plugs were cut from the St. Peter sandstone (Waverly field), the Mt. Simon sandstone (Sciota field sidewall plugs), and the Niagaran dolomite (Bell River Mills field).

Shown in Fig. 13 is a drop of water (red food dye added) placed on the surface of the St. Peter sandstone. The drop immediately spreads and is imbibed into the core; thus, the contact angle is 180° indicating a strongly water-wet surface. Rapid imbibition was also noted with the Mt. Simon side wall core. Recall that both the Waverly and the Sciota storage facilities were developed in water aquifers.

Figure 13. Water drop on St. Peter sandstone.

A water drop on the Bell River Mills dolomite core as shown in Fig. 14 is not imbibed as rapidly. Note that the drops on the first and third cores indicate that the dolomite is not water-wet. The permeability of the sandstone cores was ~ 100 md, while the dolomite cores were about 1000 md.
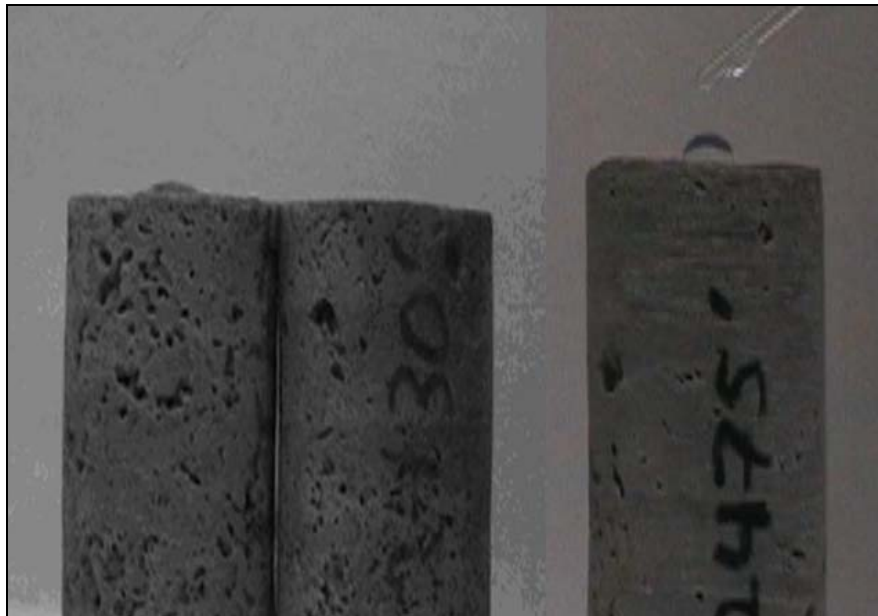
Figure 14. Water drops on untreated Niagaran dolomite core plugs.

The sandstone cores were flooded with 2% surfactant solutions (Tomadry N-4); the dolomite cores were treated with Arquad 2HT-75 and Stepanquat 300. As shown in Fig. 15 the contact angle of the water drop was less than 90°, and the water was not imbibed.

Figure 15. Water drop contact angle on treated sandstone is less than 90°.

Treating the dolomite cores with 1% surfactant solutions had little effect on the natural wettability of the core, judging by the similarity of the untreated core contact angle shown in Fig. 16.

Figure 16. Water drops on treated dolomite are similar to contact angles shown in Fig. 14.

Core Imbibition

The imbibition of reservoir water into dry reservoir cores was measured by the weight method described earlier. The St. Peter sandstone and the Niagaran reef dolomite were tested in this manner after which they were treated with surfactant solutions, and the imbibition properties were again measured.

The initial weight of the dry sandstone core was 54.750 g. Porosity was 12% and k_g was 109 md. The core was submerged in reservoir synthetic brine, and the weight of the core was measured periodically as water was imbibed. Once imbibition ceased, the core was flooded with a 2% surfactant solution of Tomadry N-4 and allowed to equilibrate overnight. The surfactant-saturated core was then flooded with dry gas to residual saturation. The initial weight of the surfactant-treated core was 54.766 g, very close to the initial dry core weight. The final weight of the surfactant-treated core increased by 1.654 g (3%), while the final weight of the non-surfactant core increased by 2.830 g (5.2%). The results are shown with a bar graph in Fig. 17. It is clear that the storage volume of the core was increased by 42% following treatment with a 2% solution of Tomadry N4.
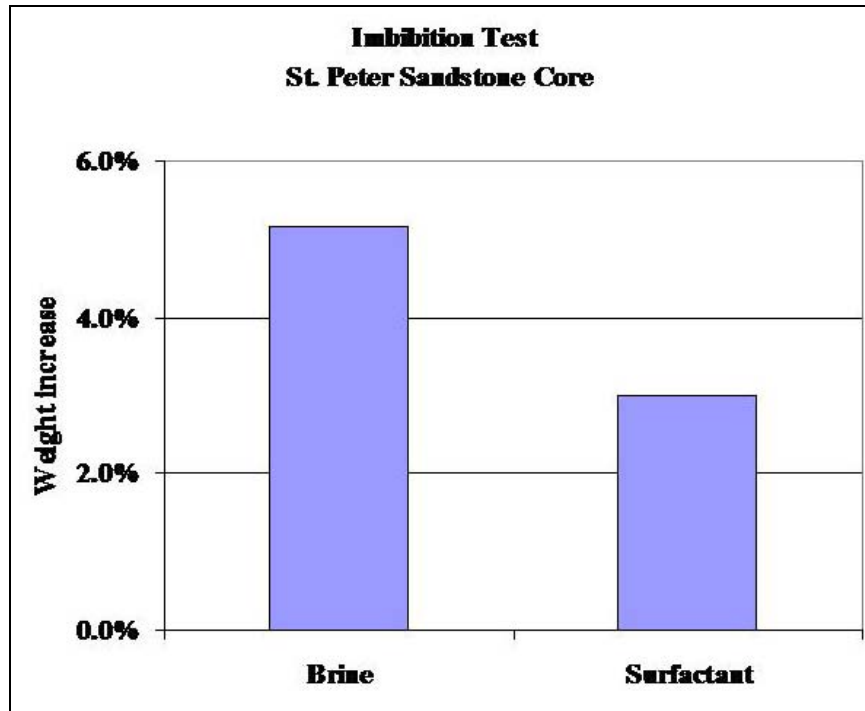
Figure 17. Forty-two percent less water was imbibed into the surfactant-treated core (17).

The imbibition-altering properties of a 1% solution of Stepanquat 300 were determined with a St. Peter Sandstone core M. The porosity was 11.2 %, and k_g was 68 md. The surfactant-treated core imbibed 0.4 g less water (2.0 g vs. 2.4 g) than the dry core. Based on an initial core weight of 54 g, the increase in storage capacity was 0.7%. The results are shown graphically in Fig. 18.
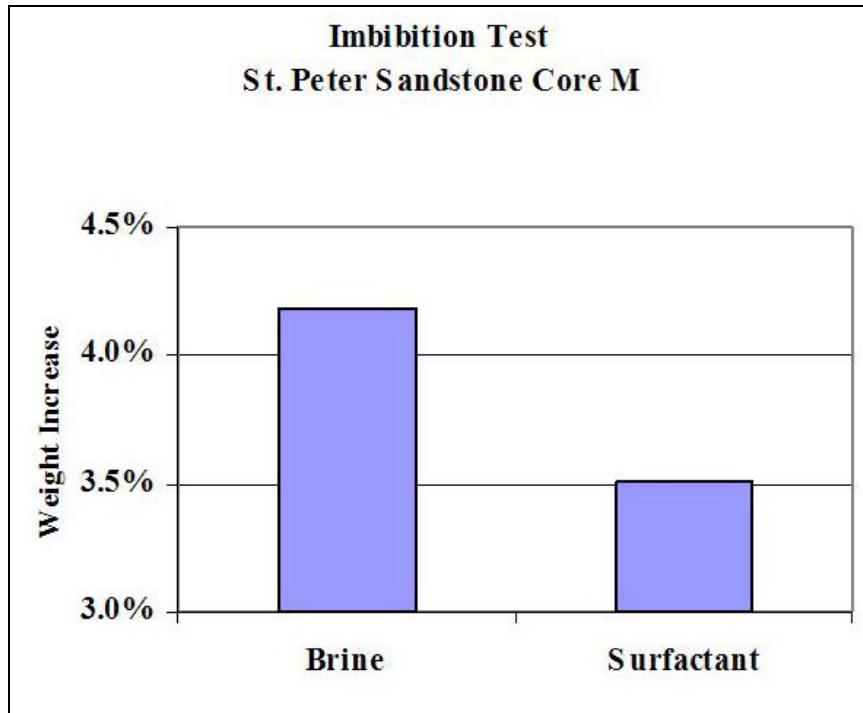
Figure 18. Seventeen percent less water was imbibed into surfactant-treated core (3).

Shown in Fig. 19 are the imbibition test results with the Niagaran reef dolomite core #2428. Pertinent core properties are 750-md k_g and 24% porosity. The surfactant was Tomadry N-4 (17). Note that the storage capacity of the core decreased suggesting that the core was not naturally water-wet.
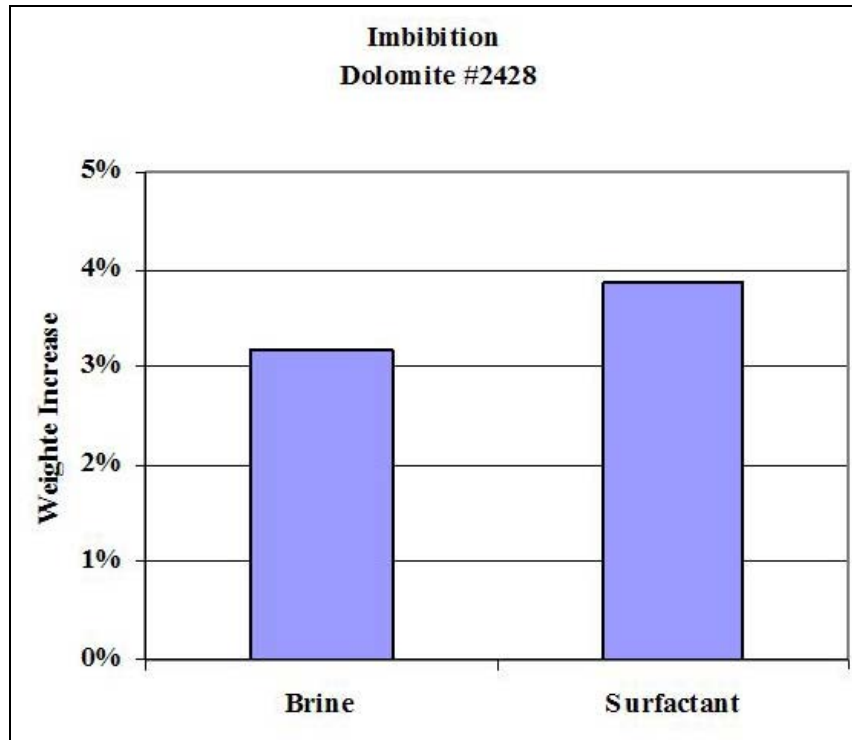
Figure 19. Imbibition test results with Niagaran dolomite core # 2428.

Since the Bell River Mills reservoir was originally a dry gas Niagaran reef field and most dry gas fields are believed to be water-wet, the imbibition test was repeated. The core properties of dolomite core #2396 are 620-md k_g and 28% porosity. The imbibition test results are quite similar to the core #2428 as shown in Fig. 20. Again, the unexpected result suggests that that the reservoir is not water-wet.
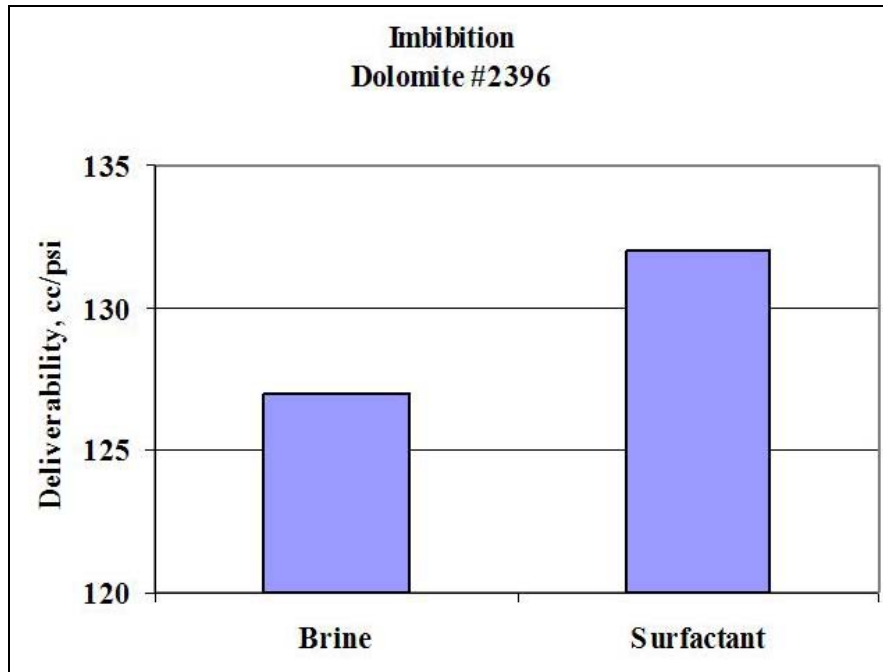
Figure 20. Bell River Mills core 2396 imbibition test result.

The core imbibition tests indicate that the aquifer storage reservoirs are water-wet. Treatment with low concentrations of surfactants, either #3 or #17, increased the storage capacity of the sandstone cores. Surfactant treatments did not increase the storage capacity of the dolomite cores.

Deliverability
  Sandstone

The effect of surfactants on the deliverability index, q/ΔP, was determined with a series of flow tests. The dimensions of the cores used for the deliverability (flow) test were ~4" long with a 1" diameter. Wet gas was injected until a stable flow rate was reached. The core was then saturated with 2% surfactant solution and again flooded with wet gas until the rate stabilized. All gas volumes were at standard conditions. The surfactant was Tomadry N-4 (17).

St. Peter sandstone core plugs were cut for testing. The Mt. Simon sidewall cores were not suitable for flow testing experiments. Results of the deliverability tests of St. Peter core A with a 109-md permeability and 12% porosity are shown in Fig. 21. A 2% solution of Tomadry N-4 was used to treat the core. The treatment improved deliverability by 59%.
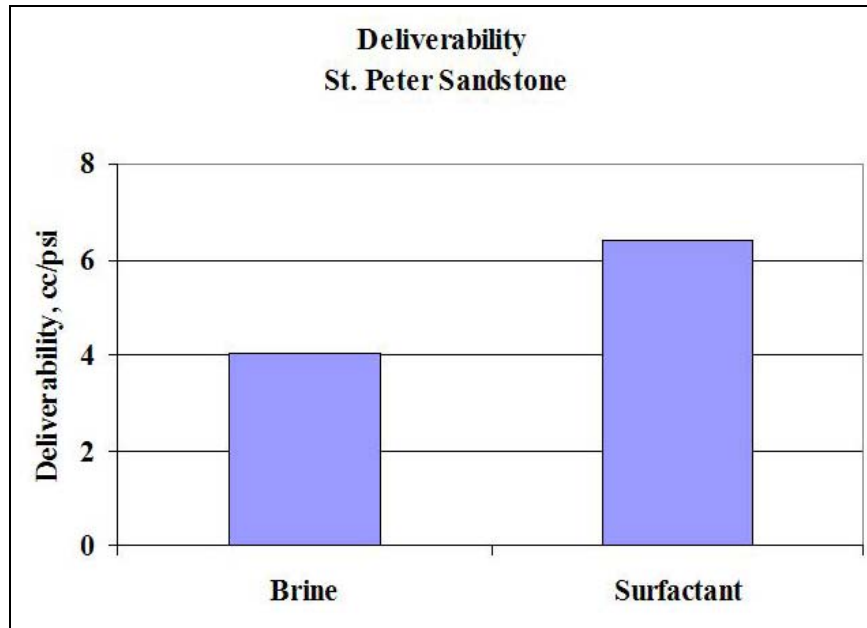
Figure 21. Gas deliverability through St. Peter 109-md sandstone.

A sandstone deliverability test was conducted with a 1% solution of Stepanquat 300 (1) using St. Peter core M with a 68-md k_g and 11.2 % porosity. The surfactant increased deliverability by 20% as shown in Fig. 22.
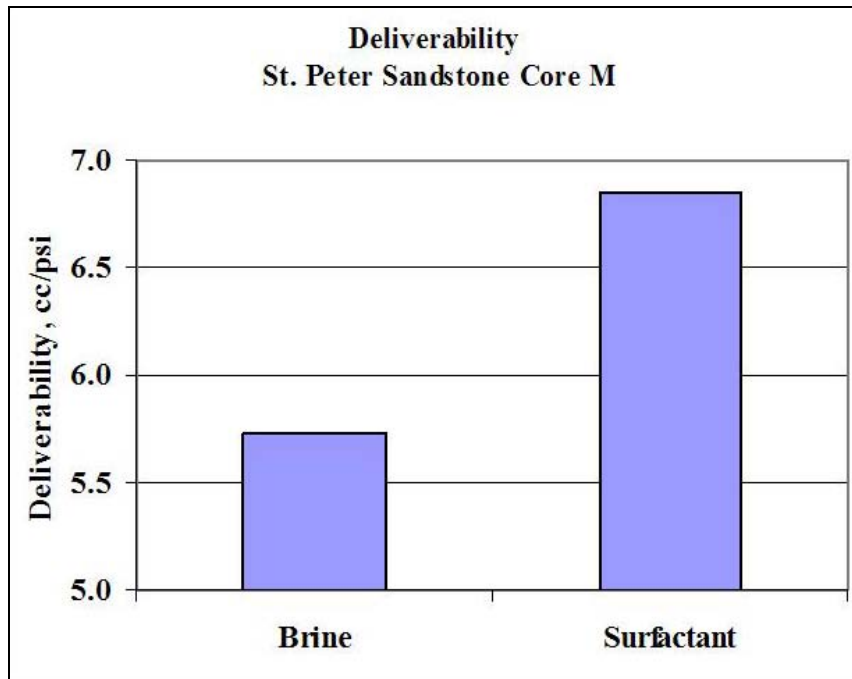
Figure 22. Deliverability test results through 68-md St. Peter sandstone.

<u>Dolomite</u>

Despite the adverse effect on storage capacity, the performance of surfactant treatment on the Niagaran reef dolomite cores on gas deliverability was measured. Dolomite core # 2428 with a 750-md k_g and 24% porosity was treated with a 2% solution of Tomadry N-4. The effect on deliverability was positive with a 1.7% increase as shown in Fig. 23.
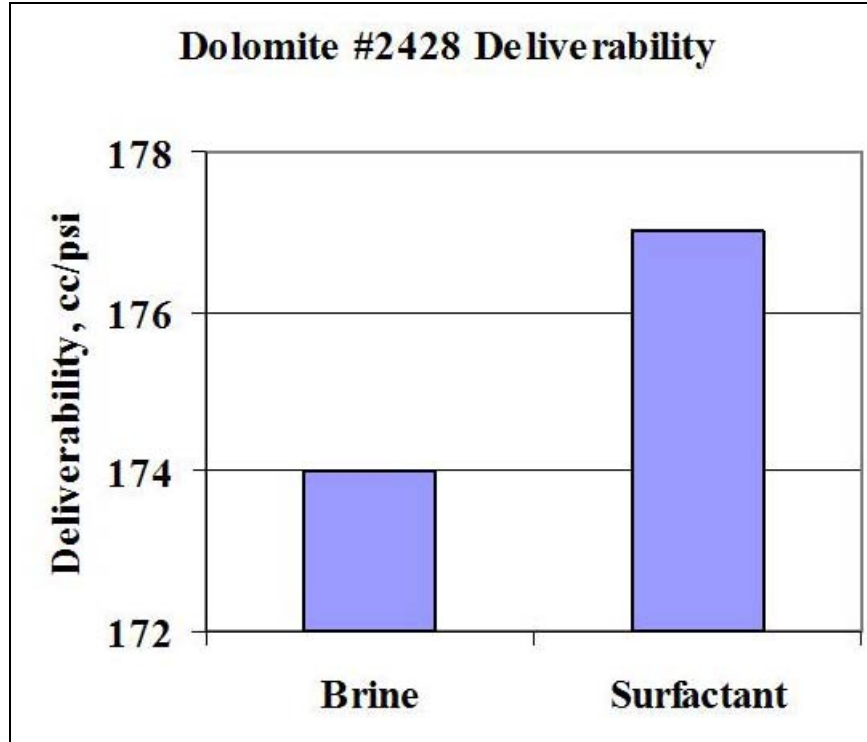
Figure 23. Marginal increase in deliverability with surfactant-treated dolomite core.

The deliverability test performed on dolomite core #2396 generated a 4% increase in this 810-md sample with 28% porosity. The marginal increase in deliverability with surfactant treatment of dolomite cores complements the dolomite imbibition test results.

The deliverability tests are presented as a function of cumulative gas injection in the appendix (Figs. A2–A5).

Engineering

A key to successful interpretation of field applications of remedial techniques is the performance history. Evaluation of the benefits of the surfactant stimulation technique requires that deliverability prior to treatment be compared to post-treatment results. The pressure-rate history of the Waverly St. Peter aquifer storage facility provided by Panhandle Energy and similar data from Bell River Mills Niagaran reef storage facility operated by Michigan Consolidated Gas was evaluated for prior-treatment trends.

Production history analysis

<u>Waverly St. Peter aquifer storage facility</u>

The Waverly storage facility monthly production history (December 2004–April 2005) served as a 25-well dataset including the withdrawal rate, flowing wellhead pressure, shut-in observation well pressure, and delta P defined as shut-in pressure squared minus flowing pressure squared. Four wells (Nos. 5, 21, 88, 91) with lengthy, continuous production records were selected for analysis to generate baseline information for potential field tests. Conventional plots of flow rate vs. time were developed. The noise in these plots was somewhat reduced by substituting cumulative gas produced for time.

Waverly is an aquifer storage facility as evident in the various production curves. The rate deteriorates until it is essentially flat when the bottom water encroaches on the perforations. This is seen with data from well 5 as shown in Fig. 24. If the withdrawal rate following the surfactant treatment is greater than the withdrawal rate without surfactant, the economics of fieldwide treatment could be investigated.
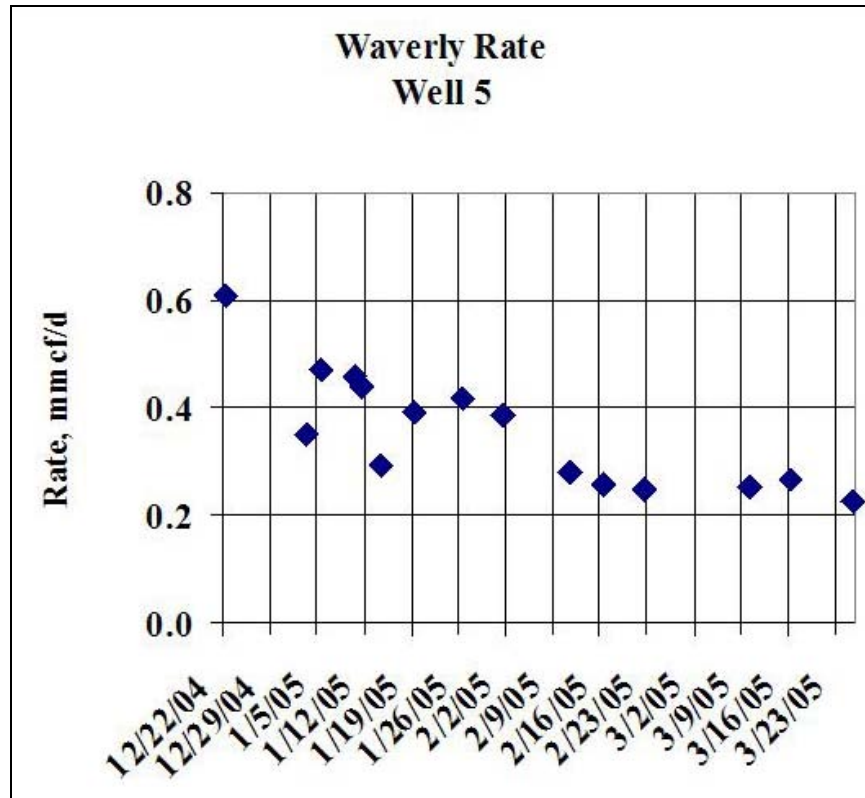
Figure 24. Waverly # 5 performance history.

The relationship between flow rate and pressure should be a continuous function with the condition of non-turbulent flow as expected at the pressure measurement points. However, two distinct trends in the rate are evident in Fig. 25. The two distinct linear trends are the result of bottom water encroachment. The fact that the trends are linear facilitates a before/after analysis.
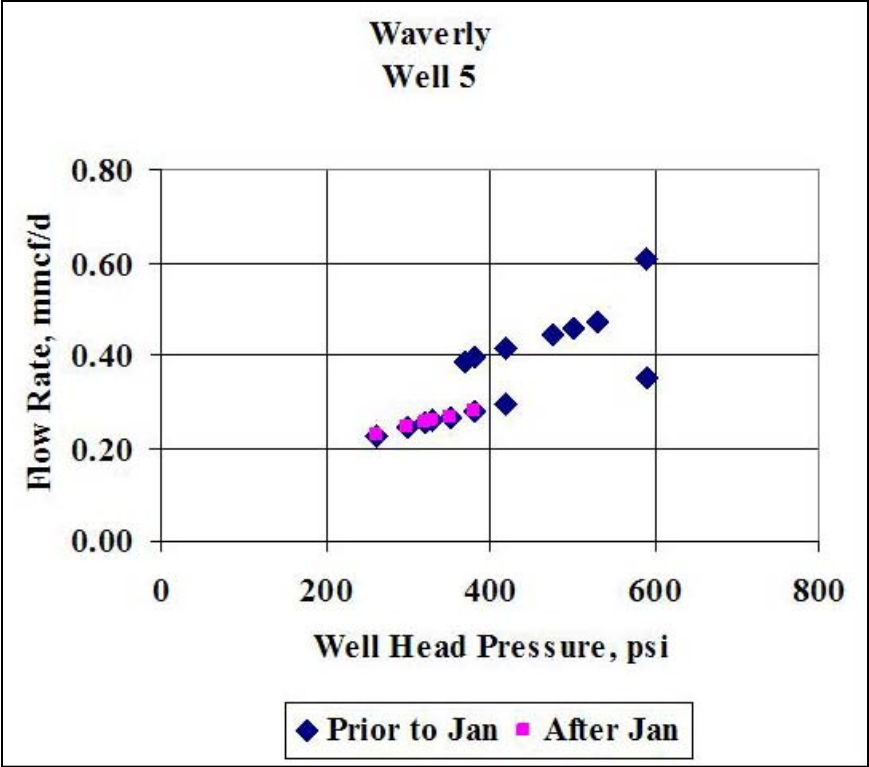
Figure 25. Well 5 flow rate vs. pressure.

Cumulative gas withdrawn was substituted for time in Fig. 26 that shows the relationship between rate, wellhead flowing pressure, deliverability defined as rate/dP, and observation well shut-in pressure. It is evident that as the reservoir pressure approaches 500 psi, the rate tends to stabilize. The same phenomenon occurs in wells 21, 88, and 91, shown in the appendix (Figs. A6–A8).
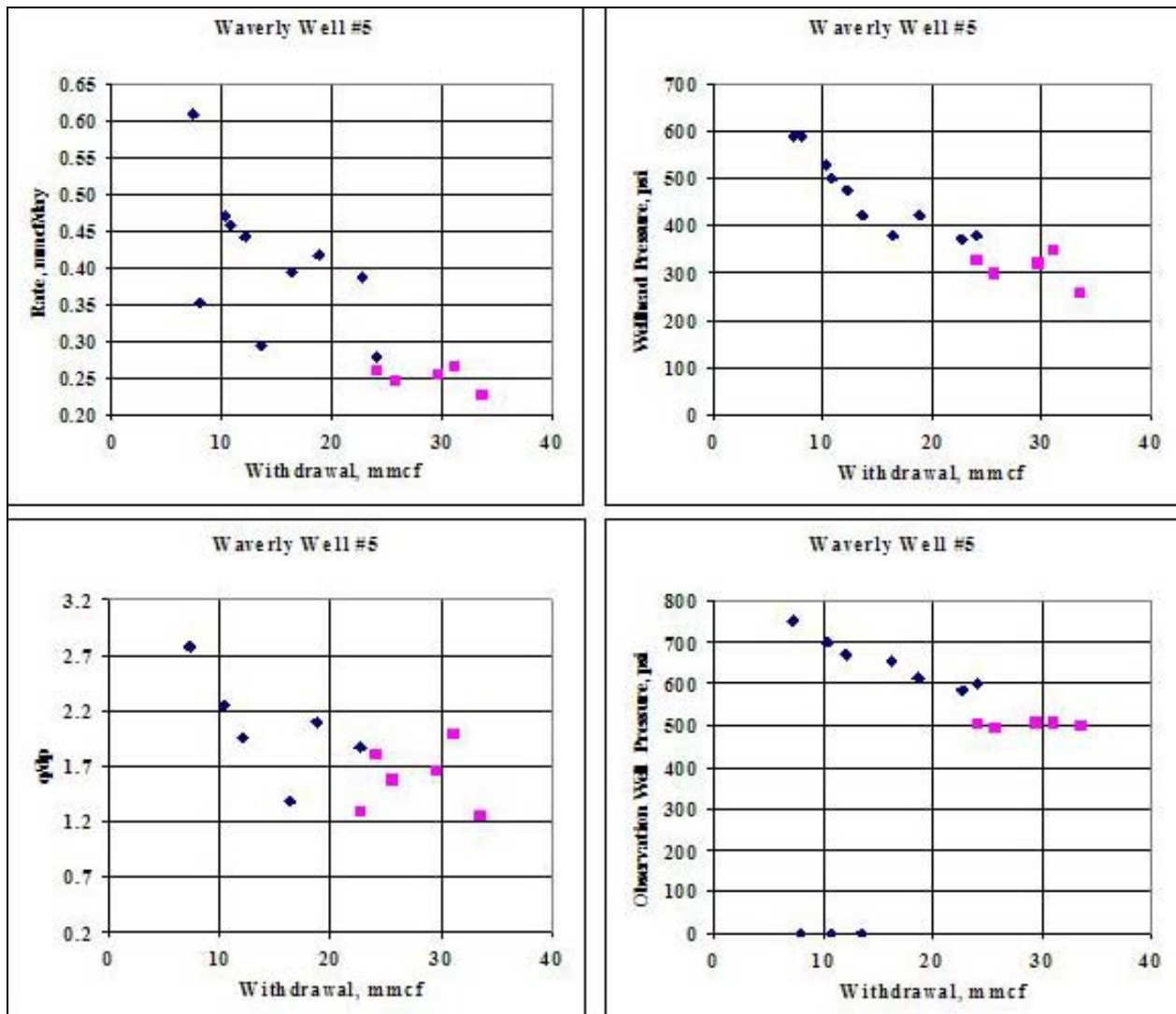
Figure 26. Rate, flowing pressure, deliverability, and observation well pressure of Well 5.

Waverly field logs were obtained to estimate porosity in the event pore volume calculations are included in the design of the surfactant volumes required for field application. Both core and log information was available from the Doolin 1-16 well. Since all wells were not cored, the Doolin 1-16 well information was used to adjust the constants in log interpretation equations to match the core-measured porosity. These tuned equations could be applied to non-cored wells.

Waverly field core cut from the stored gas interval (top @ 1821 ft; base @ 1898 ft) in the St. Peter formation Doolin 1-16 well was received along with resistivity logs and the SP log. Core plugs were drilled from core sections from 1833-34 and 1855-61 ft to obtain material for the laboratory work described earlier. The log interval was 1800–2010 ft and consisted of the ShortNormal, LongNormal, MicroInverse, and MicroNormal electrical logs, plus the SP log.

The reported core measurements are at 1-ft intervals, while the log measurements are at ½-ft intervals. The log values were averaged over 1-ft intervals and plotted vs. the core values as shown in Fig. 27. Others[8] recognized the existence of a relationship between the short normal log and porosity. However, Fig. 27 shows that the correlation is not strong. Similar correlations are observed in Figs. 28–31.
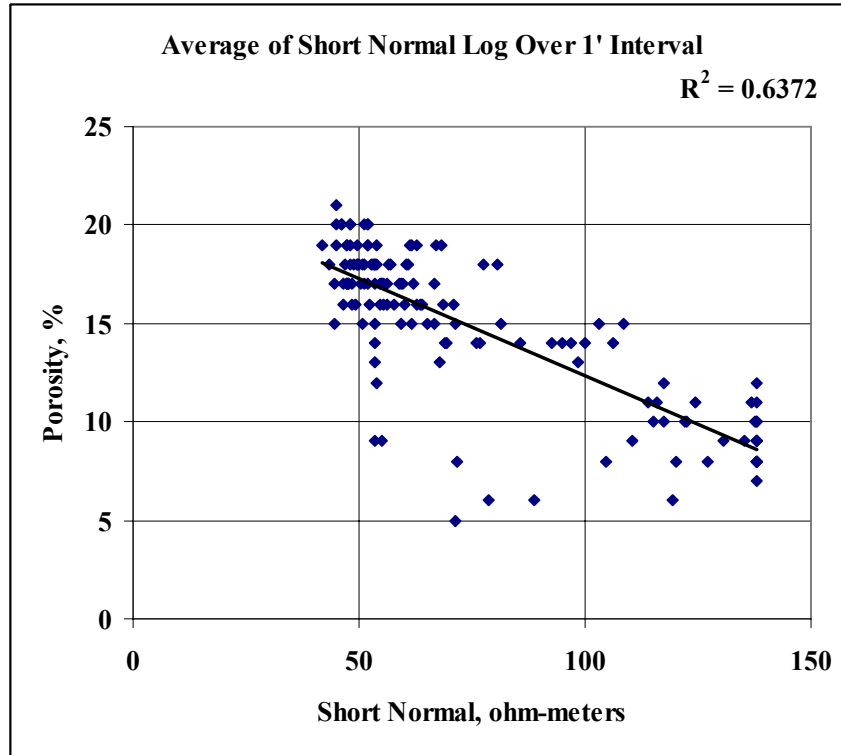
Figure 27. Core porosity vs. the average of the short normal log over 1' intervals.

Increasing the log averaging interval to 3 ft had very little effect on the correlation coefficient in Fig. 26 coefficient as shown in Fig. 27.
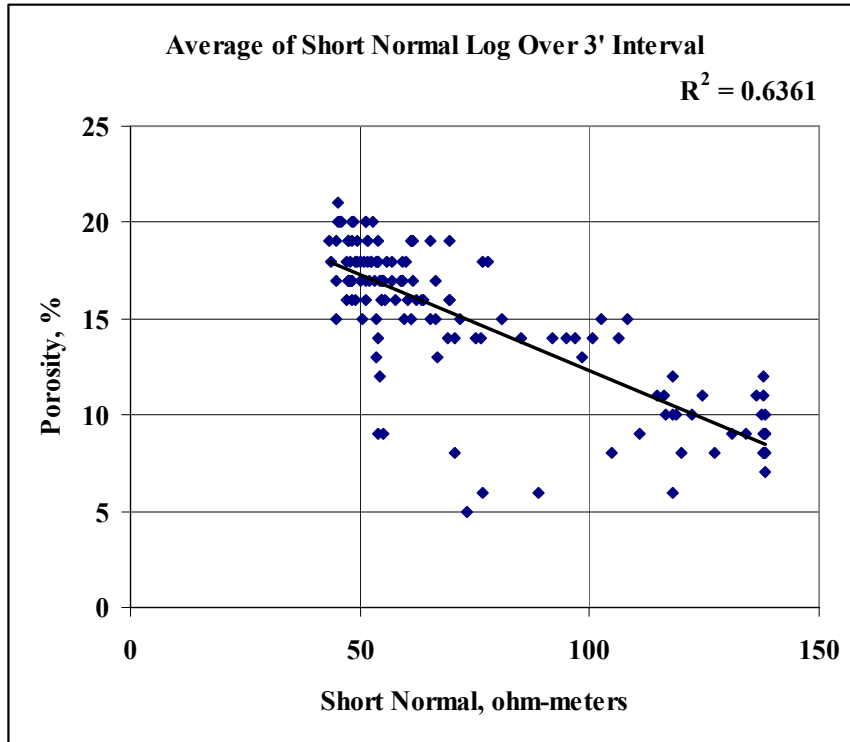
Figure 28. Core porosity vs. the average of the short normal log over 3' intervals.

The correlation between the SP log averaged over a 3-ft interval and core porosity was poor as shown in Fig. 29.
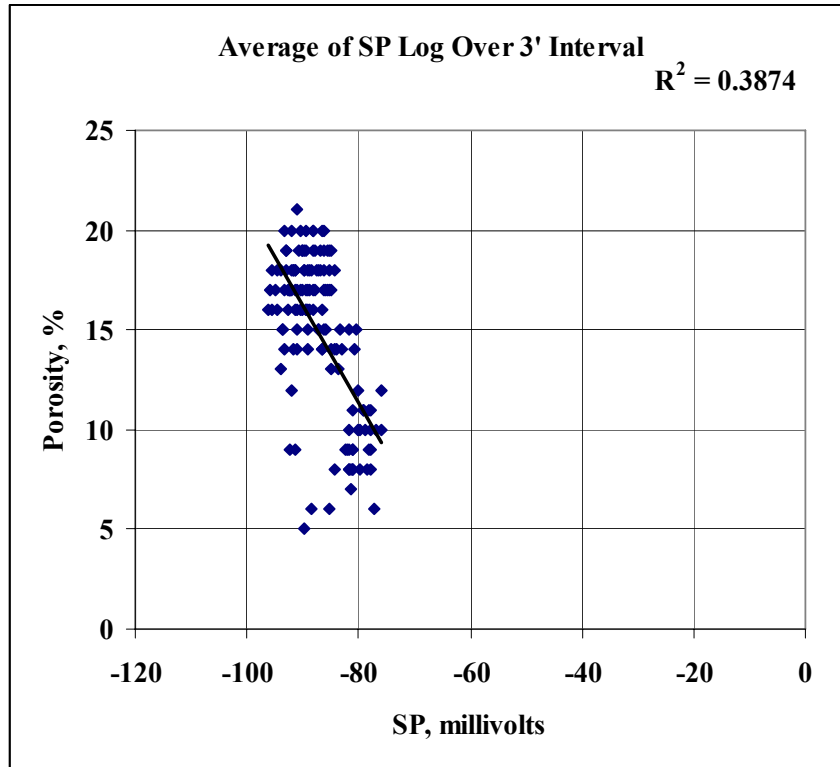
Figure 29. Core porosity vs. the average of the SP log over 3' intervals.

Derivatives of the log values have been demonstrated to be better correlating variables than measured log values.[9] The first derivative of the SP log was calculated and plotted vs. the core porosity as shown in Fig. 30. No correlation exists.
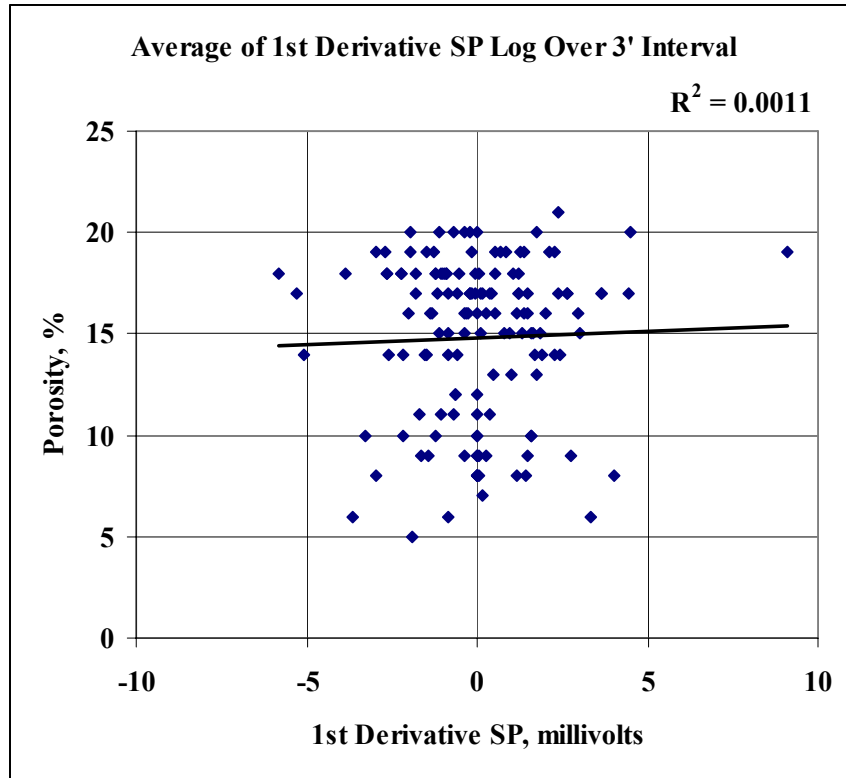
Figure 30. Core porosity vs. the 1st derivative of the average of the SP log over 3' intervals.

Datasets of the Doolin 1-16 type have been successfully correlated using fuzzy logic. The core porosity was fuzzified and plotted vs. the values of the short normal curve averaged over a 1-ft interval. The resulting fuzzy curve as shown in Fig. 31 (continuous curve) has sufficient range to be used as a tool to calculate porosity given the short normal curve. The actual core values are also shown in Fig. 31 to provide a sense for the effect of generating a fuzzy curve.
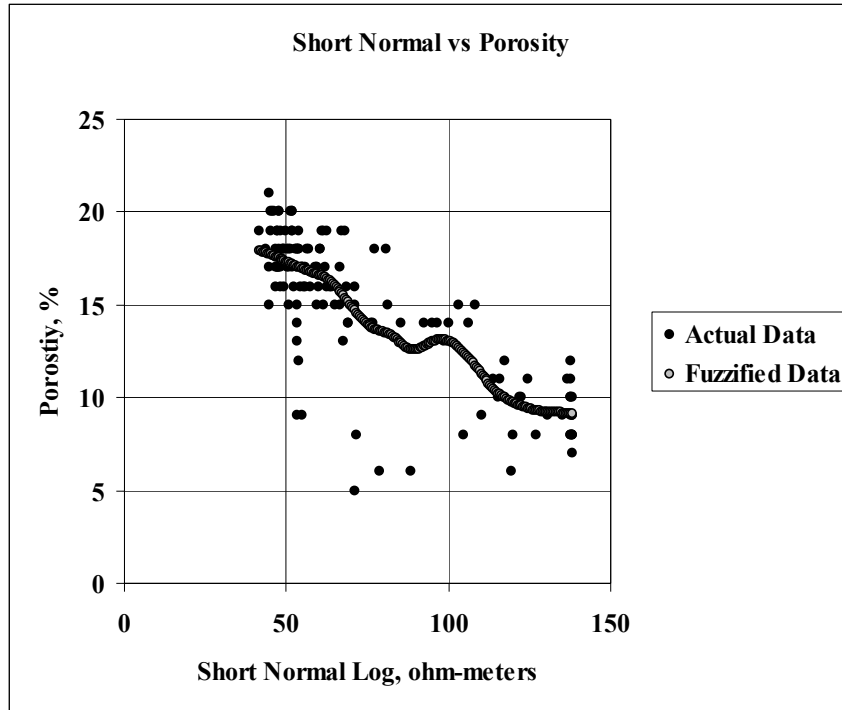
Figure 31. Fuzzified core porosity vs. the average of the short normal log over 1' intervals.

The intent of the core/log analysis was to develop a neural network to generate porosity and permeability models given log measurements. Fuzzy curves are useful when selecting input variables for neural networks. Fuzzy curves similar to Fig. 31 were generated for the ShortNormal, LongNormal, MicroInverse, and MicroNormal electrical logs, plus the SP log vs. the core porosity values. The fuzzy curves suggested that all of the resistivity curves were appropriate variables for multivariate analysis. The abundance of measured core porosity values suggested that significant multivariable correlations would result with neural network correlations. Unfortunately none of the neural network architectures generated correlations greater than the fuzzy resistivity curves alone. The SP values did not improve the neural networks based solely on the resistivity logs as inputs.

<u>Bell River Mills Niagaran reef storage facility</u>

Michigan Consolidated Gas provided about 7000 rate-pressure measurements collected during a 1-year period (Oct. 1996 to Oct. 1997). Observation well pressure data accompanied the Dietland #2 well rate-pressure history. This history was reduced to daily averages and graphed in manner similar to the format used to examine the Waverly facility information analyzed last quarter. The purpose of the analysis was to determine if stabilized trends existed that could be easily used to measure improved well deliverability should laboratory core tests support a field test.

The fill rate, withdrawal rate, fill pressure, and withdrawal pressure vs. time are plotted in Fig. 32.
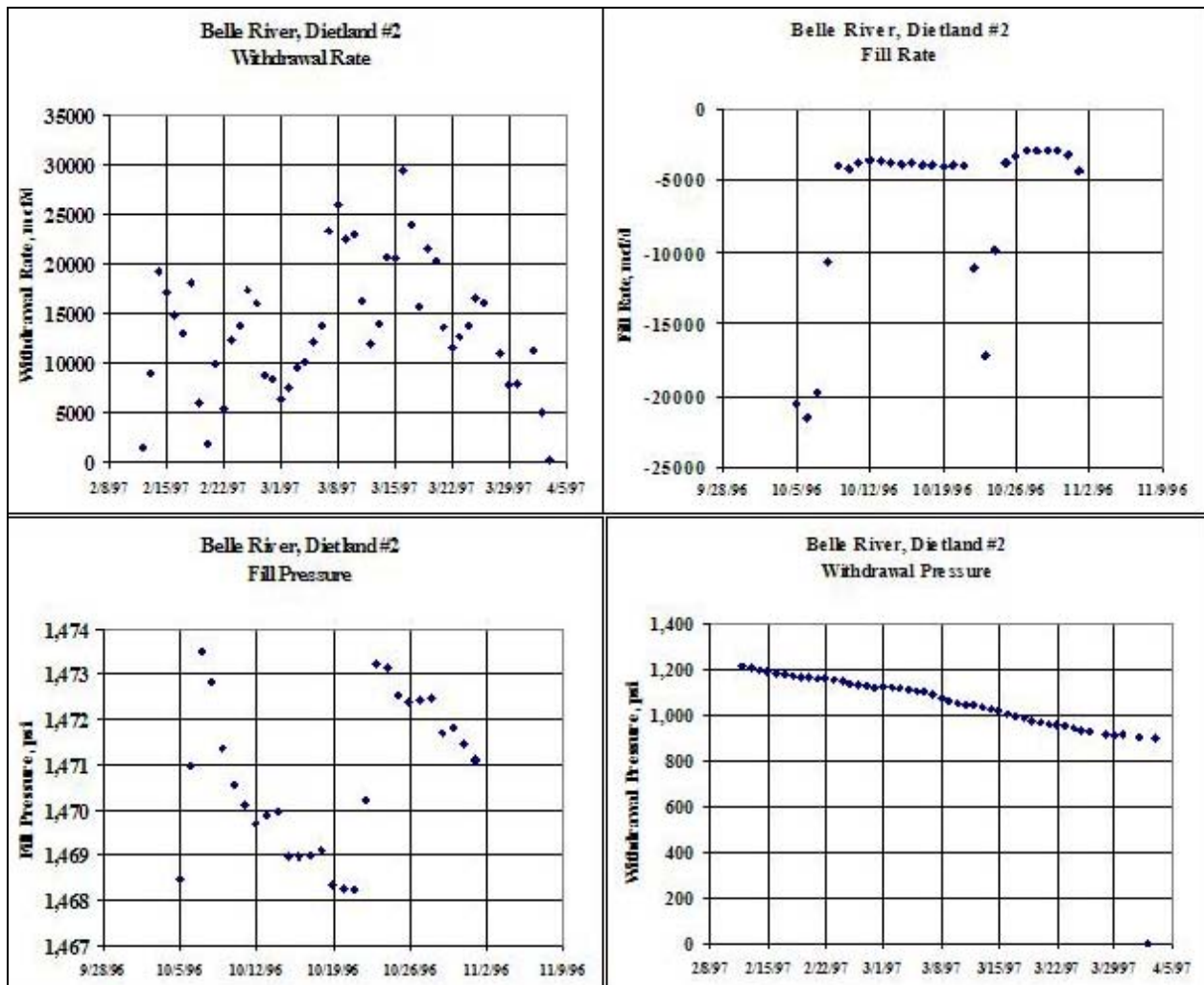
Figure 32. Fill and withdrawal rate-pressure history.

Obvious trends are evident in the fill rate and pressure plots along with the withdrawal pressure. Observation well pressure is assumed to represent static reservoir pressure in the deliverability index calculation of flow rate divided by pressure drop. Temperature and depth corrections were not applied to the wellhead pressure and rate measurements. Cumulative withdrawal volumes were substituted for time to smooth the deliverability data as shown in Fig. 33. Cumulative injection volume was substituted for time in Fig. 34. The trend in the deliverability data shown in Fig. 33 is more readily evident than the injectivity plot (Fig. 34).
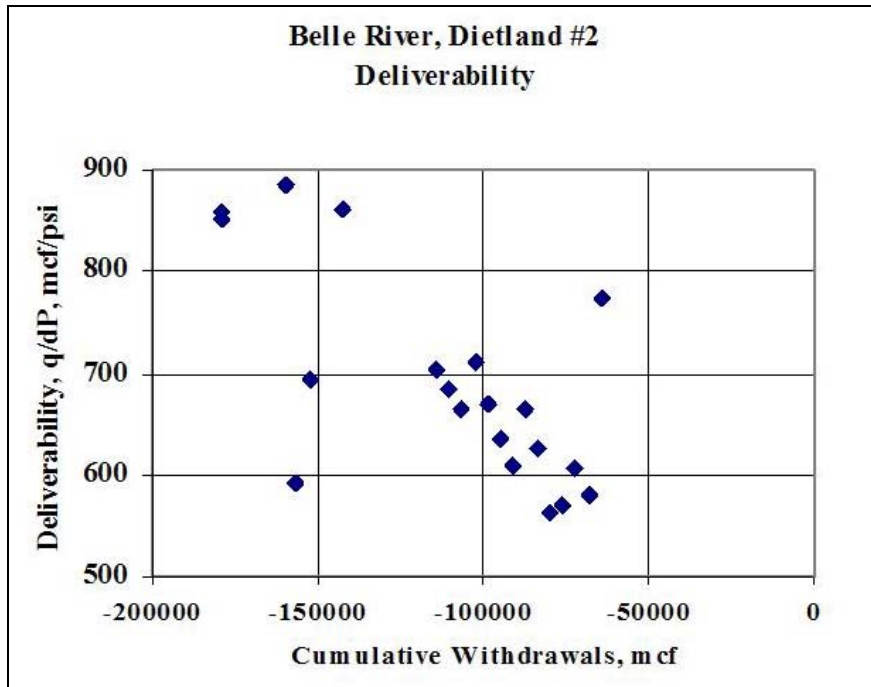
Figure 33. Deliverability vs. cumulative withdrawal.
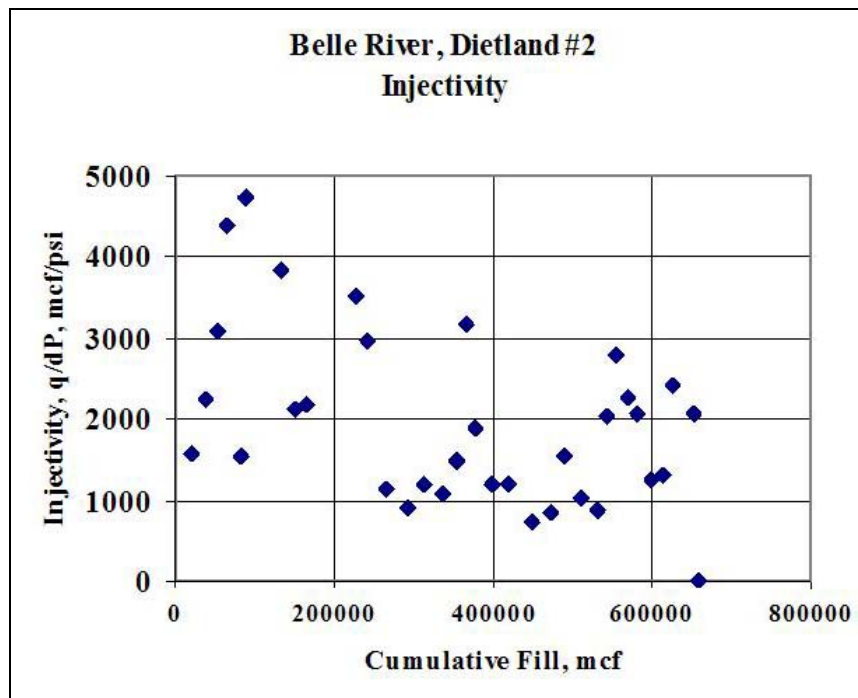
Figure 34. Injectivity vs. cumulative fill volume.

The linearity of the deliverability vs. withdrawals presentation of the pressure-rate historical data provides a baseline suitable for measuring the effect of surfactant on gas deliverability from either water-wet sandstone or non-water-wet dolomite storage facilities.

Discussion

This project evolved from an unpublished experiment conducted with a known water-wet limestone core from a Central Texas outcrop. It was observed that treating the core with an oil-soluble surfactant and then displacing the oil solution with water followed by displacement with gas doubled the gas flow rate over that at residual water saturation. Dry gas reservoirs and hence gas storage reservoirs were assumed to be water-wet, especially with the repeated fill/withdrawal cycles. After discussions concerning suitable surfactants with four vendors, requests were made for 14 surfactants that might make rocks less water-wet. The vendors supplied 11 samples. The costs of the surfactants varied from $1.50–$45.00 per lb as shown in Table 5.

Table 5. Surfactant prices*		
Chemical	Vendor	Cost $/lb
Tomadry N-4	Tomah Products	$1.47
Stepanquat 300	Stepan	$1.86
Witconic 1298	Akzo Nobel	$3.22
FC 4430	3M distributor	$44.84

*Price quotes of four potential surfactants were obtained during August 2005.

Since core tests involving preparation, precise weights, and monitoring of flow experiments require time and expense, additional methods were developed to screen the wetting properties of dilute solutions of the surfactants. Capillary tubes were used to measure the rise of water in dry tubes vs. the rise of water in tubes treated with surfactants. Another test consisted of observing a drop of water on reservoir core material. Drops that spread (contact angle to air $>90^o$) were imbibed into the core. Drops that beaded on the core surface (contact angle to air $<90^o$) did so at a much slower rate or not at all.

Stepanquat 300 and Tomadry N-4 suppressed the capillary rise of water in tubes treated with surfactant to a greater degree than the other surfactants. Both are formulated compounds of quaternary ammonium cationic surfactants. The IFT measurements (Stepanquat ~30 dyne/cm and Tomadry ~40 dyne/cm) demonstrate that IFT and contact angle are separate components in the capillary pressure equation. Both generated a 0.7 cm rise in capillary tubes treated with 1% solutions of surfactant. Young's equation (see appendix) generates a contact angle of 75.4^o for Stepanquat 300 and 76.0^0 for Tomadry N-4 suggesting that the difference in the performance of the two products in the core tests is the result of slight variations in their formulations. Since the cost effectiveness in suppressing capillary rise of the two surfactants is less than the other surfactants, they were selected for additional laboratory tests.

Generally the water-drop/contact angle on treated and untreated cores supports the precise capillary rise measurements. Both sandstone cores were water-wet, and the wetness was reduced with surfactants. However, the wetness of the dolomite appeared to be essentially constant with or without surfactant. Glass (quartz) capillary tubes are available, but availability of other materials such as dolomite or limestone is not known. Hence the advantage to using the

water-drop/contact angle tests on reservoir core material is attractive; however, additional work is required to improve the accuracy of the procedure.

The imbibition tests with reservoir cores are designed to test the effectiveness of surfactants in reducing the imbibition of water into the cores, thus increasing the volume available to store gas. The experimental results with the St. Peter core-water system demonstrate that a 2% solution of Tomadry N-4 increased the storage capacity of the core by 42%, while a 1% solution of Stepanquat 300 generated a 0.7% increase. Surfactants marginally affected the storage capacity of the dolomite cores in an adverse manner. This could be interpreted as the reservoir dolomite being naturally oil-wet.[10]

Core flow tests with reservoir cores were conducted to measure the deliverability defined as the flow rate divided by the pressure drop across the core. Laboratory experiments with a St. Peter sandstone core treated with a 2% solution of Tomadry N-4 resulted in a 59% increase in gas deliverabilty. A 40% less permeable St. Peter sandstone core treated with a 1% solution of Stepanquat 300 resulted in a 20% increase in gas deliverabilty. The gas deliverability through dolomite cores was only marginally increased.

While the Mt. Simon sandstone sidewall cores were not used in the flow tests due to size problems, the similarity in contact angle/core drop test observations suggests that the Mt. Simon sandstone would generate increased deliverability and storage capacity similar to St. Peter sandstone.

The rate-pressure history available from both the Waverly and Bell River Mills fields is adequate for field test baseline purposes. The laboratory data support a Waverly field test of the use of surfactants to increase gas deliverabilty from storage wells. If a field test could be scaled to the laboratory results, the deliverability of well 91 would increase as shown in Fig. 35.
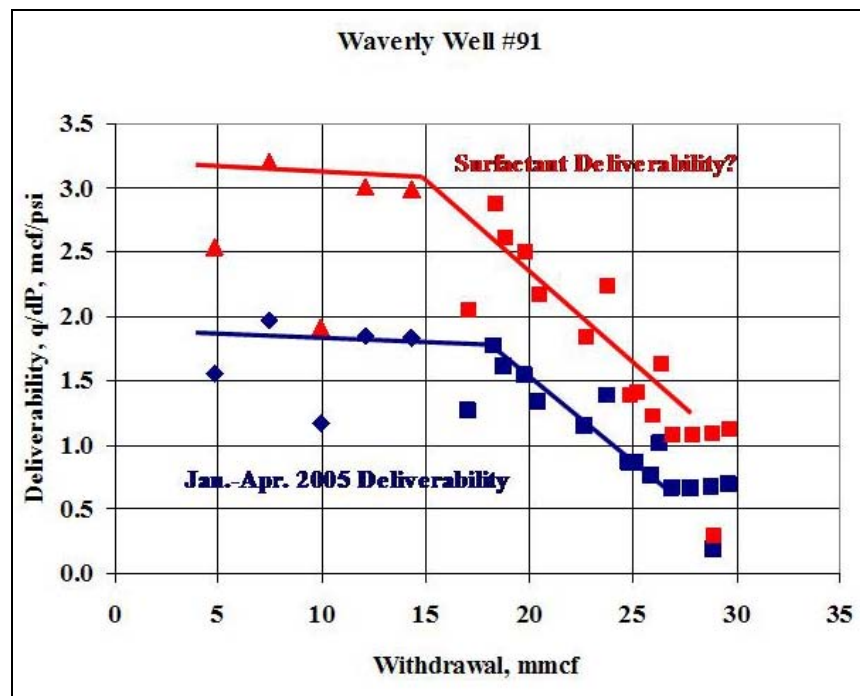
Figure 35. Potential deliverability increase with Well 91 surfactant treatment.

The laboratory data do not support a Bell River Mills field test. However, the rate-pressure history may prove useful for a salt inhibitor field test should the current laboratory work generate supporting information.

Conclusions

This project demonstrates that the wettability of gas storage reservoirs plays an important role in the void space available for storage. The deliverability of gas from a storage well is also dependent on rock wettability. It was determined through laboratory tests with cores from aquifer storage sites that some surfactants can decrease the natural water-wetness of sandstone thereby increasing gas deliverability and gas storage volume. This was not the case with dolomite cores from a storage facility that was formerly a dry gas reservoir. Transferring this new concept from the laboratory to the field should be of interest during times of limited storage capacity.

The value of laboratory testing with cores and water from specific field sites was confirmed with the surprising results obtained with dolomite cores from a storage facility that was formerly a dry gas reservoir. The notion that all dry gas reservoirs are strongly water-wet was erroneous.

References

1. Yeager, V.J., Blaush, M.E., Behenna, F.R., and Foh, S.E.: "Damage Mechanisms in Gas Storage Wells," SPE 38863 presented at the SPE Annual Technical Conference and Exhibition, San Antonio, TX (October 5–8, 1997).

2. Ammer, J.R. and Sames, G.P.: "Advances for Improved Storage: Deliverability Enhancement and New Storage Facilities," Paper SPE 65638 presented at the 2000 SPE Eastern Regional Meeting, Morgantown, WV (October 17–19, 2000).

3. Penny, G.S., Soliman, M.Y., Conway, M.W., and Briscoe, J.E.: "Enhanced Load Water-recovery Technique Improves Stimulation Results," paper SPE12149 presented at the 58th Annual Technical Conference and Exhibition, San Francisco, CA (October 5–8, 1983).

4. Al-Anazi, H.A., Walker, J.G., Pope, G.A., Sharma, M.M., and Hackney, D.F.: "A Successful Methanol Treatment in a Gas-Condensate Reservoir: Field Application," paper 80901-PA, February 2005 SPE Production & Facilities.

5. Mahadevan, J. and Sharma, M.M.: "Clean-up of Water Blocks in Low Permeability Formations," SPE 84216 presented at the SPE Annual Technical Conference and Exhibition, Denver, CO (October 5–8, 2003).

6. Fahes, M. and Firoozabadi, A.: "Wettability Alteration to Intermediate Gas-Wetting for Gas-Water Systems at Reservoir Condition," presented at the 8th International Symposium on Reservoir Wettability, Rice University, Houston, TX (May 16–18, 2004).

7. Du, L., Walker, J., Pope, G., Sharma, M., and Wang, P.: "Use of Solvents to Improve the Productivity of Gas Condensate Wells," SPE 62935 presented at the 2000 SPE Annual Technical Conference and Exhibition, Dallas, TX (October 1–4, 2000).

8. Hilchie, D.W.: *Old Electrical Log Interpretation*, IED Exploration, Inc., Tulsa OK, (1979) 118-120.

9. Weiss, W.W., Xie, X., Weiss, J.W., Subramanian, V., Taylor, A., and Edens, F.: "Artificial Intelligence Used to Evaluate 23 Single-Well Surfactant Soak Treatments," SPE Paper 89457 presented at the 14th Symposium on Improved Oil Recovery, Tulsa, OK (April 17–21, 2004).

10. Wardlaw, N.C. and McKellar, M.: "Wettability and Connate Water Saturations in Hydrocarbon Reservoirs with Bitumen Deposits." Journal of Petroleum Science and Engineering 20 (1998) 141-146.

Appendix

Additional laboratory results and Waverly production histories

Additional figures have been constructed from the laboratory test results and the Waverly production histories. Young's equation was utilized.
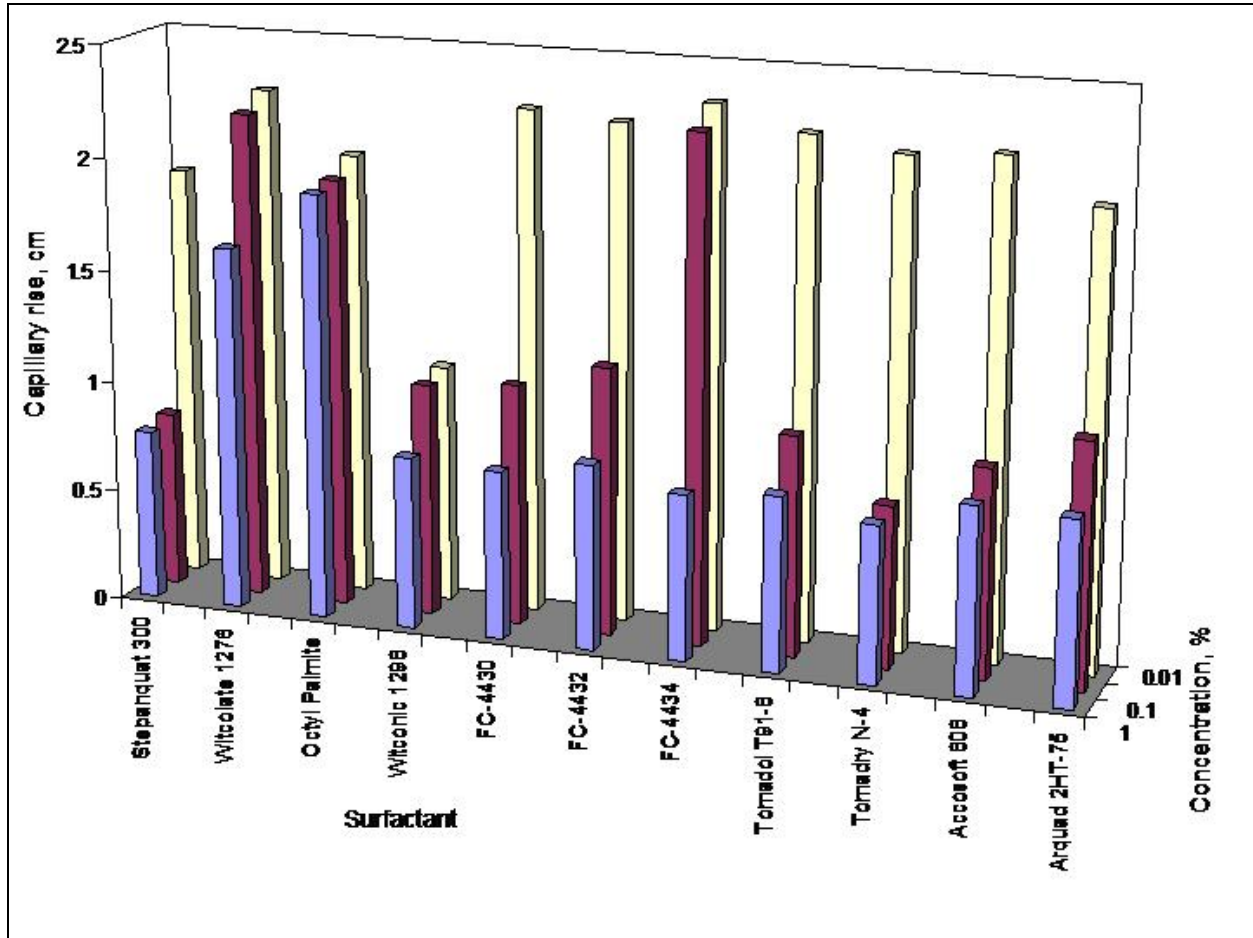
Figure A1. Summary of capillary rise tests.
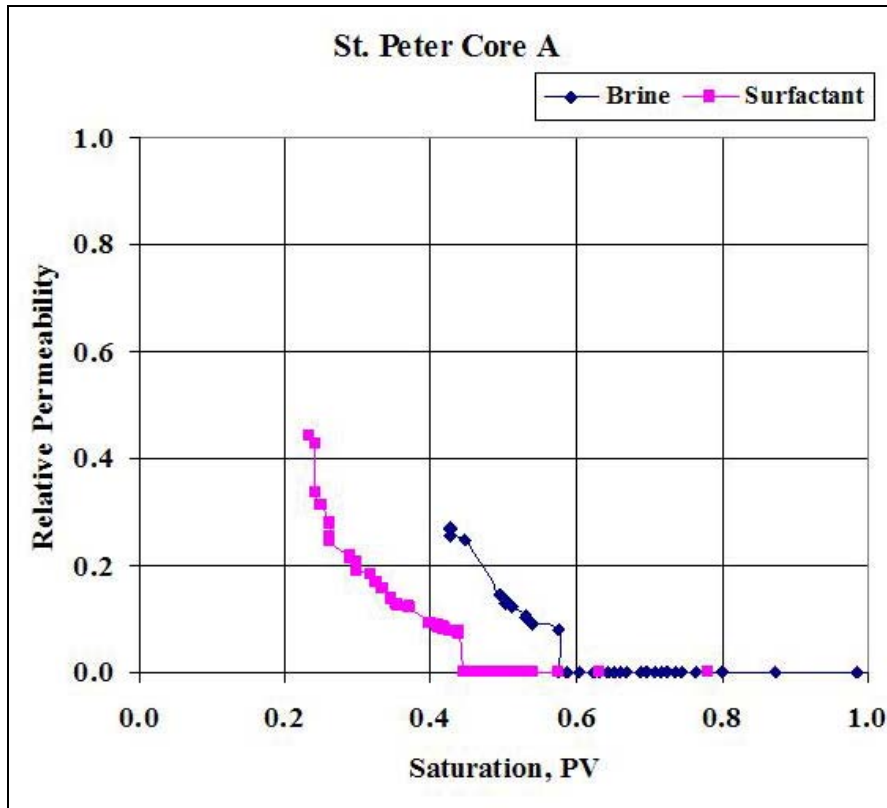
Figure A2. Krg in St. Peter sandstone core "A" with brine or Tomadry N-4.
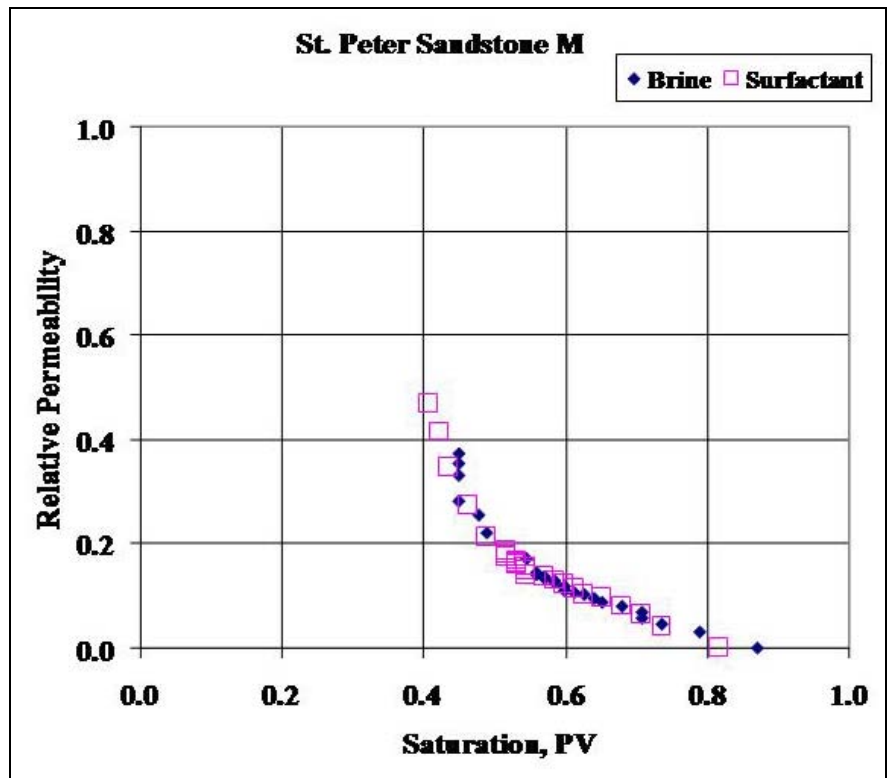
Figure A3. Krg in St. Peter Sandstone "M" with brine or Stepanquat 300.
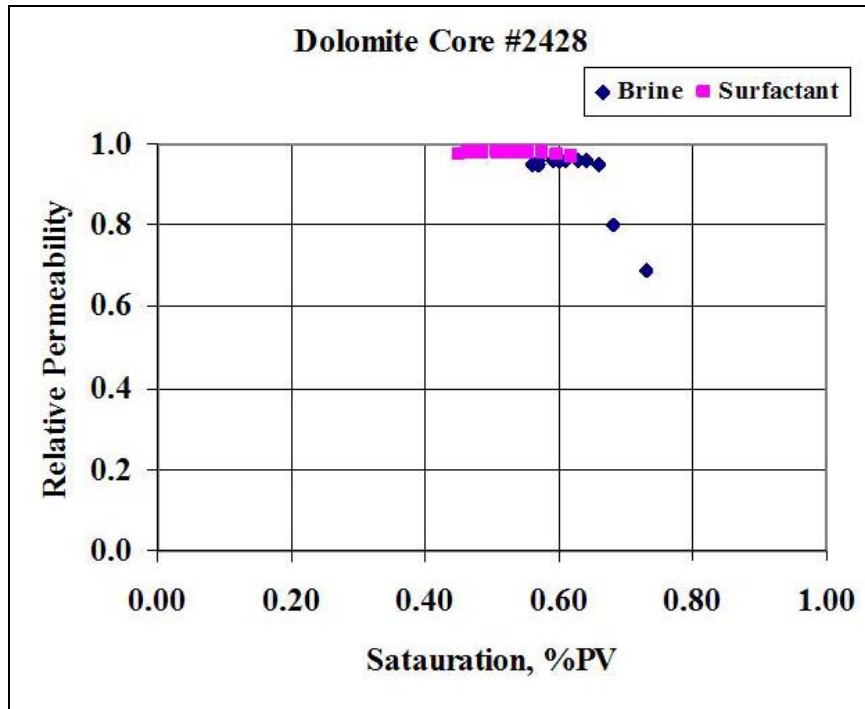
Figure A4. Krg in dolomite core #2428 with brine or N-4 Surfactant.
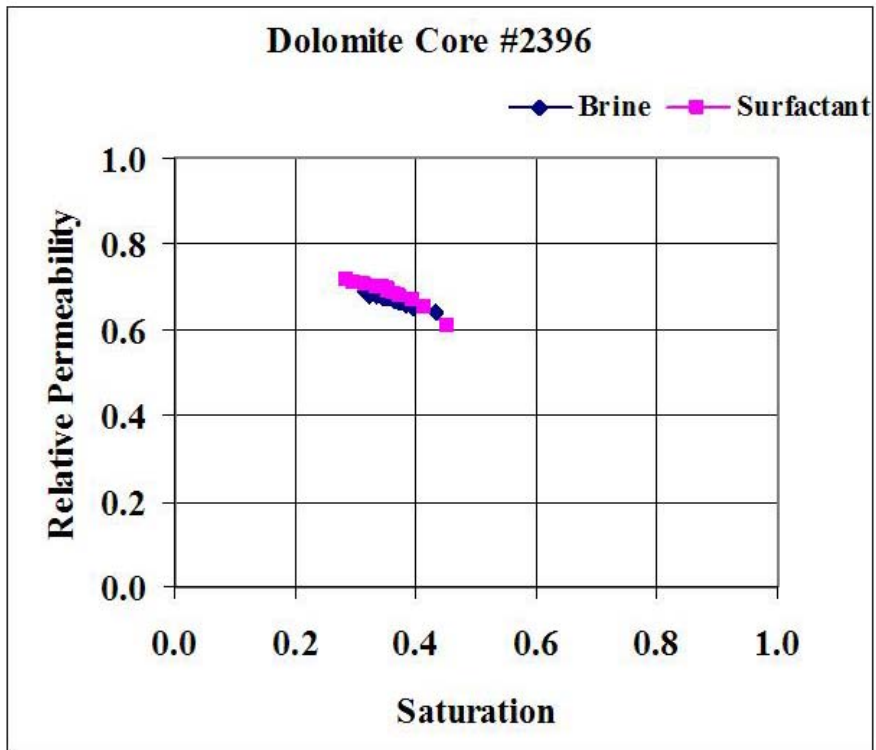
Figure A5. Krg in dolomite core #2396 with brine or Tomadry N-4.
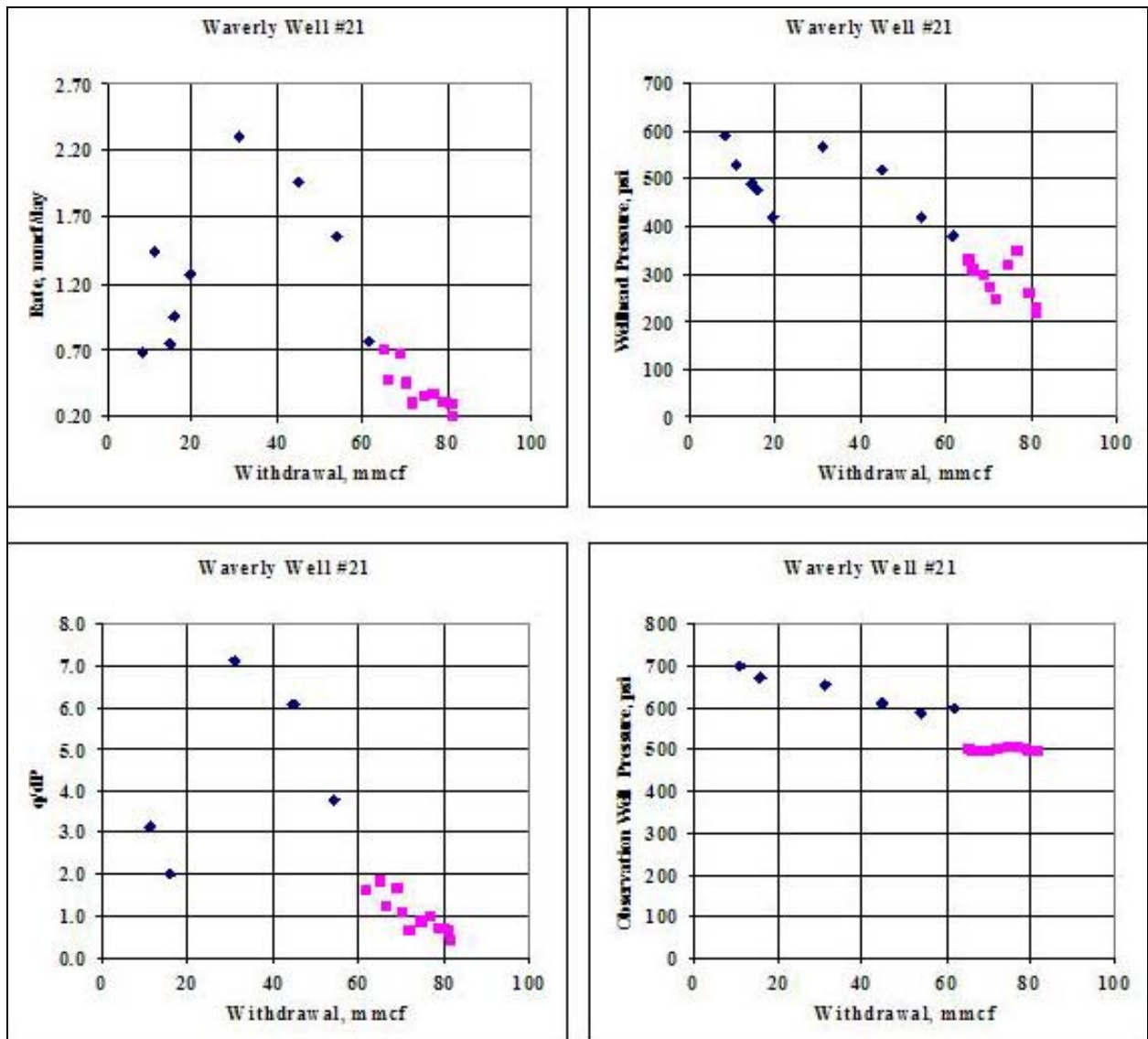
Figure A6. Performance history of Waverly well # 21 during the 2004 season.
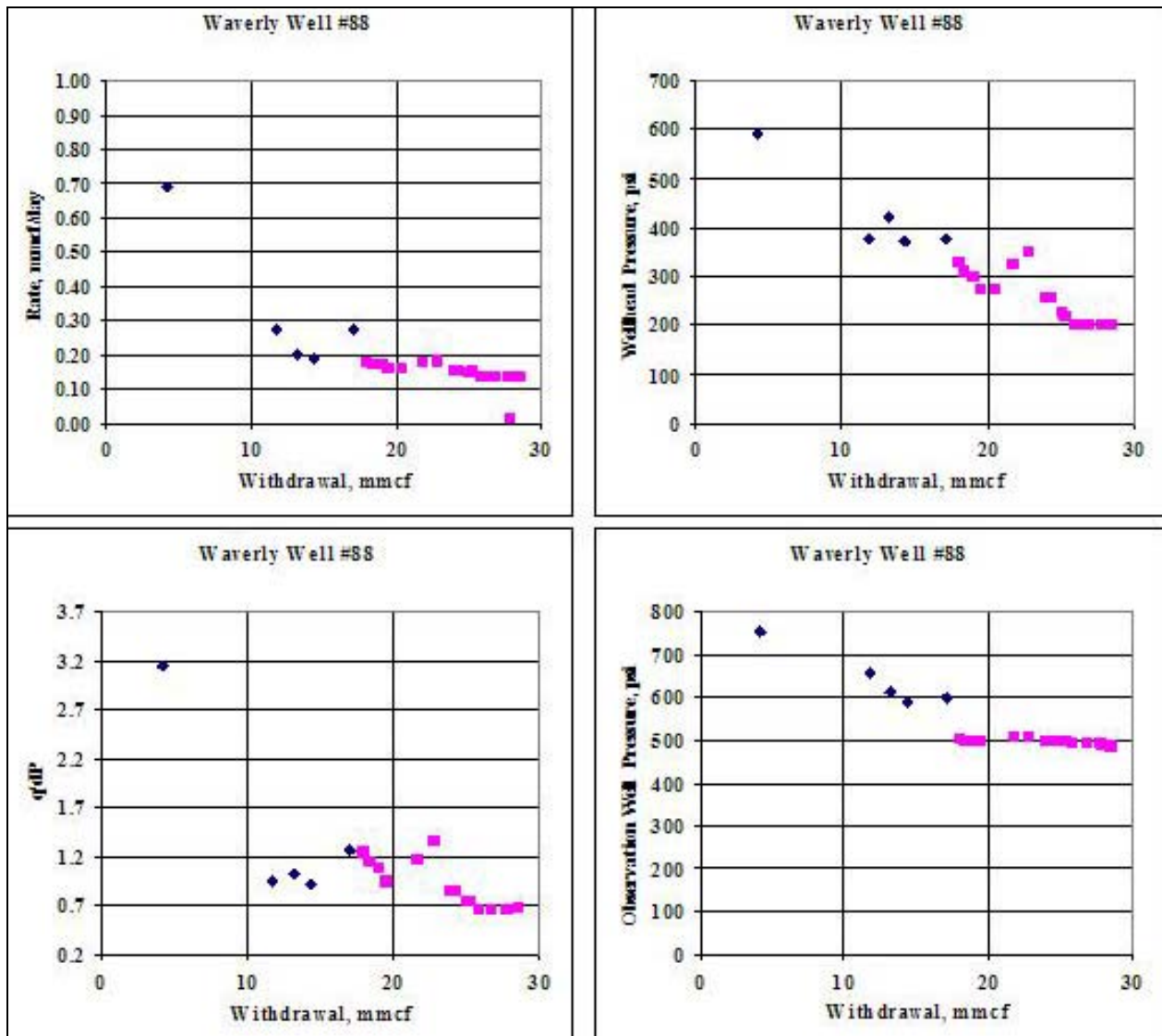
Figure A7. Performance history of Waverly well # 88 during the 2004 season.
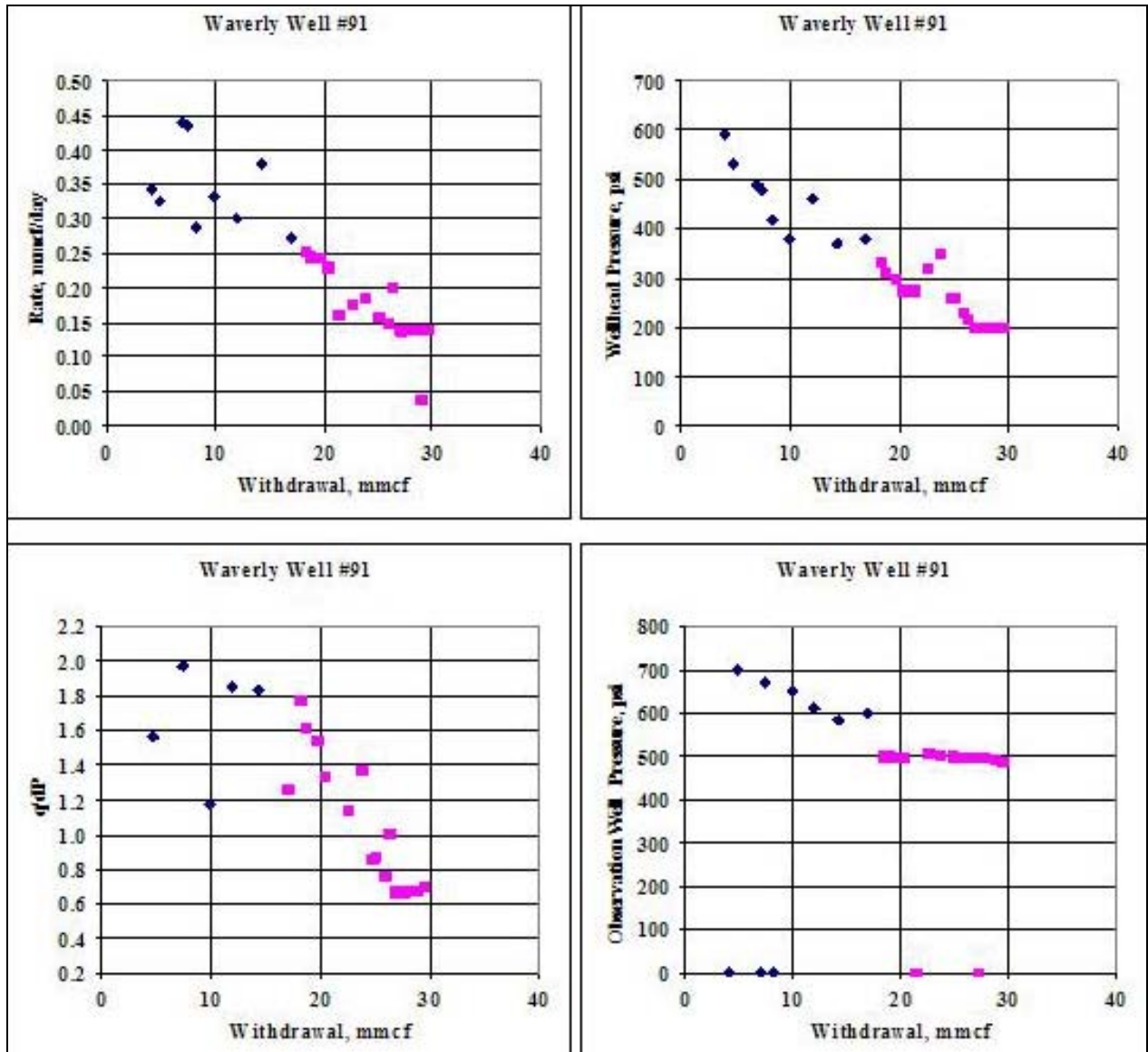
Figure A8. Performance history of Waverly well #99 during the 2004 season.

Young's Equation

Young's equation is $Pc = \dfrac{2\sigma \cos\theta}{r} = \rho g h$, where density, ρ = water density; gravity, $g = 981$ cm/s2; h = capillary rise, cm; r = capillary radius, cm; θ = contact angle, and deg; σ = water surface tension.

The application to the laboratory data results in practically identical contact angles.

TEMPERATURE EFFECTS ON THREADED COUPLINGS IN CAVERNS

DISCLAIMER

This report was prepared as an account of work sponsored by an agency of the United States Government. Neither the United States Government nor any agency thereof, nor any of their employees, makes any warranty, express or implied, or assumes any legal liability or responsibility for the accuracy, completeness, or usefulness of any information, apparatus, product, or process disclosed, or represents that its use would not infringe privately owned rights. Reference herein to any specific commercial product, process, or service by tradename, trademark, manufacturer, or otherwise does not necessarily constitute or imply its endorsement, recommendation, or favoring by the United States Government or any agency thereof. The views and opinions of authors expressed herein do not necessarily state or reflect those of the United States Government or any agency thereof.

ABSTRACT

This report documents research performed to identify if gas injection and withdrawal temperatures of typical natural gas well completions could potentially result in failure of the casing through low-frequency cyclic fatigue. Finite element analyses of two salt cavern wells and one reservoir storage well were used to estimate the state of stress in the casing resulting from: (1) casing weight; (2) product pressures; (3) thermally induced stresses; and (4) external ground pressures, including salt creep. The range of stress and temperature conditions determined during simulations of gas service cycles at the lowest casing joint was used as input to another set of finite element models to predict the casing connection response when subjected to cyclic loads caused by pressure and temperature changes. The stress history at critical points in the connections was then used in cyclic fatigue analyses to determine the expected number of cycles the couplings can withstand before failure.

EXECUTIVE SUMMARY

When natural gas is injected or withdrawn from storage, the temperature of the gas flowing through the production casing is almost never in equilibrium with the casing components or the rock mass. As a result, the production casing expands and contracts in response to the temperature fluctuations associated with cavern operation. Expansion and contraction of the casing induces cyclic loads that could have deleterious effects on the integrity of the threaded casing connections. This report documents an assessment that was performed of natural gas storage wells to determine if thermally induced cyclic loads are likely to lead to failure of the well casing. Solution of the well casing problem requires an appropriate description for the structural behavior, thermodynamics, heat transfer, and fluid flow of the gas, casing components, and geologic formation.

The geological setting, well completion practices, and operational use of natural gas storage wells in the United States provide a vast range of well designs and expected well casing loading conditions. Because it is impractical to assess all of the different well casing designs and the performance of the casings in the different geologic settings, this study was limited to the evaluation of three well casings. Candidate well casings were selected after considering which wells are expected to be subjected to the most severe loading conditions, with special consideration given to the most common casing types currently used for salt cavern and reservoir storage wells. The candidate wells selected for evaluation included two salt cavern storage wells having final cemented depths of 579 and 1,494 meters (1,900 and 4,900 feet) and a gas reservoir well drilled into a sandstone formation at a depth of 1,524 meters (5,000 feet). Both salt cavern wells modeled were completed with 340-millimeter-diameter (13⅜-inch-diameter) K-55 grade casing. The reservoir well used 140-millimeter-diameter (5.5-inch-diameter) J-55 grade production casing.

Two distinct types of finite element models were used: (1) well models that predict the casing loads from ground surface to the casing shoe and (2) connection models that predict the magnitude and location within the connection that is subjected to the most severe cyclic loading. Sources for the loads exerted on the wells modeled in this study include contributions from: (1) casing weight; (2) product pressures; (3) thermal expansion and contraction; and (4) external ground pressures, including salt creep and reservoir compaction. Although not considered by the well models, the effect of casing bending was included in the analyses of the connection models.

Conservative assumptions were made during the well model analyses where possible. These assumptions included modeling the cement as an elastic material that does not fail and using perfectly bonded interfaces between the casing, cement sheath, and adjacent rock formation. Although the axial tensions remained relatively low compared to the strength of the casing during the simulation period of the shallow salt cavern, stresses were predicted to exceed the

tensile strength of the steel casing during the analysis of the deep salt cavern well. Other than the conclusion that creep deformations around the well casing will eventually accumulate to a magnitude that will cause the casing to fail, other possibilities not simulated by the models used in this study include: (1) slip occurs along the steel/cement and/or the cement/salt interface, limiting the axial tensions that can develop in the casing, or (2) failure of the cement occurs, limiting the drag force which is causing the development of tensile stresses in the steel casing. Without physical evidence, it is difficult to identify which possibility is most likely to occur. Regardless, the modeling effort suggests that without slip along the interfaces, failure of the casing, cement, or salt is probable if relatively large vertical creep displacements are present.

For the salt cavern wells, the least-tensile (or most-compressive) vertical stresses are predicted at the beginning of the withdrawal cycle. At this time during the cycle, the temperature of the casing is the warmest and the gas pressure is the greatest. The most-tensile vertical stresses in the salt cavern casing are predicted to occur at the end of withdrawal when the gas temperature is the coolest and the pressure is the lowest. The axial stress at the lowest connection in the shallow salt cavern well was predicted to cycle between 20 and 125 mega-pascals (MPa) tension (2,900 and 18,100 pounds per square inch (psi)). It was assumed that the cement sheath cannot transmit more than 345 MPa (50,000 psi) to the casing based on supplemental analyses performed during this study. Using this limiting value, the axial stress at the lowest connection in the deep salt cavern well was predicted to cycle between 164 and 345 MPa (23,800 and 50,000 psi).

Because of the slow withdrawal rates assumed for the reservoir well, the temperature of the gas does not become significantly cooler than the storage formation temperature during gas withdrawal. As a result, the least-tensile (or most-compressive) vertical stresses are predicted to occur at the end of withdrawal when the pressure is lowest and the gas temperature is warmest. The most-tensile stresses in the reservoir well casing occur at the end of injection when the temperature is the coolest and the gas pressure is the greatest. Excluding reservoir compaction and bending stresses, the axial stress at the location of the lowest connection in the reservoir well ranges from –1 MPa to 36 MPa (–145 to 5,200 psi).

Models of the threaded connections were used to determine the fatigue life corresponding to the range of axial force and pressure cycles estimated from the well casing models. The first step of the connection analysis consisted of determining the stresses that exist in the connection following the connection make-up procedure. Next, the load cycles predicted at the lowest joint by the well models were imposed to determine the stress and strain distribution in the connection. These stress and strain values were then used to estimate the fatigue life of the connection in terms of the number of injection-withdrawal cycles that can be tolerated. The connection modeling results showed that the stress in localized areas of the connection will exceed the elastic limit of the material, resulting in plastic (unrecoverable) strain; therefore, it

was necessary to adopt a strain-based fatigue criterion that considers the magnitude of plastic strain cycles in the connection.

Based on this conservative analysis, the fatigue life for the reservoir well was estimated to be as short as 235 cycles, or 235 years, assuming an annual pressure cycle. The deep salt cavern casing could withstand approximately 3.7×10^6 pressure cycles, but since the pressure is cycled 12 times per year, the well life is estimated to be 310,000 years. Connection fatigue in the shallow salt cavern well does not appear to be a concern, with a predicted fatigue life of over a million years, assuming 12 pressure cycles per year. Two key uncertainties remain in the analyses that may have significant influence on the estimated fatigue life of the connections. The first is the fatigue performance of the casing and connection materials, which was based on analogous materials. The second uncertainty is how much of the formation movements that occur during pressure and temperature cycles are transferred through the well cement to the casing.

Welding the coupling face to the pipe body in these applications does appear to contribute somewhat to the connection strength, but in some cases, may redistribute the stresses in the connection such that failure occurs in approximately the same number of cycles but in a different location compared to connections without welds. The analyses including the weld did not consider the effects welding may have on local stress concentrations or degradation of the casing and coupling material properties in the heat-affected zone adjacent to the weld.

In conclusion, the predicted thermomechanical response of the well casing during gas storage injection and withdrawal cycles shows that the effects of operating pressure and well temperature changes are minor in comparison to the axial strains imposed by formation movements (i.e., compaction in reservoirs and salt creep in caverns). If the casing loads associated with salt creep and reservoir compaction are not considered, the conservative analyses performed in this study indicate that the minimum number of cycles necessary to cause cyclic fatigue range from about eight hundred to several hundred thousand. This study did not consider the effects of cyclic loading on the integrity of the cement sheath. Fracturing, debonding, and degradation of the cement sheath is a topic for future research.

TABLE OF CONTENTS

TABLE OF CONTENTS
(Continued)

LIST OF TABLES

LIST OF FIGURES

LIST OF FIGURES
(Continued)

LIST OF FIGURES
(Continued)

1.0 INTRODUCTION

1.1 BACKGROUND

When natural gas is injected or withdrawn from subsurface storage facilities, the temperature of the gas flowing through the production casing is almost never in equilibrium with the casing or surrounding rock mass. As a result, the production casing expands and contracts in response to the temperature fluctuations associated with operation. The weakest link for axial tensile loading of a casing string is generally the threaded connection [American Petroleum Institute, 1974]. Expansion and contraction of the casing induce cyclic loads in the connection that could have deleterious effects on the integrity of the connection. This report documents the study performed to determine if thermally induced cyclic loads could lead to failure of well casing connections used for the storage of natural gas in sandstone reservoirs and salt caverns. The report also provides insight into the expected casing loads caused by salt creep and reservoir compaction, assuming the steel casing, cement sheath, and rock mass remain perfectly bonded throughout gas storage operations.

1.2 OBJECTIVE AND SCOPE

The objective of this study is to identify if gas injection and withdrawal temperatures will result in failure through low-frequency cyclic fatigue of typical well completions. To accomplish the objective, finite element analyses were performed of three "typical" well configurations to determine the state of stress in the casing during gas storage operation. The candidate wells included two salt cavern storage wells having final cemented depths of 579 and 1,494 meters (1,900 and 4,900 feet) and a gas reservoir well drilled into a sandstone formation at a depth of 1,524 meters (5,000 feet). Two distinct types of finite element models were used: (1) well models that predict the casing loads from ground surface to the casing shoe and (2) connection models that predict the magnitude and location within the connection that is subjected to the most severe cyclic loading. The approximate number of gas injection and withdrawal cycles permissible before the connections fail is estimated based on the results of the numerical models and fatigue analysis techniques.

1.3 REPORT ORGANIZATION

An overview of the project is given in Chapter 2.0, and descriptions of the three well casing configurations evaluated are provided in Chapter 3.0. The technical approach to the numerical modeling is described in Chapter 4.0. The predicted results of the well models and connection models are provided in Chapters 5.0 and 6.0, respectively. Chapter 7.0 gives a summary of the modeling results and the study conclusions. Cited references are provided in Chapter 8.0. An appendix containing supporting information concludes this report.

2.0 PROJECT OVERVIEW

2.1 PROJECT DESCRIPTION

Under quiescent conditions, casing temperature would not deviate significantly from the in situ temperature of the rock encasing the well. However, gas is often heated above the in situ temperature of the host rock formation during injection by compression. Also, because the gas is almost always stored in a formation warmer than that penetrated by the casing, the gas being withdrawn can exceed the in situ temperature over the length of the casing. The warmer temperature of the gas relative to the casing temperature results in transfer of heat by convection and conduction between the gas and the steel casing. Conduction between the steel casing, cement, and rock formation further alters the temperature field of the casing and surrounding rock formation. During withdrawal to low pressures, the opposite response occurs, as expansion of the gas results in temperatures cooler than the in situ temperature.

Each temperature swing generated by injection and withdrawal of gas causes thermal strain in the casing. Thermal strain (ε) is usually assumed to be linearly related to the temperature change (ΔT) and the coefficient of thermal expansion (α) by the familiar one-dimensional expression:

$$\varepsilon = \alpha \Delta T \qquad (2\text{-}1)$$

In multidimensional, statically indeterminate situations, Young's modulus and Poisson's ratio become important parameters in determining the magnitude of the thermally induced stresses. The strain caused by thermal expansion or contraction can be significant. For a 610-meter- (2,000-foot-) long steel casing, a 26.67° Celsius (C) (80° Fahrenheit (F)) change in temperature would result in the casing lengthening by about 0.3 meter (1 foot) if the casing were unrestrained. However, bonding between the steel pipe, cement, and rock formation restrains the movement. This restraint produces thermally induced axial loads in the casing. Axial loads are transmitted through the connections and could potentially result in large stresses in the connection because of stress and strain localization effects associated with the complex geometry of the connection.

Under axial loads, the API STC (American Petroleum Institute–Short Threaded and Coupled) casing connections commonly used in gas storage wells will typically fail by either parting caused by tensile rupture at the smallest cross section of the pin (tension) or by a process referred to as "thread jumpout" (tension or compression). The tensile load limit of many API STC connections are approximately 80 percent of the pipe body capacity at yield.

Connection failure may also occur because of fatigue. Cyclic loading associated with the injection and withdrawal cycles in a gas storage facility can impart incremental damage to the connection even at loads well below the yield strength of the pipe body. This accumulated

damage can result in the initiation of cracks in locations where stresses are concentrated because of the loading mechanism or geometry of the connection. One of the key mechanisms that causes cyclic loading in the well casing is the change in wellbore temperature that occurs during the injection-withdrawal cycle. The primary focus of this study is to consider the possibility that these thermally induced cyclic stresses could cause failure of the well casing connections.

2.2 CASING LOADS

In addition to thermally induced loads, the well casing is subjected to other sources of loading that contribute to the total casing load. In most cases, a combination of the various loading mechanisms is most critical to casing and connection performance. The stress analyses performed in this study considered the contributions from (1) casing weight, (2) product pressures, (3) thermal expansion and contraction, (4) external ground (or fluid) pressures, and (5) casing bending. A conservative technical approach was used where possible in calculating the casing stresses. Some of the elements of the conservative analyses are discussed below.

2.2.1 Stresses From Casing Weight

During installation, the final cemented casings in the storage wells hang from the wellhead. Therefore, the lowest portion of the casing is subjected to no stress from the weight of the casing, and the shallowest portion of the casing is subjected to a stress equivalent to the entire weight of the casing. Generally, casing is installed with drilling fluids in the wellbore. Drilling fluids' buoyancy forces support some of the casing weight. For design purposes, it is commonly assumed that the loads in the casing after the cement hardens are identical to the buoyant weight in the cement. For this study, the loads in the casing following cementing were assumed to be equal to the buoyant weight of the steel casing in cement, having approximately the same density as that of drilling mud. Additionally, it was assumed that chemical reactions (i.e., heat of hydration) that occur while the cement hardens do not alter the state of stress in either the casing or cement sheath. In reality, expansion and/or contraction of the cement during curing could alter the stresses in the casing.

2.2.2 Stresses From Product Pressure

The internal pressure in a natural gas storage well varies with depth and is equal to the sum of: (1) the wellhead pressure, (2) the pressure due to the weight of the gas column above the depth of interest in the final cemented casing, and (3) frictional losses. The pressure exerted by the gas on the internal diameter of the casing will increase when compressed gas is injected into the well, raising the pressure in the formation or cavern. Similarly, expansion of the gas during withdrawal will result in a reduction in gas pressure. The gas pressure on the internal diameter of the final cemented casing produces tensile (or less compressive) tangential (hoop) stresses and compressive radial stresses in the casing. If the casing were free to expand,

an increase in the internal pressure would result in outward movement and axial shortening of the casing because of Poisson's effect. Both the outward radial movement and axial shortening are resisted by the bond between the casing and the cement. The stresses generated by a change in product pressure are a function of the material properties of the casing, cement sheath, and the rock formation.

2.2.3 Stresses From Thermal Expansion and Contraction

Rapid gas withdrawal followed by injection of gas heated through compression results in thermal cycling of the cemented casing and surrounding rock formations. The bond with the well cement restricts the casing from elongating as it is heated and from shortening as it is cooled. This constraint leads to axial loads developing within the casing body and connections. The axial load caused by a change in temperature is tensile (or less compressive) if the temperature change results in contraction of the casing. Likewise, the casing becomes more compressive (or less tensile) under conditions that result in thermal expansion of the casing. For this study, it is assumed that the casing, cement sheath, and rock formation are in equilibrium following well completion. Thus thermally induced stresses and strains occur whenever the casing temperature is different than that produced by the geothermal gradient at the depth of interest.

2.2.4 Stresses From External Ground Pressure

External pressures generally act on the final cemented casing and these external pressures produce compressive hoop stresses in the casing. The magnitude of the external pressure cannot be as accurately defined as the internal pressure and, in fact, depends very strongly on the specific geologic conditions adjacent to the casing at the depth of interest. In a salt section, it is generally accepted that the salt formation will develop a relatively uniform loading on the casing equal to the predrilling stress within the salt if no excavations exist near the casing. However, excavations in salt can alter the state of stress at distances exceeding several cavern diameters.

The external loading on the casing in natural gas reservoirs can also be complex. For example, poorly cemented intervals may exist along the casing string; in which case, the in situ fluid (e.g., product or water) will transmit an external pressure directly to the pipe body. In other cases where formation movements (e.g., subsidence) may occur, the external pressure can exceed the weight of the overburden. In any case, the external pressure results in compressive radial and hoop stresses in the casing. The compressive hoop stresses caused by external ground pressure reduce the tensile hoop stresses produced by the internal pressure on the casing. The axial stresses produced by external ground pressure can be tensile or compressive, depending on the specific geologic condition and the interval in the geological column.

In this study, two sources of external ground pressure (loading) were considered: (1) salt creep in the two salt cavern wells and (2) reservoir compaction in the reservoir storage well. As the salt creeps and flows into the cavern, it can drag the casing downward toward the cavern. This stretching of the casing will result in axial tensions. Salt creep also imparts a compressive radial pressure on the outer surface of the casing, further altering the state of stress in the casing. In addition to salt creep, the salt formation responds elastically to changes in cavern pressure. Because salt caverns can be more than 100 meters in diameter and a few hundred meters in height, the elastic response of the rock formation to gas pressure changes can be realized at great distances from the cavern. Thus the external pressures considered in this study for the salt cavern wells include those associated with the elastic and inelastic (creep) behavior of the host salt formation.

For reservoir storage wells, the gas pressure in the storage formation supports some of the overburden weight. When the reservoir pressure is lowered through withdrawal of gas, the overburden support provided by the gas is partially removed. The weight of the overburden rock that was supported by the gas must be supported by the rock within the reservoir. The additional load on the rock results in elastic compaction (shortening) of the formation. The deformations associated with this elastic process are transferred to the steel casing through the cement-rock and cement-steel bonds.

2.2.5 <u>Stresses From Casing Bending</u>

If the final cemented casing hangs perfectly vertical in the wellbore, no bending stresses exist in the casing. However, if the casing is installed in a borehole that deviates from vertical or if the casing deforms laterally by buckling or shearing over time because of formation movements, bending stresses will develop in the casing. Bending stresses cause non-axisymmetric loading of the casing where the total stress may be higher on one side of the connection than on the other. For this study, casing string bending was considered in the reservoir well by assuming it was a directional well with a 9-degree radius of curvature in the build section. However, the salt cavern wells were assumed to be vertical, so bending stresses were not considered in these wells. In addition, buckling and shear-related bending stresses caused by formation movements were not considered in this study.

2.3 OVERVIEW OF APPROACH

Solution to the well casing problems outlined above requires an appropriate description for the thermodynamics, heat transfer, fluid flow behavior of the gas, and the structural behavior of the casing components and geologic formations. Because the geometry and loading of a cemented well are too complex, closed-formed mathematical solutions do not exist that yield answers for the thermomechanical response of the casing. Therefore, numerical modeling was used to predict the well casing responses to the applied loading. Experience, good engineering judgment, and reliable programs are essential for solving the well and connection problems.

A single software program is not available to model all of the processes that contribute to the loadings on the casing and connections. However, the thermal response is usually considered independent of the structural response of the casing and rock formation. Therefore, one-way coupling can be assumed, allowing the temperature fields to be determined by an appropriate heat transfer analysis program and model, which is independent of the structural response. The computed temperature fields can then be used as input for a structural finite element program to compute the thermomechanical response of the casing and surrounding formations.

One approach for evaluating the temperature history of a natural gas storage well is to employ computational fluid dynamics (CFD). The Solution Mining Research Institute recently reviewed the use of CFD to predict the temperature distribution of gas in a salt cavern during injection and withdrawal [Nelson and Van Sambeek, 2003]. However, solution of the problem is much more complex than simply analyzing the flow of gas through the wellbore. The CFD solution requires the modeling of convection cells in the cavern and the boundary layer near the surface of the cavern. The CFD solution is sensitive to the cavern shape and properties of the boundary layer. As a result, CFD have not been routinely used to determine the temperature and pressure of gas in storage and is still being researched. Alternatively, the temperature of the gas in the well and cavern can be predicted by the software program Salt Cavern Thermal Simulator (SCTS) [Nieland, 2004].

The Gas Research Institute funded development of SCTS to provide a means to accurately determine the inventory and temperature of gas storage in salt caverns. SCTS was used in this study to predict the gas temperatures along the length of the salt cavern well casings from the wellhead to the casing shoe. SCTS was also used to compute the average temperature of the gas in the salt caverns. SCTS is limited in that it only assumes radial heat transfer. Further, SCTS does not provide output of the temperature field in the rock formation adjacent to the well or in the salt surrounding the cavern. Therefore, a heat transfer program must be used in conjunction with SCTS to determine the temperature history of the well casing system and host rock formation. For this study, the gas temperatures predicted during injection and withdrawal by SCTS were used as boundary conditions during subsequent heat transfer analyses using the finite element method. For the finite element heat transfer analyses, the temperatures specified along the inner surface of the casing and along the perimeter of the cavern were set to those determined by SCTS for a hypothetical gas storage service cycle. The time-dependent temperature boundary conditions reflect the changing gas temperatures during operation.

Given the temperature field history of the well casing system to be modeled, thermo-mechanical finite element software can be used to predict the stresses and displacements along the entire length of the well casing. The accuracy of the predicted results will depend on the application of appropriate kinematic and pressure/force boundary conditions used to represent the sources of the applied loads. Although the stresses and displacements can be determined at

discrete points by models that represent the well casing from surface to the casing shoe, they do not provide information about the contact force on individual connection threads or the stress distribution within the connection. In this study, three-dimensional finite element models of a threaded connection and short sections of pipe were used to assess the state of stress within the connections. The conditions applied to the connection models were consistent with those determined at the lowest joint location of the two salt cavern wells and one reservoir well evaluated in this study.

The geologic setting, well completion practices, and operational practices of natural gas storage wells in the United States provide a vast range of well designs and expected well casing loading conditions. Because it is impractical to evaluate all of the different well casing designs and the performance of the casings in the different geologic settings, this study was limited to evaluating three well casing configurations. Selection of the three candidate well casings proceeded by compiling well casing records that have been reported in industry surveys, technical publications, and permit applications. Additionally, service contractors and natural gas storage operators were queried to provide additional details regarding the well completion process and storage operating conditions. Candidate well casings were then selected after considering which wells are expected to be subjected to the most severe loading conditions, with special consideration given to the most common casing types currently used for salt cavern and reservoir storage wells. Candidate well descriptions used in this study are described in detail in the next chapter of this report.

3.0 CANDIDATE WELL CASING DESCRIPTION

Two salt cavern wells and one reservoir well are used in this study to assess the impact of thermal cycling on the integrity of the casing and threaded connections. Thermally induced stresses and strains produced in the casing are governed by the temperature of the gas being injected and withdrawn and the in situ temperature of the host formation. An advantage of storing gas in salt caverns is high deliverability. The higher delivery rate of salt caverns is usually accompanied by larger temperature swings of the gas entering and exiting the well compared with reservoir wells. Many salt caverns are designed to allow the cavern to be filled within 20 days and withdrawn in 10 days, with deliverability exceeding 2.01×10^7 normal cubic meters per day (Nm^3/day) (750 million cubic feet per day (MMcfd[1])). Rapid delivery of gas from the salt caverns requires the use of relatively large well casings compared with reservoir wells, which typically have lower deliverability.

Well casing information for salt caverns in the United States was compiled from state regulatory databases and from papers or reports published at technical conferences and symposia. Information regarding 36 caverns was collected, which represent more than half of the natural gas storage caverns currently operated in the United States. The caverns for which data were obtained represent approximately 70 percent of the total salt cavern storage working gas capacity currently developed in the United States. Histograms of the final cemented casing size and depth of the salt caverns are provided in Figures 3-1 and 3-2, respectively. The reported casing depths obtained ranged between 457 and 1,676 meters (1,500 and 5,500 feet). Because only two cavern wells in a salt dome are evaluated in this study, casing depths near the two extremes were chosen. Final cemented casing depths for the shallow and deep salt caverns wells used for this study are 579 and 1,494 meters (1,900 and 4,900 feet), respectively.

Casing sizes for the salt cavern wells vary from 0.1016 to 0.508 meter (4 to 20 inches) in diameter. The most common production casing size used for the salt cavern storage wells is 340 millimeters (13⅜ inches), although a significant number of caverns have casings greater than 356 millimeters (14 inches). For the salt cavern wells, 340-millimeter (13⅜-inch) production casings to depths of 579 and 1,493 meters (1,900 and 4,900 feet) were selected for further evaluation in this study. Although the casing grade was not obtained for all of the wells identified, many of wells completed with 340-millimeter- (13⅜-inch-) diameter casing used K-55 grade casing. Therefore, K-55 grade casing was assumed for the salt cavern casings modeled.

Illson and D'Arcy [2004] provide information about casing size and connection types used at 67 depleted reservoir natural gas storage facilities, representing 16 percent of those within the

---

[1] Natural gas quantities are expressed in terms of normal cubic meters (Nm^3) with reference conditions of 0°C and 0.101325 megapascals (MPa) and in terms of standard cubic feet (scf) with reference conditions of 60°F and 14.73 pounds per square inch (psi). Gas-related computations were made assuming a gas composition of 100 percent methane.
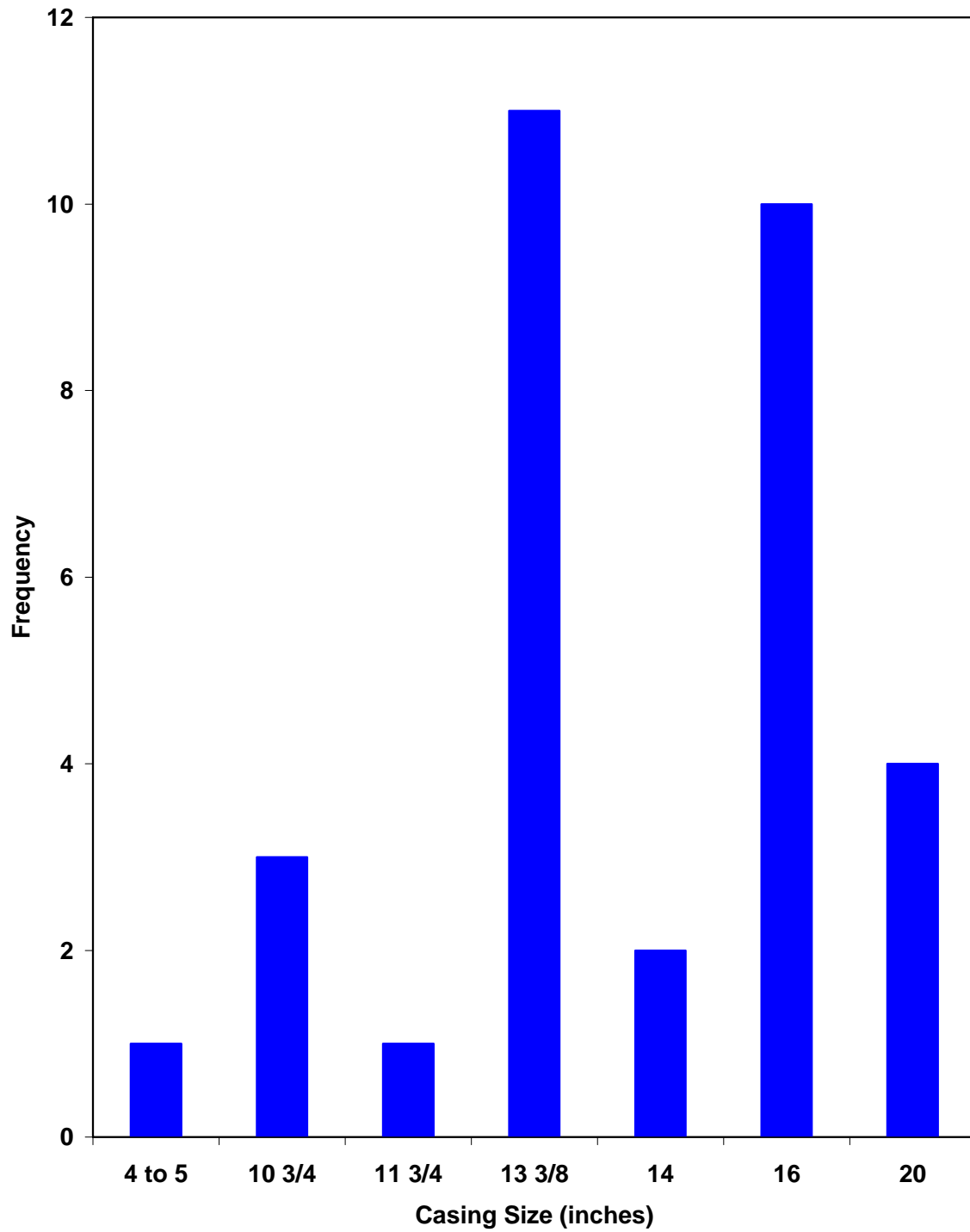
Figure 3-1. Salt Cavern Casing Size Histogram.

9
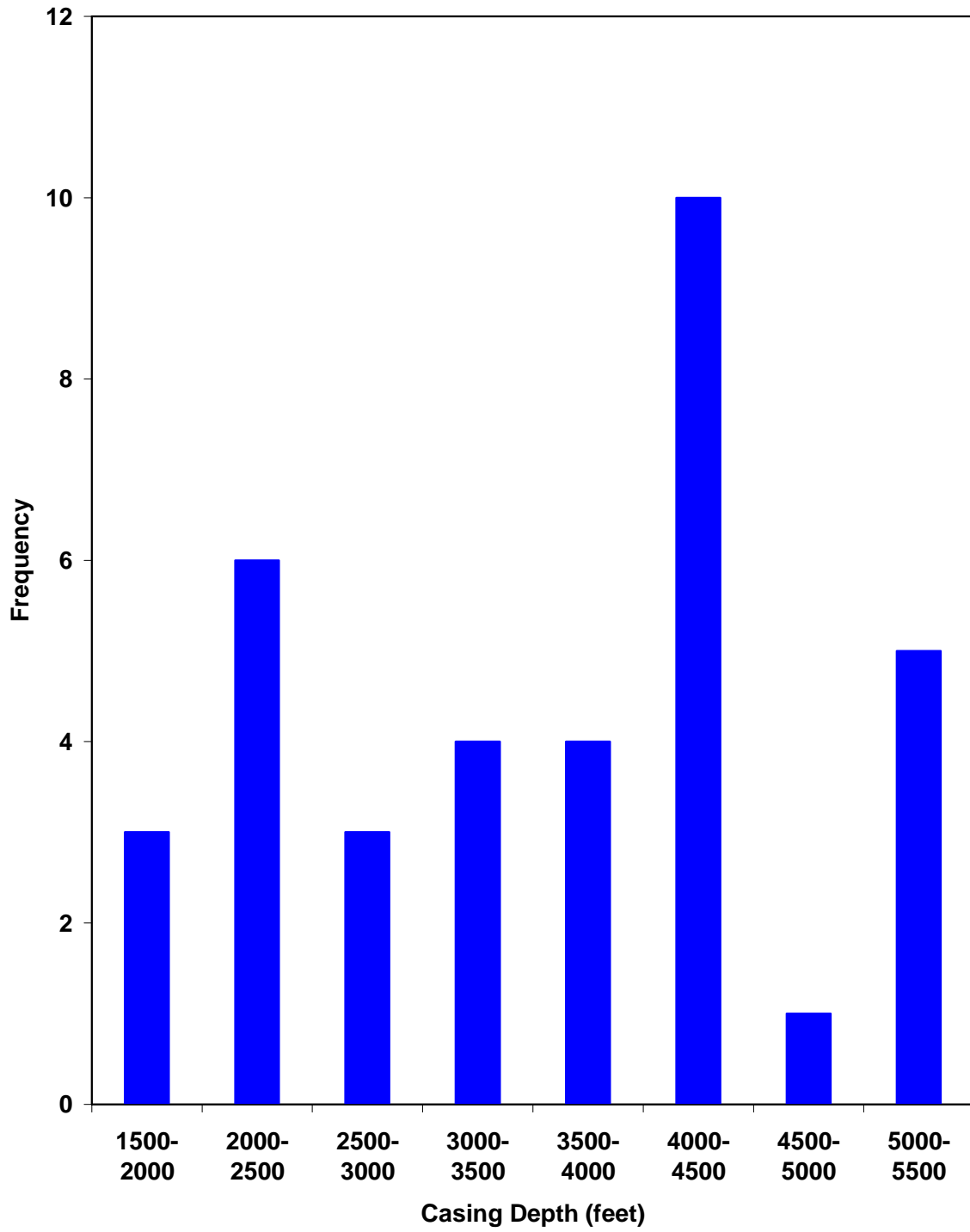
Figure 3-2. Salt Cavern Final Cemented Casing Depth Histogram.

10

United States. Casing sizes reported ranged between 0.0889 to 0.2731 meter (3.5 to 10.75 inches) in diameter. Based on the results of the survey reported by Illson and D'Arcy [2004], the most common casing size is 140 millimeters (5.5 inches) and the most common grade is J-55. Over 40 percent of the wells in the survey used 140-millimeter (5.5-inch) casing and about 60 percent of the wells used J-55 grade casing. Nearly 95 percent of the connections reported in the survey were API standard 8-R ST&C (8 round, short threaded, and coupled). The most common casing size, grade, and coupling type identified above were used in the thermomechanical evaluations of the reservoir well performed for this study.

Schematics of the three casing configurations evaluated in this study are provided in Figures 3-3 through 3-5. Additional well completion details and operating parameters are provided in Table 3-1. The salt caverns and casings sizes are sufficient to allow complete injection of gas from minimum pressure to maximum pressure in 20 days. Further, the gas can be withdrawn in 10 days without forming hydrates or exceeding a velocity of 30.48 meters (100 feet) per second. As shown in Figure 3-5, the reservoir well includes a 90-degree build section (bend) between 1,219.2 and 1,524.0 meters (4,000 and 5,000 feet) below surface. The 90-degree bend was modeled in this study to provide an additional source of loading that is created in the casing by well deviations. The effects of the cement sheath thickness were not investigated in this study. It was assumed that the cement thickness will have little impact on the results. This assumption was made on the premise that the physical properties of the cement are not significantly different than that of the host rock formation; however, additional analyses would have to be done to confirm this assumption.

As shown in Figures 3-3 through 3-5, the candidate wells are cemented along their entire length. This configuration was chosen because the fully restrained (cemented) case will result in the prediction of the maximum possible axial stress caused by thermal contraction and expansion of the casing. If the casing is only partially cemented, thermally induced stresses and strains will be uniformly distributed over the length of the section that is not cemented and equal to the average stress predicted for the fully restrained case over the same length. However, the cement sheath also limits horizontal deflection and the potential for buckling of the casing. The issue of buckling is believed to be separate from that of thermally induced cyclic fatigue and is not addressed in this study.

The remainder of this report addresses modeling details and results of the modeling effort used to assess the significance of thermal cycling in the gas storage wells. Analysis results include those determined from well models of the casing from the surface to the casing shoe and those results determined from connection models of threaded connections and short sections of pipe.

0.6604 m @ -30.48 m
(26" @ - 100 ft.)
CONDUCTOR

0.5080 m @ -60.96 m CASING
(20" @ - 200 ft.)

0.4064 m @ -152.4 m CASING
(16" @ - 500 ft.)

0.3400 m @ -579.1 m CASING
(13 3/8" @ - 1900 ft.)

WELLBORE SCHEMATIC	GSTC EXAMPLE WELL COMPLETION
SALT CAVERN STORAGE WELL No. 1	RSI-1546-05-007
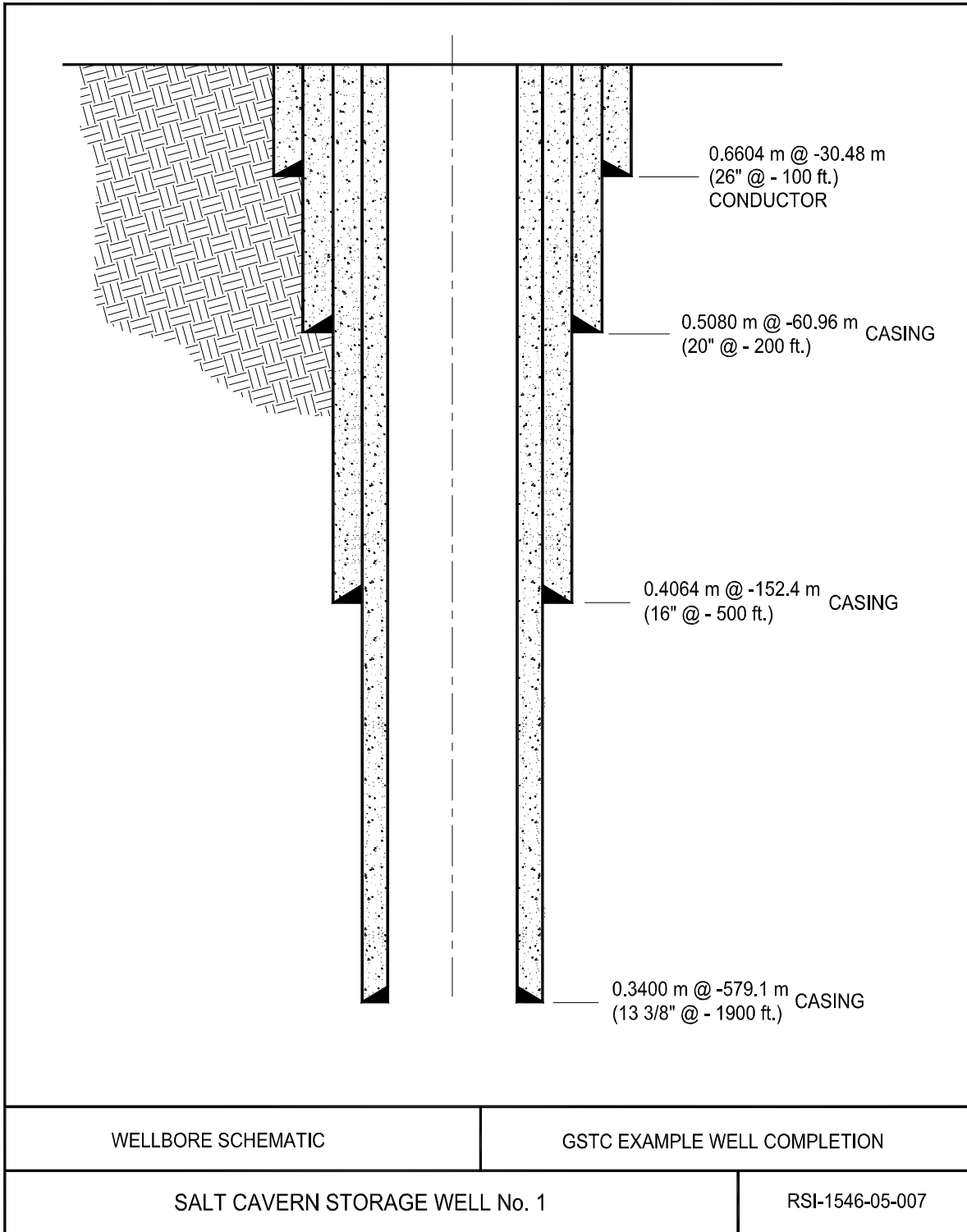
Figure 3-3. Casing Schematic of Salt Cavern Well No. 1.

0.8636 m @ -30.48 m
(34" @ - 100 ft.)
CONDUCTOR

0.6096 m @ -152.4 m CASING
(24" @ - 500 ft.)

0.4572 m @ -457.2 m CASING
(18" @ - 1500 ft.)

0.3400 m @ -1493.5 m CASING
(13 3/8" @ - 4900 ft.)

WELLBORE SCHEMATIC	GSTC EXAMPLE WELL COMPLETION
SALT CAVERN STORAGE WELL No. 2	RSI-1546-05-006
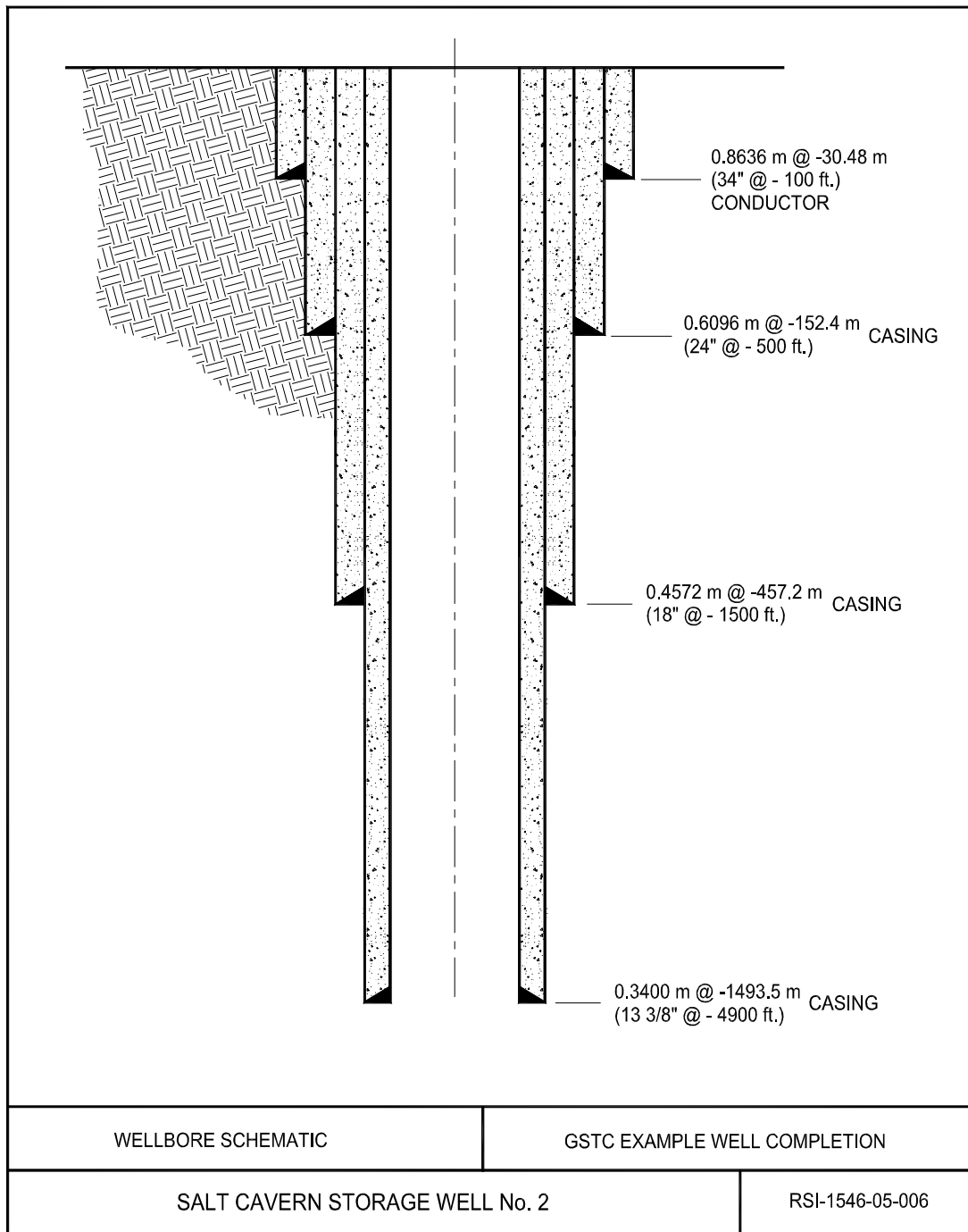
Figure 3-4. Casing Schematic of Salt Cavern Well No. 2.

0.6096 m @ -12.2 m
(24" @ -40 ft.)
CONDUCTOR

152.4 m (- 500 ft.)

0.2447 m @ -213.4 m CASING
(9 5/8" @ - 700 ft.)

0.0730 m (2.875")
PRODUCTION TUBING

-1127.8 m (- 3700 ft.)

0.1778 m @ -1219.2 m CASING
(7" @ - 4000 ft.)

0.1397 m @ -1524.0 m CASING
(5 1/2" @ - 5000 ft.)

WELLBORE SCHEMATIC	GSTC EXAMPLE WELL COMPLETION
RESERVOIR STORAGE WELL No. 3	RSI-1546-06-002
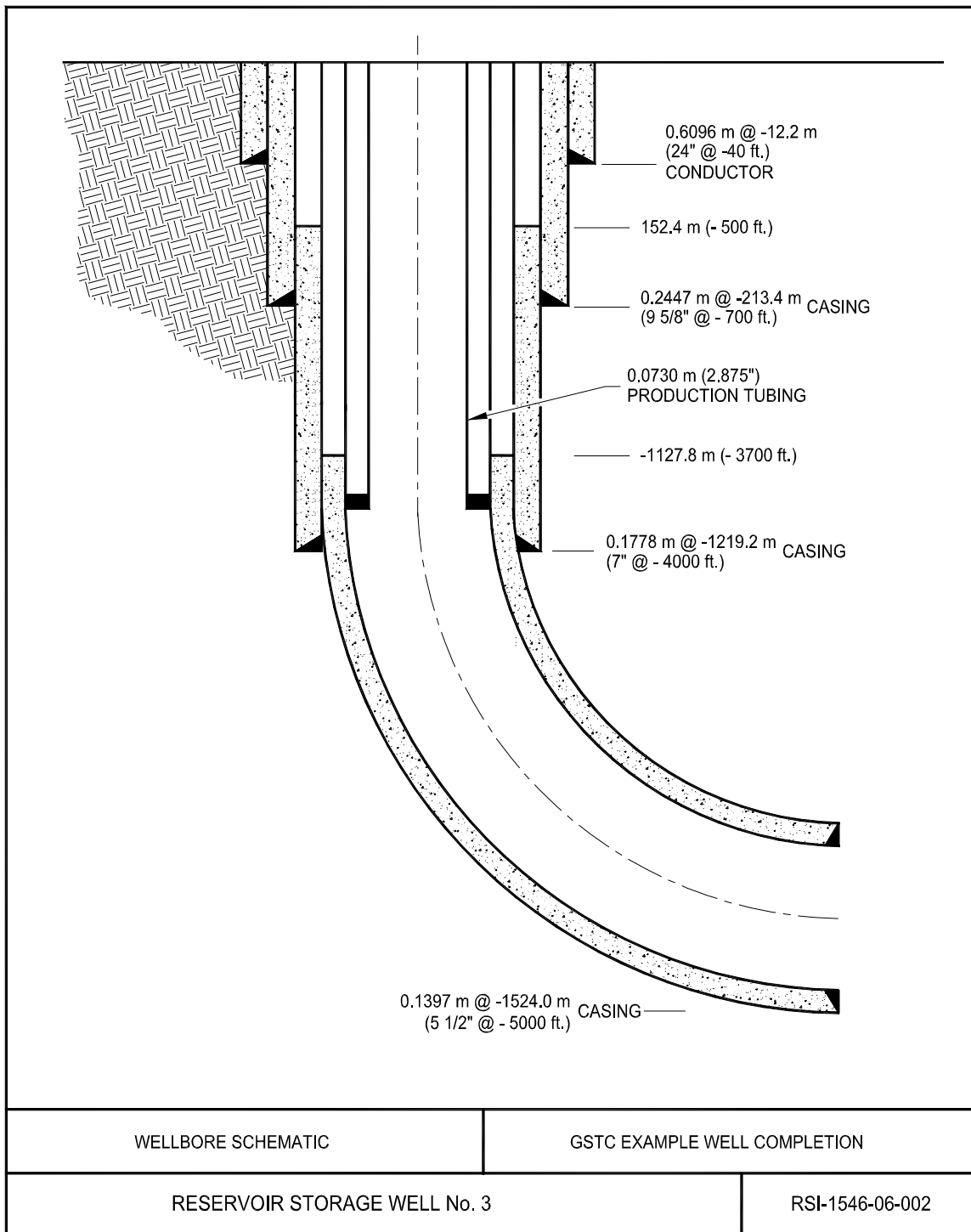
Figure 3-5. Casing Schematic of Reservoir Storage Well No. 3.

Table 3-1. Well Descriptions and Operating Conditions

	Salt Cavern Storage Well No. 1		Salt Cavern Storage Well No. 2		Reservoir Storage Well No. 3	
Final Cemented Casing Depth	579 m	1,900 ft	1,494 m	4,900 ft	1,524 m	5,000 ft
Casing Outer Diameter	0.34 m	13⅜ in	0.34 m	13⅜ in	0.1397 m	5.5 in
Casing Wall Thickness	0.0130 m	0.513 in	0.0130 m	0.513 in	0.0140 m	0.550 in
Casing Weight	107 kg/m	72 lb/ft	107 kg/m	72 lb/ft	23 kg/m	15.5 lb/ft
Casing Yield Strength	379 MPa	55,000 psi	379 MPa	55,000 psi	379 MPa	55,000 psi
Casing Ultimate Strength	655 MPa	95,000 psi	655 MPa	95,000 psi	517 MPa	75,000 psi
Cement Thickness	0.0475 m	1.87 in	0.0475 m	1.87 in	0.0508 m	1.00 in
Injection Temperature	48.89°C	120°F	48.89°C	120°F	21.11°C	70°F
Storage Formation Temperature[a]	49.17°C	120.5°F	74.17°C	165.5°F	46.11°C	115°F
Injection Rate	2.84×10^6 Nm^3	106 MMcfd	5.52×10^6 Nm^3	206 MMcfd	1.07×10^6 Nm^3	40 MMcfd
Withdrawal Rate	5.67×10^6 Nm^3	212 MMcfd	1.10×10^7 Nm^3	412 MMcfd	1.07×10^6 Nm^3	40 MMcfd
Minimum Casing Shoe Pressure	3.28 MPa	475 psi	8.45 MPa	1,225 psi	4.14 MPa	600 psi
Maximum Casing Shoe Pressure	11.13 MPa	1,615 psi	28.72 MPa	4,165 psi	22.06 MPa	3,200 psi
Gas Capacity	8.87×10^7 Nm^3	3.2 Bcf	1.90×10^8 Nm^3	7.1 Bcf	2.89×10^8 Nm^3	10.8 Bcf

(a) Storage formation temperatures for salt caverns are given at the cavern midheight.

4.0 EXPERIMENTAL

Numerical methods were used to predict the thermomechanical response of the three candidate wells within the host rock formation. The results of interest are the locations and corresponding times when the maximum and minimum stresses and strains are reached in the casing during the gas service cycle. Based on these extreme conditions, cyclic fatigue analyses were used to determine the expected number of cycles the connections can withstand before failure.

Solution to the problem requires the appropriate software programs and complete definition of the numerical models. Those inputs necessary to completely define the problem are described in this chapter. The steps followed during the assessment include:

1. Compute the temperature of the gas in the casing during natural gas storage operations.

2. Predict the temperature history of the rock formation surrounding the well using a finite element heat transfer program based on the gas temperatures along the length of the casing as boundary conditions.

3. Compute the stresses and strains in the casing during natural gas storage operation using a thermomechanical finite element program.

4. Compute the contact forces and state of stress within the connections using the extreme conditions determined by the thermomechanical analyses of the well models as boundary conditions.

5. Determine the expected number of cycles the connection can withstand before failure is expected using cyclic fatigue analysis.

The computer programs, stratigraphy, constitutive models, material properties, in situ conditions, gas service cycles, and the finite element models used to evaluate the well casings and connections are described below.

4.1 SOFTWARE PROGRAMS

Numerical modeling software was used to model the thermodynamics, heat transfer, structural behavior of the host rock formation, and mechanical behavior of the well casing components. These specialized computer programs are described in the following subsections.

4.1.1 <u>Cavern Thermodynamics Program SCTS</u>

SCTS [Nieland, 2004] is a program developed by PB Energy Storage Services, Inc. (PB ESS) and RESPEC for simulating the thermodynamics and heat transfer related to the storage of

natural gas in underground salt caverns. It accounts for the thermal effects associated with gas compression and expansion; the mass transfer during injection and withdrawal; and the heat transfer between the gas and its surroundings, both in the well and in the cavern.

SCTS was used to determine well casing and cavern temperatures throughout the simulated gas storage operations. SCTS calculates the temperature of the gas at discrete points in the well; however, the program only calculates a single bulk temperature for the gas in the cavern. The well and cavern temperatures as a function of time, determined from SCTS, were applied as boundary conditions to the thermal finite element models to estimate the temperature of the salt surrounding the caverns and/or wells as a function of time.

4.1.2 Heat Transfer Finite Element Program SPECTROM-41

SPECTROM-41 [Svalstad, 1989] is a finite element heat transfer analysis program that was developed by RESPEC to analyze thermal problems in geologic formations. The primary transport process modeled by SPECTROM-41 is conductive heat transfer with fixed, adiabatic, periodic, and convective boundary conditions. SPECTROM-41 has the capability to model complex material properties (including temperature-dependent thermal conductivity) and boundary conditions. SPECTROM-41 was used in this study to simulate the heat transfer between the wells and surrounding rock formation. The results of these calculations were then integrated into the thermomechanical analyses to account for the thermal stresses and strains that are generated by temperature changes in the rock formations and well casings.

4.1.3 Thermomechanical Finite Element Program SPECTROM-32

The finite element program SPECTROM-32 [Callahan et al., 1989] was used to perform the thermomechanical analyses of the well models. SPECTROM-32 is a finite element program developed by RESPEC for the solution of rock mechanics problems. It was designed specifically for the simulation of underground openings and structures. SPECTROM-32 not only has the capability to model the elastic-plastic response that is commonly associated with brittle rock types, but it also has the capability to simulate the viscoplastic behavior that is observed in rock salt. The features and capabilities of SPECTROM-32 required specifically for this analysis include:

- Option for modeling axisymmetric geometries.
- Kinematic and traction boundary conditions.
- Constitutive model for viscoplastic behavior of salt.
- Mohr-Coulomb plasticity constitutive model.
- Peak/residual tension constitutive model.
- Capability to represent arbitrary in situ stress and temperature fields.

4.1.4 Thermomechanical Finite Element Program ABAQUS

The threaded connection analyses were performed using the commercial finite element program ABAQUS, Version 6.5.1 [ABAQUS, Inc., 2005]. Three-dimensional models of complex, multicomponent assemblies can be built in ABAQUS using a variety of modeling elements. Complex operating scenarios can be imposed on the models simulating pressure, load, temperature, displacement, and deformation. Various temperature-, pressure-, and time-dependent behaviors can be used to describe nonlinear material properties under these complex operating scenarios.

4.2 STRATIGRAPHY

Two vastly different host rock formations were considered in the evaluation of the candidate well casing loads. The two salt cavern wells were assumed to be sited in a salt dome rather than a bedded salt formation to maximize the exposure of the casing to salt deformation. The reservoir well was assumed to be sited in a bedded formation and cemented to approximately the same depth as the deeper salt cavern well for comparative purposes. The stratigraphy used for the numerical simulations is described in the following subsections.

4.2.1 Salt Dome Cavern Storage

The two salt cavern wells selected for evaluation were assumed to be located in massive salt domes. Therefore, a simplified all-salt stratigraphy was used for the evaluation of the two salt cavern well casings. Salt domes can be found in Alabama, Louisiana, Mississippi, and Texas, as well as offshore in the Gulf of Mexico. Most of these domes have overlying sediments and caprock of varying thickness. However, it was assumed for this study that the sediments and caprock are relatively thin and sufficiently remote from the casing shoe that they do not have a significant impact on the predicted results in the lower portion of the well casing. Additionally, the gas storage caverns were modeled as being isolated from the edge of the dome and from other caverns.

4.2.2 Porous Sandstone Reservoir Storage

The 1,524-meter- (5,000-foot-) deep reservoir well was assumed to be located in a bedded formation similar to those used for storage in the northeastern United States. The formation is comprised of numerous shale, limestone, anhydrite, dolostone, and sandstone beds. Natural gas is stored in a 30.5-meter-thick (100-foot-thick) sandstone formation between 1,524 and 1,554.5 meters (5,000 and 5,100 feet) below ground surface. To simplify the problem, the rock beds more than 610 meters (2,000 feet) above the gas storage formation were combined into a massive layer that is represented by the predominate formation material, shale. Details of the stratigraphy used in the model of the reservoir well are provided in Table 4-1.

Table 4-1. Stratigraphic Detail Used in the Numerical Model of Reservoir Well No. 3

Stratigraphic Unit	Rock Type	Top (m)	Bottom (m)	Thickness (m)
Overburden	Shale	0	935.1	935.1
Tully	Limestone	935.1	961.9	26.8
Hamilton	Shale	961.9	1,428.9	467.0
Marcellus	Shale	1,428.9	1,486.2	57.3
Onondaga	Limestone	1,486.2	1,500.8	14.6
Needmore	Shale	1,500.8	1,524.0	23.2
Oriskany	Sandstone	1,524.0	1,554.5	30.5
Helderberg	Limestone	1,554.5	1,645.9	91.4

4.3 MATERIAL MODELS AND PROPERTIES

The thermal and structural models of the wells and connections include the casing components, rock strata, and cavern/reservoir fluids. A different constitutive model or material law was used for each material type represented in the conceptual models. Each constitutive model is defined by a set of model parameters that are typically determined from independent laboratory testing of the material being modeled. The model parameters for each of the materials were obtained from the literature. The models and parameters used in the analyses are presented below under separate headings.

4.3.1 <u>Steel Casing</u>

The properties of the casings used for the final cemented strings for each of the candidate wells are listed in Table 4-2. The mechanical behavior of the steel casing was assumed to be linear elastic for the well models. A nonlinear material model was used to describe the behavior of the steel casing for the connection models as described in the next subsection. For the well models, the steel was assumed to be homogeneous and isotropic so its elastic behavior could be characterized using only two elastic parameters.

4.3.2 <u>Threaded Connections</u>

The J-55 and K-55 materials specified for the connection analyses were modeled using the elastic-plastic-thermal-creep constitutive model developed previously by C-FER Technologies based on material coupon tests [Humphreys et al., 1991]. The J-55 material model has a thermal expansion coefficient of $15.6 \times 10^{-6} \, \text{K}^{-1}$ ($8.7 \times 10^{-6} \, \text{R}^{-1}$) and a Young's modulus of 200 GPa (29,000,000 psi). The yield strength for J-55 was defined on a temperature-dependent basis

and was assumed to be 425 MPa (61,640 psi) at 20°C (68°F), and 405 MPa (58,740 psi) at 200°C (392°F). The K-55 material has a thermal expansion coefficient of 14.4×10^{-6} K^{-1} (8.0×10^{-6} R^{-1}), a Young's modulus of 190 GPa (27,557,000 psi), and yield strengths of 427 MPa (61,930 psi) and 370 MPa (68,168 psi) at 20°C (68°F) and 200°C (392°F), respectively.

Table 4-2. Elastic and Thermal Material Properties of Casing Components Used for the Well Models

Material	Property	Value	Units	Reference
Steel Casing	Young's Modulus	206.9	GPa	Riley et al. [1999]
	Poisson's Ratio	0.29	—	Riley et al. [1999]
	Density	7.85	g/cm^3	Incopera [1996]
	Thermal Expansion Coefficient	12.1×10^{-6}	K^{-1}	Riley et al. [1999]
	Thermal Conductivity	60.52	W/(m-K)	Incopera [1996]
	Specific Heat	435	J/(kg-K)	Incopera [1996]
Cement	Young's Modulus	11.0	GPa	Pfeifle et al. [2000]
	Poisson's Ratio	0.286	—	Pfeifle et al. [2000]
	Density	1.86	g/cm^3	Incopera, [1996]
	Thermal Expansion Coefficient	9.54×10^{-6}	K^{-1}	Philippacopoulos and Berndt [2000]
	Thermal Conductivity	0.72	W/(m-K)	Incopera [1996]
	Specific Heat	779	J/(kg-K)	Incopera [1996]

4.3.3 Cement Sheath

The cement was also assumed to be a homogeneous, isotropic, linear elastic material. The elastic and thermal properties of cement are provided in Table 4-2.

4.3.4 Rock Salt

When a rate-dependent material is subjected to a deviatoric (shear) stress, it deforms with time (creeps). Although time-dependent deformation occurs in all materials, it is often so small that it can be neglected in most engineering problems. However, the rate-dependent deformation of some geologic materials, such as salt, is significant for the stresses, temperatures, and times of interest in underground storage caverns.

Based on analysis of multistage and other creep data from eight domal salts, Munson [1998] classified the creep of domal salt as forming two distinct groups, either soft or hard, where the

difference is roughly a factor of ten in creep rate between the two groups. Munson [1998] provided estimates for the creep model developed for the Waste Isolation Pilot Plant near Carlsbad, New Mexico, to predict both soft and hard salt behavior. This creep model is referred to as the M-D model. The M-D model is capable of predicting the steady-state and transient creep response of salt over a large range of stress and temperature through the contribution of three micromechanical mechanisms. However, for the range of stress and temperature expected in the salt during natural gas storage, the creep rate predicted by the M-D model is dominated by only one of these mechanisms (the observed and known but undefined mechanism at low temperature and low stress). This mechanism can take on the same functional form as the Norton Power Law [Norton, 1929], after appropriate rearrangement of terms. Whereas the transient nature of salt is an important feature to capture during most numerical modeling studies of natural gas storage caverns, the use of a steady-state creep model such as the Norton Power Law is adequate for the accuracy desired for this study. The Norton Power Law can be expressed as shown below:

$$\dot{\varepsilon}_c = A \exp\left(-\frac{Q}{RT}\right)\sigma^n \qquad (4\text{-}1)$$

For a triaxial compression laboratory creep test, $\dot{\varepsilon}_c$ is the axial creep strain, σ is the stress difference, R is the universal gas constant, T is absolute temperature, Q is activation energy, and A and n are material parameters.

To maintain the conservative nature of the analyses, the steady-state properties for the faster creeping salt given by Munson [1998] were used in this study. The corresponding parameter estimates of the Norton Power Law for A, Q, and n are 5.2×10^{-14} MPa^{-n}/year, 10,000 calories/mole, and 5.0, respectively.

In addition to creep, the deformation of salt includes thermoelastic deformation. The thermoelastic properties of salt used for this study are provided in Table 4-3.

4.3.5 <u>Nonsalt Strata</u>

The reservoir storage well is sited in a bedded formation comprised predominately of shale, but also includes limestone and sandstone beds as discussed in Section 4.2.2. The shale and limestone were modeled as linear elastic materials in this study. The sandstone was modeled as a poroelastic material to predict the compaction and expansion of the reservoir caused by pressure changes from gas injection and withdrawal.

The poroelastic model is based on Biot's theory of deformation for porous materials [Biot, 1955]. The poroelastic model accounts for any volumetric straining that may occur because of pore pressure by modifying the total stress tensor $\left(\sigma_{ij}\right)$ as follows:

Table 4-3. Rock Strata Elastic and Thermal Material Properties

Material	Property	Value	Units	Reference
Salt	Young's Modulus	31	GPa	Munson [1998]
	Poisson's Ratio	0.25		Munson [1998]
	Density	2.16	g/cm^3	Dahlstrom [1988]
	Thermal Expansion Coefficient	2.2×10^{-5}	K^{-1}	Senseny et al. [1992]
	Thermal Conductivity	5.19	W/(m-K)	Callahan [1981]
	Specific Heat	837	J/(kg-K)	Callahan [1981]
Shale	Young's Modulus	20.8	GPa	Croff et al. [1985]
	Poisson's Ratio	0.21		Croff et al. [1985]
	Density	2.56	g/cm^3	Croff et al. [1985]
	Thermal Expansion Coefficient	7.9×10^{-6}	K^{-1}	Croff et al. [1985]
	Thermal Conductivity	1.39	W/(m-K)	Croff et al. [1985]
	Specific Heat	796	J/(kg-K)	Croff et al. [1985]
Limestone	Young's Modulus	45.8	GPa	Croff et al. [1985]
	Poisson's Ratio	0.27		Croff et al. [1985]
	Density	2.59	g/cm^3	Croff et al. [1985]
	Thermal Expansion Coefficient	6.7×10^{-6}	K^{-1}	Croff et al. [1985]
	Thermal Conductivity	3.07	W/(m-K)	Croff et al. [1985]
	Specific Heat	743	J/(kg-K)	Croff et al. [1985]
Sandstone	Young's Modulus	20.4	GPa	Croff et al. [1985]
	Poisson's Ratio	0.20		Croff et al. [1985]
	Density	2.29	g/cm^3	Croff et al. [1985]
	Thermal Expansion Coefficient	10.0×10^{-6}	K^{-1}	Croff et al. [1985]
	Thermal Conductivity	3.40	W/(m-K)	Croff et al. [1985]
	Specific Heat	712	J/(kg-K)	Croff et al. [1985]
	Biot Coefficient	0.7		Economides et al. [1994]

$$\sigma_{ij} = \sigma'_{ij} - \alpha p \delta_{ij} \qquad\qquad (4\text{-}2)$$

where:

σ'_{ij} = the components of the effective stress tensor

α = Biot's constant

p = fluid pressure

δ_{ij} = Kronecker delta.

Table 4-3 lists the thermoelastic properties for the nonsalt rocks modeled in this study.

4.3.6 Natural Gas

Natural gas is modeled in SCTS as a real gas using the American Gas Association's Detail Characterization Method as described by Starling and Savidge [1994]. For this study, the composition of the natural gas was assumed to be 100 percent methane. For the thermomechanical analyses of the two salt cavern wells using SPECTROM-32, gas pressure was applied in the finite element models as tractions along the inside of the casing and the surface of the uncased wellbore and cavern. A linear pressure gradient was assumed for the gas in the well and cavern and is based on the casing seat pressures and bulk cavern gas densities determined by SCTS.

4.3.7 Brine

Because of the very small compressibility of brine (approximately 2.8×10^{-4}/MPa (1.9×10^{-6}/psi)), the increase in brine density associated with the hydrostatic pressure increase over the height of the model is assumed to be negligible (about 0.1 percent change per 305 meters (1,000 feet)). Consequently, the brine density was assumed to be a constant 1.2 g/cm^3 (75 lb/ft^3), resulting in a vertical pressure gradient of 0.0118 MPa/meter (0.52 psi/foot) of depth.

4.4 IN SITU CONDITIONS

Because the creep rate of salt is dependent on temperature and stress, it is important to model temperatures and stresses which are representative of those in the vicinity of the well casings. Also, the magnitude of the thermally induced stresses will depend on the initial in situ temperature for both the salt cavern wells and the reservoir well. The initial stress and temperature distributions used for the numerical models of the well casings are discussed below.

4.4.1 <u>Stress Distribution</u>

Principal in situ stresses are generally assumed to be aligned with a coordinate system that is vertical and horizontal. Assuming that the in situ stress state in salt domes and bedded salt formations is isotropic is generally accepted because most models of salt creep predict that long-term creep removes any differences in the horizontal and vertical stress components. The magnitude of the vertical principal stress is typically assumed to be equal to the weight of the overburden. An initial isotropic state of stress that varies with depth was assumed to exist within the salt formations modeled in this study.

In most nonsalt locations, the magnitudes of the vertical and horizontal principal stresses are not equal. Typically, the two principal horizontal stresses are different from the vertical stress and are also different from each other. The inequality of the principal stresses in most regions is reflected in the regional faulting. However, the axisymmetric representation of the reservoir well numerical model does not allow separate designations for the horizontal stresses. Therefore, the simulations of the reservoir well were performed assuming an isotropic initial state of stress that varies with depth. The initial state of stress within the models before creation of the well is based on an acceleration of gravity of 9.8 m/s^2 (32.15 ft/s^2) and the densities for the overlying strata given in Table 4-3.

4.4.2 <u>Temperature Profile</u>

The temperature profiles used for the analyses of the well models are based on temperatures and temperature gradients reported in the literature. Karably and White [1981] reported geothermal gradients for eight Gulf Coast salt domes ranging from a minimum of 0.01750°C/m (0.0096°F/ft) to a maximum of 0.02935°C/m (0.0161°F/ft). For the salt cavern well models used in this study, a surface temperature of 28.33°C (83°F) and a single temperature gradient of 0.02734°C/m (0.015°F/ft) were assumed.

A surface temperature of 15.56°C (60°F) and temperature gradient of 0.02005°C/m (0.011°F/ft) from ground surface to the reservoir depth of 1,542 meters (5,000 feet) were assumed for the reservoir well model. Using these properties, the temperature at the gas storage depth is 46.11°C (115°F).

4.5 GAS PRESSURE CYCLES

The gas pressure cycles used for the salt cavern well analyses were selected to provide a conservative estimate of the casing loads by using very rapid injection and withdrawal scenarios. The rapid cycles produce the largest temperature range possible for the casing because they reduce the time available for heat transfer to the surrounding rock formation. Repetitive gas injection and withdrawal periods of 20 and 10 days, respectively, were simulated for the two salt cavern well models. The injection and withdrawal rates were adjusted during each cycle in the simulations so that the pressure at the casing shoe was maintained between

the maximum and minimum allowable pressures of 0.001786 and 0.00525 MPa/m (0.85 and 0.25 psi/ft) depth at the casing shoe. The allowable pressure range at the casing shoe was selected because it spans the range used by most natural gas storage caverns in the United States.

Figure 4-1 illustrates the annual pressure cycles used for the salt cavern well models. A total of 60 cycles or 5 years of operation were simulated during the analyses of the well problems to allow sufficient time for the configuration to achieve thermal equilibrium after solution mining of the cavern. A repeatable temperature history was desired for this problem to define the magnitude of the cyclic loading to be specified for the connection analyses.

Deliverability of reservoir storage wells is typically much lower than that of salt caverns. For this study, prolonged injection and withdrawal periods were assumed for the reservoir storage well. The annual pressure cycle used for Reservoir Storage Well No. 3 is illustrated in Figure 4-1. As shown in this figure, the complete cycle requires 1 year with gas injection and withdrawal occurring during 9-month and 3-month periods, respectively. This cycle is intended to represent a storage well that is used for seasonal heating demand during the winter months. Minimum and maximum reservoir formation pressures of 4.14 and 22.06 MPa (600 and 3,200 psi) were specified, respectively. Gas is injected at a temperature of 21.11°C (70°F) and withdrawn at the reservoir storage formation temperature of 46.11°C (115°F).

4.6 FINITE ELEMENT MODELS

Axisymmetric models were used in this study to provide an accurate representation for the well configurations under investigation. A total of six finite element models were developed to complete this study: three well models and three threaded connection models. One well model was developed for each of the three candidate wells under consideration. The connection models were designed to address different casing sizes, connection assemblies (welded and nonwelded), and loading conditions (axisymmetric and nonaxisymmetric). Descriptions of the finite element meshes of the well and connection models are provided in separate sections below.

4.6.1 <u>Well Models</u>

Because the focus of this study was to evaluate casing loads, the selection of the size and shape of the salt storage cavern was arbitrary. However, the displacements caused by salt creep are of primary concern. Cylindrical-shaped caverns having a diameter and height of 60.96 and 304.8 meters (200 and 1,000 feet), respectively, were modeled in this study. The roof of each cavern is located 30.48 meters (100 feet) below the casing shoe depths of 579 and 1,524 meters (1,900 and 4,900 feet). Based on these assumptions, the caverns have a volume of 889,600 m^3 (5.6 million barrels) and provide natural gas storage of about 8.6×10^7 Nm^3 (3.2 billion cubic feet (Bcf)) for the shallow cavern and 1.9×10^8 Nm^3 (7.1 Bcf) for the deeper cavern.
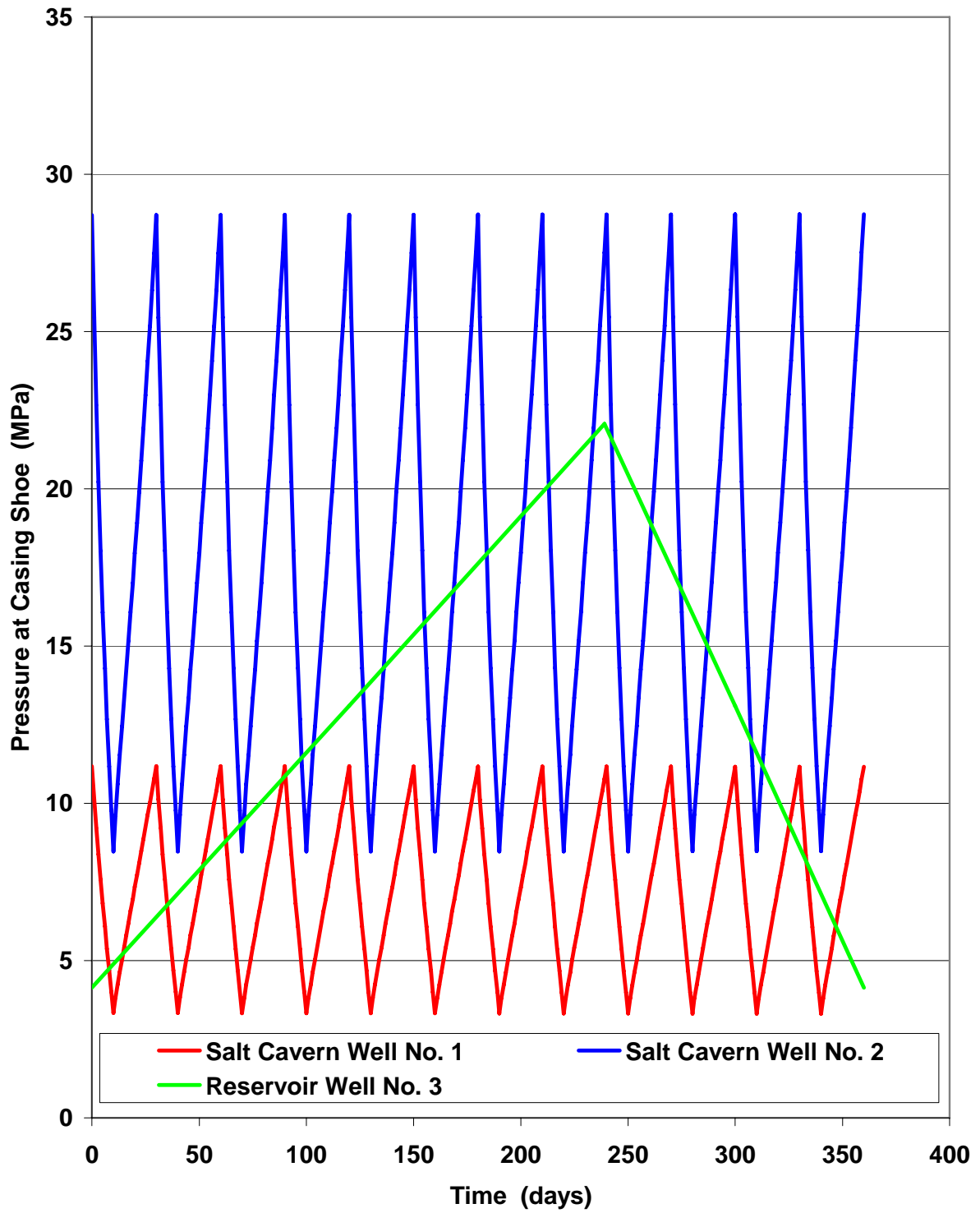
Figure 4-1. Annual Gas Pressure Cycles for the Three Candidate Wells.

26

For Salt Cavern Well No. 1, the final cemented casing is seated at a depth of 579 meters (1,900 feet). Figure 4-2 shows the axisymmetric model used for Salt Cavern Well No. 1. The model extends vertically from ground surface to a depth of 3,048 meters (10,000 feet). The model extends laterally 696 meters (2,000 feet) from the center of the well. The extent of the model was selected to isolate the response of the cavern from the influences of the radial and bottom boundaries, which are artificial truncations of the actual horizontal and vertical extents of the salt. Besides the salt and void space of the cavern, the only other components contained in the model are the 340-millimeter- (13⅜-inch-) diameter steel casing and the 50.8-millimeter (1.87-inch) cement sheath. Surface and intermediate casings are not included in the model because they are sufficiently remote as to have negligible effect on the state of stress in the lower portion of the well, which is of primary concern. The finite element mesh contains 28,533 nodes and 9,372 eight-noded finite elements. The region immediately outside the wellbore and walls of the cavern were very finely subdivided. This extremely fine subdivision was used to accurately represent the high stress and temperature gradients that are anticipated in these areas. This finite element mesh was used for both the heat transfer and thermomechanical analyses of Salt Cavern Well No. 1.

Figure 4-3 shows the axisymmetric model used for Salt Cavern Well No. 2. This model is similar to that used for Salt Cavern Well No. 1 except the top of the cavern is located at a depth of 1,524 meters (5,000 feet) and the cemented casing extends to a depth of 1,494 meters (4,900 feet). The finite element mesh of Salt Cavern Well No. 2 contains 27,933 nodes and 9,174 eight-noded finite elements.

The finite element model of Reservoir Well No. 3 extends from ground surface to a depth of 1,645 meters (5,400 feet). The model extends laterally 696 meters (2,000 feet) from the center of the well. The extent of the model was selected to isolate the response of the well from the influences of the radial and bottom boundaries. The model includes the final cemented casing to a depth of 1,524 meters (5,000 feet) in the stratigraphy identified in Section 4.2.2. Because of the axisymmetric assumption, the 90-degree bend could not be incorporated into the model. Therefore, the casing was assumed to extend to the top of the sandstone storage formation. The mesh used for the analyses of Reservoir Well No. 3 is shown in Figure 4-4. The mesh contains 31,194 nodes and 10,251 eight-noded finite elements. This model was used for both the heat transfer and thermomechanical analyses of Reservoir Well No. 3.

During heat transfer simulations of the three well models, the outer boundaries of the models were insulated and thus no heat was transferred across these boundaries. The gas temperature history in the caverns and/or well was applied to the surface of the cavern and/or well casing of the models to calculate temperatures in the casing and surrounding rock formation. This temperature history was subsequently used in the thermomechanical simulations to account for thermally induced stresses and temperature-dependent behavior of the salt in the models.
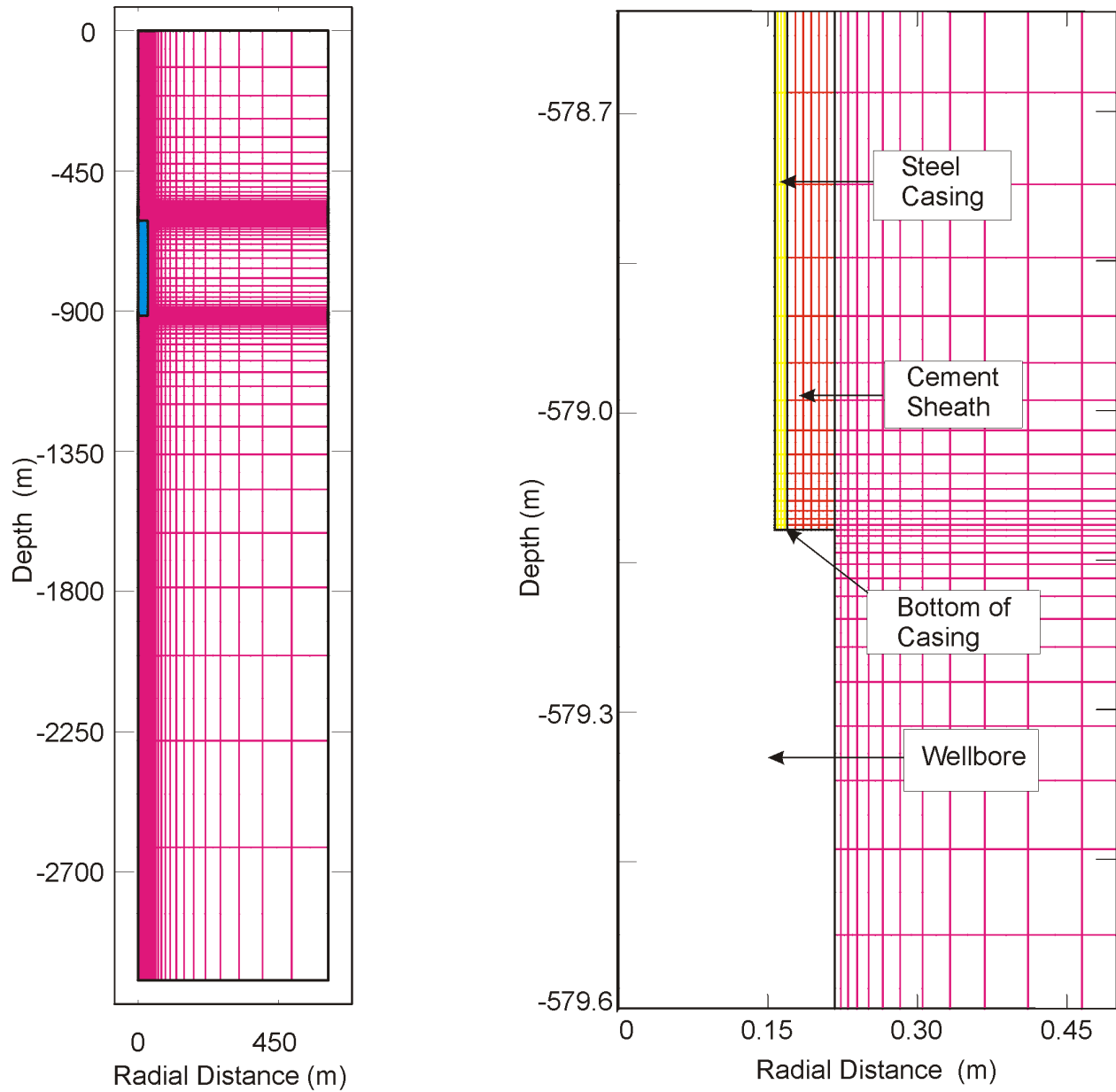
Figure 4-2. Axisymmetric Finite Element Model of Salt Cavern Well No. 1.
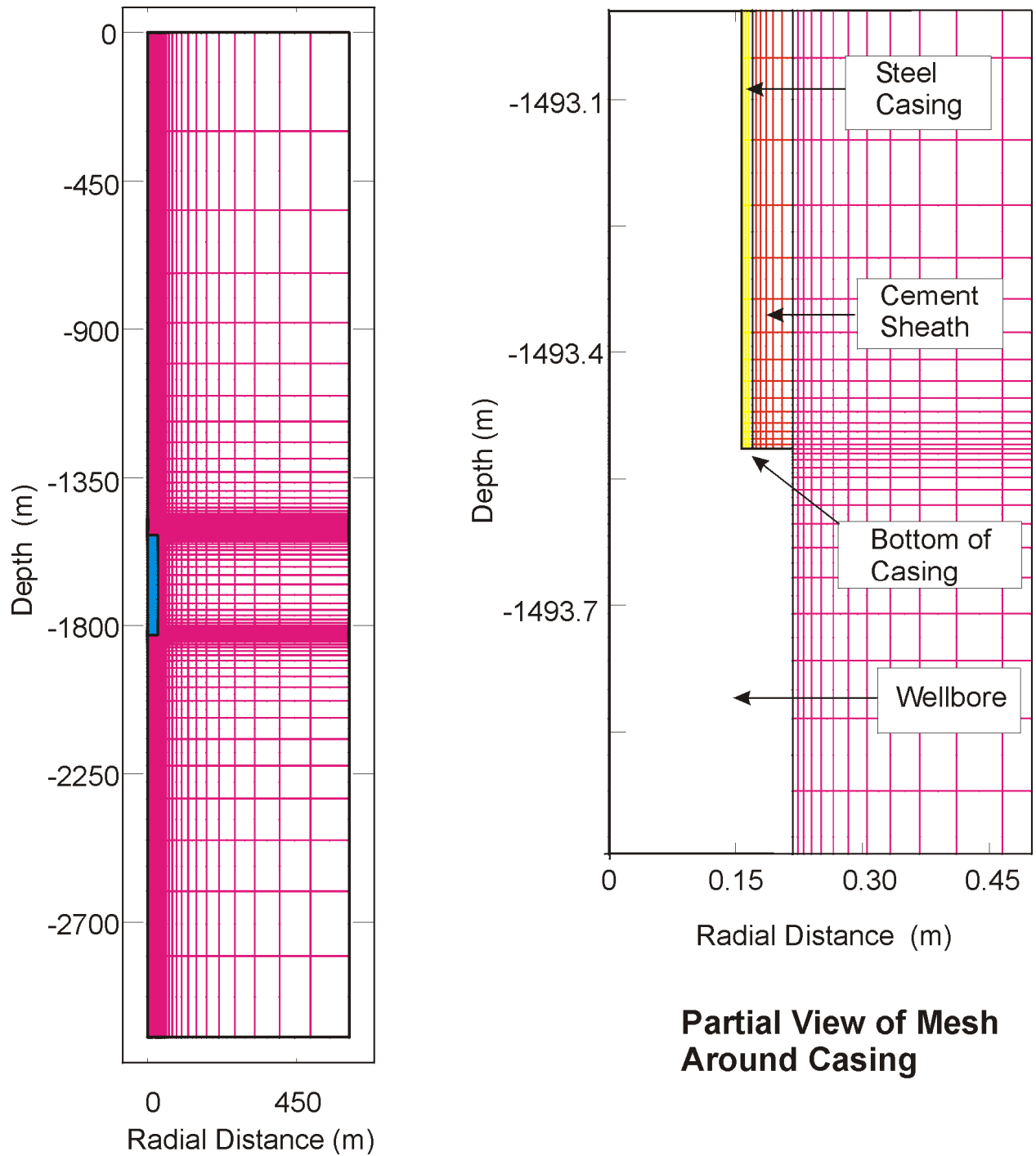
Figure 4-3. Axisymmetric Finite Element Model of Salt Cavern Well No. 2.
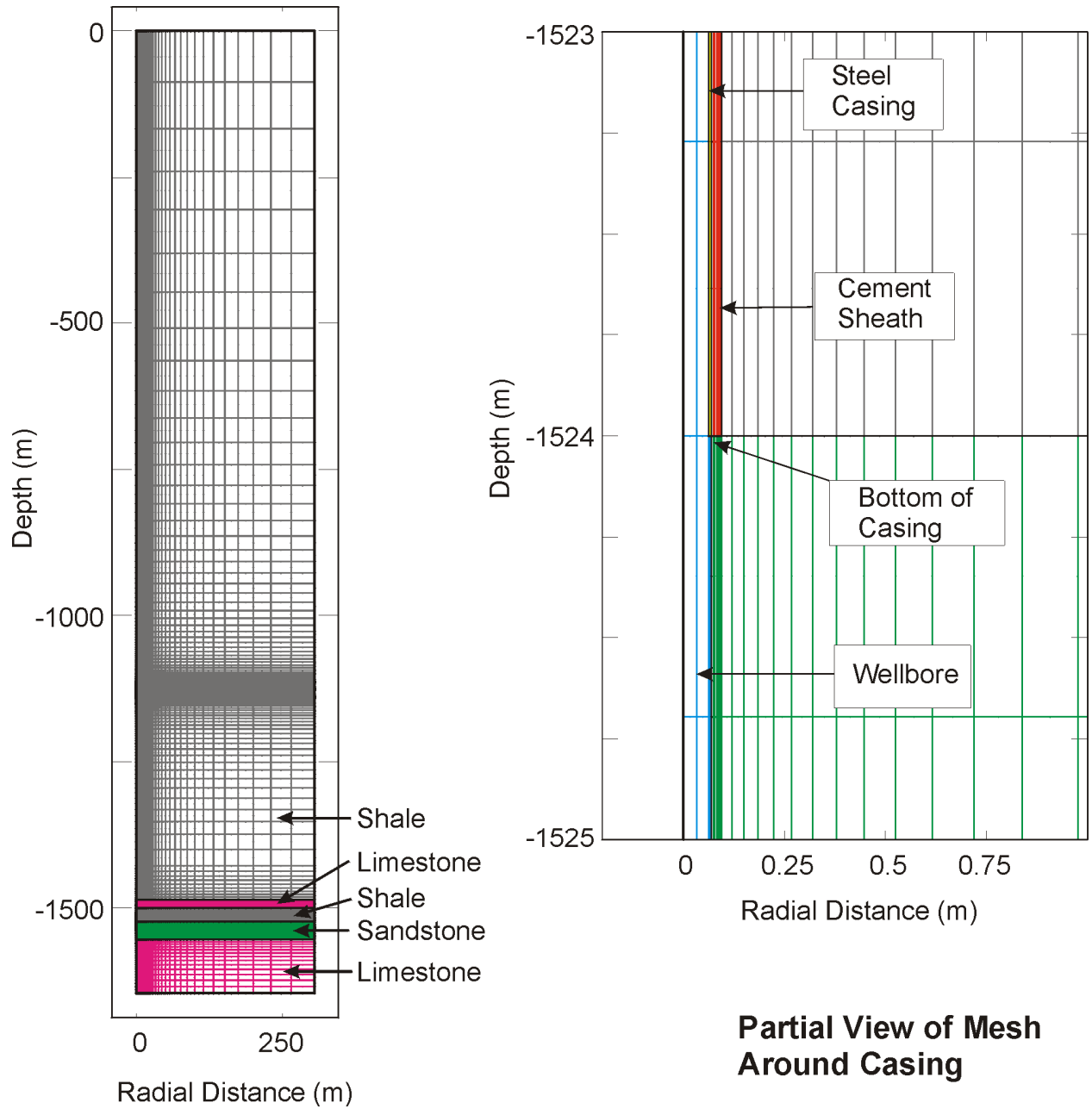
Figure 4-4. Axisymmetric Finite Element Model of Reservoir Storage Well No. 3.

During the thermomechanical simulations, the kinematic boundary conditions specified along the sides of the axisymmetric models were:

- No radial displacement along the centerline.

- No radial displacement along the outer radius.

- No vertical displacement along the bottom surface.

The upper surfaces of the models were free to move in the vertical and horizontal directions.

In the models, normal tractions were specified along the inside diameter of the steel casing to simulate the fluid pressure. For the salt cavern well models, tractions were also specified along the perimeter of the cavern and along the 30.48 meters (100 feet) of open borehole leading into the cavern. The magnitudes of these tractions were set equal to the hydrostatic pressure based on the density of brine during the solution-mining portion of the simulation and based on the respective casing seat pressure and the average cavern gas density during the natural gas storage portion of the simulated history. For the reservoir well model, the tractions along the inside of the steel casing and the pore pressure in the sandstone reservoir were updated to correspond with the downhole pressure.

4.6.2 Connection Models

The casing connections were assumed to conform to the thread profile, thread interference, and coupling length for 8-Round Short Threaded and Coupled (STC) connections as defined by the American Petroleum Institute Recommended Practice API-5B. Connection geometry was assumed to conform to the published nominal dimensions for the 140-millimeter (5.5-inch, 15.5 pound/foot (lb/ft)) and 340-millimeter (13⅜-inch, 72 lb/ft) casing. The analyses did not consider the effects of manufacturing tolerances on the connection performance. The model included one-half of a coupling and a single pipe pin end with a 127-millimeter (5-inch) length of pipe body extending from the connection as shown in Figure 4-5.

Separate models were developed to analyze axisymmetric and nonaxisymmetric loading scenarios. For the salt cavern well connections, only axisymmetric loading was considered. Both axisymmetric and nonaxisymmetric load conditions were analyzed for the reservoir storage well. The nonaxisymmetric loading condition was necessary to account for the bending stresses caused by the curvature of the casing in the deviated section of the well. For the nonaxisymmetric model, the pipe body end was constrained to a global beam node, at which the axial force and bending moment were applied. A special connection model was also developed for the reservoir storage connection analysis that included the addition of a weld between the coupling face and the pipe body after the connection is made up. Casing deformations, such as shears and buckles that impose bending on the pipe, were not considered.
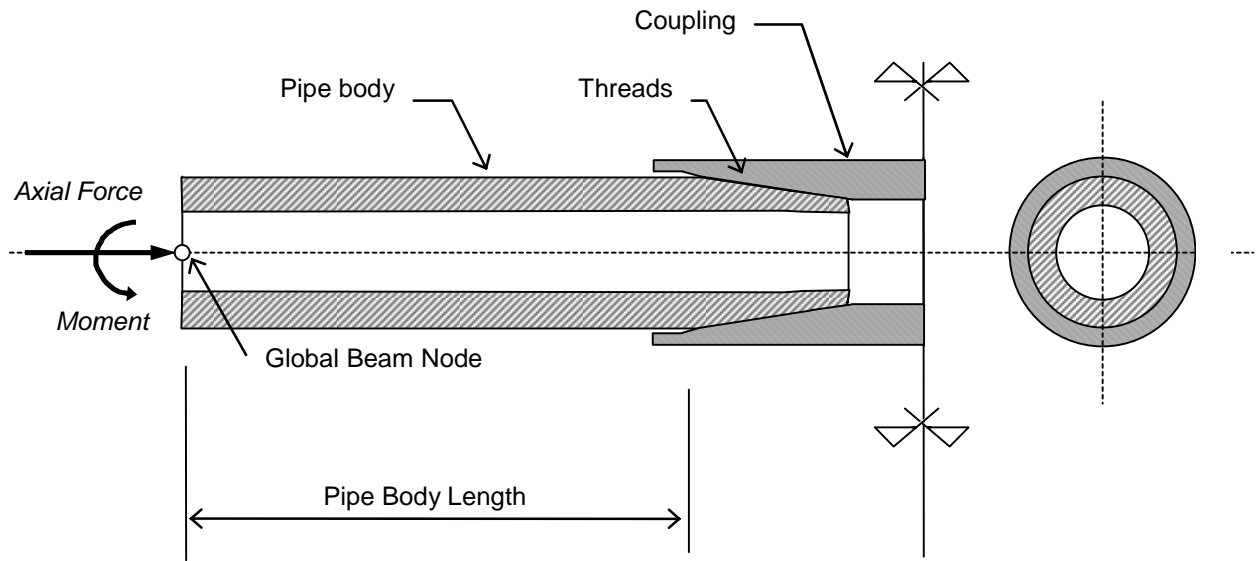
Figure 4-5. Schematic of Three-Dimensional Finite Element Connection Model.

5.0 RESULTS AND DISCUSSION OF WELL CASING MODELS

The axisymmetric finite element models of the three candidate wells described in Chapter 4.0 were used to evaluate the temperature and stress distribution in the steel casing from ground surface to the casing shoe during gas storage operation. The following sections provide a brief description of the well problems and discuss the results of the numerical modeling of the well casings. Results provided during gas storage operation include: (1) gas temperature history and distribution in the well, (2) temperature fields in the casing and rock formation along the wellbore, (3) axial (vertical) stresses in the steel casing, and (4) state of stress at the location of the lowest connection. The stresses and strains determined at the lowest connection in each well were used to define the cyclic loads that were applied to the connection models to determine the potential for cyclic fatigue. Results of the threaded connection modeling are discussed in Chapter 6.0.

5.1 PROBLEM DESCRIPTION

The stress analyses of the well casings considered contributions from (1) casing weight, (2) product pressures, (3) thermally induced stresses, and (4) external ground pressures. The problem descriptions differ for the salt cavern wells and the reservoir well. Descriptions of these two simulations are described separately below.

5.1.1 <u>Salt Cavern Well Model Simulations</u>

The analyses of the two salt cavern well models were initiated assuming a lithostatic state of stress wherein the horizontal stresses are equal to the vertical stress and vary with depth based on the density of salt. Similarly, a linear temperature distribution that varies with depth was also assumed within the modeled region. From this initial condition, the following sequential steps were simulated:

1. Instantaneously drill the 0.4348-meter- (17.12-inch-) diameter well to the depth of the cavern roof.

2. Backfill the well with a compressible, inviscid fluid having the same density as cement.

3. Hang the 340-millimeter (13⅜-inch) steel casing from ground surface.

4. Update the fluid material in the well annulus to that of hardened cement and simultaneously remove the fluid material in the central hole and apply a traction to the inside diameter of the steel casing to represent the pressure of a column of drilling mud.

5. Simulate solution mining of the cavern by injecting fresh water at a temperature of 21.11°C (70°F) over a 650-day period. The actual models simulate instantaneous excavation of the cavern to its final dimension rather than a progressive enlargement of the

cavern. However, the use of an instantaneous versus incremental mining approach is not expected to have a significant impact on the final stress and temperature fields surrounding the cavern at the end of solution-mining period.

6. Allow the brine-filled cavern to sit stagnant for 446 days. The long stagnant period was included to allow the formation temperature to recover after the extended period of solution mining. The stagnant period was included for modeling convenience because it required less effort than the simulation of additional gas service cycles to obtain a thermal equilibrium.

7. Dewater the cavern in 150 days at maximum gas pressure.

8. Simulate 5 years or 60 gas service cycles.

5.1.2 <u>Reservoir Well Model Simulations</u>

The analysis of the reservoir well model was initiated assuming an initial lithostatic state of stress that varies with depth as described in Section 4.4.1. The initial temperature of the formation was assumed to increase linearly with depth as described in Section 4.4.2. From this initial condition, the following sequential steps were simulated:

1. Instantaneously drill the 190.5-millimeter- (7.5-inch-) diameter well to the top of the storage formation.

2. Backfill the well with a compressible, inviscid fluid having the same density as cement.

3. Hang the 140-millimeter (5½-inch) steel casing from ground surface.

4. Update the fluid material in the well annulus to that of hardened cement and simultaneously remove the fluid material in the central hole and apply tractions along the inner diameter of the steel casing equivalent to that of a column of drilling mud.

5. Update the traction acting along the inside diameter of the steel casing with that produced by natural gas at minimum pressure.

6. Simulate five gas service cycles.

5.2 SALT CAVERN THERMAL SIMULATOR RESULTS

The computer program SCTS was used to determine the temperature range and distribution of the fluid flowing through the casings of the two salt cavern wells. Temperature histories predicted by SCTS for the fluid (either brine or natural gas) in the wells at depths of 579 and 1,494 meters (1,900 and 4,900 feet) are provided in Figures 5-1 and 5-2, respectively. These figures show the complete temperature history starting with solution mining of the caverns using brine. Solution mining of the caverns using brine that is cooler than the in situ temperature lowers the formation temperature in the vicinity of the cavern. However, injection

34
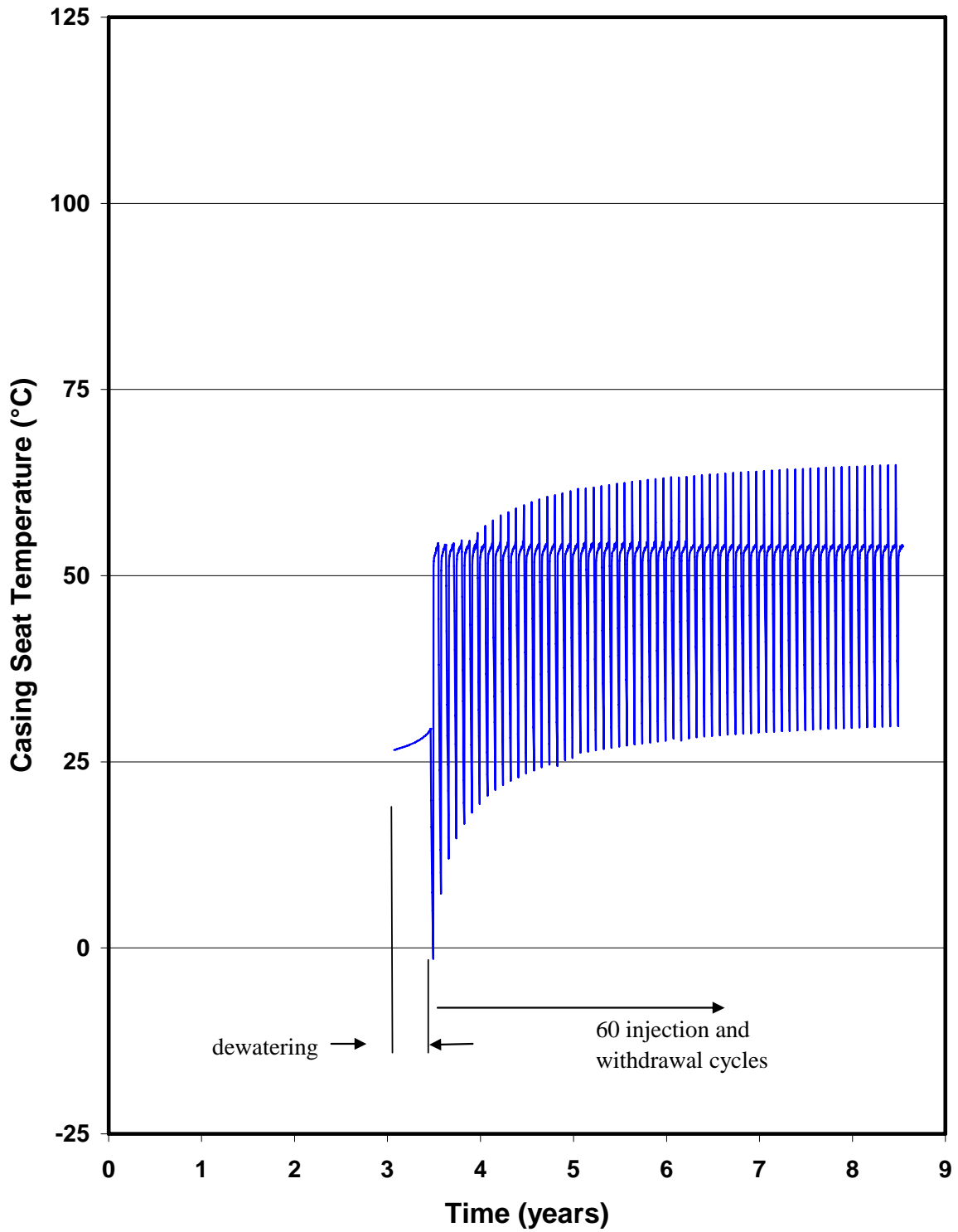
Figure 5-1. Casing Seat Temperature History for the 610-Meter (2,000-Foot) Shallow Salt Cavern Predicted by SCTS During 60 Gas Service Cycles.
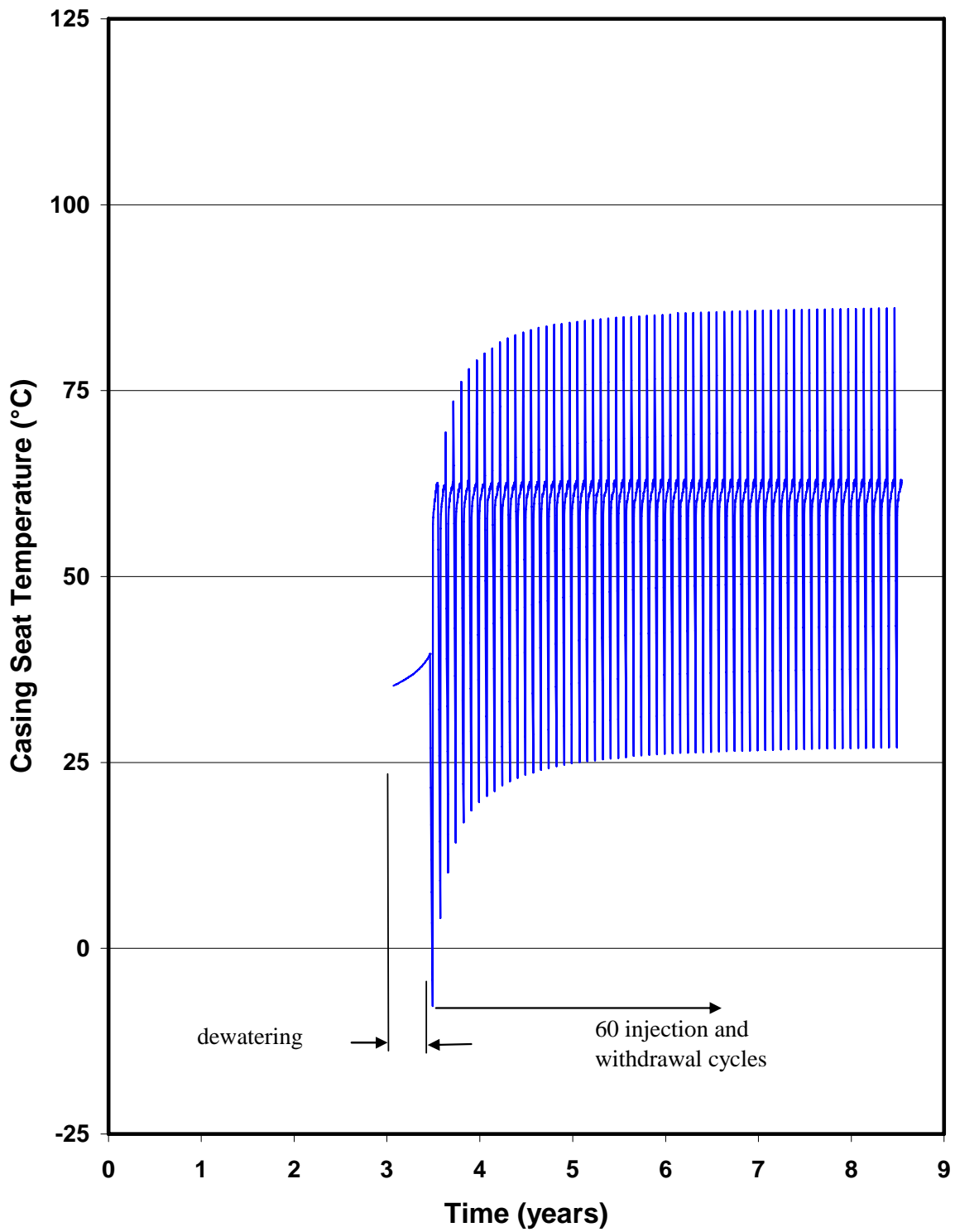
Figure 5-2. Casing Seat Temperature History for the 1,524-Meter- (5,000-Foot-) Deep Salt Cavern Predicted by SCTS During 60 Gas Service Cycles.

36

of gas at a temperature warmer than the formation temperature results in the gradual increase in the rock formation temperature surrounding the cavern with each successive gas cycle until a new thermal equilibrium is established. As shown in Figures 5-1 and 5-2, about 60 turns of working gas are necessary to provide sufficient time for the formation to obtain a new thermal equilibrium based on the repetitive injection and withdrawal cycles simulated.

In addition to the bulk temperature of the gas in the cavern, temperature histories are provided by SCTS at 15.24-meter (50-foot) increments from the wellhead to the casing shoe. Figure 5-3 illustrates the temperature profile of the gas in the well of Salt Cavern Well No. 1 at the beginning of injection, end of injection, start of withdrawal, and end of withdrawal. During withdrawal, the temperature of the casing quickly approaches that of the gas in the cavern. As a result, the warmest casing temperatures are predicted at the beginning of withdrawal when the pressure is the greatest. As shown in Figure 5-3, the temperature in the well at the beginning of withdrawal is about 10 degrees warmer than that of the casing during injection and 15 degrees warmer than the formation temperature at the cavern midheight of 49.17°C (120.5°F). After the 20-day withdrawal period, the temperature change caused by the decrease in cavern pressure results in the gas temperature becoming significantly lower. At the end of withdrawal, the casing temperature is about 25 degrees cooler than the gas injection temperature. Figure 5-4 is similar to Figure 5-3 except gas temperature profiles are provided for Salt Cavern Well No. 2.

SCTS was developed for the purpose of evaluating salt cavern gas storage operations and is not intended for the evaluation of reservoir storage. Therefore, an alternative method had to be taken to estimate the temperature of the gas in the reservoir storage well. Because of the extended injection and withdrawal periods for the reservoir well, it was assumed that the temperature of the gas remains relatively constant while the gas is flowing. This assumption appears to be valid based on SCTS simulations of salt caverns at low injection rates. Furthermore, the relatively slow flow rates would dictate that the temperature of the gas in the well is constrained between the injection temperature of 21.11°C (70°F) and the gas storage formation temperature of 46.11°C (115°F). Figure 5-5 shows the gas temperature history specified for the five gas service cycles of Reservoir Well No. 3. The gas temperature over the length of the casing was assumed to be equal to the temperature of the gas at the wellhead during injection and equal to the reservoir storage temperature during withdrawal. This approach provides conservative results because the entire casing experiences the maximum possible temperature differential.

5.3 HEAT TRANSFER RESULTS

The computer program SPECTROM-41 was used in this study to simulate the heat transfer between the casing, including the cavern if applicable, and the surrounding rock formation. The results of these calculations were then integrated into the thermomechanical analyses to
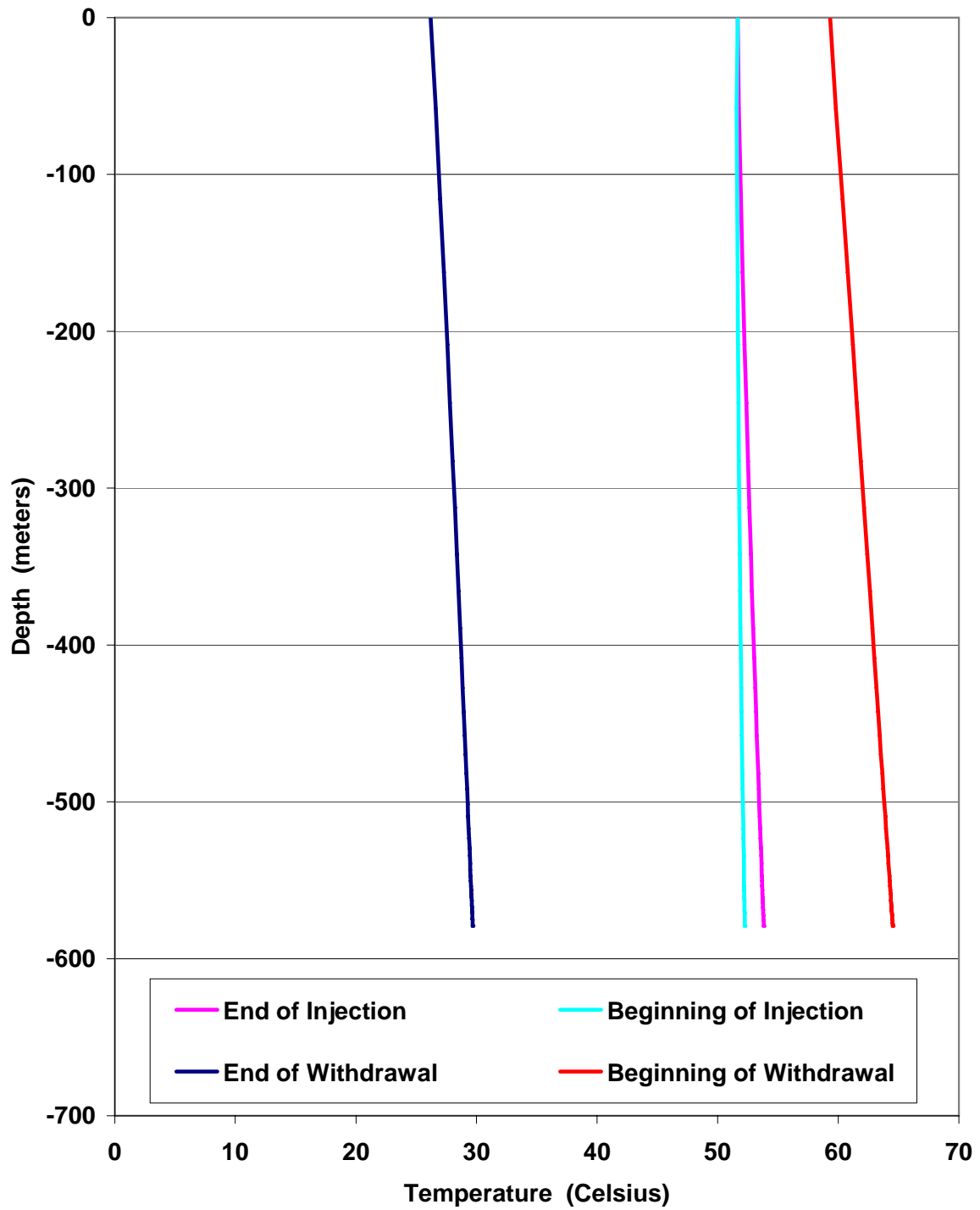
Figure 5-3. Temperature Profile of the Casing in Salt Cavern Well No. 1 During the 60th Gas Service Cycle.
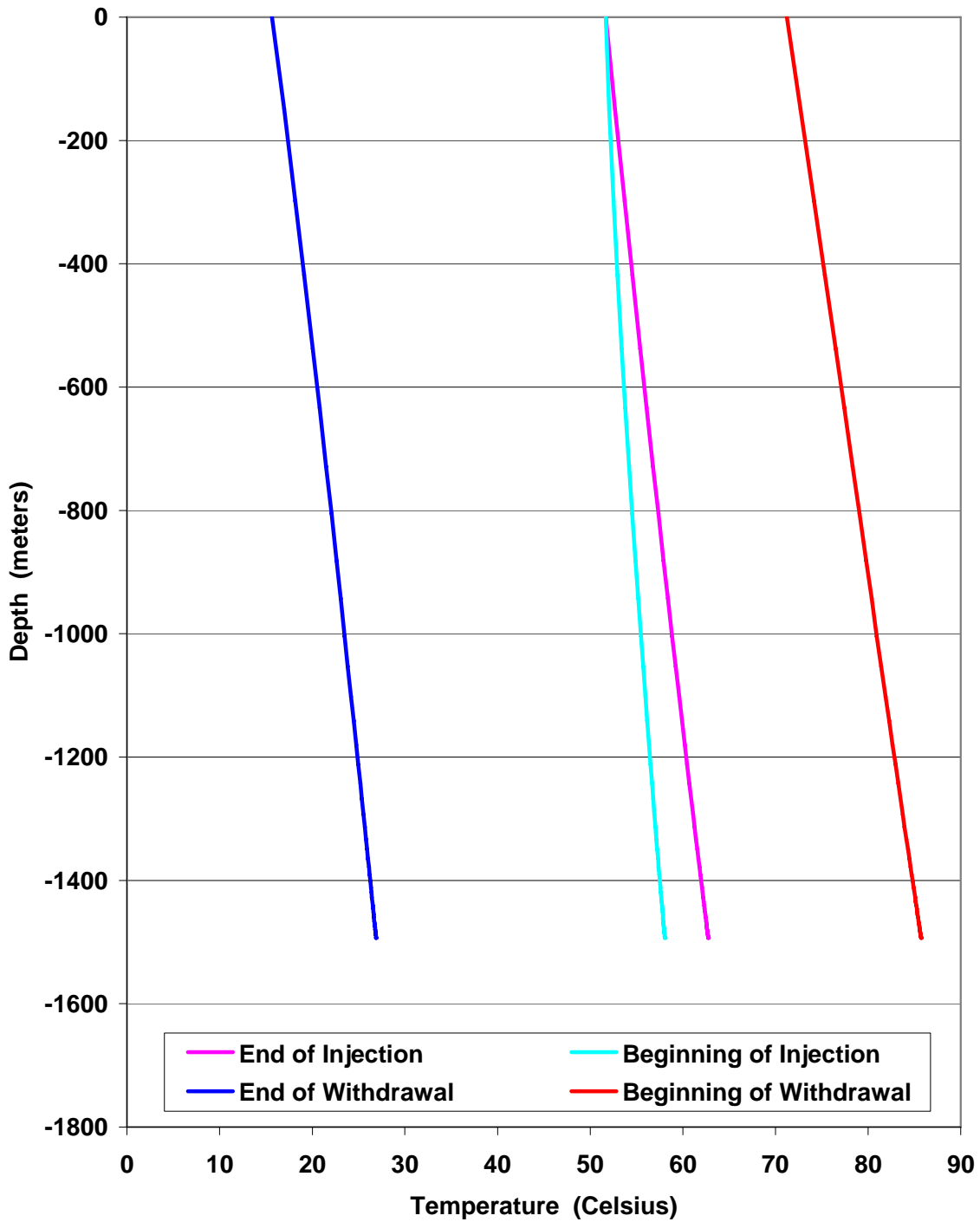
Figure 5-4. Temperature Profile of the Casing in Salt Cavern Well No. 2 During the 60th Gas Service Cycle.
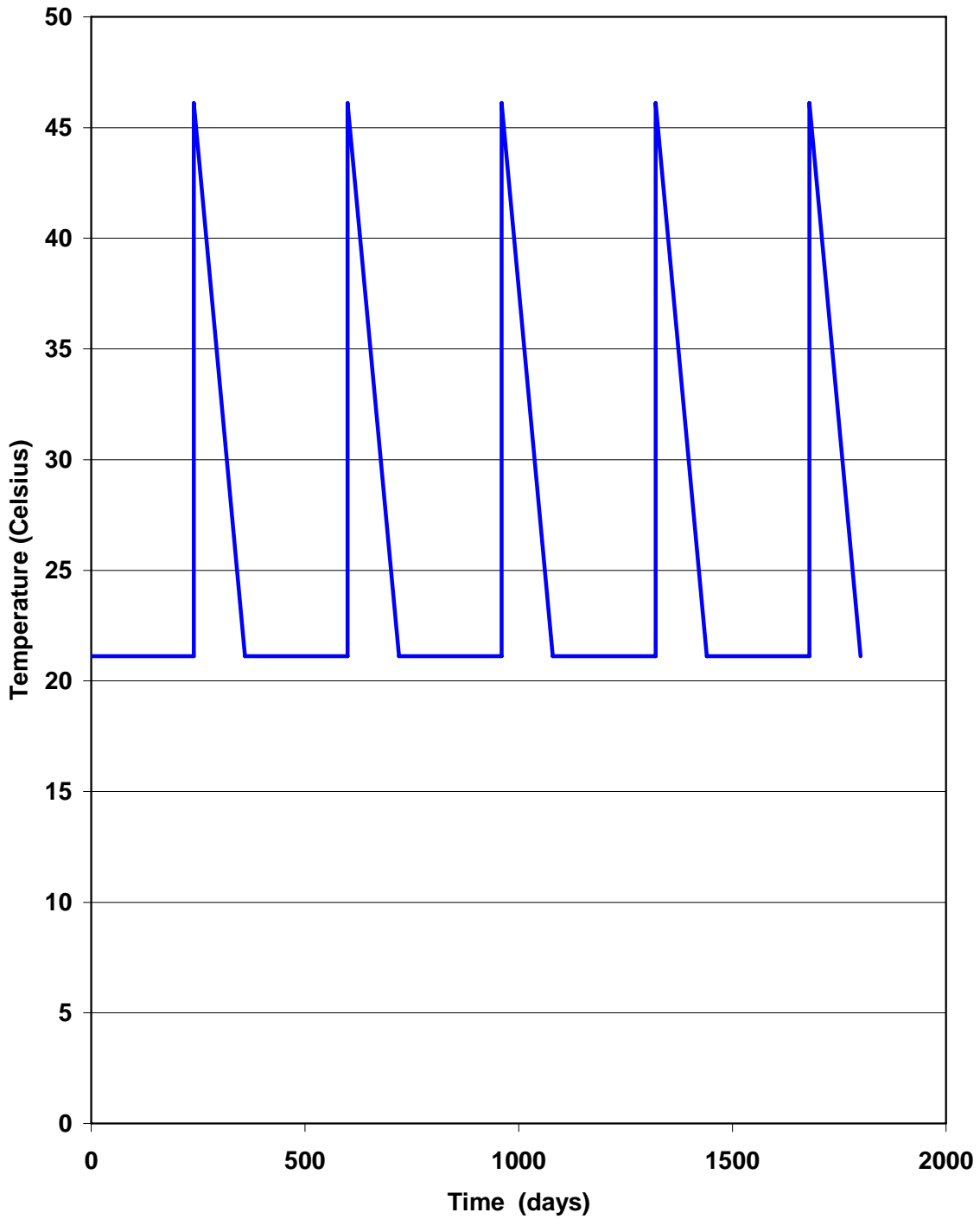
Figure 5-5. Temperature Histories at the Casing Seat of the 1,524-Meter- (5,000-Foot-) Deep Reservoir Storage Well No. 3 During Five Gas Cycles.

account for the thermal stresses and strains that are produced by temperature changes in the casing and rock formation. Because the gas temperature in the casing changes significantly during operation, the simulated gas storage cycles result in both short-term and long-term temperature changes in the casing and host rock formations. The short-term temperature changes only affect the first couple of meters of rock surrounding the casing, and in the case of the salt cavern analyses, the first couple of meters beyond the cavern walls. The long-term temperature changes affect a much larger region and are much more gradual.

Figures 5-6 and 5-7 show temperature contours around the casing shoe of Salt Cavern Wells No. 1 and No. 2, respectively, at various times throughout the 5-year gas storage simulations. These figures show the gradual long-term temperature changes that occur in the salt. Because the surface area and volume of the cavern are much larger than that of the casing, most of the long-term temperature change is caused by heat transfer between the gas in the cavern and the salt surrounding the cavern. The earliest time provided in these figures is following dewatering when the salt around the cavern has been significantly cooled by 2 years of brine production. The remaining three times correspond with when the cavern is at maximum pressure during the 1st and 60th cycle and when the cavern is at minimum pressure during the 60th cycle. After gas operations commence, the salt around the caverns gradually warms throughout the 5-year simulation. Because of the greater depth, the formation temperature is significantly warmer for Salt Cavern Well No. 2; however, the brine injection temperature was the same for both caverns.

Figures 5-8 and 5-9 show the temperatures in the casing and salt as a function of distance from the center of the well at an elevation about 12.2 meters (40 feet) above the casing shoe for Salt Cavern Wells No. 1 and No. 2, respectively. Temperature profiles are provided during the 60th gas service cycle. Profiles are provided at three times during this cycle: (1) end of injection, (2) beginning of withdrawal, and (3) the end of withdrawal. As shown in Figures 5-8 and 5-9, gas temperature changes in the well over a single cycle only affect the first few meters of salt behind the casing.

Because the modeling approach for Reservoir Well No. 3 assumes the gas temperature is constant in the sandstone reservoir, the only temperature changes predicted within the rock formation are those associated with gas flowing through the casing at a temperature different than the in situ temperature. Figure 5-10 provides profiles of temperature versus radial distance from the center of the reservoir well at a depth of 1,511 meters (4,960 feet). Profiles are provided at three times during the 5th gas cycle: (1) end of injection, (2) beginning of withdrawal, and (3) the end of withdrawal. As shown in Figure 5-10, the temperature of the rock within about 15 meters (50 feet) of the casing is lower than the in situ temperature of 45.27°C (113.5°F) at this depth. This is caused by the relatively long periods of continuous gas injection at 21.11°C (70°F).
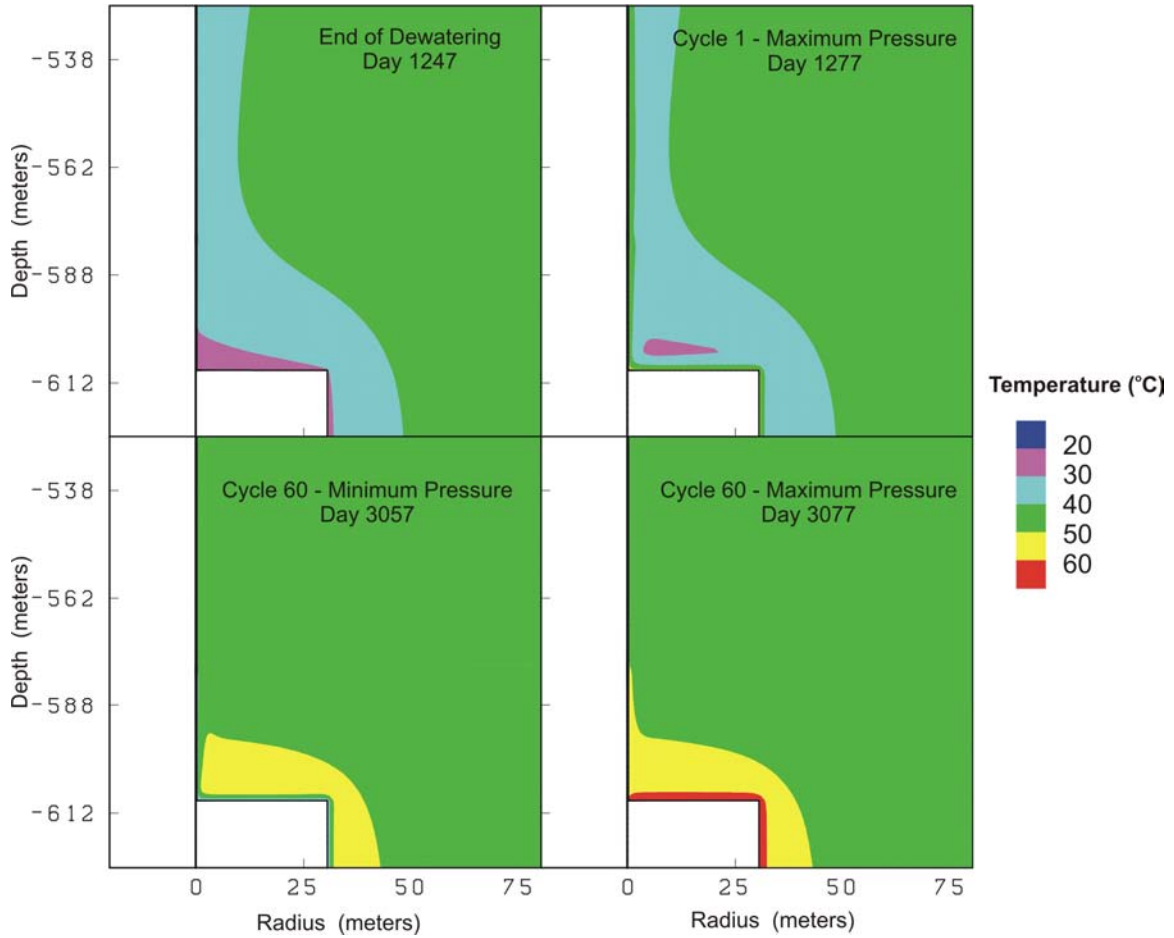
Figure 5-6. Temperature Contours in the Roof Salt Above Salt Cavern Well No. 1 at Various Times Throughout the 5-Year Gas Service Operation.
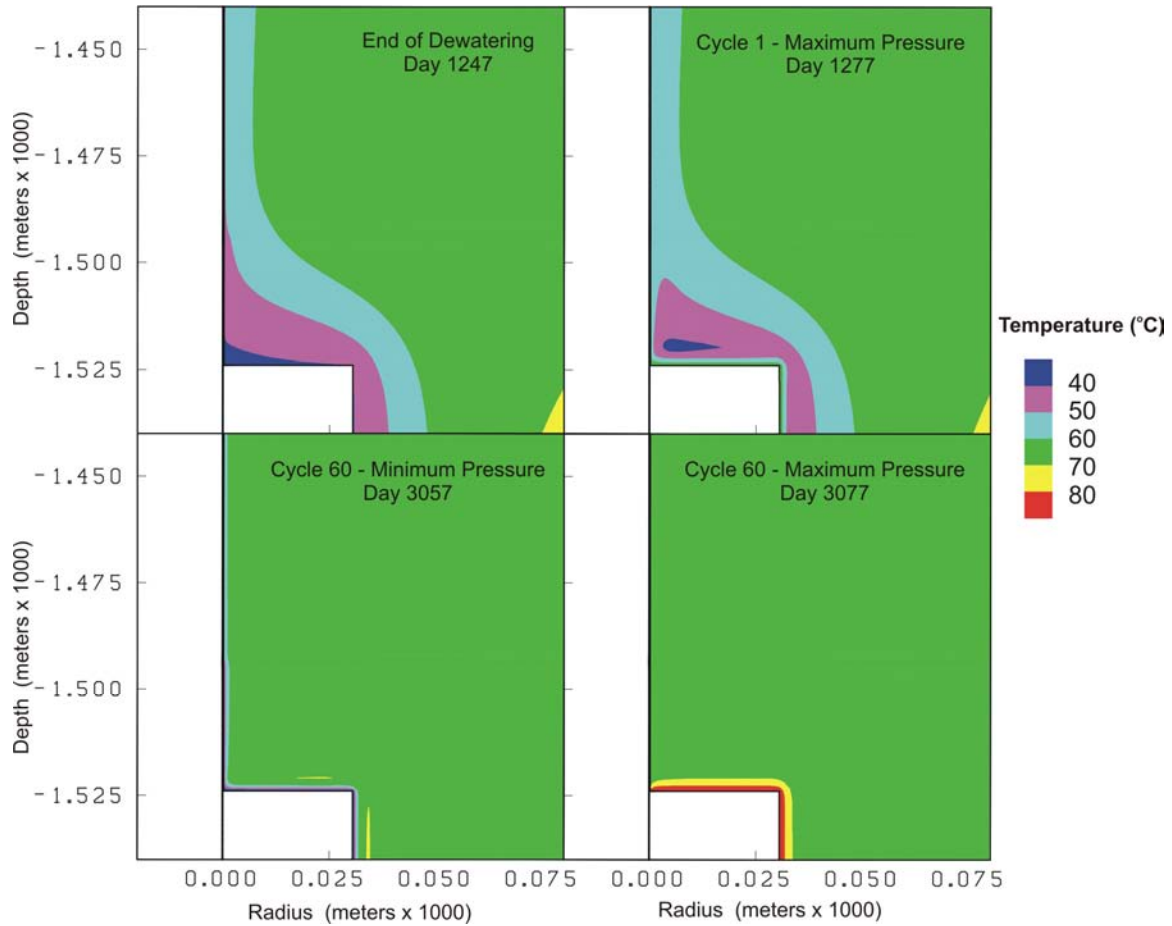
Figure 5-**7.** Temperature Contours in the Roof Salt Above Salt Cavern Well No. 2 at Various Times Throughout the 5-Year Gas Service Operation.

43
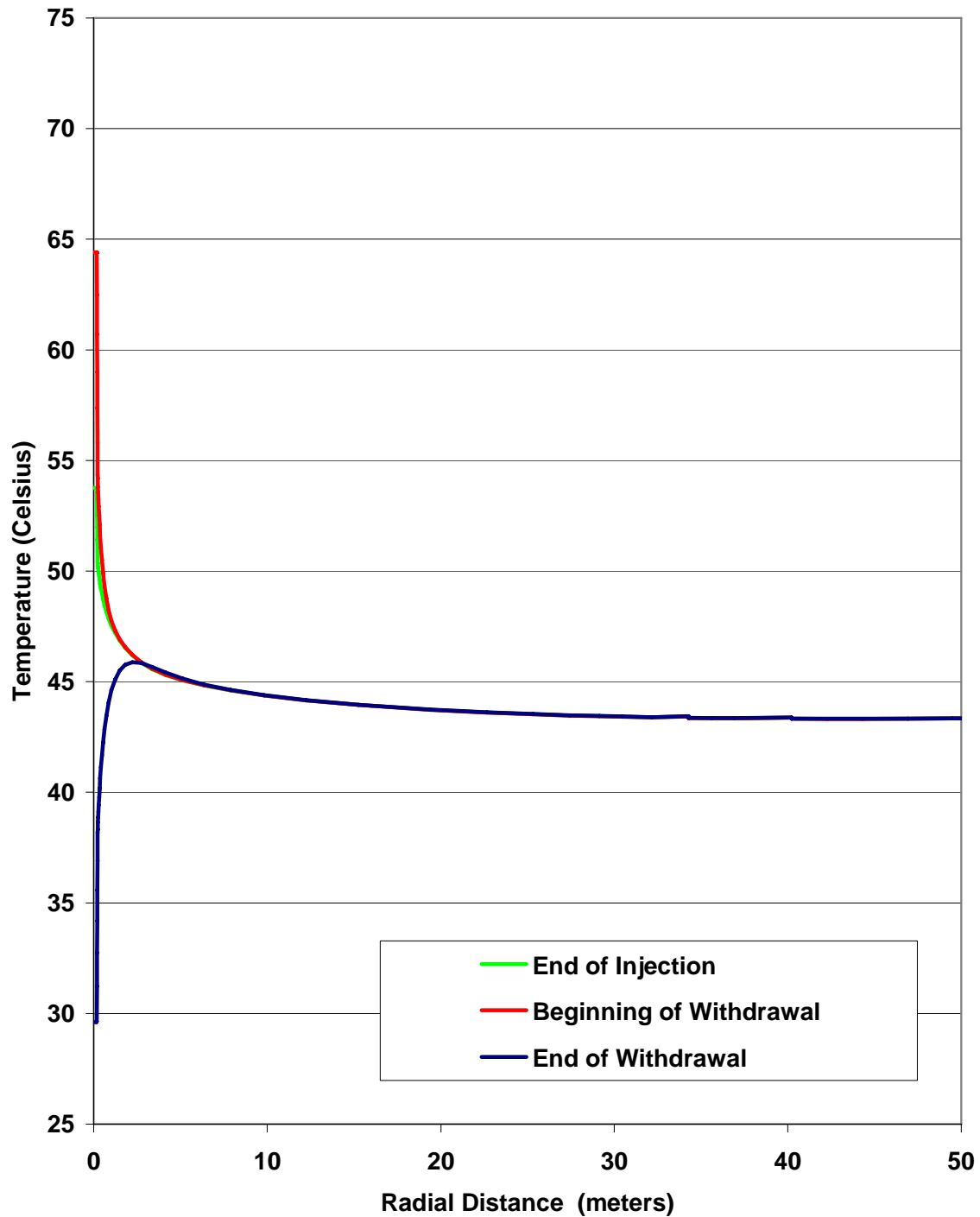
Figure 5-8. Temperature Profiles in the Casing and Salt 12.2 Meters (40 Feet) Above the Casing Shoe of Salt Cavern Well No. 1 During the 60th Gas Storage Operation Cycle.
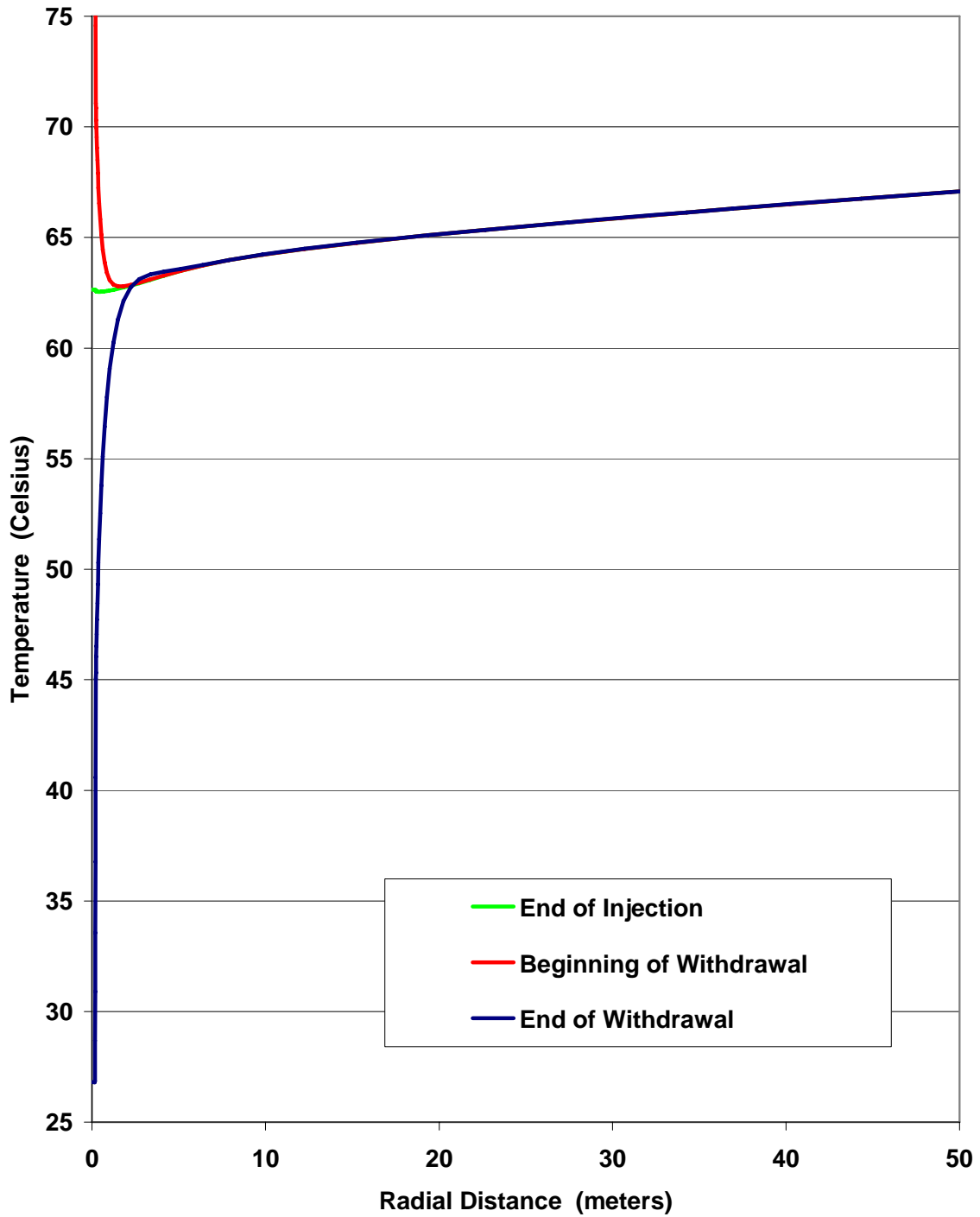
Figure 5-9. Temperature Profiles in the Casing and Salt 12.2 Meters (40 Feet) Above the Casing Shoe of Salt Cavern Well No. 2 During the 60th Gas Storage Operation Cycle.
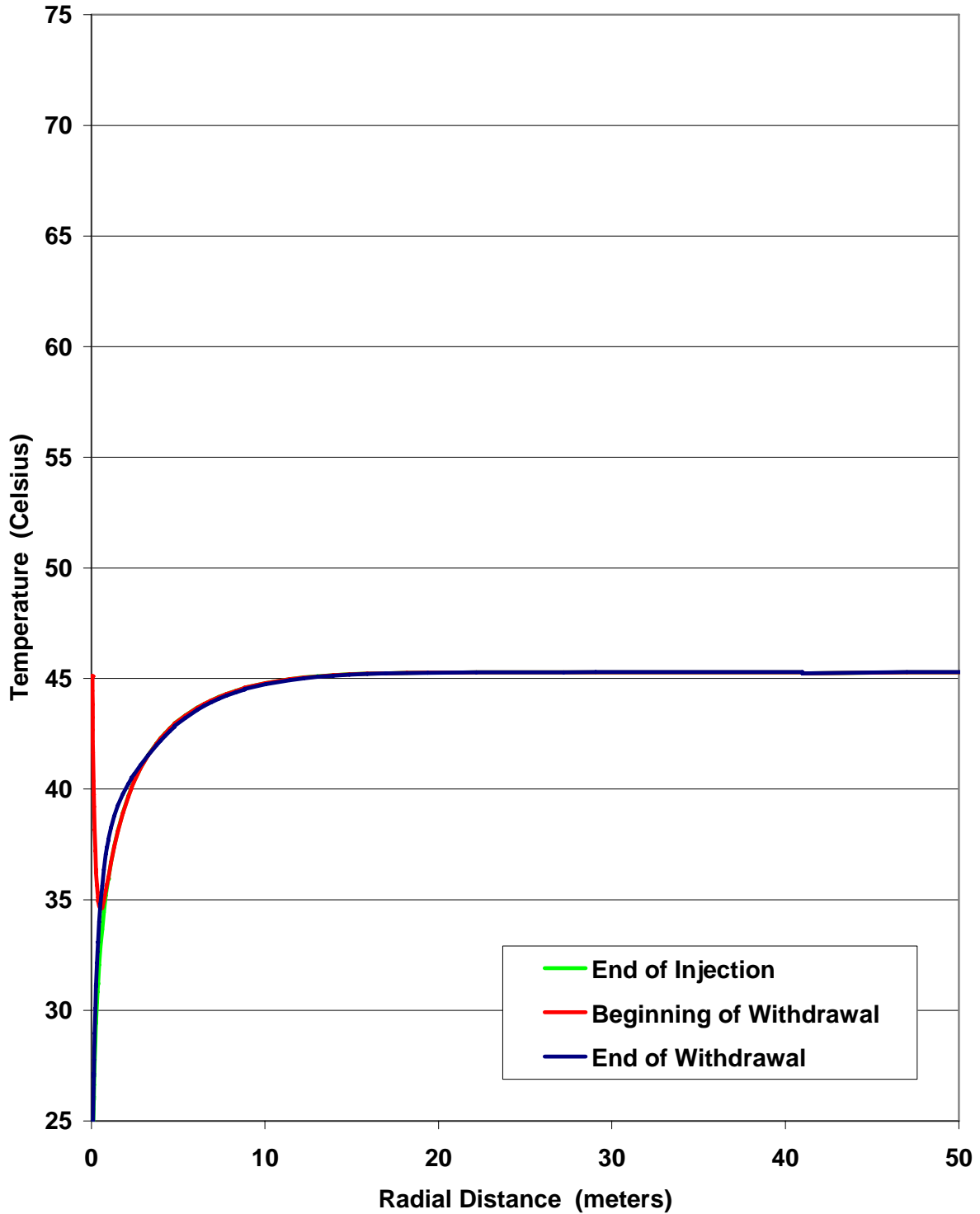
Figure 5-10. Temperature Profiles in the Casing and Rock Formation at a Depth of 1,511 Meters (4,960 Feet) During the 5th Gas Storage Operation Cycle of Reservoir Well No. 3.

5.4 THERMOMECHANICAL RESULTS

SPECTROM-32 was used to predict the structural response of the casing and host rock formation under the various operating conditions. As discussed in Chapter 2.0, the stress analyses performed considered stress contributions from: (1) casing weight; (2) product pressures, (3) thermally induced stresses, and (4) external ground pressures, including salt creep and reservoir compaction. Casing bending was not considered for these thermo–mechanical analyses. Casing bending of the reservoir well was considered during the detailed analyses of the connections provided in Chapter 6.0.

Because the problem modeled includes nonlinear aspects and the loads are not totally independent of each other, superposition of the results is not possible. Nevertheless, elastic solutions were performed to estimate the relative contribution of casing weight, product pressures, and thermally induced stresses to the total stresses induced in the casing of the three wells. Relative contribution was of interest because it provided an indication of the significance of each load type. Of particular interest was the magnitude of thermally induced stresses relative to the total axial stress. For these analyses, salt creep was not modeled, allowing the assumption that each of the casing loads acts independently of the other. However, this assumption did not allow the contribution of external ground pressure caused by salt creep or reservoir compaction to be estimated. Because the casing loads caused by ground pressures are strongly dependent on product pressure and temperature, the relative contribution of ground pressures to the casing load, independent of product pressure and temperature, cannot be determined.

Separate sections are provided below that present the results of the analyses used to estimate the relative contributions of casing weight, product pressure, and thermally induced stresses to the total state of stress expected for each of the three wells. Keep in mind that the results provided are only estimates since the loads are not independent of each other. Predicted results for the total axial stress in the casing from the combined loads of all sources follow a brief discussion regarding external ground pressure issues that were addressed in this study. The state of stress predicted at the lowest casing connection for the three wells concludes this chapter. Unless otherwise specified in this report, negative values are used to indicate compressive stresses in the casing.

5.4.1 Stresses From Casing Weight

For this study, it was assumed that the steel casing was installed with drilling fluid in the wellbore. Further, it was assumed that the drilling fluid was displaced with cement having the same density. Therefore, the drilling fluid and/or cement support some of the weight of the steel pipe through buoyancy; however, the stresses in the cement sheath are equal to that produced by gravitational loading. Figure 5-11 illustrates the vertical (axial) stresses in the steel casing following well completion for the three candidate wells.
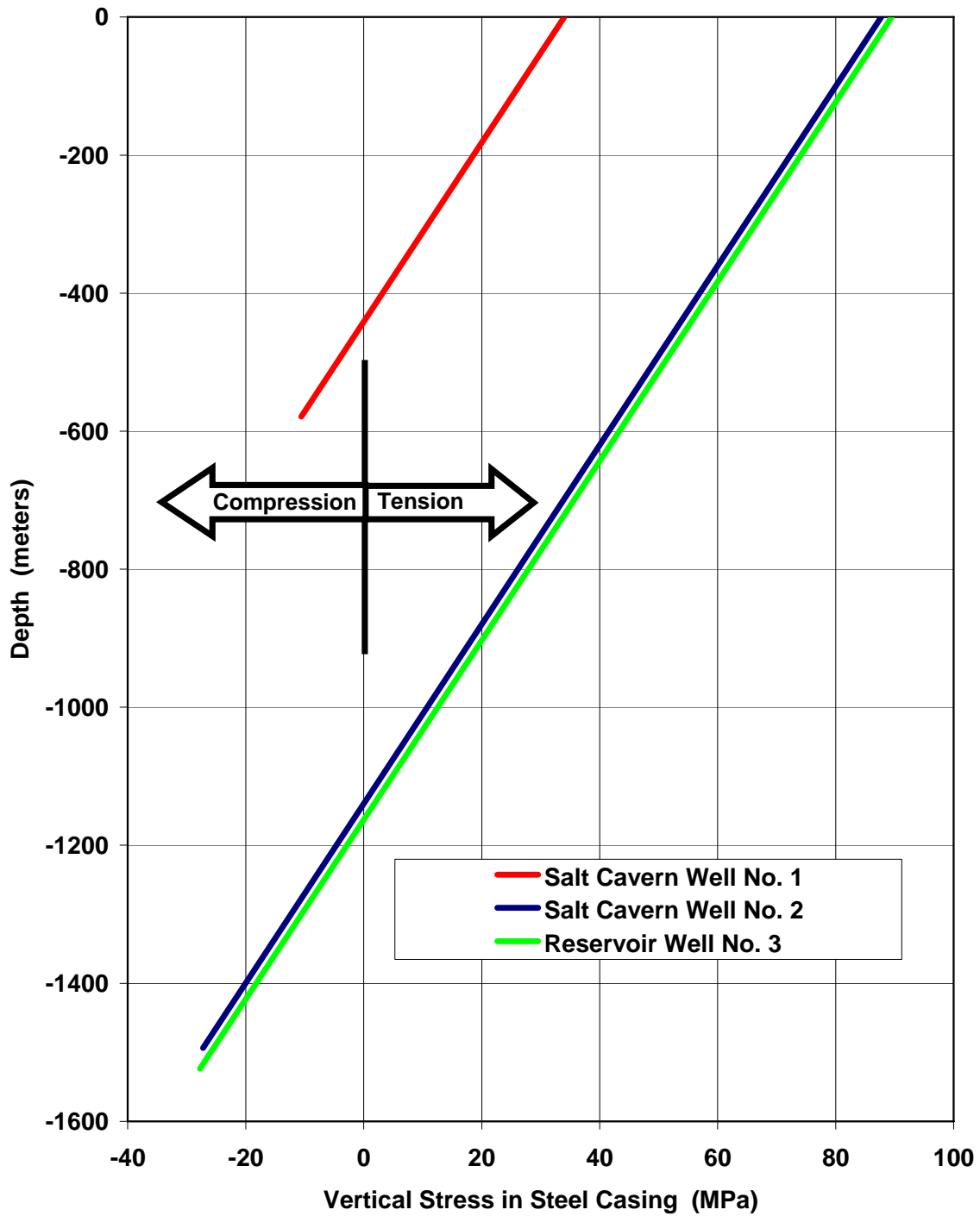
Figure 5-11. Vertical Stresses in Steel Casings of the Three Candidate Wells Following Well
Completion.

The vertical stress in the Salt Cavern Well No. 1 casing ranges from 34.03 MPa (4,935 psi) tension at the surface to a maximum compressive stress of –10.55 MPa (–1,530 psi) at the casing shoe. The vertical stress in the steel casing as a function of depth for Salt Cavern Well No. 2 and Reservoir Well No. 3 are about the same because the casing lengths differ by only 30.48 meters (100 feet). The stresses in the steel casing of Salt Cavern Well No. 2 range from 87.85 to –27.22 MPa (12,740 to –3,948 psi). Likewise, the vertical stresses in Reservoir Well No. 3 range between 89.54 and –27.77 MPa (12,986 and –4,028 psi).

5.4.2 Stresses From Product Pressures

Figure 5-12 illustrates the incremental vertical stresses in the steel casing that are produced by changes in gas pressure during storage operation of the three wells. In addition to the pressure change in the well, the predicted results include the elastic response associated with creation of the salt cavern and pressure changes in the salt cavern. Stresses associated with salt creep and pore pressure changes in the sandstone reservoir are discussed in Section 5.4.4. The stresses provided are the incremental stresses from the condition that was predicted to exist following well completion when the casing is full of drilling mud. Thus the stresses provided in Figure 5-12 are the result of replacing the pressure of the drilling mud with that of natural gas during storage plus the response associated with gas pressure changes in the caverns.

Although temperature of the gas and, therefore, the casing and rock, do not remain constant during pressurization and depressurization, isothermal conditions were assumed to compute the incremental stresses associated with changes in product pressure. The results provided in Figure 5-12 are at the two extreme cases of the gas cycle (minimum and maximum pressure) for each respective well. In general, increasing the gas pressure tends to produce a more tensile state of stress along the well axis (vertical stress). However, because of differences in wellhead pressure and fluid density, replacing the drilling mud with natural gas induces both tensile and compressive vertical stresses in the casings, depending on the depth and gas pressure. If the gas pressure is greater than the mud pressure at a given depth, incremental tensile stresses develop in the casing. Likewise, if the gas pressure becomes lower than the pressure exerted by the drilling mud, compressive axial stresses develop in the casing.

The effects of cavern creation and pressure changes in the caverns are evident by the nonlinear responses of the stress profiles in the lower portion of the casings. As shown in Figure 5-12, the curves depicting the incremental vertical stress at maximum and minimum pressure cross within the lower portion of the wells. Thus the lower portion of the casing becomes more tensile at minimum pressure compared to maximum pressure–contrary to the behavior of the rest of the well casing. This occurs because the gas pressure in the cavern pushing upward on the roof of the cavern produces more compression in the roof salt at the higher pressures. Compression of the salt induces incremental compressive stresses and strains in the casing.
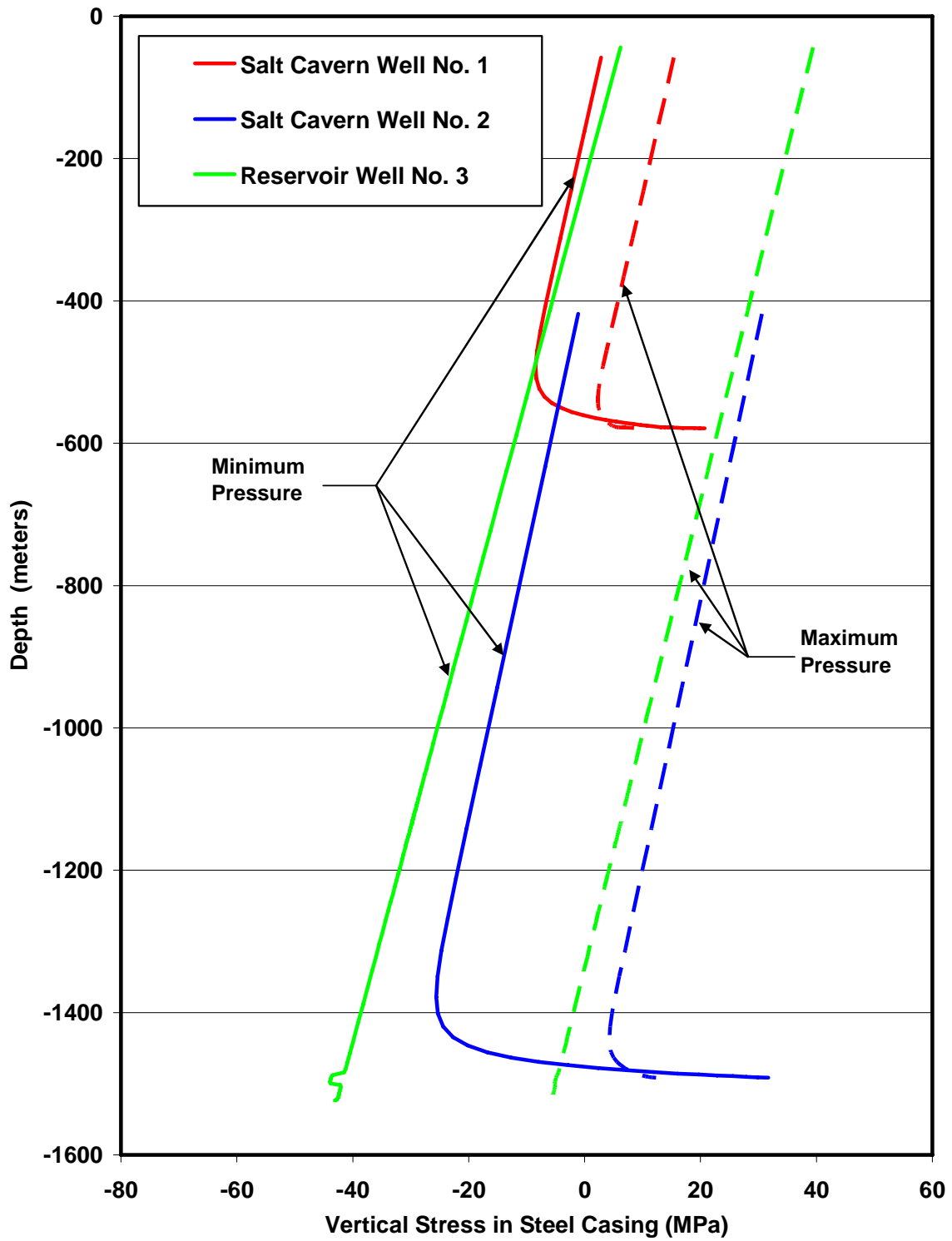
Figure 5-12. Incremental Vertical Stresses in the Steel Casings Induced by Product Pressure Changes.

5.4.3 Stresses From Thermal Expansion and Contraction

Following well completion, the temperature of the well casing is equal to the in situ temperature of the rock formation. An increase in the casing temperature above the in situ temperature results in the vertical stress becoming more compressive. Likewise, if the temperature of the casing becomes less than the in situ temperature, the vertical stress becomes less compressive. Figure 5-13 illustrates the incremental change in vertical stress associated with thermal expansion and contraction when the casings reach the two extremes in temperature during the last cycle of the simulations. In general, the thermally induced stresses become less compressive (or more tensile) with depth.

As shown in Figure 5-13, incremental tensile stresses are predicted when the casing temperatures are coolest during the gas cycle. Conversely, the entire casing becomes more compressive when the temperatures are the warmest in the casing. The influence of the cavern is evident by the nonlinear response of the temperature profiles. This is caused by the long-term temperature change of the rock formation as discussed in Section 5.3. Rock temperatures cooler than the in situ temperature induce compressive (or less tensile) strains in the casing because the salt has a higher coefficient of thermal expansion than the casing components.

5.4.4 External Ground Pressure Considerations

Whenever any underground opening is created, movement of rock toward and into the opening occurs. This is particularly the case for caverns in salt because they are typically large and the salt rock continually creeps. Following well completion, the radial force at the cement/salt interface is less than the initial in situ stress. If no other excavations are present to alter the state of stress, salt creep will increase the radial loading on the casing until it returns to the initial in situ stress. The added radial load will produce incremental radial, tangential, and axial compressive stresses in the casing.

Salt creep can also impart significant tensile loads on the casing. As the salt flows into the cavern, it can drag the casing downward toward the cavern. This stretching of the casing results in axial tensions. Because of material behavior mismatches, shear stresses will develop along the salt/cement interface. The shear stresses could potentially become great enough that the salt could flow along the cement sheath without additional elongation of the casing. However, the results of the two analyses of the salt cavern storage wells indicate that tensile stresses in the lower portion of well continually increase with each cycle. Whereas the axial tensions remain relatively low compared to the strength of the casing during the simulation period of Salt Cavern Well No. 1, stresses were predicted to exceed the tensile strength of the steel casing during the analysis of Salt Cavern Well No. 2. Thus using the conservative modeling approach, assuming that the interfaces remain perfectly bonded, indicates that elongation of the casing caused by salt creep will continue until the casing fails.
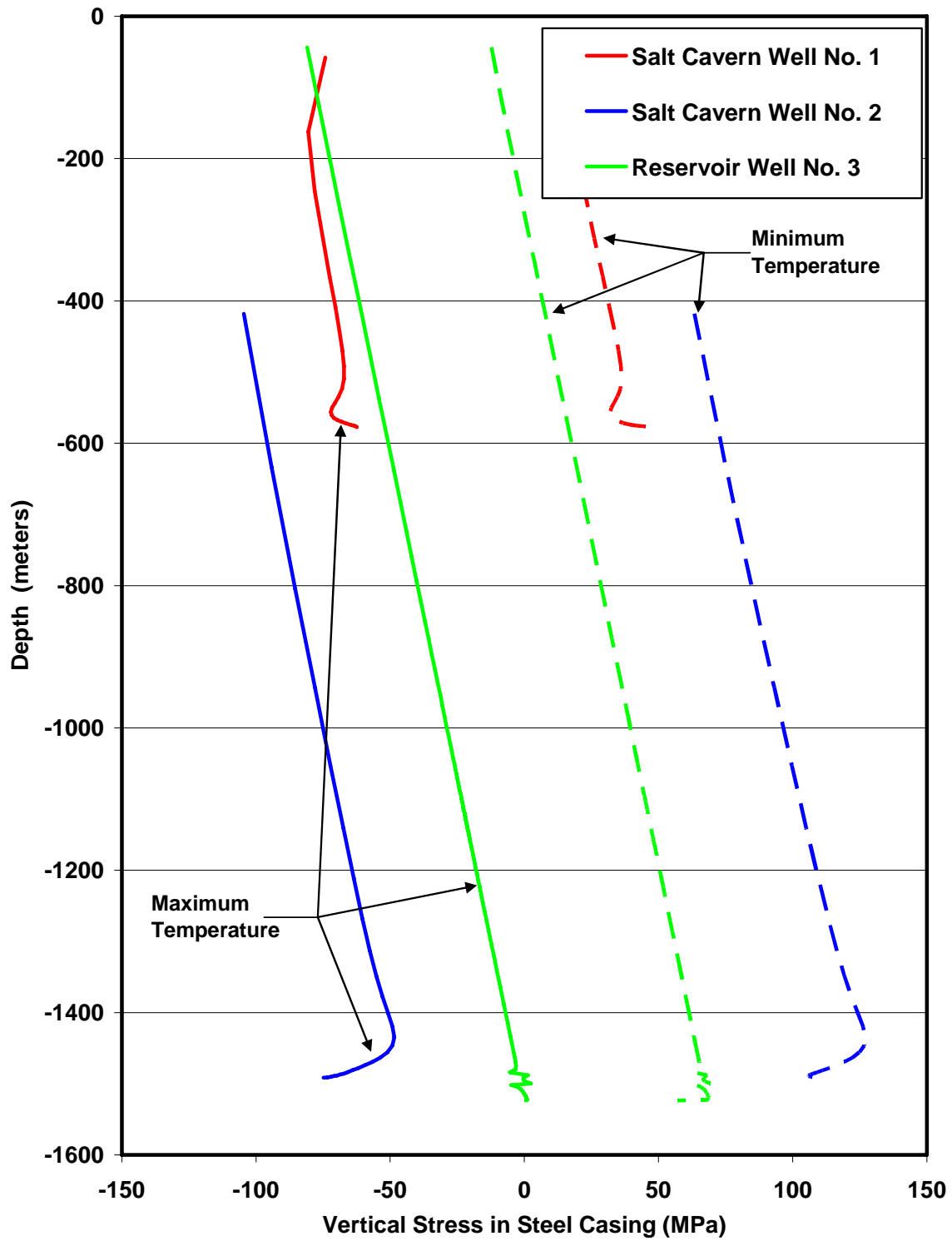
Figure 5-13. Incremental Vertical Stresses in the Steel Casings Induced by Temperature Changes.

RESPEC has considerable experience in modeling the creep deformation around underground openings in salt. Based on this experience and field validation exercises of large-scale tests in salt, it is reasonable to expect that large creep deformations would occur above deep salt caverns such as the one evaluated in this study. Other than the conclusion that creep deformations around the well casing will eventually accumulate to a magnitude that will cause the casing to fail, other possibilities not simulated by the models used in this study include: (1) slip occurs along the steel/cement and/or the cement/salt interface, limiting the axial tensions that can develop in the casing, (2) failure of the cement occurs limiting the drag force which leads to the development of tensile stresses in the steel casing, or (3) the casing seat is located sufficiently away from the cavern such that the well does not experience the large deformations predicted by this study. Little evidence has been reported that casing separations have occurred in brine production, liquid hydrocarbon, or natural gas storage wells in salt caverns in the United States, even for those caverns deeper than 1,524 meters (5,000 feet). Thus it is possible that interface slip or failure of the cement occurs for those well casings that are subject to relatively large vertical creep deformations. However, it is also possible that casing failures have occurred but remain undiscovered or have not been reported.

The modeling approach assuming the casing components and the salt remain perfectly bonded represents the worst-case scenario with regard to predicting axial stress in the casing. An investigation was performed to identify alternative approaches for evaluating the interaction between the casing components and the surrounding rock. The modeling approach had to be capable of predicting the response at the casing scale to include the potential for failure of the cement and slip along the casing interfaces and at the cavern scale to predict changes in the stress field and deformations that extend hundreds of meters from the cavern. The results of this investigation did not reveal a suitable method that was capable of predicting both the near-field and far-field responses. A few details of this investigation are given in Appendix A. The investigation did indicate that failure of the cement will precede failure of the steel pipe. Additionally, the analyses indicate that significant failure occurs within the cement before the tensile stresses in the pipe exceeds 345 MPa (50,000 psi). Based on these results, the maximum axial tensile stress in Salt Cavern Well No. 2 was limited to 345 MPa (50,000 psi) in this study. This tensile limit is unique to the assumptions, modeling approach, and properties used to evaluate the performance of Salt Cavern Well No. 2 and should not be construed as a general limit for cemented casings.

The axisymmetric assumption used for Reservoir Well No. 3 prevented the modeling of the 90-degree bend; thus, the full influence of reservoir compaction could not be determined directly using this model. To provide an estimate for the effects of ground pressure, it was conservatively assumed that the casing will experience the same strains as that of the rock formation. Gas pressures simulated in the sandstone reservoir ranged between 0.41 and 22.06 MPa (600 and 3,200 psi) during the analysis of Reservoir Well No. 3. Because it was assumed that the pressure distribution is uniform within the storage formation, the overburden formations move down uniformly over the entire formation, without bending. As a result, the

sandstone was assumed to expand and contract uniformly in response to pressure changes. The total vertical displacement across the thickness of the sandstone formation was predicted to be about 5.1 centimeters (2 inches). Assuming this deformation is evenly distributed over the 30.48-meter (100-foot) reservoir thickness results in an incremental axial strain of 0.17 percent. This translates to a cyclic stress amplitude in the casing body of 324 MPa (46,990 psi). This result was used to provide a conservative estimate for the casing loads caused by external ground pressures for Reservoir Well No. 3.

5.4.5 Total Vertical Stress From Combined Loads

Axisymmetric finite element models were used to determine the combined loads for the sources identified. The predicted results of interest are the total state of stress in the steel casing and how that stress varies during gas storage operation. Figure 5-14 shows the predicted vertical stresses in the steel casing during the final gas service cycle resulting from the combined loads. The results shown in Figure 5-14 represent the range of conditions that the casing experiences. Thus the stresses in the casing at any given depth fall between the two curves identified for the wells shown in Figure 5-14.

For the salt cavern wells, the least-tensile (or most-compressive) vertical stresses are predicted at the beginning of the withdrawal cycle. At this time during the cycle, the temperature of the casing is the warmest and the gas pressure is the greatest. The most-tensile vertical stresses in the salt cavern casing are predicted to occur at the end of withdrawal when the gas temperature is the coolest and the pressure is the lowest.

Because of the slow withdrawal rates assumed for the reservoir well, the temperature of the gas does not become significantly cooler than the storage formation temperature during the withdrawal phase. As a result, the least-tensile (or most-compressive) vertical stresses are predicted to occur at the end of withdrawal when the pressure is lowest and the gas temperature is warmest. Likewise, the most-tensile stresses in the reservoir well casing occur at the end of injection when the temperature is the coolest and the gas pressure is the greatest. The results for the Reservoir Well No. 3 shown in Figure 5-14 do not include the loads from bending or reservoir compaction. These loads occur in the lower portion of the well that was not included in the axisymmetric model. The loads from bending and reservoir compaction are considered by the connection models as discussed in Chapter 6.0.

5.4.6 Stress Condition at the Lowest Casing Connection

Based on the results shown in Figure 5-14, the largest cyclic loads and the most-tensile states of stress occur at the bottom of the salt cavern well casings. Therefore, it is anticipated that if failure were to occur, it would happen in the lower portion of the casing. The conditions at the lowest joints were selected for further evaluation using the connection models. Table 5-1 provides the predicted stresses in the pipe at the location of the lowest joint in the three
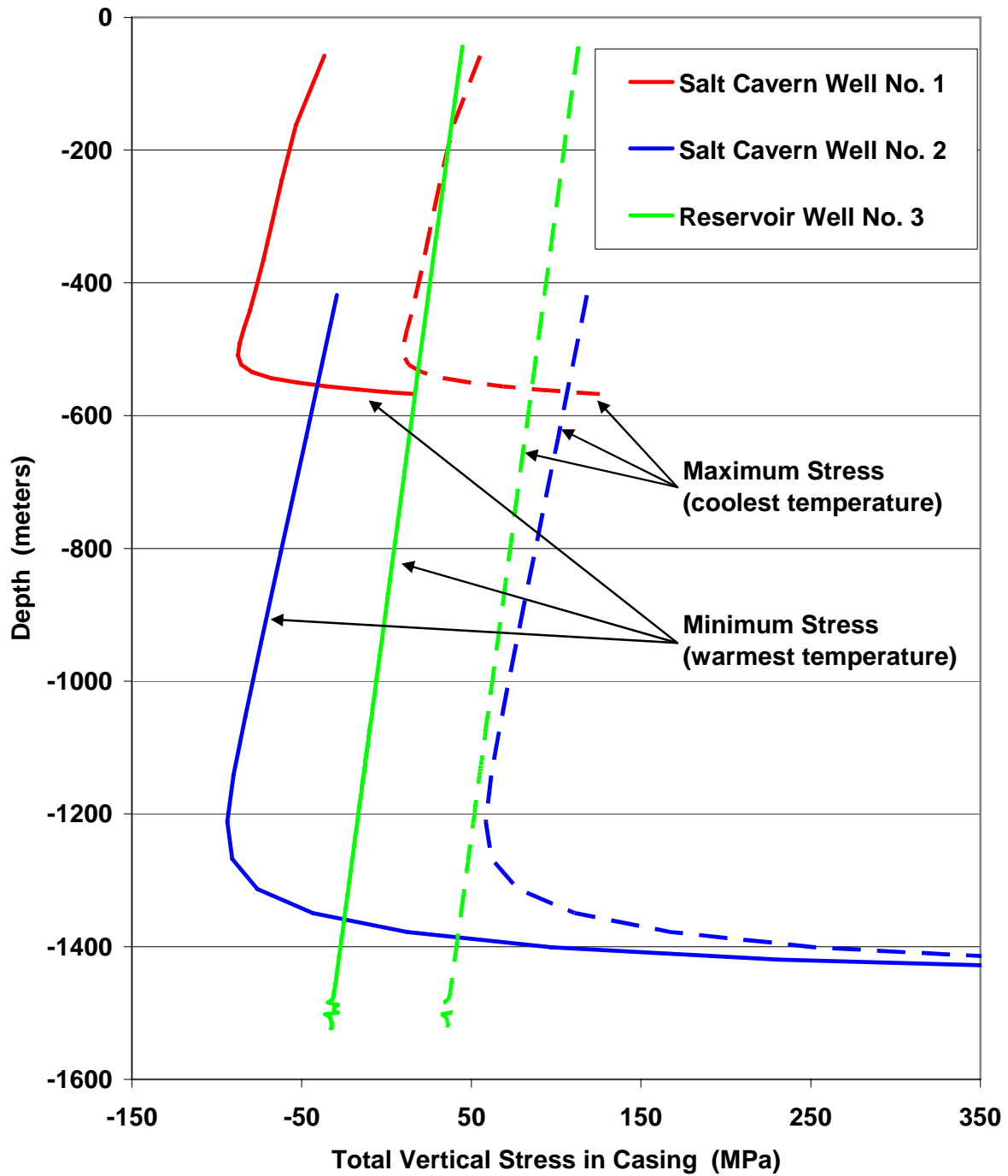
Figure 5-14. Two Extremes for Total Vertical Stress in the Steel Casings Predicted During the Last Cycle of the Simulations.

candidate wells. Stresses are provided at times either immediately preceding or following: (1) the start of injection, (2) the end of injection, and (3) the start of withdrawal. These times provide the maximum range predicted for axial stress in the casing during the final gas service cycle.

Because the model predictions of Salt Cavern Well No. 2 for axial stress exceed the limiting value of 345 MPa (50,000 psi) identified in this study, the axial stress at the start of injection was limited to 345 MPa (50,000 psi), as shown in Table 5-1. As previously mentioned, the maximum axial tensions occur in the lower portion of the salt cavern well casings at the end of withdrawal when the pressure in the cavern is at a minimum pressure and the temperature of the casing is the coolest. The net effect of increasing the casing temperature and pressure in the well and cavern during injection is to produce a more compressive state of stress in the lower portion of the casing. Based on the results of thermomechanical analyses of Salt Cavern Well No. 2, the tensile stress at the lowest connection will be reduced by 110 MPa (15,920 psi) by the time injection is complete. The tensile stress in the casing is reduced even further (an additional 71 MPa (10,295 psi)) during the early stages of withdrawal. These results provide the best available estimates for the range of cyclic loading that is expected for Salt Cavern Well No. 2 and were used in defining the conditions for the connection models for this well.

Table 5-1. Candidate Well Conditions During the Final Gas Service Cycle Simulated

Stage	Internal Pressure		External Pressure		Axial Stress		Casing Temperature	
	MPa	psi	MPa	psi	MPa	psi	°C	°F
Salt Cavern Well No. 1								
Start Injection	3.30	480	9.87	1,430	125.45	18,195	29.61	85
End Injection	11.16	1,620	16.59	2,405	49.88	7,235	49.97	122
Start Withdrawal	11.16	1,620	18.06	2,620	20.14	2,920	64.41	148
Salt Cavern Well No. 2								
Start Injection	8.47	1,230	20.38	2,955	344.74	50,000	26.81	80
End Injection	28.72	4,165	33.33	4,835	234.97	34,080	54.86	131
Start Withdrawal	28.72	4,165	36.41	5,280	163.99	23,785	85.60	186
Reservoir Well No. 3								
Start Injection	4.63	670	21.02	3,050	1.28	185	21.11	70
End Injection	24.66	3,575	25.14	3,645	35.85	5,200	21.11	70
Start Withdrawal	24.66	3,575	27.14	3,935	−32.41	−4,700	46.11	115

(a) Tensile stress in casing limited to the 345-MPa (50,000-psi) maximum.

6.0 RESULTS AND DISCUSSION OF THREADED CONNECTION MODELS

The objective of the connection modeling was to determine the fatigue life corresponding to the axial force and pressure cycles estimated from the casing load analyses given in Chapter 5.0. The first stage of the connection analysis consisted of determining the stresses that exist in the connection following the connection make-up procedure. During the next stage of the analysis, the load cycles estimated in the thermomechanical casing analyses were imposed to determine the stress and strain distribution in the connection. These stress and strain values were then used to estimate the fatigue life of the connection in terms of the number of injection-withdrawal cycles that can be tolerated.

6.1 INITIAL CONNECTION LOADS

The first step in the connection analysis was to model the make-up condition of the API 8-Round STC connection with the magnitude of the interference between the pin and coupling based on the make-up turns specified by Recommended Practice API-5B [American Petroleum Institute, 1999]. Figure 6-1 shows that because of the large amount of initial interference between the pin and coupling resulting from make-up, the stress in localized areas of the connection will exceed the elastic limit of the material, resulting in plastic (unrecoverable) strain.

RSI-1546-06-024
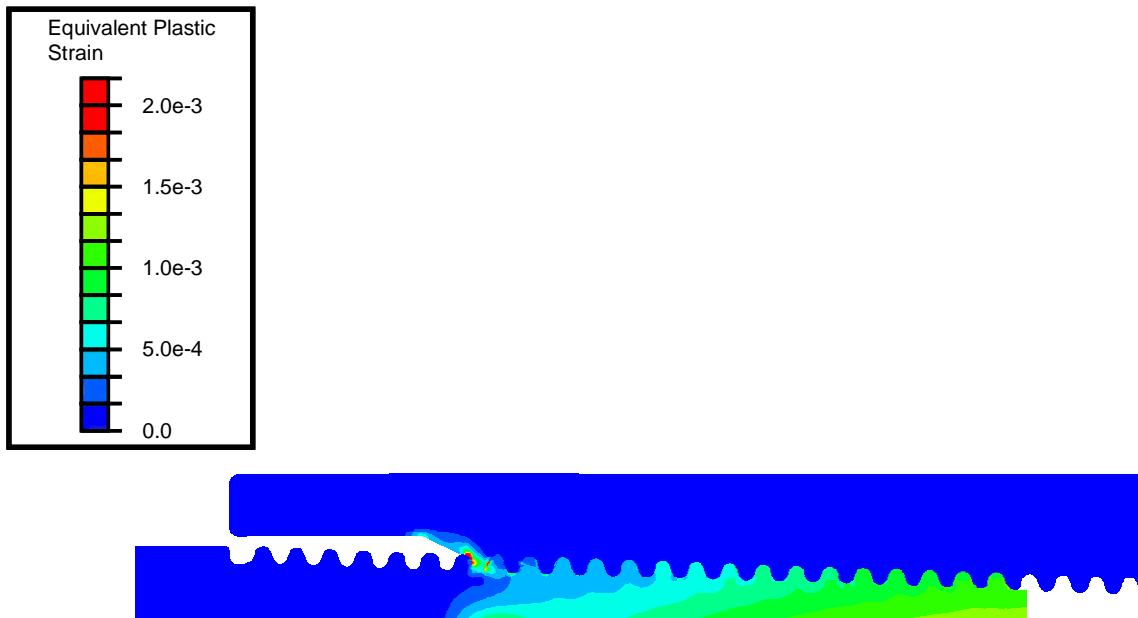
Figure 6-1. Plastic Strain Contours in an 8-Round STC Connection Following Make-Up to API-5B Specifications.

Once the casing is made up and installed in the well, storage operation cycles of gas injection and withdrawal impose temperature and pressure cycles that generate additional plastic strain in localized areas of the connection. Examples of the distribution of the axial strain in the 140-millimeter (5.5-inch, 15.5 lb/ft) J-55 connection at the end of the injection phase are presented for connections with (Figure 6-2) and without (Figure 6-3) the coupling face welded to the pipe body.

RSI-1546-06-025
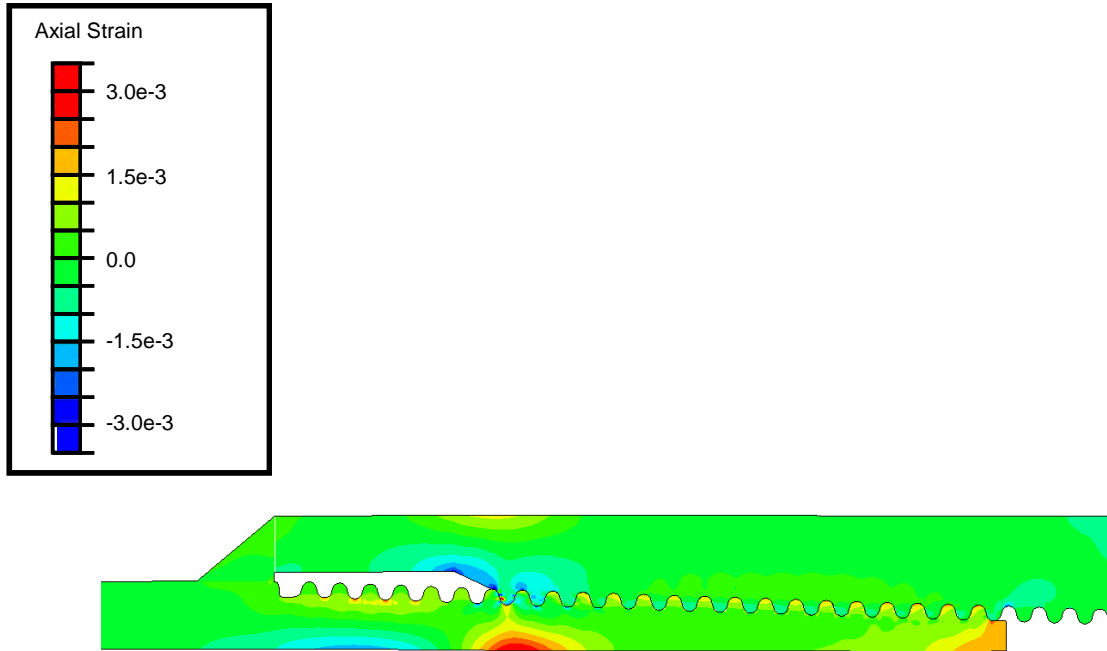
Figure 6-2. Example Results Showing Axial Strain Distribution in a Connection With a Welded Coupling Face.

Figure 6-3 identifies four areas where axial strain is localized: (1) the pin thread root at the first engaged thread, (2) the pin inside diameter (ID) surface underneath the first engaged thread, (3) the outside diameter (OD) surface of the coupling at the coupling entry plane, and (4) the ID surface of the coupling at the coupling entry plane. A multiaxial strain state typically exists at these locations (not just axial strain) both following make-up and under operating conditions. Therefore, the fatigue assessment was based on the multiaxial plastic strain state in these four key locations.

6.2 STRAIN-BASED FATIGUE ASSESSMENT CRITERIA

Traditional stress-based fatigue criteria are intended for situations where the stresses do not exceed the yield strength of the material and no plastic strain occurs. These criteria were considered to be inappropriate for this analysis because of the fact that the imposed stresses

exceed the yield strength of the material in the connection. Therefore, it was necessary to adopt a strain-based fatigue criterion that considers the magnitude of plastic strain cycles in the connection.

RSI-1546-06-026
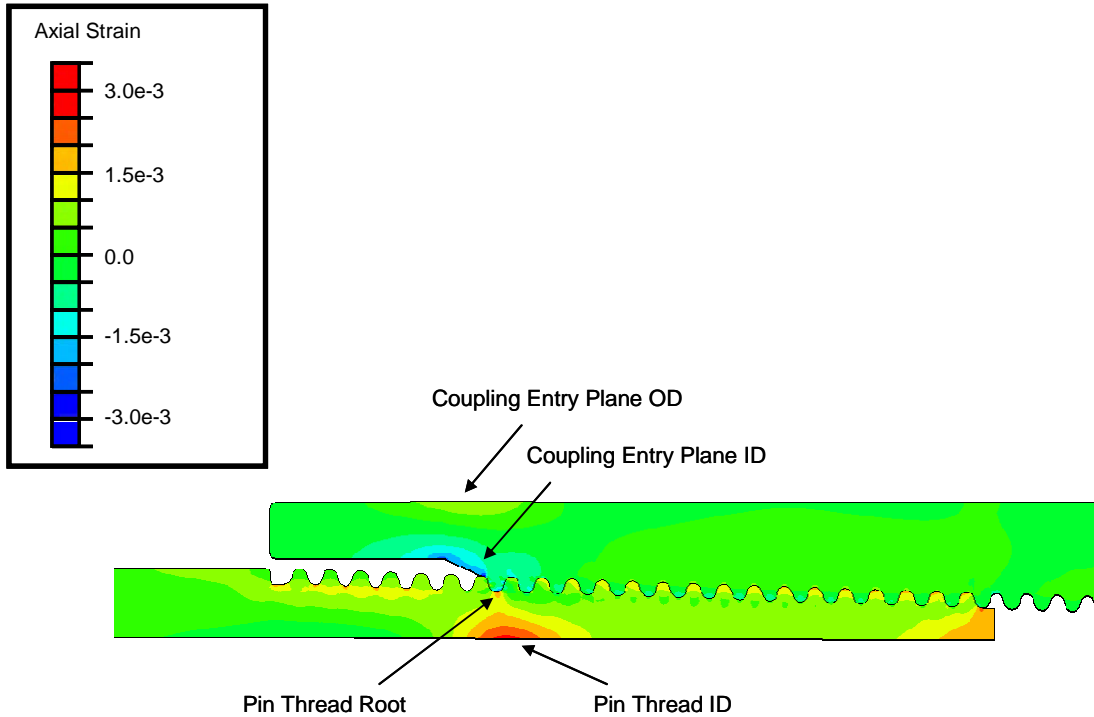
Figure 6-3. Example Results Showing Axial Strain Distribution in a Connection Without a Welded Coupling Face (Arrows Indicate Locations Where Plastic Strain Concentrations Increase the Likelihood of Fatigue-Related Failures).

As noted by Dowling [1998], the development of reliable fatigue prediction methods for multiaxial loading conditions with plastic deformations is currently an area of active research. While reasonable fatigue life estimates are possible for relatively simple situations, significant uncertainty exists as to the best procedure to use for complex nonproportional loading cases (e.g., structural components where the ratios of the principal stresses change and where the principal axes of those stresses may also rotate).

Several strain-based fatigue criteria have been developed for problems involving multiaxial strain. One of the most widely used approaches was developed by Morrow [Dowling, 1998]. The Morrow approach was later modified [Dowling, 1998], resulting in the following relationship among equivalent strain, the number of load cycles, and mean stress:

$$\overline{\varepsilon}_a = \frac{\sigma'_f}{E}\left(1 - \frac{\overline{\sigma}_m}{\sigma'_f}\right)\left(2N_f\right)^b + \varepsilon'_f + \left(2N_f\right)^c \tag{6-1}$$

where:

$$\overline{\varepsilon}_a = \text{equivalent strain}$$

$$\sigma'_f = \text{true stress at material fracture}$$

$$\varepsilon'_f = \text{true strain at material fracture}$$

$$b = \text{material fatigue constant (elastic slope)}$$

$$c = \text{material fatigue constant (plastic slope)}$$

$$E = \text{modulus of elasticity}$$

$$\overline{\sigma}_m = \text{effective mean stress}$$

$$2N_f = \text{number of full cycles.}$$

In this analysis, the static stresses and strains in the critical locations in the connection were entered in the modified Morrow equation to determine the number of load cycles $(2N_f)$ that can be tolerated.

The equivalent strain amplitude $\overline{\varepsilon}_a$ describes the multiaxial state of strain existing at one of the critical locations in the casing connection. Several alternative approaches have been proposed for calculating the equivalent strain amplitude based on the strain amplitudes along the principal axes. For this analysis, the general form of equivalent strain amplitude was assumed to be:

$$\overline{\varepsilon}_a = \beta' \sqrt{\left(\varepsilon_1 - \varepsilon_2\right)^2 + \left(\varepsilon_2 - \varepsilon_3\right)^2 + \left(\varepsilon_3 - \varepsilon_1\right)^2} \tag{6-2}$$

where $\varepsilon_1, \varepsilon_2,$ and ε_3 are the principal strain amplitudes and $\beta' = 2/3$ for the octahedral shearing strain and $\beta' = \sqrt{2}/3$ for the von Mises equivalent strain. Sines and Ohgi [1981] have suggested that the octahedral shear strain transformation correlates reasonably well with experimental results.

The material constants $\sigma'_f, \varepsilon'_f, b,$ and c are usually determined through physical tests. The true stress (σ'_f) and true strain (ε'_f) at material fracture were determined for the J-55 and K-55 materials based on C-FER's previous coupon testing programs [Humphreys et al., 1991]. However, these coupon tests did not determine the fatigue constants b and c for these materials.

An extensive review of the literature on fatigue properties of metals was not able to identify specific data for J-55 or K-55 materials. Dowling [1998] provides a general overview of the fatigue performance of various metals. It is reported that the plastic slope c ranges from –0.5 to –0.8 for most engineering metals. Relatively steep elastic slopes, with $b = -0.12$ are common for soft metals (annealed), and shallow slopes, nearer $b = -0.05$, are common for hardened metals.

According to Boller and Seeger [1987a; 1987b], the material CK-35 (which is similar in chemical composition and strength to K-55) shows a fatigue behavior described by $b = -0.075$ and $c = -0.46$. In the absence of any specific fatigue performance data for K-55 material, the values for the CK-35 material were used in this analysis.

The J-55 material is made by thermomechanically forming a sheet into a tube. The resulting microstructure of this material is that of a classic worked steel with evidence of rolling. It is expected J-55 would have a high dislocation density in the manufactured form. Upon cycling, this material is expected to soften as a result of dislocation annihilation, resulting in a cyclic work-hardening coefficient much lower than the monotonic value. This would result in a c value that is larger than the median value of -0.6, possibly being as high as -0.7. On the other hand, the b value for J-55 is likely lower than the median value of -0.085. Therefore, it was assumed that J-55 has a b value of -0.06 for this analysis. Table 6-1 summarizes the material constants used for the fatigue assessment of J-55 and K-55 materials in this report. These values were considered to be the best estimates based on the available data.

Table 6-1. Material Constants for Fatigue Assessment of J-55 and K-55 Grade Casing

Parameter	Units	J-55	K-55
σ'_f	MPa	496	869
ε'_f	%	33.6	49.8
b		-0.06	-0.075
c		-0.7	-0.46

The relationships that exist among equivalent strain, mean stress, and number of cycles for J-55 and K-55 materials based on the modified Morrow approach are shown in Figures 6-4 and 6-5, respectively. These figures indicate that pipe constructed of K-55 material should be much more resistant to fatigue than pipes constructed of J-55 material.

6.3 RESERVOIR STORAGE CONNECTION RESULTS

For the reservoir storage application, the casing strings were assumed to be 140-millimeter- (5.5-inch-, 15.5 lb/ft) diameter J-55 with API 8-Round STC connections. Six load cases were defined based on the results of the well models as summarized in Table 6-2.
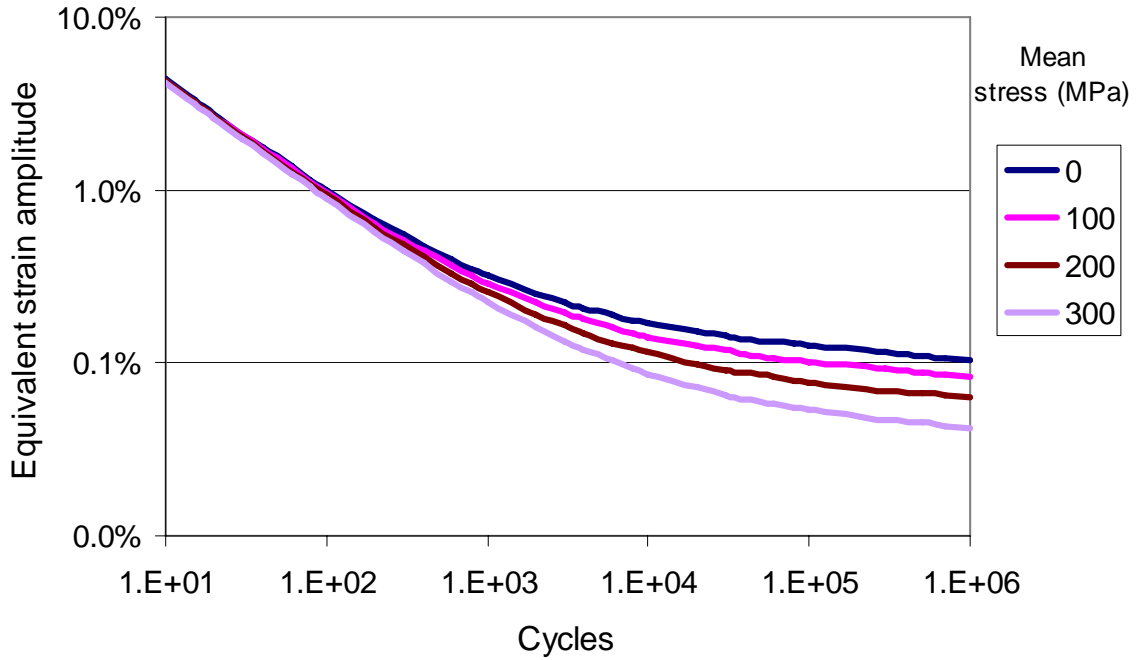
Figure 6-4. Relationship Among Equivalent Strain Amplitude, Mean Stress, and Cycles for J-55 Material Based on Modified Morrow Approach.
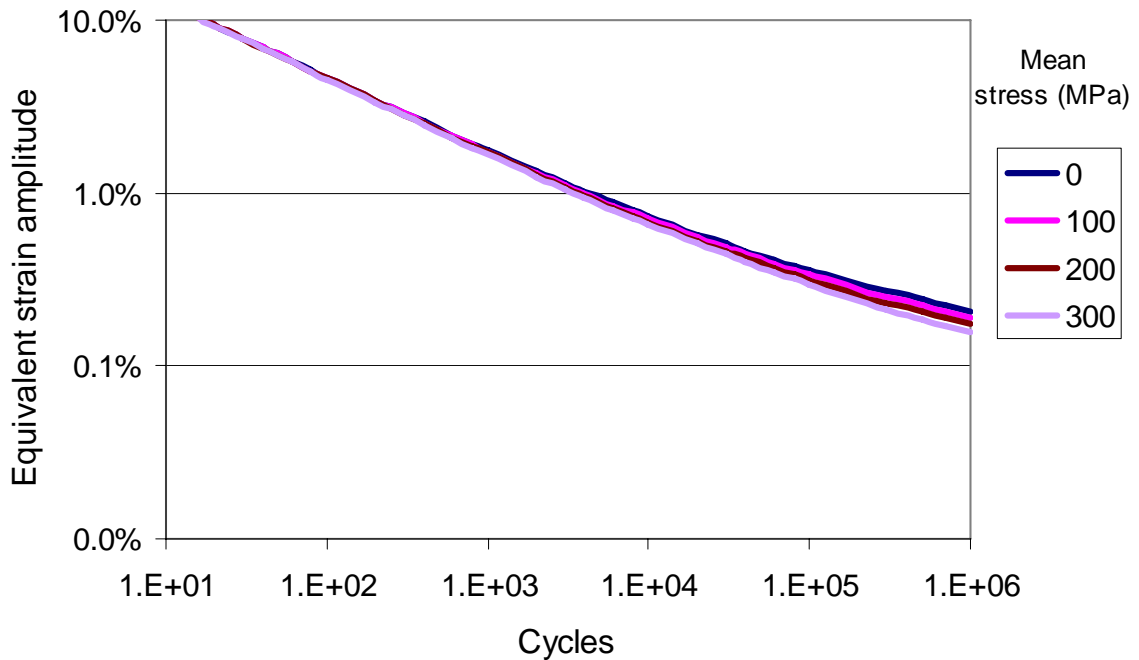
Figure 6-5. Relationship Among Equivalent Strain Amplitude, Mean Stress, and Cycles for K-55 Material Based on Modified Morrow Approach.

Table 6-2. Load Cases for the Reservoir Storage Connection Model

Load Case	Curvature (degrees/30 m)	Incremental Axial Strain (%)	Welded Coupling
1	0	N/A	No
2	9	N/A	No
3	9	−0.17%	No
4	9	0.17%	No
5	9	−0.17%	Yes
6	9	0.17%	Yes

Load Case 1 modeled the simplest case of a straight casing string without welded connections. Load Case 2 considered the impact of well curvature (9⁰ per 30 meters) associated with the build section in the directional well assumed for the reservoir storage facility. Load Cases 3 and 4 considered the incremental longitudinal (axial) strains of 0.17 percent imposed by compaction of the storage reservoir resulting from pore pressure changes during a gas cycle. Load Cases 5 and 6 considered the additional impact of welded connections (weld material connecting the coupling face to the pipe body).

The incremental strain created by pore pressure changes in the sandstone reservoir was superimposed on the loads estimated for the well casing given in Chapter 5.0. The casing strains caused by reservoir expansion/compaction can range from compressive to tensile, depending on the relative movement of the formations in different intervals of the well. As shown in Table 6-2, incremental compressive strains on the casing were simulated by Load Cases 3 and 5 and incremental tensile strains were simulated by Load Cases 4 and 6.

Each load case considered four load steps corresponding to the loading conditions determined previously at: (1) start of injection, (2) end of injection, (3) start of withdrawal, and (4) end of withdrawal, as shown in Figure 6-6. Each load step was defined with a different internal and external pressure, axial force, and temperature.

Figures 6-7 to 6-12 show examples of the results from each of the six load cases analyzed for the reservoir storage well casing at the end of injection (Load Step 2). Figure 6-7 shows a uniform band of strain at the pin thread ID that extends around the inner surface of the pipe for Load Case 1. Comparison of Figures 6-7 and 6-8 shows the effect of the well curvature by the intensification of this strain near the top of the connection and by the corresponding reduction at the bottom. Applying the incremental subsidence-related strains in Load Cases 3 and 4 appear to reduce the axial strain in this area, as shown in Figure 6-9 and 6-10. Welding the coupling tends to intensify the strain in the pin thread ID area, as shown in Figures 6-11

and 6-12. This effect appears to be related to the assumption that the weld isolates the OD of the pin threads that are not engaged from the exterior pressure on the pipe. The pressure in this area was assumed to be equal to atmospheric pressure as a worst-case scenario.

RSI-1546-06-029
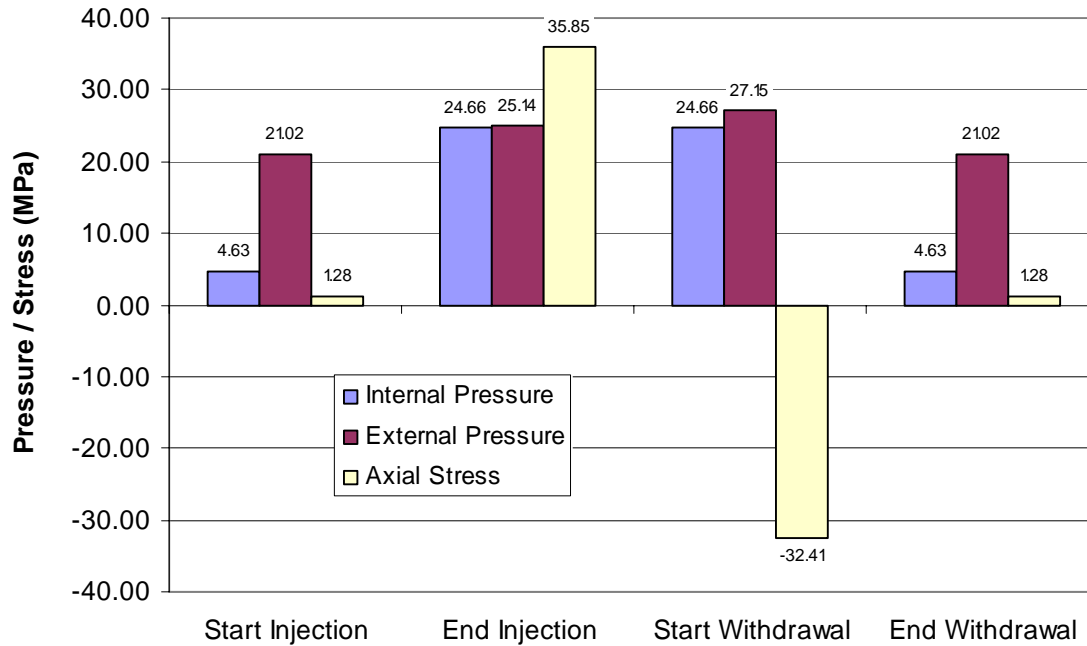
Figure 6-6. Load Steps for Reservoir Storage Well Connection Model.

For each load case, the estimated stress and peak plastic strain values at the four stress localization areas in the connection (Figure 6-3) were tabulated from each of the four load steps. This resulted in 16 combinations of stress and plastic strain in the different areas of the connection during each gas cycle. These stress and strain values were used to estimate the number of cycles to failure for each area in the connection. In each case, the area that was predicted to withstand the lowest number of cycles to failure was considered to be the critical location that would limit the performance of the entire connection. The analysis results showed that the coupling entry plane OD was never the limiting location but that fatigue failures may occur in the other three areas (coupling entry plane ID, pin thread root, and pin thread ID), depending on the combination of stress and strain imposed by the injection-withdrawal cycle.

The results of the fatigue assessment are presented in Table 6-3 and in Figure 6-13. If only the thermally induced and gas pressure induced loads are considered for a straight wellbore (Case 1), the fatigue life is approximately 1,400 cycles, with failures occurring in the coupling entry plane ID. The analysis shows that well curvature (Case 2) reduces the estimated fatigue life to 790 cycles.
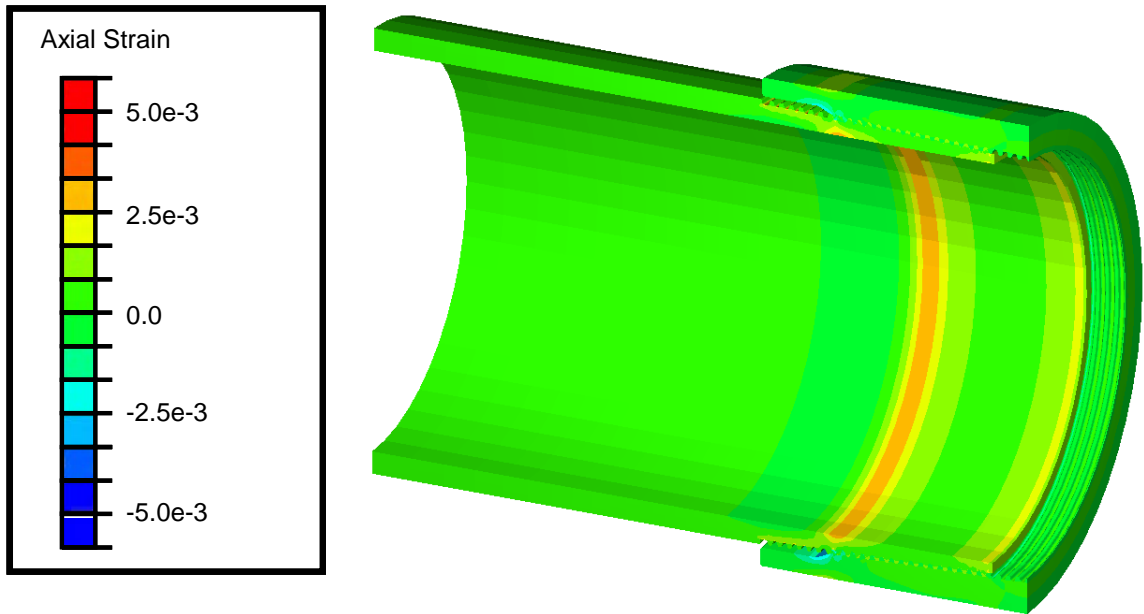
Figure 6-7. Axial Strain in Reservoir Well No. 3 for Load Case 1 at the End of Injection (Load Step 2).

RSI-1546-06-031
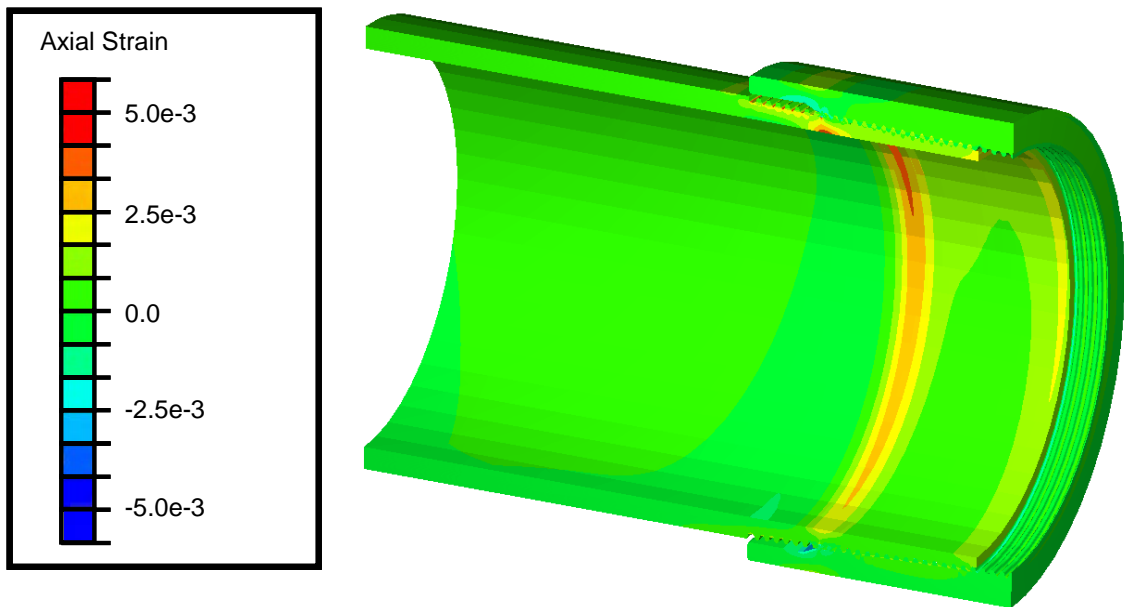
Figure 6-8. Axial Strain in Reservoir Well No. 3 for Load Case 2 at the End of Injection (Load Step 2).

65
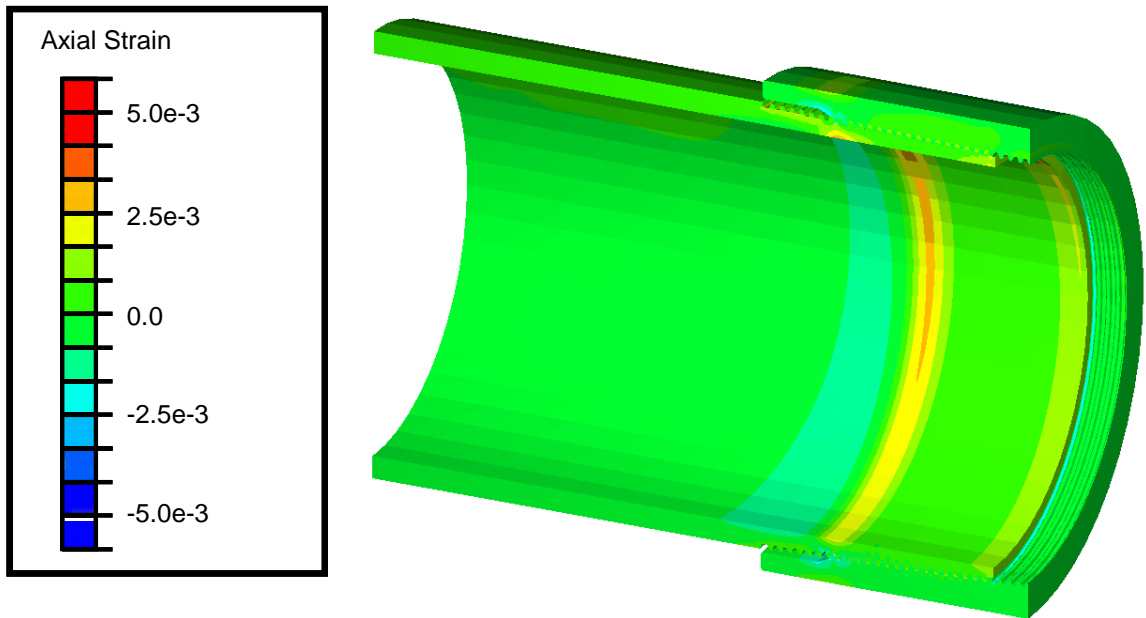
Figure 6-9. Axial Strain in Reservoir Well No. 3 for Load Case 3 at the End of Injection (Load Step 2).
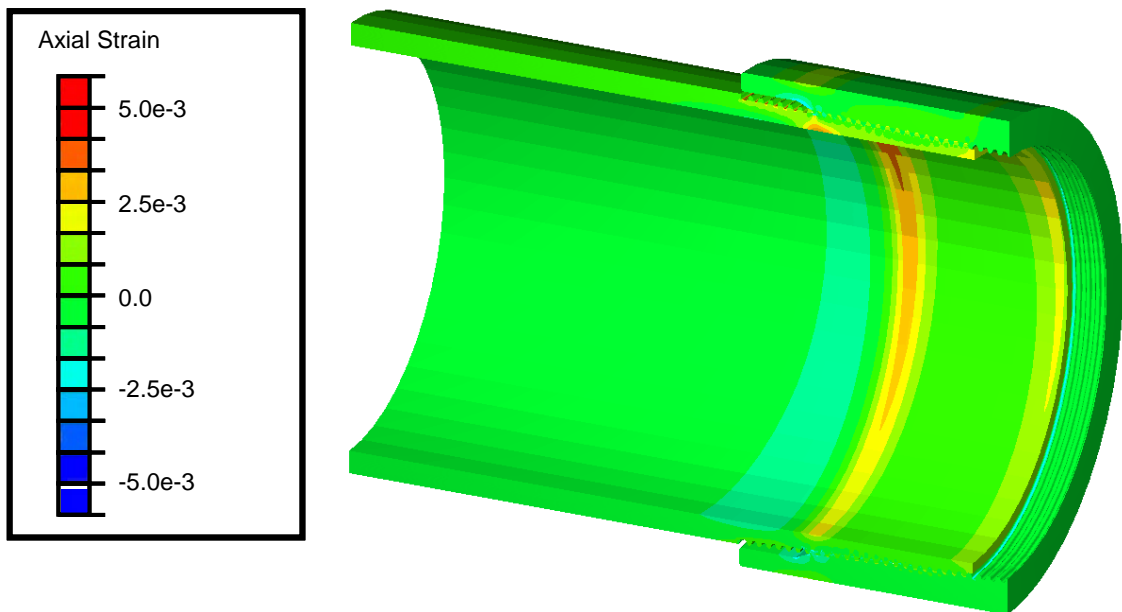
Figure 6-10. Axial Strain in Reservoir Well No. 3 for Load Case 4 at the End of Injection (Load Step 2).
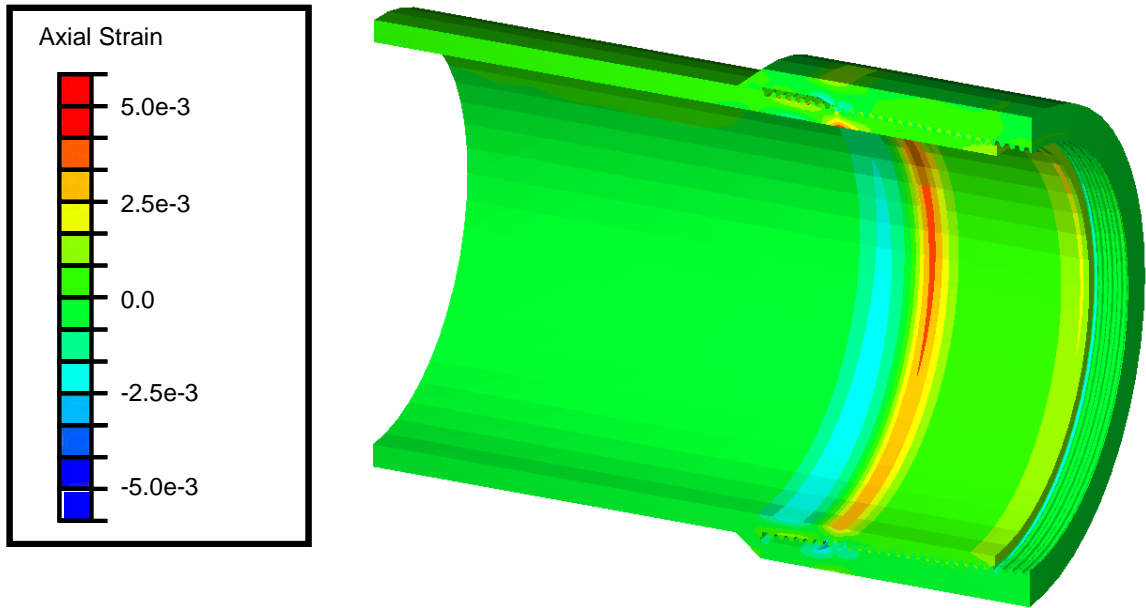
Figure 6-11. Axial Strain in Reservoir Well No. 3 for Load Case 5 at the End of Injection (Load Step 2).
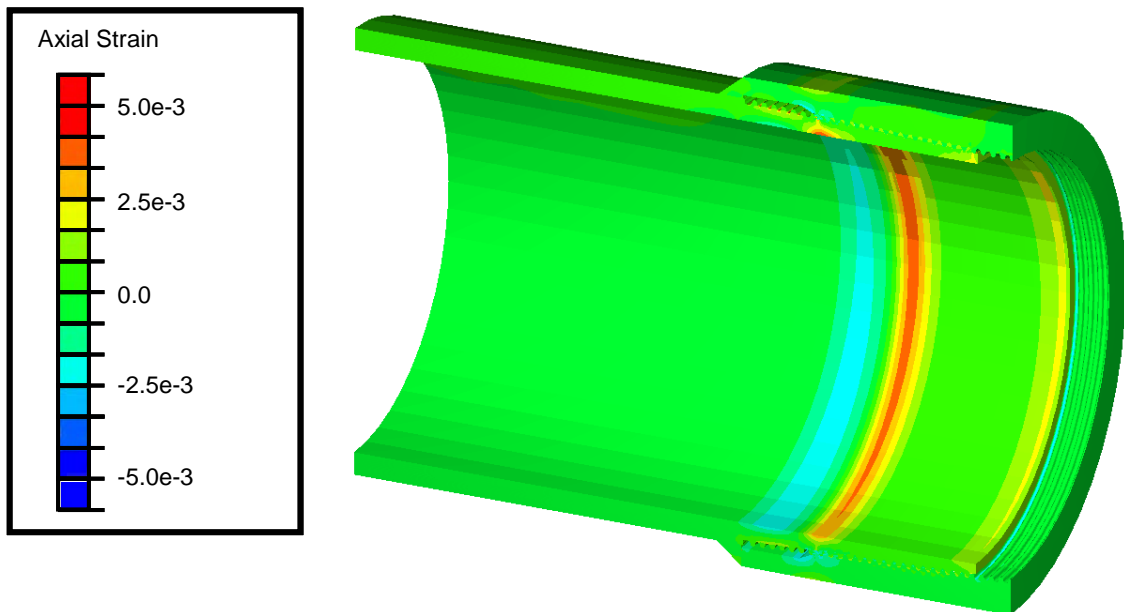
Figure 6-12. Axial Strain in Reservoir Well No. 3 for Load Case 6 at the End of Injection (Load Step 2).

Table 6-3. Fatigue Life Estimates of the Reservoir Storage Well Connection Model

Load Case	Curvature (°/30 meters)	Incremental Axial Strain (%)	Welded Coupling	Fatigue Life Pin Thread (cycles)	Fatigue Life Coupling ID (cycles)
1	0	N/A	No	2,744	1,440
2	9	N/A	No	2,005	790
3	9	−0.17%	No	1,099	1,175
4	9	0.17%	No	235	1,868
5	9	−0.17%	Yes	1,880	372
6	9	0.17%	Yes	1,732	2,631

RSI-1546-06-036
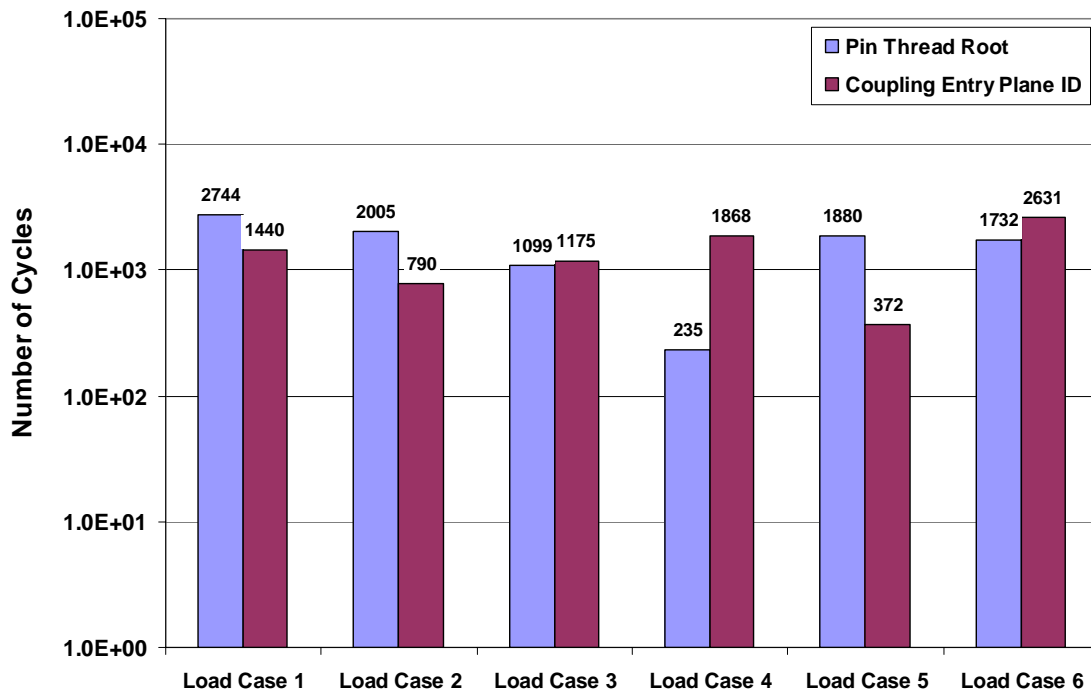
Figure 6-13. Fatigue Life for Various Load Cases of the Reservoir Storage Connection Model Assuming 5.1 Centimeters (2.0 Inches) of Formation Movement With Each Gas Cycle.

The analysis shows that where compaction imposes incremental compression on the casing (Case 3), the fatigue life decreases further and the failure location changes to the pin thread root of the connection. Compaction-related tensile strain (Case 4) reduces the fatigue life significantly to its lowest level with failures occurring in the pin thread root after 235 cycles.

These results include significant uncertainty associated with the assumed degree of formation movements caused by pore pressure changes in the reservoir. To evaluate the sensitivity of the results to these assumptions, the analysis was repeated assuming changes in axial casing stress caused by formation movements were reduced by approximately 60 percent. Figure 6-14 shows that the resulting fatigue life estimates increase dramatically for Load Case 4, where the formation movements were assumed to impart incremental tensile strain on the casing. Although Load Case 4 remains the load condition with the shortest estimated fatigue life, it is similar to other load cases and does not stand out as much as when higher load cycles are assumed.

RSI-1546-06-037
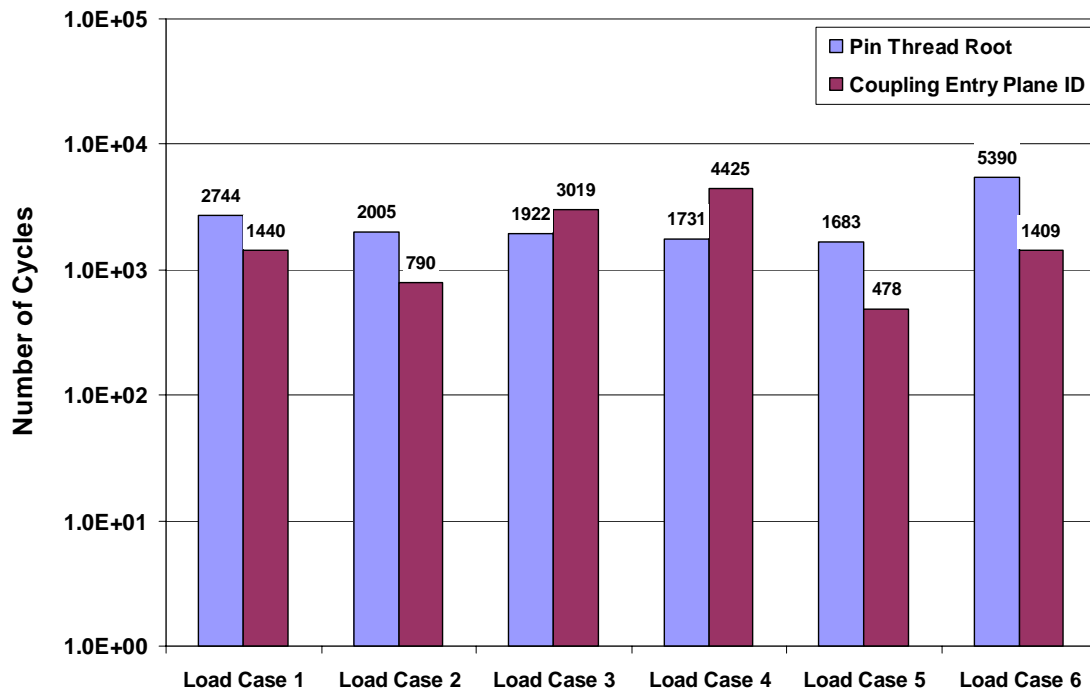
Figure 6-14. Fatigue Life for Various Load Cases of the Reservoir Storage Connection Model Assuming 2.1 Centimeters (0.8 Inch) of Formation Movement With Each Gas Cycle.

Welding the coupling face to the pipe body to strengthen the connection did not significantly change the minimum fatigue life in cases with incremental compaction-related compressive strains (Case 5 = 372 cycles compared to Case 3 = 1,099 cycles). Where compaction-related tensile strains occur, the minimum fatigue life improved with the welded connection (Case 6 = 1,732 cycles compared to Case 4 = 235 cycles). It is important to note that the analyses did not take into consideration the impact of any residual stresses or changes in material properties that may occur due to the welding of the connection.

6.4 SALT CAVERN WELL CONNECTION RESULTS

For the salt cavern application, the casing strings considered 340-millimeter (13⅜-inch, 72 lb/ft) K-55 API 8-Round STC connections. Connection analyses were performed using the load conditions provided in Chapter 5.0 determined at the lowest joint of the two salt cavern wells. The connection analyses simulated four load steps corresponding to the loading conditions determined at: (1) start of injection, (2) end of injection, (3) start of withdrawal, and (4) end of withdrawal. These load steps are shown in Figure 6-15 for the connection at a depth of 567 meters (1,860 feet) in the well of the shallow cavern (Salt Cavern Well No. 1). Figure 6-16 presents the load steps used for the lowest connection in the deeper cavern well (Salt Cavern Well No. 2). Comparison of Figures 6-15 and 6-16 shows that the deeper well casing involves much higher internal and external pressures and axial force because of the greater depth.

Figures 6-17 and 6-18 show the axial strain distribution at the end of gas injection in the shallow and deep salt cavern well connections, respectively. The strains are evenly distributed around the connections because only axisymmetric loading was assumed for these vertical wells.

Figure 6-19 presents the estimated fatigue life for the two salt cavern well completions. Both cases show that the pin thread root is the most critical location for fatigue failure. The fatigue lives are estimated to be 1.33×10^7 and 3.68×10^6 cycles (1,100,000 years and 310,000 years assuming 12 gas cycles per year) for the shallow and deep well casings, respectively.

6.5 SUMMARY OF FATIGUE LIFE ANALYSES

The fatigue life for the reservoir well was estimated to be as short as 235 cycles, or 235 years, assuming an annual pressure cycle. The deep salt cavern casing could withstand approximately 3.7×10^6 pressure cycles, but since the pressure is cycled 12 times per year, the well life is estimated to be 310,000 years. Connection fatigue in the shallow salt cavern well does not appear to be a concern, with a predicted fatigue life of 1,100,000 years, assuming 12 pressure cycles per year.

The fatigue life of 235 cycles for the reservoir well is believed to be an extremely conservative estimate. This result was obtained assuming that the casing and the sandstone formation strain equally in response to subsidence induced by depressurizing the reservoir formation. In reality, the casing, if cemented to the formation, would resist the ground movement and would experience less strain than that assumed in this study. Another possibility is that slip would occur at the casing interfaces, resulting in lower strains in the casing than the surrounding rock formation. A limited sensitivity analysis showed that the estimated fatigue life can vary significantly, depending on the magnitude of incremental axial

Figure 6-15. Load Steps for the Connection in Salt Cavern Well No. 1 at a Depth of 567 Meters (1,860 Feet).
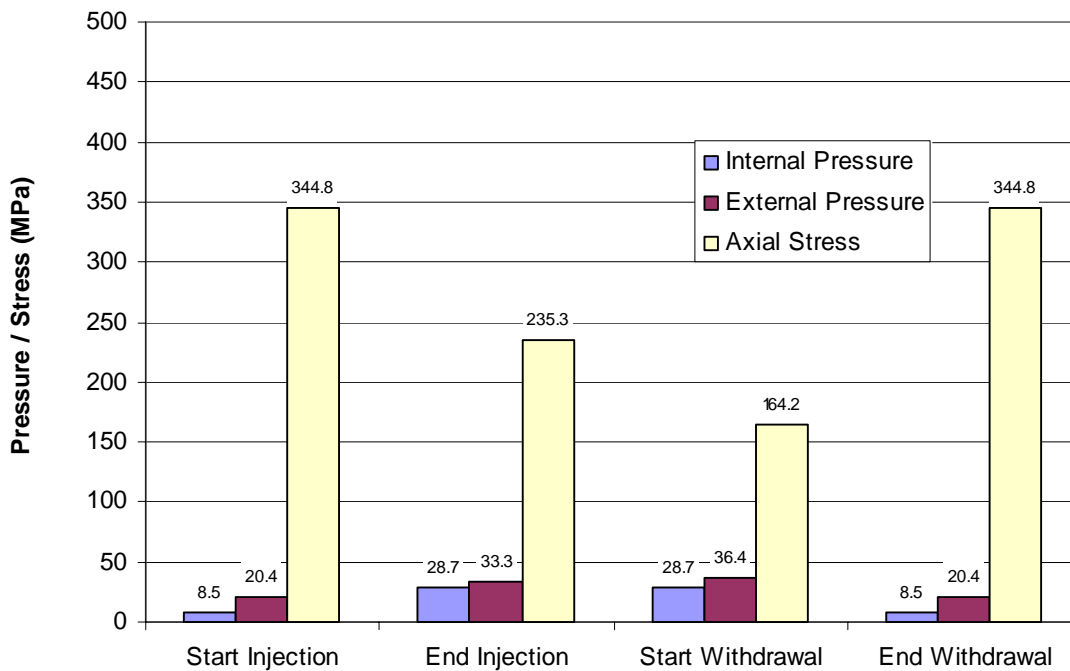
Figure 6-16. Load Steps for the Connection in Salt Cavern Well No. 2 at a Depth of 1,481 Meters (4,860 Feet).
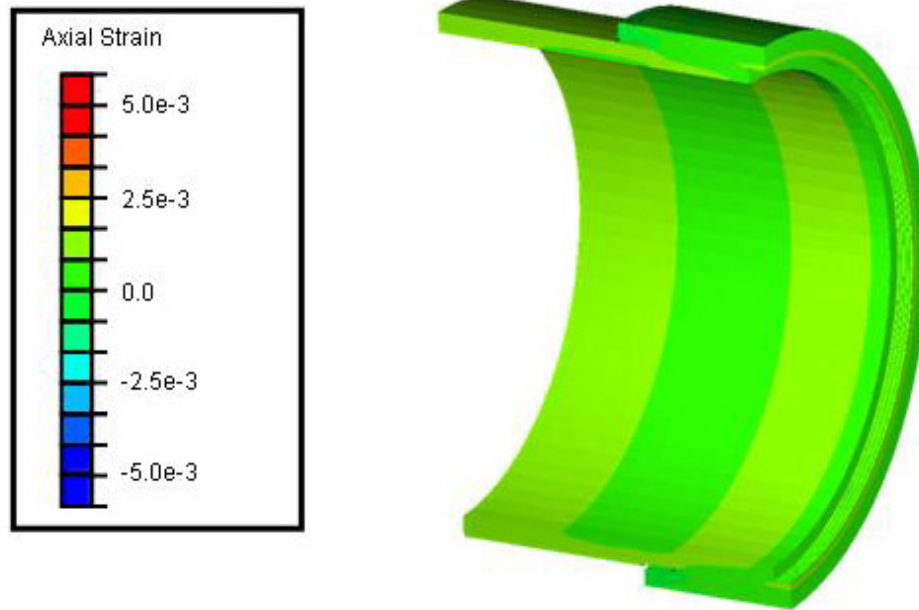
Figure 6-17. Axial Strain in Salt Cavern Well No. 1 Connection at a Depth of 567 Meters (1,860 Feet) at the End of Injection.

RSI-1546-06-041
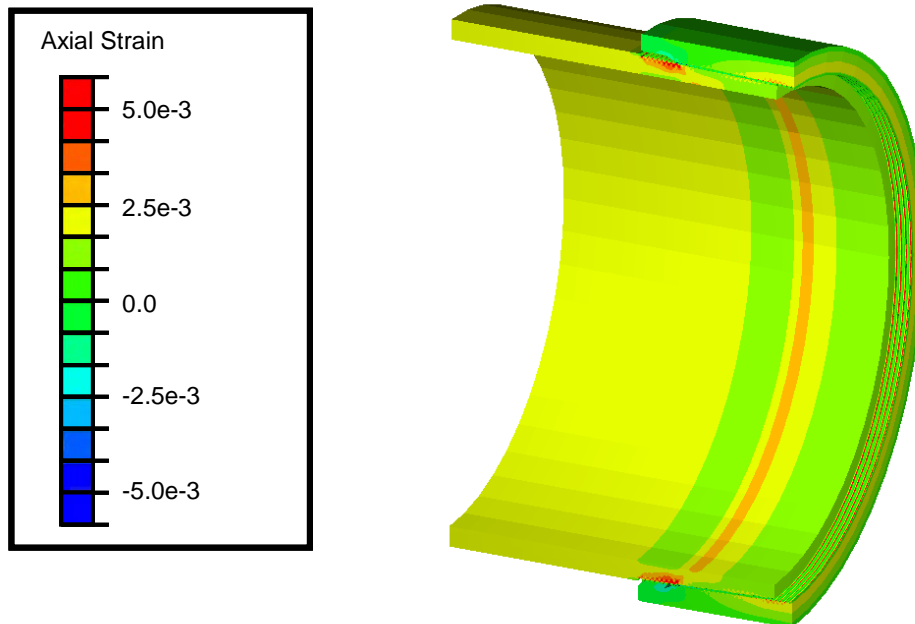
Figure 6-18. Axial Strain in Salt Cavern Well No. 2 Connection at a Depth of 1,481 Meters (4,860 Feet) at the End of Injection.

strain that is assumed to occur because of reservoir compaction. If the incremental axial strain attributable to reservoir compaction is not considered, the fatigue life of the connection increases to 790 cycles.

RSI-1546-06-042
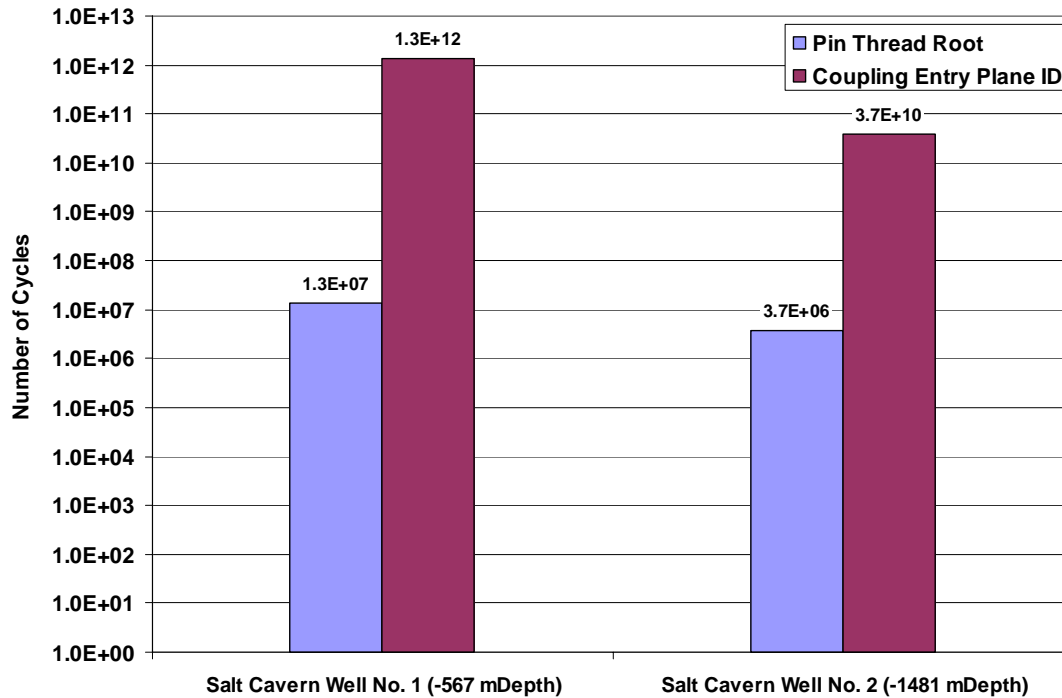
Figure 6-19. Estimated Fatigue Life for the Salt Cavern Connection Models.

Welding the coupling face to the pipe body in these applications does appear to contribute somewhat to the connection strength, but in some cases, may redistribute the stresses in the connection such that failure occurs in approximately the same number of cycles but in a different location compared to connections without welds. The analyses including the weld did not consider the effects welding may have on local stress concentrations or degradation of the casing and coupling material properties in the heat-affected zone adjacent to the weld.

There is a significant amount of uncertainty in the fatigue analysis presented here. This includes uncertainty in the fatigue performance of the connection materials, uncertainty in the effect of corrosion on the connection strength, and uncertainty how the loads (in particular, salt creep and reservoir compaction loads) are transmitted to the well casing. Considering this uncertainty, the minimum estimated fatigue life of 235 years for the reservoir well does not appear to provide a significant margin of safety to ensure adequate storage facility operating life.

The analysis did not consider the occurrence of localized casing strains that may occur because of buckling or shear of the casing that is often associated with large formation

movements. Shear and buckling deformations are common in oilfield production and injection scenarios that cause changes in the reservoir pore pressure. While many of these oilfield applications include very large changes in reservoir pore pressures, resulting in very large formation movements, the smaller pore pressure changes associated with gas storage operations likely cause similar, but smaller, formation movements in the gas storage reservoir and overburden.

Previous analyses of wells subjected to thermal strains and formation movements have shown that if the well cement provides lateral support for the casing, bending strains can be minimal because of buckling in high axial compression environments. However, even a small annular gap between the casing and cement or cement and formation can allow the casing to buckle when subjected to even moderate axial loads, resulting in localized bending strains. These bending strains can be many times greater than the average global strains attributed to thermal or pressure cycling. The effect of gap size on connection performance can be studied parametrically but it is difficult to characterize the actual gap size that might exist in a particular well.

This analysis demonstrated that API 8-Round STC connections may be susceptible to fatigue-related failures in some gas storage applications. Other connection configurations, such as Long Threaded and Coupled (LTC), buttress, and premium (proprietary) connections, are designed by various pipe manufacturers to offer significantly greater strengths. In many cases, the manufacturers report connection strengths that exceed the load capacity of the pipe body. Care must be taken in selecting a specific premium connection because some designs are intended for specific load environments and may not function any better than the 8-Round STC connection in the gas storage well scenario.

Critical pieces of information missing from this analysis of casing performance in gas storage wells are direct measurements of the casing deformations that can be used to verify the loading mechanisms and to help benchmark available models of casing-formation interaction. Conventional multifinger inspection logs can be used to characterize well deformations and provide quantitative measurements of the magnitude and direction of localized casing curvatures caused by formation movements or large casing loads. These logs are sensitive enough to identify casing deformation mechanisms before the deformations are apparent by other means (e.g., gauge rings and downhole video) or cause operational problems (e.g., casing leaks or impaired well access).

7.0 CONCLUSIONS

The analyses of the thermomechanical response of the well casings during gas storage injection and withdrawal cycles show that the effects of operating pressure and well temperature changes are minor in comparison to the axial strains imposed by formation movements (i.e., compaction in reservoirs and salt creep in caverns). Compaction in the candidate reservoir storage wells imposed an estimated 0.17 percent axial strain compared to approximately 0.018 percent strain attributed to the other loading mechanisms. The analysis of the 1,524-meter- (5,000-foot-) deep salt cavern well showed that deformations from salt creep will cause the casing to fail if the casing remains bonded to the salt and the cement does not fail. Even with the assumption that the stress transmitted to the casing is limited to 345 MPa (50,000 psi), the axial strain imposed by the formation movements is approximately 0.17 percent. This is still more than twice the 0.08-percent strain caused by temperature and pressure changes in the well.

The fatigue life of the connections in the reservoir and deep salt cavern wells was estimated to be 235 and 310,000 years, respectively. Although the axial strains imposed by formation movements were about the same for these two wells, the salt cavern well connections can withstand considerably more cycles than the reservoir well connections. This is because the formation movements impart cyclic loads on the reservoir well casing; whereas, salt creep produces monotonically increasing loads. The combined cyclic loads from formation movement and thermal cycling significantly reduce the estimated fatigue life of the reservoir well connection. Connections in both salt cavern wells do not appear to be at risk of cyclic fatigue. Two key uncertainties remain in the analysis that may influence the estimated fatigue life of the connections. The first is the fatigue performance of the casing and connection materials, which was based on analogous materials. The second is how much of the formation movements that occur during pressure and temperature cycles are transferred through the well cement to the casing.

8.0 REFERENCES

ABAQUS, Inc., 2005. *User's Manual Version 6.5.1*, Pawtucket, RI.

American Petroleum Institute, 1974. "Formulas and Calculations for Casings, Tubing, Drill Pipe, and Line Pipe Properties," *API Bulletin 5C3,* American Petroleum Institute, Washington, DC, March.

American Petroleum Institute, 1999. "Gauging and Inspection of Casing, Tubing, and Liner Pipe Threads," *API Bulletin 5B1,* American Petroleum Institute, Washington, DC.

Biot, M. A., 1955. "Theory of Elasticity and Consolidation for a Porous Anisotropic Solid," *Journal of Applied Physics*, Vol. 26, No. 2, February, pp. 182–185.

Boller, C. and T. Seeger, 1987a. "Materials Data for Cyclic Loading–Part A: Unalloyed Steels*,*" *Materials Science Nomographs,* 42A, Elsevier, New York, NY.

Boller, C. and T. Seeger, 1987b. "Materials Data for Cyclic Loading – Part B: Low-Alloy Steels," *Materials Science Nomographs*, 42B, Elsevier, New York, NY.

Callahan, G. D., 1981. *Inelastic Thermomechanical Analysis of a Generic Bedded Salt Repository,* ONWI-125, prepared by RE/SPEC Inc., Rapid City, SD, for the Office of Nuclear Waste Isolation, Battelle Memorial Institute, Columbus, OH.

Callahan, G. D., A. F. Fossum, and D. K. Svalstad, 1989. *Documentation of SPECTROM-32: A Finite Element Thermomechanical Stress Analysis Program,* DOE/CH/10378-2, prepared by RE/SPEC Inc., Rapid City, SD, for the U. S. Department of Energy, Chicago Operations Office, Argonne, IL, Vol. I and II.

Croff, A. G., T. F. Lomenick, R. S. Lowrie, and S. H. Stow, 1985. *Evaluation of Five Sedimentary Rocks Other Than Salt for High-Level Waste Repository Siting Purposes*, Volume 1: Main Report and Appendixes A and B, ORNL/CF–85/2/V1, Oak Ridge National Laboratory for the United States Department of Energy, Washington, DC.

Dahlstrom, D. J., 1988. *Thermal Properties Measurements of Avery Island Salt Core*, RSI-0334, prepared by RE/SPEC Inc., Rapid City, SD, for Stone & Webster Engineering Corporation, Boston, MA.

Dowling, N. E., 1998. *Mechanical Behavior of Material–Engineering Methods for Deformation, Fracture, and Fatigue,* 2nd ed., Prentice Hall, New Jersey, 830 p.

Economides, M. J., A. D. Hill, and C. Ehlig-Economides, 1994. *Petroleum Production Systems*, Prentice Hall PTR, Upper Saddle River, NJ.

Humphreys, K. J., S. C. Solanki, and R. A. Link, 1991. *Qualification of Grade-55 Casing for Thermal Recovery Service*, C-FER Project 88-14, prepared by C-FER Technologies, Edmonton, Alberta, Canada, for Joint Industry Members.

Illson, T. F. and C. D'Arcy, 2004. *Wellbore Integrity Assessment–Phase I Industry Survey*, Catalog No. L52134e, prepared by Advantica, Inc., Houston, TX, for Pipeline Research Council International, Inc., Underground Storage Technical Committee, Arlington, VA.

Incopera, D., 1996. *Introduction to Heat Transfer,* 3rd ed., Appendix A, pp. 746–751, John Wiley and Sons, Inc.

Karably, L. S. and R. M. White, 1981. *Geothermal Studies of Seven Interior Salt Domes*, prepared by Law Engineering Testing Company, Marietta, GA, for the Office of Nuclear Waste Isolation, Battelle Memorial Institute, Columbus, OH.

Munson, D. E., 1998. *Analysis of Multistage and Other Creep Data for Domal Salts,* SAND98-2276, Sandia National Laboratories, Albuquerque, NM.

Nelson, P. E. and L. L. Van Sambeek, 2003. *State-of-the-Art Review and New Techniques for Mechanical Integrity Tests of (Gas-Filled) Natural Gas Storage Caverns,* Research Project Report No. 2003-2-SMRI, prepared by RESPEC, Rapid City, SD, for the Solution Mining Research Institute, Encinitas, CA.

Nieland, J. D. 2004. *Salt Cavern Thermal Simulator Version 2.0 User's Manual,* RSI-1760, prepared by RESPEC, Rapid City, SD, for Gas Technology Institute, Des Plaines, IL.

Norton, F. H., 1929. *Creep of Steel at High Temperatures*, McGraw-Hill Book Company, New York, NY.

Pfeifle, T. W., K. D. Mellegard, and N. T. Skaug, 2000. *An Investigation of the Integrity of Cemented Casing Seals With Application to Salt Cavern Sealing and Abandonment*, Research Project Report No. 2000-2-SMRI, prepared by RESPEC, Rapid City, SD, for the Solution Mining Research Institute, Encinitas, CA.

Philippacopoulos, A. J. and M. L. Berndt, 2000. "Characterization and Modeling of Cements for Geothermal Well Casing Remediation," *Geothermal Resources Council Transactions,* Vol. 24, pp. 81–86.

Riley, W. F., L. D. Sturges, and D. H. Morris, 1999. *Mechanics of Materials*, 5th ed., John Wiley & Sons, Inc., New York, NY.

Senseny, P. E., F. D. Hansen, J. E. Russell, N. L. Carter, and J. W. Handin, 1992. "Mechanical Behaviour of Rock Salt: Phenomenology and Micromechanisms," *International Journal of Rock Mechanics and Mining Sciences & Geomechanics Abstracts*, Vol. 29, No. 4, pp. 363–378.

Sines, G. and G. Ohgi, 1981. "Fatigue Criteria Under Combined Stresses and Strains," *Journal of Engineering Materials and Technology,* Vol. 103, pp. 82–90.

Starling, K. E. and J. L. Savidge, 1994. *Compressibility of Natural Gas and Other Related Hydrocarbon Gases*, Report No. 8, 2nd ed., Catalog No. XQ9212, prepared for American Gas Association, Arlington, VA.

Svalstad, D. K., 1989. *Documentation of SPECTROM-41: A Finite Element Heat Transfer Analysis Program*, DOE/CH/10378-1, prepared by RE/SPEC Inc., Rapid City, SD, for the U.S. Department of Energy, Chicago Operations Office, Argonne, IL.

APPENDIX A

ADDITIONAL WELL CASING ANALYSES

APPENDIX A
ADDITIONAL WELL CASING ANALYSES

The approach used for solving the well model problems assumed that the casing/cement and cement/salt interfaces remain perfectly bonded. This approach provides a conservative estimate for axial tensions because the casing is forced to displace nearly the same magnitude as the salt. However, the predicted results could be dramatically different if the bond between the material interfaces is broken. The presence of a microannulus, defined as a very small annular gap located between the pipe and the cement sheath, is an example of a condition where the pipe is not bonded to the cement sheath. Even if a microannulus is present, the cement job may be sufficient to form a hydraulic seal and prevent fluid migration behind the pipe under normal production conditions. A microannulus may be caused by several factors, including:

- Thermal expansion of the pipe while the cement cures.

- Thermal contraction of the pipe as a result of fluids cooler than the cement sheath flowing through the pipe.

- Reducing the hydrostatic head of the fluid after holding the pressure on the casing until the cement has set.

- Contaminants, such as grease, on the external surface of the casing.

Interfaces can be modeled numerically as frictional or frictionless contacts. A frictionless contact will only allow normal forces to be transferred across the surface, providing the least conservative estimate for axial tensions in the casing. Attempts were made to model frictional interfaces without success. The scale of the regional well model prevents accurate solution of the interface behavior using convergence criteria based on global equilibrium.

To gain a better understanding of the steel/cement interaction, a finite element analysis was performed to provide an estimate of the maximum tensile load that the cement can impose on the steel pipe. The model developed for this analysis is a cylindrical representation of a 340-millimeter (13⅜-inch) casing and coupling, surrounding by a 47.5-millimeter- (2-inch-) thick cement sheath within a 1.5-meter- (5-foot-) radius salt mass. The vertical extent of the model was also limited to 1.5 meters (5 feet). Tractions were applied to the lateral boundaries to represent the confinement of the salt at a depth of about 1,481 meters (4,860 feet).

For this model, it was assumed that the bond has been broken between the steel and the cement and that only the coupling restricts the relative displacement between the two casing components. During the finite element analysis, an axial force was incrementally applied to the steel pipe in an effort to pull the pipe and coupling through the cement sheath. Mohr-

Coulomb factors of safety were monitored in the cement region to identify those regions that failed in shear based on cohesion and friction angles of 8.79 MPa (1,275 psi) and 10 degrees, respectively. Contours of factors of safety in the cement are provided in Figure A-1. As shown in Figure A-1, shear failure of the cement is initiated by the time the axial stress in the pipe reaches 275.81 MPa (40,000 psi). The zone of failure expands as the axial force in the pipe is increased. When the axial load produces 345 MPa (50,000 psi) tension in the steel, the zone of failure extends several inches from the connection and across the thickness of the cement sheath. Based on this result, it would seem unlikely that the cement could transfer an axial load greater than 345 MPa (50,000 psi) because the shear strength of the cement will be greatly deteriorated. This finding is based on the assumptions made in defining the problem, which are perceived as reasonable. Assumptions other than those identified for this problem may impact the results. However, without experimental or field observations, it is not possible to ascertain the physical condition of the cement in a zone experiencing large creep deformations. The 345 MPa (50,000 psi) tensile stress is assumed to be a conservative estimate for the maximum axial tensile stress obtainable in the casing, given the condition that the steel casing has not failed.
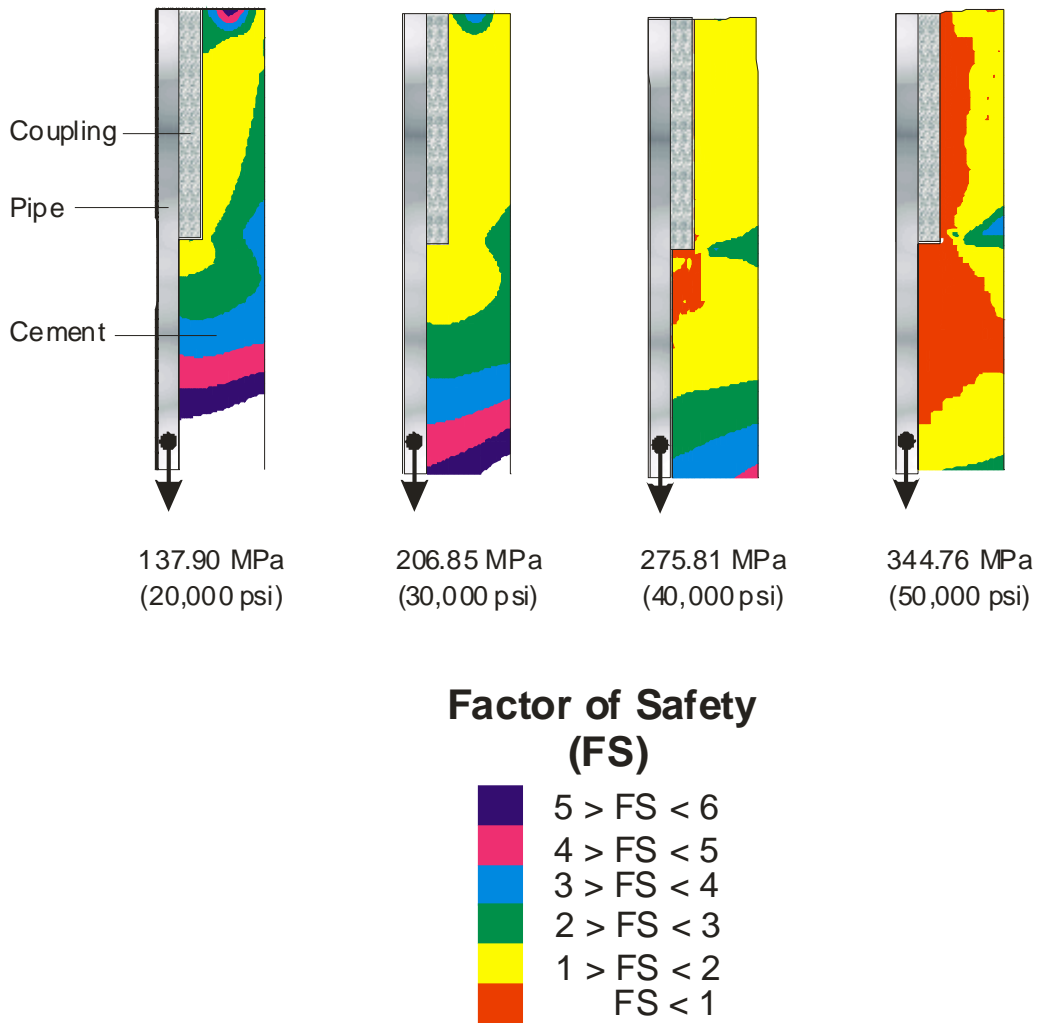
Figure A-1. Predicted Mohr-Coulomb Factor-of-Safety Contours in the Cement Sheath for Different Axial Stress Loads in the Steel Pipe.

GAS STORAGE TECHNOLOGY CONSORTIUM

Research Project

WELLBORE CEMENT BOND INTEGRITY

Final Report

Reporting Period: May 1, 2005 - December 31, 2006

DISCLAIMER

WELLBORE CEMENT BOND INTEGRITY

ABSTRACT

This program of studies combines laboratory experimental measurements and numerical simulations to investigate bonding between cement and casing, and effects of mechanical stress on cement and bond. P-waves are detected immediately upon pouring the slurry into the chamber, A dramatic increase in velocity during curing reflects the initial solidification of the slurry. Static deformation behavior was assessed by measurements of changes in wave propagation, static deformation, and failure during curing. Variations in axial stress with axial strain during triaxial deformations differ significantly for repeated deformation cycles on the same specimen. For single deformation cycles carried out on different specimens, deformation behavior follows the same trend as the dynamic moduli and the trend indicated for the unloading modulus for the multiple-deformation tests. Results for the multiple deformations on the same specimen show a tend towards lower values than those found for the multiple deformations, which is compatible with large surface-related strains in the multiple deformation tests. Permanent strains for the multiple deformations on Mix 2 (cement plus moisture-absorbing additives) indicate the presence of a non-recoverable surface deformation during the first deformation cycle, which is absent for the subsequent cycles. The amount of free water at the beginning of curing appears to significantly affect the strength of the cured cement. Numerical simulation of wave propagation in the cement-casing environment were also carried out, based on a two-dimensional discrete particle method. The simulations are compared with experimental tests in test assemblies configured to replicate bond indexing behavior. Simulations investigated wave propagation along the casing, and effects of changes in cement-casing bonds on the propagation. Non-uniform bonding affected wave amplitude in the same manner as percentage of the surface area bonded and, in some cases, completely obscured variations due to bond quality. Changes in the mechanical properties also affect amplitude. Amplitude variations scale roughly with the cumulative effect of fractional changes in bond stiffness times bond fraction, But variations in non-uniform distributions can lead to substantial deviations from this general trend. The placement of bonds with altered mechanical properties has more of an effect on wave amplitude than placement of unbonded zones. Simulations the influence of sand and porosity on cement behavior leads to attenuation of high-frequency components in the waves.

3

WELLBORE CEMENT BOND INTEGRITY

TABLE OF CONTENTS

WELLBORE CEMENT BOND INTEGRITY

EXECUTIVE SUMMARY

This program of studies combines laboratory measurements and numerical simulations to investigate bonding between cement and casing, and effects of mechanical stress on cement and bond. New apparatus and test procedures were developed for the study of cement-boundary interactions during curing and stress cycling. Systems were fabricated and used for studies of wave propagation through cement and traveling vertically along the side boundaries of the chamber. Compressional and shear wave velocities were monitored during curing periods. P-waves are detected immediately upon pouring the slurry into the chamber, and travel times during the initial 6-10 hours of curing are almost constant. A dramatic increase in velocity between 11 and 23 hours of curing reflects the initial solidification of the slurry. The earliest evidence for shear waves is seen after curing for more than 9 hours, which is consistent with the p-wave evidence that prior to this time the specimen is still a liquid. Subsequent shear waves can be identified by longer travel times. Poisson's ratios were determined from the set of shear and compressional mode velocities, and ratios were found to vary from initial values of 0.5, representative of a fluid at curing time near zero, to about 0.25, typical of intact rock, as the cement cures.

Static deformation behavior was assessed by measurements of changes in wave propagation, static deformation, and failure carried out on specimens of Type H cement during curing from slurry to rigid solids. CT images were acquired for three of the post-test specimens, to assess possible differences in cement texture. For at least one of each of the cement mixtures cured under ambient and 1kpsi confining pressure, excess water was removed from the top of the poured specimen as it was produced. At least one specimen of each cement mixture cured under ambient and 1 kpsi confining pressures was pressurized and cured without removing the water layer.

Variations in axial stress with axial strain during triaxial deformations differ significantly for repeated deformation cycles on the same specimen. Behavior for specimens that did not retain excess water during initial curing showed a gradual decrease in slope (yielding) but no evidence of failure. Specimens that retained substantial amounts of water during curing showed an initial positive curvature at low stresses, gradual yielding and failure. Wave velocities measured at the end of each of the deformation cycles were not affected appreciably by deformation, but increased systematically with curing time. CT scan images indicated in these images are the large voids

associated with absorption of free water into the cement crystal structure during curing, and deformation-related fractures.

In other tests, tri-axial single deformation cycles were carried out on different specimens of the two types of cement, after curing. Deformation behavior follows the same trend as the dynamic moduli and the trend indicated for the unloading modulus for the multiple-deformation tests. The data for the Series III tests do show a tend towards lower values than those found for the multiple deformations, which is compatible with large surface-related strains in the multiple deformation tests, suggesting that the surface effects are largely eliminated during the first loading cycle of the multiple-deformation tests, but are present for each of the single deformation cycles in the multiple deformations. Permanent strains for the multiple deformations on Mix 2 (cement plus moisture-absorbing additives) indicate the presence of a non-recoverable surface deformation during the first deformation cycle, which is absent for the subsequent cycles. The variations of the observations show a smoother and more gradual decrease in non-recoverable strain in single deformations than the multiple-cycle deformational cycles. Generally, the multiple-deformation tests show permanent strains below those for the single deformation tests Non-recoverable strains for Mix 1 and Mix 2 specimens are all significantly smaller than corresponding values for Mix 1 tests. The amount of free water at the beginning of curing appears to significantly affect the strength of the cured cement.

The third area of studies in this program is the numerical simulation of wave propagation in the cement-casing environment. The simulations are based on a two-dimensional discrete particle method (DPM). This numerical code is designed to simulate mechanical properties using an assembly of small finite particles. Macroscopic behavior is derived from first-principal micromechanical processes, coupled with a graphical user interface for the visualization of the waves. The simulations are compared with experimental tests conducted in a separate study in test assemblies configured to replicate bond indexing behavior.

The numerical simulations provide for detailed analysis of the experimental observations of wave propagation, using well-defined test conditions. The DEM simulation used in this study models the mechanical properties by treating the sample as a collection of spherical particles interacting via Newton's second law. The interaction of particles is treated as a series of springs, arising from overlap between the particles, and by elastic forces developed by deformation of inter-particle bonds. The model input parameters were determined by comparing computed wave velocities with published values, and altering the spring stiffness of the particles to match the measured wave velocities.

6

The first simulations investigated wave propagation along the casing, and effects of changes in cement-casing bonds on the propagation. Simulations of changes in the fraction of intact bonds, which is equivalent to variations in the fraction of contact area bonded in this 2D simulation, confirmed a direct relationship between wave amplitude and the percentage of intact bonds which is the essential basis for cement bond log interpretation. Examination of the effects of non-uniform bonding on wave amplitude showed that energy loss into the cement depends not only on the total percentage of the surface area bonded, but also the location of the bonds relative to the receiver. Computed amplitude variations for non-uniform distribution could, in some cases, completely obscure variations due to bond quality. Simulations of the effects of a weakening of the mechanical bond material stiffness on wave propagation showed that changes in the mechanical properties have the same effect on amplitude as fractional changes in the fraction of the bonded contact area. The results show that amplitude variations scale roughly with the cumulative effect of fractional changes in bond stiffness times bond fraction. However, variations in non-uniform distributions can lead to substantial deviations from this general trend. Simulations of the combined effect of non-uniform distribution of bonds with different stiffness shows that changes in mechanical behavior near the receiver have less effect on wave amplitude than changes further from the receiver. This behavior is similar to that observed for changes in the percentage of the contacts. The placement of bonds with altered mechanical properties has more of an effect on wave amplitude than placement of unbonded zones.

Simulations of wave propagation within the cement analyzed the influence of sand and porosity on cement behavior. Both types of inclusions alter the acoustic impedance of the cement, which will complicate bond quality evaluations, but the most important process was the attenuation of high-frequency components in the waves by scattering by void inclusions.

WELLBORE CEMENT BOND INTEGRITY

INTRODUCTION

This final report summarizes activities in the project, *Wellbore Cement Bond Integrity*. Technical, economic, environmental, and safety considerations underscore the pressing need by gas storage operators to understand the ways in which elements of a well bore and cement sheath interact during drilling, completion, and production operations. Better understanding of cement hardening, cement adhesion, and the effects of cyclic pressure and temperature-related stresses on these processes are needed for development of improvements in cement/casing/formation seals, and better techniques for assessments of seal quality with down-hole logging tools.

The components of a well-bore are physically coupled. While pressures inside the casing are easily measured and mechanical behavior of casing is well documented, little is known about the stresses, displacements, and behavioral features of the casing/cement interface outward through the cement, mud cake, plastic zone, and formation. Interface stresses, displacements, and coupling conditions change continually as well-bore pressures, pore pressures, and temperatures fluctuate. An understanding of the 3-D, time-dependent changes through all of the system components is necessary for addressing the well-bore cement bond integrity problem, especially in gas storage operations.

Concerns about cementation fall into two broad categories: 1) development of a satisfactory cement/casing/formation seal; and 2) quantitative assessments of the quality of the seal with down-hole logging tools. A better understanding of cement hardening, cement adhesion, and effects of cyclic pressure and temperature-related stresses on these processes is useful for addressing both of these concerns.

Laboratory assessments of wave propagation and deformational behavior of the cement-casing environment are especially useful in connection with these concerns. The most widely used tools for evaluating the quality of cement are based on acoustic measurements. The concept of an acoustical bond logging tool first appeared in the literature in 1959 (Tixier et al). Extensive results of laboratory and field testing of tools were published in 1961 by Grosmangin et al.; and Anderson and Walkers, and by 1962, a working tool was in use in the field. This configuration, the Cement Bond Log, is still in wide use. These tools transmit a 20 kHz spherical acoustic signal into the cased borehole. The amount of this signal lost into the formation is proportional to the acoustic coupling

between cement and formation, so that the amplitude of the propagated casing wave is inversely proportional to the integrity of the cement-casing bond. A more recent configuration, the Cement Evaluation Tool (Froelich et al., 1981), is based on ultrasonic pulse-echo technology originally developed for the Borehole Televiewer. An array of ultrasonic (nominal 0.5 MHz) transmitter/receivers placed around the circumference of the cylindrical sonde samples the relative amplitude of the echo train from approximately one square inch of the casing/cement/formation system adjacent to the transducer. Waveform amplitude is sampled during several gating windows, the latest of which provides a measure of coupling of sound energy into the formation (and a consequent loss of reflected amplitude).

Suites of laboratory tests were carried out in existing triaxial testing apparatus, and in bench-top apparatus custom designed to evaluate wave propagation in cement and along the cement-casing interface, as freshly-poured cement cures over minutes through one week. The GSTC project has been carried out in conjunction with and co-funded by a University of Texas Industrial Affiliates Research Program, *Life-Of-Well Rock, Fluid, and Stress Systems*. This program consists of three topical areas: I. Soft Sediment Systems; II. Wellbore and Near-Wellbore Casing, Cement, and Formation Interactions; and III. Pressure Management Operations. These programs overlap many concerns with the GSTC project..

In Soft Sediment Systems, the overall goal is to quantify subsurface processes and behavior of rock, fluid, and stress systems in soft, friable, poorly consolidated, weak formations. The analytical formulations of classical continuum mechanics are demonstrably inadequate for such systems, and understanding of complex, interrelated processes in very weak, granular materials is needed to develop relevant behavioral 'laws', guidelines, and correlations for field applications. Laboratory data on non-elastic rock behavior at elevated effective stresses are included in this report.

In Wellbore, Near-Wellbore, and Formation Interactions, the overall goal is to quantify the numerous stresses, strains, displacements, and interacting conditions around the wellbore region. Three, four, or more mechanical components in series (such as casing, cement, mud cake, gravel packs, liners, screens, formation) exhibit coupled interactions during drilling, completion, and production operations. Quantifications of cement shrinkage and stress transfers in wellbore and near-wellbore constituent components are the subject of the project, "Casing, Cement, and Formation Interactions During Drilling, Completion, and Production Operations". Results and

conclusions from that work useful in evaluating the cement/casing bond integrity are included in this report.

In Pressure Management Operations, the overall goal is to quantify combined static and dynamic stresses and displacements at strategic locations within and around the well bore 'U-tube' for applications such as Managed Pressure Drilling, Underbalance/Balance/Overbalance Drilling, Mud Cap Drilling, Measurements While Drilling, and Logging While Drilling. Critical pressure magnitudes and small pressure tolerances have large economic, technical, safety, and environmental consequences. Cement sheath integrity and its critical role in zonal isolation is one of several pressure/flow limiting items of concern in that work and will provide useful information to cement bond log technology.

Leverage to the Wellbore Cement Bond Integrity project from the Life-Of-Well Program has been and will continue to be substantial, owing to the large resource and support system (test facilities, data systems) utilized in Simultaneous Property System capabilities, other preparation/testing facilities on hand, and the proactive collaboration of industrial colleagues participating in the Life-Of-Well project indicated above.

The following section of this report discusses measurements of wave propagation during cement curing, and the equipment developed in the study to investigate the behavior. The next section is a detailed discussion of the deformation and wave propagation measurements carried out in the SPS system, during curing of two cement mixtures. The next section discusses the developments of numerical simulations based on the DEM techniques, and the final section is a discussion of conclusions developed on the basis of the current measurements.

EXPERIMENTAL

A preliminary sequence of graduated cylinder tests were carried out to assess the evolution of a layer of free water during curing, and to evaluate its effect on wave propagation. Photographs of the top surface of a freshly-poured specimen were taken over a period of several hours after pouring.

A bench-top experiment was then carried out. In this experiment, a 4-inch diameter by 4-inch long PVC tube was placed between end platens containing s- and p-wave transducers, and the chamber was filled with cement slurry. In this geometry, the 2-inch diameter end platens extend

into the cement, and the aqueous layer should be above the bottom surface of the top pedestal (and out of the wave propagation pathway).

The next test was carried out in the same bench-top apparatus, but using 3 sets of 0.17" shims placed on top of the PVC tube. These shims increased the distance between the end platens, and hence the length of the cement between the platens. By progressively removing the shims one set at a time at various times during the initial 12-hour curing stage – while the cement was still in a liquid state - the top platen was progressively pressed into the cement. In this way we hoped to force out the aqueous layer between the top platen and the specimen.

In these benchtop tests, the presence of the water layer and associated chemical interaction between the fluid and the aluminum platens effectively prevented detection of ultrasonic waves traveling through the cement during the early stages of curing. The difficulties in measuring wave propagation led to the design of a new apparatus for investigation of curing behavior and corresponding changes in propagation behavior. A primary concern was the development of techniques for measuring waves propagating through cement during the very earliest curing times.

The basic approach was to mount transducers well below a top surface, in an apparatus in which waves travel horizontally through the cement. The 4" x 4" apparatus shown in Figure 1 was designed and fabricated. A larger (4" x 8" chamber; Figure 2) was also constructed, to investigate features of waves traveling along different path-ways representative of the down-hole casing/cement environment. It provides for measurements of waves traveling vertically along the side boundaries of the chamber – but still well removed from the specimen top and the accompanying layer of free water. Side panels were either plexiglass (as in Figure 2) or steel (not shown).

A large suite of wave propagation measurements was carried out with these test assemblies, using the initial cement mixture (only Type H Portland cement). Cement slurry was mixed according to API #10 procedures, and poured immediately into the test box. Travel times for p-waves across the sample were monitored for the entire duration of the tests. Shear waves were not observed until after curing times of approximately 10 hours, and were generally not monitored until after curing overnight. Waveforms of waves propagating across the chambers (for 4"x4" and 4"x8" boxes) and along the chamber side walls (for the 4"x8" box) were captured and stored at nominal 1-day intervals as the specimens cured.

Suites of mechanical deformation and failure measurements and simultaneous changes in wave propagation were carried out over a nominal one-week time period, during which specimens

prepared from slurry at time zero cured to a rigid solid. The investigation was carried out using triaxial measurements in the Simultaneous Property System (SPS) shown in Figure 3. This test system has been developed and refined over four decades of operation at the UT Center for Earth Science and Engineering. A jacketed cylindrical test specimen is subjected to lateral stresses from a confining fluid and an independent axial load. Simultaneous measurements of axial and radial displacements, and ultrasonic shear and compressional wave propagation were carried out during loading and unloading deformations. Deformation parameters are measured by load and displacement transducers, and stored in digital files in the computer-based data acquisition system.

The specimen for these tests were cement slurry, poured immediately after mixing into the jacket attached to the bottom platen. Two cement mixtures were used. The first mixture, Mix 1, was composed only of Class H Portland cement. The second mixture, Mix 2, was a recipe provided by one of the Life-of-Well sponsors. It contained bentonite and BA-90, both of which absorb excess water and thereby reduce the amount of free water present during early stages of curing. Both mixtures were prepared according to API 10A.

After filling the jacket with the cement slurry (and removing excess water from the top of the specimen), the top platen was inserted into the jacket, and the three alignment rods were secured to the bottom and top end platens. At this point the sample-end platen assembly was a continuous column, and - except for specimens #2, #3, and #4 – axial specimen length was determined directly by measurement of the spacing between the platens. The reference axial displacement transducer output corresponding to this initial state was measured and recorded. No subsequent adjustments of the axial displacement transducer position were made, and all subsequent changes in length were relative to this initial position.

The sample assembly was placed in the pressure vessel and the confining pressure (200 psi or 1 kpsi) was applied. Shear wave propagation measurements proved to be problematic for this series of measurements. No s-wave propagation is possible prior to solidification of the cement, and the lead shims used for isolation of platens and specimen led to a degradation of signal quality, so that determinations of first arrival times for velocity determinations was not reliable. No shear wave velocity measurements are reported for these tests.

Also, no lateral displacement measurements were carried out for this series of tests. The lateral displacement transducers in the SPS are spring loaded on to the specimen, and the stress exerted by the springs led to significant (permanent) deformation of the slurry specimens. Out of

concern for spurious behavior introduced by such changes in cross-section geometry, the lateral transducers were not attached for this series of tests.

For each of the specimens, the test sequence was as follows.

1. Freshly poured cement was cured for 24 hours under various confining pressures.
2. Hydrostatic confining pressure was increased to 1kpsi, and a triaxial loading cycle up to a deviatoric axial stress of 1kpsi was carried out, and the specimen was unloaded to the hydrostatic 1kpsi stress.
3. For some of the specimens, p-wave velocities were measured at several pointes during the loading /unloading cycle.
4. The p-wave velocity was measured in all specimens after the initial triaxial loading cycle (at 1kpsi hydrostatic confining pressure).
5. Additional 1 kpsi triaxial loading cycles were carried out for some of the specimens at 24 – 48 hour intervals. P-wave velocities were measured after each of these loading cycles, at a hydrostatic confining pressure of 1kpsi.

The specimens were cured for 24 hours under ambient, 200 psi, and 1 kpsi confining pressures.   Within minutes after pouring each of the specimens, a layer of free water was observed on the top surface. Left alone, this free water was re-absorbed into the specimen over the next 24 hours.   For at least one of each of the cement mixtures cured under ambient and 1kpsi confining pressure, this water layer was removed from the top of the poured specimen as it was produced, for approximately 30 minutes prior to the application of confining pressure. At least one specimen of each cement mixture cured under ambient and 1 kpsi confining pressures was pressurized and cured without removing the water layer. The water layer was not removed for any of the specimens cured under 200 psi confining pressure.

After the sequence of deformations, three of the specimens (#11, a Mix 1 specimen with no adjustment of water content; #9, a Mix 1 specimen in which excess free water was removed prior to curing; and #6, a Mix 2 specimen) were examined in the UT Geology Computerized Axial Tomography (CT) scanner. This provides a high resolution (nominal 100 micron) view of porosity within the specimen. This porosity includes initial pore space as well as fractures associated with deformation-induced failure. Results from this series of multiple-deformation tests are designated as Series II tests.

Uncertainties in observed behavior in this series of tests led to a modification of the test sequence, carried out in the final series of static deformation tests. In these tests fresh Mix 1 and

Mix 2 specimens were poured at the beginning of the test sequence, and the specimen was allowed to cure – undisturbed – for a time period of 14, 24, 36, 48, or 168 hours. After the curing period, the specimen was deformed by carrying out a loading cycle, and the sample was removed. A new specimen was poured into the specimen chamber, and the sequence was repeated for a different curing time. The revised sequence was repeated for Mix 2 specimens. These tests are designated as Series III and Series IV tests, for Mix 1 and Mix 2 slurries, respectively.

RESULTS AND DISCUSSION

1. Wave Propagation

Observations during the preliminary shakedown tests of wave propagation demonstrated that the quality of waveforms is generally poor during the first 24 hours of curing. A photograph of the top layer of free water after curing for 24 hours is shown in Figure 4. Four representative images over a 24 hour period are shown in Figure 5. Subsequent to 24 hours of curing, waveforms were still of poor quality until the specimens were axially loaded. A primary source of difficulties in wave propagation measurements is the development of a small layer of water at the top end of cement slurry. This water is re-absorbed during the first 18 hours of curing. This aqueous layer can have significant impact on wave propagation – especially shear waves – along such a vertical column.

One consequence of this water layer is corrosion of the aluminum end platen in testing systems, and deposition of cement minerals from the aqueous layer. This behavior is shown in Figures 6 and 7. These photographs show the upper and lower end platens and specimen surfaces. There is considerable residue on the top platen, while the bottom platen remains flat and relatively clean.

The quality of wave-forms shown in Figure 8 illustrates the problem with the aqueous layer. Post test observations of the end platens revealed that the bottom specimen surface and end platen were clearly damaged, consistent with the poor wave-forms. Water in the aqueous layer in this test was apparently trapped by the low permeability of the partially cured specimen.

The use of shims during cement curing was clearly effective in improving coupling for the later-stage curing for p-waves, shown in Figure 9. Computed velocities for these waveforms are shown in Figure 10. Post-test observation of the top platen and test specimen surfaces were much cleaner and flatter than those in the previous bench-top tests. However, none of the wave-forms shown were captured during the initial 12 hours of curing, as the cement cured from slurry to solid. The signal

14

qualities during these early stages were too poor to provide useable measures of travel times. Coupling across the free water layer is apparently insufficient to provide useable waveforms.

These observations led to the design of the new 4" x 4" test chamber shown in Figure 1. The illustration of compressional waveforms in the 4" x 4" chamber shown in Figure 11 shows the success of the chamber design for monitoring wave propagation during curing. Well-defined p-waves are detected immediately upon pouring the slurry into the chamber. Travel times during the initial 6-10 hours of curing are almost constant, indicating that the slurry remains in a predominately liquid state during this period. The dramatic increase in velocity between 11 and 23 hours of curing – reflecting the initial solidification of the slurry – is clearly reflected in the decrease in corresponding arrival times. Additional, more gradual increases in velocity are observed through curing times of 100 hours, but subsequent changes (out to 167 hours) are small.

Measurements of shear waveforms are more problematic, but can still be clearly detected in this apparatus. An example of signals measured and detected by a shear wave transducer is shown in Figure 12. Initial signals detected for travel times of about 20 microseconds are p-wave precursors, created by mode conversions at the specimen-surface boundary. The earliest evidence for shear waves is seen after curing for more than 9 hours, which is consistent with the p-wave evidence that prior to this time the specimen is still a liquid. After 9 hours of curing, a shear wave can be identified by its longer travel time and the similarity of waveforms moving to progressively shorter travel times. Again, large changes in travel times - reflecting increases in velocity - are evident in travel times observed for signals which have cured between 9 and 24 hours.

Wave velocities for these tests were determined by procedures in which waveforms were shifted in time until a best-fit overlap between waveforms captured at different times was obtained (Figures 5, 6, 13, and 14). Aligned waveforms for the p-waves in Figure 11 are shown in Figure 13, and those for aligned shear wave-forms from Figure 12 are shown in Figure 14. An initial velocity was determined, based on the first arrival for the un-shifted wave for a curing time at which there is a well-defined arrival (arrow in Figure 12, vertical line in Figure 13). Subsequent travel times – and, hence, velocities – were determined by shift times necessary to align the waveforms. The waveform changes significantly, so only the initial portion (the first break for the signal) is aligned. The same procedure was used for both compressional and shear waves, except that the precursor signal in the shear wave-forms (presumably from mode conversion into p-waves) at short travel times was ignored.

15

Summaries of variations in p- and s-wave velocities with curing time are shown in Figures 15 and 16, respectively. Note that these data are taken from several different test specimens. The results for both p- and s-waves are very reproducible, supporting the reliability of the measurement methodology and the reproducibility of the curing process. The results are re-plotted on a common scale in Figure 17, along with variations in computed dynamic Poisson's ratio.

Further evidence for the reliability of the measurements – and, in this case, specimen uniformity - is provided by wave propagation measurements in the second new apparatus (4"x 8" assembly; Figure 2). This system is configured with 4 compound (ie., s- and p-wave) transducers, so that waves propagating across the top of the poured specimen (which is left open to the atmosphere) could be compared with those traversing the specimen bottom. Results for shear waves traveling across the top and bottom of the specimen are shown in Figures 18 and 19, respectively. In both cases, the waveforms for equivalent pathways are virtually identical..

The behavior of p-waves is also similar for waves generated and detected by transducers on the same sides of the chamber (Figures 20 and 21), indicating similarities of cement-sidewall adhesion. Corresponding waveforms generated and detected by s-wave transducers are shown in Figures 22 and 23. The s-waves for different faces differ by a 180^0 phase shift, but are otherwise the same.

2. Static Deformation Behavior

The studies described in this section were designed to assess the evolution of static and dynamic mechanical behavior of cement slurry as it cured. Plots of stress - strain behavior for each of the Mix 1 test specimens are shown in Figures 24-37. Figure 24 includes a graphical illustration of yield, failure, Young's modulus, and permanent strain. All strains are shown positive for shortening, and, except for specimens 2, 3, and 4 (as noted above), were computed relative to the initial axial length of poured slurry. For all specimens, stress-strain behavior during the first deformation cycle was significantly different than that for all subsequent deformation cycles. Variations in the first cycle are generally non-linear and exhibit substantial permanent axial strains. Subsequent cycles are almost linear, and result in almost no permanent strain. Deformation behavior in this first cycle is similar for all specimens except #7, #8, #11, and #12 (Figures 24, 27-29):

1. an initial linear region of increasing stress with strain;
2. a gradual decrease in slope (yielding) at approximately 1.4 to 1.8 kpsi.

3. at the end of axial loading where the load ram was stopped to re-configure the apparatus for unloading (nominally 5 minutes), axial stress decreased and axial strain (shortening) increased, linearly; and

4. during unloading, deviatoric axial stress decreased in a linear fashion, down to the hydrostatic confining pressure.

Loading behavior for the Mix 1 specimens that were not wicked (#7, #8, #11, and #12; Figures 27, 24, 28, and 29, respectively) is qualitatively and quantitatively different from that for the other specimens. The initial loading, also non-linear, has an initial positive curvature at low stresses, gradual yielding at intermediate stresses (1.5-1.8 kpsi), and failure at approximately 1.8 kpsi.

Non-recoverable strain (NRS, defined as the difference between axial strain before and after the first deformation cycle) provides a quantitative measure of non-elastic behavior. The largest NRS's were observed for Specimens #7, #8, #11, and #12, all of which were Mix 1 samples with no removal of excess water. These specimens all show evidence of failure (Figures 27, 24, 28, and 29, respectively) at a deviatoric axial stress of approximately 1.7 kpsi. However, specimen #10 (Figure 30; also a Mix 1 sample with no removal of excess water) did not give an indication of failure during deformation. None of the Mix 2 specimens or Mix 1 specimens with excess water removed, showed evidence of failure during the triaxial deformations.

The linear unloading behavior is generally considered to represent elastic material behavior, and the slope of the unloading curve is designated as the elastic Young's modulus. (Note that not all the deformation cycles are included in the plots, because after 2 or 3 cycles the stress-strain data are virtually identical for each subsequent cycle. However, unloading slopes (Young's moduli) for all the deformations are included in the tabular summations below).

Several test parameters derived from these plots are summarized in Table 1 for the Mix 1 specimens, and Table 2 for the Mix 2 specimens. Wave velocities measured at the end of each of the deformation cycles are also included in the tables. The tabulated parameters, in the order they appear in the tables are

1. Specimen ID;

2. WRI (water removal interval) - Length of time, in hours, free water on the top of the poured slurry was removed by wicking;

3. P_{CUR} (curing pressure, psi) – confining pressure during initial 24 hour cure;

4. NRS (non-recoverable strain, milli-strain) – permanent shortening of the specimen after the first triaxial stress cycle (immediately after 24 hour cure);

5. SS (stress-strain cycle) – ID for the loading / unloading cycles carried out over the total duration of testing for the specimen;

6. E (static Young's modulus) – slope of the linear portion of unloading stress-strain variations for the triaxial deformation designated by the SS ID;

7. V_P (p-wave velocity) – measured p-wave velocity for the indicated measurement ID; and

8. C_P (dynamic constrained modulus, kpsi) – computed from V_P and a density of 2.85 gm/cc.

Table 1. Mechanical properties of Mix 1 cement specimens, measured during curing and deformation.

Test #	El Time (hr)	Wick-t(hr)	P(cure)	NRS(milli)	SS #	E (kpsi)	Vp (ft/sec)	Cp(kpsi)
2	25.1	2	0	2	b	1553	10042	3872
	25.8				b	1553	10314	4084
	26				b	1553	10332	4098
	49.6				c	3661	11223	4835
	72.3				d	5759	11680	5238
	95.6				e	6154	12049	5573
	167.9				f	6929	12387	5891
9	23.9	0.5	1000	2	b	1120	8674	2889
	24.6				b	2148	8867	3018
	49.1				c	2149	10880	4545
	78.8				d	3838	11619	5183
	122.4				e	4685	11967	5498
16	22.5	0.5	0	3	a	1330	8004	2460
	23.0				a	1330	9112	3187
	23.8				a	1330	9552	3503
	24.1				a	1330	9805	3691
	24.4				a	1330	9805	3691
7	23.2	0	1000	5	b	1006	8328	2662
	24.1				b	1006	8506	2778
	25.4				b	1006	8629	2859
	25.5				b	1007	8629	2859
8	23.7	0	1000	10	b	1537	8569	2819
	25.8				b	1537	9384	3381
	48.8				c	1537	11153	4776
	73.5				d	3038	11705	5260
11	23.8	0	1000	9	b	995	9384	3381
	25.6				b	995	9845	3721
	27.0				b	996	10354	4116
	27.4				b	996	10354	4116
12	22.6	0	200	10	b	848	8060	2494
	24.5				b	848	8436	2732
	25.8				b	849	8644	2869
	27.3				b	849	8707	2911
10	24.2		0	1	b	1115	8269	2625
	48.2	0			c	2822	10463	4203
	72.2				d	2969	11049	4687
	72.5				d	2970	11111	4740

Table 2. Mechanical properties of Mix 2 cement specimens, measured during curing and deformation.

Test #	ElTime (hr)	WickTim(hr)	P(cure)	NRS(milli)	SS #	E (kpsi)	Vp (ft/sec)	Cp (kpsi)
4	24.4	0.5	0	1	a	1340	9257	3290
	25				a	1340	9410	3400
	25.2				a	1340	9504	3468
	48.4				b	2657	11736	5288
	72.5				c	3363	12373	5878
	144				d	5055	12935	6424
15	23.6	0.5	0	1	a	1538	8403	2711
	24.1				a	1538	8718	2918
	24.6				a	1538	8989	3102
	25.0				a	1538	9030	3131
	25.4				a	1538	9059	3150
5	0.2	0.5	1000	1	a		6085	1422
	24				b	2001	9077	3163
	25.3				b	2001	9223	3266
	26.1				b	2001	9374	3374
	26.3				b	2001	9374	3374
	49.2				c	4561	10788	4468
	121.6				d	4880	11668	5226
	145.6				e	5042	11668	5226
13	22.6	0	200	1	b	913	8004	2460
	24.0				b	913	8226	2598
	24.7				b	913	8401	2710
	25.2				b	913	8401	2710
3	25.6	0	0	3	a	1170	7765	2315
	26.2				a	1170	8093	2514
	26.5				a	1170	8116	2529
	26.8				a	1170	8116	2529
	48.2				b	2701	10079	3900
	71.7				c	3843	10638	4345
	95.6				d	4396	10942	4597
	167.7				e	4914	11263	4871
14	21.3	0	0	2	a	1273	9107	3184
	21.6				a	1273	9326	3339
	22.1				a	1273	9634	3563
	22.5				a	1273	9714	3623
	23.4				a	1273	9730	3635
6	24.9	0	1000	1	b	1683	9221	3265
	48.2				c	3927	9221	3265
	97.2				d	5029	10729	4419
	144.3				e	5259	11347	4943

CT Images of one slice of scans for Specimens #11, #6, and #9 are shown in Figures 38-40. The images are from approximately midway along the axis of the specimens. The principal features indicated in these images are the large voids associated with absorption of free water into the cement crystal structure during curing, and deformation-related fractures. The image of the failed

specimen #11 (Figure 38), shows considerable internal fracturing, consistent with the failure seen in the stress-strain plot (Figure 28). Scans of a Mix 2 specimen (#6, Figure 39) and a Mix 1 specimen with water removal (#9, Figure 40) showed no evidence of internal fracturing. Neither of these specimens, nor any other Mix 1 wicked specimens or Mix 2 specimen, wicked or unwicked, showed evidence of failure during the triaxial deformation.

Water content appears to affect the strength of the cured cement, as evidenced by the observation of failure (and larger values of NRS) during deformation of Mix 1 specimens for which excess free water was removed by wicking. However, this may not be related to the strength of the cement matrix. Specimen #10, also a Mix 1 sample with no wicking, gave no indication of failure, either in the stress-strain behavior (Figure 30) or from visual inspection of the post-deformation specimen. The principal difference between curing in Specimen #10 and all the other un-wicked Mix 1 specimens is that only Specimen #10 was cured while unconfined.

No CT scan was carried out for Specimen #10. However, a visual comparison of Specimen #10 with Specimen #11, shown in Figure 41, does suggest a possible mechanism for the difference in failure behavior: differences in effective stress. Few of the large vugs seen in CT images were visible on the visual observation of specimen surfaces in, but the ones that are visible for Specimen #10 appear to be significantly larger than those for Specimen #11. The un-wicked Mix 1 specimens have the greatest volume of free water prior to deformation, and post test observations (several days after mixing) still show remnant free water. This would indicate that specimens still have significant quantities of pore water during the initial deformation cycle. If this were the case, pore pressure could be created during the early stage of the triaxial loading, leading to a lowering of effective stress and a corresponding decrease in compressive strength. On the other hand, the larger pore volume created in Specimen #10 during unconfined curing, would accommodate a greater volume of pore water without a significant decrease in effective stress, and an apparent increase in compressive strength.

Variations in p-wave velocities with curing time are shown in Figure 42, for all test specimens. There is more scatter in these data than for velocities determined in the 4"x4" Box Tests (Figure 8), reflecting the greater loss of signal strength for the SPS transducers, propagation through longer test specimens (nominal 2 ½ inches in the SPS versus 1 inch in the box), and the well documented (Chapter 1) presence of water and an associated top specimen roughness in the SPS configuration. Nevertheless, the pattern of variations and asymptotic values is the same for both test series (Figures 14 and 42).

21

Variations in static Young's moduli with curing time are summarized in Figure 43. The overall behavior indicates that static deformation behavior of these cement mixtures are similar to those in the dynamic moduli (Figure 42). Again, no systematic relationship between Young's moduli and curing pressure is evident.

The magnitudes of the non-recoverable strains for this series of tests are significantly larger, and the unloading moduli are significantly smaller, for the first deformational cycles than those for subsequent deformations. Differences between loading and unloading slopes, and the magnitudes of non-recoverable strains, decrease with subsequent deformations, becoming negligible by the third cycle. Loading behavior for the un-wicked Mix 1 specimens after 24 hours (#7, 8, 11, and 12; Figures 24, 27 – 29) shows a large positive curvature at low stresses, gradual yielding at intermediate stresses (1.5kpsi), and failure at approximately 1.8 kpsi. These specimens have the largest non-recoverable strain of all multiple-deformation specimens. Deformation of the Mix 2 specimen #6 and the wicked Mix 1 specimen #9 are initially more linear than deformations of specimen #8, and show a gradual decrease in slope (yielding) at 1.4 to 1.8 kpsi. None of the Mix 2 or wicked Mix 1 specimens show evidence of failure.

However, the variations in behavior observed for this series of tests may be related to two different processes: 1) deformation and failure of the cement surface at the end(s) of the specimen; and 2) hardening and strengthening of the cement as it cures. Clear evidence for the development of surface irregularities is visible on the top of the specimens at the ends of the tests, and the deformation of small-scale surface features could lead to additional strain, and obscure behavior due to the curing process. In order to assess this surface-related behavior, a modified sequence of curing and deformation measurements were carried out.

Deformation behavior for the Series III tests are shown in Figures 44 - 48. Variations in computed Young's moduli with curing time are shown in Figure 49. The modulus variations again show the large scatter associated with determinations of static Young's moduli, but the behavior follows the same trend as the dynamic moduli (Figure 16) and the trend indicated for the unloading moduli for the Series II tests Figure 43): a rapid increase after curing for about 14 hours, slowing rate of increase through the next few days, and settling to an asymptotic value after 5 – 7 days. In spite of the large scatter the data for the Series III tests do show a tend towards lower values than those found for the Series II results, which is compatible with larger surface-related strains in the Series III tests. The data support the hypothesis that the surface effects are largely eliminated

22

during the first loading cycle of the Series II tests, but are present for each of the (single) deformation cycles in the Series III tests.

Non-recoverable strains for the Series III tests at different curing times are shown in Figure 50. Also shown in the plot are results from the Series II Mix 1 tests, with and without removal of the initial free water by wicking. The permanent strains for the Series II Mix 2 tests, on both wicked and un-wicked specimens, again indicate the presence of a non-recoverable surface deformation during the first deformation cycle, which is absent for the subsequent cycles. The variations of the Series III strains, all of which include the first-cycle surface strains, show a smoother and more gradual decrease in non-recoverable strain than the multiple-cycle deformational cycles of the Series II tests. Except for the initial deformation cycle after curing for 24 hours, all the Series II tests have permanent strains below those for the Series III tests

Measured behavior during deformation cycles of Mix 2 specimens (Series IV tests) is shown in Figures 51-55. The amount of permanent strain is clearly smaller, and the stress-strain slopes are clearly larger, for all the Mix 2 tests. Results from the Series III and Series IV are compared in Figure 57. They exhibit the same type of behavior as Mix 1 specimens (Figure 43; data is re-plotted on Figure 58 for comparison), but all Mix 2 values of Young's modulus are larger than corresponding Mix 1 values. Results from the repeat deformations are re-plotted in Figure 59.

As noted, permanent strains for Mix 2 (Series IV) specimens are all significantly smaller than corresponding values for Mix 1 (Series III). In fact, all permanent strains for Mix 2 are effectively zero, except for the single test for the 14-hour curing time. Note that two different specimens were tested for curing times of 24 hours; results for the two tests were approximately identical.

The Series III and IV tests again show a weakening effect of excess water on deformational behavior, and confirm the presence of surface-related deformations in addition to the deformations related to material hardening with curing time. Test results from the previous test sequence, in which a cement specimen was repeatedly deformed at various intervals of curing, showed that the magnitudes of the non-recoverable strains are significantly larger, and the unloading moduli are significantly smaller, for the first deformational cycle than those for subsequent deformations. The separate test specimens aged for time periods of 14, 24, 36, 48, or 168 hours before deformation show lower values of non-recoverable strain, and larger values of unloading moduli than those found for the Series II results in support of the hypothesis that the surface effects are largely eliminated during the first loading cycle of the Series II tests, but are present for each of the (single)

23

deformation cycles in the Series III tests. The amount of permanent strain is clearly smaller for Series III tests, and the stress-strain slopes are clearly larger, than for all the Series IV (Mix 2) tests.

3. Discrete Element Modeling

The third area of investigation in the program of studies was a numerical simulation of wave propagation in the well-bore/casing/cement environment, using a simulator which is based on micromechanical deformational processes. In work through this program year, formalism for such a treatment of wave propagation has been established. In the following discussion of activities to date, several examples of simulated behavior are presented, to demonstrate the utility of the approach in understanding behavior observed in the experimental program. The numerical simulations are based on a two-dimensional discrete particle method PFC2D, (Potunday and Cundal, 2004), a commercial discrete element model (DEM). PFC2D is designed to simulate mechanical properties using an assembly of small finite particles. Macroscopic deformational and wave propagation behavior are derived from first-principal micromechanical processes, coupled with a graphical user interface for the visualization of the waves.

The DEM simulation used in this study models the mechanical properties by treating the sample as a collection of spherical particles interacting via Newton's second law. The interaction of particles is treated as a series of springs, arising from overlap between the particles, and by elastic forces developed by deformation of inter-particle bonds. The inter-particle bonds represent cement with a finite volume, and are designated here as cement bonds. These bonds are also referred to as parallel bonds, because they contributed forces in addition to – or in parallel with – contact forces arising from overlap between particles. The various particle-particle interactions are shown schematically in Figure 60. In this study, mechanical properties of the particles and of the cement bonds are the same.

The particles in this simulation represent a basic cell of cement or steel, into which porosity will be introduced later. The sample consists of a two-dimensional assembly with hexagonal packing of circular particles, for which the aerial porosity between the particles is 9%. In order to reduce the porosity to zero, cement (parallel bond material) between the particles is assigned a mass and size to completely fill the void space. The particles are treated as a collection of spheres whose centroids all lie within the same plane.

The inter-particle bonds in the cement and in the steel are uniform within the assembly, but the bonds at the steel-cement interface have mechanical properties which are adjusted or removed to

simulate variations in bonding. The properties and position of each bond were set individually, allowing for conditions such as channeling and poor cement bonding to be simulated. The particles and the cement have both shear and normal stiffness.

Waves in PFC2D are modeled by imposing a velocity to a subset of the particles (transmitters). The imposed particle velocities propagate through the assembly via inter-particle forces, in the same manner as elastic disturbances in a physical system. Waves are detected at another subset of designated particles (receivers). Wave forms are determined by the time dependence of particle velocities at specified positions.

A portion (approximately half of the total length) of the model assembly is shown in Figure 61. The total assembly contains about 20,000 particles. Selected groups of particles are configured to act as wave transmitters or receivers. The 'transducer' groups are placed in the same positions in the model assembly as in the laboratory assembly discussed in the previous chapter. Additional transmitters and receivers are placed within the assembly to record the wave behavior as it propagates in the assembly. The gray particles in assemblies represent the cement, the yellow particles steel, and the reddish-brown lines between the steel and the cement are the parallel bonds at that interface. The purple particles are wave transmitters in the assembly, and the other colors represent wave receivers.

The receivers in the steel as depicted in Figure 61 are spaced 5 centimeters apart. Transmitters and receivers were also placed in the cement, with the receivers shown in Figure 61 placed 5 centimeters apart in position to measure wave propagation vertically in cement. The transmitters and receivers which measure horizontal wave propagation from left to right through the cement are 5.08 centimeters apart. Additional receivers, not shown in Figure 61, were placed in the cement along the left to right propagation path. Waves are created by specification of particle velocities.

Figure 62 illustrates the process of p-wave generation, by imposing a sinusoidal particle velocity in the horizontal direction, shown in red, onto the red-colored transmitter particles on the left-hand surface. Figure 63 shows the distribution of particle velocities after the initial particle oscillations have propagated across the width of the assembly. The p-wave velocity is given by the assembly width divided by the elapsed time for the detection of motions of particles in the right-hand receiver (purple balls).

The model input parameters for the model were determined by comparing computed wave velocities with published values, and altering the spring stiffness of the particles to match the

measured wave velocities. Initial values of normal and shear stiffness values for the particles were determined by the relationship between the particle stiffness, (spring constant), k^n and k^s, and the corresponding elastic constant (E_C; Itasca, 2002):

$$k^n = \frac{AE_c}{L} \tag{3.1}$$

$$k^s = \frac{12IE_c}{L^3} \tag{3.2}$$

In equation 3.1, k^n and k^s are the normal and shear stiffness of the particle, A is the cross-sectional area at the contact, E_c is the contact Young's modulus, E_c, and L is the length between the particle centers. I is the moment of inertia of the particles. The contact Young's modulus is found to be related to the material Young's modulus by a factor of four (Park, 2006). The relation between the mechanical properties of the bonding to the input properties of the parallel bonds is (Itasca, 2002):

$$\bar{k}^n = \frac{\bar{E}_c}{L} \tag{3.3}$$

$$\bar{k}^s = \frac{3\bar{R}\bar{E}_c}{4\tilde{R}L} \tag{3.4}$$

where $\bar{R}$ is the radius of the parallel bond and $\tilde{R}$ is the particle radius.

Two particle assemblies were used for the model calibrations. Each of these assemblies contained 20,000 particles of only one material (steel or cement). The model contained a transmitter and two receivers and the wave velocity was measured between the first and second receivers. The velocities were considered matched if they were within 30 m/s of the actual velocity of the materials.

A comparison of actual wave velocities for cement (Gray, 2006 a,b), steel (Rose, 1999), and quartz (Best, 1997) to wave velocities determined from the PFC simulation are shown in Table 3. From the tabulation, the wave velocity for the modeled steel and cement is within an acceptable margin of error. Quartz particles, which are used later in the study, were also modeled.

Table 3. Wave velocities of assembly materials for model calibration

Material	V_p (m/s)	V_s (m/s)	$V_{p\ modeled}$ (m/s)	$V_{s\ modeled}$ (m/s)
Steel	5820	2950	5836	2939
Class H Cement	3386	1924	3361	1895
Quartz, Solid	6047	4092	6048	4304
Quartz, un-Consolidated	1000		981	

This calibrated DEM model was then used to carry out several simulations to characterize different aspects of wave propagation behavior in detail. Variations in bond quality, fraction of intact bonds, and bond stiffness at the steel-cement interface were introduced to investigate the effects on wave behavior in the model. The simulations were fashioned to replicate wave paths used in the experimental tests in Section b.

WAVE PROPAGATION IN CASING - VARIATIONS IN FRACTION OF BONDS

Figure 64 shows the initial portion of waveforms for simulated p-waves traveling vertically through the steel portion of the assembly, for three different fractions of intact bonds between cement and steel particles at the interface. Figure 65 plots the normalized amplitude as a function of the fractions of intact bonds (equivalent to the percentage of contact area bonded in this 2D simulation). The plot clearly displays a linear relationship between wave amplitude and the percentage of intact bonds. Hence, wave propagation simulated by PFC confirms the essential aspect of cement bond log theory: the amplitude of waves propagating in the steel 'casing' should decrease as the percentage of the bonds between cement and steel at the cement-steel interface increases (Pardue et al., 1963).

In the above simulation the un-bonded particles were uniformly distributed along the interface between transmitter and receiver. The effects of non-uniform bonding on wave amplitude were also examined. For this simulation, two non-uniform distributions of bonds were used, in which the density of cement-steel bonds adjacent to the receiver differs from the average bond density between the transmitter and receiver. In Case 1 (Figure 66), all bonds between transmitter and receiver are intact. In Case 2 (Figure 67) only half the bonds along the interface between transmitter and receiver, and none of the bonds adjacent to the transmitter are intact. In both non-uniform distributions a total of 66% of all bonds along the left hand interface are intact. The locations of the bonds are displayed as blue lines in Figures 66 and 67 for the two different distributions. Note that the assemblies in Figures 66and 67 show only a portion (approximately half) the total assembly of particles. Computed wave forms for these distributions are shown in Figure 68.

For non-uniform bonding Case 1, the computed wave amplitude is indistinguishable from that for the 100 percent uniformly bonded case (in which all touching particles are bonded). The measured energy loss into the cement depends not only on the total percentage of the surface area

27

bonded, but also the location of the bonds relative to the receiver. Computed amplitude variations for non-uniform distribution Case 1 are indistinguishable from the 100 percent (uniform) bonded case (all touching particles are bonded). In this example, 66% of the total number of touching particles over the cement-steel interface on the left side of the sample were bonded, but the all of touching the particles on the surface area between the transmitter and the receiver were bonded.

In the next example 50 percent of the touching particles in the steel-cement interface between the transmitter and the receiver were bonded. There are no bonds in the zone adjacent to the transmitter in this case; all of the bonds between the transmitter and the receiver are located near the receiver. Again, 66% of the total number of touching particles on the left side steel-cement interface were bonded.

These simulations indicate that non-uniform bonding leads to significant uncertainty in bond index determinations. The results show that the bond index measures the percentage of the steel-cement interface bonded between the transmitter and receiver, but it is especially sensitive to changes in bonding near the receiver. This is supported by Table 4, which gives the bond index measurement compared to the percentage of the surface area at the steel-cement bonded between the transmitter and the receiver. The large error of the bond index measurement in non-uniform case 2 was also found in several other non-uniform bonding cases (not shown). The simulations indicate that bonding in the region adjacent to the receiver has a greater effect on the amplitude of the recorded wave than bonds located away from the receiver.

Table 4. Bond Index determinations for distributions in which 66% percent of the total steel-cement interface is bonded. These values were calculated from the simulations shown in Figure 68.

Case	Bond Index	Actual Percent Bonded Between Receivers
66% uniform	0.68	0.66
66% non-uniform 1	1.00	1.00
66% non-uniform 2	0.37	0.50

WAVE PROPAGATION IN STEEL, VARIATION IN BOND STIFFNESS

The next simulations were carried out to investigate the effects of a weakening of the chanical properties of the bond material on wave propagation. For this simulation the stiffness of the bonds at the steel-cement interface was reduced. Only the bonds at the steel-cement interface were altered. Figure 69 illustrates the changes in wave amplitude due to changes in the mechanical bonding at the steel-cement interface. The samples in Figure 70 were completely bonded at the steel-cement interface, while the bond stiffnesses of the interface bonds were varied. The summary

of results in Table 5 shows that changes in the mechanical properties have the same effect on amplitude as fractional changes in the fraction of the bonded contact area.

Table 5. Bond index measurement for a fully bonded steel-cement interface; with changes to the mechanical properties of the bonds. The measurement was calculated using the amplitudes from the simulations shown in Figure 69.

Case	Bond Index
10% Stiffness	0.118
50% Stiffness	0.587
90% Stiffness	0.901
100% Stiffness	1.000

WAVE PROPAGATION IN STEEL, VARIATIONS IN MECHANICAL PROPERTIES AND BONDING FRACTION.

The next simulations were carried out for cases in which both the mechanical properties of the bonds (bond stiffnesses) and the percentage of the intact bonds at the steel-cement interface were varied. A value for the percentage of bonds was first selected, and for each value, simulations were carried out for four different values of stiffness. A new value of bond fraction was then selected, and the simulations were again carried out for the four stiffness values. Simulations were carried out for stiffness values of 100%, 90%, 50% and 10% of the cement bond stiffness value, and for fractions of intact bonds of 100%, 90%, 50% and 10% percent of the total value. Figure 71 shows amplitudes of p-wave traveling in steel, for the case of a uniform distribution of 90 percent of intact bonds along the interface, with the indicated stiffnesses.

Table 6. Bond Index simulations on samples with various mechanical properties, for 90% uniformly bonded contact area. Values were calculated from the simulations shown in Figure 70.

Percent of Contact area Bonded	Bond Mechanical Properties	Bond Index
90%	10%	.118
90%	50%	.447
90%	90%	.874

The results in Table 6 show that these bond index measurements can be approximated by the product of contact area bonded multiplied by the percentage of the mechanical properties of the cement present in the bond mechanical properties. For instance, when 90 percent of the contact area of the steel-cement interface was bonded, and the bond mechanical properties were 90 percent of the cement mechanical properties, the bond index measurement was 0.874, close to the value of 0.81 expected for 90% bonding fraction with bond material with 90% stiffness. Table 7 shows the

variations in p-wave amplitude with variations in bond stiffness, for a specimen with 50% bonding fraction. Again, computed bond index roughly scales with the product of bond fraction and percentage of bond stiffness. Additional simulations with different bond fractions and stiffnesses all showed the cumulative effect on amplitude.

Table 7. Bond index measurement on modeled sample with altered bond mechanical properties and 50% of contact area bonded uniformly

Percent of Contact area Bonded	Bond Mechanical Properties	Bond Index
50%	10%	0.076
50%	50%	0.356
50%	90%	0.461

Simulations were next carried out for specimens in which half (50%) of the bonds are intact, but are not uniformly distributed along the cement-steel interface. Intact bonds shown in Table 8 were clustered at three locations along the steel-cement interface. In the first case, there were two clusters of bonds at the interface: one located between the transmitter and the receiver, with no bonds immediately before the transmitter or after the receiver; a second cluster of bonds that started just before the receiver; and a the third case for which bonding at the interface started at the base of the sample and continued to the midpoint of the sample height where the receiver is located. These results show that amplitude variations scale roughly with the cumulative effect of conditions at the steel-cement interface, but variations in non-uniform distributions can lead to substantial deviations from the general trend.

Table 8. Bond index determinations in a simulation of variations in bond mechanical properties, for an average of 50% area bonded non-uniformly. The bonding in the first case was clustered between the transmitter and the receiver, with no bonding just before the transmitter and after the receiver. In the second case the bonding between the transmitter and the receiver was just before the receiver. The majority of the bonding in this case was not located between the transmitter and the receiver. In the third case the interface was fully bonded between the transmitter and the receiver.

Total Percentage of surface area bonded	Bond Mechanical Properties	Percent of Surface area between Receivers Bonded	Bond Index
50%	10%	100%	0.181
50%	10%	5%	0.034
50%	10%	100%	0.138

WAVE PROPAGATION IN STEEL: DISTRIBUTION OF MECHANICAL PROPERTIES

From the foregoing discussion, alteration of the mechanical properties of bond material at the steel-cement interface affects the amplitude of waves propagating in the steel in the same

manner as the percent of the interface bonded. It has also been shown that placement of unbonded and bonded zones affects the p-wave amplitude. The next series of simulations were carried out to investigate the combined effect of non-uniform distribution of properties and bonds on wave amplitudes. This simulation was carried out on a sample with 90 percent of the bonds between the transmitter and the receiver bonded. The mechanical properties for half of the distance between the transmitter and the receiver were decreased to 10 percent of the cement mechanical properties. The results of these simulations were compared to the same sample with bond mechanical properties that were 10 percent and 100 percent of the cement mechanical properties for all bonds at the steel-cement interface. Figure 71 shows that changes in the steel-cement interface near the receiver have less effect on wave amplitude than changes further from the receiver. This behavior is similar to that observed when testing the percentage of the contact area bonding. Changes in the mechanical properties near the receiver have less effect on the recorded amplitude.

The results shown in Table 9 indicate that placement of altered bond mechanical properties at the interface have more of an affect on wave amplitude than placement of unbonded zones. The method of estimating the bond index measurement by multiplying the percent of the contact area bonded by the percentage of the original mechanical properties present between the transmitter and the receiver is not accurate enough to be used with any confidence. Similar behavior was found for other simulations.

Table 9. Effect of Placement of altered bond properties between transmitter and receiver. Half of the length (referenced in the Case description) has altered properties. The other half has of the mechanical properties of the cement.

Case	Bond Stiffness	Bond Index
Near transmitter	10%	0.735
Near receiver	10%	0.375
reference	10%	0.118
reference	100%	0.921

WAVE PROPAGATION THROUGH CEMENT; VARIATIONS OF BONDING FRACTION

The discussion thus far has considered the effects of bonding and mechanical properties on p-wave transmission through the steel 'casing'. In the next discussion, consider horizontal p-wave propagation within the cement zone. The experimental study clearly demonstrated that the quality of the bonding at the steel-cement interface significantly affects wave behavior through the cement. In the simulations of this behavior, the percentage of the steel-cement interface bonds on the left side of the sample were altered, while the bonding at the steel-cement interface on the right side of

the sample was fixed at 100% of the steel-cement interface bonds. Waves were input at a transducer on the left edge of the sample and detected at a receiver located on the right edge. The effects of varying mechanical properties of the bond were also investigated by altering the bond stiffnesses at the steel-cement interface on the left side of the sample.

Results of simulations for different distributions of interface bonds are shown in Figure 72. The amplitudes decrease as the percentage of intact bonds at the steel-cement interface on the left side of the sample decreases, although the amplitude is not reduced to zero with 0% bonding (wave energy is still transmitted across the interface by physical contacts between steel and cement particles). Simulations of the effects of altered bond mechanical properties (not shown here) also show a decrease in amplitude with decreasing stiffness of the bonds.

Figure 73 presents results from the same simulations plotted on an expanded time scale, which shows high frequency (nominal 1MHz) oscillations caused by multiple reflections of the wave at the surfaces of the steel plate. Similar behavior was observed in some of the measured waveforms in the experimental study (see Figure 17 or 18). These high-frequency oscillations are not attenuated in the same manner as the main pulse (see below). The oscillations probably arise from multiple reflections within the steel on the left side of the specimen. They have potential as a means for more precise determination of the quality of bonding between cement and casing, and will be treated in some detail in the following discussion.

WAVE PROPAGATION IN CEMENT: EFFECTS OF QUARTZ CONTENT

The next simulations were carried out to investigate the effects of inclusions in the cement. Two types of inclusion were investigated: quartz and void space (porosity). The inclusions were introduced by replacing cement particles at randomly selected positions. Cement bonds were used to bond the cement to the quartz. The steel-cement interface in this sample was 100% bonded for both the left and the right interface. The waves were introduced into the sample on the left side and detected on the right side.

Both types of inclusions alter the acoustic impedance of the cement. Figure 74 shows that the inclusion of quartz into the cement generally increases the amplitude. However, an upper limit is reached at a concentration of about 10 percent quartz, and the computed amplitude of the waveform for a quartz concentration of 10 percent was higher than that for 15 percent quartz. From visual inspection of the assembly, it appears that this anomaly was caused by the placement of the

quartz grains. The sample with 10% quartz had a higher percentage of quartz between the transmitter and receiver than the sample with 15% quartz.

The addition of quartz to the sample increases the propagation velocity in the sample, as shown by the decreases in arrival times in Figure 75. The effect of the addition of quartz on the acoustic impedance of the cement is displayed in Table 10. The inclusion of quartz in the model assembly increased the impedance. The high-frequency oscillations in this simulation are not significantly affected by quartz content.

Table 10. Acoustic impedance in the cement with the addition of quartz in the cement.

Percent Quartz in Cement	Z_o (kg/m^2s)
0.00%	6.40E+06
1.00%	6.42E+06
5.00%	6.53E+06
10.00%	6.67E+06
15.00%	6.87E+06
20.00%	7.06E+06

WAVE PROPAGATION THROUGH THE CEMENT; EFFECTS OF VOIDS

In the next simulations, void spaces were introduced by removing cement particles at randomly selected locations. The additional porosity reduces propagation speed, as shown in Figure 76. The variation in acoustic impedance with inclusions of voids is listed in Table 11.

In addition to the changes in acoustic impedance, the introduction of voids into the assembly leads to waveform scattering. The large discontinuity in mechanical behavior at the void locations leads to local reflections, and this scattering leads to a corresponding decrease in signal amplitude. The scattering is sensitive to wavelength, and should be greatest when the wavelength is on the same order as the size of the voids. Wavelengths in this simulation are not this small, but scattering should be greater for the higher-frequency waves created by the multiple-reflection within the steel, than for the lower frequencies input directly. This is the behavior exhibited for signals shown in Figure 76.

The decrease in high-frequency content is clearly shown in Figure 76 for specimens with void content. At a concentration of 5 percent the high frequency oscillations are still present, but they have almost completely disappeared for a void concentration of 10%. At the same time, the amplitudes of the lower-frequency waveforms increase with void concentration, as energy from the high-frequency signals is converted by the scattering into the lower-frequency signals.

Table 11. Variations in acoustic impedance in cement with the addition of voids.

Void Concentration in Cement	Z_o (kg/m^2s)
0.00%	6.40E+06
1.00%	6.31E+06
5.00%	5.83E+06
10.00%	5.30E+06
15.00%	4.74E+06
20.00%	4.27E+06

WAVE PROPAGATION THROUGH THE CEMENT: COMBINED EFFECTS OF QUARTZ AND VOIDS

In the next simulations both quartz and voids were added to the cement. The steel-cement interfaces were fully bonded for these simulations. A wave was introduced at a transmitter on the left edge of the assembly, and detected by the receiver on the right edge.

The computed waveforms in Figure 77 show effects from variations in void concentration for a fixed (5%) quartz concentration. The observed behavior is similar to that in Figure 76 for the addition of voids only, except that that the high-frequency oscillations are still present to some degree for 15 percent void concentration in the sample.

Figure 78 shows the variations in p-waveforms with void concentration, for waves in samples with fixed 10% quartz content. The waveforms differ only slightly from those for 5% quartz content. This is shown in greater detail in Figure 79, which shows variations with quartz content for fixed (15%) void content. This plot is very similar to the plot of amplitude variations shown in Figure 74. The addition of quartz has little impact on computed waveform amplitudes.

Three cases without high frequency oscillations, as determined by the graphical display of particle velocity, are compared to the case with no quartz in the cement, in which the high frequency oscillations did occur. In cases where destructive scattering occurred, an increase in quartz caused the amplitude to decrease and the smoothness of the waveform to increase. All cases of destructive scattering had significant increases in amplitude compared to the reference case.

EVOLUTION OF HIGH-FREQUENCY SIGNALS

The final set of simulations looks at the evolution of the high-frequency waves, presumably generated by the multiple reflections in the steel plates, and attenuated by scattering of the waves by voids in the cement. These waves may – or may not - impact interpretations of signals in bond quality tools. Analysis of their behavior illustrates the utility of PFC simulations, in which wave

behavior within the interior of material. Such observations are completely outside the realm of possibility for experimental measurements in the laboratory.

One of the concerns about wave propagation in the bore-hole environment is whether the observed behavior is due to interface processes, or due to changes within the body of cement. For this investigation direct observations of particle motion of cement particles during wave propagation are combined with 'virtual' receivers (designated particles used for detecting wave behavior). This approach permits the viewing of waveforms at any stage of their generation and propagation, and to completely isolate interface behavior from changes during wave propagation.

Figure 80 shows waves detected from such a receiver located just beyond the steel-cement interface on the left side of the sample. It shows an initial half cycle of the high-frequency introduced on the left side of the specimen, and several cycles of the high-frequency signal from multiple reflections in the steel on the left side. None of these high-frequency signals ultimately reach the external receiver on the right side of the assembly (cf., Figure 79). The plot shows graphically that the disappearance of the high frequency signal is not from inadequate coupling of the signal into the specimen.

Figure 81 the wave-form detected at a receiver placed midway along the path within the cement. It shows that the high-frequency waveforms were still present midway through the cement, although at reduced amplitudes resulting from scattering within the cement. All the signal wavelengths have increased in Figure 81, also due to the scattering.

The wave-forms detected at the external receiver on the right side of the model assembly was shown in Figure 79. None of the high-frequency waveforms are evident in this figure. The apparent wavelength of the measured wave has increased significantly, due to overlapping scattering fields recorded at the receiver. Much of the high-frequency attenuation was due to scattering (Figure 81), but some of the losses were at the right side interface (Figure 82).

Using PFC's graphical display, effects of cement inclusions on wave propagation can be visually assessed. The following series of simulations tracks waveforms by the locations and magnitudes of particle velocities (red arrows) associated with wave propagation. The first set of figures, Figures 83 through 85, show particle displacements during wave propagation in a cement sample with no voids (no scattering). The high-frequency cycles are clearly evident in all three plots, as the wave travels across the cement and as it is reflected back by the interface on the right (Figure 85).

The next set of simulations show the propagation of the same wave-form introduced in the previous figures, into cement with a small (5%) void content. Some wave-form degradation is evident from the beginning (Figure 86), but the wave front (first arrival) is still clearly defined. After traversing the cement, much of the high-frequency content is absent (Figure 87), while the distinct wave front persists. Some evidence for the presence of the high-frequency signal still exists in Figure 88, after reflection from the right side interface, but the wave-form has been substantially dispersed by the scattering..

The last set of simulations show the wave behavior in the cement with 15% voids. The wave-form is already dispersed by the first cycle of input signal (Figure 89). After the wave-front has almost traversed the cement (Figure 90) almost all high-frequency content has disappeared, and the wave-form is reduced to a uniform distribution of particle motions behind a distinct wave-front (Figure 91). Further dispersion of the wave-form, and a less-well defined wave-front are evident in the wave reflected from the right side (Figure 92). The simulation results clearly show that the attenuation of the high-frequency signal (s) if due to scattering from voids within the cement, and not from coupling the signals at the steel-cement interface.

CONCLUSIONS

It has been more than ten years since the last significant advances in commercial cement evaluation tools. In this time, significant changes have taken place in the nature of wells and the requirements of the cement that is used. The increase in the popularity of gas storage wells and the prospect of large numbers of carbon dioxide storage or sequestration wells presents new problems. The cost of logging must be balanced by the fact that even a good log is not a guarantee of a good seal. In many cases the operator's judgment is based on the understandings of older economic calculations. This may require rethinking to fully utilize newer technology and adapt to the changes that are taking place in the industry. It is our belief that coordinated laboratory testing and numerical simulations can best address these needs. This study has demonstrated the viability of this approach in several test sequences.

New test procedures and apparatus were developed for the study of cement-boundary interactions during curing and deformation. Compressional and shear wave velocities were monitored during nominal one-week curing periods. P-waves are detected immediately upon pouring the slurry into the chamber, and travel times during the initial 6-10 hours of curing are almost constant. A dramatic increase in velocity between 11 and 23 hours of curing reflects the initial solidification of the slurry. The earliest evidence for shear waves is seen after curing for more than 9 hours, consistent with the p-wave evidence that prior to this time the specimen is still a liquid. Measured behaviors for both p- and s-waves are highly reproducible. Dynamic Poisson's ratios determined from the set of shear and compressional mode velocities were found to vary from initial values of 0.5, representative of a fluid at curing time near zero, to about 0.25, typical of intact rock, as the cement cures. A second assembly was also developed, which provides for simulations of wave propagation along a casing-cement interface.

Experiments carried out in an in-house triaxial testing system, during curing of cements from slurry to rigid solid, provide further information on cement-casing bonding, and simultaneous wave velocity measurements correlate with the static behavior. Variations in axial stress with axial strain after overnight curing are generally non-linear and exhibit substantial permanent axial strains. Subsequent cycles are almost linear, with almost no permanent strain. Stress-strain variations are strongly affected by the amount of water retained in the cement during curing. The observed variations suggest that the variations of strength with water content are the consequence of excess

37

pore pressure.   The strong dependence of cement mechanical behavior on water content will be a concern of subsequent studies.

Test results from test in which cement was repeatedly deformed at various intervals of curing, showed that the magnitudes of the non-recoverable strains are significantly larger, and the unloading moduli are significantly smaller, for the first deformational cycle than those for subsequent deformations. In the present research separate test specimens aged for different time periods before deformation show lower values of non-recoverable strain, and larger values of unloading moduli than those found for the multiple-deformation results. The results suggest that the surface effects are largely eliminated during the first of several repeated loading cycle, but are present for each of the (single) deformation cycles in the single-cycle tests.   The amount of permanent strain is clearly smaller for single-cycle tests on Mix 1 (cement only) material, and the stress-strain slopes are clearly larger, than for all the single-cycle tests on Mix 2 (cement plus moisture-absorbents) specimens.

The companion numerical simulation tests were able to reproduce central features of the experimental tests, and illustrate the potential for utilizing the simulations to better understand cement bond quality. The study achieved two goals: 1) It has provided a numerical framework, based on a discrete particle computation, to quantitatively analyze details of the propagation of waves in the well-bore – cement environment; and 2) Preliminary analysis using the simulation has provided information that is directly useful for interpreting bond quality in log tools. Computed changes in the fraction of the area bonded at the steel-cement interface (bond quality) are consistent with those predicted by cement bond log theory. However, the simulations show quantitatively that changes in the mechanical properties of material at the interface lead to behavior which can be indistinguishable from that of poor bonding. This can be an important cause of error when interpreting the quality of the bond between the cement and casing from the bond index measurement.

Simulations of wave propagation within the cement show details of wave-particle interactions, and demonstrate that interactions within the cement are as important as behavior at the cement-casing interface. This behavior has direct application to measurements using the variable density log. Additional simulation of wave propagation in a casing coupled, with varying degrees of bond quality, to cement with varying degrees of material properties (porosity, bond and particle stiffness) provide for comprehensive evaluation of the existing wireline tools.

This preliminary analysis of wave propagation with a discrete particle simulation indicates that the behavior can be predicted in considerable detail. Further activity, with more rigorous material properties and boundary conditions, could lead to significant improvements in bond log interpretation. The wave propagation model in PFC2D can be expanded to the bond between the cement and the formation. Ultimately, simulations of wave propagation in full three-dimensional models should be carried out.

REFERENCES

Best, A. I., Sams, M.S., 1997, Compressional Wave Velocity and Attenuation at Ultrasonic and Sonic Frequencies in Near-Surface Sedimentary Rocks, *Geophysical Prospecting*, Vol. 45, No. 2, pp. 327-344.

Froelich, B., Pittman, D., and Seeman, B.: Cement Evaluation Tool - A New Approach to Cement Evaluation, *Journal of Petroleum Technology*, Aug., 1982, pp. 1835-41.

Gray, K. E., 2006a, Acoustic Signatures During Cement Slurry Hardening: Part 2, GSTC Quarterly Report #1, June 1, 2006 - August 31, 2006. DE-FC26-03NT41779 (3139-UT-DOE-1779).

Gray, K. E., 2006b, Acoustic Signatures During Cement Slurry Hardening: Part 3, GSTC Quarterly Report #2, September 1, 2006 - November 30, 2006 (DE-FC26-03NT41779 (3139-UT-DOE-1779).

Grosmangin, M., Kokesh, F.P., and Majani, P.: A Sonic Method of Analyzing The Quality of Cementation of Borehole Casings, *Journal of Petroleum Technology*, Feb., 1961, pg 165.

Itasca Consulting Group, Inc., 2002, PFC^{2D} (Particle Flow Code in 2 Dimensions), Minneapolis, MN.3

Pardue, G.H., Morris, R., Gollwitzer, L.W., and Moran, J. H., 1963, Cement Bond Log - A Study of Cement and Casing Variables, *Journal of Petroleum Technology*, May, pp. 545-555.

Park, N., 2006, *Discrete Element Modeling of Rock Fracture Behavior: Fracture Toughness, and Time Dependent Fracture Growth*, Dissertation, University of Texas at Austin.

Potyondy, D. O. and Cundall, P. A., 2004, A Bonded-Particle for Rock, *International Journal of Rock Mechanics and Mining Sciences*, Vol. 41, No. 8, pp. 1329-1364.

Rose, J. L., 1999, *Ultrasonic Waves in Solid Media*, Cambridge University Press, New York.

Tixier, M. P., et al.: Sonic Logging, *Journal of Petroleum Technology*, Vol. 216, 1959, p. 106.
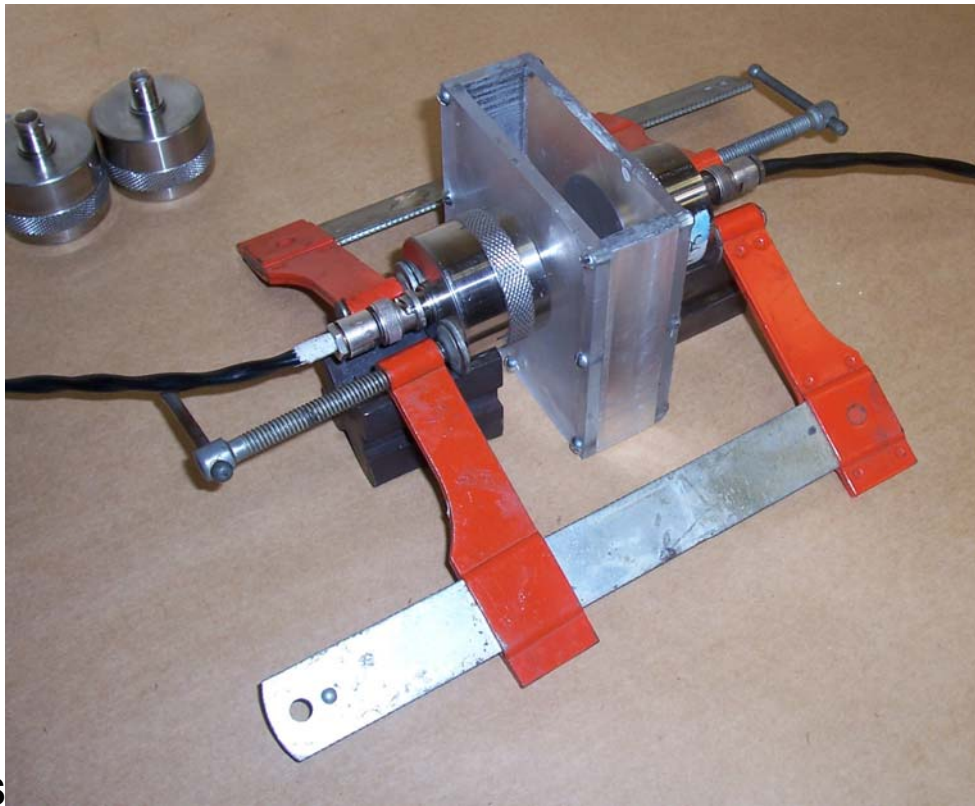
FIGURES

*Figure 1.   Chamber for measurements of wave propagation during curing. Cement slurry is poured into 1"
thick chamber between 4" x 4" side walls (plexiglass in this figure). Transducers clamped to the side walls,
as shown for the bottom transducer, are used for transmitting and receiving both shear and compressional
mode waves travelling through the cement.*
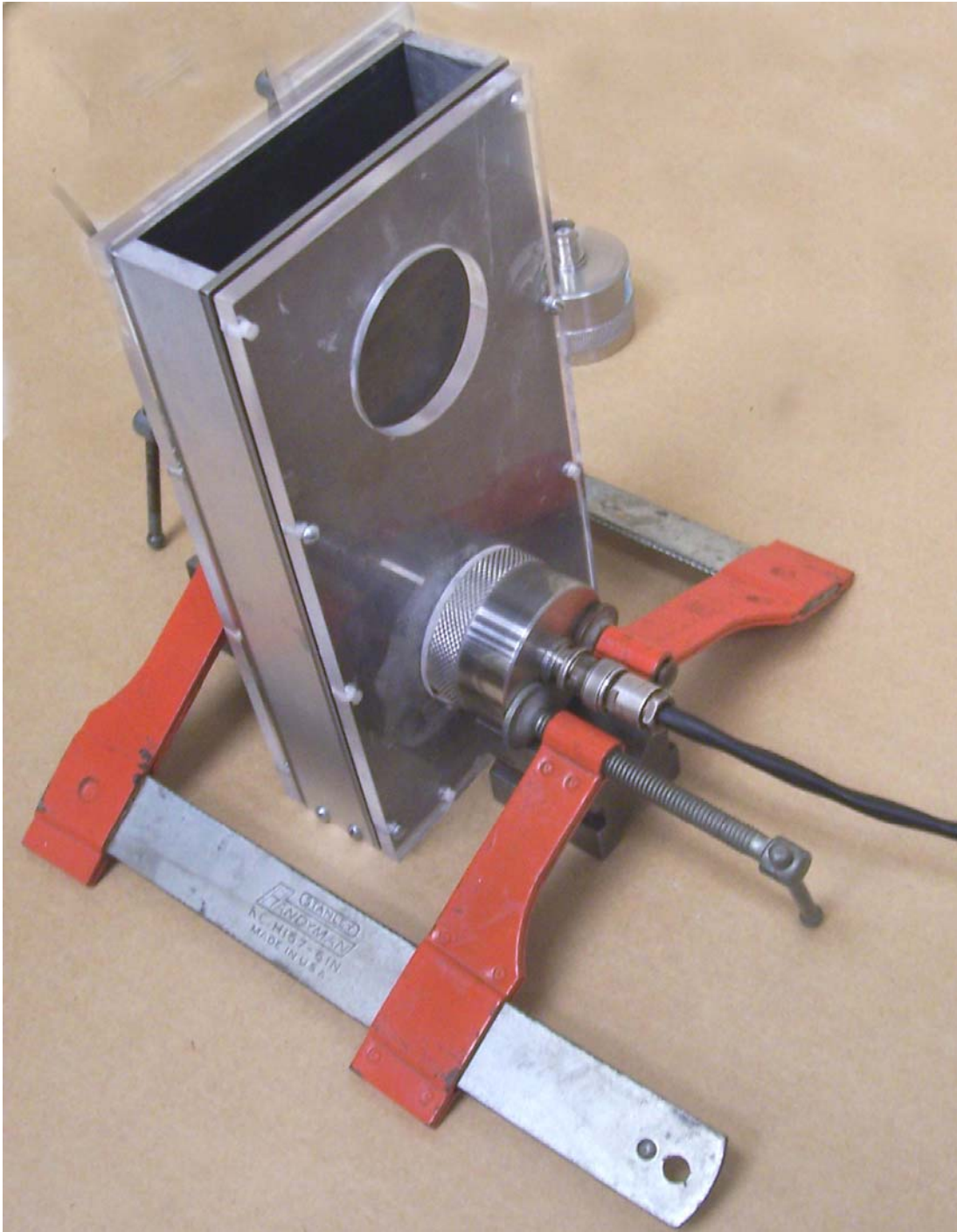
Figure 2. Large test assembly for wave propagation measurements using 4 ultrasonic transducers clamped to the 4" x 8" side walls. Different locations of the transducers provide for s- and -p waves traveling through the cement and along the side faces the specimen.

Simultaneous Property System

Computer-Controlled:
- Overburden
- Confining Pressure
- Pore Pressure
- Load Path
- Load Rate
- Flow Rate
- Pressure Drop
- Data Access
- Data Handling
- Servo-Controlled Feedback Looping
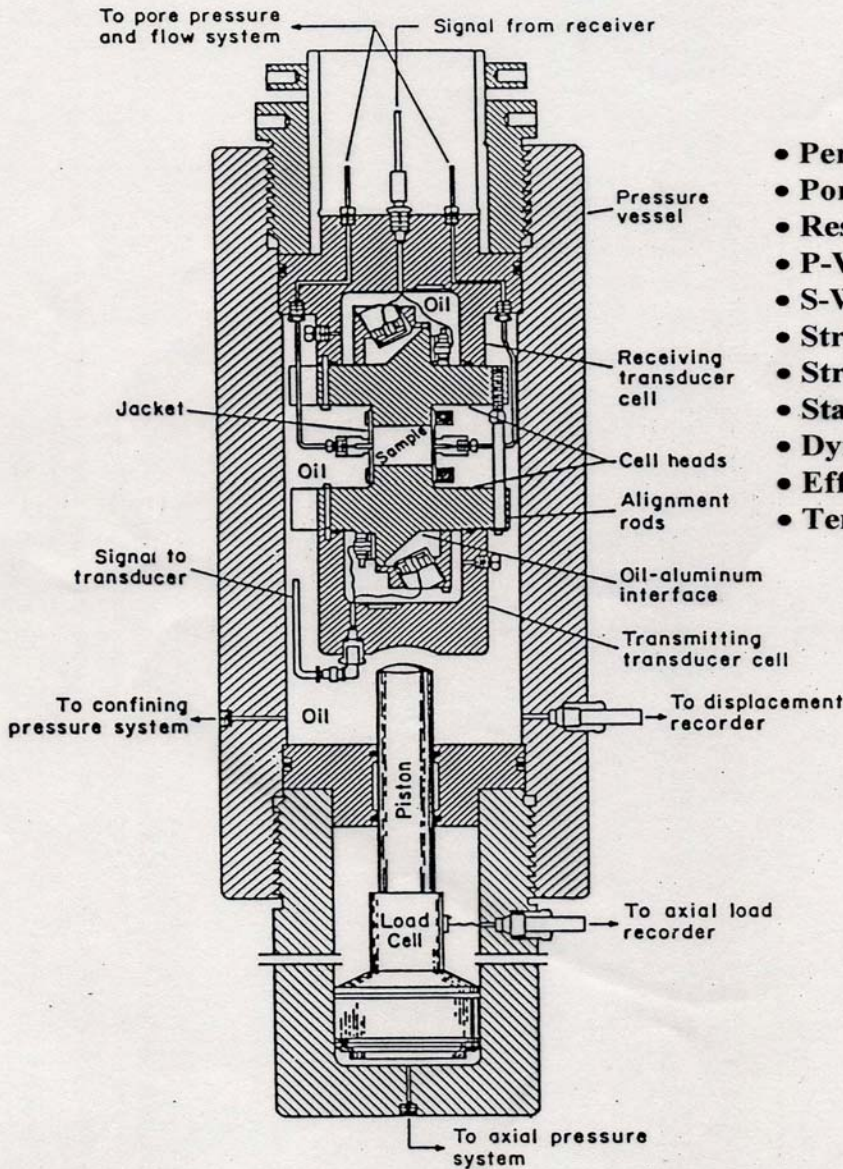
- Permeability
- Porosity
- Resistivity
- P-Wave Velocity
- S-Wave Velocity
- Stress-Strain (Vertical)
- Stress-Strain (Lateral)
- Static Moduli
- Dynamic Moduli
- Effective Stress: 60,000 Ft.
- Temperature: 550 °F

Figure 3. Schematic diagram of Simultaneous Property System, for testing of borehole components under simulated downhole conditions. (Life-Of-Well Rock, Fluid, and Stress Systems, University of Texas at Austin, July 1, 2004).

Figure 4. Side view of a graduated cylinder (250 ml) filled with cement slurry, after curing overnight. The white line around the circumference at the top of the cement column delineates the zone initially occupied by water expelled from the cement, and later re-absorbed

.
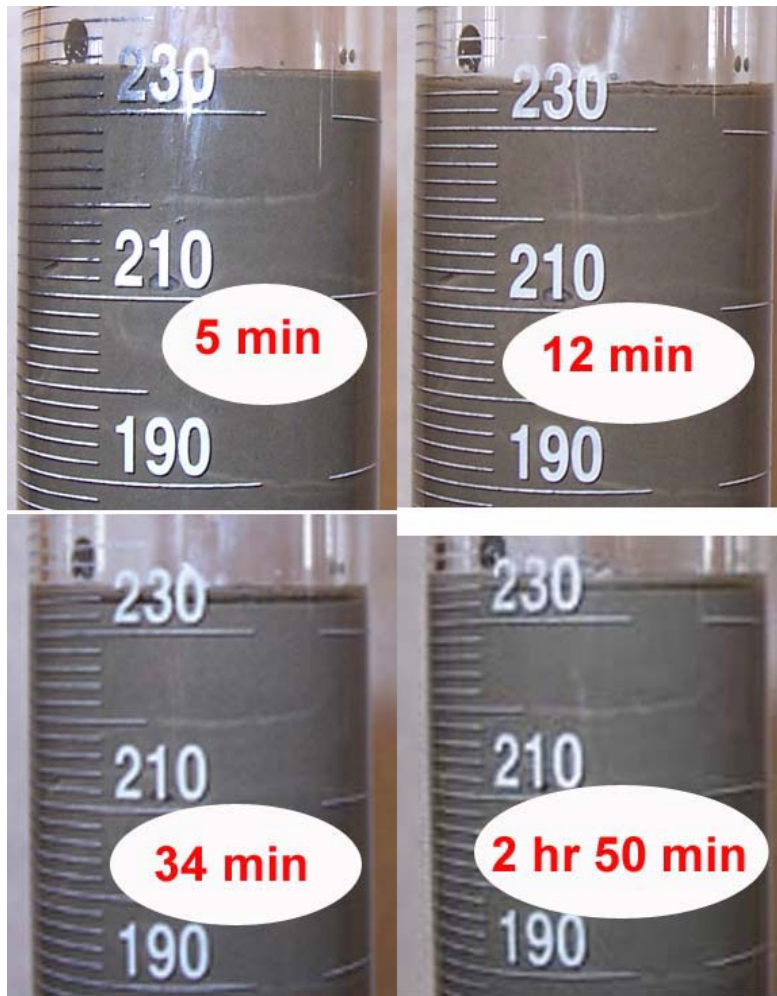
Figure 5. Photographs of a graduated cylinder filled with a freshly mixed cement slurry at time zero. Note the formation of the water layer at the top of the specimen, which persists throughout the sequence. The water layer was absent on the following day, but no shrinkage or expansion of the cement column was observed.

Figure 6. Particulate material deposited on the upper end platen, presumably from within an aqueous layer during several days in which the cement specimen was in the vessel.

Bottom Surfaces

Top Surfaces

Figure 7. Post test photographs of top (right side) and bottom (left side) surfaces of test specimen (top) and end platens (bottom).
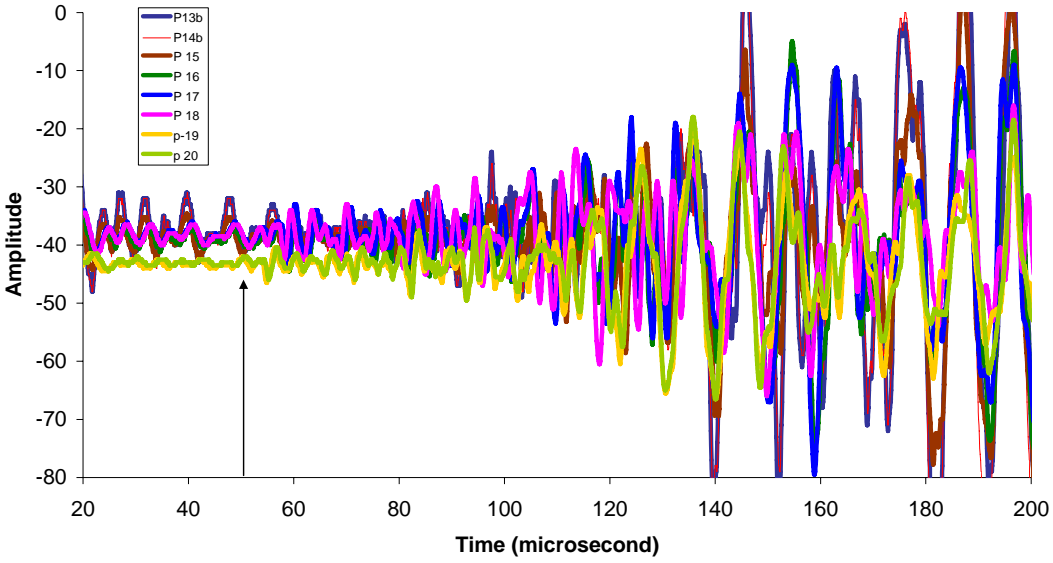
Figure 8. Waveforms for p-waves in the bench-top configuration with a rigid separation between end platens.
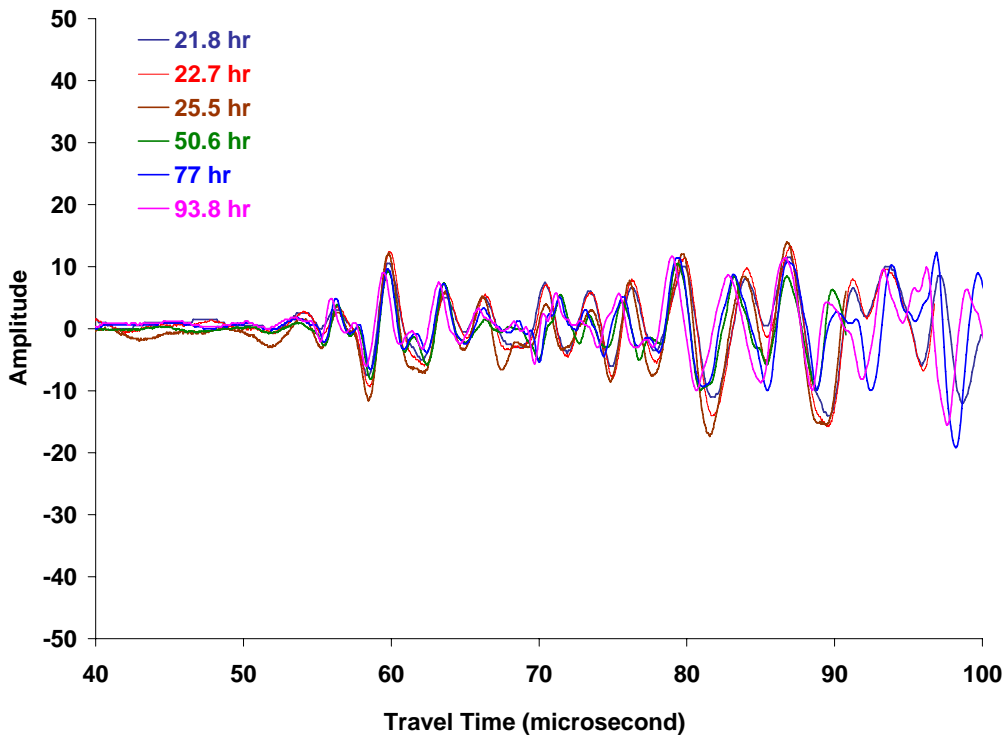
Figure 9. P-wave waveforms observed at elapsed times indicated in legend, in which the end platens were progressively pressed into the cement during curing of the still-liquid cement (not shown). The signals have been offset in time to provide optimum overlap. Wave forms offset to provide approximate overlap and estimated common first arrival (arrow) used to compute p-wave velocities (Figure 10).

48
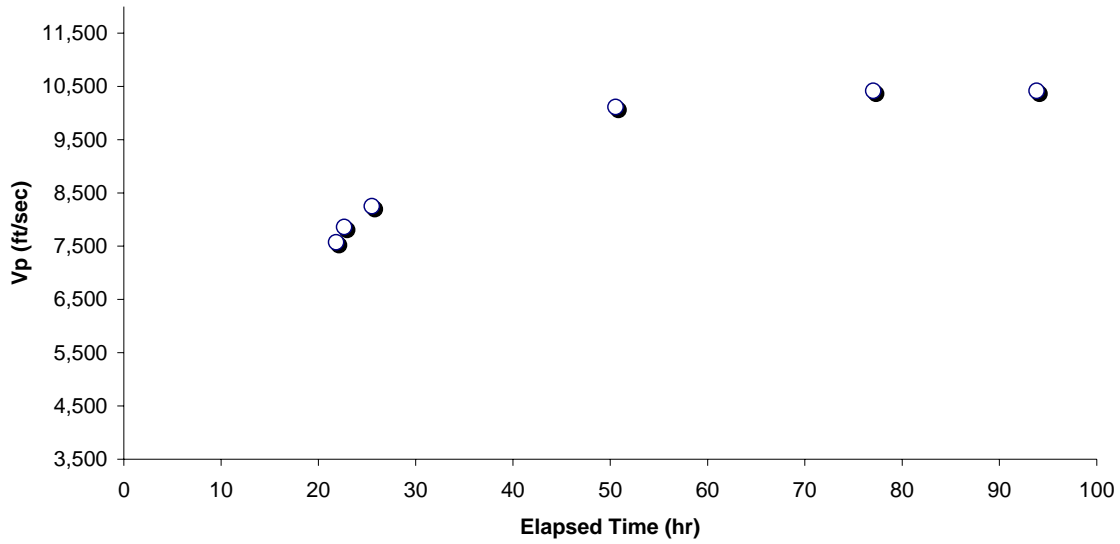
Figure 10. P-wave velocities computed from offsets used in Figure 9, during later stages of curing.
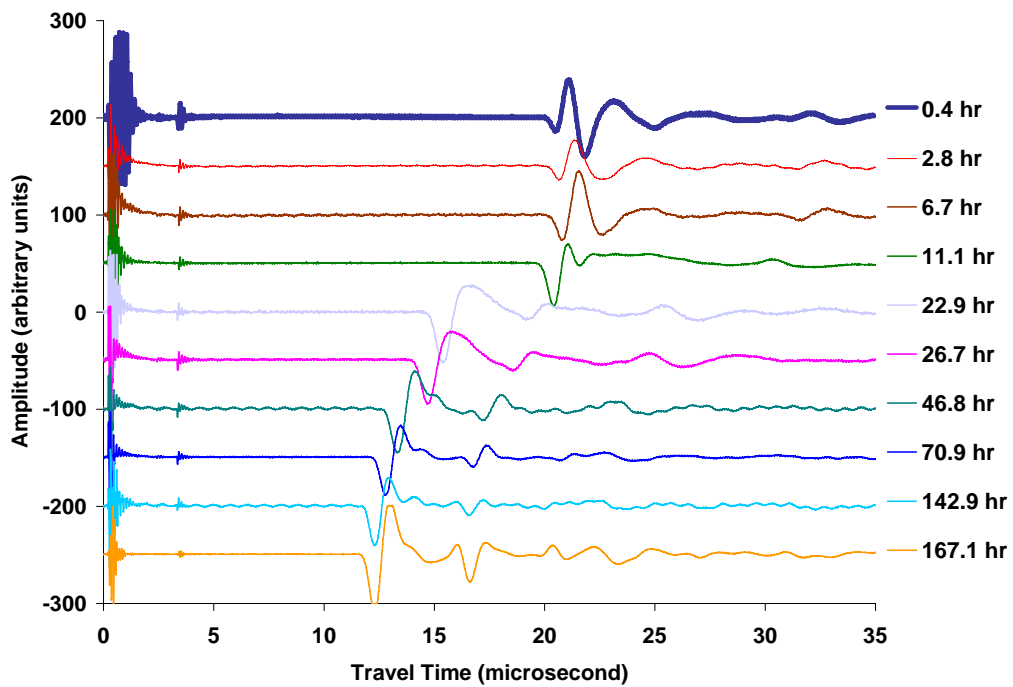
Figure 11. Compressional waveforms traveling through a cement slurry poured into the 4" x 4" chamber (Figure 1) from time 0, after successively greater curing times shown on the right side of the plot.

49
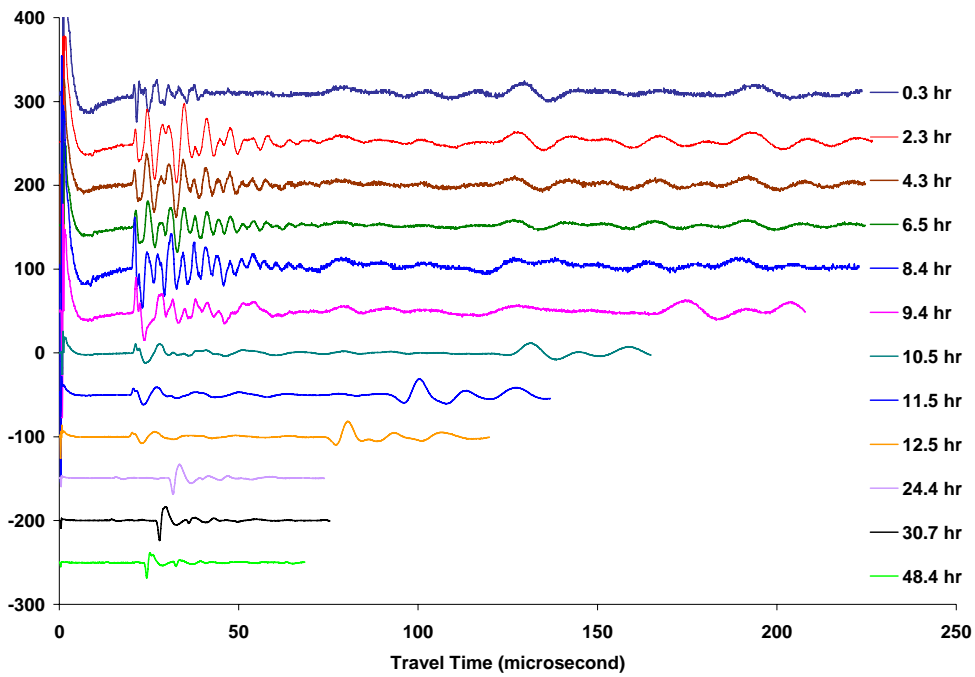
Figure 12. Shear waveforms traveling through a cement slurry poured into the 4" x 4" chamber (Figure 1) from time 0, with curing times shown on the right side of the plot.
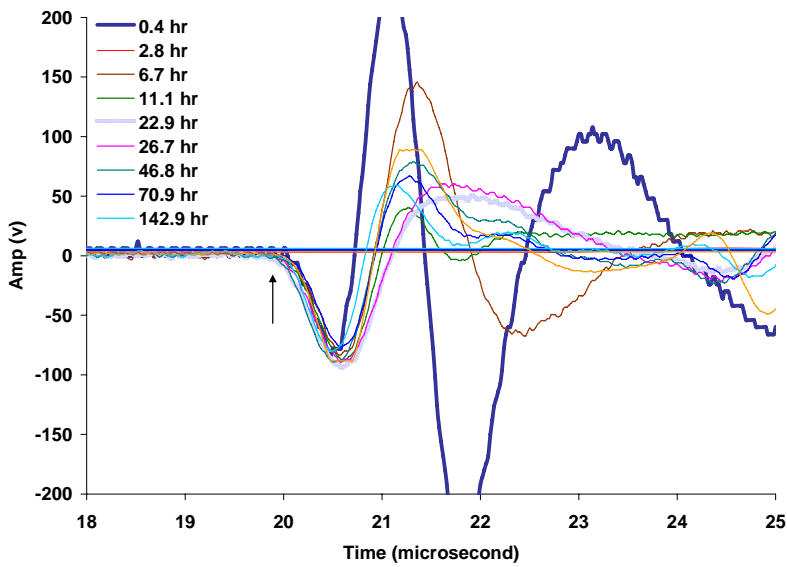
Figure 13. Shifted compressional mode waveforms for different curing times in the 4x4" apparatus (Figure 1), aligned for velocity computations.

50
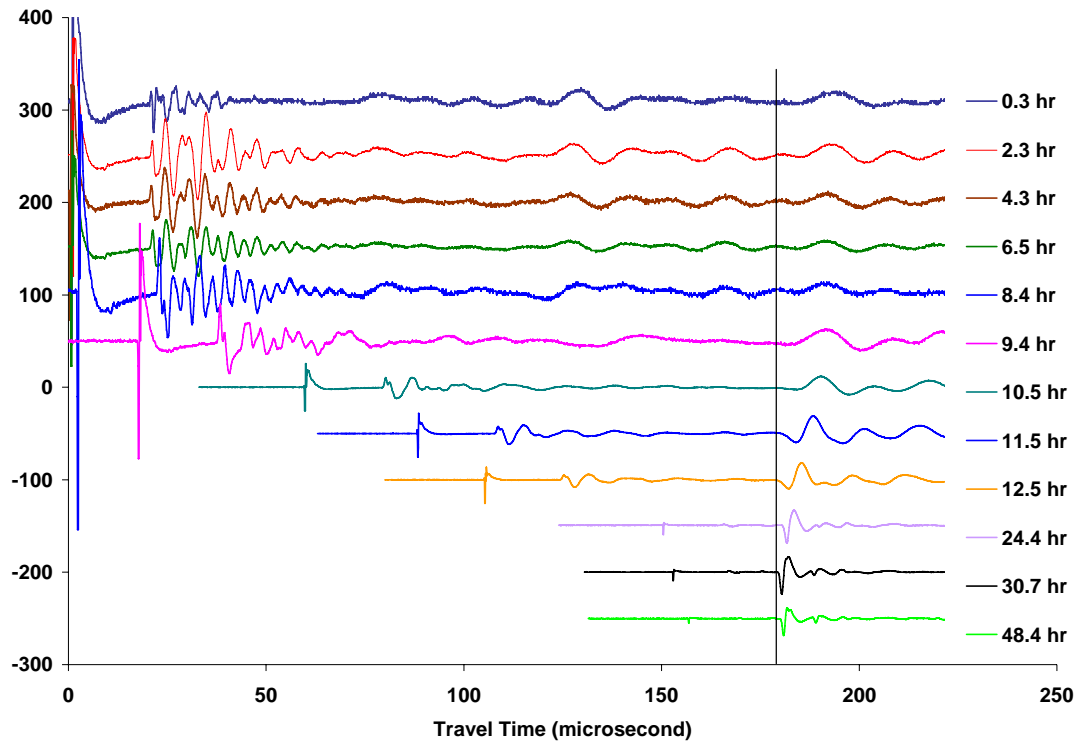
Figure 14. Aligned shear mode waveforms in 4x4" chamber (Figure 1) for velocity computations. Signal for early travel times is a p-wave precursor, which is ignored in waveform shifting.
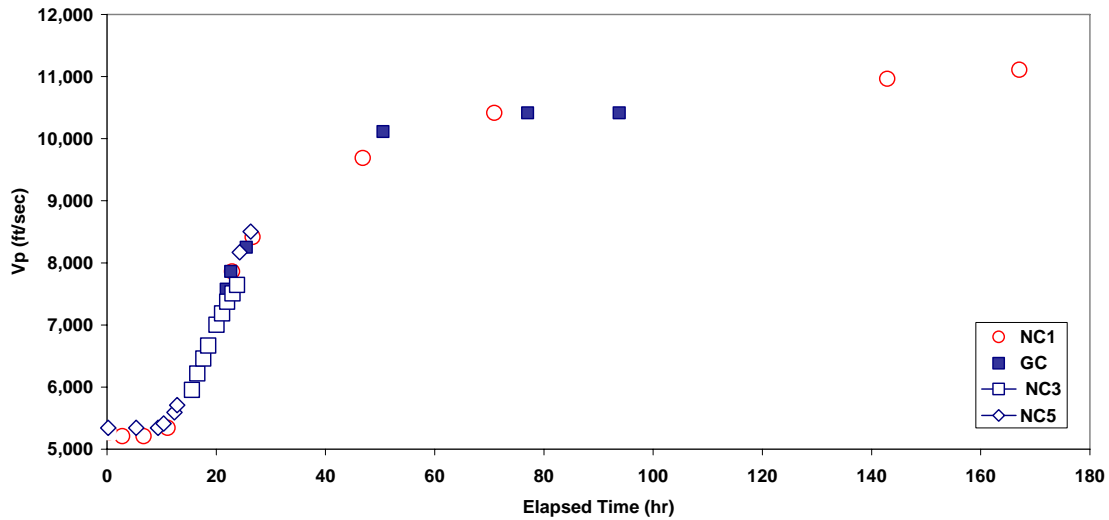
Figure 15. Cumulative plot of p-wave velocity variations during curing of cement. Data taken from measurements on 4 different specimens: one in the Gulf Cell (GC), and 3 different specimens in the new 4"x 4" cell (NC1, 3, and 5, apparatus shown in Figure 1).

51
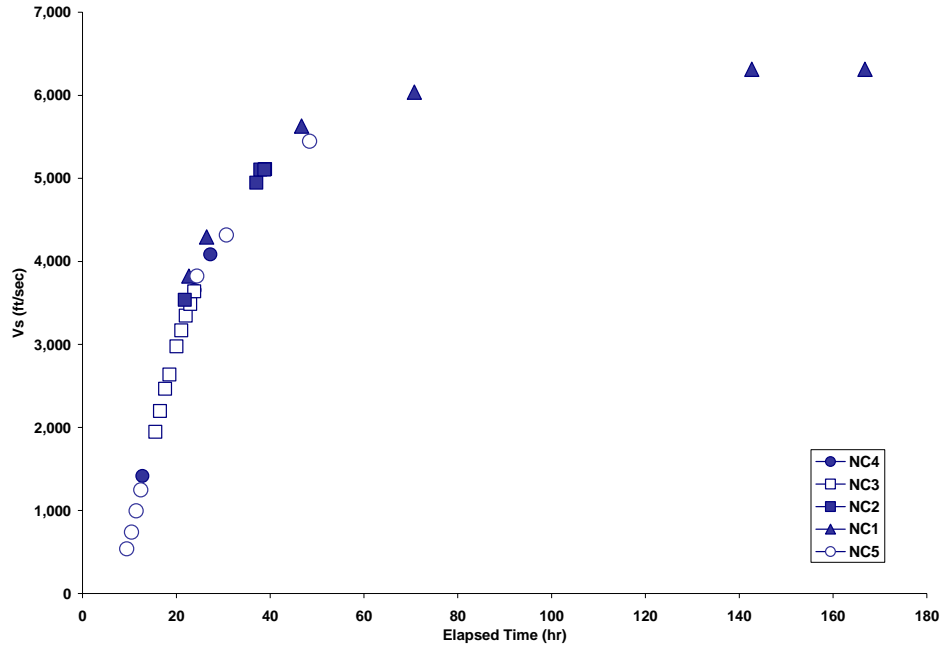
Figure 16. Cumulative plot of s-wave velocity variations during curing of cement. Data taken from measurements on 5 different specimens in the new 4"x4" apparatus (NC1-5; Figure 1).
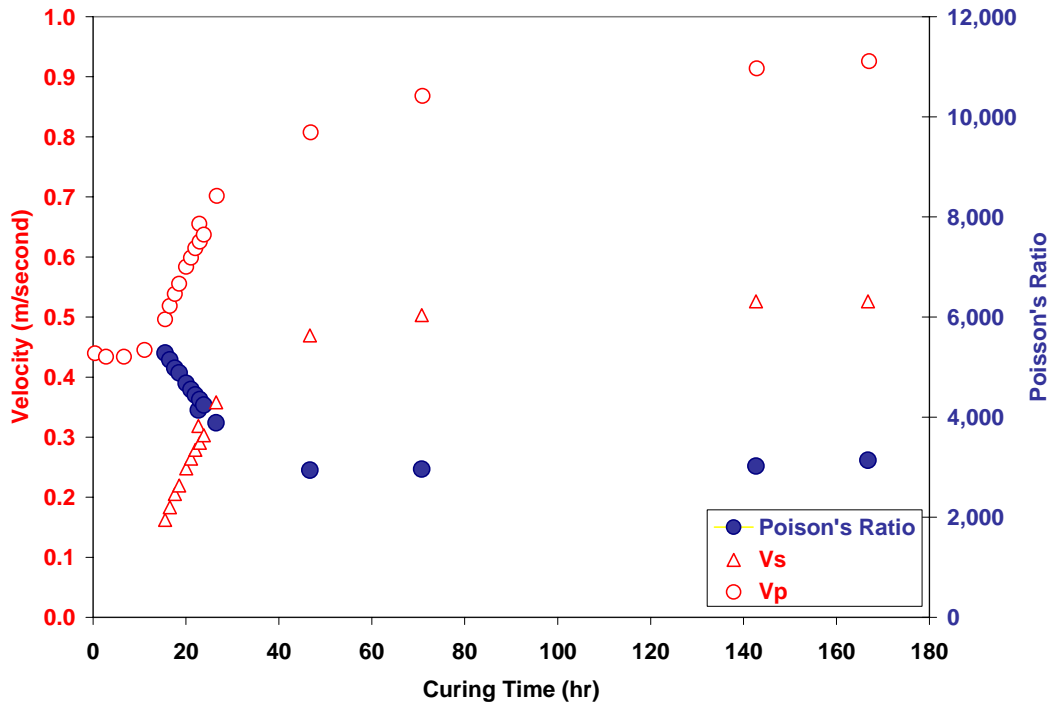
Figure 17. Variations in dynamic Poisson's ratio with curing time. S- and P-wave velocity variations from Figures 15 and 16 are repeated for comparison.
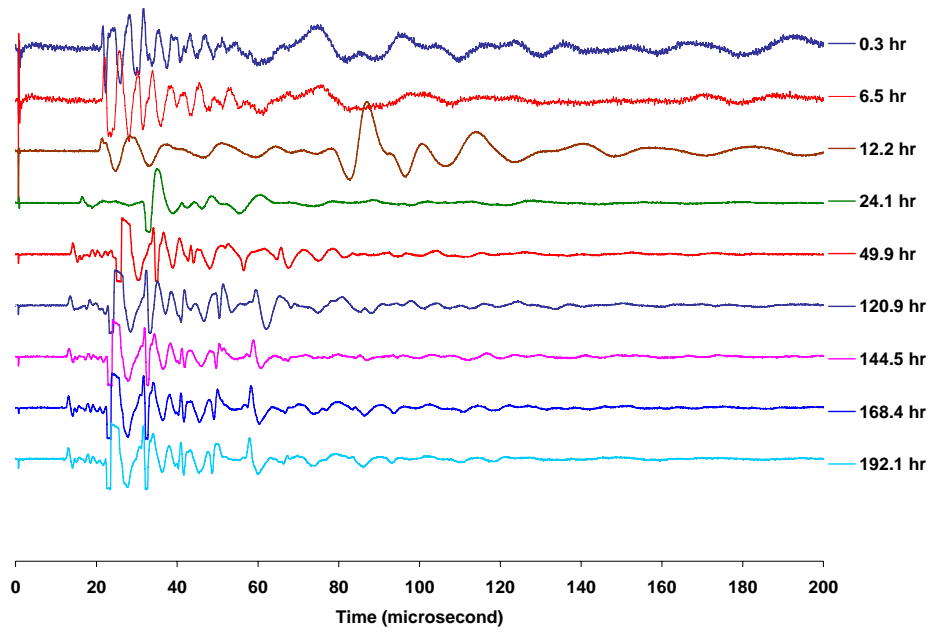
Figure 18. Waveforms for shear waves traveling across the bottom of a cement specimen in the 4" x 8" chamber (Figure 2), for different curing times shown on the right side.
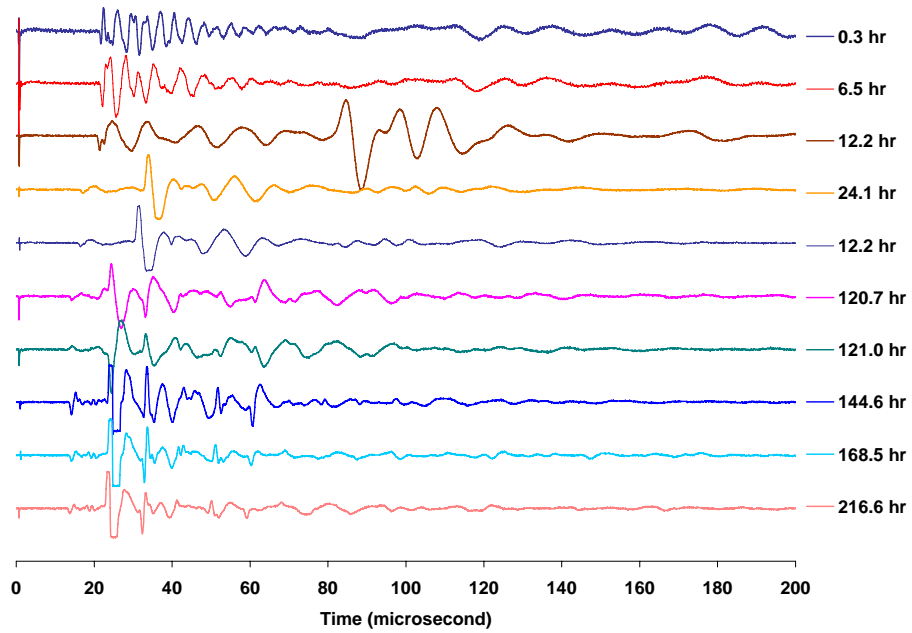
Figure 19. Corresponding plot for shear waves traveling across top end of specimen in 4" x 8" chamber (Figure 2).
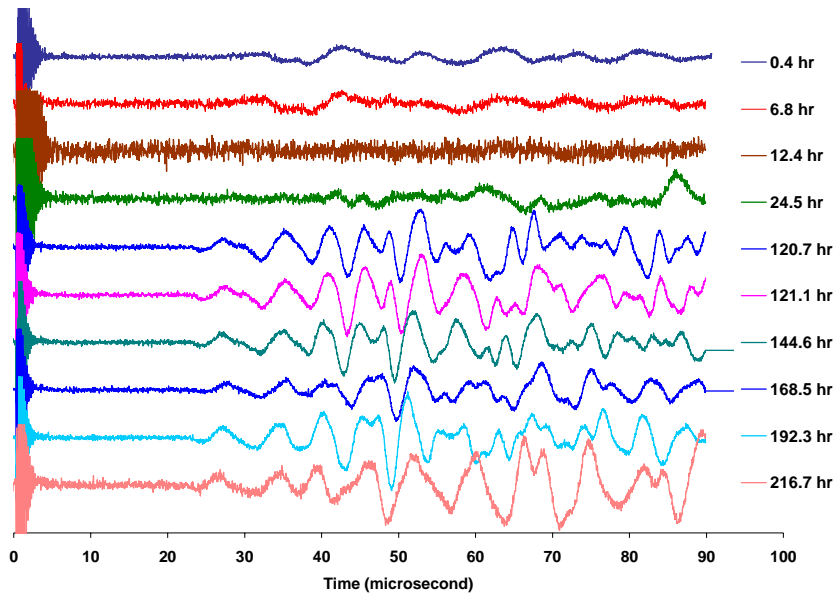
Figure 20. Wave patterns for propagation of signals generated and detected by p-wave transducers on the right face of the apparatus shown in Figure 2.
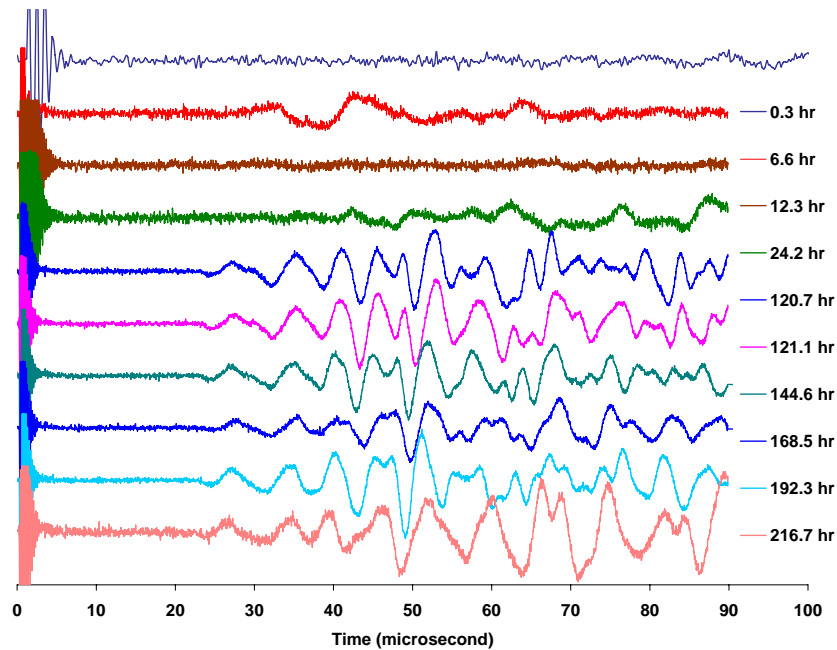
Figure 21. Corresponding plot for waves generated by p-wave transducers, traveling along the left face of the 4" x 8" apparatus (Figure 2).

54
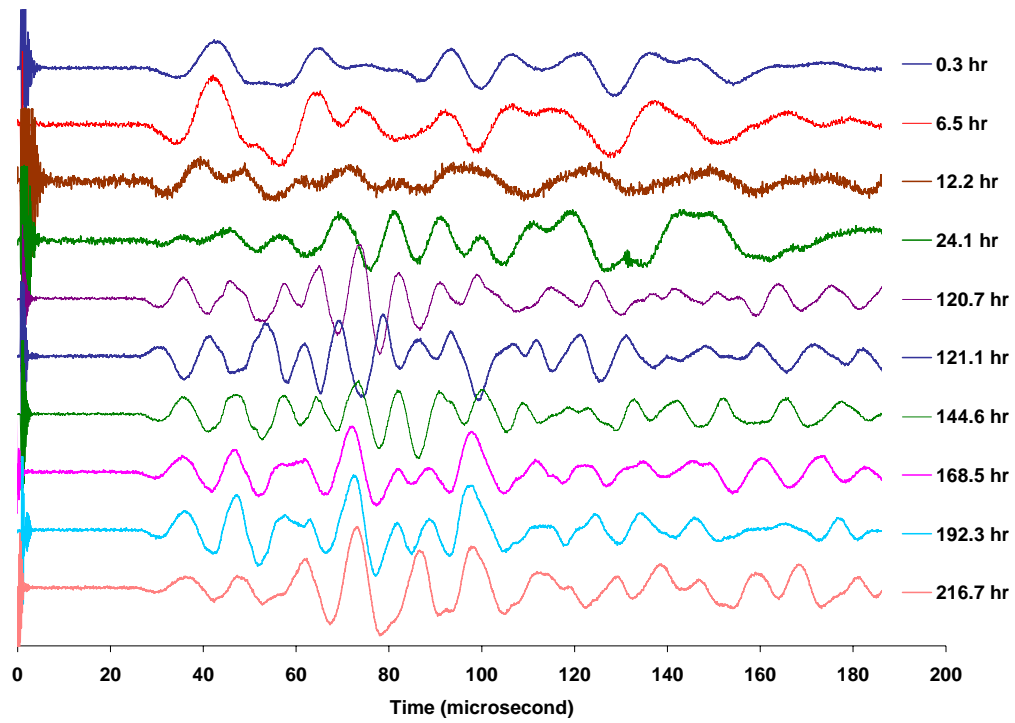
Figure 22. Wave forms for waves generated and detected by shear transducers mounted on the right side of the 4" x 8" chamber (Figure 2).
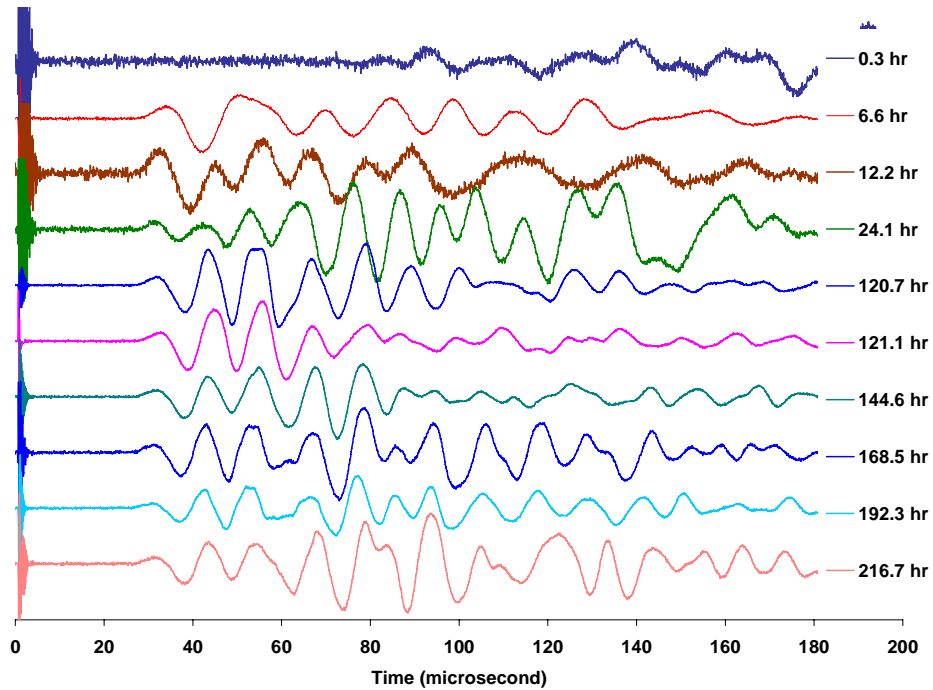
Figure 23.   Wave forms for waves generated and detected by shear transducers mounted on the left side of the 4" x 8" chamber (Figure 2)

55
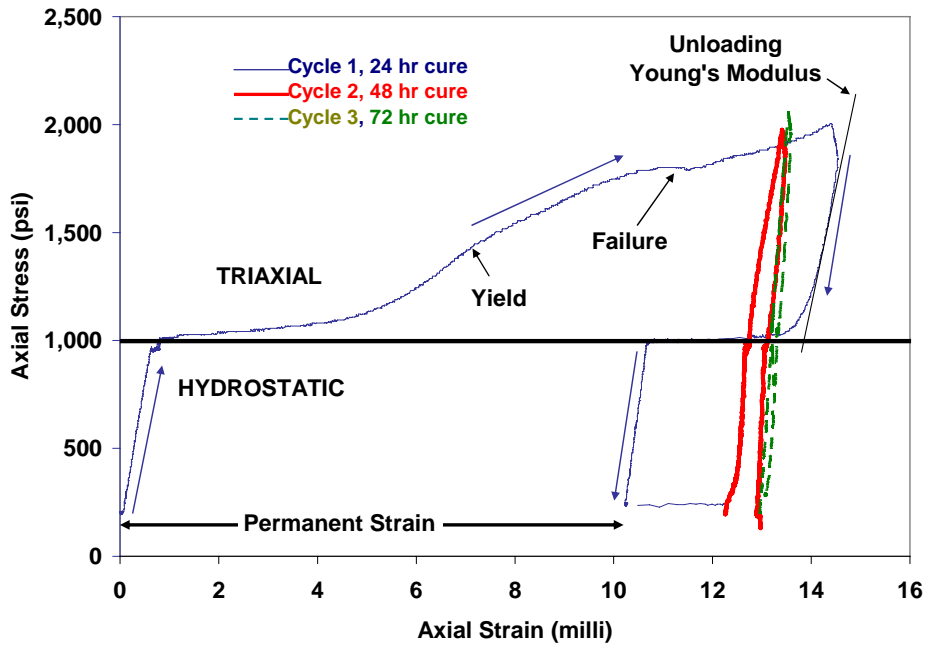
Figure 24. Axial stress - strain behavior of Mix 1 Specimen #8 after deformations at indicated times. Graphical definitions of yield, failure, Young's modulus, and permanent strain are also shown.
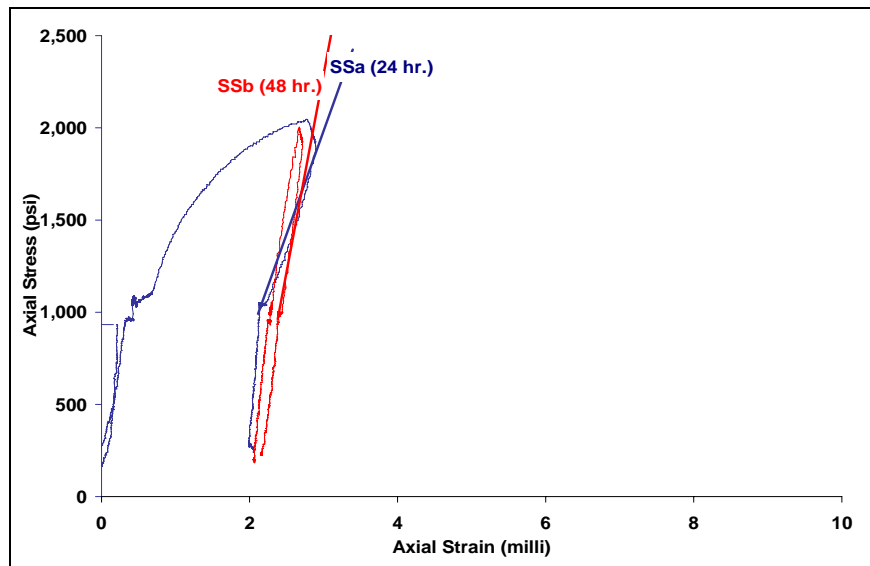
Figure 25. Axial stress - strain behavior of Mix 1 specimen #9 during curing and deformations at indicated times. Young's moduli computed from linear stress strain slopes are listed in Table 1.
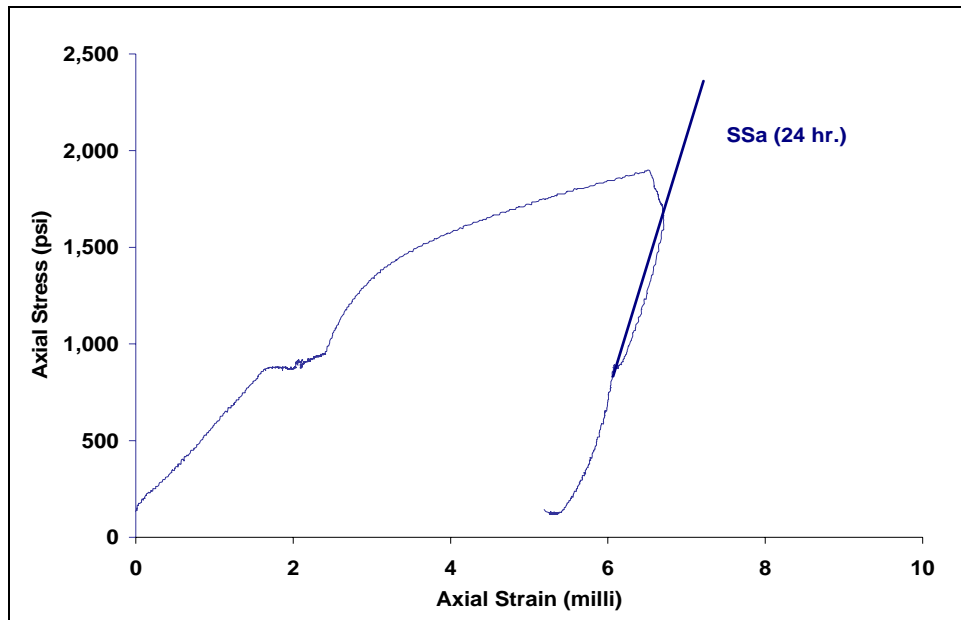
Figure 26. Axial stress-strain behavior in Mix 1 specimen #16 after curing (Pc = 0) and deformation. Young's modulus computed from linear stress-strain slope is listed in Table 1.
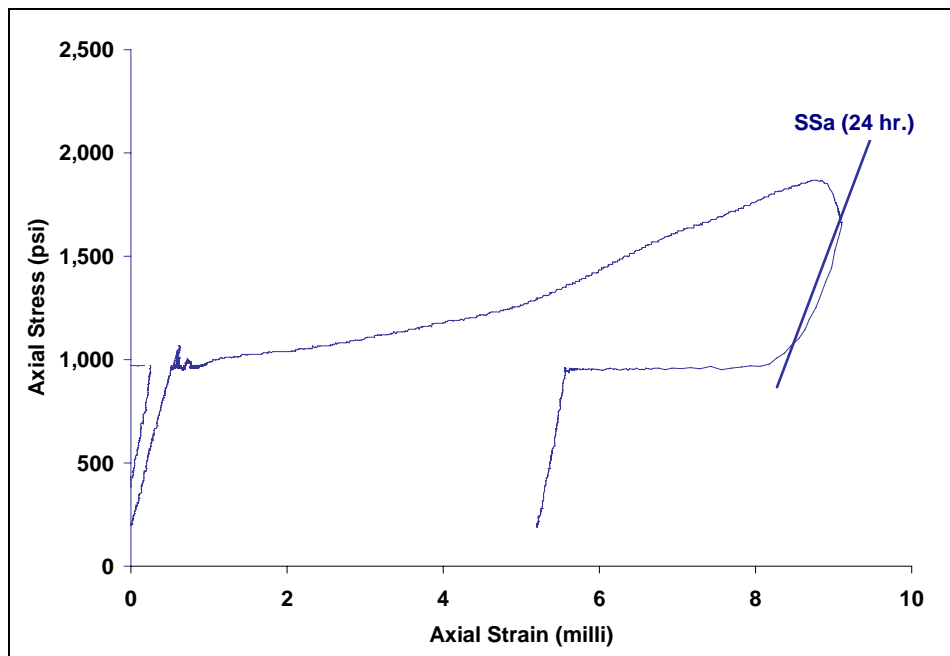
Figure 27. Axial stress-strain behavior during curing and deformation of Mix 1 specimen #7. Some evidence of failure is indicated by break in slope at an axial stress of approximately 1.7 kpsi. Young's modulus computed from linear stress-strain slope is listed in Table 1.

57
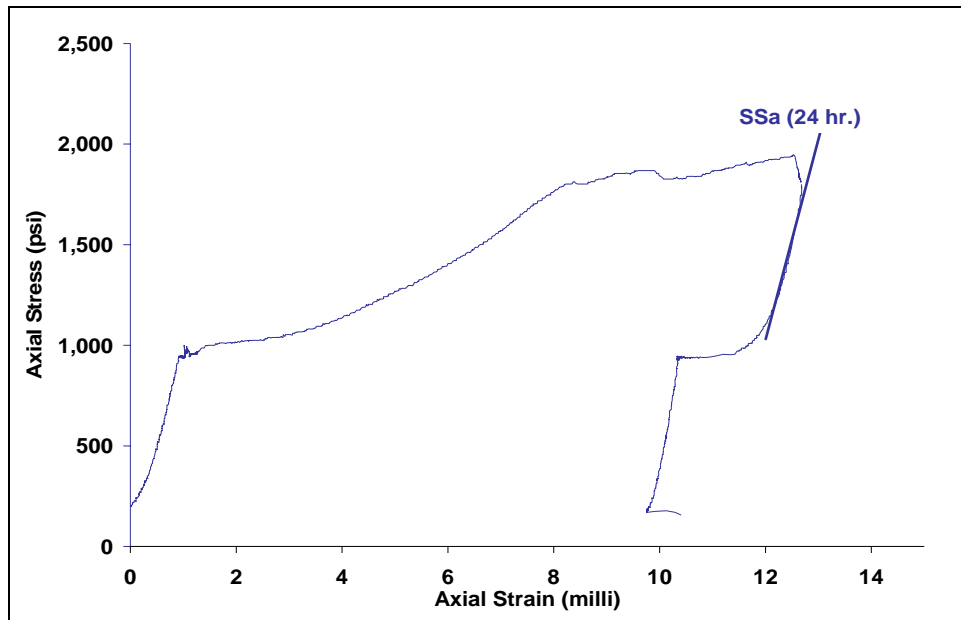
Figure 28. Axial stress - strain behavior of Mix 1 specimen #11 during curing and deformation. Note clear evidence of failure at an axial stress of approximately 1.8 kpsi. Young's modulus computed from linear stress-strain slope is listed in Table 1.
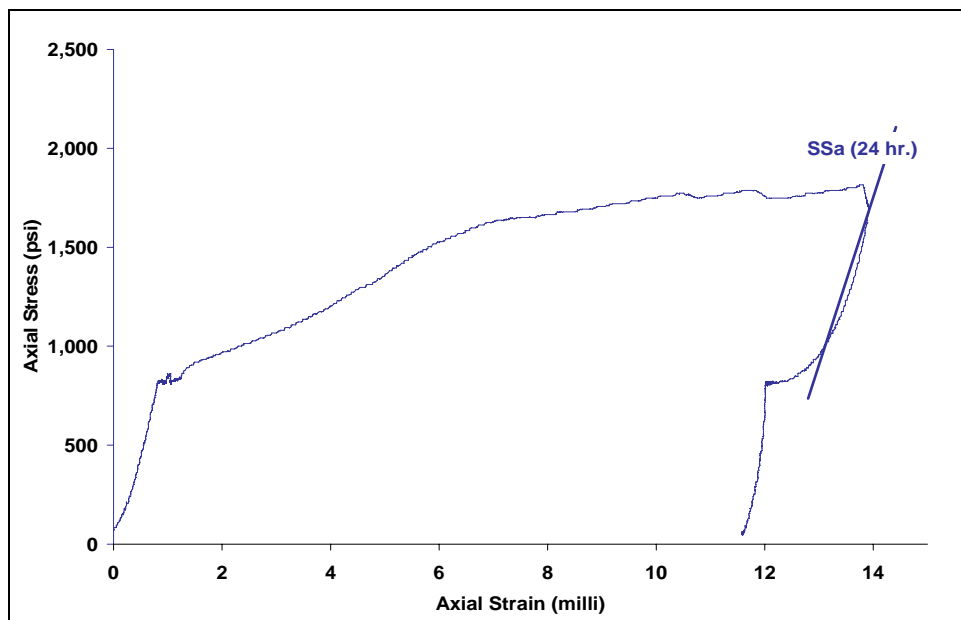
Figure 29. Axial stress - strain behavior during curing (Pc = 200 psi) and deformation of Mix 1 specimen #12. Note clear evidence of specimen failure at an axial stress of approximately 1.7 kpsi. Young's modulus computed from linear stress-strain slope is listed in Table 1.

58
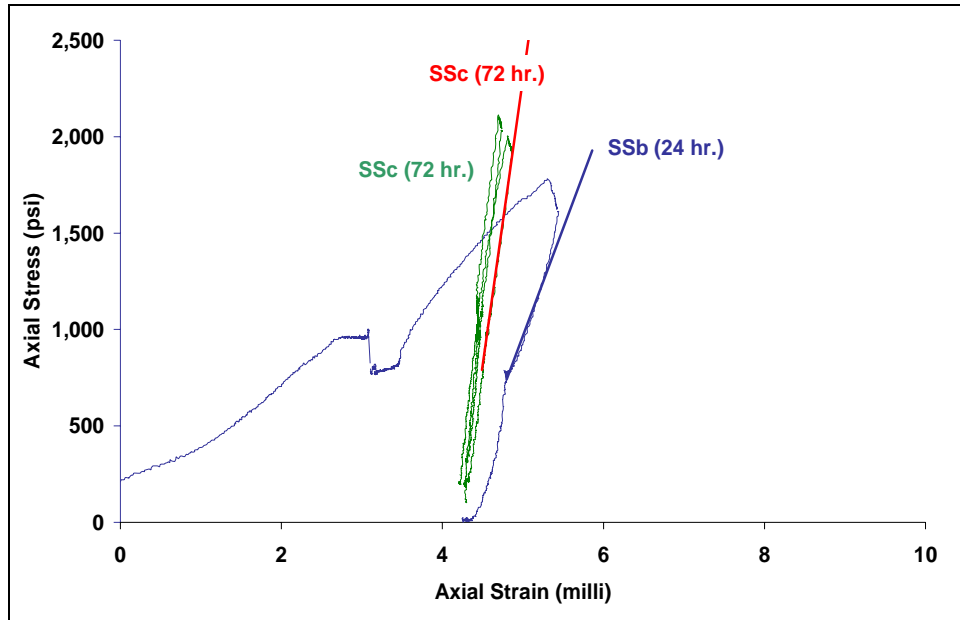
Figure 30 Axial stress - strain behavior of Mix 1 specimen #10 during curing (Pc = 0; apparent drift in axial stress during initial curing was due to load cell drift) and deformation at indicated times. Young's moduli computed from linear stress-strain slopes are listed in Table 1.
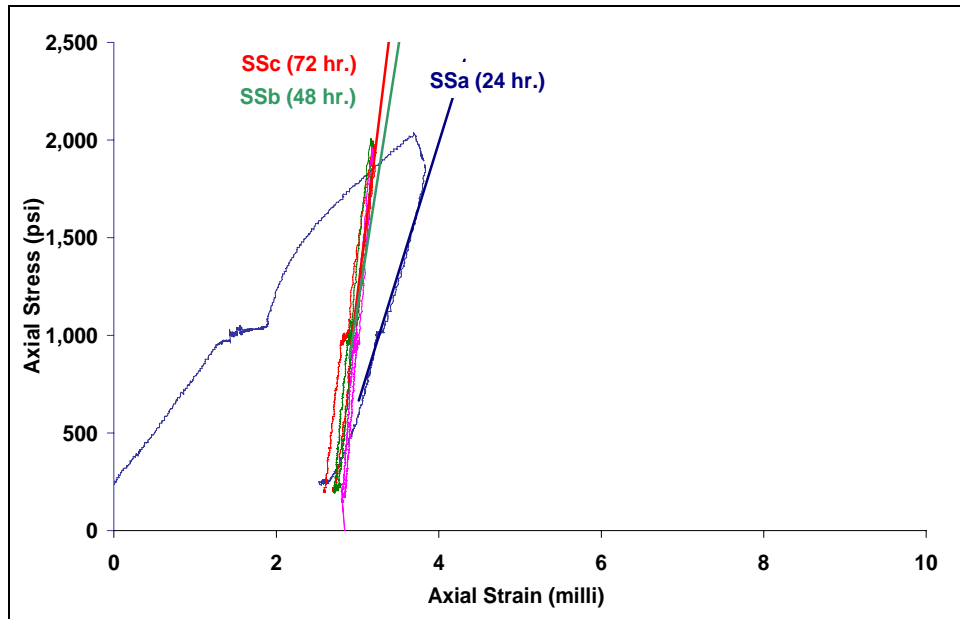
Figure 31. Axial stress-strain behavior in Mix 2 specimen # 4 after curing and deformation at indicated times. Young's moduli computed from linear stress-strain slopes are listed in Table 2.
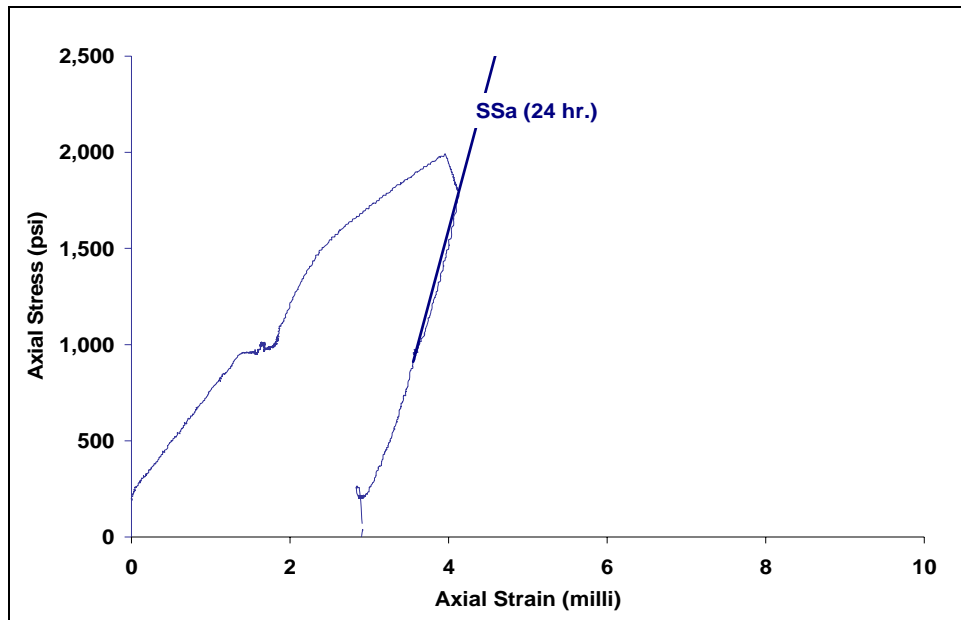
Figure 32. Axial stress-strain behavior in Mix 2 specimen #15 during curing (Pc = 0) and deformation. Young's modulus computed from linear stress-strain slope is listed in Table 2.
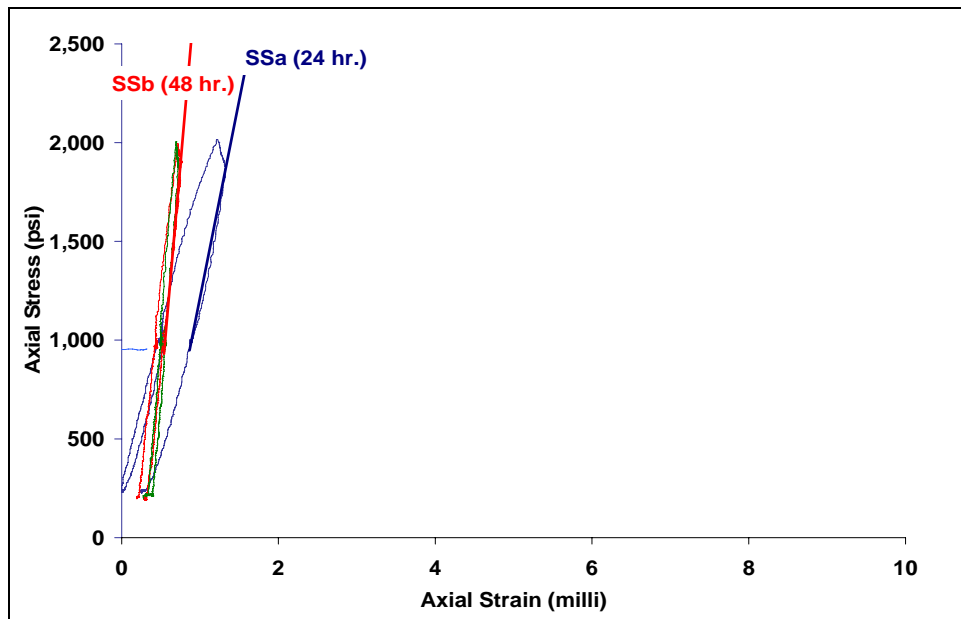
Figure 33. Axial stress-strain behavior of Mix 2 specimen #5 during curing and deformation at indicated times,. Young's moduli computed from linear stress strain slopes are listed in Table 2.
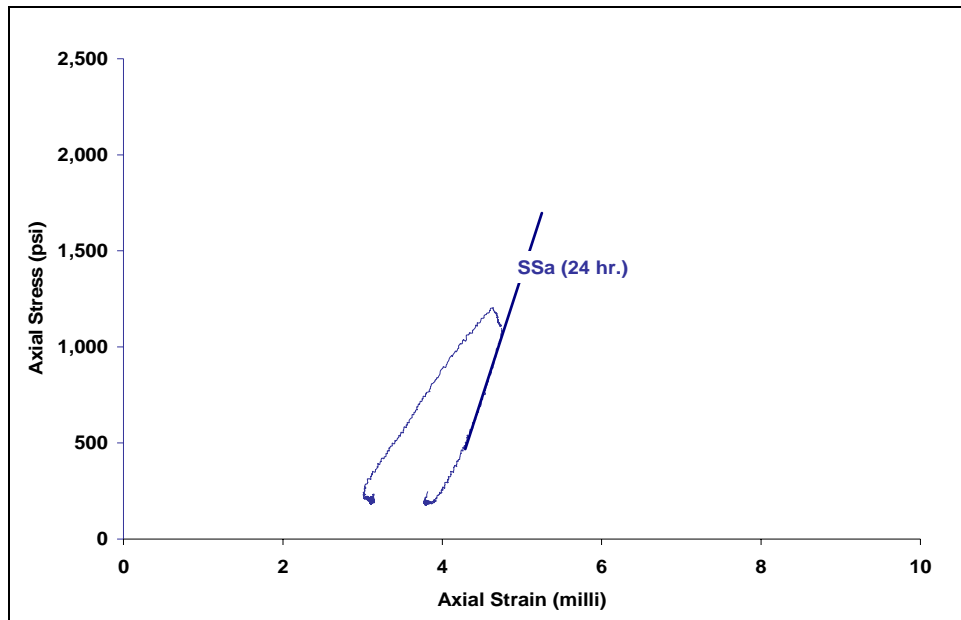
Figure 34. Axial stress-strain behavior of Mix 2 specimen #13 during curing (Pc = 1 kpsi) and deformation at indicated times. Young's moduli computed from linear stress strain slopes are listed in Table 2. Note lower confining pressure (200 psi) for this deformation

.
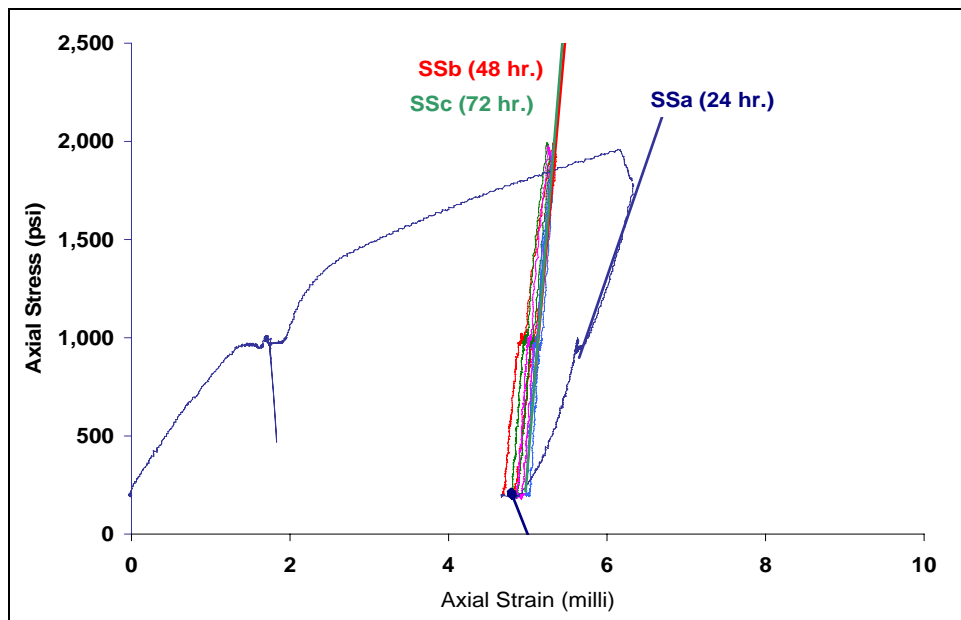
Figure 35. Axial stress-strain behavior in Mix 2 specimen #3 after curing and deformation at indicated times. Young's moduli computed from linear stress-strain slopes are listed in Table 2.

61
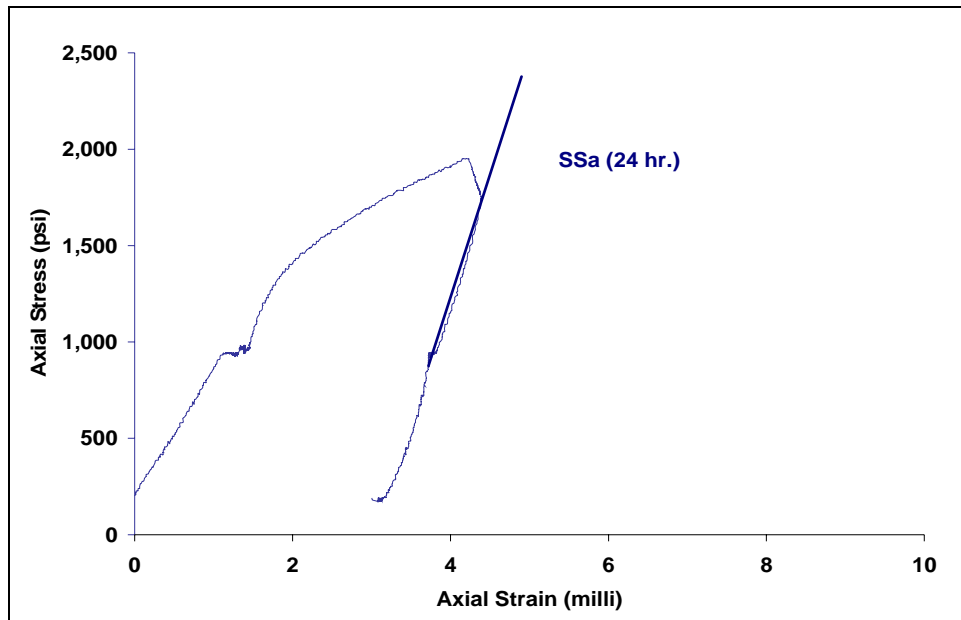
Figure 36. Axial stress-strain behavior in Mix 2 specimen #14 during curing and deformation. Young's modulus computed from linear stress-strain slopes is listed in Table24.
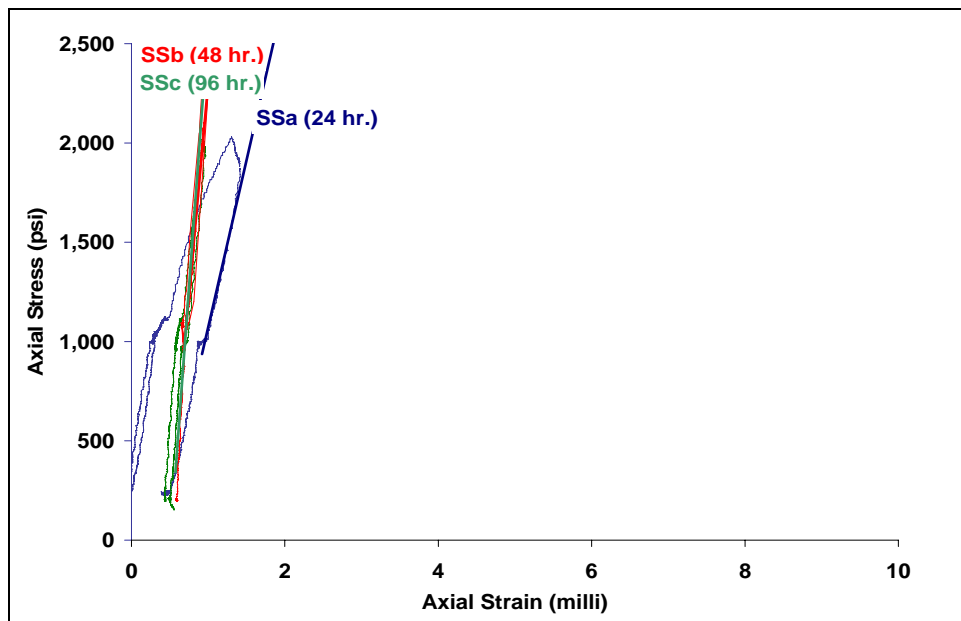
Figure 37. Axial stress-strain behavior in Mix 2 specimen #6 after curing and deformation at indicated times. Young's moduli computed from linear stress-strain slopes are listed in Table 2.
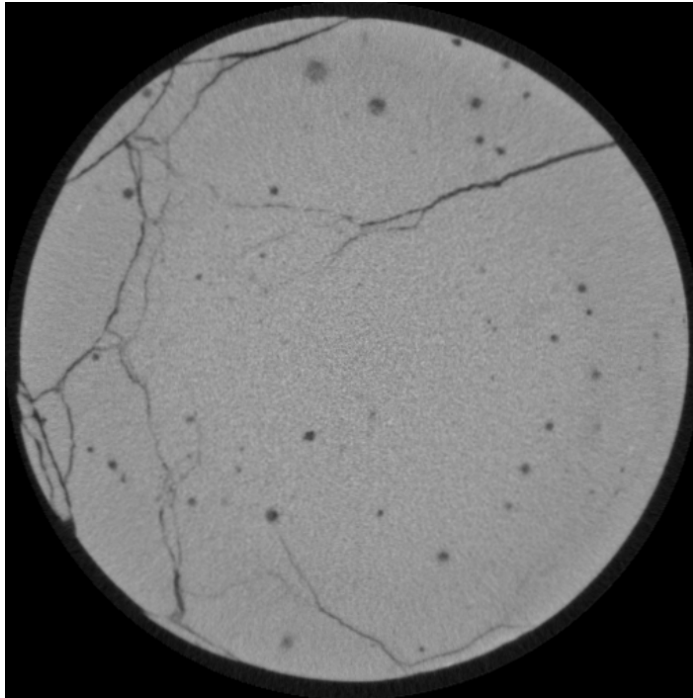
Figure 38. Single slice, approximately midway along cylinder axis, of post-test CT image of specimen #11 (Mix 1, excess water not removed), showing extensive internal fracturing from failure during triaxial deformation (Figure 28).
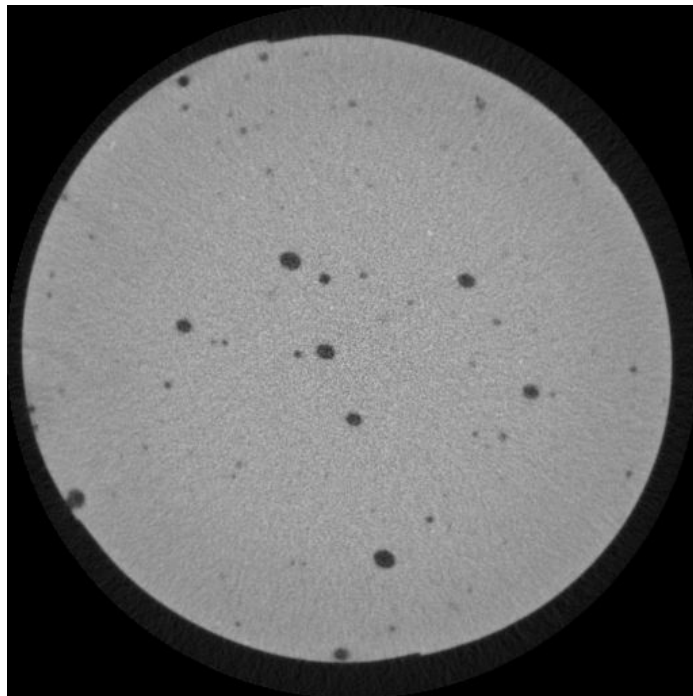
Figure 39. Single slice, approximately midway along cylinder axis, of post-test CT image of specimen #6 (Mix 2, excess water not removed), showing lack of internal fracturing after triaxial deformation. Deformation gives no indication of failure (Figure 37).
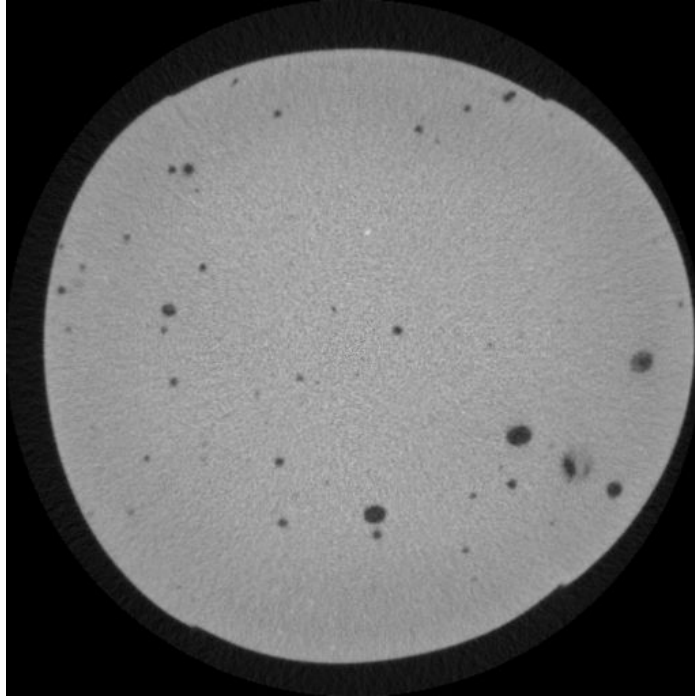
Figure 40. Single slice, approximately midway along cylinder axis, of post-test CT image of specimen #9 (Mix 1, excess water removed by wicking), showing lack of internal fracturing after triaxial deformation. Specimen gives no indication of failure (Figure 25).

Figure 41. Photographic comparison of post-test Specimen 10 (left side) and 11 (right side), showing greater porosity in Specimen 10.
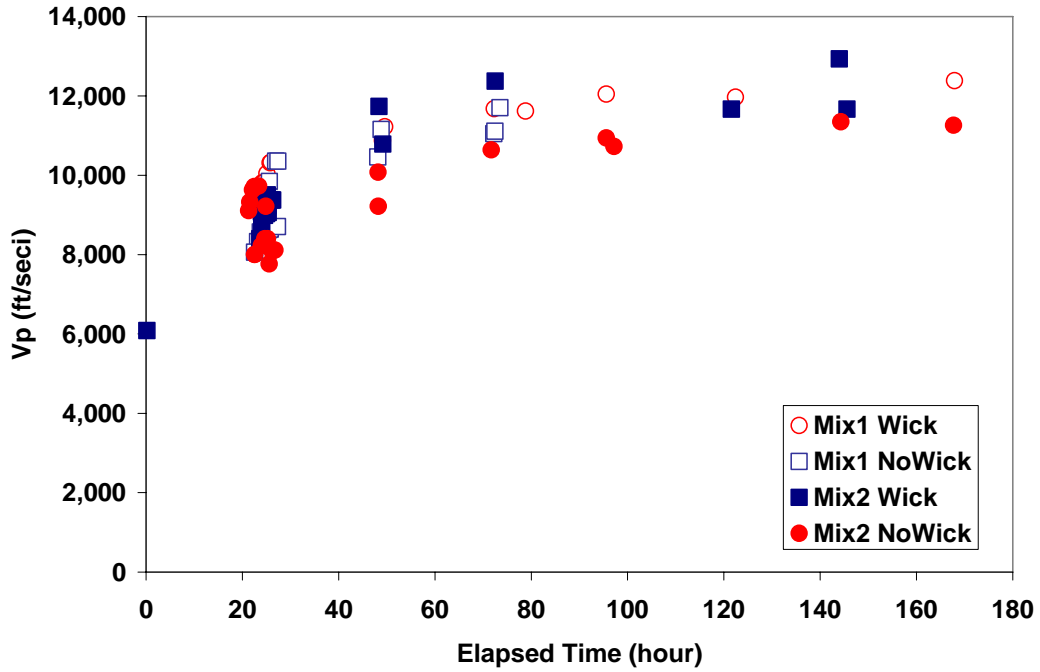
Figure 42. Variations in p-wave velocity for all specimens.
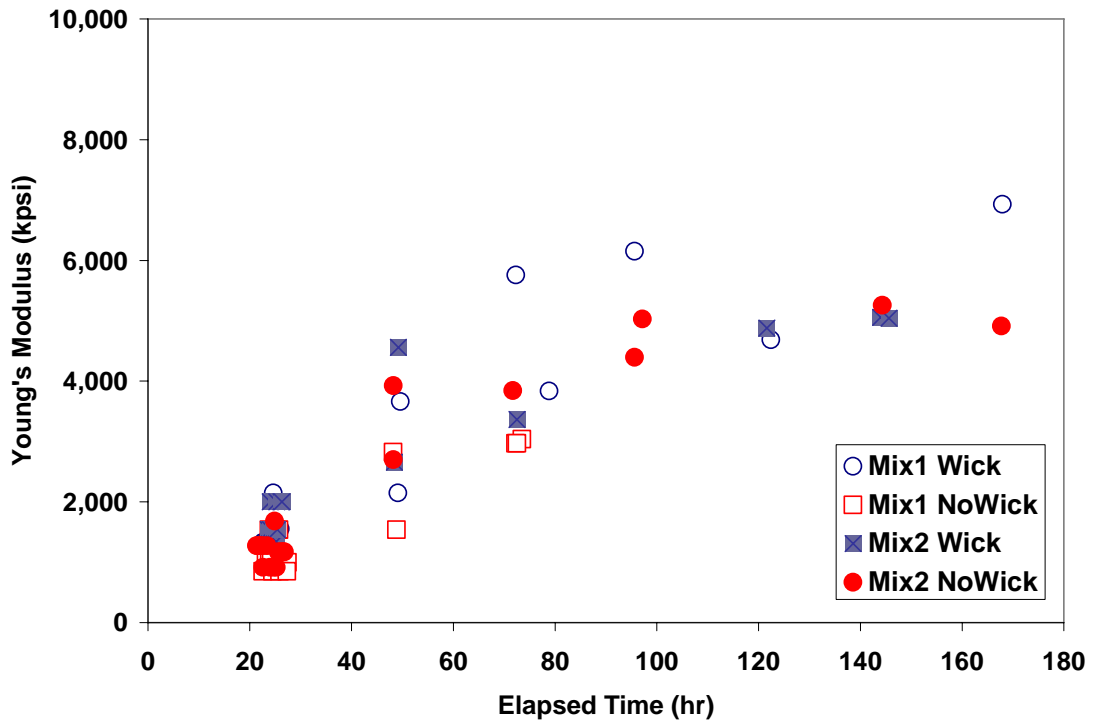
Figure 43. Variations of static Young's moduli with curing time.

65
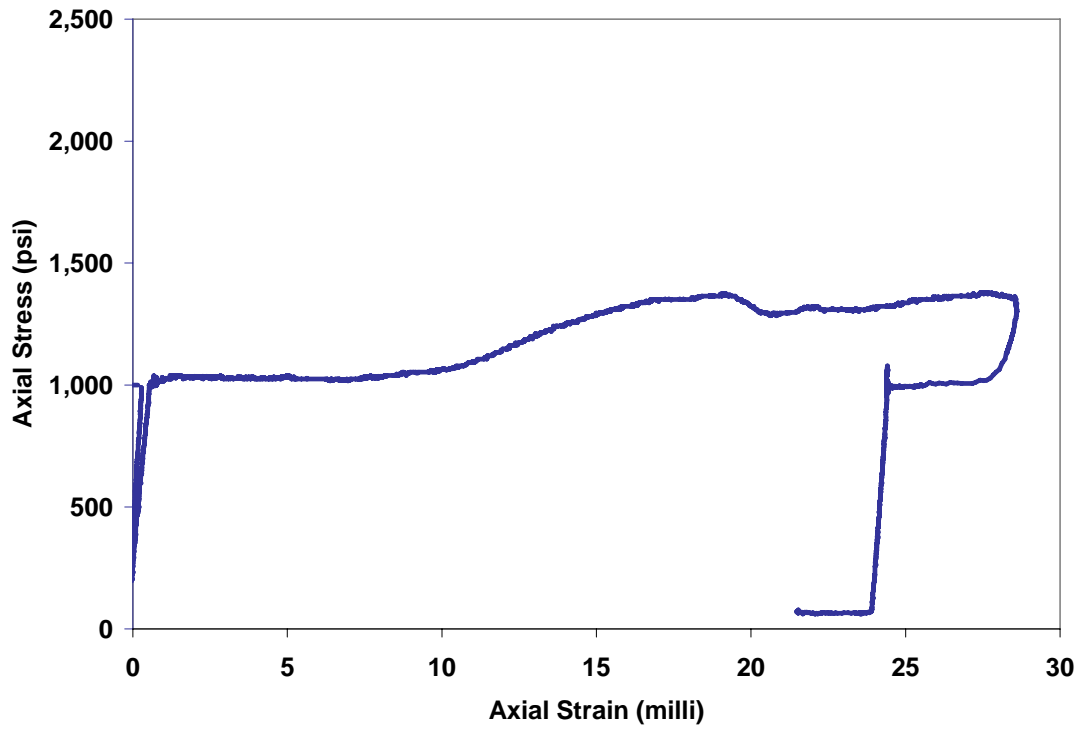
Figure 44. Stress-strain behavior of Mix 1 specimen #III-2 after curing for 14 hours.
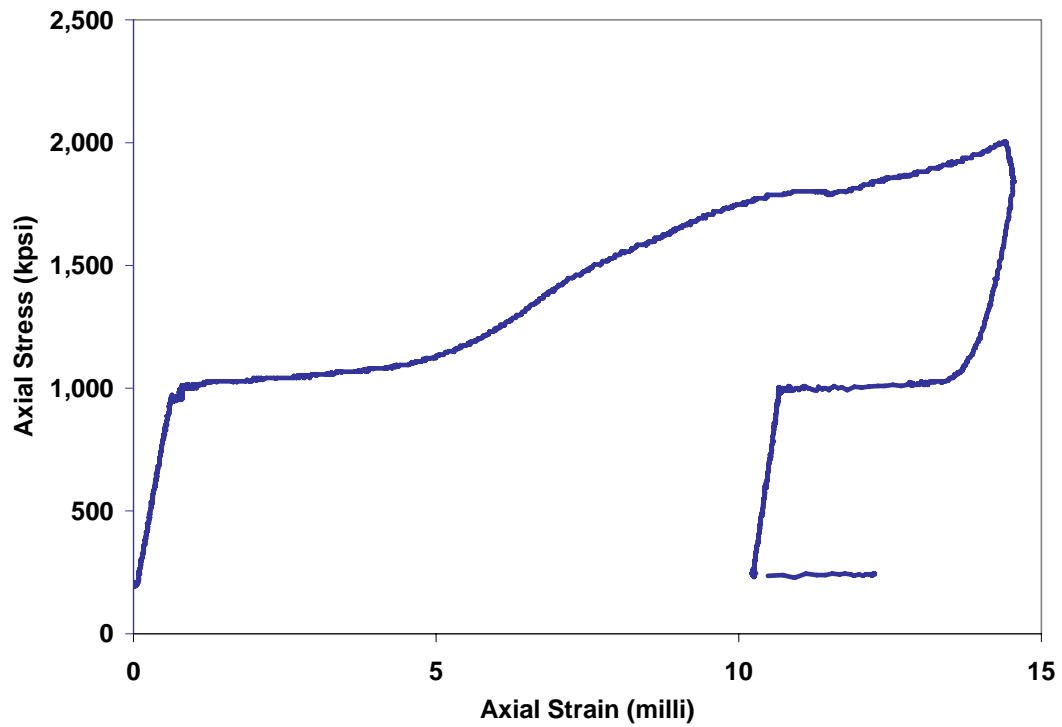
Figure 45. Stress strain behavior of Mix 1 specimen # II-8 (data from Figure 24) after curing for 24 hours.
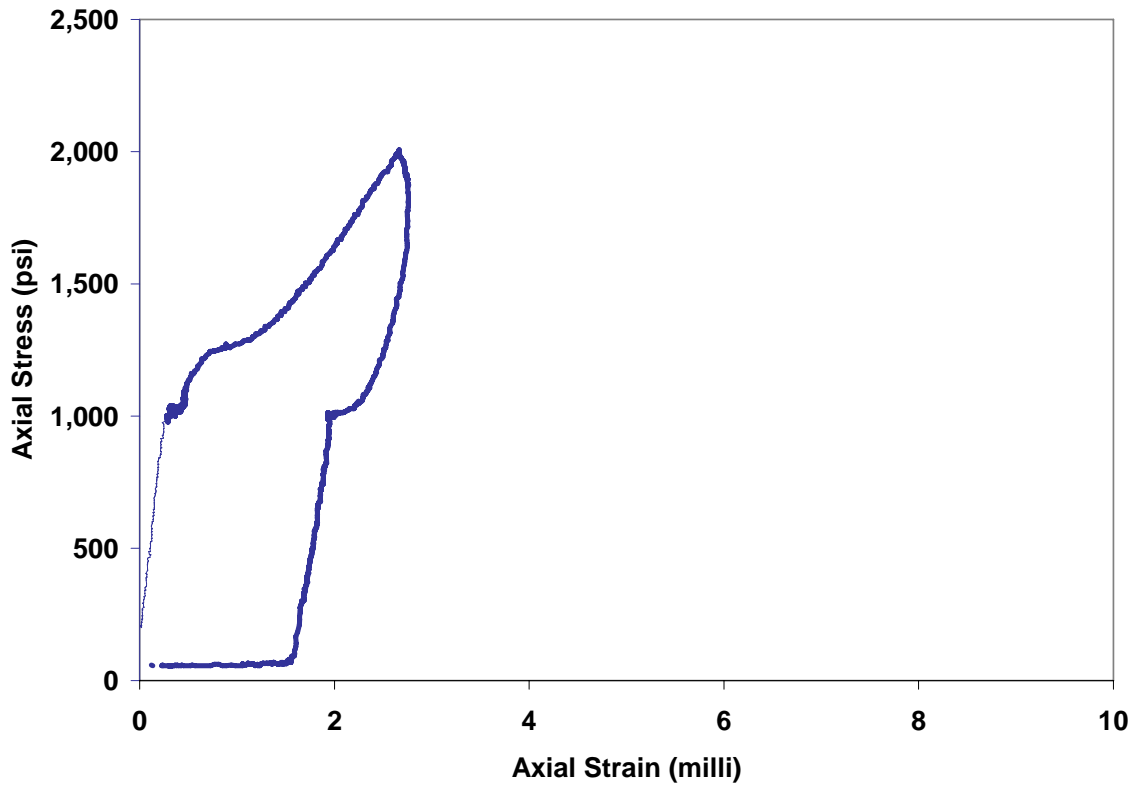
Figure 46. Stress strain behavior of Mix 1 Specimen #III-1 after curing for 36 hours.
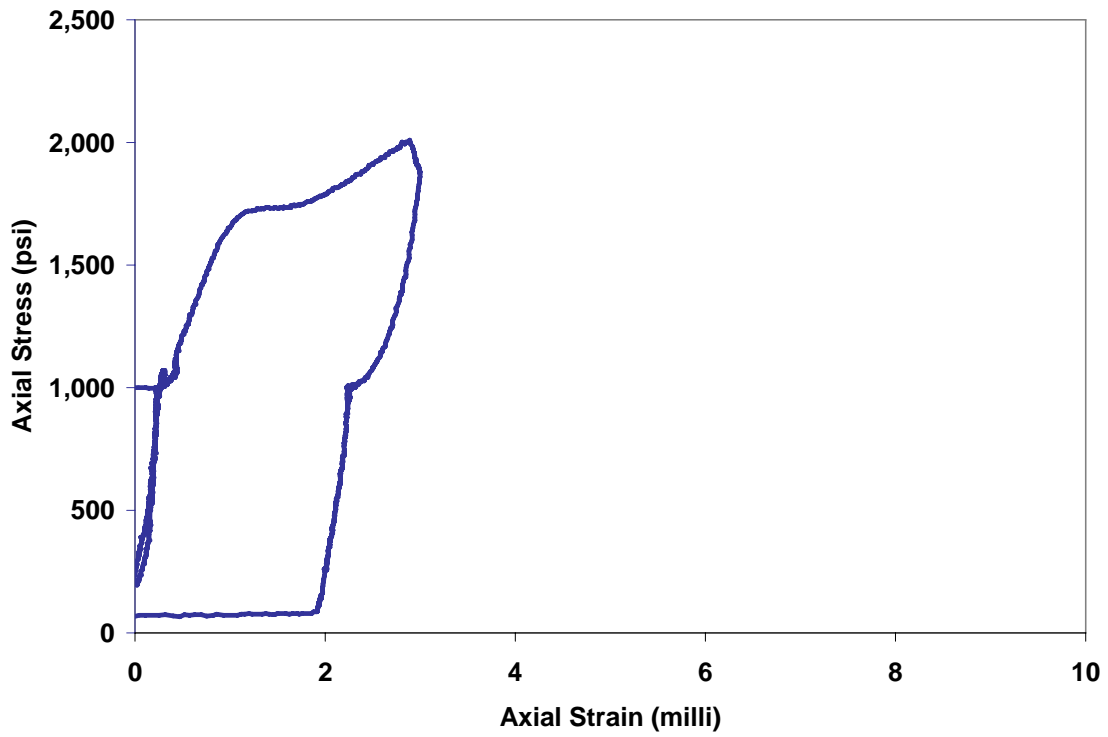
Figure 47. Stress strain behavior of Mix 1 specimen #III-3, after curing for 48 hours.
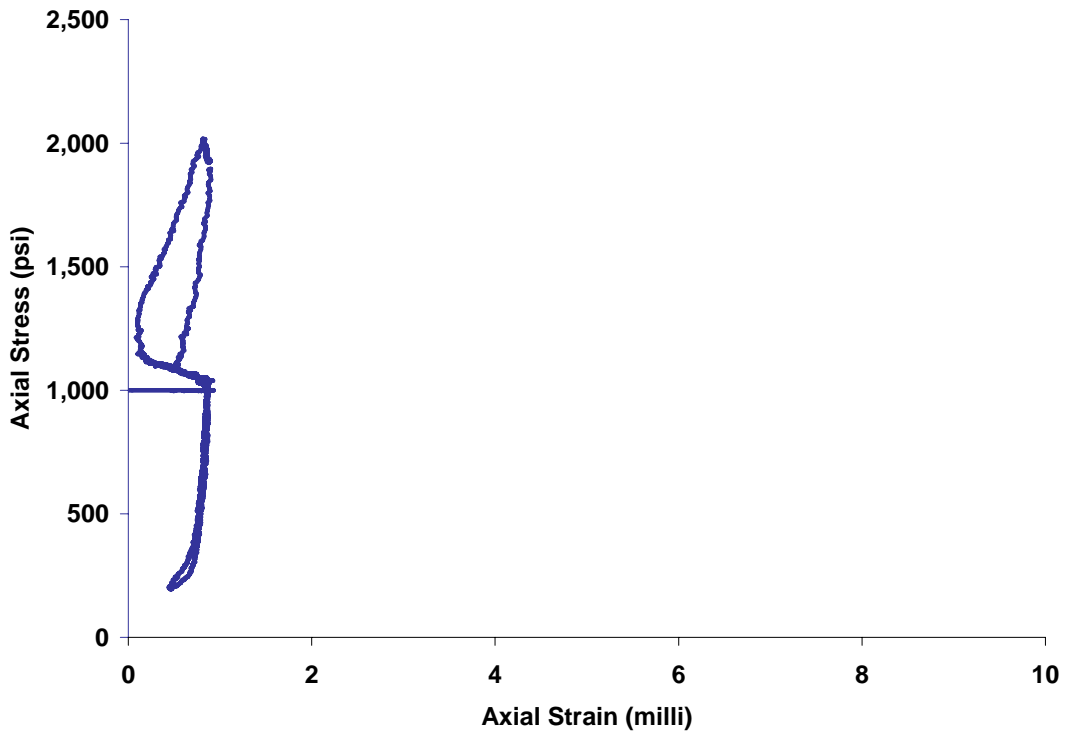
Figure 48. Stress strain behavior of Mix 1 specimen #III-4 after curing for 5 days.

68
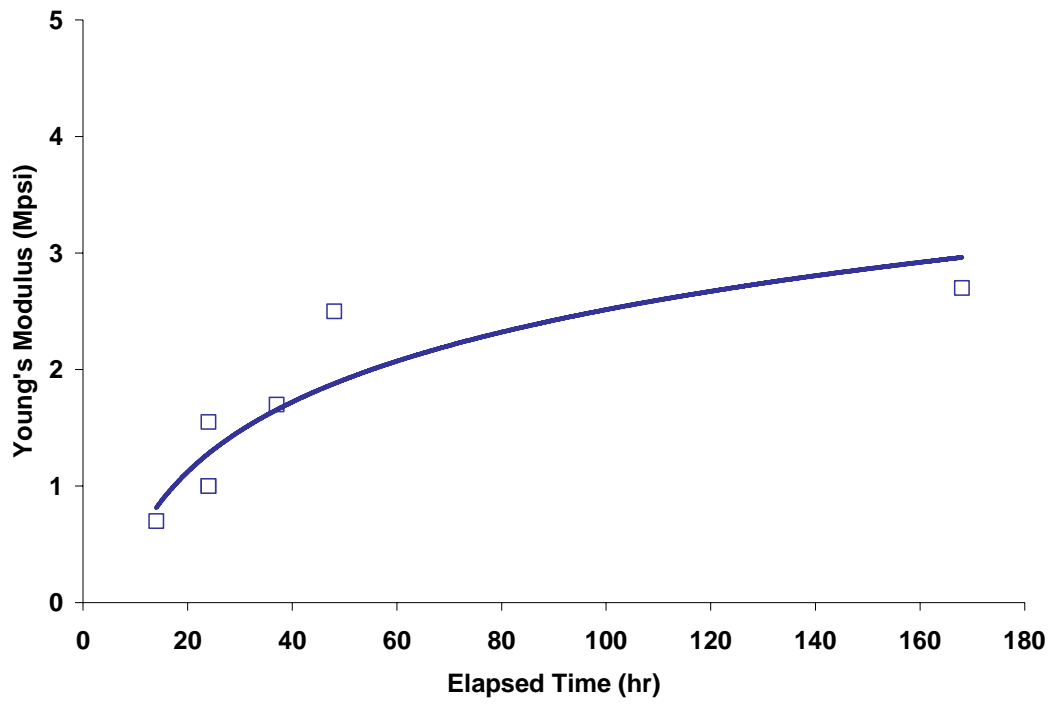
Figure 49. Variations in Young's modulus for Series III tests (data from Figures 44-48), for indicated curing times.
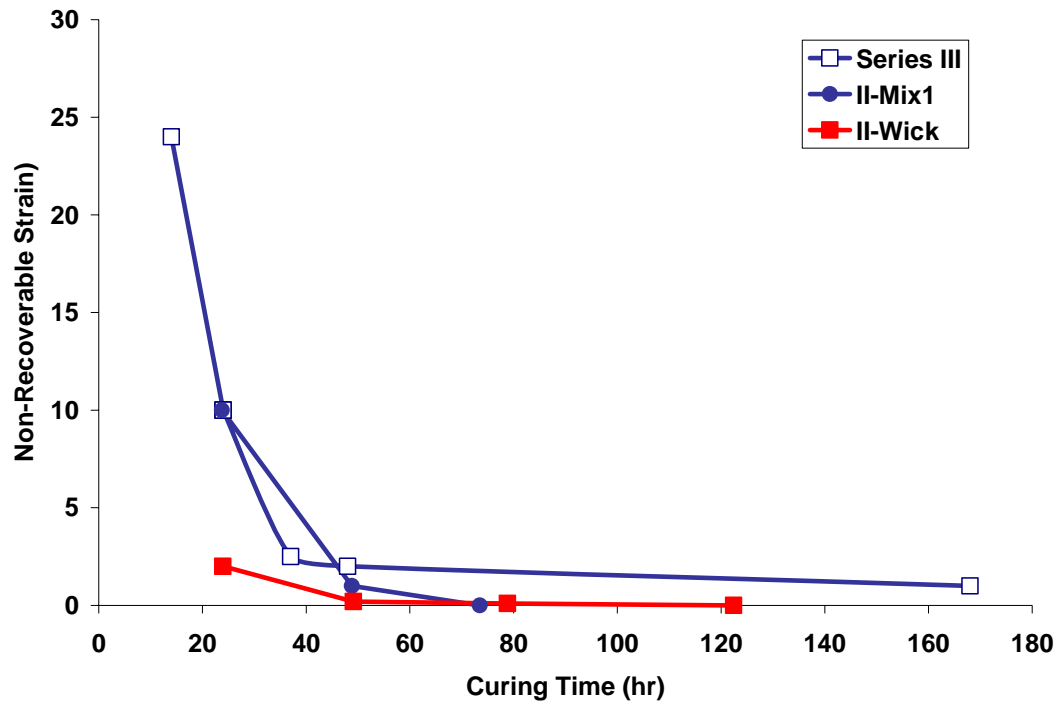
Figure 50. Non-recoverable strain from Series III tests (open squares; data shown in Figures 44 – 48) for indicated curing times. Mix 1 (filled circles) and wicked (filled squares) results from Series II tests shown for comparison.
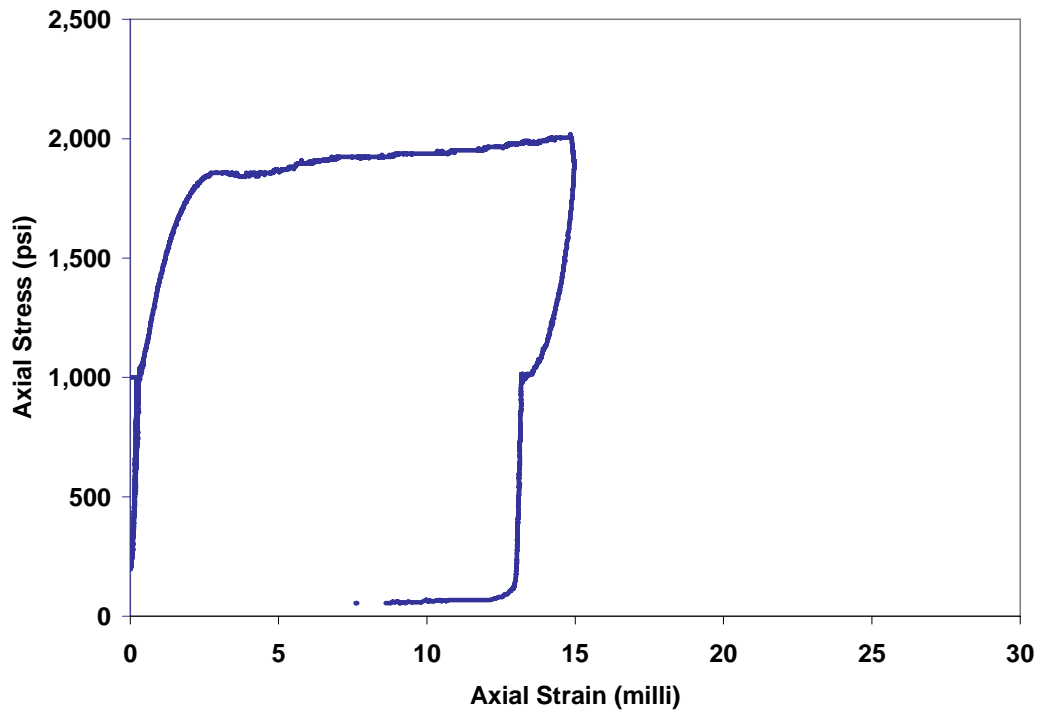
Figure 51. Stress – strain behavior for Mix 2 Specimen #IV-5, after curing for 14 hours.
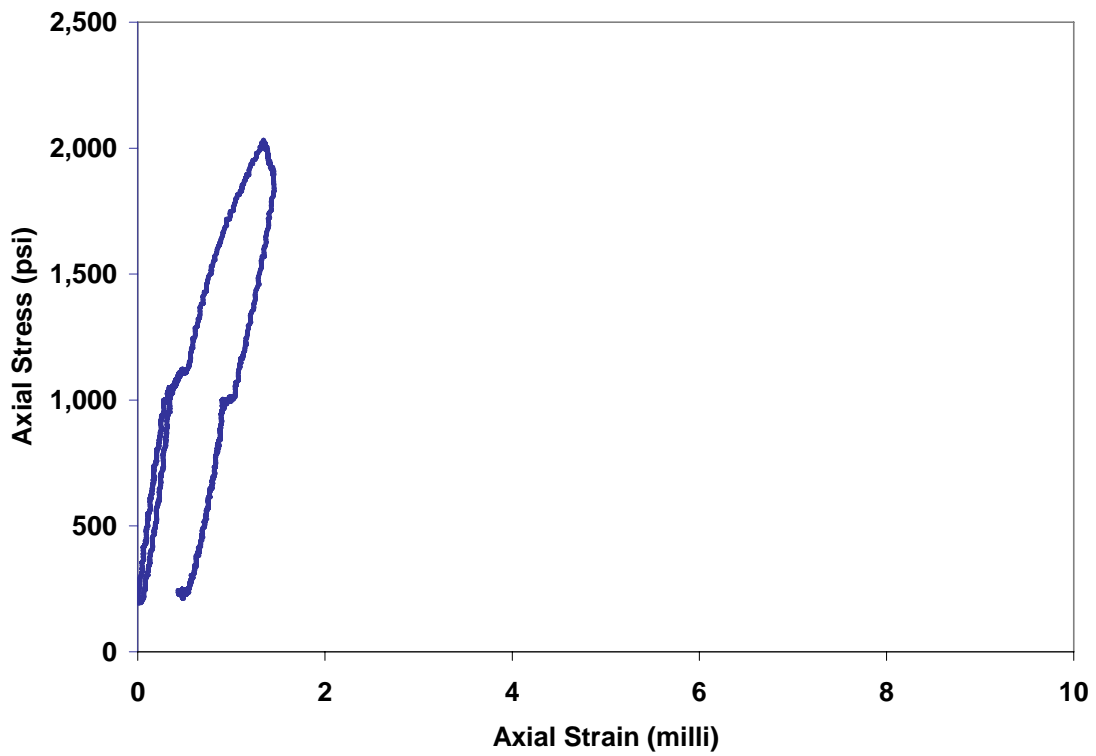
Figure 52. Stress – strain behavior for Mix 2 Specimen #II-6, after curing for 24 hours.
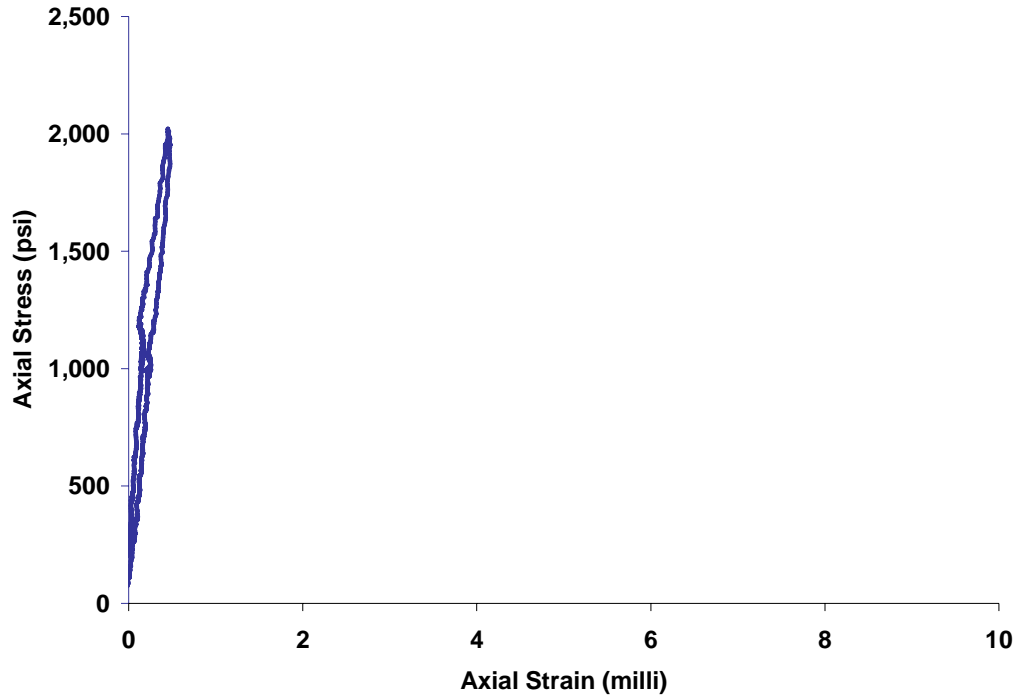
Figure 53. Stress – strain behavior for Mix 2 Specimen #IV-2, after curing for 36 hours
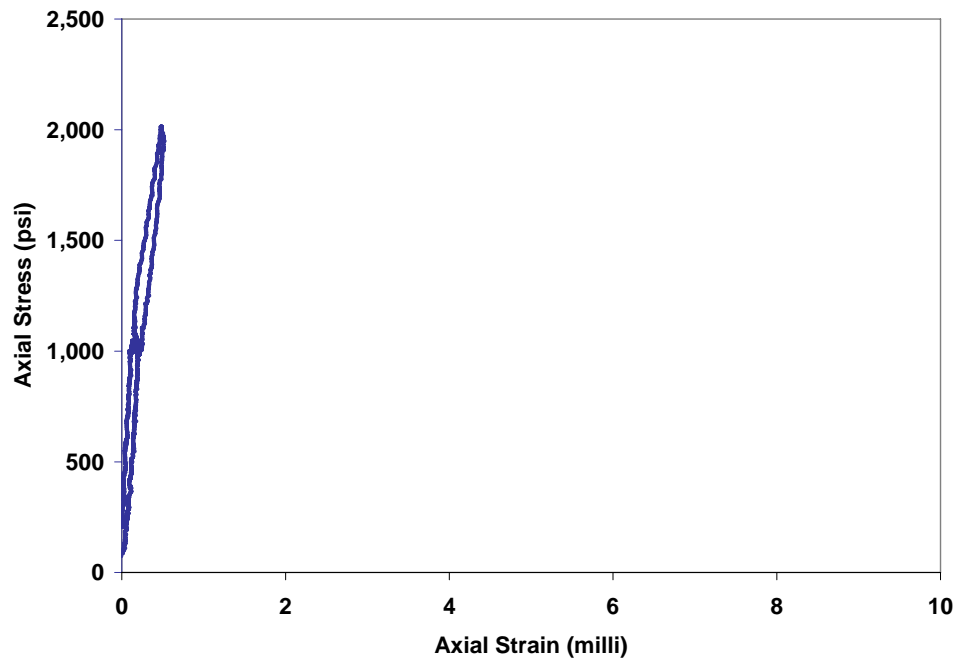
Figure 54. Stress – strain behavior for Mix 2 Specimen #IV-3, after curing for 48 hours

72
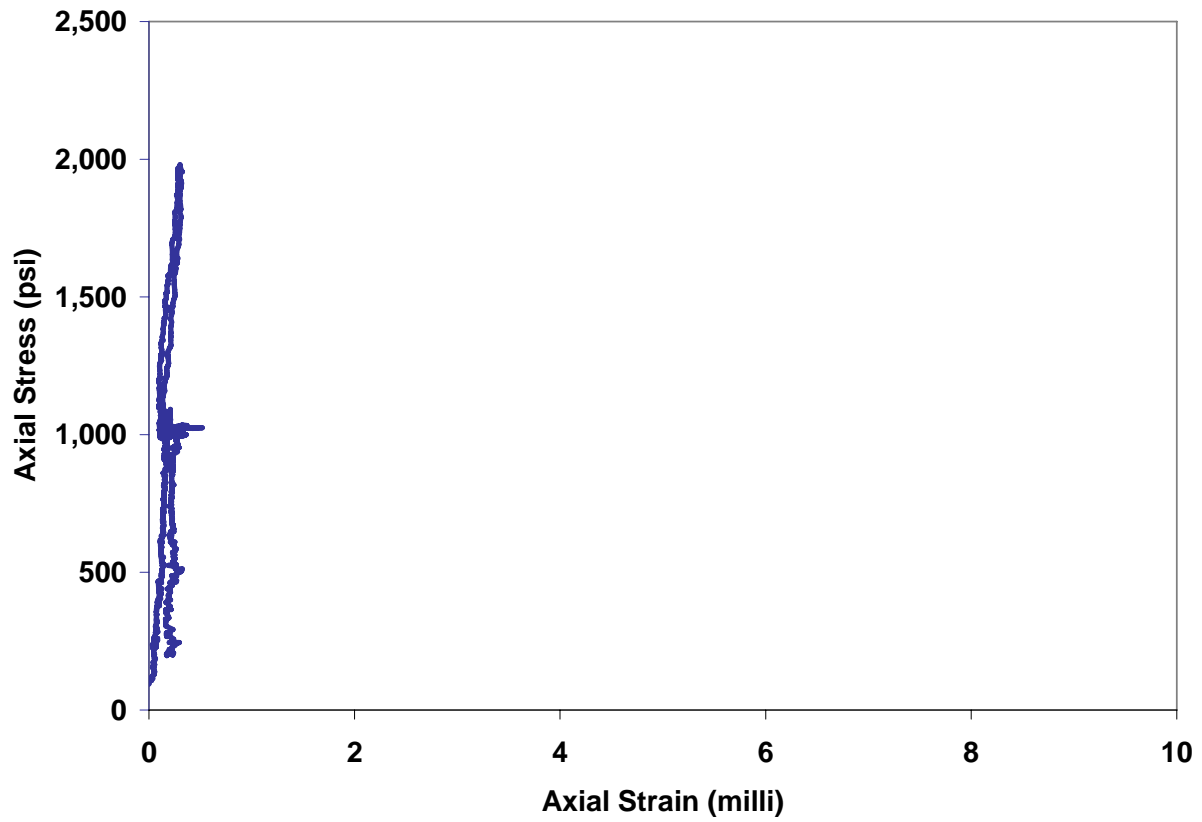
Figure 55. Stress – strain behavior for Mix 2 Specimen #IV-3, after curing for 48 hours.
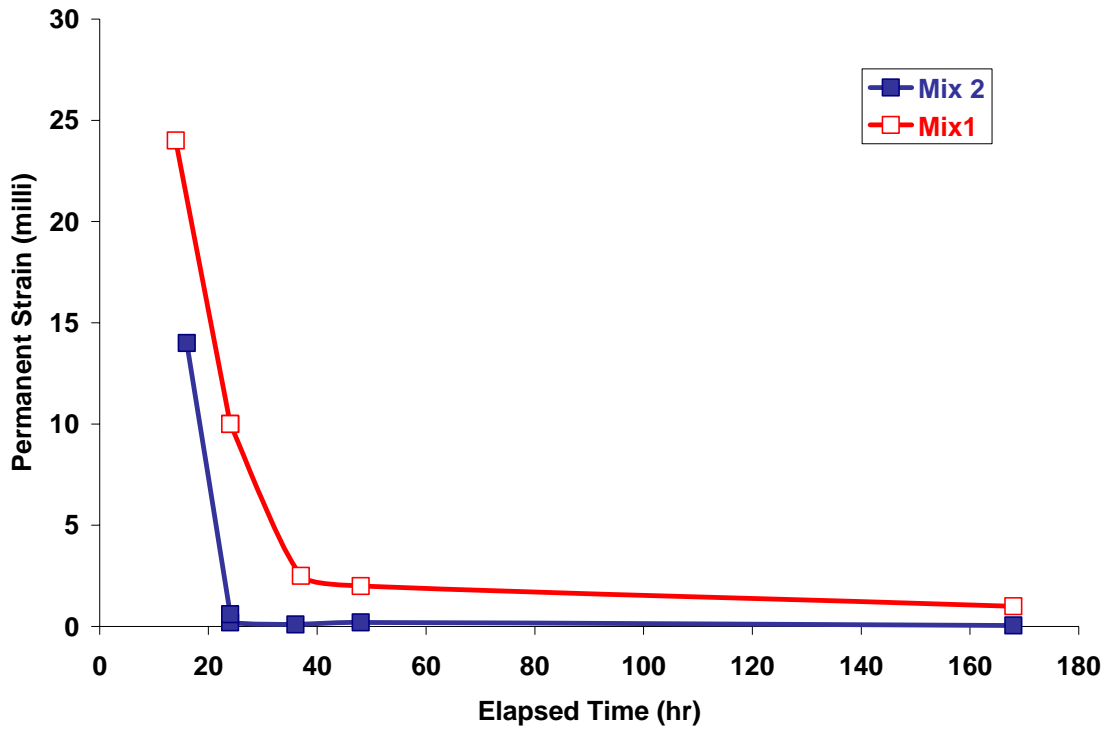
Figure 56. Variations in non-recoverable strain with curing time Series IV tests (Mix 2) specimen (filled squares). Series III test results (Mix 1, open squares) shown for comparison.
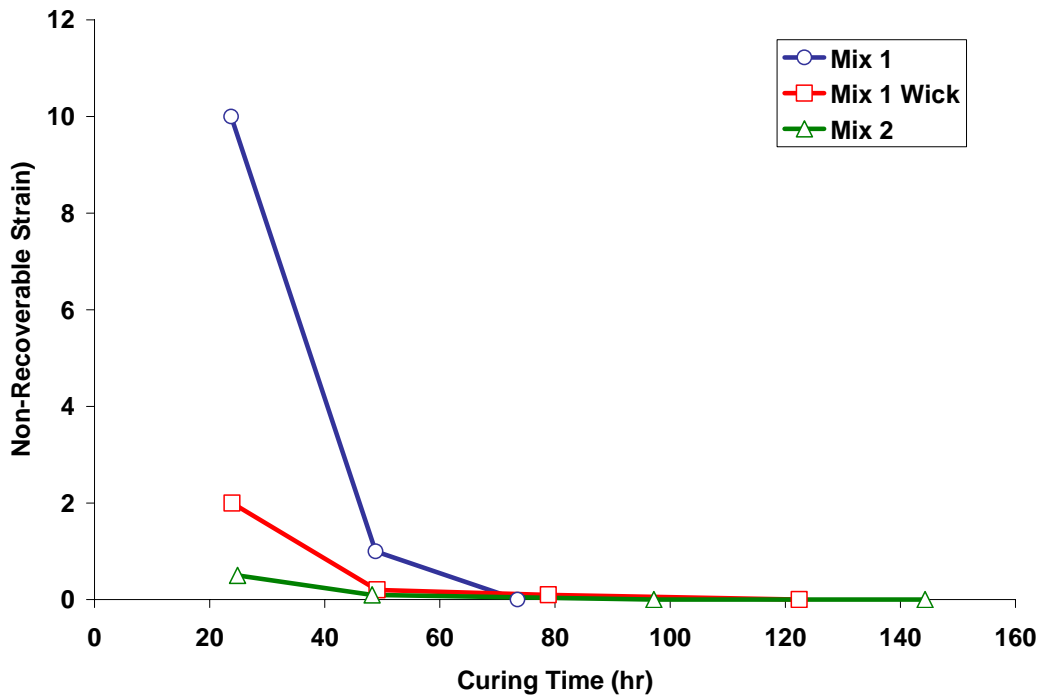
Figure 57. Non-recoverable strain for repeated deformations as functions of curing times,, from data shown in Figures 44-48.
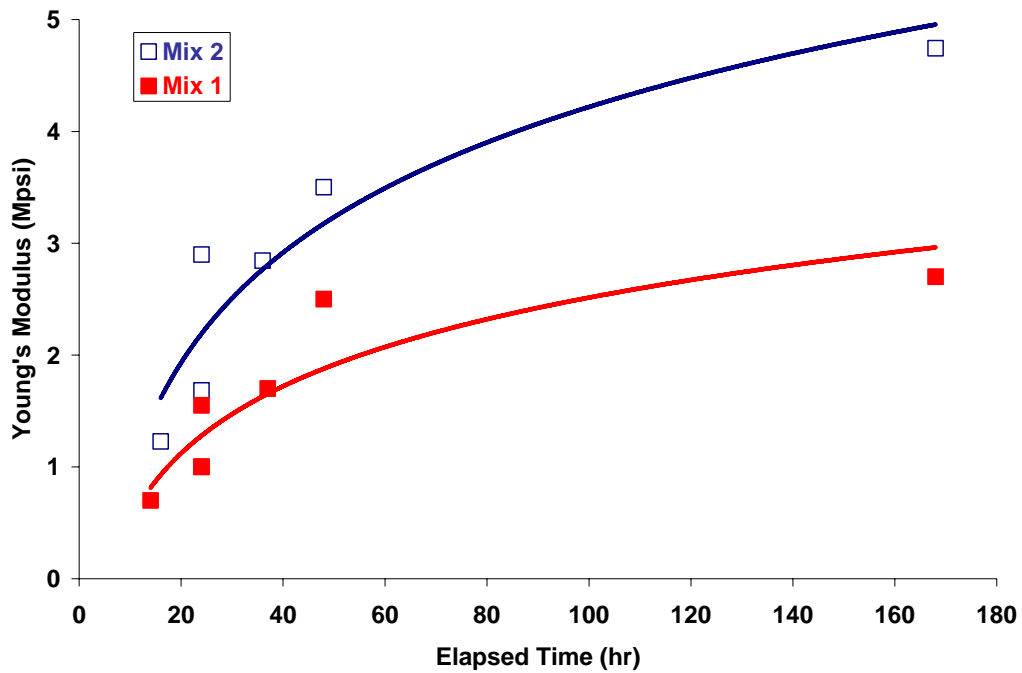
Figure 58. Variations in Young's modulus with curing time for Series IV tests (Mix 2) specimen (open squares)s. Series III test results (Mix1, filled squares) shown for comparison.
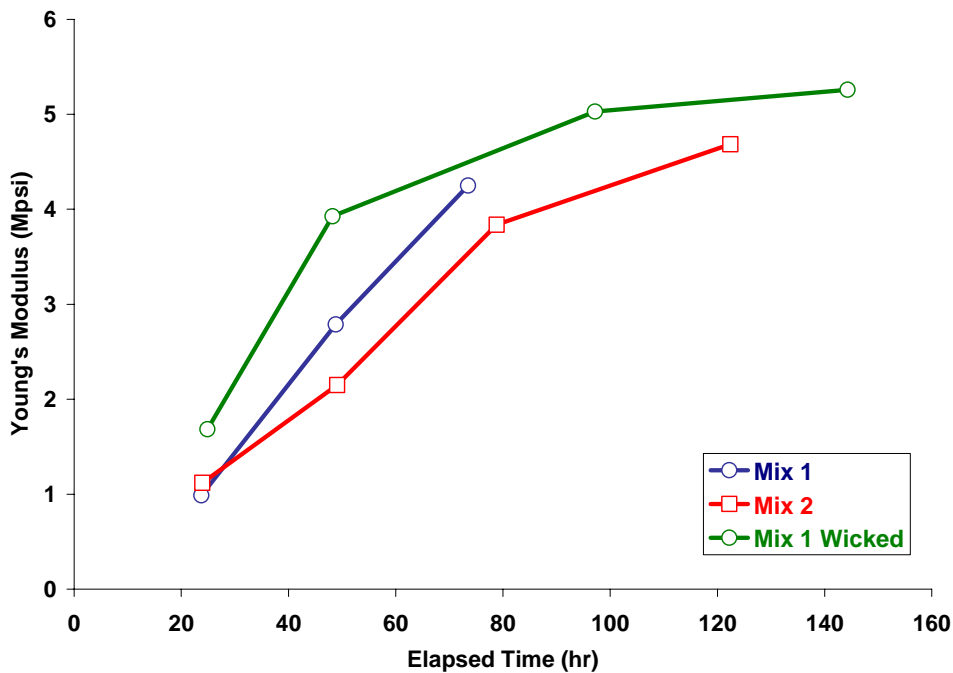
Figure 59. Variations in Young's modulus from unloading data of repeat tests on specimens as function of curing time, from data shown in Figures 44-48.
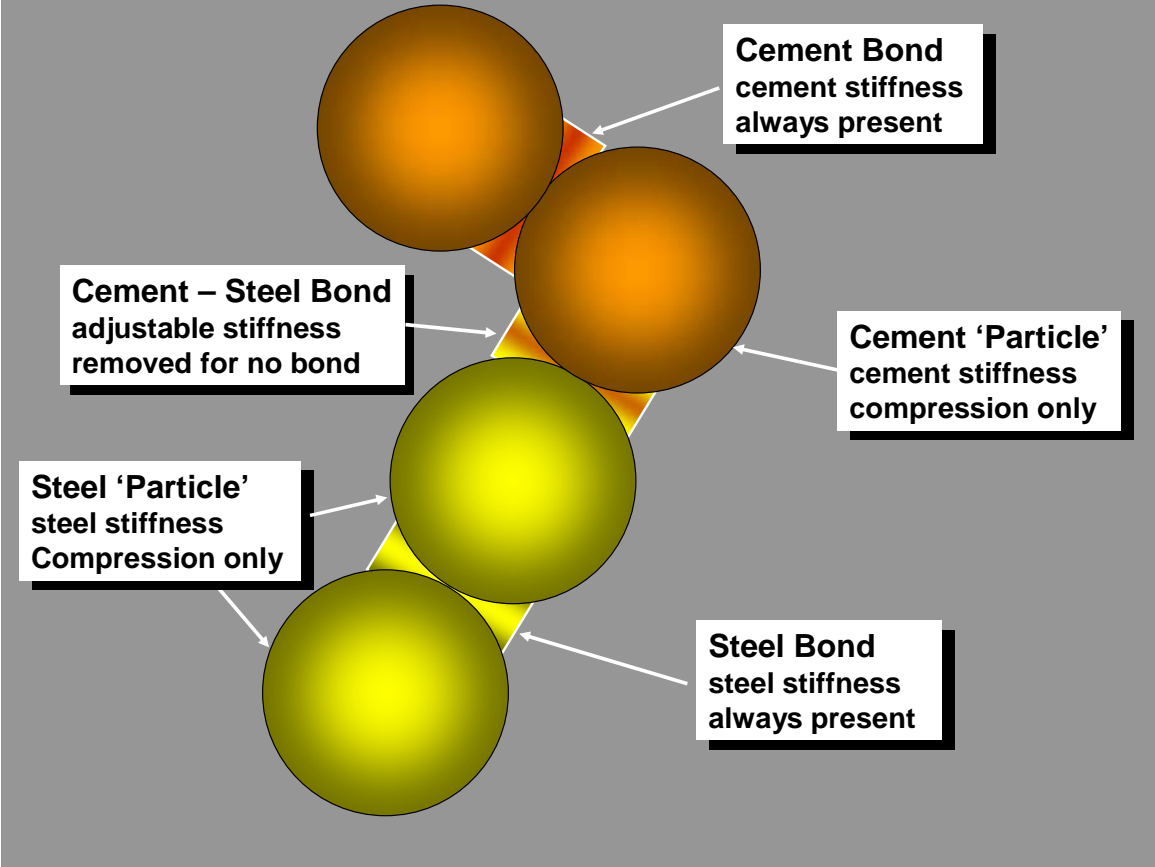
Figure 60. Particle interaction in PFC2D assembly.
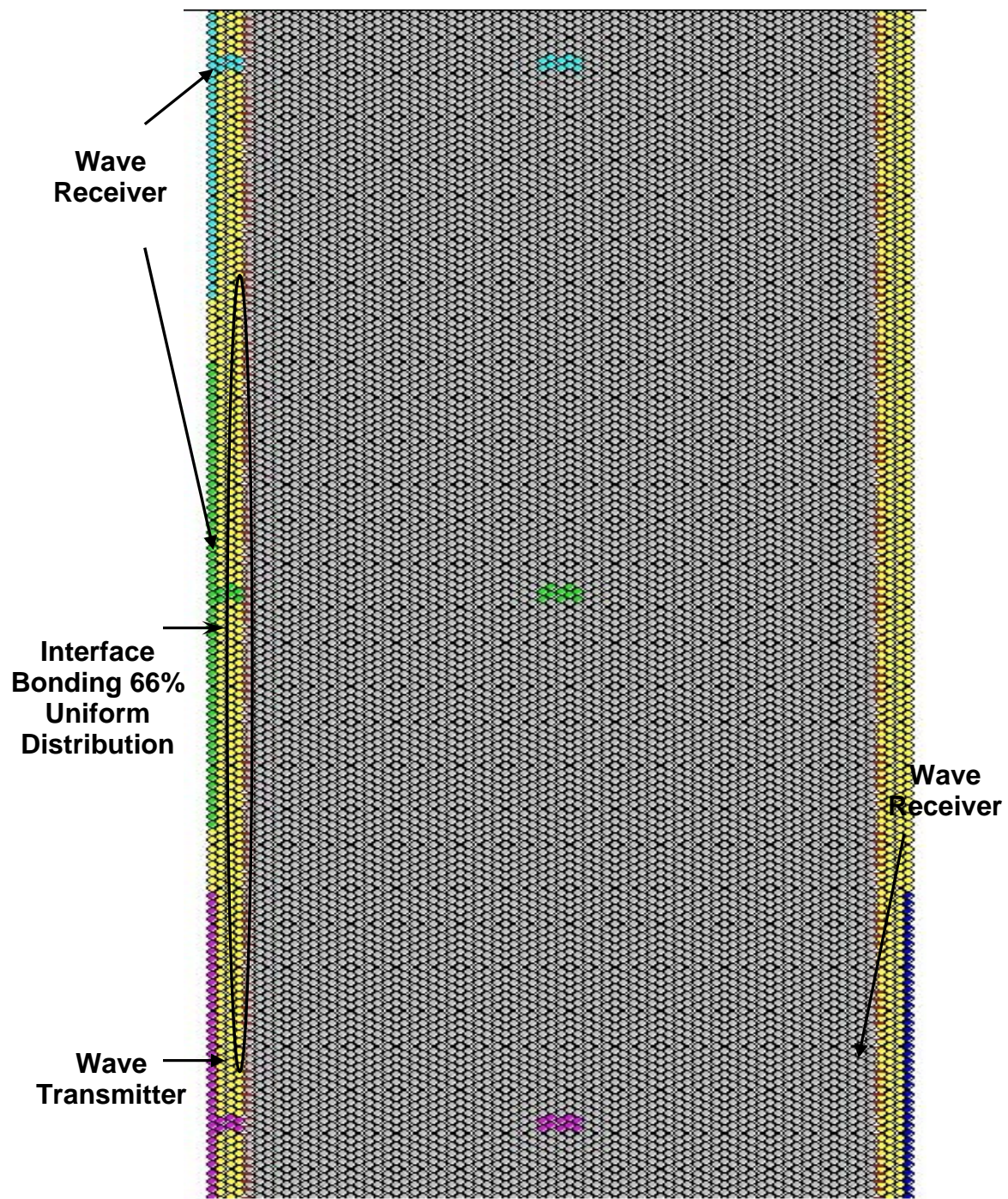
Figure 61. Model assembly in PFC2D with imbedded wave transmitter and receivers. The figure has been enlarged slightly to provide more detail; not all of the assembly is shown.
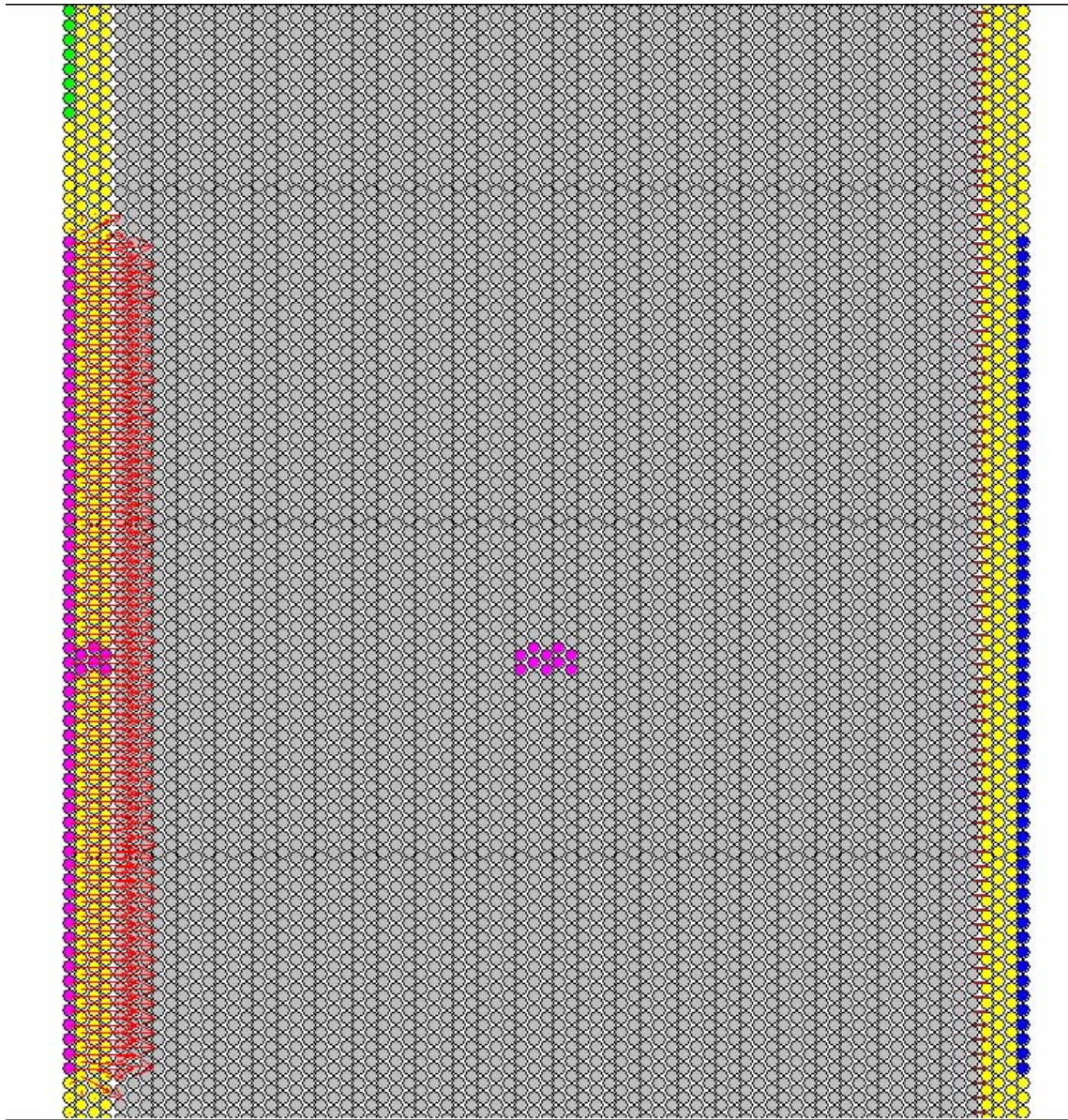
Figure 62. Wave input in modeled assembly. Red arrows, which represent the velocity of the particles, designate the location of wave in the sample
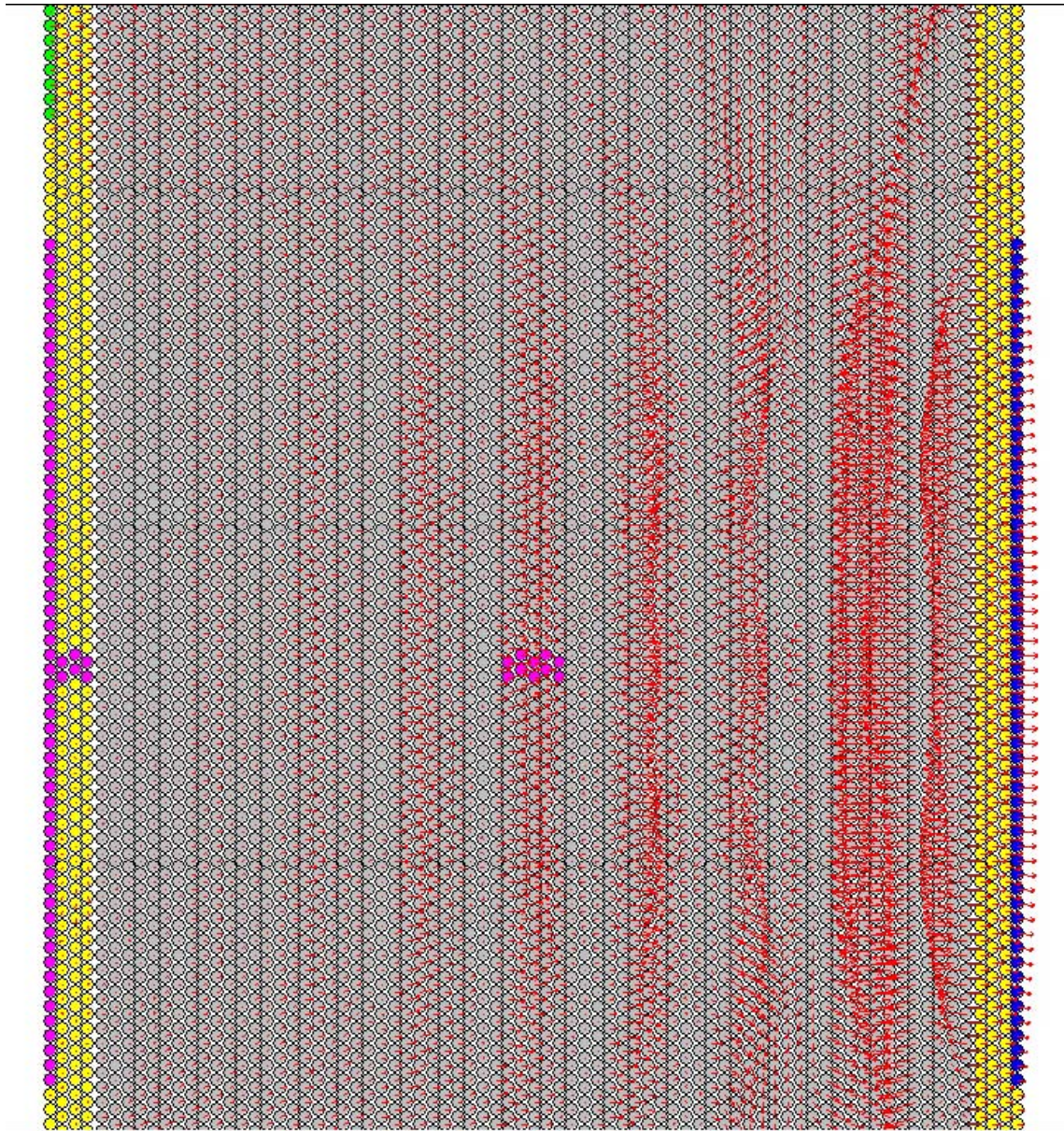
Figure 63. Wave input in model assembly after a lapse in time.
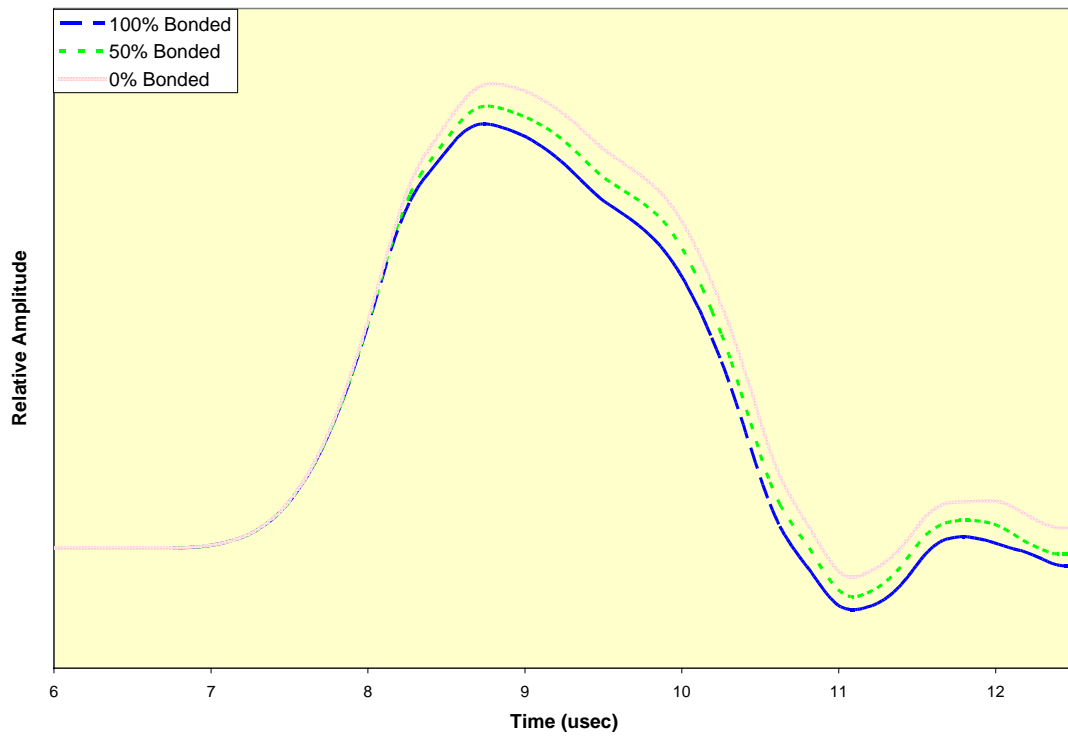
Figure 64.   Effects of incomplete bonding on wave amplitude. The wave propagation propagates through the steel parallel to the steel-cement interface. The percentage of the steel-cement interface that is bonded is specified in the legend.
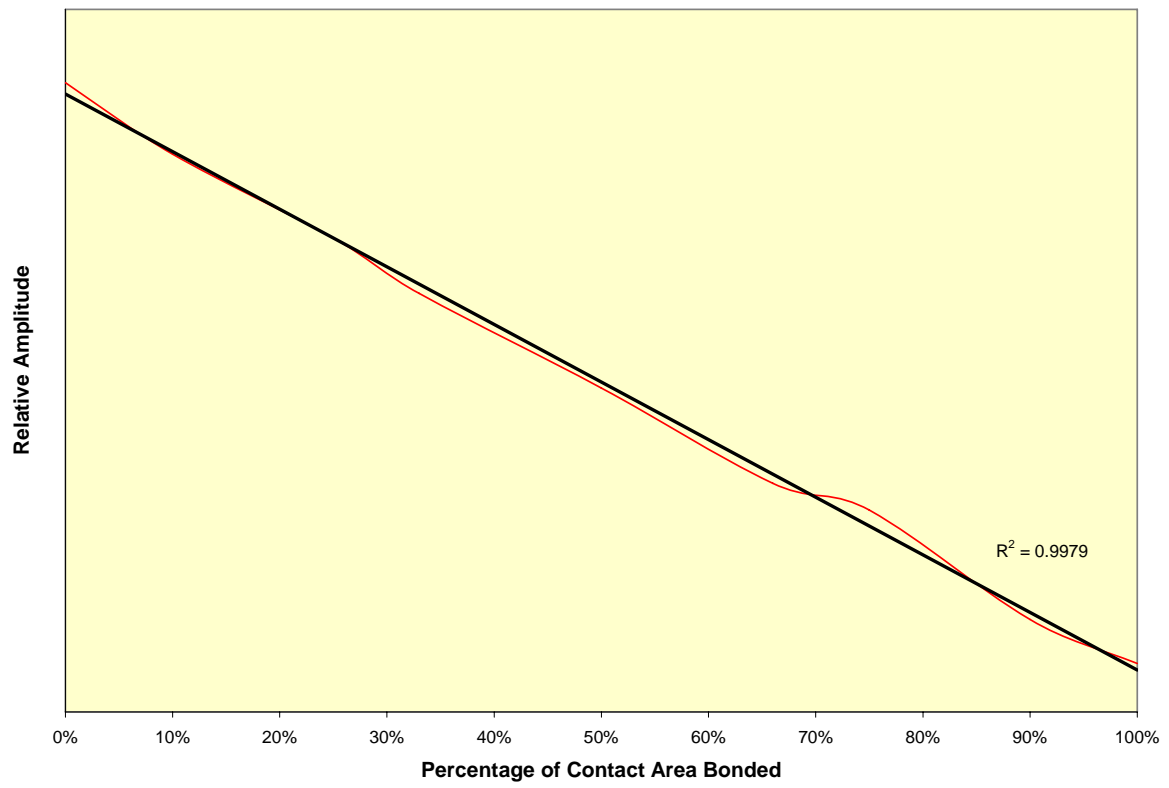
Figure 65. Relationship between p-wave amplitude and the fraction of intact bonds between the steel and the cement.
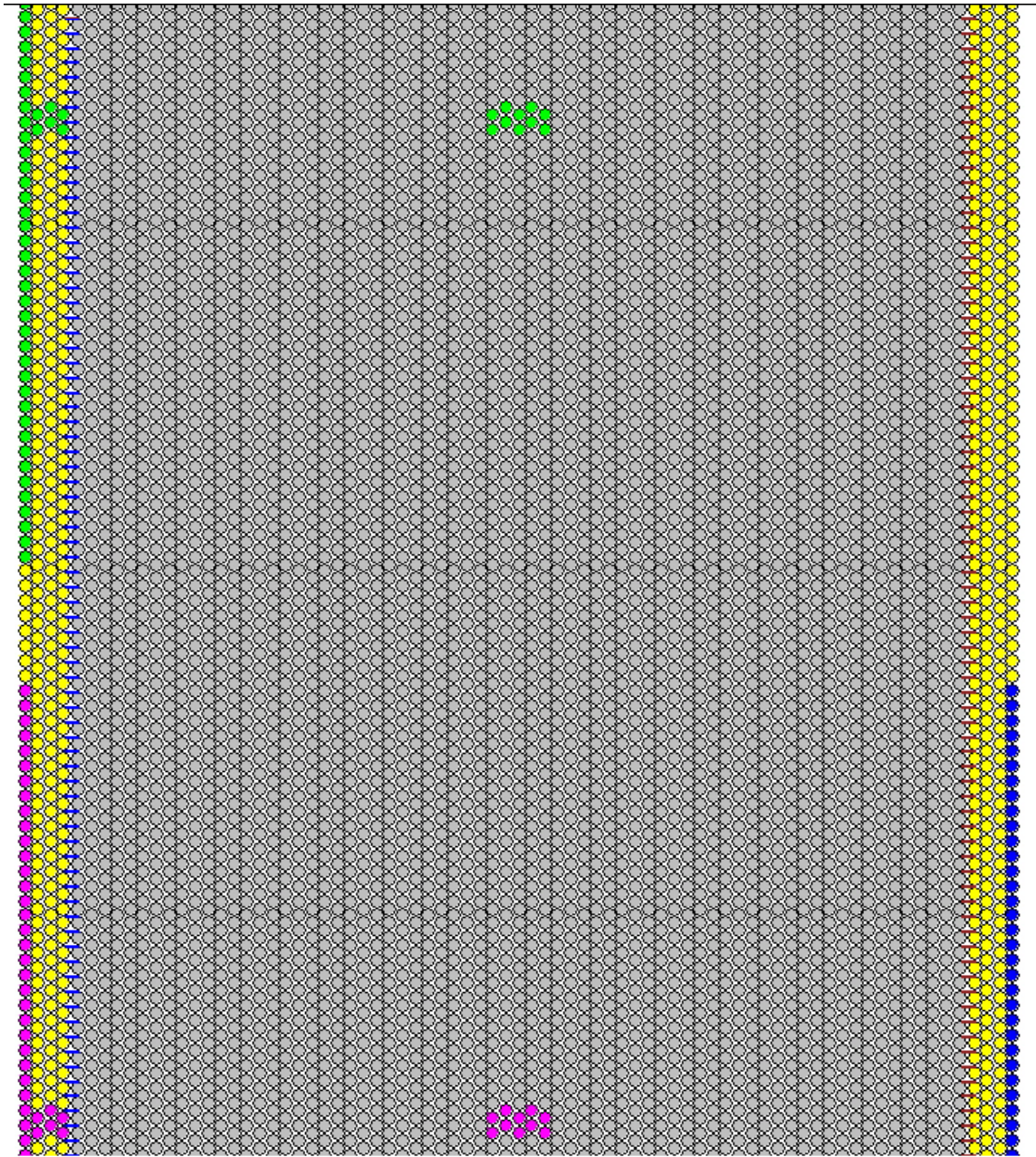
Figure 66. Model assembly with non-uniform distribution of intact bonds (blue lines) across the steel-cement interface on the left side of the assembly. Although all bonds in the portion of the interface shown are intact, only 66% of the total number of interface bonds on the left side of the assembly are intact. This distribution of interface bonds is designated as non-uniform Case 1 in Figure 68.
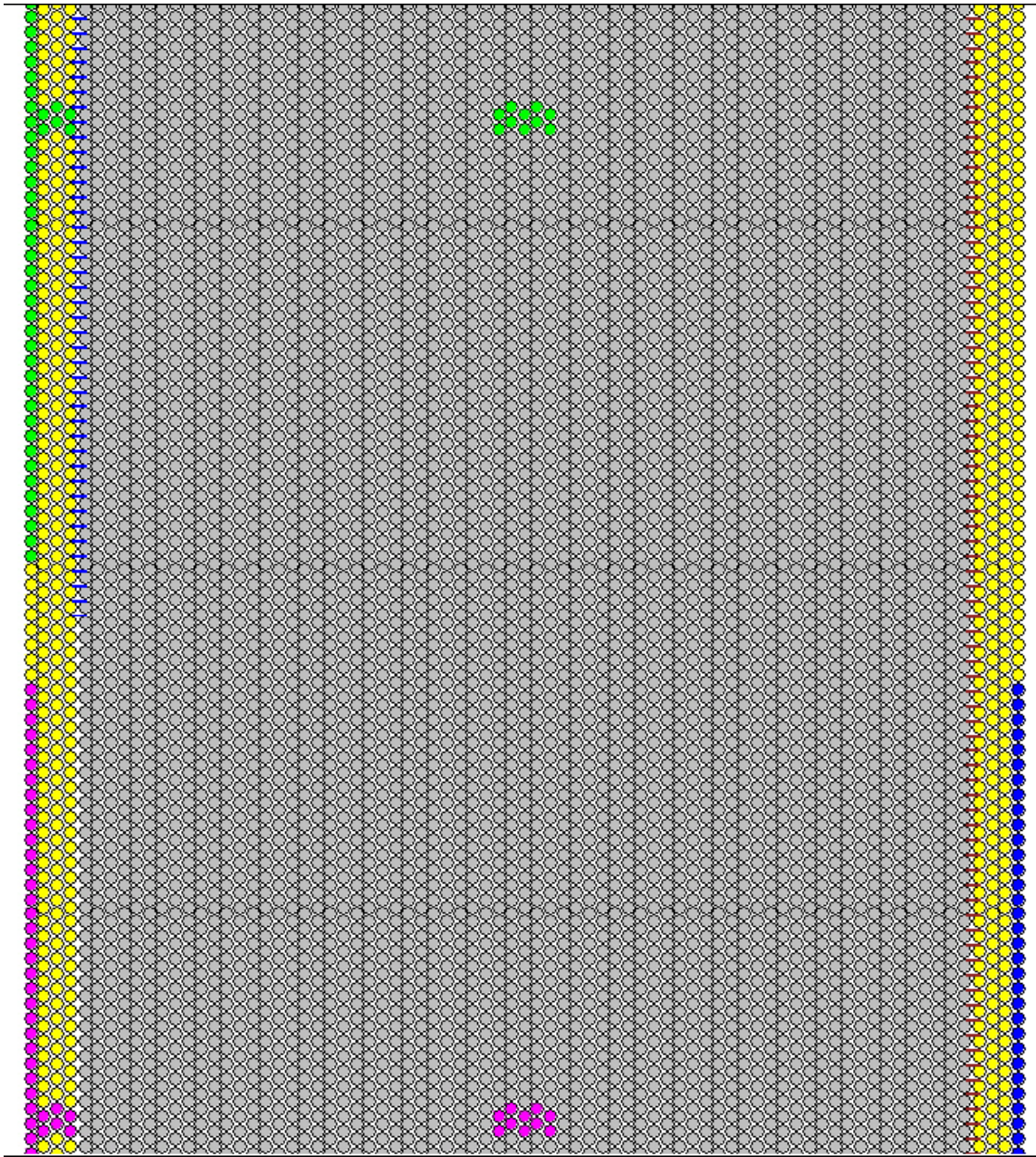
Figure 67. Model assembly with non-uniform distribution of intact bonds (blue lines) across the steel-cement interface on the left side of the assembly. Bonds in this assembly are clustered in the top half of the sample; 66% of total particle pairs along the left side interface are bonded, whereas the steel-cement interface is bonded for only half of the distance between the transmitter and the receiver, and totally un-bonded along the transmitter region. This distribution is labeled as non-uniform Case 2 in Figure 68.
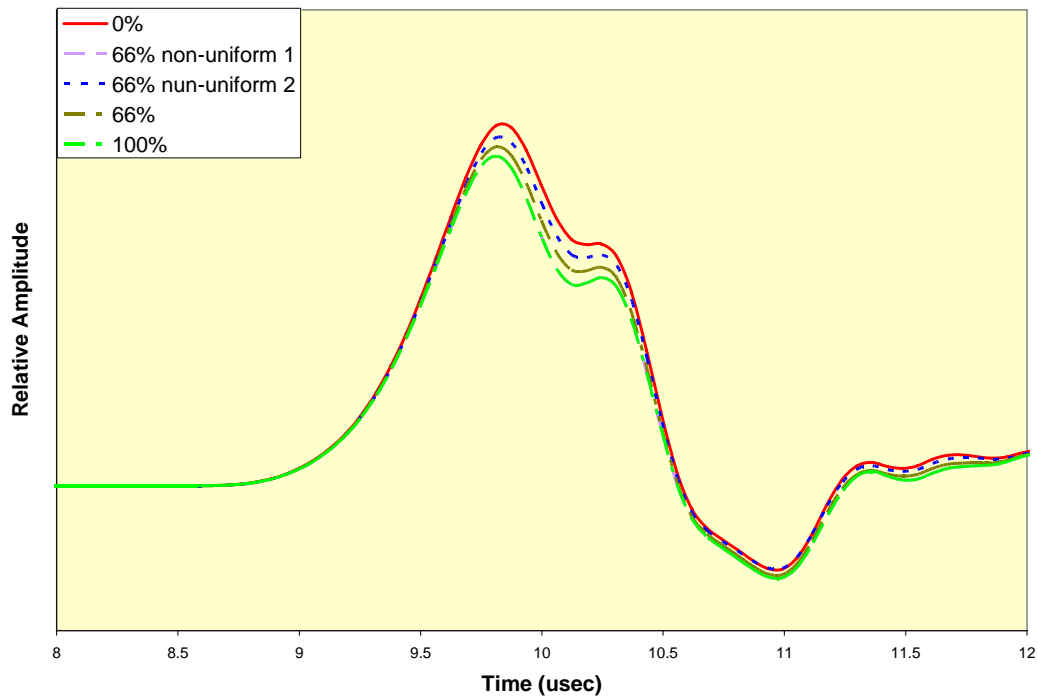
Figure 68. Non-Uniform bonding with uniform bonding waveforms as a reference. Waves propagated through the steel, parallel to the steel-cement interface on the left side of the sample. The bonding at the steel-cement interface is indicated in the legend. Non-uniform 1 and non-uniform 2 refer to the bonding states depicted in Figures 66 and 67, respectively.
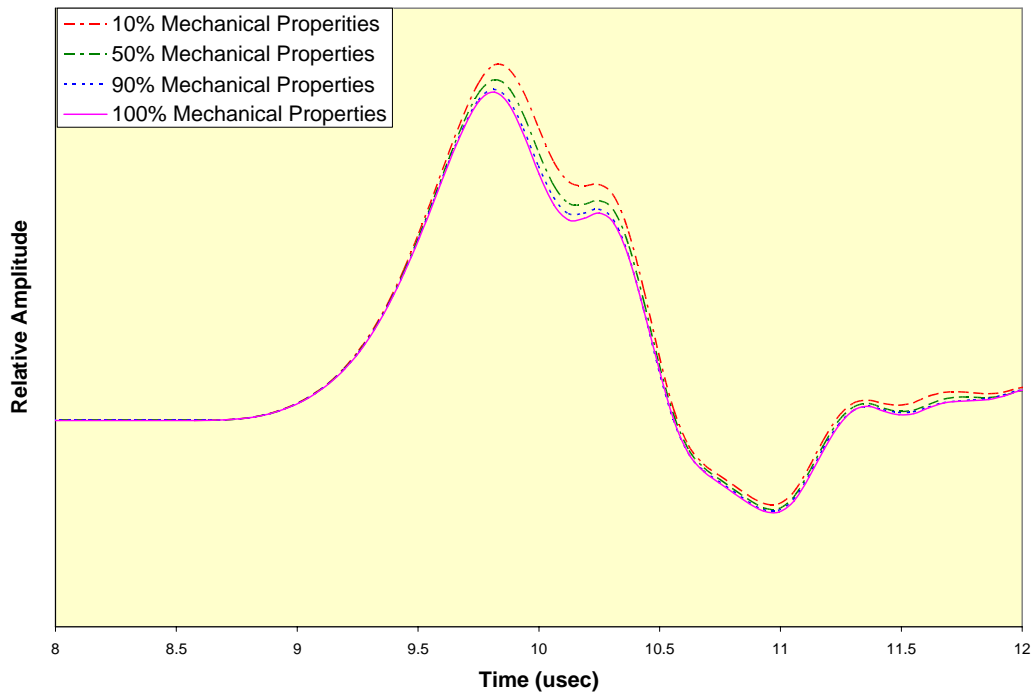
Figure 69. Wave propagation in steel, with 100% of contact area bonded at the steel-cement interface. Mechanical Properties of the bonds for each waveform is given in the legend, as a percentage of the mechanical properties of the cement.

84
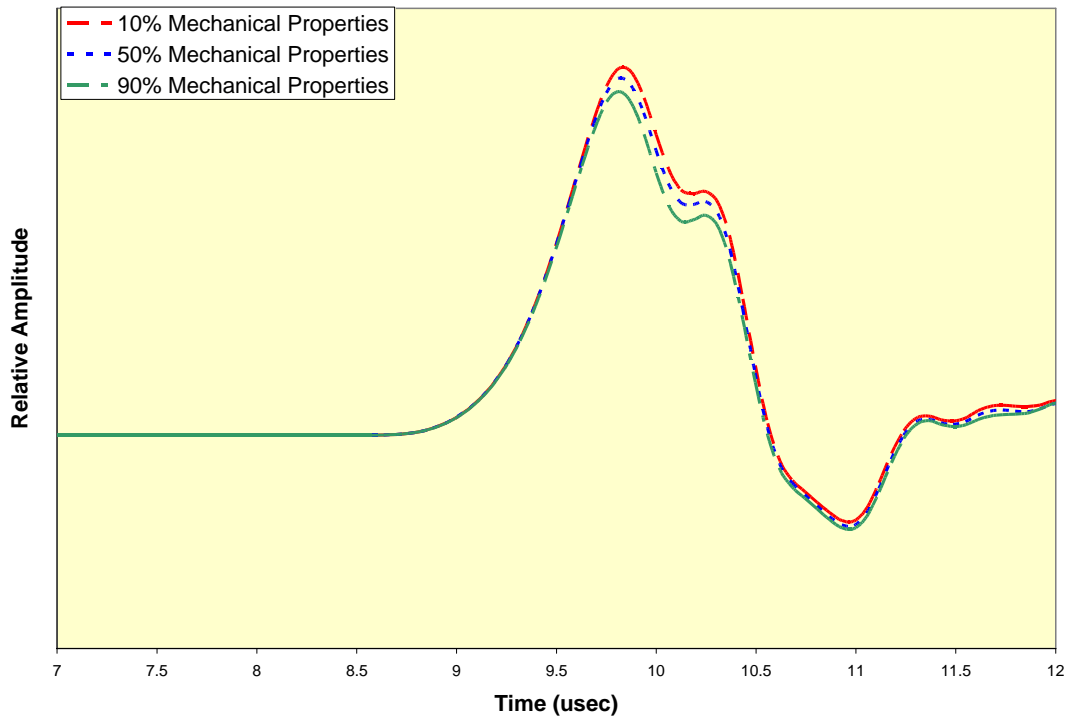
Figure 70. Wave propagation in steel 90% of contact area bonded uniformly, with changing mechanical properties of the bonding at the steel-cement interface
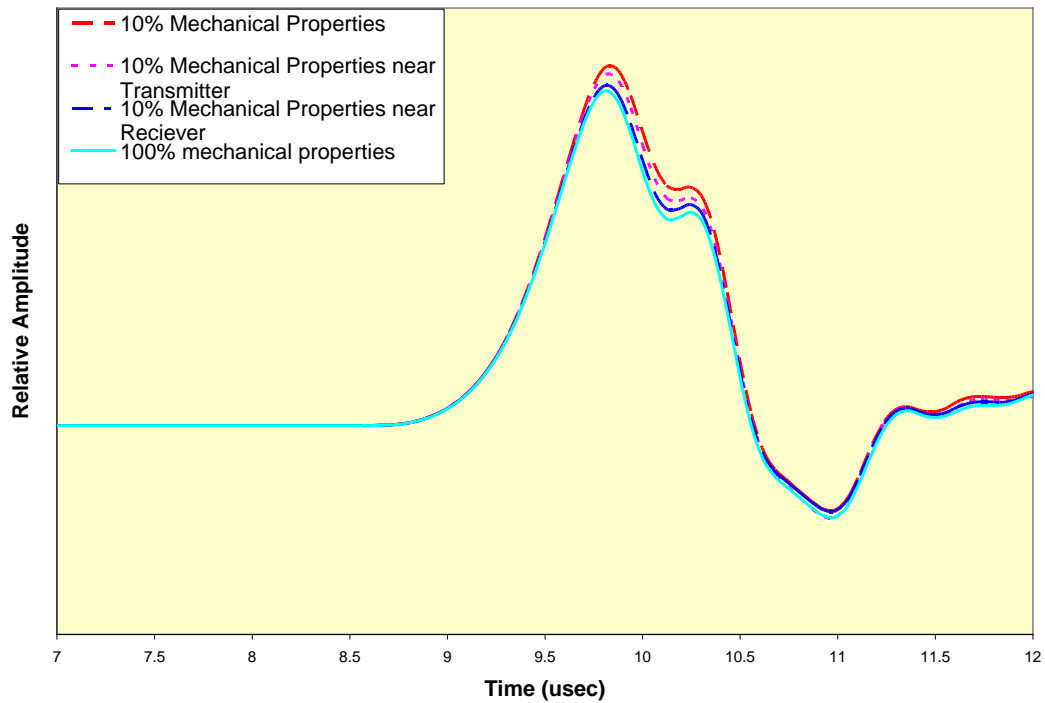
Figure 71. Effects of placement of zones of altered mechanical properties between the receivers. In these simulations 90% of the bonds at the steel-cement interface are intact. The simulations were carried out with altered mechanical properties for half the distance between the transmitter and receiver, in a region located either near the transmitter or the receiver. The behavior for these distributions are compared with that of uniformly distributed bonds with altered properties.

86
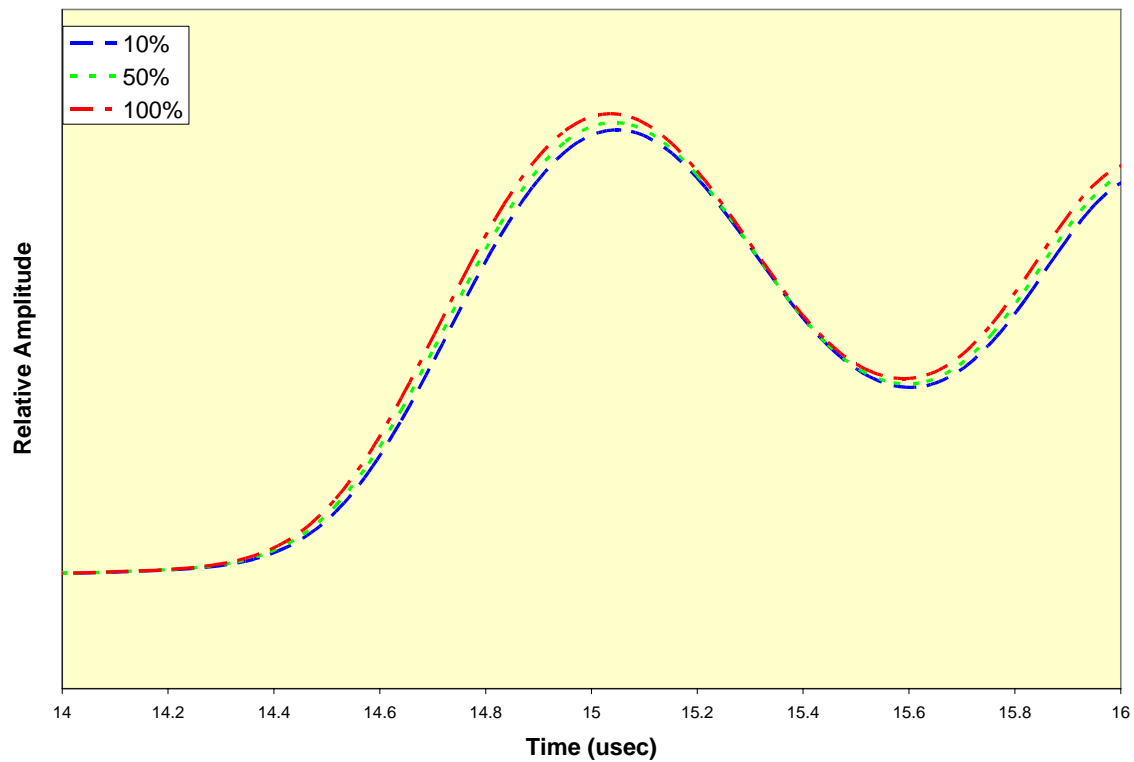
Figure 72. Amplitudes of detected p-waves propagating through the assembly from left to right, through steel, cement and then steel, with changing fractions of intact bonds at the steel-cement interface on the left side of the sample.
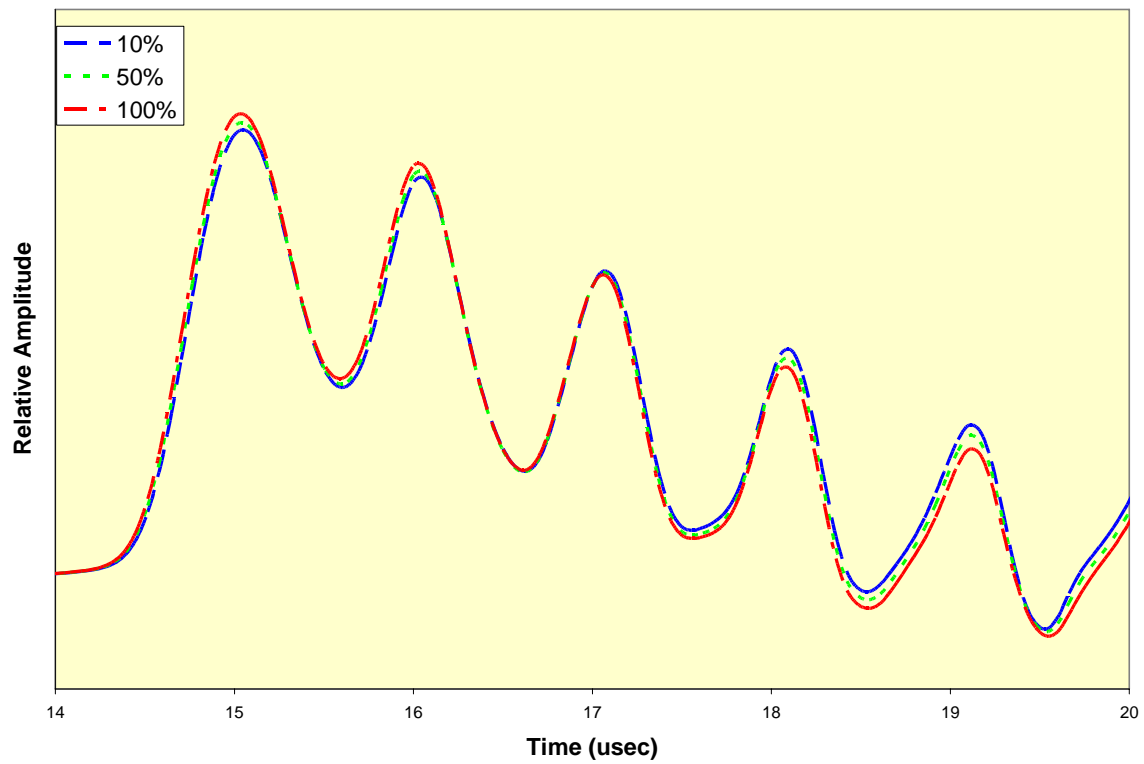
Figure 73. Same p-wave as in Figure 72, with expanded time scale to show high-frequency oscillations from multiple reflections within the steel 'casing'.
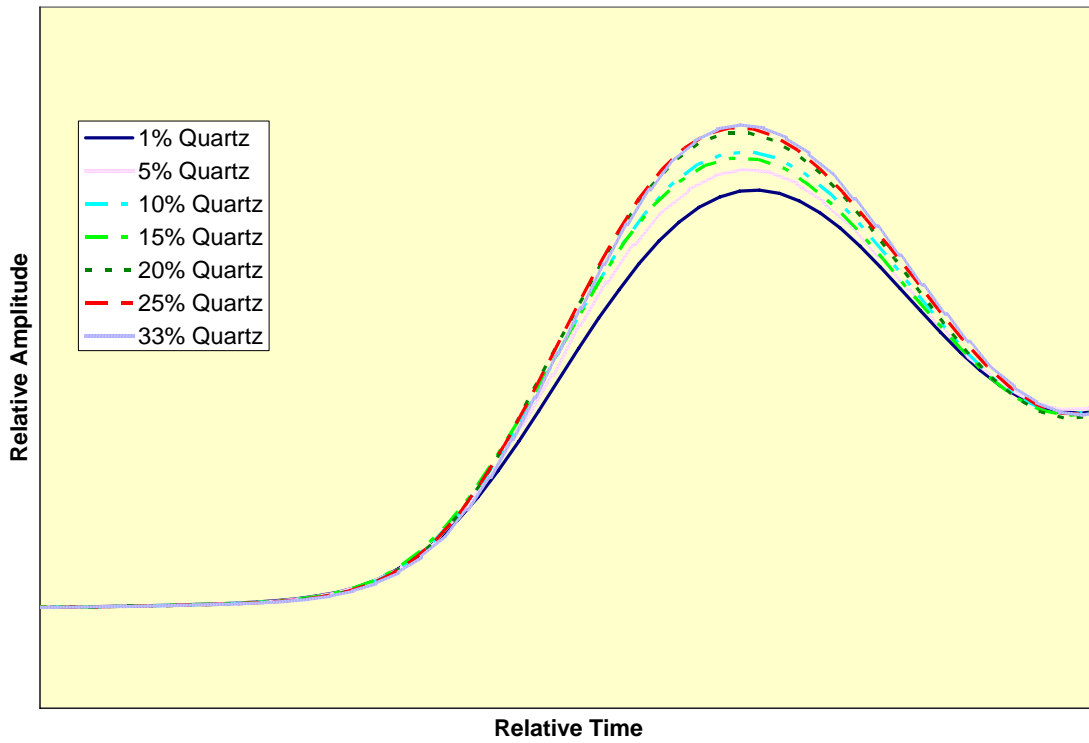
Figure 74. Propagation through assembly with the inclusion of quartz. The time scale has been altered so that the first arrival time of each waveform is the same. Arrival times were between 14 and 14.2 microseconds.
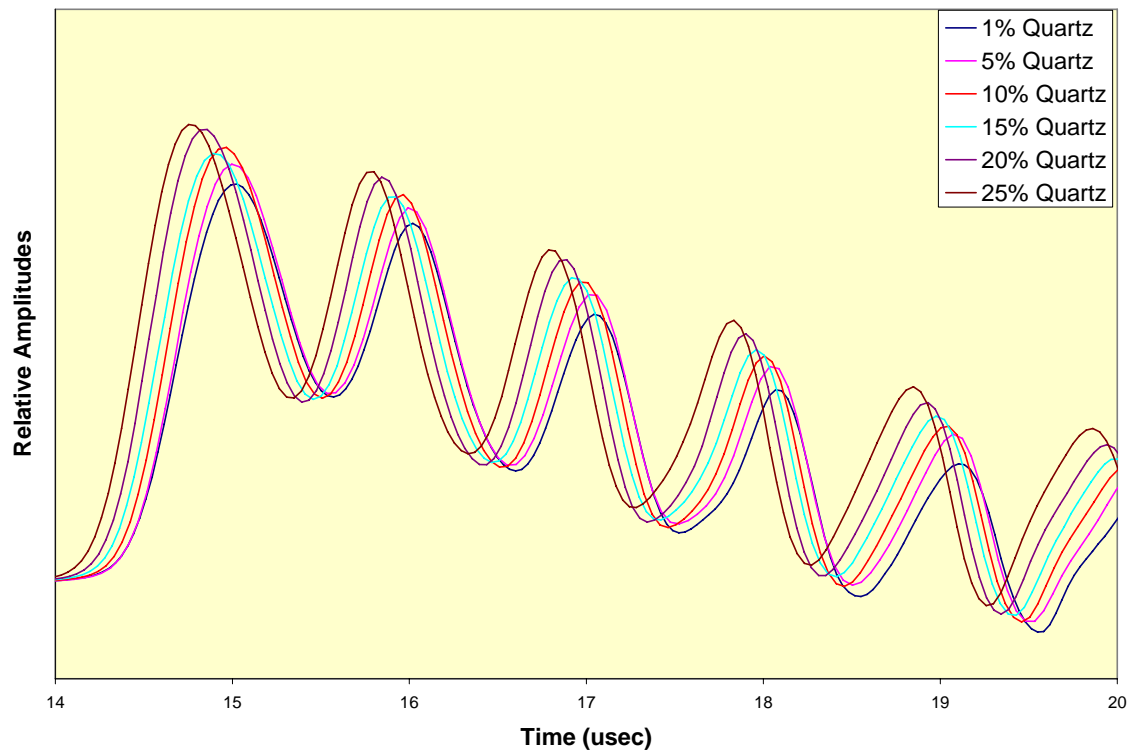
Figure 75. P-wave propagation through sample with added quartz, with expanded timescale to show high-frequency reflected waveforms.
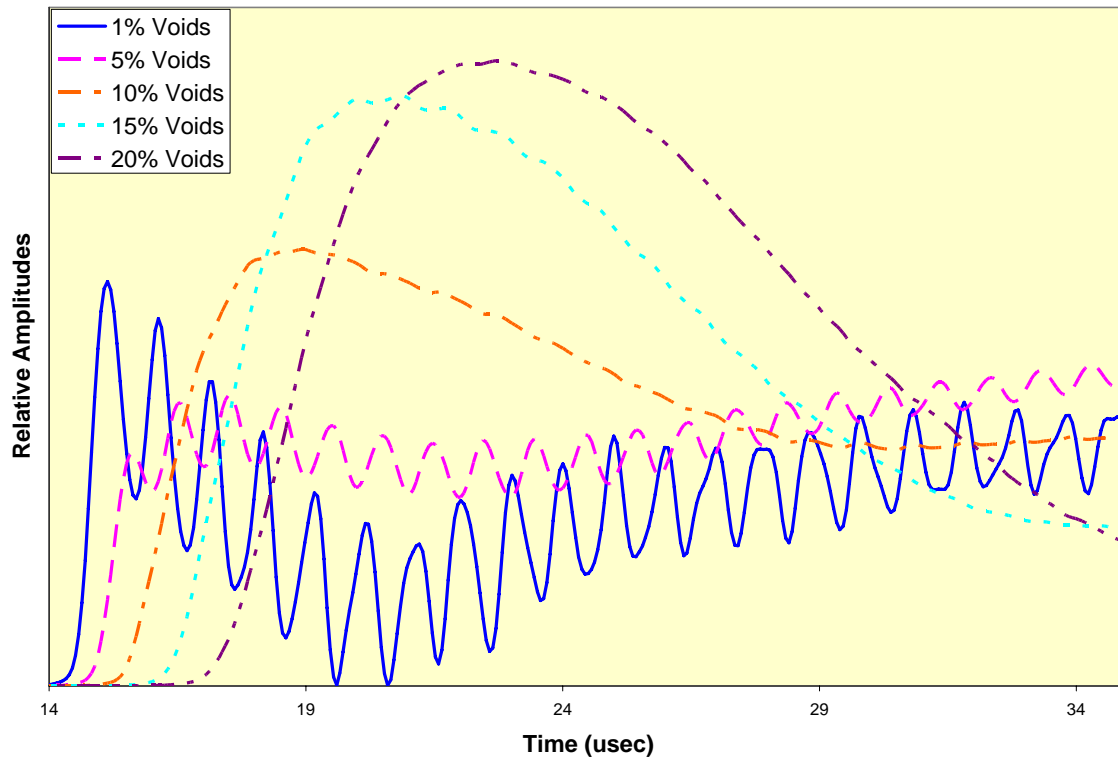
Figure 76. Propagation through the sample with void spaces added to the cement. Steel-cement interfaces are 100 % bonded with no quartz inclusions.
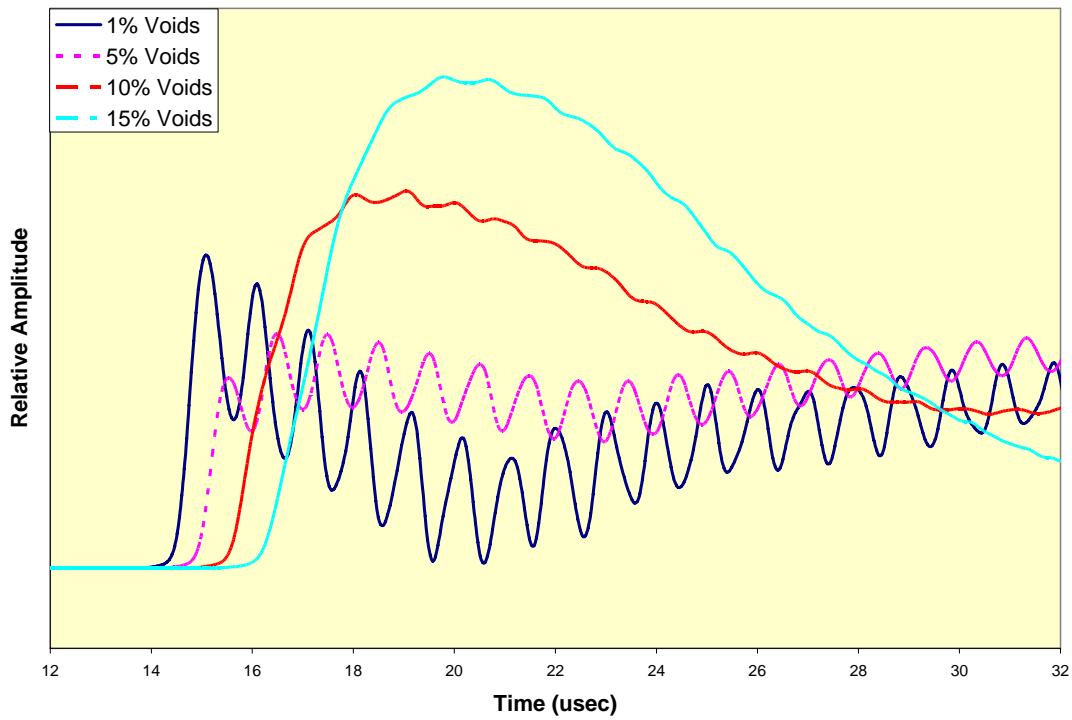
Figure 77. Detected p-waveforms for horizontal propagation through sample with a fixed 5% quartz and the indicated voids contents. All of the steel cement interface was bonded and the wave was propagated from a transducer on the left side of the sample to a receiver on the right side of the sample.
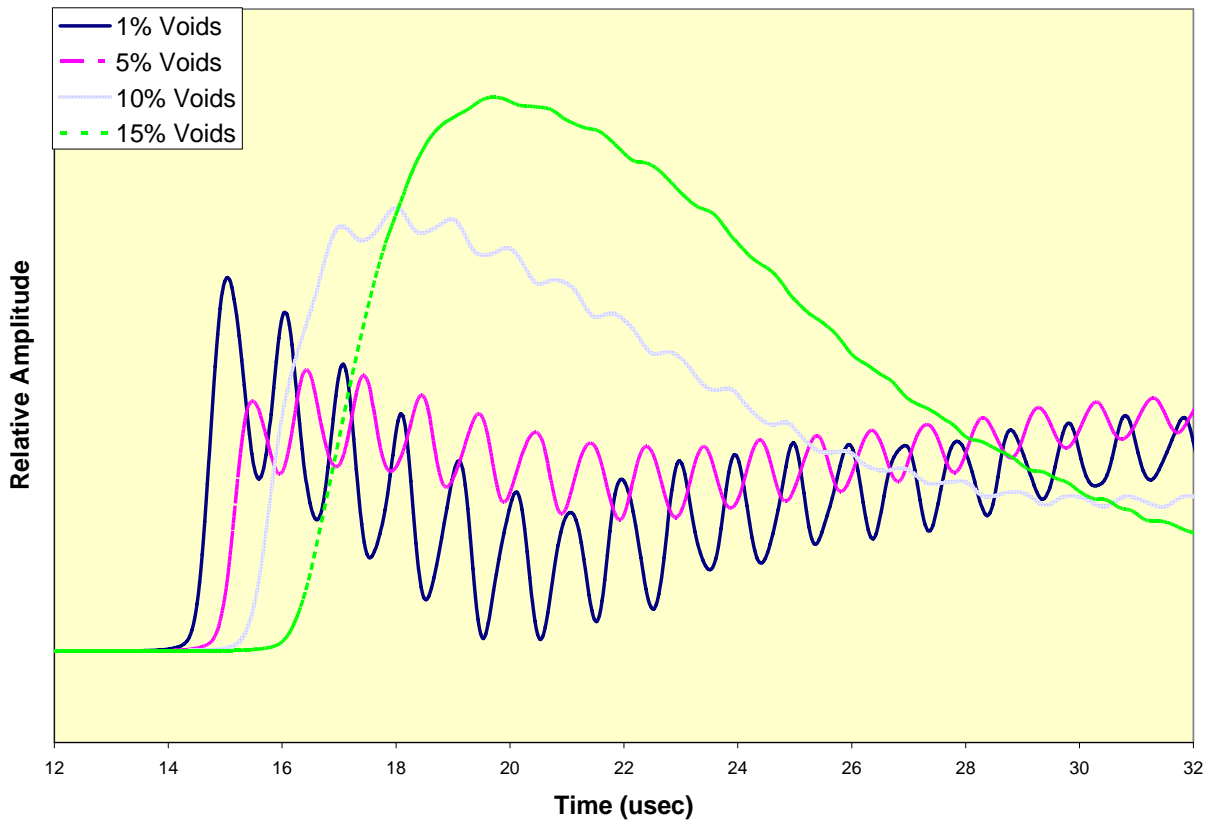
Figure 78. Horizontal propagation through assembly with 10% quartz.
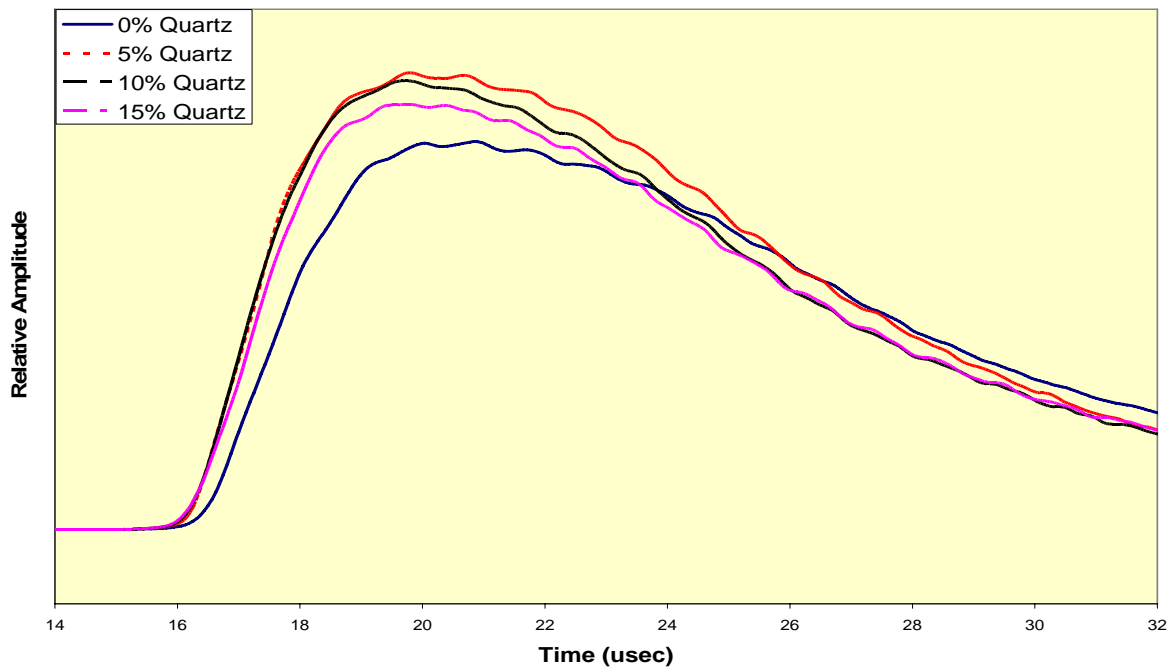
Figure 79. Horizontal propagation through cement with 15% voids. 100% of the steel cement interface was bonded and the wave was propagated from a transducer on the left side of the sample to a receiver on the right side of the sample
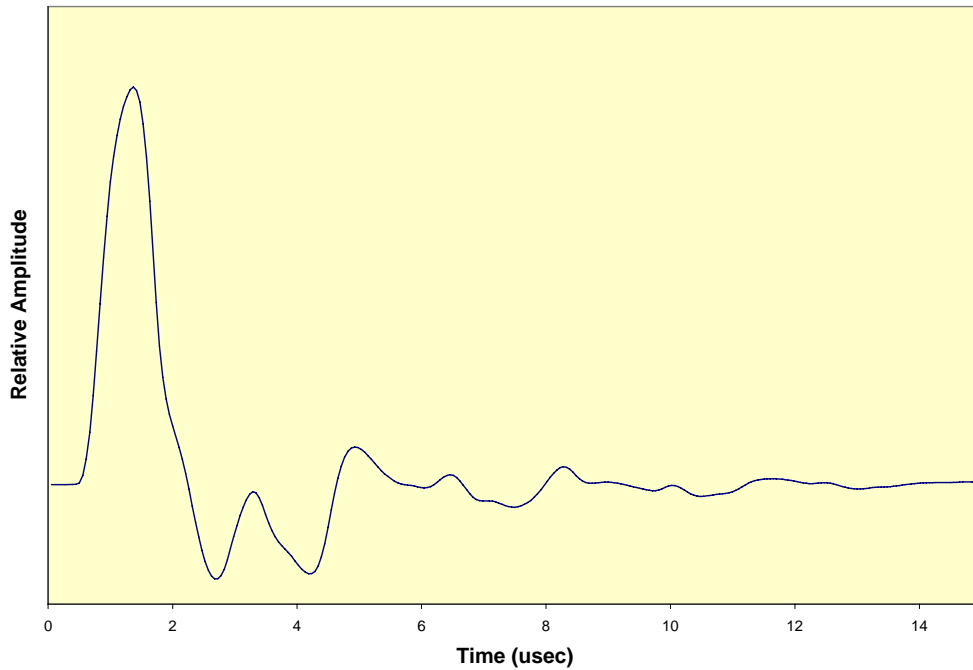
Figure 80. Horizontal p-wave in a sample with 5% quartz and 15% voids. Waveforms detected at a receiver near the steel-cement interface on the left side of the sample.

94
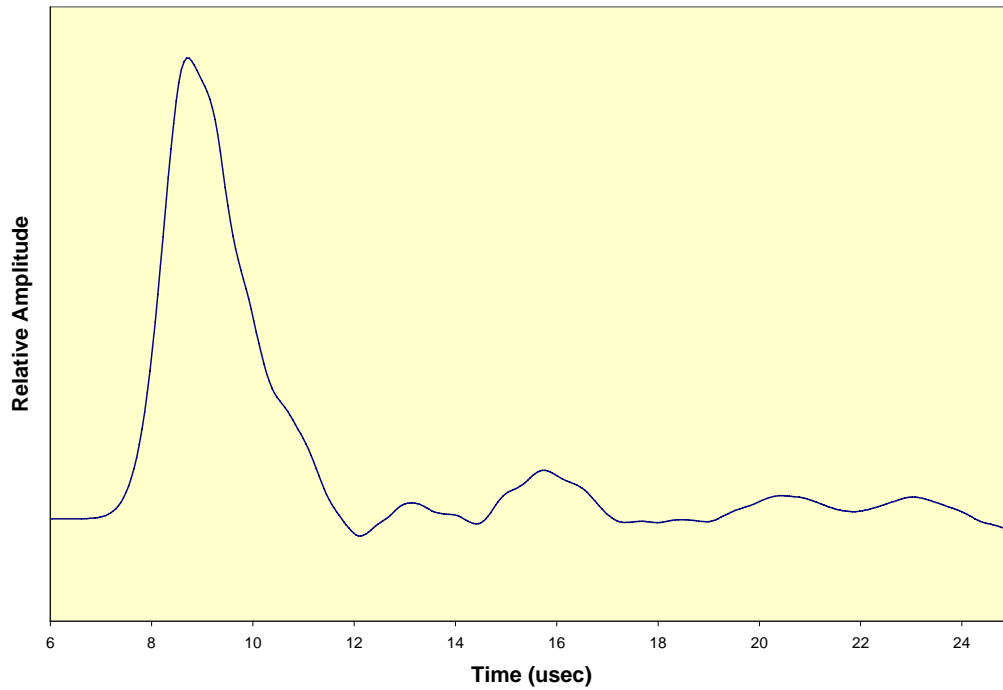
Figure 81. Horizontal wave in sample with 5% quartz and 15% voids. Waveforms detected midway through the cement.
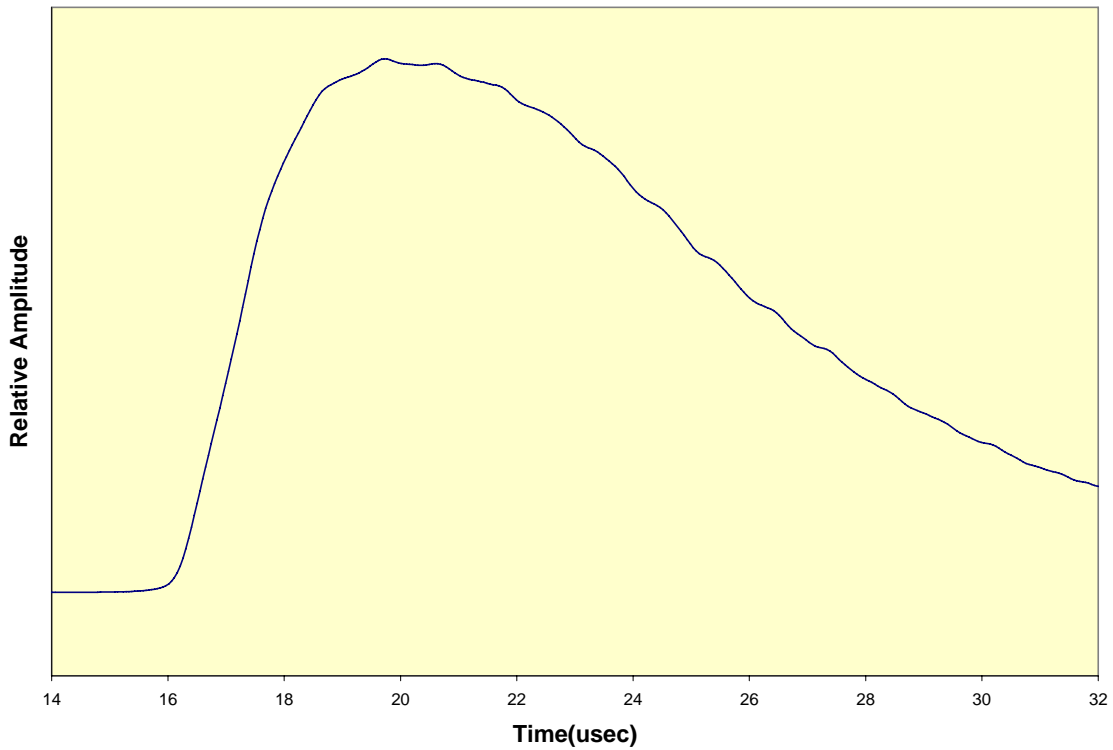
Figure 82. Horizontal wave input in sample with 5% quartz and 15% voids. Waveforms measured at steel receiver on right hand side of the sample.

95
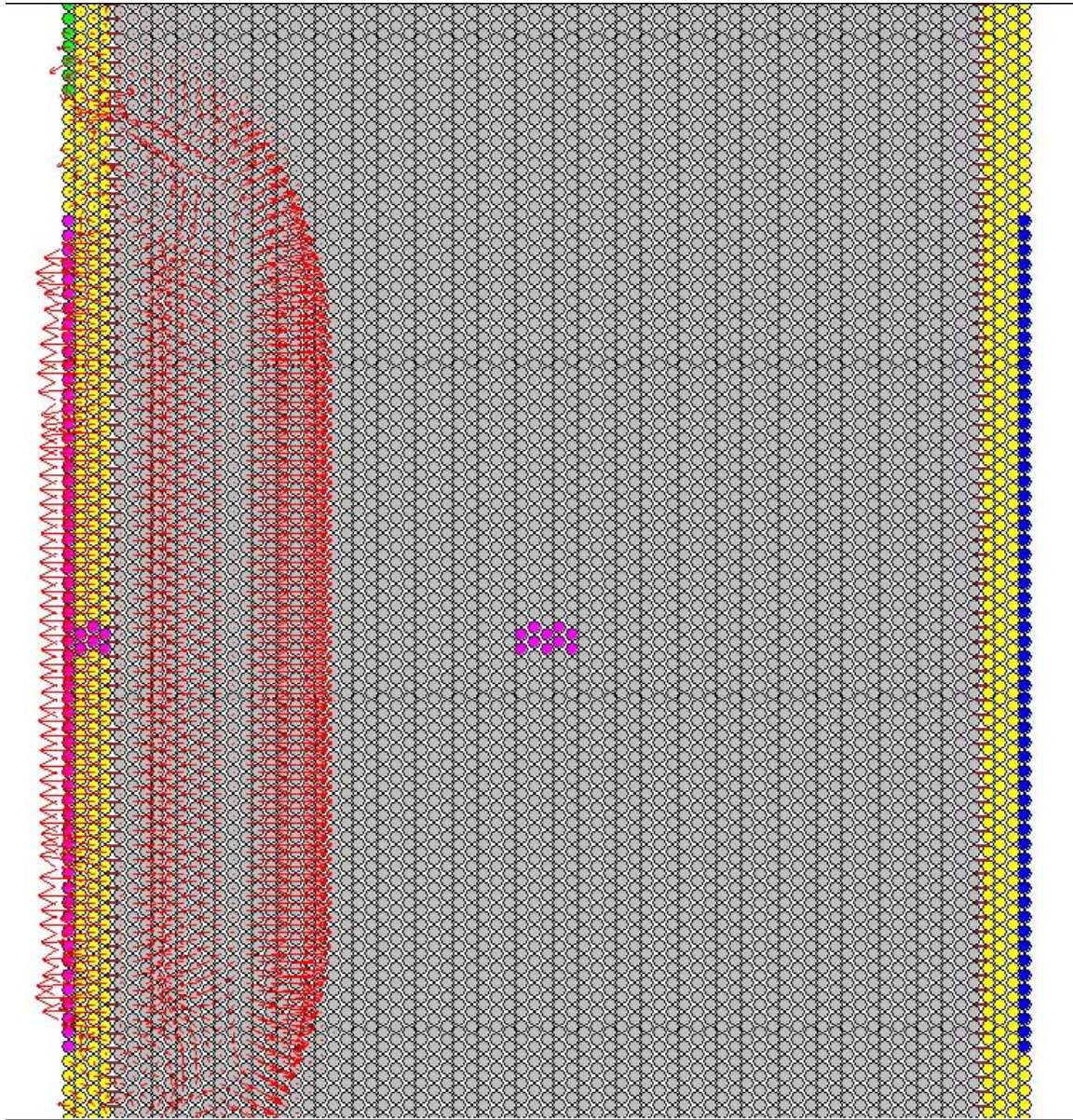
Figure 83. Waveforms in cement with no voids. Red arrows indicate particle velocities associated with propagating wave.
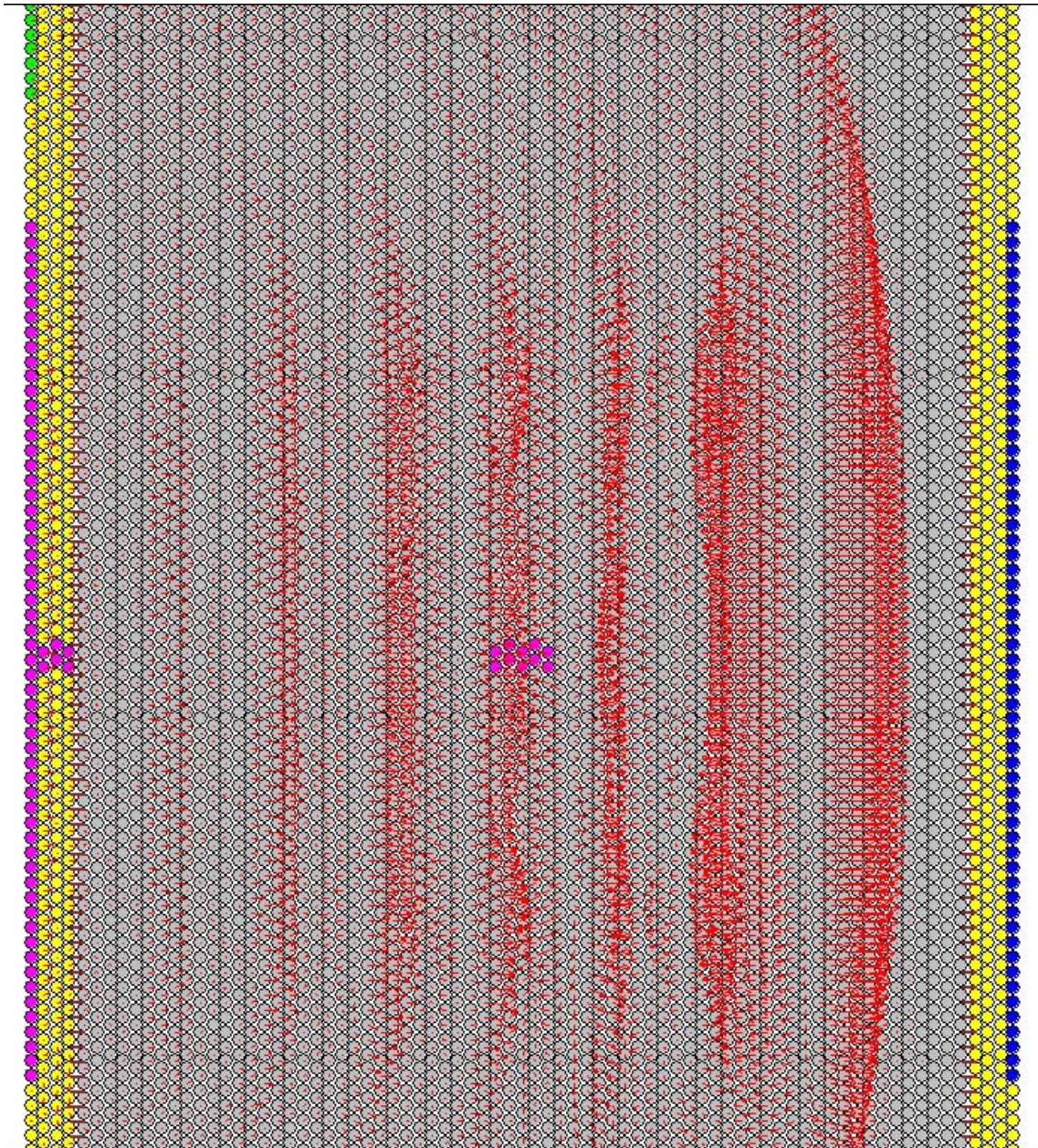
Figure 84. Waveforms in assembly with no voids, after propagation across cement.
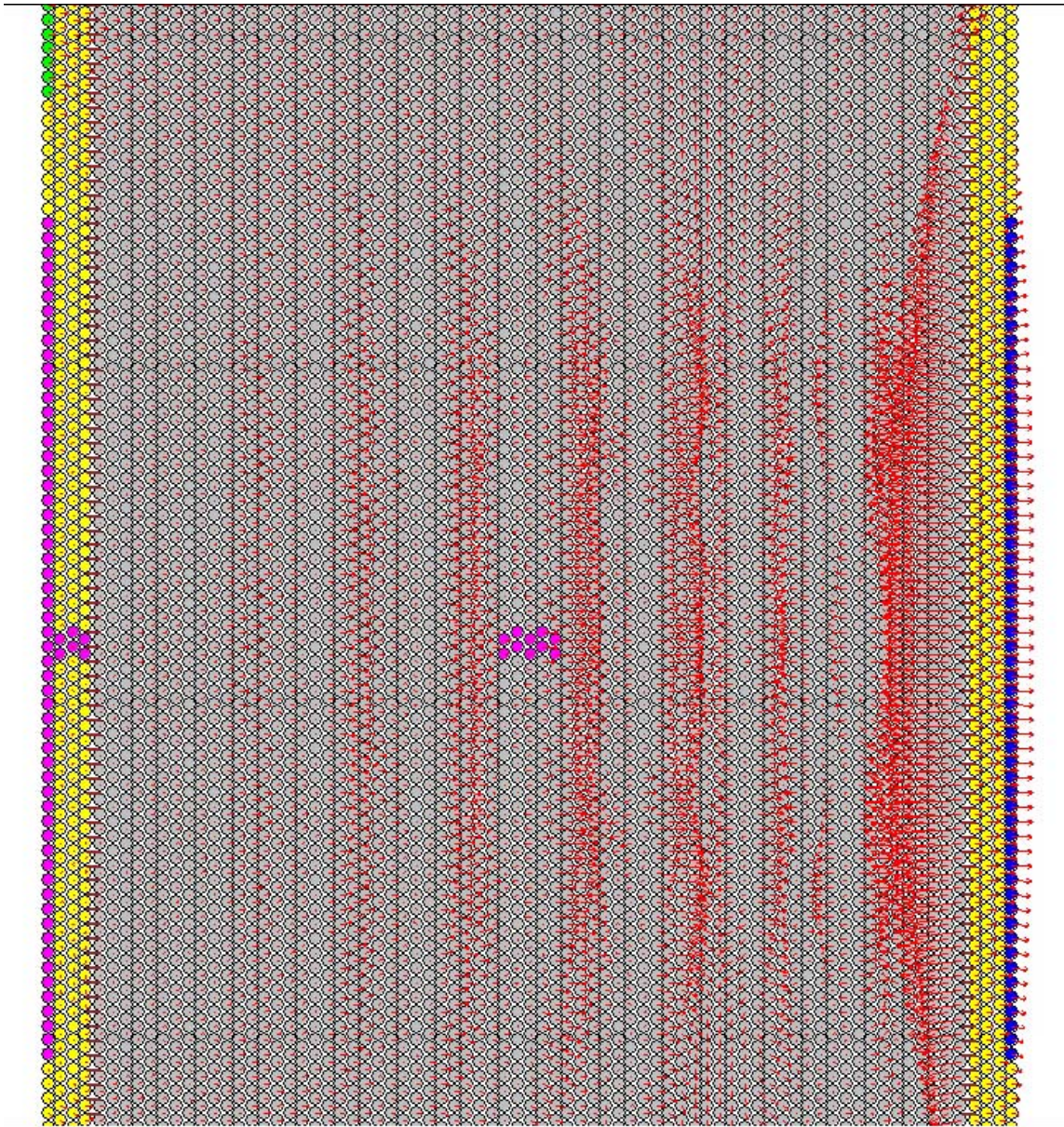
Figure 85. P-waveforms in sample with no voids (no scattering), after transit across the cement and reflecting from the right interface.
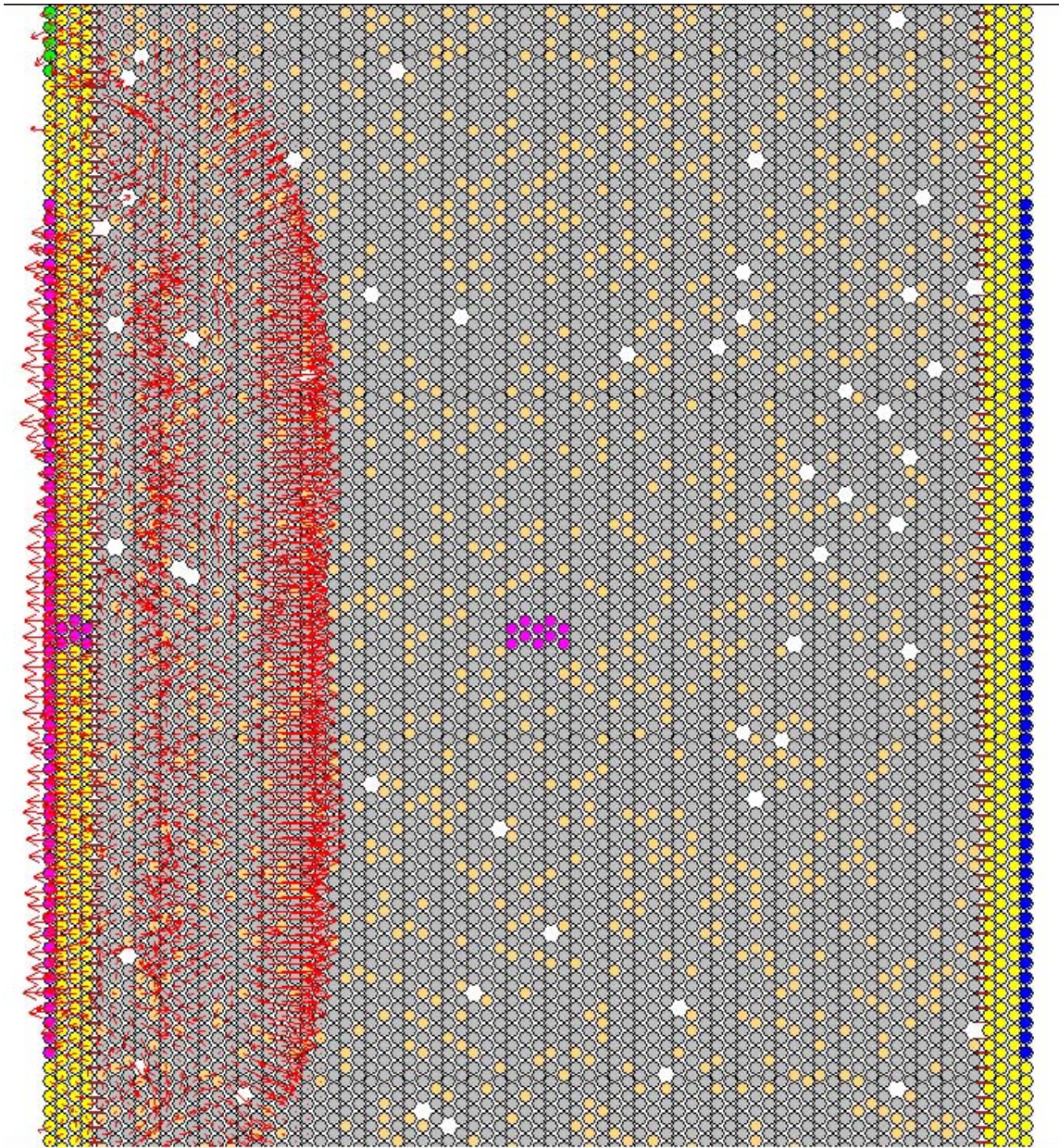
Figure 86. P-wave propagation in cement with 5% voids, after introducing the first wave-form cycle.
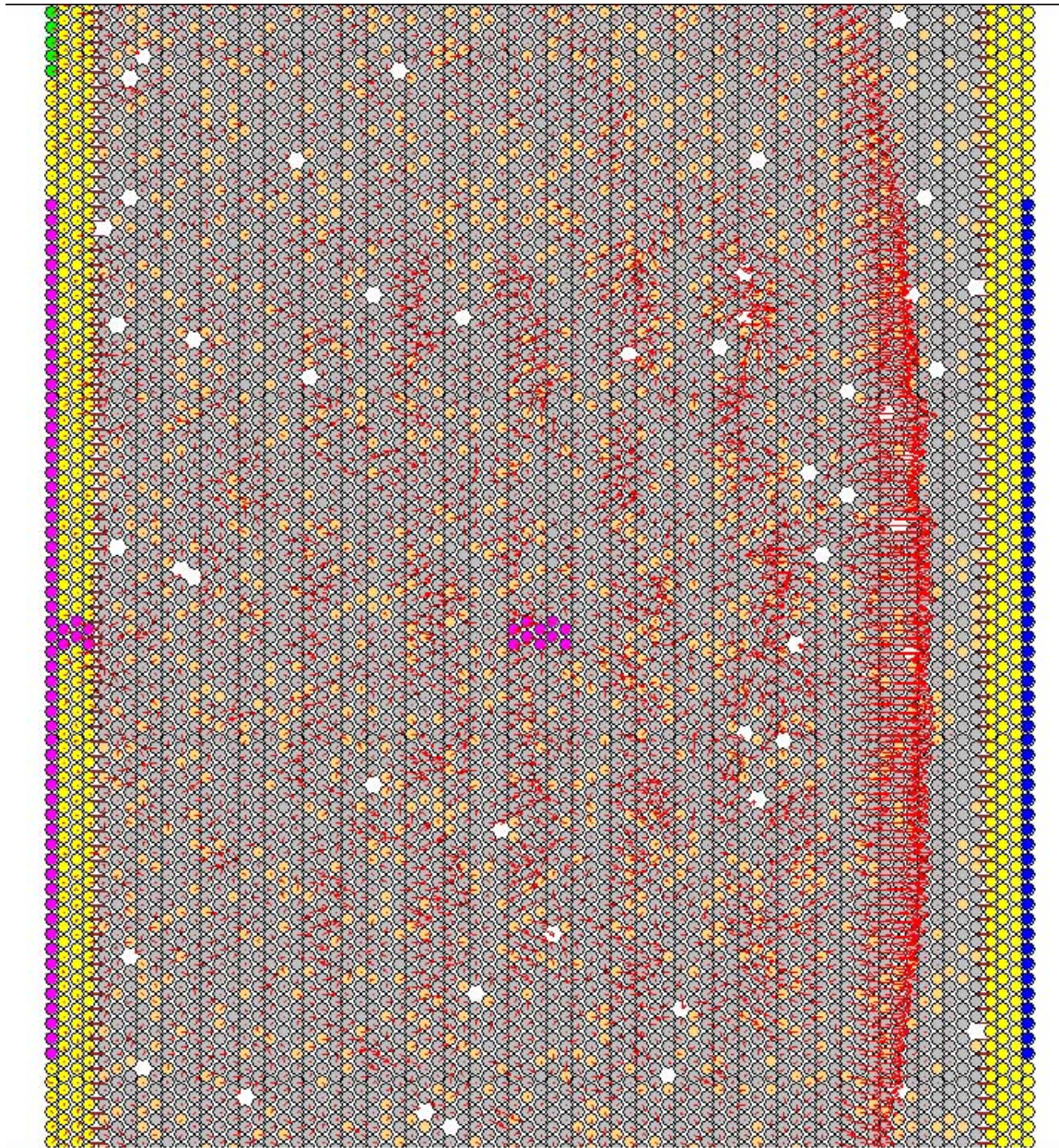
Figure 87. P-wave propagation in cement with 5% voids, after transit through the cement zone.
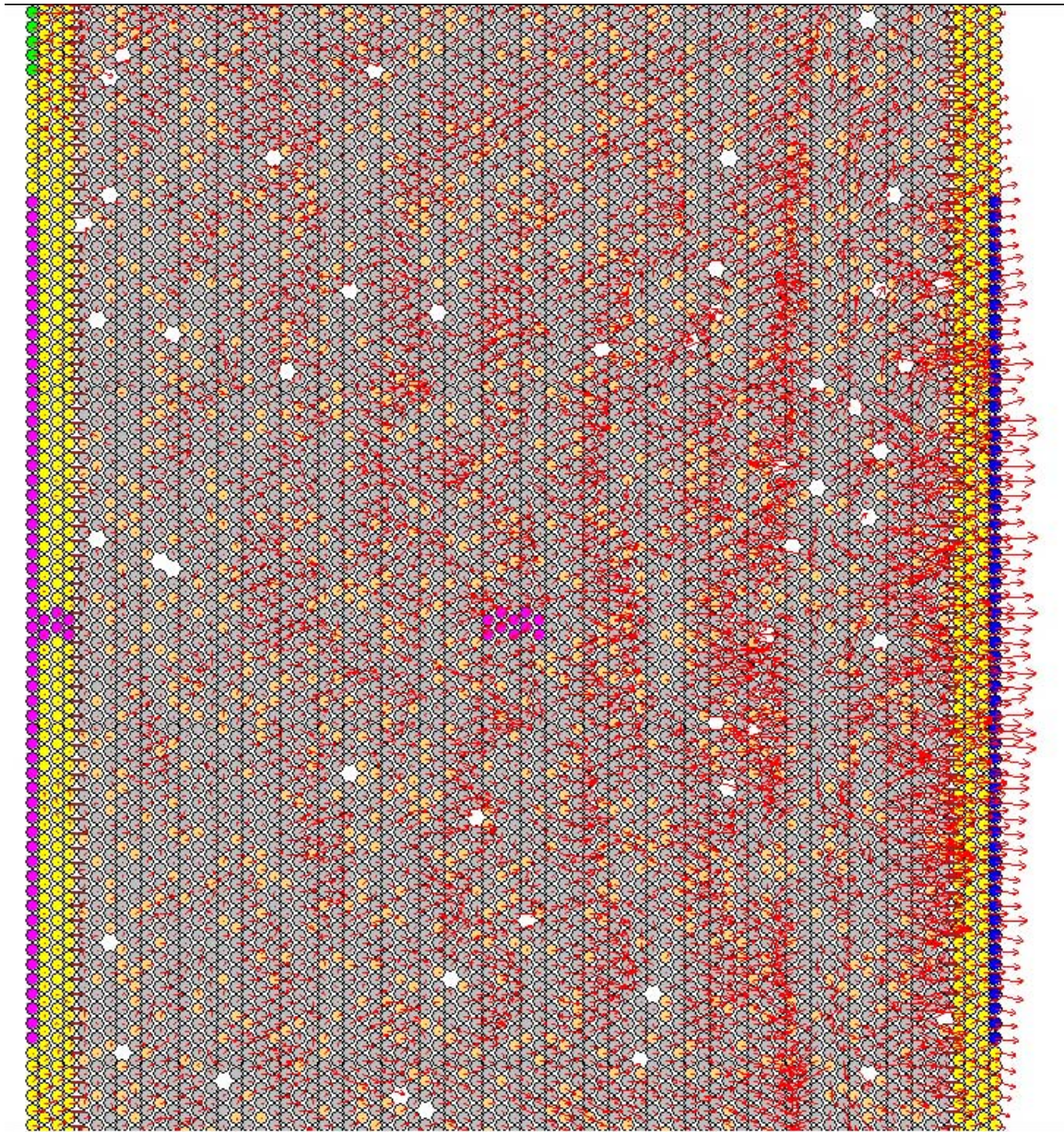
Figure 88. P-wave propagation in cement with 5% voids, after passage through the cement zone and reflection at the right side interface.
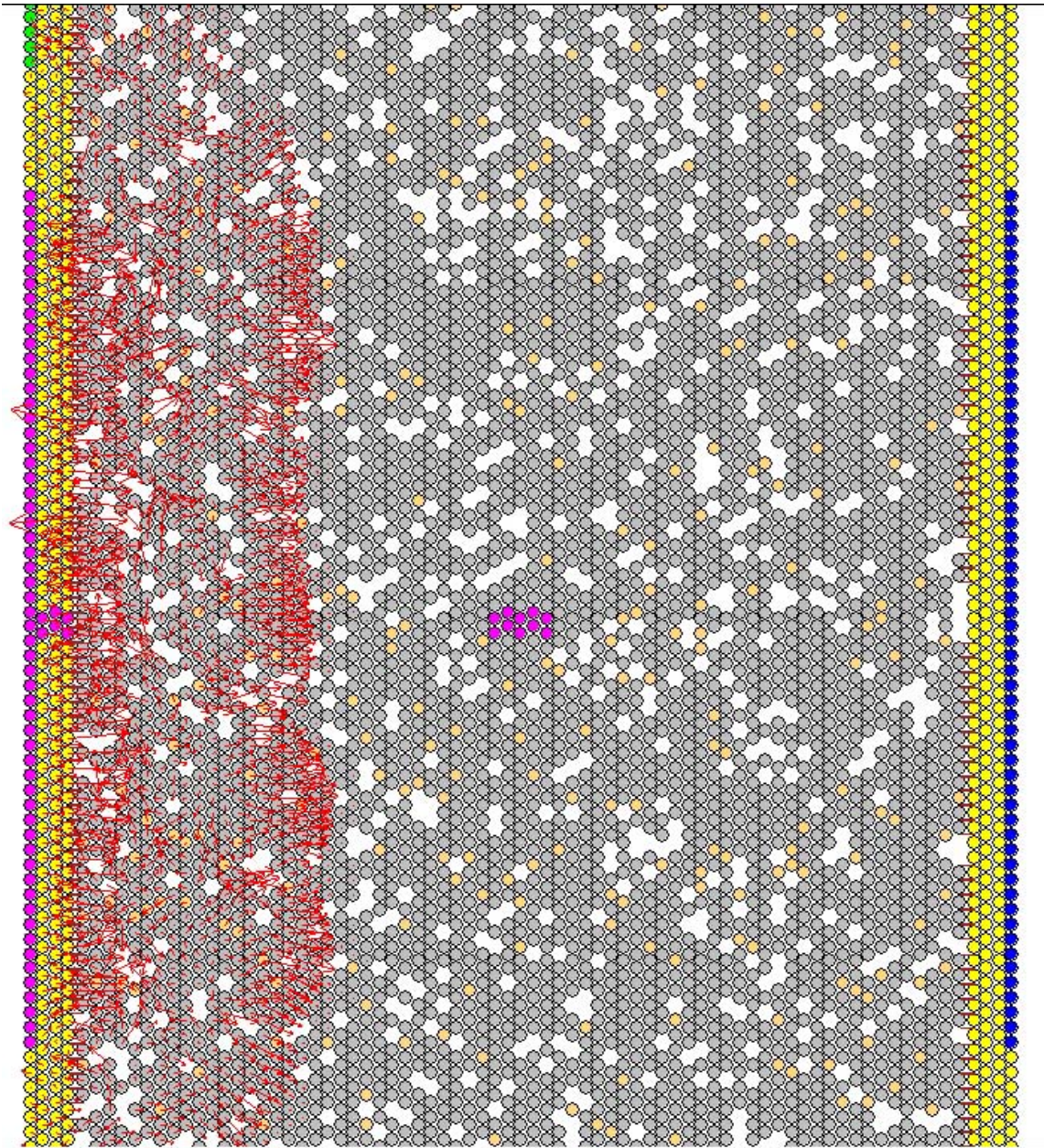
Figure 89. P-wave propagation in cement with 15% voids, after introduction of one cycle of the waveform.
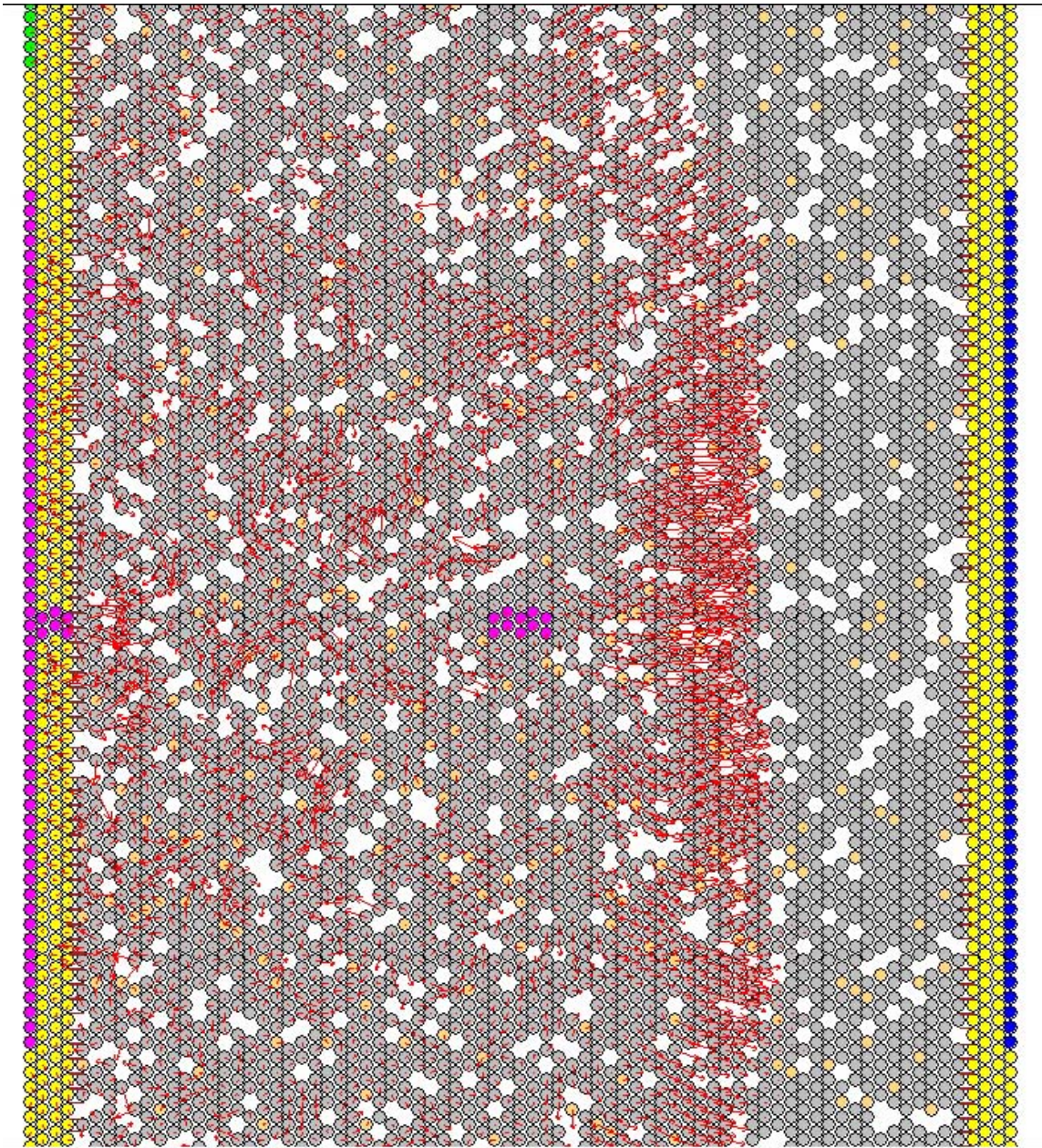
Figure 90. P-wave propagation in cement with 15% voids, after passage through most of the cement zone.
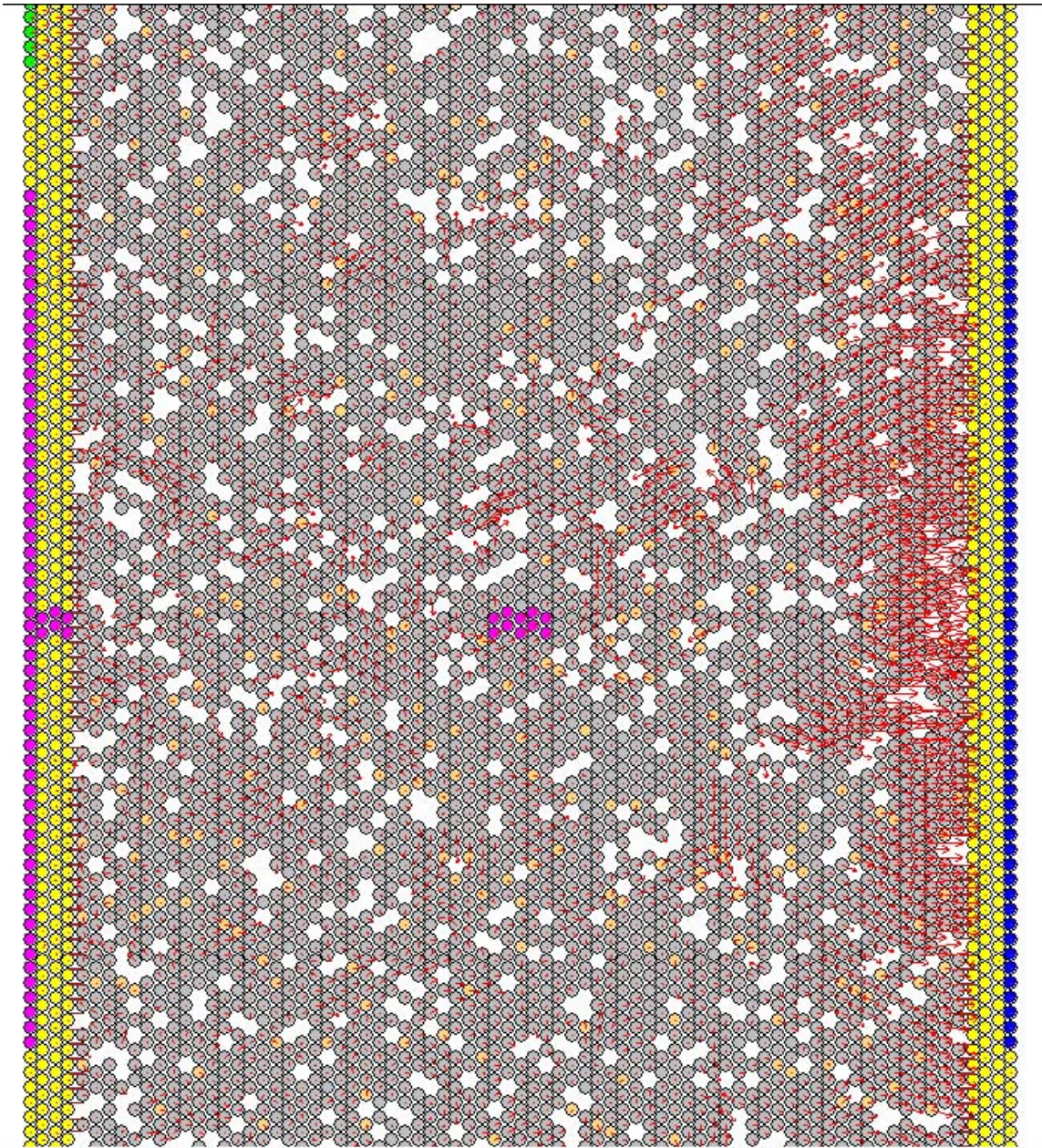
Figure 91. P-wave propagation in cement with 15% voids, after passing through the cement zone.
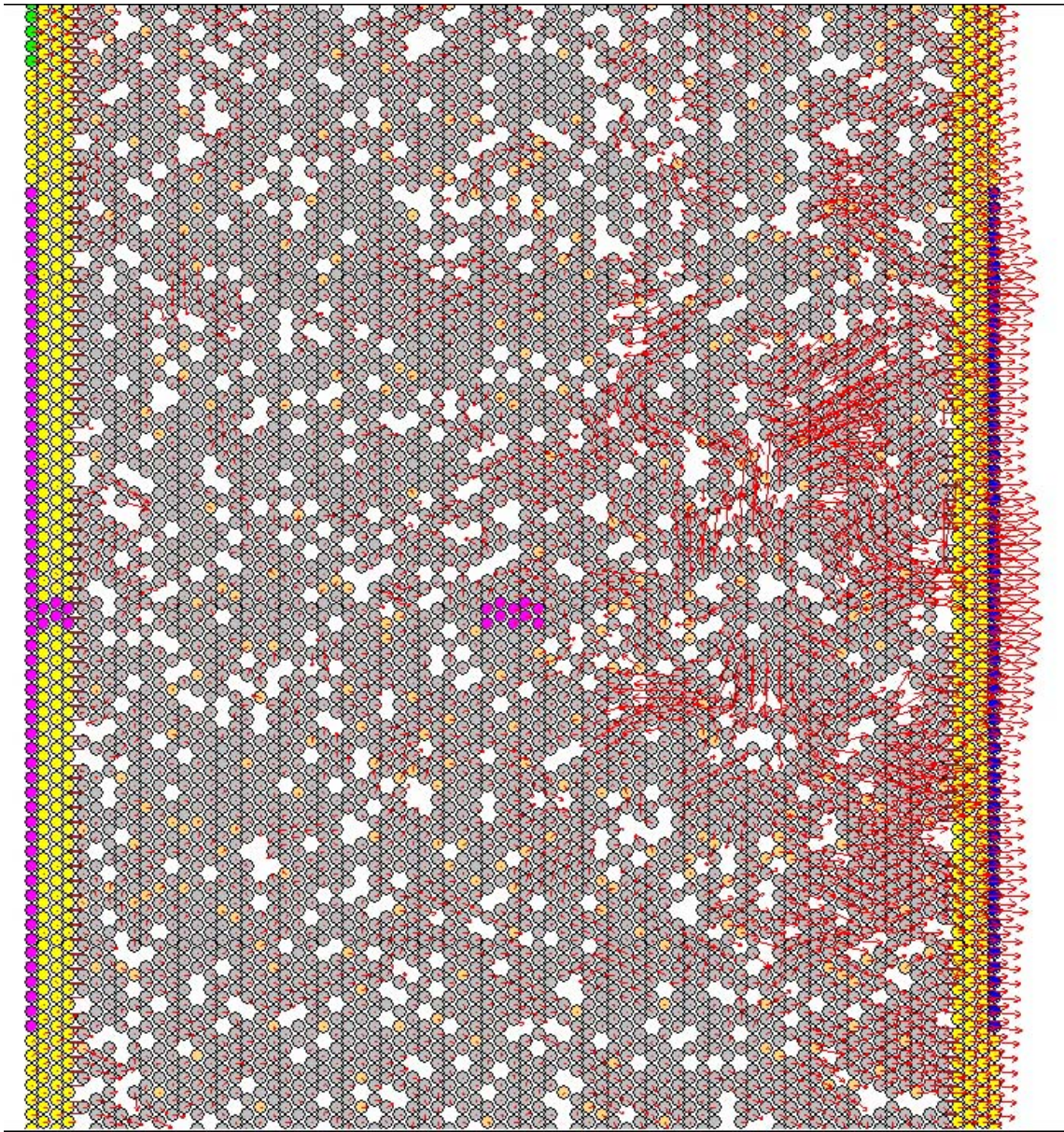
Figure 92. P-wave propagation in cement with 15% voids, after passage through the cement zone and reflection at the right side boundary.

Appendix C 2006 Reports

Storage Field Wellbore Flow Data Containing Water and Hydrates

Jeffrey Savidge
Colorado Engineering Experiment Station
54043 WCR 37
Nunn, CO 80648

No report received, no funds expended

Protocol Evaluation for Scale Prevention and Remediation in Gas Storage Reservoirs and Formations

Larry Chorn
Colorado School of Mines
1500 Illinois
Golden, CO 80401

Project terminated, no funds expended

Predicting and Mitigating Salt Precipitation

Final Report

Reporting Period Start Date:
June 1, 2006
Reporting Period End Date:
June 30, 2007

Principal Author:
William W. Weiss

DOE Award No.
DE-FC26-03NT41779
Subaward No.
3145-CC-DOE-1779

Report Issue Date
July20, 2007

Prime Awardee
The Pennsylvania State University
110 Technology Center Building
University Park, PA 16802

Subawardee
Correlations Company
P.O. Box 730
115 Court Street
Socorro, NM 87801

Table of Contents

List of Graphical Materials

Abstract

Storage operations often involve the production of brines along with stored gas or liquid products. As the produced brine encounters changing pressure and temperature in the wellbore, wellhead, and gathering system, salt can precipitate. The objectives of this study were to assess the effectiveness of current methods used to prevent and mitigate salt precipitate and to provide guidance on making choices. Physical laboratory experiments coupled with numerical modeling were the methods used to investigate sodium chloride or NaCl deposition problems reported by members of the Gas Storage Research Consortium.

A protocol was developed to conduct static laboratory experiments with pure solutions of NaCl that resulted in salt deposition. A numerical model based on thermodynamics was used to match the laboratory results and then used to model field conditions difficult to simulate in the laboratory. It was determined that two commercial salt inhibitors worked well with solutions of pure sodium chloride; however, the performance deteriorated in the presence of calcium and iron typically found in field brines. Compatibility of the two commercial inhibitors was tested with widely used scale and corrosion inhibitors. At use concentrations, the nitrilotriacetamide-based inhibitor was judged compatible with both the scale and corrosion inhibitors; the ferrocyanide-based inhibitor was not compatible.

It was determined that field brines in excess of 300,000 ppm total dissolved solids (TDS) usually result in NaCl scale problems. However, salt scale problems were surprisingly reported where the brine TDS was much lower. Evaporation during the fill cycle with dry gas explained this contradiction. Numerical simulation established that fill volumes on the order of 1 Bcf were sufficient to vaporize enough water from the wellbore, leaving water with 300,000 ppm TDS and the accompanying NaCl precipitate.

Executive Summary

The development of a laboratory protocol to precipitate sodium chloride or NaCl was the initial step in this project. A practical method was developed and used to conduct salt precipitation experiments in order to evaluate the effectiveness of two commercial salt inhibitors. One inhibitor was a ferrocyanide formulation and the other a nitrilotriacetamide compound. Both inhibitors prevented precipitation from pure supersaturated solutions of NaCl. In pure solutions, the efficiency of ferrocyanide was about five times greater than nitrilotriacetamide. However, performance deteriorated in the presence of calcium ions, iron content, and low pH. The ferrocyanide formulation was particularly sensitive to dissolved iron and low pH.

Thermodynamic software was used to numerically model the precipitation of salt under field conditions of temperature, pressure, and water chemistry that are difficult to match in the laboratory. The accuracy of the numerical model was confirmed by matching laboratory results. The modeling work led to an improved laboratory technique for producing supersaturated solutions based on weight rather than volume measurements and temperature conditions at the onset of boiling. Both the numerical model and laboratory tests demonstrated that small amounts of fresh dilution water prevent NaCl precipitation

Gas Storage Research Consortium members provided field water analyses from facilities with salt precipitation problems. The analyses along with the facility temperature and pressure conditions were used to numerically model salt precipitation. The model established that brines containing a high calcium content with total dissolved solids (TDS) exceeding 300,000 ppm result in salt precipitation under most operating conditions. Under the conditions studied, the numerical modeling demonstrated that cooling of the produced fluid had a much greater effect on salt deposition than pressure decrease.

A number of the field brines were less than 300,000 ppm TDS, and salt deposition could not be numerically modeled; yet, salt scale was observed in the field. The thermodynamic model was used to determine the volume of dry gas required to vaporize water sufficient to generate remaining brines greater than 300,000 ppm TDS under reservoir temperature and pressure conditions. Salt then precipitated. The modeling results demonstrate that reservoir brines in the range of 200,000 ppm TDS can be increased to 300,000 ppm with Bcf-type volumes of gas that are typically injected during the fill cycle. The reservoir brine analyses from one facility that reported salt deposition problems was about 30,000 ppm TDS, and it required Tcf-type volumes of dry gas to reach the 300,000 ppm threshold, clearly beyond fill cycle volumes. However, the answer to the salt scale in that particular facility lay in the 10 lb/gal calcium chloride or KCl workover fluids used to kill the well. An analyses of a bailed brine sample from such a well was found to be 200,000 ppm TDS.

Excess KCl was added to a saturated solution of NaCl (359,000 ppm) at 90°C and allowed to cool to room temperature to determine the usefulness of nitrilotriacetamide as a KCl salt inhibitor. KCl precipitate was observed. In an accompanying test, the nitrilotriacetamide inhibitor prevented all but a trace of precipitation.

While the field application of commercial salt inhibitors has been documented in the drilling and production arenas, consortium members reported little or no experience with either chemical. Members reported using fresh water to dissolve salt scale after its formation at a cost varying from $500 for a simple water truck application to $25,000 for a coiled tubing application.

Static adsorption tests were done with the two commercial salt inhibitors using core material from sandstone and dolomite reservoirs to determine suitability of the chemicals in squeeze applications. The ferrocyanide inhibitor adsorbed to both materials while the nitrilotriacetamide at high concentrations retained only on the sandstone. The nitrilotriacetamide was compatible with a frequently used commercial scale inhibitor as well as an often-used corrosion inhibitor. The scale inhibitor caused the ferrocyanide to decompose to Prussian Blue and was not compatible with the water-soluble corrosion inhibitor.

This project generated insight into the sensitivity of NaCl precipitation to fresh water dilution, effectiveness, and stability conditions of two inhibitors; adsorption characteristics of the two inhibitors on a sandstone and a dolomite; methods to improve inhibitor efficiency based on the addition of sequestrants; a method to automate the addition of chemicals/fresh water; and the need to understand the water chemistry of salt cavern development.

Introduction

Storage operations often involve the production of brines along with stored gas or liquid products. As the produced brine encounters changing pressure and temperature in the wellbore, wellhead, and gathering system, salt can precipitate. A number of products claim prevention or removal of salt precipitates. However, the effectiveness of these products varies from situation to situation for reasons not well understood. There is a need to determine how to choose methods that will be effective for particular sets of conditions.

The objectives of the study were to assess the effectiveness of current methods in order to prevent and mitigate salt precipitate and to provide guidance on making choices. Both laboratory experimental work and engineering analyses were applied to meet the objectives.

The scope of work included assessing the effectiveness of current methods of preventing and mitigating salt precipitate, analyzing successes and failures of current field applications to determine the reasons for salt deposition, and developing guidance that storage operators can use to choose methods that have the highest chance of success for their systems, including wellbores, wellheads, and gathering lines.

Assessing the effectiveness of current methods involved working with storage operators who have had both good and bad results in preventing or mitigating salt precipitation. Pertinent collected data included the products used and system variables: pressure, temperature, brine composition, application method, well completions, and system configuration.

Analysis involved evaluating the successes and failures and attempting to relate them to the products used as well as the system variables. The products are described in generic chemical classes rather than specific formulations. Laboratory experiments were conducted to physically model the water chemistry involved in salt precipitation. These experiments provided a baseline for evaluating commercially available products that inhibit salt formation. The laboratory work was also the basis for numerically modeling the thermodynamics of salt precipitation. An analytical method to predict NaCl precipitation based on the numerical model results was developed.

Experimental Results

Generating supersaturated solutions

First it was necessary to develop a method of producing supersaturated brines. The published methods of Earl and Nahm[1] and Kirk[2] were tried in this laboratory and either failed to produce any quantity of precipitate upon cooling or could not be used to introduce increasing levels of calcium ion and/or the different inhibitors. After experimentation a procedure was developed using two solutions that were mixed together just as they reached the boiling point. One solution contained NaCl saturated at ambient temperature and inhibitor, or an equivalent amount of distilled water; the other contained $CaCl_2$ or $CaCl_2$ with $MgCl_2$ and KCl. For supersaturated NaCl only solutions, it was necessary to add solid NaCl at the boiling point. In the first series of experiments with nitrilotriacetamide and ferrocyanide, this procedure had not yet been developed, and these experiments were done with only one solution to which solid NaCl was added at the boiling point. The second step was deciding on an analytical method to quantify the results. A chloride titration with $AgNO_3$ on the final solutions after measuring solution volumes was selected. A more precise method was filtering, drying, and weighing the

resulting precipitates, but in many instances this was not possible because the amount of precipitate was very small or extremely fine.

Chloride titration

The determination of Cl by titration and subsequent calculation of the amount of NaCl precipitate sometimes predicted solid NaCl even when no precipitate was visible in the flasks. The reason for this is probably experimental error in that large dilutions must be made to titrate Cl, and it was difficult to accurately measure final solution volumes. To determine the amount of error, a series of six NaCl-saturated samples were titrated for chloride. The results are presented in Table 1. The range of soluble NaCl is large enough when subtracted from the initial NaCl to account for the observed differences. For the purposes of these experiments, this amount of error was considered acceptable.

Table 1. Chloride titration statistics		
Soluble Cl (g)	NaCl (g soluble)	NaCl (g solid)
14.30	23.58	3.42
13.53	22.31	4.69
14.81	24.42.	2.58
14.40	23.75	3.25
14.82	24.44	2.56
14.45	23.83	3.17
Average = 14.39	**23.72**	**3.28**
Ave Dev = 0.47	**0.78**	**0.52**

Initial solutions contained 27 g NaCl and 73 ml H_2O.

Published studies by Ralston et al.[3] and Kleinitz et al.[4] have shown that the precipitate from saturated brines is NaCl, even when large amounts of other ions are present. To confirm this in our laboratory, a portion of scale obtained from a Six Lakes gas storage well was analyzed (Appendix I). The scale was determined to contain 97.50% NaCl, 1.09% insoluble residue, and 0.7% bound water (total=99.29%). Thus, to determine the amount of precipitate when laboratory solutions contained cations other than Na, the precipitate was assumed to be only NaCl. Knowing the amount of Cl contributed by $CaCl_2$ and KCl to the solution, this amount was subtracted from the Cl determined by titration and the amount of soluble NaCl calculated from the remaining chloride. The amount of NaCl precipitate was determined by subtracting the soluble NaCl from the amount of NaCl initially added.

Numerical modeling

The laboratory procedure was used to generate NaCl deposition from saturated solutions with increasing Ca concentrations. The precipitate resulting from cooling the supersaturated solutions to room temperature and atmospheric pressure was weighed and recorded for numerical modeling. The chemistry of the laboratory procedure was reconciled using software that ensures that the modeled samples are electrically neutral, see Appendix I, prior to simulating NaCl precipitation under test conditions. The model results are compared to the physical experiments in Fig. 1.
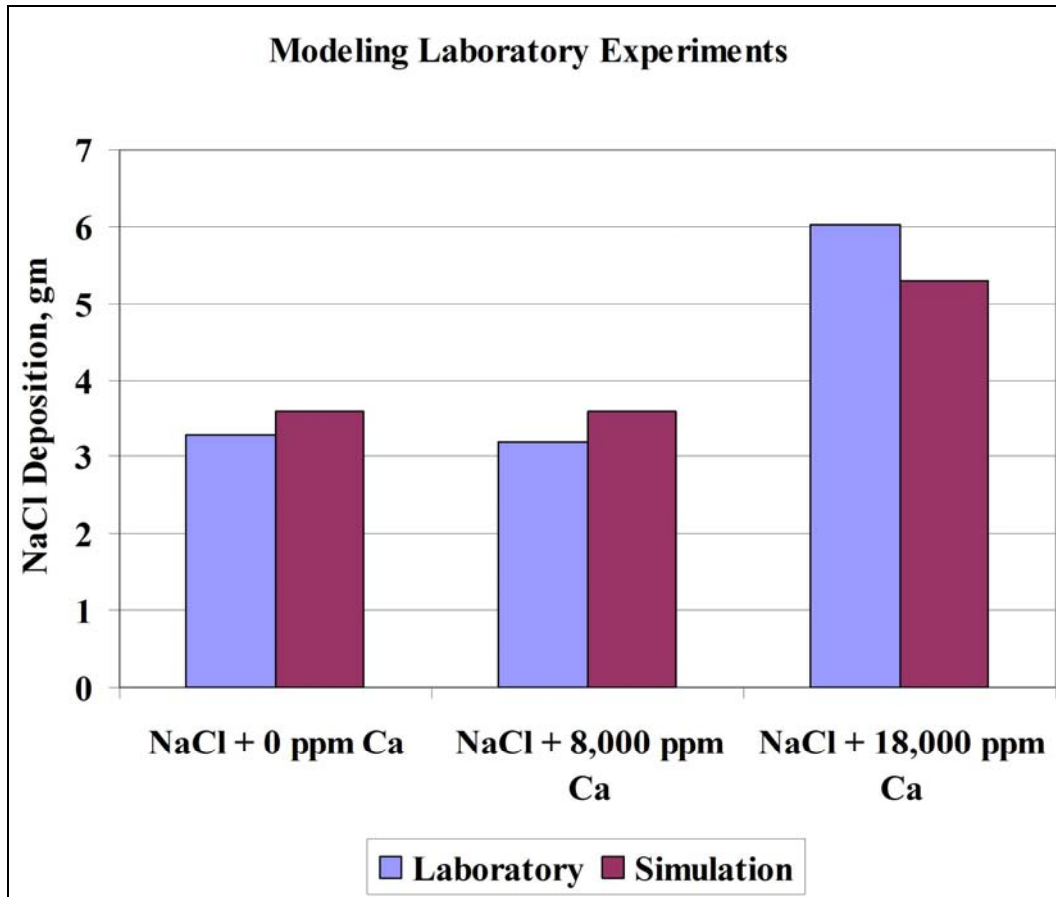
Figure 1. Physical experiments vs. numerical model.

As shown in Fig. 2, the model was used to simulate the effect of temperature and pressure on NaCl precipitation. Notice that 5-fold increase in temperature results in a decrease to 0.67 gm from 1.41 gm at 32°F of precipitate in the 1-liter system; whereas a 147-fold increase in pressure reduces the precipitate to 0.12 gm. Temperature is a key variable in the mechanism of salt deposition.
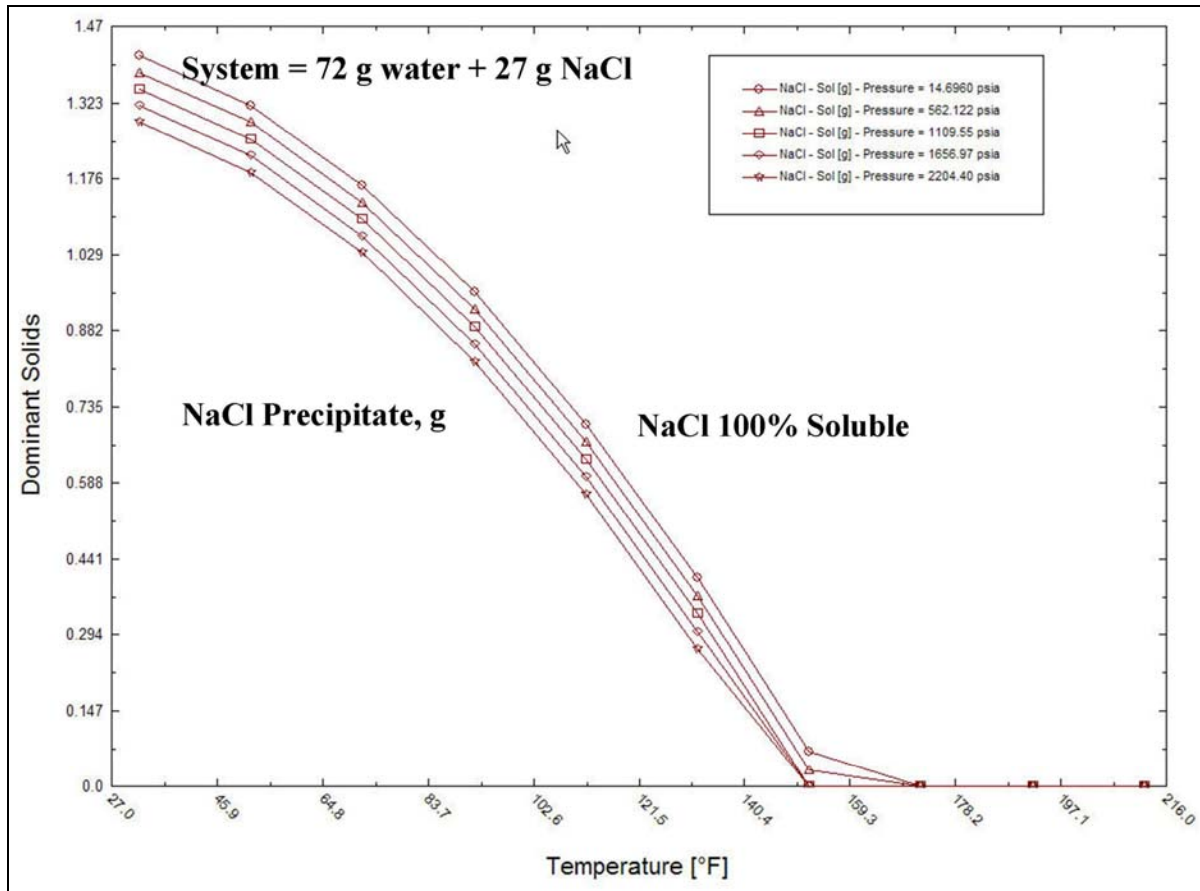
Figure 2. Effect of temperature and pressure on NaCl precipitation.

Nitrilotriacetamide and ferrocyanide as inhibitors of salt precipitation in the absence and presence of calcium

Nitrilotriacetamide and salts of ferrocyanide have been employed in the oilfield as drilling-fluid additives to prevent salt precipitation during oil recovery operations. But no studies have been published as to the particulars of using these inhibitors in gas recovery operations where brines are produced with varying degrees of hardness. These inhibitor studies were designed to this end. Initially we used the inhibitors in their pure chemical form rather than as the commercially available products. Later the commercial products were evaluated and compared.

Sodium chloride brine that contained no inhibitor and no calcium produced rather large cubic-shaped crystals that tended to clump (Fig. 3). When low levels of the ferrocyanide inhibitor were added, the resulting precipitate was fine grained and amorphous with less of a tendency to stick together. At higher levels of inhibitor, there was no precipitate. Similar results were found with nitrilotriacetamide.

11

Figure 3. Three views of NaCl brine solutions; left to right, brine solution with no inhibitor, brine solution with 0.01% of Fe(CN)$_6$ inhibitor, and brine solution with 0.05% Fe(CN)$_6$ inhibitor.

Details and experimental data for the calcium hardness studies are included in Appendices II (nitrilotriacetamide) and III (ferrocyanide). Ferrocyanide proved to be about 5 times more effective in preventing salt deposition than nitrilotriacetamide regardless of the presence of calcium hardness, although both inhibitors declined in effectiveness as the amount of calcium increased (Figs. 4 and 5). Ferrocyanide is also a less expensive chemical. However, it decomposes in the presence of Fe or at low pH (addition of scale inhibitors can reduce pH). This greatly limits its applicability.
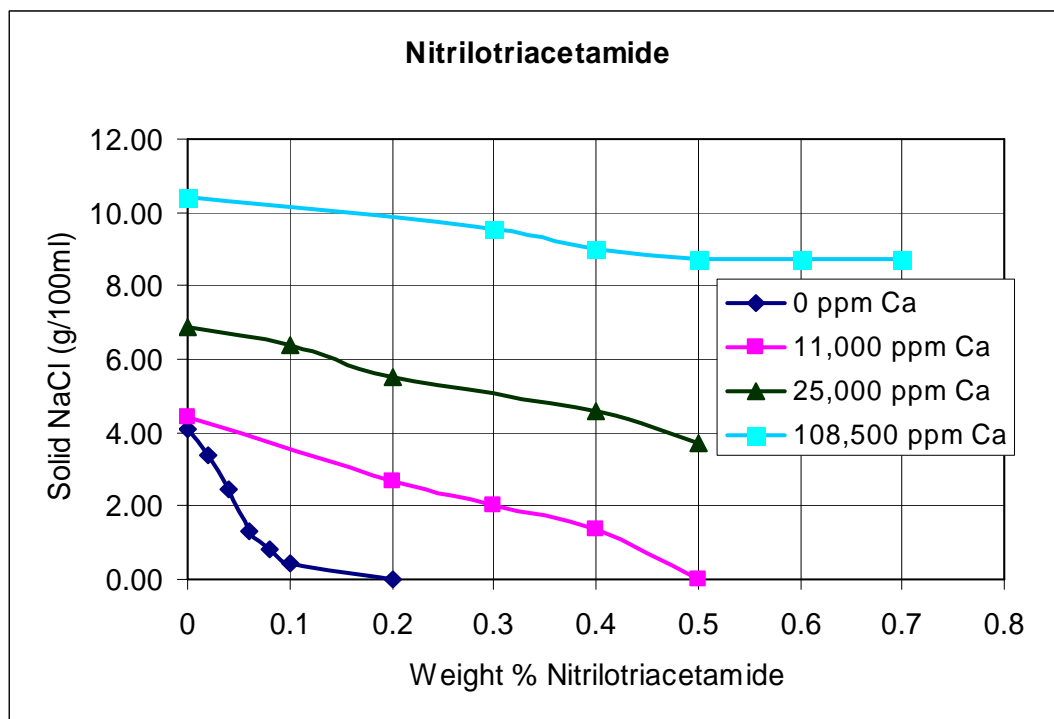
Figure 4. Effectiveness of nitrilotriacetamide in preventing salt deposition in the presence of calcium hardness.
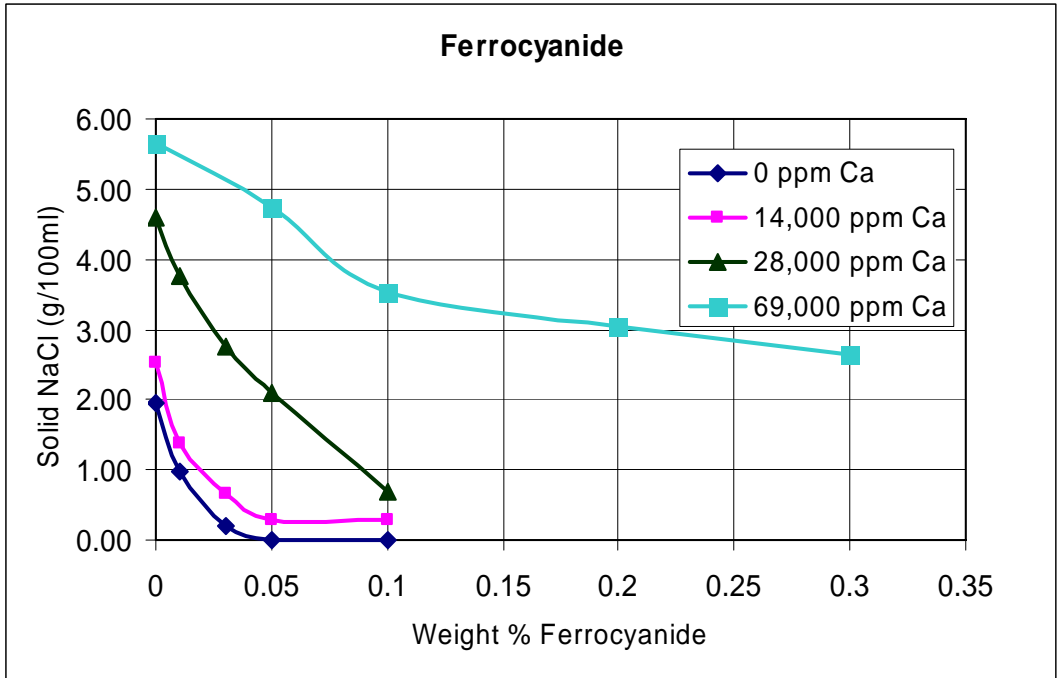
Figure 5. Effectiveness of ferrocyanide in preventing salt deposition in the presence of calcium hardness.

The change in structure of the NaCl precipitate when inhibitor is added as noted in Fig. 3 is also apparent when calcium hardness is present (Fig. 6). The precipitates formed from saturated NaCl brine were large cubic crystals, which tended to clump—eventually forming blocks. When Ca was present (32,000 ppm), the crystals formed were smaller with less of a tendency to clump. When an inhibitor (7,400 ppm nitrilotriacetamide) was present, the crystals were even smaller and had even less of a tendency to clump. Thus, if a precipitate was formed in waters with a high hardness, total salt blockage might not occur. This precipitate might also be easy to remove.

Figure 6. Left to right: precipitate from supersaturated NaCl solution, precipitate from supersaturated NaCl solution with Ca hardness, and precipitate from supersaturated NaCl solution with Ca hardness and salt inhibitor.

Calcium-sequestering agent experiments

Salt deposition inhibitors are thought to work by surface interference with crystal formation and can be effective when present in very small amounts compared to the amount of salt present in the brine. As calcium is added to NaCl solutions, however, it requires more and more of the inhibitor to prevent salt deposition. At very high levels of Ca (73,484 ppm), neither nitrilotriacetamide nor potassium ferrocyanide is effective as a salt inhibitor. Calcium in some manner prevents the inhibitor from interfering with the formation of salt crystals, although the shape and size of the crystals change from large cubic to very small noncubic.

This study investigated whether the addition of a calcium-sequestering agent would improve the inhibitor's ability to prevent salt deposition in high calcium chloride-sodium chloride brine. The procedure and details are given in Appendix IV. Ferrocyanide was chosen for the study since it had been shown in earlier work to be the better inhibitor. However, it did not prevent salt deposition at a level of 300 ppm in a 20,000 ppm Ca; hence, these levels of inhibitor and calcium were chosen and used in all tests.

The following reagents were examined:

1. EDTA. Resulted in more precipitate than the control.
2. Citric acid. Solution turned blue, and a dark blue precipitate formed on cooling. Solution was very acidic.
3. Sodium citrate. A large amount of precipitate formed.
4. Potassium phosphates (monobasic and dibasic). An amorphous precipitate was formed upon heating, and the solutions also turned blue, although not as intense a blue as with the sodium citrate.
5. Sodium hexametaphosphate. White precipitate formed when the reagent was added to test solution.
6. Commercial scale inhibitor (AS-216**;** a soluble organo-phosphate). Solution turned dark blue upon heating before NaCl was added. The commercial product CS-71 gave similar results.
7. Sodium borate. Reagent was not very soluble, and precipitate formed upon cooling.
8. Trisodium nitrilotriacetic acid. A large amount of white precipitate was formed when the reagent was added to the test solution.
9. Tripotassium nitrilotriacetic acid. A bluish-white precipitate formed when NaCl was added to hot solution.
10. Ascorbic acid. A fine bluish precipitate formed upon cooling and remained suspended for considerable time. The ascorbic acid did prevent the precipitation of some NaCl, the control sample contained 2.92 g solid NaCl, while the solution with ascorbic acid contained only 0.84 g, indicating that about 66% of the Ca was sequestered.
11. Glycine (aminoacetic acid). Some sequestering was apparent. The control contained 2.6 g of solid NaCl, while the sample containing glycine contained only 1.95 g of solid NaCl.

Many of the above listed compounds (citric acid, potassium phosphates, ascorbic acid, scale inhibitors, and tripotassium nitrilotriacetic acid) produced very acidic solutions, causing the ferrocyanide to decompose to Prussian Blue. The compounds might be useful if the pH was adjusted to neutral before combining with the NaCl brine, or they might be effective when

nitrilotriacetamide is used as an inhibitor. In addition, they might have to be added in higher concentration. Of the compounds tested, glycine appeared the most promising.

Because the ferrocyanide is unstable under certain conditions (low pH and presence of Fe^{+3} ions), it is not the best salt inhibitor for field operations where in many cases iron would be present. An inhibitor that contains nitrilotriacetamide would be a better choice.

Comparison of Alpha 1655 and JACAM salt inhibitors

Previous testing established that ferrocyanide was a more effective inhibitor than nitrilotriacetamide.   This series of tests compared the effectiveness of two commercial preparations containing these inhibitors: Alpha 1655 (nitrilotriacetamide) and JACAM (sodium ferrocyanide). Each commercial inhibitor was tested with increasing calcium concentrations for its ability to prevent salt deposition from sodium chloride-saturated solutions. Four sets of tests were run, and the details are listed in Appendix V.

As the calcium concentration was increased, larger concentrations of salt inhibitor were required to prevent precipitation until at a calcium level of 87,566 ppm, even a 10% weight concentration failed to prevent salt precipitation. However, the precipitates that did form were very fine and tended to stay suspended for long periods of time.

Fig. 7 compares graphically the amounts of the two commercial forms of the inhibitors needed to prevent salt deposition as the amount of calcium was increased. Previously when ferrocyanide was compared with nitrilotriacetamide, the ferrocyanide was more effective. When the commercial preparations were compared, the one containing the nitrilotriacetamide, Alpha 1655, was more effective. This is perhaps due to the Alpha 1655 containing more of the active ingredient or less of other additives that might interfere. At the highest level of calcium, 88 g/kg, neither of the inhibitors, at concentrations of 10.6 weight %, prevented salt from precipitating so the columns are shown extending off scale. However, even at this level of calcium, the Alpha 1655 inhibitor produced less salt deposition. If the Alpha 1655 inhibitor were introduced with low TDS fresh water at levels of 10% inhibitor and 5% fresh water in relation to the amount of water being produced, complete inhibition of salt precipitation could probably be attained.
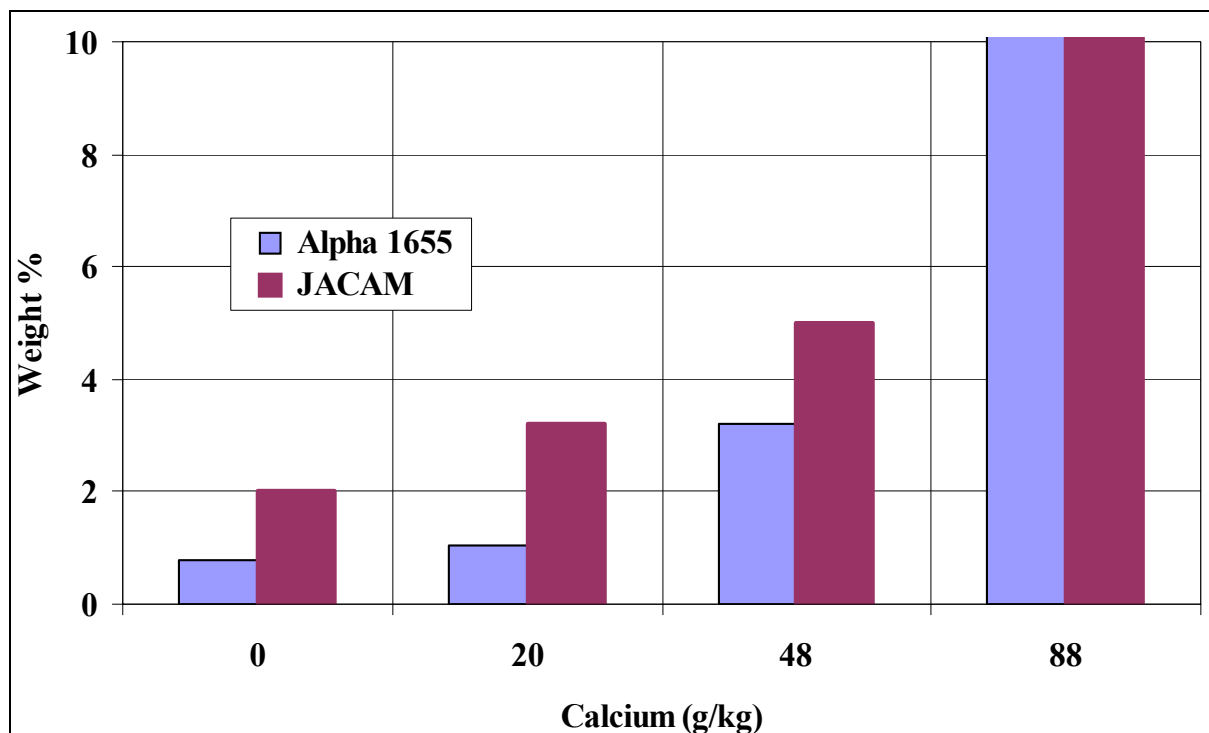
Figure 7. Amount of inhibitor needed to prevent NaCl precipitation in the presence of calcium.

Previous studies of calcium-complexing agents during this project were done using potassium ferrocyanide as the salt deposition inhibitor. Ferrocyanide was chosen because it was more effective than nitrilotriacetamide in pure NaCl solutions. These experiments were not successful. In some cases this was because low pH caused the ferrocyanide to breakdown to Prussian Blue, and in other cases the high Ca concentration caused the added chemical to form an insoluble calcium compound. In their commercial forms, as demonstrated in this experiment, the nitrilotriacetamide containing Alpha 1655 is more effective on a weight percent basis. Because nitrilotriacetamide is not subject to the same decomposition problems as ferrocyanide, calcium-complexing agent experiments should be repeated with the Alpha 1655 inhibitor.

Determination of nitrilotriacetamide in Alpha 1655

The active ingredient in Alpha 1655, nitrilotriacetamide, can be determined by the Kjeldahl nitrogen method without the usual digestion procedure because the three amide nitrogens can be removed and converted to ammonia by steam distillation. The ammonia is then determined by an ammonia-specific electrode. This method is very sensitive, and the amount of ammonia generated from Alpha 1655 is high, so the samples need to be diluted by 1/10 or 1/100. The complete procedure is given in Appendix VI.

Pure nitrilotriacetamide, formula weight=188.14 g/mole, contains three amide nitrogen groups or 22% N. Analysis of Alpha 1655 by the Kjeldahl method yielded a value of 8.18% amide nitrogen. By calculation the Alpha 1655 then contains 36.9% nitrilotriacetamide.

16

Determination of ferrocyanide in JACAM

Ferrocyanide can be determined by converting it to dark blue colored Prussian Blue by the addition of acidic Fe^{+3} and measuring the intensity of the color spectrophotometrically at 700 nm. The intensity of the color is directly proportional to concentration. Complete details of the procedure are given in Appendix VII. Using this method JACAM was found to contain 2% ferrocyanide.

Salt precipitation, brine concentration, and temperature

Solubility of NaCl at three different temperatures and three different concentrations was determined experimentally in the laboratory. Flasks were all pre-weighed. All solutions contained the same amount of NaCl (27 g), and at each temperature the water volume was varied. The control sample contained 73.0 ml, the sample with a 5% increase in fresh water contained 76.7 ml, and the sample with a 9.5% increase in water contained 80 ml of water. All samples were heated to boiling, allowed to cool to the stated temperatures, and held there for 24 hours. Then the flasks were weighed to determine the final weight of H_2O. Chloride was determined by titration with silver nitrate solution. Solid NaCl was determined by subtracting the soluble NaCl from the original NaCl. Results are presented below in Tables 2 to 4.

Table 2. NaCl solubility at 72^oF			
	Control	5% Increase in H_2O	9.5% Increase in H_2O
Temperature	23^oC (72^oF)	23^oC (72^oF)	23^oC (72^oF)
NaCl	27.0 g	27.0 g	27.0 g
Final H_2O	68.2 g	73.1 g	76.58 g
Soluble NaCl	23.45 g	26.53 g	26.99 g
Solid NaCl	3.56 g	0.48 g	0.0 g

Table 3. NaCl solubility at 53^oF			
	Control	5% Increase in H_2O	9.5% Increase in H_2O
Temperature	12^oC (53^oF)	12^oC (53^oF)	12^oC (53^oF)
NaCl	27.0 g	27.0 g	27.0 g
Final H_2O	69.47 g	73.49 g	76.44 g
Soluble NaCl	23.97 g	26.15	26.92 g
Solid NaCl	3.03 g	0.81 g	0.07 g

Table 4. NaCl solubility at 39^oF			
	Control	5% Increase in H_2O	9.5% Increase in H_2O
Temperature	4^oC (39^oF)	4^oC (39^oF)	4^oC (39^oF)
NaCl	27.0 g	27.0 g	27.0 g
Final H_2O	65.9 g	73.59 g	76.53 g
Soluble NaCl	23.08 g	26.40 g	26.96 g
Solid NaCl	3.92 g	0.61 g	0.04 g

The laboratory experiments were numerically modeled with thermodynamic software as shown in Fig. 8. The numerical model and the physical results demonstrate that relatively small volumes of fresh water can prevent NaCl deposition.
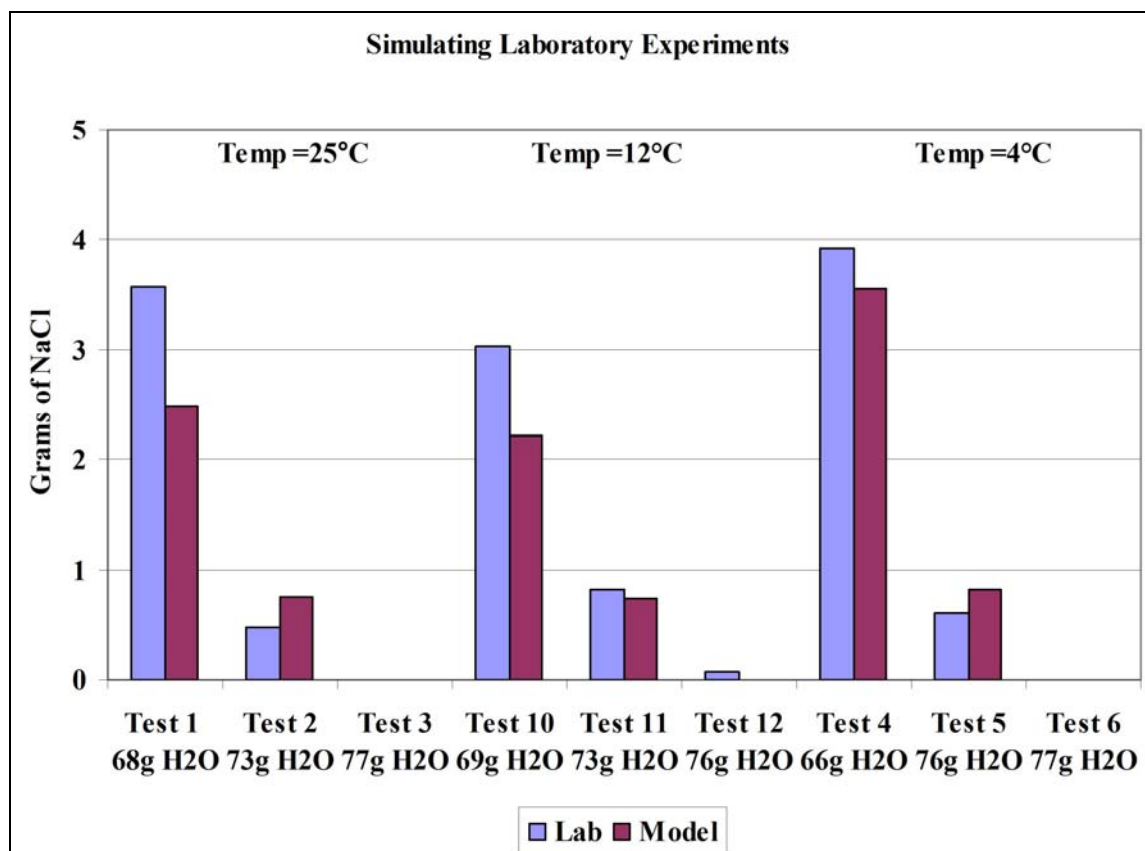
Figure 8. Both laboratory and model support the use of fresh water to prevent NaCl deposition.

Gravimetric analysis of Alpha 1655

Alpha 1655 was analyzed for nitrilotriacetamide content by precipitating, drying, and weighing. One ml of Alpha 1655 was added to 25 ml of acetone. A sticky white precipitate, which formed immediately, was filtered, dried, and weighed. A 1000-ppm solution of the precipitate was prepared by weighing 0.1 g, dissolving it in distilled water, and diluting to 100 ml.

> **Calculations**
> Weight of precipitate=0.3289 g
> Weight of 1 ml of Alpha 1655=1.14 g
> (0.3289/1.14) x 100=37.5 % nitrilotriacetamide in Alpha 1655

Kjeldahl analysis of Alpha 1655 and Na minus 55

Clearwater International has replaced Alpha 1655 with Na minus 55. Hence, Na minus 55 will now be used after testing to show that the two inhibitor preparations are comparable. Diluted aliquots of both products were analyzed for amide nitrogen content by the Kjeldahl method as described previously in Appendix VI. One ml of each was diluted to 50 ml with distilled water. Three and 5 ml aliquots of the dilutions were taken for distillation. The ammonia was distilled and then determined by ammonia-specific ion electrode. The amount of ammonia was then used to calculate the amount of amide nitrogen in each. Since the percent of

amide nitrogen in nitrilotriacetamide is 22%, the amount of nitrilotriacetamide in the products can be calculated. Results are presented in Table 5.

Table 5. Kjeldahl analysis of Alpha 1655 and Na minus 55

Inhibitor	Sample size	Ammonia (ppm)	% Amide-N	% Nitrilotriacetamide
Alpha 1655	3 ml	113	8.25	37.0
Alpha 1655	5 ml	185	8.11	36.8
Na minus 55	3 ml	104	7.74	35.0
Na minus 55	5 ml	167	7.46	33.9

The percent nitrilotriacetamide in Alpha 1655 as determined gravimetrically (37.5%) is close to the same as that determined by Kjeldahl analysis (average=36.9%). The difference between the two results is probably due to the difficulty of separating and filtering the very sticky precipitate in the gravimetric method and/or losses in evolution and trapping of the ammonia in the Kjeldahl method. The amount of nitrilotriacetamide found in Na minus 55 (average=34.5%) is slightly lower than that found in Alpha 1655 (37.2%) but similar.

Comparison of Alpha 1655 and Na minus 55 as salt deposition inhibitors
Flasks containing 50 ml of saturated NaCl solution (17.96 g NaCl; 59.7 g total weight) and the appropriate volume of inhibitors were heated to boiling. The volumes of all the solutions were the same with the difference made up with distilled water. Ten ml portions of a $CaCl_2$ solution containing 0.2 g/ml of Ca (equivalent to 88,000 ppm Ca), also heated to boiling, were combined, stirred, and allowed to cool to room temperature. After 24 hours the volumes were measured, and aliquots of each solution were titrated for Cl. Soluble NaCl was calculated followed by the amount of precipitated NaCl.

The amounts of NaCl precipitated from the Alpha 1655 solutions are comparable to the amounts precipitated from the Na minus 55 solutions (Table 6). The two inhibitor solutions were comparable.

Table 6. Comparison of Alpha 1655 and Na minus 55 as salt inhibitors		
Inhibitor	Soluble NaCl (g)	Solid NaCl (g)
0	10.63	7.3
2 ml Alpha 1566	12.6	5.4
2 ml Na minus 55	12.75	5.2

Static adsorption of Na minus 55 and JACAM on dolomite and sandstone
The static adsorption of the commercial inhibitors Na minus 55 and JACAM on sandstone and dolomite was determined by the method of Sorbie et al.[5] The sandstone was obtained from cores from the Waverly St. Peter formation in Illinois. The dolomite was from a Niagaran Reef well in Belle River Mills, Illinois. The cores were crushed to pass through a standard #28 Tyler sieve producing particle sizes ranging from 32 to 600 µm (surface area of 0.93 m^2/g). The composition of the synthetic brine used in these studies is given in Table 7 (from Sorbie et al.[5]).

Table 7. Composition of synthetic brine			
Compound Composition (g/l)		Ion Composition (mg/l)	
NaCl	24.0738	Na^{+1}	10,890
$CaCl_2 \cdot 6H_2O$	2.3395	Ca^{+2}	428
$MgCl_2 \cdot 6H_2O$	11.4362	Mg^{+2}	1,368
KCl	0.8771	K^{+1}	460
Na_2SO_4	4.376	SO_4^{-2}	2,960
TDS	35,875	Cl^{-1}	19,766

Solutions were prepared by diluting various amounts of the inhibitors to 50 ml with the synthetic brine. Fifteen milliliters of each inhibitor/brine solution were added to 15-g amounts of dolomite and sandstone in small plastic bottles (60 ml). The bottles were placed on a wrist action shaker and shaken for 6 hours. Then the bottles were allowed to stand undisturbed for 12 hours, and finally they were shaken again for 6 hours. All experiments were conducted at room temperature. The samples were vacuum filtered through 0.45 µm Millipore filter paper. The concentrations of ferrocyanide in the JACAM solutions were determined spectrophotometrically by the method described in Appendix VII. The concentrations of nitrilotriacetamide in Na minus 55 were determined by the Kjeldahl method described in Appendix VI.

The absorption of the ferrocyanide in JACAM onto dolomite and sandstone is shown graphically in Fig. 9 where the initial ferrocyanide concentration in ppm is plotted against the milligram of inhibitor adsorbed per gram of core material. Fig. 10 presents the same information for the adsorption of the nitrilotriacetamide in Na minus 55 onto dolomite and sandstone. The ferrocyanide adsorbs strongly initially onto dolomite and appears to reach a maximum at about 0.09 mg/g. It adsorbs onto the sandstone but not as well either initially or maximally.
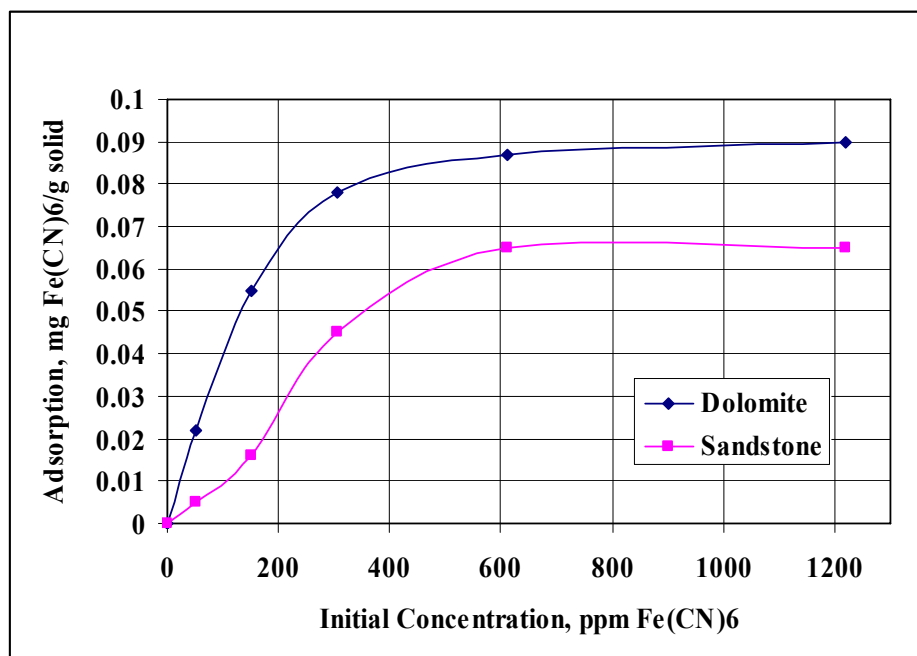
Figure 9. Static adsorption of ferrocyanide in JACAM by dolomite and sandstone.
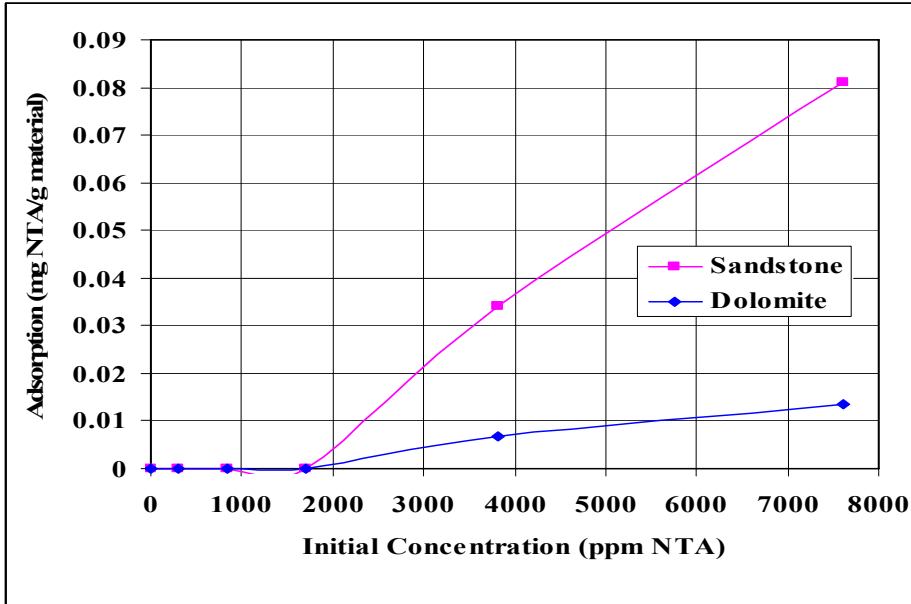
Figure 10. Static adsorption of nitrilotriacetamide (NTA) in Na minus 55 by dolomite and sandstone.

In the static test of nitrilotriacetamide (Fig. 10), no adsorption is observed until the amount of inhibitor in the initial solution is high (2000 ppm). Even at a high level of inhibitor, very little nitrilotriacetamide was adsorbed onto the dolomite. Since the filtered solids were not washed, it is possible that the apparent adsorption at the very high levels of the nitrilotriacetamide inhibitor is an artifact due to the solids simply retaining some of the inhibitor by occlusion and not by adsorption. The indication then is that the nitrilotriacetamide is not adsorbed to a great enough extent to be used in "squeeze" applications by either mineral.

Na minus 55 as a salt inhibitor for KCl precipitation

The solubility of KCl is very dependant on temperature, for example, the solubility of KCl at 20^oC in saturated NaCl solutions is 15 g/100 g and at 100^oC is 35 g/100 g. So if 35 g of KCl were dissolved in a 100 g solution of saturated NaCl at 100^oC and allowed to cool to room temperature, KCl would precipitate out of solution. The nitrilotriacetamide in Na minus 55 will prevent NaCl precipitation from supersaturated NaCl solutions. The following test was run to explore the possibility of the inhibitor preventing KCl from precipitating out of a saturated NaCl solution containing 350,000 ppm TDS.

Flasks were prepared containing the following:

Flask #1	Flask #2
50 ml saturated NaCl brine	50 ml saturated NaCl brine
2 ml distilled water	2 ml of Na minus 55

The solutions were heated to 90° to 100^oC, and 7.0 g of KCl were dissolved in each. Solutions were then allowed to cool to room temperature. After 3 hours, there was precipitate in the control, Flask #1 but no precipitate in Flask #2. After 24 hours, there was more precipitate in Flask #1 and a small amount of precipitate in Flask #2. This is shown visually in Fig. 11. The

cloudiness in the photo of Flask #2 is light reflection and not precipitate. Flask #2 contained very few crystals. These conditions remained the same for the next 96 hours. It is apparent that the salt inhibitor could prevent precipitation of KCl from a saturated NaCl solution.
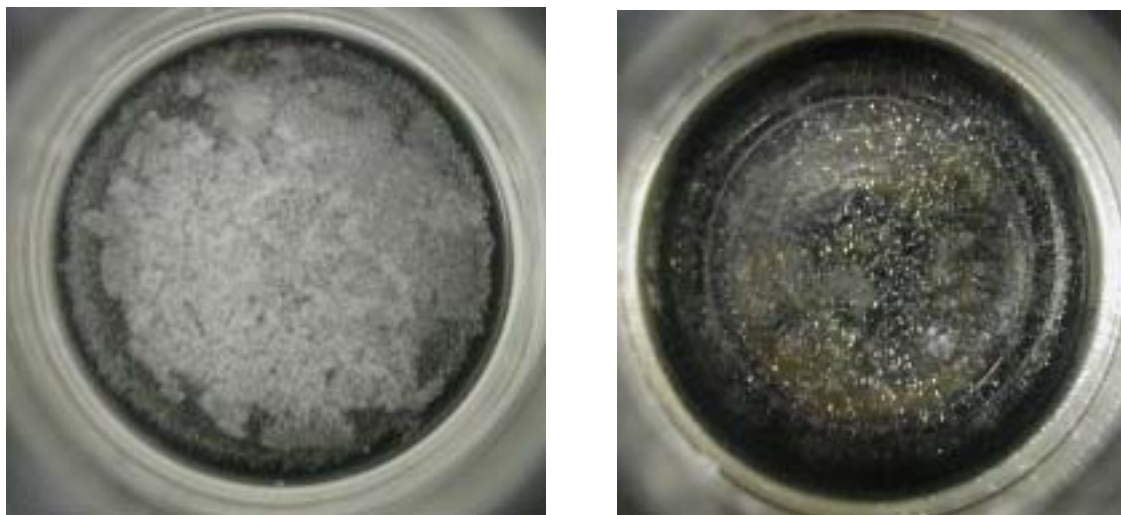
Figure 11. Effect of Na minus 55 on KCl precipitation from saturated NaCl solution: Flask #1 on the left (control) and Flask #2 on the right (inhibitor).

Compatibility tests

The compatibility of the two commercial salt inhibitors at two concentrations was determined via visual observations of mixtures of the salt inhibitors with a commonly used scale inhibitor and a corrosion inhibitor. The experimental results are shown in Figs. 12-15.

JACAM is based on ferrocyanide chemistry and Alpha 1665 is based on nitrilotriacetamide chemistry. The scale inhibitor is a phosphonate-based inhibitor, and the corrosion inhibitor is a water-soluble amine. Based on core flow tests we have observed that solutions that clabber such as the JACAM and the corrosion inhibitor seen at different concentrations of corrosion inhibitor in Figs. 12 & 13 do reduce the flow through cores. However hazy solutions such as the Alpha 1665 and the corrosion inhibitor seen in Fig. 14 & 15 do not result in core plugging. Hence, Alpha 1665 is judged to be compatible with both the scale inhibitor and the corrosion inhibitor. The JACAM is not compatible with the corrosion inhibitor. While JACAM is compatible with the scale inhibitor, the blue color indicates the effectiveness as a salt inhibitor is diminished.

Figure 12. Left to right: Visual observation of JACAM (30,000 ppm), mixture of JACAM + scale inhibitor (9,460 ppm), and mixture of JACAM + corrosion inhibitor (1,300 ppm).
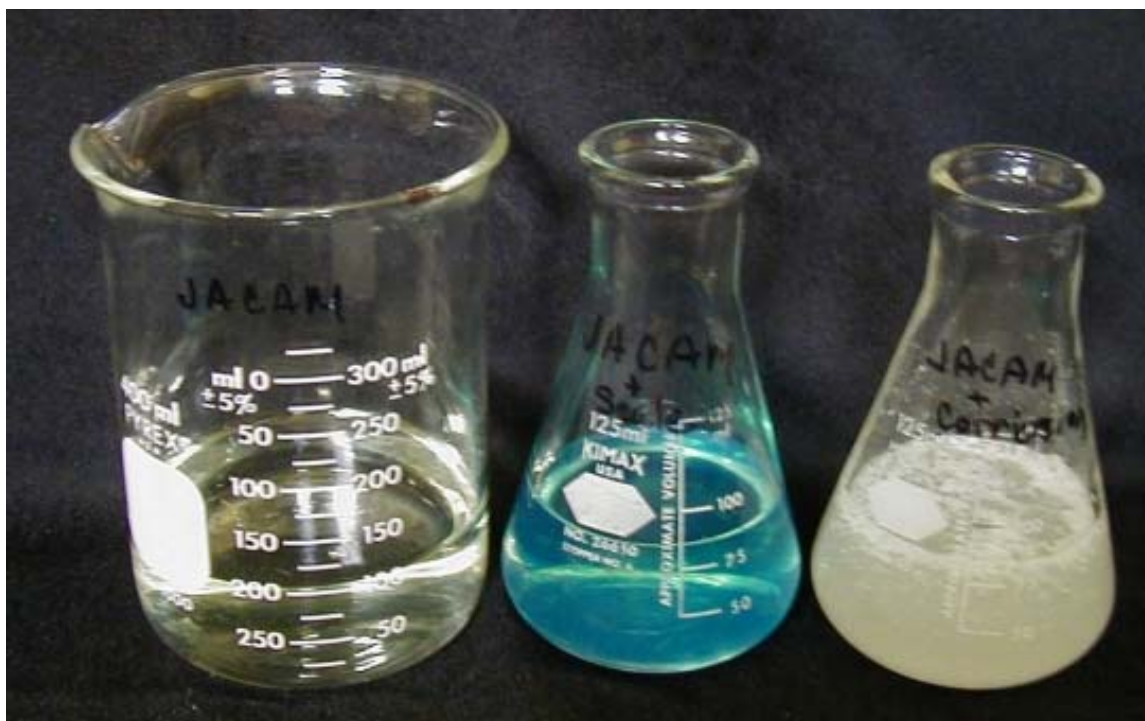
Figure 13. Left to right: Visual observation of JACAM (30,000 ppm), mixture of JACAM + scale inhibitor (12,600 ppm) ,and mixture of JACAM + corrosion inhibitor (2,600 ppm).

Figure 14. Left to right: Visual observation of Alpha 1655 (30,000 ppm), mixture of Alpha + scale inhibitor (12,600 ppm), and mixture of Alpha + corrosion inhibitor (2,600 ppm).

Figure 15. Left to right: Visual observation of mixture of Alpha 1655 (30,000 ppm), mixture of Alpha + scale inhibitor (12,600 ppm), and Alpha + corrosion inhibitor (2,600 ppm).

*Numerical modeling of storage facility brines (*see Appendix IX for information on the software)

Gas Storage Research Consortium members provided water analyses from nine facilities located in the northeastern part of the country and from three California facilities. NaCl scale was reported to be a problem in the 12 facilities. Note that the California reservoirs are much hotter (~175°F) than the northeastern reservoirs that are ~65°F. As mentioned earlier, temperature plays a key roll in salt deposition, as well as water vaporization. The TDS of the brine samples from the 12 facilities are listed in Table 8.

Table 8. Facility water analyses and predicted solid salt deposition					
Facility	TDS, ppm	NaCl, lb/bbl	Facility	TDS, ppm	NaCl, lb/bbl
Muehleisen	280,157	0	Sharrow	318,143	25
Goodwell	274,718	0	Belle River	343,061	5.1
Smith	275,326	0	Brine Pond	336,540	12.5
Lincoln	254,967	0	Aliso Canyon Bailer	201,431	0
Reed City	289,641	0	Aliso Canyon Reservoir	15,247	0
Whitewater	465,964	49	Goleta Reservoir	10,970	0

The water analyses from these facilities were used along with bottomhole temperature and pressure ranges to model salt precipitation. The water analyses are included in Appendix X. The model predicts that salt will precipitate at 50°F in four of the 12 facilities, yet all facilities report that salt scale is a problem. Shown in Fig. 16 is a plot of theoretical NaCl precipitate versus the brine TDS for the northeastern reservoirs. Note that the correlation coefficient is strong and intercepts the zero precipitation axis at ~300,000 ppm TDS.
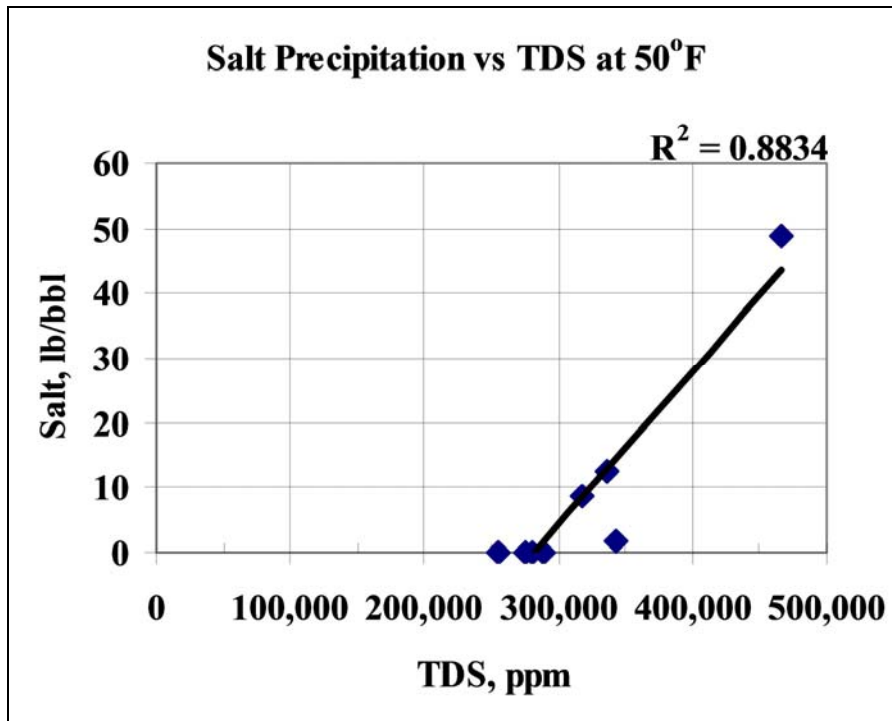
Figure 16. Correlation between predicted salt scale at 50°F and the TDS of field brines.

Two northeastern analyses that predicted salt deposition were Sharrow and Whitewater. The Sharrow lease precipitated ~2 lb/bbl NaCl as the water cooled from 140°F to 40°F where it

precipitated ~10 lb/bb. Minor amounts of calcium and barium sulfate scale were predicted to precipitate. Pressure drop from 15 psi to 500 psi had very little effect on NaCl deposition in this system. The Whitewater lease with an extremely high TDS content of 466,000 mg/l precipitated 43 lb/bbl of salt at 140°F and 50 lb/bbl at 40°F. Neither barium nor calcium sulfate scale was expected to form with this water. Again, pressure drop had little effect on the formation of NaCl scale in this system.

As demonstrated with laboratory experiments, the addition of fresh water to the brine is an effective method of preventing salt scale formation. The analysis of typical Michigan fresh water from a shallow well is shown in Table 9.

Table 9. Typical Michigan fresh dilution water analysis.							
Component	Na	Ca	Mg	Ba	HCO_3	SO_4	Cl	TDS
mg/l	55	400	831	8	85	200	600	2179

This dilution water was used in numerical experiments to determine the volume of dilution water required to prevent salt deposition in the Sharrow and Whitewater lease waters. By trial and error, it was determined that a 9% dilution of the Sharrow brine reduced the NaCl scale deposition from 9 lb/bbl to 0.0 lb/bbl. The very high TDS Whitewater water required a 49% dilution with fresh water to prevent salt scale. Dilution of both Sharrow and Whitewater brines with the fresh water generated minor amounts of calcium and barium scale on the order of 0.01 lb/bbl (30 ppm) of brine-fresh mixture.

We accept 300,000 ppm TDS as the threshold for salt precipitation at 50°F. The outlying point at 343,000 ppm TDS and 1.8 lb/bbl salt is due to the common ion (Cl) being low (see water analyses in Appendix X) relative to points with higher chloride concentrations; thus, the driving force for salt precipitation is less.

The water analyses from five laboratory experiments with pure salt solutions were used to numerically predict salt precipitate. The results are shown in Fig. 17. Note that the trend is clear with the intercept at ~350,000 ppm TDS due to the abundance of the common ion Cl and the resulting effect on driving NaCl out of solution.
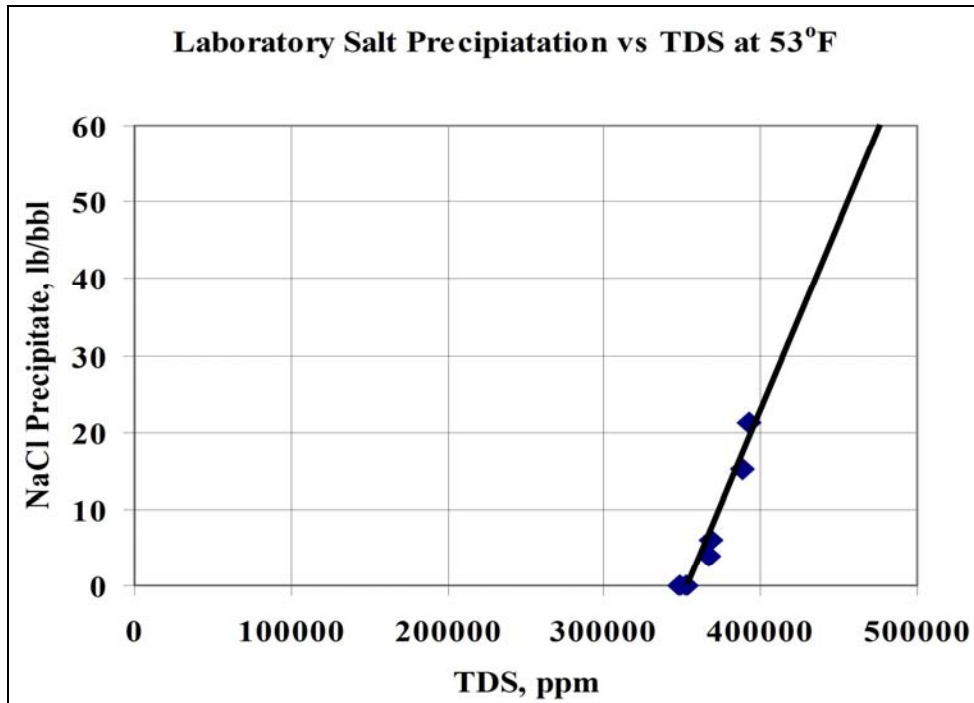
Figure 17. Correlation between predicted salt scale at 50°F and the TDS of laboratory brines.

Understanding that dry gas will vaporize water resulting in brine with an increased concentration of TDS and recognizing that salt will precipitate at 50°F when the TDS level reaches 300,000 ppm, a series of numerical experiments were conducted to determine the volume of gas required to generate 350,000 ppm TDS brine. The purpose of the experiments was to determine if the estimated volumes are within the range of fill-cycle injection volumes. The experiments were based on pure CH_4, the brines listed in Table 8 and the water analyses in Appendix X, and bottomhole conditions of 500 psi and 63°F for the northeastern reservoirs and 1600 psi and 175°F for the California reservoirs. The results shown in Table 10 were generated using a trial and error method.

	Muehleisen	Goodwell	Smith	Lincoln	Aliso Canyon Bailer	Aliso Canyon Reservoir
Table 10. Gas required to generate brine TDS greater than 300,000 ppm						
Gas, mcf/bbl	3,830	5,044	3,308	4,030	813	5,600

The relatively low bottomhole temperature (63°F) of the Michigan reservoirs requires 3 to 5 MMcf/bbl of gas to generate brines that will deposit salt at 50°F. Since salt scale threshold of 350,000 ppm TDS was used, the volume requirements are judged to fall within the range of gas injected during the fill cycle. With the exception of the bailer sample, the high-temperature California reservoir has a similar requirement.

Salt deposition consisting of calcium, sodium, and potassium chloride has been reported in three facilities operated by SoCal. The TDS content of water samples collected at various points throughout the three California facilities varied from ~1000 ppm to 277,000 ppm. Pressure and temperature conditions are shown in Table 11.

Table 11. California storage reservoir temperature and pressure			
	Minimum pressure, psia	Maximum pressure, psia	Temperature, ^{o}F
Honor Rancho	1100	4210	190
La Goleta	1500	2040	150
Aliso Canyon	1600	3600	175

The Aliso Canyon facility had a relatively complete set of data consisting of analyses of reservoir brine, a bailer sample of workover kill-fluid, and a scale analysis of solids, all from the Porter 69 well. The bailer sample was a mixture of 10 lb/gal $CaCl_2$ kill-fluid used during times of maximum bottomhole pressure and 9.4 lb/gal KCl used for pressure control during low-pressure delivery periods.

Numerical models were developed to estimate the volume of dry gas required to reduce the volume of one barrel of 30,000 ppm TDS reservoir water to 300,000 ppm TDS. By trial and error, dry methane was added until 90% of the water was evaporated at specified conditions of temperature and pressure. Conditions were selected to encompass the range seen in Table 10. The results of these numerical experiments were used to generate Fig. 18.
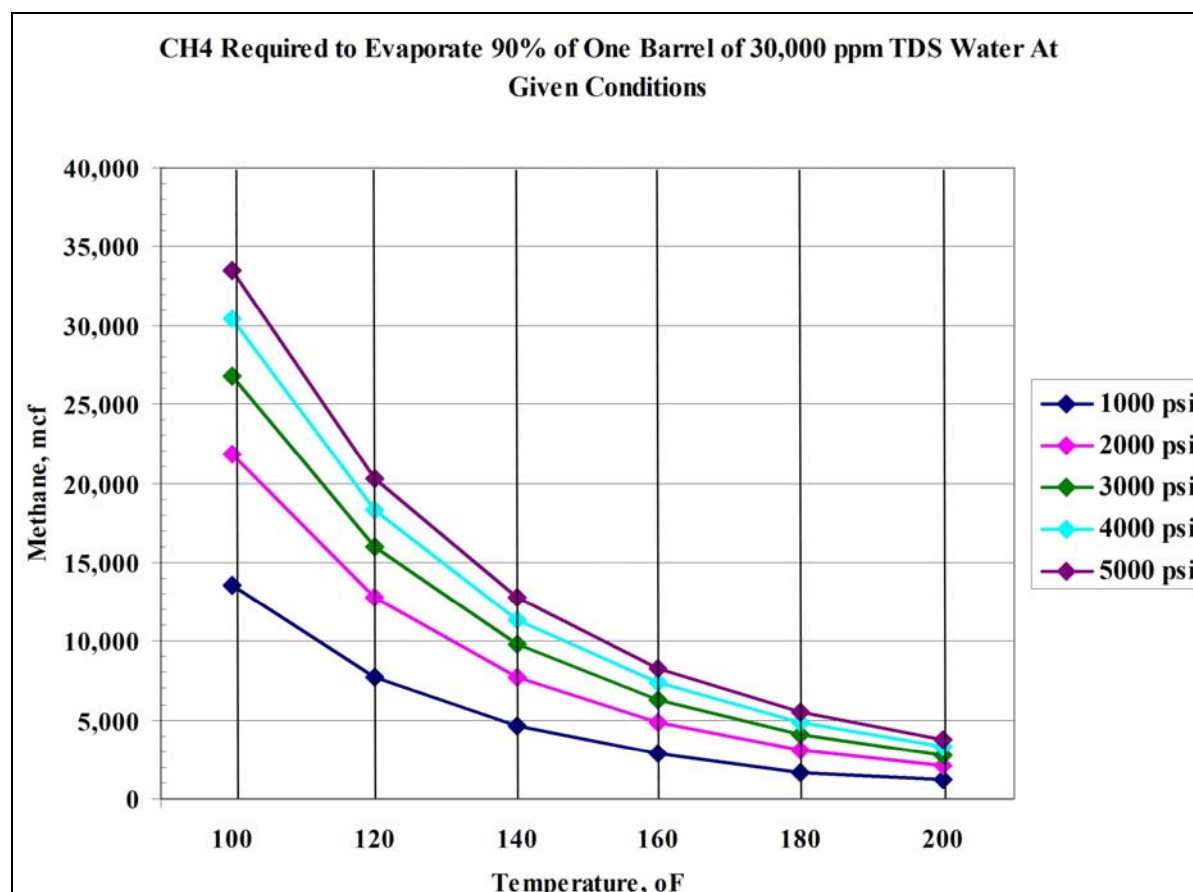
Figure 18. Dry methane required to evaporate sufficient water from 1 bbl of 30,000 ppm TDS brine to generate 300,000 ppm TDS brine.

The information in Table 11 was used in conjunction with Fig. 18 to determine the volume of dry gas required to increase the concentration of one barrel of 30,000 ppm TDS to 300,000 ppm TDS brine for three California reservoirs as shown in Table 12.

Table 12. Volume of dry methane required to increase 30,000 ppm TDS to 300,000 ppm TDS		
Honor Rancho	La Goleta	Aliso Canyon
4,200 mcf/bbl	6,300 mcf/bbl	5,600 mcf/bbl

The absolute volume requirements are dependent on the source of 30,000 ppm TDS brine. If the wellbores are dry and reservoir connate water is the source, one can assume that with typical well spacing of 40 acres with a 10-ft interval with 20% porosity and 20% water saturation, the interval contains about a 124,000 bbl of water requiring about 700 BCF dry gas to generate scale. If the 30,000 ppm TDS brine exists in the wellbore, the requirement is about 3 BCF; if the wellbore contains the bailer fluid shown in Table 8, the requirement is about 0.4 BCF. The dry gas requirements suggest that the salt scale is a result of wellbore water vaporization.

A series of numerical experiments were conducted with the Aliso Canyon workover fluid analysis (Appendix X to estimate the amount and type of scale formed at bottomhole temperature and pressure. All components except sulfide were included. Temperature was varied from 50°F to 175°F and pressure from 1600 psia to 3600 psia. The TDS of the workover brine was increased via evaporation from 200,000 ppm to 288,000 ppm to 300,000 ppm, and 360,000 ppm.

The predicted scales are shown in Fig. 19 with units of pounds of scale per pound of water. Larger versions of the component figures are shown in Appendix XI.
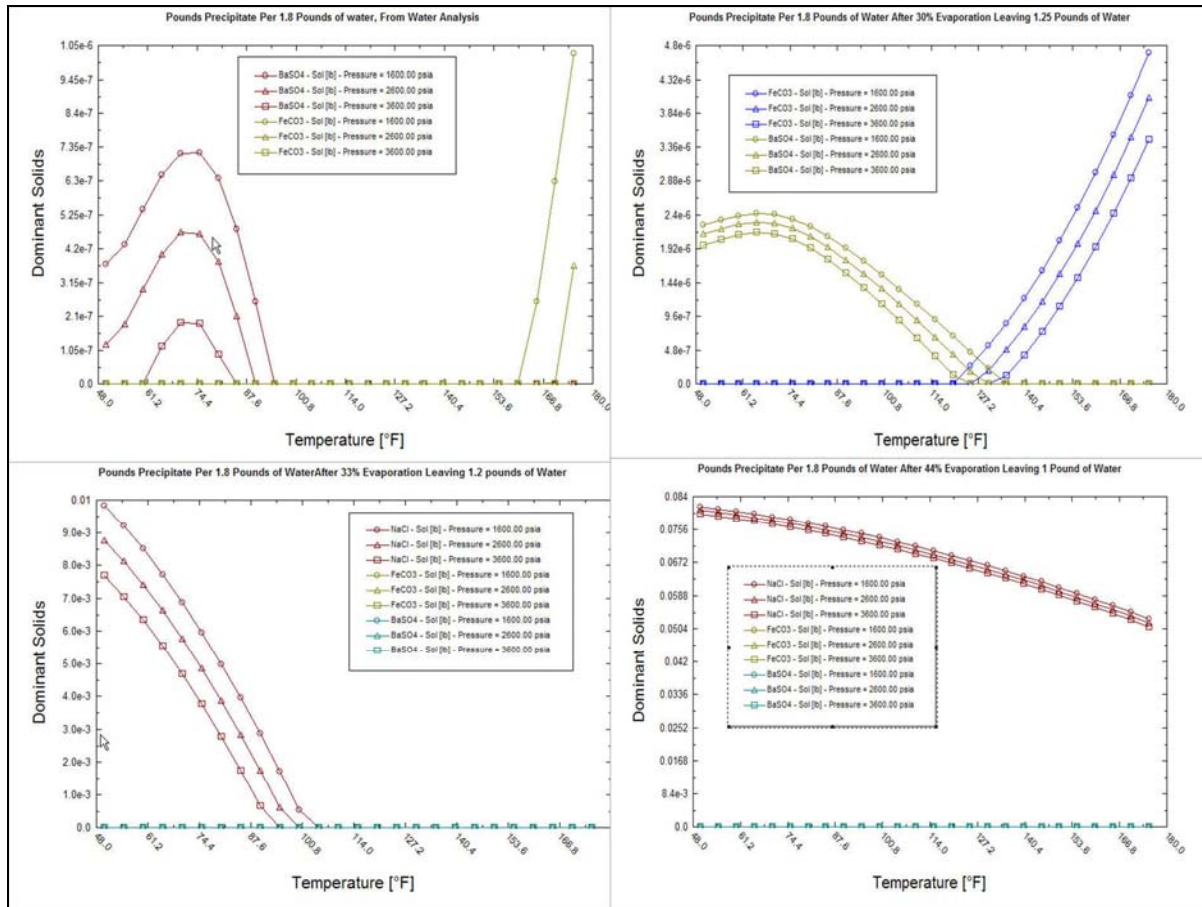
Figure 19. Predicted scale formation from 200 k, 288 k, 300 k, and 388 k TDS workover fluids.

If no water evaporates (upper left of Fig. 19), about 0.0001 lb/bbl of BaSO$_4$ precipitates from about 50°F to 90°F, and a similar small amount (0.006 lb/bbl) precipitates if the brine TDS increases to 288,000 ppm. In the 125°F to 175°F range, both the 200,000 and 288,000 ppm TDS brines precipitate small amounts (0.0001 to 0.006 lb/bbl) of iron carbonate, FeCO$_3$, but BaSO$_4$ ceases to precipitate.

Once the 300,000 ppm TDS threshold is reached, NaCl scale at about 1.5 lb/bbl becomes an issue in the 50°F to 90°F temperature range as seen in the lower left of Fig. 19.   If the TDS increases to 388,000 ppm, salt precipitates throughout the temperature range at about 25 lb/bbl, which is a significant problem. Both BaSO$_4$ and FeCO$_3$ precipitate at the higher TDS range, but are insignificant compared to NaCl.   No calcium scales were predicted with this set of experiments.   The reported CaCl$_2$ scale may have precipitated during the time the well was loaded with 10 lb/gal kill fluid. The bailer sample analyses used as the starting point in this set of experiments consisted of fluid collected following the use of 9.4 lb/gal KCl to kill the well.

It appears that salt deposition occurring downstream of the perforations is the result of evaporation at or below the perforations. KCl precipitation was simulated as shown in Fig. 20 by adding 125,000 ppm of KCl (~9.4 lb/gal kill fluid) to the bailer water concentrated to 300,000 ppm TDS. The model predicts a maximum of 6 lb/bbl of KCl and 19 lb/bbl of NaCl along with negligible amounts of BaSO$_4$ and FeCO$_3$.
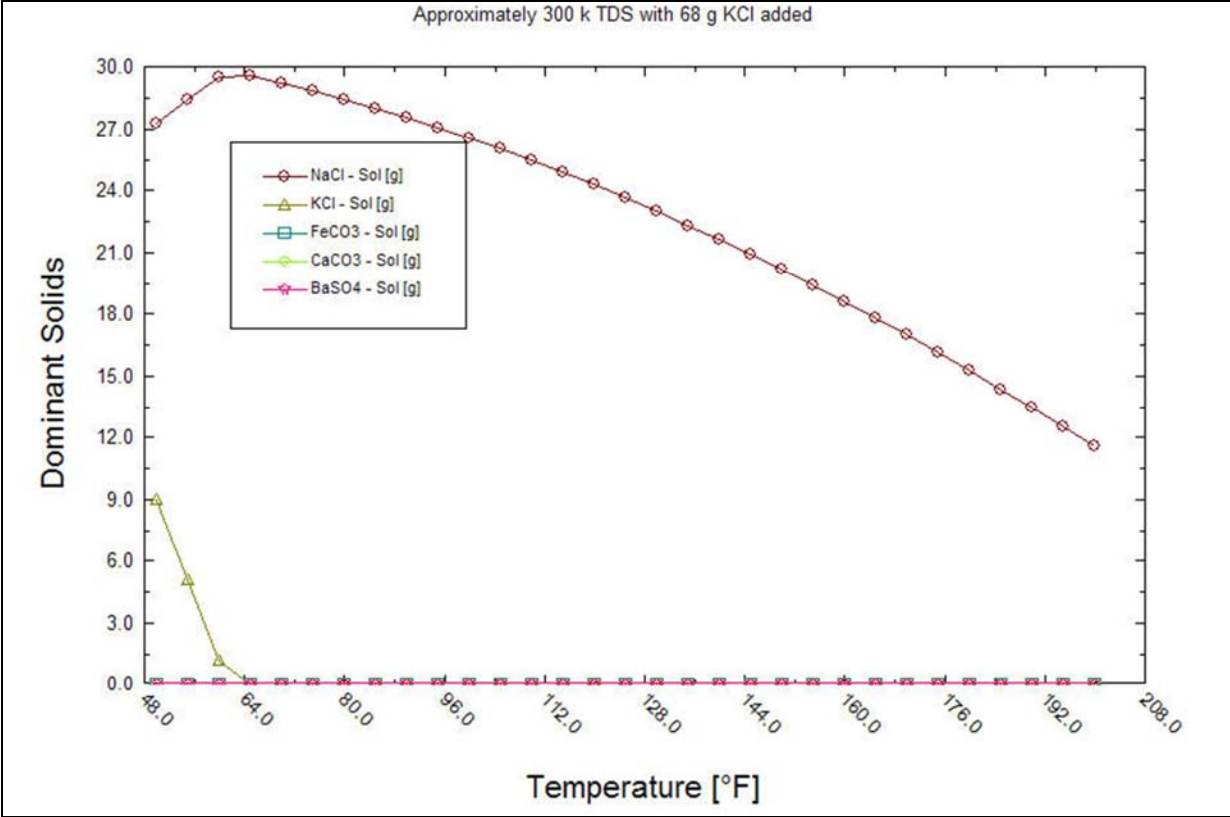
Figure 20. Simulated KCl precipitation from workover fluid.

The laboratory results reported earlier suggest that the nitrilotriacetamide-based inhibitor could be added to the kill fluid to mitigate both NaCl and KCl scales.

Discussion

The development of a laboratory protocol to generate repeatable NaCl precipitation experiments with supersaturated salt solutions facilitated the evaluation of two commercial salt inhibitors and provides a format for future work with new inhibitors if they are developed. The nitrilotriacetamide-based inhibitor may be more useful than the ferrocyanide-based inhibitor. The ferrocyanide is unstable under certain conditions (low pH and presence of Fe^{+3} ions); therefore, it is not the best salt inhibitor for field operations where in many cases iron would be present. An inhibitor that contains nitrilotriacetamide would be a better choice for preventing salt scale resulting from the vaporization of $CaCl_2$- and KCl-based kill fluids that contain incompatible scale and/or corrosion inhibitors and sit in the wellbore for long periods where they become contaminated with iron.

Operators have little experience with either the ferrocyanide- or the nitrilotriacetamide-based inhibitors. They instead prefer to use fresh dilution water as a means to prevent and remove salt scale. Both numerical and laboratory experiments support the dilution water approach. However, if brine TDS exceeds 400,000 ppm the volume of dilution water may become excessive and approach 50%. In such cases the cost of salt inhibitors may be justified. While the less expensive ferrocyanide is considerably more effective than nitrilotriacetamide in pure NaCl solutions, performance deteriorates in the presence of Fe^{+3}. Neither inhibitor performs well once Ca^{+2} exceeds 25,000 ppm, a condition found many times in supersaturated field brines. Sequestering additives might reduce the negative effect of Ca^{+2} on salt inhibitor performance.

The laboratory data suggest that neither salt inhibitor will provide long-term squeeze life when compared to phosphonate scale inhibitors. Ferrocyanide adsorption is about 10% that of phosphonate scale inhibitors. If field conditions necessitate squeeze treatments for the prevention of salt scale, large volumes of fresh water should be included. In cold climates the use of fresh water might be restricted due to freezing; in such cases, ferrocyanide could be included in a fresh water squeeze to increase squeeze life, especially in dolomite reservoirs that are generally free of dissolved iron.

Conclusions

The project generated insight into the following areas:
- The sensitivity of NaCl precipitation to fresh water dilution
- Effectiveness and stability conditions of two inhibitors
- Adsorption characteristics of the two inhibitors on a sandstone and a dolomite
- Methods to improve inhibitor efficiency based on the addition of sequestrants
- A method to automate the addition of chemicals/fresh water
- The need to understand the water chemistry of salt cavern development.

References

1. Earl, S.L. and Nahm, J.J., Use of chemical salt precipitation inhibitors to maintain supersaturated salt muds for drilling salt formations, SPE 10097, 58th Annual Fall Technical Conference and Exhibition of the Society of Petroleum Engineers of AIME, San Antonio, TX, 1981.

2. Kirk, J.W., Methods for the inhibition of salt blockages in oil and gas wells, US Patent No. 7,028,776 B2, 2006.

3. Ralston, P.H., Park, B., and Persinski, L.J., Inhibiting salt deposition, U.S. Patent 3,367,416, 1968.

4. Kleinitz, W., Koehler, M., and Dietzsch, G., The precipitation of salt in gas producing wells, SPE 68953, European Formation Damage Conference, The Hague, The Netherlands, 21-22 May 2001.

5. Sorbie, K.S., Wat, R.M.S., Todd, A.C., and McCloskey, T., Derivation of scale inhibitors adsorption isotherms for oil reservoir squeeze treatments, *Chemicals in the Oil Industry: Developments and Applications,* P.H. Ogden, Ed., pp. 199-214, 1991.

Appendix I. Analysis of solid from a Six Lakes gas storage well

A portion of the sample was first dried at 105°C, then weighed and dissolved in distilled water in duplicate. The resulting solutions were analyzed for potassium, calcium, iron, and magnesium by atomic absorption spectroscopy, and none was detected. Sodium was then assumed to be the only cation present. Acidified portions of the solutions were tested for sulfate by adding a saturated solution of $BaCl_2$, and none was detected. Chloride was determined by titration with silver nitrate. Bound water was determined by heating a weighed portion to 300°C. Insoluble residue was determined by dissolving a weighed portion in boiling distilled water and weighing the residue.

Appendix II. Experimental data for nitrilotriacetamide inhibitor studies

Table II-1. Effect of nitrilotriacetamide inhibitor in saturated NaCl solutions prepared by adding 27 g NaCl to 73 ml boiling water

Sample Description	ppm Inhibitor	Cl (g)	Na (g)	Ca (g)	K (g)	NaCl (soluble) (g)	NaCl (solid) (g)
No Ca Control	0	14.4	9.3	0.0	0.0	23.72	3.3
1 drop Inhibitor	600	14.8	9.7	0.0	0.0	24.55	2.5
2 drops Inhibitor	1200	15.3	9.9	0.0	0.0	25.23	1.8
3 drops Inhibitor	1800	15.8	10.2	0.0	0.0	26.03	1.0
4 drops Inhibitor	2400	15.9	10.3	0.0	0.0	26.22	0.8
5 drops Inhibitor	3000	16.1	10.4	0.0	0.0	26.55	0.5
10 drops Inhibitor	6000	16.1	10.4	0.0	0.0	26.55	0.5

No precipitation of NaCl was visible in the flasks at 25ºC containing four drops to 10 drops of inhibitor.

Table II-2. Effect of nitrilotriacetamide inhibitor in saturated NaCl solutions containing 2.979 g CaCl$_2$·2H$_2$O, 1.6 g KCl, and 24.05 g NaCl in 72 ml of boiling water

Sample Description	ppm Inhibitor	Cl (g)	Na (g)	Ca (g)	K (g)	NaCl (soluble) (g)	NaCl (solid) (g)
0.81 g Ca Control	0	14.85	8.20	0.81	0.84	20.84	3.21
10 drops Inhibitor	6000	15.60	8.68	0.81	0.84	22.08	1.97
15 drops Inhibitor	9000	15.90	8.88	0.81	0.84	22.57	1.48
20 drops Inhibitor	12000	16.20	9.08	0.81	0.84	23.07	0.98
25 drops Inhibitor	15000	16.60	10.44	0.81	0.84	23.73	0.32

No precipitation of NaCl was visible in the flasks at 25ºC containing 15 drops to 25 drops of inhibitor.

Table II-3. Effect of nitrilotriacetamide inhibitor in saturated NaCl solutions prepared with 6.77 g CaCl$_2$·2H$_2$O, 3.7 g KCl, and 21.77 g NaCl in 72 ml of boiling water

Sample Description	ppm Inhibitor	Cl (g)	Na (g)	Ca (g)	K (g)	NaCl (soluble) (g)	NaCl (solid) (g)
1.85 g Ca Control	0	15.19	6.59	1.85	1.94	16.75	5.02
5 drops Inhibitor	3000	15.40	6.73	1.85	1.94	17.10	4.67
10 drops Inhibitor	6000	15.80	6.99	1.85	1.94	17.76	4.01
20 drops Inhibitor	12000	16.20	7.08	1.85	1.94	18.42	3.35
25 drops Inhibitor	15000	16.60	7.26	1.85	1.94	19.08	2.69

No precipitation of NaCl was visible in the flasks at 25ºC with 25 drops of inhibitor.

Table II-4. Effect of nitrilotriacetamide inhibitor in saturated NaCl solutions prepared with 28.7 g CaCl$_2$·2H$_2$O and 11.0 g NaCl in 72 ml of boiling water

Sample Description	ppm Inhibitor	Cl (g)	Na (g)	Ca (g)	K (g)	NaCl (soluble)(g)	NaCl (solid) (g)
7.83 g Ca Control	0	15.89	1.32	7.81	0.00	3.38	7.62
15 drops Inhibitor	9000	16.28	1.57	7.81	0.00	4.02	6.98
20 drops Inhibitor	12000	16.54	1.74	7.81	0.00	4.42	6.58
25 drops Inhibitor	15000	16.67	1.82	7.81	0.00	4.62	6.38
30 drops Inhibitor	18000	16.67	1.82	7.81	0.00	4.62	6.38
35 drops Inhibitor	21000	16.67	1.82	7.81	0.00	4.62	6.38

Precipitate was in all of the flasks at 25ºC.

Appendix III. Experimental data for ferrocyanide inhibitor studies

Table III-1. Effect of $Fe(CN)_6$ inhibitor in saturated NaCl solutions containing 27 g NaCl in 73 ml water

Inhibitor (wt. %)	Ca (g)	Cl (soluble)(g)	NaCl (soluble)(g)	NaCl (solid) (g)	pH	Vol
0	0.0	15.53	25.60	1.4	6.8	73
0.01	0.0	15.95	26.30	0.7	6.8	73
0.03	0.0	16.25	26.80	0.2	6.8	73
0.05	0.0	16.31	26.90	0.1	6.8	73
0.1	0.0	16.31	26.90	0.1	6.8	73

No precipitation of NaCl was visible in the flasks containing from 0.03% inhibitor to 0.1% inhibitor.

Table III-2. Effect of $Fe(CN)_6$ inhibitor in saturated NaCl solutions containing 3.67 g $CaCl_2 \cdot 2H_2O$ and 23.0 g NaCl in 73 ml of water

Inhibitor (wt. %)	Ca (g)	Cl (soluble)(g)	NaCl (soluble) (g)	NaCl (solid) (g)	pH	Vol
0	1.00	14.62	21.19	1.81	6.9	73
0.01	1.00	15.60	22.34	1.00	6.9	75
0.03	1.00	15.43	22.52	0.48	6.98	75
0.05	1.00	15.60	22.80	0.20	6.95	75
0.1	1.00	15.60	22.80	0.20	6.95	75

No precipitation of NaCl was visible in the flasks at 25ºC from 0.05% inhibitor to 0.1% inhibitor.

Table III-3. Effect of $Fe(CN)_6$ inhibitor in saturated NaCl solutions containing 7.52 g $CaCl_2 \cdot 2H_2O$ and 21.5 g NaCl in 73 ml of water

Inhibitor (wt. %)	Ca (g)	Cl (soluble)(g)	NaCl (soluble) (g)	NaCl (solid) (g)	pH	Vol
0	2.00	14.73	18.19	3.31	6.9	73
0.01	2.00	15.26	19.00	2.70	6.94	74
0.03	2.00	15.46	19.51	1.99	6.92	75
0.05	2.00	16.00	20.00	1.50	7.3	76
0.1	2.00	16.55	21.00	0.50	7.6	76

No precipitation of NaCl was visible in the flask containing 0.1% inhibitor at 25ºC.

Table III-4. Effect of $Fe(CN)_6$ inhibitor in saturated NaCl solutions containing 18.35 g $CaCl_2 \cdot 2H_2O$ and 14.5 g NaCl in 73 ml of water

Inhibitor (wt. %)	Ca (g)	Cl (soluble)(g)	NaCl (soluble) (g)	NaCl (solid) (g)	pH	Vol
0	5.00	15.18	10.44	4.07	6.93	73
0.05	5.00	15.58	11.10	3.41	6.9	74
0.1	5.00	16.11	11.97	2.54	7.02	75
0.2	5.00	16.2	12.12	2.20	7.13	74
0.3	5.00	16.5	12.61	1.90	7.18	75

Precipitate was in all of the flasks at 25ºC.

Appendix IV. Calcium-Sequestering Agent Experiments

The test solution consisted of the following:

> 7.52 g CaCl$_2$·2H$_2$O in 10 ml of H$_2$O (20,000 ppm in final solution)
> 21.5 g NaCl
> 30.0 mg of ferrocyanide in 3 ml of H$_2$O (300 ppm in final solution)

The final volume of the solution including the calcium chloride solution, the ferrocyanide solution, and the calcium-complexing agent was 73 ml. Then NaCl was added. The following reagents were tested.

1. EDTA (0.2 g). When the brine solutions were cooled to room temperature, more NaCl precipitated in the solution containing EDTA than in the control.
2. Citric acid (0.75 g). When the solutions were heated to dissolve the NaCl, the solution containing the citric acid turned blue, and a dark blue precipitate formed on cooling. The pH of the solution containing the citric acid was less than 1.0. The pH of the control was 6.9.
3. Sodium citrate (1 g). Sodium citrate was added to calcium-inhibitor solution and heated slightly to facilitate dissolution. Upon cooling to room temperature, a large amount of precipitate formed. The solubility of sodium citrate is 72 g/100 ml, and the solubility of calcium citrate is 0.22 g/100 ml, so the precipitate is probably calcium citrate. Calcium citrate is probably soluble in acid, which is why it did not precipitate out of solution in the preceding test. The low pH in the previous test probably caused the ferrocyanide to decompose to Prussian Blue (Fe^{+3}(Fe^{+3}Fe^{+2}(CN)$_6$)$_3$). Citric acid might be an effective calcium complexer when nitrilotriacetamide is used as an inhibitor.
4. Potassium phosphates (monobasic and dibasic) (1 g). Both potassium phosphates were tested as complexing agents. An amorphous precipitate was formed upon heating, and the solutions also turned blue, although not as intense a blue as with the sodium citrate. The pH of these solutions was 1 to 3. The precipitate was most likely calcium phosphate.
5. Sodium hexametaphosphate (1 g). Precipitate was formed when the reagent was added to test solution.
6. Commercial scale inhibitor (AS-216**;** a soluble organo-phosphate)(1 ml). Solution turned dark blue upon heating before NaCl was added. The pH of solution was less than 1. This experiment was rerun, and solutions containing the calcium, ferrocyanide, and scale inhibitor were adjusted to pH=4, pH=6, and pH=8 using 1.0 N NaOH. The pH=4 solution turned a dark cloudy blue when heated, and 24 hours later dark blue and white precipitates had settled leaving a clear colorless solution. The white precipitate was 1.34 g NaCl determined by loss from solution. The pH=6 and pH=8 solutions turned cloudy with a fine white precipitate, when NaCl was added to the hot solutions, which settled out after 24 hours. The pH=6 flask contained 0.69 g NaCl, and the pH=8 flask contained 1.02 g NaCl. The pH-adjusted flasks all contained more volume than the control due the varying amounts of NaOH solution added. The commercial product CS-71 gave similar results.
7. Sodium borate (0.7 g). Reagent was not very soluble (0.7 g used instead of 1 g), and precipitate formed upon cooling. However, the precipitate was finely divided and did not clump together. The pH of the solution was 7.11.

8. Trisodium nitrilotriacetic acid (1 g). A large amount of precipitate was formed when the reagent was added to the test solution.

9. Tripotassium nitrilotriacetic acid (1 g). A bluish-white precipitate formed when NaCl was added to hot solution.

10. Ascorbic acid (1 g). A fine bluish precipitate formed upon cooling and remained suspended for considerable time. The ascorbic acid did prevent the precipitation of some NaCl: the control sample contained 2.92 g solid NaCl, while the solution with ascorbic acid contained only 0.84 g, a complexation of about 66%. Ascorbic acid forms a 1:1 soluble complex with calcium on a mole weight basis. The 1 g of ascorbic acid added was only 0.006 moles, while the calcium in solution was 0.05 moles. More ascorbic acid would have to be added for complete complexation, although the amount might only need to be doubled. The pH of this solution was 2.23. The solution would need pH adjustment to at least 5.0.

11. Glycine (aminoacetic acid) (1 g). Some complexing ability was apparent. The control contained 2.6 g of solid NaCl, while the sample containing glycine contained only 1.95 g of solid NaCl. The pH of this solution was 6.11. Glycine should complex Ca on a 1:1 mole weight basis. The solution contained 0.05 mole of Ca (2 g), and 1 g of glycine was added, which is only 0.03 moles. When the experiment was rerun adding 0.05 mole (3.75 g) of glycine, only 0.81 g of solid NaCl precipitated. The 1:1 mole ratio did not completely negate the effect of the calcium, but it did reduce it by about 60%. The solution turned cloudy with a fine precipitate when the NaCl was added. After several hours at room temperature, the fine precipitate settled. After 24 hours large cubic crystals formed on top of the fine precipitate. The pH of the solution was 5.6.

Appendix V. Comparison of Alpha 1655 and JACAM salt inhibitors

Test 1.   0 Ca Control…..containing no inhibitor
                Weight % inhibitors: 0, 0.54, 1.08, and 3.3
                Volume after addition of inhibitor=73 ml
                27 g NaCl

Test 2.   2.0 g Ca Control…..containing no inhibitor
                Weight % inhibitors: 0, 0.54, 1.08, and 3.3
                2.0 g Ca (19,640 ppm) as $CaCl_2 \cdot 2H_2O$
                Volume after addition of inhibitor and Ca=73 ml
                21.5 g NaCl

Test 3.   5.0 g Ca Control…..containing no inhibitor
                Weight % inhibitors: 0, 0.54, 1.08, and 3.3
                5.0 g Ca (47,920 ppm) as $CaCl_2 \cdot 2H_2O$
                Volume after addition of inhibitor and Ca=73 ml
                14.0 g NaCl

Test 4.   10.0 g Ca Control…..containing no inhibitor
                Weight % inhibitors: 0, 0.54, 1.08, and 3.3
                10.0 g Ca (87,566 ppm) as $CaCl_2 \cdot 2H_2O$
                Volume after addition of inhibitor and Ca=73 ml
                4.5 g NaCl

        For each test, the solutions were prepared and heated to boiling in order to dissolve the NaCl, and then allowed to cool to room temperature. After 24 hours each flask was observed for precipitate formation, pH and solution volume were measured, and 2 ml taken for chloride analysis by titration with $AgNO_3$.

Appendix VI. Distillation of ammonia for determination by specific ion electrode

Equipment and Reagents

- All glass steam distillation unit equipped with a steam-generating vessel with an immersion heater
- 30 ml pharmaceutical graduated cylinder
- Lab Jack
- 50% (w/w) NaOH solution
- Indicator solution: 0.1% Methyl Red and 0.5% Brom-cresol green in alcohol
- Saturated boric acid solution: ~40 g /L in ammonia-free water and 5 ml of indicator solution.

Procedure

- Fill steam generator with ammonia-free water. Turn on Variac and bring water to a boil. Use steam to clean apparatus
- Set Variac at 40 to 50 to keep water in generator close to boiling (higher may be required).
- Add 5 ml of boric acid solution to 30 ml graduated cylinder. Place under the delivery tube using the Lab Jack so that tip of condenser is under the solution
- Open clamp under funnel. Rinse sample, using a minimum amount of RO water, into the funnel
- Add enough NaOH (about 6 ml) solution through the funnel quickly to make sure that the pH is 9.4 or above. Close clamp
- Turn Variac to maximum setting to boil water rapidly, and then set between 70 to 90
- Collect 20 to 25 ml of condensate; after the first 5 ml are collected use the Lab Jack to lower the cylinder to keep the tip of the delivery tube just under the solution. The collection solution should turn from red-brown to blue green
- Rinse off tip of delivery tube
- Remove collection vessel (cylinder)
- Turn Variac down to about 40. Distillation residue will be sucked into the waste vessel
- Rinse funnel and allow this to all be sucked out
- Dilute sample to 50 ml volume with 18 megaohm water.

Ammonia Electrode Procedure

Equipment and Reagents
- pH/mV meter--easiest to use are the direct concentration specific ion meters. A pH/mV meter with readability to 0.1 mV can be used
- Magnetic stirrer
- 4 cycle semi-log paper if direct concentration meter is not available
- Ionic strength adjustor: 5M NaOH/0.05M disodium EDTA and enough 0.1% thymolphthalein in methanol to give a medium blue color

- Internal electrode filling solution (for Orion Ammonia Electrode--951202)
- Stock Ammonium Standard: (200 ppm NH_3-N). Dissolve 3.3 gm of dried $(NH_4)_2SO_4$ in RO water and bring to 1000 ml volume (NH_4Cl can be used, but be careful in drying)

Ammonia Electrode Preparation
- Prepare and condition electrode as described in the instruction manual for the ammonia electrode referenced below.

Standardization for Ammonia Nitrogen
- Select a standard range suitable to the expected concentration in samples. For nitrogen analysis of the Alpha 1655 inhibitor, this range is 2 to 200 ppm. Prepare standards in this range using the stock standard. Prepare a blank using the same water as used to make up the standards. The final volume of the standards and blank should be the same as the samples. This is usually 50 ml
- Place the electrode in the blank/standard and stir gently. The stirring should continue through the analysis
- Ideally the mV difference for a 10-fold change in concentration would be 59.6 mV; usually you will only get close to this.
- Add 2.0 ml of the ISA solution. The solution should turn blue.
- When the reading is stable, record the mV or concentration. Repeat until all standards and the blank have been recorded. Generate a standard curve. Repeat the readings for the samples.

Reference
Ammonia Electrode Instruction Manual for Model 95-12 Electrode, Orion Research, Inc. Beverly, MA.

Appendix VII. Spectrophotometric ferrocyanide analysis

In this method ferrocyanide $[Fe(CN)_6^{-4}]$ is analyzed by converting it to dark blue colored Prussian Blue by the addition of acidic Fe^{+3} and measuring the color spectrophotometrically at 700 nm. The intensity of color is directly proportional to concentration.

Reagents
- Acidic Fe^{+3} indicator: dissolve 1.5 g $FeCl_3$ in 20 ml of distilled water, add 3 ml of concentrated HCl, and dilute to 30 ml.
- Ferrocyanide standard solution (100 ppm): Weigh 0.1994 g of potassium ferrocyanide, dissolve, and dilute to 1000 ml with distilled water.

Standard Curve

Prepare standards of 0, 5, 10, 15, and 20 ppm by diluting 0, 5, 10, 15, and 20 ml of the standard solution to 100 ml in volumetric flasks. Add three drops of Fe^{+3} indicator solution and mix. Wait for 12 minutes and measure the color at 700 nm. Plot a standard curve (Fig. VII-1).
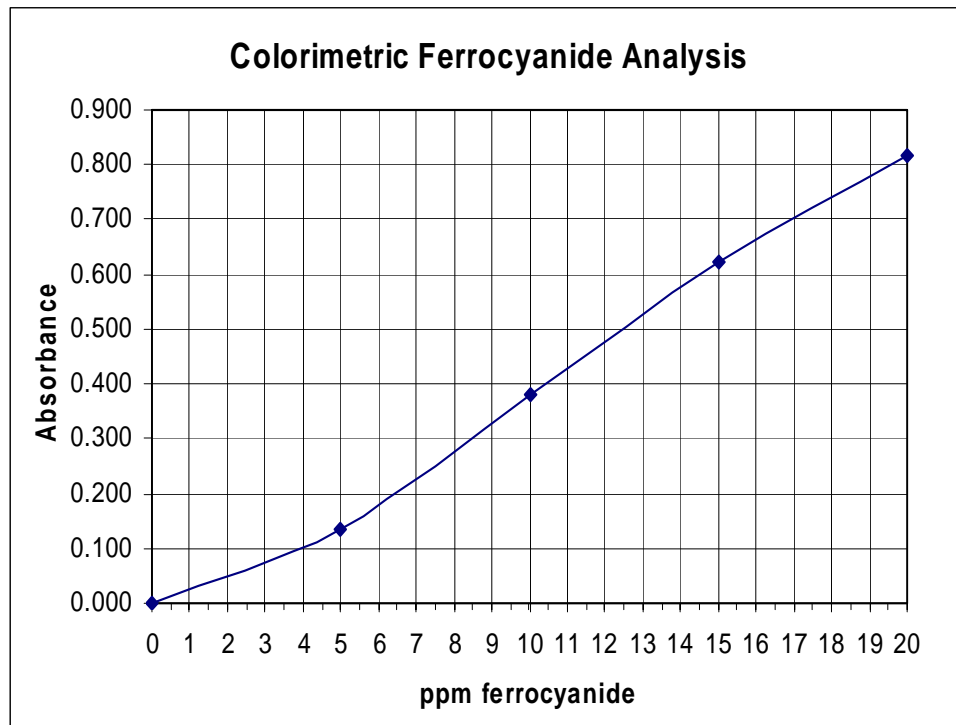
Figure VII-1. Color adsorbtion at 700 nm.

Reference

McGivney, S.E. and Shelton, S.P., Detection and treatment of ferrocyanide generated by the photographic and electroplating industries, Conference on Cyanide and the Environment, Tucson, AZ, 1984.

Appendix VIII. Compatibility test procedure

Prepare 30,000 ppm solutions of Desalt liquid salt inhibitor and Alpha 1665 Salt inhibitor. Photograph brine only (standard seawater, SW) and the prepared chemical solutions (Table VIII-1). Divide prepared chemical solution and add the corrosion inhibitor and scale inhibitor dropwise (record concentration) to test the compatibility of the chemicals. Photograph the results to record change in solution clarity.

Table VIII-1. Test brine composition and concentration (g/L)	
Component	SW brine
NaCl	28
KCl	0.935
$CaCl_2$	1.19
$MgCl_2$	5.368
Na_2SO_4	0
$NaHCO_3$	0
Total dissolved solids, ppm	35,493

If the solution clabbers, chemical incompatibility is indicated. Haze does not mean incompatibility.

Appendix IX. Software application notes

Numerically modeling the thermodynamics of salt precipitation Oli Stream Analyzer thermodynamic software (www.olisystems.com)

Initially the Oli Stream software checks the accuracy of laboratory water analysis by calculating the ion concentrations in the solution and balancing them since water is essentially electro neutral. This is referred to as reconciliation in the software. Once the analyses have been reconciled, the software can be used to predict concentrations and compositions under different conditions of temperature and pressure. Additionally, the software can be used to predict the amount of water that would be required to prevent salt deposition. The layout of the software is straightforward. Inputs required are concentrations of the different chemical constituents of water, which are typically reported as dissolved solids in lab analyses, pH, and temperature. The reporting units English or metric can be changed to suit the needs of the user. The software automatically computes the conversions between different unit systems .
The main window presents the user with the options of adding a water analysis or a stream to compute the required parameters. Shown in Figure IX-1 is the main window presented when the software is invoked.
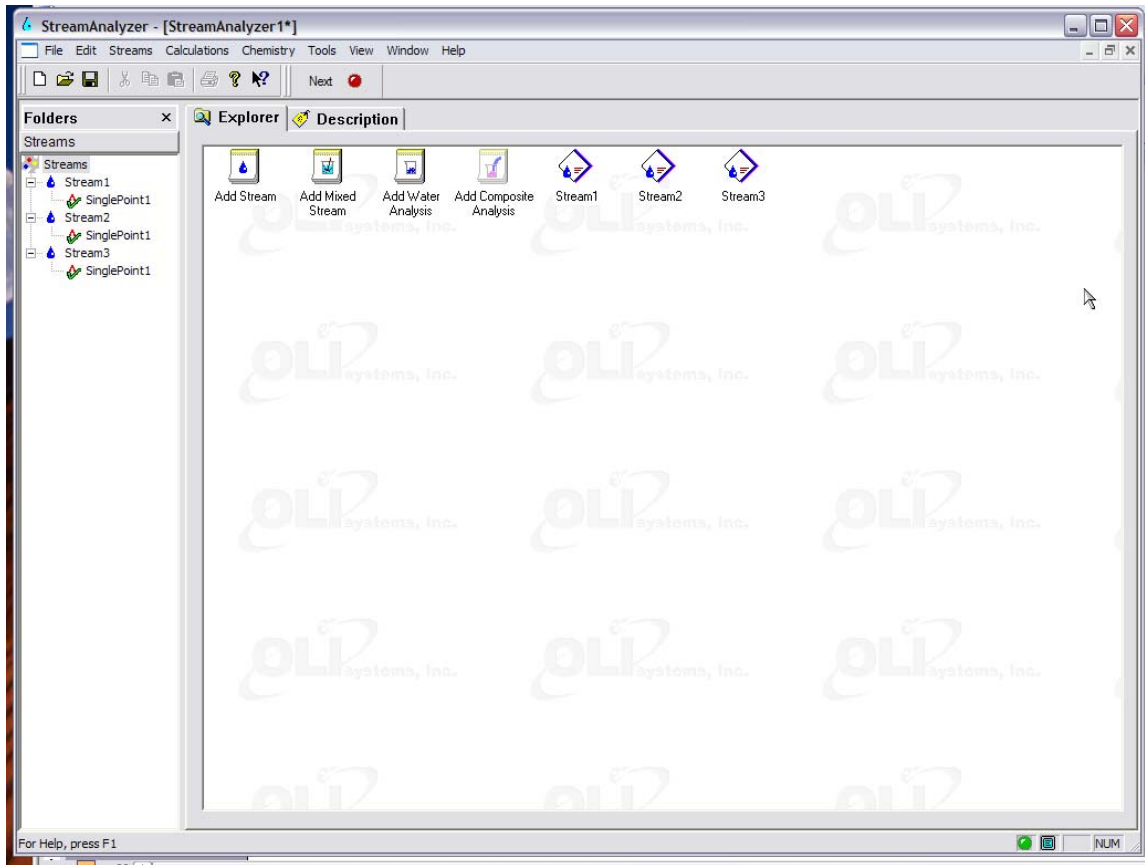
Figure XI-1. Main window of StreamAnalyzer.

The first option of adding a water analysis presents the user with fields in which data from the analytical lab reports can be entered. Typical entries include the temperature at which the analysis was carried out, pH, specific gravity, and the concentrations of the anions and cations in the water. Figure XI-2 shows the data input screen when the water analysis option is selected. The concentrations and the temperature are the most important entries here. The flow is usually assumed to be 1 liter. Once the data is entered, the sample is reconciled to test conditions.
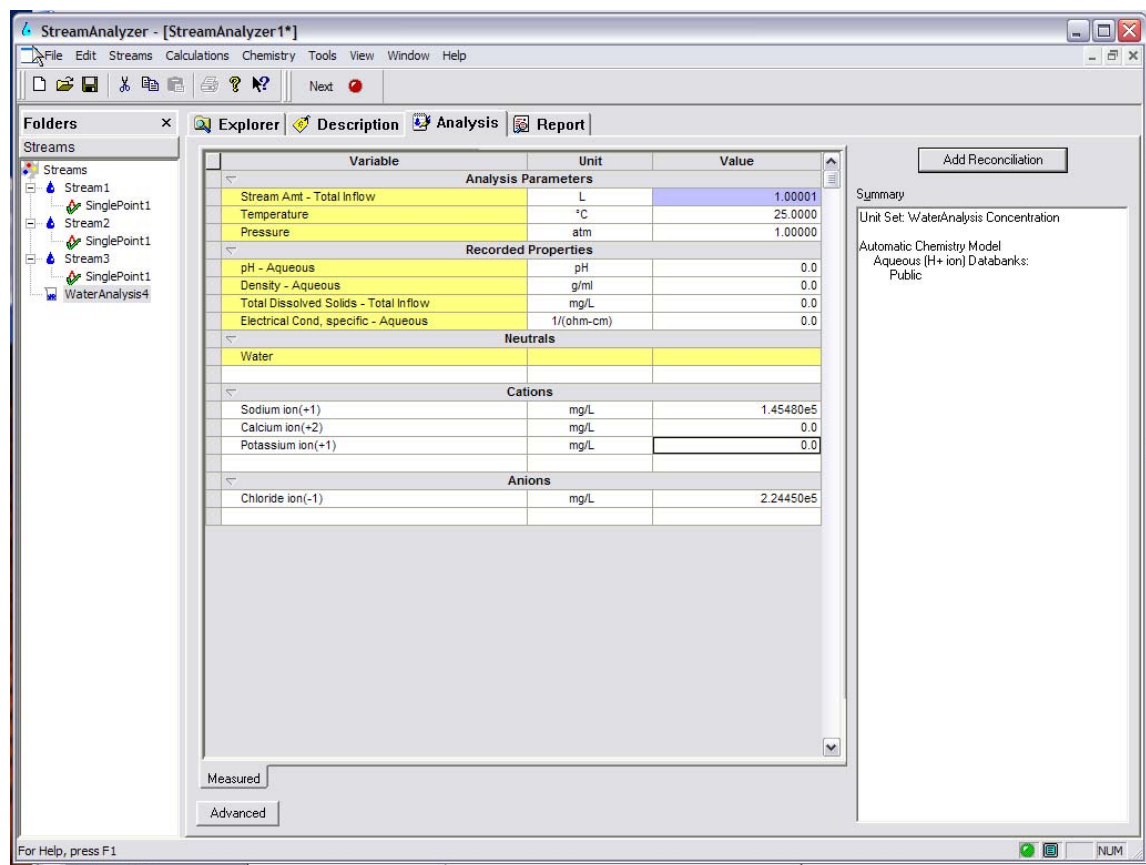
Figure IX-2. Data input screen when Water Analysis is selected.

As stated earlier, reconciliation is a process in which the software checks for electro-neutrality of the solution. This is a very important step because all water samples are electrically neutral, and calculations based on lab tests could be erroneous because the chemical model of the software assumes that all samples are at equilibrium before the measurements are made. The user has several options of choosing which method the software uses to reconcile the sample. The default method calculates the total positive and negative ions present in the solution. The software then calculates the number of cations or anions that have to be added to the solution to neutralize the ion with the greatest concentration.

Other options include choices where the ion used to balance the sample can be selected. The software also allows for reconciliation of the pH. If the pH is not available, then this need not be performed, but if the pH is reported, then the reconciliation can be performed by two methods. The first is to let software automatically reconcile the pH using NaOH and HCl. The

second method allows the user to select the titrants used to do the reconciliation. In most cases, where a pH is reported, the automatic pH reconciliation is used.

This software is designed to solve steady-state problems. Once the sample has been reconciled, it can be added as a stream so that compositions or calculations based on various conditions such as temperature or pressure can be solved. When the reconciled sample is added as a stream, the software converts the sample into the various ionic constituents so that calculations can be performed.

The second option (add mixed stream) directly adds a stream of known components, which can then be analyzed. This requires knowledge of the actual components and their quantities that constitute the inflow other than the ambient conditions such as temperature and pressure. The total inflow here is the sum of the individual components of the inflow streams. Figure XI-3 shows the data input screen when the Add Stream option is selected.
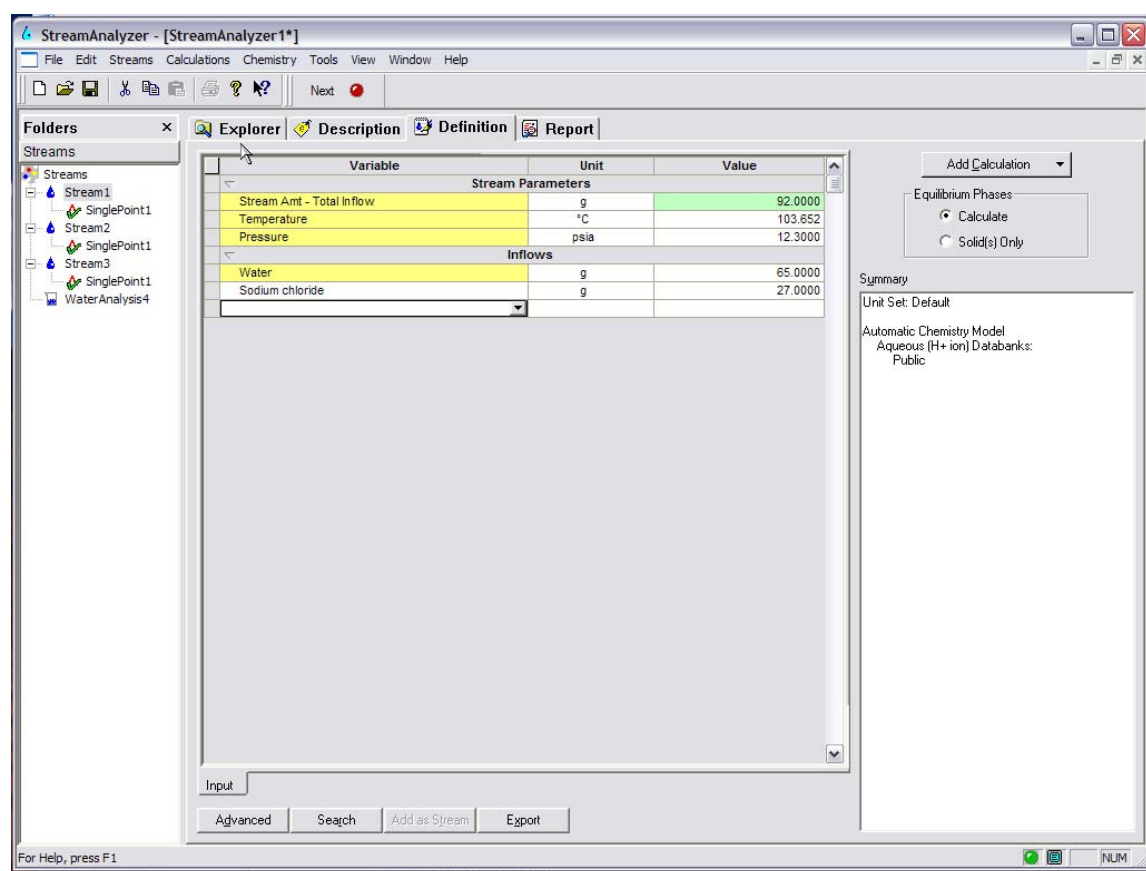
Figure IX-3. Data input screen when Add Stream option is selected.

Once the streams have been defined, the software can then be used to perform calculations. There are three computation algorithms, a single point, survey, and chemical diagram. In a single point calculation, the user specifies conditions at which the calculations are to be performed. An example of this type of calculation is cooling a solution to a specified temperature given initial conditions. A survey calculation is when the variation of the sample solution characteristics (temperature, pressure, or both) is required. An example of this is calculating the solubility of NaCl as a function of temperature. A survey calculation includes a

graph of the variables. The result of a calculation is presented in a report, which gives the details (concentration, enthalpies, Gibbs free energy, for example) of all the species present in solution at the endpoint conditions along with other physical conditions such as temperature and pH. The report also includes the scaling tendencies of the salts in the solution. A scaling tendency close to 1 indicates the likelihood that the precipitating salt is greater than salts that have a lower scaling tendency.

The software has 10 different types of calculations. The default type is constant temperature. Other types of calculations of interest are bubble point calculation (can be used to calculate the boiling point of solutions), dew point calculation (can be used to calculate the condensation point of vapors), and precipitation point. This calculation computes the amount of inflow required to prevent the precipitation of a user-specified salt. This is very useful in estimating the quantity of fresh water to be added to prevent NaCl scaling.

The software was used to simulate a condition where a solution was cooled from $100^{\circ}C$ to $25^{\circ}C$. These results were then compared to actual lab test results. The lab tests consisted of three simple solution recipes containing varying amounts of NaCl, $CaCl_2.2H_2O$, and KCl in water. Solution 1 consisted of 27 g of NaCl in 72 ml of water; Solution 2 consisted of 18.65 g of NaCl, 1.6 g KCl, and 2.979 g of $CaCl_2.2H_2O$ in 72 ml of water; and Solution 3 consisted of 21.77 g of NaCl, 3.7 g KCl, and 6.77 g $CaCl_2.2H_2O$ in 72 ml of water. The static water analysis method was first used to simulate the lab test in a manner similar to that expected with field problems.

To conform to the software input requirements, the concentrations of the individual anions and cations in the solutions were calculated and input into the software. The simulated result for each test was then compared to the lab test result. The two did not agree. This led to an initial conclusion that the chemistry model within the software was not accurate in reproducing actual test results. Further investigation revealed that data from the lab tests were input as g/Kg instead of g/L.

To avoid conversion errors and better simulate the lab tests, the second option of directly inputting the test data as a stream was used. This method generated better agreement with the lab test results; however, the amount of NaCl precipitate predicted was off by a factor of 2. This was a water density problem, caused by the conversion of milliliters to grams. Initially the density used to make the conversion was for pure water at boiling point. This was no longer the case since the addition of the salts to the water caused density changes by as much as 15%. Taking into account the change in the density, the weight of water going into the system was recalculated as shown in Table IX-1. This resulted in predictions that were in better agreement with the lab results. The boiling temperatures of the different samples used to simulate the lab tests were calculated using the software. The key comparative result is that NaCl precipitated, ppt, in the table. The lab and simulation results are compared in Table IX-1.

Table IX-1. Comparison of software results and lab tests									
Sample 1: 27 g NaCl in 72 ml boiling water									
	Cl^{-1} (g)	Na^{+1} (g)	Ca^{+2} (g)	K^{+1} (g)	NaCl (g)	NaCl (ppt) (g)	Water (g)	pH	Vol. (ml)	Temp. (^{o}C)
Lab Test	16.4	10.6	0.0	0.00	27.00	0	--	--	--	106
	14.4	9.3	0.0	0.00	23.72	3.3	--	ND	73	25
Simulation	--	--	--	--	27.00	0	65	--	--	103.7
	14.17	9.19	0.0	0.00	--	3.6	--	6.9	73.5	25
Sample 2: 2.979 g CaCl$_2$·2H$_2$O, 1.6 g KCl, and 24.05 g NaCl in 72 ml of boiling water										
Lab Test	20.87	9.07	0.81	0.84	24.05	0.00	--	--	--	106
	14.85	8.20	0.81	0.84	20.86	2.19	--	ND	72	25
Simulation	--	--	--	--	24.05	0	63	--	--	102
	14.49	7.98	0.81	0.83	--	3.6	--	6.4	72.6	25
Sample 3: 6.77 g CaCl$_2$·2H$_2$O, 3.7 g KCl, and 21.77 g NaCl in 72 ml of boiling water										
Lab Test	18.23	8.56	1.85	1.94	21.76	0.00	--	--	--	106
	14.58	6.19	1.85	1.94	15.75	6.01	--	6.9	72	25
Simulation	--	--	--	--	21.77	--	61.5	--	--	104
	15.02	6.50	1.84	1.92	--	5.30	--	6.15	71.9	25

The results were not absolutely accurate, perhaps because the laboratory system never reached equilibrium. As stated earlier, the chemistry models used in this software assumed that the system is in equilibrium. In the lab, the solution was heated to the boiling point and then cooled immediately; water vapor was not in equilibrium. Therefore, the software could not be used to precisely duplicate the lab test results. However, the software did do a sufficient job of simulating the laboratory test results.

Water analyses for the northeastern storage facilities are shown in Table X-1. Table X-2 shows the water analyses for the California facilities.

	Goodwell	Reed City	Lincoln	Muehleisen	Smith	Whitewater	Sharrow	Belle River	Brine Pond
Table X-1. Brine analyses of northeastern storage facilities									
	mg/L	mg/L	mg/L	mg/L	mg/L	mg/L	mg/L	mg/L	mg/L
B	14.6	4.07	4.7						
P	15.19	7	9.22						
Si	5.4	6.77	3.96						
Al	3.47	4.66	2.47						
Ba	2.9	0.66	0.7	19	22	23	24		
Ca	41133	34937	3233	57600	64400	99600	60400	74000	48900
Mg	825	8020	7833	7739	20447	12258	13359	8000	5540
Mn	9986	24	26						
K	1790	3677	11422					4500	
Na	49146	58589	56556	44396	30050	70046	54083	42000	61100
Sr	937	575	522						
Zn	6.44	1.43	2.39						
Pb	6.61	3.08	3.96						
Fe	0	356	744	5	50	0.5	10	3.6	
Br	1459	1718	1318						
Cl	168584	181245	172667	170000	160000	284000	190000	214500	221000
F	316	242	277						
SO$_4$	487	230	342	300	150	5	200	57	
HCO$_3$				98	207	31.1	67		
Total Hardness				175000	244000	298000	205000	185000	
TDS	274,718	289,641	254,967	280,157	275,326	465,964	318,143	343,061	336,540

	Goleta Miller #7	Goleta Production Tank #4	Aliso Canyon Bailer Sample	Aliso Canyon Reservoir Brine
Table X-2. California water analyses				
SI, mg/l	17	28.7		
B(OH), mg/l				114
Na, mg/l	7,945	890	85,400	4,840
Ca, mg/l	82,500	727	1,480	341
Mg, mg/l	2,400	92	43	275
Ba, mg/l		4	1.1	
Fe, mg/l	18,250	169	61	
Mn, mg/l				0.18
K, mg/l		26.2	4,110	37
Sr, mg/l				
Zn, mg/l				
Pb, mg/l				
Br, mg/l				
Al, mg/l				
Cu, mg/l			0.1	
Cl, mg/l	164,875	2600	110,000	9,640
HCO$_3$, mg/l	100	430	16	
SO$_4$, mg/l	240	210	320	
TDS, mg/l	277,390	10,970	201,431	15,247
Hardness, mg/l				1880

Appendix XI. Enlarged Version of Figure 19

Upper left of Fig. 19.

Pounds Precipitate Per 1.8 Pounds of water, From Water Analysis

Upper right Fig. 19

Pounds Precipitate Per 1.8 Pounds of Water After 30% Evaporation Leaving 1.25 Pounds of Water

Lower left of Fig. 19

Pounds Precipitate Per 1.8 Pounds of WaterAfter 33% Evaporation Leaving 1.2 pounds of Water

Lower right of Fig. 19

Pounds Precipitate Per 1.8 Pounds of Water After 44% Evaporation Leaving 1 Pound of Water

Legend:
- NaCl - Sol [lb] - Pressure = 1600.00 psia
- NaCl - Sol [lb] - Pressure = 2600.00 psia
- NaCl - Sol [lb] - Pressure = 3600.00 psia
- FeCO3 - Sol [lb] - Pressure = 1600.00 psia
- FeCO3 - Sol [lb] - Pressure = 2600.00 psia
- FeCO3 - Sol [lb] - Pressure = 3600.00 psia
- BaSO4 - Sol [lb] - Pressure = 1600.00 psia
- BaSO4 - Sol [lb] - Pressure = 2600.00 psia
- BaSO4 - Sol [lb] - Pressure = 3600.00 psia

Y-axis: Dominant Solids
X-axis: Temperature [°F]

EWI Project Numbers: 49745GTH and 49658CSP
PRCI Project No.: PR-185-06702
GSTC Project No.: 3138-EWI-DOE-1779

State-of-the-Art Assessment of Alternative Casing Repair Methods

Final Technical Report

Reporting Period:
June 1, 2006 through May 31, 2007

Principal Authors:
Matt Boring and Nancy Porter

Report Issued: June 27, 2007

DOE Award No.: DE-FC26-03NT41779

Submitted By:
Edison Welding Institute
1250 Arthur E. Adams Drive
Columbus, OH 43221

DISCLAIMERS

DOE NETL Disclaimer

This report was prepared as an account of work sponsored by an agency of the United States Government. Neither the United States Government nor any agency thereof, nor any of their employees, makes any warranty, express or implied, or assumes any legal liability or responsibility for the accuracy, completeness, or usefulness of any information, apparatus, product, or process disclosed or represents that its use would not infringe privately owned rights. Reference herein to any specific commercial product, process or service by trade name, trademark, manufacturer, or otherwise does not necessarily constitute or imply its endorsement, recommendation, or favoring by the United States Government or any agency thereof. The views and opinions of authors expressed herein do not necessarily state or reflect those of the United States Government or any agency hereof.

PRCI Disclaimer

This report is furnished to Pipeline Research Council International, Inc. (PRCI) under the terms of PRCI contract (PR-185-06702), between PRCI and EWI. The contents of this report are published as received from EWI. The opinions, findings, and conclusions expressed in the report are those of the authors and not necessarily those of PRCI, its member companies, or their representatives. Publication and dissemination of this repot by PRCI should not be considered an endorsement by PRCI of EWI, or the accuracy or validity of any opinions, findings or conclusions expressed herein.

In publishing this report, PRCI and EWI make no warranty or representation, expressed or implied, with respect to the accuracy, completeness, usefulness, or fitness for purpose of the information contained herein, or that the use of any information, method, process, or apparatus disclosed in this report may not infringe on privately owned rights. PRCI and EWI assume no liability with respect to the use of, or for damages resulting from the use of, any information, method, process, or apparatus disclosed in this report.

The text of this publication, or any part thereof, may not be reproduced or transmitted in any form by any means, electronic or mechanical, including photocopying, recording, storage in an information retrieval system, or otherwise, without the prior, written approval of PRCI.

DOE NETL ACKNOWLEDGEMENT

Measurement Units -- SI Metric System of Units are the primary units of measure for this report followed by their U.S. Customary Equivalents in parentheses ( ).

Note: SI is an abbreviation for "Le Systeme International d'Unites."

ABSTRACT

The objective of this project was to review current state-of-the-art casing repair technologies to identify more cost effective alternatives. The most prominent form of underground U.S. gas storage is depleted reservoirs. American Petroleum Institute specification 5CT contains the industry standard design guidance for new casings; however, there are no industry standard repair procedures and each state has their own. The most common state required repair integrity test is pressure testing. Casings must withstand tensile, burst, and collapse loads. Most state repair procedures do not specify a target mechanical property that defines repair success. It is therefore easy to assume that a repair should return a casing back to its original integrity level; however, it may not be necessary. The major types of damage mechanisms are corrosion, threaded connection separation, sealant leaks, split casings, and drill bit damage. While a literature search indicated that the most commonly used types of cost effective repair processes are squeezes, liners, and plating, industry feedback indicated that liner repair is the most commonly used repair process. Adhesively bonded, helically-wound, steel strip repair and magnetic pulse welding are the most promising alternative repair technologies identified, mainly because both are applicable for a broad range of damage types and as an alternative to both traditional casing liner and expandable tubular repair technologies.

TABLE OF CONTENTS

LIST OF GRAPHICAL MATERIALS

LIST OF TABLES

LIST OF EQUATIONS

1.0 INTRODUCTION

Many natural gas storage wells suffer damage during normal storage operations. Storage operators spend upwards of $100 million per year recovering lost deliverability.[1] Damage to casings in gas storage wells is largely the result of localized loss of metal from corrosion; however, other types of damage do occur. Individual corrosion pits can be found either on the inside or outside of the casing wall.[2]

Repair methods that are currently used for natural gas storage well casings include patches, plugs, liners, etc. While currently-used repair methods can be a cost-effective means of repairing damaged casings as compared to the cost of running an entirely new casing, there is a need to identify and develop alternative casing repair methods that are more economical and/or do not have inherent operational disadvantages. Many of the current repair methods are proprietary, and as a result, are relatively costly to perform. In addition, many of these repair methods (e.g., tube and packer system repairs) result in a decreased cross-sectional area, which creates operational limitations due to flow restrictions and reduces the ability to perform well logging operations.

The objective of this project was to survey state-of-the-art repair technologies used to repair casing damage and to identify better alternatives to currently-used methods. Alternative repair methods for natural gas storage well casings are needed to lower the costs of casing repairs and to reduce operational constraints that result from repair methods that reduce the inside diameter of the casing.

Project work featured surveys and literature searches that focused on both the oilfield industry and other industries that have developed repair technologies that could be adapted to storage wells casings. An example of the latter is the pipeline industry, where work on methods of repairing line pipe might be adapted for storage well casing repairs.

Several repair methods that are commonly applied to the inside of pipelines (e.g., gas distribution lines, water lines, etc.) to restore leak tightness are, in theory, applicable to natural gas storage well casings. It may also be possible to identify novel repair methods that have potential to restore both leak tightness and structural integrity. In order to evaluate the

---

[1] Watson, B., Johnson, D., and Driscoll, D., "Consortium to Research U.S. Storage System," GasTIPS, Volume 10, Number 3, Gas Technology Institute, Chicago, Illinois, Summer 2004.

[2] Swanson, R.K., De Los Santos, A., Miller, D., "Improved Methods for Inspecting Gas Storage Well Downhole Casing," Final Report for PR-15-614 to Pipeline Research Council International, Southwest Research Institute, San Antonio, Texas, January 1, 1987.

applicability of a new casing repair technology, at a minimum, the following issues need to be addressed:

- Equipment must be developed to perform repairs remotely.

- The feasibility of mobilizing the repair equipment through the casing to areas that require repair must be determined.

- How well the repair methods meet the structural integrity requirements of natural gas storage well casings must be quantified.

- The ability of the repair to survive in a natural gas storage well environment must be tested.

This project focused primarily on the needs of natural gas storage well operators. However, the repair needs of operators of liquid petroleum product systems (e.g., liquid propane gas, crude oil, propylene, ethylene, brine, etc.) were also considered. Where appropriate, repair methods that are applicable only to certain types of service were differentiated from those that have universal applicability.

2.0 EXECUTIVE SUMMARY

The objective of the project was to survey current state-of-the-art storage well casing repair technologies and to identify preferred alternative repair methods, which have the potential to reduce repair cost and operational constraints after repair.

EWI provided overall project management, interfacing with the Gas Storage Technology Consortium (GSTC) of The Pennsylvania State University, Pipeline Research Council International, Inc. (PRCI), and industry (i.e., GSTC and PRCI member companies). GSTC provided $45,000 and PRCI provided $30,000; the total project budget was $75,000. The PRCI funding was used to accomplish Tasks 1, 2, 3, 4 and a portion of Task 5. The GSTC funding was used to complete Task 5 activities and for all of Tasks 6, 7, and 8 activities. Following is a summary of all project accomplishments.

Task 1 – Review of Design Requirements
With input from the gas storage industry, design requirements for natural gas storage well casings were reviewed, including industry code requirements, company specifications, industry guidelines, etc. The vast majority of existing U.S. gas storage is in depleted reservoirs that are close to consumption centers. The most common design guidance for new casing fabrication is American Petroleum Institute 5CT, which does not include repair requirements for damaged casings. There is no standardized U.S. document for casing repair procedures; however, each state and/or company has their own casing repair requirements.

Task 2 – Review of Service Loads and Service Environments

With input from the gas storage industry, service loads and environmental conditions that natural gas storage well casings are exposed, both in service and during workover, were reviewed. The most important loads that a casing must withstand are tensile, burst, and collapse. Other factors that affect casing loads are earth movements and temperature variations. All in all, there is very little published literature on casing loads. Since the majority of state and company mandated repair procedures do not specify mechanical properties, it is easy to assume that a repair should return the casing integrity back to the original state, but this may not be the most appropriate measure of repair success.

Task 3 – Review of Damage Mechanisms

With input from the gas storage industry, scenarios that require repair were identified. The major types of casing damage mechanisms are corrosion, threaded connection separation, thread sealant leak, parted or split casings due to internal defect, and drill damage. In underground structures, internal and external corrosion causes include joining of dissimilar metals, non-homogeneous soil, differential aeration, and microbiological attack. Internal corrosion is reduced by using products to inhibit microbiological corrosion. The potential of external corrosion can be reduced by a good cement job or cathodic protection.

Task 4 – Review of Existing/Currently-Used Repair Technologies

With input from the gas storage industry and an extensive literature survey, current methods that are used to repair natural gas storage well casings were reviewed. The most expensive and complex options that companies use to repair casings are full string casing repair and cut out and replace. The most commonly used type of cost effective repair process used by industry is a liner repair.

Task 5 – Review of Candidate Alternative Repair Methods

With input from the gas storage industry, a variety of technologies were reviewed including mechanical sleeves, fiber reinforced composites, other composite systems, epoxy repair technology, etc. Four candidate alternative casing repair methods were identified: weld deposition repair; adhesively bonded, helically-wound, steel strip repair (a.k.a., helical strip repair); laser cement drilling; and magnetic pulse welding (MPW).

Task 6 – Assessment of Alternative Repair Method Capabilities

A matrix of the four alternative repair methods was created to compare and contrast the attributes of the candidate alternate casing repair methods. The two most promising alternative repair processes are the internal helical strip repair and MPW. EWI conducted one set of hydrostatic burst tests to determine the feasibility of using the helical repair technology to repair casings that are bent as a result of earth movements. The results of the hydrostatic burst tests using the helical strip repair on bent casing with simulated corrosion was not as promising as

the previous experimental results using straight pipe. Therefore, the experimental results did not support future development of helical strip repair for bent casings due to earth movements.

<u>Task 7 – Development of Recommendations</u>
Both helical strip repair and MPW show the greatest promise for a broad range of damage types and as an alternative to both traditional casing liner and expandable tubular repair technologies. Preliminary cost estimates show that while helical repair is quite economical, it takes several days to install. On the other hand, MPW is quite expensive in terms of capital equipment, but can be completed in minutes. Both the helical strip repair and MPW should be further evaluated as alternatives for improved casing repair.

3.0   EXPERIMENTAL

3.1   Project Team

Edison Welding Institute (EWI) performed the activities supported by this award with $45,000 provided by the Gas Storage Technology Consortium (GSTC) of The Pennsylvania State University (via Subaward No. 3138-EWI-DOE-1779) under Department of Energy (DOE) Award No. DE-FC26-03NT41779 between GSTC and DOE. Additionally, Pipeline Research Council International, Inc. (PRCI) provided a cash cost share contribution of $30,000 (via contract No. PR-185-06702), which represents a 40% cost share. The total project budget was $75,000. The PRCI cost share contribution was used to accomplish Tasks 1, 2, 3, 4 and a portion of Task 5. The GSTC funding was used to complete the remaining Task 5 activities and all of Tasks 6, 7, and 8 activities. EWI provided overall project management (interfacing with GSTC, PRCI and industry) and lead the assessment of alternative casing repair methods.

Based in Columbus, OH, EWI is North America's leading engineering and technology organization dedicated to welding and materials joining. EWI's staff provides materials joining assistance, contract research, consulting services, and training to over 3,300 member company locations representing world-class leaders in the energy and chemical, aerospace, automotive, defense, energy, government, heavy manufacturing, medical, and electronics industries. EWI is an internationally recognized leader in pipeline welding, nondestructive evaluation (NDE), fitness-for-purpose technology, and pipeline repair.

Based at Pennsylvania State University, the Gas Storage Technology Consortium is industry-driven, membership based organization created to assist in the development, demonstration and commercialization of technologies to improve to improve the integrity, flexibility, deliverability, and cost-effectiveness of the nation's underground natural gas/hydrocarbon storage facilities.

PRCI is a not-for-profit corporation comprised of energy pipeline companies. Although originally focused on technology development for the gas transmission pipeline industry across the research spectrum from basic to applied, over the years PRCI has increasingly focused on near-term integrity and reliability solutions to design and operating problems and realizing the opportunities that an industry-managed program generates. As the focus of the work has evolved and broadened, so too has PRCI's membership with an increasing focus on oil and petroleum products pipelines.

3.2 Scope of Work

The project focused primarily on the needs of natural gas storage well operators. However, the repair needs of operators of liquid petroleum product systems (e.g., liquid propane gas, crude oil, propylene, ethylene, brine, etc.) were also considered. Where appropriate, repair methods that are applicable only to certain types of service were differentiated from those that have universal applicability.

Natural Gas Storage Industry Feedback

Input from the natural gas storage industry was critical to the success of this project. Two methods were employed to collect input: an Email inquiry[3] and a formal online survey.[4] The Email inquiry and online survey were designed to benchmark current repair practices and operating conditions. Appendix A contains the Email Inquiry and its resultant industry input. Appendix B contains the formal online survey and Appendix C contains the industry response to the online survey as of March 23, 2007.

Task 1 – Review of Design Requirements

No experimental methods or apparatus were used to accomplish this task. With the help of industry,[3,4] EWI engineers reviewed the design requirements for natural gas storage well casings. This review included code requirements, company specifications, industry guidelines, etc.

Task 2 – Review of Service Loads and Service Environments

No experimental methods or apparatus were used to accomplish this task. With the help of industry,[3,4] EWI engineers reviewed the service loads and environmental conditions that natural

---

[3] Email Inquiry from Matt Boring of EWI to GSTC Member Companies on November 10, 2006.

[4] State-of-the-Art Assessment of Alternative Casing Repair Methods, online survey conducted by EWI via SurveyMonkey.com from March 13, 2007 through April 20, 2007

gas storage well casings are exposed to, both in-service and during workover. This included pressure (hoop stress), axial loads (longitudinal stress), transient loads, loads due to temperature fluctuation, and exposure to corrosive environments.

Task 3 – Review of Damage Mechanisms

No experimental methods or apparatus were used to accomplish this task. With the help of industry,[3,4,5] EWI engineers identified scenarios that require repair. The vast majority of repairs are required for corrosion although the need for repair of other damage (e.g., perforations, split casings, drill damage, etc.) were also identified. The need for restoration of leak tightness vs. the need for the restoration of structural integrity (i.e., the ability to carry hoop and longitudinal stress) was also addressed.

Task 4 – Review of Existing/Currently-Used Repair Technologies

No experimental methods or apparatus were used to accomplish this task. With the help of industry,[3,4] EWI engineers reviewed existing methods that are currently used to repair natural gas storage well casings. This review consisted of a literature search, a web-based search, and interviews with natural gas storage facility operators (e.g., PRCI member companies) and service providers (e.g., Halliburton, Schlumberger, Baker Hughes, etc.). The literature search portion of this task was conducted using online, subscription-based scientific data bases.

Task 5 – Review of Candidate Alternative Repair Methods

No experimental methods or apparatus were used to accomplish this task. EWI engineers identified candidate alternative repair methods for natural gas storage well casings. In a recently completed EWI project for the DOE's National Energy Technology Laboratory (NETL), alternative repair methods for natural gas transmission pipelines were identified and assessed.[6] The NETL project focused on repair methods that could be deployed from inside the pipeline (internal or trenchless repair methods). The repair methods included mechanical sleeves, fiber reinforced composites, other composite systems and epoxy repair technology and served as a valuable starting point for the current project. Welding repair, adhesively bonded, helically-wound, steel strip repair (a.k.a., helical strip repair) and magnetic pulse welding (MPW) were also reviewed as part of this task.

---

[5] Private Communication, John Rogers Smith, Louisiana State University, August 28, 2006.

[6] Bruce, W., Boring, M., Porter, N., Ritter, G., Harris, I., Mohr, W., Harwig, D., Dierksheide, J., Gordon, R., Neary, C. and Sullivan, M., "Internal Repair of Pipelines" Final Report to National Energy Technology Laboratory, U.S. Department of Energy, DOE Award No.: DE-FC26-02NT41633, Edison Welding Institute and Pacific Gas & Electric, July 2004.

Task 6 – Assessment of Alternative Repair Method Capabilities

A matrix of alternative repair methods was created to compare and contrast the various attributes of each repair method. The results from the comparison indicated that two alternative repair technologies showed the most promise: helical strip repair and MPW. Feasibility categories were established and subdivided into capabilities; each were ranked with respect to different damage mechanisms. During a teleconference with GSTC, DOE and GSTC member companies on March 26, 2007, this task was modified to include one set of hydrostatic burst tests to determine the feasibility of using helical strip repair technology to repair casings that are bent as a result of earth movements. Three pipe sections were hydrostatically tested until rupture. The first pipe was in the "virgin" condition (i.e., unbent) with no repair. This established the baseline strength of undamaged pipe and was used to determine the acceptability of the repaired pipe. The second pipe was bent to simulate damage due to earth movement and hydrostatically tested to determine the effect bending the pipe had on the burst pressure to establish the "as damaged" strength. The third pipe was bent with simulated corrosion and a through hole, which was repaired with the helical strip repair. A through hole was added to the damaged pipe, because the results of the previous tasks indicated that repairs are made mainly to repair leak tightness of the casing. This pipe was burst tested to determine the "as repaired" strength. Burst test results were then compared to determine whether this technology shows promise for repairing casings bent due to earth movements.

Task 7 – Development of Recommendations

With the help of industry, EWI engineers developed recommendations for either the use of repair methods that are fully developed and readily adaptable to natural gas storage well casings or for further development of methods that are not fully developed that would require adaptation for natural gas storage well casing repair. For methods that are not fully developed, the time and resources required for development were estimated.

Task 8 – Reporting

EWI engineers produced a comprehensive final report describing all aspects of the project. The same report was provided to GSTC and PRCI. Quarterly technical reports were delivered in accordance with the schedule (contract Attachment 4) and format (Section D.4.10 Guidelines for Organization of Technical Reports) as specified in the GSTC/EWI Subaward No. 3138-EWI-DOE-1779. The GSTC quarterly technical reports were also provided to PRCI in accordance with Exhibit A of the PRCI/EWI Agreement No. PR-185-06702. In addition, this task included time and travel to two project review meetings.

4.0 RESULTS AND DISCUSSION

4.1 Task 1 – Review of Design Requirements

This report section summarizes the literature search results and industry input for natural gas storage industry demographics, casing design guidance requirements, and currently-used casing materials.

4.1.1 Natural Gas Storage Industry Demographics

There are three main types of underground natural gas storage facilities: depleted reservoirs, aquifers, and salt caverns. The most prominent and common form of underground storage is depleted reservoirs (86% of total), which consists of formations that have already been tapped of all their recoverable natural gas. Aquifers are the next largest form of underground storage (10% of total). Aquifers are underground porous, permeable rock formations that act as natural water reservoirs. In certain situations, these water containing formations may be reconditioned and used as natural gas storage facilities. Underground salt formations are another option for natural gas storage and represent the least number of storage facilities (4% of total). Underground salt formations are well suited to natural gas storage because, once formed, they allow little injected natural gas to escape from the formation unless specifically extracted. A graphical representation of the percent of underground natural gas storage facilities by type is shown in Figure 1.[7,8]
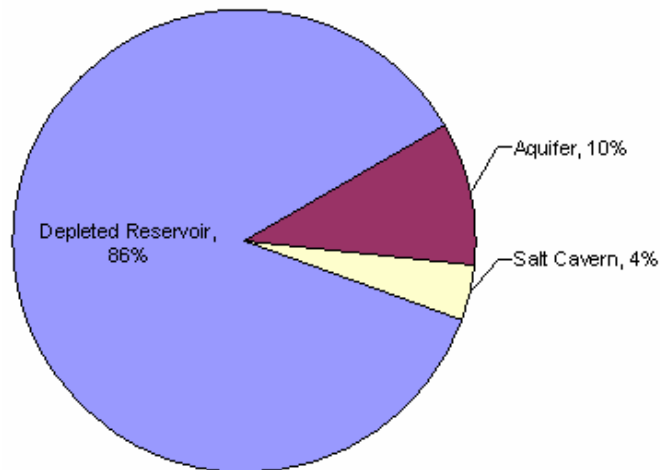
Figure 1. Working Gas Capacity by Type of Storage[8]

---

[7] Storage of Natural Gas, from http://www.naturalgas.org/naturalgas/storage.asp

[8] The Basics of Underground Natural Gas Storage, from http://www.eia.doe.gov/pub/oil_gas/natural_gas/analysis_publications/storagebasics/storagebasics.html. Energy Information Administration (EIA), EIA Gas Tran Geographic Information System Underground Storage Data Base

The vast majority of existing U.S. gas storage is in depleted reservoirs that are close to consumption centers. Conversion of a field from production to storage duty takes advantage of existing wells, gathering systems, and pipeline connections. Aquifers and salt caverns, on the other hand, normally require a substantial amount of resources to prove the viability as a natural gas storage facility, as well as, developing the required infrastructure. Figure 2 shows the location of underground natural gas storage facilities in the lower 48 states.[7,8]
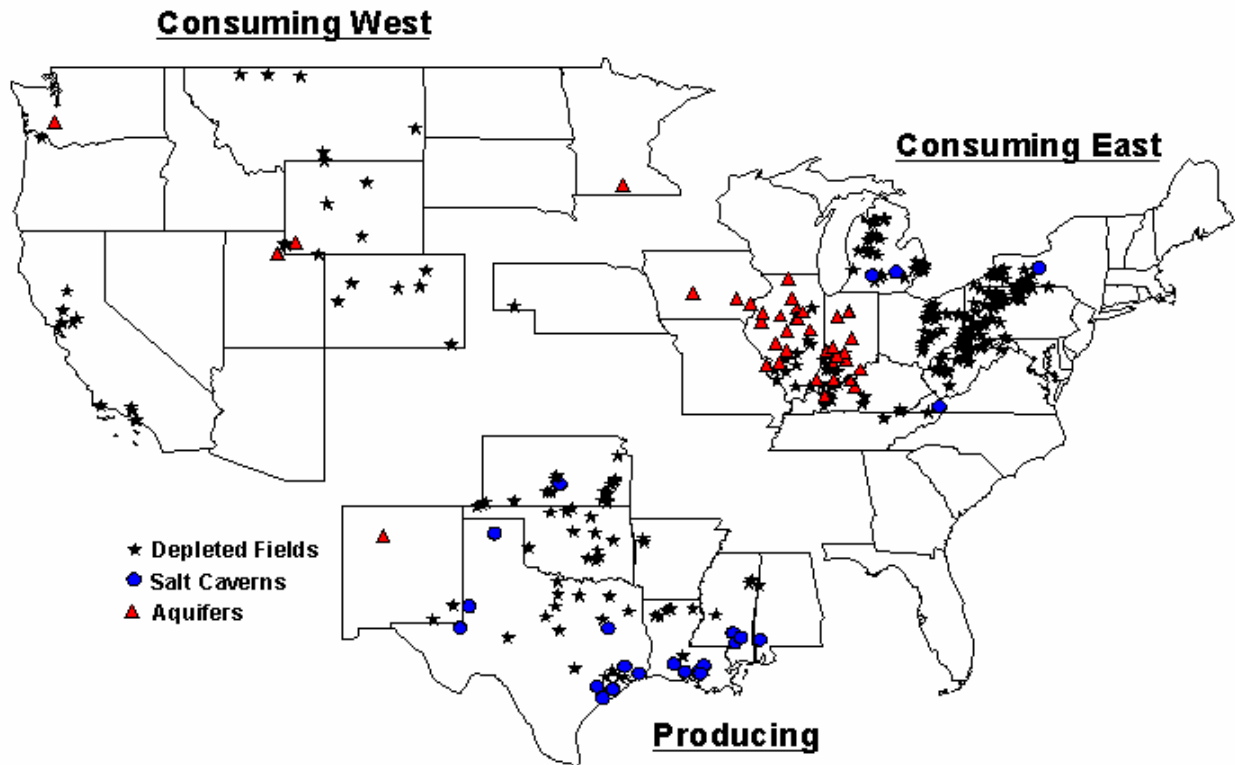
Figure 2. Natural Gas Storage Facilities in the Lower 48 States[8]

Fourteen of fifteen survey[4] respondents indicated that their companies own or operate depleted reservoirs; two respondents also operate aquifers; one also operates a salt cavern. The remaining respondent only operates a salt cavern (see Figure 3). Compared to the demography of the underground natural gas storage industry (Figure 1), survey[4] respondents represented a realistic cross section of the industry (Figure 3).
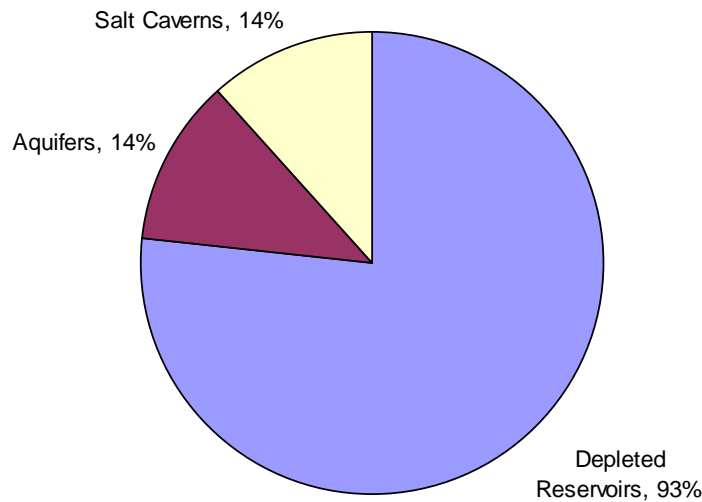
Figure 3. Gas Storage Facilities Operated by Survey Respondents[4]

4.1.2 Casing Design Guidance

The most common design guidance for casing fabrication is American Petroleum Institute (API) specification 5CT.[9] The scope of API 5CT states, "this International Standard specifies the technical delivery conditions for steel pipes (casing, tubing, plain end casing liners and pup-joints) and accessories." API 5CT does not include the qualifications for a repair of a damaged casing.

4.1.3 Survey Responses to Currently-Used Casing Materials Questions

Thirteen respondents[4] provided outside diameters, lbs./ft. ratings, and material specifications for the casing materials that they use. One respondent divided their materials into "surface" casings (Table 1) and "production" casings (Table 2); another identified his as "liquid service well" casings (Table 3); and a third respondent specified his as "flowstring" casings (Table 4). Wall thickness data was not reported for the materials in Table 1 through Table 4 but can be

---

[9] American Petroleum Institute, Specification for Casing and Tubing – API Specification 5CT. 2001, ISO 11960:2001, Petroleum and Natural Gas Industries – Steel Pipes for Use as Casing and Tubing for Wells. 2002.

inferred from the lb./ft. rating. The remaining respondents[4] did not specify their casing application; this data is contained in Table 5, which is the only table that contains reported wall thickness data.

Table 1. Surface Casing Materials Used by 1 Survey Respondent

Diameter (in.)	Rating (lbs./ft.)	Material Type
10.75	32.75	H-40
10.75	40.5	H-40
13.375	48	H-40

Table 2. Production Casing Materials Used by 1 Survey Respondent

Diameter (in.)	Rating (lbs./ft.)	Material Type
5.5	14	K-55
5.5	15.5	K-55
7	20	J-55
7	23	L-80

Table 3. Liquid Service Well Materials Used by 1 Survey Respondent

Diameter (in.)	Rating (lbs./ft.)	Material Type
9.625	54	K-55
10.75	54	K-55
13.38	61	K-55
13.38	72	S-95

Table 4. Flowstring Materials Used by 1 Survey Respondent

Diameter (in.)	Rating (lbs./ft.)	Material Type
3.5	9.2	J-55
4.5	10.5	J-55
4.5	11.6	N-80
5.5	15.5	J-55
5.5	17	J-55
7	20	J-55
7	23	N-80

Table 5. Unspecified Casing Materials Used by Remaining Survey Respondents

Diameter (in.)	Wall (in.)	Rating (lbs./ft.)	Material Type
4.5		10.5	K-55
4.5	0.224	10.5	K-55
4.5		11.6	N-80
4.5		17-23	J-55
5.5	0.244	14	H-40
5.5	0.263	15	J-55, K-55
5.5	0.275	15.5	J-55
5.5		15.5	J-55
5.5	0.275	15.5	K-55
5.5		17	N-80
5.5	0.304	17	K-55
5.5		17-23	J-55
5.5			J-55
6.625		20	K-55
7	0.231	17	H-40
7	0.301	22	J-55, K-55
7	0.317	23	K-55
7		23	K-55
7		26	N-80
7		26	K-55
7.625	0.328	26.4	K-55
8.625	0.264	24	J-55, K-55
8.625		24	H-40
8.625		32	J-55
8.625		32	H-40
8.625	0.352	32	K-55
8.625		32	K-55
9.625		36	J-55
9.625	0.352	36	J-55
9.625		36	K-55
9.625		48	H-40
13.375	0.38	54.5	J-55
13.38		61	J-55

The median diameter size of all reported casing materials is 7-in. Survey respondents[4] did not indicate the quantity of each pipe diameter used; therefore, it is not possible to definitively identify the most commonly used pipe diameter.

The percentage of pipe materials used is shown in Figure 4. K-55 and J-55 are used most often. Again, survey respondents[4] did not indicate the quantity of each pipe grade used; therefore, it is not possible to definitively identify the most commonly used material.
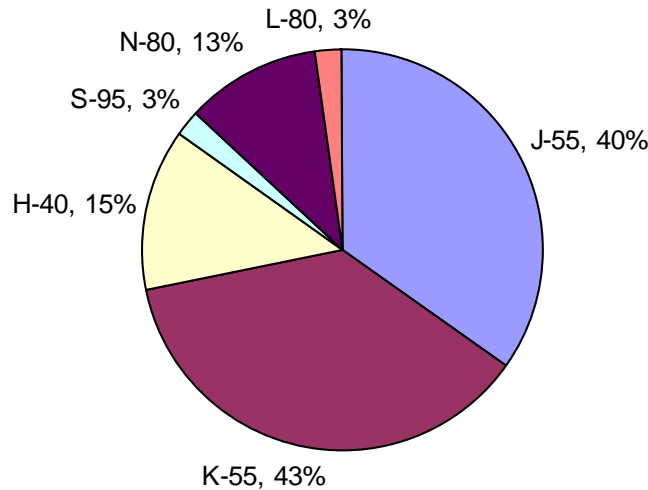
Figure 4. Percentage of Pipe Materials Used

4.2 Task 2 – Review of Service Environments and Service Loads

This report section summarizes the literature search results and industry input for service environments and service loads.

4.2.1 Service Environments

Casings are exposed to a wide variety of environments many of which result in casing corrosion. Well environments can contain carbonates or are highly alkaline, while others can contain hot salty gas water that contains elemental sulfur. Any of these environments can exist in the same type of rock formation. Since all wells are different, the casing will corrode differently depending on the environment. The corrosion can be external or internal and is influenced by the composition of the surrounding rock formation and the product in the well.

Each well and/or storage facility has specific characteristics that are dependent on the rock formations and the downhole environment, which includes the products that are precipitating out of the rock formations. Each well acts differently; the service loads and environments that the each downhole casing is exposed to cannot easily be compared. For this reason, it is extremely difficult to make general statements that are applicable to all storage wells.

In spite of these differences, there are typically three rock types that make up the outer layers of the earth: igneous, sedimentary, and metamorphic. Igneous rocks (e.g., granite and obsidian) are solidified products of magmatism and volcanism that seldom host any significant accumulations of hydrocarbon concentrations. Sedimentary rocks (e.g., sandstone, limestone,

and shale) are composed of materials derived from weathering and erosion of preexisting rocks and soils. Sedimentary rocks are the main rock formations that contain hydrocarbon concentrations. Metamorphic rocks (e.g., marble and slate) are rocks that undergo a textural or composition change due to substantial heat and pressure. These temperature and pressure changes usually result in pore volume reduction. As a result, metamorphic rocks seldom make a suitable storage media for hydrocarbons. Each type of rock presents different problems with respect to the performance of the casing.[10] Typical strength values, density values, and percent porosity values of several rock formations and steel are listed in Table 6.[11]

Table 6. Typical Properties of Rock Formations[11]

Typical Rock Types	Compressive Strength (MPa)	Tensile Strength (MPa)	Shear Strength (MPa)	Bulk Density (Mg/m^3)	Porosity %
Granite	100-250	7-25	14-50	2.6-2.9	0.5-1.5
Diorite	150-300	15-30	N/A	N/A	N/A
Diabase	100-350	15-35	25-60	2.7-3.05	0.1-0.5
Gabbro	150-300	15-30	N/A	2.8-3.1	0.1-0.2
Basalt	100-300	10-30	20-60	2.8-2.9	0.1-1.0
Gneiss	50-200	5-20	N/A	2.8-3.0	0.5-1.5
Marble	100-250	7.2	N/A	2.6-2.7	0.5-2
Slate	100-200	7.20	15-30	2.6-2.7	0.1-0.5
Quartzite	150-300	10-30	20-60	2.6-2.7	0.1-0.5
Sandstone	20-170	4-25	8-40	2.0-2.6	5-25
Shale	5-100	2-10	3-30	2.0-2.4	10-30
Limestone	30-250	5-25	10-50	2.2-2.6	5-20
Dolomite	30-250	15-25	N/A	2.5-2.6	1-5
Steel	900-1,500	N/A	N/A	N/A	N/A

Other factors that affect casings are temperature and pressure. Rock temperature intends to increase with depth and can be high enough to affect the strength and fracture toughness of the steel casing. New reservoirs at the bottom of a well can have pressures large enough to increase the probability of some types of casing failure mechanisms.

Corrosion is the common denominator in all service environments. Corrosion is affected by the amount of oxygen, carbon dioxide, hydrogen sulfide, salts, organic acids and/or other factors such as stress, the composition of the corrosive environment, the casing surface condition, temperature, and differences in electrical potential of the materials. When corrosion occurs on

---

[10] Lyons, W. C., Plisga, G. J., "Standard Handbook of Petroleum and Natural Gas Engineering," Second Edition, Elsevier/Gulf Professional Publication, Burlington, MA (2005)

[11] Retrieved from
http://www.geocities.com/unforbidden_geology/rock_properties.htm#a%29%20Rock%20hardness,
February 28, 2007.

casings, it can take many forms including uniform attack, crevice corrosion, pitting corrosion, galvanic corrosion, intergranular corrosion, microbial or cavitation corrosion. It is important to note that the loading conditions and environment do interact to degrade the casing. Such combined mechanisms include corrosion fatigue, erosion-corrosion, stress corrosion cracking, and environmental caused cracking.[3,10]

4.2.1.1 Survey Responses to Service Environment Questions

When asked what types of service environments survey[4] respondent's casings were exposed to (Q8), the answers varied. While there was some commonality, it was not possible to graph the responses. Individual responses follow.

- We have H_2S in two of our fields. All of our fields produce some water and the gas in our fields has some CO_2 (<1%).

- Some are exposed to H_2S and most see brine with a pH in the 5 to 5.6 range.

- Two of our fields have cathodic protection (CP) on well casings, others do not. Gas is generally pipeline quality (little or no H_2S, CO_2 <3%), no oxygen internally except during a workover. One field does have H_2S in parts of the field of up to 500 ppm, but this has not seemed to cause problems. Exposure to brine varies from a little to a lot. Where a well has a dead annulus with fluid, microbiologically influenced corrosion (MIC) corrosion has been a problem. Have experienced some external corrosion due to varying external water table with oxygenated water. Major source of casing damage has found to be drill pipe wear. Also, many wells flow up through a packer and out into the tubing-casing annulus through a sliding sleeve, and sand erosion has been a problem at this point.

- The natural gas has contained minute quantities of oxygen and up to 2% CO_2. Brine, fresh water and compressor oil liquids also come in contact with the casing. Salt deposits and paraffin have been found in some cases. Evidence of bacteria also found.

- Salt brine (10.4 lbs./ft., saturated brine) in one field.

- Salt and iron sulfate/sulfide precipitated. Bacteria, [specifically] sulfate reducing bacteria (SRB) and acid producing bacteria (APB) are a problem.

- Salt precipitation, paraffin build-up, hydrate formation, CO_2 (0.5% - 1.5%), and saturated brine (chlorides = 250,000 ppm).

- Saline water, fresh water, mercaptan (methylethylsulfide), and electrical potential.

- 2% to 3% CO_2.

- Annulus between tubing and casing is filled with inhibited fluid. Some wells have CP. No abnormal downhole conditions or surface conditions exist at our facilities.

- Brine corrosive environment, no free oxygen, salts, inorganic, high solid velocity of unabsorbed salts.

- High carbon dioxide levels in the gas stream, exterior bacterial attack in outside annuli, corrosive salts in annuli, bacterial attack (pitting) in the gas stream.

4.2.2 Service Loads

A casing is subjected to different loads during landing, cementing, drilling, and production operations. The most important loads that the casing must withstand during each stage are: tensile, burst, and collapse loads. Tensile loads can be a result of the weight of the casing, bending and dragging during installation, shock loads and pressure testing of the completed strings after installation. The different loading mechanisms act in an accumulative manner; in other words the tensile loads from the weight of the casing and the pressure test are additive stresses and need to be taken into account. Burst loads are a result of internal or operating pressure of the well or storage facility. Collapse loads are a result of external pressure.[12]

There are other factors that may be of equal or greater importance, which often influence the selection of casing grades. These factors include: wear, corrosion, vibration and pounding by drill pipe, the effect of gun perforating, and erosion.[12] Even though the typical loading experienced by casings is described separately above, it is important to note that the loading mechanisms rarely if ever act alone. The casing is always subjected to biaxial loading, which may increase the frequency of failures.

There is little published literature on the magnitude of the loads that casings are exposed to and even less literature on the magnitude of the loads that casing repairs may experience in the field. Several of the design requirements for casings outlined in Task 1 do not specify the mechanical properties for a casing repair. Because of the lack of repair requirements, it is easy to assume that the repair should return the casing integrity back to the original state of construction. This may not be the most accurate method to determine a successful repair, because the loads acting on existing storage wells may not be as severe as the loads on casings in production wells for which the original casing was designed.

All the loads that apply to newly drilled and cased wells do apply to existing casings in storage wells; however, the mechanisms that apply the loads are reduced. For example, the load caused by the pounding of the drill pipe would not apply to storage well casings. The loads that are present in storage well casings are typically a result of the operating conditions of the storage well, which can be as high as 4,000 psig.[3] Other factors that can affect the magnitude of the loads on storage well casings are earth movements and temperature variations.

---

[12] Rahman, S. S., Chilingarian, G. V., "Casing Design Theory and Practice," Elsevier, Amsterdam/New York (1995)

4.2.2.1 Survey Responses to Service Loads Questions

When asked what types of loads that casings are exposed to, twelve respondents[4] (100%) indicated that their casings are exposed to well pressure. Of the twelve, two respondents also experience temperature variations. One respondent indicated that his casings are exposed to well pressure, temperature variations and that casings can be in compression at top of cement. This respondent also commented that earth movements occur very rarely. Two of the twelve also described other loadings. One person said their casing is packed off and casing tubing annulus is filled with corrosion inhibited fluid. The other said their loads are associated with directionally drilled wells (i.e., horizontal wells). A graphical representation of these responses is shown in Figure 5.

Figure 5. Typical Casing Loads Reported[4]

When asked to provide well pressure ranges, twelve survey[4] respondents reported ranges that were converted to psig for comparison purposes. Typical ranges are found in Table 7and graphically represented in Figure 6. The average minimum pressure reported is 363 psig; the average maximum reported pressure is 2,313 psig. 100% of the twelve respondents[4] indicated that they could not quantify any other types of loading besides well pressure.

Table 7. Typical Well Pressure Ranges

Maximum Pressure (psig)	Minimum Pressure (psig)	Average Pressure (psig)
785	385	585
1,003	400	702
1,085	0	543
1,235	285	760
1,750	150	950
2,300	300	1,300
2,350	200	1,275
2,485	485	1,485
2,485	135	1,310
3,000	800	1,900
3,600	90	1,845
3,985	1,485	2,735
4,000	0	2,000

Figure 6. Typical Well Pressure Ranges

4.3 Task 3 – Review of Damage Mechanisms

This section summarizes the literature search results and industry input for damage mechanisms.

Damage mechanisms are normally caused by the service load, service environment or some form of mechanical damage from drilling. Typical types of damage mechanisms are: corrosion, threaded connection separation, thread sealant leaks, collapse, parted or split casings due to internal defect, and rotational failure.[5] The results of the Email inquiry[3] and the survey[4] indicate that the main damage mechanisms for natural gas storage wells appear to be corrosion and mechanical damage from re-drilling. These responses indicate that all other damage mechanisms may occur, but they are more likely to be one-off situations and not a common occurrence.

4.3.1 Corrosion Damage

Casing damage in gas storage wells is largely the result of localized loss of metal from corrosion. Corrosion causes in underground structures include joining of dissimilar metals, non-homogeneous soil, differential aeration and microbiological attack.[13] There can be both internal and external corrosion. Internal corrosion is reduced by using products that kill or reduce the possibility for microbiological corrosion such as biocides.[14] External corrosion is prevented by using a good cement job. The Manitoba informational Notice 04-02 recommends circulating a non-corrosive inhibited fluid once a year to retard internal corrosion.[15] This point is supported by the responses to the Email inquiry,[3] four respondents indicated that they have corrosion issues. A fifth respondent said he didn't have any type of damage. Three of the five respondents to Email inquiry[3] questions 6 and 7 indicated that the extent of corrosion is used as the only defect that requires repair. One of the other two respondents[3] listed severed casings as the only damage requiring repair.

4.3.1.1 Survey Responses to Corrosion Damage Questions

Ten out of eleven survey[4] respondents experience pitting corrosion. The full spectrum of corrosion damage types experienced by survey respondents is shown in Figure 7. One

---

[13] Gas Field Technology, Retrieved from http://www.pttc.org/solutions/sol_2005/547.htm, September 19, 2006.

[14] Private Communication, Ronald Walden, Dominion Transmission, September 19, 2006

[15] Manitoba Industry, Economic Development and Mines, Informational Notice 04-02, Retrieved from http://www.gov.mb.ca/iedm/petroleum/infonotes/04-02.pdf, September 19, 2006.

respondent[4] said that differential aeration was common; bacterial and AM5 has been identified in gathering lines but not in wells.
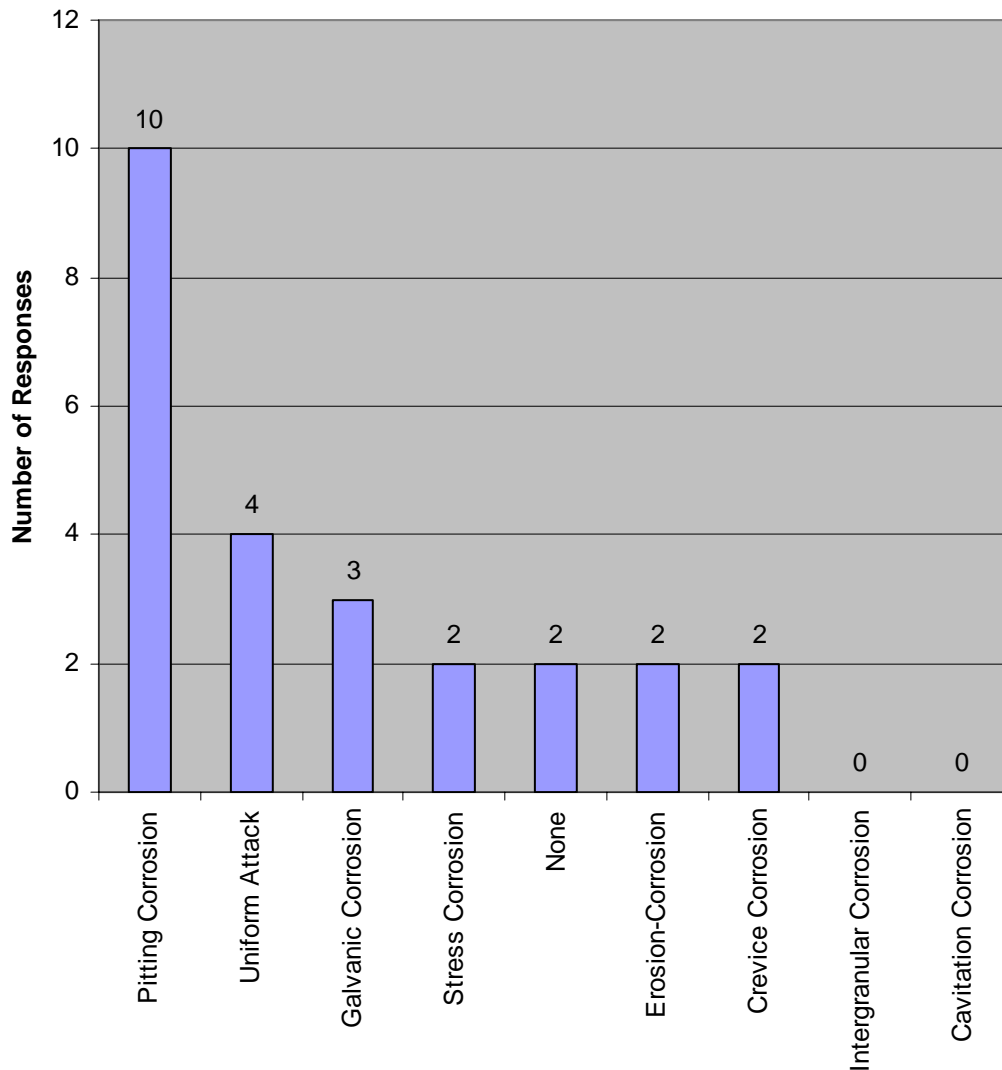
Figure 7. Types of Corrosion Experienced by Survey Respondents

When asked what their company does to prevent these forms of corrosion damage, three respondents[4] indicated that they use CP to protect each well. One respondent said that his company does nothing. Other individual responses are listed below.

- Use biocide and corrosion inhibitor in completion and workover fluids. New wells are designed to have cement to surface (not always achieved). Where interference with other wells/substructures is not a problem, CP is applied to well casings. Sand control is used to minimize sand erosion.

- Use a spring loaded check valve to keep oxygen out of the annulus. Some annulars contain corrosion inhibitor. Do not use CP on wells (gathering lines protected, wells isolated). Gas quality standards keep O_2 and CO_2 levels low.

- Atmospheric corrosion program for surface facilities. When O_2 is removed from surface facilities, corrosion is minimized.

- Chemical treatments on a regular basis.

- We also equip our casing strings with modified couplings and seal rings.

- Run caliper tools and inspections tools every workover period (7 years) and repair as needed.

- Biocides and corrosion inhibitors are used, and annuli are protected from sources of oxygen.

83% of survey[4] respondents consider corrosion the most pervasive damage mechanism; 17% do not. One respondent indicated that they consider mechanical damage from well work the most prevalent casing damage. They provided the following examples of such damage:

- Acid treatments.

- Fracing.

- Coiled tubing clean out.

Another respondent[4] indicated that they used to consider corrosion the most pervasive damage mechanism. With their new prevention policies in place (outlined in Q14, Appendix C), they experience very little corrosion. With more and more horizontal wells, they find bit and drill string related mechanical damage, but have taken steps to prevent those as well.

4.3.2 Survey Responses to Non-Corrosion Damage Mechanisms Questions

The second most common form of damage identified by the Email inquiry[3] was mechanical damage as reported by three out of four respondents. When asked additional questions about what constitutes mechanical damage, a typical example was when a drill head did not remain centered in the casing when it was reinserted into the well to drill out a packer. Another type of reported mechanical damage was caused by casing tongs.

Survey[4] respondents were asked to identify all of the types of non-corrosion damage that they experience. 44% experience threaded connection separation; 33% have threaded connection leaks; 33% see bends due to earth movements; and 22% report parted/split casings due to internal defect and drill damage. The full spectrum of reported damage is shown in Figure 8.
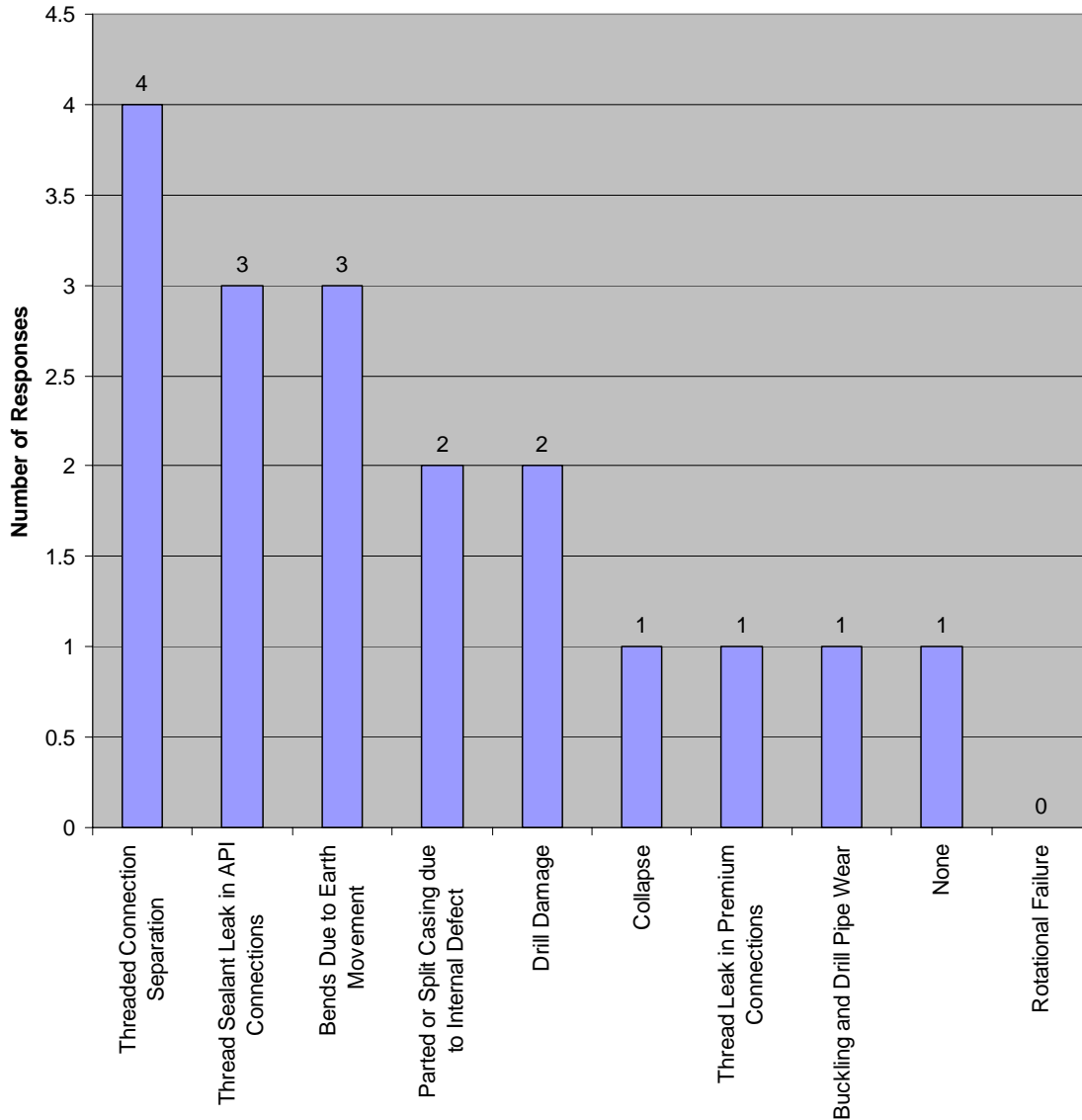
Figure 8. Non-Corrosion Damage Experienced by Survey Respondents

One respondent's[4] company does not experience any non-corrosion type damage. Three respondents[4] listed some form of bit damage, as well as, the following additional types of non-corrosion damage:

- External mechanical damage from casing make up or internal from drilling equipment.

- Internal wear due to rotating drill pipe. Thread leak in premium connections. Combination of buckling and drill pipe wear at top of cement. Where casing was not hung in sufficient tension and temperature changes cause it to be in compression at top of cement. Many 1979's era wells used stage cementing collars in middle of casing string and most of these eventually develop a leak when exposed to varying gas pressure.

Three survey[4] respondents do nothing to prevent these types of non-corrosion damage; seven companies indicated that they take the following precautions.

- Exercise proper precautions when running casing to not impart mechanical damage.

- Don't rotate the bit while it's in the casing.

- Be careful when handling, running and cementing casings in new wells.

- Modified couplings and seal rings.

- Inspect every workover period and make repairs as needed.

- Limit introduction of oxygen into annuli, use of biocides and corrosion inhibitors in packer fluids.

4.3.3 Survey Responses to Un-Repairable Damage Questions

4.3.3.1 Limits of Repairable Damage

Eight survey respondents[4] listed the following limits to damage that they will repair.

- Would assess on a case by case basis.

- Very severe wall thickness loss where there is a potential for not being able to get to bottom to properly plug well.

- If excessive, would plug and drill offset well.

- Excessive corrosion on smaller diameter (4 1/2', 5 1/2') casing.

- Hard to answer this.

- Corrosion must be over 80% and growing.

- Depends on the extent of the damage and state regulations and industry practice.

- Economics of repair vs. plug and drill replacement well.

4.3.3.2 Types of Non-Repairable Damage

50% of survey respondents[4] (6 people) listed the following criteria for damage they would not repair.

- Would assess on a case by case basis.

- Casing part.

- A poor well would be plugged rather than repaired.

- Casing collapse due to coal mine subsidence.

- Depends on the extent of the damage and state regulations and industry practice.

- Mill defects or inactive corrosion pitting resulting in acceptable reduced burst pressure ratings.

4.3.3.3 Circumstances that Require Well or Reservoir Abandonment

50% of survey respondents[4] (6 people) listed the following criteria for capping off a well or abandoning a reservoir:

- Usually when the field is no longer needed for storage or the well is no longer needed for storage. Have not plugged a well due to damage.

- Significant casing damage and near well bore plugging of reservoir in combination.

- Cost of well replacement greater than revenue from storage.

- It would have to be in extremely poor condition and pose a safety concern before it would be plugged.

- High corrosion and gas outside casing in annular area.

- If no suitable repair methods are available, a well may be plugged and abandoned. The well may be replaced with an offsetting new well. No experience abandoning an entire reservoir, because of well defects.

4.4 Task 4 – Review of Existing/Currently-Used Repair Technologies

This section summarizes the literature search results and industry input for existing and currently-used casing repair technologies.

4.4.1 Casing Repair Standard Guidance

During communications with the casing industry,[16] each state was found to have their own casing repairs procedures for underground storage wells. To determine casing repair design requirements, several state documents where obtained including Kansas, Texas, and Louisiana. In addition to the state requirements, the guidelines for repairing wells with casing leaks in Manitoba, Canada was also obtained.

---

[16] Private Communication, David Dauterive, Shell, September 2006.

The Kansas Department of Health and Environment Procedure UICLPG-12 for internal casing repair specifies that, the casing shall be repaired in a manner that will ensure the integrity of the well is maintained.[17] Procedure UICLPG-12 only describes casing patch repairs, not squeezes, and specifies that the pressure requirements for the patch designed for the size and weight of casing being repaired and, upon completion, a pressure test should be performed.[17] The procedures for performing and reporting a casing pressure test are outlined in the Kansas Department of Health and Environment Procedures UICLPG-17 and UICLPG-15, respectively.[18,19] UICLPG-17 states that the minimum test pressure shall be the maximum allowable operating injection pressure of the weld head. The pressure test shall be conducted for a minimum of one hour and will be considered acceptable if the pressure loss is equal to or less than 5% of the initial test pressure. If the pressure increases greater than 5% of the initial test pressure is not acceptable and may indicate the well has not reached thermal equilibrium.[18]

The Texas Administrative Code Title 16, Part 1, Chapter 3 gives rules for underground storage of gas in productive or depleted reservoirs and salt formations. The governing rules are Rule 3.96 and Rule 3.97. Rule 3.96 states that prior to operating a gas storage well, an integrity test shall be performed. The guidance states that the operator shall pressure test the long string casing, or the tubing-casing annulus if the well is equipped with the tubing set in a packer. Gas storage wells in which injection occurs through a casing shall be tested at a maximum authorized injection pressure. Gas storage wells in which injection occurs through a tubing and packer shall be tested at no less than 500 psig. After the gas storage well is in operation, the integrity of the well shall be checked by a pressure test once every five years in operation or the tubing-casing annulus pressure may be monitored in lieu of a pressure test every five years. However, there is no mention of how to repair leaks if one occurs.[20] Rule 3.97 is similar to Rule 3.96 in that the casing needs to be pressure tested every five years of operation.[21] Rule 3.97, for storage in salt formations, also calls out similar integrity pressure tests for new and operating wells especially after each workover that involves physical changes to any cemented casing

---

[17] Kansas Department of Health and Environment, "Procedure for Internal Casing Repair," Procedure #: UICLPG-12, Bureau of Water – Geology Section, February 2003.

[18] Kansas Department of Health and Environment, "Procedure for the Pressure Mechanical Integrity Test for the Casing of an Underground Hydrocarbon Storage Well," Procedure #: UICLPG-17, Bureau of Water – Geology Section, February 2005.

[19] Kansas Department of Health and Environment, "Procedure for Conducting a Casing Pressure Test for Underground Hydrocarbon Storage Wells," Procedure #: UICLPG-15, Bureau of Water – Geology Section, December 2003.

[20] Texas Administrative Code, "Underground Storage of Gas in Productive or Depleted Reservoirs," Title 16 Economic Regulation, Part 1 Railroad Commission of Texas, Chapter 3 Oil and Gas Division, Rule 3.96, Retrieved from http://info.sos.state.tx.us/pls/pub/readtac$ext.ViewTAC?tac_view=4&ti=16&pt=1&ch=3, September 18, 2006.

string; however, there is no guidance on how to repair the casing string.[21] Texas Administrative Code Title 16, Part 1, Chapter 3 also has Rule 3.13, *Casing, Cementing, Drilling, and Completion Requirements*. Rule 3.13 is referenced in Rule 3.96 and 3.97. Rule 3.13 discusses integrity pressure testing or other means of monitoring the integrity, but similar to Rule 3.96 and 3.97, there is no mention of any requirements for repairing damaged casings or how to test the completed repair.[22]

The Louisiana Administrative Code Title 43, Part XVII, Chapter 3 gives guidelines for underground storage of gas in salt formations. Like the Texas rules, the Louisiana rules state the casing string shall have adequate tensile and collapse strengths as established by the commissioner for the setting depth.[23] In addition, the casing string is subjected to several pressure tests prior to operation. The Louisiana rules also make no mention of requirements for the repair of damaged casings.

In the Guidance and Polices section of the New York Regulations for Casing and Cementing Practices, it states that all surface casings need to be pressure tested and all production casings shall be of sufficient strength to contain any expected formation or stimulation pressures. Part 556 Operating Practices states for the operation of a gas well, the department may require periodic testing of any gas well in such a manner as the department may prescribe in order to establish the producing capacity and characteristics of the well. Part 557 Secondary Recovery and Maintenance states wells used for injection of gas, air, water or other extraneous fluids shall be cased with safe and adequate casing in such a manner as to prevent migration, leakage or damage to oil, gas, or fresh potable water reservoirs. In none of these sections is there any mention of how to repair damaged casing or casings that fail the integrity test. [24]

The Pennsylvania Department of Environmental Protection (PADEP) requires a pressure integrity test once every five years for storage wells. PADEP also recommends a testing

---

[21] Texas Administrative Code, "Underground Storage of Gas in Salt Formations," Title 16 Economic Regulation, Part 1 Railroad Commission of Texas, Chapter 3 Oil and Gas Division, Rule 3.97, Retrieved from http://info.sos.state.tx.us/pls/pub/readtac$ext.ViewTAC?tac_view=4&ti=16&pt=1&ch=3, September 18, 2006.

[22] Texas Administrative Code, "Casing, Cementing, Drilling, and Completion Requirements," Title 16 Economic Regulation, Part 1 Railroad Commission of Texas, Chapter 3 Oil and Gas Division, Rule 3.13, Retrieved from http://info.sos.state.tx.us/pls/pub/readtac$ext.ViewTAC?tac_view=4&ti=16&pt=1&ch=3, September 18, 2006.

[23] Louisiana Administrative Code, "Hydrocarbon Storage Wells in Salt Dome Cavities," Title 43 Natural Resources, Part XVII Office of Conservation, Injection and Mining, Subpart 3 Statewide Order No. 29-M, Chapter 3, Dated December 2004, Retrieved from http://www.state.la.us/osr/lac/43v17/43v17.pdf, September 18, 2006.

[24] New York State Department of Environmental Conservation, Title 6 of the Official Compilation of Codes, Rules and Regulations of the State of New York (6NYCRR), Retrieved from http://www.dec.ny.gov/energy, June 12, 2007.

program that may consist of gas storage field monitoring, pressure testing or other procedures approved by PADEP, but similar to other states, there is no repair methods mentioned or repair acceptance guidelines.[25]

The Manitoba Informational Notice 04-02 does not specify design requirements, but it does give a list of typical casing repair techniques, which include cement squeezes, running a casing liner or patch, polymer water shut-off job, removal/replacement of the casing and packer to isolate the leak. To verify repair acceptance for a well with a packer repair, the well is subjected to a pressure test at a minimum pressure of 507.6 psi (3,500 kPa) for a 15 minute period. For the test to be acceptable, the pressure variation (increase or decrease) must not exceed 5% over the fifteen minute duration of the test and the final pressure must be 507.6 psi (3,500 kPa) or greater.[15]

4.4.1.1 Survey Responses to Casing Repair Standard Guidance Questions

45% of survey[4] respondents indicated that they use an industry standard to define repair procedures; 27% use an in-house code; 27% use no guidance; and 18% use state regulations (see Figure 9). Overall, 73% use some sort of a standardized repair procedure while 27% use no standard guidance.
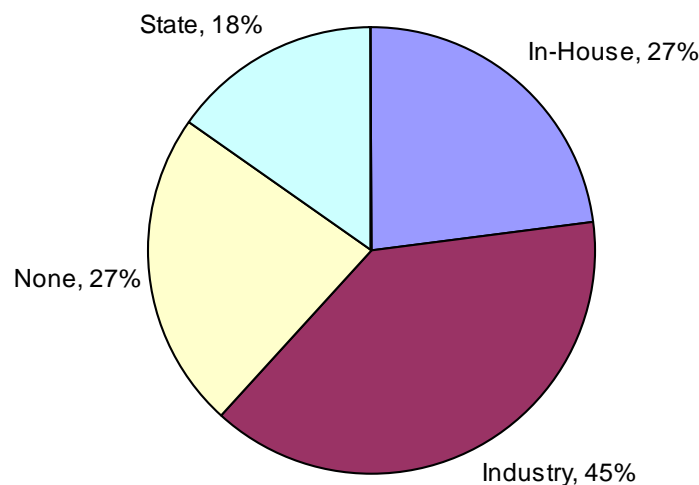
Figure 9. Types of Casing Procedure Specifications used by Respondents

One respondent[4] indicated that his company has had very few casing failures. The few they have experienced were very close to the surface and were repaired by unscrewing the bad pipe and replacing it with a new casing.

---

[25] Pennsylvania Code: Oil and Gas Regulations, Chapter 78: Oil and Gas Wells, Retrieved from http://www.pacode.com, June 12, 2007.

Three people[4] said that they do not use a code or standard procedure to define repair procedures/requirements. One respondent[4] even indicated that he did not understand the question. The lack of knowledge about standardized repair procedure specifications (represented by 28% of the respondents) and the lack of any one code being used by the majority of respondents imply that there is no minimum acceptable quality control among the reservoir operators that responded to this survey. Again, each storage facility has specific characteristics that are dependent on the rock formations and the downhole environment. As a result, each facility acts differently and the service loads and environments that each downhole casing is exposed to cannot easily be compared. For this reason, it is extremely difficult to make general statements that are applicable to all storage wells.

Without collecting data from a larger number of natural gas storage industry professionals, we cannot conclude that repairs are so rare that standards are not needed. It does appear that the underground natural gas industry needs to establish some standardized repair guidance for minimum acceptable quality levels to define an acceptable vs. rejectable repair.

Four respondents[4] provided the following input regarding their in-house repair practices.

- Wells are repaired in one of the following ways:
    - Tubing packer system.
    - Casing patch.
    - Cemented liner.
- Back off and replace the bad joint if possible, or run a liner or plug the well. Casing patches have been considered but not done to date.
- No welding on gas production string; threading only. Welding allowed on surface or water protection string.
- Repairs are driven by magnetic flux-leakage log run results and interpretations. 'Reduced burst pressures' are calculated for flowstrings using B31.G methodology. Candidate wells are prioritized based on calculated reduced burst pressures vs. required service pressures. A subset of the candidate list is slated for repairs each year based upon budget availability.

These responses[4] also imply that there is no minimum acceptable quality control among the reservoir operators who responded to this survey.[4]

Five survey[4] respondents define an acceptable repair as follows:

- Not having the defect in the casing exposed to well pressure and the repair method used being able to withstand the highest well pressure it will see.

- Replacing the bad joint with a good one, covering up the bad joint with good tubing, or plugging the well.

- Replace badly corroded casing.

- Restore to full strength.

- If possible, the pipe is removed and replaced. If not, alternate repairs methods may be employed, such as casing patches and expandable sleeves, liners and smaller diameter flowstrings. If none of these repair methods is possible, the well may be plugged and, if the situation warrants, a replacement well may be drilled.

Again, these responses[4] imply that there is no minimum acceptable quality control among the reservoir operators that responded to this survey.

Three survey[4] respondents (60%) indicated that they use API 5CT; one of these respondents also uses the Louisiana code. (Again, API 5CT contains design guidance, not repair guidance.) One of the other respondents indicated that they use Title 6 of the Official Compilation of Codes, Rules and Regulations of the State of New York (6NYCRR) and follow the requirements of the PADEP. The last respondent indicated that his company has no regulatory requirements; their selections are made based upon integrity monitoring of casing corrosion. Answers to this question are graphically shown in Figure 10.
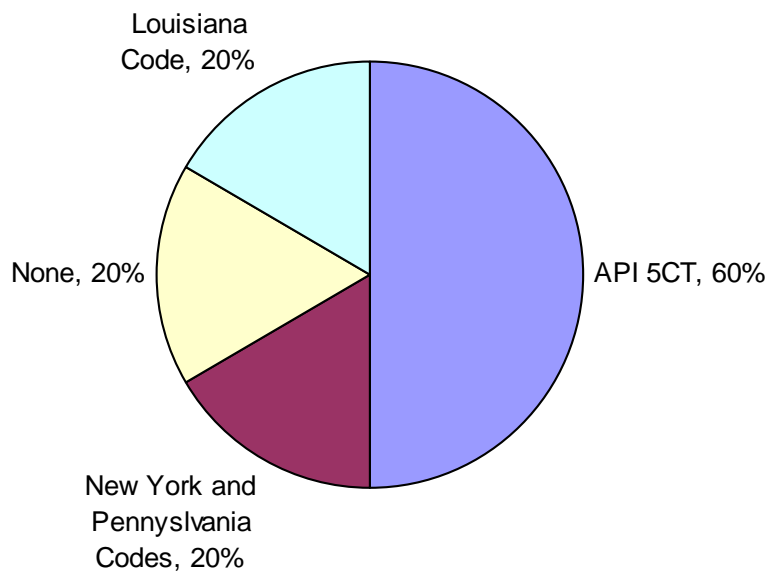
Figure 10. Reported Standardized Code Usage

4.4.2   Existing and Currently-Used Casing Repair Technologies

The most expensive and complex options that companies use to repair casings are full string casing repair and cut out and replace. The most commonly used types of repair processes are squeezes, liners, and plating, which are inherently more cost effective than remove/replace options. Many of these repair methods are proprietary, and as a result, are relatively costly to perform. In addition, many of these repair methods (e.g., tube and packer systems) result in decreased cross-sectional area, which create flow restrictions and subsequent operational limitations, and reduce the ability to perform well logging operations.

4.4.2.1   Squeeze Repairs

A squeeze repair operation consists of forcing a material through the damaged casing (or perforations in the casing) into the cavities that form behind the casing. Prior to performing the squeeze it is common practice to clean the inside diameter (ID) of the casing to help assure a good bond. The squeeze operation is normally performed by using one of two types of packers. The first is a drillable packer that is drilled out after the squeeze is complete. The second is a retrievable packer. There are several types of materials that can be used in a squeeze operation which include cement, sealants and metallic materials. Typical reasons for using a squeeze operation are to reduce water production, to mitigate annular fluid migration, to repair casing holes due to corrosion or split casings, to repair primary cement sheath channels, and to fix insufficient height of the primary cement.[26,27,28] Figure 11 is an illustration of a typical squeeze repair procedure with a drillable packer.

---

[26] Goodwin, K.J., "Principles of Squeeze Cementing," SPE 12603, Presented at the 1984 Permian Basin Oil & Gas Recovery Conference, Midland, TX March 8-9, 1984.

[27]Wasnik, A. and Mete, S., "Application of resin system for sand consolidation, mud-loss control, and channel repairing," SPE/PS-CIM/CHOA 97771, PS2005-349, presented at 2005 SPE International Thermal Operations and Heavy Oil Symposium, Calgary, Alberta, Canada, 1-3 November 2005.

[28] Toor, I. A., "Problems in squeeze cementing," SPE 11499, presented at the Middle East Oil Technical Conference of the Society of Petroleum Engineers, Manama, Bahrain, March 14-17, 1983.

Damaged Casing   **Casing After Clean**   **Repair Area Dammed**

After Squeeze   **After Squeeze is Drilled Out**
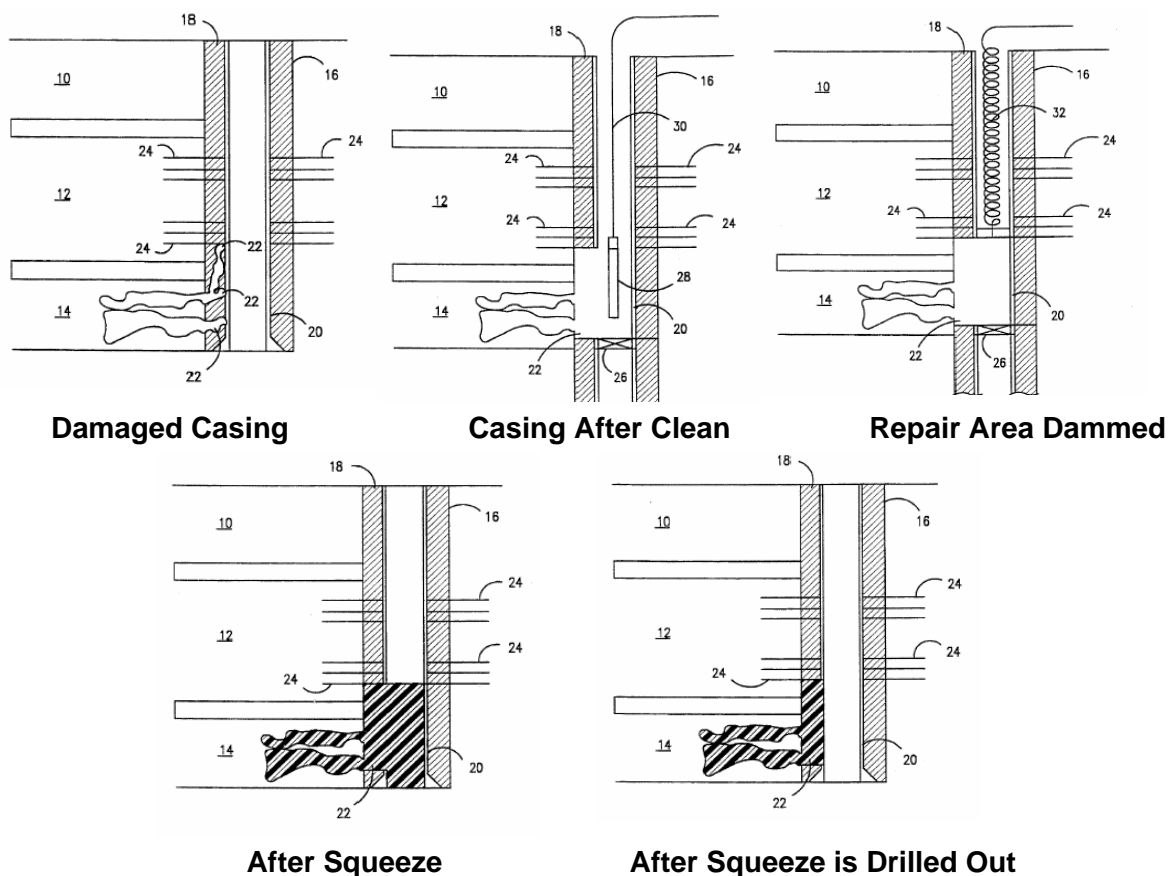
Figure 11. Typical Squeeze Repair Operation

4.4.2.1.1   Cement Squeeze Repair

Cement squeezes are the most common type of squeeze repair. The repair is performed by forcing cement out into the formation where cement dehydration occurs allowing the cement to deposit onto the adjoining surfaces; or by placing the cement in the damaged areas, such as casing splits or corrosion holes. After curing, the deposited cement forms a nearly impermeable solid. There has been some advancement in cement squeeze technology with the introduction of ultra-fine cement. Ultra-fine cement particles are 5 to 10 times smaller than standard API cement. The average particle size for ultra-fine cement is 4 microns, whereas the average particle size for standard API cement is 30 microns. Since ultra-fine cement does not contain large particles, it is able to penetrate and repair damage that standard cement cannot repair.[26,28,29]

---

[29] Harris, K.L., and Johnson, B.J., "Successful Remedial Operations using Ultra Fine Cement," SPE 24294, presented at the SPE-MidContinent Gas Symposium, Amarillo, Texas, April 3-14, 1992.

4.4.2.1.2 Sealant Squeeze Repair

Sealant squeezes are used for pinhole casing leaks, which cannot be repaired or that require a substantial number of subsequent cement squeezes to be successful. There are several types of sealants that are used: sodium silicate gel, in situ polymerizing monomer (IPM), crosslink polymer gel, epoxy, or resin. The main advantage of using sealants is the fact that they are squeezed in liquid form, which allows them to penetrate smaller orifices as compared to small-particle cement.[27,30,31]

4.4.2.1.3 Metallic Squeeze Repair

A squeeze technology for casing repair that uses molten metal has recently been developed that is similar to a soldering process. The metal consists of 58% bismuth and 42% tin, which has a melting temperature of 137ºC (278.6ºF). The solid metal is heated with an inductive heating element and the molten metal is forced outward in a manner similar to other squeeze techniques. The molten metal solidifies forming an impermeable plug in the well's annulus. The metallic squeeze technique has been successfully applied in field applications since 2004.[32,33]

4.4.2.1.4 Survey Responses to Squeeze Repair Questions

Approximately 80% of the survey respondents[4] do not use cement squeezes. One respondent reports that his company has not used a cement repair in 15 years. The respondents that do, indicated that they use cement squeezes to repair the following damage types:

- Everywhere there is through-pipe hole.

- Cement not to surface as per NYDEC or PADEP requirements.

- Small hole leaks.

- MIC-damaged surface casings.

As for the cement squeeze trade name products used, one respondent[4] indicated that his company uses various unidentified cement blends. Another respondent indicated that his company uses regular class C cement. No other respondents claim to use cement squeezes.

---

[30] Creel, P. and Crook, R., "Gels, Monomer Solutions Fix Pinhole Casing Leaks," Oil and Gas Journal, October 13, 1997, pg 44.

[31] Ng, R. C. and McPherson, T. W., "Low Temperature Underwater Epoxy System for Zone Isolation, Remedial Cementing, and Casing Repair," United States Patent 5531272, July 2, 1996.

[32] Schmidt, Victor, "What's new in production," World Oil, Vol. 227, No. 4, April 2006.

[33] Canitron System, Inc., Retrieved September 18, 2006 from http://canitron-sys.com.

The two respondents[4] that currently use cement squeezes listed the following limitations for the technology.

- Squeeze cementing is rarely used as the sole repair method, because it will not reliably hold gas pressure. Cement is used to stabilize and protect the exterior of the casing, with a patch or inner casing string used to hold pressure.

- The rate of pumping is a limitation during application.

100% of survey[4] respondents indicated that they do not use sealant or metallic squeeze repairs. Again, one respondent indicated that he has not used a squeeze repair in 15 years.

4.4.2.2 Casing Liner Repairs

Casing liners (or casing patches) are normally in the form of a smaller sized casing that is transported downhole and placed at the location of the repair. Typically, the ID of the casing is larger than the outside diameter (OD) of the patch/liner. Because the repair liner has a smaller ID than the damaged casing, there is some reduction in cross-sectional area of the well after repair. Before a casing liner is installed, the casing is typically cleaned by scrapping or brushing. Liners are made from a metallic or composite material and can be applied in addition to a squeeze operation.

4.4.2.2.1 Metallic Liner Repairs

Metallic liners fall into two categories: non-expandable and expandable. In both cases an elastomer, metal-to-metal seal or some other material is commonly used to produce the seal after the repair is completed.[34,35]

4.4.2.2.1.1 Non-Expandable Liner Repair

An example of a non-expandable liner is a tube and packer system (e.g., scab liner). A scab liner is a section of casing with a smaller diameter, which is used to repair an existing larger diameter damaged casing. An illustration of a scab liner is shown in Figure 12. Packers are used to isolate the damaged area of the casing and to act as the pressure seal. Non-expandable liners are usually accompanied with a squeeze.[12]

---

[34] Fischer, P.A., and Schmidt, V.A.," Suppliers show progress in expandables innovation," World Oil, July 2006, Vol 227, Issue 7, pg 33-39.

[35] Neely, J.D., "The use of casing patches to improve workover success rates," SPE 13996, Offshore Europe 85, Aberdeen, 10-13 September 1985.
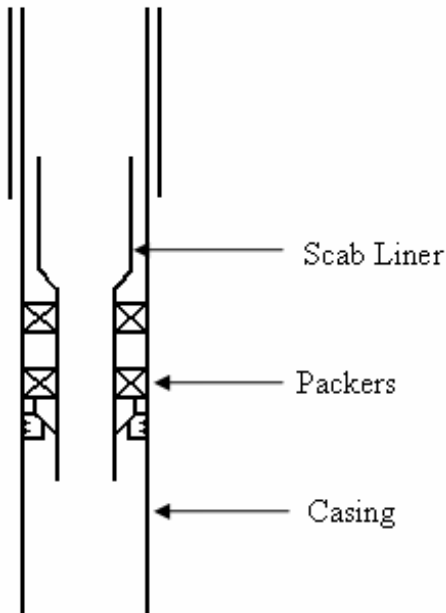
Figure 12. Illustration of a Scab Liner

4.4.2.2.1.2 Expandable Liner Repair

Expandable liners typically use the same casing repair materials as non-expandable liners. The main difference is expandable liners are "expanded" out to produce the pressure seal between the OD of the expandable liner and the ID of the casing while minimizing loss of casing ID. Figure 13 shows a typical example of an expandable liner repair process. Figure 14 is a cross section of a casing with an installed expandable liner. The expandable casings repairs can be expanded by using either a bottom-up driven method or a top-down driven method.[36] There are basically two kinds of expandable casing repairs. One is to use solid expandable casing tubular and to expand every joint of the whole liner; the other is to use expandable elements at the top and bottom of the patch and non-expanded joints in between.[37] It is important to note that until recently, expandable liner repairs could not be used in H_2S service since the elastomer seal may corrode in such environments.

---

[36] Bargawi, et. al, "Expandable tubular successfully scab off severe casing leaks," SPE/IADC 97357, presented at SPE/IADC Middle East Drilling Technology Conference & Exhibition, Dubai, U.A.E, 12-14 September 2005.

[37] Wright, et. Al., "Expandable tubing casing repairs: four case histories," SPE 84049, presented at SPE Annual Technical Conference and Exhibition, Denver, Colorado, U.S.A., 5-8 October 2003.

| Clean Out Casing | Run & Position Expandable Liner | Pump Dart Start Expansion | Expand Liner | Expand Hanger Joint | Drill Out Shoe |
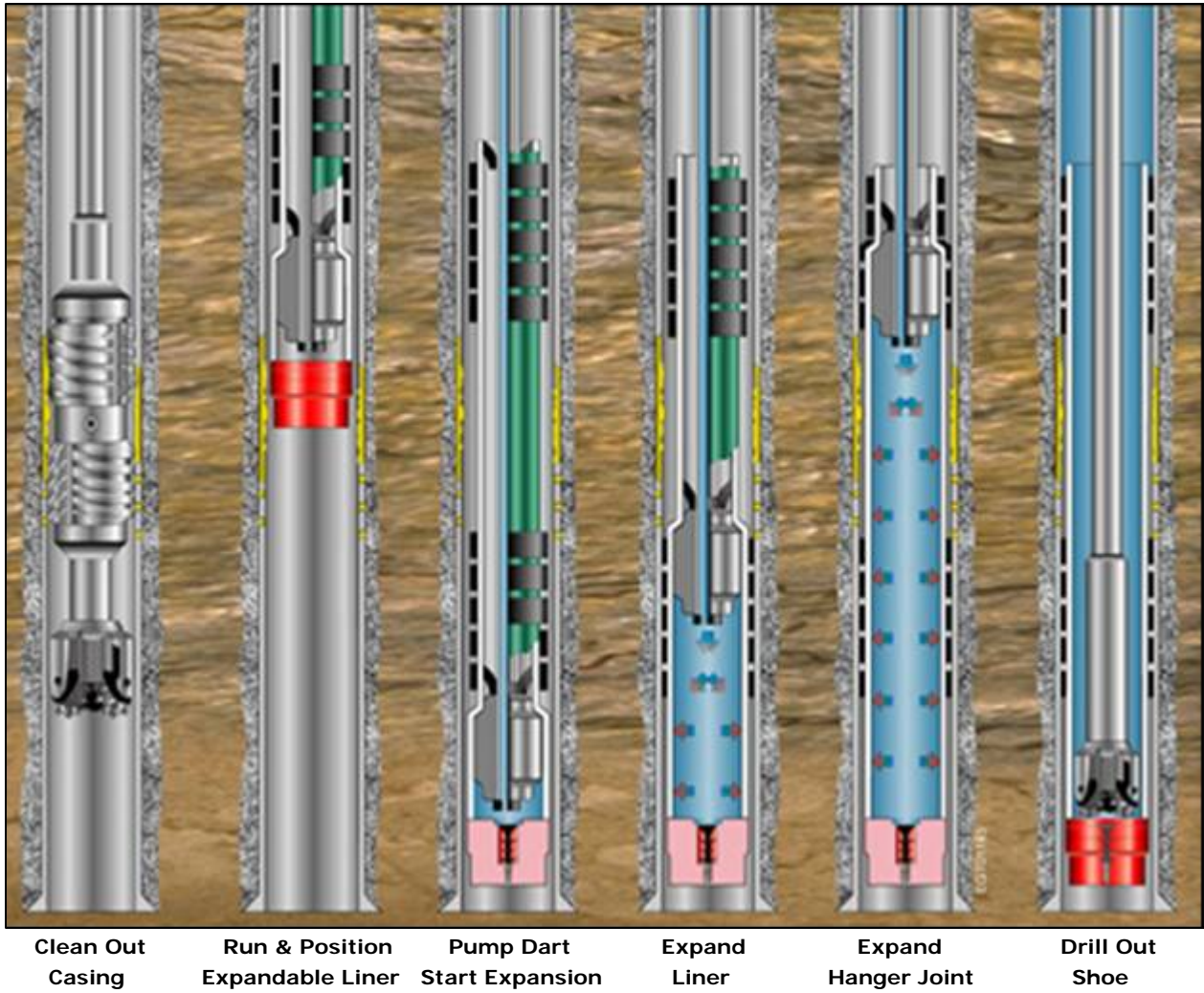
Figure 13. Enventure's Cased-Hole Liner (CHL™) System Expandable Liner Process[38]

---

[38] Enventure Global Technology, L.L.C. Retrieved December 12, 2006 from
http://www.enventuregt.com/assets/base/pdfs/productlit/CHL_letter_DataSheet.pdf.
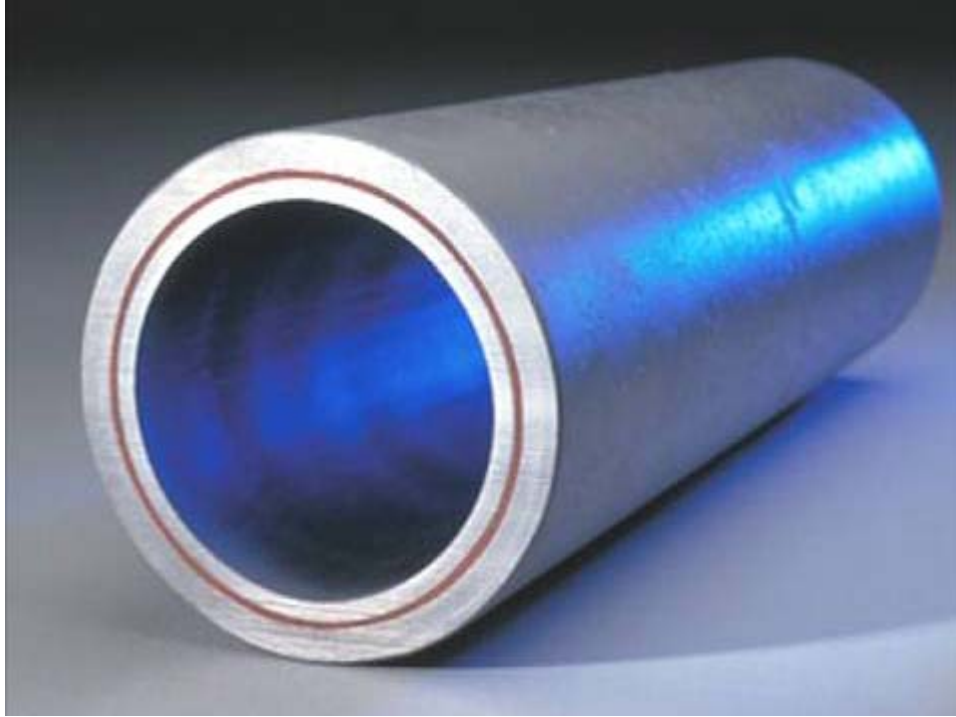
Figure 14. Installed Expandable Eventure Cased-Hole Liner (CHL™)[38]

4.4.2.2.2 Composite Liner Repair

As an alternative to using steel as the casing liner material, successful liner repairs have been made using a high-density polyethylene (HDPE) or other composite materials. The installation of the composite liner requires it to be drawn down to an OD slightly larger than the ID of the casing. The liner is then stretched by using weights to reduce the OD, so the liner can be transported downhole. Once the liner is in position, the weights are removed and the liner expands making an "interference fit" between the OD of the composite liner and the ID of the steel casing along the entire length of the composite liner.[39]

4.4.2.2.3 Survey Response to Liner Repair Questions

46% of survey respondents[4] use non-expandable liners to repair corrosion. Five respondents listed the following specific damage types that they repair with this process.

- Corrosion in the casing. Liner is run the entire length of the well bore with cement pumped behind the liner to seal it.

- High corrosion and collar leaks.

---

[39] King, et. Al, "Economic in-place casing lining and repair," Journal of Petroleum Technology, October 1997, Vol. 49, No. 10, pg 1115-1117.

- Any.

- Corrosion pits, split casing.

- Corrosion pitting near shoe in open hole completions.

36% of survey respondents[4] indicate that they would use a squeeze operation in conjunction with a non-expandable liner repair. One person indicated that he would use combination, but it depends on the size and depth of the casing hole and the cause of the casing damage. His company is more likely to squeeze if external corrosion or buckling exists.

Three survey respondents[4] report using the following non-expandable liner products.

- Halliburton (Pengo) patch; inner casing string landed on packer at bottom and wellhead at top.

- Weatherford.

- Various liner hangers.

Two survey respondents[4] provided the following limitations on the use of non-expandable liner repair technology.

- Pengo patches have not been reliable.

- Will follow industry standards as well as Louisiana regulations.

46% of survey respondents[4] use expandable liner repairs. The most commonly reported types of damage repaired with expandable liners are corrosion and leaks. Six of thirteen respondents reported the following specific damage types.

- Casing collar leak.

- Corrosion in casing or threaded connection leak.

- Where significant wall thickness remains.

- Squeezed perforations and leaky collars.

- Corrosion, split casing.

- Corrosion defects in cemented pipe, usually uphole.

Four of the five survey respondents[4] indicated that they use Weatherford patches; two of the five indicated that they use Baker systems. One respondent indicated that they have used an old style Weatherford patch, which was corrugated with epoxy on the outside. This respondent also said that they have looked at newer expandable patches but have not used them yet due to cost and issues with reduced ID.

Five survey respondents[4] provided the following temperature and pressure ranges associated with the expandable liner repair systems that they've used:

- Patches we have used meet our pressure range and temperature range of 10° to 23.9°C (50° to 75°F).

- Lower end of our pressure and temperature range for patches that use epoxy.

- 12.8° to 37.8°C (55° to 100°F); 3,447 to 27,579 kPa (500 to 4,000 psi).

- Casing needs to be real clean.

- Depends on product specifications.

Two survey respondents[4] answered the question about limitations of expandable liner repair technology. The first person indicated that they are not aware of any limitations. The second respondent said that liner repairs may restrict future ability to work on the well due to the permanent ID reduction.

One survey respondent[4] indicated that he has used a Weatherford composite liner to repair corrosion. Interestingly enough, he also listed "Weatherford" as a limitation to the process. Another respondent indicated that he was not familiar with any commercially available composite liner repair systems.

4.4.2.3 Plating Repair

There are at least two patents on mechanisms to repair downhole casing damage by depositing materials onto the ID of the casing; one by Halliburton, the other by Schlumberger. The Halliburton patent describes a method and apparatus for downhole work to repair a damaged casing in a well bore, to close an opening in a casing or to fill openings between casings. As shown in Figure 15, this method uses technologies, such as flame spray, plasma spray, welding or other technologies to apply the metallic material.[40]

---

[40] Surjaatmadja, J.B., "Downhole Casing Repair," European Patent Number EP 1 251 241 A1, October 23, 2002.
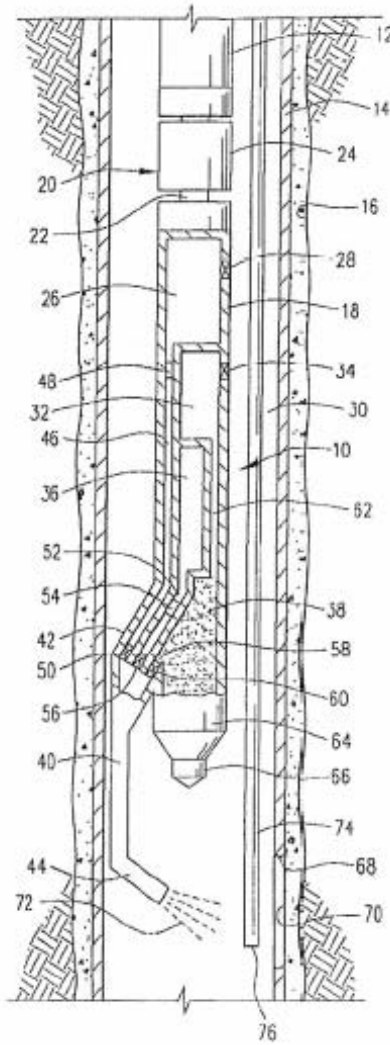
Figure 15. Halliburton Patented Plating Repair Apparatus[40]

The Schlumberger patent describes the method and apparatus for cleaning the ID of the casing and electrolytically plating the cleaned casing ID with a new metallic layer over the corroded area (Figure 16). Instead of using an electrolytic process, this method can be adapted to include a chemical plating process that uses reducing agents instead of current to deposit metal ions onto the cleaned casing ID.[41]

---

[41] Zhang, W. and Walter, J., "Method and Apparatus for Downhole Pipe or Casing Repair," International Publication Number WO 2004/001178 A2, December 31, 2003.
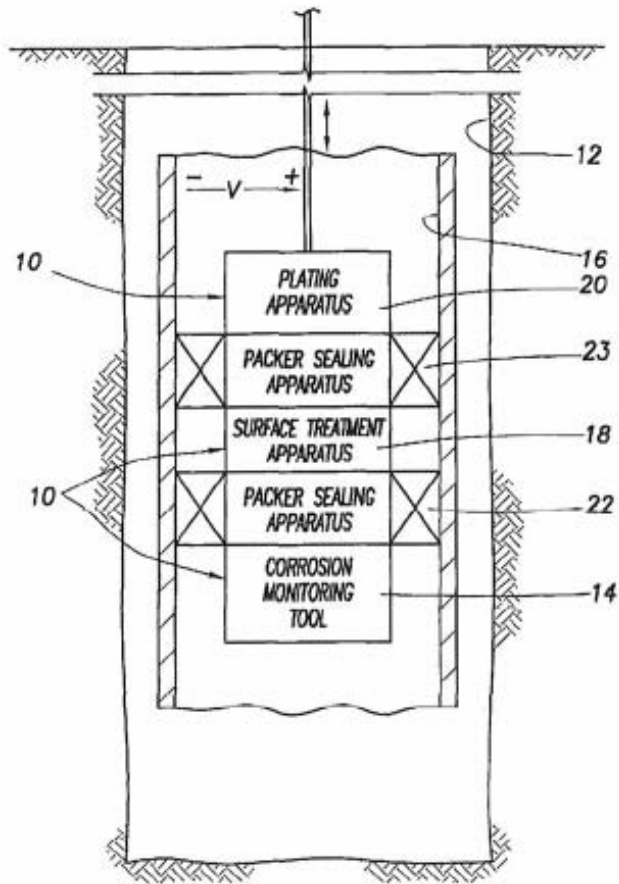
Figure 16. Schlumberger Patented Plating Repair Apparatus[41]

There is a recent development in downhole repair that uses welding. The Visual Robotic Welding System (VRWS) process allows for hands free welding in areas inaccessible to a human and where automated welding is not possible because of unknown or changing weld conditions. Visual robotic welding has been designed for remote internal pipe repair, but this technique could be adapted to other situations. The VRWS presently travels through a pipe by means of motorized winches located at each end of the pipe under repair. The current prototype is sized to repair pipes from 12- to 24-in. diameter, but the basic design can be adapted to larger or smaller spaces.[42]

---

[42] Anderson, J.,Kendziora, C., "Visual Robotic Welding,"kendziora.net/vrw.htm, May 25, 2007

Figure 17. Artist Rendition of the Visual Robotic Welding System[42]

4.4.2.4   Other Repair Methods

Ten of thirteen survey respondents[4] indicated that they do not use any other types of casing repair technologies. One respondent said that his company is lucky not to have casing problems; not that they won't have problems in the future. Another respondent uses the following "other" repair technology: back off, pull and replace.

4.4.3   Repair Assessment Conclusions from the Survey Responses

Thirteen survey respondents[4] indicated that they operate storage facilities, but did not indicate whether they repair them. One storage facility operator indicated that they perform repairs; another indicated that they specifically do not perform repair activities. The respondent that operates a liquid service salt cavern well did not indicate whether they perform repair activities. The responses to this question are graphically shown in Figure 18. Based on this feedback, it appears that 7% of survey respondents make casing repairs.
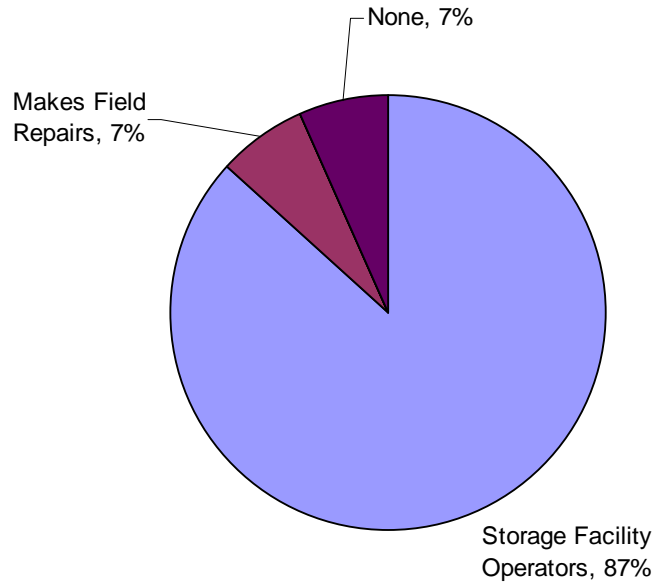
Figure 18. Repair Activities Performed by Respondents

Overall, 73% of survey respondents[4] report that they use some sort of a standardized repair procedure while 27% indicate that they use no standard guidance. Three survey respondents indicated that they use API 5CT (which in fact does not contain repair guidance); one of these respondents also uses the Louisiana code. Other respondents indicated that they use Title 6 of the Official Compilation of Codes, Rules and Regulations of the State of New York (6NYCRR) and follow the requirements of the PADEP. Another respondent indicated that his company has no regulatory requirements; their selections are made based upon integrity monitoring of casing corrosion.

Without collecting data from a larger number of natural gas storage industry professionals, it is not possible to definitively conclude that repairs are so rare that codes or standards are not needed. It does; however, appear that the underground natural gas industry needs to establish some standardized repair guidance for minimum acceptable quality levels to define an acceptable repair compared to a unacceptable repair. The guidance could also include ratings for the repair methods or a methodology for determining which repair method is preferred to repair each specific type of casing damage.

Since the objective of this project was to determine repair methods for existing casings, the initial literature search addressed all published repair methods for downhole casing repairs. Other methods such as casing replacements, running tubing, or plugging and abandoning the wells were not included in the literature review. It was assumed that it is more cost and time effective to repair casings versus replacing whole sections of damaged casing or by running tubing down the inside of the casing. It was also assumed that plugging the well was not an

option. From the responses to the Email inquiry[3] and the survey[4] it appears that these two assumptions were incorrect.

For near surface damage (i.e., outer casing strings) Email inquiry respondents[3] typically remove and replace casings. Respondents[3] are equally likely to repair a casing with tubing/packer system that isolates the leak with a casing patch. A casing patch is a non-expandable liner repair (Figure 12), which appears to have a high failure rate due to leaking packer seals. One respondent mentioned the use of a liner depends on the extent and severity of the damage. Another respondent[3] said they cement long casing strings to the surface. When it is not economical (or possible) to repair the damaged casing, the last resort for several companies[3] is to plug and abandon the well. The decision to plug the well is typically determined by a cost analysis between the cost of the repair, capacity of the well, and the type of defect.

4.5   Task 5 - Alternative Repair Processes

This section summarizes previous EWI research and industry input reviewed during the identification of alternative repair technologies for improved casing repair.

While currently used methods can be an effective means of repairing damaged casing, whereby the cost of running an entirely new casing can be avoided, there is a need to identify or develop alternative casing repair methods that are not high cost, reduce operational disadvantages, and repair casing damage that is now un-repairable which causes the well to be plugged and abandoned. For these reasons, alternative repair methods for natural gas storage well casings are needed.

4.5.1   Alternative Repair Process Conclusions from *Internal Repair of Gas Transmission Pipelines Project*[6]

In December 2005, EWI completed a research program[6] for DOE NETL that identified and assessed alternative repair methods for internal repair of natural gas transmission pipelines. There are many points of synergy between the previous NETL DOE research[6] and the current research program for GSTC. In this section, the conclusions from the previous project[6] are presented as a starting point for the assessment of alternative repair processes for casing repair.

During the course of the previous DOE NETL project,[6] the most common cause for repair of gas transmission pipelines was determined to be external corrosion causing loss of wall thickness.[43] Other transmission pipeline defects that commonly require repair include internal corrosion, original construction flaws, service induced cracking, and mechanical damage. To prevent an area of damage from causing a gas transmission pipeline to rupture, the area containing the damage must be reinforced. These damage types are also found in casings used for underground gas storage, which also require some remedial action to prohibit the casing from leaking.

An extensive survey[6] was conducted of the gas transmission pipeline industry. One of the goals of the survey[6] was to identify current repair processes for OD repair that were promising for ID repair. Matrices were created to assess the attributes and feasibility of each repair process; the weighted scores for each process are shown in Figure 19. This information was used to design the subsequent experimental program.
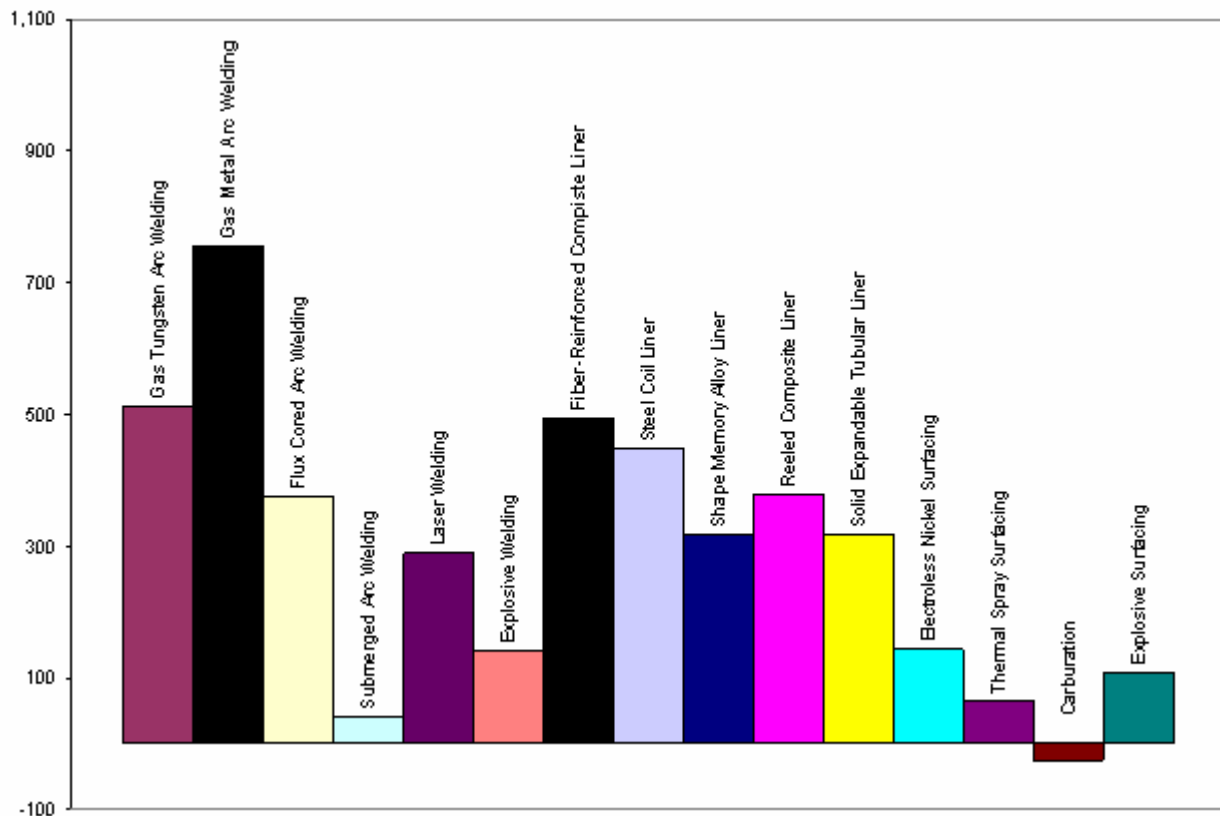
Figure 19. Weighted Scores of Potential Internal Pipeline Repair Methods

[43] Wang, Y.-Y., and Bruce, W. A., "Examination of External Weld Deposition Repair for Internal Wall Loss," Final Report for EWI Project No. 07723CAP to PRC International, Contract No PR-185-9633, March 1998.

To benchmark gas transmission pipeline material performance, pipe sections in the virgin condition and in the un-repaired simulated corrosion damaged condition were hydrostatically tested until rupture. Hydrostatic pressure testing was then conducted on pipe sections with the same simulated corrosion damage, but repaired with:

- Glass fiber-reinforced composite liners.

- Carbon fiber-reinforced composite liners.

- Weld deposition.

- Adhesively bonded steel patch.

- Adhesively bonded, helically-wound steel strip (a.k.a., helical strip repair).

Of the five repair technologies tested, weld deposition and adhesively bonded steel patch repair technologies exhibited burst pressures that were lower than the burst pressures of the un-repaired pipe sections (10% below and 1% below respectively). The other three repair technologies exhibited burst pressures greater than the burst pressures of the un-repaired pipe sections:

- Glass fiber-reinforced liner repair had burst pressures ranging from 1% to 7% higher.

- Carbon fiber-reinforced liner repair had burst pressures ranging from 4% to 17% higher.

- Helical strip repair exhibited the highest performance with burst pressures ranging from 0.4% to 144% higher.

Physical testing indicated that helical strip repair was clearly the most promising technology evaluated, because of its ability to effectively restore a damaged pipe section in excess of 100% of the specified minimum yield strength, it lends itself well to field deployment, and the material itself is inexpensive. The helical coils can be sized to accommodate any length of corrosion damage, cinched down to allow deployment through pipe bends, and compressed down to a single strip width. Future evaluation of this repair technology was recommended to optimize its application and to develop a prototype repair systems to deploy this repair technology.

4.5.2 Alternative Repair Processes for Casing Repair

This report section is a discussion of alternative processes that were considered for improved casing repair.

4.5.2.1 Alternative Repair Process 1 - Weld Deposition Repair

Weld deposition repair was assessed as the first alternative casing repair technology. It has believed that weld deposition could be performed to specific damage that may not require the entire ID of the casing to be reduced. Such situations could be for isolated corrosion pits, leaking threads or split casings.

During the previous NETL DOE research[6] project, welding deposition repair was also considered as an option to repair the inside of a gas transmission pipeline while the pipeline was in-service. The effect of methane on weld quality was the first litmus test for the welding repair for the previous project and it was assumed to be the initial test for casing repair as well. It is not practical for a storage facility to be emptied before the repair process can be applied and it was assumed that it would be unacceptable to plug the casing to apply the repair. The following narrative is a summary of previous EWI research on the effect of methane on weld quality and the subsequent effects of weld distortion and residual stress on pipe integrity in the as-repaired condition.

During any arc welding operation on steel, the material is exposed to temperatures that range from ambient to well above the melting temperature 1,536°C (2,736°F). When steel at temperatures above 1,130ºC (2,066ºF) is exposed to methane, eutectic iron can form as the result of diffusion of carbon from the methane into the steel and carburization can occur.[44,45] In previous work at EWI,[45] welds were made on the outside of a thin-wall [3.2 mm (0.125 in.)[pipe containing methane gas pressurized to 4.5 MPa (650 psi) with a flow rate of 6.1 m/sec (19.9 ft./sec). Figure 20 shows the equipment setup used to perform these welding trials.

---

[44] Eiber, R. J., Bubenik, T. A., and Leis, B. N., "Pipeline Failure Mechanisms and Characteristics of the Resulting Defects," Eighth Symposium on Line Pipe Research, Paper No. 7 (Houston, TX: American Gas Association, 1993).

[45] Bruce, W.A., "Welding onto In-service Thin-Walled Pipelines," Pipeline Research Council International, Edison Welding Institute EWI Project No. 41732, Columbus, Ohio, July 2000.

Figure 20. Set-Up for Welding Thin Wall Pipe with Pressurized Methane Gas

Figure 21 shows the external appearance of welds 2M7, 2M9, and 2M8 made on the outside of the thin-wall pipe under these conditions. Figure 22 shows the appearance of these welds from the inside.

Figure 21. Welds Made in Pressurized Methane - Appearance from OD

Figure 22. Welds Made in Pressurized Methane - Appearance from ID

Figure 23 is a metallographic cross section thru Weld 2M9 (from Figure 21 and Figure 22).
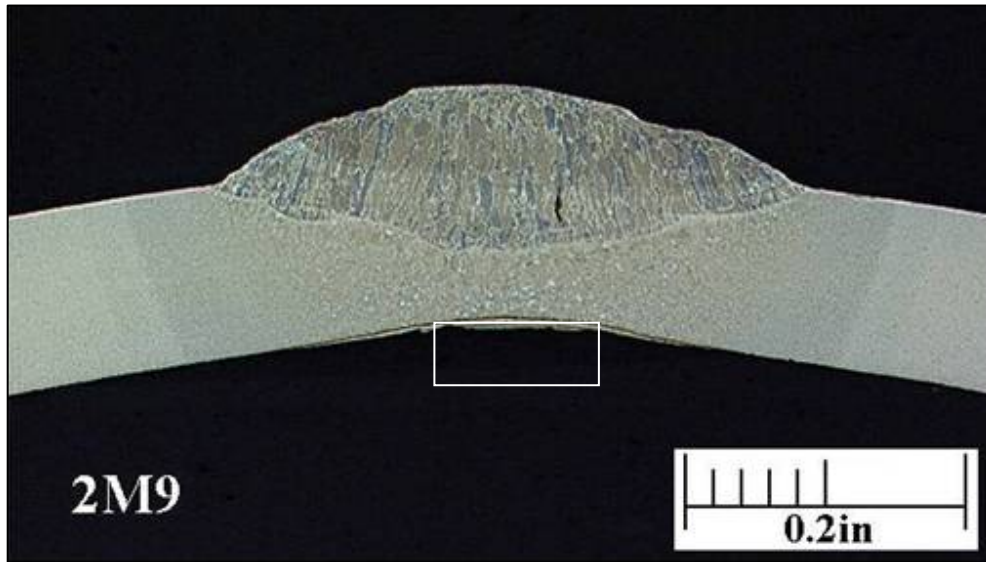
Figure 23. Metallographic Cross Section of Weld 2M9

Figure 24 is a magnified view inside the white box in Figure 23. Figure 24 clearly shows carburization and the formation of thin layer of eutectic iron.
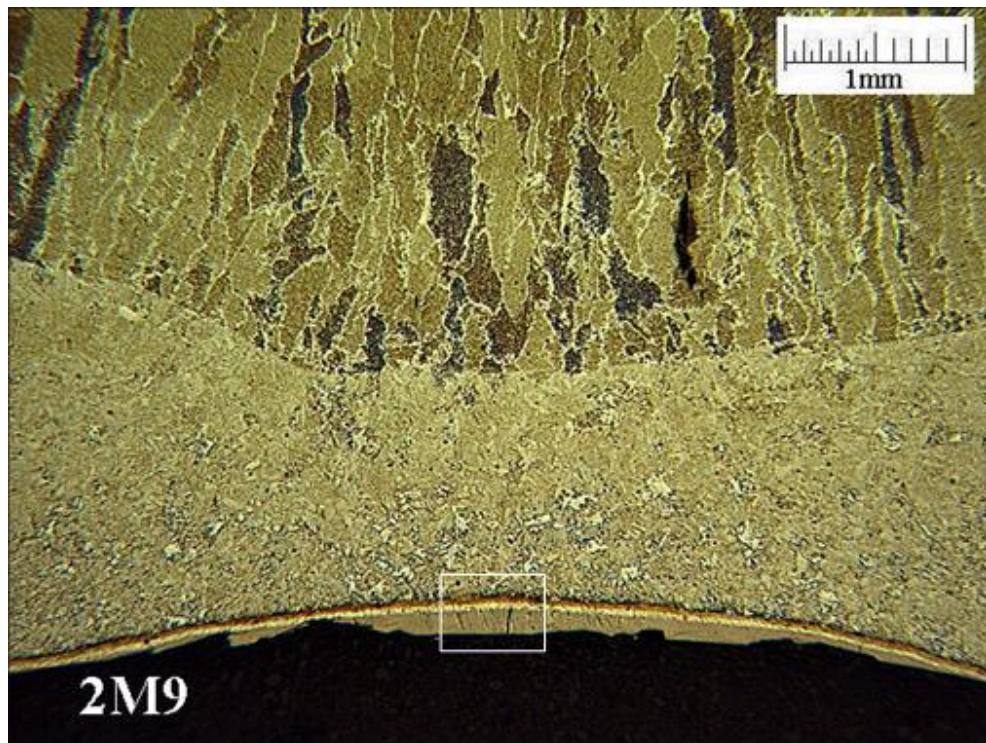
Figure 24. Eutectic Iron Layer on Backside Surface of Weld 2M9

This phenomenon was previously reported by Battelle during experiments with liquid propane.[46] Figure 25 is a magnified view inside the white box in Figure 24 and shows small cracks associated with the eutectic iron layer, which were attributed to the limited ductility of eutectic iron.
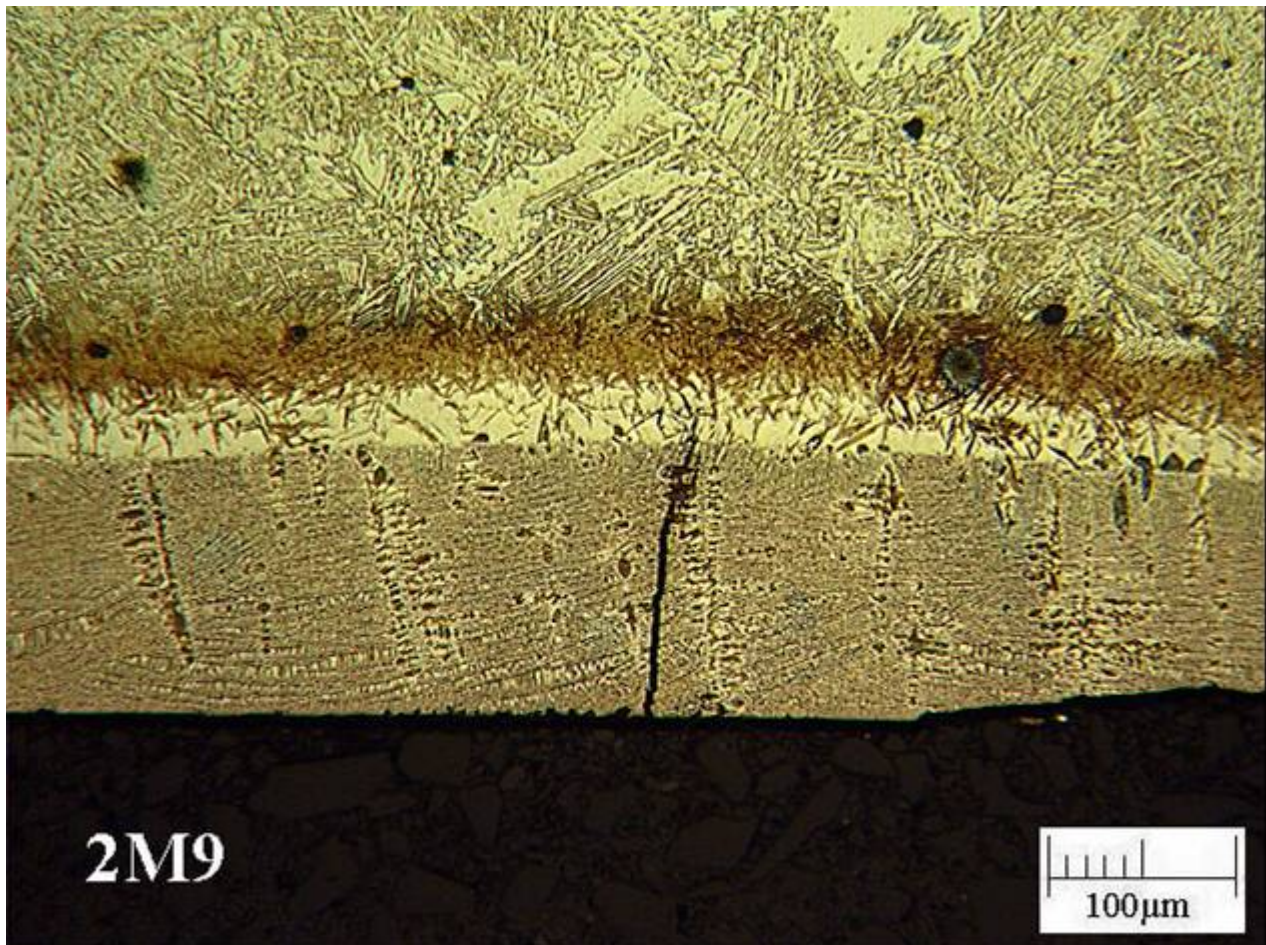
Figure 25. Cracks in Eutectic Iron Layer of Weld 2M9

Because of the detrimental quality effects of exposing steel to methane at an elevated temperature,[46] the DOE NETL project,[6] needed to evaluate the effect methane may have on the weld quality if methane was present in the welding arc and weld pool. To evaluate the effect methane has on the welding arc and weld pool, weld trials were conducted with a shielding gas containing various levels of methane.

---

[46] Kiefner, J. F., Barnes, C. R., Gertler, R. C., Fischer, R. D., and Mishler, H. W., "Experimental Verification of Hot Tap Welding Thermal Analysis. Final Report - Phase II - Volume 2, Liquid Propane Experiments," Repair and Hot Tap Welding Group, Battelle Columbus Laboratories, May 1983.

The welds were deposited using an internal, automatic gas metal arc welding (GMAW) system (Magnatech Pipeliner II) with a 0.89-mm (0.035-in.) diameter AWS ER70S-6 electrode. Seven bead-on-pipe welds were deposited on the ID of a 558.80-mm (22-in.) diameter API 5L Grade B pipe in 6 o'clock position. The travel speed of the welds was not recorded as they were held constant for all weld trials. The shielding gas was supplied by two independent gas bottles: one bottle contained a mixture of 95% Ar + 5% CO_2; the other bottle contained a mixture of 10% methane with a balance of 95% Ar + 5% CO_2. The amount of methane was raised by increasing the flow rate of the bottle containing methane. Methane welding parameters are found in Table 8.

Table 8. Average Weld Metal Hardness and Carbon Content for Methane Weld Trials

| Weld ID | Shielding Gas Flow Rate | | | | Volume Percent Methane | Average Weld Metal Hardness (Hv-10kg) | Weld Metal Carbon Content (%) | Comments |
| | 95% Ar + 5% CO_2 | | 10% Methane + 4.5% CO_2 + 85.5% Ar | | | | | |
	(m^3/hr)	(ft^3/hr)	(m^3/hr)	(ft^3/hr)				
325-2	1.42	50	0.00	0	0.0	169.7	0.073	No Porosity
325-3	1.13	40	0.28	10	2.0	174.7	0.074	No Porosity
325-4	0.99	35	0.42	15	3.0	175.0	0.062	Porosity
325-5	0.85	30	0.57	20	4.0	175.3	0.071	Porosity
325-6	1.22	43	0.20	7	1.4	169.7	0.075	No Porosity
325-8	0.99	35	0.28	10	2.2	176.7	0.071	No Porosity
325-9	0.85	30	0.42	15	3.3	171.3	0.081	Porosity

The resultant welds were then prepared for metallographic examination. Three weld metal hardness measurements were made and the results were averaged for each weld. The chemical composition for each weld was also measured to determine if the presence of methane affected the carbon content of the weld deposit. Table 8 contains a summary of hardness measurements and the percent carbon contents that were measured.

Figure 26 is a graph of the average weld metal hardness values and percent carbon content from Table 8. In Figure 26, the weld metal hardness scale is on the left axis and the percent carbon content of the weld metal is shown on the right axis. From this figure, it can be seen that increasing the volume percent of methane in the shielding gas did not consistently increase either weld metal hardness or percent carbon content of the weld metal.
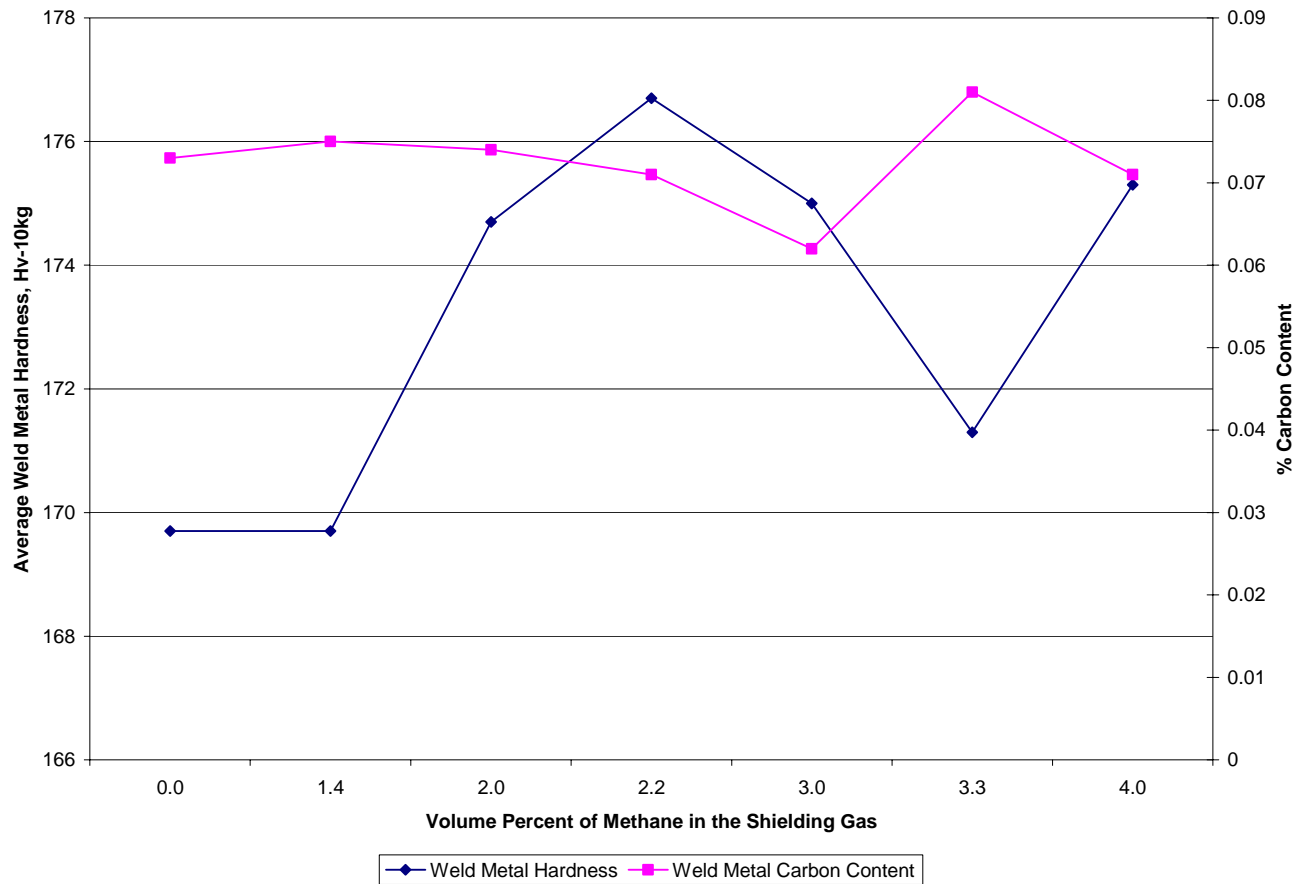
Figure 26. Graphs of Table 8 Hardness Values and Carbon Content

Photos of welds that were made during this portion of the investigation[6] are shown in Figure 27 through Figure 33. A visual examination of the samples revealed that a volume percent of methane greater to or equal to 3% in the shielding gas caused porosity in weld specimens [e.g., 325-4 with 3% methane (Figure 29), 325-5 with 4% methane (Figure 30), and 325-9 with 3.3% methane (Figure 33)].

Figure 27. Methane Weld Specimen 325-2

Figure 28. Methane Weld Specimen 325-3

Figure 29. Methane Weld Specimen 325-4
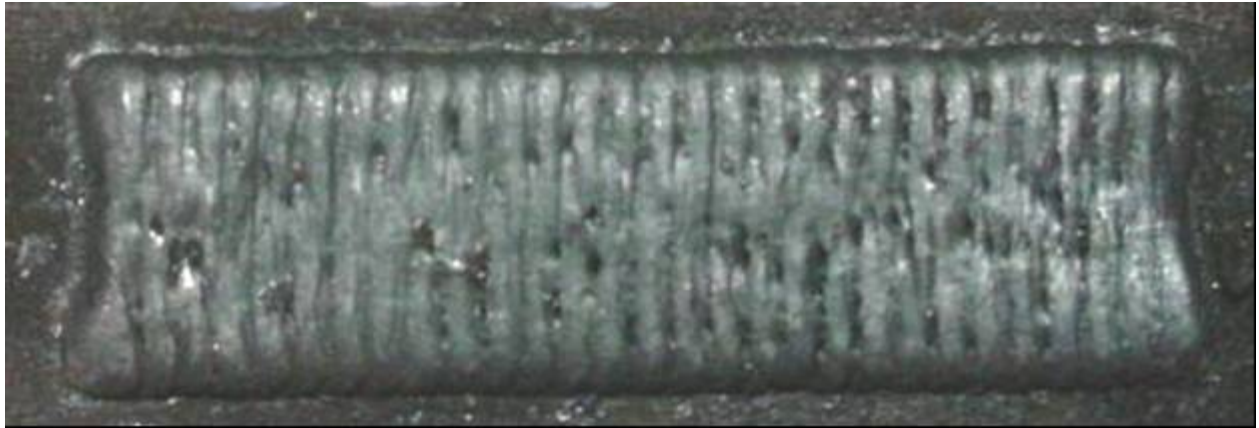
Figure 30. Methane Weld Specimen 325-5

Figure 31. Methane Weld Specimen 325-6

Figure 32. Methane Weld Specimen 325-8

Figure 33. Methane Weld Specimen 325-9

These results[6] clearly indicate that adequate shielding gas protection is critical to creating sound, defect free welds in a methane rich environment and that an increased volume of methane in the weld shielding gas produces welds with porosity defects that decrease pipeline structural integrity. Therefore, weld deposition repair was not recommended for pipelines with methane present and consequently casing repairs. Extensive high risk research and development is required to develop adequate gas shielding methods in the laboratory before field repair can even been attempted. This is years if not decades away.

To further evaluate the use of weld deposition repair for internally repairing pipelines, a pipe section with simulated corrosion damage was repaired with weld deposition repair deposited on the ID of the pipe (Figure 34).[6] The pipe was then subjected to a hydrostatic burst test to determine the adequacy of the repair. Prior to hydrostatic burst testing the pipe it was noticed that the circumference of the pipe has changed and was attributed to the weld residual stresses (Figure 35).

Figure 34. Test 01 Finished Patch Type Weld Repair
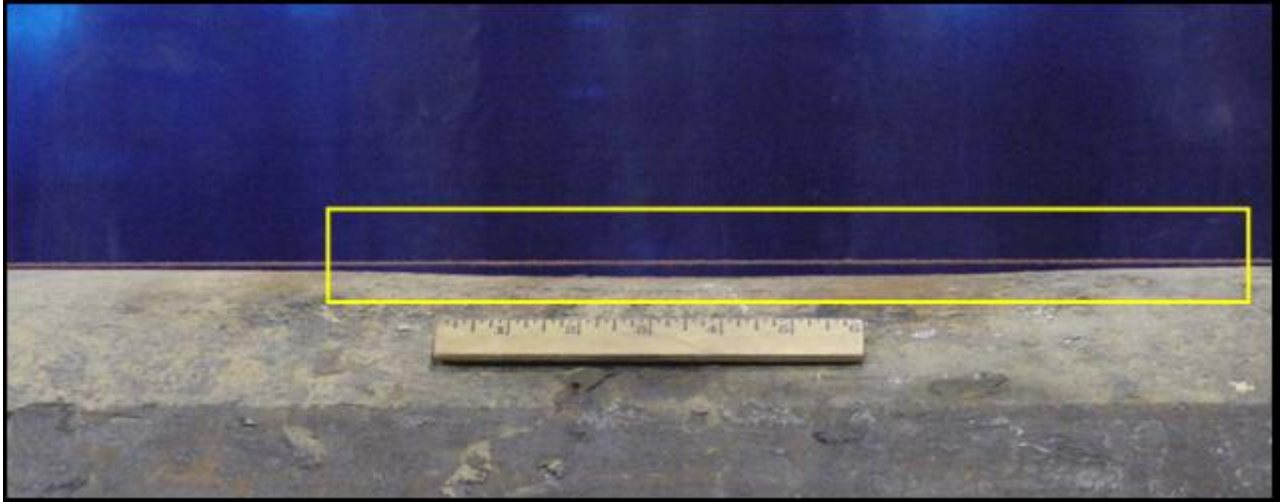
Figure 35. Profile of Dent in Pipe OD after Internal Weld Repair Test 01[6]

The results of the hydrostatical burst test showed that the repaired pipe exhibited a 10% lower burst pressure when results were compared to the burst pressure of an un-repaired pipe section. The reduction of burst pressure between the repaired and un-repaired pipe sections could easily be attributed to the distortion caused by welding residual stresses. The weld distortion area could have acted like a dent in the pipe and, then pressurized, the "dent" tried to re-round which could have reduced the burst pressure of the pipe.[6]

Table 9. Summary of Predicted vs. Actual Hydrostatic Burst Pressure Values Test 01

Pipe Diameter	Pipe Condition	Predicted Burst Pressure		Actual Burst Pressure	
		(MPa)	(psi)	(MPa)	(psi)
558.8 mm (22 in.)	Virgin	10.91	1,583	12.69	1,841
	Simulated Damage Short/Deep Un-Repaired	5.15	747	10.78	1,563
	Simulated Damage Repaired with High Grade CF Liner (Test 01)	-	-	9.68	1,404

The potential of methane in the welding environment and the reduced burst pressure shown in the internally weld deposition trials indicates that weld deposition repair is not the preferred repair technology for casing repairs. There is also concern that the welding arc could ignite the methane rich environment present in casings during repair since there is a higher potential for oxygen to be present. Weld deposition repair was consequently dropped from the test program[6] for internal repair of gas transmission pipelines and therefore weld deposition, although promising in principal, was considered less than ideal for casing repair for similar reasons.

4.5.2.2   Alternative Repair Process 2 - Internal Helical Strip Repair

Internal helical strip repair (developed by EWI for the previous DOE NETL project[6]) was assessed as a second alternate casing repair process. Helical strip repair is viewed as particularly promising for applications where bent casings need to be repaired and current repair technologies do not lend themselves to such applications (e.g., expandable tubular repair cannot transverse the bend to repair the damaged area).

Physical testing[6] indicated that the helical strip repair was clearly the most promising technology evaluated for internal gas transmission pipeline repair due of its ability to effectively restore a damaged pipe section to a pressure in excess of 100% of the specified minimum yield strength (SMYS), the potential for field deployment, and the inexpensive repair materials. The helical coils can be sized to accommodate any length of damage, cinched down to allow deployment through pipe bends, and compressed down to a single strip width.

To deploy a helical strip repair a helical coil is rolled to an OD that is slightly larger than the ID of the pipe section to be repaired. The helical coil is then compressed to an OD smaller than the ID of the pipe by pulling the ends of the helical coil (Figure 36). As illustrated in Figure 36, the OD of the compressed helical strip is coated with adhesive and is inserted into a pipe section where the ID has also been coated with adhesive. The compressed helically-wound coil is then released and is allowed to expand to the ID of the pipe. An inflatable bladder is inserted into the ID of the expanded helical coil and inflated to hold the OD of the steel strip in intimate contact with the pipe ID during the adhesive curing process. Figure 37 shows a single layer of helically-wound steel strip installed in a pipe section. The repair can be made with single or multiple layers of steel strip depending on the operating requirements of the repair.
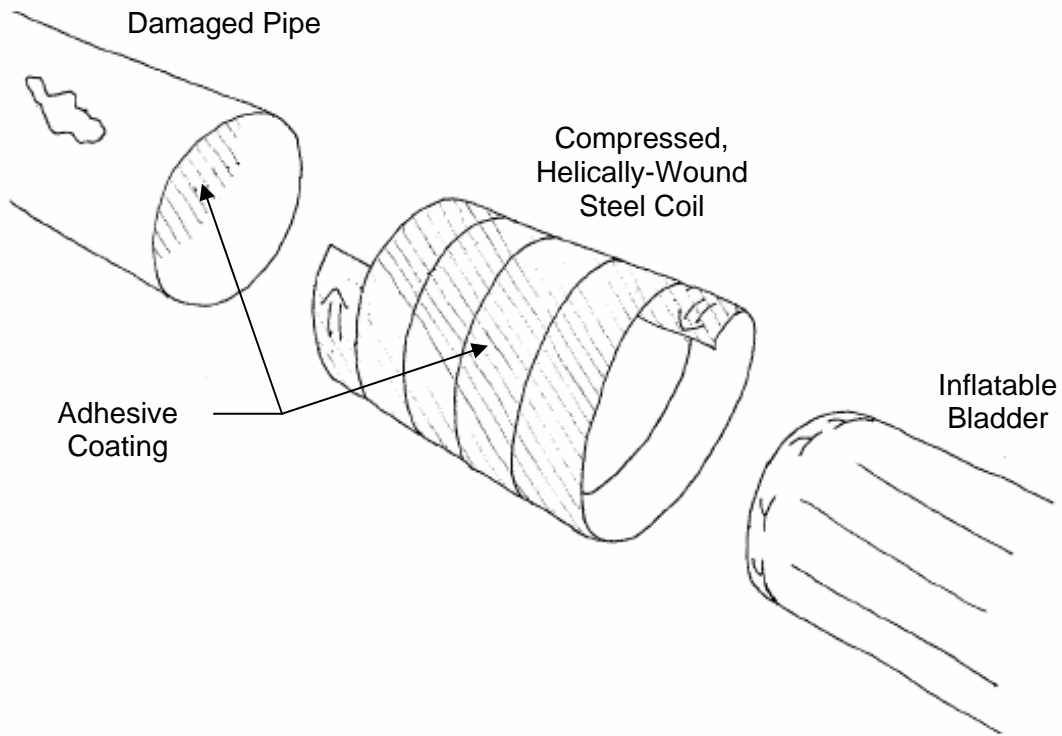
Figure 36. Internal Helical Strip Repair Process
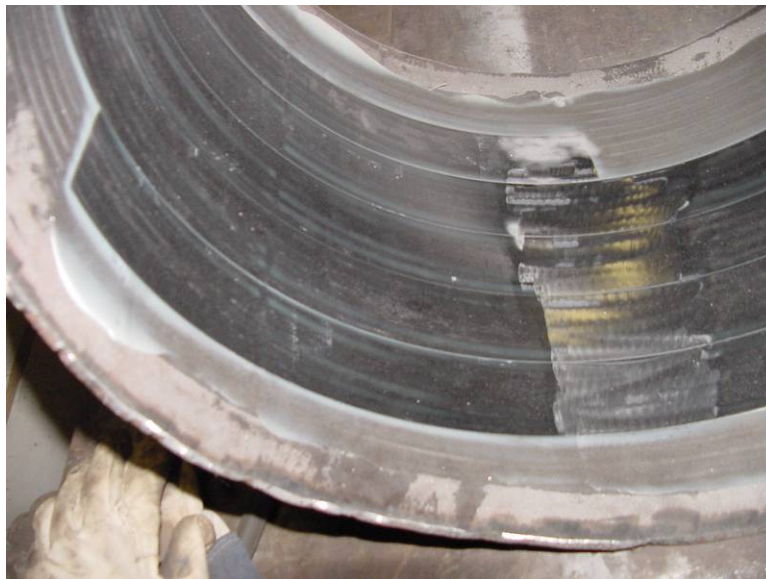
Figure 37. Installed Internal Helical Strip Repair

In the previous DOE NETL project conducted by EWI,[6] a program was developed to evaluate full-size pipe sections repaired with the helical strip repair. Similar to other test programs, one pipe section in the "virgin" (i.e., undamaged) condition was hydrostatically burst tested until

rupture to establish the baseline strength of the pipe. A second pipe section was prepared with an area of simulated corrosion damage, left un-repaired and was hydrostatically tested until failure to establish the "damaged/un-repaired" strength of the pipe. A third pipe was prepared with identical simulated corrosion damage repaired with the helical strip repair and hydrostatically tested until rupture to establish the "as repaired" strength of the pipe. In this way, improvements shown by the helical repair were experimentally quantified with respect to the undamaged pipe and damaged pipe. The following results of the test program conducted on helical strip repair are taken directly from EWI's previous DOE project report.[6]

A 24-in. (609.6-mm) OD by 0.312-in. (7.9-mm) thick wall X65 pipe was cut into three sections. Identical corrosion was simulated on two pipe sections by machining a 0.234-in. (5.9-mm) deep by 9-in. (228.6-mm) long slot on the OD of the pipe. A ball mill was then used to produce a hole through the wall of the pipe of one of the simulated corrosion pipe sections (Figure 38). The undamaged pipe section and damaged/un-repaired pipe section were pressure tested until failure. The damaged pipe section with the through hole was repaired with a helical strip repair and pressure tested until failure.

Figure 38. Short, Extra Deep Damage with Through Hole for 609.6 mm (24 in.) Pipe

RSTRENG® software[47] was used to predict the burst pressure for the damaged/un-repaired pipe section with simulated damage. To establish baseline material performance for the 24-in. pipe, Barlow's equation (Equation 1) was used to calculate the pressure that corresponds to 100% SMYS (i.e., X65 pipe). To determine the predicted burst pressure for the virgin pipe section, the measured ultimate tensile strength of the X65 pipe was used as S in Equation 1.

$$P = \frac{2St}{D}$$

Equation 1. Barlow's Formula

---

[47] Kiefner, J. F. and Vieth, P. H., "A Modified Criterion for Evaluating the Remaining Strength of Corroded Pipe" Final Report to A.G.A. Pipeline Corrosion Supervisory Committee, Project PR-3-805, Battelle, Columbus, OH, December 1989.

Test results and calculated burst pressures for all the conditions are summarized in Figure 39. Figure 40 and Figure 41 show the simulated corrosion damage after the repaired pipe section ruptured. Based on these results shown in Figure 39 and discussions with industry, it was determined that the helical strip repair should be further evaluated as an alternative to casing repair.
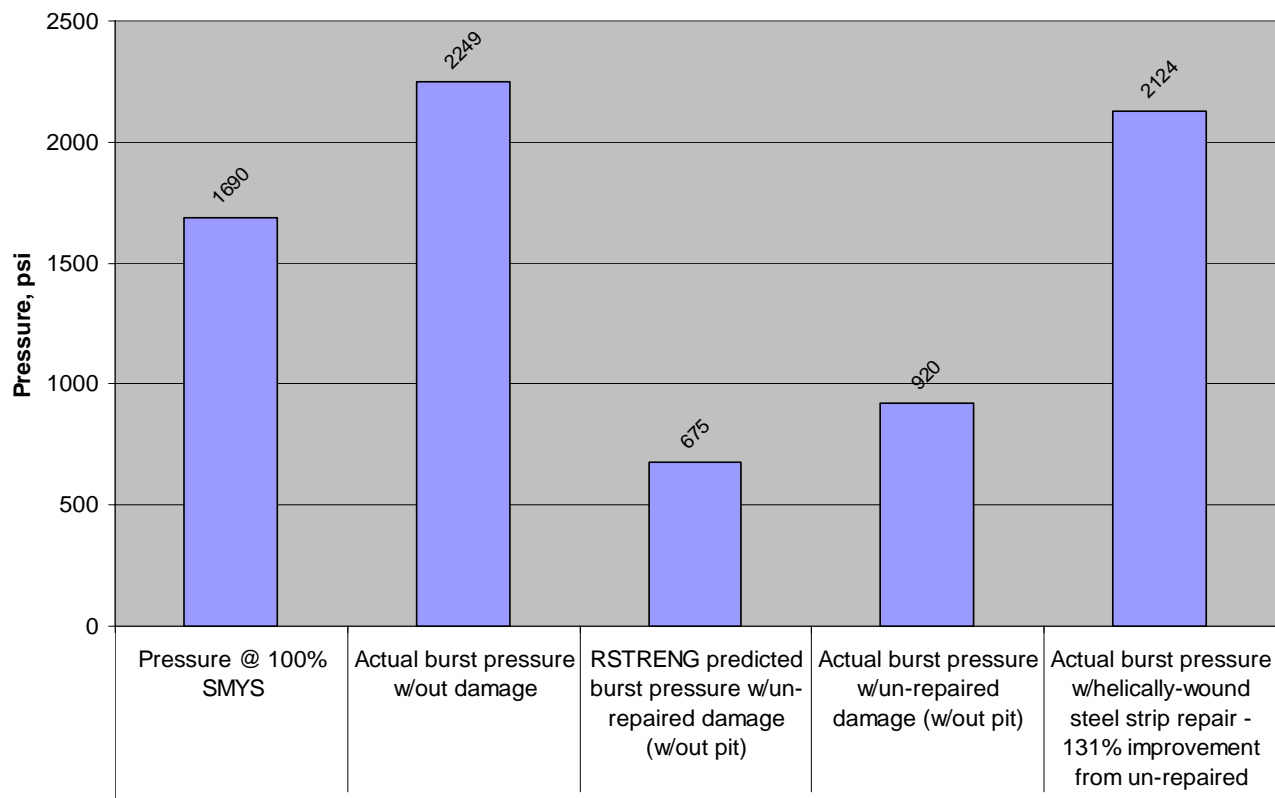
Figure 39. Burst Pressures for Internal Helical Strip Repair Analysis

Figure 40. Simulated Corrosion Area after Burst Test

Figure 41. Close-Up of Simulated Corrosion Area after Burst Test

4.5.2.3   Alternative Repair Process 3 - Laser Cement Drilling

During the literature review and discussions with industry it was mentioned that during cement squeeze repairs, it is common for the liquid cement to occlude corrosion holes before the voids on located at the OD of the casing are filled with cement. This issue can lead to several squeeze attempts before a success pressure test can be performed. The idea for this alternative is to drill holes, downhole, were the cement squeeze will be performed to improve the one-time squeeze success rate.

Five years ago, California mandated that all hospitals in southern California complete a seismic retrofit to improve their building's resistance to earthquakes. The mandate requires strategically reinforcing existing concrete structures and necessitates concrete cutting, surfacing, drilling and pouring of new concrete. Loma Linda University Medical Center in Loma Linda, CA wanted to retrofit their hospital while it was occupied to minimize revenue loss. At the time, the only options to put holes in cement were slow, loud mechanical processes such as jack hammering and drilling. Unfortunately these processes are extremely disruptive to patients. Over the past 5 years, EWI has successfully developed a portable ytterbium (Yb) fiber laser cement drilling system for Loma Linda that is highly productive and minimally disruptive to patients (Figure 42). The current system is an IPG Photonics fiber laser with II-IV, Inc. custom laser optics that produces a collimated beam capable of cutting or drilling a variety of hole sizes (Figure 43) and is light weight and can be operated by one person (Figure 44).
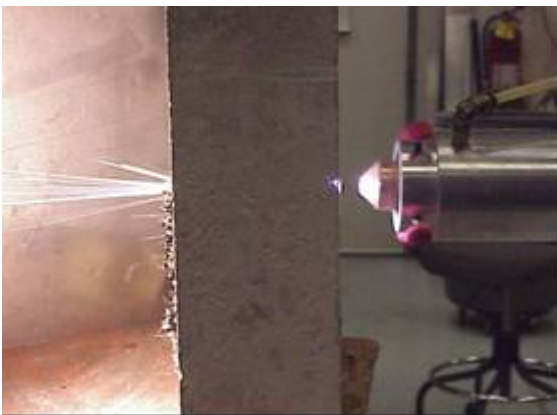
| **Side View of Laser Cutting Concrete** | **Back View of Beam Penetrating Concrete** |
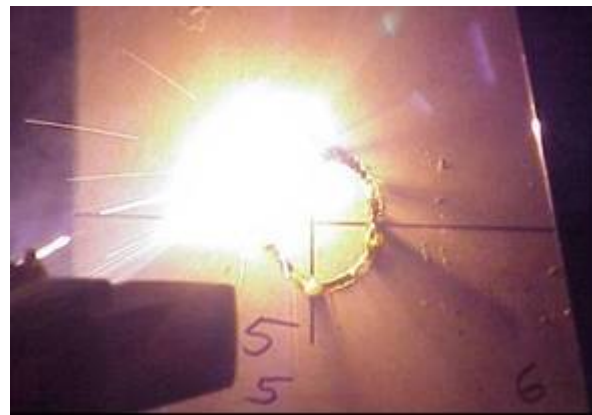
Figure 42. Laser Cutting Cement
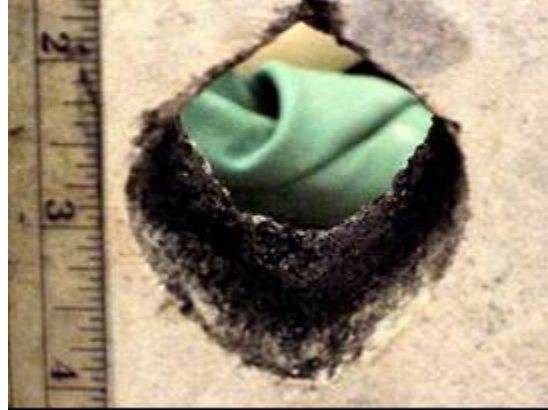
| 0.25-in. Blind Hole | 2-in. Through Hole |

Figure 43. Laser Drilled Holes Variations

Figure 44. EWI Laser Cement Drilling Head on Cement Wall

Given the size of the EWI fiber laser drilling system, laser cement drilling could be used downhole to open up as intended but this alternative repair technology is not recommended for future evaluation for several reasons. One reason for not selecting this alternative came from industry by way of the Email inquiry[3] and online survey[4] responses both suggesting that squeeze repairs are not common. Also the selection of squeeze materials is a mature process. Designer squeeze materials (e.g., gels or epoxies) can be selected to penetrate any size of corrosion pit; therefore, while laser drilling to enlarge orifice size is promising, it is may not be necessary. There is also concern that the heat from the laser cutting process may ignite the methane rich environment present in casings during repair.

4.5.2.4 Alternative Repair Process 4 - Magnetic Pulse Welding (MPW)

Magnetic pulse welding (MPW) was the fourth proposed alternate for casing repair and is an adaptation to the current expandable tubular repair method. As mentioned in the literature review, the use of an expandable tubular repair may be limited to the temperature, pressure, or service environment of the well which are attributed to the elastomer used for the pressure seal. A potential application for MPW technology for casing repair is for joining a metallic linear to a damaged/leaking casing to return it to full capacity. This process could also potentially create high temperature/high pressure (HP/HT) seals for H_2S service or for severe loading environments, such as cavern storage and thermal heavy oil operations.[34,48]

Figure 45 is a picture of the 90-kJ Magneform MPW system at EWI. MPW is a single-shot joining process, i.e., the weld is made instantaneously by pressing a button. The basic configurations, phenomena, and mechanisms of MPW are described and documented in numerous publications.[49,50,51,52,53] MPW essentially uses a magnetic field to accelerate one component (i.e., a flier) against another component (i.e., a target). When the impact conditions are correct, a joint is formed in a similar manner to an explosion bond[53] (Figure 46). A basic schematic of the MPW system is shown in Figure 47.

---

[48] Private Communication, Brian Wagg, C-Fer Technologies, February, 20, 2007.

[49] Powers, H. G. 1967. Bonding of aluminum by the capacitor discharge magnetic forming process. Welding Journal, 46(6):507-510.

[50] Khrenov, K. K. and Chudakov, V. A. 1968. Magnetic-Pulse Welding. *Avtomat Svarka*, (2):74-75.

[51] Masumoto, I., Tamaki, K., and Kojima, M. 1985. Study on electromagnetic welding. Report 1: Electromagnetic welding of aluminum tube to aluminum or dissimilar metal cores. *Transactions of the Japan Welding Society*, 16(2):110-116.

[52] Hokari, H., Sato, T., Kawauchi, K., and Muto, A. 1998. Magnetic impulse welding of aluminum tube and copper tube with various core materials. *Welding International*, 12(8):619-626.

[53] Shriban, V., Livshitz, Y., Gafri, O., and Kimchi, M. 2000. The magnetic pulse welding process. *Third International TWI/EWI Workshop on Joining of Aerospace Materials*.

(a) 90-kJ Capacity Bank   (b) Coil System

Figure 45. EWI's 90-kJ Magneform MPW System
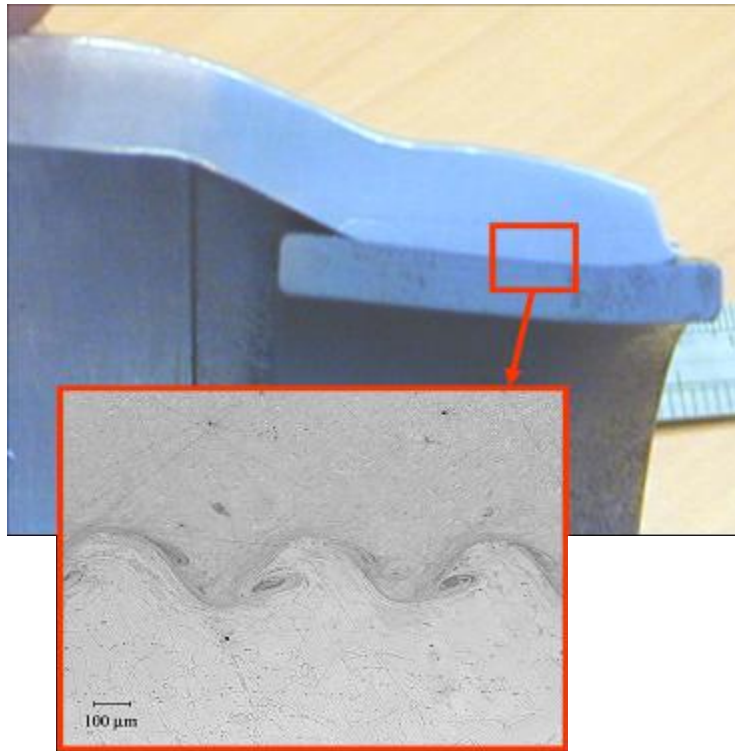
Figure 46. MPW Bonded Interface
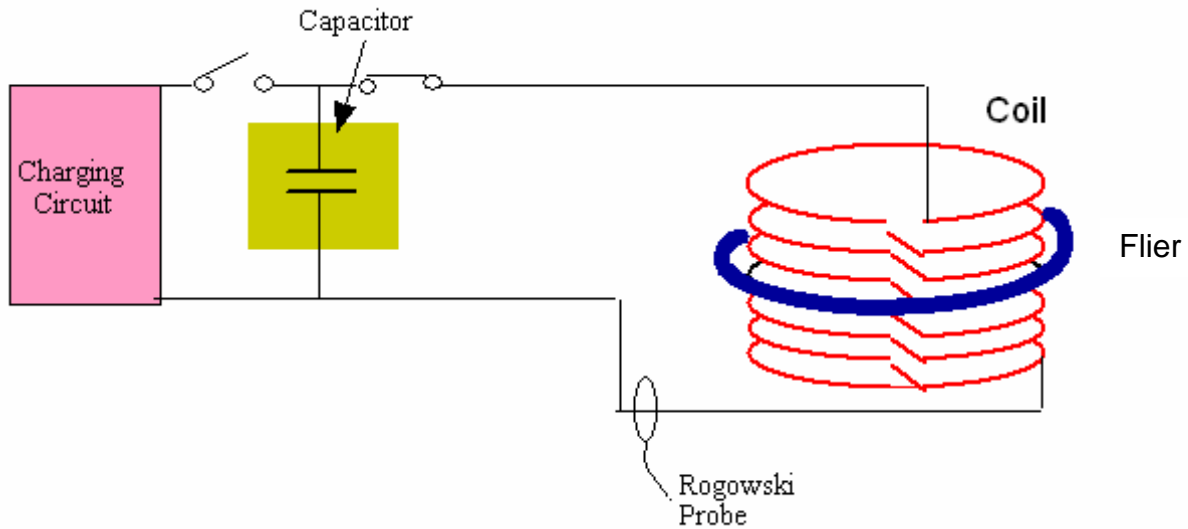
Figure 47. Magnetic Pulse Welding Process Schematic

To perform a MPW a charging circuit (high-voltage DC power) is used to charge a bank of capacitors. The capacitors are then discharged into an accelerator or coil. The short-time (10- to 100-µs) pulse in the coil then induces a reaction current flow in the nearby flier. The currents in the coil and flier then repel causing the flier to have a high repulsion force. The high repulsion force drives the flier with a high velocity toward the target component causing a strong impact between the two metals causing a metallurgical bond (Figure 46). The impact pressure sweeps away the surface contaminants and forces atomic bonding over the interface. Figure 48 gives another schematic representation and a force diagram of MPW for tubular applications were the outer tube is compressed onto an inner tube.
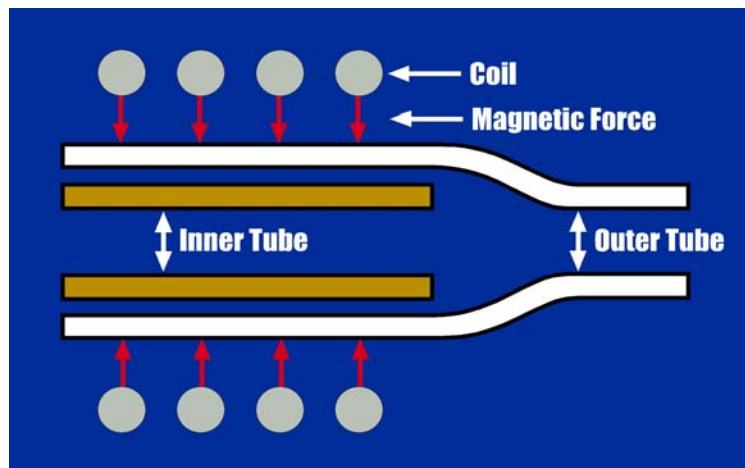
Figure 48. MPW Magnetic Force Diagram

Since MPW technology is relatively new, there are no industry standard recommended practices defining set-up conditions to develop weld joints for a given application. Additionally, there is little information on the effects of manufacturing variables. The key to successful implementation of MPW is understanding MPW's tolerances to manufacturing variations like part concentricity (i.e., parallel alignment of the two components), angular alignment, and cleanliness.

While the field of MPW is quite broad, EWI has a lot of experience in the field of MPW. EWI owns or has rights to patent applications, know-how, and trade secrets related to methods of MPW for low-ductility materials, split concentrator designs for MPW, split coil for MPW (U.S. Patent Application #20060185412), and internal/expansion coil designs for MPW.

EWI has conducted extensive work to relate electrical and mechanical characteristics in an effort to define critical processing conditions for a range of applications.[50,51] As a result, the most critical MPW welding parameters have been identified and are listed below:

- Peak Pulse Current

    - The maximum coil current, seen in the first cycle of discharge power.

- Pulse Frequency

    - The frequency implied by the first half cycle pulse width.

- Stand-Off Distance

    - The gap between the flier and the target.

- Lap Distance

    - The overlap between the components being joined).

- Implied Angle on the Target

    - The contact angle between the target surface and collapsing flier surface.

- Gap Between the Coil and Flier

    - The radial distance between the ID of the concentrator and the surface of the flier.

Although the basics of MPW are known, information on how to adapt the process to potential applications and its robustness in production environments is not available. Each application must be thoroughly evaluated by a combination of numerical analysis and design-of-experiment (DOE) methodologies to determine the coil design and the range of process parameters each coil design is capable of producing.

EWI performs the numerical analysis using software called MP*one* (previously known as multi-physics analysis code or MAC). The software is capable of modeling the magnetic field distribution generated within the main coil and magnetic field coupling between the coil and the concentrator. The software is also used to perform a stress analysis in the concentrator during the welding process. The results assist in concentrator (*i.e.*, coil) design and selection of the initial process parameters.

From the numerical analysis results, several coil designs can be built and evaluated to determine which design is the most robust for a specific set of process parameters. The evaluation of each coil design is typically done be developing and performing a DOE. The DOE welds are then destructively tested (e.g., peel and metallographic testing) and the welding parameter traces are analyzed for quality assurance. For example, a typically DOE can be designed to address flier-to-target concentricity (i.e., parallel alignment of the two components), flier gap, flier lap onto the concentrator (i.e., the degree the flier is extended over the concentrator land), surface cleanliness, and voltage. The weld analysis is then normalized and subjected to regression curve fitting which produce process robustness curves that allow the effect of each variable to be assessed as it is varied from its best-practice condition. The final DOE results identify the best-practice conditions and the development of process robustness curves for each coil size (and/or joint) under investigation. This approach for MPW evaluation has been demonstrated for a wide range of tubular applications; most notably material combinations of Aluminum 6061-T0 to 6061-T6, Aluminum to Copper, Aluminum to Steel, and Steel to Steel.

MPW has been used extensively for externally welding tubular structures with a compression type of operation using an external coil, with the specimens inserted in the coil opening (Figure 48). For internal welding, an expansion-type operation is needed which is constructed from multi-turn coils of copper (Cu) wire wound in a helix and embedded into a non-conductive core. To prevent the Cu wire from moving during operation, an epoxy is used to mold the core and the Cu windings. This type of coil works fine for small scale forming operations but has not been proven for larger diameter tubes because MPW typically requires high electromagnetic pressure in localized areas. The capacity to provide sufficient localized pressure is limited in current internal coil designs. In addition, windings could fail in areas generating high pressure demanded by certain applications, windings could move after a few operations creating arcing between neighboring windings in a coil and between the coil and work piece. To eliminate these issues in current internal coil designs, EWI has developed and tested a more durable internal coil system. Preliminary results show that the internal coil system is more robust than multi-turn coils; however, the efficiency needs to be improved for internal welding of high strength materials such as those used in casings. Future development is therefore needed to improve coil design in order to fully explore the feasibility of MPW for casing repair.

The estimated cost to conduct such a feasibility study is estimated to be $150,750. A detailed description of such a feasibility study is located in EWI Proposal No. 50687GTH, which was submitted to GSTC on May 3, 2007.

4.5.2.5   Other Alternative Repair Processes

Twelve survey[4] respondents indicated that they were not aware of any emerging casing repair technologies not covered by the survey. One respondent was familiar with the expandable patch repair technology and indicated that this repair shows promise.

4.6   Task 6 – Assessment of Alternative Repair Method Capabilities

This section summarizes the assessment of alternative repair technology for casing repair, which includes the creation of a matrix of alternative methods that compares and contrasts the various attributes of the four alternative casing repair technologies discussed in Section 4.5. In addition to the assessment a further feasibility study of the helical strip repair was performed.

4.6.1   Assessment Matrix of Candidate Alternate Casing Repair Methods

Starting with the feasibility categories identified in the previous DOE NETL project[6], the results of the casing repair literature search and the survey[4] responses were reviewed to identify feasibility categories unique to the natural gas storage industry needs. The following major feasibility categories were identified:

- Technical feasibility of candidate repair process.

- Feasibility of inspecting the candidate repair process with NDE inspection processes commonly used by the gas storage and transmission industries.

- Feasibility of substituting the candidate alternate repair for currently-used casing repair methods.

- Maturity level of the candidate repair process.

- Candidate repair process costs.

Each feasibility category was then subdivided into capabilities or characteristics to rank. Each capability or characteristic was assigned a unique weight factor to distinguish its importance in the overall repair process feasibility. Weight factors were based on the literature search and survey[4] responses associated with the feasibility capability/characteristic, with the sum of all weight factors being equal to 100%.

For each potential repair process, individual feasibility capabilities were rated on a scale from (-1) to (5) as defined in Table 10.

Table 10. Key to Ratings in Potential Repair Process Matrices

Rating	Definition
-1	Unacceptable
0	Doubtful Potential - High Risk
1	Development Required - High Risk
2	Development Required - Medium Risk
3	Development Required - Low Risk
4	Acceptable - Low Risk
5	Ideal - No Risk

Each rating was then multiplied by its unique weight factor to arrive at the weighted score for the individual capability. Four characteristics were determined to be "show stoppers", given the fact that an unacceptable rating for these capabilities would negate repair process feasibility entirely.

The four show stoppers were identified as:

- Affinity of the process to ignite methane.
- Ability to perform repair process in the vertical pipe axis position.
- Process technical feasibility.
- Deployable in methane rich environment.

The rating of each show stopper was multiplied by 25 to produce the corresponding weighted score. The assessment matrix of candidate casing repair methods is shown in Table 11. Figure 49 is a bar chart that contains the total weighted scores for each candidate alternate casing repair technology.

Table 11. Matrix of Alternative Casing Repair Methods

Feasibility Category	Weight Factor	Capability or Characteristic to Rank	Welding Repair		Adhesively Bonded, Helically-Wound, Steel Strip Repair		Laser Drilling for Squeeze Repairs		Magnetic Pulse Welding	
			Rating	Weighted Score	Rating	Weighted Score	Rating	Weighted Score	Rating	Weighted Score
Technical Feasibility of Candidate Repair Technology		Affinity of Technology to Ignite Methane	-1	-25	5	125	-1	-25	2	50
		Vertical Pipe Axis Deployment Position	4	100	3	75	5	125	3	75
		Process Technical Feasibility	4	100	3	75	3	75	3	75
		Deployable in Methane Rich Environment	0	0	3	75	1	25	3	75
	3%	Ability to Match Material Properties of Casing	4	12	4	12		0	4	12
	1%	Near Surface Deployment	2	2	2	2	2	2	2	2
	10%	Downhole Deployment	1	10	1	10	1	10	1	10
	10%	Repair Permanence	5	50	4	40		0	5	50
	5%	Ability to Repair Corrosion Damage	3	15	3	15	-1	-5	3	15
	4%	Ability to Repair Through Holes	2	8	3	12	2	8	3	12
	4%	Ability to Repair Split Casings	1	4	3	12	0	0	3	12
	5%	Ability to Restore Leak Tightness	2	10	3	15	1	5	3	15
	1%	Ability to Negotiate Bends during Deployment	1	1	2	2	2	2	1	1
	1%	Ability to Survive in H2S Environment	2	2	2	2	1	1	3	3
	1%	Ability to Survive Bacteria in Environment	2	2	2	2	1	1	3	3
	1%	Ability to Survive Acid Treatments	2	2	1	1	1	1	3	3
	1%	Ability to Survive at Well Pressure Maximum	2	2	3	3	1	1	3	3
	2%	Ability to Survive CP in Environment	2	4	1	2	1	2	3	6
	4%	Ability to Survive Exposure to Corrosion Inhibitors	3	12	1	4	1	4	3	12
Inspectability of Candidate Repair Process	1%	Physical Measurement Device	5	5	5	5	5	5	5	5
	5%	Pressure Test	5	25	5	25	5	25	5	25
	1%	Magnetic Flux-Leakage	5	5	2	2	5	5	5	5

Feasibility Category	Weight Factor	Capability or Characteristic to Rank	Welding Repair		Adhesively Bonded, Helically-Wound, Steel Strip Repair		Laser Drilling for Squeeze Repairs		Magnetic Pulse Welding	
			Rating	Weighted Score	Rating	Weighted Score	Rating	Weighted Score	Rating	Weighted Score
Ability of Candidate Repair to Substitute For or to Improve Currently-Used Repair Methods	1%	Cement Squeeze Repair	1	1	3	3	3	3	3	3
	1%	Sealant Squeeze Repair	1	1	3	3	3	3	3	3
	1%	Metallic Squeeze Repair	1	1	3	3	3	3	3	3
	10%	Metallic Liner Repair	1	10	3	30	-1	-10	3	30
	1%	Composite Liner Repair	1	1	3	3	-1	-1	3	3
	3%	Tubular Packing Systems	0	0	3	9	0	0	3	9
	3%	Back Off, Pull or Replace	0	0	0	0	0	0	0	0
Technical Maturity of Candidate Repair Method	5%	EWI Experience with Technology	5	25	5	25	5	25	5	25
	1%	Laboratory Deployable	0	0	5	5	5	5	5	5
	1%	Technology Development Required	1	1	3	3	1	1	2	2
	1%	Vendors That Offer Technology	1	1	-1	-1	-1	-1	-1	-1
	1%	Field Deployable	1	1	1	1	0	0	1	1
	1%	Industry Experience with Technology	1	1	-1	-1	-1	-1	-1	-1
Cost of Candidate Repair Process Application	2%	Equipment/Hardware Costs	2	4	2	4	0	0	0	0
	2%	Power Requirements	1	2	1	2	0	0	0	0
	2%	Repair Surface Preparation Requirements	1	2	1	2	3	6	1	2
	2%	Process Application Time	2	4	1	2	4	8	4	8
	2%	Material Cost	4	8	3	6	5	10	3	6
	100%			**409**		**615**		**318**		**567**
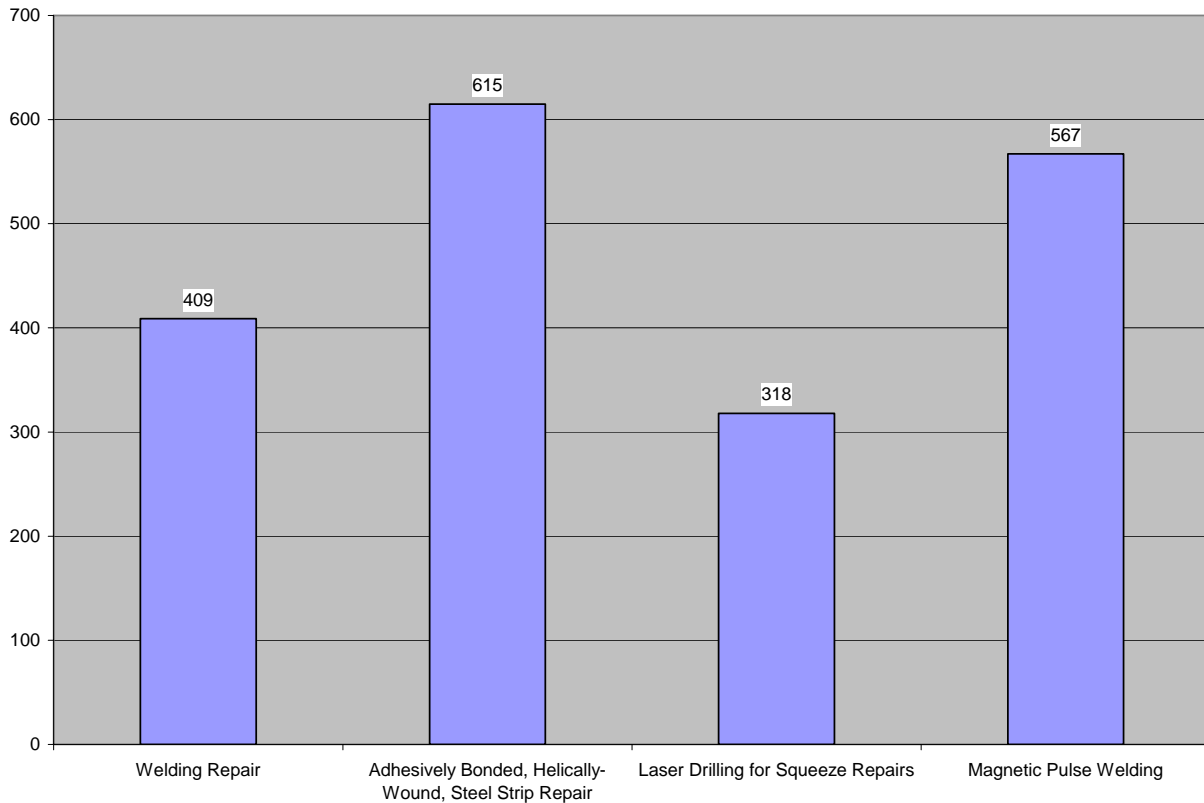
Figure 49. Weighted Scores of Candidate Alternate Casing Repair Methods

4.6.2   Technology Readiness Level Assessment of Candidate Alternate Casing Repairs

A technology readiness level (TRL) assessment is routinely used to identify a technology's performance risk and its integration risk. TRLs provide a common language and standard to assess the performance maturity/risk of a technology and the path for system maturation. Using the NASA developed TRL system[54] as a template, the TRL chart in Figure 50 was developed specifically for the development of new casing repair technologies.

---

[54] Author unknown, http://www.hq.nasa.gov/office/codeq/trl/trlchrt.pdf.
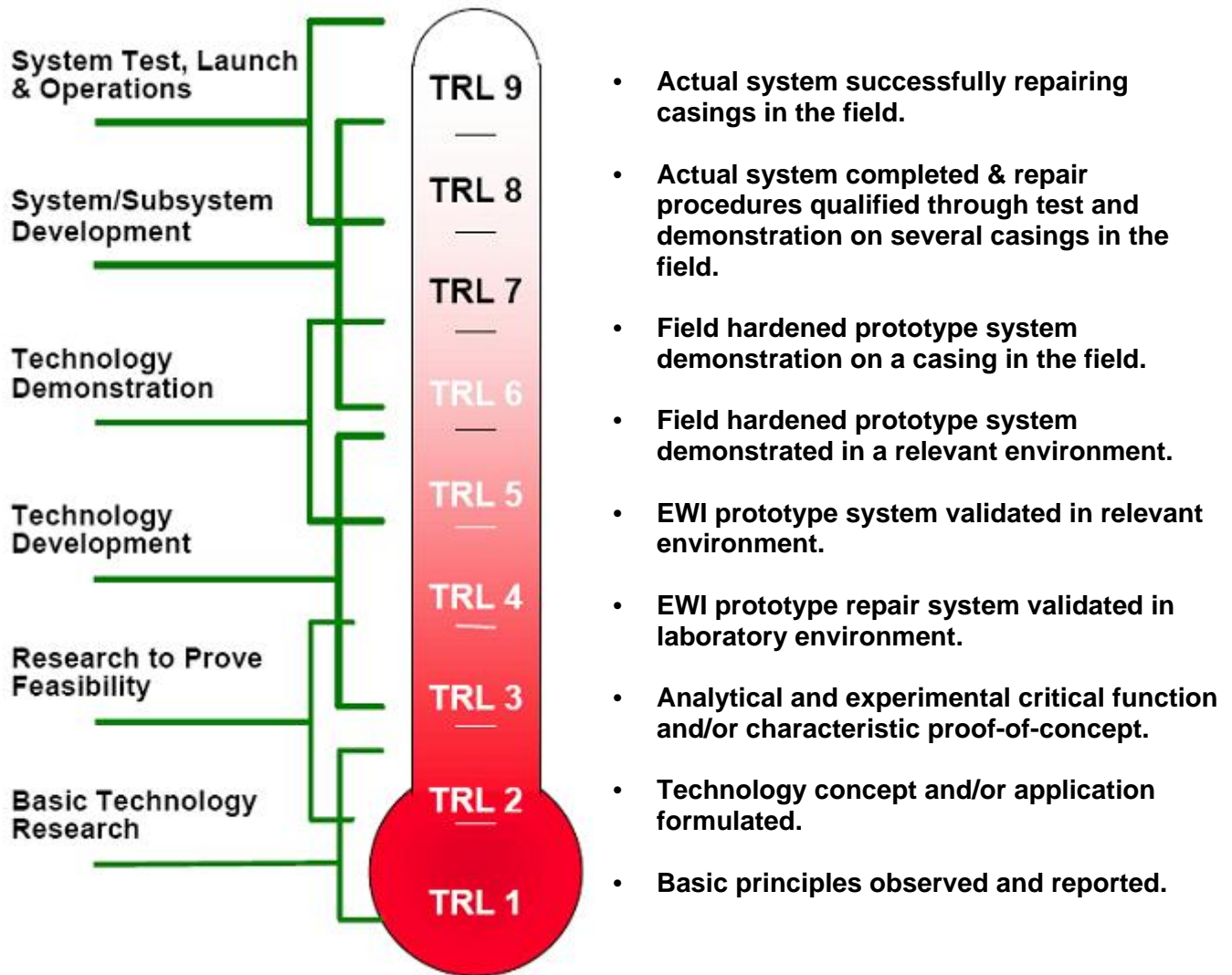
Figure 50. Technology Readiness Level of Automated Welding System

Using the TRL chart in Figure 50, internal helical steel strip repair is clearly a TRL 3, because
EWI has demonstrated analytical and experimental critical function through the proof-of-concept
testing in the DOE NETL project.[6] Similarly, MPW is clearly a TRL 2. MPW technology concept
has been formulated; however, a proof-of-concept needs to be conducted.

4.6.3   Internal Helical Strip Repair Feasibility Study

Based on the assessment in Section 4.6.1, the results of the DOE NETL program[6], and the fact
that helical strip repair is a TRL 3, the project team decided to conduct a limited study of the
helical repair with respect to casing repair. In an attempt to further explore the feasibility of the
helical strip repair for casings, EWI performed a set of hydrostatic burst tests during the project.
Tests were conducted on simulated field bent pipe sections to represent casings that have been

bent as a result of earth movements. The first pipe was in the "virgin" condition (i.e., unbent) with no repair to established the baseline strength of an undamaged pipe. The second pipe was bent to simulate damage due to earth movements and tested without a repair to establish the "as damaged" strength. The third pipe was bent and simulated corrosion damage with a through hole was repaired with the helical strip repair to determine the "as repaired" strength. A through hole was used in the feasibility trials to simulate a casing that was bent and corroded that could not contain pressure. From discussions with industry, the ability to maintain pressure is the main measure of an acceptable repair.

The material used to perform the helical strip repair feasibility was a 254-mm (10-in.) diameter by 9.3-mm (0.365-in.) thick, X42 grade pipe. The pipe used had a similar diameter, wall thickness and strength values highlighted by the survey responses.[4] Casing material was not used because of the difficulty in locating a casing supplier. The first pipe section had only test heads welded onto it. The other two pipe sections were field bent to a 10⁰ angle using field induction bending equipment. There was no postweld processing after the bend in an attempt to keep the bending stress in the pipe during the hydrostatic burst test. The first bent pipe section had the test heads welded onto it (Figure 51).

Figure 51. Bent Pipe Section for Helical Strap Repair Feasibility

The second bent pipe section had simulated corrosion machined into the pipe. This was done by first drilling an 3.2-mm (0.125-in.) diameter hole through the pipe wall. A grinder was then used to machine away an elliptical area approximately 139.7-mm (5.5-in.) long by 50.8-mm (2-in.) wide with the hole in the center of the ellipse (Figure 52).

Figure 52. Simulated Corrosion with Through Hole

The adhesive and steel strap material that was used for the helical strip repair were the same materials used in the previous DOE NETL project.[6] The material properties and dimensions of the strap and pipe material are listed Table 12 (the strength of the pipe listed in the table is the SMYS of the pipe).

Table 12. Helical Repair Material Dimensions and Properties

Material	Thickness		Yield Strength		Ultimate Tensile Strength	
	in.	mm	ksi	MPa	ksi	MPa
Strap	0.044	1.12	101.5	698.29	143.25	987.95
Pipe	0.365	9.271	42	289.66	60	413.69

Since the strap material was stronger than the pipe material it was decided to use less than a full wall thickness of the strap material for the repair. Consequently, there was a total of four layers used in the helical repair. Four layers were selected to restore the structural integrity with respect to the strength/thickness of the repair compared to the pipe material. The hydrostatic burst test results are listed in Table 13 and are plotted in Figure 53.

Table 13. Burst Test Results for the Helical Strap Repair Feasibility.

Specimen Identification	Specimen			Test Conditions				Failure Location
	Dia.	Length	Thick	Temp.		Burst Pressure		
	(in.)	(ft.)	(in.)	(°C)	(°F)	(MPa)	(psi)	
Unbent Pipe	10.75	5.0	0.375	20	68	32.30	4,684	Center
Bent Pipe	10.75	5.0	0.375	20	68	34.52	5,005	Outside Bend
Bent and Damaged Pipe	10.75	5.0	0.375	20	68	17.03	2,469	Repair Area

Figure 53 shows that the bent pipe failed at a higher pressure than the unbent pipe and failure occurred outside the bend. This result would indicate that the pipe was work hardened as a result of the bend causing the bent section to have a higher strength then the unbent section.
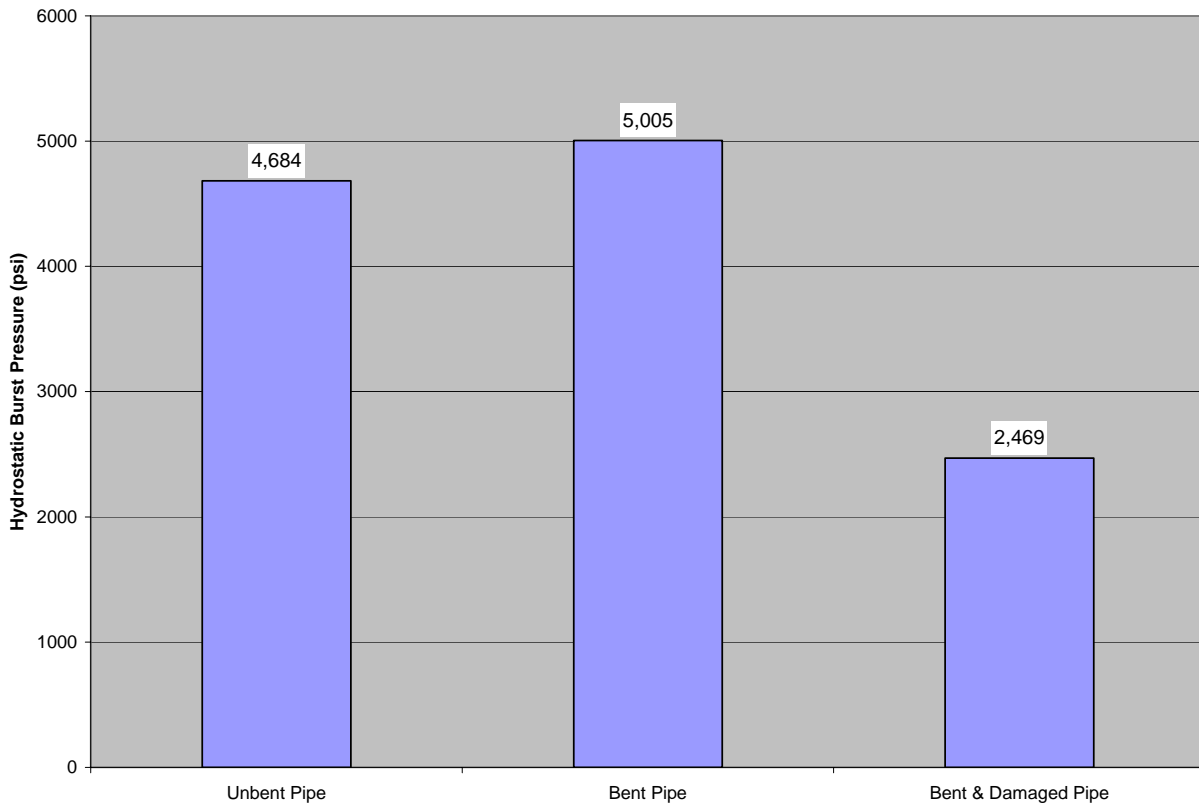
Figure 53. Graphical of Hydrostatic Burst Test Results

The post hydrostatic burst tested pipe sections for the unbent and bent pipe sections are shown in Figure 54 and Figure 55, respectively.

Figure 54. Unbent Pipe Section after Hydrostatic Burst Test

Figure 55. Bent Pipe Section after Hydrostatic Burst Test

The repaired pipe section failed at about half the pressure of the unbent pipe, which was less than anticipated and was less than promising. A short failure analysis was conducted to investigate the cause of the failure. Figure 56 shows a close up of the failure location of the repaired pipe section.

Figure 56. Failure Location of the Repaired Pipe Section

The failure was not a blow out of the pipe that was present in Figure 54 and Figure 55, nor did it have excessive plastic deformation, which is typically present when a blow out occurs. The failure was a small leak that came from the machined through hole. The pipe was sectioned at the failure location and the cross section is shown in Figure 57.
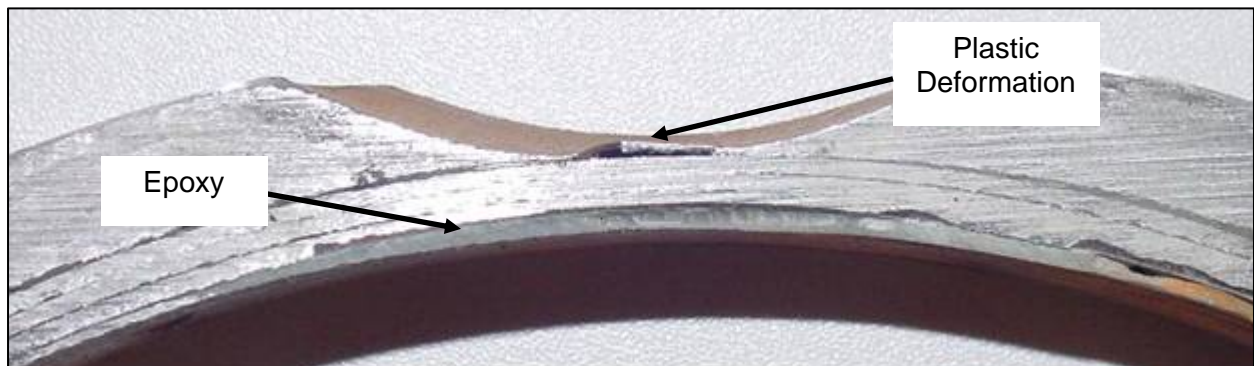
Figure 57. Cross-Section of the Repaired Pipe Section at the Failure

Figure 57 shows local plastic deformation near the failure location that indicates that the repair did not contain the pressure prior to the pipe wall yielding. There are several factors that could have contributed to the failure at a pressure lower than expected. One factor could be the inability to apply the helical coils adjacent to each other (Figure 58), which may reduce the strength of the repair by allowing the stress to be applied to a material with lesser strength.

Figure 58. Coil Spacing Observed During Failure Analysis of Repaired Pipe Section

The spacing between the coils appeared to be present at the failure location on the fourth layer of the repair (Figure 57). A second factor that could have contributed to the low burst pressure may be not having enough coils in the repair. The intent of using only four layers for the repair was to replace the strength of the pipe that was lost due to the simulated corrosion and not to replace the total wall thickness of the pipe. If more layers were used in the repair, the burst pressure may have increased. Also, with more layers in the repair, the effect of not having the coils adjacent to one another in each layer may be reduced.

Even though the results from the helical strip repair of a bent pipe section were not as promising as previously witnessed[6] on straight pipe, the helical strip repair may be still be applicable to specific casing damage with further development.

4.7   Task 7 – Development of Recommendations

This section summarizes recommendations for the most promising alternative repair technology identified for improved casing repair.

4.7.1   Weld Deposition Repair Recommendations

Weld deposition, although promising in principal, is less than ideal for casing repair. The results of the previous DOE NETL project[6] clearly indicate that adequate shielding gas protection is critical to creating sound, defect free welds in a methane rich environment and by increasing the volume percent of methane in the weld shielding gas that porosity defects will be present that decrease the pipeline structural integrity. There is also concern that the welding arc could ignite the methane rich environment present in casings during repair. Extensive high risk research and development will be required to develop adequate gas shielding methods in the laboratory before casing repair can even been attempted. Also, it has been shown, when applying weld deposition repair on the ID to repair a defect creates distortion caused by welding residual stresses (Figure 35) which may detrimental effect the structural integrity of the casing.[6] In addition to the experimental testing, the assessment carried out in Section 4.6.1 resulted the

third lowest rating of 409. All these factors consequently led to weld deposition repair being eliminated as a reasonable option for casing repair.

4.7.2   Laser Cement Drilling Recommendations

Although the use of laser cement drilling appears to have some potential, this technology was not recommended for further evaluation for casing repair for several factors. The first factor is that the selection of squeeze material is a mature process. Designer squeeze materials (e.g., gels or epoxies) can be selected to penetrate any size of corrosion pit; therefore, while laser drilling to enlarge orifice size could help in squeeze repair success, it is not necessary. Secondly, laser processing, similar to weld deposition, could ignite the methane environment. These assumptions were further supported by the Email inquiry[3] and online survey[4] responses both suggest that squeeze repairs are not common and the assessment carried out in Section 4.6.1 resulted the worst rating of 318. For these reasons, laser cement drilling is therefore not recommended for improved casing repair.

4.7.3   Helical Repair Recommendations

Based on the results of the preliminary feasibility study conducted during the DOE NETL project,[6] the additional testing performed during this project (although not completely successful), and the highest rating of 625 of all the alternative repair methods assessed in Section 4.6.1, it is believed that the helical strip repair should be further evaluated as an alternative to casing repair. Helical strip repair can be a direct replacement for tube and packer repairs and an alternative repair to expandable tubulars.

The estimated equipment and material costs to apply helical repair in the laboratory environment are listed in Table 14. At the current level of development, it takes one day to apply one layer of the helical strip repair in order to allow the adhesive to cure. An average repair requires three layers of helical strip. Thus, depending on the number of strips the repair requires, the repair time can be quite long.

Table 14. Laboratory Costs of Adhesively Bonded, Helically-Wound, Steel Strip Repair

Item	Cost
Adhesive for 1 Repair	$ 10
Steel Strip for 1 Repair	$ 10
Internal Air Pressure Bladder	$1,000
Plastic Sheet to Protect Bladder	$ 5
Air Compressor	$1,145
Total	**$2,170**

Although the helical strip repair technology is currently considered "laboratory" mature, there are several aspects of the technology that must be experimentally evaluated in order to determine its ability to repair the full spectrum of casing damage types. (Whether helical steel strip can handle a separated casing must specifically be determine to maximize potential applications.) Research is needed to determine the number of steel strip layers that are needed to restore pipeline integrity for various pipe grades and wall thickness combinations. The maximum bend angle (due to earth movements) the process can repair must also be determined.

After the limits of the helical strip repair are experimentally determined for casing repair, the next step is to evaluate the deployment of the process in a methane rich environment. The affects of methane on the installation process and materials must be thoroughly evaluated as well as the resultant repair quality (i.e., physical performance).

Once the details of applying helical strip repair in a methane rich environment are determined, a vendor must be identified to commercialize the technology. Working closely with the commercialization vendor, the next step is to determine the best way to deploy the repair technology in the field. Field hardened tooling must be identified and evaluated for deployment in the pipe axis vertical position. A comprehensive series of field trials is then recommended in order to determine the practicality of this technology for casing repair. At this time, it will be possible to determine the cost of applying this repair. After the field repairs are made, the repairs must then be studied over time in order to determine repair performance and durability.

4.7.4   MPW Recommendations

Based on the assessment results carried out in Section 4.6.1, MPW had the second highest rating of 567. For this reason and discussions with industry, it is believed that MPW should be further evaluated as an alternative to casing repair. MPW is viewed as a potential modification to expandable liner repairs that would increase the quality of the repair and expand the potential use of the repair technology (e.g., higher pressures, higher temperatures, and more severe environments). An improvement of technology over the current technology is the use of a metallurgical bond instead of an elastomer seal.

The estimated costs associated with applying internal MPW and equipment costs (in the laboratory environment) are summarized in Table 14. While capital equipment costs are quite high, the MPW process is a fast, single-shot joining technology (i.e., the weld is made instantaneously by pressing a button) that could recover the start up cost be applying the technology to wells that would normal be plugged.

Table 15. Laboratory Costs of Internal MPW Repair

Item	Cost
Liner for 1 Repair	$10
Internal Coil	$TBD
Capacitor Bank	$TBD

Although external MPW is also considered "laboratory" mature, internal MPW is an emerging application. An internal welding coil must be successfully designed for repetitive use with a typical liner and pipe material combination. With this process, an experimental program similar to that in the previous DOE NETL program[6] must be conducted in order to determine the ability of this process to restore straight, corrosion damaged pipe sections to full structural integrity. After that, other aspects of the technology must be experimentally evaluated in order to determine MPW's ability to repair the full spectrum of casing damage types. (Whether MPW can handle a separated casing should also be determined to maximize repair applications.) Research is then needed to determine the thickness of liner material needed to restore pipeline integrity for various pipe grades and wall thickness combinations.

After the limits of internal MPW are experimentally determined for casing repair, the next step is to evaluate the deployment of the process in a methane rich environment. The affects of methane on the MPW installation process must be thoroughly evaluated, as well as the resultant repair quality (i.e., physical performance). In addition to the effect of methane on weld quality, an ID casing cleanliness needs to be thoroughly evaluated to determine the surface preparation requirements for MPW.

Once, the details of applying internal MPW a methane rich environment and surface preparation guidelines are developed, a vendor must be identified to commercialize the technology in the field. Working closely with the commercialization vendor, the next step is to determine the best way to deploy the repair technology in the field. Power sources and deployment distances (e.g., applicable down hole depths) must be determined. Field hardened tooling must be identified and evaluated for deployment in the pipe axis vertical position. A comprehensive series of field trials should then be carried out to determine the practicality of this technology for casing repair. At this time, it will be possible to determine the cost of applying this repair. After the field repairs are made, the repairs must then be studied over time in order to determine repair performance and durability.

4.7.5 Summary of Recommendations

Both internal helical strip repair and MPW show the greatest promise for a broader range of damage types and as an alternative to both traditional casing liner and expandable tubular

repair technologies. The main questions about these proposed alternatives is whether they can repair damaged casings, including bent casings, back to the casings original strength and if the process can be field deployable.

5.0   CONCLUSIONS

The most common form of underground storage is depleted reservoirs, followed by aquifers, and underground salt formations. The vast majority of existing U.S. gas storage is in depleted reservoirs that are close to consumption centers. The most common design guidance for new casing fabrication is API 5CT, which does not include repair qualifications for damaged casings. There is no standardized U.S. code for casing repair procedures; each state has their own procedures for casing repair requirements. Pressure testing is the most common repair integrity test called out in the state requirements.

Casings experience different loads during landing, cementing, drilling, and production operations. The most important loads that it must withstand are: tensile, burst, and collapse loads but other loads affect the casing such as earth movements and temperature variations. All in all, there is very little published literature on casing loads. Since the majority of state mandated repair procedures do not specify mechanical properties, it is easy to assume that a repair should return the casing integrity back to the original state, but this may not be the most appropriate determination of repair success.

The major types of casing damage mechanisms are: corrosion, threaded connection separation, thread sealant leaks, parted or split casing due to internal defect, and mechanical damage (e.g., damage from drilling). In underground structures, corrosion causes include joining of dissimilar metals, non-homogeneous soil, differential aeration and microbiological attack. Corrosion can be both internal and external. Internal corrosion is reduced by using products to inhibit microbiological corrosion. External corrosion is prevented by a good cement job and cathodic protection.

 While the literature search indicated several types of repair processes such as squeezes, liners, and plating, the industry feedback indicated that liner repair is the most commonly used and reliable technology. The most expensive and complex options that companies use to repair casings are full string casing repair and cut out and replace.

Helical strip repair and MPW are the two most promising alternative repair technologies evaluated to date. Mainly, because both are applicable for a broad range of damage types and are promising alternatives or adaptations to traditional casing liner repair technology. A limited feasibility study showed that helical strip repair is suitable for unbent casing repair but more

research is needed to thoroughly evaluate both recommended processes for improved casing repair.

6.0   RECOMMENDATIONS

Internal helical strip repair should be further evaluated as an alternative to casing repair for the full spectrum of casing damage types. After the limits of the helical strip repair are experimentally determined for casing repair, the next step would be to evaluate the deployment of the process in a methane rich environment. The affects of methane on the installation process and repair quality must be thoroughly evaluated.

Internal magnetic pulse welding (MPW) should be further developed and subsequently evaluated as an alternative to casing repair for the full spectrum of casing damage types. After the limits of the internal MPW repair technology are experimentally determined for casing repair, the next step is to evaluate the deployment of the process in a methane rich environment. The affects of methane on the installation process and repair quality must be thoroughly evaluated.

7.0   REFERENCES

1. Watson, B., Johnson, D., and Driscoll, D., "Consortium to Research U.S. Storage System," GasTIPS, Volume 10, Number 3, Gas Technology Institute, Chicago, Illinois, Summer 2004.

2. Swanson, R.K., De Los Santos, A., Miller, D., "Improved Methods for Inspecting Gas Storage Well Downhole Casing," Final Report for PR-15-614 to Pipeline Research Council International, Southwest Research Institute, San Antonio, Texas, January 1, 1987.

3. Email Inquiry from Matt Boring of EWI to GSTC Member Companies on November 10, 2006.

4. State-of-the-Art Assessment of Alternative Casing Repair Methods, online survey conducted by EWI via SurveyMonkey.com from March 13, 2007 through April 20, 2007

5. Private Communication, John Rogers Smith, Louisiana State University, August 28, 2006.

6. Bruce, W., Boring, M., Porter, N., Ritter, G., Harris, I., Mohr, W., Harwig, D., Dierksheide, J., Gordon, R., Neary, C. and Sullivan, M., "Internal Repair of Pipelines" Final Report to National Energy Technology Laboratory, U.S. Department of Energy, DOE Award No.: DE-FC26-02NT41633, Edison Welding Institute and Pacific Gas & Electric, July 2004.

7. Storage of Natural Gas, from http://www.naturalgas.org/naturalgas/storage.asp

8. The Basics of Underground Natural Gas Storage, from http://www.eia.doe.gov/pub/oil_gas/natural_gas/analysis_publications/storagebasics/storagebasics.html. Energy Information Administration (EIA), EIA Gas Tran Geographic Information System Underground Storage Data Base

9. American Petroleum Institute, Specification for Casing and Tubing – API Specification 5CT. 2001, ISO 11960:2001, Petroleum and Natural Gas Industries – Steel Pipes for Use as Casing and Tubing for Wells. 2002.

10. Lyons, W. C., Plisga, G. J., "Standard Handbook of Petroleum and Natural Gas Engineering," Second Edition, Elsevier/Gulf Professional Publication, Burlington, MA (2005)

11. Retrieved from http://www.geocities.com/unforbidden_geology/rock_properties.htm#a%29%20Rock%20hardness, February 28, 2007.

12. Rahman, S. S., Chilingarian, G. V., "Casing Design Theory and Practice," Elsevier, Amsterdam/New York (1995)

13. Private Communication, John Rogers Smith, Louisiana State University, August 28, 2006.

14. Gas Field Technology, Retrieved from http://www.pttc.org/solutions/sol_2005/547.htm, September 19, 2006.

15. Private Communication, Ronald Walden, Dominion Transmission, September 19, 2006

16. Manitoba Industry, Economic Development and Mines, Informational Notice 04-02, Retrieved from http://www.gov.mb.ca/iedm/petroleum/infonotes/04-02.pdf, September 19, 2006.

17. Private Communication, David Dauterive, Shell, September 2006.

18. Kansas Department of Health and Environment, "Procedure for Internal Casing Repair," Procedure #: UICLPG-12, Bureau of Water – Geology Section, February 2003.

19. Kansas Department of Health and Environment, "Procedure for the Pressure Mechanical Integrity Test for the Casing of an Underground Hydrocarbon Storage Well," Procedure #: UICLPG-17, Bureau of Water – Geology Section, February 2005.

20. Kansas Department of Health and Environment, "Procedure for Conducting a Casing Pressure Test for Underground Hydrocarbon Storage Wells," Procedure #: UICLPG-15, Bureau of Water – Geology Section, December 2003.

21. Texas Administrative Code, "Underground Storage of Gas in Productive or Depleted Reservoirs," Title 16 Economic Regulation, Part 1 Railroad Commission of Texas, Chapter 3 Oil and Gas Division, Rule 3.96, Retrieved from http://info.sos.state.tx.us/pls/pub/readtac$ext.ViewTAC?tac_view=4&ti=16&pt=1&ch=3, September 18, 2006.

22. Texas Administrative Code, "Underground Storage of Gas in Salt Formations," Title 16 Economic Regulation, Part 1 Railroad Commission of Texas, Chapter 3 Oil and Gas Division, Rule 3.97, Retrieved from http://info.sos.state.tx.us/pls/pub/readtac$ext.ViewTAC?tac_view=4&ti=16&pt=1&ch=3, September 18, 2006.

23. Texas Administrative Code, "Casing, Cementing, Drilling, and Completion Requirements," Title 16 Economic Regulation, Part 1 Railroad Commission of Texas, Chapter 3 Oil and Gas Division, Rule 3.13, Retrieved from http://info.sos.state.tx.us/pls/pub/readtac$ext.ViewTAC?tac_view=4&ti=16&pt=1&ch=3, September 18, 2006.

24. Louisiana Administrative Code, "Hydrocarbon Storage Wells in Salt Dome Cavities," Title 43 Natural Resources, Part XVII Office of Conservation, Injection and Mining, Subpart 3 Statewide Order No. 29-M, Chapter 3, Dated December 2004, Retrieved from http://www.state.la.us/osr/lac/43v17/43v17.pdf, September 18, 2006.

25. New York State Department of Environmental Conservation, Title 6 of the Official Compilation of Codes, Rules and Regulations of the State of New York (6NYCRR), Retrieved from http://www.dec.ny.gov/energy, June 12, 2007

26. Pennsylvania Code: Oil and Gas Regulations, Chapter 78: Oil and Gas Wells, Retrieved from http://www.pacode.com, June 12, 2007

27. Manitoba Industry, Economic Development and Mines, Informational Notice 04-02, Retrieved from http://www.gov.mb.ca/iedm/petroleum/infonotes/04-02.pdf, September 19, 2006.

28. Goodwin, K.J., "Principles of Squeeze Cementing," SPE 12603, Presented at the 1984 Permian Basin Oil & Gas Recovery Conference, Midland, TX March 8-9, 1984.

29. Wasnik, A. and Mete, S., "Application of resin system for sand consolidation, mud-loss control, and channel repairing," SPE/PS-CIM/CHOA 97771, PS2005-349, presented at 2005 SPE International Thermal Operations and Heavy Oil Symposium, Calgary, Alberta, Canada, 1-3 November 2005.

30. Toor, I. A., "Problems in squeeze cementing," SPE 11499, presented at the Middle East Oil Technical Conference of the Society of Petroleum Engineers, Manama, Bahrain, March 14-17, 1983

31. Harris, K.L., and Johnson, B.J., "Successful Remedial Operations using Ultra Fine Cement," SPE 24294, presented at the SPE-MidContinent Gas Symposium, Amarillo, Texas, April 3-14, 1992.

32. Creel, P. and Crook, R., "Gels, Monomer Solutions Fix Pinhole Casing Leaks," Oil and Gas Journal, October 13, 1997, pg 44.

33. Ng, R. C. and McPherson, T. W., "Low Temperature Underwater Epoxy System for Zone Isolation, Remedial Cementing, and Casing Repair," United States Patent 5531272, July 2, 1996.

34. Schmidt, Victor, "What's new in production," World Oil, Vol. 227, No. 4, April 2006

35. Canitron System, Inc., Retrieved September 18, 2006 from http://canitron-sys.com.

36. Fischer, P.A., and Schmidt, V.A.," Suppliers show progress in expandables innovation," World Oil, July 2006, Vol 227, Issue 7, pg 33-39.

37. Neely, J.D., "The use of casing patches to improve workover success rates," SPE 13996, Offshore Europe 85, Aberdeen, 10-13 September 1985.

38. Bargawi, et. al, "Expandable tubular successfully scab off severe casing leaks," SPE/IADC 97357, presented at SPE/IADC Middle East Drilling Technology Conference & Exhibition, Dubai, U.A.E, 12-14 September 2005.

39. Wright, et. Al., "Expandable tubing casing repairs: four case histories," SPE 84049, presented at SPE Annual Technical Conference and Exhibition, Denver, Colorado, U.S.A., 5-8 October 2003.

40. Enventure Global Technology, L.L.C. Retrieved December 12, 2006 from http://www.enventuregt.com/assets/base/pdfs/productlit/CHL_letter_DataSheet.pdf

41. King, et. Al, "Economic in-place casing lining and repair," Journal of Petroleum Technology, October 1997, Vol. 49, No. 10, pg 1115-1117.

42. Surjaatmadja, J.B., "Downhole Casing Repair," European Patent Number EP 1 251 241 A1, October 23, 2002.

43. Anderson, J.,Kendziora, C., "Visual Robotic Welding,"kendziora.net/vrw.htm, May 25, 2007

44. Zhang, W. and Walter, J., "Method and Apparatus for Downhole Pipe or Casing Repair," International Publication Number WO 2004/001178 A2, December 31, 2003.

45. Wang, Y.-Y., and Bruce, W. A., "Examination of External Weld Deposition Repair for Internal Wall Loss," Final Report for EWI Project No. 07723CAP to PRC International, Contract No PR-185-9633, March 1998.

46. Eiber, R. J., Bubenik, T. A., and Leis, B. N., "Pipeline Failure Mechanisms and Characteristics of the Resulting Defects," Eighth Symposium on Line Pipe Research, Paper No. 7 (Houston, TX: American Gas Association, 1993).

47. Bruce, W.A., "Welding onto In-service Thin-Walled Pipelines," Pipeline Research Council International, Edison Welding Institute EWI Project No. 41732, Columbus, Ohio, July 2000.

48. Eiber, R. J., Bubenik, T. A., and Leis, B. N., "Pipeline Failure Mechanisms and Characteristics of the Resulting Defects," Eighth Symposium on Line Pipe Research, Paper No. 7 (Houston, TX: American Gas Association, 1993).

49. Kiefner, J. F., Barnes, C. R., Gertler, R. C., Fischer, R. D., and Mishler, H. W., "Experimental Verification of Hot Tap Welding Thermal Analysis. Final Report - Phase II -

Volume 2, Liquid Propane Experiments," Repair and Hot Tap Welding Group, Battelle Columbus Laboratories, May 1983.

50. Kiefner, J. F. and Vieth, P. H., "A Modified Criterion for Evaluating the Remaining Strength of Corroded Pipe" Final Report to A.G.A. Pipeline Corrosion Supervisory Committee, Project PR-3-805, Battelle, Columbus, OH, December 1989.

51. Private Communication, Brian Wagg, C-Fer Technologies, February, 20, 2007.

52. Powers, H. G. 1967. Bonding of aluminum by the capacitor discharge magnetic forming process. Welding Journal, 46(6):507-510.

53. Khrenov, K. K. and Chudakov, V. A. 1968. Magnetic-Pulse Welding. *Avtomat Svarka*, (2):74-75.

54. Masumoto, I., Tamaki, K., and Kojima, M. 1985. Study on electromagnetic welding. Report 1: Electromagnetic welding of aluminum tube to aluminum or dissimilar metal cores. *Transactions of the Japan Welding Society*, 16(2):110-116.

55. Hokari, H., Sato, T., Kawauchi, K., and Muto, A. 1998. Magnetic impulse welding of aluminum tube and copper tube with various core materials. *Welding International*, 12(8):619-626.

56. Shriban, V., Livshitz, Y., Gafri, O., and Kimchi, M. 2000. The magnetic pulse welding process. *Third International TWI/EWI Workshop on Joining of Aerospace Materials*.

57. Private Communication, Brian Wagg, C-Fer Technologies, February, 20, 2007.

58. Author unknown, http://www.hq.nasa.gov/office/codeq/trl/trlchrt.pdf.

8.0 LIST OF ACRONYMS AND ABBREVIATIONS

Acronym or Abbreviation	Definition
AGA	American Gas Association
APB	Acid Producing Bacteria
API	American Petroleum Institute
CP	Cathodic Protection
DOE	Department of Energy
DOE	Design of Experiments
EWI	Edision Welding Institute
GMAW	Gas Metal Arc Welding
GSTC	Gas Storage Technology Consortium
HDPE	High-Density Polyethylene
IPM	In Situ Polymerizing Monomer
MIC	Microbiologically Influenced Corrosion
MPW	Magnetic Pulse Welding
NDE	Nondestructive Evaluation
NETL	National Energy Technology Laboratory
PADEP	Pennsylvania Department of Environmental Protection
PRCI	Pipeline Research Council International
RP	Recommended Practices
SMYS	Specified Minimum Yield Strength
SRB	Sulfate Reducing Bacteria

Appendix A. November 10, 2006 Email Inquiry and Industry Feedback

At the end of last quarter, an Email inquiry was circulated to 23 GSTC member companies. Some of the companies had two contacts in different divisions, which resulted in a total 29 contacts. The eight Emailed questions follow:

1. What are the typical casings that are used for natural gas storage (*e.g.*, diameter, wall thickness, material)?
2. What are the typical pressure ranges to which the casing are exposed?
3. What type of casing damage occurs?
4. How do you currently repair the casing damage?
5. Are there any types of damage that you do not repair and as a result require shutting down the well?
6. Are there limits to the amount of damage that you do repair (e.g. excessive corrosion, excessive buckle angle, etc.)?
7. Does your company have guidance to select which repair type can remedy specific types of damage?
8. Are there limits to any repair technologies that you have seen during repair applications?

Of the twenty-nine Emails sent to the member companies, five people responded during this third quarterly reporting period. The responses are summarized in Table 16. The results of the Email Inquiry were incorporated in the Task 1 - 5 narratives where applicable and relevant.

Table 16. Summary of Email Inquiry Responses

			Comments
Question 1	Minimum Outside Diameter	4.5-in.	
	Maximum Outside Diameter	9.625-in.	
	Minimum Wall Thickness	0.224-in.	
	Maximum Wall Thickness	0.545-in.	
	Minimum Casing Grade	J-55	75 ksi minimum tensile strength per API 5CT
	Maximum Casing Grade	N-80	100 ksi minimum tensile strength per API 5CT
Question 2	Minimum Pressure	0 psig	
	Maximum Pressure	4,000 psig	
Question 3**	Corrosion (4 of 5)		1 Respondent gave no details
	Mechanical (3 of 5)		
	Leaking Seals in Cement Collars (1 of 5)		
	Buckling (if not set in tension) (1 of 5)		
Question 4**	Replacement (2 of 4)		1 Respondent gave no details
	Plugged (2 of 4)		
	Tubing/Packer System (2 of 4)		
	Casing Patch (non-expandable casings) (2 of 4)		
	Run a Linear (1 of 4)		
	Cement to Surface (1 of 4)		
Question 5**	Repair if possible (4 of 4)		1 Respondent gave no details
Question 6**	80% of wall (1 of 4)		1 Respondent gave no details
	Class IV Corrosion (1 of 4)		
	Severed Casing (1 of 4)		
	No Limits (1 of 4)		
Question 7**	Will Repair 60% of wall (1 of 3)		2 Respondents gave no details
	Engineering Judgment/Case-by-Case (2 of 3)		
Question 8**	No Limits (3 of 4)		1 Respondent gave no details
	Cost (1 of 4)		
	Casing Patches have High Failure Rates (non-expandable casings) (1 of 4)		

** The numbers in parentheses indicate how many responses had each characteristic

Appendix B. March 13, 2007 Formal Online Survey

During the third quarterly reporting period, a more extensive online survey was conducted in an effort to extract more detailed information from GSTC members in support of Tasks 1 - 5. Thirty-six GSTC members were invited to take the survey; twelve responded (a 33% response rate). The following narrative describes the online survey and summarizes industry input as of March 23, 2007. The online survey will remain open until April 20, 2007 in an effort to solicit more information.

Structure of Online Survey

The survey was created and administered online via SurveyMonkey.com. SurveyMonkey.com allows the user to create professional online surveys with a web browser. There is no software to purchase; the online survey editor is intuitive and easy to use. For each question composed, the user selects from over a dozen types of questions including single choice, multiple choice, rating scales, drop-down menus, etc. EWI created the survey from the Email Inquiry[3] and the last quarterly report. GSTC provided a list of Email addresses for people that have participated in project teleconferences and members of the GSTC Executive Council. These addresses were combined with the addresses used for the November 2006 Email Inquiry[3] to create a master distribution list for the online survey. SurveyMonkey then generated Email invitations like the one shown in Figure 59.
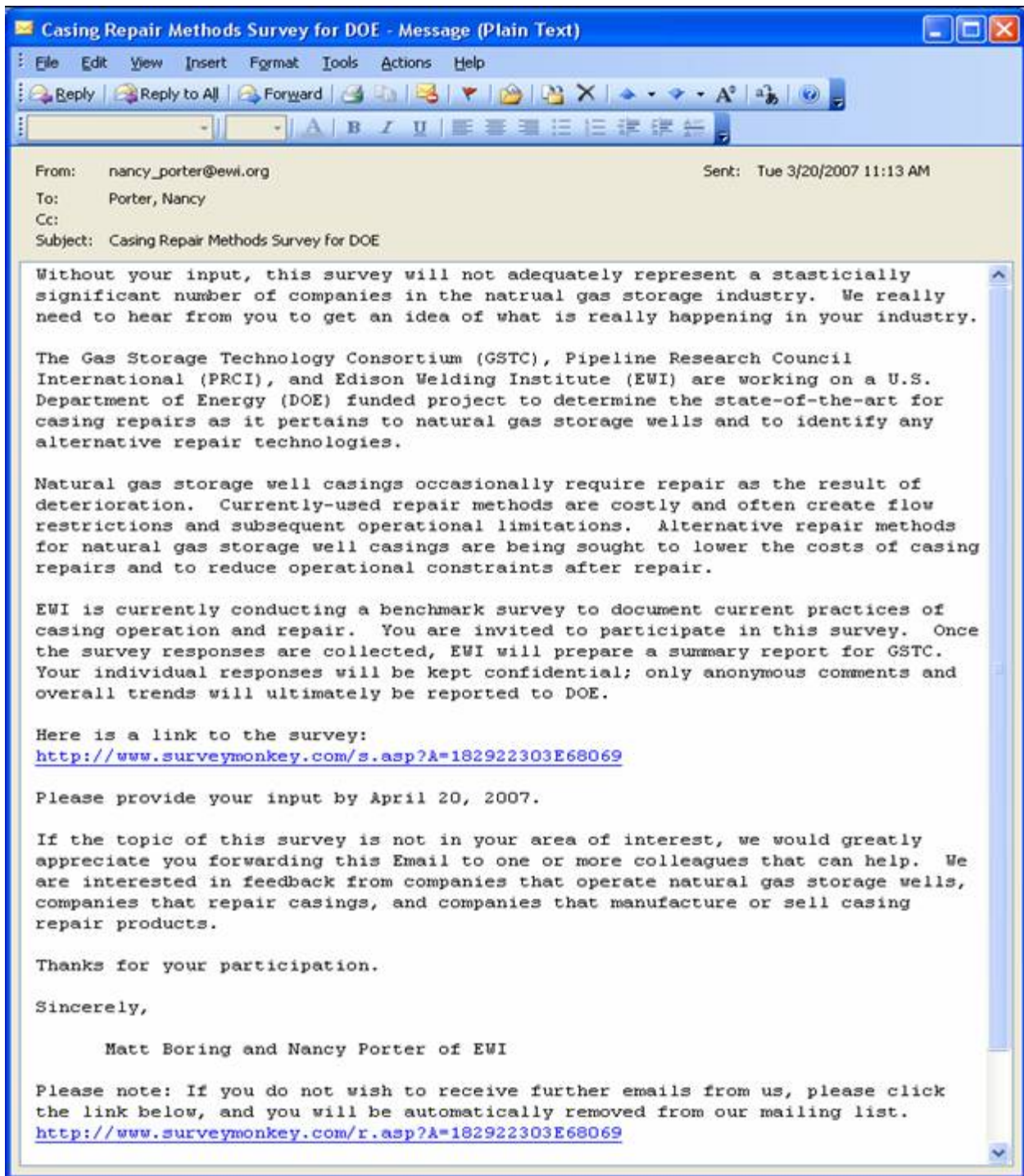
Figure 59. Survey Invitation Email

Although the survey is still open online until April 20, 2007, EWI does not anticipate any additional input. If any data is received next quarter, it will be incorporated in to the next quarterly report.

Responses were automatically tracked online and were subsequently downloaded into an Excel spreadsheet for further analysis. Upon completion of the survey, respondents were allowed to view aggregate survey results online in the form of bar charts.

The screen capture in Figure 60 is the introduction (or first) screen a survey respondent saw when directed to the survey link on SurveyMonkey.com.
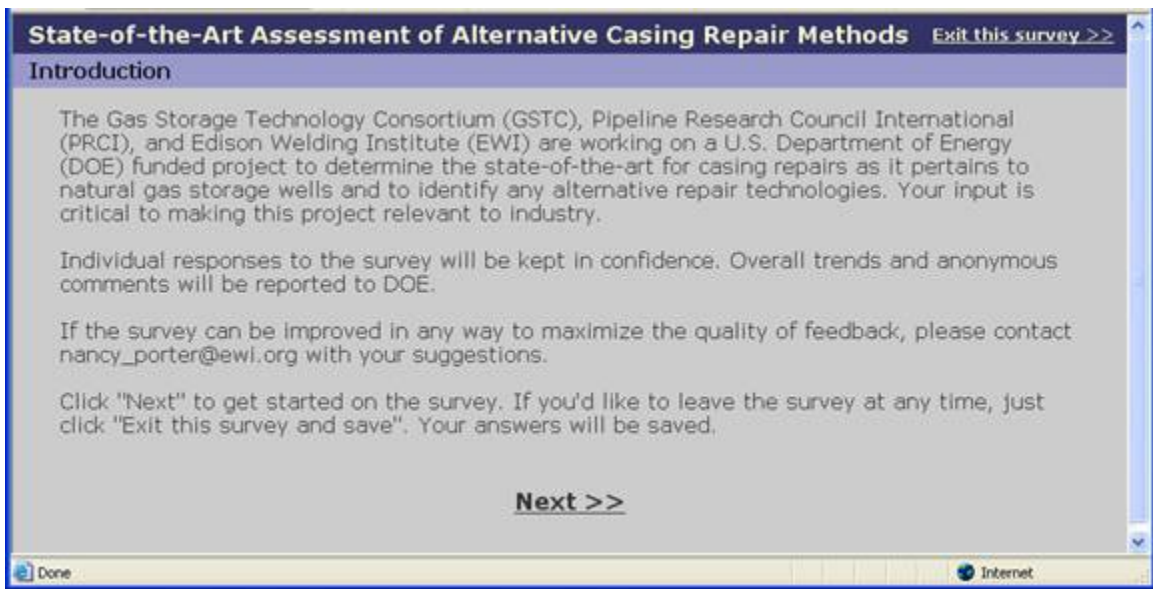
Figure 60. Introduction Screen for Online Survey

The following screen captures (Figure 61 through Figure 86) show the progression of online survey screens and questions.

Figure 61. Questions to Define Respondent's Background

Figure 62. Open Ended Question to Identify Casing Materials Used

Figure 63. Questions to Capture Casing Operating Loads

Figure 64. Open Ended Question to Characterize Service Environments

Figure 65. Question to Identify Repair Procedure Specifications
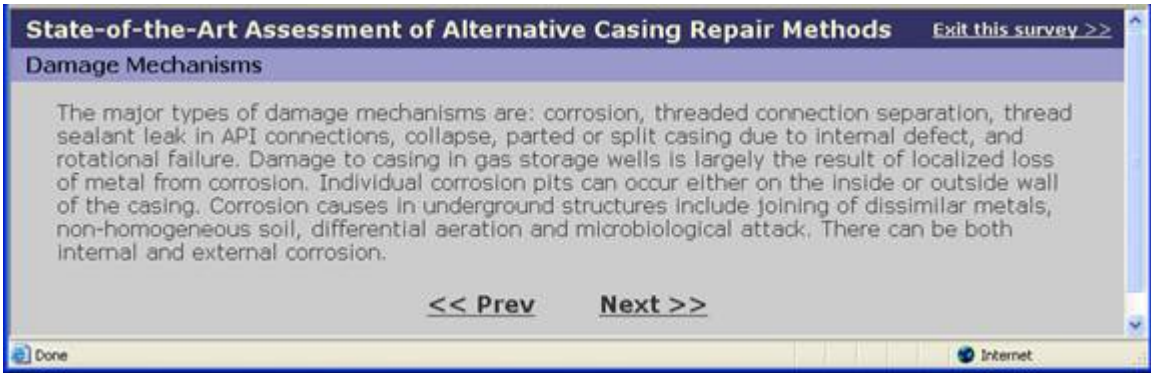
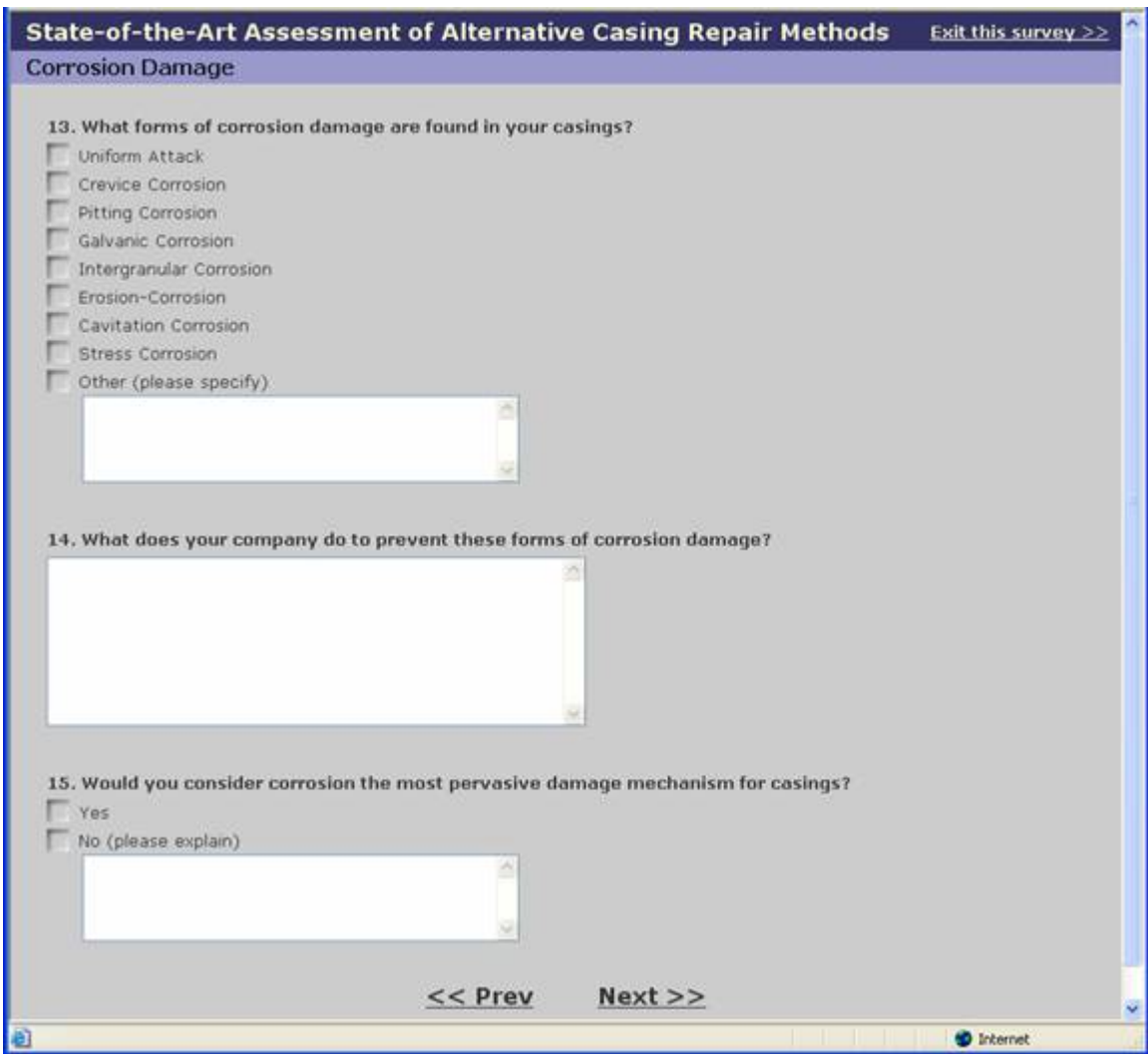**Figure 66. Question About Non-Industry Standard Repair Procedure Specifications**

Figure 67. Question to Identify Industry or Government Repair Procedure Specifications

Figure 68. Description of Damage Mechanisms to Set Up Next Set of Questions

Figure 69. Questions to Characterize Corrosion Damage

Figure 70. Questions to Characterize Non-Corrosion Damage

Figure 71. Description to Setup Next Section of Questions

Figure 72. Description of Squeeze Repairs to Set Up Next Set of Questions

Figure 73. Questions to Capture Current Cement Squeeze Repair Use

Figure 74. Questions to Capture Current Sealant Squeeze Repair Use

Figure 75. Questions to Capture Current Metallic Squeeze Repair Use

Figure 76. Description to Set Up Next Set of Questions

Figure 77. Questions to Capture Current Non-Expandable Metallic Liner Repair Use

Figure 78. Questions to Capture Current Expandable Liner Repair Use

State-of-the-Art Assessment of Alternative Casing Repair Methods   Exit this survey >>

Composite Liner Repairs

40. Does your company use a composite liner repair?
○ Yes
○ No

41. What types of damage do you repair with composite liner repair?
☐ None
☐ Please specify damage types

42. Please list the trade name(s) and types of composite liner repair system(s) that you use.
☐ Not applicable
☐ Please specify trade name(s)

43. Are there any limits to composite liner repair technology that you have seen during the application of such repair?
☐ Not applicable
☐ Please specify limitations

<< Prev   Next >>

Figure 79. Questions to Capture Current Composite Liner Repair Use

Figure 80. Questions to Capture Other Current Repair Technologies in Use

State-of-the-Art Assessment of Alternative Casing Repair Methods   Exit this survey >>

Types of Damage You Would Not Repair

There are certain types or levels of damage (or circumstances) that would cause a well to be capped off and the reservoir abandoned.

48. Under what circumstances do you cap off a well and abandon a reservoir?
☐ None
☐ Please specify circumstances

49. Is there any type of damage that you do not repair?
☐ No
☐ Please describe damage you do not repair

50. Are there limits to the amount of damage that you do repair, such as excessive corrosion, excessive buckle angle, etc.?
☐ No
☐ Please specify limitations

51. Do you have any additional comments about damage that is not repaired.
☐ No
☐ Please list additional comments

<< Prev   Next >>

Figure 81. Questions to Identify Damage that would not be Repaired

Figure 82. Questions to Identify Emerging Repair Technologies

Figure 83. Questions to Capture Additional of Missed Information

Figure 84. Question to Solicit Future Feedback
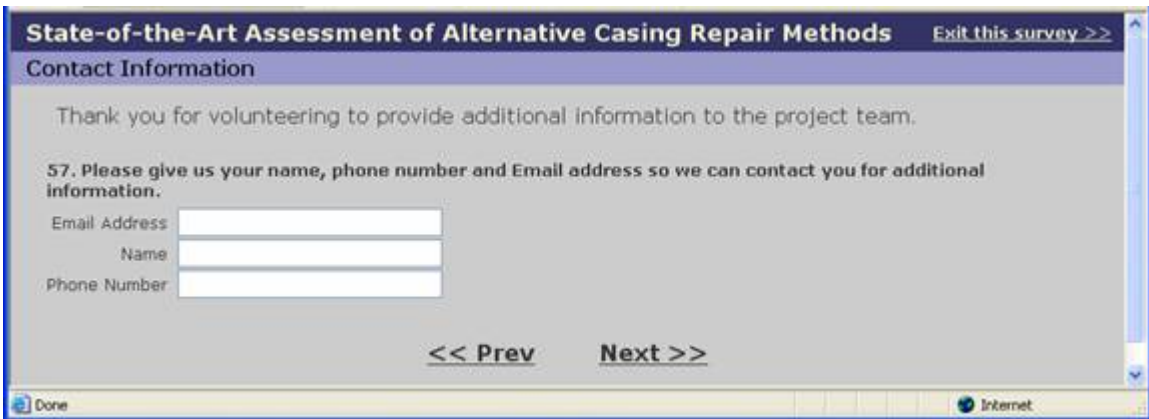
Figure 85. Input Screen for Contact Info for Future Feedback
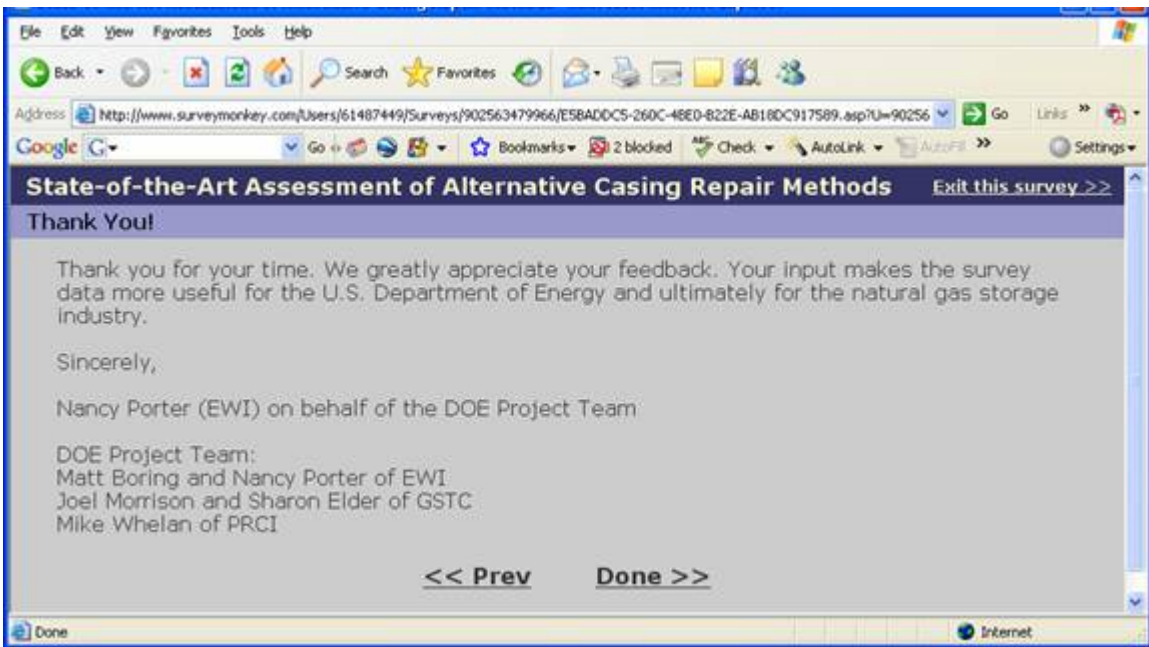
Figure 86. Final Screen of Online Survey

Survey respondents were able to view real-time results after submitting their answers. An example of the online results summary for questions 1 and 2 is shown in Figure 87.
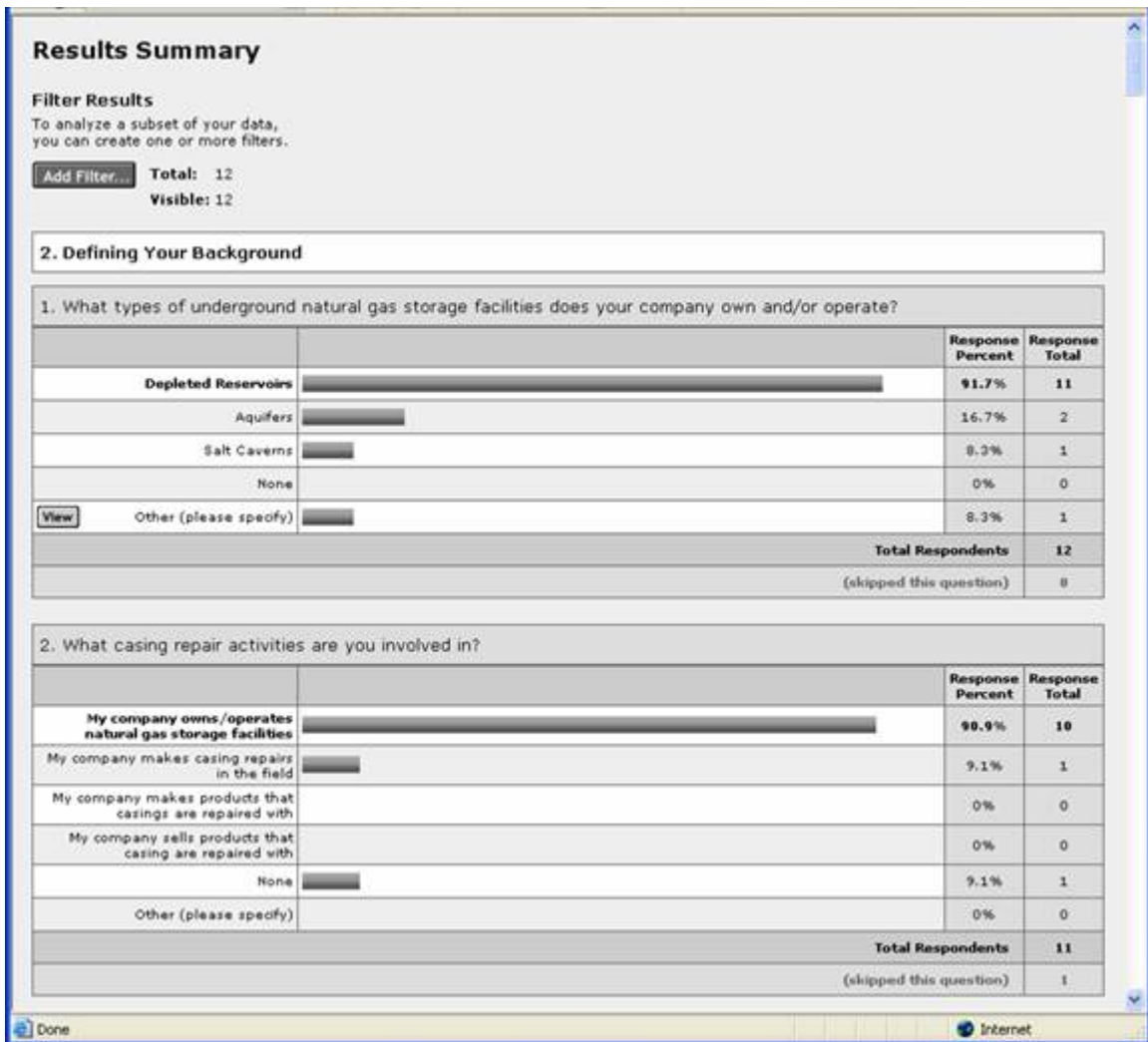
Figure 87. Real-Time Survey Results Available Online

Appendix C. Online Survey Feedback as of May 1, 2007

The following is a presentation of the online survey responses, organized by questions (shown in bold). A 1% response rate is typical for unsolicited surveys. This survey was sent to a total of 36 Email addresses; a total of 16 responses were received, thus representing a 44% response rate (as of May 1, 2007). However, respondents did not answer all of the questions, so it is not known how well the given responses reflect the gas storage industry as a whole.

Q1. What types of underground natural gas storage facilities does your company own and/or operate?

Fourteen of the fifteen respondents indicated that their companies own or operate depleted reservoirs; two respondents also operate aquifers; and one also operates a salt cavern. One of the fifteen respondents operates a salt cavern. The results are graphically displayed in Figure 88.

Salt Caverns, 14%

Aquifers, 14%

Depleted Reservoirs, 93%
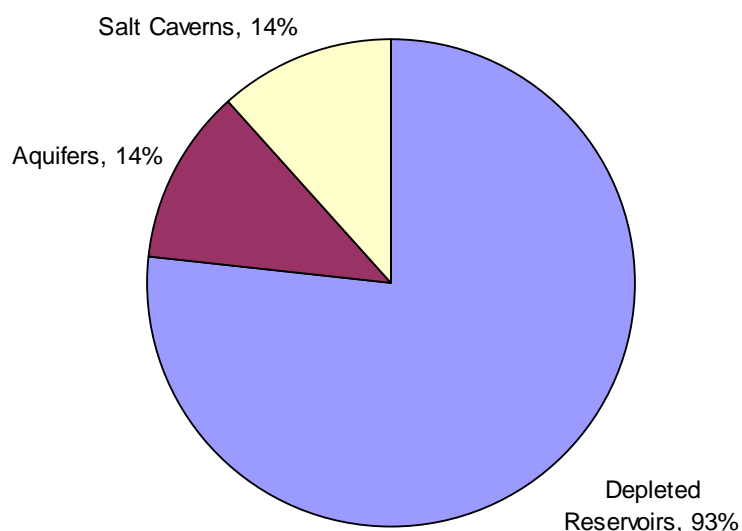
Figure 88. Types of Natural Gas Storage Facilities Operated by Respondents

Q2. What casing repair activities are you involved in?

Of the fifteen survey respondents that answered this question, thirteen respondents indicated that they operate storage facilities, but did not indicate whether they repair them. One storage facility operator indicated that they perform repairs; another indicated that they specifically do not perform repair activities. One respondent operates liquid service salt cavern wells and did

not indicate whether they perform repair activities. The responses to this question are graphically shown in Figure 89.
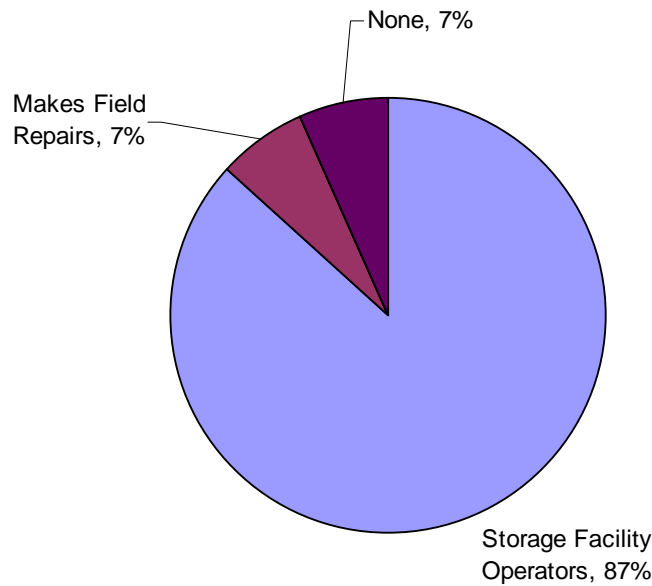
Figure 89. Repair Activities Performed by Respondents

Q3. Is there anything other unique role that you play in the natural gas storage industry that was not covered by the questions above?

One depleted reservoir operator indicated that they are a member of the AGA Underground Storage Committee and GSTC. A salt cavern operator indicated that his company is a member of PRCI and GSTC.

Q4. Please list typical casing diameters, wall thicknesses, and casing material types that are used in the natural gas storage facilities that you work with.

Thirteen respondents answered this question, providing outside diameters, lbs./ft. ratings, and material specifications. One respondent divided their materials into "surface" casings (Table 17) and "production" casings (Table 18); another identified his as "liquid service well" casings (Table 19); and a third respondent specified his as "flowstring" casings (Table 21). A few respondents provided wall thicknesses (shown in Table 21).

Table 17. Surface Casing Materials Used by 1 Survey Respondent

Diameter (in.)	Rating (lbs./ft.)	Material Type
10.75	32.75	H-40
10.75	40.5	H-40
13.375	48	H-40

Table 18. Production Casing Materials Used by 1 Survey Respondent

Diameter (in.)	Rating (lbs./ft.)	Material Type
5.5	14	K-55
5.5	15.5	K-55
7	20	J-55
7	23	L-80

Table 19. Liquid Service Well Materials Used by 1 Survey Respondent

Diameter (in.)	Rating (lbs./ft.)	Material Type
9.625	54	K-55
10.75	54	K-55
13.38	61	K-55
13.38	72	S-95

Table 20. Flowstring Materials Used by 1 Survey Respondent

Diameter (in.)	Rating (lbs./ft.)	Material Type
3.5	9.2	J-55
4.5	10.5	J-55
4.5	11.6	N-80
5.5	15.5	J-55
5.5	17	J-55
7	20	J-55
7	23	N-80

Table 21. Unspecified Casing Materials Used by Remaining Survey Respondents

Diameter (in.)	Wall (in.)	Rating (lbs./ft.)	Material Type
4.5		10.5	K-55
4.5	0.224	10.5	K-55
4.5		11.6	N-80
4.5		17-23	J-55
5.5	0.244	14	H-40
5.5	0.263	15	J-55, K-55
5.5	0.275	15.5	J-55
5.5		15.5	J-55
5.5	0.275	15.5	K-55
5.5		17	N-80
5.5	0.304	17	K-55
5.5		17-23	J-55
5.5			J-55
6.625		20	K-55
7	0.231	17	H-40
7	0.301	22	J-55, K-55
7	0.317	23	K-55
7		23	K-55
7		26	N-80
7		26	K-55
7.625	0.328	26.4	K-55
8.625	0.264	24	J-55, K-55
8.625		24	H-40
8.625		32	J-55
8.625		32	H-40
8.625	0.352	32	K-55
8.625		32	K-55
9.625		36	J-55
9.625	0.352	36	J-55
9.625		36	K-55
9.625		48	H-40
13.375	0.38	54.5	J-55
13.38		61	J-55

The median diameter size of all reported casing materials is 7-in.; however, the respondents did not indicate the quantity of each size used.

The percentage of pipe materials used is shown in Figure 90. K-55 and J-55 are used most often.
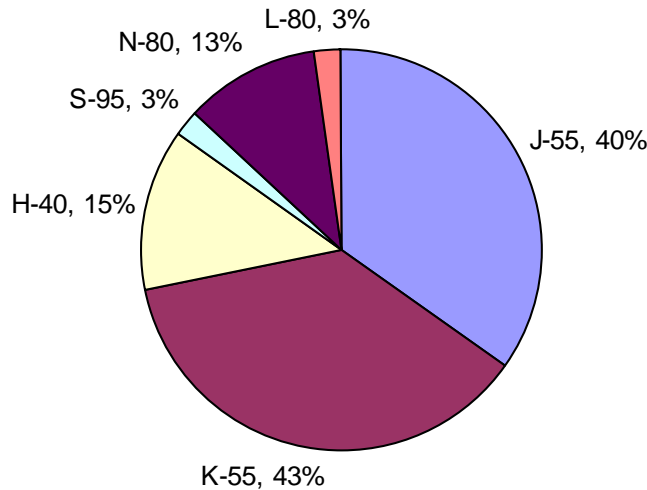
Figure 90. Percentage of Pipe Materials Used

Q5. What types of loads are your casings typically exposed to?

Twelve respondents (100%) to this question indicated that their casings are exposed to well pressure. Of the twelve, two respondents also experience temperature variations. One respondent indicated that his casings are exposed to well pressure, temperature variations and that casings can be in compression at top of cement. This respondent also commented that earth movements occur very rarely. Two of the twelve also described other loadings. One person said their casing is packed off and casing tubing annulus is filled with corrosion inhibited fluid. The other said their loads are associated with directionally drilled wells (i.e., horizontal wells). A graphical representation of these responses is shown in Figure 91.

Figure 91. Typical Casing Loads

Q6. What well pressure ranges are your casings typically exposed to?

Twelve survey respondents provided typical pressure ranges. Ranges were reported in a variety of units; all pressures were converted to psig for comparison purposes. Typical ranges are found in Table 22 and graphically represented in Figure 92. The average minimum pressure reported is 363 psig; the average maximum reported pressure is 2,313 psig.

Table 22. Typical Well Pressure Ranges

Maximum Pressure (psig)	Minimum Pressure (psig)	Average Pressure (psig)
785	385	585
1,003	400	702
1,085	0	543
1,235	285	760
1,750	150	950
2,300	300	1,300
2,350	200	1,275
2,485	485	1,485
2,485	135	1,310
3,000	800	1,900
3,600	90	1,845
3,985	1,485	2,735
4,000	0	2,000

Figure 92. Typical Well Pressure Ranges

Q7. Can you quantify any stress/pressure ranges that your casings are exposed to for the other types of loadings?

100% of the twelve respondents indicated that they could not quantify any other types of loading besides well pressure.

Q8 What types of service environments are your company's casings exposed to?

The answers to this question varied drastically. While there was some commonality, it was not possible to graph the responses. Individual responses are listed separately below.

- We have H_2S in two of our fields. All of our fields produce some water and the gas in our fields has some CO_2 (<1%).

- Some are exposed to H_2S and most see brine with a pH in the 5 to 5.6 range.

- Two of our fields have cathodic protection (CP) on well casings, others do not. Gas is generally pipeline quality (little or no H_2S, CO_2 <3%), no oxygen internally except during a workover. One field does have H_2S in parts of the field of up to 500 ppm, but this has

not seemed to cause problems. Exposure to brine varies from a little to a lot. Where a well has a dead annulus with fluid, MIC corrosion has been a problem. Have experienced some external corrosion due to varying external water table with oxygenated water. Major source of casing damage has found to be drill pipe wear. Also, many wells flow up through a packer and out into the tubing-casing annulus through a sliding sleeve, and sand erosion has been a problem at this point.

- The natural gas has contained minute quantities of oxygen and up to 2% CO_2. Brine, fresh water and compressor oil liquids also come in contact with the casing. Salt deposits and paraffin have been found in some cases. Evidence of bacteria also found.

- Salt brine (10.4 lbs./ft., saturated brine) in one field.

- Salt and iron sulfate/sulfide precipitated. Bacteria, [specifically] sulfate reducing bacteria (SRB) and acid producing bacteria (APB) are a problem

- Salt precipitation, paraffin build-up, hydrate formation, CO_2 (0.5% - 1.5%), and saturated brine (chlorides = 250,000 ppm).

- Saline water, fresh water, mercaptan (methylethylsulfide), and electrical potential.

- 2 to 3% CO_2

- As mentioned earlier, annulus between tubing and casing is filled with inhibited fluid. Some wells have CP. No abnormal downhole conditions or surface conditions exist at our facilities.

- Brine corrosive environment, no free oxygen, salts, inorganic, high solid velocity of unabsorbed salts.

- High carbon dioxide levels in the gas stream, exterior bacterial attack in outside annuli, corrosive salts in annuli, bacterial attack (pitting) in the gas stream

Q9.   Does your company use in-house or industry repair procedures for casing repair requirements for underground storage wells?

Eleven people responded to this question. No survey respondents use federal, state or local regulations to define repair procedures. The answers are graphically displayed in Figure 93. 72% use some sort of a standardized repair procedure while 28% use no standard guidance.
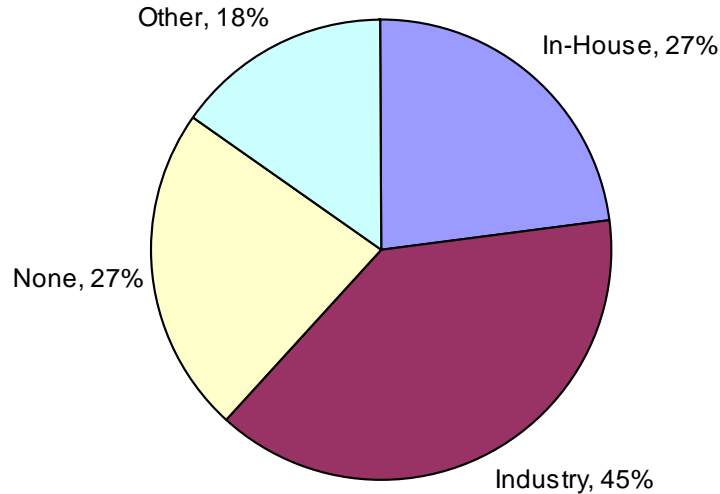
Figure 93. Types of Casing Procedure Specifications used by Respondents

One respondent indicated that his company has had very few casing failures. The few they had were very close to the surface and were repaired by unscrewing the bad pipe and replacing it with new casing.

Three people said that they do not use a code or standard procedure to define repair procedures/requirements. One respondent even indicated that he did not understand the question.

Q10 Summarize key points of your in-house repair standard or repair practices.

Four respondents provided the following input.

- Wells are repaired in one of the following ways:
    - Tubing packer system
    - Casing patch
    - Cemented liner
- Back off and replace the bad joint if possible, or run a liner or plug the well. Casing Patches have been considered but not done to date.
- No welding on gas production string; threading only. Welding allowed on surface or water protection string.
- Repairs are driven by magnetic flux-leakage log run results and interpretations. 'Reduced burst pressures' are calculated for flowstrings using B31.G methodology. Candidate wells are prioritized based on calculated reduced burst pressures vs. required

service pressures. A subset of the candidate list is slated for repairs each year based upon budget availability.

Again, these responses imply that there is no minimum acceptable quality control among the reservoir operators that responded to this survey.

Q11 What constitutes an acceptable repair? For example, restoring the casing to full base metal strength, simply plugging up the hole, etc.

Five respondents provided the following input.

- Not having the defect in the casing exposed to well pressure and the repair method used being able to withstand the highest well pressure it will see.

- Replacing the bad joint with a good one, covering up the bad joint with good tubing, or plugging the well.

- Replace badly corroded casing.

- Restore to full strength

- If possible, the pipe is removed and replaced. If not, alternate repairs methods may be employed, such as casing patches and expandable sleeves, liners and smaller diameter flowstrings. If none of these repair methods is possible, the well may be plugged and, if the situation warrants, a replacement well may be drilled.

Again, these responses imply that there is no minimum acceptable quality control among the reservoir operators that responded to this survey.

Q12 Please check all industry standards or federal, state or local regulations that apply to your casing repairs.

The multiple choice question consisted of the following options (from the Task 1 literature review):

- API Specification 5CT.

- Kansas Department of Health and Environment, Procedure #: UICLPG-12.

- Kansas Department of Health and Environment, Procedure #: UICLPG-17.

- Kansas Department of Health and Environment, Procedure #: UICLPG-15.

- Texas Administrative Code, Title 16 Economic Regulation, Part 1 Railroad Commission of Texas, Chapter 3 Oil and Gas Division, Rule 3.96.

- Texas Administrative Code, Title 16 Economic Regulation, Part 1 Railroad Commission of Texas, Chapter 3 Oil and Gas Division, Rule 3.97.

- Texas Administrative Code, Title 16 Economic Regulation, Part 1 Railroad Commission of Texas, Chapter 3 Oil and Gas Division, Rule 3.13.

- Louisiana Administrative Code, Title 43 Natural Resources, Part XVII Office of Conservation, Injection and Mining, Subpart 3 Statewide Order No. 29-M, Chapter 3.

- Manitoba Industry, Economic Development and Mines, Informational Notice 04-02.

Only five people responded to this question. Three respondents (60%) indicated that they use API Specification 5CT; one of these respondents also uses the Louisiana code. One of the other respondents indicated that they use Title 6 of the Official Compilation of Codes, Rules and Regulations of the State of New York (6NYCRR) and follow the requirements of the Pennsylvania Department of Environmental Protection (PADEP). The last respondent indicated that his company has no regulatory requirements; their selections are made based upon integrity monitoring of casing corrosion. Answers to this question are graphically shown in Figure 94.
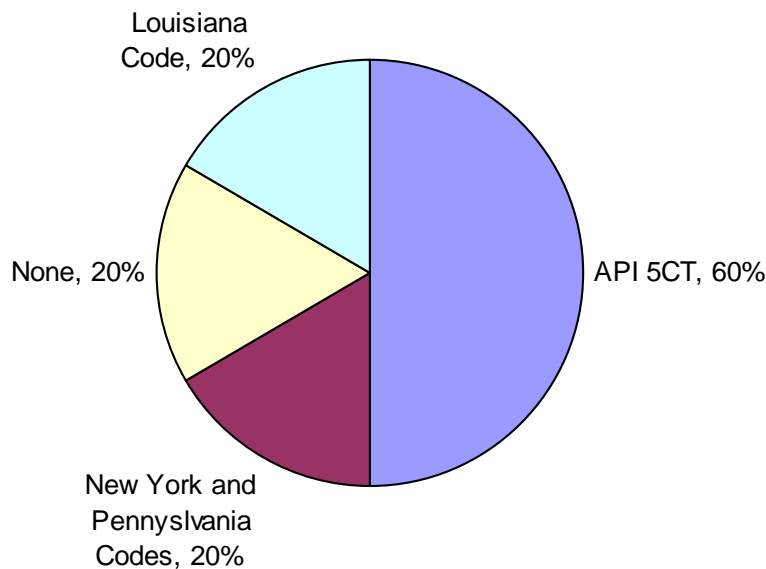
Figure 94. Reported Standardized Code Usage

Q13 What forms of corrosion damage are found in your casings?

Eleven people responded to this question; 10 experience pitting corrosion. The full spectrum of corrosion damage types experienced by the respondents is shown in Figure 95.
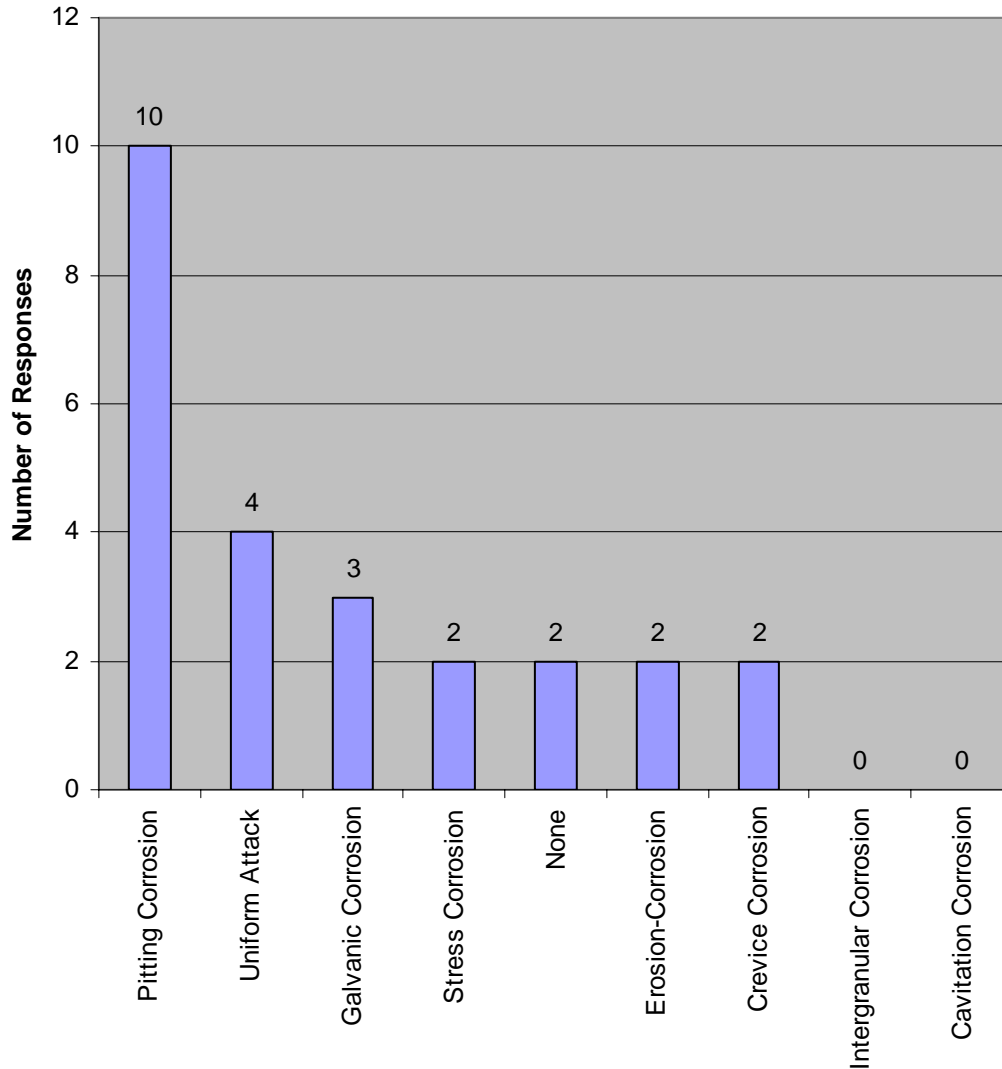
Figure 95. Types of Corrosion Experienced by Survey Respondents

One respondent said that differential aeration was common; bacterial and AM5 has been identified in gathering lines but not wells.

Q14 What does your company do to prevent these forms of corrosion damage?

Eleven people responded to this open-ended question. Three respondents indicated that they use CP to protect each well. One respondent said that his company does nothing. Other individual responses are listed below.

- Use biocide and corrosion inhibitor in completion and workover fluids. New wells are designed to have cement to surface (not always achieved). Where interference with

other wells/substructures is not a problem, CP is applied to well casings. Sand control is used to minimize sand erosion.

- Use a spring loaded check valve to keep O_2 out of the annulus. Some annulars contain corrosion inhibitor. Do not use CP on wells (gathering lines protected, wells isolated). Gas quality standards keep O_2 and CO_2 levels low.

- Atmospheric corrosion program for surface facilities. When O_2 is removed from surface facilities, corrosion is minimized.

- Chemical treatments on a regular basis.

- We also equip our casing strings with modified couplings and seal rings.

- Run caliper tools and inspections tools every workover period (7 years) and repair as needed.

- Biocides and corrosion inhibitors are used, and annuli are protected from sources of oxygen.

Q15 Would you consider corrosion the most pervasive damage mechanism for casings?

Twelve people responded to this question, 83% consider corrosion the most pervasive damage mechanism; 17% do not.

One respondent indicated that they consider mechanical damage from well work the most prevalent casing damage. They provided the following examples of such damage:

- Acid treatments.

- Fracing.

- Coiled tubing clean out.

Another respondent indicated that they used to consider corrosion the most pervasive damage mechanism. With their new prevention policies in place (outlined in Q14), they experience very little corrosion. With more and more horizontal wells, they find bit and drill string related mechanical damage, but have taken steps to prevent those too.

Q16 What other types of casing damage are found in your casings?

The multiple choice question consisted of the following options:

- Threaded connection separation.

- Thread sealant leak in API connections.

- Collapse.

- Parted or split casing due to internal defect.

- Rotational failure.

- Bends due to earth movement.

- Drill damage.

- Thread leak in premium connections.

- Buckling and drill pipe wear.

- None.

- Other.

44% of respondents experience threaded connection separation; 33% have threaded connection leaks and bends due to earth movements; and 22% report parted/split casings due to internal defect and drill damage. The full spectrum of reported damage is shown in Figure 96.
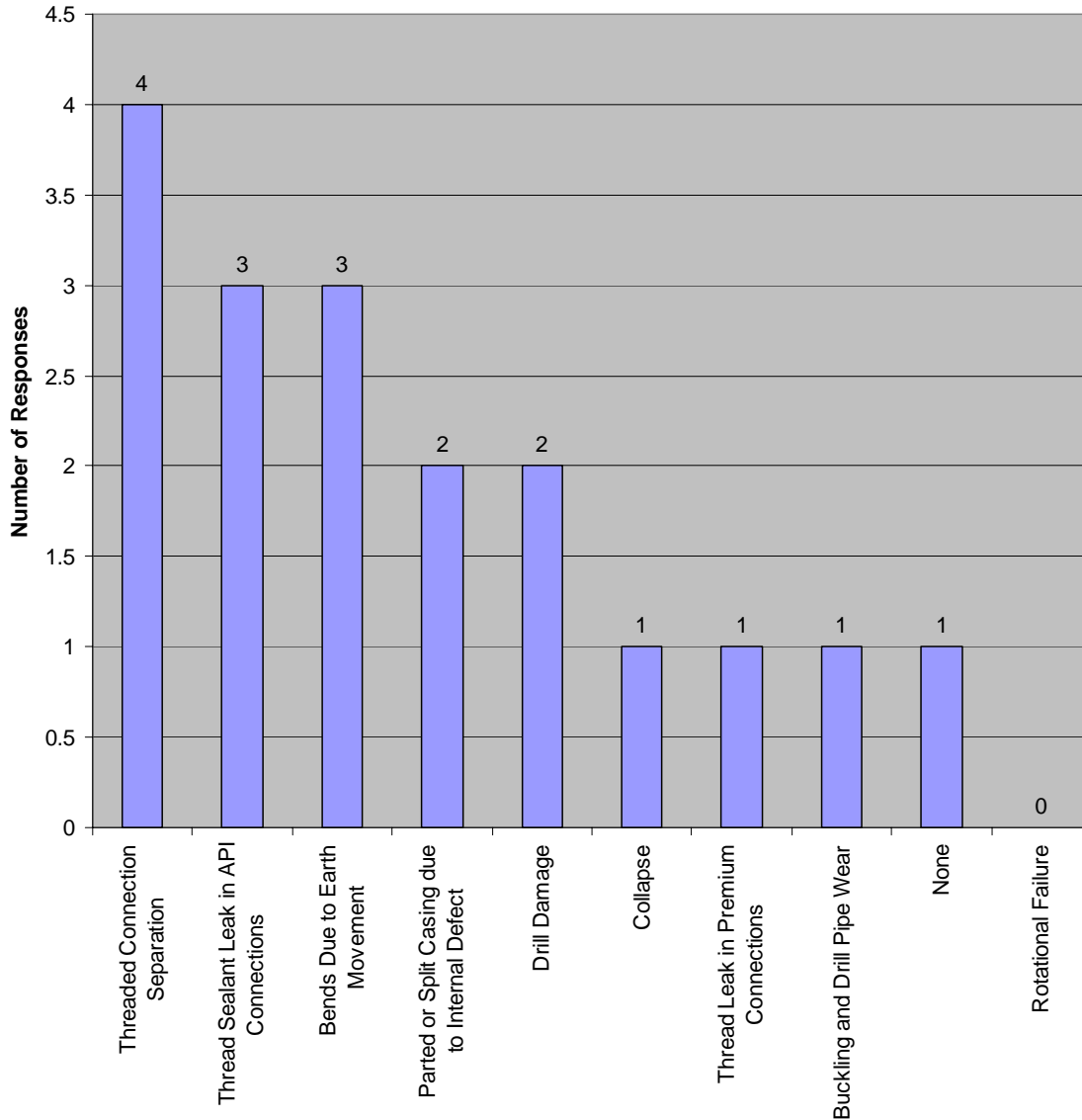
Figure 96. Non-Corrosion Damage Experienced by Survey Respondents

Three respondents listed some form of bit damage, as well as, the following additional types of non-corrosion damage:

- Internal and external corrosion, external mechanical damage from casing make up or internal from drilling equipment

- Internal wear due to rotating drill pipe. Thread leak in premium connections. Combination of buckling and drill pipe wear at top of cement. Where casing was not hung in sufficient tension and temperature changes cause it to be in compression at top of cement. Many 1979's era wells used stage cementing collars in middle of casing

string and most of these eventually develop a leak when exposed to varying gas pressure.

One respondent's company does not experience any damage and another reports external MIC pitting corrosion.

Q17 What does your company do to prevent these forms of damage?

Ten people responded to this question. 3 companies do nothing; 7 respondents indicated that their companies take the following precautions.

- Exercise proper precautions when running casing to not impart mechanical damage.

- Don't rotate the bit while it's in the casing.

- Be careful when handling, running and cementing casings in new wells.

- Modified couplings and seal rings.

- Inspect every workover period and make repairs as needed.

- Limit introduction of oxygen into annuli, use of biocides and corrosion inhibitors in packer fluids.

Q18 Does your company use cement squeeze casing repairs?

Thirteen respondents answered this question; 54% (7) do not use cement squeezes.

Q19 What types of casing damage do you repair with cement squeeze repair?

Of the 14 responses to this question, 36% (5) respondents that use (or have used) cement squeezes, provided the following input:

- Everywhere there is through-pipe hole.

- Cement not to surface as per NYDEC or PADEP requirements.

- Small hole leaks.

- MIC-damaged surface casings.

- Have not used a cement repair in 15 years.

Q20 Please list the trade name(s) of the cement squeeze repair system(s) that you use.

Twelve people responded to this question. 83% (10) report that they do not use cement squeezes. One respondent indicated that his company uses various cement blends, but did not

provide any additional information. Another respondent indicated that his company uses regular class C cement.

Q21 Are there any limits to cement squeeze repair technology that you have seen during the application of such repair?

Twelve people responded to this question; again, 83% do not use squeeze repairs. The two respondents that use cement squeezes listed the following limitations.

- Squeeze cementing is rarely used as the sole repair method, because it will not reliably hold gas pressure. Cement is used to stabilize and protect the exterior of the casing, with a patch or inner casing string used to hold pressure.

- The rate of pumping is a limitation during application.

Q22 Does your company use sealant squeeze repairs?

Thirteen people responded to this question and none use sealant squeeze repairs. Again, one respondent indicated that he has not used a squeeze repair in 15 years.

Q23 What types of damage do you repair with sealant squeeze repair?

None were identified. Ten people responded to this question and none of them use sealant squeeze repairs.

Q24 Please list the trade name(s) and types of sealants squeeze repair system(s) that you use. (These include sodium silicate gel, in situ polymerizing monomer, crosslink polymer gel, epoxy, or resins.)

No sealant squeeze repair trade names were listed, as none of the respondents use this type of repair.

Q25 Are there any limits to sealant squeeze repair technology that you have seen during the application of such repair?

None were identified. Of the thirteen people who responded to this question, none use sealant squeeze repairs. Again, one respondent indicated that he has not used a squeeze repair in 15 years.

Q26 Does your company use metallic squeeze repairs?

Twelve people answered this question and none use metallic squeeze repairs. Again, one respondent indicated that he has not used a squeeze repairs in 15 years. Another respondent said that he was not aware of such a product being commercially available.

Q27 What types of damage do you repair with a metallic squeeze repair?

None were identified. Eight people responded to this question and none of them use metallic squeeze repairs. Again, one respondent indicated that he has not used a squeeze repairs in 15 years.

Q28 Please list the trade name(s) of the metallic squeeze repair system(s) that you use.

Ten people responded to this question and none use metallic squeeze repairs.

Q29 Are there any limits to metallic squeeze repair technology that you have seen during the application of such repair?

None were identified. Eleven people responded to this question and none use metallic squeeze repairs. One respondent indicated that he was not aware that a product like this was commercially available.

Q30 Does your company use a non-expandable liner repair such as a scab?

Thirteen people responded to this question; 6 respondents (46%) use non-expandable liner repair and 7 (54%) do not.

Q31 What types of damage do you repair with non-expandable liner repair?

Eleven people answered this question. Corrosion is the most common damage type repaired with non-expandable liners. Five respondents listed the following candidate damage types.

- Corrosion in the casing. Liner is run the entire length of the well bore with cement pumped behind the liner to seal it.

- High corrosion and collar leaks.

- Any.

- Corrosion pits, split casing.

- Corrosion pitting near shoe in open hole completions.

Q32 Do you use a squeeze operation in conjunction with a non-expandable liner repair?

Eleven people responded to this question; 64% (7) indicate that they would not use a squeeze operation in conjunction with a non-expandable liner repair. Only one indicated that they would use a squeeze operation in conjunction with a non-expandable liner and that it depends on size and depth of hole and cause. They are more likely to squeeze if external corrosion or buckling.

Q33 Please list the trade name(s) and types of non-expandable liner repair system(s) that you use.

Twelve people responded to this question; three have used the following non-expandable liner products.

- Halliburton (Pengo) patch; inner casing string landed on packer at bottom and wellhead at top.
- Weatherford.
- Various liner hangers.

Q34 Are there any limits to non-expandable liner repair technology that you have seen during the application of such repair?

Eleven respondents answered this question. Two provided the following limitations on the use of non-expandable liner repair technology.

- Pengo patches have not been reliable.
- Will follow industry standards as well as Louisiana regulations.

Q35 Does your company use an expandable liner repair?

Thirteen people answered this question; 6 (46%) use expandable liner repairs and 7 (54%) do not.

Q36 What types of damage do you repair with expandable liner repair?

One respondent indicated that they have experienced no problems in the past 15 years. Thirteen people responded to this question and the most common types of damage repaired with expandable liners are corrosion and leaks. Six of thirteen respondents reported the following specific damage types.

- Casing collar leak.

- Corrosion in casing or threaded connection leak.

- Where significant wall thickness remains.

- Squeezed perforations and leaky collars.

- Corrosion, split casing.

- Corrosion defects in cemented pipe, usually uphole.

Q37 Please list the trade name(s) and types of expandable liner repair system(s) that you use.

Four of the five respondents indicated that they use Weatherford patches; two of the five indicated that they use Baker systems. One respondent indicated that they have used an old style Weatherford patch, which was corrugated with epoxy on the outside. This respondent also said that they have looked at newer expandable patches but have not used them yet due to cost and issues with reduced ID.

Q38 What typical temperature and pressure ranges are associated with each expandable liner repair system that you use?

Twelve people responded to this question. Five respondents provided the following data:
- Patches we have used meet our pressure range and temperature range of 50° to 75°F.

- Lower end of our pressure and temperature range for patches that use epoxy.

- 55° to 100°F; 500 to 4,000 psi.

- Casing needs to be real clean.

- Depends on product specifications

Q39 Are there any limits to expandable liner repair technology that you have seen during the application of such repair?

Two respondents answered this question. The first respondent indicated that they are not aware of any limitations. The second respondent said that liner repairs may restrict future ability to work on the well due to the permanent ID reduction.

Q40 Does your company use a composite liner repair?

One of thirteen people responding to this question indicated that they use a composite liner repair. One respondent was not familiar with any commercially available composite liner repair systems.

Q41 What types of damage do you repair with composite liner repair?

The one respondent who uses composite liner repair technology deploys it to fix corrosion. One person reiterated that they have not experienced any problems in 15 years.

Q42 Please list the trade name(s) and types of composite liner repair system(s) that you use.

The one person who familiar with composite liners uses a Weatherford system.

Q43 Are there any limits to composite liner repair technology that you have seen during the application of such repair?

One respondent indicated that they were not familiar with any commercially available composite liner repair systems. The other respondent simply listed "Weatherford" as a limitation.

Q44 What other casing repair technologies does your company currently use?

One respondent said that his company is lucky not to have casing problems; not that they won't have problems in the future. Ten of thirteen respondents indicated that they do not use any other types of casing repair technologies. Another respondent uses the following "other" repair technology : back off, pull and replace.

Q45 What types of damage do you repair with these other casing repair technologies?

Eleven people responded to this question; eight do not repair damage with other procedures. One respondent theorized that he would expect these processes would be used to repair corrosion problems or collar leaks. The respondent that uses tubing packer systems said that they use them to repair corrosion and threaded coupling leaks. The respondent that uses back off, pull and replace uses this technique to repair internal and external pitting in uphole joints.

Q46 Please list the trade name(s) and types of the other casing repair system(s) that you use.

The respondent that uses tubing packer systems did not list a trade name for the system that his company uses.

Q47 Are there any limits to the other casing repair system(s) that you have seen during the application of such repair(s)?

The respondent that uses tubing packer systems did not list any limitations during application. The respondent that uses back off, pull and replace indicated that they need to avoid backing off pipe in open hole intervals; backoffs are tough as you get deeper; some thread forms are hard to correctly tighten and torque.

Q48 Under what circumstances do you cap off a well and abandon a reservoir?

Twelve respondents answered this question; 6 (50%) said they will not cap off a well or abandon a reservoir. The remaining 6 (50%) of respondents listed the following criteria for capping off a well or abandoning a reservoir:

- Usually when the field is no longer needed for storage or the well is no longer needed for storage. Have not plugged a well due to damage.

- Significant casing damage and near well bore plugging of reservoir in combination.

- Cost of well replacement greater than revenue from storage

- It would have to be in extremely poor condition and pose a safety concern before it would be plugged.

- High corrosion and gas outside casing in annular area.

- If no suitable repair methods are available, a well may be plugged and abandoned. The well may be replaced with an offsetting new well. No experience abandoning an entire reservoir, because of well defects.

Q49 Is there any type of damage that you do not repair?

Twelve respondents answered this question; 6 (50%) said there is no type of damage they would not repair. The remaining 6 (50%) of respondents listed the following criteria for damage they would not repair.

- Would assess on a case by case basis.

- Casing part.

- A poor well would be plugged rather than repaired.

- Casing collapse due to coal mine subsidence.

- Depends on the extent of the damage and state regulations and industry practice.

- Mill defects or inactive corrosion pitting resulting in acceptable reduced burst pressure ratings.

Q50 Are there limits to the amount of damage that you do repair, such as excessive corrosion, excessive buckle angle, etc.?

Twelve respondents answered this question; four listed no limits to the amount of damage that they will repair. Eight respondents provided the following:

- Would assess on a case by case basis.

- Very severe wall thickness loss where there is a potential for not being able to get to bottom to properly plug well.

- If excessive, would plug and drill offset well.

- Excessive corrosion on smaller diameter (4 1/2', 5 1/2') casing.

- Hard to answer this.

- Corrosion must be over 80% and growing.

- Depends on the extent of the damage and state regulations and industry practice.

- Economics of repair vs. plug and drill replacement well.

Q51 Do you have any additional comments about damage that is not repaired.

Twelve responded to this question; eleven had nothing to add. One respondent said that they have found mill defects in some joints.

Q52 Are you aware of any emerging casing repair technologies that are not covered by this survey?

Twelve respondents indicated that they were not aware of any emerging casing repair technologies not covered by this survey.

Q53 Are you aware of any emerging technologies that show promise as a casing repair technology?

Of the twelve people who answered this question, one was familiar with expandable patch repair technology and indicated that this repair shows promise.

Q54 Do you have any additional comments about the survey?

Twelve respondents answered this question. One is interested in more information on the metal squeeze/welding process that was mentioned in the survey.

Q55 Are there any questions that we should have asked, but didn't?

Twelve respondents indicated that there were no additional questions that should have been asked.

Q56 Are you interested in providing additional information to the project team?

Five people volunteered to provide additional information as the project progresses.

Effects of Tensile Loading on the Remaining Strength of Corroded Casing

Robert Francini
Kiefner and Associates
585 Scherers Ct.
Worthington, OH 43085

Project extended until June 30, 2008, report due at later date

Brine String Integrity-Case History Survey and Model Evaluation

Joseph Ratigan
PB Energy Storage Services
PO Box 725
Rapid City, SD 57709

Project extended until June 30, 2008, report due at a later date

GAS STORAGE TECHNOLOGY CONSORTIUM

Research Project

WELLBORE CEMENT BOND INTEGRITY

Final Report
June 1, 2006 – May 31, 2007

Prepared and Submitted by

Dr. K. E Gray
The University of Texas at Austin
Petroleum & Geosystems Eng. 1
University Station CO 300
Austin, TX 78712-0228

Phone (512) 471-3242 Fax (512) 471-9605

Disclaimer

This report was prepared as an account of work sponsored by an agency of the United States Government. Neither the United States Government nor any agency thereof, nor any of their employees, makes any warranty, express or implied, or assumes any legal liability or responsibility for the accuracy, completeness, or usefulness of any information, apparatus, product or process disclosed, or represents that its use would not infringe privately owned rights. Reference herein to any specific commercial product, process, or service by trade name, trademark, manufacturer, or otherwise does not necessarily constitute or imply its endorsement, recommendation, or favoring by the United States Government or constitute or imply its endorsement, recommendation, or favoring by the United States Government or any agency thereof. The views and opinions of authors expressed herein do not necessarily state or reflect those of the United States Government or any agency thereof.

WELLBORE CEMENT BOND INTEGRITY

Abstract

Activities during this project focused on two related concerns: 1) relationships between cement – casing bond quality and the properties of acoustic wave propagation, and 2) an assessment of the reliability of laboratory acoustic systems for estimating mechanical properties of cement.   For the laboratory investigation of cement bonding, a bench-top apparatus was designed and built to simulate relevant features of the down-hole environment of a cemented casing. Freshly-prepared test specimens were poured into the assembly and allowed to cure for nominal one-week periods. After the period of curing, the assembly was cycled to temperatures of 100F, 150F, 175F, 195F, or 0F. As a result of these relatively modest temperature cycles, waves traveling through cement and the cement-casing bond were reduced in amplitude, while most of the waves traveling along the steel plate increased in amplitude. On the basis of observations from these initial studies, several modifications in system design and test methodology were incorporated into the experiments. Behavior observed in the modified system was very systematic, and in general agreement with the initial tests.

Assessment of acoustic measurement systems used to predict mechanical behavior was based on comparisons of measurements of the same specimens in both an ultrasonic cement analyzer and a load frame. Measurements showed that consistent behavior in the MPro system, and in bench-top wave propagation measurements, but values of UCS from load frame measurements show considerable scatter. Large discrepancies between MPro and load-frame values were found, and the measurements suggest that a more comprehensive assessment is needed.

WELLBORE CEMENT BOND INTEGRITY

Table of Contents

WELLBORE CEMENT BOND INTEGRITY

Executive Summary

Activities during this project focused on two related concerns: 1) relationships between cement – casing bond quality and the properties of acoustic wave propagation, and 2) an assessment of the reliability of laboratory acoustic systems for estimating mechanical properties of cement.

For the laboratory investigation of cement bonding, a bench-top apparatus was designed and built to simulate relevant features of the down-hole environment of a cemented casing. The apparatus consists of a layer of cement sandwiched between two steel plates. This geometry provides for generation and detection of P- and S-waves traveling through cement-casing bonds on either side of a layer of cement and several waves traveling vertically through the steel plate adjacent to the bonded cement layer. These waves include waves generated by compressional–and shear-mode transducers at one end of the specimen assembly and detected by another composite transducer at the other end. This geometry is a first-order approximation of the down-hole conditions appropriate for tools designed to assess cement bond quality. In particular, waves traveling through the steel plates should be affected by coupling of wave energy into and out of the cement, in a manner similar to waves used in cement logs. Energy coupled into a (steel) casing propagates with a high velocity (probably a p-wave), while energy is continuously lost into the cement casing through the cement-casing interface. The better the cement-steel bond, the lower the amplitude of waves traveling in the steel plate (casing), as a greater amount of energy is lost into the cement.

The basic test methodology for the wave propagation tests was as follows. Class H Portland Cement slurry was mixed and poured immediately into the test assembly. Waveforms of waves propagating across the chambers and along the chamber side walls were captured and stored at nominal 1-day intervals as the specimens cured. After curing for approximately 100 hours, the ultrasonic transducers were removed from the apparatus, the apparatus was immersed in a water bath heated to temperatures of 100F, 150F, 175F, or 195F, or a brine-saturated water bath cooled to 0F, and allowed to

5

stabilize for a period of one hour. The specimen was then removed from the water bath, transducers were re-attached, and the combinations of S- and P-wave forms were measured again.

A noticeable change in the character of horizontal P- and S-waves was observed after these relatively modest temperature cycles. Waves traveling through cement and the cement-casing bond are virtually undetectable after most of the temperature cycles. Travel times for waves traveling through the cement increase measurably after temperature cycles. A two-fold increase in amplitude is observed for waves traveling within the steel plate adjacent to the cement layer. These features are consistent with a decrease in energy loss into the cement from a degradation of bond quality between the plates and cement.

However, some inconsistencies were observed, which suggest that other factors contributed to the observed behavior. In the second phase of measurements, modifications in testing apparatus were developed to eliminate spurious behavior from transducer clamping and those due to the presence of water contact with the specimen assembly during immersion in water baths.   Subsequent measurements with the revised apparatus and test methodology provided highly reproducible measurements of effects of curing and temperature cycling on wave propagation in experimental simulations of cement bond log evaluations.

With the modified procedures and apparatus, observed behavior is now very systematic, and in general agreement with the initial tests. Namely:

- amplitudes and velocities of P- and S-waves traveling through the cement increase with curing times of up to 150 hours;
- amplitudes of P- and S-waves traveling horizontally through the cement are significantly reduced, but not eliminated, by temperature cycling;
- travel times for waves traveling through the cement increase measurably (one or two microseconds out of total travel times of several 10's of microseconds) after temperature cycles to elevated (150F or more) and to reduced temperatures;

6

- the variations in amplitudes of waves traveling horizontally through the cement is approximately the same for cycles to elevated temperatures of 150F – 195F as for cycles to reduced temperatures of 0F;

- the amplitudes of all waves traveling vertically (through the steel plates adjacent to the cement) increase noticeably (nominal 10%, well outside the measurement scatter) after all temperature cycles to 150F or greater and 0F or lower; and

- no changes in waves (amplitudes or travel times) are observed after immersion of the specimen assembly in a water bath at room temperature, but the normal amplitude decrease and travel time increase are still observed after temperature cycling immediately following the water bath immersion.

The assessment of acoustic measurement systems used to predict mechanical behavior was based on direct measurements of the same specimens in both an ultrasonic cement analyzer and a load frame. However, prior to this comparative assessment, an initial set of measurements were carried out to document system performance of the load frame. Deformation and failure tests were carried out for 10 one-inch diameter by two-inch long Berea sandstone specimens. Observations from the tests demonstrated that the load-frame measurements are highly reproducible. Observed discrepancies in deformation behavior measured in the load frame should be attributed to testing methodology or material behavior.

Comparative measurements in the MPro, load frame, and bench-top velocity systems showed that variations between different tests in the MPRO system were small, values of wave velocity measured in the MPro system were close in magnitude to those measured independently on the bench-top, predicted values of UCS from the MPro system show little measurement scatter, but load frame measurements of UCS show considerable scatter. No systematic trends in UCS values or discrepancies between MPro and load frame measurements were seen in this preliminary study. The large discrepancies between MPRO and load-frame values are of concern, and a more comprehensive assessment is needed.

WELLBORE CEMENT BOND INTEGRITY

Chapter 1: Introduction

This report concerns laboratory testing carried out during the period June 1, 2006 to May 31, 2007 for *Wellbore Cement Bond Integrity,* a 2-year program carried out in conjunction with and co-funded by the *Life-Of-Well Rock, Fluid, and Stress Systems* and *Rock Mechanics* Joint Industry Programs (JIP) at The University of Texas at Austin under the direction of Dr. K. E. Gray. Specific to this GSTC project is the Life-Of-Well JIP project: *Casing, Cement, and Formation Interactions during Drilling, Completion, and Production Operations.* This project is sponsored by BJ Services, Chevron, ExonMobil, and Schlumberger. The *Casing, Cement, and Formation Interactions During Drilling, Completion, and Production Operations* project is investigating what happens to the cement slurry in the wellbore and the effects of those changes on wellbore and near-wellbore stresses. The GSTC *Wellbore Cement Bond Integrity* project seeks to quantify the effects of stress and temperature variations on casing-cement bond integrity. Both projects require and utilize extensive laboratory tests to quantify mechanical and acoustical behavior of commonly used cement formulations, from tests being carried out under simulated in situ conditions.

Activities during this project focused on two related concerns: 1) relationships between cement – casing bond quality and the properties of acoustic wave propagation, and 2) an assessment of the reliability of laboratory acoustic systems for estimating mechanical properties of cement. The overall objective of the research is to improve the design and characterization of well bore cements by developing a better understanding of wave propagation in the cement – well bore environment and its relationship to cement behavior. Both components of the study are based on experimental measurements in the laboratory.

For the laboratory investigation of cement bonding, a bench-top apparatus was designed to simulate relevant features of the down-hole environment of a cemented casing, and a large number of measurements of waveforms propagating along simulated well bores bonded to a cement layer were carried out. Measurements of variations in

cement bonding, and the impact of that variation on wave propagation, were carried out during a one week curing period and after temperature cycles to four higher and one lower temperature.

The assessment of acoustic measurement systems is based on direct measurements of the same specimens in both an ultrasonic cement analyzer and a load frame. Results from this investigation of ultrasonic system performance should be of general applicability for use of the system in predicting mechanical behavior of cement. However, the immediate need for such a documentation of system performance is in connection with new studies to be carried out. The new study will be a comprehensive assessment of cement performance in a well bore environment - and the impact of changes in cement recipe and curing environment on cement performance. This assessment will be carried out using a bench-top ultrasonic system to rapidly monitor cement mechanical behavior. A comprehensive assessment of ultrasonic cement evaluation systems will be necessary to document the reliability of ultrasonic systems for estimating static mechanical behavior of cement.

A preliminary assessment has been carried out in the current project. For this assessment, two sets of specimens were prepared and cured in the ultrasonic system, and then load frame measurements of mechanical behavior were carried out on the same specimen. Results from this preliminary assessment are presented in this report.

Predictions of well-bore failure and the degradation of the cement-casing bond performance during the life of the well are often based on numerical simulations of cement and bore-hole behavior. These simulations require knowledge of deformation and failure behavior to predict in-situ state of stress in the vicinity of the bore-hole, and to predict failure of well-bore and near-well-bore components (Thiercelin et al., 1997). The most relevant mechanical properties for this purpose are elastic moduli and compressive strengths. This includes a working knowledge about rheological behavior of the cement slurry as it is injected into a well-bore, and as it transitions from a liquid to solid states during curing. A significant amount of this kind of information is provided by measurements of wave propagation in cement as it cures.

9

Mechanical measurements in a load frame provide stress-strain relationships and failure behavior of materials, determined directly from measured data. Young's modulus (E) is the ratio of stress to the corresponding strain in the region of linear behavior in a uniaxial stress (no lateral constraint) deformation:

$$E = \frac{Axial\ Stress}{Axial\ Strain} = \frac{\sigma_x}{\varepsilon_y} \qquad (1)$$

Published test data (Prabhakar et al., 1982) indicates that Young's modulus of cement varies from 0.6×10^6 psi to 2.5×10^6 psi.

Poisson's ratio (v) is the ratio of transverse (lateral) strain to the corresponding axial (longitudinal) strain, also under uniaxial stress conditions:

$$v_{yx} = -\frac{\varepsilon_x}{\varepsilon_z} \qquad (2)$$

Representative stres-strain curves for a cement specimen are shown in Figure 1. Magnitudes of the computed Young's modulus, (unconfined) strength, and Poisson's ratio are also indicated, adjacent to the straight lines used for the determinations. The bulk modulus (B, the ratio of pressure change to volume change) is not generally measured directly in load frame tests, but can be computed from the measured Young's modulus and Poisson's ratio:

$$B = \frac{E}{3(1 - 2v)} . \qquad (3)$$

The unconfined compressive strength (UCS) is the maximum value of applied stress prior to failure of an unconfined specimen. The magnitude of UCS can be read directly from the stress-strain curve. This number is a good indicator of material strength, and is widely used as a model input parameter.

The mechanical parameters measured in a load frame are static moduli and strength, which are most appropriate as input to bore-hole simulations. However, these measurements are lengthy and expensive, and cement behavior is more commonly

10

described in terms of wave propagation data. Although actual deformation and failure in a bore-hole take place in a high-pressure, high-temperature environment – and measurements under simulated in-situ conditions are possible (Reddy et al., 2005) - laboratory measurements of cement behavior are commonly carried out at atmospheric conditions, and these data are extrapolated to down-hole conditions.

Measurements of wave velocities are fast and require less specimen preparation than load frame tests, and they are non-destructive. In typical laboratory tests, compression and shear wave transducers are attached to the ends of the specimen. The velocity of the wave is calculated from the travel time of the pulse through the specimen. The appropriate modulus, C, is then determined by

$$V = \sqrt{\frac{c}{\rho}} \qquad (10)$$

where C is the constrained modulus, M, for compression waves (P-waves) or the shear modulus, G, for shear waves (S-waves). These moduli are dynamic moduli which are always greater than their static counterparts because the response of the specimen to low stress levels and short strain duration is purely elastic (Lacey and Richards, 1996). Dynamic values of Young's modulus, E_d , Poisson's ratio, v_d , and bulk modulus, $\boldsymbol{B_d}$, can be determined from the velocities by the relations:

$$E_d = \rho V_s^{\;2} \frac{(3V_p^{\;2} - 4V_s^{\;2})}{V_p^2 - V_s^2}, \qquad (11)$$

$$v_d = \frac{V_p^2 - 2V_s^2}{2(V_p^2 - V_s^2)}, \text{ and} \qquad (12)$$

$$\boldsymbol{B_d} = \frac{\rho(3V_p^2 - 4V_s^2)}{3} \qquad (13)$$

where V_s is the S-wave velocity, V_p is the P-wave velocity, and ρ is the density of the material. The measured propagation behavior must then be quantitatively correlated to the static mechanical behavior, and several patented packages have been developed and are in use. Note that, for a liquid, Poisson's ratio is ½, both E and G are zero, and M is equal to B.

11

Two devices that provide for characterization of cement behavior via ultrasonic wave propagation measurements are the Mechanical Properties Analyzer (MPro, manufactured by Chandler Engineering), and the Ultrasonic Cement Analyzer (UCA). The basis for their operation is empirical correlation of the wave velocities to uniaxial deformation and compressive strength.

The UCA apparatus consists of a heating jacket and pressure cell, and two sets of ultrasonic shear and compressional transducers used for measuring transit time. Transit time data are used to calculate the set time and the compressive strengths using in-built equations. In acoustic measurements, as the cement slurry hardens and gains static gel-strength, the amplitude of the acoustic signal also increases, and thus a change in this amplitude directly relates to the cement slurry's gel strength. Thus this method is useful for providing continuous, accurate measurements of static gel-strength cement slurry samples. A freshly-mixed and poured sample is used to test the unconfined compressive strength development history and the initial set of the cement slurry. Temperatures and pressures can be varied over a range encompassing virtually any condition encountered in a well bore environment. A schematic diagram of the system is shown in Figure 2.

The MPro system provides for monitoring a greater variety of cement properties during the curing and aging stages of slurry; a schematic diagram of the test vessel is shown in Figure 3. The cement slurry is poured into this cell, which is then placed horizontally in the system. Two transducers inside each end of the cell generate and detect shear and compressional waves as the cement slurry cures. The maximum settings for temperature and pressure are 400 F and 10,000 psi respectively. The ultrasonic measurements are used to determine the dynamic Young's modulus, bulk modulus and Poisson's ratio from Equations 10 - 13. The compressive strength is determined using compressional wave velocities in a proprietary correlation, incorporated into the data acquisition system. The MPro provides continuous measurement of mechanical properties. Down-hole conditions are simulated using a temperature and pressure control panel which can be programmed to different specifications.

Systems such as MPro make it possible to conveniently evaluate the effects of modifications to preparation procedures on cement properties. In addition to variations in

cement mixtures with additives, cement behavior may be affected by curing temperature, moisture content, and pressure conditions during curing. It is the intent of this research program to carry out a comprehensive series of tests with a variety of environmental conditions, using the MPro system housed in the CESE, to assess the potential for altering and improving cement quality. However, in preparation for this testing, it is first necessary to confirm the reliability of mechanical behavior predicted by the system, by comparison with direct load-frame measurements. The present phase of study, summarized in this report, is a preliminary assessment of this comparative study. For two cement mixtures, a suite of curing-time dependent velocity measurements were carried out, the cured (nominal one week time) specimen was removed, and direct bench-top measurements were carried out on the same specimen cured in the MPro system. Two suites of preliminary measurements are reported here: bench top ultrasonic wave velocities, using the independent apparatus housed in the CESE, and unconfined deformation and failure tests in a CESE load frame.

The design and operation of the ultrasonic and load frame measurement systems are described in the following section. Results from the tests carried out for this project are presented and discussed in Chapter 3. Observations and conclusions based on these studies are given in Chapter 4.

Chapter 2: Experimental Equipment and Test Procedures

Acoustic Signatures

The bench-top apparatus used for the study of wave propagation in a simulated well bore environment is shown in Figure 4. It consists of a 4" x 8" x 2" chamber bounded by steel plates on all surfaces except the top, into which is poured a freshly-mixed cement slurry at the beginning of each set of measurements. Composite ultrasonic transducers, each with capabilities for generating compressional and plane-polarized shear waves, are positioned at the three locations shown schematically in Figure 5. This geometry provides for generation and detection of P- and S-waves traveling horizontally (left – to – right) and several waves traveling vertically. The vertically-traveling waves include waves generated by the compressional – mode transducer at the top of the assembly, traveling vertically down the specimen assembly, and detected by the bottom compressional-mode transducer, and two waves generated by shear wave transducers at the top of the assembly, traveling vertically on the same side of the specimen and detected by shear transducers at the bottom of the assembly. These waves are likely to be converted modes - most likely P-waves in all cases – but they are distinct and are designated here by the properties of the shear waves generated initially: P waves, S_H, and S_V waves, (corresponding to horizontal or vertical polarizations. The first arrivals for all the waves traveling from top to bottom should be primarily P-waves propagating in the steel plate, while the waves traveling horizontally should be waves propagating through the cement (plus a small travel interval as waves traveling through the thickness of the steel plates).

This geometry provides for generation and detection of several waves:

1. P-waves traveling horizontally (left – to – right);
2. S-waves traveling horizontally (left – to – right). Depending on the orientation of the transducer, the shear wave can be polarized vertically (S_V waves) or horizontally (S_H waves), but the two waves are degenerate for this pathway.

3. Waves generated by the top (left or right) compressional – mode transducer, traveling vertically down the specimen assembly, and detected by the bottom compressional-mode transducer. These waves are likely to be P-waves;

4. Waves generated by the top shear-mode transducer, and detected by the bottom shear mode transducer on the same side.

As noted in Chapter 1, this apparatus geometry is a first-order approximation of the down-hole conditions appropriate for acoustic tools designed to assess cement bond quality. Waves traveling through the steel plates in this apparatus should be affected by coupling of wave energy into and out of the cement, in a manner similar to waves used in cement logs. Energy coupled into a (steel) casing propagates with a high velocity (probably a P-wave), while energy is continuously lost into the cement casing through the cement-casing interface. The better the cement-steel bond, the lower the amplitude of casing waves, as wave energy is lost into the cement. Wave attenuation inversely reflects the quality of the cement bond.

The basic test methodology for the wave propagation tests was as follows. Class H Portland Cement slurry (no additives) was mixed according to API #10 procedures, and poured immediately into the test assembly. Waveforms of waves propagating across the chambers and along the chamber side walls were captured and stored at nominal 1-day intervals as the specimens cured. After curing for approximately 100 hours, the ultrasonic transducers were removed from the apparatus, the apparatus was immersed in a water bath heated to temperatures of 100F, 150F, 175F, or 195F, or a brine-saturated water bath cooled to 0F, and allowed to stabilize for a period of one hour. The specimen was then removed from the water bath, transducers were re-attached, and the combinations of S- and P-wave forms were measured again.

Additional measurements were carried to assess the effects of multiple temperature cycles on observed behavior. A suite of waveform measurements was carried out for a fresh specimen, and the specimen was immersed for one hour in water at a temperature of 150F. Then another set of measurement were carried out. On the following day, another set of pre-heating waveform measurements were carried out, the specimen was again immersed in the water bath at 150F, and a final set of waveform

measurements was carried out. Measurements to assess the effects of shear wave polarization on observed behavior were also carried out.

Modifications in system design and test methodology were incorporated into the test matrix prior to a subsequent series of tests. In order to avoid possible complications from specimen exposure to water during immersion, the assembly was placed in a sealed plastic bag prior to immersion. Measures to avoid the variations in signal amplitude with clamping of the transducers to the specimen were incorporated into a modified apparatus configuration, shown in Figure 6. In this configuration bonding force is applied to the transducers via two saddle brackets (one for each side of the assembly). The single C-clamp contacts the saddle brackets in the center, so that equal amounts of force are applied to each transducer. A torque wrench is used for applying the force, so that a reproducible total force can be applied in each clamping operation. Sequences of measurements were carried out for both modifications, to document the improvements resulting from the modifications. A complete set of wave propagation and temperature cycling measurements were carried out using this test configuration.

MPro Assessment

A photograph of the MPRO system is shown in Figure 7. The module shown on the left side of the photo is the pressure and temperature control unit, which applies water pressure and temperature specified by the controller to the cement slurry. The heater is housed inside the right side. At the start of a test, the vessel containing the cement slurry is placed in the housing on the lower rear of the right hand unit, and appropriate cables and pressure lines are connected to the vessel for monitoring temperature, pressure, and wave velocities. The drawing in Figure 8 (inset) shows a 3-dimensional image of the pressure vessel. The cable connected to the center of the vessel (in Figure 7) is the electrical output from the ultrasonic receiver transducers; the transmitter transducer is at the opposite end of the chamber. The test specimen is a nominal 2-inch diameter by 4-inch long cylinder with irregular surfaces. The travel path length for the ultrasonic signals is 2 inches.

Test specimens of cement slurry for the MPro system were prepared according to API standard 10. Two mixtures were used: Mix 1 and Mix 2, as defined in Chapter 2. A Constant Speed Cement Mixer (CCSM) was used to mix the cement slurries. The mixed slurry was poured into the test vessel. After the cell was filled and sealed, the thermocouple was inserted and the ultrasonic signal leads were attached. The test specimens for these tests were normally allowed to cure in the test chamber for several days, while continuously monitoring travel times through the test specimen. A photograph of one of the test specimens after curing and removal from the test chamber is shown on the left side of Figure 9.

Comparative bench-top velocity measurements were carried out on this set of post-test MPRO specimens, using the Panametrics ultrasonic wave generation transducers from the box tests reported in GSTC Quarterly Reports #1 and 2 (Gray and Holder, 2006B,C). A photograph of the test assembly for one of the tests is shown in Figure 10 (from Gray and Holder, 2007B).

For these bench top ultrasonic measurements, the ends of the two-inch diameter cement specimen from the MPro test were machined to be flat and parallel. The S- and P-waveforms were digitized and recorded with a digital oscilloscope; representative waveforms are shown in Figure 11. The quality of the waveforms is inferior to the conditioned signals in the MPRO system (Figure 8), and a precursor (electronic broadcast signal from transmitter to receiver, and some mode conversion of shear waves to P-waves during pulse input) to the shear wave arrival signal is clearly evident in Figure 11. However, both S- and P-wave arrival times are easily discernable, and travel times can be determined by visual inspection of the oscilloscope traces.

The load frame apparatus used for measurements of the static moduli and unconfined compressive strength is shown in Figure 12. The load frame is equipped with a motorized hydraulic ram to move the lower load platen, and an axial load transducer and axial and lateral displacement transducers. All transducers are coupled to a computer-based data acquisition system. Uniaxial compression test procedures followed ASTM D 2938 standards. The test specimens were cylindrical with a length to width ratio (H/D) of 2 - 2.5. Loading rates for the load frame tests were approximately 10^{-5} per

second. The plot of representative behavior in a load frame results shown in Figure 1 were measured in this apparatus.

Prior to the comparative load-frame measurement sequence to assess MPro performance, a preliminary suite of load frame measurements was carried out on samples of Berea sandstone. Deformation and failure tests were carried out for 10 one-inch diameter by two-inch long specimens (cored along bedding), to provide a measure of repeatability for the load frame measurements. Some of these tests included a small unloading cycle during the deformation sequence. In porous material such as cement, some of the deformation is due to non-recoverable (inelastic) processes. These processes are largely stress-dependent, which are no longer active during the unloading phase. Hence, this unloading stress-strain behavior is predominantly elastic.

For the comparison of deformation behavior determined in the MPro system with direct measurements in the load frame, the sequence of activities was as follows. Initially, 10 cement samples were prepared and tested in the MPro system. After test completion and removal from the MPro vessel, end surfaces were machined flat and parallel, and bench-top S- and P-wave travel time measurements were carried out. Subsequently, ten additional specimens were prepared and tested in the MPro system, and the sequence of MPro comparison of MPro results with load frame measurements was carried out. For the load frame measurements, test specimens were prepared by coring plugs from the MPRO specimens following ASTM C170 standards. A photograph of a prepared 1" x 2" cylindrical specimen, inside the MPro specimen from which it was cored, is shown on the right side of Figure 9. Finally, additional one-inch diameter by two-inch long test specimens for the load frame tests were cored from the first set of MPro test samples (used for velocity comparisons, above). Nine of the tests for comparison with load frame tests were completed satisfactorily, and 9 of the specimens from the initial set of MPro tests were successful.

18

Chapter 3: Results and Discussion

Acoustic Signatures

Wave forms for different test conditions, wave types, and travel paths for Specimen #1 are shown in Figures 13 -16. For each of the figures, waveforms are shown for P- and S-waves traveling along horizontal travel paths, and for vertical propagation of S waves, measured after curing times of 1, 21, 46, 72, and 117 hours, and immediately after immersing the specimen assembly in a water bath at 195F. Two waveforms are shown for each propagation direction for waves traveling between upper and lower transducers (horizontal propagation) and between left and right transducers (vertical propagation). The labels to the immediate right of each pair of waveforms designate the pathway, mode, and curing time. For example, bl-br_P-a (1.0) designates the P-wave traveling between bottom-left to bottom-right transducers, after curing for 1.0 hours. The 'a' – 'e' designators in the labels are used to distinguish file names for the different curing times. The S-waves traveling vertically were polarized so particle displacements were normal to the plane of the steel plates (designated as S_V waves, although the character of the waves is probably altered by mode conversions; see below).

Curing behavior in the horizontally-traveling waves (Figure 13 and 14) is similar to observations in previous phases of this research program (Gray and Holder, 2006A): a large increase in amplitude, and a sharp decrease in travel time through the cement, between initial pouring and after curing for 24 hours; subsequent changes in wave forms with curing are small. Shear waves traveling (horizontally) through the cement are seen only after curing overnight (Figure 13), and shear wave arrival times are approximately twice that of P-waves. Waves traveling vertically through the side plates are remarkably similar for each of the two paths (left and right). P-wave precursors are evident in shear waveforms (Figure 13).   There is a noticeable difference in travel times (a few microseconds) between the two different horizontal pathways (upper and lower) for all curing times.

There is a noticeable change in the character of horizontal P- and S-waves after temperature cycling (waves labeled with 'e' in Figures 13-16, after 121 hours of curing).

The waves traveling horizontally between the top transducers are virtually undetectable after the temperature cycle, and waveforms traveling between the bottom transducers are significantly reduced in amplitude after the cycle. There is an increase in amplitude (approximately by a factor of 2) for the vertically traveling waves generated and detected by the P-wave transducers (Figure 15). This increase in amplitude, and the decrease in amplitudes of waves traveling horizontally through the cement and cement-steel bond, is consistent with a decrease in energy loss into the cement due to a degradation of bond quality between the plates and cement. The coupling is different between the two pathways even before the temperature cycle. However, a similar increase in the amplitude of waves generated and detected by S-wave transducers was not found.

The sequence of waveform measurements at curing times between one hour and one week was repeated for specimen #2, followed by temperature cycling by immersion in a water bath at 175F. The waveforms are shown in Figures 17 – 20. The behavior is virtually identical to that observed for Specimen #1, Figures 13 – 16:

1)   amplitudes and velocities of P- and S-waves traveling through the cement increase dramatically after overnight curing, but subsequent increases with curing time are small;

2)   amplitudes of P- and S- waves propagating horizontally through the cement decrease substantially after temperature cycling to 175F;

3)   amplitudes of vertically-traveling waves generated and detected by P-wave transducers increase; and

4)   no significant change in amplitudes of vertically traveling waves generated and detected by S-wave transducers was observed.

Again, observed behavior is consistent with a degradation of the cement-steel bond during the temperature cycle.

The sequence of tests carried out for the next specimen (#3) assessed the effects of repeated temperature cycles on propagation behavior. For this sequence, no waveform measurements were carried out as the specimen cured over the first 5 days after mixing. After curing for 5 days, a complete suite of waveform measurements was carried out. Then the specimen was immersed for one hour in water at a temperature of 150F, and a

subsequent set of waveform measurement were carried out. On the following day, another set of pre-heating waveform measurements were carried out, the specimen was again immersed in the water bath at 150F, and a final set of waveform measurements was carried out. Waveforms traveling horizontally in the test apparatus are shown in Figures 21 – 22.

Again, signal amplitudes for both S- and P-waves traveling horizontally (through the cement and cement-steel bond) are substantially reduced after the temperature cycles. However, the signal amplitudes of all waves – with the exception of the P-wave traveling between the upper transducers - are largely restored after a subsequent overnight cure. Following the second temperature cycle one day later, both S- and P-wave amplitudes for waves traveling between the upper transducers are again reduced substantially, while the amplitudes of the waves traveling between the lower transducers are not reduced as much. This behavior could be an indication that water in the temperature bath has affected coupling of energy from the upper transducers (the top of the specimen chamber is open) into the cement. The nature of this process is not clear, however. Further investigation is discussed below.

Vertically-propagating waveforms for Specimen #3, generated and detected by P- and S-wave transducers, are shown in Figures 23 and 24, respectively. An increase in amplitude of the vertical P-wave signal is again evident, and the shear wave signals are relatively unchanged, after the first temperature cycle to 150F.

It has been noted that all vertically-propagating waves in this laboratory test configuration, as well as waves traveling through steel casings in the down-hole environment, are likely to involve mode conversions at the steel-cement boundaries. These waves should travel at least partially within the steel plates, and energy losses for the waves are likely to depend on wave modes. In the measurement sequences thus far, the vertically-traveling waves generated and detected by S-wave transducers were polarized such that the particle displacements were vertical. The behavior of S-waves generated and detected by S-wave transducers with horizontal particle displacements may be different, however, and measurements to assess this difference were carried out in this sequence. These waveforms are designated in this discussion as S_H waves (although, as

21

noted, the character of the waves traveling in the steel plates may be altered by mode conversions). Measured waveforms for the same curing and temperature conditions as for Figures 21-24 are shown in Figure 25.

Indeed, the S_H waves in Figure 25 are significantly different from the S_V waveforms shown in Figure 24. The initial highest S_V signal amplitude arrives at the beginning of the waveform (at about 15 microseconds for both S_H and S_V waves) while the highest amplitude S_H signal does not arrive until much later (approximately 30 microseconds). Neither S_V nor S_H waveforms are significantly changed by the temperature cycle to 150F. Measurements of the behavior of both S_V and S_H waveforms were carried out for all subsequent curing/temperature cycle sequences.

The full suite of waveform measurements at nominal 1-day curing intervals and a temperature cycle to only 100F, was carried out for Specimen #4; results are shown in Figures 26 – 30. The usual progression of arrival times for waves traveling horizontally through the cement as it cures is observed, and the amplitudes are dramatically decreased after immersion in water - more so for the waves traveling between the upper transducers. Little change is observed for either of the S-waves traveling vertically. In contrast to the earlier tests, the amplitude of the P-wave traveling vertically through the steel plate is not significantly changed by immersion of the assembly in water at 100F. This diminished effect with a smaller temperature cycle is consistent with lower thermal stresses. Some evidence for a larger post-cycle amplitude is indicated for the S$_H$ waves, but the magnitude is within measurement scatter.

Most of the general trends observed in Specimens 1 – 3 are reproduced in the tests for Specimen #4, but some inconsistencies are seen. Of particular concern is the large reduction of the amplitudes of waves traveling through the cement for temperature cycles of less than 150F – even though, in contrast to tests for Specimens 1 – 3, no significant increase is found in the amplitudes of P-waves traveling vertically in the steel plate. Furthermore, the amplitude reductions are slightly greater for wave paths through the cement near the open end of the specimen containment box. These inconsistencies could indicate a variation in behavior due to the introduction of water from the bath at the open end of the test box, rather than that due to temperature cycling. Based on these concerns,

the sequence of measurements was repeated for one-week curing and subsequent immersion of a specimen in a bath of water at ambient room temperature (ie., water immersion but no temperature change). Results from these experiments are shown in Figures 31– 35.

Although some measurement difficulties are indicated in Figure 31, these test results show most of the features observed for Specimens 1-4. In particular, the amplitudes of waves traveling horizontally through the cement are substantially reduced – but less so than for Specimens 1 - 4 – and the amplitudes of waves generated and detected by P-wave and horizontally–polarized shear wave transducers traveling vertically through the steel plates are again increased by immersion in room temperature water. The behavior suggests a problem with the immersion methodology used to create the temperature cycles. This problem could obscure the observed changes in bond quality due to temperature cycling, and must be resolved before reaching meaningful conclusions about the impact of temperature cycling on cement bond quality.

An additional experimental concern was the potential for variations in observed behavior from removal and installation of clamps used to attach the ultrasonic transducers to the test apparatus. The clamps were removed prior to immersion of the apparatus into the heated water bath, and re-installed after the one-hour residence in the bath. Spurious behavior from this procedure could also obscure effects due to temperature-induced changes in bond quality.

Towards this end, two modified test sequences were carried out:

1. A test specimen (# III-1) was prepared and cured for 116 hours according to the normal test sequence. The ultrasonic transducers were un-clamped and removed from the assembly. The specimen was then subjected to a temperature cycle to 195F by immersion in heated water. However, prior to immersing the specimen assembly in the water bath, the assembly was placed in a sealed plastic bag to prevent exposure of the assembly to water.

2. Another specimen (#III-2) was prepared and cured for 118 hours. At each of the waveform sampling stages (after curing for 0.5, 24, 48, 72, and 118 hours), however, the attachment procedures for the wave transducers were altered. One

23

set of wave forms was measured with the original clamps (Figure 4) very loosely attached (only enough clamp force to prevent the clamp from dropping from the assembly in its erect position). Immediately following this set of measurements for loosely-clamped transducers, the forces from all 4 clamps were increased as high as possible (hand-tight), and another set of wave form captures were carried out.

Results from the first of these measurement sets (Specimen III-1) are shown in Figures 36-40. It does appear that the decrease in amplitudes of the waves traveling horizontally through the cement following immersion is not as large as for the previous tests in which the sample and assembly were exposed directly to water. Also, the post-immersion increases in amplitude for waves traveling vertically are not as prominent as they were for the previous tests. Unfortunately, this set of measurements was compromised by leakage of water into the bagged specimen during the immersion. The heated bag used for encapsulation of the specimen was very weak at the elevated temperature, and the jacket was punctured in several places where the bag came in contact with sharp corners of the apparatus.

Regardless of the uncertainty of water leakage, all subsequent temperature cycles were carried out by bagging the sample prior to the immersion. The problem with punctures from sharp edges of the apparatus was avoided by taping all the corners prior to bagging. No evidence of water leakage into the bags was seen in any of the subsequent tests.

Results for the wave-form measurements for the loosely-clamped transducers (Specimen # III-2) are shown in Figures 41-45 (No temperature cycling was carried out for this specimen). The corresponding plots of waveforms for tightly-clamped transducers, measured immediately after the measurements for loosely-clamped transducers, are shown in Figures 46-50. The tightly clamped signals that travel through the cement are clearly larger than the loosely clamped signals. On the other hand, waves traveling vertically through the apparatus have significantly lower amplitudes for the loosely-clamped case, reflecting less energy loss from these waves into the cement. It is

apparent that variations in clamping pressure could significantly complicate assessments of the small changes associated with changes in bond quality.

Measures to avoid the variations in signal amplitude with clamping were therefore incorporated into a modified apparatus configuration. The modified assembly is that shown in Figure 6. In this configuration force is applied to the transducers via two saddle brackets (one for each side of the assembly). The C-clamps contact the saddle brackets in the center, so that equal amounts of force are applied to each transducer. A torque wrench is used for applying the force, so that a reproducible total force can be applied in each clamping operation.

A preliminary assessment of the modified assembly was provided by a third set of waveform measurements on Specimen # III-2. Prior to testing, this specimen remained in the test assembly during fabrication of the new saddle brackets, where it cured for an additional week. The transducers were then attached to the assembly and clamped to a standard force (for a torque wrench indication of 40 in-lb) with the new saddle brackets, and another sequence of wave-form measurements were carried out. The clamps were then removed, the specimen assembly (with taped edges to avoid puncturing of the bag) was bagged, and the assembly was immersed in a water bath at 195F for one hour. Following the temperature cycle, the bag was removed, the new clamping brackets were affixed with the same torque (40 in-lb), and a final sequence of wave-form measurements was carried out. The captured wave forms are shown in Figures 51-55

The wave forms captured before and after removal of the clamps and temperature cycling are virtually identical. Curing for these specimens was almost complete (310 hours), and the integrity of the cement-steel plate bond was much better than for the previous sequences (temperature cycles were carried out after curing for about 5 days for those tests). Therefore, this replication of wave shapes after removal and re-installation of the new transducer/clamp assembly is taken as strong evidence for the reliability of measurements carried out with the modified clamps. All subsequent measurements were carried out using the new apparatus, with an intermediate amount of applied torque (40 in-lb).

A complete repetition of the suite of the temperature cycling measurements was carried out with the modified equipment, to substantiate the conclusions derived from the initial set of measurements (Gray and Holder, 2006B). As before, temperature cycles were carried out by immersion into water baths at room temperature, 150F, 175F, and 195F. For each these specimens, the specimen was cured for 120 to 150 hours, during which the sequence of 5 wave forms were captured at curing times of 1 hour, 24 hours, 48 hours, 72 hours, and either 120 or 150 hours. After curing, the transducers were removed, the sample assembly was placed in a cellophane bag, and the bagged assembly was immersed in the water bath for one hour. After the temperature cycle, a final set of (post-cycle) wave form measurements were carried out. In addition to the elevated-temperature cycles, one specimen was subjected to a low-temperature cycle by immersion into a brine bath at 0F. Another specimen was immersed in water at room temperature, to check for possible non-thermal effects. The captured wave forms are shown in Figures 56-60 (195 F bath), Figures 61-65 (175F bath), Figures 66-70 (150F bath), Figures 71-75 (room temperature bath), and Figures 76-80 (0F brine bath).

The behavior exhibited by the captured wave forms is now very systematic. It is in general agreement with the previous conclusions for effects of curing and temperature cycling on wave propagation in the box assembly, but some features are quantified:

- amplitudes and velocities of P- and S-waves traveling through the cement increase with curing times of up to 150 hours;
- amplitudes of P- and S-waves traveling horizontally through the cement are significantly reduced, but not eliminated, by temperature cycling;
- travel times for waves traveling through the cement increase measurably (one or two microseconds out of total travel times of several 10's of microseconds) after temperature cycles to elevated (150F or more) and to reduced temperatures;
- the variations in amplitudes of waves traveling horizontally through the cement is approximately the same for cycles to elevated temperatures of 150F – 195F as for cycles to reduced temperatures of 0F;

26

- the amplitudes of all waves traveling vertically (through the steel plates adjacent to the cement) increase noticeably (nominal 10%, well outside the measurement scatter) after all temperature cycles to 150F or greater and 0F or lower; and

- no changes in waves (amplitudes or travel times) are observed after immersion of the specimen assembly in a water bath at room temperature, but the normal amplitude decrease and travel time increase are still observed after temperature cycling immediately following the water bath immersion (Figures 71-75).

One final set of measurements was carried out for the new assembly and test methodology, to assess the effects of varying water content on the wave propagation. For these measurements, two test specimens were prepared and tested. Both were mixed according to the Mix 1 recipe used for all tests in this series, but for one of the specimens (V-1) 10% more water than the standard recipe was used. For the second specimen (V-2), 10% less water than the standard recipe was used. Captured wave forms for the specimen with 10% more water are shown in Figures 81-85; wave forms for specimens with 10% less water are shown in Figures 85-90.

The additional water has little impact on the observed wave propagation, as indicated by comparison with waveforms measured for the phase IV specimens (Figures 56-60), except for a small increase in the high frequency content of the P-wave traveling through the cement (Figure 83). Decreasing the water content appears to substantially alter the wave forms, however. Waves traveling through the reduced-water cement are considerably reduced in amplitude and the travel times are shorter than those for normal and enhanced-water cements (Figures 86 and 87). Neither travel times nor amplitudes were significantly altered for vertically traveling waves, however (Figures 88-90). No clear explanation is available for these observations, although the poorer quality of wave propagation behavior for the normal and increased water specimens suggests that the water content for the standard Mix 1 cement is close to optimal. Tests with Mix 2 specimens, as well as other mixtures, should contribute to a better understanding of relevant factors, and subsequent testing will address this concern.

MPro Assessment

        Results from the series of initial load frame measurements on specimens of Berea sandstone, carried out to assess uncertainty in measured behavior in the load frame system, are shown in Figure 91. This figure is a composite plot of stress-strain behavior for all 10 tests, plotted in the same figure. A tabulation of moduli (*E* and *v*) and UCS for all the load-frame tests on sandstone is presented in Table 2.   Bulk density for the specimens was also determined for these specimens, and the results are also included in Table 2. The uniformity of the density measurements confirms the uniformity of the Berea specimens. The observed behavior clearly shows that the load-frame measurements are highly reproducible. Observed discrepancies in deformation behavior measured in the load frame should be attributed to testing methodology or material behavior.

        Representative test results for an MPro measurement of wave velocities in cement specimens, collected over a 75-hour curing time, are shown in Figure 92. The p-wave transit times are constant at about 17 microseconds/inch during the first few hours, during which no shear waves were detected. After curing for about 5 hours the presence of a well-defined shear wave signal is seen, indicating that the slurry has solidified. From this point onward, the shear wave travel time is approximately twice that of the p-wave (s-wave velocity is about half the p-wave velocity), as is generally observed (Gray and Holder, 2006A). Travel times for both S- and P-waves steadily decrease (velocities increase) for the remainder of the test. Test pressure and temperature are also displayed on the upper plot in Figure 92. Computed dynamic moduli (B, v, and E) and the predicted values of UCS are shown in the lower plot in Figure 92. Test pressure was 3 kpsi and the temperature was 250 F.

        The MPro results for the initial set of tests on 8 cement specimens are tabulated in the first block of data in Table 3. The tabulation includes P- and S-wave travel times (inverse of velocity); computed values of dynamic Young's modulus, Poisson's ratio, and bulk modulus; and predictions of UCS, based on the proprietary MPro algorithm. The bench-top velocity measurements were carried out for the same specimens as for the MPro tests, and were measured shortly after the nominal one-week MPro test. The third

block of data in Table 2 shows results of load-frame tests on the same specimens used for both the MPro tests and the bench-top wave propagation tests. These results are discussed below, along with those of the load-frame tests in Table 3.

Three cement mixtures are included: a Chandler propriety mixture used for initial system calibration, and the two mixtures labeled Mix 1 and Mix 2 (cf. Chapter 2). Two tests, for Specimens 5 and 10, were not successful; the cement test chamber for Test 5 was apparently over-filled, and results for Test 10 were not consistent with the other tests. Results for these tests are not reported.

Travel times for the MPro measurements are relatively consistent (about 10% scatter). The measurement scatter for travel times, Young's modulus, and Poisson's ratio from the MPro system (Table 2) is correspondingly small: about 10% for the travel times and Young's modulus, and 5% for Poisson's ratio. In view of the small scatter in static moduli in the Berea sandstone specimens (Table 1), the MPro variations in measured cement moduli are likely to be the result of material variations.

Composite plots of the digitized P- and S-waves from the nine bench-top Panametrics measurements are shown in Figures 93 and 94, respectively. These specimens were completely cured prior to the bench-top measurements (more than 2 weeks from initial mixing). The bench-top travel time measurements show an even greater degree of reproducibility than the MPro tests; measurement scatter is only about 2%. The magnitudes of the bench-top travel times are in good agreement with those for the MPro measurements. These features are illustrated clearly in the plot of bench-top vs. MPro velocity measurements shown in Figure 95. The solid red line represents equal values for the two velocity determinations.

The ten additional specimens (9 Mix 1 and 1 Mix 2) were tested in the MPro system, and then core plugs were tested in the load frame. Results from these tests are shown in Table 3. Three of the specimens broke during coring, and no lateral strains were measured for Test 2 in the load frame. The first set of specimens, for MPro and bench-top velocity measurements, were plugged subsequent to the velocity measurements. Load frame tests were then carried out on the plugs. Results from these tests are included in Table 2.

The observed scatter in Young's moduli from MPro tests in both Table 2 and Table 3, although small, is much larger than for the Berea tests (about 10% for cement but only about 5% for sandstone). Magnitudes of the load frame measurements of Young's moduli are significantly lower than those for the MPro, reflecting the general trend of lower static moduli than dynamic (MPro) values. Scatter in Poisson's ratio is substantially greater for the load frame measurements. The values of UCS for all MPro tests is larger than that for the sandstones, but much of the variation can be attributed to differences between Mix 1 (nominal 5 kpsi) and Mix 2. (nominal 3 kpsi).

The greatest amount of scatter is within the load frame measurements of UCS. Values differ by more than a factor of two (nominal 6kpsi to 12 kpsi), and the variations do not correlate with MPRO values. The measurement scatter is much larger than that for the load frame tests on sandstone, even though the magnitudes of cement and sandstone UCS values are similar. The discrepancy between MPro and load frame values of UCS are likely to be associated with cement material variations.

Chapter 4: Summary and Conclusions

Two sets of experimental studies were carried out to: 1) characterize the behavior of waves traveling in a casing/cement environment as it is subject to stresses due to temperature variations; and 2) document the reliability of bench-top systems such as the MPro apparatus from Chandler Engineering for predicting mechanical behavior of cement. The objective of the first set of measurements was to improve the understanding of cement bond quality derived from wire line acoustic instruments. The system reliability measurements were carried out in preparation for subsequent studies of improvements in cement behavior from systematic tests with the MPro system.

The laboratory simulations of wave propagation in a well-bore /cement / casing environment demonstrated that significant changes in wave energy can result from relatively modest variations in temperature. The measured changes in wave behavior relate directly to the performance of cement bond logs. The principal observations were:

1. wave amplitudes and velocities of P- and S-waves traveling through the cement increase with curing, up to a static value after about one week;

2. amplitudes of P- and S-waves traveling through the cement and cement-casing bond are significantly reduced by temperature cycles by immersion in a water bath at elevated temperature;

3. with some exceptions, the amplitudes of waves traveling through steel plates adjacent to a bonded cement layer increase slightly (nominal 10%) after temperature cycles to 150F or greater, but not after cycling to 100F ;

4. the amplitudes of waves generated and detected by vertically polarized shear wave transducers, traveling through steel plates adjacent to an adjacent bonded cement layer are not noticeably changed by temperature cycling; and

5. the amplitudes of waves generated and detected by horizontally polarized shear wave transducers, traveling through the steel plates adjacent to an adjacent bonded cement layer, increase slightly.

These observations are consistent with a degradation of cement-casing bonding by temperature cycling, which significantly reduces both S- and P-wave energy coupled

directly into the cement. The loss of energy by coupling into the cement leads to a corresponding increase in P- and S_H-wave energy within the steel plate.

However, some similar variations were found after immersion of the cement-casing bond in a bath of water at room temperature (no temperature change), which suggest that other factors, probably the introduction of water into the specimen during the immersion process, contributed to the observed behavior. The determination and elimination of these factors was the major concern of the second phase of this set of studies.

In the second phase of measurements, modifications in testing apparatus were developed to eliminate spurious behavior from transducer clamping and those due to the presence of water contact with the specimen assembly during immersion in water baths. Subsequent measurements with the revised apparatus and test methodology provided highly reproducible measurements of effects of curing and temperature cycling on wave propagation in experimental simulations of cement bond log evaluations. The repeat measurements with modified apparatus established, beyond any measurement uncertainty, that

- amplitudes of p- and s-waves traveling horizontally through the cement are significantly reduced, but not eliminated, by temperature cycling,
- travel times for waves traveling through the cement increase measurably (one or two microseconds out of total travel times of several 10's of microseconds) after temperature cycles to elevated (150F or more) and to reduced temperatures;
- the variations in amplitudes of waves traveling through cement and the cement-casing bond is approximately the same for cycles to elevated temperatures of 150F – 195F as for cycles to reduced temperatures of 0F;
- the amplitudes of all waves traveling through the steel plates adjacent to the cement increase noticeably (nominal 10% after all temperature cycles to 150F or greater and 0F or lower;
- no changes in waves (amplitudes or travel times) were observed after immersion of the specimen assembly in a water bath at room temperature; and

- no significant changes in behavior were observed for specimen mixtures with 10% greater water content than the standard Mix 1, but clear degradations of signal quality were found for specimens mixed with 10% less water. The behavior is taken to indicate optimal water content in the Mix 1 cement recipe.

The objective of the preliminary assessment of the reliability of bench-top systems for characterizing mechanical behavior of cement from ultrasonic measurements was to assess the feasibility of using measurements from an MPro testing system in developing techniques for improving cement quality. This assessment was based on comparisons of MPro predictions and direct measurements of wave propagation and load frame deformation and failure tests. The principal observations were:

1. variations between different tests in the MPro system, which are all based on ultrasonic wave propagation measurements, are small;

2. values of wave velocity measured in the MPro system are close in magnitude to those measured independently on the bench-top;

3. predicted values of UCS from the MPro system show little measurement scatter;

4. MPro predictions of UCS values are generally smaller than values measured directly; and

5. load frame measurements of UCS show considerable scatter(more than a factor of two).

No systematic trends in UCS values or the discrepancies between MPro and load frame measurements were seen in this preliminary study. Possible factors include pre-test specimen condition of the test specimens – particularly the presence of an existing network of fractures - and excess degradation of cement strength with aging in ambient conditions. In any case, the large discrepancies between MPRO and load-frame values are of concern, and call for a more comprehensive assessment. This assessment is currently being carried out to confirm or deny the discrepancy, and, if confirmed, to determine its source and remedy.

References

Gray, K.E. and Holder, J. (2006A), "Acoustic Signatures During Cement Slurry Hardening: Part 1", *Gas Storage Technology Consortium*, *Number DE-FC26-03NT41779, (2910-UT-DOE-1779),* **Quarterly Report #3.**

Gray, K.E. and Holder, J. (2006B), "Acoustic Signatures During Cement Slurry Hardening: Part 2", *Gas Storage Technology Consortium*, *Number DE-FC26-03NT41779, (3139-UT-DOE-1779),* **Quarterly Report #1.**

Gray, K.E. and Holder, J. (2006C), "Acoustic Signatures During Cement Slurry Hardening: Part 3", *Gas Storage Technology Consortium*, *Number DE-FC26-03NT41779, (3139-UT-DOE-1779),* **Quarterly Report #2.**

Gray, K.E. and Holder, J. (2007A), ""Determining Strength Parameters of Oil Well Cement", *Gas Storage Technology Consortium*, *Number DE-FC26-03NT41779, (3139-UT-DOE-1779),* **Quarterly Report #3.**

Gray, K.E. and Holder, J. (2007B), "Laboratory Determination of Oilwell Cement Strength: Preliminary Comparison of MPro and Load-Frame Methods", *Gas Storage Technology Consortium*, *Number DE-FC26-03NT41779 (3139-UT-DOE-1779),* **Quarterly Report #4**.

Lacy, Lewis L. and Rickards, Allan (1996) "Analyzing Cements and Completion Gels Using Dynamic Modulus", *SPE 36476-MS, SPE Annual Technical Conference and Exhibition, 6-9* October, Denver.

Prabhakar P., Rao, David L., Sutton, Jerry D., Childs, Willis C. Cunningham (1982) "An Ultrasonic Device for Nondestructive Testing of Oilwell Cements at Elevated Temperatures and Pressures" *SPE 9283-PA, Journal of Petroleum Engineering*.

Reddy, B.R., Santra, A., McMechan, D. Gray, D., Brenneis, C. and Dunn, R. (2005) "Cement Mechanical Property Measurements Under Wellbore Conditions", *SPE 95921-MS, SPE Annual Technical Conference and Exhibition*.

Thiercelin, M.J., Dargaud, Bernard, Baret, J.F. Dowell, and Rodriquez, W.J. (1997) "Cement Design Based on Cement Mechanical Response", *SPE 38598-MS. SPE Annual Technical Conference and Exhibition*.

Tables

Table 1: Cement Slurry MIX 1 components.

MIX1				Slurry Volume(mls)	600		
Yield (cu ft/sk)	1.054			Slurry (SG)	1.975	District:	Applied Tech
Total Fluid (gps)	4.285			Total Fluid (%)	38.019	Analyst	DTM
Cement Brand		Name	Class	Grams	Mix H20 Ab Vol		Desired Mix H20
Cement Mix H20		Cement	H	857.83	Fresh	0.1199	Ab Vol.
GPS	4.285	POZ			Sea	0.1169	0.1199
%	38.019	Slag/Other					
		NaCl					
		KCl					
		Additive					
		ASA-301		1.29			
		Fresh H20		326.14			

Table 2. Summary of load frame tests on Berea Sandstone.

Specimen	E(kpsi)	UCS(kpsi)	v	Den(g/cc)
Berea4b	2,420	5.960	0.24	2.168
Berea5	2,467	5.646	0.27	2.160
Berea6	2,405	5.965	0.32	2.175
Berea7	2,311	5.430	0.30	2.173
Berea8	2,439	5.179	0.32	2.172
Berea9	2,253	4.751	0.29	2.170
Berea10	2,369	5.289	0.31	2.159
Berea11	2,194	4.638	0.41	2.154
Berea12	2,260	5.523	0.30	2.169
Berea13	2,285	5.442	0.31	2.157

Table 3. Measured and computed data from MPRO and bench-top transducers on MPRO specimens. Specimen lengths, L, for bench-top measurements are also included. Path lengths for all MPRO tests are 2 inches.

Sample	Mix	t_P(µs/in)	t_S(µs/in)	E(Mpsi)	v	UCS(kpsi)	E(Mpsi)	v	UCS(kpsi)	L (in)	t_P(µs/in)	t_S(µs/in)
		MPRO Tests					Load Frame Tests			Bench-top Tests		
Test 1	Prop.	7.32	12.49	2,671	0.24	4,207				1.942	7.31	12.26
Test 2	1	6.90	11.67	3,039	0.23	5,487				1.911	7.01	12.35
Test 3	2	7.76	13.80	2,243	0.27	3,273				1.917	7.36	12.83
Text 4	1	6.89	11.86	2,977	0.24	5,416	1,606	0.17	5,753	1.936	7.33	12.19
Test 6	1	7.03	11.58	3,030	0.21	5,015	1,046		4,858	1.904	7.25	12.50
Test 7	2	7.15	12.17	2,809	0.24	4,670	1,434	0.15	4,023	1.875	7.31	12.59
Test 8	2	7.00	11.64	3,019	0.22	3,019	1,739	0.18	9,965	1.900	7.19	12.55
Test 9	1	7.45	12.45	2,651	0.22	1,810	1,455		6,881	1.900	7.39	12.64

Table 4. Measured and computed data fro MPro tests, and load frame measurements on plugs taken from MPro specimens.

Sample	Mix	t_P(µs/in)	t_S(µs/in)	E(Mpsi)	v	UCS(kpsi)	E(Mpsi)	v	UCS(kpsi)	L (in)
		MPRO Tests					Load Frame Tests			
Mix 1 Test 1	1	7.04	11.65	3,004	0.21	4,987	1,963	0.37	6,369	1.969
Mix 1 Test 2	1	7.16	11.72	2,945	0.20	4,601	1,957		11,363	1.719
Mix 1 Test 3	1	6.92	11.46	3,108	0.21	5,411				
Mix 1 Test 4	1	6.96	11.59	3,052	0.22	5,790				
Mix 2 Test 2	2	8.26	13.25	2,266	0.18	2,486	1,324	0.14	5,682	1.803
Mix 1 Test 6	1	7.07	11.86	2,926	0.22	4,915	1,729	0.11	11,018	1.766
Mix 1 Test 1(Repeat)	1	7.08	11.93	2,905	0.23	4,868	1,406	0.20	12,406	1.982
Mix 1 Test 2(Repeat)	1	7.06	11.66	2,995	0.21	4,881				
Mix 1 Test 5(Repeat)	1	7.00	11.74	2,988	0.22	5,060	1,680	0.29	7,495	1.801

Figures
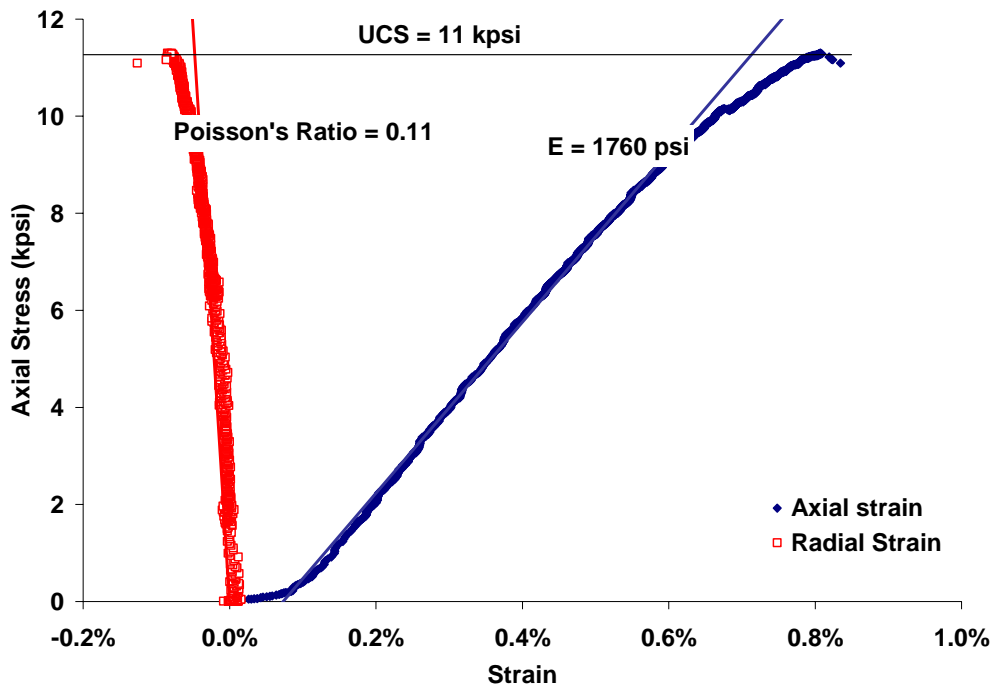
Figure 1. Representative unconfined deformational behavior.
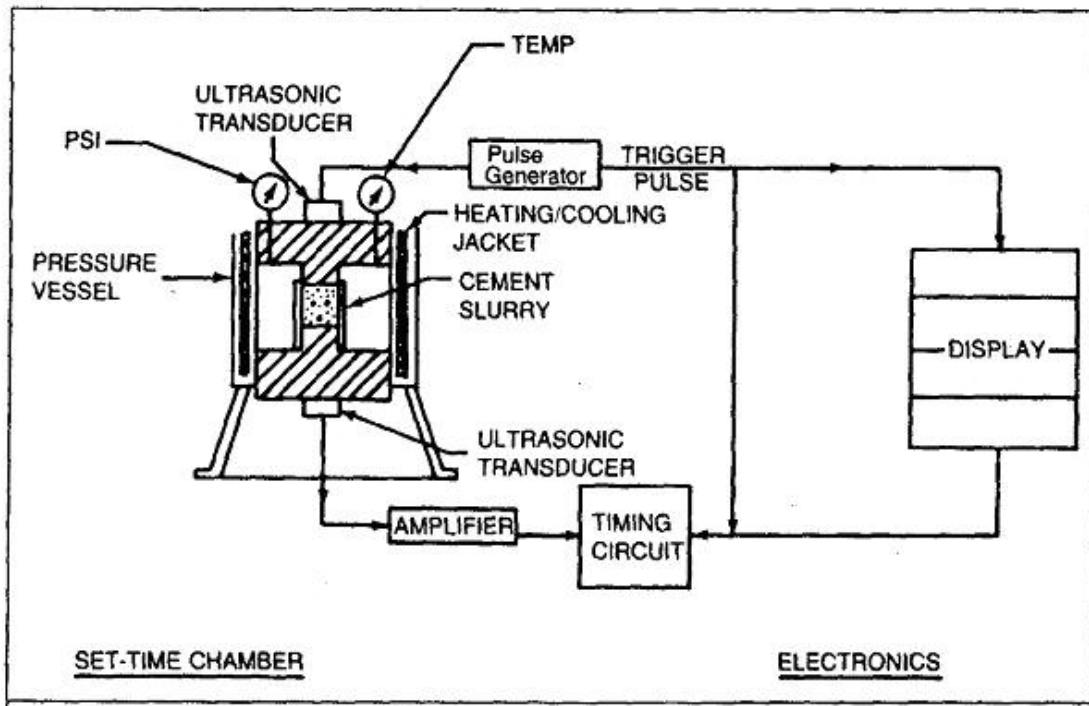
Figure 2. Ultrasonic Cement Analyzer (from Gray and Holder, 2007A).

Top Plug
Assembly

Seals

Vessel (large end
of internal taper is
down)

Bottom Plug
Assembly
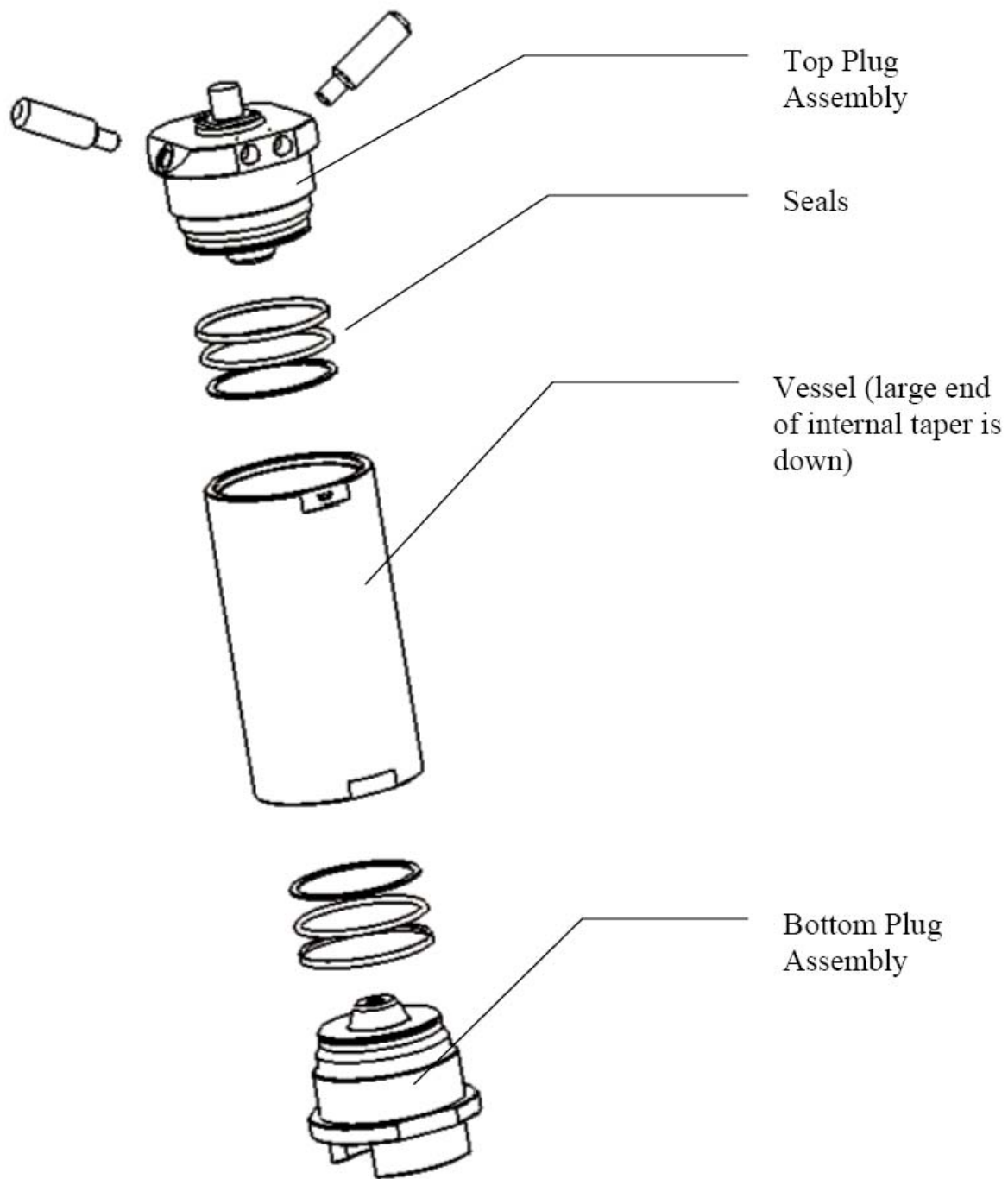
Figure 3. Exploded view of MPRO steel cell (from Gray and Holder, 2007A).
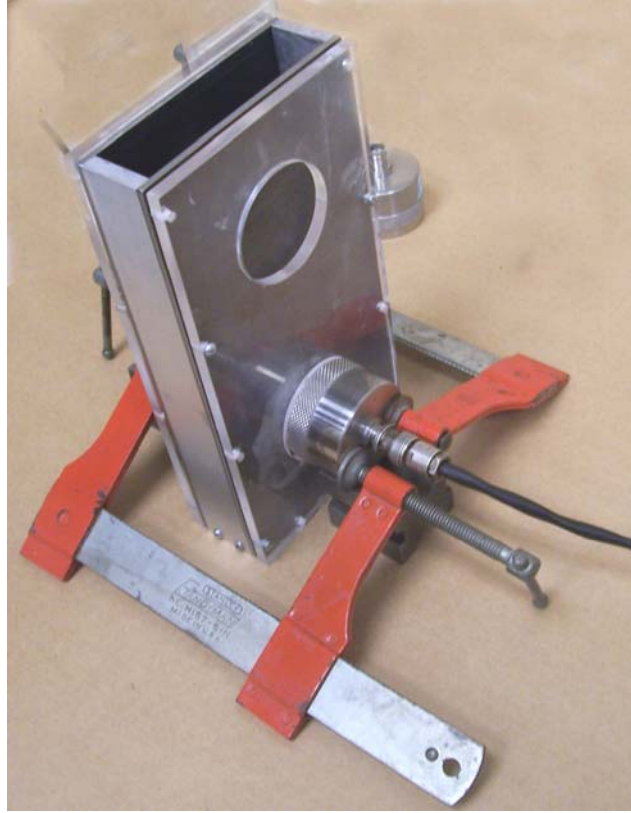
Figure 4. Test assembly for wave propagation measurements using 4 ultrasonic transducers clamped to the 4" x 8" side walls.
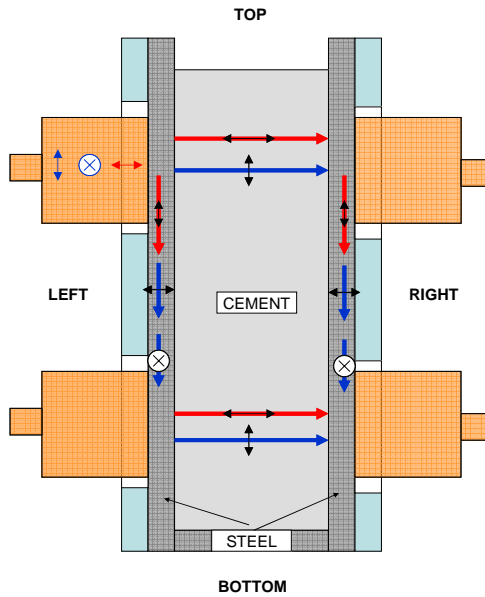
Figure 5. Schematic diagram of travel paths for waves generated by shear and compressional mode transducers.

39
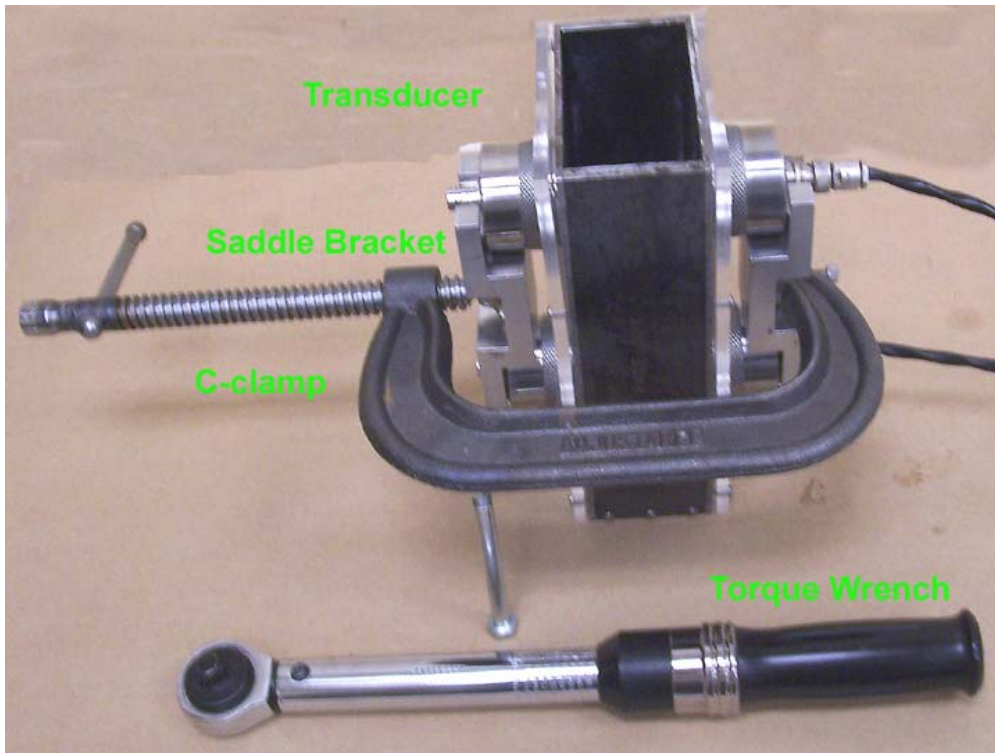
Figure 6. Modified sample assembly, with saddle brackets and torque wrench, designed to reproducibly clamp transducers to test specimens.

Figure 7. Model 6265 Mechanical Properties Analyzer (from Gray and Holder, 2007A).
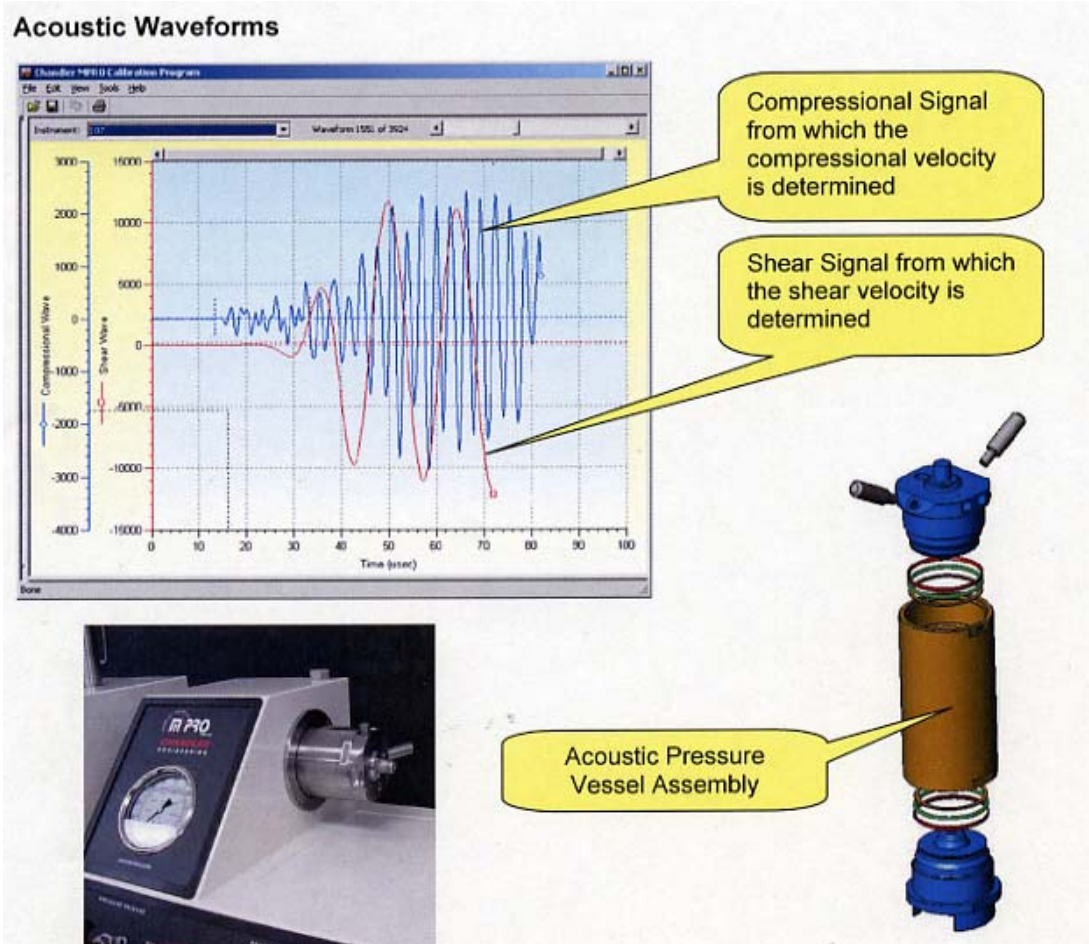
Figure 8. MPro test apparatus and acoustic waveforms.

Figure 9. Photograph of MPro specimens, after curing and removal from test vessel (left), showing indentations from transducers, and after coring 1" diameter plug (right), with machined end surfaces, for load frame tests.

41
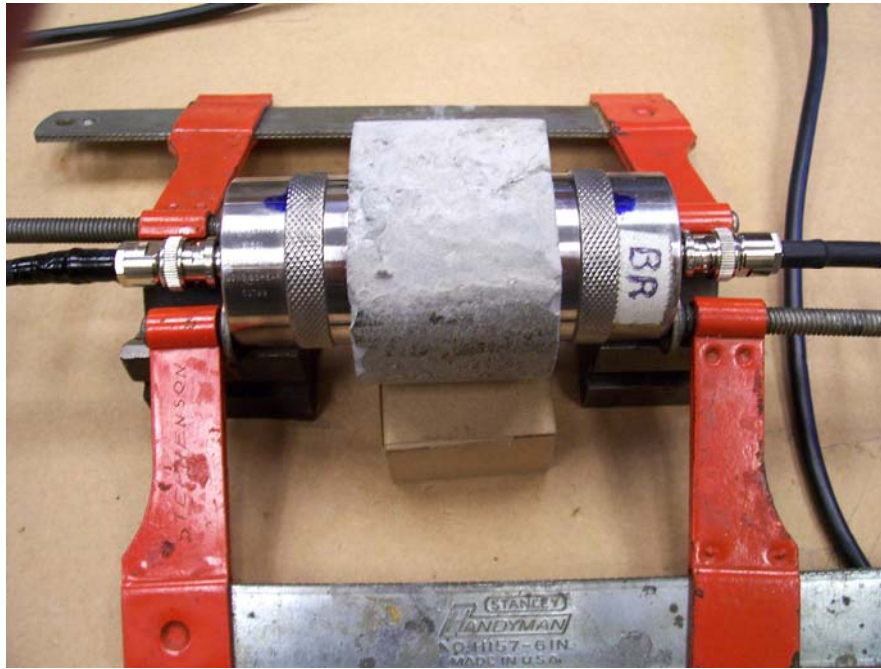
Figure 10. Specimen and ultrasonic transducer configuration for bench-top velocity measurements.
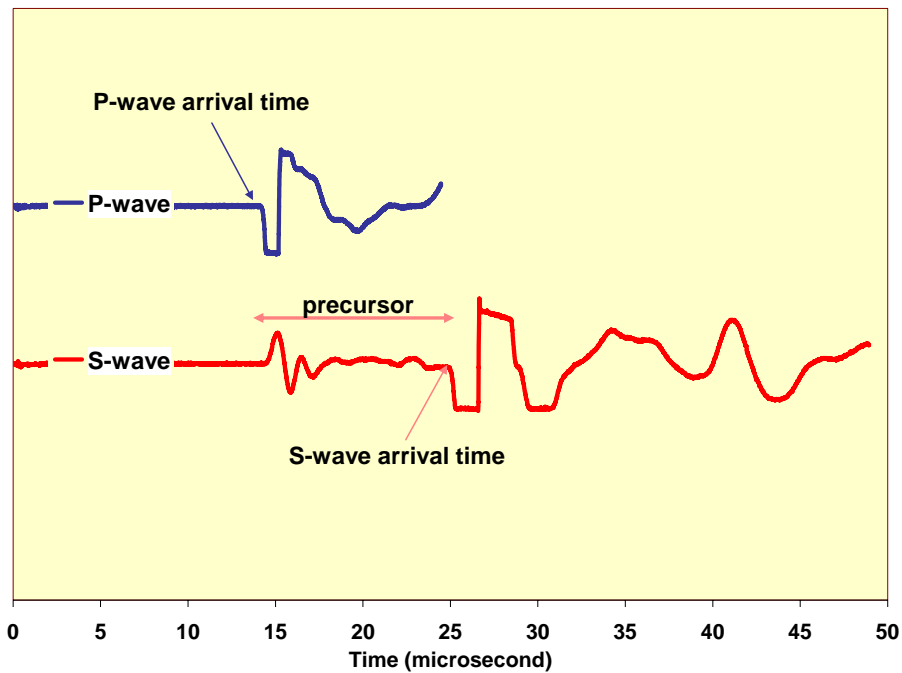
Figure 11. Example wave forms for bench-top measurements with Panametrics ultrasonic transducers.

Figure 12. Load frame (center), with ancillary electronics and meters for static deformation tests.
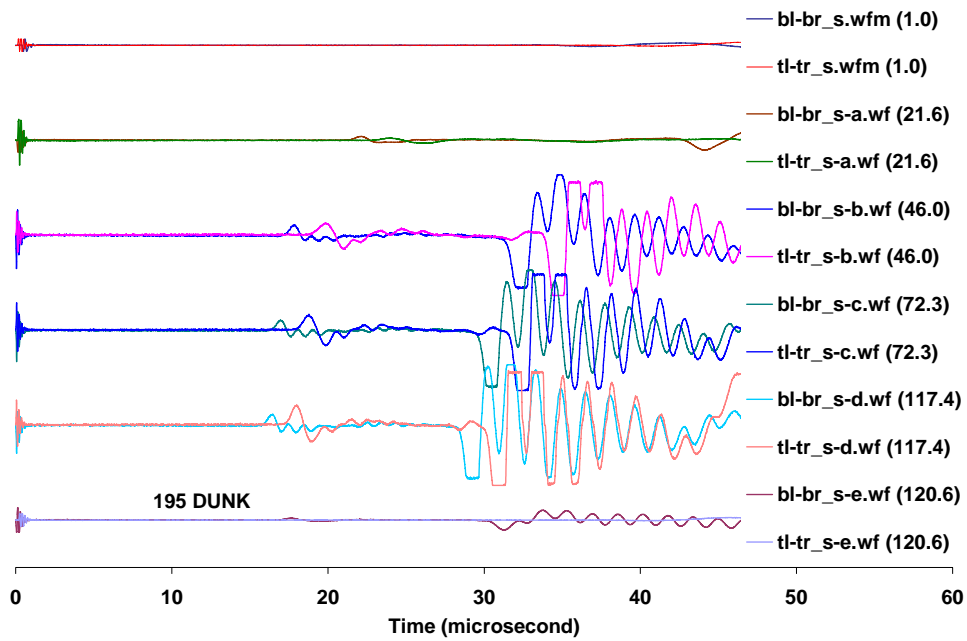
Figure 13. Shear wave forms traveling horizontally through cement #1 after curing for indicated times, and after immersion in water at 195F. Early arrival signals are p-wave precursors.

43
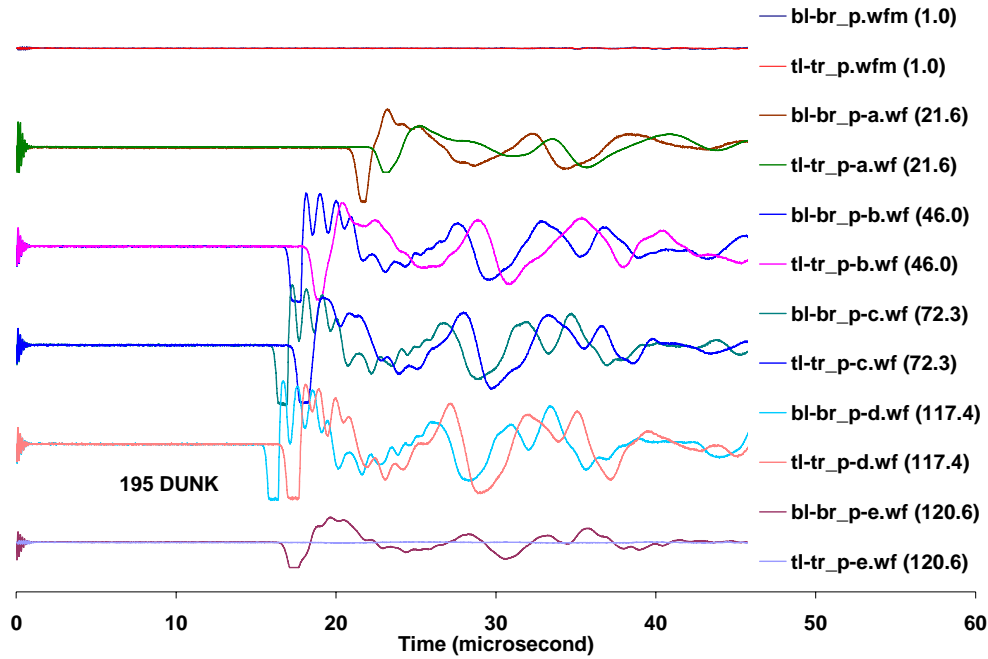
Figure 14. P-waves traveling horizontally through cement Specimen #1, for different curing times, and after immersion in a water bath at 195F.
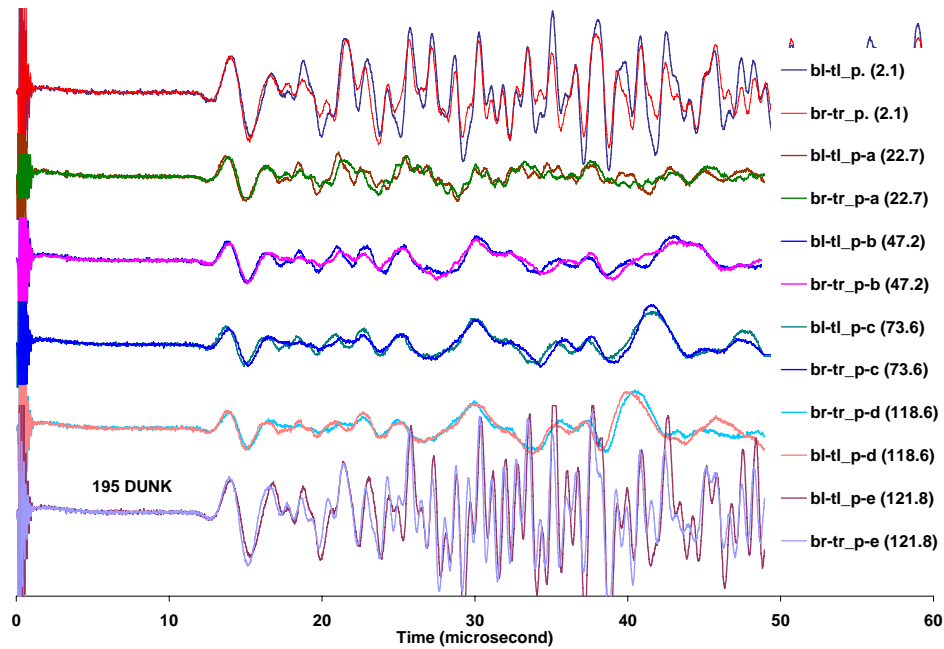
Figure 15. Waveforms generated and detected by p-wave transducers, traveling vertically through test chamber containing Specimen #1, at indicated curing times and after immersion in water bath at 195F.

44
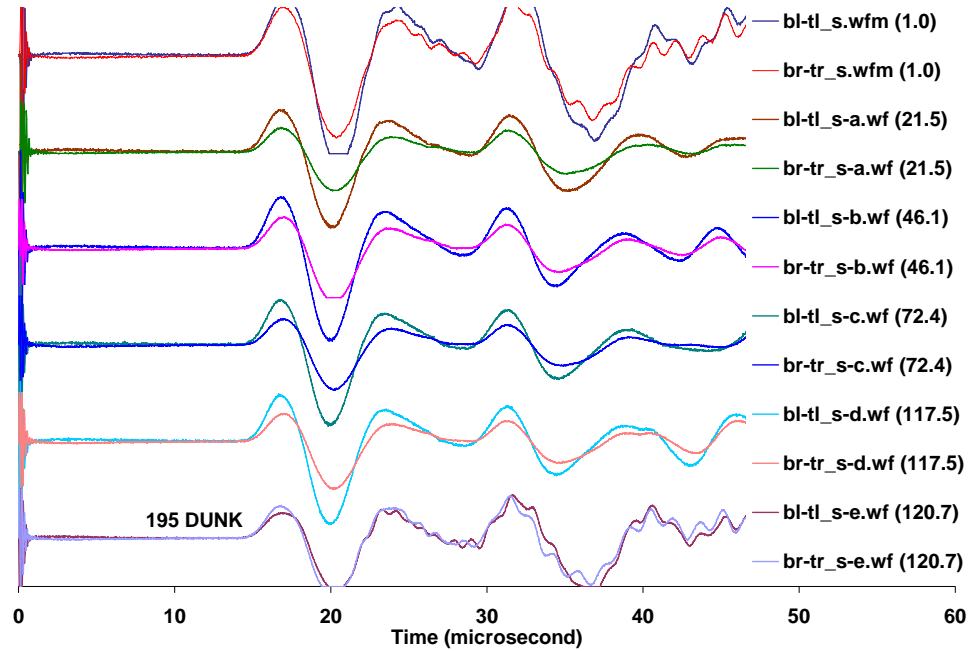
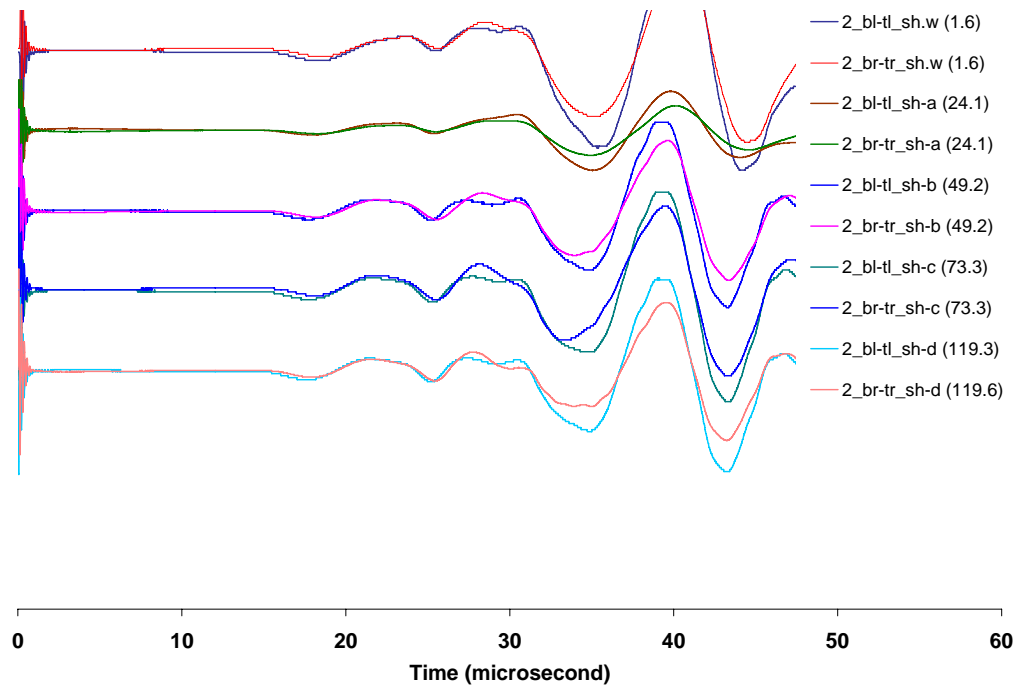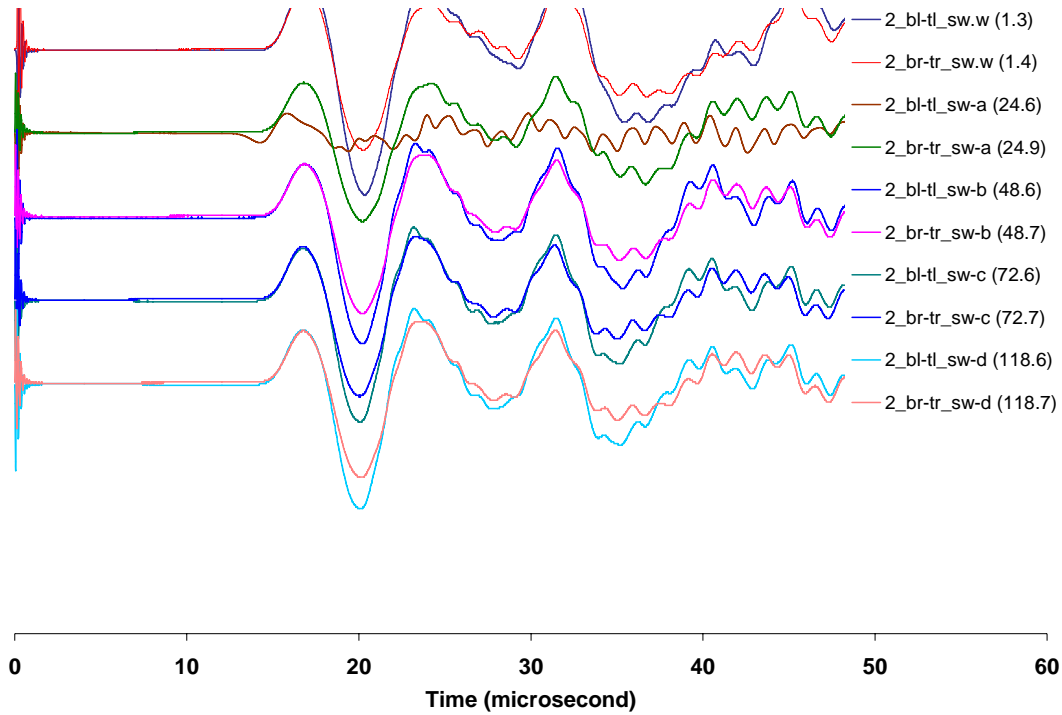*Figure 16. Waveforms generated and detected by s-wave transducers, traveling vertically through test chamber containing Specimen #1, at indicated curing times and after immersion in water bath at 195F*

.
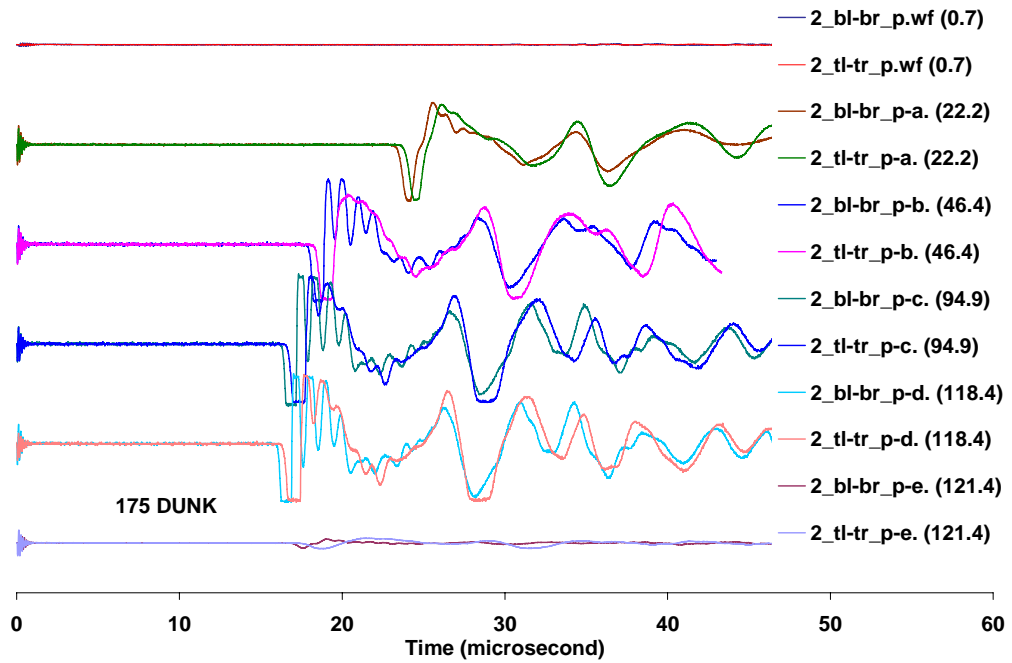
Figure 17. P-waves traveling horizontally through test chamber containing Specimen #2, for different curing times and after immersion in a water bath at 175F.
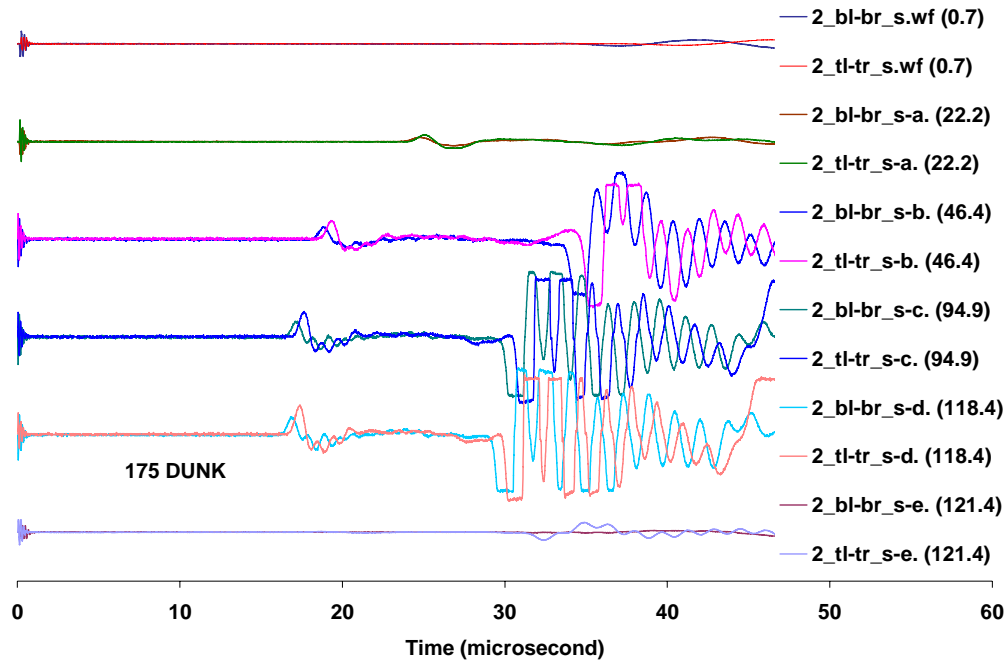
Figure 18. S-waves traveling horizontally through test chamber containing Specimen #2, for different curing times and after immersion in a water bath at 175F.
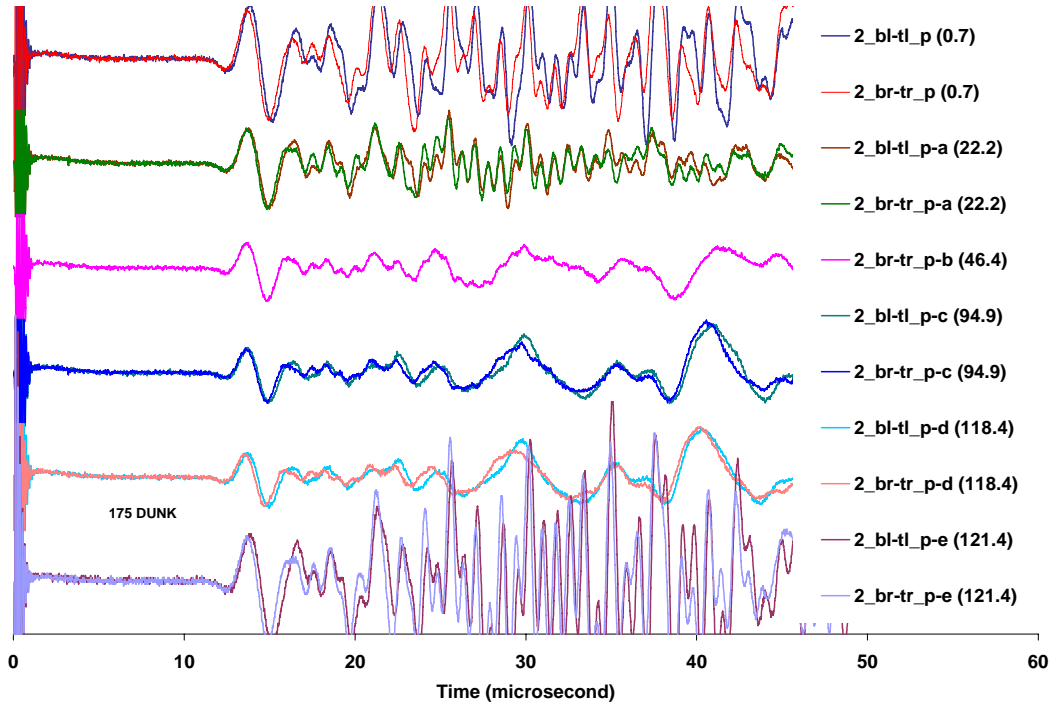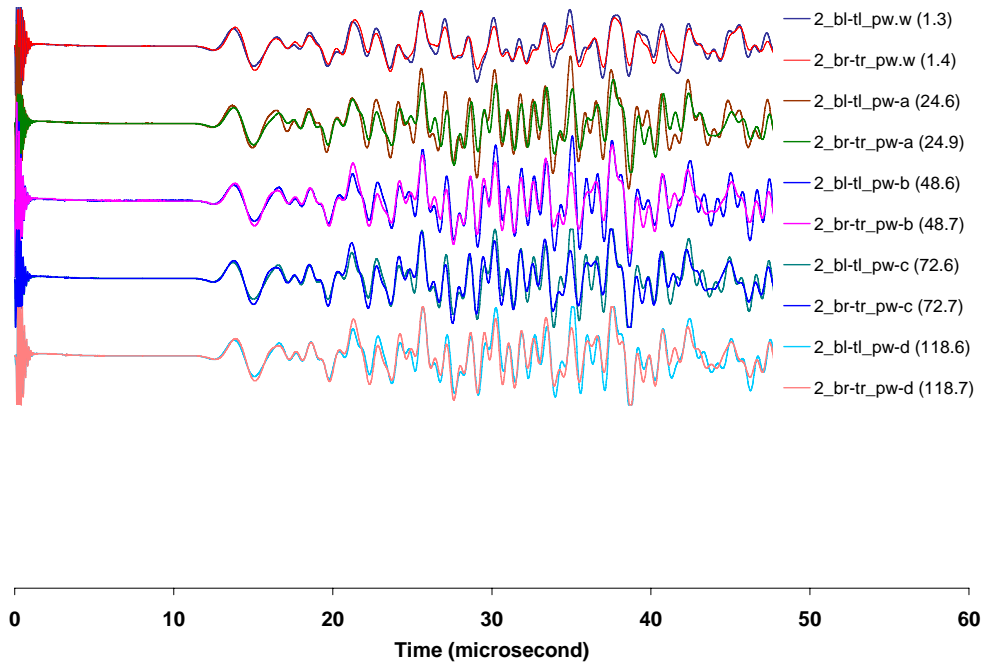

Figure 19. Waveforms generated and detected by p-wave transducers, traveling vertically through test chamber containing Specimen #2, at indicated curing times and

46

after immersion in water bath at 175F.
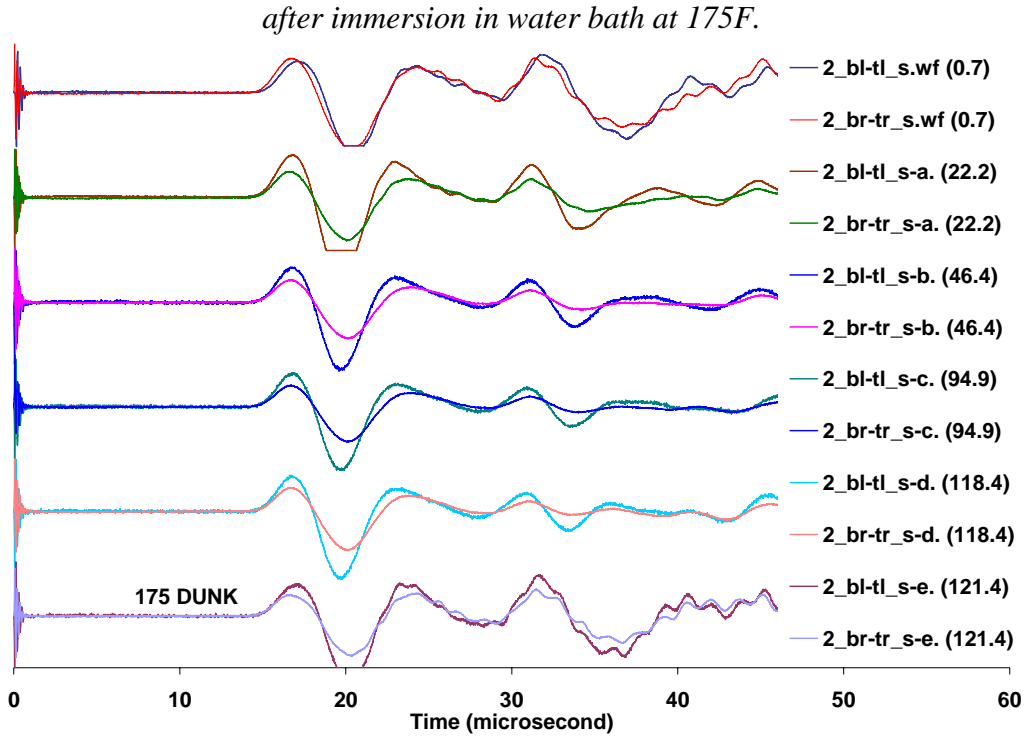
Figure 20. Waveforms generated and detected by shear wave transducers, traveling vertically through test chamber containing Specimen #2, at indicated curing times and after immersion in water bath at 175F
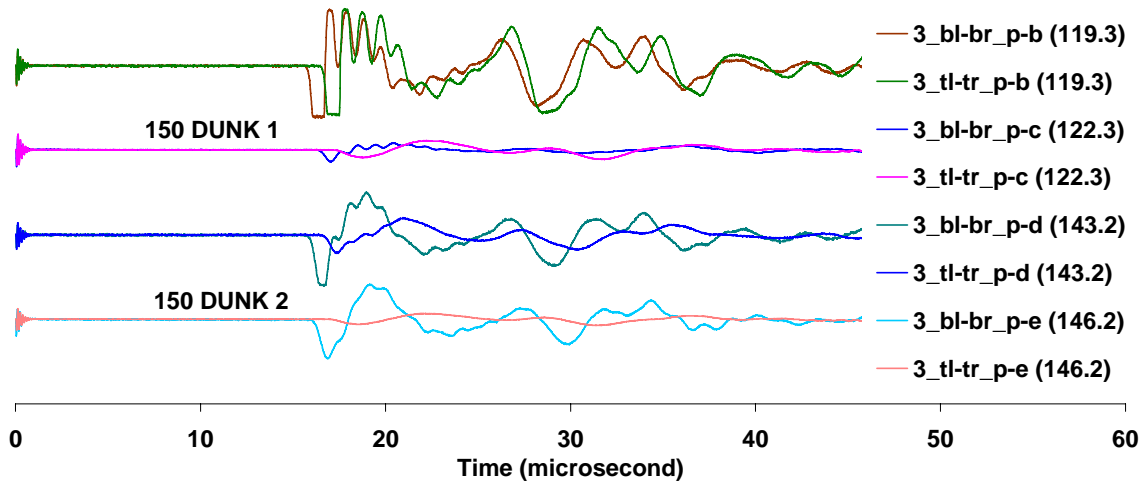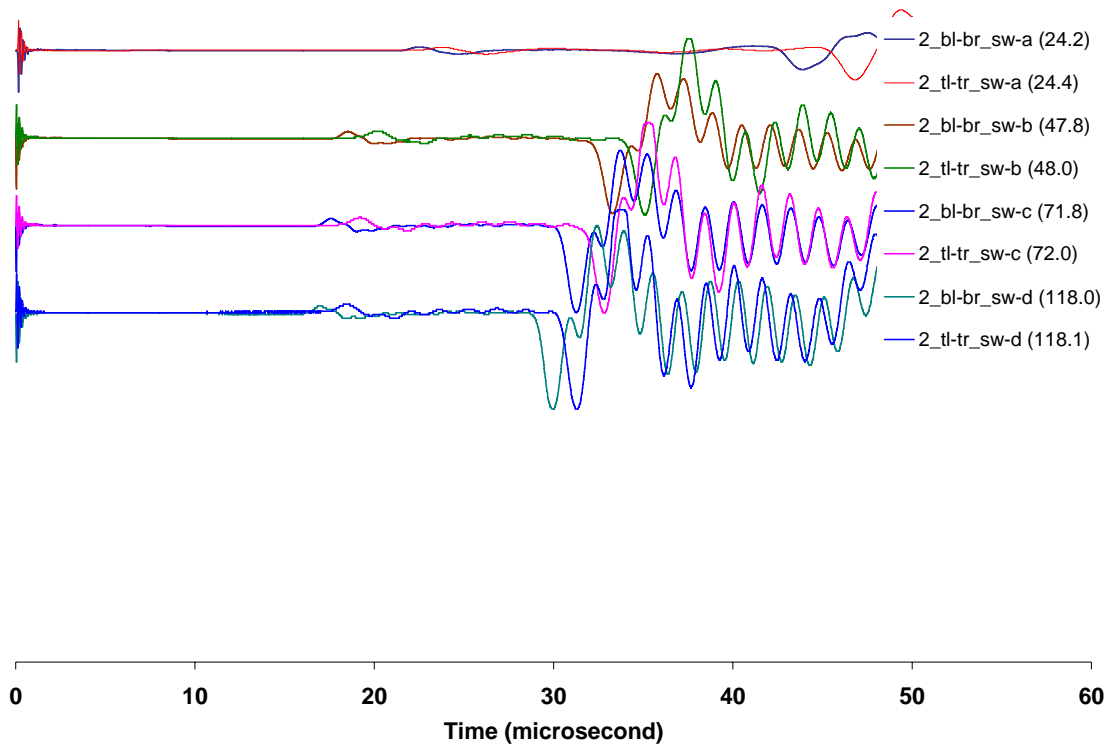

Figure 21. P-waves traveling horizontally through cement Specimen #3 after curing times of 5 and 6 days, with two temperature cycles to 150F.

47
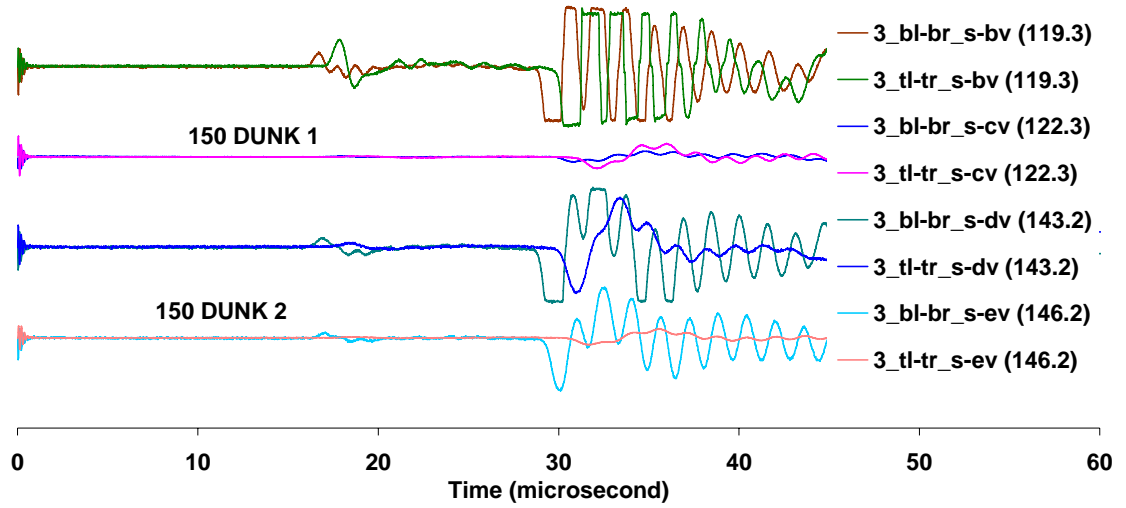
Figure 22. Vertically-polarized shear-waves traveling horizontally through cement Specimen #3 after curing times of 5 and 6 days, with two temperature cycles to 150F.
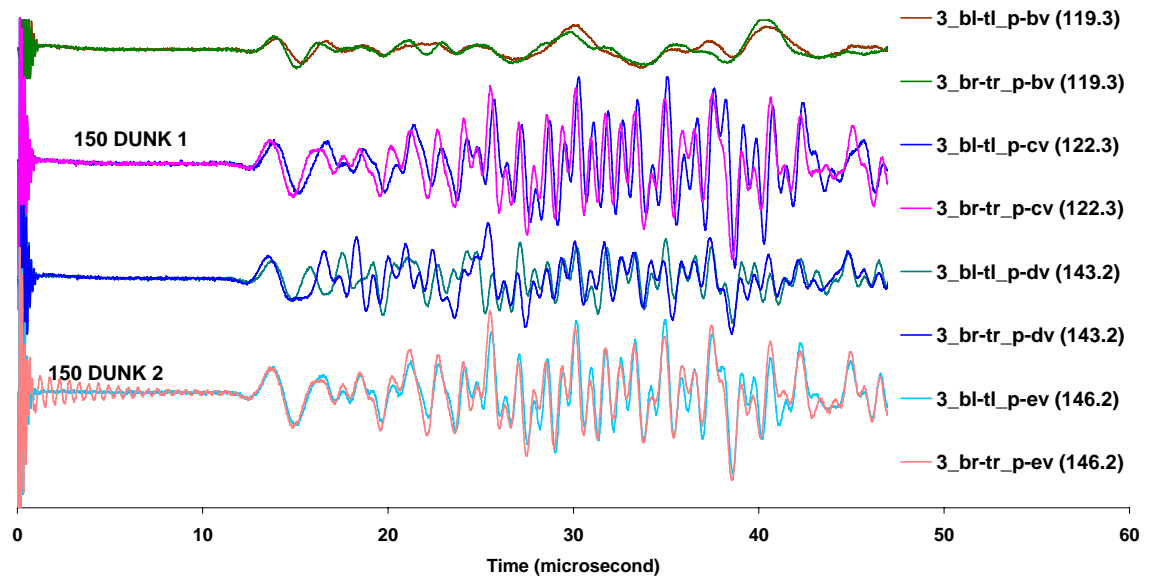
Figure 23. Waveforms generated and detected by p-wave transducers, traveling vertically through test chamber containing Specimen #3, after curing times of 5 and 6 days, and two temperature cycles to 150F
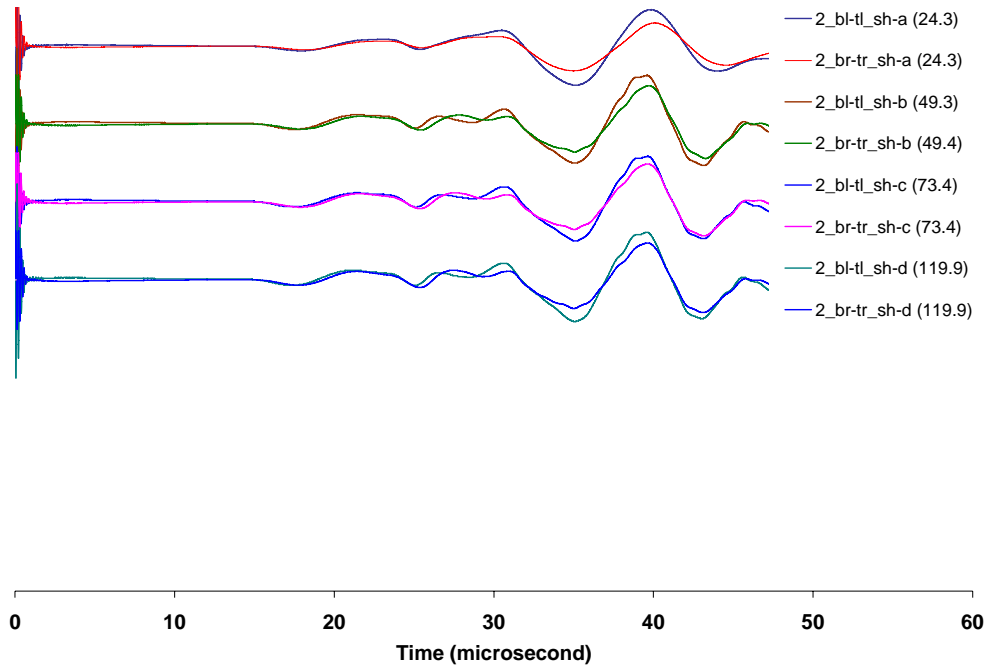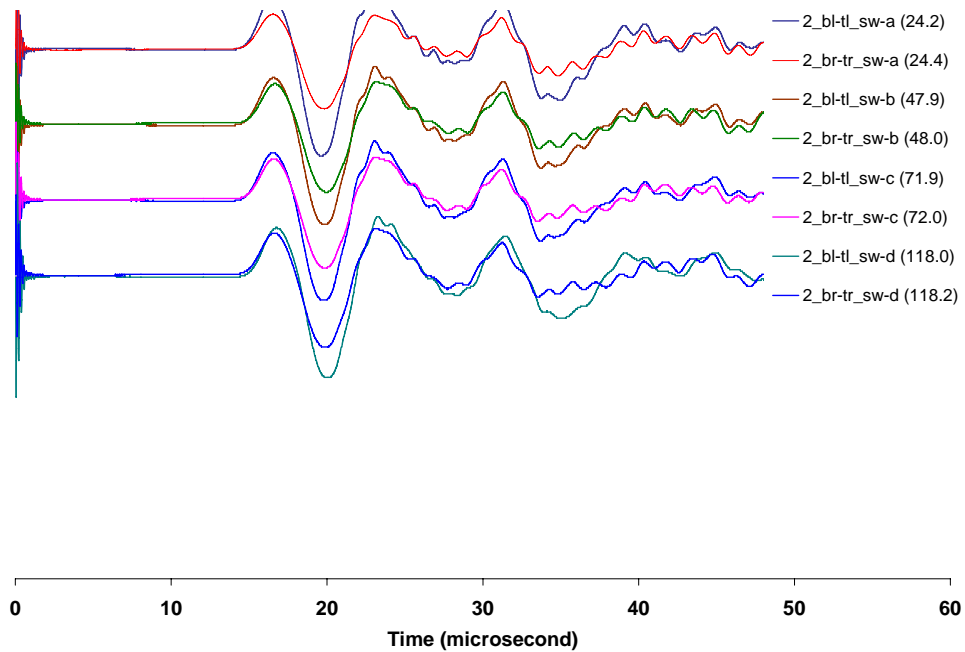
48
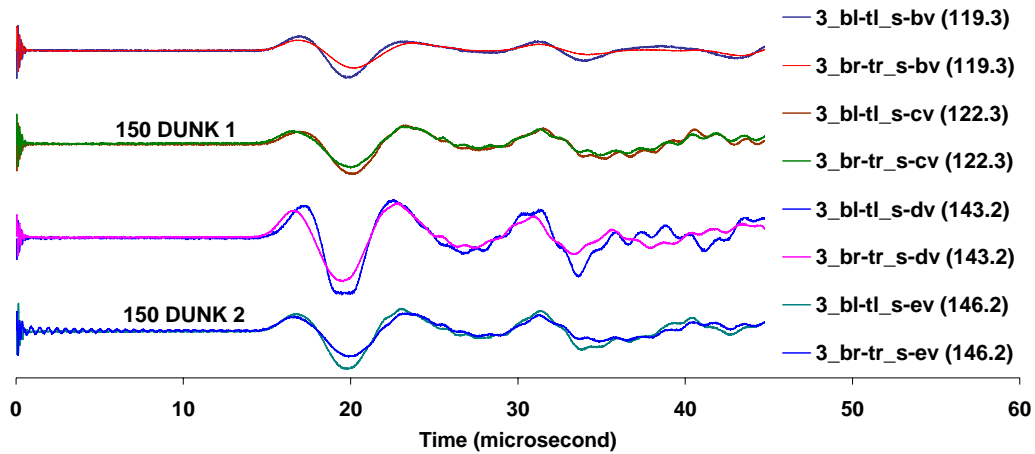
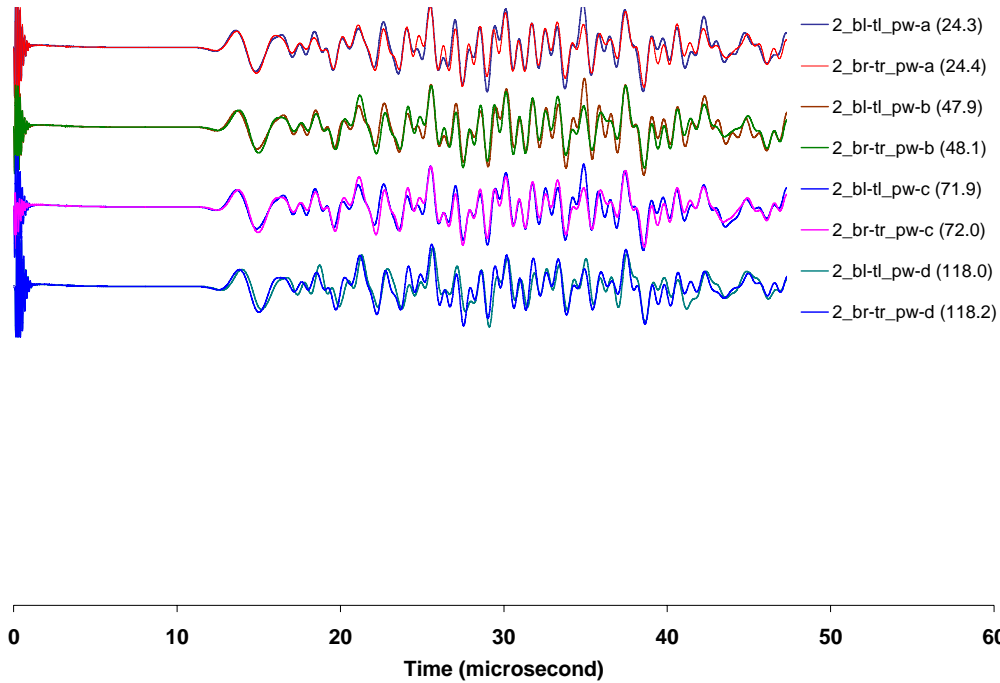*Figure 24. S$_V$ wave forms, generated and detected by vertically-polarized s-wave transducers, traveling vertically through test chamber containing Specimen #3, after curing times of 5 and 6 days, and two temperature cycles to 150F.*
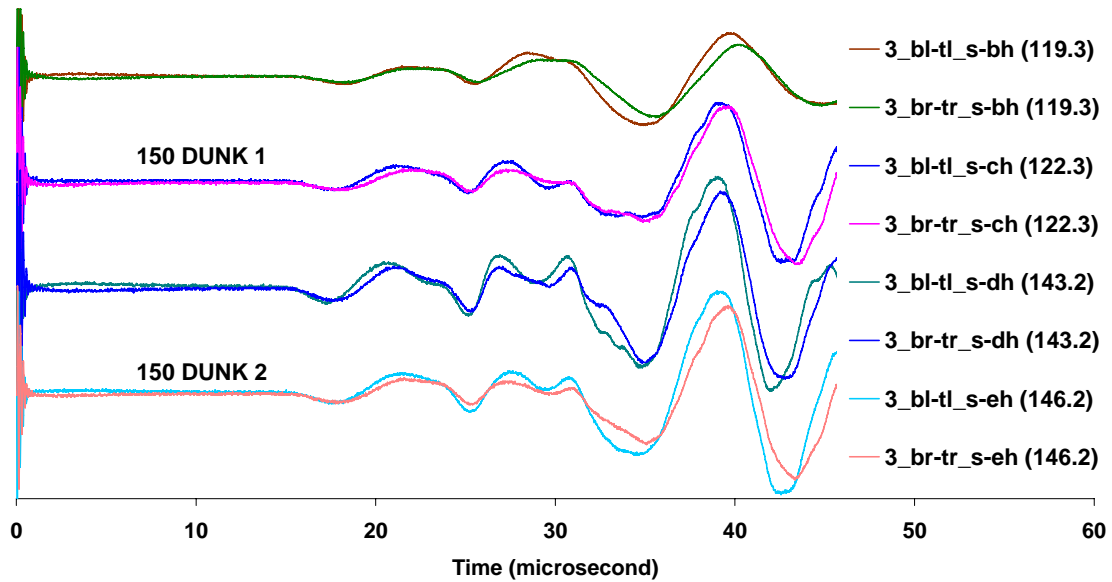
Figure 25. S$_H$-waves traveling vertically in the test chamber for Specimen #3, curing 5 and 6 days, two temperature cycles to 150F. Waves are polarized such that particle displacements are horizontal (see text).
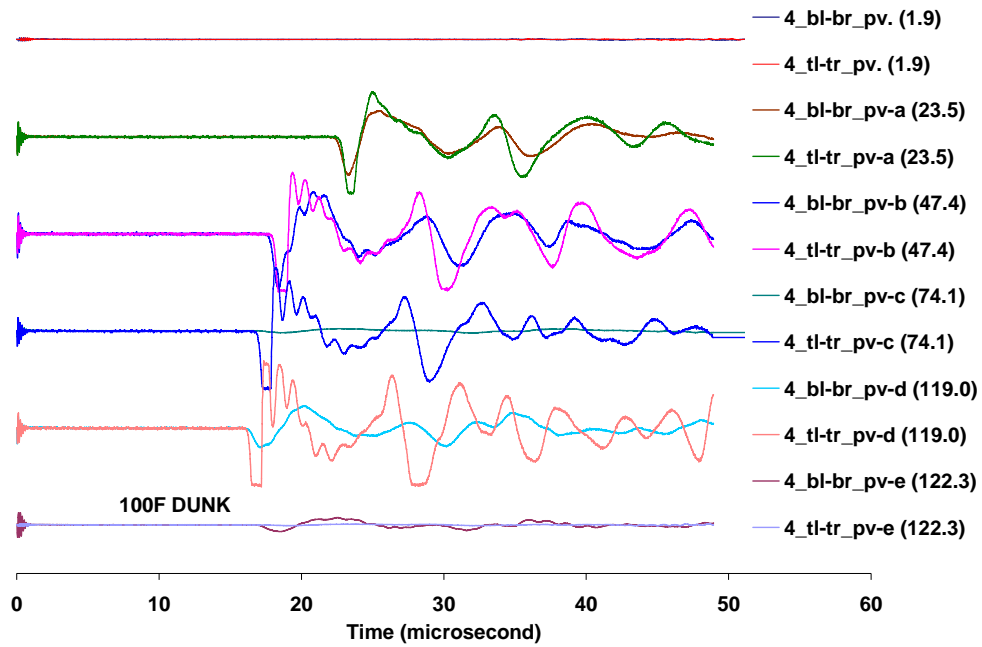
Figure 26. P-waves traveling horizontally through test chamber containing Specimen #4, for indicated curing times and after immersion in a water bath at 100F.
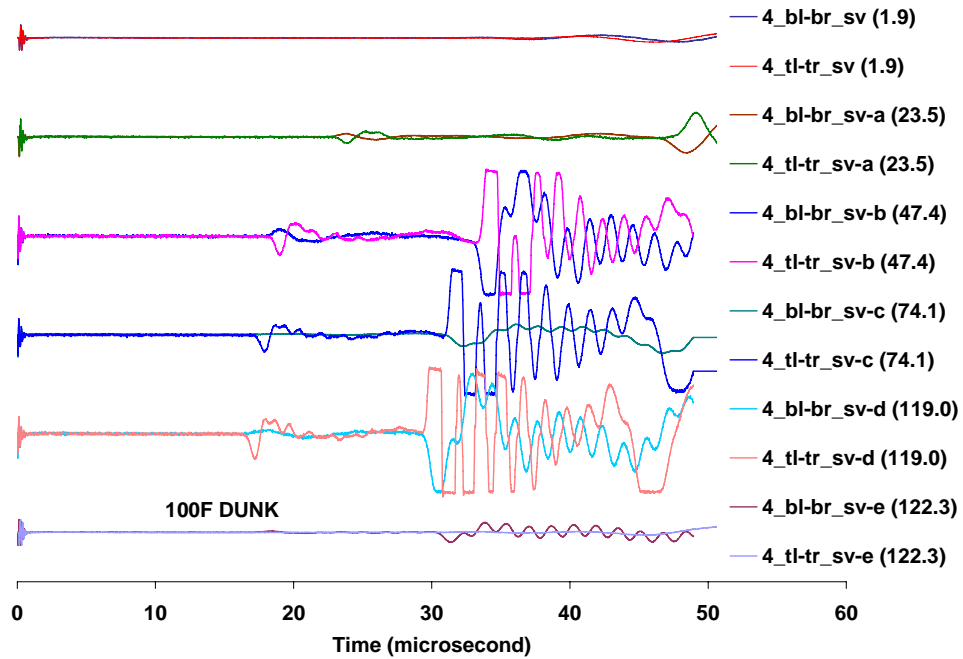
Figure 27. S-waves traveling horizontally through test chamber containing Specimen #4, for indicated curing times and after immersion in a water bath at 100F.

50
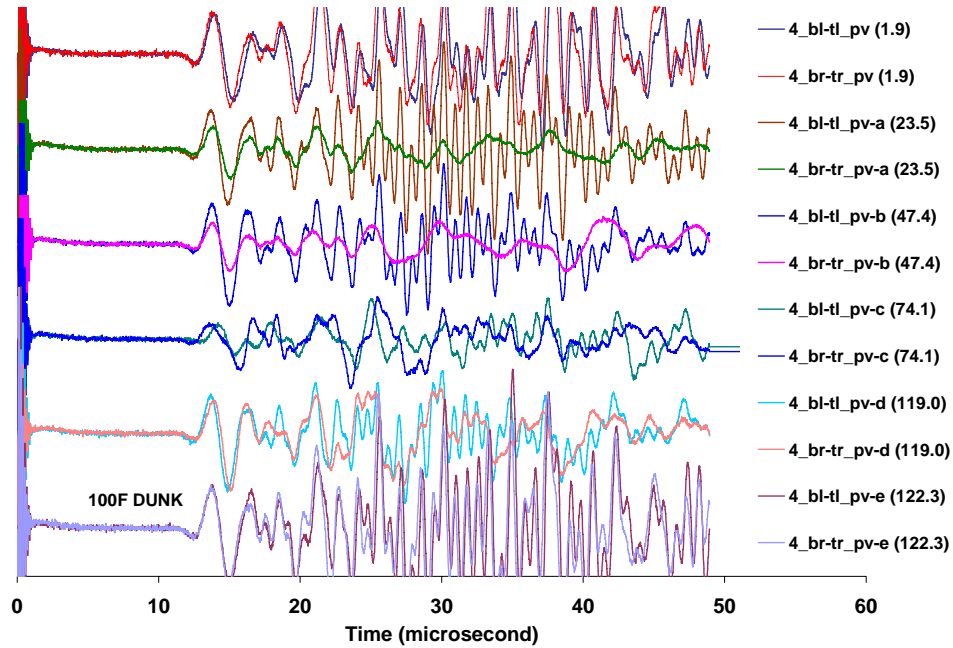
*Figure 28.   Waveforms generated and detected by p-wave transducers, traveling vertically through test chamber containing Specimen #4, at indicated curing times and after immersion in a water bath at 100F.*
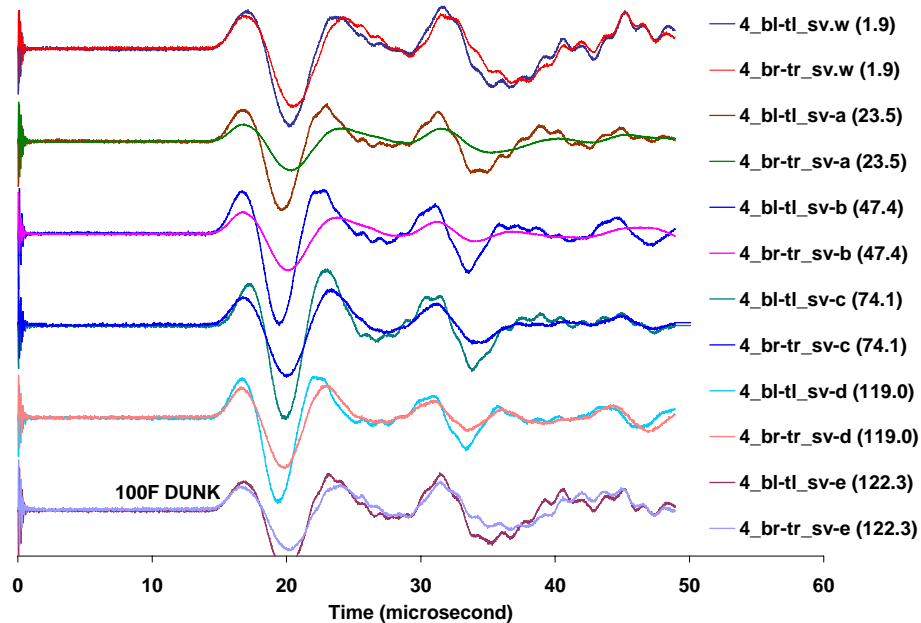
Figure 29. S_V waveforms generated and detected by vertically polarized s-wave transducers, traveling vertically through test chamber containing Specimen #4, at indicated curing times and after immersion in water bath at 100F
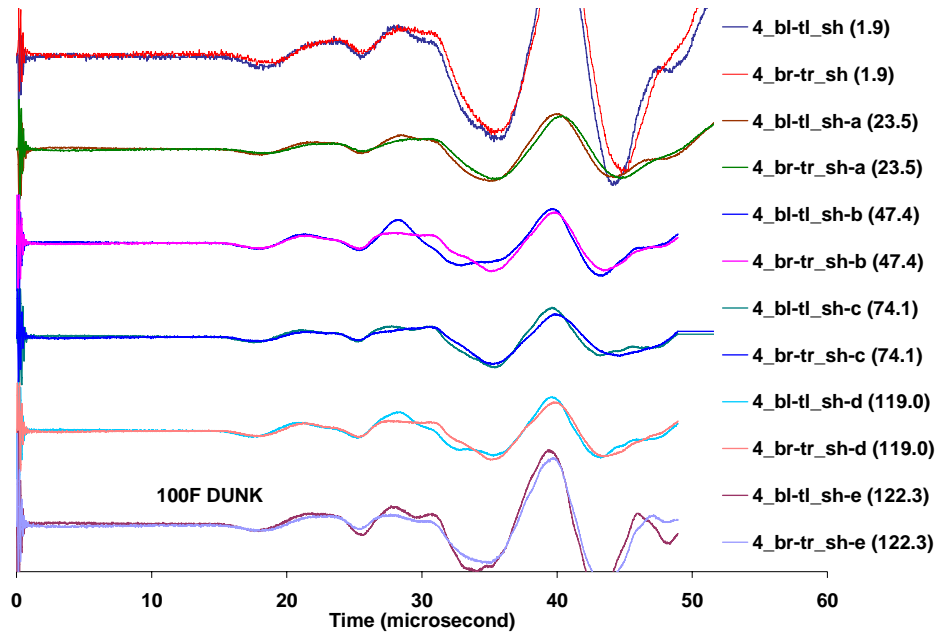
Figure 30. S_H wave forms, generated and detected by horizontally-polarized s-wave transducers, traveling vertically through test chamber containing Specimen #4, after indicated curing times and a temperature cycle to 100F.
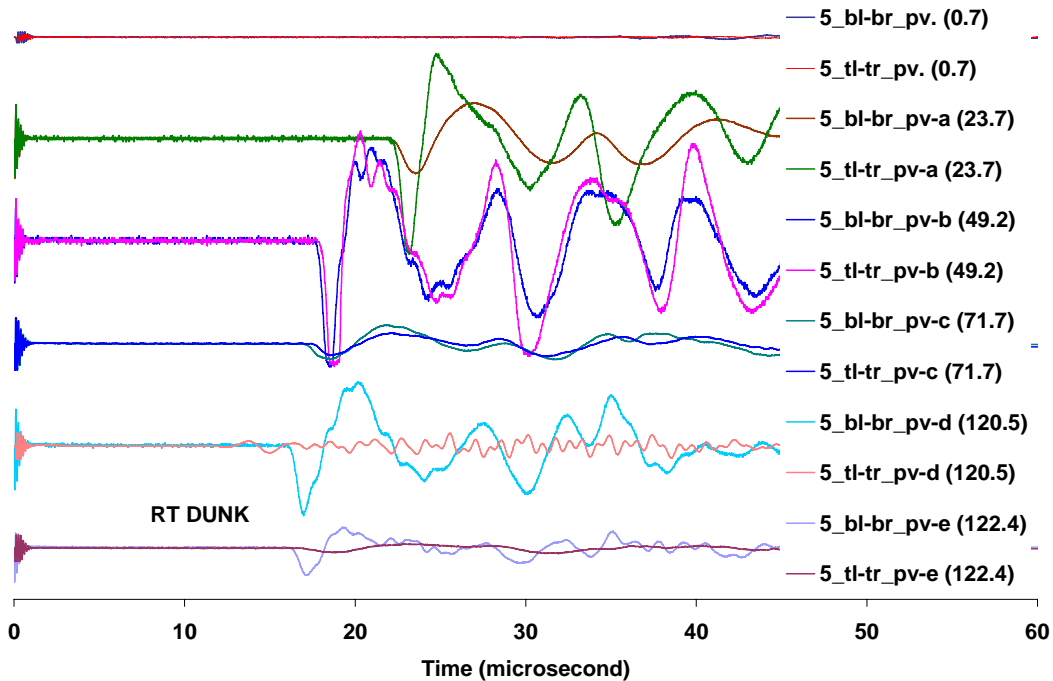
Figure 31. P-waves traveling horizontally through test Specimen #5, for indicated curing times and after immersion in a water bath at room temperature. Differences in amplitudes of waves after annealing for 24 hours and 72 hours are probably due to poor bonding of the transducers.
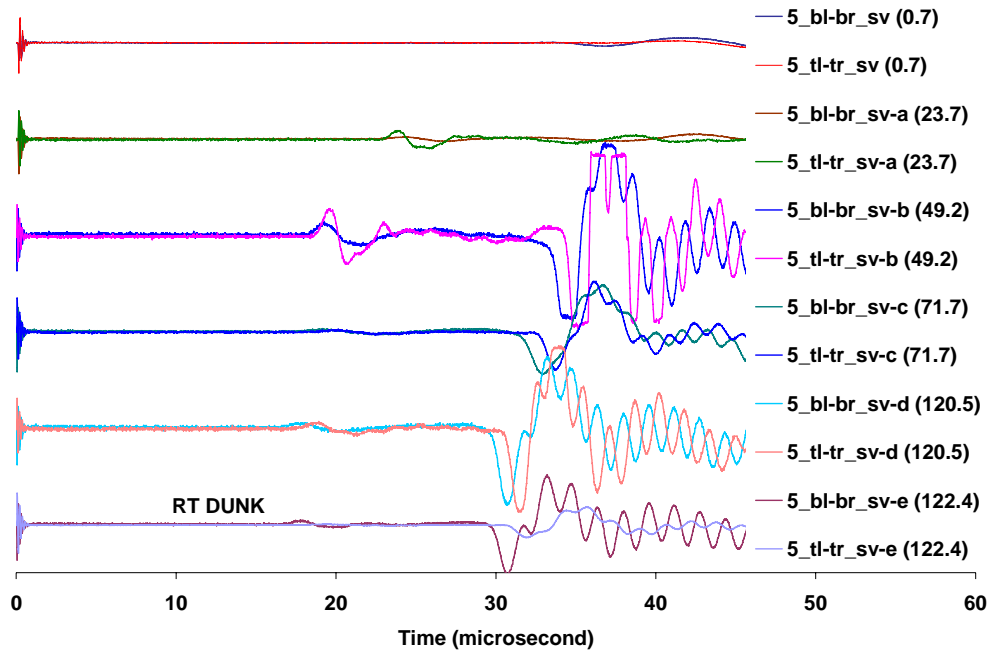
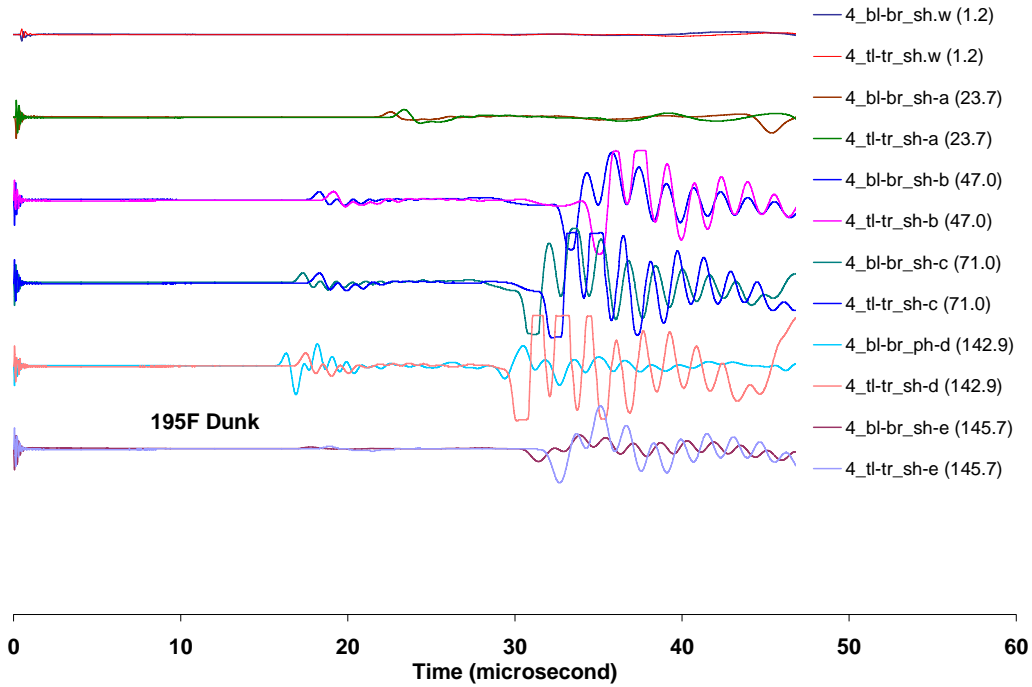*Figure 32. S-waves traveling horizontally through test Specimen #5, for indicated curing times and after immersion in a water bath at room temperature.*
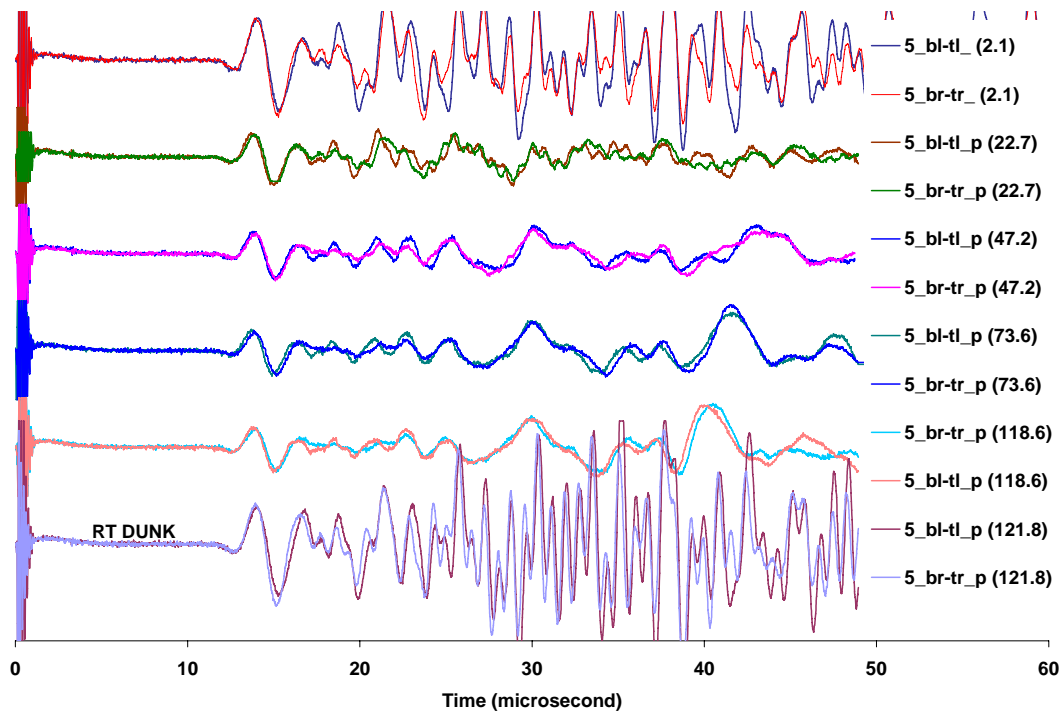
Figure 33. Waveforms generated and detected by p-wave transducers, traveling vertically through test chamber containing Specimen #5, at indicated curing times and after immersion in a water bath at room temperature.
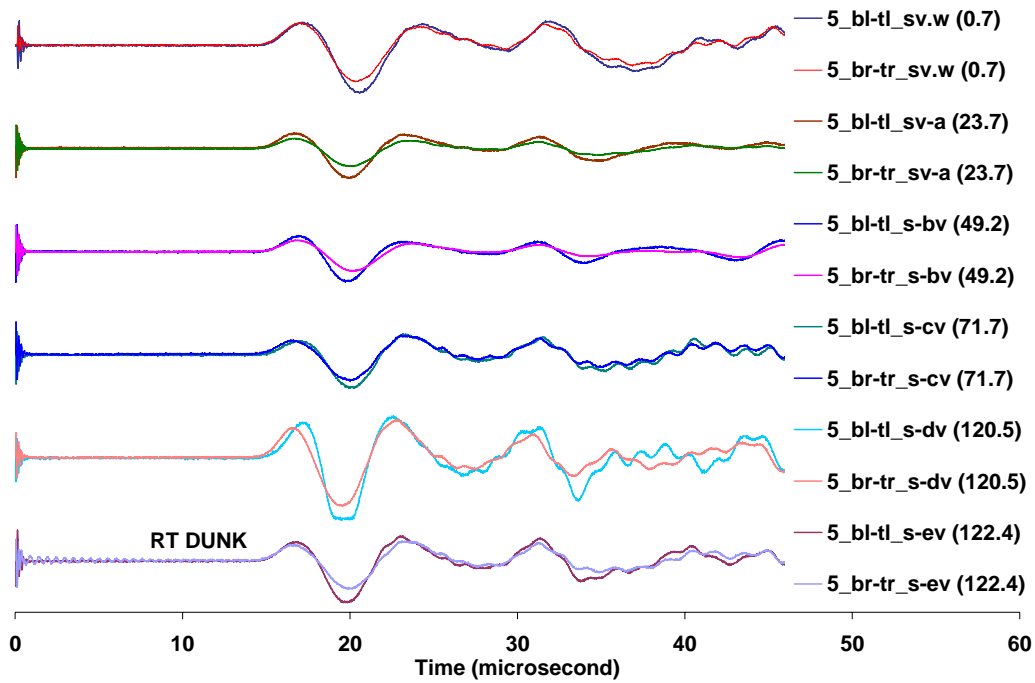
Figure 34. SV waveforms generated and detected by vertically polarized s-wave transducers, traveling vertically through test chamber containing Specimen #5, at indicated curing times and after immersion in water bath at room temperature.
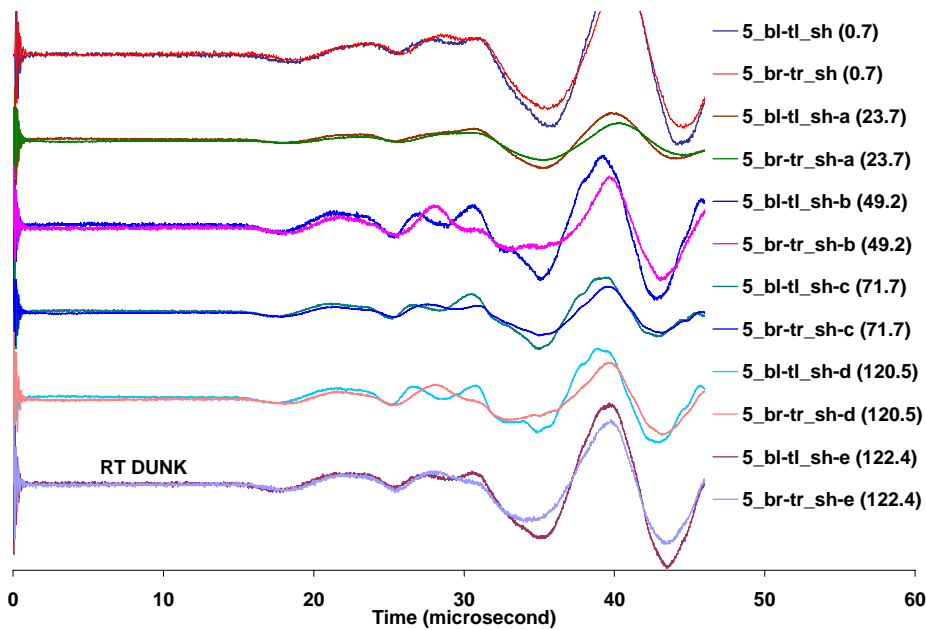
Figure 35. SH wave forms, generated and detected by horizontally-polarized s-wave transducers, traveling vertically through test chamber containing Specimen #5, after indicated curing times and after immersion in a bath of water at room temperature.
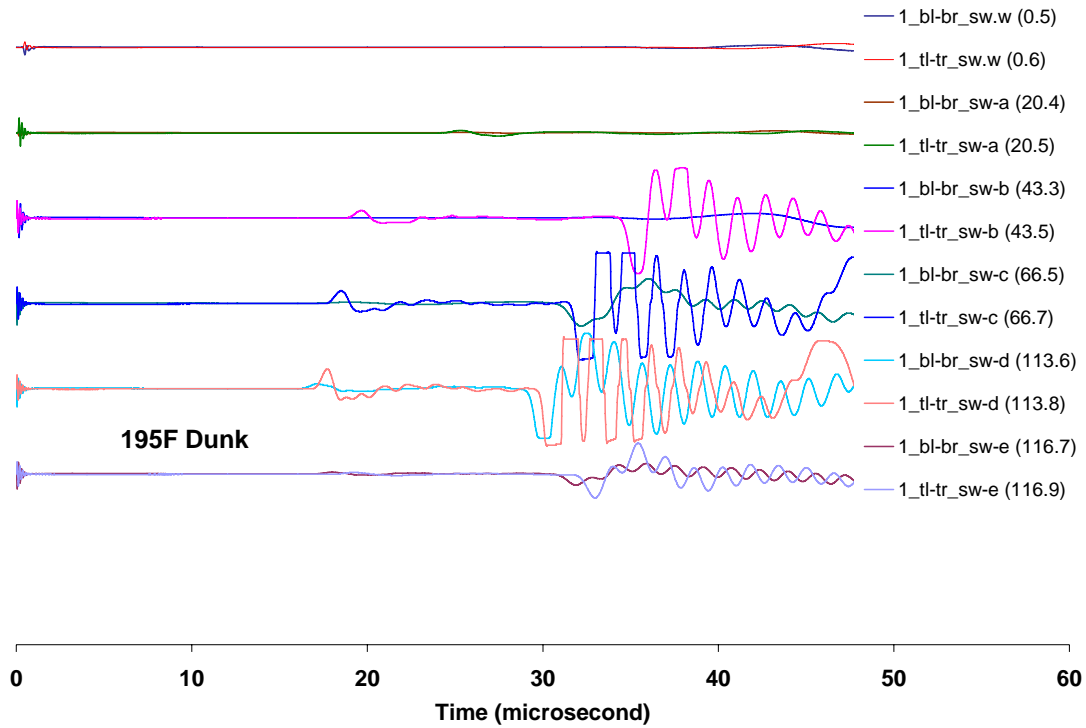
Figure 36. Compressional wave forms traveling horizontally through cement #III-1 after curing for indicated times, and after bagging and immersion in water at 195F. Some water leakage into the bag was observed.
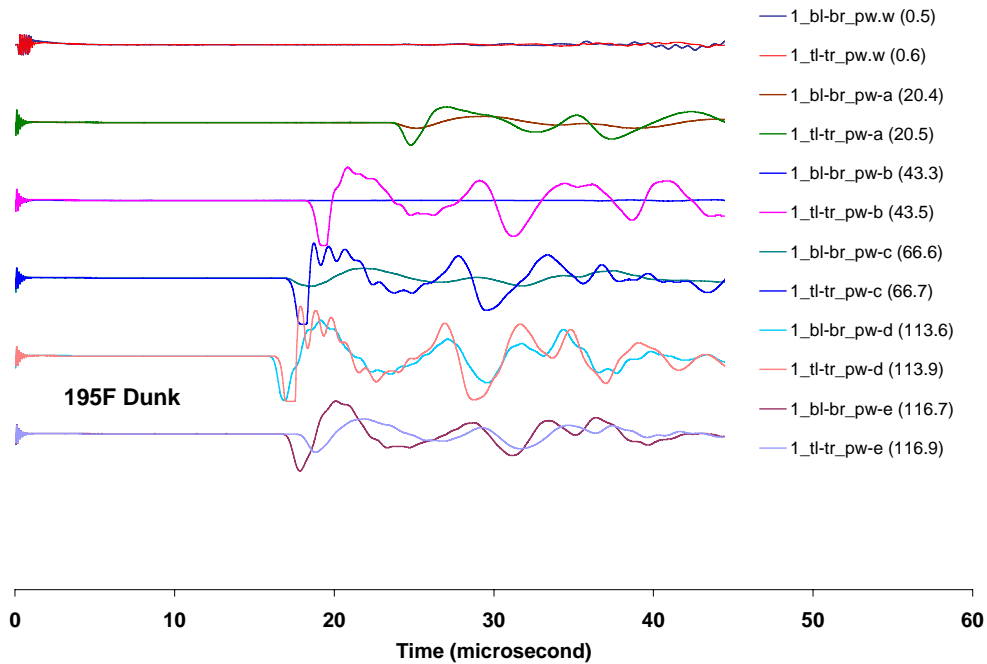
Figure 37. Shear waves traveling horizontally through cement Specimen #III-1, after indicated curing times and after bagging and immersion in water at 195F. Some water leakage was observed.
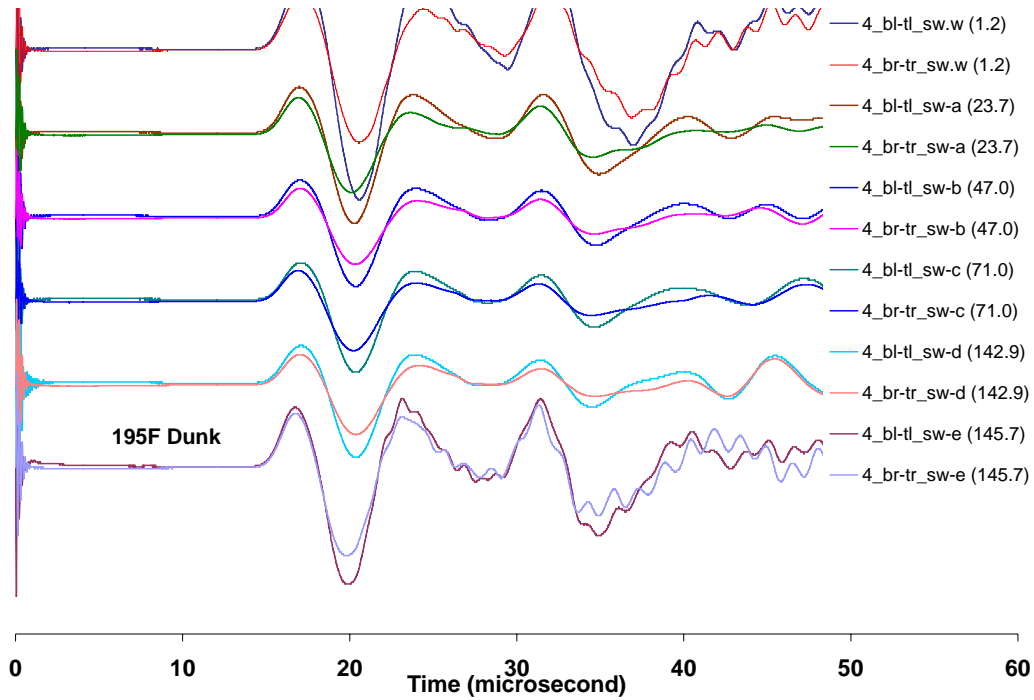
55
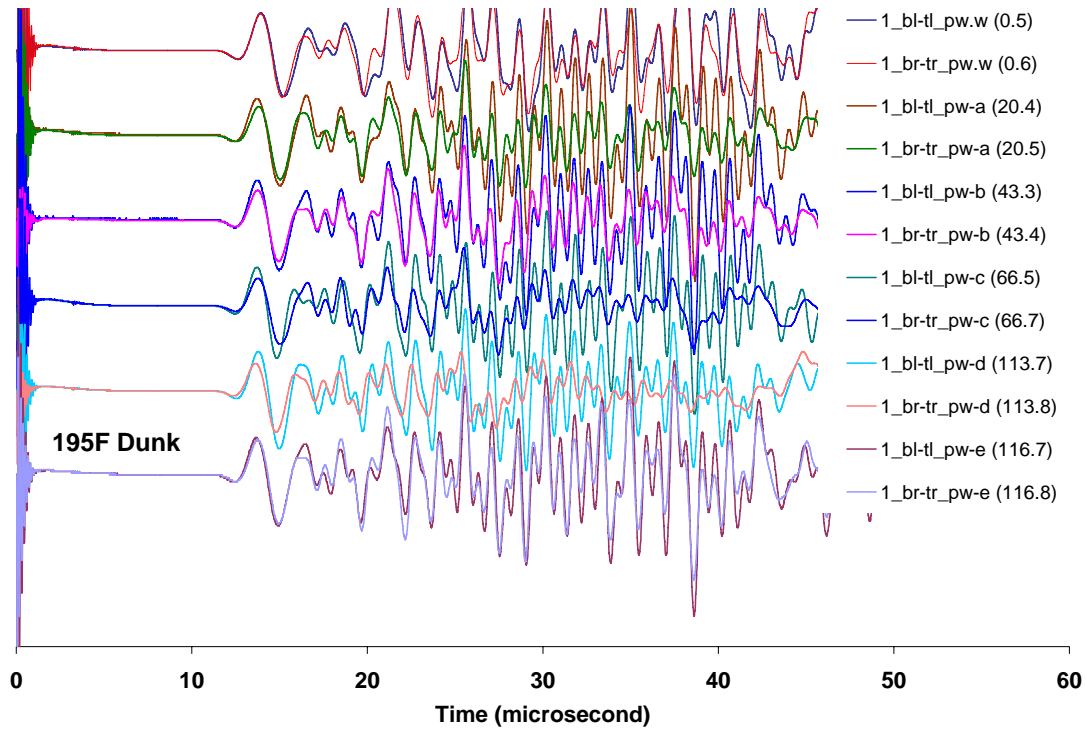
Figure 38. Waveforms generated and detected by p-wave transducers, traveling vertically through test assembly containing Specimen #III-1, after indicated curing times and after bagging and immersion in water at 195F. Some water leakage was observed.
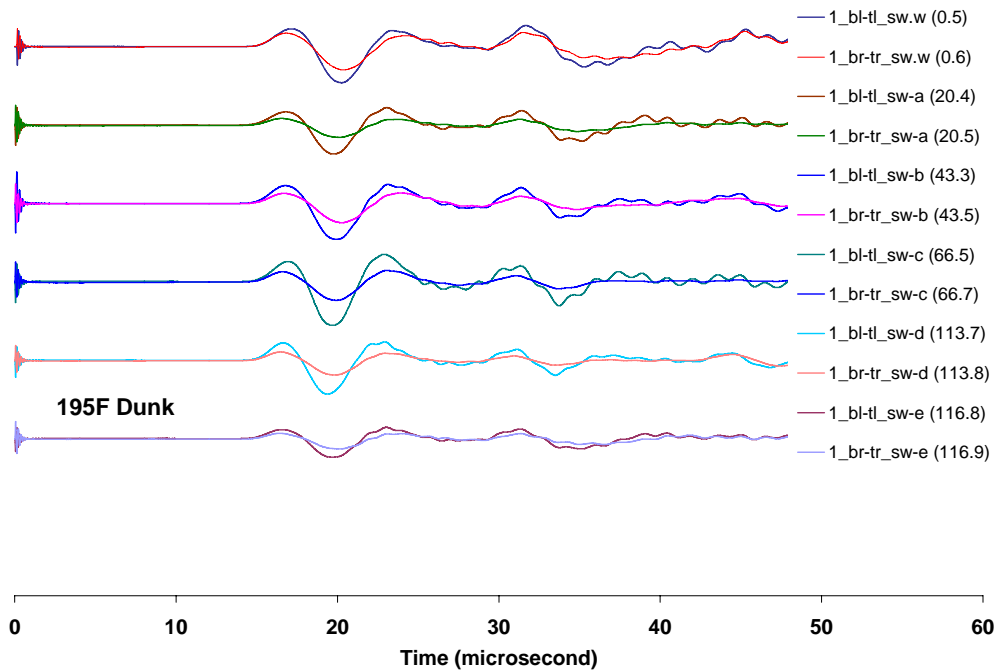
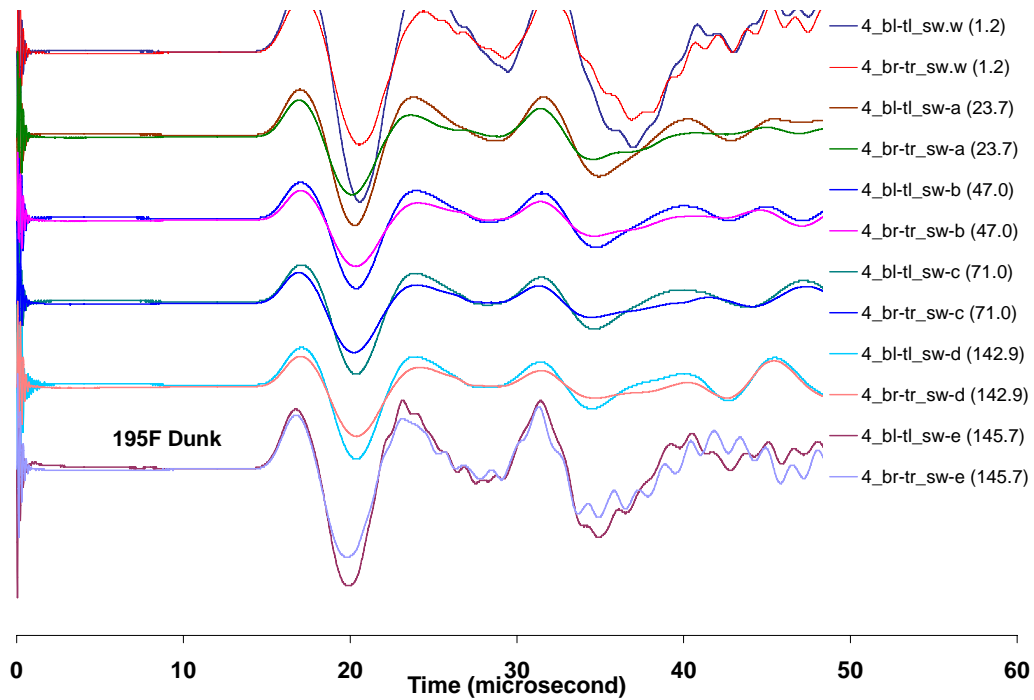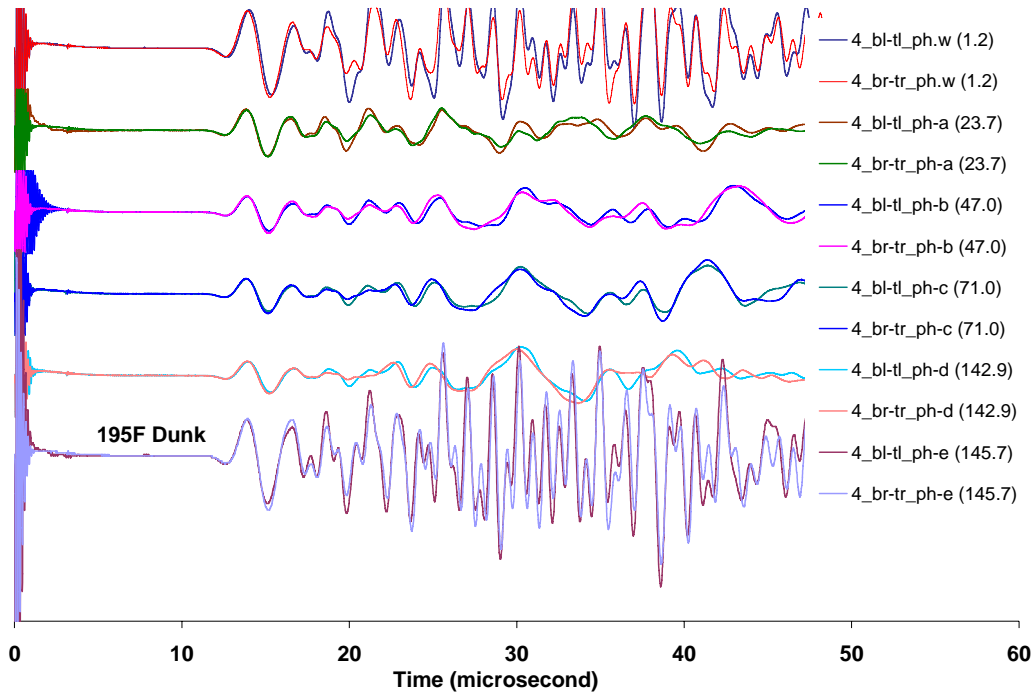*Figure 39. Waveforms generated and detected by vertical-polarized s-wave transducers, traveling vertically through test assembly containing Specimen #III-1, after indicated curing times and after bagging and immersion in water at 195F. Some water leakage was observed.*

56
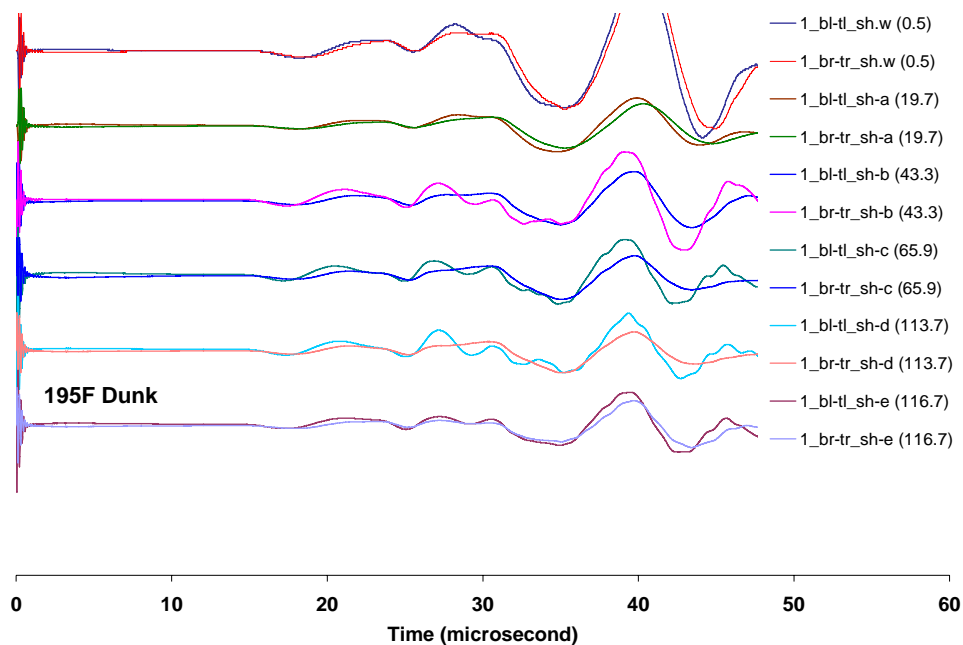
Figure 40. Waveforms generated and detected by horizontal-polarized s-wave transducers, traveling vertically through test assembly containing Specimen #III-1, after indicated curing times and after bagging and immersion in water at 195F. Some water leakage was observed.
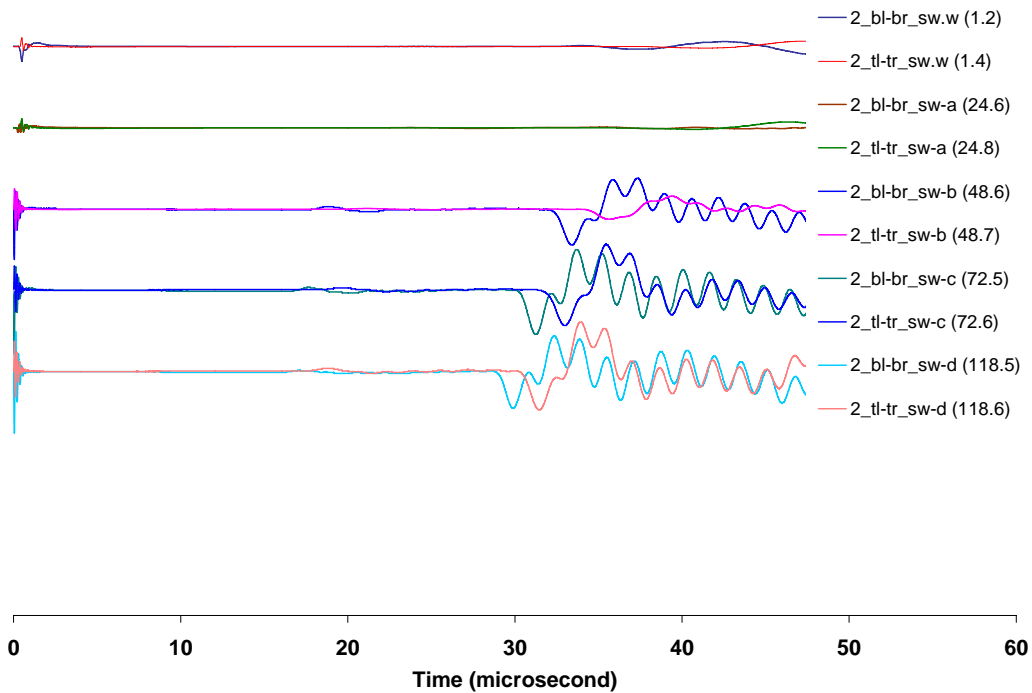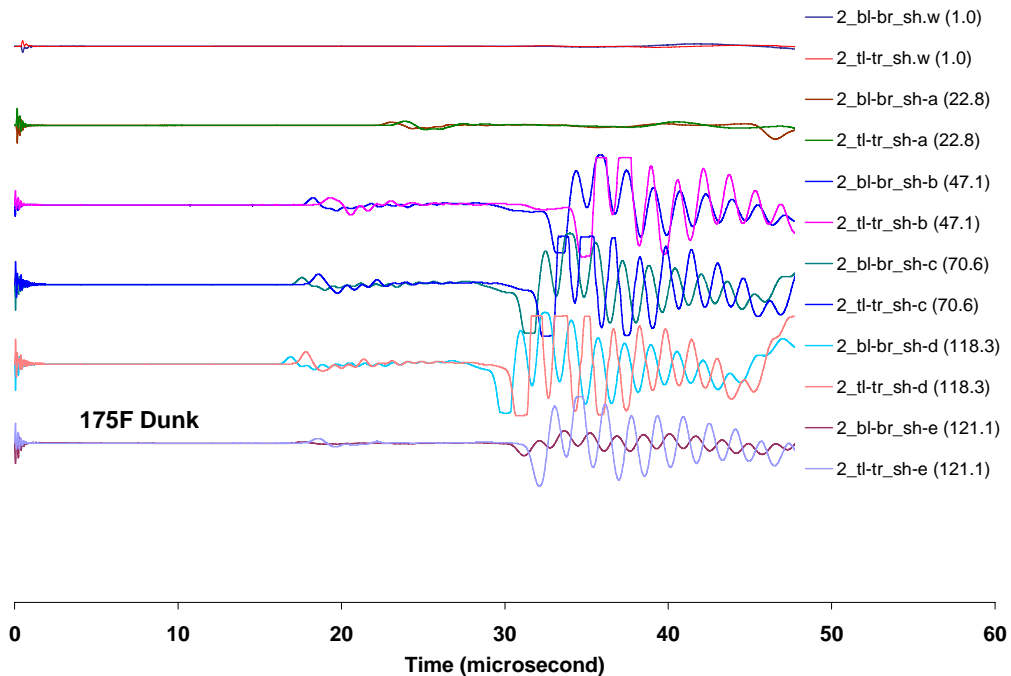

Figure 41. S-waves traveling horizontally through test chamber containing Specimen #III-2 with loosely clamped transducers, for indicated curing times.
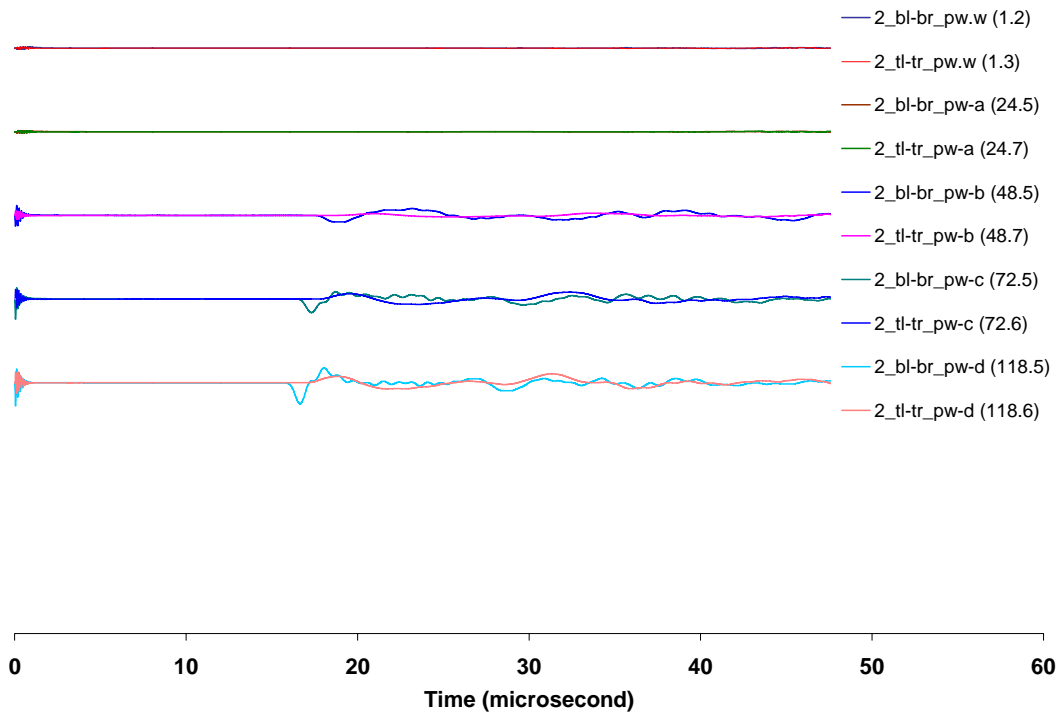
Figure 42. P-waves traveling horizontally through test chamber containing Specimen #III-2 with loosely clamped transducers, for indicated curing times.
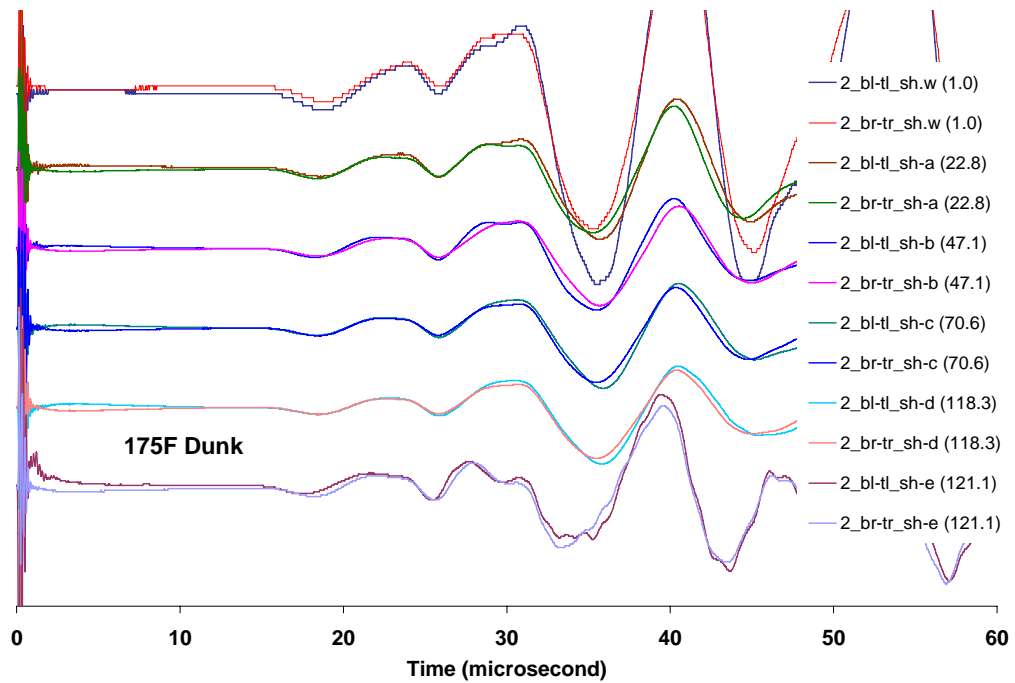

Figure 43. Waveforms generated and detected by horizontally polarized transducers, traveling vertically through test chamber containing Specimen #III-2, at indicated curing times.
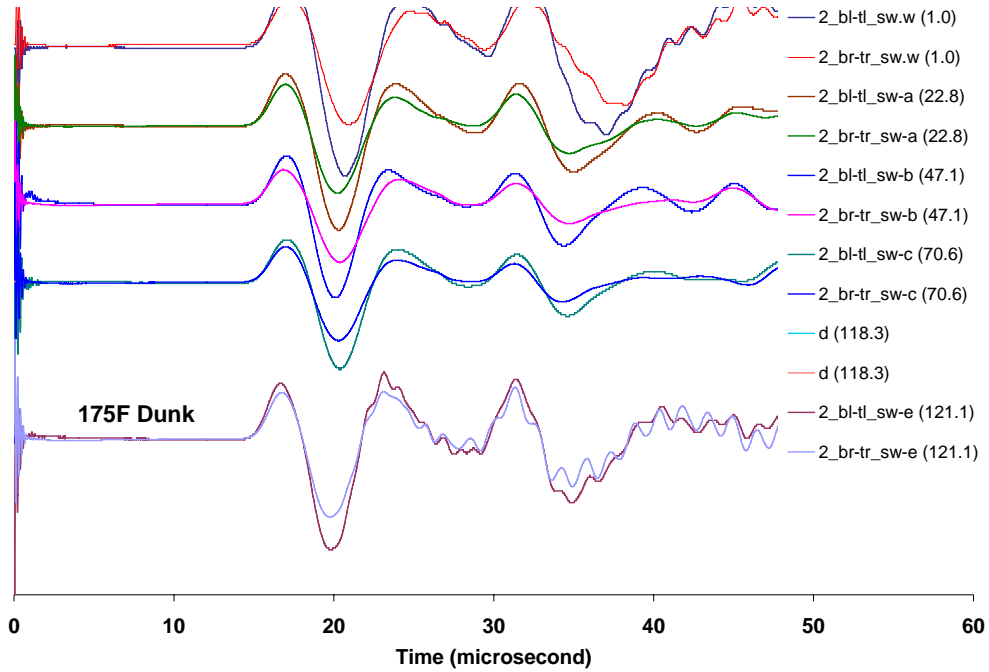
Figure 44. Waveforms generated and detected by vertically polarized transducers, traveling vertically through test chamber containing Specimen #III-2, at indicated curing times.

Figure 45. Waveforms generated and detected by tightly clamped p-wave transducers, traveling vertically through test chamber containing Specimen #III-2 at indicated curing times.

59

Figure 46. S-waves traveling horizontally through test chamber containing Specimen #III-2 with tightly clamped transducers, for indicated curing times.
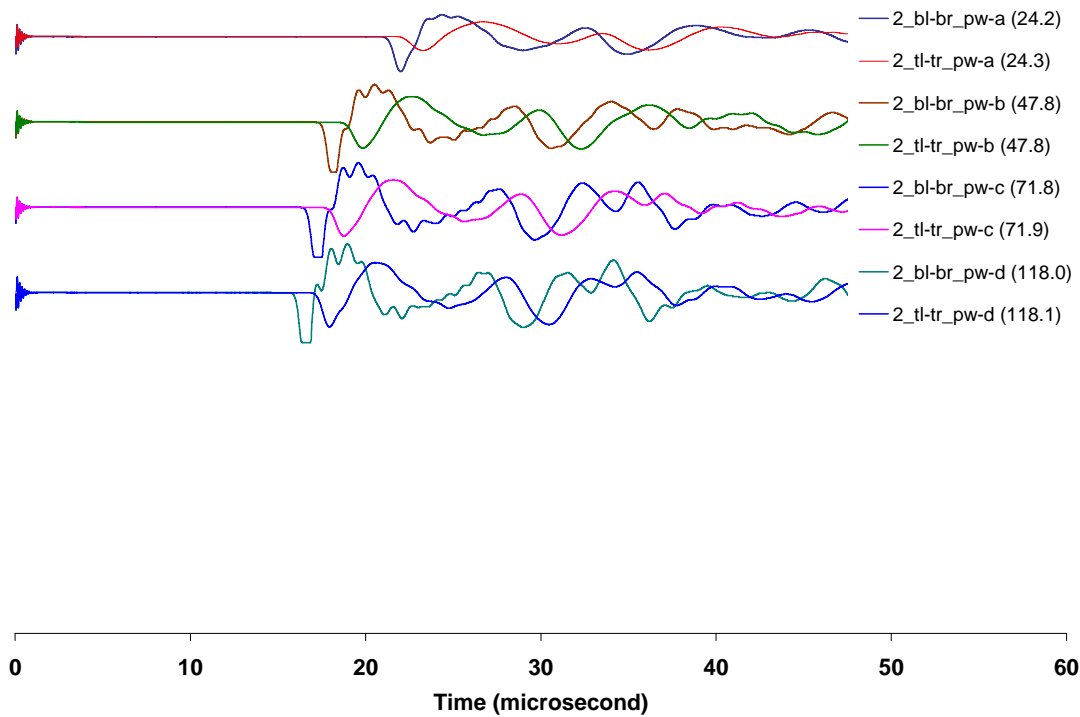
Figure 47. P-waves traveling horizontally through test chamber containing Specimen #III-2 with tightly clamped transducers, for indicated curing times.

60

Figure 48. Waveforms generated and detected by tightly clamped horizontally polarized transducers, traveling vertically through test chamber containing Specimen #III-2 at indicated curing times.

Figure 49. Waveforms generated and detected by tightly clamped vertically polarized transducers, traveling vertically through test chamber containing Specimen #III-2 at indicated curing times.

61

Figure 50. Waveforms generated and detected by tightly clamped p-wave transducers, traveling vertically through test chamber containing Specimen #III-2 at indicated curing times.
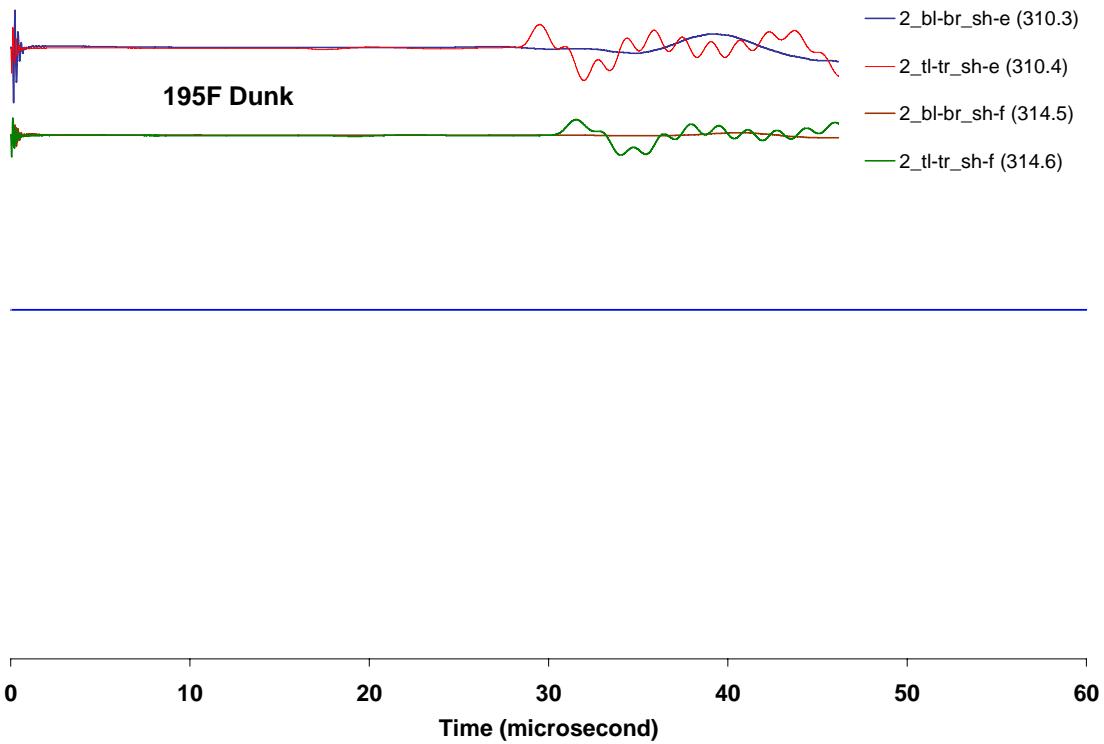
Figure 51. S-waves traveling horizontally through cement Specimen# III-2a in modified sample assembly, before and after immersion in water bath at 195F.
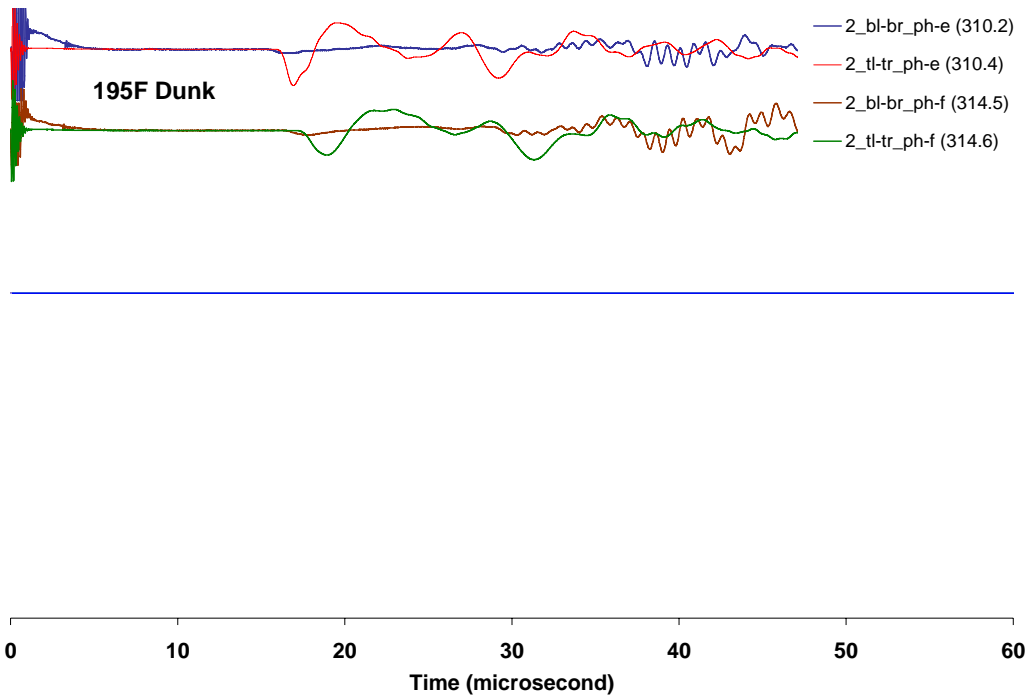
Figure 52. P-waves traveling horizontally through cement Specimen# III-2a in modified sample assembly, before and after immersion in water bath at 195F.
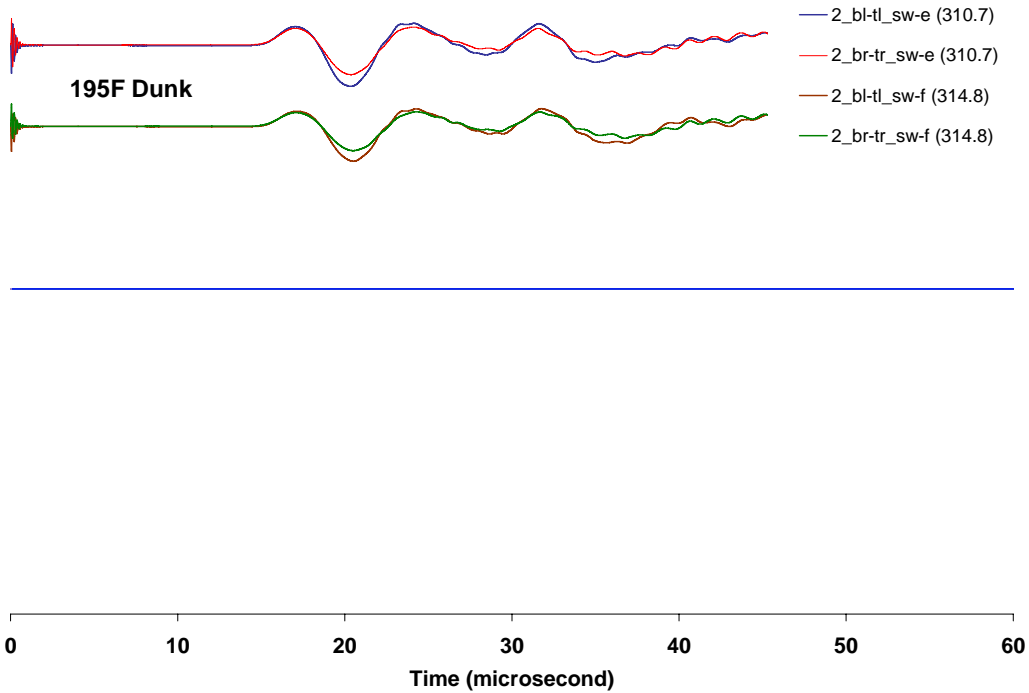
Figure 53.   Waveforms generated and detected by vertically polarized s-wave transducers, traveling vertically through Specimen #III-2a in modified apparatus, before and after immersion in water bath at 195F.

63
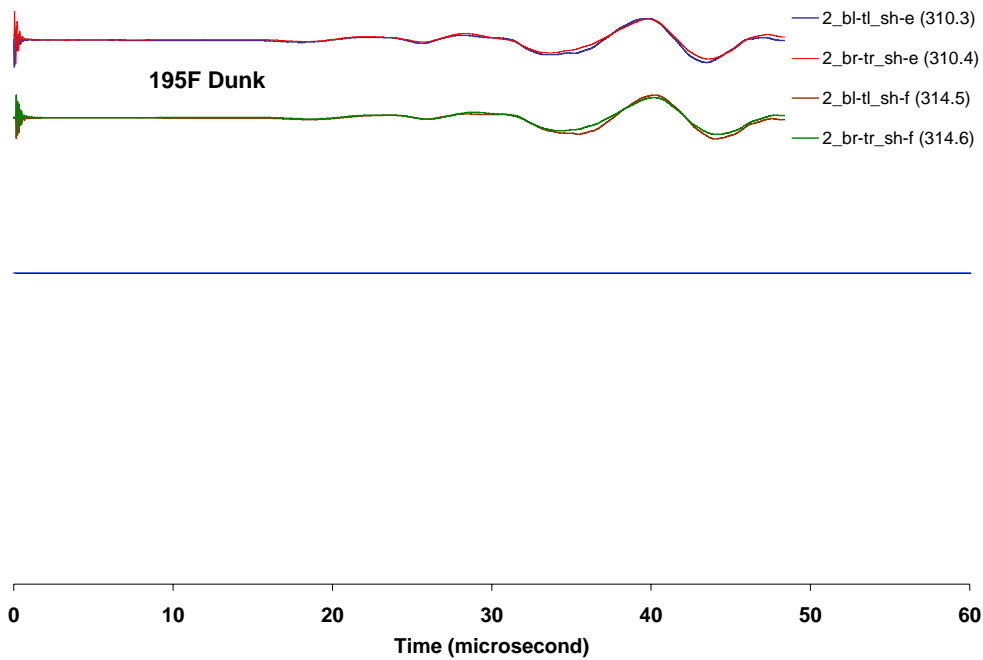
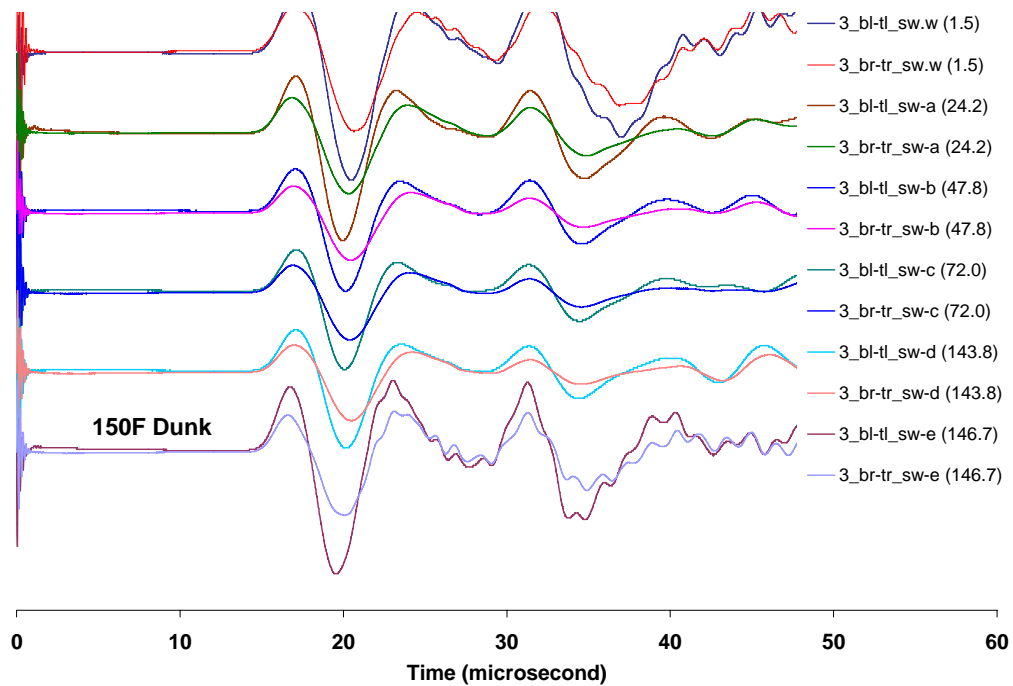*Figure 54. Waveforms generated and detected by vertically polarized s-wave transducers, traveling vertically through Specimen #III-2a in modified apparatus, before and after immersion in water bath at 195F.*
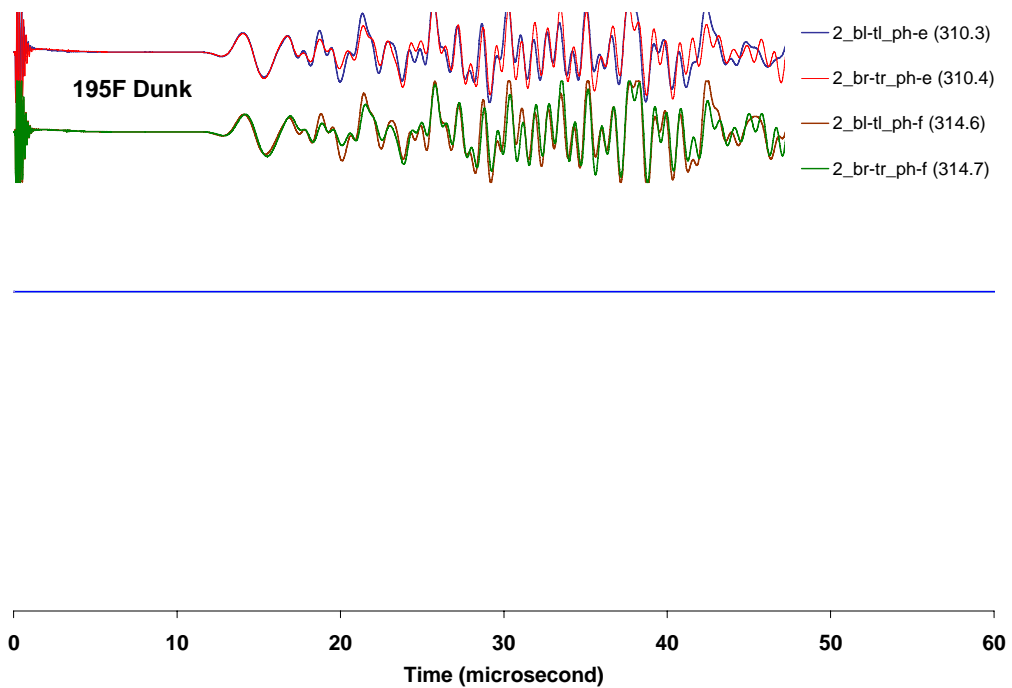
Figure 55. Waveforms generated and detected by p-wave transducers, traveling vertically through Specimen #III-2a in modified apparatus, before and after immersion in water bath at 195F.

64

Figure 56. S-waves traveling horizontally through Specimen #IV-4 in modified apparatus, at indicated curing times and after immersion in water bath at 195F.
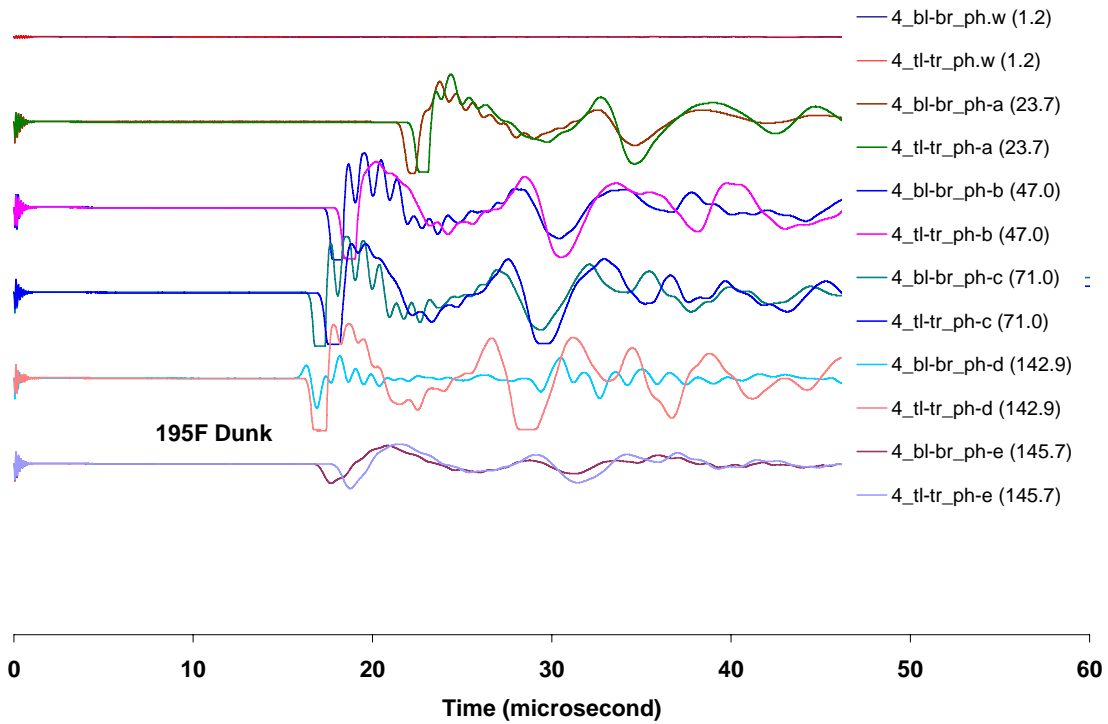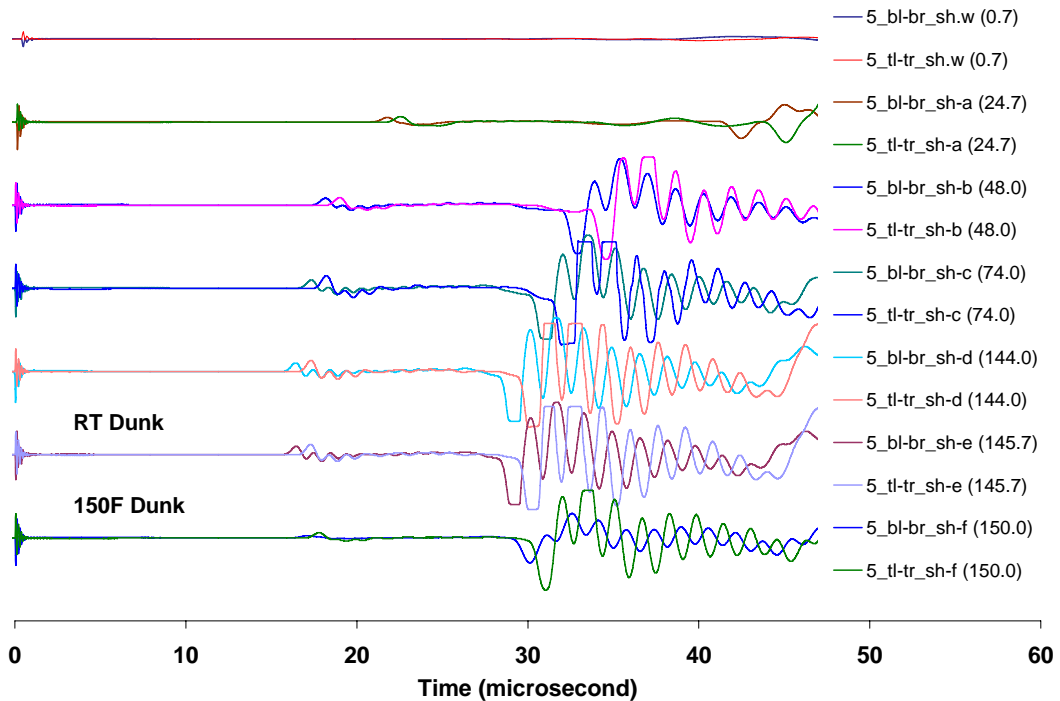

Figure 57. P-waves traveling horizontally through Specimen #IV-4 in modified apparatus, at indicated curing times and after immersion in water bath at 195F.

Figure 58. Waveforms generated and detected by horizontally polarized s-wave transducers, traveling vertically through modified assembly containing Specimen #IV-4, at indicated curing times and after immersion in a water bath 195F.

Figure 59. Waveforms generated and detected by vertically polarized s-wave transducers, traveling vertically through modified assembly containing Specimen #IV-4, at indicated curing times and after immersion in a water bath at 195F.

Figure 60. Waveforms generated and detected by p-wave transducers, traveling vertically through modified assembly containing Specimen #IV-4, at indicated curing times and after immersion in a water bath at 195F.
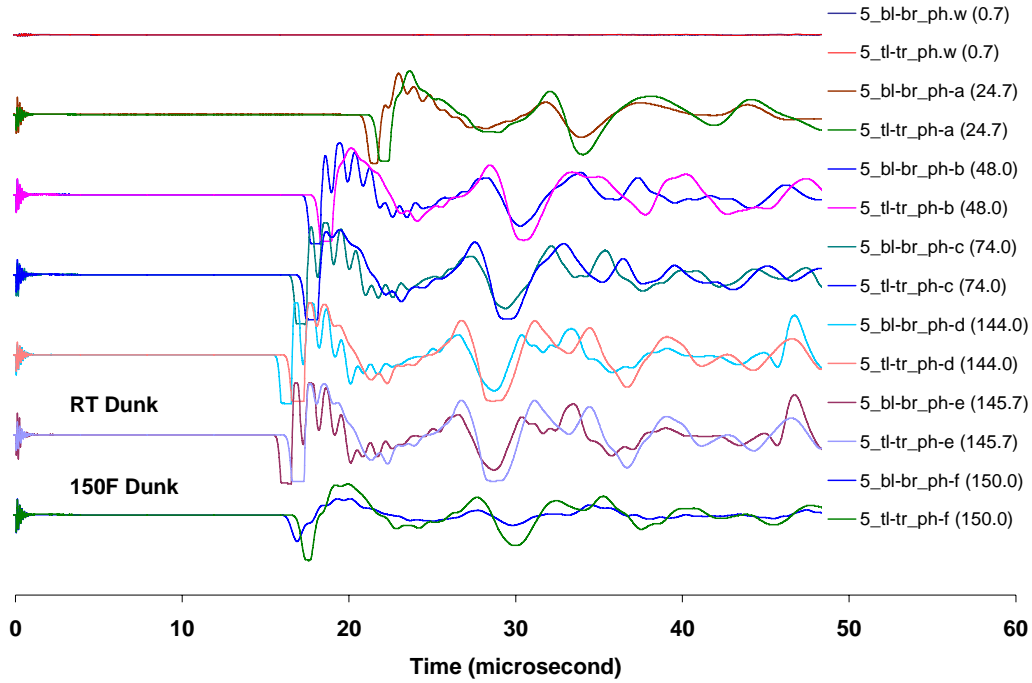

Figure 61. S-waves traveling horizontally through Specimen #IV-2 in modified apparatus, at indicated curing times and after immersion in water bath at 175F.
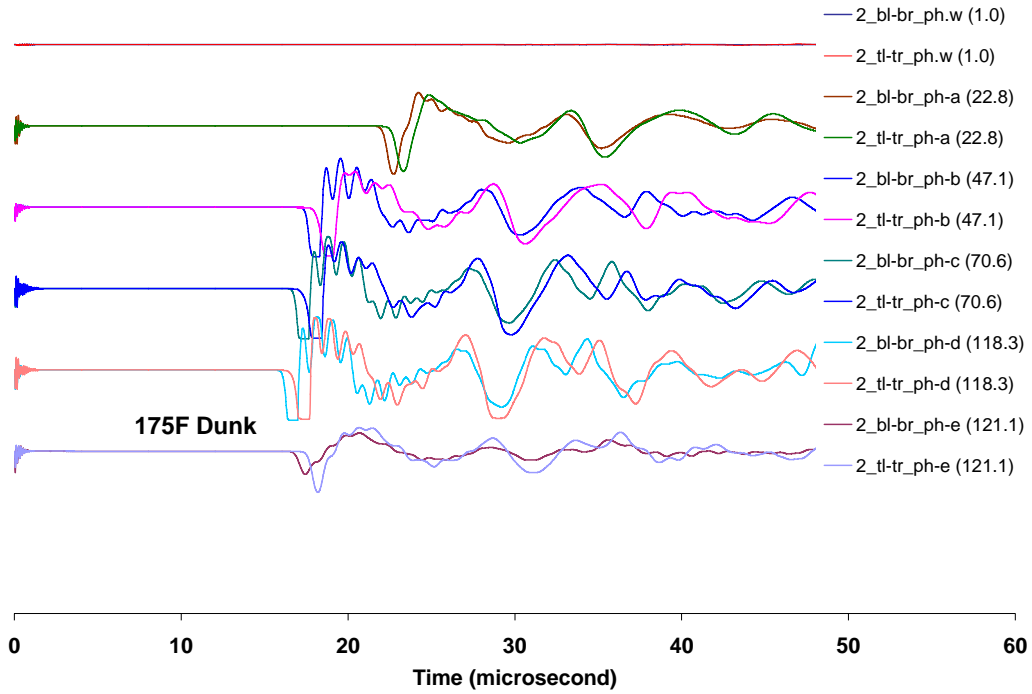
Figure 62. P-waves traveling horizontally through Specimen #IV-2 in modified apparatus, at indicated curing times and after immersion in water bath at 175F.
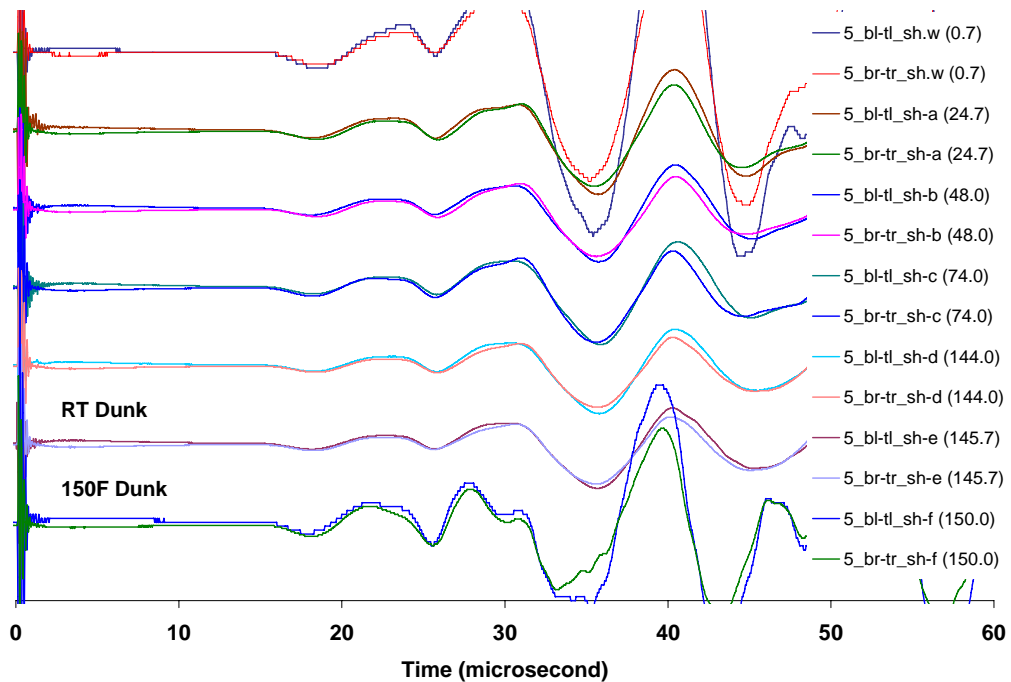

Figure 63. Waveforms generated and detected by horizontally polarized s-wave transducers, traveling vertically through modified assembly containing Specimen #IV-2, at indicated curing times and after immersion in a water bath at 175F.
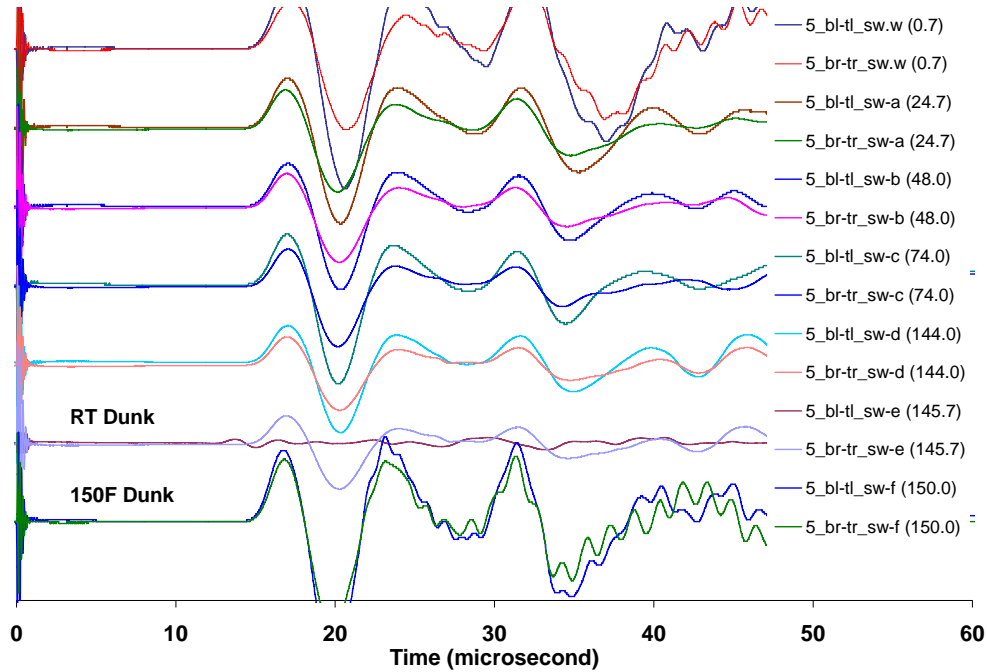
Figure 64. Waveforms generated and detected by vertically polarized s-wave transducers, traveling vertically through modified assembly containing Specimen #IV-2, at indicated curing times and after immersion in a water bath at 175F.
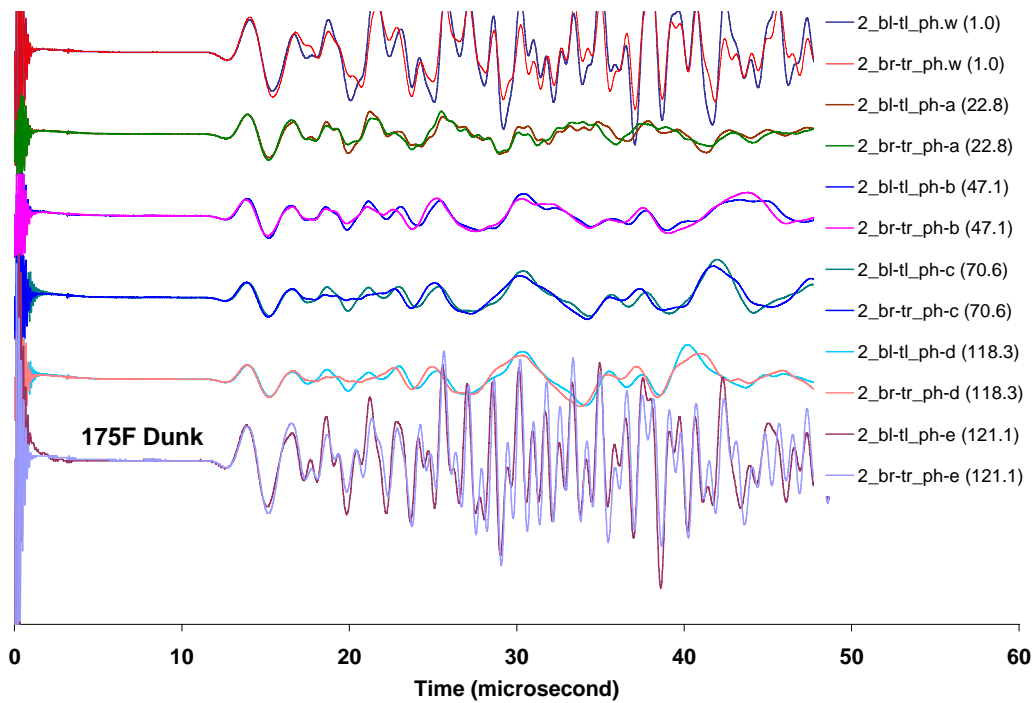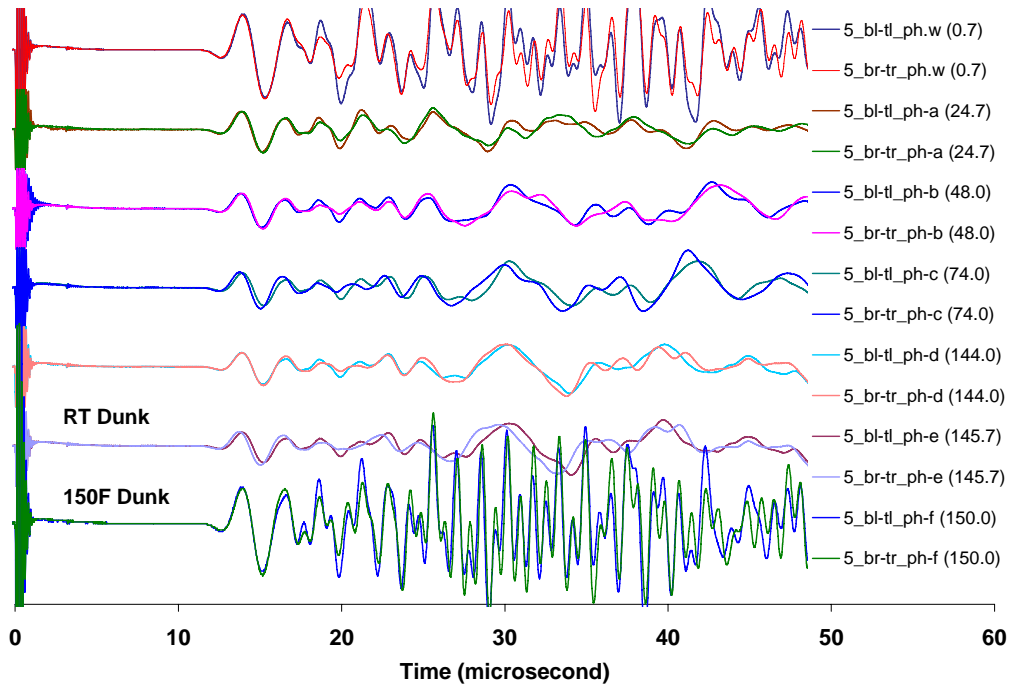

Figure 65. Waveforms generated and detected by p-wave transducers, traveling vertically through modified assembly containing Specimen #IV-2, at indicated curing times and after immersion in a water bath at 175F.
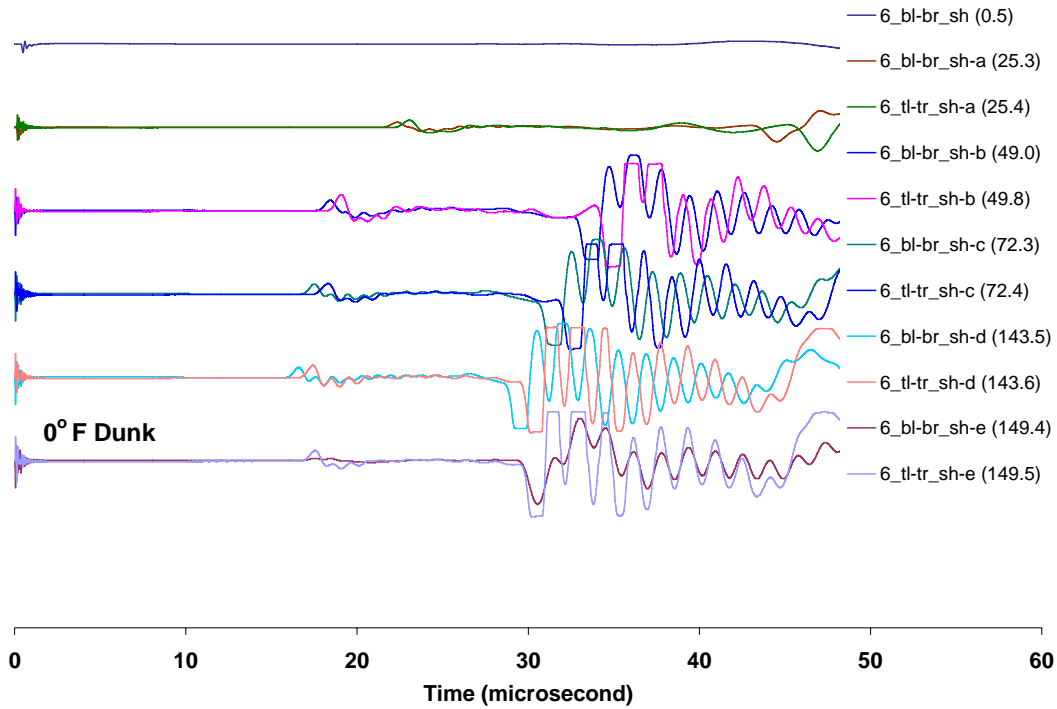
69
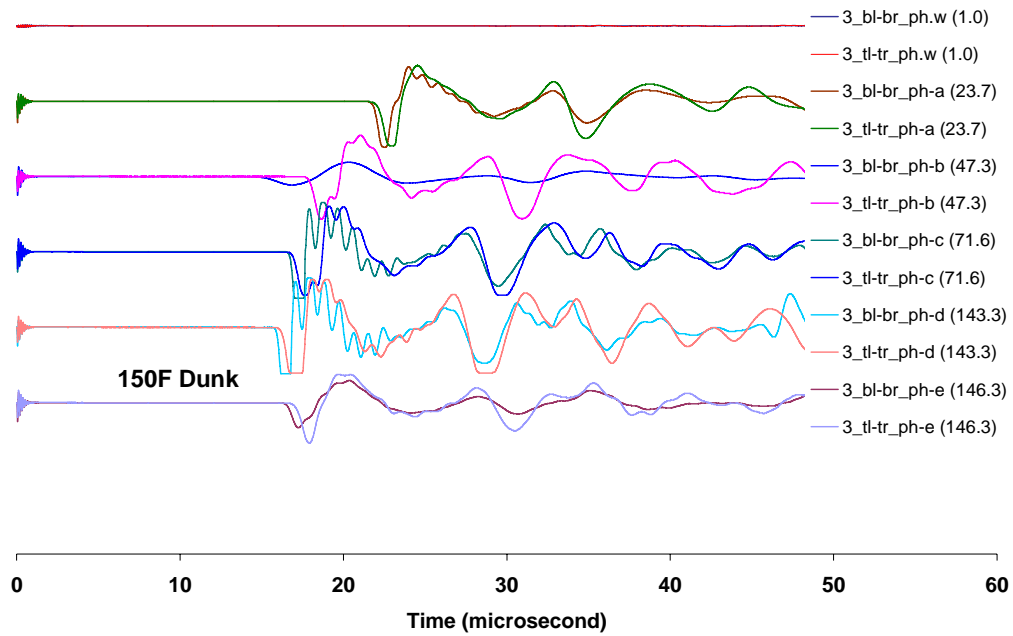
Figure 66. S-waves traveling horizontally through Specimen #IV-3 in modified apparatus, at indicated curing times and after immersion in water bath at 150F.
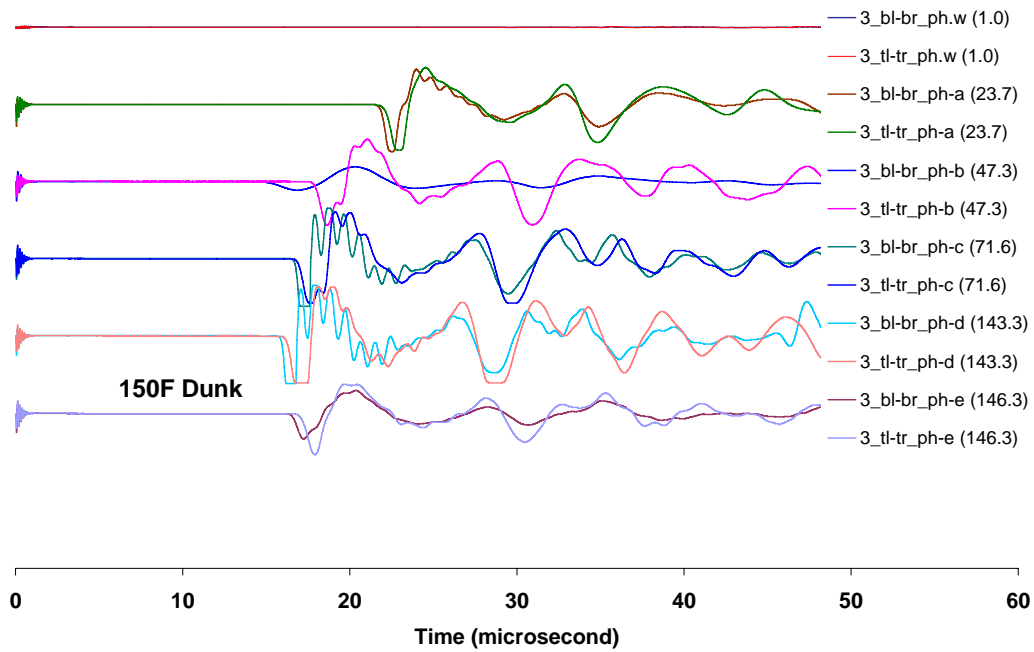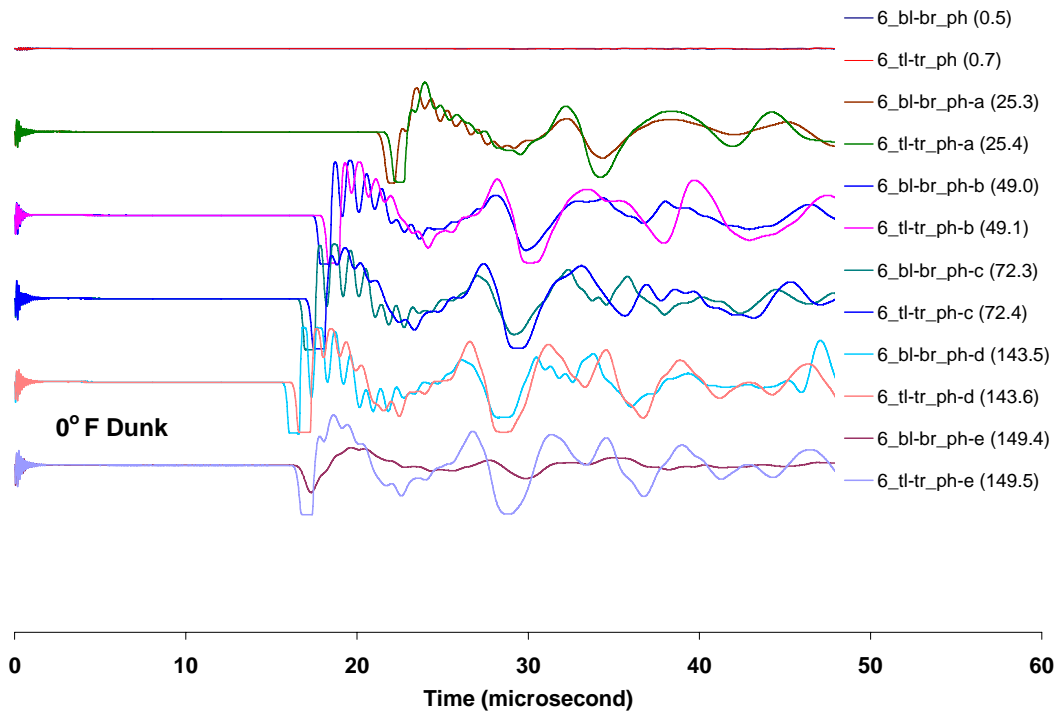

Figure 67. P-waves traveling horizontally through Specimen #IV-3 in modified apparatus, at indicated curing times and after immersion in water bath at 150F.
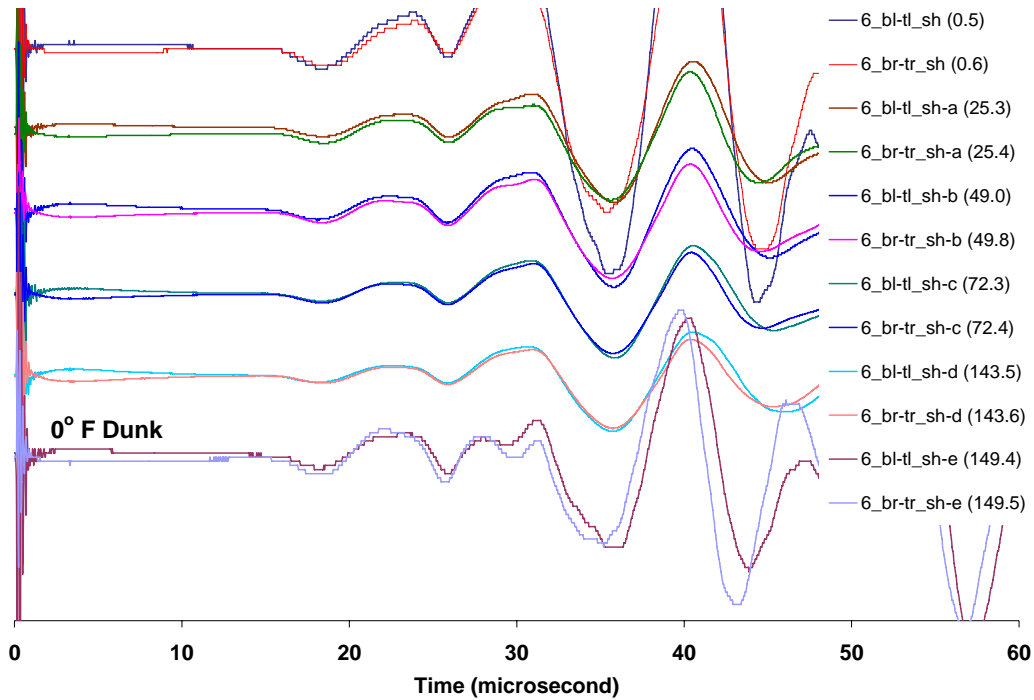
70
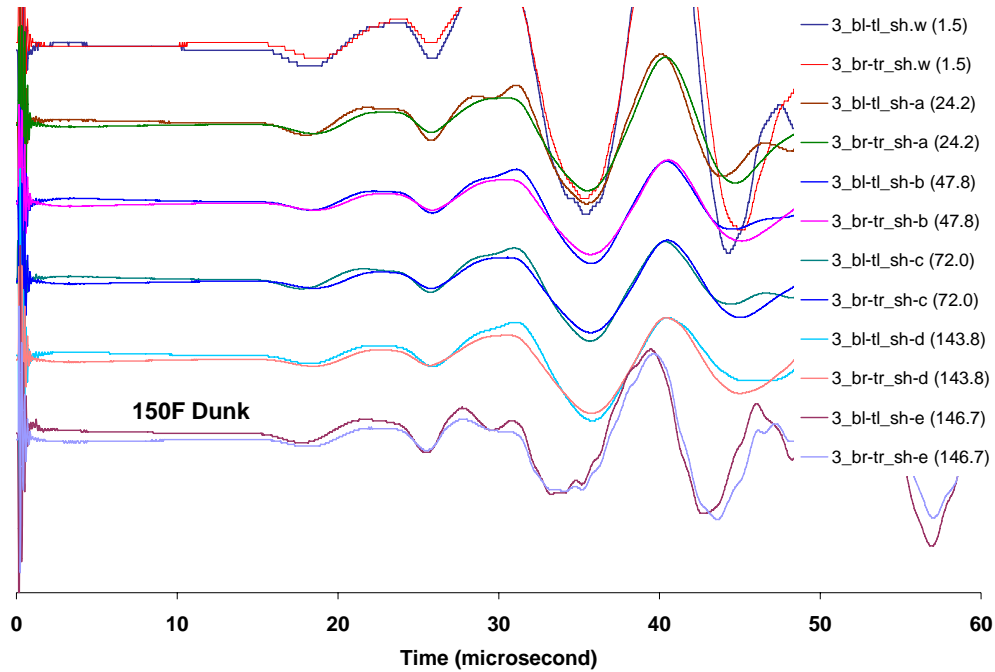
Figure 68. Waveforms generated and detected by horizontally polarized s-wave transducers, traveling vertically through modified assembly containing Specimen #IV-3, at indicated curing times and after immersion in a water bath at150F.
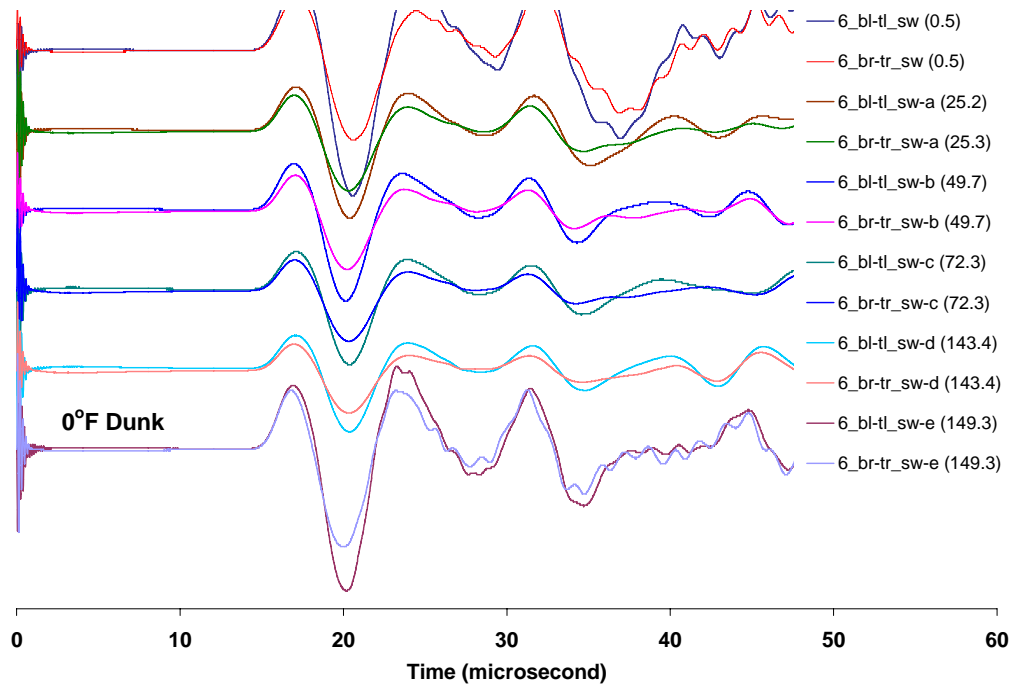

Figure 69. Waveforms generated and detected by vertically polarized s-wave transducers, traveling vertically through modified assembly containing Specimen #IV-3, at indicated curing times and after immersion in a water bath at 150F.
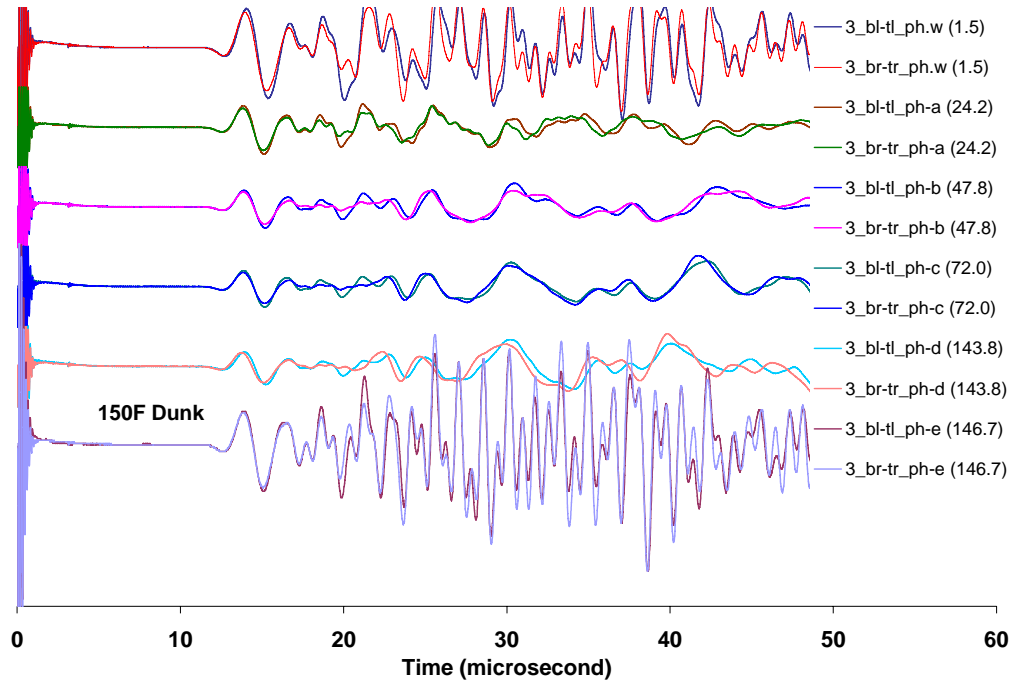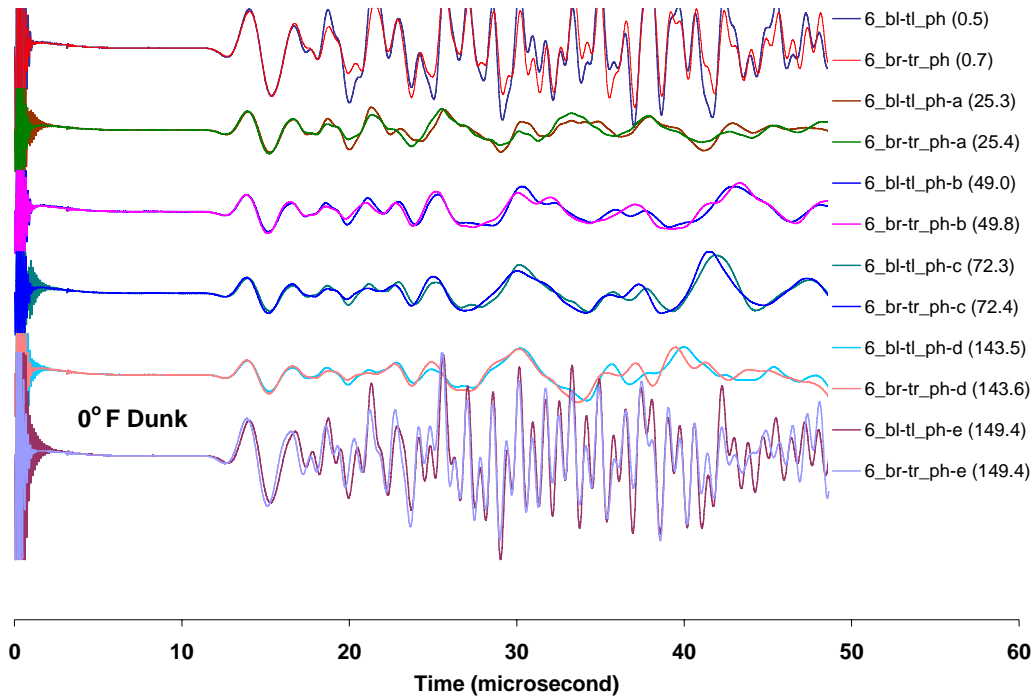
Figure 70. Waveforms generated and detected by p-wave transducers, traveling vertically through modified assembly containing Specimen #IV-3, at indicated curing times and after immersion in a water bath at 150F.

Figure 71. S-waves traveling horizontally through Specimen #IV-4 in modified apparatus, at indicated curing times and after immersion in water bath at room temperature and 150F.

Figure 72. P-waves traveling horizontally through Specimen #IV-4 in modified apparatus, at indicated curing times and after immersion in water bath at room temperature and 150F.

Figure 73. Waveforms generated and detected by horizontally polarized s-wave transducers, traveling vertically through modified assembly containing Specimen #IV-4, at indicated curing times and after immersion in a water bath at room temperature and 150F.
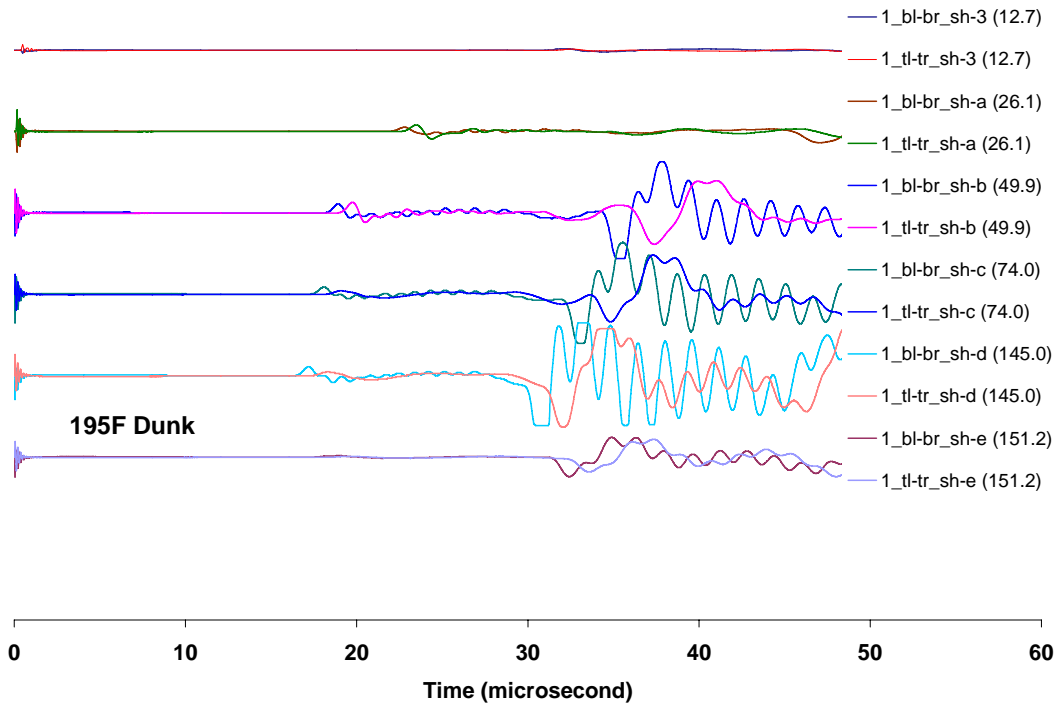
73

Figure 74. Waveforms generated and detected by vertically polarized S-wave transducers, traveling vertically through modified assembly containing Specimen #IV-4, at indicated curing times and after immersion in a water bath at room temperature and 150F.

Figure 75. Waveforms generated and detected by P-wave transducers, traveling vertically through modified assembly containing Specimen #IV-4, at indicated curing times and after immersion in a water bath at room temperature and 150F.

74

Figure 76. S-waves traveling horizontally through Specimen #IV-6 in modified apparatus, at indicated curing times and after immersion in brine bath at 0F.

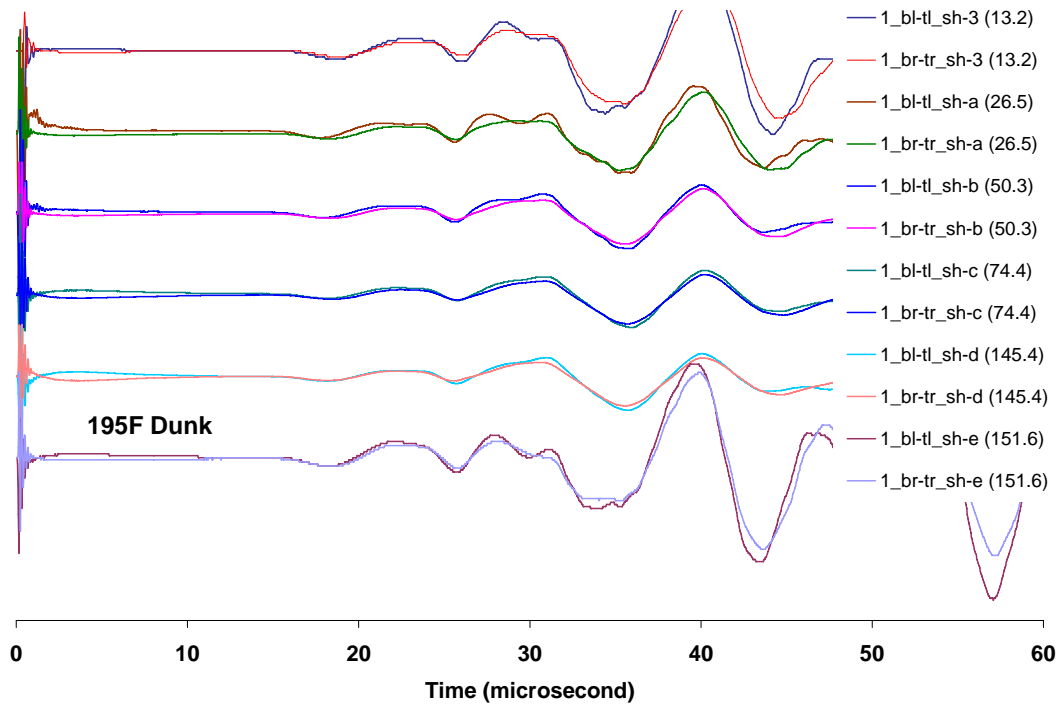*Figure 77. P-waves traveling horizontally through Specimen #IV-6 in modified apparatus, at indicated curing times and after immersion in brine bath at 0F.*

75

Figure 78. Waveforms generated and detected by horizontally polarized s-wave transducers, traveling vertically through modified assembly containing Specimen #IV-6, at indicated curing times and after immersion in a brine bath at 0F.
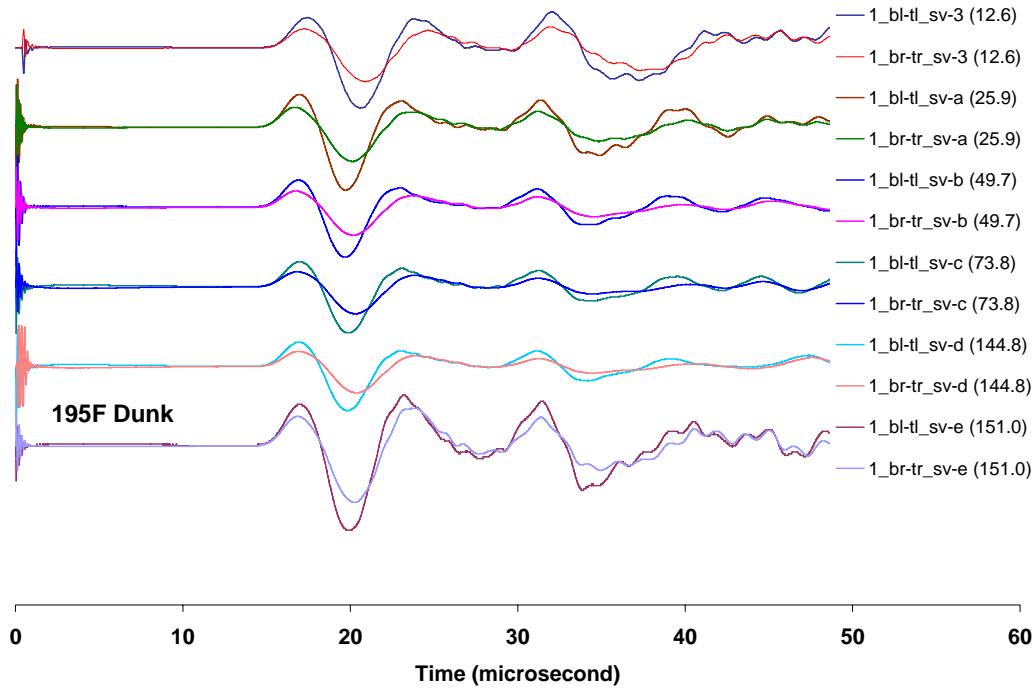

Figure 79. Waveforms generated and detected by vertically polarized s-wave transducers, traveling vertically through modified assembly containing Specimen #IV-6, at indicated curing times and after immersion in a brine bath at 0F.

76

Figure 80. Waveforms generated and detected by p-wave transducers, traveling vertically through modified assembly containing Specimen #IV-6, at indicated curing times and after immersion in a brine bath at 0F.

Figure 81. S-waves traveling horizontally through Specimen #V-1, mixed with 10% more water than standard, at indicated curing times and after immersion in 195F water.
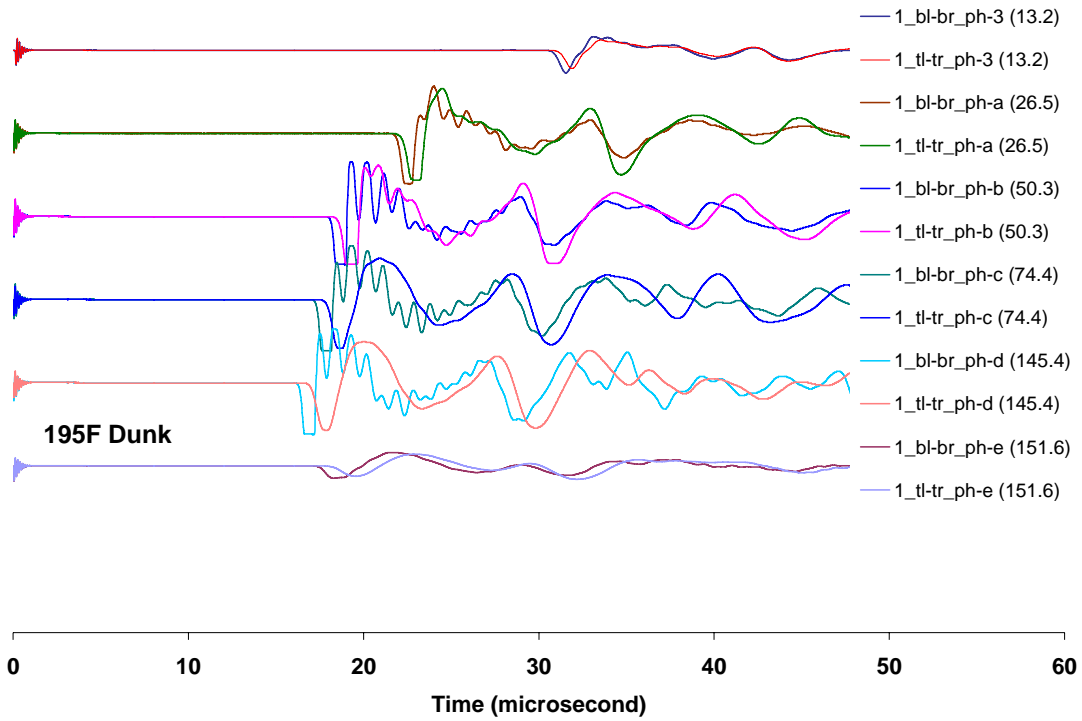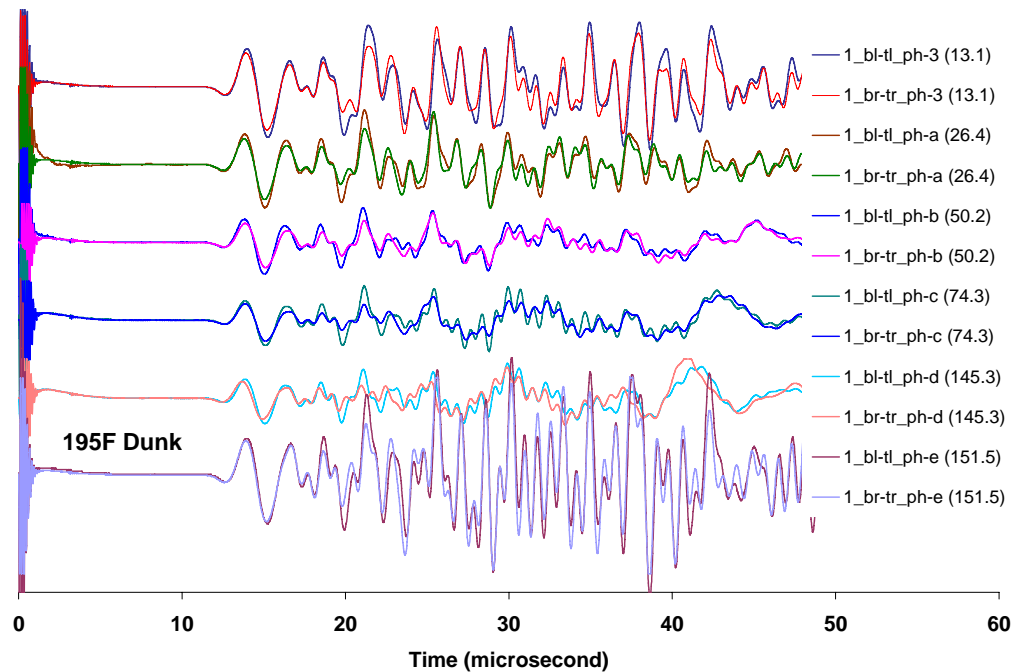
Figure 82. P-waves traveling horizontally through Specimen #V-1, mixed with 10% more water than standard, at indicated curing times and after immersion in 195F water.

Figure 83. Waveforms generated and detected by horizontally polarized s-wave transducers, traveling vertically through Specimen #V-1 mixed with 10% more water than standard, at indicated curing times and after immersion in 190F water.
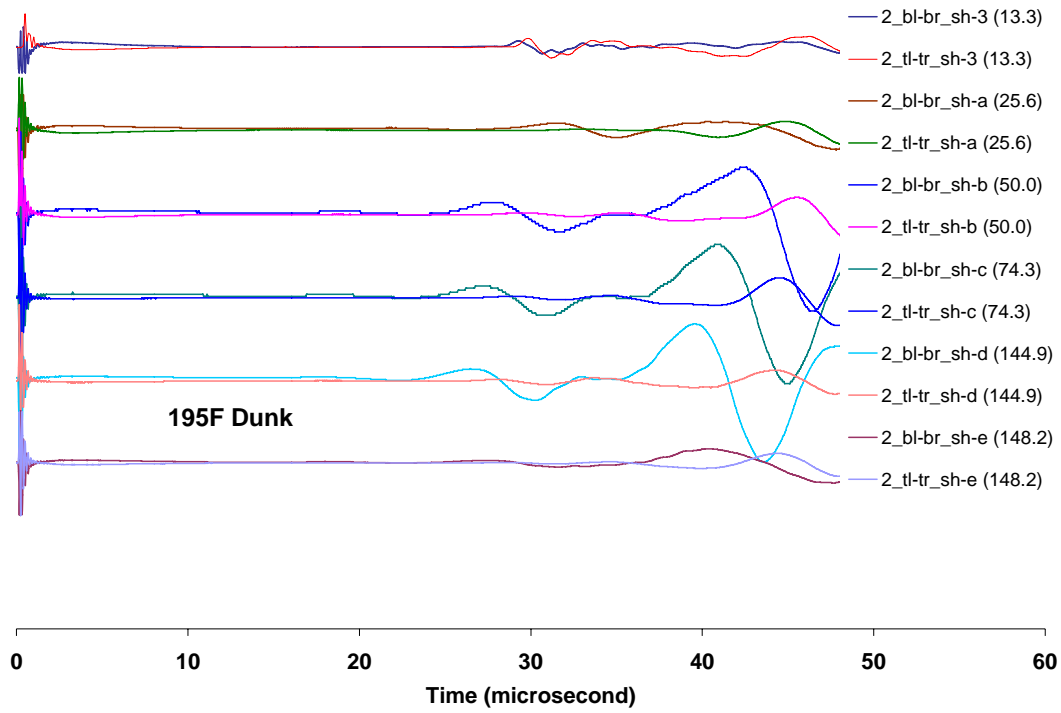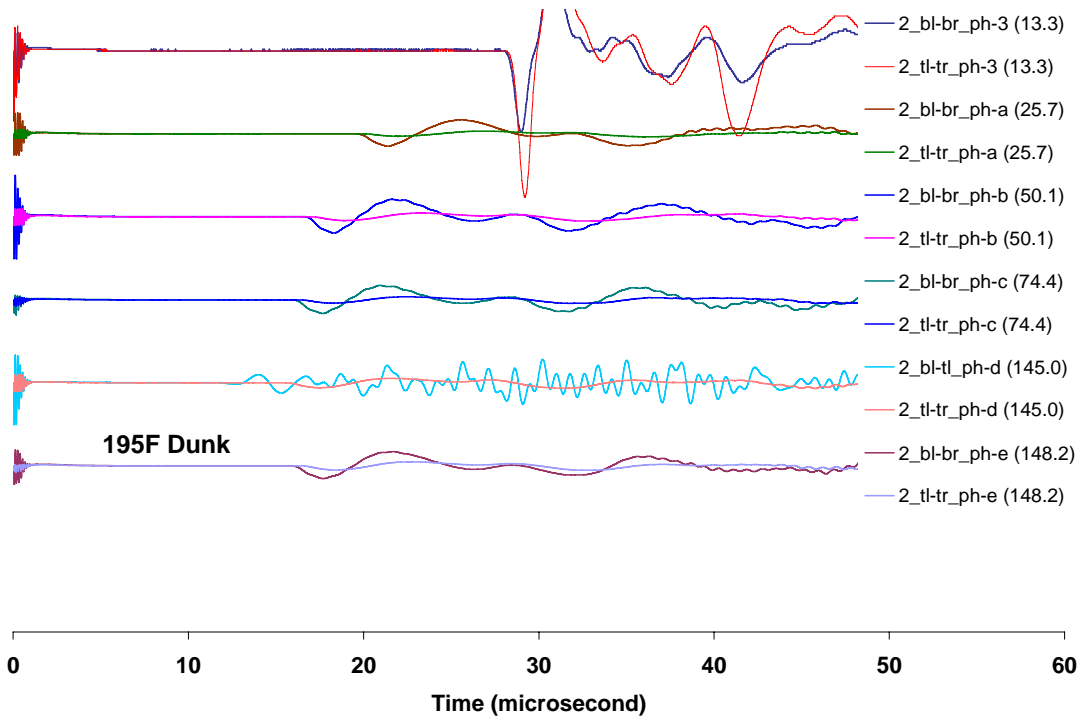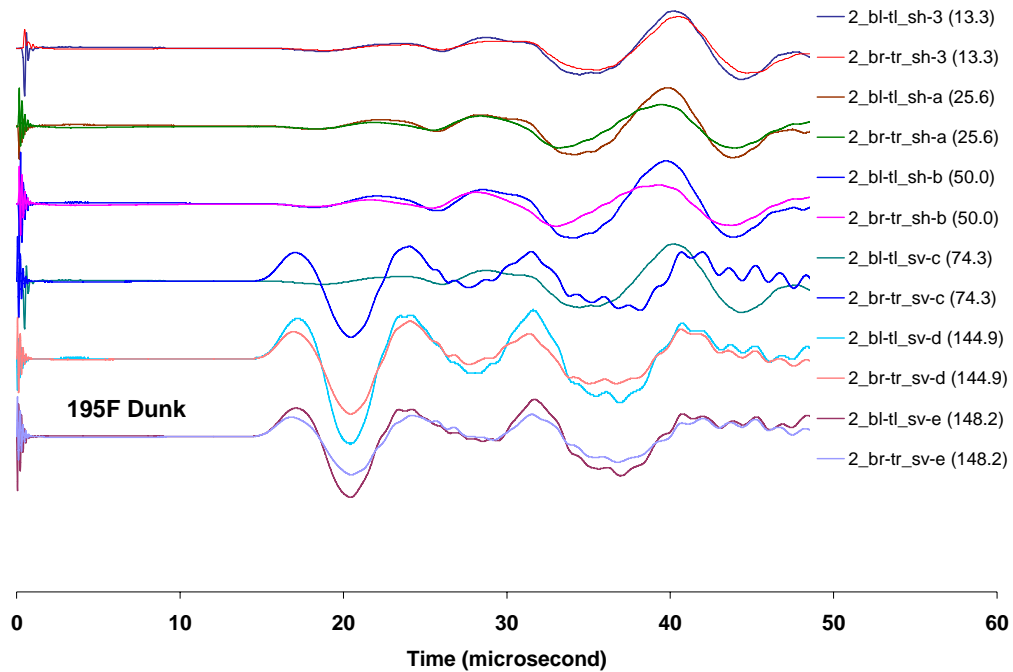
78

Figure 84. Waveforms generated and detected by vertically polarized S-wave transducers, traveling vertically through Specimen #V-1 mixed with 10% more water than standard, at indicated curing times and after immersion in 190F water.

Figure 85. Waveforms generated and detected by p-wave transducers, traveling vertically through Specimen #V-1 mixed with 10% more water than standard, at indicated curing times and after immersion in 190F water.
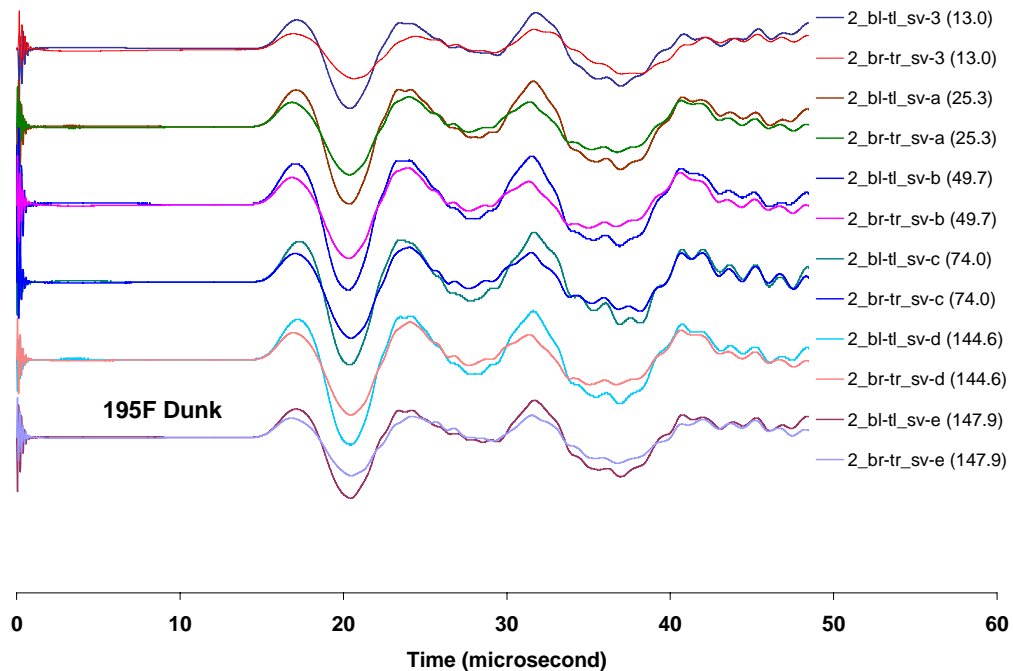
79

Figure 86. S-waves traveling horizontally through Specimen #V-2, mixed with 10% less water than standard, at indicated curing times and after immersion in 195F water.

Figure 87. P-waves traveling horizontally through Specimen #V-2, mixed with 10% less water than standard, at indicated curing times and after immersion in 195F water.

Figure 88. Waveforms generated and detected by horizontally polarized s-wave transducers, traveling vertically through Specimen #V-2 mixed with 10% less water than standard, at indicated curing times and after immersion in 190F water.
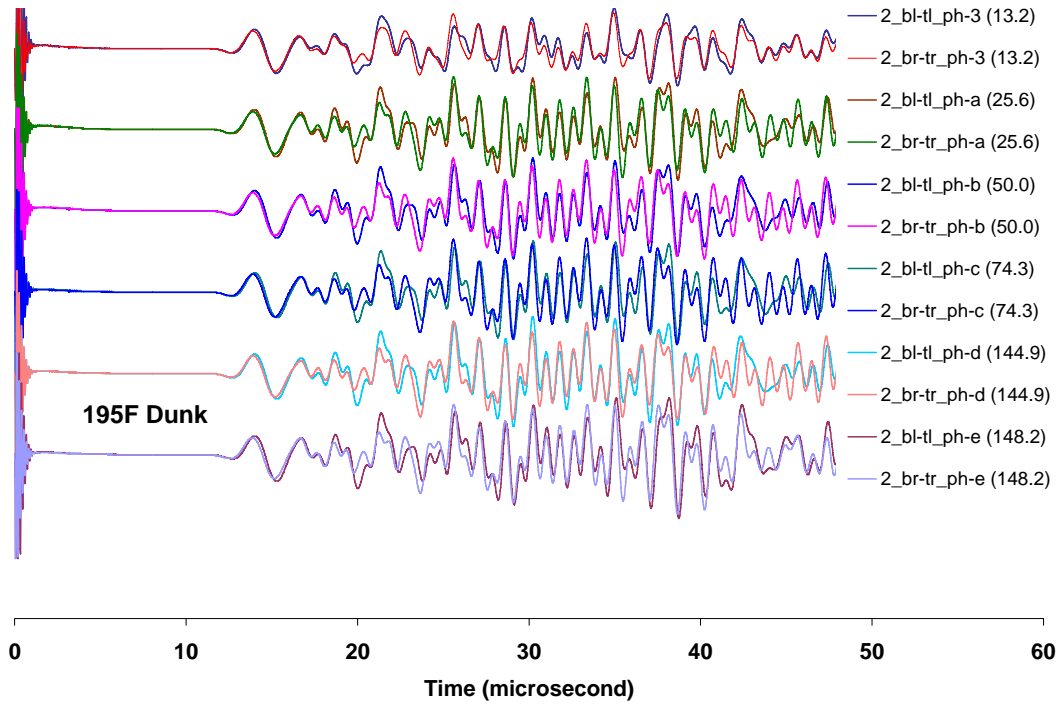

Figure 89. Waveforms generated and detected by vertically polarized s-wave transducers, traveling vertically through Specimen #V-2 mixed with 10% less water than standard, at indicated curing times and after immersion in 190F water..

81

Figure 90. Waveforms generated and detected by p-wave transducers, traveling vertically through Specimen #V-2 mixed with 10% less water than standard, at indicated curing times and after immersion in 190F water.
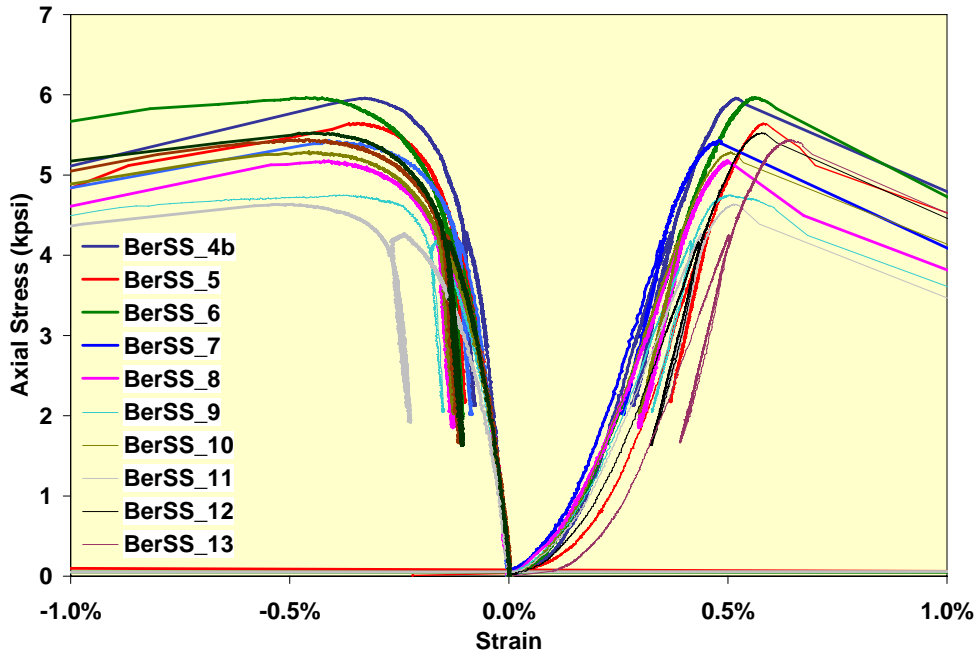

Figure 91 Composite plot of load frame measurements for Berea sandstone samples. Curves with increasing axial stress to the right show axial stress-strain behavior, and curves with increasing stress to the left show axial stress – radial strain changes.
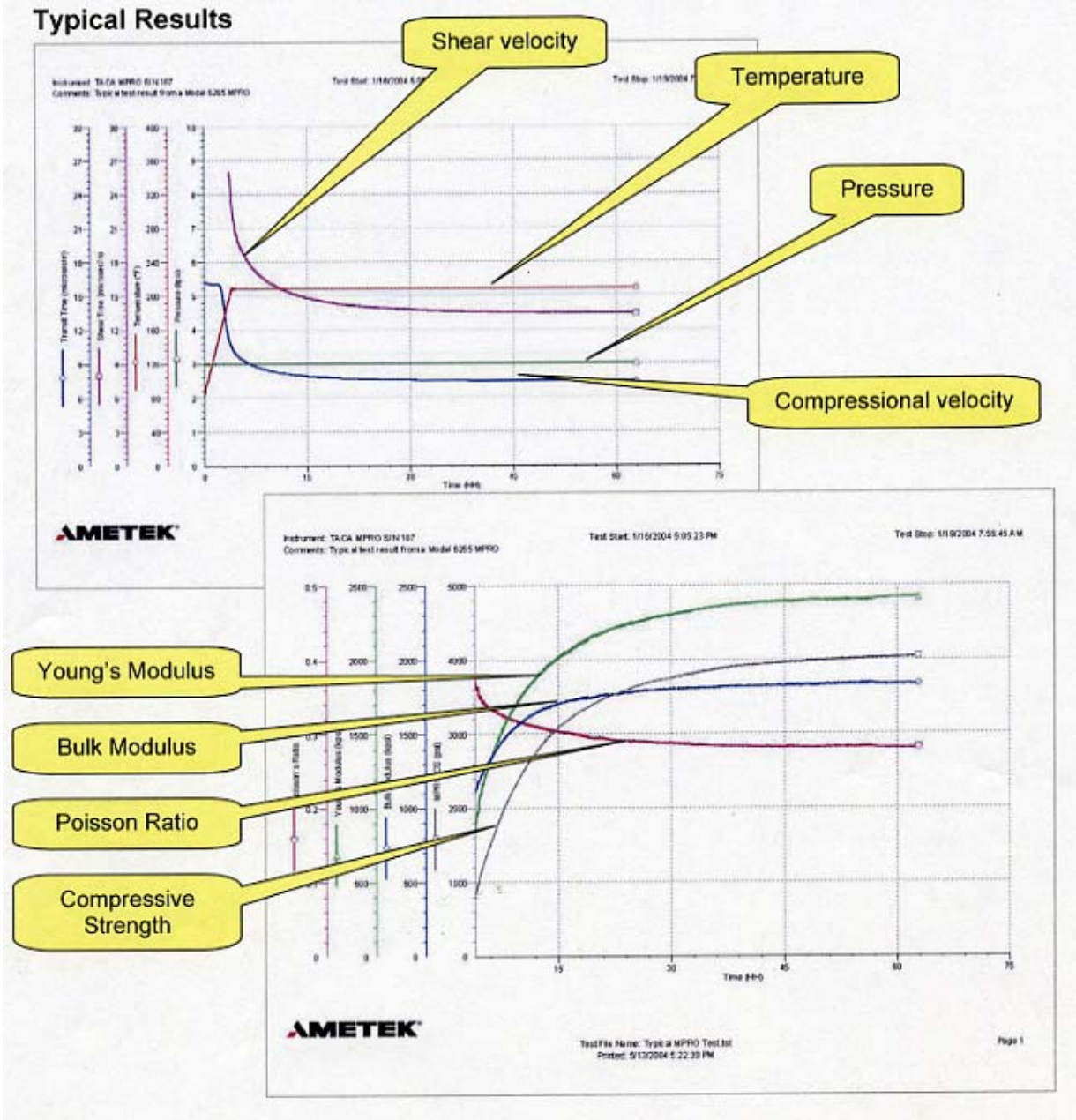
82

Figure 92. Representative plots of wave traveltimes and test environment (top), computed moduli (bottom), from Equations 11-13, and predicted compressive strength, for a complete MPro test.
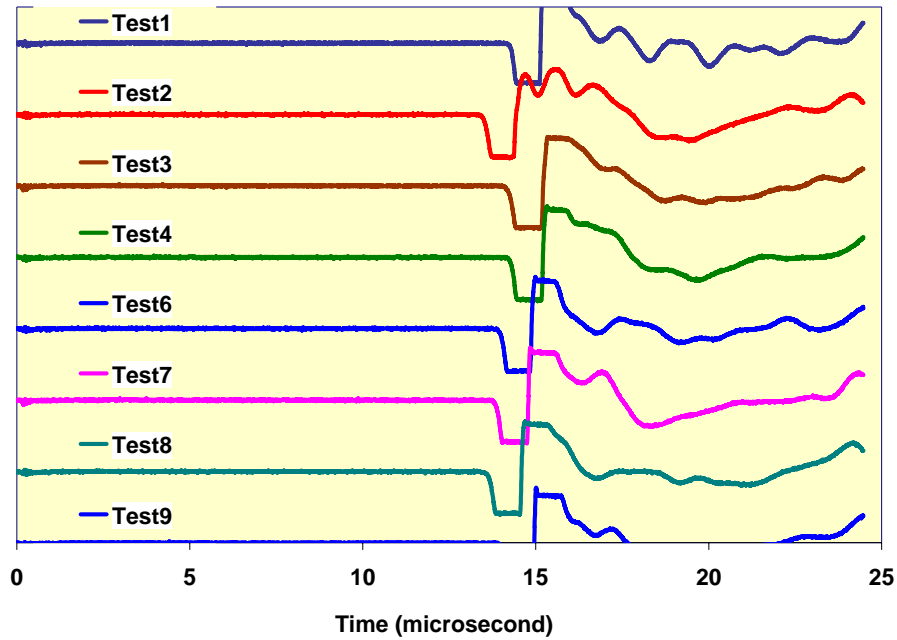
Figure 93. Composite plot of all bench-top P-waves for bench-top measurements with Panametrics transducers, for specimens tested in the MPRO system.
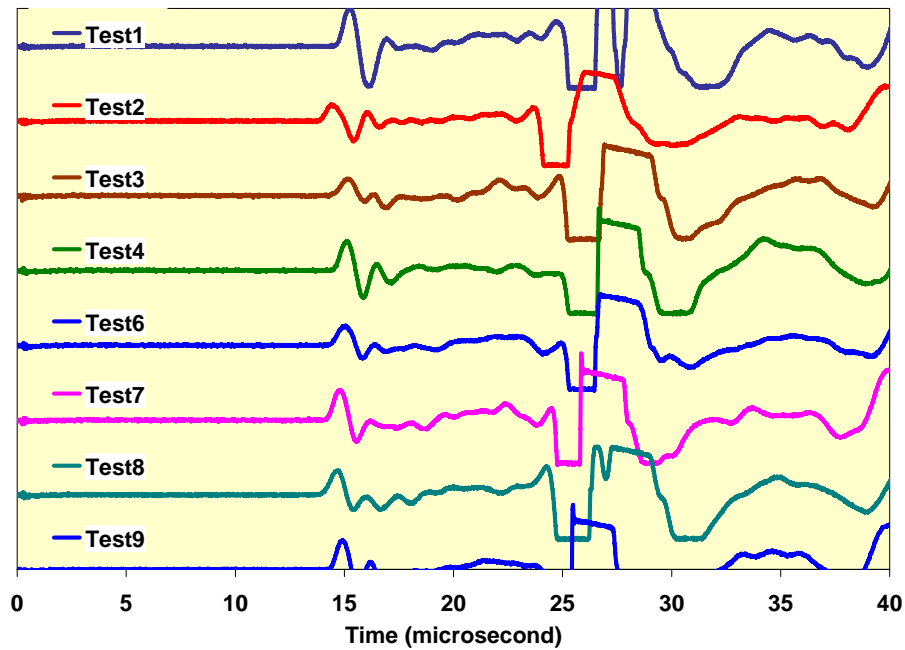

Figure 94. Composite plot of all bench-top P-waves for bench-top measurements with Panametrics transducers, for specimens tested in the MPRO system.
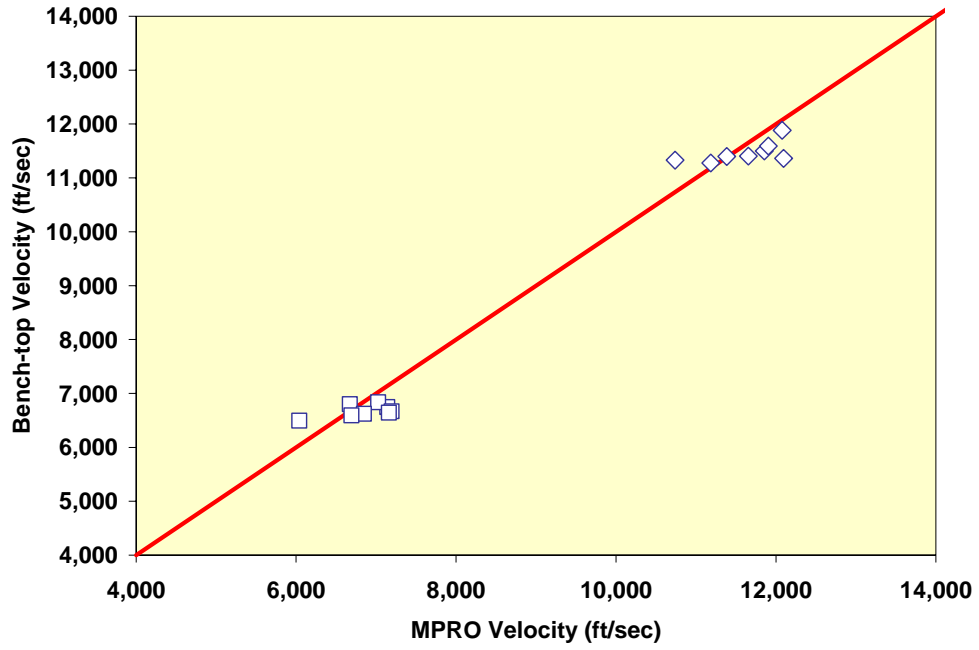
Figure 95. Graphical summary of bench-top P– and S-wave velocity measurements (open diamonds and squares, respectively) in cement, plotted versus corresponding MPRO measurement.

Technical Feasibility Evaluation of Non-Intrusive Optical Detection, Monitoring and Preliminary Characterization of Casing Cement Leaks for Gas Wells

Glenn DeWolf
URS Corporation
9400 Ambeylen Boulevard
Austin, TX 78729

Report due at a later date